esa

WPP-161
Volume I

ESAMS '99 – European Symposium on

Atmospheric Measurements from Space

GOME 14

ESTEC, Noordwijk, The Netherlands
18–22 January 1999

European Space Agency
Agence spatiale européenne

WPP-161
Volume I
ISSN 1022-6656
March 1999

'ESAMS '99'

European Symposium on

Atmospheric Measurements from Space

ESTEC, Noordwijk, The Netherlands
18-22 January 1999

Organised by :
ESA Earth Sciences Division

european space agency/agence spatiale européenne

The Organising Committee

Dr. J-L. Bertaux	Service d'Aéronomie du CNRS, France
Mr. S. Bruzzi	ESA Headquarters, France
Prof. J. Burrows	University of Bremen, Germany
Dr. B. Carli	IROE/CNR, Italy
Dr. K.V. Chance	Smithsonian Astrophysical Obs., USA
Prof. Dr. H. Fischer	Forschungszentrum Karlsruhe, Germany
Dr. E. Kyrolä	Finnish Meteorological Institute, Finland
Mr. E. Attema	ESA/ESTEC, The Netherlands
Mr. A. Hahne	ESA/ESTEC, The Netherlands
Mr. J. Langen	ESA/ESTEC, The Netherlands
Mr. G. Levrini	ESA/ESTEC, The Netherlands
Mr. C.J. Readings (Chair)	ESA/ESTEC, The Netherlands

Workshop Secretariat

ESTEC Conference Bureau
P.O. Box 299
2200 AG Noordwijk
Tel. +31 71 565 5005
Fax +31 71 565 5658
E-mail confburo@estec.esa.nl

Contents

VOLUME I

Algorithm Review

Scientific Sessions

[END OF VOLUME I]

VOLUME II

Scientific Poster Sessions

Algorithm Review

Introduction

THE EUROPEAN SYMPOSIUM ON ATMOSPHERIC MEASUREMENTS FROM SPACE (ESAMS '99) – INTRODUCTION

C.J. Readings

The Earth Sciences Division,
ESTEC, Noordwijk,
The Netherlands
Phone: +31 71 565 5673, Fax: +31 71 565 5675, e-mail: creading@estec.esa.nl

1. THE CONFERENCE

Given the anticipated launch of Envisat in the year 2000, with its group of three atmospheric chemistry instruments, it is clear that the time is opportune to encourage interactions between the various groups of scientists working on these instruments and those already exploiting data from the GOME (Global Ozone Monitoring Experiment) instrument currently flying on ERS-2.

The European Space Agency (ESA) therefore decided to organise a meeting at Estec, namely ESAMS '99, with two specific objectives in mind:

- to describe the three "chemistry" instruments which will be flown on Envisat and to present for review the algorithms being developed for them;
- to provide a working forum for scientists to exchange information on scientific activities linked to GOME and the chemistry instruments on Envisat.

The actual meeting starts with a review of the algorithms being developed for the three Envisat 'chemistry' instruments before moving on to a series of scientific sessions (see agenda). During the first part of the meeting the scene is set by some presentations describing Envisat and its ground segment. These are followed by presentations on all three atmospheric chemistry instruments i.e. GOMOS (Global Ozone Monitoring by the Occultation of Stars), MIPAS (Michelson Interferometer for Passive Atmospheric Sounding) and SCIAMACHY (Scanning Imaging Absorption Spectrometer for Atmospheric Chartography)

However, the main concern of this part of the meeting is the review of the algorithms to be used to process data from these three instruments. This review is mainly based on the Algorithm Theoretical Baseline Documents (ATBD's) which are presented by invited speakers. As a spur to the subsequent discussion specialists have been commissioned by the Agency to formulate critiques on these algorithms. The audience is encouraged to seek clarifications as well as to comment in depth on the various algorithms.

The second part of the meeting is intended to build on the success of the informal 'workshops' that, for many years, have preceded meetings of the advisory groups supporting the GOME and SCIAMACHY instruments. The aim is to foster scientific co-operation by expanding this circle to include scientists involved in the other Envisat atmospheric chemistry instruments.

This part of the meeting is intended to be used by scientists to informally brief their colleagues on recent work, highlighting problems as well as successes. The presentation of preliminary findings and 'work in progress' has always been a hallmark of the GOME/SCIAMACHY sessions. It is hoped that during ESAMS '99 this will be extended to encompass both the MIPAS and GOMOS scientific communities. It is clear from the list of presentations (poster and oral) that this has been quite successful.

The agenda includes papers and posters addressing a wide range of topics including retrieval and radiative transfer, spectroscopy, geophysical validation and in-flight calibration and data assimilation as well as scientific analyses and the interpretation of results. Furthermore, the presentations cover not only ozone but also many other trace gases as well as clouds and aerosols. My regret is that there is time for only a limited number of oral presentations. The result is an impressive collection of posters for which special provision has been made in the agenda.

2. THE ENVISAT MISSION

ENVISAT is an advanced Earth Observing satellite which has been designed to observe the atmosphere, the oceans, the land and the cryosphere over a five year period. Its broad objectives are a) to help ensure the continuity of ERS observations for the monitoring of coastal zones, open oceans, ice and land surface processes, b) to extend the ERS oceanic mission by the observation of biological components and ocean colour and c) to make a major contribution to understanding, monitoring and modelling of atmospheric chemistry processes. The latter is the particular concern of this meeting.

The package of instruments to be flown on this satellite (Figure 1) will provide an almost unique opportunity for the synergetic use of satellite data. Together these instruments exploit not only the ultraviolet and visible parts of the spectrum, but also the near and middle infrared to observe trace gases. More information will be found in *Envisat Mission: Opportunities for Science and Applications*, ESA SP-1218 and in <http://envisat.estec.esa.nl>; the Envisat web site. A full

listing of all the products that it is planned to make available shortly after the end of the commissioning phase will be found in *Envisat Mission: Product Summary Overview*. ESA SP-1221.

The span of species that can be observed by the three chemistry instruments (Figure 2) is very wide and it is already clear that the scientific community has grasped the unique opportunity afforded by Envisat for the synergetic use of data to address scientific problems. Responses to the recent Envisat Announcement of Opportunity make interesting reading – 80% of the SCIAMACHY proposals also requested GOMOS data; 70% of all atmospheric chemistry proposals involve the use of data from all three chemistry instruments; 85% of MIPAS proposals also requested GOMOS data.

However, the synergy extends beyond the three chemistry instruments *per se* as there are other instruments on Envisat which can supply complementary information. Here particular mention must be made of the AATSR - Advanced Along Track Scanning Radiometer (cloud parameters, cloud type, water/ice discrimination, particle size distribution, aerosol information), the MERIS - Medium Resolution Imaging Spectrometer (aerosol optical thickness and type, cloud reflectance, cloud top height, water vapour column amounts) and the MWR - MicroWave Radiometer (water vapour and liquid water column amounts). Again it is clear from the responses to the Announcement of Opportunity that the scientific community is well aware of this and it is notable that proposals involving the use of data from the three chemistry instruments span the full range of "disciplines" listed in the Announcement of Opportunity.

3. CONCLUDING REMARKS

This meeting will hopefully help pave the way for the future by bringing together scientists from across Europe and beyond, encouraging them to exploit the unique opportunities afforded by Envisat. However, it is important to look beyond this and to consider the long term future.

Here it is very important to note that the Member States of the European Space Agency (ESA) have not only approved the Envisat mission but, in addition, they have supported the formulation of long term strategy for Earth Observation which envisages a series of research and/or demonstration missions called the Earth Explorer Missions.

More information on these missions, including their research objectives, will be found in *Earth Explorers: The Science and Research Elements of ESA's Living Planet Programme*, ESA SP-1227. *The Living Planet Programme* includes mission preparation and data exploitation as well as the missions themselves.

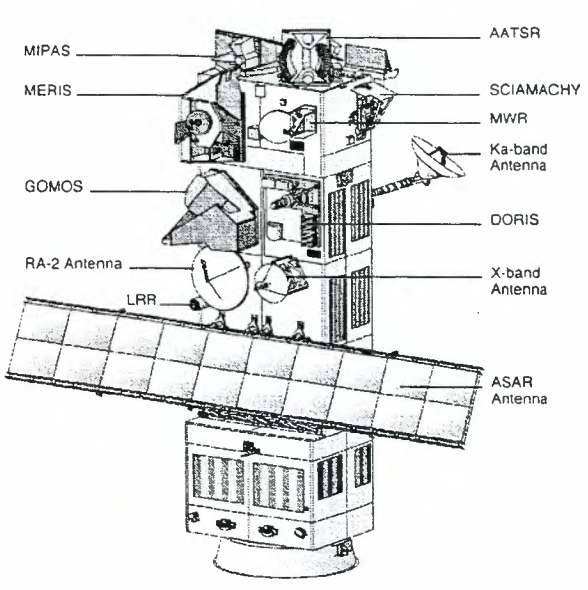

Figure 1: Envisat and its payload

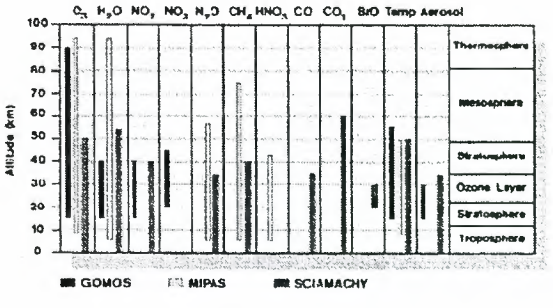

Figure 2: The altitude ranges over which some atmospheric constituents are measured by GOMOS, MIPAS and SCIAMACHY

ENVISAT Mission & Ground Segment Overview

Jacques Louet

ESA ESTEC ENVISAT System and Payload Project Manager

ABSTRACT

This paper provides an overview of the ENVISAT System & Mission with particular emphasis on the operations strategy related to the atmospheric payload, the corresponding data acquisition data processing and data distribution strategy in Near Real time as well as Offline. It also provides an overview of the User Services being implemented. Finally, a brief programme development status is given.

1. Mission & System

The main objective of the Envisat programme is to endow Europe with an enhanced capability for the remote sensing of the Earth from space, increasing Europe's capacity to take part in the study and monitoring of the Earth and its environment. Its primary objectives are:

- to ensure the continuity of the observations started with the ERS satellites, including those obtained using radar-based observations;
- to provide for the enhancement of the ERS mission, notably its ocean and ice missions, by improving the quality of the measurements;
- to extend the range of the geophysical parameters observed to meet the need to increase knowledge of the factors determining the environment;
- to make a significant contribution to environmental studies, notably in the areas of atmospheric chemistry (through three instruments, MIPAS, GOMOS and Sciamachy) and in ocean studies and marine biology with MERIS.

These are coupled with two secondary objectives:

- to allow more effective monitoring and management of the Earth's resources;
- to better understand solid Earth processes.

Envisat is carrying a package of instruments to observe the Earth and its atmosphere from space in a synergetic fashion, addressing crucial matters such as global warming, climate change, ozone depletion and ocean and ice monitoring. As such, it will be a major contributor to the global study and monitoring of the Earth and its environment as expressed by international cooperative programmes such as the International Geosphere and Biosphere Programme (IGBP) and the World Climate Research Programme (WCRP).

The Envisat system consists of two main elements:

- the Satellite,
- the Ground Segment.

As a complement to the direct X-bands links between the satellite and the ground, Envisat will also utilise a Ka-band link with the Artemis Data Relay Satellite for instrument data recovery.

The satellite, having a design lifetime of five years, will be launched from the Kourou Space Centre in French Guyana by an Ariane-5 launch vehicle.

2. The satellite & the payload

The Envisat satellite is composed of the payload complement and the Polar Platform on which the instruments are mounted.

The payload comprises a set of ESA-Developed Instruments (EDI's) complemented by Announcement-of-Opportunity Instruments (AOI's).

ESA-Developed Instruments (EDI's)

- MERIS (Medium-Resolution Imaging Spectrometer)
- MIPAS (Michelson Interferometric Passive Atmospheric Sounder)
- ASAR (Advanced Synthetic Aperture Radar)
- GOMOS (Global Ozone Monitoring by Occultation of Stars)
- RA-2 (Radar Altimeter 2)
- MWR (Microwave Radiometer)
- LRR (Laser Retro-Reflector)

Announcement-of-Opportunity Instruments (AOI's)

- SCIAMACHY (Scanning Imaging Absorption Spectrometer for Atmospheric Chartography)
- AATSR (Advanced Along-Track Scanning Radiometer)
- DORIS (Doppler Orbitography and Radiopositioning Integrated by Satellite).

Part of the instruments is focussed on ensuring the continuity of the data acquired by the ERS-1/2 missions: ASAR, AATSR, RA-2 with its supporting instrumentation (MWR, DORIS and LRR), with improved accuracy and coverage.

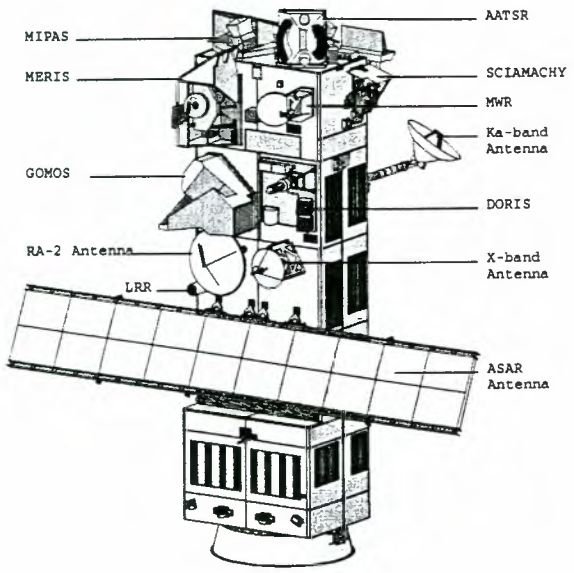

Dimensions:
- Launch configuration: length 10.5m
  (envelope diameter 4.57m)
- In-Orbit Configuration: 26m x 10m x 5m

Mass:

-	Total satellite	8140 Kg	
	(including 319 Kg hydrazine)		
-	Payload	1700	1750
-	Satellite	3275	2870

Launch vehicle: Ariane 5 (single launch)

The observation of the ocean and coastal waters (with the retrieval of marine biology constituent information) is the primary objective of the MERIS instrument.

The ability to observe the atmosphere, following on from the GOME instrument on ERS-2, is significantly enhanced by 3 instruments on Envisat which offer complementary measurement capabilitites:

- observation of a large quantity of atmospheric species by analysis of the absorption lines through the atmosphere;
- characterisation of the atmospheric layers as well as total column content by complementary limb and nadir observations.

2.1 The Orbit

To fulfil its mission objectives, the orbit selected for the Envisat satellite is sun synchronous, with a mean altitude of 800 km and a descending node mean local solar time of 10:00 am.

The selected orbit provides a 35-day repeat cycle with the same ground track as ERS-2.

This orbit will be maintained so as to ensure that the deviation of the actual ground track is kept within 1 km of the reference orbit track and the mean local solar time is maintained within 1 minute.

Table 1. Characteristics of the orbit

Semi-major axis: 7159.5 km
Mean altitude: 799.8 Km
Inclination: 98.55 deg.
Repeat cycle: 35 days
No. of orbits in 1 cycle: 501
Reference ascend. node: 0.1335° E
Desc. node mean local solar time: 10.00

2.2 The Satellite

Envisat will be the largest free-flying and probably the most complex satellite ever built in Europe. Ten instruments, accommodated on the Polar Platform, compose its payload.

Two major modules constitute the Polar Platform itself:

- the *Service Module (SM)* accommodates most of the satellite support subsystems such as:
  - power generation, storage and distribution
  - Attitude & Orbit Control System (AOCS)
  - communication in S-band
  - support structure and launcher interface.

  The SM is derived from the concept and design of the Spot MkII service module with a number of important new developments (in particular new solar array and new structure).
- the *Payload Module (PLM)* carries the instruments and the payload dedicated support subsystems:
  - instrument control and data handling
  - instrument data recording with 3 tape recorders and one solid-state recorder
  - communication in X- and Ka-bands
  - power distribution
  - support structure and thermal control.

This modular approach facilitates parallel development and integration of the Service and Payload Modules and allows for an efficient satellite AIT programme where only a minimum of system level activities are needed for final verification.

The major driver for the Envisat satellite configuration has been the need to maximise the payload instrument mounting area and to meet very different and stringent viewing requirements whilst staying within the constraints of the Ariane-5 fairing and interfaces.
This configuration concept provides a large, modular construction, with sufficient Earth-facing mounting surface for payload instruments and an anti-sun face, free of occultation by satellite subsystem equipment.

3. The Ground Segment

The Ground Segment is split into two major elements:

- the Flight Operation Segment (FOS) which manages and controls the satellite;
- the Payload Data Segment (PDS) which receives and processes the data produced by the instruments and disseminates and archives the generated products. Furthermore, it provides a single interface to the users to allow optimum utilisation of the system resources in line with the users' needs.

3.1 Flight Operation Segment (FOS)

The FOS is composed of the Flight Operations Control Centre (FOCC), located at ESOC, Darmstadt (D), and the associated command and control stations. It provides control of the satellite through all mission phases:

- satellite operation planning
- mission planning interface with Artemis
- command & control of the satellite, up-loading of operation schedules on a daily basis via the TT&C station at Kiruna-Salmijarvi (north Sweden).

Furthermore the FOCC will support:

- satellite configuration and performance monitoring
- software maintenance for PPF and payload elements
- orbit prediction, restitution and maintenance.

3.2 Payload Data Segment (PDS)

The PDS comprises all those elements which are related to payload data acquisition, processing, archiving as well as those concerning the user interfaces and services. The PDS will thus provide:

- all payload data acquisition for the global mission
- all regional data acquisition performed by ESA stations
- processing and dissemination of ESA near-real-time (NRT) products within three hours from data sensing
- data archiving, processing and delivery of ESA off-line products with support of Processing & Archiving Centres (PAC's)
- interfaces with the national and foreign stations authorised to receive Envisat-1 regional data
- interfaces to the users from order handling to product delivery.

The PDS centres and stations will be co-ordinated by the Payload Data Control Centre (PDCC) located at ESRIN, Frascati (I). The PDCC will interface with the FOCC for all mission planning activities.

The PDS ESA stations include:

- a Payload Data Handling Station (PDHS-K) providing X-band data reception and located at Kiruna Salmijarvi;
- a Payload Data handling Station (PDHS-E) located at Esrin and receiving via an User Earth Terminal (UET) the data relayed via Artemis in Ka-band;
- a Payload Data Acquisition Station (PDAS) receiving X-band data and located in Fucino (Italy).

PDS Deployment over Europe

NRT services (Global & Regional products)
PDHS (Payload data handling Stations) at Kiruna and ESRIN
PDAS (Payload Data Acquisition Station) at Fucino

Offline Services (Global & Regional products)
Low Rate Archiving Centre (LRAC) at Kiruna for all level 1b global mission products
D-PAC for all atmospheric products (with FMI for GOMOS)
F-PAC for RA-2, MWR, Wave and Doris Orbit products
D-PAC, I-PAC and UK-PAC for ASAR High resolution products
UK-PAC, I-PAC and E-PAC for MERIS Full resolution products
S-PAC at Kiruna for MERIS Reduced Resolution products
UK-PAC for AATSR products

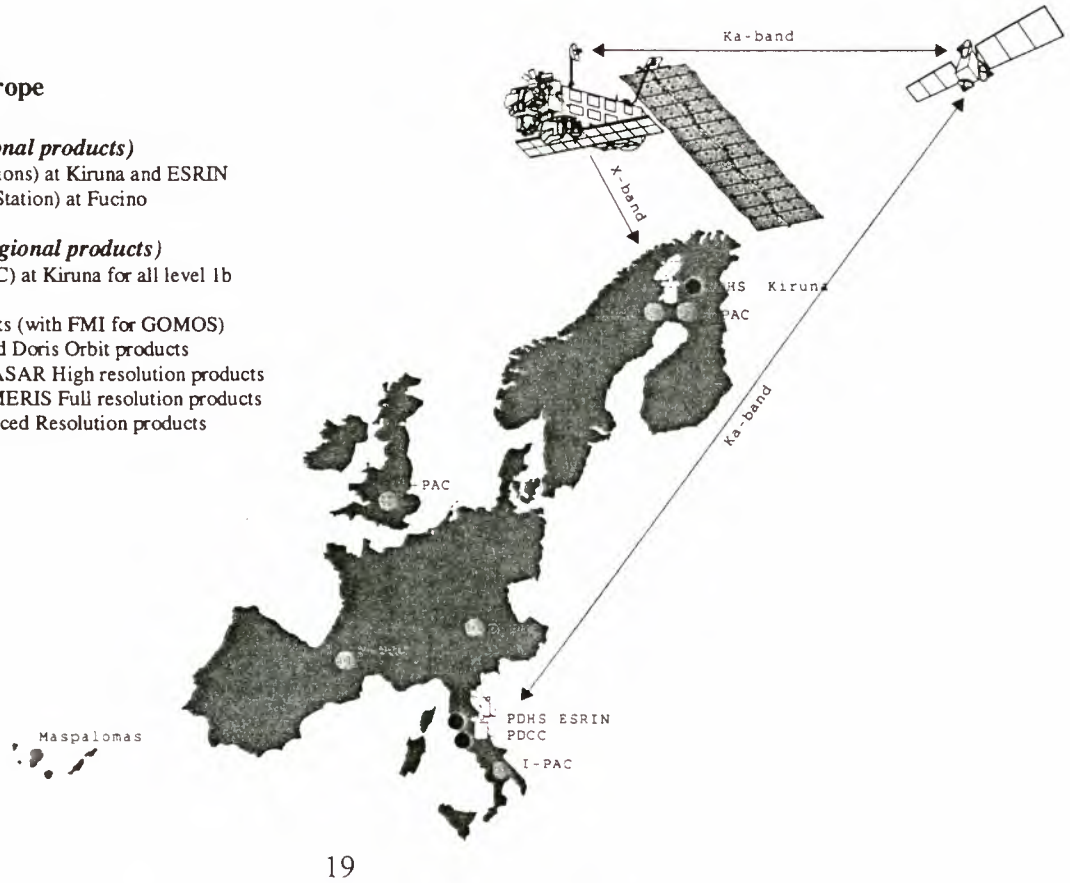

4. Approach to Mission Operations

The mission objectives imply global and regional operations to provide both global and regional data to the user communities on various time-scales.

4.1 Regional Operations

The Regional Operations cover those instruments and instrument modes which are not operated systematically but are governed by specific user requests. The resulting datasets correspond in general to the high-rate modes of ASAR and MERIS. All Regional Operations data acquired by the ESA PDS will be systematically processed at medium-resolution and browse level. High-resolution products will be provided in response to user requests.

4.2 Global Operations

The Global Mission operation includes all ENVISAT-1 instruments which have global coverage objectives. These instruments are operated systematically and their operation is not governed by specific user requests but by the user community's need to get a continuous and coherent global dataset. It implies:

- continuous operation of the low rate instrument around the orbit (for MERIS, Sun illumination constraints limit the observation to about 43.5 minutes per orbit);
- on board recording of all instrument data;
- data recorder playback at least once per orbit to ensure availability of FD products within less than 3 hours from observation;
- systematic processing of all acquired data

The global mission strategy is defined in the High Level Operation Plan (HLOP) approved by the programme participants.

The corresponding detailed operation requirements for the FOS and PDS are defined in the Reference Operation Plan (ROP).

4.3 Data Recovery

The onboard recording system is composed of:

- 3 Tape Recorders (TR), 30 Gbits capacity each
- 1 Solid-State Recorder (SSR), 60 Gbits (EOL) capacity.

The TR record the data from the low-rate operating modes of the instruments (corresponding to Global Operations).

The SSR can record ASAR high-rate data or MERIS full-resolution data as well as low-rate data in parallel with any of these two data streams.

All instruments contributing to the global mission deliver data at rates compatible with the on-board TR capability. Therefore, for the low-rate global data, the nominal strategy is to record the data and to perform one tape dump per orbit via either the Artemis link, with data reception at the Artemis User Earth Terminal (UET) of ESRIN. or a direct X-band link with data reception at Kiruna. In both cases, the tape dump is performed at 50 Mbit/s and completed in less than 10 minutes. This strategy will permit the distribution to users of global near-real-time (NRT) products within less than 3 hours of observation.

The regional mission includes the imaging modes of the ASAR (single swath or Scansar wide swath), and MERIS, in its 250 m full-resolution mode. These data, acquired on a regional basis, can be either recorded on-board using the SSR or transmitted directly via the X-band and/or Ka-band data down links

The satellite is capable of providing simultaneous operation of the X-band and Ka-band channels. For the regional mission, it permits data acquisition by an X-band regional station in parallel with Ka-band operation via Artemis and reception at the ESA UET.

For recovery of the Global Mission, the nominal scenario is based on equal workload sharing between the Kiruna station and the ESRIN UET. Each station will receive daily a sequence of about seven consecutive orbits of tape recorder data dumps. All received data will be systematically processed in near-real time and the corresponding products disseminated to the users.

ENVISAT-1 ON BOARD DATA SYSTEM

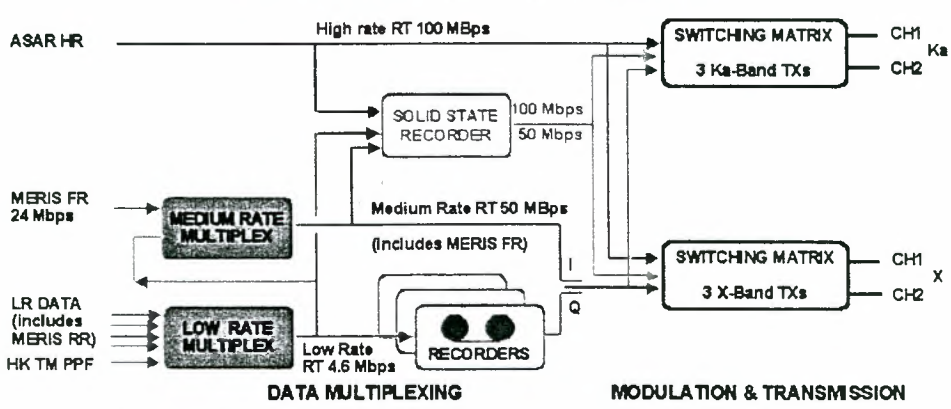

Whenever a request for regional mission operation is requested, the mission management control system will plan the instrument operation and the corresponding data recovery. The nominal scenario is to down-link the data in X-band to the two ESA stations of Kiruna and Fucino for data reception within their coverage (European coverage). Data outside this coverage will be acquired using the SSR or via the Artemis link, within the Artemis coverage limits. Direct X-band down link will be planned when requested by duly authorised national or foreign station

4.4 Near Real Time Services and Products

Systematic processing, within 3 hours from sensing, of all global data will be performed at ESA PDS stations to generate:

- level 1b engineering geolocated and calibrated products
- level 2 geophysical geolocated products (including meteo products: wind, wave, significant wave height, SST atmospheric P,T and constituent profiles, clouds...)

Meteo products are systematically disseminated within 3 hours from sensing via GTS and via a satellite dissemination channel.

All imaging instrument data are systematically processed to generate:

- medium resolution products (150m resolution for ASAR, 1km for MERIS and AATSR)
- Browse products for immediate on line access by users

High resolution ASAR and MERIS images are processed and disseminated on user request.

Products are disseminated via satellite dissemination channels, on line retrieval via user service internet access is possible for small products.

4.5 Offline Services and Products

Off-line services are offered by Processing Archiving Centres.
The ESA standard products are made available (same formats and same processing algorithms as for NRT services with updated auxiliary data).
For access to the Off-line services, the following alternatives are offered to the users:

- Subscription basis (systematic distribution of the products, once a month, on physical media, typically for global low rate data)
- On request basis for high and medium resolution images (delivery on physical media)
- On line retrieval by user request (possible for all products systematically processed, provided size of extracted product is compatible with network transmission throughput).

5. DATA PRODUCTS

5.1 ESA PRODUCT LIST

The approved ESA Ground Segment Concept includes a Complete list of ESA products with type of processing (Systematic or On Request), dissemination, time delivery, centre or station providing the service as well as algorithm development scheme. This list ensures coherency between Near Real Time and Offline products.

Slight corrections have been made, due to improved knowledge during the detailed definition phase involving Expert Support Laboratories (ESLs), Supporting Industries and the Scientific Advisory Groups.

5.2 Product Levels definition

The following type of products are identified in the ESA PDS:

- Raw Data	as received from the satellite (serial data stream, no de-multiplex)
- Level 0	reformatted, time ordered (no overlap) satellite data, computer compatible format
- Level 1B	geolocated engineering calibrated product (Near Real Time and Offline)
- Level 2	geolocated geophysical product (Near Real Time and Offline).

5.3 Algorithms & Products Development Approach

According to the agreed GS Concept strategy, clear distinction has been made between:

- The algorithm development/validation activities performed by the ESLs and some supporting industries ;
- The algorithm implementation activities to be performed within the PDS contract for the PDS operational processors.

The PDS contractor is implementing the algorithms provided by ESA as CFIs (Customer Furnished Items) in the form of detailed algorithm specifications for all products, except ASAR image products. Test data as well as definition of the input and output interfaces of the processing algorithms are also provided to the PDS contractor as CFIs. ESA ensures that the phasing of the algorithm development activities and corresponding CFI deliveries are compatible with the PDS development contract.

5.4 Product Standards

To ensure overall coherency in between all ENVISAT-1 Products, the following common elements have been specified by ESA and made applicable to all products and related algorithm development activities:

- Use of a suite of Mission Software provided by ESA as CFI (Orbit propagator & interpolator, Target pointing software for data localisation, etc...)
- ENVISAT-1 Product Format Guidelines (ref: PO-TN-ESA-G-00242, Issue 5.0, Nov. 95)

- ESL Documentation Requirements for the documents to be delivered to the PDS
- Applicable Software Standards (a subset of ESA PSS-05) for the production of the ESL prototype software.

5.5 Data Product format

The ESA products are such that one Product => one File.

Each product has the following structure:

MPH	Main Product Header
SPH	Specific product header

Followed by Data Sets:

SQADS	Summary Quality Auxiliary Data Set
LADS	Localisation Auxiliary Data Set
MDS	Measurement Data Set(s) as many as necessary
ADS	Auxiliary Data Set(s) as many as necessary
GADS	Global auxiliary data Set(s) for auxiliary data not timely related to the MDS record time entries.

Product Generation and Extraction

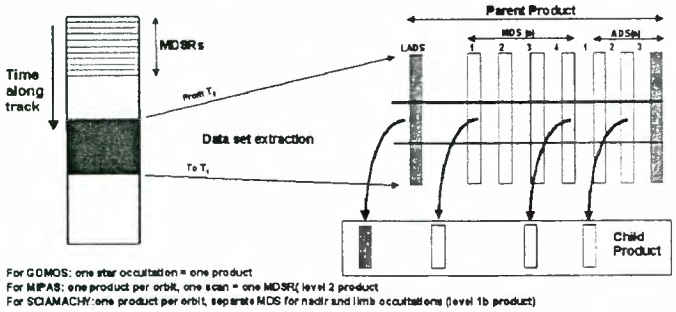

All Data sets are filled with Data Set Records (DSR), each DSR starts with a time entry (the GADS is the only exception to this rule); the time entry permits correlation between all Data Sets at record level and permits extraction of subset extraction

6. USER SERVICES

The User Services will be accessible via INTERNET. Wherever the user enters the PDS, any station or centre offering ESA services, he will have access to:

- a unified user interface (all stations and centres will be equipped with a standard User Service Facility);
- a unified search mechanism to find all available products and to order them, without the need to know where the data are physically stored, all stations and centres being linked by a PDS internal network,
- on-line browse, for all imaging instruments, and possibility to obtain direct on-line delivery of small products.
- a unified ordering interface, the order being processed automatically by the appropriate centre or station (ordering of products requiring specific data acquisition will be routed automatically to the PDCC).
- Help Desk and Order Desk at the PDCC.

USER SERVICE ACCESSS

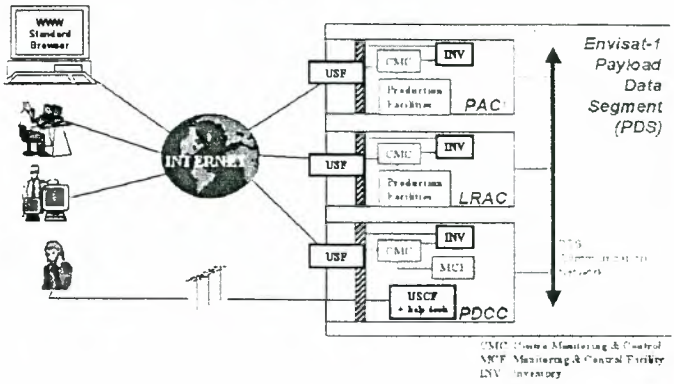

All PDS products will strictly adhere to ENVISAT PDS Standard formats (identical product formats for Near Real Time or Offline) and standard quality by use of the PDS Generic Processors. Software tools will be made available for opening the products.

Product delivery will be made via:
- satellite links (used mainly for NRT service),
- ground network (for any service, NRT or Offline, provided the product size is compatible with the network throughput),
- standard physical media (used mainly for Offline service).

INTER-ACTIVE PRODUCT SEARCH

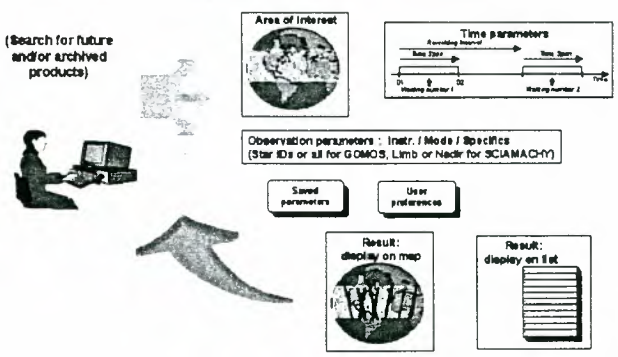

7. SYSTEM OPERATION CONCEPT

- Overall Mission Management is controlled by the Envisat-1 Mission Management (EMM),
- The EMM defines the operation strategy via the ROP (Reference Operation Plan),
- The ROP defines completely the Global Mission Operation (satellite operation including links and tape recorder data recovery, data acquisition, processing and systematic dissemination),

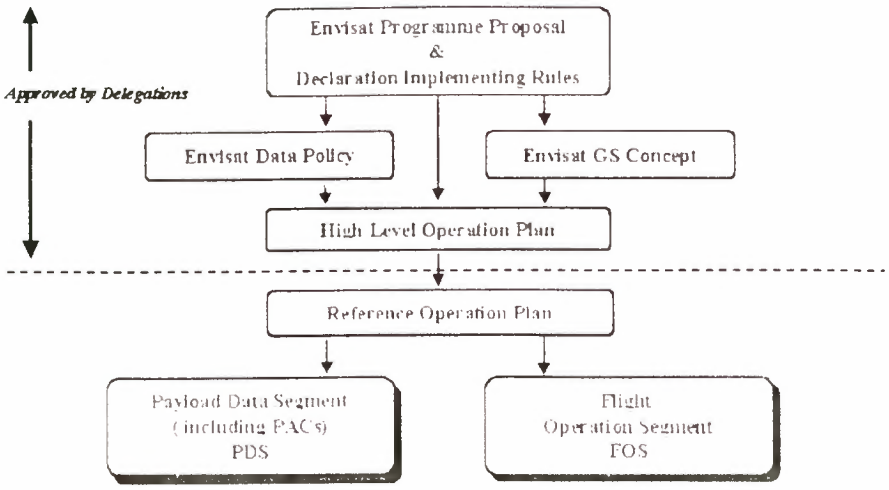

- The ROP defines, for the Regional Mission, the strategy for handling user requests, according to data policy rules, and specifies a Background Regional Mission according to HLOP agreed rules,
- The ROP Global Mission is directly implemented by the FOS,
- The Regional Mission is handled by the PDCC, registering and handling the user requests, merging them with the Background Regional Mission according to ROP rules and building up the Preferred Exploitation Plan (PEP),
- The PEP is submitted to the FOCC which answers with the Detailed Mission Operation Plan (DMOP), providing the detailed satellite operation (all instruments, recorders and links),
- The PDCC plans the acquisition and NRT processing accordingly.

8. PROGRAMME DEVELOPMENT STATUS

The
the following stage:

- The EM satellite programme is planned to be completed by end March 1999,
- The Integration of FM instruments on the FM satellite is on going: MWR, GOMOS, RA-2 are already integrated, MIPAS F-EQM and CESA FM are delivered and ready for integration, the remaining instruments are planned to be delivered in the coming months (the ASAR antenna, being the last delivery, planned for August 1999),
- The satellite is planned to arrive at ESTEC in May 1999 and will remain there until completion of the FM test programme and then transported to Kourou for the launch campaign.

For the Ground Segment (FOS & PDS), the status is as follows:

- The FOS development is well advanced, intermediate versions of all major components are delivered and integrated in the FOCC at ESO,.
- The next major compatibility test with the satellite (SVT 1) is planned for mid March 1999.
- The compatibility tests of the mission planning softwares at FOS and PDS are already initiated.
- The PDS V1 is integrated on the Reference Platform at DATAMAT Rome, an initial acceptance test has been conducted in December 1999, the test completion of PDS V1 is planned for end March 1999.
- The acceptance of the PDS V2, including complete version of all Instrument processors based on the ESL documentation and test data already delivered, is planned for September 1999.

The ENVISAT launch is presently planned for the fall 2000.

9. Conclusion

With a design lifetime of 5 years, ENVISAT will continue and extend the science and application objectives of the ERS-1/2 missions. As such, ENVISAT is part of a coherent European Earth Observation Programme ensuring the long-term provision of continuous data-sets, essential for addressing environmental and climatological issues, as well as aiming at the promotion of application and commercial use of Earth Observation data.
With its three complementary atmospheric instruments, addressed in detail in this ESAMS Symposium, ENVISAT will make a major contribution to environmental research studies.

For further information on Envisat-1, please visit our Web site at:

http://envisat.estec.esa.nl

Algorithm Review

MIPAS

MIPAS MISSION OBJECTIVES

Herbert Fischer

Institut für Meteorologie und Klimaforschung (IMK), Forschungszentrum Karlsruhe/Universität Karlsruhe,
P.O. Box 3640, D-76021 Karlsruhe, Germany
e-mail: Herbert.Fischer@imk.fzk.de

The Michelson Interferometer for Passive Atmospheric Sounding (MIPAS) is a cooled high resolution mid-infrared (4.1-14.6 μm) Fourier Transform Spectrometer which will be launched aboard ESA's ENVISAT satellite (Ref. 1). The instrument will scan across the earth limb in order to detect vertical profiles of temperature and more than 20 atmospheric trace species (Ref. 2). Further important parameters to be derived from MIPAS observations are the distribution of aerosol optical depth, tropospheric cirrus clouds and polar stratospheric clouds.

The simultaneous and global measurements allow to study a number of important scientific objectives as the dynamics and chemistry of the stratosphere, the stratospheric/tropospheric exchange processes, the chemistry of the upper-troposphere, the energy balance as well as physical and chemical processes in the mesosphere and lower thermosphere and also climatology. Even for the weather forecast MIPAS can contribute by providing near real-time global temperature and ozone distributions. Measurements of existing MIPAS instruments like the balloon and the aircraft device have already proven the enormous scientific capabilities of the MIPAS space experiment (Ref. 3).

Due to this wide range of scientific applications it is obvious to define different observation scenarios for optimum measurements. This is possible because the MIPAS experiment comprehends a very flexible scanning unit. Besides the nominal observation mode covering atmospheric layers between the upper troposphere and the lower mesosphere a considerable number of special observation modes are planned like polar chemistry/dynamics mode, tropospheric/ stratospheric exchange mode, aircraft emission mode, atmospheric dynamics mode and diurnal change mode. In addition, observation scenarios for the upper atmosphere have been specified including non-Local Thermodynamic Equilibrium investigations.

The MIPAS software for data processing is developed along three lines. The operational near real time products, namely vertical profiles of temperature, O_3, H_2O, CH_4, N_2O and HNO_3, are generated by ESA facilities. The off-line data processing with a time delay of about three weeks will be performed by the DLR center in Oberpfaffenhofen/Germany. During the first phase the data products are the same as the near real time data products; at a later stage further trace gases may be added. Scientific software development is carried out by a few scientific institutes in Europe, in order to further exploit the information content of the MIPAS spectra. It is foreseen that also global distributions of trace gases like NO_2, N_2O_5, HNO_4, $ClONO_2$, CFC's as well as NO and CO will be available some time after launch.

The MIPAS data validation is divided in three phases: prelaunch activities, self-consistency tests and inflight validation. The prelaunch activities comprise the test of various in situ and remote sensing instruments and the use of realistic data from existing MIPAS instruments for algorithm validation. The self-consistency tests consist of checks on measurement precision, internal consistency and long-term stability of the MIPAS data. For the in-flight validation a considerable number of validation experiments have to be performed including aircraft, balloon and ground based instrumentation.

In conclusion, MIPAS measurements will yield a novel global set of distributions of atmospheric parameter (from pole to pole). Several years of MIPAS data will allow to study various dynamical, radiative and chemical processes in the upper troposphere, stratosphere, mesosphere and lower thermosphere.

REFERENCES:

1. Endemann, M & Fischer H 1993, Envisat's high-resolution limb sounder, *ESA Bulletin*, 76, 47-52
2. Fischer H, & Oelhaf H 1996, Remote sensing of vertical profiles of atmospheric trace constituents with MIPAS limb emission spectrometers, *Applied Optics*, 35, 2787-2796
3. Fischer H 1993, Remote sensing of atmospheric trace gases, *Interdisciplinary Science Reviews*, 18, 185-191

MIPAS Instrument Concept and Performance

M. Endemann

ESA-ESTEC, P.O.Box 299, NL-2200AG Noordwijk, The Netherlands

ABSTRACT

The Michelson Interferometer for Passive Atmospheric Sounding (MIPAS) is the first high resolution Fourier-transform spectrometer for limb sounding from satellite. This measurement concept puts high demands on the instrument technology, as it requires several highly precise mechanisms to operate constantly at low temperatures over several years lifetime. Since MIPAS's selection as an ESA-developed instrument for flight on the ENVISAT environmental satellite some 10 years ago, it has evolved through various iterations on the design concepts of its subsystems. The instrument could be considered a good compromise between complexity and performance, but it still utilises a number of critical technologies that are employed the first time in space.

This paper summarises the performance requirements imposed on MIPAS, outlines the design challenges and their solutions, and presents the performance demonstrated in the characterisation measurements.

1 INTRODUCTION

The Michelson Interferometer for Passive Atmospheric Sounding MIPAS is a space borne Fourier Transform spectrometer (FTS), conceived for global observations of atmospheric trace species. It detects the atmospheric limb emissions over wide spectral intervals throughout the mid infra-red with high spectral resolution. These IR-spectra contain characteristic emission features of most gases. Thus a series of limb spectra from different altitudes can be processed to determine concentration profiles of numerous atmospheric trace species, including the complete NOy-family and several CFC's, atmospheric temperature and pressure, as well as the distribution of aerosol particles, tropospheric Cirrus and stratospheric ice clouds (including Polar Stratospheric Clouds).

As MIPAS is observing the thermal emission of the atmosphere, measurements can be performed independent of illumination conditions. Thus, as a unique feature of MIPAS, these atmospheric parameters are determined

- all simultaneously with each measurement,
- with complete global coverage,
- during day- and night time conditions (allowing to observe the diurnal variation of trace species), and
- throughout its mission duration of four years.

Thus MIPAS provides unique capabilities and promises to become an important research tool for atmospheric sciences. For this reason, MIPAS thus has been selected as an ESA payload for the next European earth observation spacecraft ENVISAT.

2 MIPAS's CAPABILITIES

2.1 Performance Requirements

To provide useful measurements, MIPAS has to meet ambitious performance requirements. Tab.1 summarizes the key pointing, spectral and radiometric requirements.

Fig.1 indicates the basic observation geometry of MIPAS. The instantaneous field-of-view (IFOV) is only 3 km high to achieve a good vertical resolution, but 30 km wide to collect sufficient radiance, which corresponds to an angular range at the

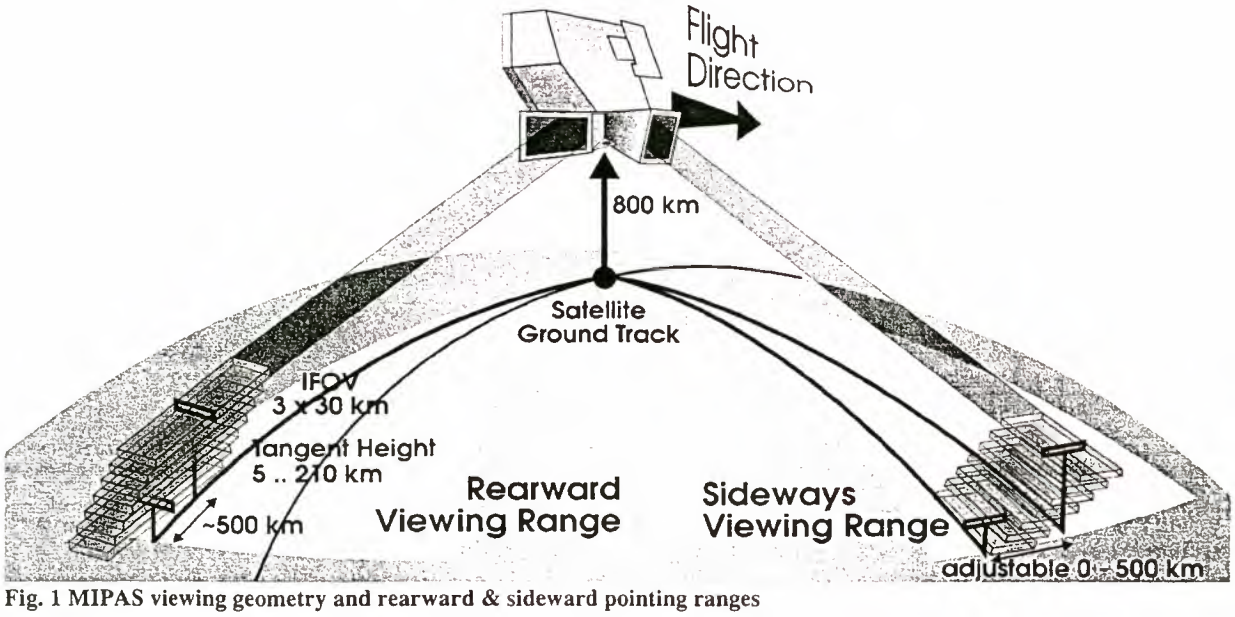

Fig. 1 MIPAS viewing geometry and rearward & sideward pointing ranges

Table 1 MIPAS Performance Requirements

Pointing Requirements	
Instantaneous Field-of-View	3 x 30 km^2 (height x width)
elevation pointing	5 ... 210 km above earth limb
azimuth pointing	35° rearwards, 30° sideways
pointing stability (1-sigma)	0.08 mrad over 4 s 0.14 mrad over 75 s
pointing knowledge	0.28 mrad
Spectral Requirements	
spectral range	685 .. 2410 cm^{-1} (14.6 .. 4.15 µm)
spectral resolution	0.035 cm^{-1} (unapodized)
spectral resolution modes	down to 1/10 full spectral resolution
Radiometric Requirements	
radiometric sensitivity NESR	50 ... 4.2 nW/cm^2/sr/cm^{-1}
absolute radiometric accuracy	1% (@14.6 µm) ... 3 % (@4.15 µm) (relative to input radiance)
Operations Requirements	
max. time per spectrum	4.6 s (full spectral resolution) 1.0 s (1/10 spectral resolution)
time per elevation scan	75 s (500 km ground trace)
spectra per elevation scan	16 (full spectral resolution) 75 (1/10 spectral resolution)

instrument of 0.9 mrad (vertical) by 9 mrad (horizontally).

MIPAS is capable to steer the IFOV within two pointing regimes: rearwards (in the anti-flight direction) within a 35° wide range, and sideways (in the anti-sun direction) within a 30° wide arc. For all routine measurements the IFOV will be in the rearward viewing range, as it provides a good earth coverage including the polar regions. The sideways range is important for observation of 'special events', like volcano eruptions, trace gas concentrations above major air traffic routes, or concentration gradients along the dusk/dawn lines.

As a result of the limb viewing geometry, the distance between instrument and tangent point is about 3300 km. Thus, in order to measure at a predetermined limb height, the pointing of instrument and satellite in elevation direction must be excellent. It is possible to determine the geometric limb height by pointing information from the spacecraft with a standard deviation below 900 m, corresponding to a Line-of-Sight elevation pointing accuracy of better than 0.28 mrad (1-sigma) will be required. A very high stability of all assemblies affecting the pointing is a design driver for MIPAS as well as for the ENVISAT satellite. To compensate bias angles (e.g. from launch shifts) and harmonic pointing variations during the orbit, the Line-of-Sight will be recalibrated during flight by viewing stars, as discussed in the next section 2.2.

Pointing stability during one interferometer sweep (4 s duration) will be much higher - predictions indicate a worst case height variance below 300 m (0.1 mrad).

The spectral coverage ranges from 685 cm^{-1} (14.6 µm) to 2410 cm^{-1} (4.15 µm). This range covers most of the mid-infrared region, and contains numerous strong, characteristic emission lines of most atmospheric species. A Fourier-Transform spectrometer is ideally suited to perform measurements of such wide spectral coverage with highest possible sensitivity.

Fig. 2 shows a typical atmospheric radiance spectrum from a tangent altitude of 10 km. The large amount of atmospheric emission features in this spectral region is evident. Also shown are those spectral regions where key atmospheric species show strong emission lines that can be identified. Concentration profiles of these species can be determined by analyzing the effective strength of specific lines from spectra with different tangent altitudes. The sensitivity goals for detection of the indicated species are derived for single line. In fact, however, many emission lines will be used in the retrieval, thus increasing the noise tolerance significantly.

The high spectral resolution (unapodized) of better than 0.035 cm^{-1} (corresponding to 1 GHz resolution or 0.006 nm at a wavelength of 4.15 µm) is necessary to reduce the interference of overlapping spectral features. With this high spectral resolution, MIPAS provides a total of about 60.000 independent spectral samples in each spectrum.

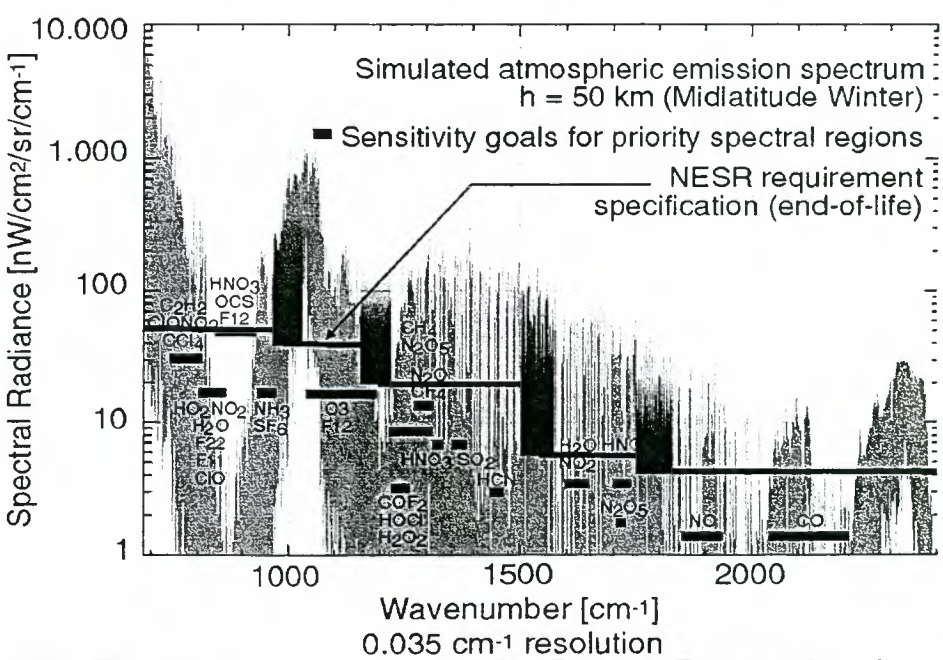

Fig. 2 MIPAS sensitivity requirements, expressed in NESR (Noise Equivalent Spectral Radiance), superimposed to anticipated limb radiance from high altitudes. The black regions indicate the overlap of the MIPAS spectral bands where noise may be higher.Also shown are NESR-goals for interesting species, assuming single line detection.

A complete high resolution spectrum is obtained all 4.5 s. MIPAS can also perform measurements with a lower spectral resolution in shorter time.

The radiometric requirements on MIPAS are highly demanding. A good radiometric sensitivity is a major design driver to allow detection of weak atmospheric signals without additional averaging. Radiometric sensitivity is expressed here by the Noise Equivalent Spectral Radiance (NESR), which characterizes the instrument noise in terms of incident radiance. The required sensitivity must be better than 50 nW/cm^2 sr cm^{-1} at the long wavelength side, decreasing to 4.2 nW/cm^2 sr cm^{-1} at the short wavelength side. The actual instrument performance (as predicted for the flight model) is also indicated in Fig. 2. It meets the requirements in all bands.

A good absolute knowledge of the received radiance is important for the retrieval of species concentrations and temperatures. This need for data with an excellent radiometric accuracy is quite challenging: a calibration accuracy in the 1 - 3 % range is difficult to achieve even for ground based instruments. But the test results of MIPAS indicate that this demanding requirement will be met as well.

2.2 *MIPAS Operation*

MIPAS performs continuously measurements, which are either atmospheric observations (i.e. useful atmospheric spectra are derived), or are used for instrument calibrations (subdivided into radiometric calibration and pointing calibration). Fig. 3 indicates the envisaged time line for the different measurement types: most of the time, MIPAS performs elevation scan sequences in nominal or special event measurements. Deep space calibration is performed relatively often (after a few elevation scan sequences) to compensate for instrument temperature variations along the orbit, while gain calibration is performed much rarer (on the order of days) to compensate slow drifts of the electronics. Pointing calibration finally is performed very rarely (once per months) to compensate for slow drifts of the satellite pointing. The exact times will be established in orbit during the commissioning phase.

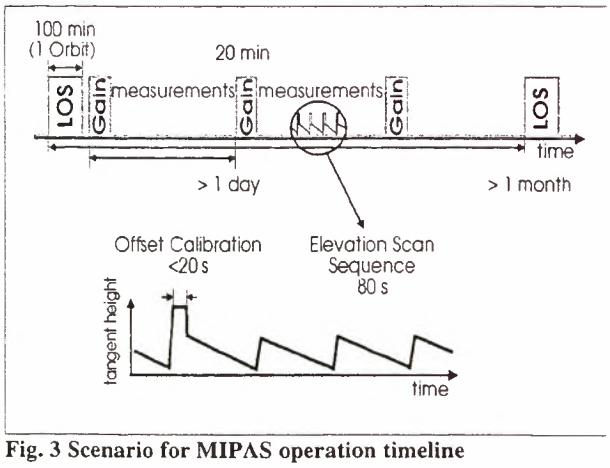

Fig. 3 Scenario for MIPAS operation timeline

2.2.1 Atmospheric Measurements

To retrieve concentration profiles, MIPAS obtains a series of spectra with different tangent altitudes, typically starting at about 70 km altitude, and then descending in 5 or 3 km steps down to 7 km. As one spectrum is obtained in about 4.5 s, such an elevation scan sequence of 18 spectra takes 80 s. During this time, the spacecraft covers a ground-track distance of about 530 km, but due to the downward scanning the measurement distance increases during the scan, so that the actual spread of tangent points is only 400 km.

For most measurements, MIPAS will view the atmosphere through the rear baffle, and will autonomously move the azimuth mirror within the 35° wide range to cover both, the arctic and the antarctic polar regions.

The actual elevation scan sequence can be updated in flight to allow an adaptation to the user needs. In addition, time tagged 'special events' can be commanded with free azimuth and elevation angle ranges, which allow observations for more specific research interest, like pollution monitoring along air traffic routes, observation of concentrations changes along the dawn/dusk line, concentration profiling near volcanic eruptions or support of regional measurement campaigns.

2.2.2 Radiometric Calibration

Radiometric calibration of MIPAS is performed with two measurements:

- **Offset calibration**, by observation of cold space to determine the thermal emission of MIPAS (which will be the major source for offset in the spectra),
- **Gain calibration**, by observation of the well characterized internal calibration blackbody source to calibrate the instrument response throughout the spectral bands. Gain calibration also provides the information about phase distortions used for the phase correction of the interferograms during ground processing.

Offset calibration has to be performed relatively frequently (several times per orbit) to determine all variations of the instrument self emission due to temperature variations. It takes about 20 s. It comprises several low resolution interferometer sweeps that are co-added by the ground segment to reduce noise.

Gain calibration is planned to be performed much less frequently (once per day or less). It comprises a number (about 500) of blackbody-cold space measurements performed at low spectral resolution, which are co-added on ground to reduce the random noise. The temperature of the calibration blackbody is also down linked to provide the basis for the conversion into an absolute radiance units.

The phase correction of interferograms is very critical for the correct radiometric calibration. After long trade-offs between various different phase correction schemes it was decided early on that for an emission sensing interferometer like MIPAS the best correction is performed together with the radiometric calibration: the (complex) offset spectrum must be subtracted from both, the scene spectrum and the calibration blackbody spectrum. These offset-corrected spectra then are divided by each other for the proper gain- and phase correction. However, this scheme only works if the phase shifts of the interferograms remain constant throughout the time between two blackbody

measurements. This requirement of an excellent long-term phase stability is one of the design drivers for the MIPAS instrument.

2.2.3 Pointing Calibration

Another set of calibration measurements is performed in-flight to determine the actual Line-of-Sight (LOS) pointing biases and harmonic variations, which in turn set the tangent altitude of a particular measurement. This LOS-calibration is based on the observation of stars moving through the IFOV with the short wavelength channels. The actual time of star observation is correlated with the expected time as computed by the pointing information from the Attitude & Orbit Control System (AOCS) of ENVISAT. Thus all biases and slow pointing variations between the star tracker package of ENVISAT (providing the pointing reference for the AOCS) and the LOS of MIPAS are derived and used for pointing corrections. The LOS-calibration will be repeated rather infrequently, like once per month.

2.3 *Ground Processing*

On-board data processing is reduced to the minimum required to reduce the data rate (i.e. analog and digital filtering of the detector outputs, decimations of the data streams and word length reduction of transmitted data blocks).

During the Level-1 processing in the ENVISAT ground segment, the interferograms to the different channels are converted to a fully (radiometrically and spectrally) calibrated spectrum, which is also corrected for the Doppler-shift from the moving platform.

The available pointing data are converted into the tangent height (including the correction for atmospheric refraction), and the geographic coordinates of the tangent point.

Level-2 processing at the ENVISAT ground segment uses these Level-1 spectra from a complete elevation scan sequence to derive the profiles of temperature and pressure in a first step, and the concentration and mixing ratio profiles of selected species of highest priority: ozone O_3, water vapor H_2O, methane CH_4, nitrous oxide N_2O, and nitric acid HNO_3.

Other species contained in the spectra will be retrieved by other data centers or by research groups using similar algorithms as those in the ENVISAT ground segment.

3 DESIGN OVERVIEW

3.1 *Functional Description*

How does MIPAS work? Fig. 4 shows a strongly simplified optical layout of a Fourier-Transform Spectrometer (FTS) like MIPAS. The atmospheric limb radiance is collected by some optics (mainly steering mirrors and a telescope) and directed to the two-beam interferometer (derived from a 'Michelson' interferometer) which allows to measure broad-band spectra with a very good spectral resolution. The second input port to the interferometer is closed with a cold blackbody to suppress disturbing radiance.

Within the actual interferometer, the input radiance is divided at the beamsplitter into two beams of similar intensity. They are directed to the moving retro reflectors (in MIPAS: cube-corners), which return the light to the beam combiner where the beams are superimposed and interfere.

As the optical path of the two beams differs due to the moving retro reflectors, the phase between the two beams changes as well, which causes a modulation of the light intensity in the output ports. At equal path length in both arms (ZPD = zero path difference), constructive interference in one output port increases the intensity to (almost) twice the average value, while destructive interference in the other port reduces the intensity there to (almost) zero. When the optical path difference is changed, interference causes the intensity to fluctuate between the two output ports (but the sum of the intensity in both ports stays constant).This interference-modulated signal as a function of optical path difference is an interferogram.

This interferogram is the Fourier transform of the spectrum of the recorded radiation, so the original spectrum can be reconstructed from the recorded interferogram by the inverse Fourier transform.

The spectral resolution of an FTS is mainly determined by the maximum path difference (MPD) achievable in the particular interferometer. For MIPAS, the MPD must be ±20 cm to achieve the required spectral resolution of 0.35 cm^{-1} (FWHM). As the both cube-corners move, this corresponds to a mechanical motion over a ±5 cm long path for each of them.

To record a useful interferogram, the modulated output has to be sampled at very regular optical path difference intervals (for MIPAS, the required sampling accuracy is about 30 nm). This is usually done with the help of a laser beam transmitted in the same optical set-up, which is used to trigger the sampling electronics behind the detector at very precise increments.

Furthermore, to achieve the tight sampling accuracy and a high modulation efficiency, the retro-reflectors must be guided with very high precision (lateral jitter below 20 mm) and constant velocity (variation below 1 %) over the full path (for MIPAS 100 mm). Thus an FTS has to meet very demanding requirements on its mechanical design. In the case of MIPAS, the alignment constraints become even more challenging as the

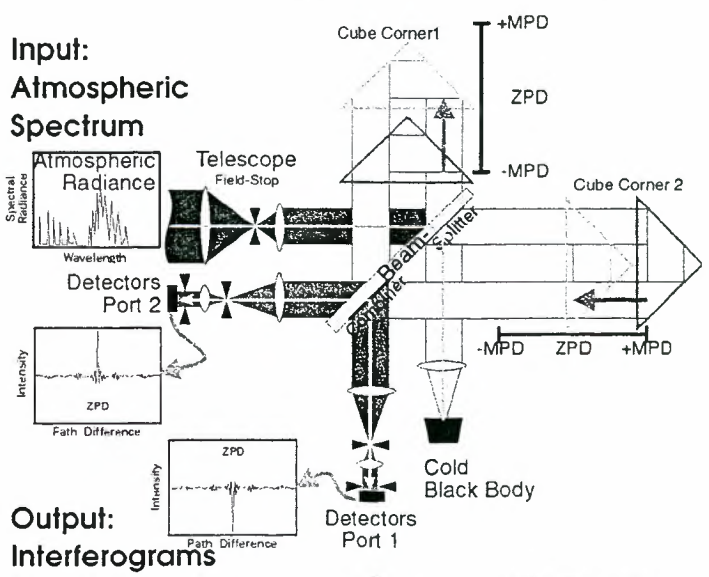

Fig. 4 Generic layout of an Fourier Transform Spectrometer like MIPAS

optics has to be cooled down to -70°C to reduce the thermal self emission.

In spite of its mechanical complexity, an FTS has unique features and shows key advantages over spectrometers with dispersive elements (like gratings or prisms) in two areas:

(i) In an FTS, a single detector receives all spectral elements present in a broad-band spectrum simultaneously throughout the full interferometer sweep duration. As long as the photon noise is not dominant (as is the case for MIPAS), this provides a clear advantage over spectrometers using dispersive elements (like gratings or prisms) employing a scanning device sending one by one the spectral elements to the detector (resulting in poor utilization of the received radiance). A large detector array would negate this advantage, but it simply doesn't exist yet in the mid-infrared.

(ii) An FTS can accept light coming from a much larger solid angle as input for a given spectral resolution. This property is essential to observe an extended source like the sky with high spectral resolution.

Thus an FTS is the only means currently available to obtain complete high resolution infrared spectra of the atmosphere with adequate sensitivity.

3.2 *Basic Design Trades*

During the first design phase of MIPAS, numerous trade-offs were performed to derive the overall instrument configuration. The trades were always driven by the need for the simplest, most reliable design solution available to achieve the performance. As a result, the main design features for MIPAS can be summarized as follows:

- A **dual slide interferometer** was selected to minimize overall dimensions and mass, reduce the residual momentum during slide reversal, and provide some redundancy in case of a single drive failure.
- The **interferometer slides** are carried by dry-lubricated roller bearings to allow easier ground testing than with magnetic bearings, and to make use of available bearing technology as far as possible.
- A **diode-laser** based reference interferometer was selected as the simplest design solution. No absolute frequency stabilization is implemented, as the spectral scale can easily be calibrated by known emission features of the atmosphere.
- **Single mode optical fibers** are used to get the laser radiance into the cooled interferometer without adding to the heat dissipation there.
- All optics is **passively cooled** to temperatures on the order of 200 K to reduce their thermal emission, which forms a major noise source.
- A **Stirling-cycle cooler** was selected for cooling of the detectors, which allows to achieve detector temperatures of about 70 K. This eliminates use of Si:Ga detectors, which would be more sensitive than the Hg:Cd:Te-detectors now employed.
- To make fast profiling measurements, linear detector arrays had been considered. However, **single element Hg:Cd:Te-detectors** will be used instead to ease the development of the sensitive detectors and their read out electronics.
- **On ground data processing** will be perfomed wherever possible to simplify the demands on the in-flight software. Only functions to reduce the data rate will be performed in the flight segment of MIPAS.

3.3 *Architecture*

The functional block diagram of MIPAS and its ground segment is outlined in Fig. 5. The atmospheric radiance enters MIPAS through the **Front End Optics (FEO)**, which comprises Azimuth and Elevation Scan Units for the selection of the line-of-sight, an anamorphotic telescope and a calibration blackbody for in-flight radiometric calibration.

From the telescope, the radiance is directed to the **Interferometer (INT)**, which could be considered the 'heart' of the instrument. Its slide motion is controlled to close tolerances using a laser

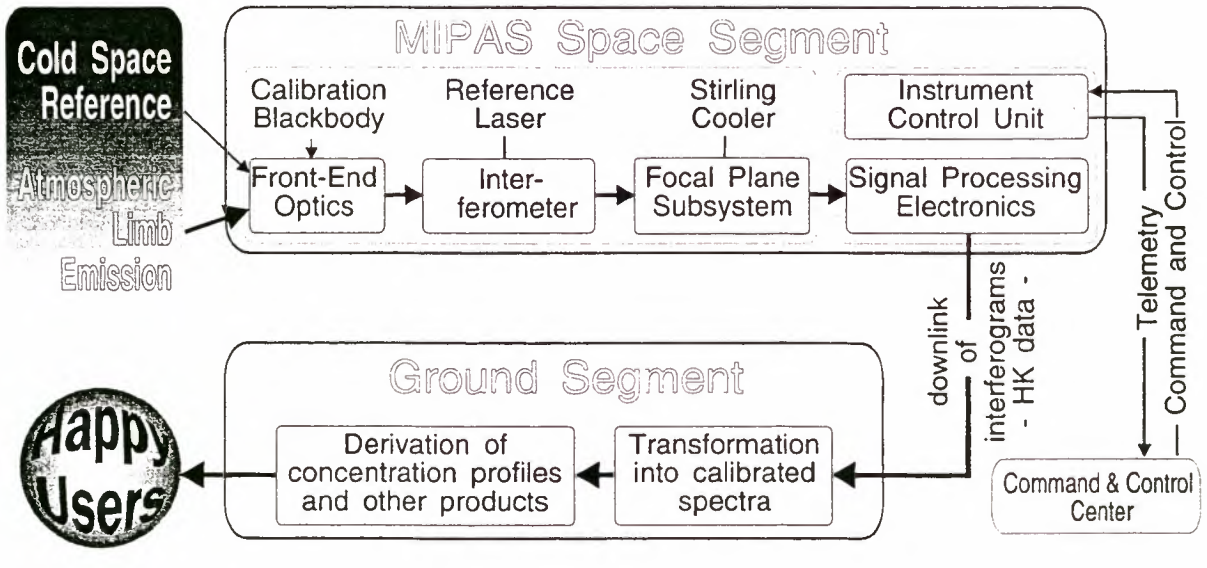

Fig. 5 Functional subsystem layout, indicating the major building block of the instrument and the ground segment

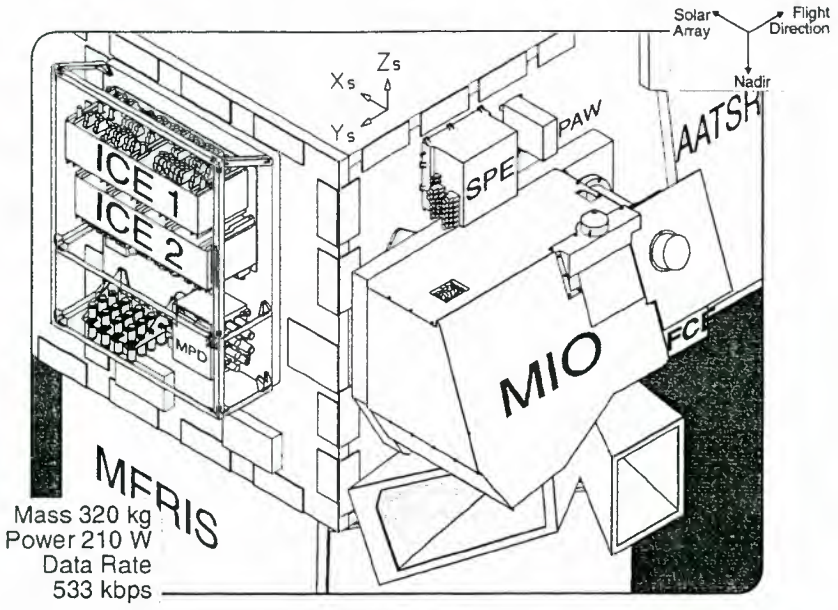

Fig. 6 MIPAS on the tip of ENVISAT

interferometer.

The interferograms are detected by the **Focal Plane Subsystem (FPS)**, which divide the incoming light into various spectral channels for detection by the eight Hg:Cd:Te-detectors. The detectors are cooled by a pair of synchronized Stirling-cycle coolers to 70 K for maximum sensitivity.

The detector output is filtered and decimated in the **Signal Processing Electronics (SPE)**, which outputs the interferograms and the ancillary data required for the on-ground processing to the Platform Data Handling & Transmission interface of the PPF for on-board storage and downlinking to the ground station.

In the **Ground Segment**, the downlinked interferograms are converted into calibrated atmospheric spectra. In the next processing levels, these spectra are used to retrieve the concentration profiles of the relevant atmospheric species and other, higher data products.

An **Instrument Control Electronics (ICE)** contains all electronics modules to supervise and to execute macro-commands for MIPAS, and it also houses the plug-in modules to drive the FEO and INT subsystems. The Stirling-cycle coolers of the FPS are controlled by a dedicated electronics box.

All electronics units are fully redundant: in the case of the ICE, two identical units are used, while the cooler control electronics is internally redundant, and the SPE uses redundant submodules which can be switched by tele-command to bypass faulty components.

3.4 Accomodation on ENVISAT

Fig. 6 shows the overall layout of MIPAS as mounted on the tip of ENVISAT. It comprises the following modules:

- The MIPAS Optics module (MIO) with the azimuth and elevation scan units and the receiving telescope, the interferometer and the focal plane subsystem, mounted on the tip of ENVISAT . It is radiatively cooled to about 205 K to reduce the thermal emission of its optical components, but two Stirling-cycle coolers keep the temperature of the detection module to about 70 K.

- The MIPAS Electronics module (MIE) on the side of ENVISAT, with redundant Instrument Control Electronics boxes (ICE 1 & 2), the MIPAS Power Distribution unit (MPD) mounted on a common carrier plate and under a common radiator for thermal control, and

- Signal Processor Electronics (SPE), Detector Preamplifiers (PAW) and Stirling-cycle cooler drive electronics (FCE) surrounding the Optics Module on the deep-space side of ENVISAT.

All units with power dissipation are removed from the MIO to achieve a lower temperature of the optics. However, this distributed concept results in a rather complex instrument harness, as the units in the optics module have to be connected to primary and redundant control and monitoring units (it has over 300 connectors).

The total mass of the instrument is about 327 kg, and its power consumption amounts to 210 W.

4 Design Description

4.1 The MIPAS Optics Module (MIO)

The MIPAS Optics Module is the actual 'measurement head' of MIPAS, housing the Front End Optics, the Interferometer, the Focal Plane Subsystem and the Stirling-cycle coolers. Fig. 7 illustrates the layout of the subsystems in the MIO. The module is about 1.36 m long (in flight direction), 1.46 m high (nadir direction) and about 0.74 m deep (cold space direction). It has a mass of about 170 kg.

The housing of the Optics Module carries several radiators:

- a large radiator to cool all optical components of the instrument to about 205 K to reduce the thermal background of the instrument,

- two separate radiators to cool the compressor of the Stirling-cycle coolers and to precool the Focal Plane Subsystem that keeps the detectors at about 70 K.

All radiators are tilted away from nadir by 20° to reduce the earth shine and thus to improve their efficiency.

Below the Optics Module are the two baffles that reduce the amount of straylight entering MIPAS. The baffle for the rearward viewing range extends sufficiently far from the first optical component to avoid sunlight to enter, when the south pole region is observed during the summer period. In this case, the minimum angle between sun and line-of-sight could become

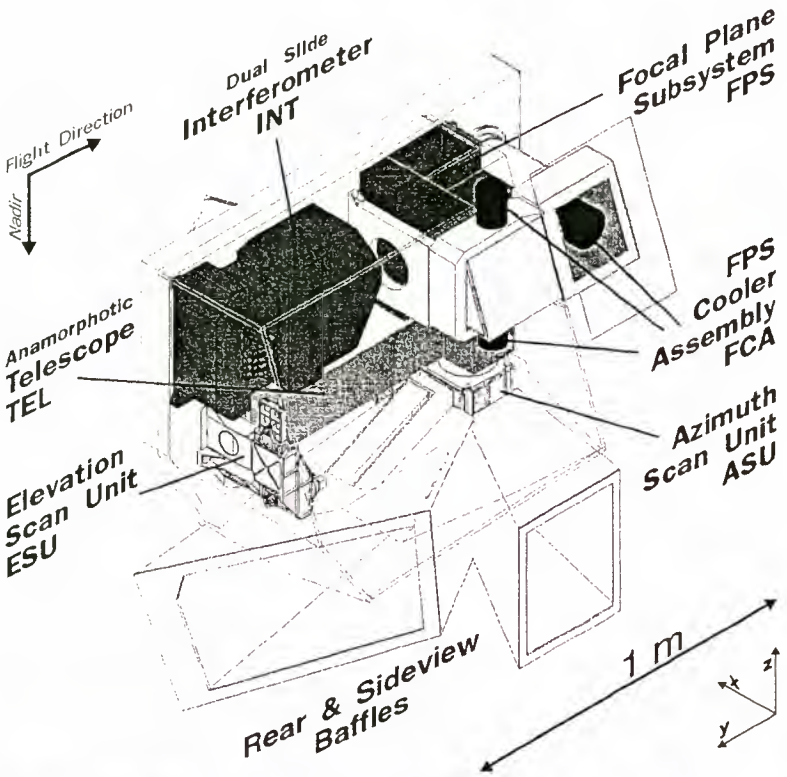

Fig. 7 Subsytem layout of the MIPAS Optics Module

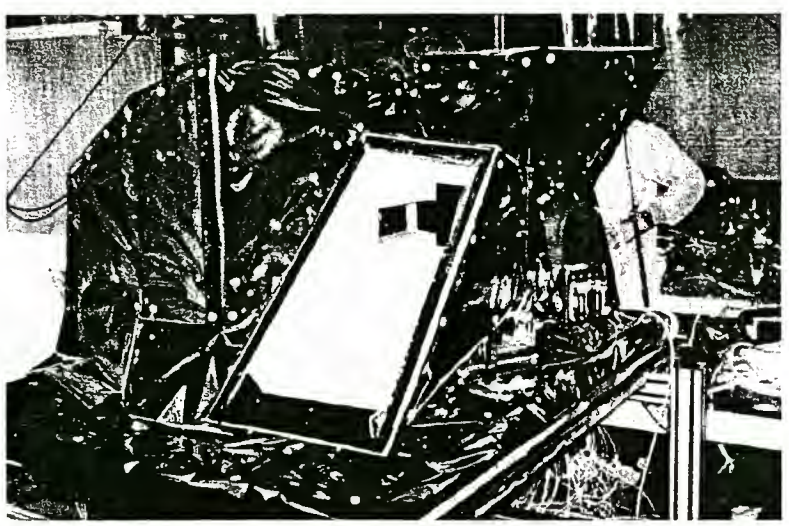

Fig. 8 The MIPAS Optics Module during the preparation for the thermal vacuum testing

as small as about 8°. It is cut short on the sun illuminated side to reduce its heat input. Further reduction of the baffle temperature is achieved by using a white coating (in the thermal IR it is black).

Fig. 8 is a picture of the MIO during the preparation for the thermal vacuum testing, lying on the mounting side to the satellite (thus nadir would be to the right) and seen from the rearward direction. It shows clearly the white aft-baffle and (pointing upwards) the side baffle. The outside of the MIO is covered in multi-layer insulation to minimize heating from sun and earth shine. This view gives an impression for the size of the MIO.

4.1.1 Optical Design Features

Fig. 9 indicates the optical path of MIPAS from the entrance baffle to the detector elements in the cold unit. Another overview of the optical design is given in Fig. 9, which shows beam sizes and view angles at the various locations within the optical train. For clarity, it shows the beam path for only one interferometer output port and one detector channel.

The entrance aperture of MIPAS accepts an input beam of 165 mm height and 55 mm width. This free aperture is reduced by two Lyot-stops (in the interferometer and a cold aperture before the detectors) to an effective size 135 mm by 45 mm for efficient stray light rejection.

The telescope of the Front-end optics reduces the beam by a factor of 6 in azimuth and 1 in elevation. It houses the field stop which determines the instrument field-of-view of 0.9 * 9 mrad (elevation / azimuth).

The interferometer is indicated as a simple straight light path, although its actual implementation is rather more complex. The output side of the beam combiner carries the first Lyot stop for straylight supression.

Behind the interferometer, the beams from the two output ports are reduced in size to 4.5 mm by 9 mm by another mirror telescope, the Afocal Reducer. This telescope is part of the Focal Plane Subsystem (FPS).

The entrance of the cooled part of the FPS acts as a second Lyot stop. A second field stop ('cold stop') is mounted behind some relay optics. As there is a cold stop in each of the two output ports from the interferometer, a slight relative misalignment between them would lead a slightly different field-of-view of the individual detectors. To avoid this problem, the cold stops are somewhat oversized.

The detector elements are acting as aperture stops and thus average the scene radiance even for scene with large radiance gradients. Thus response variations over the detector surface (which are rather strong for the photo-conductive detectors) will not affect the radiometric accuracy of MIPAS.

4.1.2 Front End Optics (FEO)

The FEO contains all assemblies that determine the line-of-sight, the instantaneous field-of-view and the receiving area:

4.1.2.1 Azimuth Scan Unit (ASU)

The ASU allows to select the Line-of-Sight within the two field-of-

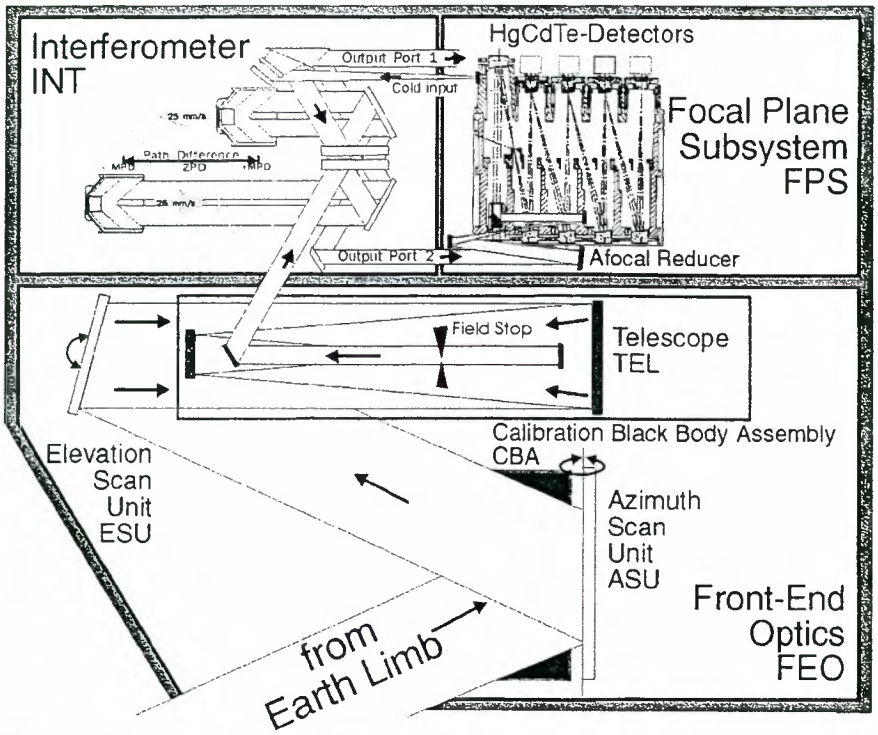

Fig. 9 Optical path through the subsystems

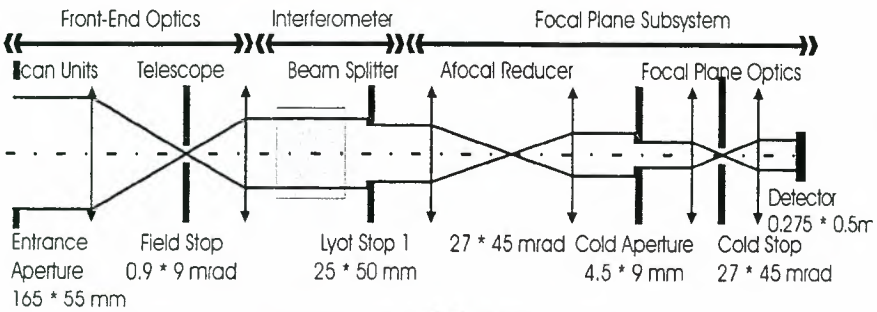

Fig. 10 Optical scheme with beam sizes and divergence angles

view regions, and also to access an internal blackbody source for gain calibration. A flat steering mirror rotates about an axis parallel to nadir to direct the incoming infrared radiation into the instrument. This steering mirror has a dimension of 346 mm in height and 122 mm in width and thus forms the largest optical component of MIPAS.

4.1.2.2 Elevation Scan Unit (ESU)

The ESU is used to adjust the actual tangent height of a particular measurement, and thus requires a very high pointing accuracy over a limited angular range. It comprises a flat steering mirror rotating about an axis that is orthogonal to both nadir and flight direction. The angle covered by this mirror is less than 3° which is sufficient to reach tangent heights between 5 km and 220 km; the highest tangent height is used for measurements of cold space to determine the instrument self emission for offset calibration.

4.1.2.3 Telescope (TEL)

Driven by the demand for an atmospheric object size with a large edge ratio (30 km horizontal to 3 km vertical dimension), the telescope is an anamorphotic design with a high magnification in elevation compared with azimuth. A trade-off to reduce the overall volume of telescope and interferometer resulted in a design with a magnification of 6 in elevation and 1 in azimuth. It uses a folded design with a 5 mirrors (two mirrors focus the incoming light on the field stop, and the remaining ones collimate the beam for the interferometer).

TEL uses an Aluminium-honeycomd structure and specially designed mirror mounts to maintain its optical performance over the wide temperature range, and to survive the launch vibrations.

4.1.2.4 Calibration Blackbody Assembly (CBA)

The calibration blackbody, that is used for the in-flight calibration of the instrument responsivity, is mounted in the Azimuth Scan Unit. It requires a rather large clear aperture (220 x 75 mm^2). Its design is derived from the blackbody design for the Along-Track Scanning Radiometer ATSR, presently flying on the ERS-1 satellite. Its emissivity is above 99.6 %, so that a high accuracy for the gain calibration can be achieved. For precision gain calibration measurements, it can be heated up to about 50 K above the ambient instrument temperature to deliver sufficient radiance at short wavelengths. It will be heated in flight to temperatures between about 220 and 250 K. Measurements at different temperatures are required for the in-flight characterisation of the detector non-linearities.

4.1.3 Interferometer

4.1.3.1 Overview

MIPAS uses a symmetrical dual slide interferometer with dual input and output as it provides highest detectable signal at the outputs, highest degree of redundancy, and most compact dimensions. The optical arrangement is indicated in Fig. 11: the incident angle of the radiation onto the beamsplitter is 30° to reduce polarisation effects by this component when compared to 45° incidence. To achieve the specified spectral resolution, the maximum path difference (MPD) at the beam combiner must be at least ±20 cm, corresponding to a mechanical motion of ±5 cm for each corner cube.

Fig. 12 outlines the overall design. Fig. 13 shows the actual MIPAS Interferometer Flight Model with the remotely located laser boxes before integration in the MIO.

4.1.3.2 Interferometer Optics (INO)

The INO comprises the beam splitter assembly, flat steering mirrors and the corner cubes on the moving slides. The beam splitter coatings are quite critical, as they have to provide a reflectivity near 50 % throughout the broad spectral range. More difficult to manufacture are actually the broad-band anti-reflection coatings on the other surfaces of the substrate to reduce undesired interference effects that would modulate the transmission.

The beam splitter assembly also has to compensate the phase delays caused by the dispersive nature of the substrate throughout the spectral range. This is done with a second substrate of same thickness as the beam splitter itself and mounted with a narrow gap to the beam splitter coatings. Both substrates are slightly wedged to reduce the residual etalon effects.

4.1.3.3 Interferometer Drive Units (IDU)

The two identical IDUs perform the actual translation of the cube corners. Linear magnetic actuators ('voice coils') generate the drive force. The slides are guided by mechanical bearings. The lifetime requirement of four years continuous operation corresponds to about 40 million interferometer sweeps. Dry-lubricated (MoS_2 - coated) ball bearings running on steel rails have been selected and have demonstrated this lifetime.

A locking mechanism off-loads the slides during launch. It uses two hot-paraffin actuators to unlock the slides in flight.

4.1.3.4 Optical-Path Difference Sensor (ODS)

The optical path difference signal for interferogram sampling, and the accurate difference speed of the corner cubes are derived from a laser interferometer. It uses a single-mode 1.3 µm-diode laser which is located in a temperature stabilised box mounted onto MIO. The output from the diode laser is guided to the interferometer via a Single Mode, Polarising-optical fibre.

The 1.3 µm-radiation from the ODS laser is circularly polarised and injected into the interferometer via special coatings on the beam splitter substrate. The polarisation allows to retrieve both sine- and cosine components of the superimposed beams, and thus to determine the direction of the retro-reflector motion. This direction information is important as the interference fringes of the ODS provide an absolute position reference, that must be accurately maintained between two gain calibration sequences.

It should be noted that the ODS laser does not have an absolute frequency stabilisation, although it is designed to have a good short term frequency stability (less than 50 MHz drift over 75 s). The absolute frequency calibration is performed during the ground processing using isolated emission lines of know position.

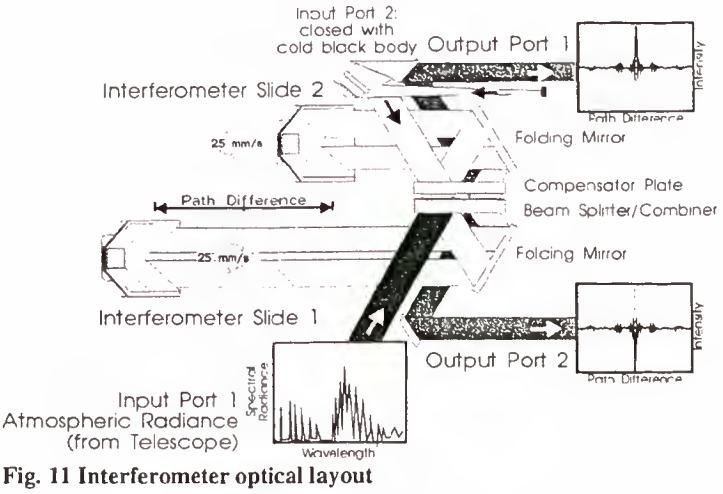

Fig. 11 Interferometer optical layout

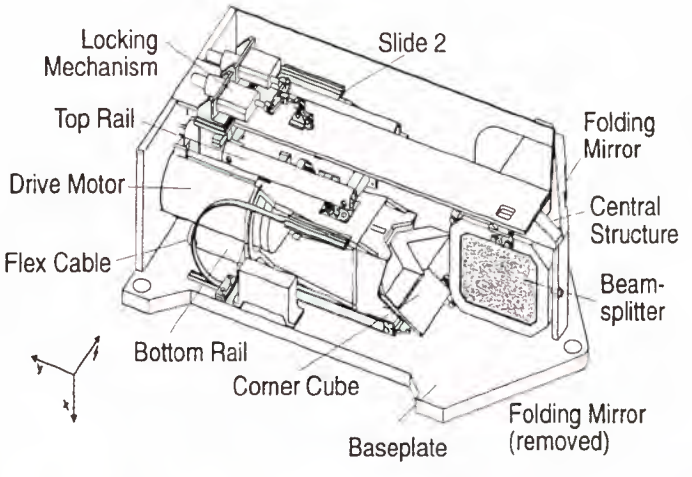

Fig. 12 Interferometer mechanical layout

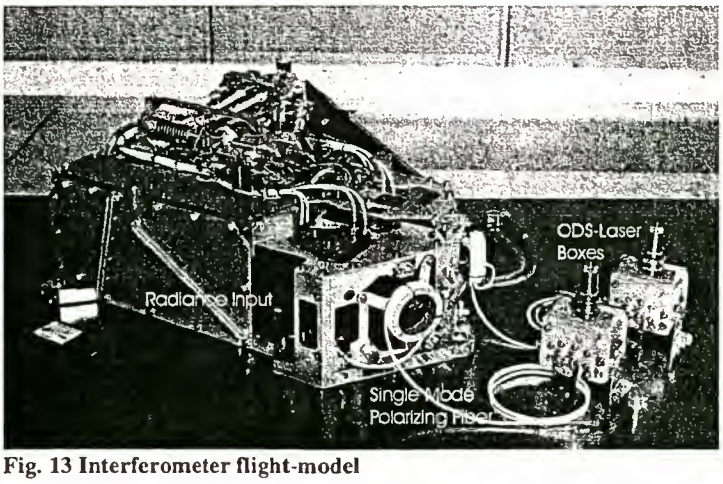

Fig. 13 Interferometer flight-model

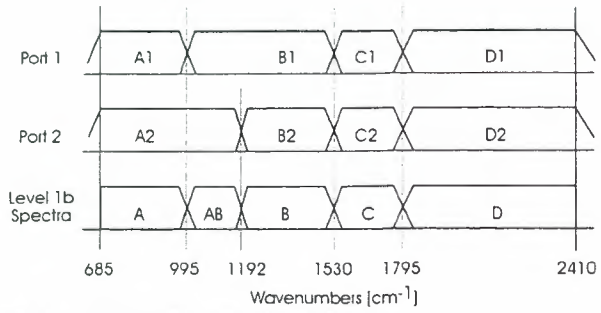

Fig. 14 MIPAS spectral channels

4.1.4 Focal Plane Subsystem (FPS)

The two output beams of the interferometer is reduced in size by the Afocal Reducer (two small off-axis Newton telescopes), and directed into the cold part of the FPS. The latter houses the signal detectors with their interfaces to the active coolers, as well as the associated optics required for spectral separation and beam shaping.

To achieve best radiometric sensitivity, a set of four Hg:Cd:Te detectors in each output port (thus a total of eight detectors) is used, each optimised for highest sensitivity in a particular spectral band. Fig. 14 shows the spectral bands for each of the output port, and also shows the final spectral band assignments after pre-processing in the signal processing electronics and on-ground.

The detectors for the two long wavelength bands A and B are photo-conductive, those for the shorter wavelength bands photo-voltaic types. The response of the photo-conductive detectors reduces somewhat with increasing radiance fluxes. This non-linear behavior causes distortions of the interferograms which are corrected during the ground processing.

The preamplifiers are individually optimized for each detector to fulfil the stringent requirements on noise, phase distortions and linearity. The cold part of the preamplifiers is mounted in

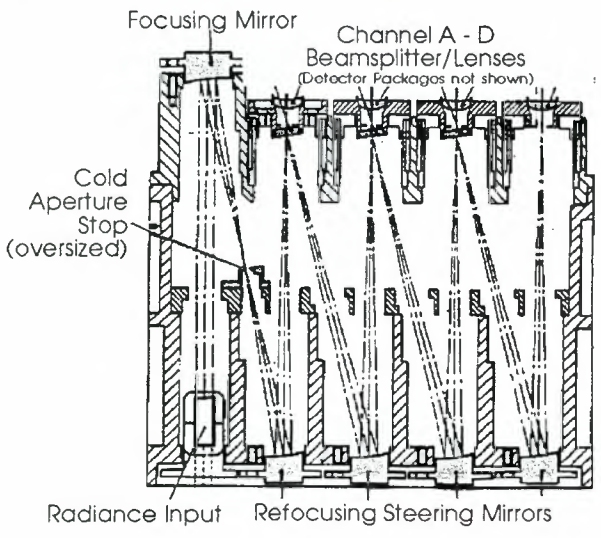

Fig. 15 Focal Plane Optics layout

the detector housing, while final amplification is performed in an externally mounted preamplifier (called Preamplifier Warm (PAW)). The PAW is located above the MIO in close proximity to the FPS. The preamplifier gain is programmable by tele-command. However, it is adjusted once to achieve the full dynamic range of the analog-to-digital converters, but the gain stays constant during interferometer sweeps and also the elevation sweeps.

Fig. 15 indicates the layout of the cooled optics, that directs the radiance from the two output ports through a series of long-pass filters to separate the radiance into the various spectral channels. Only the optics for one interferometer output port is shown, the radiance from the other output port is divided by a symmetrical arrangement in the same housing. All optics and the detectors are cooled to 70 K to reduce their thermal emission and increase the sensitivity.

Cooling is performed by a pair of active Stirling-cycle coolers that easily satisfy the cooling requirements (500 mW heat lift at a temperature of 70 K). A twin cooler arrangement is used, comprising two identical compressors and displacer units operating with opposing movements of the compressor and displacers to compensate vibrations to a large degree.

Thus, although the FPS is conceptually simple, the numerous interfaces between the optics, the detectors and the coolers under the constraints of good thermal insulation and high alignment stability turn it into a quite intricate and complex subsystem.

4.2 MIPAS Electronics (MIE)

4.2.1 Signal Processing Electronics (SPE)

On-board signal processing electronics performs the following functions:

- analog anti-alias filtering of the detector signals,
- digitization (16 bit, 77 kHz) of each signal,
- digital filtering to reduce the signal bandwidth and decimation to reduce the data rate,
- combination of some detector outputs, word length reduction and data compressing to reduce the data rate below 550 kbits/s,
- formatting and transmission to the Platform Data Handling & Transmission interface.

Interferograms and pointing data are downlinked to ground, where the Fourier-transformation and radiometric and spectral calibration (including the phase correction) will be performed to yield atmospheric spectra.

Complex digital FIR filters (512 taps) are used to limit the signal bandwidth and to shift the frequencies to the baseband, as this allows the most efficient data decimation. As a result, however, the interferograms get complex.

The on-board digital filtering and decimation steps can be disabled by tele-command. However, in this case the data rate increases to 8 Mbit per second, which can be used only for a short time. Thus the nominal operation utilises the on-board digital filtering and decimation capabilities of the SPE.

During the formatting of the data stream, the word length of the interferogram data is reduced. As the full dynamic range of the ADC is used only near the zero-path difference points, the remainder of the interferogram uses significantly fewer bits

which allows another significant reduction of data rate.

4.2.2 Instrument Control Electronics (ICE)

The ICE is the 'brain' of MIPAS and will perform all tasks required to control and monitor the subsystems. It comprises two decoupled parts in the same electronics box:

- the Instrument Control Unit (ICU), which is the instrument controller and communicates via ENVISAT with the control station on ground to exchange commands and house keeping data, and
- the Functional Dedicated Electronics (FDE), which is a bus system to support the electronics modules from the other subsystems.

After being powered, the ICU will activate all other required units by commanding the respective power switching. In this way also redundancy selection will be performed. The ICU controls via the FDE the whole instrument and performs commanding of the operating modes. These control functions also include the monitoring of all status and housekeeping signals.

5 MEASUREMENT PERFORMANCE

5.1 Measurement Set-up

All specified performance parameters have to be verified on ground. For MIPAS, this requires some extensive measurement set-up as the instrument can only be operated in cold vacuum. Thus a dedicated MIPAS test facility has been established, which comprises

- a vacuum tank with cold shrouds for the MIPAS optics module,
- a smaller vacuum chamber that generates optical test inputs, enlargens and collimates them to fill aperture and field-of view of MIPAS is mounted to the front end of the MIPAS chamber and also cooled to reduce its thermal emission, and
- a precision blackbody on top of the MIPAS chamber to validate the radiometric accuracy requirements.

Fig. 16 shows the general arrangement as well as the actual implementation. A cold blackbody to simulate deep space is included in the smaller tank to allow the offset calibration of MIPAS. The instrument line shape has to be characterized with high precision. For that purpose, radiance from a hot blackbody outside the vacuum envelope is filtered by a cold narrow band pass filter in the vacuum chamber to limit the total radiance seen by MIPAS. This radiance then passes through a gas cell which is filled with a low pressure gas with sharp features in one of the MIPAS spectral bands. These absorption features are used to determine the actual spectral properties, such as the instrument line shape or the spectral calibration.

The instantaneous field-of-view is characterized by moving a cooled aperture with a pin-hole through the radiance of a hot blackbody and recording the MIPAS response as function of pin-hole position.

The calibration blackbody is cooled with liquid nitrogen to reach the required low temperatures. The actual emission temperature then is set with electrical heating elements and carefully controlled with precision resistor thermometers.

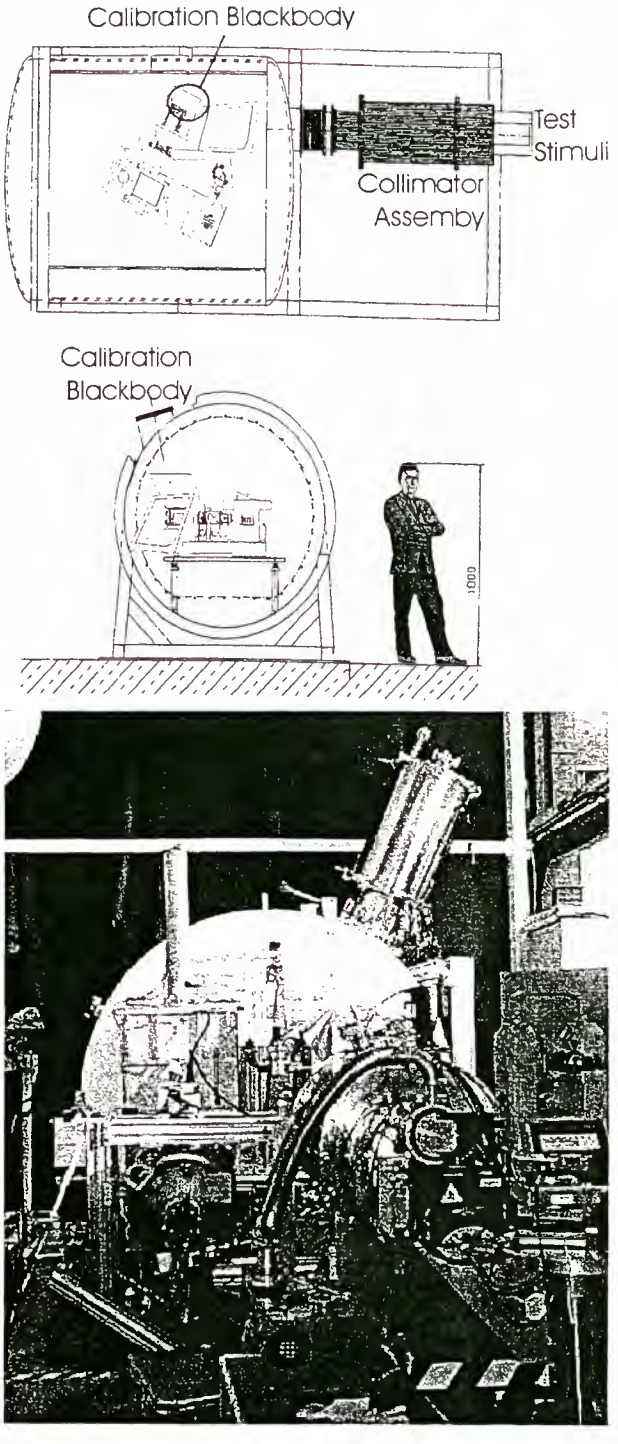

Fig. 16 The MIPAS test chamber: the overview drawing indicates the dimensions, while the lower picture shows the actual set up during measurements. The calibration blackbody is on top, the stimulus generator in front.

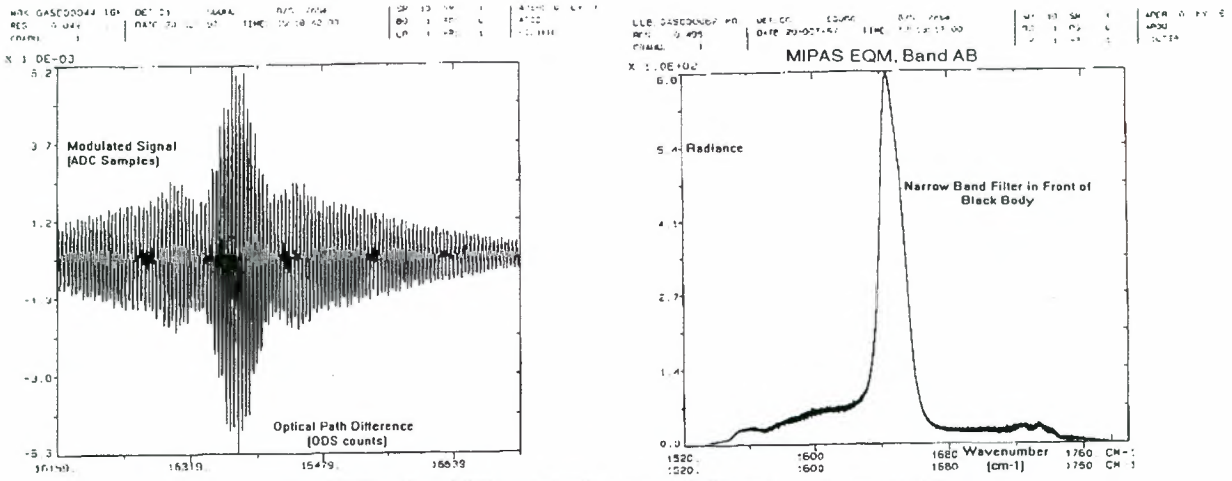

Fig. 17 The first MIPAS interferogram (left) and spectrum (right)

5.2 *General Observations*

After initial problems with the measurement set-up and the instrument operation, first interferograms were finally obtained from MIPAS in Nov. 1998. Fig. 17 shows this first instrument interferogram and the corresponding magnitude spectrum.

In general, the MIPAS interferograms were surprisingly close to the expectations. In particular, the adjustment of the digital filters was verified, and the absence of narrow spectral features in the instrument was confirmed. However, a few observations should be reported here in more detail:

- Detector Non-linearities

The first investigations on MIPAS data output were done using non-calibrated spectra obtained in the raw-data (unfiltered) mode. Fig. 18 shows a magnitude spectrum of the output from Channel A1 (670 to 1000 cm^{-1}), viewing into a blackbody source. Besides the strong signal of the base band of this spectral channel, a significant signal is also visible at the harmonic frequencies. These artifacts are resulting from the non-linearities of the photo-conductive Hg:Cd;Te detectors. For channels C and D, where photo-voltaic detectors are used, these harmonic contributions are not observed. These strong non-linearities have been expected, and are corrected during the on-ground processing.

- Spectral Spikes

A more surprising feature was discovered during the initial testing of MIPAS: when the interferograms are filtered and thus their frequencies are shifted around the zero-frequency point, any clipping or truncation of the digitized interferogram samples can result in an offset of the zero-frequency point in the spectral domain. As this point is shifted back into spectrum during ground-processing, it may show up as a spike. Fig. 19 shows an example of one of these 'sampling spikes'.

As the clipping of the interferogram samples is not predictable, the magnitude of this spike varies for all interferometer sweeps. Thus, the spike also exist in calibrated spectra as well. But as the frequencies of the spectral points where sampling spikes occur are deterministic and as only one point per spectral band is affected, this effect is not considered critical.

- Channel Spectra

Fig. 19 shows a detail of a magnitude spectrum that is obtained by averaging 500 interferograms of a blackbody – note the large offset from the zero-radiance line. Under these conditions, a periodic modulation of the blackbody emission with a 1 cm^{-1} periodicity and an amplitude of 0.22 % becomes clearly visible. This modulation is an instrument artifact ('channel spectrum') that is observable in band A and (to a lesser extent) Band B. Due

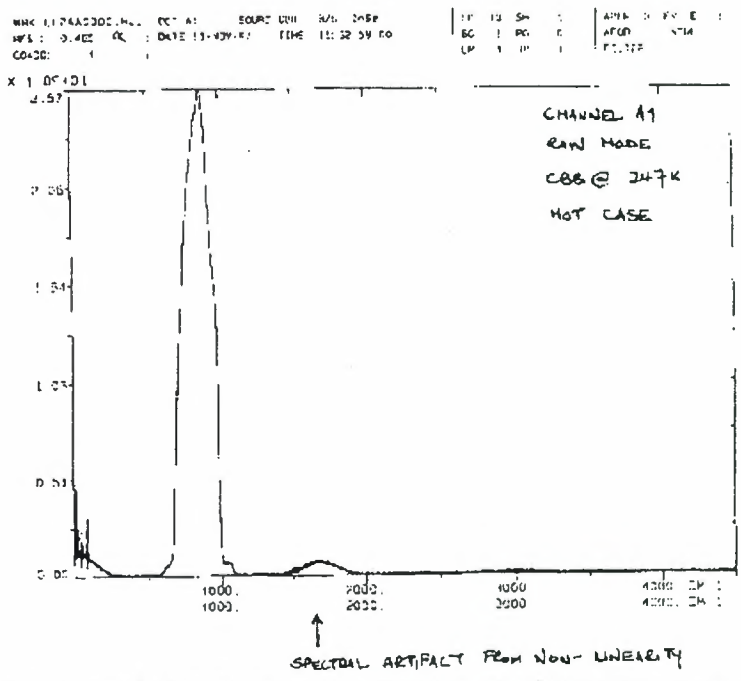

Fig. 18 Raw data spectrum, showing the harmonics due the the detector non-linearities

to the small amplitude, this channel spectrum vanishes in the

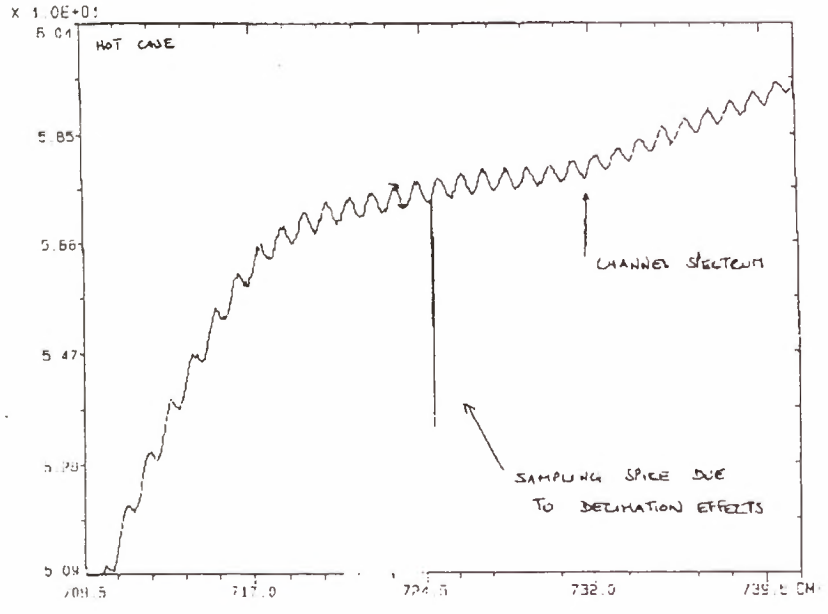

Fig. 19 Magnification of low noise blackbody spectrum (500 coadditions), indication sampling spike and channel spectrum of 0.2 % amplitude. Note the offset to the radiance scale, showing the region from 5.09 to 6.04 only.

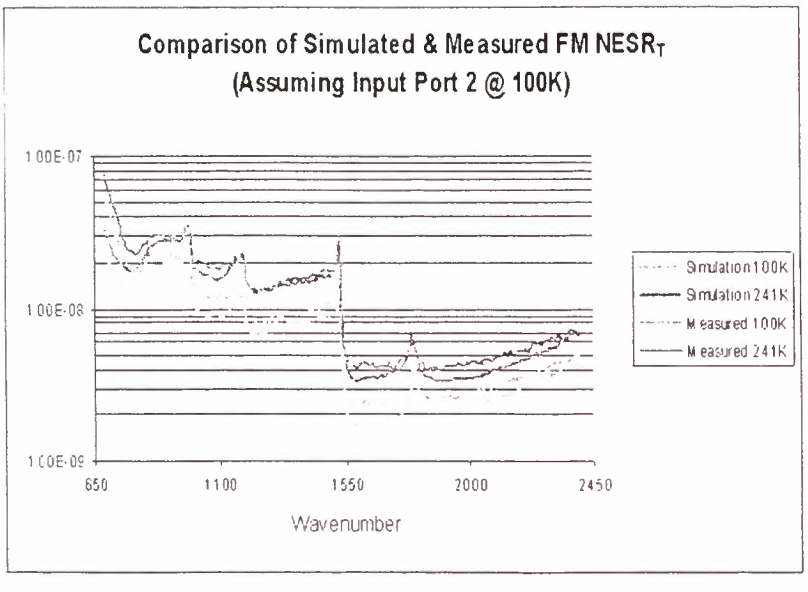

Fig. 20 NESR measurements for the MIPAS Flight Model for two different input radiance levels, compared with the predictions that were based on subsystem characterization data

random noise when no co-addition is performed.

The channel spectrum results from a slight etalon effect of the dichroic beam splitter in the Focal-Plane Subsystem. These beam splitter substrates are wedged and use a rather broad-band anti-reflection coating on one side to reduce this effect, and the observed modulation is the residual effect. As the temperature within the FPS is very well controlled, the phase of the channel spectrum is expected to remain unchanged between gain calibration and measurements; in this case, the channel spectrum disappears in calibrated spectra.

5.3 Performance Characterization Measurements

The following investigations were made using fully calibrated spectra, which were generated with the same algorithms as for the ground segment (although the implementation of the algorithms differs from the ground segment). Thus a measurement is performed by first doing a gain calibration (600 MIPAS sweeps blackbody / deep space simulator with low spectral resolution), followed by the actual scene measurement (deep space simulator, absorption cell or the facility blackbody) and another deep space simulator measurement with low spectral resolution.

- NESR

Fig. 20 shows the NESR data obtained during the first measurement campaign with the Flight Model, looking into different scenes. It also shows the predictions from the MIPAS performance model (which was developed six years before the measurements), and using component characterization data as inputs. The correlation between predicted and measured NESR is quite remarkable. This demonstrates that the noise behavior of MIPAS is rather well understood.

- Radiometric Accuracy

Similarly, the radiometric accuracy was determined by using the facility blackbody as input source. The observed radiometric errors were significantly less than specified, also for channel A and B which are affected by the non-linear detectors. Thus it is shown that the correction algorithms are suitable. However, with the ground testing it can not be measured how large the zero-line offset gets for high average radiances. This offset can be investigated using the MIPAS simulation programme, and will be assessed during the commissioning phase as well.

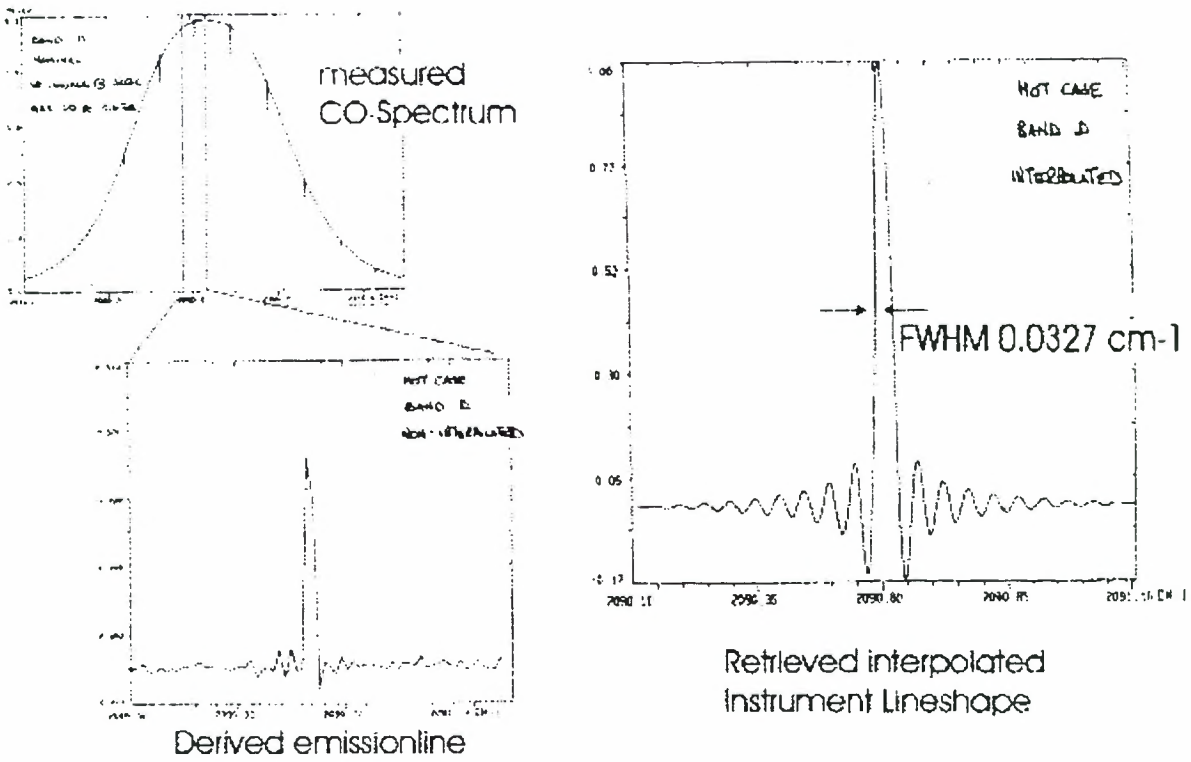

Fig. 21 Lineshape retrieval step: one line from an absorption spectrum is numerically transformed into an equivalent emission line. This lineshape is interpolated to obtain the relevant line shape parameters.

- Lineshape and spectral resolution

Fig. 21 shows the steps involved in a lineshape retrieval, in this case for the shortest wavelength band D (which is most sensitive for misalignment). The original spectrum is obtained by measuring an absorption spectrum of CO (low optical density), and co-addition of 500 interferograms to reduce noise. The resulting absorption spectrum is recomputed as emission spectrum, and the line shape of the CO-line is deconvolved to obtain the instrument line shape. This line then is interpolated to result in a smooth curve, as shown in the figure.

The line width (Full-Width at Half Maximum) as shown here was obtained with the Engineering-Qualification Model, for which the line width is 0.033 cm^{-1}.

The line shape of the Flight Model is shown in Fig. 22. It has a slightly wider line width of 0.034 cm^{-1}, but it still meets the requirement with margins. However, the side lobes are slightly different, which can be explained by a slight misalignment of the interferometer.

As the lineshape is a sensitive indicator for any misalignment, it was used to verify the alignment stability throughout the mechanical qualification tests. The instrument lineshape obtained after . It was very pleasing to observe that the lineshape remained almost unchanged (peak variation is about 1 %), although the instrument had undergone vibration levels which are significant higher than expected for launch. Thus it was demonstrated that MIPAS is structurally sound.

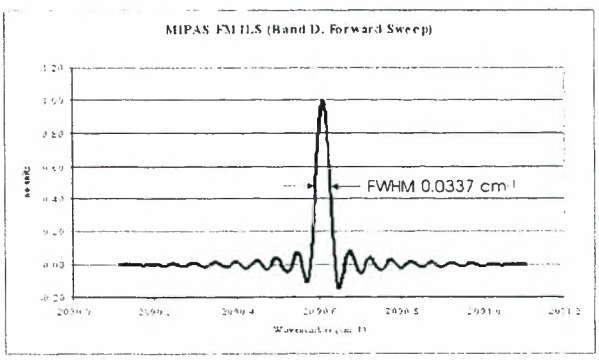

Fig. 22 Line shape of the MIPAS Flight Model

6 CONCLUSION

MIPAS for the ENVISAT satellite presents a new type of space borne instrumentation that promises to deliver important data about the composition of the middle atmosphere and upper troposphere. It will be the first cooled FTS in space and will allow to measure concentration profiles of many trace constituents around the globe, in particular also in the polar regions.

The performance requirements are demanding, in particular the need for high radiometric sensitivity and the radiometric accuracy. The measurements of the actual Flight Model indicate that the overall performance requirements are as expected, and thus it will meet its requirements in flight as well.

The MIPAS Flight Model has completed a first performance characterization campaign in its thermal vacuum facility. After vibration testing and electromagnetic-compatibility testing, a second, full characterization campaign will follow. The delivery to the ENVISAT satellite is expected for summer 1999.

The last figure shows MIPAS with its integration team, who have performed an excellent job during MIPAS programme.

7 ACKNOWLEDGMENTS

The design work has been performed by the following industrial team: Dornier Satelliten Systeme GmbH DSS-FH (Friedrichshafen, Germany) is the ENVISAT mission prime contractor, and DSS-OTN (Ottobrunn, Germany) is the MIPAS instrument prime contractor, with Bomem (Quebec, Canada) for support of the system and interferometer engineering tasks;

Oerlikon Contraves (Zürich, Switzerland) is responsible for the Front-End Optics with subcontractors **SENER** (Madrid, Spain) for the Azimuth and Elevation Scan Electronics, **SESO** (Aix-en-Provence, France) for the anamorphotic telescope, and **AEA-Technology** (UK) for the calibration blackbody;

DSS-OTN is responsible for the Interferometer, which will be realized together with the subcontractors **Officine Galileo** (Florence, Italy) for the mechanism assembly and the drive electronics, **REOSC** (Paris, France) for the interferometer optics, and **Kongsberg Aerospace** (Kongsberg, Norway) for the Laser Interferometer;

Fokker Space B.V. (Leiden, Netherlands) is responsible for the Focal Plane Subsystem, with subcontractors **TPD/TNO** (Delft, Netherlands) for the optical design, **GMIRL** (Southampton, UK) for the detectors, and **Com Dev Europe** (Aylesbury, UK) for the preamplifiers; **Matra Marconi Space-Bristol** (Bristol, UK) supplies the Stirling-cycle coolers, and **Rutherford Appleton Laboratories** (Chilton, UK) the low vibration drive electronics;

the Signal Processing Electronics is developed by **Com Dev Canada** (Cambridge, Canada), and the Instrument Control Electronics is designed by **CRISA** (Madrid, Spain), the MIPAS Power Distribution unit by **Delft Sensor Systems** (Delft, Netherlands), and the MIPAS Instrument Harness by **OHB System GmbH** (Bremen, Germany).

Bomem (Quebec, Canada) is responsible for the on-ground calibration facilities, and **AFI** (Sollentuna, Sweden) designs the electronic ground support equipment, and **ORS** (Vienna, Austria) supplies the mechanical ground support equipment and the Thermal Control Hardware.

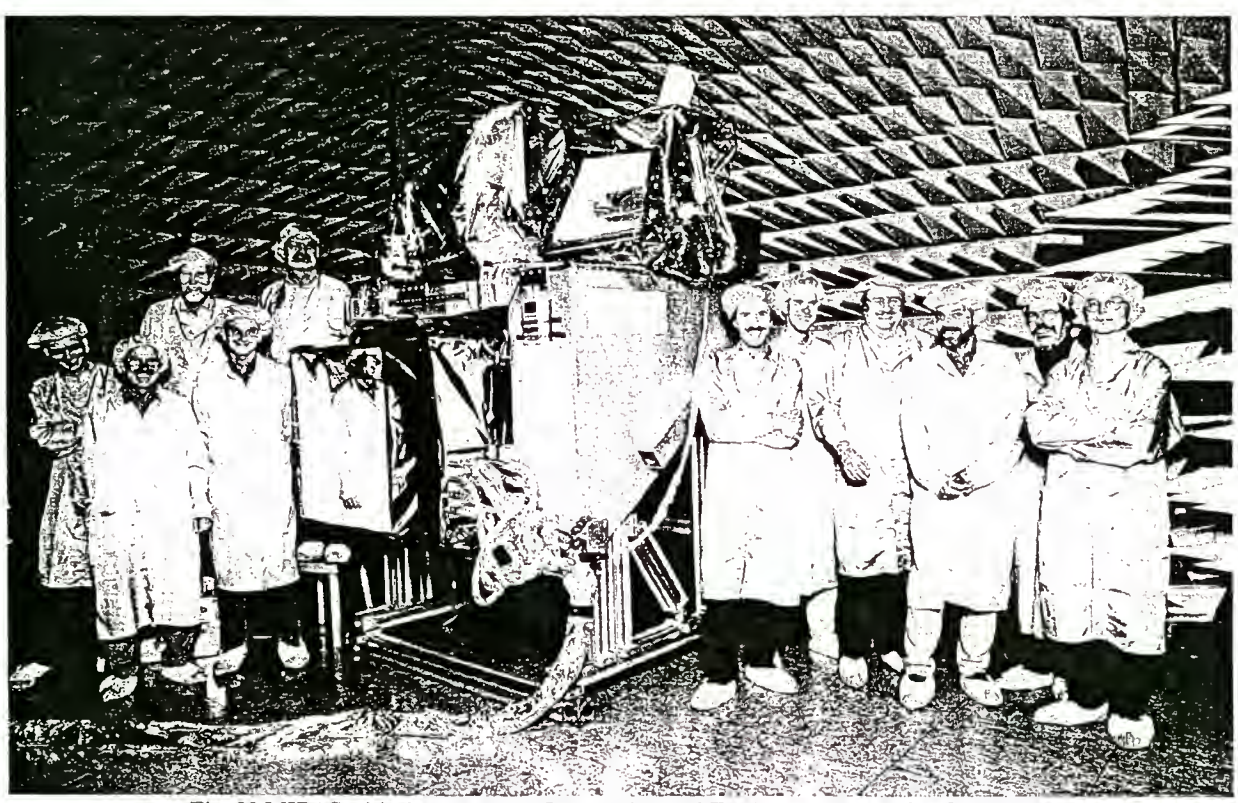

Fig. 22 MIPAS with the Assembly, Integration and Testing team at DASA/Ottobrunn

MIPAS DATA PRODUCTS

Herbert Nett

ENVISAT Systems/Payload Division

ESA/ESTEC,P.O. Box 299 NL-2200 AG Noordwijk

(e-mail: hnett@jw.estec.esa.nl)

ABSTRACT

MIPAS (Michelson Interferometer for Passive Atmospheric Sounding) will be one of the ESA provided payload instruments on board ENVISAT. During its operational phase it will provide a number of routine data products of primary interest in various disciplines of atmospheric research. The list of products comprises instrument raw data (Level 0), geolocated and calibrated limb radiance spectra (Level 1B) and a number of geophysical parameters, in particular vertical profiles of atmospheric pressure, temperature and volume mixing ratios of the primary MIPAS target species O_3, H_2O, CH_4, N_2O, HNO_3 (Level 2).

This paper shall provide an overview of the MIPAS products and describe the general data structures. The included parameters, resulting from the Level 1B & 2 ground processing chain, will be discussed. These cover, in addition to the primary geophysical data, various quantities which support the user in the interpretation of MIPAS data and allow the monitoring of instrument and ground processor performance throughout the mission lifetime.

1. INTRODUCTION

During nominal in-orbit operation MIPAS will acquire limb emission measurements while periodically varying the line-of-sight (LOS) tangent height in discrete steps. For each tangent height a scene interferogram will be recorded, corresponding to a single stroke of the interferometer ('sweep'). With an orbit period of 100.6 minutes and a measurement time of 4.45 s per sweep (max. resolution, incl. turn around time), typically 75 elevation scans will be acquired per orbit, with 16 sweeps per scan, ranging from 8 km to 65 km in tangent height. This includes deep space ('offset') calibrations interleaving the scene measurements in periodic time intervals of approximately 300 s.

The downlinked MIPAS raw data will be stored on ground in a computer compatible format, yielding the so-called Level 0 products. Starting from a Level 0 set the MIPAS Level 1B processor will convert the scene interferograms into fully calibrated radiance spectra, making use of pre-processed radiometric offset and gain calibration data, and of spectral axis correction parameters. In the subsequent Level 2 stage extracted Level 1B spectra will be analysed yielding a set of geophysical profile data and related output parameters, to be included in the Level 2 data products. Besides instrument raw data (Level 0) and calibrated limb radiance data (Level 1B) the ground processor will require additional input data, e.g., instrument parameters, orbit/attitude information and atmospheric/spectroscopic data. These parameters, referred to as auxiliary data, will be formatted according to the same - ENVISAT specific - product structures as used for the Level 1B/2 products. This allows to archive and retrieve both types, auxiliary sets and data products, using the same mechanisms.

In the following sections a brief outline of the routine MIPAS processing scheme and of the relevant components of the ENVISAT Payload Data Segment (PDS) will be given, as well as a description of the MIPAS Level 1B/2 and auxiliary products. Basic concepts related to product structures, extracted data sets, and product dissemination will be discussed.

2. MIPAS PRODUCTS: A REVIEW

Generation of Level 1B and Level 2 data sets

In nominal in-orbit operation MIPAS raw data will be stored on board ENVISAT using tape recorders. These data will be downlinked to one of two receiving ground stations typically once per orbit, according to station visibility or availability of a Data Relay Satellite link. Each downlinked sequence will be stored as a Level 0 product file that covers a time ordered set of data units ('instrument source packets') as well as header and annotation information. As a consequence of the downlink scenario the processing of MIPAS Level 0 data up to Level 2 will be performed on an orbit basis, and the information contained in the various data products will apply to the entire data set acquired over periods of approximately 100 minutes.

The information included in the Level 1B data product covers:

- scene geolocation parameters (for individual sweeps and for elevation scans)
- additional geometry data (e.g., line-of-sight (LOS) tangent height & error information, Doppler correction parameter, local Earth surface curvature)
- copy of processed deep space calibration data included in the Level 0 input data
- spectral calibration parameters computed for and valid over the processed orbit segment
- copy of radiometric gain calibration data (if such data were acquired within the processed orbit segment)
- product confidence data, extracted from instrument raw data or derived during processing of scene and calibration data
- information on actually valid processing input data (by direct inclusion in the product or via references to separately stored auxiliary data sets)
- processor setup and configuration parameters

- parameters supporting the identification and extraction of individual data sets.

Starting from the Level 1B data set, the Level 2 processor will extract specific subsets of the calibrated radiance data and perform retrievals of atmospheric pressure, temperature and trace gas volume-mixing-ratio (VMR) profiles. Again, a number of supplementary parameters will be computed for inclusion in the Level 2 data product, together with the retrieved profile and related variance/covariance (VCM) data. In summary, the information included in the Level 2 data product comprises:

- elevation scan geolocation and LOS tangent height data
- retrieved tangent pressure and temperature profiles, LOS tangent height corrections, related VCM data
- VMR profiles of the target species O_3, H_2O, CH_4, N_2O, HNO_3, VCM data
- derived trace gas concentration profiles and vertical column densities
- information on processed spectral intervals ('microwindows') and used height ranges for each target gas (CO_2 (for p, T), O_3, H_2O, CH_4, N_2O, HNO_3)
- fitted radiance offsets and continuum absorptions in processed microwindows and height ranges
- product confidence data (PCD)
- fitted radiance offsets and continuum absorptions in the processed spectral intervals ('microwindows)
- information on valid/used auxiliary data
- processor setup and configuration parameters
- parameters supporting the identification and extraction of individual data sets.

Table 1 summarises the MIPAS products and related auxiliary data.

TABLE 1. Summary of MIPAS products

1. Level 1B		
Product ID	**Description**	**Size**
MIP_NL__0P	MIPAS raw (source packet) data in nominal measurement mode, time ordered. Header and general quality information	320 MBytes/ orbit
MIP_NL__1P	*Data Sets:* Calibrated limb radiance data in the MIPAS spectral bands (A: 685 - 970 cm^{-1}. AB: 1,020 - 1,170 cm^{-1}. B: 1,215 - 1,500 cm^{-1}. C: 1,570 - 1,750 cm^{-1}. D: 1,820 - 2,410 cm^{-1}) *Annotation data:* Geolocation data, product confidence data, processing parameters, NESR data, offset cal. data	330 MBytes/ orbit
MIP_xx1__AX (xx = CG, CO, CL, CS, CA, PS, MW)	**Auxiliary products** * Calibration data (gain, offset validation, LOS, ILS) * others (characterisation data, processing parameters, ...) * orbit state vector/attitude data	variable size & update rates
2. Level 2		
MIP_NL__2P	*Data Sets:* Vertical profiles of p, T, O_3, H_2O, CH_4, N_2O, HNO_3. Variance/covariance data. *Annotation data:* Geolocation data, product confidence data, used microwindows & height ranges, fitted continuum/offset data, processing parameters	5.5 MBytes / orbit
MIP_xx2__AX (xx = CS, SP, MW, OM, IG, PI, PS)	**Auxiliary products** * Cross-section LUT's, (spectroscopic line data), microwindows data, atmospheric profiles, a priori pointing data, processing parameters * ECMWF: Meteorology forecast data	variable size & update rates

Product Confidence Data (PCD) and performance monitoring

Both Level 1B and Level 2 products contain various types of quality information that are routinely derived either directly from instrument raw data or during individual on-ground processing steps. These so-called product confidence data (PCD) serve the following purposes:

- indicate health status of main instrument components and check settings of vital operational parameters
- monitor critical instrument performance parameters and detect possible long term drifts
- check overall L1B/L2 processor performance and verify correct settings of parameters controlling numerical accuracies and runtime performance
- generate input parameters for use in subsequent ground processing steps (e.g., spectral band validity information in Level 1B data, used in Level 2 pre-processing)
- provide the users with supplementary information required for a correct interpretation of data products.

The analysis of PCD information may result in a modified calibration scenario, in changed settings of instrument parameters (e.g., on board signal processing) or in a change of ground processing auxiliary data. Examples: Optimisation of control parameters for in-flight spectral calibration/ILS retrieval (Level 1B) or of critical tuning parameters of the Level 2 profile retrievals.

TABLE 1. MIPAS Product Confidence Data (list not complete)

Product	Data Set	Description[a]
Level 0	Specific Product Header (SPH)	Summary quality information
	Measurement Data Set (MDS)	Information on detected transmission errors
Level 1B	Summary quality annotation data set (SQADS)	General PCD's (no. of corrupted sweeps in product due to different error sources, ...)
	MDS	Information on detected fringe counts, spurious spikes; scene data validity flags (per spectral band)
	Scan Information ADS	Spectral calibration fit parameters, NESR assessment data
Level 2	SQADS	General PCD's (total no. of unsuccessful retrievals in product, per target species, ...)
	MDS # 1 ... 7	Last χ^2, ID of convergence criterion terminating iterations Var./covariance data of retrieved profiles and related fit parameters (partial χ^2, radiance offsets, continua in processed microwindows, ...)
	ADS (various)	* Number of macro/micro-iterations * Evolution of χ^2 & retrieved parameters during iterations * Residual spectra in microwindows, averaged over orbit segments.

a. See Ref. 2 & 3 for a detailed definition of these fields.

A number of PCD's will be monitored in the so-called Instrument Engineering Calibration Facility (IECF). For this purpose, subsets of Level 0/1B/2 data products are provided to the IECF and analysed on a regular basis. The IECF will be operated during the full ENVISAT mission lifetime, including the initial in-orbit phase (commissioning), and provide functionalities to adjust critical operational settings and on-board parameter tables. In addition, it will routinely monitor all generated calibration data and produce regular reports on the overall instrument and ground processor performance.

A summary of the primary MIPAS PCD is given in Table 2 (for a definition of Data Sets and Annotation Data see Section 3).

3. FILE STRUCTURES AND EXTRACTED PRODUCTS

General product structures and 'time stamps'

MIPAS product files are structured according to the general ENVISAT formatting rules. These distinguish the following 'generic' building blocks:

- **Main Product Header (MPH).** Fixed size standard header, identical for all ENVISAT products. It specifies basic product information such as origin of data, processing site, software version, UTC time of data sensing&processing
- **Specific Product Header (SPH).** Product specific header, containing information applicable to the whole product, such as geographical coverage of scene data, spectral band/grid parameters
- **Data Set Descriptors (DSD).** Provide information on structure, number and size of included data set records, and on referenced or included annotation data
- **Measurement Data Sets (MDS).** Include the actual radiance spectra (Level 1B) and the retrieved geophysical parameters and related quantities (Level 2), respectively
- **Annotation Data Sets (ADS).** Include MDS specific information related to acquisition or processing of individual data segments
- **Global Annotation Data Sets (GADS).** Include annotation parameters not linked to individual scene data but applicable to the entire processed data set.

An MDS is formatted according to a data set specific record structure. Each record corresponds to an individual processed measurement data unit and is identified by a unique time parameter, the so-called 'time stamp'. In a Level 1B product each record (MDSR) contains the spectral data of an individual sweep, with the time stamp corresponding to the time of interferometer zero path difference crossing (t_{zpd}). In the Level 2 product the MDS records contain sets of retrieved profiles and related output parameters. In this case the time stamp of the 'center of scan' sweep (i.e., the sweep closest in time to the center of scan) is chosen as reference. This accounts for the fact that the smallest data unit in Level 2 processing corresponds to a complete evevation scan sequence.

Similar to the MDS an ADS provides a sequence of records, each provided with a time stamp parameter. The time stamp is used to identify the ADS record (ADSR) corresponding to a particular MDSR. In general, each ADSR is linked to a single or a group of MDSR, spanning a specific sensing time interval. Since the time stamp of the first MDSR in a group to which a given ADSR refers is chosen as a common reference, a unique relation between each MDSR and a corresponding ADSR exists.

Figures 1 a) and b) illustrate the general structures of MIPAS Level 1B and Level 2 product files, respectively.

Extracted products

This 'time stamp' concept allows to extract subsets of MDS / ADS data from any Level 0, Level 1B or Level 2 product, according to a selected sensing time interval (or orbit segment). Any extracted data set, referred to as a 'child product', will be re-formatted in the same way as the full orbit product and contains the complete header information.

In addition to extraction by time interval, individual MDS or ADS can be extracted from a full orbit product ('parent product'). In any case, the included data sets and the covered sensing time interval in a child product can be identified by inspecting the SPH and DSD information.

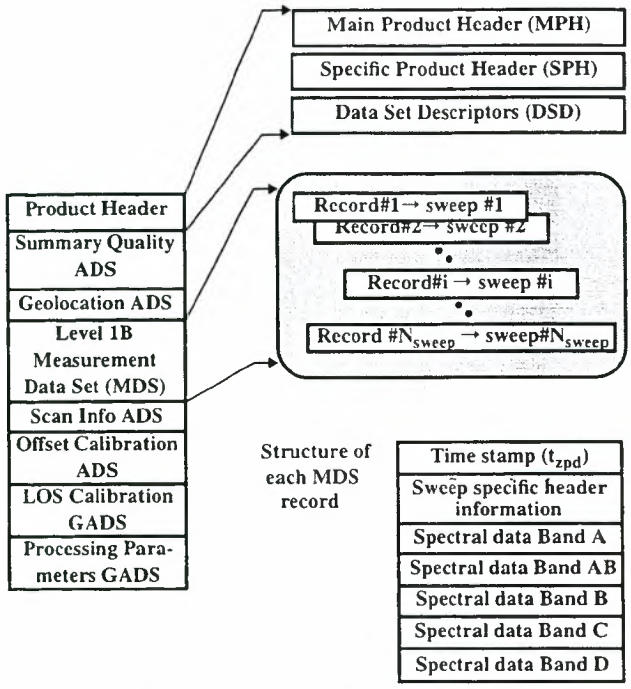

Figure 1 a) *Structure of a Level 1B product file*

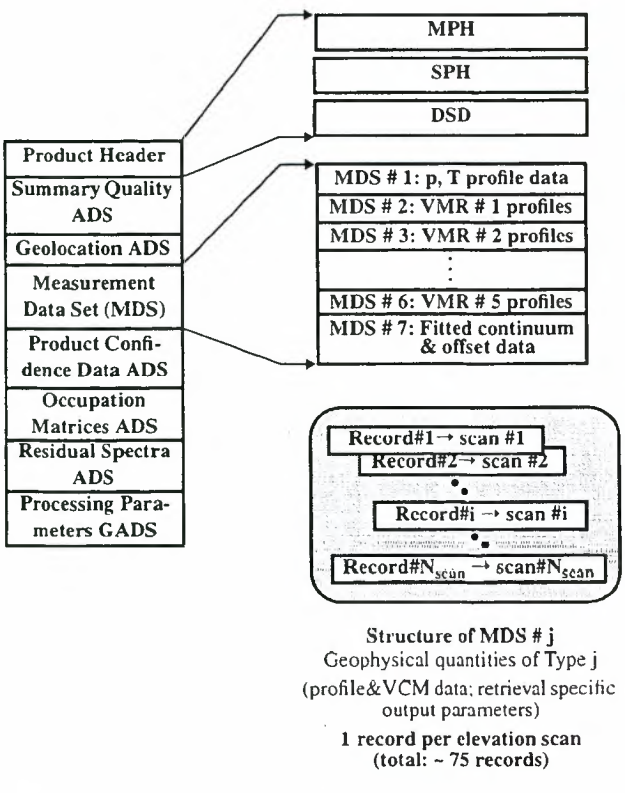

Figure 1 b) *Structure of a Level 2 file*

4. PROCESSING STRATEGY AND DISSEMINATION

Near Real Time (NRT) processing concept

As already discussed the recorded MIPAS raw data will be 'dumped' to one of two receiving ground stations, located in Kiruna (S) and at ESRIN/Frascati (I), respectively. Co-located with the receiving stations are the so-called Payload Data Handling Stations, PDHS-K (Kiruna) and PDHS-E (ESRIN). The PDHS will perform the processing the re-formatted instrument raw data (Level 0 data) up Level 1B & 2 data products immediately after reception of the payload data. Since both PDHS host MIPAS processing facilities and maintain local archives they are capable of generating and disseminating data products within approx. 3 hours after sensing. This so-called near real time (NRT) concept allows users to access MIPAS Level 1B and Level 2 data in a period from ca. 3 hours to 4 weeks after sensing. After that period the so-called consolidated Level 1B products (reformatted to cover orbit periods from ascending node to ascending node and using refined orbit information) and off-line Level 2 data products will be accessible. The Level 2 off-line products will be generated at the German Processing and Archiving Center, D-PAC[1]. Whereas Level 0 and Level 1B data, along with the Level 1B auxiliary sets, will be archived in the so-called Low Rate Reference and Archiving Center (LRAC) all Level 2 products (NRT and off-line) and corresponding auxiliary data will be archived in the D-PAC.

Handling of auxiliary data and overall data flows

The Instrument Engineering Calibration Facility (IECF) will perform a number of routine calibration activities, in addition to the already discussed monitoring tasks. In general, the IECF will process, monitor and systematically update all auxiliary data required by the Level 1B/Level 2 processing chain, with the exception of orbit state vector information and meteorology forecast/analysis data. Those data sets are provided by the Flight Operations Segment (FOS) and by the European Centre for Medium-Range Weather Forecasts (ECMWF), respectively, and routed to the PDHS via dedicated interfaces.

Fig. 2 provides a simplified view of the ENVISAT Ground Segment facilities relevant for MIPAS and indicates the primary data flows.

[1] The Level 2 off-line algorithm and corresponding auxiliary data will be implemented by the D-PAC. They are not discussed here.

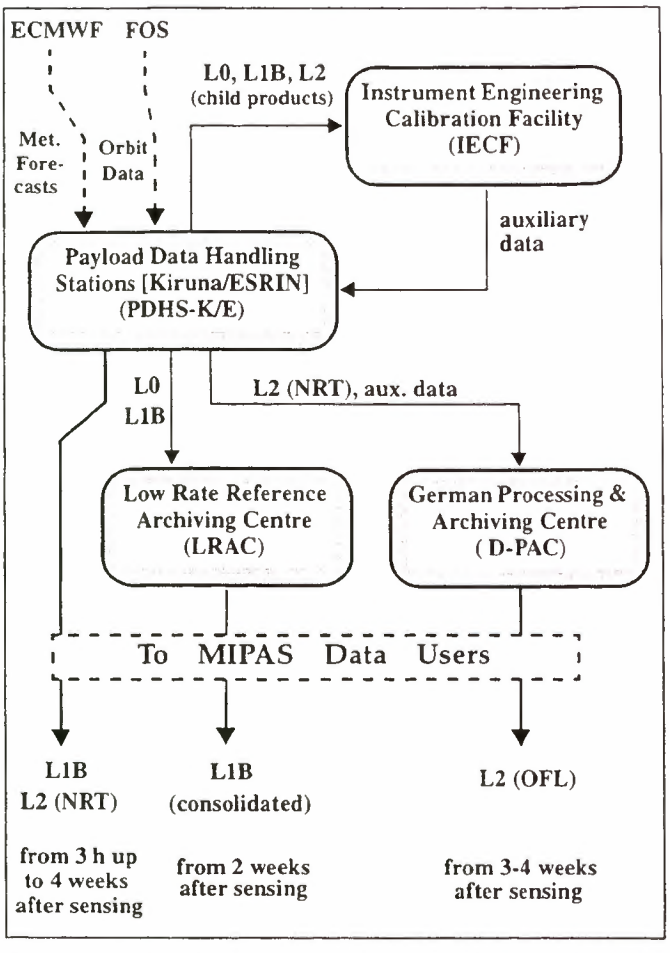

Figure 2 MIPAS Ground Segment facilities and primary data flows

5. CONCLUSIONS

The MIPAS ground processing scenario foresees routine generation, dissemination and archiving of MIPAS Level 0 / 1B / 2 products as well as the archiving of corresponding auxiliary data sets. Detailed file formats have been defined and implemented, for use in ongoing algorithm development and testing activities. The formats are in line with the generic ENVISAT product structures allowing to identify individual data sets and data set records. The extraction of Level 1B / 2 subsets is supported through Data Set Descriptors as well as sensing time and scene geolocation parameters, contained in header fields and annotation data. The monitoring of Product Confidence Data and the systematic updating of auxiliary data in the Instrument Engineering Calibration Facility will ensure the correction for primary sources of instrumental drifts and support the early detection of performance degradation of both instrument and ground processor components.

6. REFERENCES

1. Endemann, M., *MIPAS Instrument Concept and Performance* (this conference).

2. Lachance, R.L. et al, *Algorithm Theoretical Baseline Document (ATBD) for MIPAS Level 1B Processing*, PO-TN-BOM-GS-0012, Technical Note, ESA Contract 12303/97/NL/GS.

3. Carlotti, M. et al, *High Level Algorithm Definition and Physical and Mathematical Optimisations'*, TN-IROE-RSA9601, Technical Note, ESA Contract 11717/95/NL/CN.

MIPAS LEVEL 1B ALGORITHM TECHNICAL BASELINE DOCUMENT: AN OVERVIEW

Richard L. Lachance, Ph.D.†

BOMEM Inc., 450 St-Jean-Baptiste, Québec, Canada, G2E 5S5

ABSTRACT

This paper describes the Level 1B algorithms needed for the ground segment in order to produce meaningful data meeting all the requirements of the MIPAS instrument. Level 1B data is geolocated, radiometrically and spectrally (frequency) calibrated spectra with annotated quality indicators. The present paper summarizes the Algorithm Technical Baseline Document (Ref. 1) intended to the user community and all MIPAS related people.

1. INTRODUCTION

The Michelson Interferometer for Passive Atmospheric Sounding (MIPAS) is an ESA developed instrument to be operated on board ENVISAT-1 as part of the first Polar Orbit Earth Observation Mission program (POEM-1).

MIPAS will perform limb sounding observations of the atmospheric emission spectrum in the middle infrared region in the spectral range from 4.15 to 14.6 μm (685 – 2410 cm^{-1}). At the core of the instrument is a Fourier transform spectrometer that measures with one sweep the spectral features within the entire spectral range with high spectral resolution (less or equal than 0.035 cm^{-1} FWHM unapodized) accuracy and throughput.

Horizon will be observed with an instantaneous field of view that corresponds at the tangent point to 3 km in vertical direction and 30 km in horizontal direction. MIPAS is equipped with two scan mirrors that allow making measurements in either of two pointing regimes. One regime covers horizontally a 35 deg range in anti-flight direction (rearward) whilst the other one covers a 30 deg wide range sideways in anti-sun direction. The majority of measurements will be made in rearward viewing, as the observation geometry provides good coverage including the polar regions. For special events monitoring, the instrument can be commanded in both rearward and sideways viewing geometries. Vertical pointing range covers the tangent height from 5 to 150 km.

An elevation scan sequence comprises a sequence of interferometer sweeps (data recording for a single interferogram) within a fixed time interval at variable elevation and azimuth with respect to the MIPAS local normal reference frame.

One basic elevation scan sequence will comprise sixteen high-resolution atmospheric scene measurements (or up to 75 scene measurements but with reduced spectral resolution (1/10)) and will take about 75 seconds. A typical elevation scan will start at about 50 km tangent height and descend in 3 km steps to 5 km. As the initial angles and the step sizes of the azimuth and elevation scan mirror are programmable any other elevation scan sequence can be realized.

The MIPAS interferometer has a dual port configuration, i.e. it has two input ports and two output ports. Only one input port is actually needed to acquire data from a given scene. Thus, the second input port is designed to look at a cold target in order to minimize its contribution to the signal. The signals detected at both output ports are, in principle, similar and can be combined in order to improve signal-to-noise ratio. This setup has also the advantage of providing a certain redundancy. If a detector fails on one output port, the corresponding detector of the other port still provides useful data.

The MIPAS detectors are designed to cover the spectral range from 685 cm^{-1} to 2410 cm^{-1}. Eight detectors are used and the spectral range is split into five bands, each band being covered by one (two) specific detector(s). The chosen detectors and band arrangements assure redundancy and providing backup should one or more channels be lost.

The spectral bands and contributing detectors in Nominal Operation of the detectors are depicted in the following table:

Table 1. Spectral bands and detector arrangement

Band	Detector	Decimation factor	Optical Range [cm^{-1}]
A	A1 & A2	21	685 – 970
AB	B1	38	1020 – 1170
B	B2	25	1215 – 1500
C	C1 & C2	31	1570 – 1750
D	D1 & D2	11	1820 – 2410

For more details about MIPAS, consult (Ref. 3).

Essentially, the Level 1B algorithms consist of calibrating the incoming raw interferograms coming from the instrument. Calibration, in the sense used within the ENVISAT-1 program, is the procedure for converting instrument measurement output data into the required physical units. For MIPAS, the output of the ground processor is an atmospheric spectrum showing radiance as a function of wavenumber. Calibration refers not only to the assignment of absolute values in radiance units (noted [r.u.] expressed in $W/(cm^2\ sr\ cm^{-1})$) to the intensity axis (y-axis), but also to the assignment of absolute spectral values in cm^{-1} to the wavenumber axis (x-axis). A third geometric calibration is also required to assign an absolute LOS pointing value to each atmospheric spectra. All of these three calibrations must be performed within a specified accuracy.

Validation will also be performed, converting instrument measurement data into a representative indicator of the quality of the measurement.

† Further author information – tel: (418) 877-2944, fax: (418) 877-2834, richard.lachance@bomem.com

January 15, 1999

2. GROUND PROCESSING PRINCIPLES

Generally speaking, the ground processing system has to mathematically retransform the scene interferograms from the MIPAS instrument into spectral information useful to scientists, considering all relevant data from calibration measurements, from characterization measurements for calibration and from characterization measurements for validation in order to yield fully calibrated spectra. All this information will enable to retrieve atmospheric key parameters that will be computed by the Level 2 algorithms not described here.

2.1 Measurement principle

In order to properly calibrate the radiometric output from the instrument, it is also necessary to acquire regularly, during the course of the mission, two additional types of measurements on well-defined targets. The first one is done with an internal high-precision calibration blackbody (CBB). For the second measurement, the instrument is simply looking at the deep space, which represents a source of low (negligible) radiance.

Of all the measurement types, only the scene measurements contain the desired scientific information, i.e. spectra of the atmosphere. All other measurements are characterization measurements for calibration. Following the acquisition, the ground segment has to perform a Fourier transform of the interferograms and a calculation of the instrument response, based on the calibration measurements, in order to recover the original spectrum in calibrated radiance units (Section 2.3).

No dedicated measurement is taken on board for precise spectral calibration because it is assumed that spectral calibration will be possible using known features in nominal scene measurements (Section 4.4).

Finally, it is necessary to perform geometric calibration measurements to assess line-of-sight pointing errors. For that purpose, the instrument is operated as a simple radiometer measuring the signal from stars crossing the instrument field of view.

The on-board recording of MIPAS data and the data downlink to different ground stations is performed independently of the actual measurements performed. The Level 1B ground processor has therefore to cope with raw data packages (Level 0 data) which do not start necessarily with an offset calibration or the first sweep in a limb sequence.

2.2 Measurement modes

The default operational mode of MIPAS is in *measurement mode*. In this mode either IR-radiation from the atmosphere, from the deep space or sequentially from the deep space and from an internal blackbody source is entering the spectrometer. In nominal measurement mode, measurements of radiation originating from the atmosphere are taken at high resolution.

2.2.1 Scene Measurements

MIPAS will take measurements of the atmosphere at different altitudes. The elevation range is scanned in discrete steps using the elevation mirror. A single scene measurement is taken at each elevation value.

2.2.2 Deep Space Measurements

Looking at the deep space (DS) provides a "cold" scene, i.e. a scene with negligible IR radiance. The measured interferogram is then related to self-emission of the instrument. This offset is subtracted from the scene and blackbody measurement during on-ground data radiometric calibration processing. DS measurements are performed frequently (once every four elevation scan) in order to account for changing instrument self-emission due to temperature variations in the orbit. Offset measurements are performed at reduced resolution (1/10).

2.2.3 Calibration Blackbody Measurements

For radiometric (gain) calibration, the instrument is sequentially looking at the deep space and at a well-characterized internal blackbody source to characterize the instrument responsivity. These measurements are also repeated regularly because of the expected responsivity variations. In order to improve the signal to noise ratio and consequently the achievable gain calibration accuracy, many interferograms from the deep space and the internal blackbody reference source are recorded and co-added on the ground. Radiometric calibration measurements are performed at reduced resolution (1/10). The baseline is to perform this calibration every week.

2.3 Calibration Equation

The basic approach for determining absolute radiance measured by a FTIR spectrometer is the same as that used for filter radiometers and has been used successfully for many other interferometric applications (Ref. 2). The detectors and electronics are designed to yield in principle an output which is linear in the incident radiance for all wavenumbers in the optical passband of the instrument, and two reference sources are viewed to determine the slope and offset which define the linear instrument response at each wavenumber.

The measurement obtained by the system is proportional to the spectral power distribution at the detector. The latter is composed of the emission coming from each input port, along with thermal emission of the spectrometer.

The general relationship between an interferogram and its equivalent spectrum can be expressed as:

$$\tilde{S}(\sigma) = \mathcal{F}\{I(x)\} \qquad (1)$$

where the left side of the equation (spectral domain) denotes the spectrum as a function of wavenumber (σ), and the right side (spatial domain) denotes the Fourier transform of the interferogram as a function of the optical path (x). As the measured interferogram is not symmetrical (because for example of dispersion effects in the beamsplitter and electronics), the resulting spectrum will be complex (represented here by the tilde notation).

Measurements can be expressed as:

$$\tilde{S}^M = \tilde{G}(L^M + \tilde{O}) \qquad (2)$$

$\tilde{S}^M(\sigma)$ is the calculated complex spectrum from the measurement (arbitrary units, commonly referred to as digitalization units [d.u.]).

$L^M(\sigma)$ is the true incident spectral radiance from the *scene* (in [r.u.]).

$\tilde{G}(\sigma)$ is the overall spectral responsivity of the instrument, referred to as *gain*. it is a complex function to include interferogram phase delays,

$\tilde{O}(\sigma)$ is the instrument emission, referred to as *offset*, it is the stray radiance, including all modulated radiance that does not come from the scene (in [r.u.]).

To be more precise, we should state that the instrument line shape (ILS) is implicitly included in these terms, as:

$$L^M(\sigma) = L^M_{TRUE}(\sigma) \star ILS(\sigma, \sigma_0) \qquad (3)$$

where the $\star$ represents the convolution operator. Moreover, zero-mean noise is also present in this equation and its standard deviation is given by the NESR of the instrument.

Equation (2) expresses the linear relationship between the true spectral radiance and the measured, uncalibrated spectrum. Two non-equivalent calibration observations made at cold (T^C) and hot (T^H) temperatures are required in order to determine the two unknowns, that are the gain and the offset radiance as defined in Equation (2). The offset is the radiance, which, if introduced at the input of the instrument, would give the same contribution as the actual emission from various parts of the optical train.

For the MIPAS instrument, as the cold reference measurement obtained by looking at the deep space corresponds to an emission at a very low temperature ($T^C \approx 4$ K « T^M), one can safely make the approximation that the cold term has a negligible spectral radiance ($L^C \approx 0$). The calibration equation can then be expressed in the simplified form:

$$L^M = \left(\frac{\tilde{S}^M - \tilde{S}^C}{\tilde{S}^H - \tilde{S}^C} \right) L^H \qquad (4)$$

where L^H is the hot calculated blackbody radiance, modeled by the theoretical spectral radiance of the observed internal calibration blackbody.

If no error distorts the measurement, this expression for the calibrated radiance given in Equation (4) leads to radiance L^M with no imaginary part. When non-linearity is present, a special correction must be applied on different interferograms coming from affected detectors.

2.4 Filtering and decimation

In order to lower the size of the signals to be transmitted, measured interferograms will be filtered and decimated.

Neglecting the dispersion phenomenon inducing a non-null phase, an observed interferogram is basically a real and symmetrical function. The symmetry is about ZPD and, by extension about every multiple of MPD. The Fourier transform of such an interferogram is a real and symmetrical spectrum with symmetry about every multiple of the sampling frequency. In other words, the full spectrum will show on one half the true physical spectrum and on the other half the image of this spectrum. Depending on the convention, this second half may be displayed as negative frequencies or as frequencies above the sampling frequency divide by 2, as displayed in Figure 1

For a given sampling rate of σ_s (equal to 7692 cm^{-1} for MIPAS, corresponding to a laser operating at 1.3 μ), the Nyquist sampling theorem states that this sampling frequency defines a fixed spectral band of maximum width $\sigma_s/2$. This spectral band is quite large and can be reduced. The principle of data compression is to sample at a lower rate by decimating the interferogram (taking one point out of n) already sampled by the metrology laser system. The result is a reduced number of interferogram data points that permits a smaller data throughput.

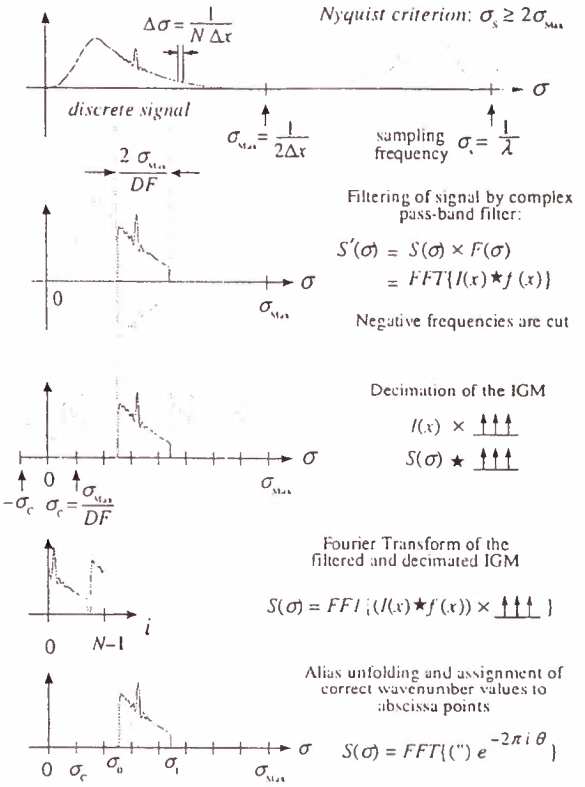

Figure 1: Filtering and decimation scheme

When a spectrum is band limited between σ_0 and σ_1, the sampling frequency can be reduced up to $2\sigma_1$ without any information loss as stated by the Nyquist sampling theorem. Reducing the sampling frequency further can produce spectral overlap that disturbs the interesting information (aliasing effect). However, since there is a useless spectral region from 0 to σ_0, it is possible to sample at a lower rate than $2\sigma_1$ and still keep all the information. For a real filtered signal, where both the desired physical band and its image are present, the lowest possible sampling frequency preserving the information is twice the spectral bandwidth $\sigma_s = 2(\sigma_1 - \sigma_0)$.

For MIPAS, complex filters have been devised in such a way that it has no image passband, by defining its imaginary part anti-symmetrical such that it produces a compensating negative image. After such a filtering, the only undersampling condition is:

$$\sigma_s = \sigma_1 \quad \sigma_0 \qquad (5)$$

Thus, the decimation factor can be two times larger after complex filtering. The integer ratio of the initial sampling frequency to the new one is called the *decimation factor*, noted

DF. Since the folding frequencies are not restricted to be out of the band of interest, there is no additional restriction on the decimation factor. It is then possible to better optimize the decimation factor. This is where a gain can be made with respect to data reduction.

The shape of the apodization function applied to the filtering impulse response (FIR) is critical. It must produce sufficient smoothing of the filter, but must avoid widening it to the point of reducing too much the effective bandwidth of the pass bands and the possible data compression. MIPAS FIR filters respect these criteria and are defined over 256 taps using 16-bit coefficients. The isolation of the various MIPAS filters range from 65 to 87 dB (Ref. 4).

The processing needed for the proper recovery of the wavenumber axis for each spectrum consists of computing a Fourier transform of the decimated signal, unfolding of the spectral axis (for cases where spectral limits do not exactly correspond to an integer factor of the band width), followed by axis limit identification. Further details about this procedure can be found in (Ref. 1).

3. Special Considerations

In this section, we will consider special aspects of the ground processing. The present topics are considered because of their inherent complexity or criticality.

3.1 Spikes detection/correction

This function has the purpose of detecting spurious spikes in an interferogram. The presence of spikes in an interferogram can be caused by cosmic radiation or transmission errors. The affected points in a scene interferogram are corrected by taking the mean between immediate non-affected points. This scene will be flagged of having corrected for one or more spikes. If a spike is detected in a gain or in an offset measurement, this measurement will be discarded in order to avoid corrupting all of the subsequent calibrated spectra (Ref. 5).

The algorithm performing spike detection scans groups of points in the interferogram (odd number with central block corresponding to ZPD block) in search of spikes. In each block, except for the central ZPD region of the middle block, the standard deviation of the interferogram values is computed, and a spike is identified if a given point amplitude exceeds a predefined threshold for values in the real or the imaginary parts. To improve the accuracy of the algorithm, A second pass is done excluding the data points identified as spikes to calculate the final standard deviation of the group.

For each detected spike, the value at the specific wavenumber is replaced by a mean of the two immediate points in the interferogram vector. The real part and the imaginary part are corrected independently.

The spike correction will always cause some distortions with respect to the original spectrum, but it has been shown that this distortion is within the radiometric accuracy requirement.

3.2 Fringe count errors detection and correction

The basic ground processing for MIPAS contains no explicit phase correction or compensation. For a given interferometer sweep direction, it is assumed that the gain and offset calibrations and also the scene measurements have the same phase relationship, i.e. they are sampled at precisely the same intervals. This sampling is determined by a metrology fringe counting system using a reference laser source within the interferometer subsystem, with the fringe counts forming a "clock" signal to the ADC in the on-board signal processor electronics (SPE). The fringes trigger the sampling of the IR interferogram. If, for any reason, a fringe is lost, then the phase of subsequent measurements will be affected and if these are calibrated using a gain or offset measurement taken before the occurrence of the fringe loss, then errors will be introduced into the final spectrum. The ground processing scheme includes a method for detecting and correcting fringe losses by analyzing the residual phase of calibrated spectra, computed from the central ZPD region of each interferograms. Hence there is no specific measurement required as part of calibration for this aspect.

In the following, we summarize the philosophy adopted for fringe count errors (FCE) detection and correction. The proposed approach assumes that fringe count errors occur at turn-around, i.e. between two measurements. Under this assumption, the effect of a fringe count error is to shift all measurements following the error by N points. The problem manifests itself at calibration because all the measurements involved may not have the same sampling positions, i.e. they do not have the same phase relationship.

Fringe count errors occurrence within a measurement is believed much less probable, and its effect is the same as if the error would have been at the turn-around. Thus it will be covered by the above assumption.

Fringe count errors can occur in all types of measurements done by the MIPAS instrument, except of course the LOS calibration measurements during which the sweeping mechanism is stopped. Depending on the type of measurement, the effect is not the same and therefore, the detection and correction approach will be different. Because the phase is not strictly the same for forward and reverse sweeps, the fringe count error detection and correction will be done independently for the two sweep directions. For all measurements, the fringe count reference interferogram of a given sweep direction will be the last gain interferogram of that sweep direction. The last gain interferogram can be either a deep space or a blackbody interferogram, depending on the acquisition scenario requested.

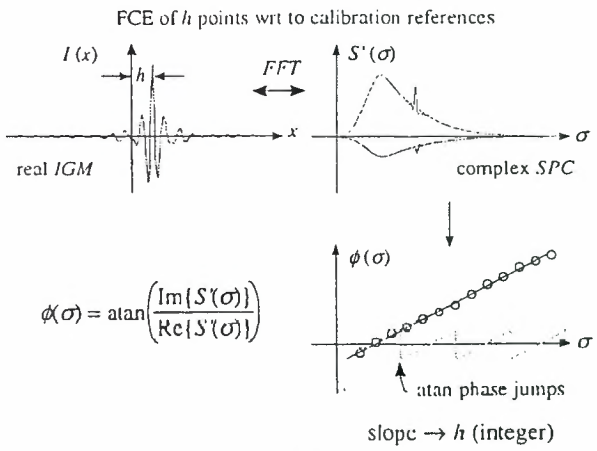

Figure 2: Fringe Count Error handling

3.2.1 Fringe count errors detection

The approach selected for fringe count error detection consists in a coarse radiometric calibration of the actual measurement at very low resolution, followed by an analysis of the residual phase. The radiometric calibration is done using the last available gain measurement. When the optical path difference (OPD) axis definition of the actual measurement is the same as the gain used for radiometric calibration, then the residual phase should be zero. A shift will produce a phase error increasing linearly with wavenumber.

Starting from Equation (1) relating the observed interferogram to the corresponding complex spectrum, we can re-write it for shifted signals in the following way using the shift theorem:

$$\tilde{S}'(\sigma) = \tilde{S}(\sigma)\, e^{-2\pi i \sigma k} = \mathcal{F}\{I(x-k)\} \qquad (6)$$

The algorithm simply performs a linear regression on the residual phase of the calibrated spectrum to reveal an integer shift k due to a fringe count error on the observed interferogram. The spectral phase is expressed as:

$$\phi(\sigma) = \tan^{-1}\left(\frac{\mathrm{Im}\{\tilde{S}'(\sigma)\}}{Re\{\tilde{S}'(\sigma)\}}\right) \qquad (7)$$

the shift k is extracted from the phase according to the relation:

$$2\pi k\, \lambda = slope = \frac{\Delta\phi}{\Delta\sigma} \qquad (8)$$

3.2.2 Fringe count errors correction

Once the OPD shift is known, the decimated interferogram must be shifted by a fractional number of points corresponding to this shift divided by the current *DF*. This requires some sort of interpolation. The current approach is to perform a multiplication of the Fourier transformed of the shifted IGM by the phase function obtained in the detection procedure.

$$I(x) = \mathcal{F}^{-1}\left\{\tilde{S}'(\sigma)\, e^{+2\pi i \sigma k}\right\} \qquad (9)$$

With this method, no manipulation is done on the OPD axis of the interferogram, but each data point is corrected to represent the value of its desired current OPD position.

It should be mentioned that fringe count errors will affect interferograms of all bands. For the MIPAS instrument, detection is done only for bands C and D.

The approach for fringe count error detection and correction will be the same for all types of measurements. However, the implementation will be somewhat different for the different types. This is discussed below. The fringe count error detection will be performed systematically on all incoming interferograms. However, the correction procedure will be applied only if a non-zero shift is detected.

3.2.3 FCE handling in offset measurements

Detection and correction are done with respect to the last available gain calibration. All the offsets corresponding to one orbit are aligned to the fringe count phase of this last gain. If one or more fringe count errors occur during the computation of one orbit, the ground processing will detect the same shift for all subsequent offset interferograms and will apply the same (always recalculated) correction on these offsets until the end of the processing of the orbit.

3.2.4 FCE handling in gain measurements

At the beginning of a gain measurement sequence, there is no reference against which one can check for fringe count errors. Thus, there is no relation between the actual measurement and the previous fringe counting reference. This is the main reason why we start with a new gain measurement.

Fringe count errors during gain calibration are checked by comparison with the first measurement of the sequence, typically a blackbody measurement (either forward or reverse). The first step is to determine the OPD shift between that measurement and the previous gain. The same procedure as for normal error detection and correction is then followed.

This corrected gain will then be used for detection of fringe count errors on all subsequent interferograms. In principle, the calibrated spectra obtained with this corrected gain should show no additional phase until a fringe count error occurs. Then, all error-free measurements will be coadded normally. Each time a fringe count error will be detected, a new coaddition group will be formed. When the complete calibration sequence is over, then all the coadded measurements are corrected with respect to the last measurement and the remaining processing of the radiometric calibration is performed normally. Correcting the gain with respect to the last measurement presents the advantage that all subsequent error-free measurements need no correction.

After processing the data corresponding to one orbit, if one or more FCE are detected, the current gain is shifted according to the last fringe count error measured. This is done in order to avoid correcting all the offsets and scenes in subsequent orbits.

3.2.5 FCE handling in scene measurements

When a scene is measured, its fringe count is checked against the last available gain calibration. All the scenes corresponding to one orbit are aligned to the fringe count phase of this last gain. If one or more fringe count errors occur during the computation of one orbit, the ground processing will apply the same correction on these scenes until the end of the processing of the orbit.

After that, the gain is shifted according to the last FCE to match the offsets and scenes of subsequent orbits. This way, the worst that could happen is that all the scenes of only one orbit would need to be shifted. All the subsequent processing of the orbits to follow would not suffer needlessly of a single previous FCE event.

This approach also minimizes the accumulating of numerical error on gains, that can be modified only after successive orbits. In practice, FCE are expected to occur very infrequently during processing of one orbit; but even if this would be the case, the fact of aligning offsets and scenes to the last available gain calibration would limit the error accumulation on the gain calibration vector.

This procedure will slightly increase the throughput for the reference gains used for the ground segment computation. There will be one each time at least one fringe count is detected during one orbit. But, as fringe count errors are expected to occur infrequently, there would usually still only be one gain vector per week and, should an error occur, only the gain would be modified after the processing of the corresponding orbit. The fact of realigning gain calibration vectors between orbits should save a lot of operations, as one

would otherwise be correcting every interferogram until the next gain calibration (the saving occurs independently of whether there are frequent fringe errors or not).

3.3 Non-linearity correction

The detectors from the first three MIPAS bands (A, AB, and B) are photoconductive (PC) detectors, subject to non-linearity depending on the total photon flux falling on them. Here, the non-linearity means that the response of the detector differs from a linear behavior as a function of the incoming flux. This phenomenon occurs at high fluxes.

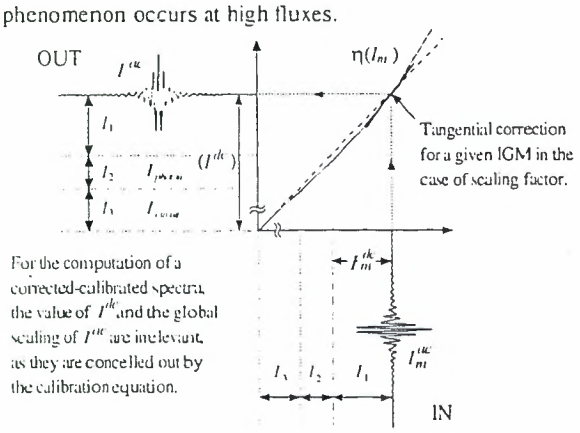

Figure 3: Non-linearity responsivity curve

With the MIPAS detectors, the non-linearity can be a source of significant radiometric errors if it is not properly handled (as much as 40% in band A). As explained in (Ref. 6), the non-linearity produces a change in the effective responsivity as well as the apparition of spectral artifacts. The present method corrects for the decrease of responsivity with DC photon flux in the radiometric calibration, within the required radiometric accuracy. The approach is the following:

A characterization must first be performed on ground, and then in space at specific intervals, at instrument level, of the total height of the unfiltered and undecimated interferogram (ADC^{Max} and ADC^{Min} values) with the on-board calibration blackbody at different pre-selected temperatures. These values will be used during the characterization phase for a computation of the non-linear responsivity coefficients. These values will be used to correct for the non-linearity of the detectors by means of a specific algorithm called the Adaptive Scaling Correction Method (ASCM).

Although they are intended to be combined in a single band, the optical ranges of the detectors A1 and A2 are not the same. They will then exhibit a different behavior with respect to photon flux. As a result, they will require different non-linearity corrections. Because of this, the signals from these detectors are not equalized and combined on board the instrument in the SPE. This operation is instead performed by the ground processor following non-linearity correction. The other two PC detectors, B1 and B2, are not combined in any case as they produce the bands AB and B. Other than the need to keep A1 and A2 separate in the baseline output set up at the SPE, the non-linearity measurements and correction has no impact upon the calibration scenario.

The important effect of detector non-linearity is on the radiometric accuracy performance. The present radiometric error budget allocated to the non-linearity in the 685 – 1500 cm^{-1} (where the detectors are the most non-linear) shall be better than the sum of 2 $NESR_T$ and 5% of the source spectral radiance, using a blackbody with a maximum temperature of 230K as source (Ref. 3).

A polynomial correction is then applied on each incoming interferogram, at the very beginning in the processing chain, with the purpose of compensating for the global effects of responsivity.

For the measured responsivity curves of the MIPAS engineering and demonstration model (EDM), the correction of the non-linearity error due to the change of effective responsivity and from the cubic artifacts have shown to lead to an accuracy within the allocated budget (Ref. 7).

3.4 SPE and PAW responsivity scaling

In practice, three scaling items need to be considered, as a result of the pre-amplifier warm (PAW) system:

1) A scaling to account for a commanded gain change

The gains are predefined and are commanded by an 8-bit word sent via the instrument control unit (ICU). Since different gains may be commanded, a data scaling in the ground segment to equalize performance must be foreseen. The commanded gain is available in the auxiliary data stream and so this is a simple scaling effect based on the extracted word.

2) A temperature dependent scaling to account for changes in responsivity of the detectors.

The detector units are specified to provide a stable response based upon assumed knowledge of their temperature (i.e. the responsivity may vary but it must be well characterized). For this reason, a correction of performance with time/temperature must be foreseen. This is made based on the measured detector temperature (available via thermistor values in the auxiliary data) and using characterization curves generated during characterization tests on ground.

3) A temperature dependent scaling (gain & possibly phase) to account for the variations in the performance of the electronics of the PAW and the SPE around the orbit.

At present, it is not thought necessary to correct for these effects around the orbit as predictions show the variations will not cause the units to drift out of specification. The In-Flight Calibration Plan (Ref. 8) foresees to make around orbit measurements during Commissioning Phase to check whether there are any such variations.

4. Ground Processing functions

The overall processing chain, divided into its high-level functions, will be processed in the following order:

1– Load Data
2– Calculate Offset Calibration
3– Calculate Gain Calibration
4– Calculate Spectral Calibration
5– Calculate Radiance
6– Calculate ILS Retrieval
7– Calculate Pointing
8– Calculate Geolocation
9– Format Product

Each of these functions is described in the following sections. Figure 4 summarizes the control flow between these various ground processing modules, while Figure 5 summarizes the data flow between the modules.

The *Format Product* function performs the packaging of all the processed spectra, computed calibrations and diverse processings performed on the raw incoming data into the Level 1B product, as defined in document (Ref. 9).

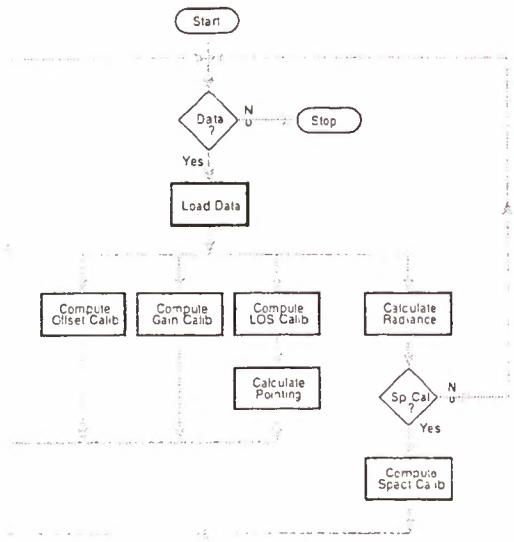

Figure 4: Ground Processing Control Flowchart

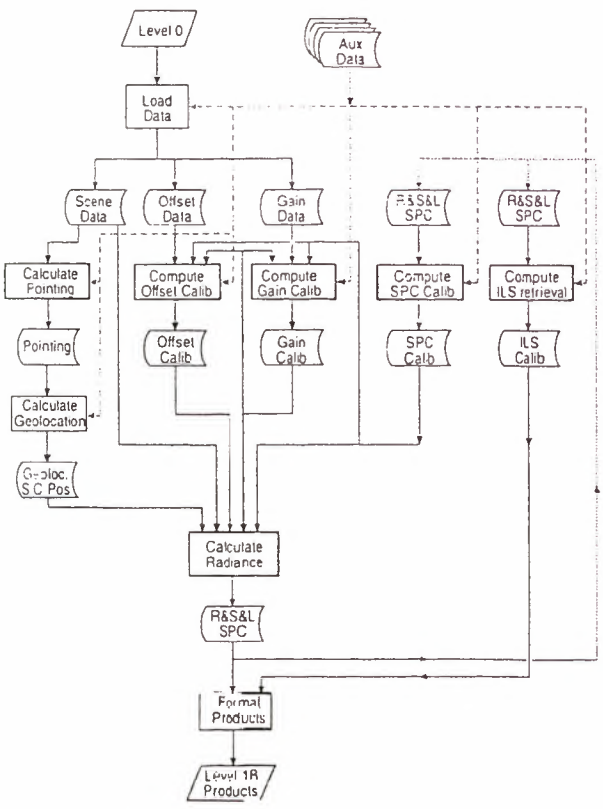

Figure 5: Ground Processing Data Flowchart

The conventions used in the flowchart of this paper are described below.

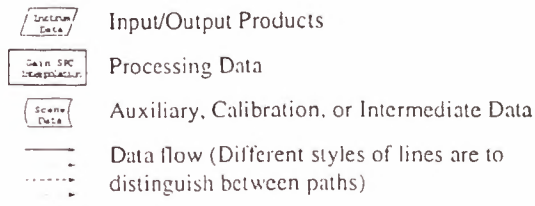

4.1 LOAD DATA

The *Load Data* function performs the initial processing of all incoming on-board instrument data. It converts data packets into single measurements properly identified and grouped. Auxiliary data is properly calibrated and complete reconstructed interferograms are sent to the proper function depending on the type of data.

It is assumed that incoming data have been demultiplexed and time ordered. These operations are normally common to all instruments of the platform and they will not be covered in the present document.

Specific objectives of the function are

- Receive MIPAS data source packets from the on-board instrument (Level 0)
- Extract data packets and form single measurements
  - Perform Error Correction (transmission errors)
- Calibrate relevant auxiliary data
  - UTC time computation
  - CBB PRT reading conversion into Kelvin degrees
- Sort measurement data according to the type of measurement (i.e. scene, blackbody, or deep space)
- Stack the calibration measurements into the relevant groups
- Generate and deliver preprocessed data (Level 1A)

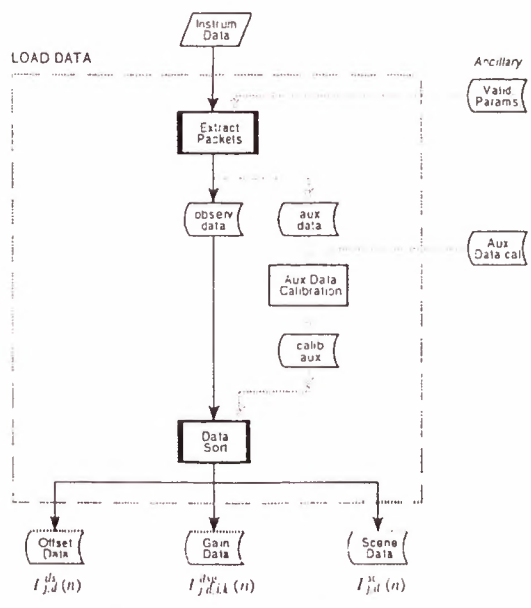

Figure 6: *Load Data* Flowchart

4.2 CALCULATE OFFSET CALIBRATION

The main objective of the *Calculate Offset Calibration* function is to deliver offset calibration measurement data in a form suitable for radiometric calibration of the spectra by the *Calculate Radiance* function. The computational sequence of this function is illustrated by the flowchart of Figure 7.

This estimate of the instrument contribution is made by simply pointing the instrument to deep space and performing a measurement cycle as in the nominal case. For practical reasons, the deep space measurement is taken at a tangential height of around 150 km. Also, due to the potential difference in phase between different sweep directions of the instrument, a measurement is taken in each of the forward and reverse directions of the interferometer. In the ground segment, the closest in time offset measurement (in the correct sweep direction) is simply subtracted from each interferogram during processing.

The signals detected during offset measurements arise mainly from noise sources in detectors/ amplifiers and from thermal emission of the optical components within the interferometer. Even if the spectrum will be weak, it is believed that fringe count errors can be effectively determined. The scheme applied to scene and calibration measurements will most probably detect the occurrence of fringe errors, and the use of all interferograms (including offsets) maximizes the chance of detecting and correcting the errors as soon as possible after their occurrence.

The zero offset measurements will be subtracted from the relevant individual interferograms. Logically, these measurements should be made at the same spectral resolution as the scene measurements themselves, in order that the vectors are directly comparable. However, it is not expected that any high resolution features will be present in the offset spectra, which means that the measurements may be made at low resolution, with an interpolation on the ground segment. This has the advantage of reducing the duration of the offset measurement.

The Offset Calibration will be performed every four scans, and use six sweeps at low resolution (three forward and three reverse), which must be combined to reduce the noise level to acceptable level. The total duration of the offset measurement is 16.15 seconds (including transition times), and measurements will then be made every 300.5 seconds.

For an orbit of 100 minutes, assuming all measurements are performed with the same scan scenario, there will be about 20 offset measurements per orbit, which is well above the necessary minimum computed by an examination of temperature variations.

Offset calibration will be performed such that the closest in time available valid offset measurement is used until a new valid offset measurement becomes available. If no offset data are found at the beginning of the Level 0 product input data set, then the first available offset found leading to valid measurement shall be used for all initial scenes. If one or more invalid offset measurements are detected in the middle of the input stream, then a "closest in time strategy" shall be applied, which means that complete scans shall be calibrated with the closest valid offset. If no valid offset at all is found in the input data, then the offset calibration data contained in the offset validation file shall be used.

Specific objectives of the function are:

- Perform spikes detection
- Sort offset data according to the direction of interferometer sweep.
- Coadd six interferograms in each band.
- Detect and correct fringe count errors in spectral bands C and D.
  - Gain spectral interpolation
  - Calculate coarse spectra
  - Calculate calibrated spectra
- Responsivity scaling
- Correct for detector non-linearity.
- Equalize and combine interferograms in band A.
- Assess NESR performance.
  - Accumulate statistics from deep space readings to obtain the NESR of the instrument
  - Check the validity of incoming readings

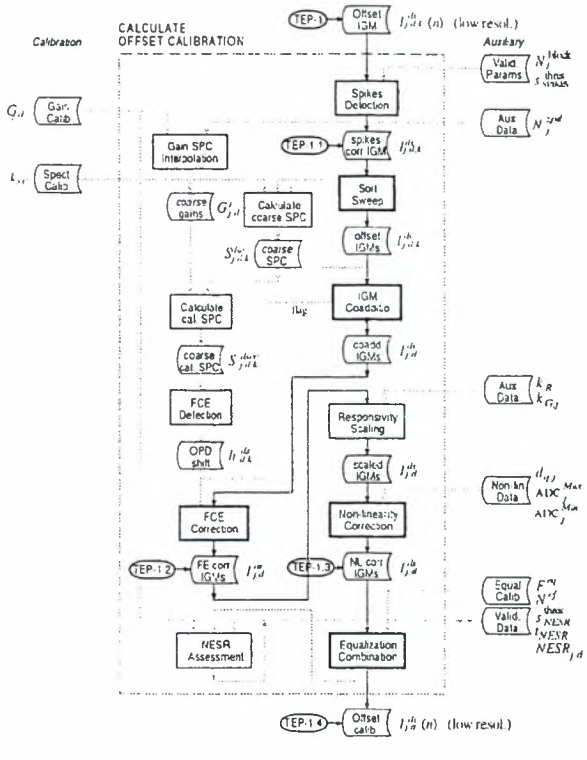

Figure 7: *Calculate Offset Calibration* Flowchart

4.3 CALCULATE GAIN CALIBRATION

The main objective of the *Calculate Gain Calibration* function is to deliver a file representing the radiometric gain of the instrument, computed using gain calibration measurements, in a form suitable for radiometric calibration of the spectra by the *Calculate Radiance* function. The computational sequence of this function is illustrated by the flowchart of Figure 8.

The radiometric gain calibration requires all deep space and blackbody measurements of the gain calibration sequence. Since in this case the instrument is again contributing to the observed signal, it is also necessary to perform deep space

measurements before the blackbody measurements in order to subtract the appropriate instrument offset. (In this instance, the term "Deep Space Radiometric Calibration" is used to distinguish the measurements from the regular Offset Calibration made with the scan sequences. The Deep Space (DS) Radiometric Calibrations are used only to correct the Calibration Blackbody (CBB) measurements and must be explicitly commanded. In fact, several measurements of each kind will be needed. This is because the signal to noise ratio of a single, offset-corrected, blackbody measurement is not high enough, particularly in band D, to achieve the required radiometric accuracy. Therefore a single gain calibration implies several successive measurements.

It is expected that there will be no high frequency features in either the CBB spectrum or in the instrument contribution (as assumed also for the offset calibration). These assumptions will be verified on the ground during instrument Assembly and Integration Test (AIT), but the assumption is reasonable. Therefore, each CBB or Deep Space sweep of the instrument will be made at low-spectral resolution, i.e. with a duration of 0.4 seconds. The baseline scenario uses 300 sweeps at low resolution in both forward and reverse directions for both CBB and DS measurements.

Specific objectives of the function are:

- Perform spikes detection
- Sort the gain calibration measurements according to types of measurement and sweep direction.
- Coadd interferograms to increase SNR.
- Detect and correct fringe count errors in spectral bands C and D.
  - Gain spectral interpolation
  - Calculate coarse spectra
  - Gain shift correction
  - Calculate calibrated spectra
- Responsivity scaling
- Correct DS and CBB measurements for non-linearity of each affected detector.
- Subtract offset due to contribution of the instrument.
- Equalize and combine interferograms in band A.
- Compute coarse spectra using a FFT algorithm applied on the zero-padded interferograms.
- Interpolate gain spectral vectors to provide the gain on a predefined spectral axis.
- Calculate expected blackbody radiance from temperature readings corresponding to blackbody measurements.
- Calculate the complex ratio of theoretical to calculated spectrum.
- Gain coaddition
- Check for radiometric accuracy of the incoming data.

Radiometric gain calibration will be performed after the instrument slides have been stopped in order to re-establish a phase reference. The gain sequence will therefore be commanded as the first operation in any nominal measurement sequence. Radiometric Deep Space Calibration measurements precede those made looking towards the CBB to cover the worst case condition of the instrument entering measurement mode directly after the boost heater phase of the CBB.

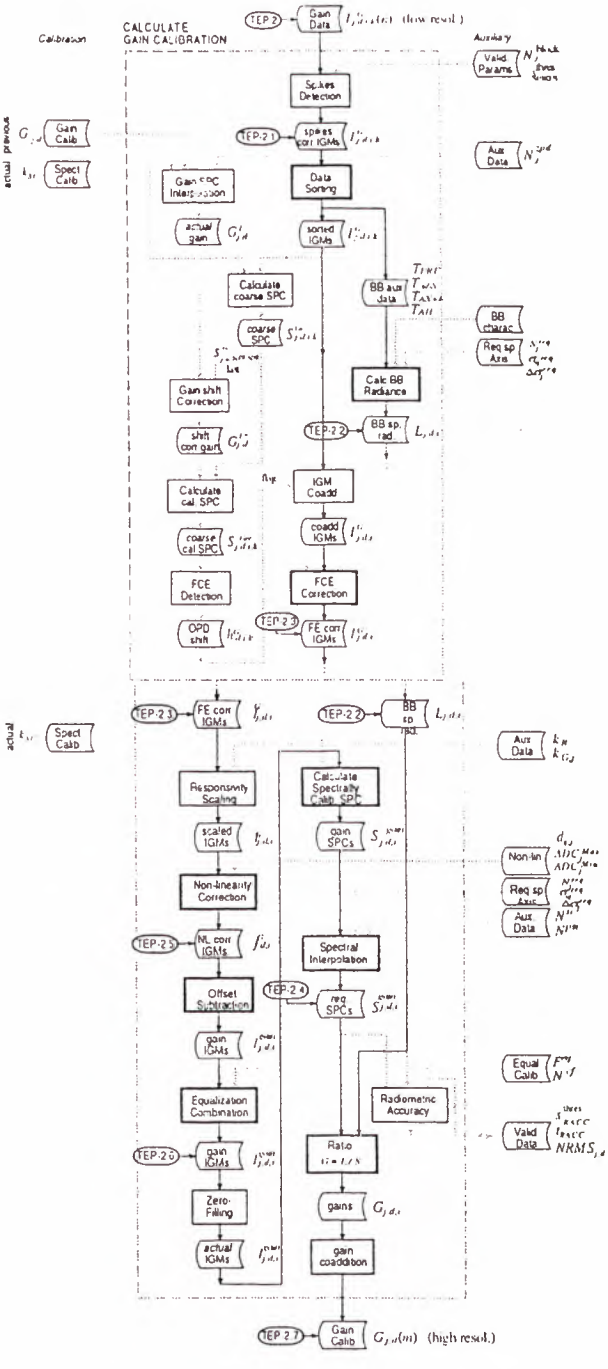

Figure 8: *Calculate Gain Calibration* Flowchart

The radiometric gain calibration has two commanded sequences, each of 600 low-resolution sweeps. In addition to the duration of the sweep sequences themselves, there will be two commanded transitions followed by an automatic transition. Each commanded sequence has a duration of 520.6 seconds. The total duration of the radiometric gain sequence (DS and CBB) is 17.35 minutes. With this duration required once par week, the baseline radiometric calibration easily satisfies the requirement.

The gain data shall be processed by the Level 1B processor at the beginning before scene data. During processing, the gain file shall not be modified by the processor.

4.4 CALCULATE SPECTRAL CALIBRATION

The *Calculate Spectral Calibration* function performs the processing of some selected (radiometrically) calibrated scene measurements and generates the spectral calibration data. The computational sequence of this function is illustrated by the flowchart of Figure 9.

Spectral calibration is performed in MIPAS using standard limb measurements from the atmosphere already corrected for the Doppler effect by the *Calculate Radiance* function. Specific reference spectral lines will be retrieved in the observed spectra according to the extremities of specific microwindows listed in a reference lines database. From these microwindows will be performed the line position identification, with respect to a database containing the exact known theoretical position of the reference lines. In order to reduce noise, equivalent scenes are coadded, i.e., scenes with altitude included in the range of the processing parameter file. The computed known values of the reference lines positions will be used to establish the assignment of the calibrated wavenumber to the index of spectral data points. Following this operation, spectral calibration will be used for the wavenumber assignment of all subsequent measurements until a new spectral calibration is performed.

The *Calculate Spectral Calibration* will be performed when it is appropriate to update the spectral calibration, with a current baseline of twice per day.

Because it is related to the same parameters, the spectral shift can be considered as a part of the instrument line shape. The disadvantage is that it is then necessary to perform a deconvolution of the ILS from an observed spectrum to get the proper wavenumber assignment. Here we will assume that the spectral shift is included in the spectral calibration, i.e. it is calibrated out by the spectral calibration procedure without any ILS deconvolution.

It is also assumed that the spectral calibration will be the same throughout the spectral range. It is assumed that the definition of the optical axis is common to all four detectors on the output ports, for both output ports. It is also assumed that the residual misalignment between the two output ports is low enough so that the difference in wavenumber is negligible.

Two algorithms have been proposed to perform spectral calibration: the Peak Finding Method (PFM) and the Cross-Correlation Method (CCM). The feasibility of both these methods have been demonstrated, and both algorithms have demonstrated strengths and weaknesses. The PFM has shown to be a little simpler to implement and faster to execute, but the CCM presents the advantage of giving information related to the precision of a given fit. Only the PFM is presented here, as it is the current baseline for operation.

The precision of the peak identification algorithm is proportional to the number of equivalent scenes that are coadded, as the noise affecting the signal decreases when multiple readings are superposed. This number will probably vary between 1 and 5 (to attain stability and a precision equal or less than 0.001 cm^{-1} (Ref. 10)), and will be defined in auxiliary data.

4.4.1 Fit peak

The Fit Peak subfunction consists in determing the position of the incoming selected spectral line. The peak fitting algorithm proceeds by the minimization of the sum of square residuals between a parametric mathematical function of the line shape and the measured spectrum data. Initial guesses are supplied to the mathematical function and a Simplex algorithm (Ref. 12, 13) iterates on these parameters until a minimum is reached. The final peak position is given by the horizontal position parameter b.

One of the mathematical model $f(\sigma, \text{params} = a,b,c,d)$ used for the fitting is a parametric sinc profile, where a represents the radiance intensity, b the spectral position, c the HWHM of the central peak, and d the DC offset of the signal:

$$g_s(\sigma) = a\,\mathrm{sinc}\left(\frac{\sigma - b}{c}\right) + d \tag{10}$$

4.4.2 Spectral axis definition

This subfunction calculates the basic parameters defining the spectral axis for each band, based on the computed peaks position. The basic parameters are the lower wavenumber, the spectral spacing between data points, and the number of data points. The scaling factor computed is also given as one of the spectral calibration parameters.

- $\Delta\sigma_j$ the spacing between spectral data points in the band
- σ_{0j} the starting wavenumber of the band
- N_j^{req} the number of points in the band
- k_{SC} the spectral calibration correction factor

With these parameters and the index of points m, the numerical vector can be generated according to the following formula:

$$\sigma = \sigma_{0j} + m \cdot \Delta\sigma_j \tag{11}$$

The spectral axis of a given band is defined by the spacing $\Delta\sigma$ between spectral data points in the band, σ_0 the starting wavenumber of the band, N the number of points in the band, and k_{SC} the spectral calibration correction factor

$$\sigma'_{0j} = \sigma_{0j} \times k'_{SC} \tag{12}$$

$$\Delta\sigma'_j = \Delta\sigma_j \times k^j_{SC} \tag{13}$$

Once the position of a selected experimental peak is known up to a given precision, the ratio k_{SC} between the reference and the retrieved position is computed, with a mean taken over each considered reference lines (with valid fit):

The operation of taking the mean for each peak shift is based on the assumption that the shift is linear as a function of wavenumber. This way, a simple linear correction by the multiplication of the spectral axis by a constant may be applied.

If the distribution appears to be non-linear, a polynomial fit (with zero origin) could be performed in order to correctly evaluate the amount of stretch of the spectral axis as a function of the wavenumber.

Spectral calibration will be performed such that the latest available valid spectral measurement is used until a new valid spectral measurement becomes available. If in the middle of the input stream invalid spectral calibration are calculated, then a "previous closest in time strategy" shall be applied,

which means that complete scans shall be calibrated with the previous valid spectral calibration. If no valid spectral calibration at all is available, then the spectral calibration data contained in the current ILS and spectral calibration file shall be used. Spectral calibration data shall be written to auxiliary file simultaneously with ILS retrieved data (see Section 4.6). Otherwise the file shall not be modified by the processor.

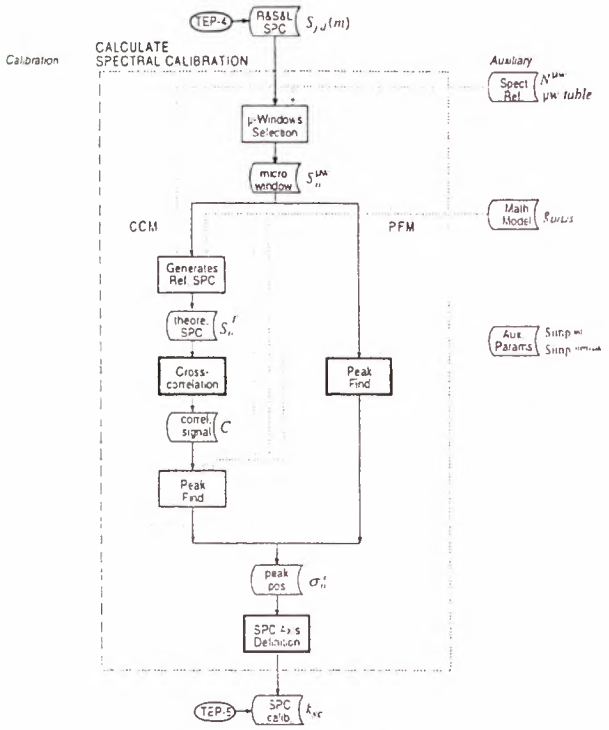

Figure 9: *Calculate Spectral Calibration* Flowchart

4.5 CALCULATE RADIANCE

The *Calculate Radiance* function performs the processing of the scene measurements and generates a radiometrically calibrated spectrum. This function assumes that gain, offset and spectral calibrations are available as soon as they are produced, so that they can be used for the processing of all scene measurements following these calibrations. If this is not the case, then processing will proceed with the latest available calibration data. The computational sequence of this function is illustrated by the flowchart of Figure 10.

Specific objectives of the function are:

- Perform spikes detection
- Detect fringe count errors in spectral bands C and D, and in the case of misalignment adjust the phase of the gain and offset according to the current fringe count.
  - Gain spectral interpolation
  - Calculate coarse spectra
  - Calculate calibrated spectra
- Responsivity scaling
- Correct scene measurements for non-linearity of each affected detector.
- Equalize and combine interferograms in band A.
- Subtract offset due to contribution of the instrument.
- Compute spectra using a FFT algorithm applied on the zero-padded interferograms.
- Correct spectral axis for Doppler shift and perform spectral interpolation onto a predefined uniform spectral axis.
- Interpolates spectrum over a pre-determined user's grid
- Radiometric calibration by a complex multiplication of the actual scene spectrum with the actual gain.
- Perform scene measurement quality verification.
- Report of NESR

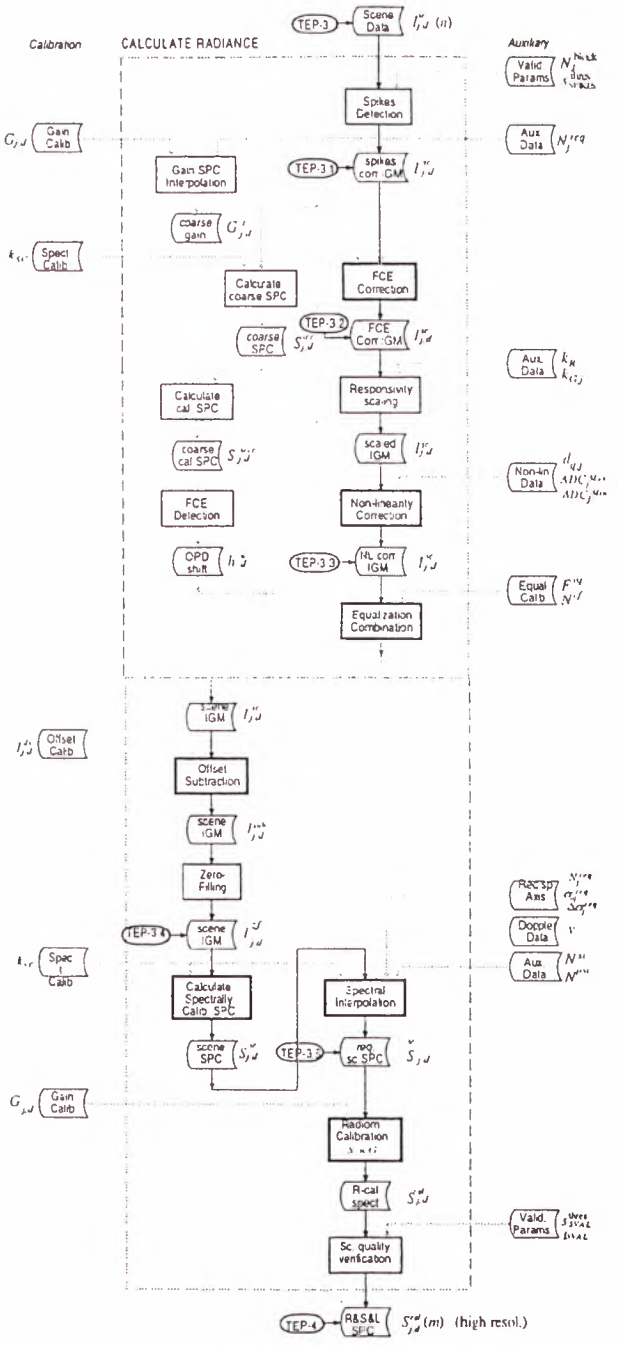

Figure 10: *Calculate Radiance Calibration* Flowchart

4.6 CALCULATE ILS RETRIEVAL

The *Calculate ILS Retrieval* function performs the instrument line shape (ILS) retrieval from radiometrically and spectrally calibrated spectra. The result of this operation is made available to the output data products. The computational sequence of this function is illustrated by the flowchart of Figure 11.

ILS retrieval has been studied extensively in the technical note (Ref. 10). A deconvolution approach has shown to be inadequate, but a second approach has shown to give good enough results. The chosen ILS retrieval method is called the "Parametric ILS Fitting Method" (PIFM). This method proceeds with a theoretical ILS, obtained by a modelization with a limited number of parameters, convolved with the theoretical line and iteratively fits the results onto the experimental data.

Appropriate peaks for spectral calibration that represent known features of standard scene measurements have been identified and studied in the document (Ref. 10). The precision of the peak identification algorithm is proportional to the number of equivalent scenes that are coadded, as the noise affecting the signal decreases when multiple readings are superposed. This number will probably vary between 2 and 10, and will be defined in auxiliary data.

The operation of ILS retrieval is more computer intensive than others tasks presented up until now, but this operation will be requested only from time to time, not on a regular basis as the computation of spectral calibration for example. Topics of the exact frequency at which the ILS retrieval shall be done is addressed here.

It has been chosen to extract the ILS in each detector band of the instrument on an appropriate spectral line located anywhere inside the band. The list of reference spectral lines will be stored in a table kept as auxiliary data.

The auxiliary data file containing retrieved ILS parameter data and spectral calibration data shall be produced by the Level 1B processor according to the processing parameter file. An initial ILS and spectral calibration auxiliary file will be given as an input to the processor at all processing stations and shall be used until the next file will be made available. ILS and spectral calibration data will be written to the auxiliary file simultaneously (i.e., only ca. once per week). Otherwise the file shall not be modified by the processor.

Specific objectives of the function are:

- Select specific microwindows containing precisely one reference peak of well-known wavenumber.
- Obtain or generate the reference theoretical spectral line corresponding to this microwindow.
- Fit an ILS to the incoming raw spectrum by minimizing residuals between the reference line and the parametric ILS.
- Store the iterated parameter set and the specific wavenumbers as a Level 1B product.

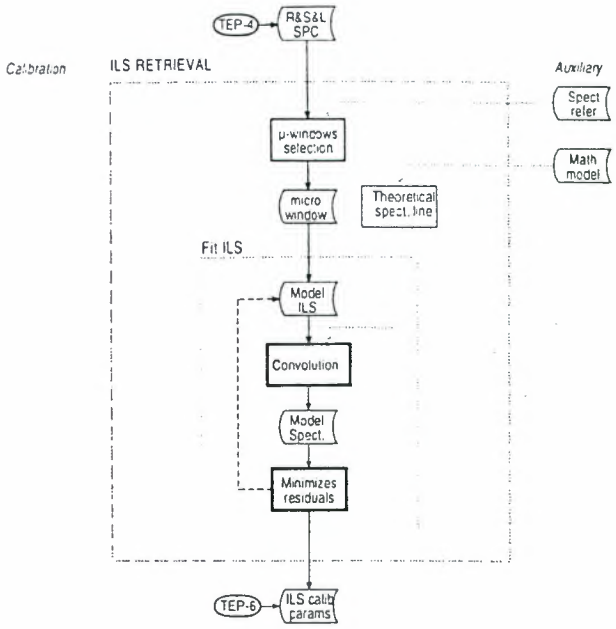

Figure 11: *Calculate ILS Retrieval* Flowchart

4.7 CALCULATE POINTING

The *Calculate Pointing* function performs the line of sight (LOS) pointing calibration in order to generate corrected LOS pointing angles. The algorithms are covered in details in document (Ref 11). The main objectives of the Calculate Pointing function are

- Compute correction of elevation pointing angle,
- Compute corrected pointing angles of actual scene (sweep).

The *Calculate Pointing* function is based on the following assumptions. It is assumed that commanded elevation angles are only partially corrected with respect to known pointing errors according to the best knowledge based on-ground characterization and LOS calibration measurements. The remaining elevation error, obtained from LOS calibration measurements, shall be computed in the ground segment (PDS) and be used to correct in measurement mode the measured elevation angles. The corrected elevation angles and the measured azimuth angles are used to compute the geolocation (height/longitude/latitude) of the actual scene (target).

Specific objectives of the function are:

- Compute the actual pointing error at time of ZPD crossing
- Compute actual azimuth pointing angle
- Compute correction of elevation angle
- Compute actual elevation pointing angle

The computational sequence of the *Calculate Pointing* function is illustrated by the flowchart of Figure 12.

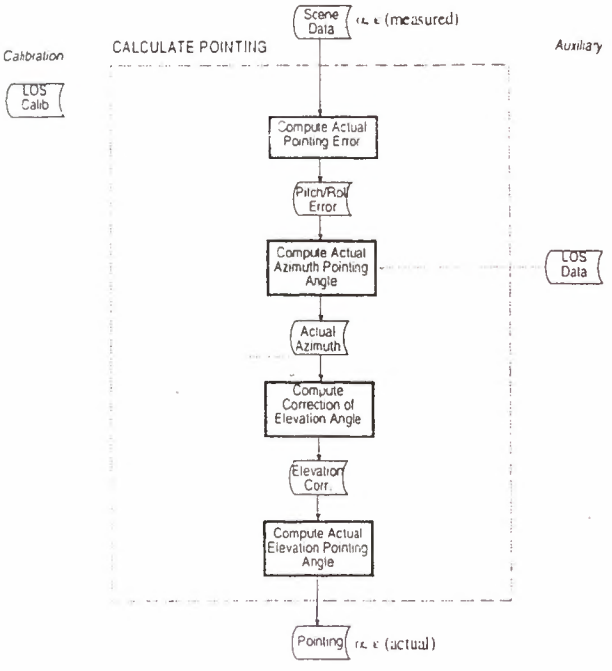

Figure 12: *Calculate Pointing* Flowchart

4.8 CALCULATE GEOLOCATION

The *Calculate Geolocation* function calculates the tangent point geolocation and related information. The function has as input the orbit state vector and corrected pointing angles and it makes use of the CFI softwares (Customer Furnished Items).

The main objectives of the Calculate Geolocation function are

- Compute tangent height of actual scene,
- Compute RMS error of tangent height of actual scene,
- Compute longitude / latitude of actual scene.

Specific objectives of the function are:

- Compute orbital position of S/C at ZPD time
- Compute tangent height, longitude and latitude
- Estimate error on computed tangent height

The computational sequence of the *Calculate Geolocation* function is illustrated by the flowchart of Figure 13.

5. Conclusions

This paper presented a summary of the current baseline adopted for the Ground Segment processing aimed at the generation of Level 1B algorithms. The presented processing scheme of fringe count handling is not definitive and still under revision. The non-linearity algorithm was verified on the MIPAS Engineering Demonstration Model, and its design has proved to be valid under the expected instrument operating conditions.

The final validation of the Level 1B algorithms will be done during Commissioning Phase, where the whole set of functions will be put to test together, and modifications, corrections, or refinement will be applied if necessary.

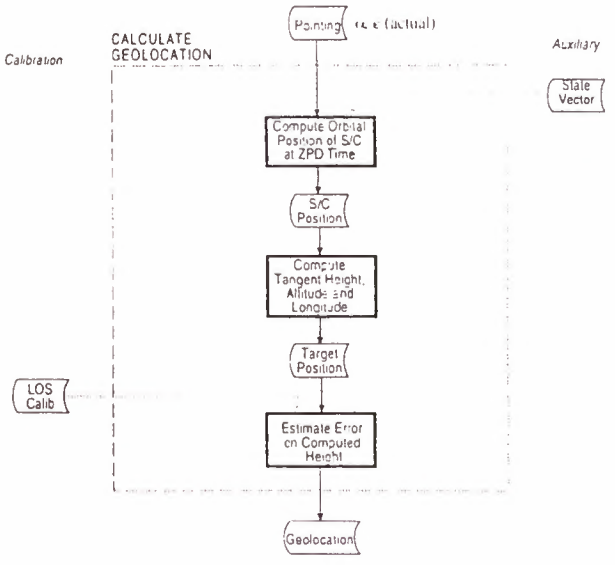

Figure 13: *Calculate Geolocation* Flowchart

6. REFERENCES

1. "Algorithm Technical Baseline Document (ATBD) for MIPAS Level 1B Processing", ENVISAT-1 Ground Segment Technical Note, PO-TN-BOM-GS-0012, Issue 1, September 1998.

2. H. E. Revercomb, H. Buijs, H. B. Howell, D. D. Laporte, W. L. Smith, and L. A. Sromovsky, "Radiometric calibration of IR Fourier transform spectrometers: solution to a problem with the High-Resolution Interferometer Sounder". Appl. Opt., Vol. 27, No 15, pp. 3210-3218, Aug. 1988.

3. "MIPAS Instrument Specification", PO-RS-DOR-MP-0001, Issue 6, February 1993.

4. "SPE Design & Analysis Document", PO-RP-CDC-MP-0001, 1992.

5. "Detection of Spurious Spikes in an Interferogram", PO-TN-BOM-GS-0005, Issue 1, April 1995.

6. "Non-Linearity Characterization and Correction", PO-TN-BOM-MP-0019, Issue 1A, September 1996.

7. "MIPAS Detector Non-linearity Correction Critical Revision", PO-RP-BOM-GS-0017, Issue 1, May 1998.

8. "In-Flight Calibration Plan", PO-PL-DAS-MP-0031, Issue 2A, June 1997.

9. "MIPAS Level 1B Processing I/O Data Definition", PO-TN-BOM-GS-0010, Issue 4, October 1997.

10. "MIPAS In-flight Spectral Calibration and ILS retrieval", PO-TN-BOM-GS-0006, Issue 2A, June 1997.

11. "MIPAS Assumptions on the Ground Segment", PO-RS-DOR-SY-0029, May 1996.

12. W. H. Press *et al.*, *Numerical Recipes in C: The art of scientific computing*, Second Ed., Cambridge University Press, 1992.

13. M. S. Caceci and W. P. Cacheris, *Fitting curves to data: The Simplex algorithm is the answer*, BYTE Magazine, May 1984, pp. 340–362.

MIPAS LEVEL 2 ALGORITHM

Bruno Carli[a], Emiliano Battistini[b], Massimo Carlotti[b], Thomas von Clarmann[e], Bianca M. Dinelli[b], Anu Dudhia[c], George Echle[e], Jean-Marie Flaud[d], Alessandro Gignoli[a], Michael Höpfner[e], Eugenio Lunedei[b], Francesco Mencaraglia[a], Paul E. Morris[c], Piera Raspollini[a], Marco Ridolfi[a], Gabriele Stiller[e], Alessandro Vigiani[b] and Robert J. Wells[c]

[a] IROE - CNR Via Panciatichi, 64 I-50127 Firenze (Italy)
[b] Dip. Chimica Fisica e Inorganica Università di Bologna (Italy)
[c] Atmospheric, Oceanic and Planetary Physics - Clarendon Laboratory - Oxford University (UK)
[d] Laboratoire de Photophysique Moleculaire Université de Paris Sud (France)
[e] Forschungszentrum Karlsruhe GmbH, Institut fuer Meteorologie und Klimaforschung (Germany)

Abstract. An ESA supported study was carried out for the development of an optimized code for near real time retrieval of altitude profiles of pressure, temperature (p, T) and volume mixing ratio (VMR) of five key species (O_3, H_2O, HNO_3, CH_4 and N_2O) from infrared limb sounding spectra recorded by MIPAS (Michelson Interferometer for Passive Atmospheric Sounding), which will be operated on board ENVISAT-1 satellite.
The implemented model is based on the Global Fit approach, i.e. all the limb-scanning spectra are simultaneously fitted, and on the analysis in narrow spectral intervals (microwindows).
The trade-off between run time and accuracy of the retrieval was optimized from both the physical and mathematical point of view, with improvements in the program structure, in the radiative transfer model and in the computation of the retrieval Jacobian.
The attained performances of the retrieval code are as follows: noise error on temperature < 2 K at all the altitudes covered by the standard MIPAS scan (8-53 km), noise error on tangent pressure < 3 %, noise error on VMR of the target species < 5 % at most of the altitudes of scientific interest covered by the standard MIPAS scan, with a total run time of less than 6 minutes on a SUN SPARC station 20.

1. INTRODUCTION

MIPAS (Michelson Interferometer for Passive Atmospheric Sounding) is an ESA developed instrument to be operated on board ENVISAT-1 as part of the first Polar Orbit Earth Observation Mission program (POEM-1). MIPAS will perform limb sounding observations of the atmospheric emission spectrum in the middle infrared region. Concentration profiles of numerous trace gases can be derived from MIPAS observed spectra.
According to the current baseline, from MIPAS measurements altitude profiles of atmospheric pressure and temperature (p,T), and of volume mixing ratio (VMR) of five high priority species (O_3, H_2O, HNO_3, CH_4 and N_2O) will be routinely retrieved in near real time (NRT). The retrieval of these parameters from calibrated spectra (Level 1b data) is indicated as NRT Level 2 processing.
Level 2 processing is expected to be a critical part of the Payload Data Segment (PDS) because of both the long computing time that may be required and the need for a validated algorithm capable of producing accurate and reliable results.
In the frame of the on-going ESA supported study "Development of an Optimised Algorithm for Routine p,T and VMR Retrievals from MIPAS Limb Emission Spectra" a scientific code has been developed for NRT Level 2 analysis, suitable for implementation in ENVISAT PDS and optimized for the requirements of speed and accuracy. The scientific code is called Optimized Retrieval Model (ORM) and includes p,T and VMR retrieval components. It is the result of the primary study objective, which was to optimise the overall retrieval scheme with respect to the initial baseline, by introducing various mathematical and physical optimisations and by verifying the performance improvements on the basis of simulated test scenarii. The required accuracy performances of the retrieval code are the following:

- Temperature error < 2 K at all the altitudes covered by the standard MIPAS scan (8-53 km)
- Tangent pressure error: < 3%
- Error on the retrieved VMR of the key species: < 5 % at all the altitudes covered by the standard MIPAS scan.

The required run-time to perform p,T and VMR retrieval of the five MIPAS target species from a limb-scanning sequence of 16 limb-views should be less than 1 hour on a SUN SPARCstation 20.
In order to cope with accuracy and speed requirements, even if the MIPAS instrument is designed to measure earth limb emission in five broad spectral channels (685 - 970 cm^{-1}, 1020 - 1170 cm^{-1}, 1215 - 1500 cm^{-1}, 1570 - 1750 cm^{-1}, and 1820 - 2410 cm^{-1}), data analysis is performed by considering only narrow (less than 3 cm^{-1} width) spectral subintervals, called 'microwindows'. This baseline offers several advantages. It is efficient, because data analysis can concentrate on those parts of the entire measured spectrum, which contain most information on the target parameters, and a large fraction of the measured data, which contain minor or redundant information, can be ignored. Spectral regions can be avoided which are characterized by: uncertain spectroscopic data, interference by non-target species, Non-Local Thermal Equilibrium and line mixing effects. Weakly temperature-dependent transitions can be chosen for constituents retrieval in order to minimize mapping of temperature uncertainties on the resulting concentration vertical profiles.

By analyzing the sensitivity of the radiance to changes of target parameters, lists of appropriate microwindows have been selected for retrieval of H_2O, O_3, HNO_3, CH_4, and N_2O (Ref. 1) as well as for the joint retrieval of pressure and temperature (Ref. 2). A microwindow database has been created and is currently being refined with respect to minimization of retrieval errors, following the approach of Clarmann and Echle (Ref. 3).

2. THE INVERSION METHOD

The problem of retrieving the altitude distribution of a physical or chemical quantity from limb-scanning observations of the atmosphere, drops within the general class of problems that require the fitting of a theoretical model, that describes the behavior of the observed system, to a set of available observations. The theoretical model describes the system through a set of parameters so that the retrieval procedure consists in the search for the set of values of the parameters that produce the "best" simulation of the observations. The most commonly adopted criterion to accomplish the objective is the minimization of the χ^2 function (generally defined as the weighted squared summation of the differences between observations and simulations) with respect to the value of the parameters. This criterion is referred as Least Squares Fit (LSF). When the theoretical model does not depend linearly on the unknown parameters the problem, called Non-linear Least Squares Fit (NLSF), cannot be solved directly by using a solution formula, and an iterative procedure must be used. Several methods exist for the NLSF; the one adopted for our purposes is the Gauss Newton (GN) method modified following the Marquardt's criterion (GNM) (Ref. 4).
In order to provide the framework of the subsequent discussion, the general mathematical formulation of the problem is herewith briefly reviewed.

THE DIRECT PROBLEM

The signal S that reaches the spectrometer can be modeled, by means of the radiative transfer equation (see Sect. 3), as a function $S = S(x, q_z)$ of the observation parameters x and of the distribution profile q_z of the atmospheric quantity which is to be retrieved. In general the radiative transfer does not represent a linear transformation. In this case, a linear relationship between S and q_z can be obtained by operating a Taylor expansion of the radiative transfer equation, around an assumed profile $\tilde{q}_z$. In the hypothesis that $\tilde{q}_z$ is near enough to the true profile to drop in a linear behavior of the function S, the Taylor expansion can be truncated to the first term to obtain:

$$S(x, q_z)=S(x, \tilde{q}_z)+\int_0^{\infty}\left[\frac{\partial S(x, q_z)}{\partial q_z}\right]_{\tilde{q}_z}\left[q_z-\tilde{q}_z\right]dz \quad (2.1)$$

Note that the use of the integral is required in the above equation since the profile q_z is here considered as a continuous function. Eq. (2.1) can be written as:

$$N(x)=\int_0^{\infty} K(x, z)\ y_z\ dz \quad (2.2)$$

where:

$$N(x) = S(x,q_z) - S(x,\tilde{q}_z) \quad (2.3)$$

$$K(x,z)=\left[\frac{\partial S(x,q_z)}{\partial q_z}\right]_{\tilde{q}_z} \quad (2.4)$$

$$y_z = [q_z - \tilde{q}_z]\,. \quad (2.5)$$

Equation (2.2) is an integral equation that represents a linear transformation of the unknown y_z leading to the observations $N(x)$ by way of the kernel $K(x, z)$.

THE GAUSS NEWTON METHOD

In the case of practical calculations, the mathematical entities above defined are represented by discrete values. Actually, we will deal with a finite number (n) of observations and a finite number (m) of values to represent, in a vector $\mathbf{q}_z$, the altitude distribution of the unknown quantities (these m values will be denoted as "parameters" from now on). As a consequence the integral operator of Eq. (2.2) becomes a summation and the equation itself can be expressed in matrix notation as:

$$\mathbf{n} = \mathbf{K}\,\mathbf{y} \quad (2.6)$$

In equation (2.6):

- $\mathbf{n}$ is a vector of dimension n. The entry n_j of $\mathbf{n}$ is the difference between observation j and the corresponding simulation calculated using the assumed profile $\mathbf{q}_z$ (Eq. 2.3).
- $\mathbf{K}$ is a matrix (usually denoted as Jacobian matrix) having n rows and m columns. The entry k_{ij} of $\mathbf{K}$ is the derivative of observation i made with respect to parameter j (Eq. 2.4)
- $\mathbf{y} = \mathbf{q}_z - \tilde{\mathbf{q}}_z$ is a vector of dimension m. The entry y_i of $\mathbf{y}$ is the correction needed to the assumed value of parameter $\tilde{\mathbf{q}}_z$ in order to obtain its correct value $\mathbf{q}_z$. The goal of the retrieval is the determination of this vector.

The problem is therefore that of the search for a "solution matrix" $\mathbf{D}$ (having m rows and n columns) that, multiplied by vector $\mathbf{n}$ provides $\mathbf{y}$. If the vector $\mathbf{n}$ is characterized by the variance-covariance matrix $\mathbf{V}^n$ (square of dimension n), the χ^2 function which must be minimized is defined as:

$$\chi^2 = \mathbf{n}^T(\mathbf{V}^n)^{-1}\mathbf{n} \quad (2.7)$$

and matrix $\mathbf{D}$ that satisfies the least squares condition is equal to:

$$\mathbf{D} = (\mathbf{K}^T(\mathbf{V}^n)^{-1}\mathbf{K})^{-1}\mathbf{K}^T(\mathbf{V}^n)^{-1} \quad (2.8)$$

If the inverse of $\mathbf{V}^n$ does not exist, its generalized inverse must be used instead (Ref. 5). If the unknown quantities are

suitably chosen, the inverse of matrix $(\mathbf{K}^T(\mathbf{V}^n)^{-1}\mathbf{K})$ always exists.

If the real minimum of the χ^2 function is found and $\mathbf{V}^n$ is a correct estimate of the errors, the quantity defined by equation (2.7) has an expectation value equal to $(n - m)$ and a standard deviation equal to $\sqrt{n-m}$. The value of the quantity $\chi^2/(n-m)$ provides therefore a good estimate of the quality of the retrieval. Values of $\chi^2/(n-m)$ which deviate too much from unity indicate the presence of incorrect assumptions in the retrieval.

The unknown vector $\mathbf{y}$ is then computed as:

$$\mathbf{y} = \mathbf{D}\,\mathbf{n} \qquad (2.9)$$

and the new estimate of the parameters as:

$$\mathbf{q'}_z = \tilde{\mathbf{q}}_z + \mathbf{y} \qquad (2.10)$$

The errors associated with the solution of the inversion procedure can be characterized by the variance-covariance matrix ($\mathbf{V}^q$) of $\mathbf{q'}_z$ given by:

$$\mathbf{V}^q = \mathbf{D}(\mathbf{V}^n)\mathbf{D}^T = (\mathbf{K}^T(\mathbf{V}^n)^{-1}\mathbf{K})^{-1} \qquad (2.11)$$

Matrix $\mathbf{V}^q$ permits to estimate how the experimental random errors map into the uncertainty of the values of the retrieved parameters. Actually, the square root of the diagonal elements of $\mathbf{V}^q$ measures the root mean square (r.m.s.) error of the corresponding parameter. The off-diagonal element V_{ij} of matrix $\mathbf{V}^q$, normalized to the square root of the product of the two diagonal elements V_{ii} and V_{jj}, provides the correlation coefficient between parameters i and j.

If the hypothesis of linearity about the behavior of function S is satisfied, Eq. (2.10) provides the result of the retrieval process. If the hypothesis is not satisfied, the minimum of the χ^2 function has not been reached but only a step has been done toward the minimum and the vector $\mathbf{q'}_z$ computed by Eq. (2.10) represents only a better estimate of the parameters than $\tilde{\mathbf{q}}_z$. In this case the whole procedure must be reiterated starting from the new estimate of the parameters. Convergence criteria are therefore needed in order to establish when the minimum of the χ^2 function has been approached enough to stop the iterations.

THE MARQUARDT METHOD

The Marquardt method (Ref. 6) introduces a modification to the procedure described in the previous sub-section. The modification consists in introducing in Eq. (2.8) a factor damping the amplitude of the parameters correction vector. Marquardt method permits a faster convergence especially in cases of strongly non-linear problems.

CONVERGENCE CRITERIA

The convergence criteria adopted in our code must represent a compromise between the required accuracy and speed performances of the algorithm. To this purpose, the following two conditions are used:

- At the current iteration the relative difference between the actual χ^2 and the chi-square computed in the linear approximation (χ^2_{LIN}) must be less than a fixed threshold t_1:

$$\left|\frac{\chi^2(\mathbf{q}_z) - \chi^2_{LIN}(\mathbf{q}_z)}{\chi^2(\mathbf{q}_z)}\right| < t_1 \qquad (2.12)$$

where χ^2_{LIN} is computed using the expression:

$$\left((\mathbf{1}-\mathbf{KD})\mathbf{n}\right)^T\left(\mathbf{V}^n\right)^{-1}\left((\mathbf{1}-\mathbf{KD})\mathbf{n}\right) \qquad (2.13)$$

- The maximum relative correction that has to be applied to the parameters for the next iteration is below a fixed threshold t_2 i.e.:

$$\mathrm{Max}_j\left|\frac{(\mathbf{q}_z^{iter-1})_j - (\mathbf{q}_z^{iter})_j}{(\mathbf{q}_z^{iter})_j}\right| < t_2 \qquad (2.14)$$

different thresholds are used for the different types of parameters depending on their required accuracy. Furthermore, whenever an absolute accuracy requirement is present for a parameter, the absolute variation of the parameter is checked instead of the relative variation considered in Eq. (2.14). The non-target parameters of the retrieval, such as continuum and instrumental offset parameters are not included in this check. Parameters equal to zero are excluded from this check as well.

The logical operation 'OR' between conditions (2.12) and (2.14) is then used in order to establish whether the convergence has been reached.

THE GLOBAL FIT ANALYSIS

In global fit approach (Ref. 7) the whole altitude profile is retrieved from simultaneous analysis of all the limb-views of a scan. The retrieval is based on the least-squares criterion and looks for a solution profile that has a number p of degrees of freedom smaller than or equal to the number of the observed data points. In practice the profile is retrieved at p discrete altitudes and at intermediate altitudes an interpolated value is used in the radiative transfer model (see Sect. 2).

In this approach, the vector $\mathbf{n}$ appearing in Eq. (2.9) is the difference between all the selected observations and the corresponding simulations (all the spectral intervals and all the limb-scanning measurements are included in this vector).

The unknown vector $\mathbf{y}$ may contain different variables depending on the retrieval we are performing. In general it includes an altitude distribution sampled at a number of discrete altitudes (the tangent altitudes of the measurements, in our case) as well as some spectroscopic and instrumental parameters (e.g. atmospheric continuum).

USE OF COMPLEMENTARY (NON-RADIOMETRIC) INFORMATION IN THE INVERSION MODEL

When some complementary information on the unknown parameters is available, the quality of retrieved parameters can be improved by including this information in the retrieval process. Assuming this complementary information as consisting of a vector $\mathbf{n_1}$ connected by means of the jacobian $\mathbf{K_1}$ with the unknowns $\mathbf{y}$, and of a variance covariance matrix $\mathbf{V}^{n_1}$ relating to $\mathbf{n_1}$, the combination of the MIPAS measurements with the information $\mathbf{n_1}$ can be made using the optimal estimation (Ref. 8) formula:

$$\hat{\mathbf{y}} = \left[\mathbf{K}^{\mathrm{T}}(\mathbf{V}^{n})^{-1}\mathbf{K} + \mathbf{K}_1^{\mathrm{T}}(\mathbf{V}^{n_1})^{-1}\mathbf{K}_1\right]^{-1} \cdot \left[\mathbf{K}^{\mathrm{T}}(\mathbf{V}^{n})^{-1}\mathbf{n} + \mathbf{K}_1^{\mathrm{T}}(\mathbf{V}^{n_1})^{-1}\mathbf{n}_1\right] \quad (2.15)$$

Implicitly this expression is always used in the retrieval to combine the information provided by the different microwindows, more generally it can be used also for the exploitation of non-radiometric information obtained from sources external to the MIPAS interferometer.

The complementary information can either be of 'external' type (as in the case of climatological data or model forecasts) which do not relate to a specific MIPAS scan, or of 'specific' type.

The exploitation of 'external' information is not recommended because, when the same information is used for the retrievals of several scans, the results of these retrievals are not independent of each other and are affected by a common bias. Therefore, this approach would prevent the users from building averages of profiles retrieved using the same 'external' complementary information.

Inversely, complementary information relating to the 'specific' MIPAS scan we are actually analyzing, (e.g. line of sight data, or data relating to the same air mass actually sounded by the considered MIPAS scan) can be profitably included in the retrieval using Eq. (2.15) instead of Eq. (2.9). In fact, in this case, also the complementary information is updated at each scan and therefore the retrieved profiles do not suffer of any bias.

INCLUSION OF LOS ENGINEERING INFORMATION IN P,T RETRIEVAL

Engineering data defining the instrument Line Of Sight (LOS) are updated at each scan and therefore constitute an effective and 'specific' source of information which we routinely use in p,T retrievals without introducing a bias in the retrieved profiles.

The LOS engineering information consists of both a vector $\mathbf{z}$ containing the tangent altitudes of the sweeps of the current scan and of a Variance-Covariance Matrix (VCM) $\mathbf{V}^z$ related to the vector $\mathbf{z}$; a relationship between the engineering tangent heights and the unknowns of the retrieval (p,T) is provided by the hydrostatic equilibrium constraint. Hydrostatic equilibrium is a condition that applies to an ideal atmosphere which is perfectly stratified. The differential form of the equation that describes this condition in an atmospheric layer within the altitudes z_i and z_{i+1} is:

$$\Delta z_i = \frac{R}{Mg} \cdot \overline{T}_i \cdot \ln\left(\frac{p_i}{p_{i+1}}\right) \quad (2.16)$$

where the notations are:

p_i pressure at altitude z_i,

M average molecular weight of the atmosphere,

R universal gas constant,

$\overline{T}_i$ mean temperature of the atmospheric layer i,

Δz_i thickness of the atmospheric layer i

$(\Delta z_i = z_{i+1} - z_i)$

Now, a linear relation between (p,T) and the tangent heights $\mathbf{z}$ can be obtained by locally linearizing Eq. (2.16). In this assumption, instead of equation (2.6) we have a couple of equations defining the retrieval problem:

$$\begin{aligned} \mathbf{n} &= \mathbf{K}\mathbf{y} \\ \mathbf{z} &= \mathbf{K}_z\mathbf{y} \end{aligned} \quad (2.17)$$

where the first equation is still Eq. (2.9) and the second equation is derived from the hydrostatic equilibrium condition. Matrix $\mathbf{K}_z$ is the jacobian connecting the tangent altitudes with the unknowns p,T and is obtained by deriving Eq. (2.16) with respect to p and T. The solution (optimal estimation) formula providing the vector $\hat{\mathbf{y}}$ which minimizes the χ^2 function of the new inversion problem is:

$$\hat{\mathbf{y}} = \left[\mathbf{K}^{\mathrm{T}}(\mathbf{V}^{n})^{-1}\mathbf{K} + \mathbf{K}_z^{\mathrm{T}}(\mathbf{V}^{z})^{-1}\mathbf{K}_z\right]^{-1} \cdot \left[\mathbf{K}^{\mathrm{T}}(\mathbf{V}^{n})^{-1}\mathbf{n} + \mathbf{K}_z^{\mathrm{T}}(\mathbf{V}^{z})^{-1}\mathbf{z}\right] \quad (2.18)$$

3. ATMOSPHERIC MODEL

FORWARD MODEL

The purpose of the forward model is to simulate the spectra measured by the instrument in case of known atmospheric composition. The signal measured by the spectrometer is determined by the atmospheric radiance which reaches the spectrometer and by instrumental effects, arising from the finite spectral resolution of the instrument and the finite angular size of the input diaphragm (finite Field of View, FOV). In general, the instrument signal $S_I(z_t, \sigma)$ due to atmospheric limb sounding at a given tangent altitude z_t can be calculated convolving the atmospheric radiance $L(z_t, \sigma)$ with the Apodized Instrument Line Shape (*AILS*) and with the MIPAS FOV function ($FOV(z_t)$):

$$S_I(z_t,\sigma) = \iint \left(L(\sigma-\sigma', z_t - z_{t'}) \cdot AILS(\sigma')d\sigma'\right) \cdot FOV(z_{t'})dz_{t'} \quad (3.1)$$

- *Radiative Transfer*

The atmospheric radiance which reaches the instrument when pointing to the limb at tangent altitude z_t is calculated by means of the radiative transfer formula:

$$L(\sigma,z_t)=\int_{x_t}^{x_0}\left[B(\sigma,x)c(\sigma,x)\eta(x)\right]\exp\left(-\int_{x}^{x_0}c(\sigma,x')\eta(x')dx'\right)dx \qquad (3.2)$$

where x is some position along the line of sight of the spectrometer between the observation point x_0 and the point x_t anterior to the tangent point at the furthest extend of the limb, $B(\sigma, x)$ is the radiative source function, $c(\sigma,x)$ is the molecular absorption coefficient, $\eta(x)$ is the number density of absorbing molecules and the exponential term represents the atmospheric transmittance between x and x_0.
In the case of local thermal equilibrium $B(\sigma, x)$ is equal to the Planck function.
The line of sight in the atmosphere is determined by the viewing direction of the instrument and the refractive index: due to refraction, the ray-path is not a straight line and bends towards the earth.

- *Refraction*

The refractive index is a function of both pressure and temperature (the dependence on water vapor and frequency is negligible for MIPAS measurements) and it is determined by the Edlen (Ref. 9) model. Assuming a spherical earth and spherical atmospheric layers, the optical path x is linked to the altitude r by the following expression:

$$dx=\frac{1}{\sqrt{1-\dfrac{n(r_t)\cdot r_t}{n^2(r)\cdot r^2}}}\cdot dr \qquad (3.3)$$

with r altitude referred to the center of the earth, $n(r)$ refractive index and r_t tangent altitude.

- *Use of Curtis-Godson pressure and temperature*

The curvilinear integral (3.2) is computed by dividing the integral over x into a sum over discrete thin layers l, each characterized by an appropriate 'equivalent' pressure and temperature, namely the Curtis-Godson (Ref. 10) quantities, calculated weighting the pressure and temperature along the ray-path inside each layer with the corresponding number density of each absorbing molecule. In particular, Curtis-Godson parameter G (pressure and temperature) relative to gas g, layer l and limb view t, is calculated as follows:

$$G^{e}_{g,l,t}=\frac{\displaystyle\int_{z_{l-1}}^{z_l}G(z)X_g(z)\cdot\eta(p(z),T(z))\cdot\frac{dx_t}{dz}\cdot dz}{\displaystyle\int_{z_{l-1}}^{z_l}X_g(z)\cdot\eta(p(z),T(z))\cdot\frac{dx_t}{dz}\cdot dz} \qquad (3.4)$$

z is the altitude, z_l and z_{l-1} are the heights on the boundaries of the layer, $X_g(z)$ represents the Volume Mixing Ratio of the g-th gas, x_t is the line of sight characterized by the tangent altitude z_t, $\eta(p(z),T(z))$ is the air number density.

The normalization factor of these expressions represents the column of the considered gas, layer and limb view: $col^{g}_{l,t}$.
If for each couple of 'equivalent' pressure and temperature characterizing a layer, the value of the absorption coefficient $c^{g}_{l,t}\left(p^{e}_{g,l,t},T^{e}_{g,l,t}\right)$ is computed, equation (3.2) can be written as:

$$L=\sum_{l=1}^{N}B_{l,t}\left(1-\exp\left(-\tau_{l,t}\right)\right)\left(\prod_{k=l+1}^{N}\exp\left(-\tau_{k,t}\right)\right) \qquad (3.5)$$

where $\tau_{l,t}$ is the single layer optical depth:

$$\tau_{l,t}=c^{cont}_{l,t}col^{air}_{l,t}+\sum_{g=1}^{Ngas}c^{g}_{l,t}col^{g}_{l,t} \qquad (3.6)$$

l is the index for the layers with layer '1' the farthest and N the nearest layer with respect to the satellite, t is the index of the limb view, $B_{l,t}$ is the Planck function computed for the equivalent temperature of the main gas of the retrieval in layer l and limb view t. $c_{l,t}{}^{cont}$ is the absorption cross section of the continuum (the atmospheric continuum emission is taken into account as an additional species with VMR =1), $col_{l,t}{}^{air}$ the partial air column of layer l and limb view t and col^{g} the partial column of gas g, layer l and limb view t.

INSTRUMENT MODEL

- *AILS*

The high resolution spectrum computed with the radiative transfer model is convolved with the Apodized Instrument Line Shape (AILS) function, which takes into account the finite spectral resolution of the instrument, the asymmetries introduced by the spectrometer and the apodization of the measured spectra. The ILS function does not take into account the instrument responsivity and phase error corrections, since retrieval is performed using calibrated and phase-error corrected spectra provided by the Level 1B processing.
Measured spectra, as well as simulated spectra, are apodized with the Norton-Beer (Ref. 11) strong function, in order to reduce the interference of lines outside the individual microwindows.

- *FOV*

The input diaphragm of the interferometer has non-zero angular size and light from an extended source, characterized by a radiance gradient, is observed. These factors produce a modification in the ILS and a modification in the 'effective' tangent altitude of the spectrum.
The antenna pattern of the field of view is presently represented by a spread in the altitude domain which is assumed to be independent of tangent altitude and of shape equal to a trapezium with the greater base of about 4 km and the smaller base of about 3 km.
The effect of field of view is taken into account performing, for each spectral frequency, the convolution between the spectrum and the antenna pattern. In general, this convolution can be performed numerically after repeating forward model calculation for a number of lines of sight that span the

vertical range of 4 km around the tangent altitude. In order to reduce the number of computations, in ORM an analytical convolution is performed using the spectrum as a function of altitude determined interpolating spectra calculated at contiguous tangent pressures.
Whenever interpolation between contiguous measurement tangent pressures introduces too large approximations due to discontinuities in the rate of change of temperature and of molecule density with altitude, additional spectra are simulated at intermediate tangent levels.

4. OPTIMISATIONS

In order to cope with the speed requirements of the retrieval algorithm, several optimizations of both mathematical and physical type have been employed. Some optimizations have already been discussed in the previous section. These namely:

- Global-fit approach. Avoids repeating calculation of quantities which are common to all the limb-views of the considered scan.
- Use of Curtis-Godson equivalent quantities. This technique allows to implement a coarse discretization of the atmosphere for radiative transfer integral calculation.
- FOV convolution approach. Together with the global-fit approach, it allows to save unnecessary computation of several limb-views with close tangent altitudes.
- Use of LOS engineering information in p,T retrieval. Stabilizes the retrieval and reduces the number of iterations.

In the present section we describe further, very effective, optimizations that have been implemented in our forward model.

SECANT LAW APPROXIMATION FOR THE CALCULATION OF CURTIS-GODSON QUANTITIES

In principle, Curtis-Godson pressures and temperatures have to be computed for each gas, each layer and each limb view. However, assuming the layers flat and the line of sight a straight line, the secant law applies and the same values of p^e and T^e are obtained independently from the angle θ between the line of sight and the vertical direction, that is independently from the limb-view. We have verified that the use of secant law approximation causes very small errors at all altitudes, except at the tangent layer.
Exploiting this result, it is sufficient to calculate the values of p^e and T^e for all the layers of the lowest limb view, and only for the lowest layer of the other limb-views, all the other layers being characterized by the same values of p^e and T^e as the lowest limb view.
This optimization is crucial, not only because less equivalent pressures and temperatures have to be calculated, but mainly because absorption cross-sections have to be calculated and stored for a smaller number of paths (combination of layer and limb-view).

CALCULATION OF THE JACOBIAN DURING THE CALCULATION OF THE SPECTRUM

Since the developed Optimized Forward Model (OFM) is optimized for running in the environment provided by the retrieval algorithm, the fast determination of derivatives of the radiance with respect to the parameters is a very important issue besides the calculation of the spectrum. In the following we will first present the four different types of derivatives which are produced and then explain the procedure implemented for their calculation. The retrieval parameters are: (1) volume mixing ratios of atmospheric trace gases at tangent pressure, (2) atmospheric continuum values at tangent pressure, (3) temperature at tangent pressure and (4) the tangent pressure itself. While the number of parameters in (1), (3) and (4) is equal to the number of tangent points, the continuum (2) is assumed to be constant in one microwindow, but variable from one microwindow to another. Thus, the number of continuum parameters is equal to the number of microwindows times the number of tangent geometries at which the individual microwindows are used.
As derivatives (1) and (2) are handled in the same way, they are described together. The aim is the calculation of the derivatives of the spectrum L provided by Eq. (3.5) with respect to the atmospheric retrieval parameters q_n on each tangent level n. The expression for these derivatives reads:

$$\frac{dL}{dq_n} = \sum_{j=1}^{N} \left(\frac{dL}{dB_j} \frac{dB_j}{dq_n} + \frac{dL}{d\tau_j} \frac{d\tau_j}{dq_n} \right) \qquad (4.1)$$

In the following we neglect the 2nd order dependence of equivalent temperatures on the parameters q_n. Therefore, we have to consider only the second term in the parenthesis of Eq. (4.1). Parallel to the radiative transfer calculation the derivative of the radiance with respect to the optical depths is determined by:

$$\frac{dL}{d\tau_j} = B_j \exp(-\tau_j) \left(\prod_{k=j+1}^{N} \exp(-\tau_k) \right) - \sum_{i=1}^{j-1} B_i (1 - \exp(-\tau_i)) \left(\prod_{k=i+1}^{N} \exp(-\tau_k) \right) \qquad (4.2)$$

The first term is the derivative of the emission of layer j attenuated by all layers between j and the observer, while the second term is the derivative of the attenuation for the radiation of each layer up to layer j. For the evaluation of the summation appearing in Eq. (4.1), the derivative of the optical depth of each layer with respect to the parameters must be known. In case of continuum parameters, this derivative reads simply:

$$\frac{d\tau_j}{dq_n^{cont}} = \sum_{l=1}^{N} \frac{d\tau_j}{dc_l^{cont}} \frac{dc_l^{cont}}{dq_n^{cont}} = \sum_{l=1}^{N} col_l^{air} \frac{dc_l^{cont}}{dq_n^{cont}} \qquad (4.3)$$

where c_l^{cont} are the continuum cross-sections for each layer and q_n^{cont} the continuum parameters (the continuum cross section values at the tangent levels). Except some layers above and below the tangent level $dc_l^{cont} / dq_n^{cont}$ is equal to zero. The formula for the derivative of the optical depth with respect to the trace gas parameters is:

$$\frac{d\tau_j}{dq_n^g} = \sum_{l=1}^{N}\left(\frac{d\tau_j}{dc_l^g}\frac{dc_l^g}{dq_n^g} + \frac{d\tau_j}{dcol_l^g}\frac{dcol_l^g}{dq_n^g}\right) = \sum_{l=1}^{N}\left(col_l^g\frac{dc_l^g}{dq_n^g} + c_l^g\frac{dcol_l^g}{dq_n^g}\right) \quad (4.4)$$

Neglecting the dependence of equivalent temperature and pressure on the VMR parameters q_n^g results in $dc_l^g / dq_n^g = 0$. During the calculation of the Curtis-Godson equivalent quantities, only the derivatives of the partial columns of each layer with respect to the VMR at the tangent level have to be determined.

While the procedure for the calculation of (1), (2) and (4) is analytic (in the sense that the analytical formulas of the derivatives are implemented in the program), the temperature derivatives (3) are determined in a 'fast numerical' way. In contrast with slow numerical derivatives, which are determined by as many total reruns of the forward model as there are fitting parameters, in the 'fast numerical' calculation the derivatives are computed in parallel with the spectra, avoiding unnecessary repeated calculations. The implemented fast numerical derivatives with respect to tangent temperature make use of the limited influence of the change of one temperature parameter on the overall temperature profile: only the Curtis-Godson equivalent temperatures are affected of the neighboring layers above and below the tangent altitude to which the considered temperature parameter refers. Hence, we calculate only cross-sections and radiative transfer corresponding to the unperturbed original temperature profile, needed for the forward calculation; plus, cross-sections relating to the layers affected by the current temperature parameter change and radiative transfer as modified by the changed cross-sections.

The analytical derivative of the spectrum with respect to the tangent pressure (4) can be very complicated, since changes in the column, in the line-shapes and in the temperature have to be considered when tangent pressure is perturbed. The problem was overcome by exploiting the fact that the effect of FOV convolution is to shift the 'effective' tangent pressure of the spectrum. Therefore, the derivative of the spectrum with respect to tangent pressure is calculated performing an analytical derivative of the expression which provides the convolution between the interpolated spectrum as a function of tangent pressure and the FOV pattern. The accuracy of the derivative calculated in this way is strictly connected with the accuracy of the interpolated spectrum in the range where the FOV pattern is defined.

The additional computing effort required for the Jacobian calculation is only two times the effort needed for one forward model run. This is a very interesting result, considering that the full numerical calculation of the derivatives would require as many forward model re-runs as many are the fitting parameters (≈ 100).

CROSS-SECTION LOOK-UP TABLES AND IRREGULAR SPECTRAL GRIDS

The most time consuming parts of the forward model are the calculation of the absorption coefficients and the calculation of the radiative transfer. A spectral resolution of $\Delta\nu$ = 0.0005 cm^{-1} is usually considered necessary in order to resolve the shape of Doppler-broadened lines. To avoid repeated line-shape and radiative transfer calculations at this high resolution, two optimisations have been implemented:

1. Tabulating absorption coefficients $c_\nu^g(p,T)$ for a range of (p,T) values for each absorber g,
2. Determining an 'irregular grid' containing a subset of the spectral points used in the radiative transfer calculation such that a rapid interpolation of the remaining values is adequate.

Both the look-up tables and irregular grids are microwindow-specific and are precalculated.

LOOK-UP TABLES

In principle, it is straightforward to precalculate the absorption coefficient at each spectral grid point for a range of (p,T) conditions. However, for a single microwindow (typical width 0.5 cm^{-1}), the number of data points required is of the order of:

1000 spectral pts. x 100 pressures x 10 temperature pts. = 10^6 grid points (4.5)

Such a tabulated function is shown in Figure 1. Within a retrieval, up to 100 such tables have to be stored (10s of microwindows with 4 or 5 absorbers per microwindow), requiring too much memory for most practical applications.
A solution suggested by Strow (Ref. 12) is to compress this information using 'Singular Value Decomposition'. Any matrix $\mathbf{K}$ (m x n) can be decomposed as the product of three other matrices:

$$\mathbf{K} = \mathbf{U}\Sigma\mathbf{V} \quad (4.6)$$

where $\mathbf{U}$ (m x n) and $\mathbf{V}$ (n x n) are orthonormal matrices, and Σ is a diagonal matrix containing n singular values. Assuming that most of the information is contained in the l ($<< n$) largest singular values, the decomposition matrices can be truncated in the n dimension to give:

$$\mathbf{K} \approx \mathbf{U}'\Sigma'\mathbf{V}' = \mathbf{U}'\mathbf{W}' \quad (4.7)$$

where the reduced matrices $\mathbf{U}'$ (m x l) and $\mathbf{W}'$ (l x m) are much smaller matrices than the original matrix $\mathbf{K}$.

In this application, the matrix $\mathbf{K}$ contains $\ln c^g(\nu,x)$ where x represents any pair of (p,T) conditions. This is decomposed and stored as matrices $U'(\nu,l)$ and $W(l,x)$, where typically $l \leq$ 10 singular values, giving compression factors of the order 10 - 100.

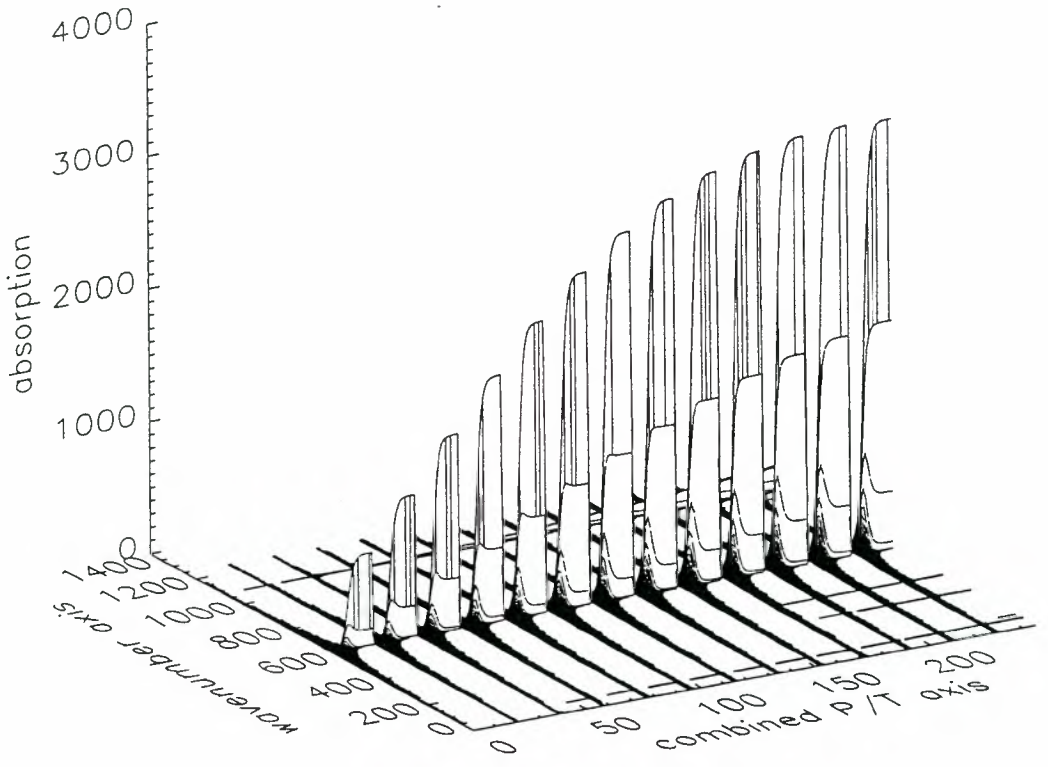

Figure 1. Plot of the CO_2 absorption coefficient look-up table for the PT004A microwindow. The wavenumber axis extends from 693.45-693.725 cm^{-1}. Each of the 13 (p,T) major cycles corresponds to a different temperature, and within each are 19 different -ln(p) values varying from Lorentz to Doppler broadening.

IRREGULAR GRIDS

Limb radiance spectra contain spectral features on a range of scales varying from the narrow, isolated, Doppler-broadened line centers at high altitudes, to wide, overlapping, Lorentz-broadened line wings from low altitudes.

The task is to determine the subset of spectral grid points that are required to reconstruct full radiance spectra, applicable over a range of tangent altitudes and atmospheres. Full radiative transfer calculations are then only required for this subset of points. The subset will be a function of the microwindow boundaries, the chosen interpolation scheme and the spectral convolution represented by the Instrument Line Shape.

Several interpolation functions were investigated, but since the same interpolation is also required for the calculation of Jacobians (which, unlike the radiances, can have negative values) logarithmic and inverse interpolations were avoided and a simple cubic interpolation was chosen.

The procedure is to start with a set of full-resolution limb radiance spectra for different tangent point altitudes. Then, for each point, a `cost' function is determined, representing the maximum radiance error (at any altitude, following ILS convolution) that would arise if the point were to be replaced by an interpolated value. The point with the smallest interpolation cost is then eliminated and the process repeated for the remaining grid. The iteration continues until no further points can be removed without exceeding some maximum error criterion, chosen to be 10 % of the noise-equivalent signal radiance.

Typically it is found that only 5-10 % of the full resolution grid is required for reconstruction. When combined with the use of Look-Up Tables, this also means that absorption coefficient c only has to be reconstructed at the same fraction of grid points, and the U' matrix only has to be stored for these points resulting in even further compression.

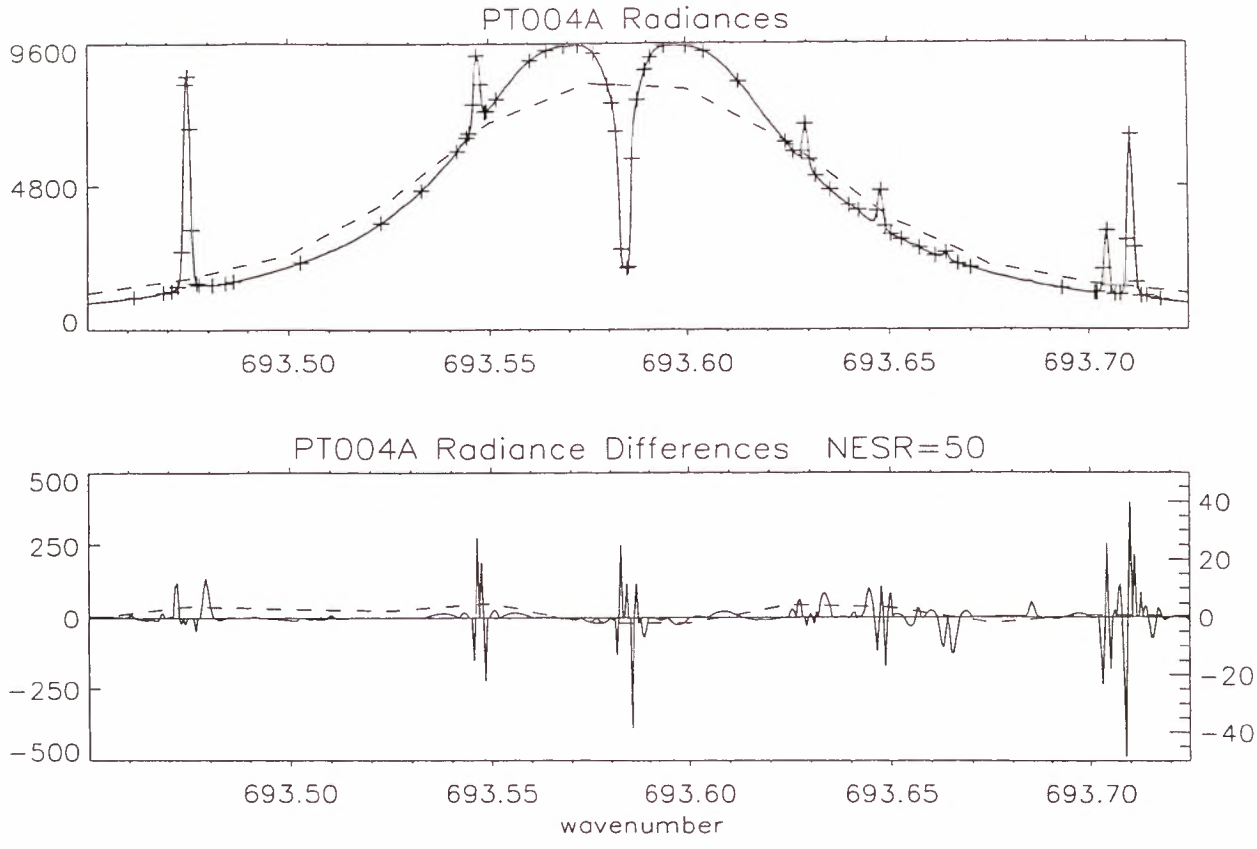

Figure 2. 44 km tangent height radiance from the PT004A microwindow. The upper plot shows the high-resolution radiance (solid line) with the interpolation points (+), and the convolved radiance (dashed line). The lower plot shows the difference between the original and interpolated radiances, on both the high-resolution grid (solid line, left axis) and the convolved radiances (dashed line, right axis).

DIRECT INTERPOLATION / CONVOLUTION

Without irregular grids, the low resolution spectrum is given by the convolution between the high resolution spectrum and the high resolution AILS function ($\Delta\sigma_{fine} = 0.0005\,\mathrm{cm}^{-1}$), performed only in correspondence of the coarse grid points ($\Delta\sigma_{coarse} = 0.025\,\mathrm{cm}^{-1}$). When irregular grids are available, instead of performing first the interpolation of the spectrum in the regular fine grid and then the convolution with the AILS in correspondence of only the coarse grid spectral points, it is possible to save time computing both operations at the same time.

5. ACCURACY PERFORMANCE OF THE RETRIEVAL MODEL

The retrieved profiles accuracy is determined by the following error sources:

1. forward model error, i.e. error due to imperfect modeling of the atmosphere,
2. retrieval error, due to the fact that the inversion procedure stops when the convergence criteria are satisfied, and therefore the real minimum of the χ^2 function is not exactly matched,
3. noise error, due to the mapping of measurement noise in the retrieved profiles (this error is evaluated from Eq. (2.11)),
4. systematic error due to incorrect assumptions in the forward model.

In our algorithm, the forward model error has been evaluated comparing the spectra of the forward model internal to our retrieval model with the spectra generated by a Reference Forward Model (RFM) developed at Oxford University.

The total effect of errors type 1., 2. and 3. has been evaluated by carrying-out test retrievals using as observations the spectra generated with the RFM to which artificial noise was added, and comparing the retrieved profiles with the assumed atmospheric profiles (reference profiles).

Regarding errors of type 4., a dedicated algorithm for precise evaluation of the systematic error components is still under construction. However, systematic errors, such as spectroscopic errors or errors due to imperfect knowledge of the concentration profiles of non-target species, are already taken into account in the algorithm for the definition of optimized spectral microwindows (see Sect. 1). We therefore

expect systematic errors to contribute less than the noise error to the total error budget.

COMPARISONS WITH REFERENCE FORWARD MODEL

To validate the approximations employed in the OFM, comparisons were made with a line-by-line code, the Reference Forward Model, based on GENLN2 (Ref. 13). The analysis is described in document PO-TN-OXF-GS-0007, but the principle results are:

Ray-Tracing For N_2O, 10 km tangent-height path (representing the most 'difficult' case involving both large VMR gradients and refraction effects) RFM-OFM calculations differ by <0.7% absorber mass, <0.004% Curtis-Godson pressure and <0.002 K Curtis-Godson temperature.

Absorption Coefficient Calculations Significant differences were initially observed due to the RFM using the older '92 HITRAN Total Internal Partition Sum (TIPS) data and a different (GENLN2-like) implementation of the CKD_21 H_2O continuum. However, when using the '96 TIPS and conventional continuum implementation, RFM and OFM full spectral calculations for typical microwindow regions agree to better than 1 % near major absorption features.

Limb Spectral Calculations Excluding FOV convolution, RFM-OFM limb radiance calculations agree to within NESR/4. However, at low altitudes (10 km) the calculated radiances are sensitive to the FOV representation, largely caused by the step-nature of the H_2O profile at the tropopause. This effect determined the implementation (in the OFM) of the calculation of spectra at intermediate tangent levels in the cases of strong gradients in the atmosphere.

ESTIMATION OF THE TOTAL ERROR

The results of test retrievals carried-out starting from observations generated with the RFM are shown in Figure 3. From this type of retrievals it is possible to evaluate the overall effect of forward model errors, retrieval errors and noise errors, by just comparing retrieved profiles with the 'reference' profiles that have been assumed for the generation of the observations.

Figure 3 reports the reference profiles with the corresponding retrieved data points (left panels) as well as the differences between retrieved and reference profiles and the profiles Estimated Standard Deviation (ESD) obtained from the measurement noise through Eq. (2.11) (right panels). From these results it turns out that, as the differences between retrieved and reference profiles are consistent with the ESD for most of the target species, forward model errors and retrieval errors are only a fraction of the noise error. The case of tangent pressures is however an exception: in this case the US standard atmosphere pressure profile used for generating RFM observations does not satisfy the hydrostatic equilibrium around 30 km. As the hydrostatic equilibrium is an assumption of our retrieval model, this implies that a model error biases (≈ 2%) the retrieved pressures above 30 km.

From Figure 3 it is also clear that the initially desired accuracy requirements are not satisfied at all the MIPAS altitudes and for all the target gases. However, in case the obtained accuracy is not satisfactory, the errors affecting the retrieved profiles can be reduced including further microwindows in the analysis. Of course, this operation can be made only at the expense of additional computing time.

6. RUN-TIME PERFORMANCE OF THE RETRIEVAL MODEL

The runtime performances of the Optimized Retrieval Model have been tested using different computers. Assuming the following framework:

- a set of microwindows is used which provides accuracy of the retrieved profiles as reported in Figure 3,
- the initial guess profiles of the retrieval are not 'too different' with respect to the reference profiles, so that convergence is reached in only one iteration,

the time required to perform p,T and five target gases retrievals amounts to 348 seconds while using a SUN SPARCstation 20 with 128 Mb of RAM memory. In the same conditions, the runtime can be as short as 210 seconds when using a 200 MHz PENTIUM PC with 256 Mb of RAM, running LINUX Operating System or 51 seconds when using a Digital DEC-SERVER, Mod.4100, with 1Gb of RAM and 600 MHz of CPU installed at Bologna University .

7. CONCLUSIONS

An Optimized Retrieval Model was developed for near real-time MIPAS retrievals employing the following optimizations:

- Global-fit approach
- use of Curtis-Godson equivalent quantities
- FOV convolution exploiting interpolation in pressure domain
- use of LOS engineering information in p,T retrieval.
- secant law approximation in radiative transfer
- calculation of the jacobian during the calculation of the spectrum, using analytical derivatives whenever convenient
- use of compressed absorption cross-section look-up tables and use of 'irregular' frequency grids
- combined interpolation and convolution for the calculation of the low resolution spectrum.

Test retrievals have shown that, using a realistic set of spectral microwindows, the VMR profiles of the five MIPAS target species can be retrieved with an accuracy within the requirements in most of the altitude ranges of scientific interest explored by the MIPAS scan. In these conditions, the run-time required to perform p,T and VMR retrieval of the five MIPAS target species from a limb-scanning sequence of 16 limb-views is only 348 seconds on a SUN SPARCstation 20.

A further reduction of the noise error on the retrieved profiles can be attained by including in the analysis further microwindows. However, this can be done only at the expenses of the runtime required to perform the retrievals.

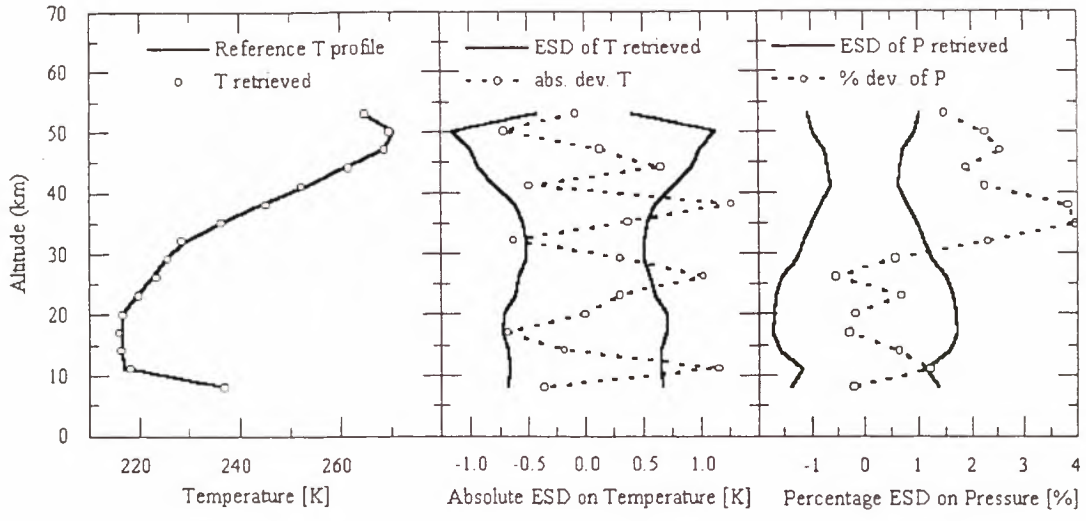
Reference T profile
T retrieved
ESD of T retrieved
abs. dev. T
ESD of P retrieved
% dev. of P
Altitude (km)
Temperature [K]
Absolute ESD on Temperature [K]
Percentage ESD on Pressure [%]

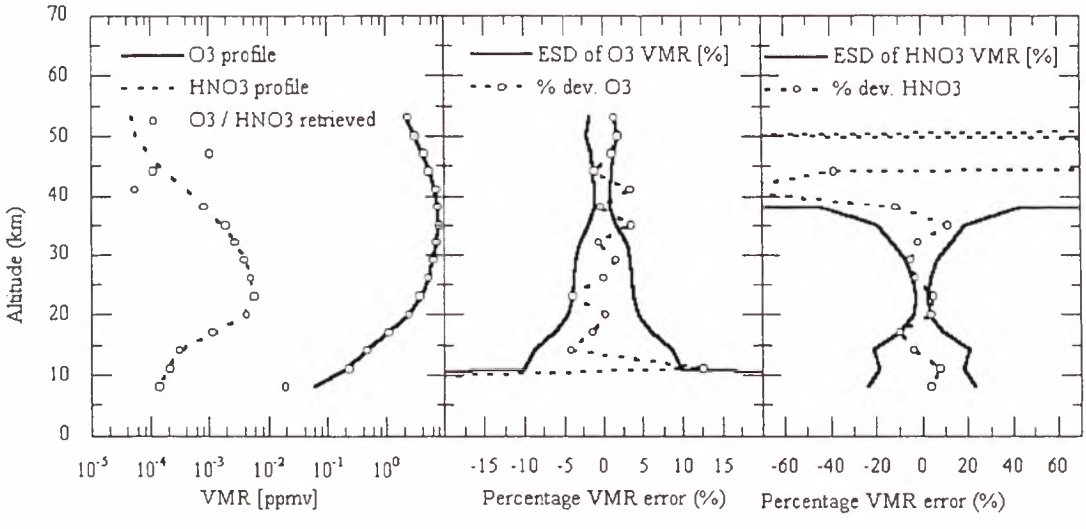
O3 profile
HNO3 profile
O3 / HNO3 retrieved
ESD of O3 VMR [%]
% dev. O3
ESD of HNO3 VMR [%]
% dev. HNO3
Altitude (km)
VMR [ppmv]
Percentage VMR error (%)
Percentage VMR error (%)

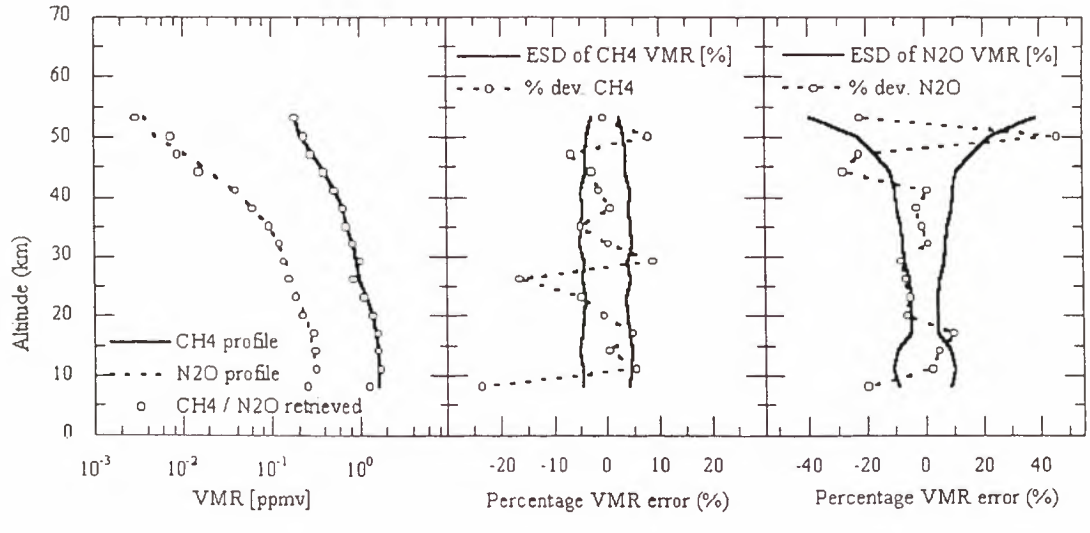
ESD of CH4 VMR [%]
% dev. CH4
ESD of N2O VMR [%]
% dev. N2O
CH4 profile
N2O profile
CH4 / N2O retrieved
Altitude (km)
VMR [ppmv]
Percentage VMR error (%)
Percentage VMR error (%)

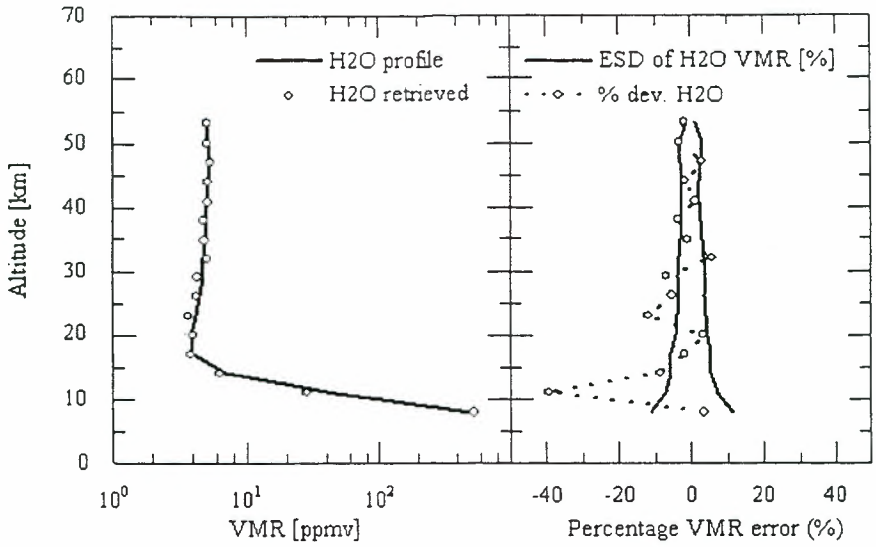

Figure 3. Results of test retrievals carried-out starting from observations generated with the RFM. Each panel reports the reference profiles (*profiles*) with the corresponding retrieved data points (left plots) as well as the deviations (*dev.*) of the retrieved data points from the reference profiles (center and right plots). The Estimated Standard Deviation (*ESD*) of the retrieved profiles is also reported as a solid line in the center and right plots.

AKNOWLEDGEMENTS

This study is supported by ESA contract 11717/95/NL/CN. The study team is grateful to Herbert Nett and Jörg Langen for the fruitful discussions and for the efforts dedicated to an efficient coordination of the overall MIPAS system development.

REFERENCES

1. G. Echle, H. Oelhaf, T.v. Clarmann, and M. Schmidt, "Definition of spectral intervals for the retrieval of trace gas concentrations from MIPAS limb emission spectra", ESA contract: 10993/94/NL/PR, Final Report, (1995).
2. T.v. Clarmann, A. Linden, G. Echle, A. Wegner, H. Fischer, and M. Lopez-Puertas, "Retrieval of pressure and temperature from MIPAS-ENVISAT limb emission spectra", *SPIE* 2961, 128-135, (1996).
3. T.v. Clarmann, and G. Echle, "Selection of Optimized Microwindows for Atmospheric Spectroscopy", *Applied Optics* 37, 7661-7669, (1998).
4. D.W.Marquardt, "An Algorithm for the Least-Squares Estimation of NonLinear Parameters", *J. Soc. Appl. Math.* 11, 431 (1963).
5. R.E.Kalman, "Algebraic aspects of the generalized inverse of a rectangular matrix", in *Proceedings of Advanced Seminar on Generalized Inverse and Applications*, M.Z.Nashed, ed. (Academic, San Diego, Calif., 1976), p.111.
6. W.H.Press, S. A. Teukolsky, W. T. Wetterling, B. P. Flannerly: *"Numerical Recipes in Fortran"*, Second Edition Cambridge University Press (1992).
7. M.Carlotti, "Global-fit approach to the analysis of limb-scanning atmospheric measurements", *Appl. Optics* 27, 3250-3254 (1988).
8. C.D.Rodgers "Retrieval of Atmospheric Temperatire and Composition From Remote Measurements of Thermal Radiation", *Reviews of Geophysics and Space Physics*, Vol. 14 N. 4, p.609, (1976).
9. Edlen, B. Metrology, 2, 12, (1966).
10. Houghton, J.T. "The Physics of Atmospheres" , *2nd Ed, CUP*, Cambridge, (1986).
11. R.H.Norton, R.Beer, "New apodizing functions for Fourier spectrometry", *J. Opt. Soc. Am.* Vol. 66, No. 3, 259, (1976).
12. L.L.Strow, Motteler H.E., Benson R.G., Hannon S.E. and De Souza-Machado S. Fast Computation of monochromatic infrared atmospheric transmittances using compressed look-up tables. J. Quant. Spectrosc. Radiat. Transfer, 59, p481-493, (1998).
13. Edwards, D.P. "GENLN2: A general line-by-line atmospheric transmittance and radiance model. Version 3.0 description and users guide", Rep. NCAR/TN-367+STR, Natl.Cent.for Atmos.Res., Boulder, Colo., (1992).

Algorithm Review

GOMOS

GOMOS MISSION OBJECTIVES

Jean-Loup Bertaux

ABSTRACT

On board ENVISAT, the GOMOS instrument will measure the vertical profile of stratospheric ozone with an unprecedented absolute accuracy , thanks to the advantages of the technique of stellar occultations. In particular, this self-calibrated method is protected from long term drifts, and the study of ozone trend is therefore the major mission objective assigned to GOMOS. The study of scintillations will bring new data on the vertical temperature profile with a high resolution , connected to dynamics and ultimately with vertical mixing of minor species in the stratosphere.The problem of ozone deficit budget at 40 km is discussed as an example of a scientific question in which GOMOS data would certainly contribute for the improvement of chemisty/transport models, necessary for a better forecast tool for the future evolution of ozone in the stratosphere. Simultaneous measurements of NO_2, NO_3, H_2O, O_2 and aerosols with GOMOS are also important in this respect.

1. Introduction

The presence of ozone (O_3) in the Earth's atmosphere is a natural consequence of the presence of molecular oxygen (O_2), itself a by-product of biological activity. In return, the particular optical properties of ozone, namely its powerful absorption of UV radiation, promote the atmospheric ozone layer to the role of a protective shield for life on Earth by preventing the harmful solar UV radiation to reach the ground. Abiotic ultraviolet band B (wavelength 290-320 nm) and band C (200-290 nm) are strongly absorbed by the DNA molecules of living cells. Its absorption can alter or stop reproductive processes of these cells. A well known example is the relation between ultraviolet B exposure and human skin cancer ; the other biological effects are numerous , in particular the increase of cataracts.

This biosphere equilibrium is now threatened by the demographic explosion and related human activities. Stratospheric ozone content has declined worldwide since the 1970s. Apart from the spectacular Antarctic ozone hole, at northern mid-latitudes, above Europe and other heavily populated areas, total ozone is declining by between 4 and 8% per decade. This decline is believed to be related to the massive injection of chlorofluocarbons (CFCs) in the atmosphere at ground level which ends up, many years later, to the liberation of chlorine atoms (Cl) in the stratosphere. There, a series of catalytic chemical reactions allow a single chlorine atom to destroy up to 100,000 ozone molecules before being eliminated.
The almost perfect fulfilment of the Montreal protocol is reducing the production of CFCs and Halons, and this is in principle expected to stop the decline in total ozone , which should reverse over the next few decades.

Although measurements suggest that most of this decline in ozone occurs in the lower stratosphere, in agreement with hypotheses of its detailed mechnism, these measurements of trends in ozone profile (as oppposed to trends in total ozozne) lack sufficient accuracy to make definitive statements. Worse, current models of stratospheric chemistry do not predict the observed decline in ozone. Hence it is essential to continue to monitor trends in ozone, and trends in its profile but with enhanced accuracy. Only in this way can we confirm that our hypotheses about the details of ozone depletion are accurate and that the provision of the Montreal protocol are having the desired effect.

Our understanding of the complex atmospheric machinery is far from being perfect ; a big surprise came with the unpredicted ozone hole, and many other may come later. Clearly, model simulations, which are absolutely necessary to project in the future, must be based on our best understanding of this machinery, constantly improved by comparison with measurements.

GOMOS on ENVISAT platform is one of several instruments that the European Space Agency has selected to develop and fly in space, in order to collect the corpus of ozone data (and other atmospheric parameters) necessary to answer the following questions :
- what is the time evolution of ozone in the stratosphere (the trend) all over the world ?
- what is the effect of CFCs release limitations?
- is the measured ozone trend equal to the trend predicted by our best simulation model predictions ?
- if not, is there anything in the data that can indicate where are the shortcomings of our models and how can they be improved for more reliable predictions ?

Among the three instruments devoted to atmospheric chemistry, the particular role of GOMOS is to establish the 3-D distribution of ozone in the stratosphere and to monitor its trend as a function of altitude, latitude, season and longitude. thanks to the particularly high absolute accuracy offered by the occultation of stars. GOMOS is the acronym of Global Ozone Monitoring by Occultation of Stars, and was first proposed to ESA by a group of european scientists (Bertaux *et al.* , 1988). An industrial Phase A study was conducted by MMS for CNES in 1989-1990. Then it was decided at the ESA countries minister conference of Madrid in 1992 that GOMOS would fly on ENVISAT platform as an ESA funded instrument.

2. Principle and highlights of the stellar occultation measurement.

GOMOS is implemented on ENVISAT opposite to the velocity vector, allowing to look near the horizon the successive setting down of various stars while the platform is moving along its orbit. The principle of the stellar occultation is quite simple (figure 1). When the star is high above the horizon, the light spectrum of the star $F_0(\lambda)$ is recorded by GOMOS, free of any atmospheric absorption. A few seconds later, the light spectrum of the same star seen through the atmosphere (just above the horizon) is again recorded. The spectrum $F(\lambda,z)$ is modified by the absorption of all atmospheric constituents integrated over the line of sight from ENVISAT to the star, according to the Beer-Lambert law :

$$F(\lambda,z) = F_0(\lambda) \exp(-\sigma_\lambda N(z)) \qquad (1)$$

where λ is the wavelength, z is the altitude of the line of sight above the horizon, N(z) (mol./cm^2) is the integrated quantity of ozone along the line of sight and σ_λ the cross section of ozone. Here, only ozone absorption is considered for clarity.

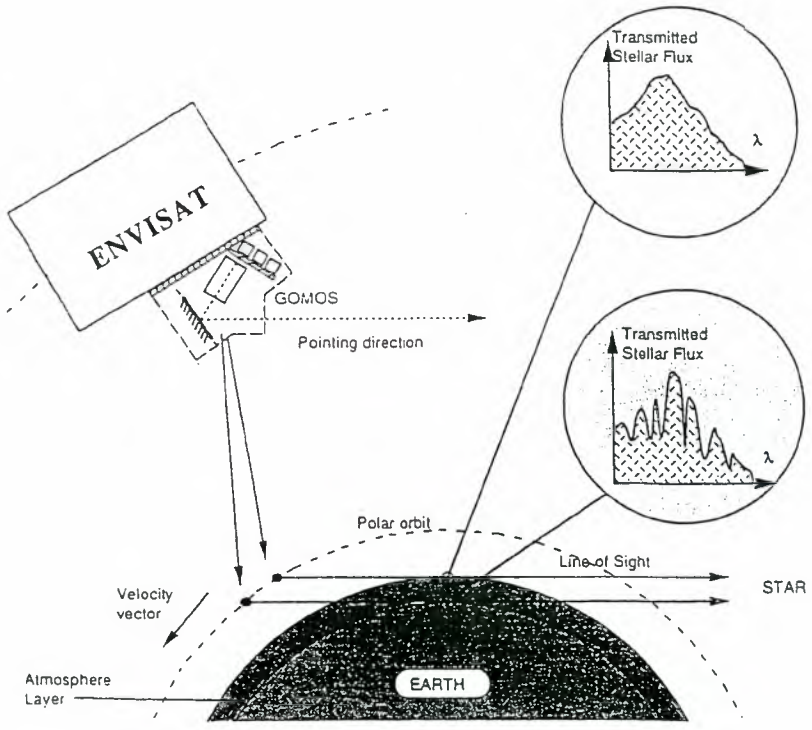

Figure 1. Principle of the stellar occultation used by GOMOS on board ENVISAT. The measured spectral transmission of the atmosphere is interpreted in terms of quantities of absorbers species along the line of sight through the atmosphere (i.e., ozone).

From equation (1) one derive :

$$N(z) = -\frac{1}{\sigma_\lambda} \log_e \frac{F(\lambda,z)}{F_o(\lambda)} \qquad (2)$$

During one single occultation, a series of tangential column densities are obtained at various altitudes z_j. This series can be inverted (vertical inversion) to yield the vertical distribution of the local density of O_3 (mol.cm^{-3}), assuming that the atmosphere is locally spherically symmetric. This vertical inversion is straightforward with the so-called onion-peeling technique.

Besides the extreme simplicity of the retrieval algorithm when compared to other methods, the occultation technique has one enormous advantage readily expressed from the mathematical form of equation (2) : an absolute estimate of N(z) is obtained from the ratio of two measurements taken with the same instrument at a few seconds of interval. The method is inherently self-calibrated, and even if the spectral sensitivity of the instrument is changing with time, the ratio will be measured correctly and hence the column density N(z). This protection against long-term drift is of course ideal for the study of trends of ozone and other constituents.

As shown on figure 2 , the weight function provided by the occultation geometry are very much peaked, with no contribution at all from all the region below the altitude z of the line of sight, and a rapidly decreasing contribution of upper layers. This ensures a well-behaved situation for the vertical inversion.

The altitude of the measurement is entirely defined by the direction of the star and by the position of the spacecraft. ENVISAT position will be known with an accuracy of ± 30 m or better , ensuring the same accuracy on the knowledge of z. The altitude accuracy is important, because an error of 100 m would result in 1% error in ozone density estimate in the altitude region above the peak of ozone. At variance with other limb emission techniques, the altitude of the measurement does not depend on the attitude of the spacecraft and instrument, therefore protecting from long term drift of the accurate attitude knowledge (1 arcsec is projected at the distance of the limb, 3 400 km, as Δz = 20 m).

GOMOS will integrate the stellar light during 0.5 sec., which corresponds in the worst case (occultation in the orbital plane) to an interval of Δz = 1.7 km of altitude projected at the limb, which corresponds to a quarter of a scale height ≅ H/4. The weight functions are accordingly modified as is seen on figure 2. What is important however is that, though the vertical resolution has a finite extension of 1.7 km (or less) the altitude boundaries of the integration slot are known with an accuracy of ± 30 meters.

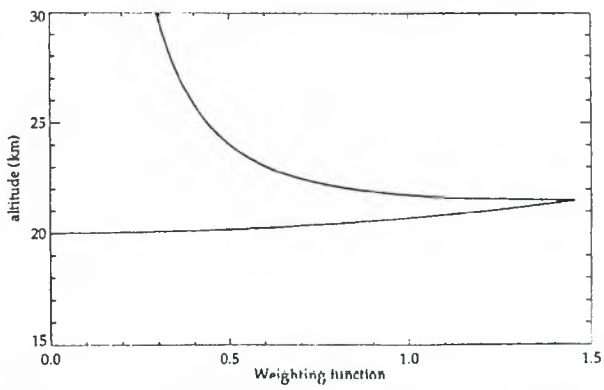

Figure 2 : The weighting functions of tangential lines of sight, integrated over Δz = 1.7 km of altitude.

3. A brief description of the GOMOS instrument and its capabilities

GOMOS is described elsewhere in greater details (Popescu, ESAMS proceedings). Simulations of the atmospheric transmission $T(\lambda,z)$ as a function of tangent altitude z and wavelength λ show that ozone absorbs highly in the UV, which allows to measure it at high altitudes ; at lower altitudes where there is no more UV light, the Chappuis band of ozone in the visible, showing a conspicuous "V shape" absorption, is used to retrieve tangential column densities of ozone. GOMOS includes two different spectrometers with CCD detectors, A and B. Spectrometer A covers the whole UV-visible range 250-675 nm with a resolution of 1.1 nm, while two different orders of spectrometer B are used to cover the O_2 band at 756-773 nm and the H_2O band at 926-952 nm with a resolution of 0.13 and 0.16 nm (figure 3).

The atmospheric refraction causes a loss of light by dilution when lower parts of the atmosphere are probed (below 30 km), and the ray path is no longer a straight line; but moreover, the fine structure of the vertical temperature profile provokes scintillations : these fast variations of light intensity do not occur simultaneously at all wavelengths, and the spectrum of the star seen through the atmosphere is not only absorbed, but also deformed by the scintillations. This problem is taken care of by the use of two fast photometers with bandwidth in the blue and the red which allow to measure scintillations at 1kHz sampling rate , reconstruct the actual deformation of individual spectra, and correct for it in the spectral inversion process.

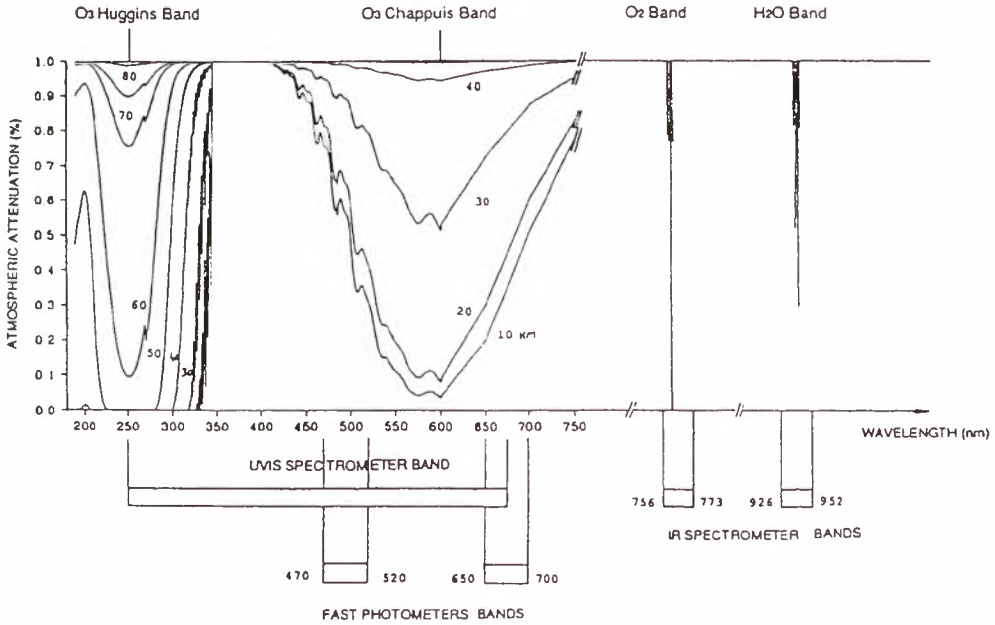

Figure 3. Atmospheric ozone transmission simulated at various altitudes (10-80 km) as a function of Wavelength and domaines of GOMOS spectrometers and fast photometers.

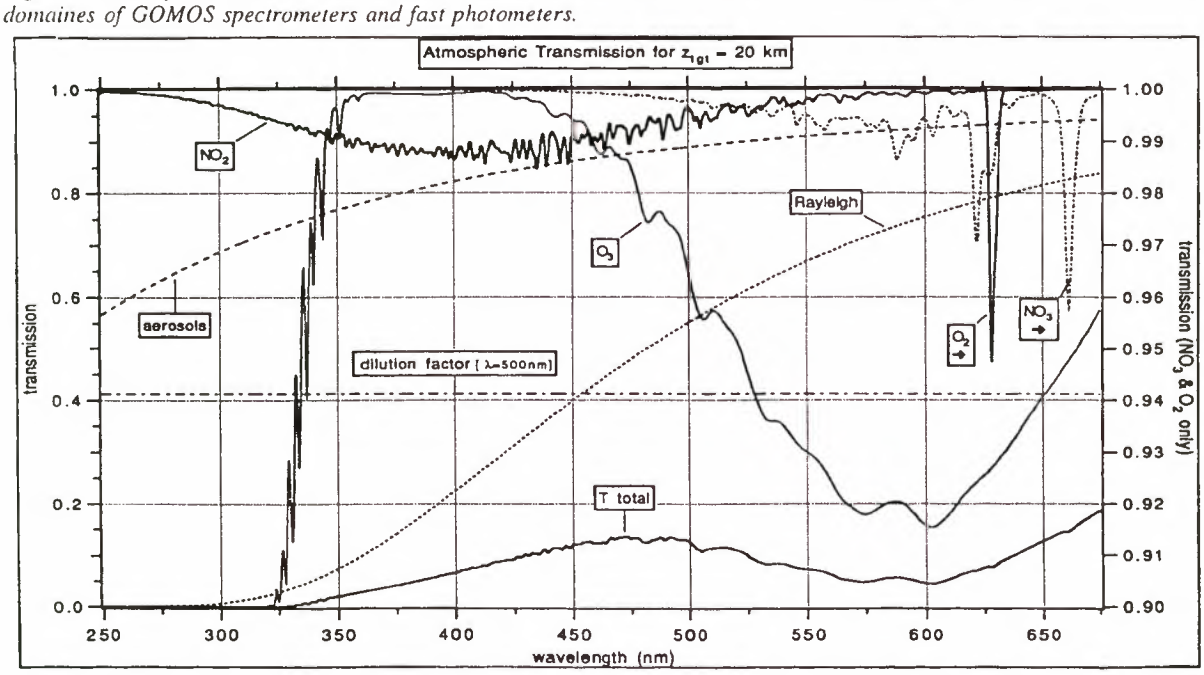

Figure 4. Forward simulation of the atmospheric transmission. The contribution of various absorbers at p = 20 km are indicated as well as the total transmission.The dilution factor is due to atmospheric refraction.

Geographical coverage: Simulations have shown that the occultation of 25 to 45 stars can be observed in one single orbit, distributed over all latitudes. It can be noted that when a star is occulted at one orbit, it will also be occulted at the following almost at the same latitude (figure 5). The star is fixed in an inertial system, the orbital plane has moved only by a small fraction of a degree (≡1/15°) and the Earth has rotated by 25 degrees. Therefore, the succession of points of occultation of the same star are aligned along a constant latitude circle, regularly spaced in longitude. In addition, because of the number of orbits per day (14 and 11/35), nearly the same longitude sampling apply three days later, and sampling of day 2 and day 3 are interlaced with the ones of day 1. Since the correlation time of ozone is more than 3 days (Frederik, 1984), it will be of great interest to regroup 3 days of orbit for a more complete global coverage.

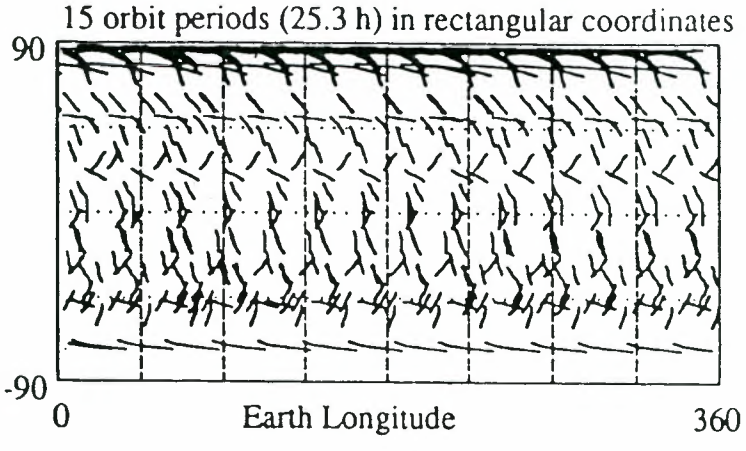

Figure 5. Global coverage obtained with GOMOS in 25. 3 hours (15 orbits)(after Korpela, 1991)

Ozone accuracy retrieval and trend capability:
The brightest stars are giving the best ozone retrievals. Also the color of the star is important, hot stars being favored for the UV and ozone at high altitudes, while cool stars are preferred for H_2O at 936 nm. Along a typical orbit, the number of stars that can be occulted with their brightness and corresponding ozone local density retrieval accuracy δ[O3] are listed below:

	star magnitude	δ[O3]
1 Sirius	mv = -1.44	<1%
3 stars	mv <0	<1%
3 stars	0 < mv<1	1-3%
7 stars	1<mv<2	3-10%
12 stars	2<mv<3	10-30%

An estimate of the trend capabilities was made (Bertaux et al., 1991). During the nominal 4 years mission of GOMOS on ENVISAT, taking a 4% variance of ozone at 40 km, the minimum ozone trend that can be detected by GOMOS in 9 latitudes bands of 20° each is :

$\delta_{GOMOS}(lat) = 0.5 \times 10^{-3}$ (± 0.05 % per year)
and
δ_{GOMOS} (K = 100) = 1.5×10^{-3} (± 0.15% per year)

when the world is divided in 100 geographical regions where the ozone trend must be studied.It can be remarked that a higher precision on integrated line densities is obtained than on local concentrations, and all these primary data will be archived also for trend studies.

Other measured constituents: Stratospheric water vapor H_2O is known to be one of the catalytic scavenger of ozone ; it is therefore important to determine possible long term trends of H_2O in the stratophere, in order to interpret the trends that will be observed for ozone. The chemistry of ozone is also very much connected to the NO_x family ; NO_2 absorbs in the whole visible domaine and NO_3, existing only at night, can be observed around 650 nm . Therefore, the GOMOS spectral range allows to measure the vertical profiles at each occultation site of :
- ozone, H_2O, NO_2, NO_3, aerosols, O_2 and temperature, as seen below.
This will be done both on the night side and the dayside,to check for an expected diurnal variation of ozone above ≅ 40 km from photochemical models. The extent, and the altitude distribution of this diurnal variation, when measured, would provide a test of the photochemical models. In addition, the ozone trend might be different on the night side and on the dayside, and one must test this possibility with measurements on both sides.

4.Temperature retrieval with GOMOS

There is an important wavelength domaine (310-350 nm, the Huggins bands) where the O_3 cross-section are strongly dependent on the atmospheric temperature. Therefore, a long-term variation of absorption in the UV as measured by GOMOS might be due to a temperature variation and wrongly attributed to an ozone density variation. It was felt necessary to include a temperature measurement within GOMOS. This is possible with the A band of O_2 at 760 nm ; since O_2 is a perfectly mixed gas and the air is in hydrostatic equilibrium, its scale height H is directly connected to the atmospheric temperature .This measurement of O_2 allows also to relate all measurements of ozone density (and other species) to the air density to yield the mixing ratio [O3]/[air], which is often a quantity used in the models : comparison of GOMOS measurements with models may be easier with

mixing ratios than with absolute densities. The ILAS instrument recently launched on ADEOS is presently performing measurements of O_2 in the A band by solar occultation.

Another method (invented by Hauchecorne and Dalaudier) will be to use the two photometers. Scintillation spikes observed in the 1 kHz curves will not occur at the same time for the two photometers, but with a small lag time (fig.6) , due to chromatic refraction (the air index of refraction varies with wavelength). Simulations have shown that the fine structure of the temeperature profile, as well as the bulk profile, can be retrieved with an accuracy of 2-4 K (Theodore, 1998). Finally, these scintillations data can be also interpreted to get an estimate of the vertical eddy diffusion coefficient K_Z, which characterizes the vertical mixing of minor species.

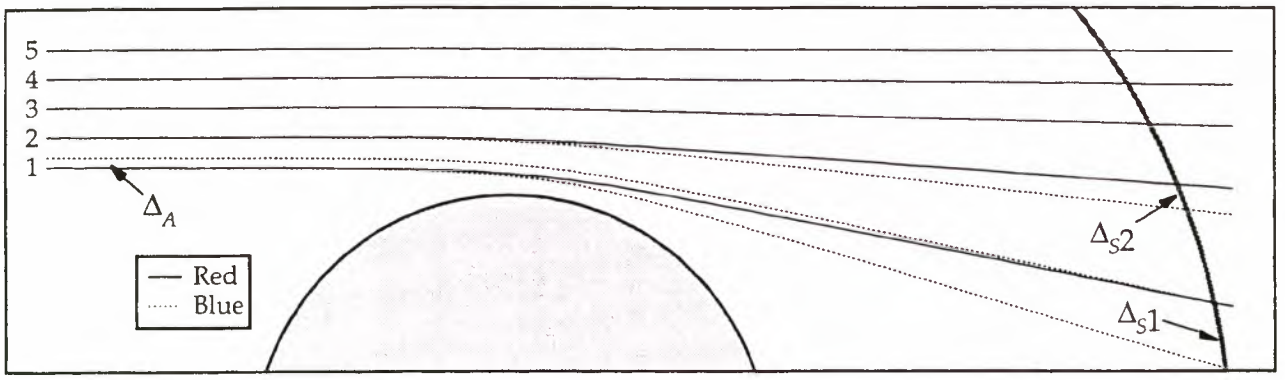

Figure 6 . Schematic representation of the trajectories of rays with various tangent altitudes showing the increasing divergence of the ray tubes after crossing of the atmosphere. Refractive dilution is a consequence of energy conservation within ray tubes. Chromatic effects are illustrated with an exaggerated refractivity ratio m = 1.50. The chromatic lag Δ_S at the satellite level is proportional to the refraction angle while the chromatic shift Δ_A saturates for low altitudes (dilution q smaller than 0.5)(from Dalaudier, 1999)

5. Other mission objectives .

The natural variability of ozone is actually not very well documented. The subset of the brightest stars, yielding high precision vertical profiles of ozone (< 1%), can be used to actually measure the natural variability of ozone as a function of the altitude.

In addition to ozone, the trends on other constituents (NO_2, NO_3, H_2 O, T, aerosols...) will also be measured, and correlated with ozone trends for possible explanations of ozone depletion mechanisms, by confrontation to models (see sections 6 and 7).

In polar hole conditions, OClO might be measured with bright stars. In condition of volcanic activity, SO_2 might be also detected in the lower stratosphere with its strong spectral signature around 310 nm. Aerosols of volcanic origin may also be characterized from their spectral signature, different from the background aerosol loading.

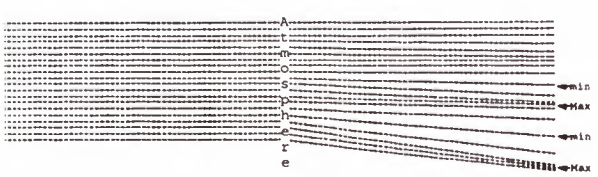

Fig. 7 : Schematic of variable bending of atmospheric rays. Regions marked min and max indicates variations of intensities producing the scintillation effect (after Dalaudier)

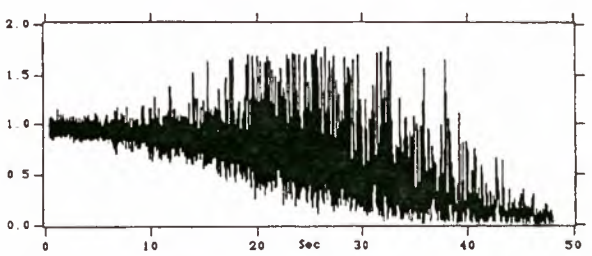

Fig. 8 Stellar scintillations observed from space.

Scintillations are representative of motions in the atmosphere (waves, turbulence, advection, convection,...). These motions, coupled with molecular diffusion, are transporting the various chemical species through the atmosphere. Single wavelength scintillations during a stellar occultation have already obtained from MIR space station (Fig. 8, Gretchko et al, 1997) and interpreted in terms of vertical structure situation. They show detached layers of turbulence above 50 km. The same analysis may be applied with GOMOS at each occultation, yielding for the first time a climatology of atmospheric motions and transport parameters on a global scale. During tangential occultations, occuring at 90° from the orbital plane, the horizontal displacement of the tangent point to the star is much larger than the vertical displacement. Scintillations will therefore probe the horizontal structure of turbulent regions and line densities.

In the equatorial region where the tropopause is at 17 km, water vapor is injected from the troposphere into the stratosphere through convection above cumulo-nimbus. The hygrometry of the extremely dry air which penetrates the stratosphere is controlled by the lowest temperature along the vertical profile, - 80 to -85°. In fact, gravity waves provide temperature variations along the vertical, and hygrometry above the tropopause will depend on the history of temperature above a given point. Due to the extreme sensitivity of H_2O abundance to atmospheric temperature at

the hygropause, GOMOS might be able to detect trends on this temperature based upon a potentially observed H_2O trend. At mid latitudes, H_2O may be injected in the stratosphere from lateral motions of air masses along isentropic trajectories.

Polar Stratospheric Clouds (PSC_S) are high altitude clouds encountered during very cold conditions in polar regions. They are of several types, according to the nature of the condensate, besides H_2O. It is likely that their horizontal optical thickness is so large that the stellar signal will be lost by the star tracker. The main information will therefore be obtained from the very sudden loss of the signal, also observed with the fast photometers. At least the detection of the cloud will be ensured, allowing to make statistics of PSCs occurence and their altitude cloud top.

Noctilucent clouds (NLC) are seen from the ground during twilight. They are the "visible" part of the Polar Mesospheric Clouds (PMC), most of which can be only observed from space. It is a thin layer (2 km) of small ice particles ($r<0.1$ mm) at 83-85 km of altitude, which vertical optical thickness is $\tau_v = 10^{-4}$, and tangential optical thickness around $\tau_h = 10^{-2}$. It is connected to condensation of water vapor during the cold conditions of summer mesosphere.
In emission, they would be detected by the spectrometers, mainly in the two background bands. The actual brightness is about the same as Rayleigh scattering at 50 km of altitude and should give a significant signal which could be interpreted in terms of Mie theory and particle size and nature. In absorption, the 1% absorption over 2 km of altitude would be measurable very well with the fast photometers, which would give the exact height, vertical extent and vertical distribution. This small absorption of 1% on the spectrometers would affect only one or two 0.5 s sampling and might be useful only for the brightest stars while the emission spectrum would always be significant.

PMC appear only at high latitudes during summer. This feature is explained easily by the fact that mesospheric air is descending during summer conditions at high latitudes, and the temperature is at its minimum value (below 150 K, the coldest region of the entire planet). Then water vapor abundance becomes higher than the local saturation vapor pressure, and icy particles condensate around condensation nuclei, which could be either meteoritic dust particles or large water cluster ions .

In his review of the subject, Thomas (1991) advocates that the appearance of PMC is a strong evidence of Global Change. The explanation would be that methane has been increasing steadily since ≅ 1850 (growing population and associated development of agriculture and livestock), with a present growth rate of 1% per year. Indeed , oxydation of methane CH_4 is an important source of H_2O above ≅ 50 km, and therefore an increase of CH_4 at ground level will reflect some years later as an increase of H_2O at mesopause level and a higher probability to encounter frost point temperature conditions. The saturation vapor pressure descreases by a factor of 5 for only a decrease of 4 K for summer mesopause conditions. Therefore, even a moderate climatic temperature change (as induced for instance by increased CO_2 cooling at these altitudes) could reflect on a larger PMC cover over the globe. With its capability to detect the presence of PMC at each occultation, GOMOS will allow to establish an unprecedented corpus of data over the whole globe. Of particular interest will be to document the North-South asymmetry, and to monitor the evolution of PMC cloud cover and the location of its equator boundary.
The chemistry of the mesosphere will be addressed, because GOMOS is able to measure the ozone concentration in the mesosphere by absorption at 250 nm, where O_3 cross-sction ismaximum.

On the dayside, the limb radiance (background) due to Rayleigh and aerosols scattering of solar light might also be used to retrieve ozone and other gases, with a technique used by Sciamachy. The spectrum of the recorded light is influenced by ozone absorption (and also other gases) and may be analyzed in terms of ozone (and other gases) vertical profile. This technique was used on SME spacecraft and will be used by Sciamachy on ENVISAT. Though the retrieval algorithm is much more complex than the occultation one, it will be useful to compare values of ozone retrieved by the two techniques. Included in GOMOS is the capability to perform a "dummy" occultation, in which the tracking mirror is no longer piloted by the image of a star in the star tracker, but rather programmed to perform a motion as if there were a star to be occulted, sweeping the whole range of altitudes across the bright limb.

6. GOMOS and the problem of the ozone deficit budget

In this section we want to illustrate, with a particular scientific question taken as an example, the high diagnostic potential of GOMOS, related to the very high accuracy of O_3 GOMOS measurements and altitude retrieval.

The question is the long standing puzzle of the stratospheric ozone deficit ; we will rely in the following on the recent study performed by Khosravi et al (1998), where they tried to solve the problem by modifying a number of parameters in their 3D model. In the upper stratosphere region (say, 35-50 km), the measured ozone is consistently more abundant than all chemical model predictions by about 10 to 25%, depending on altitude and latitude. This is surprising, since in this range of altitude, ozone is in photochemical equilibrium : the chemical lifetime of O_3 (actually, $O_x = O+O_3$) is only 10^4 s (Brasseur and Solomon, 1984). Therefore, deficiencies in the modelling of transport cannot be blamed for this discrepancy, and the solution should probably be found in a deficiency on the chemical part of the modelling.

Khosravi et al (1998) have established a 2D distribution (altitude -latitude) of ozone measured by HALOE (Halogen Occultation Experiment) on UARS, after a zonal average over a ≅ one month period (from January 6 to February 13, 1992). This distribution is then compared to a similar average in their baseline model, containing the widely accepted standard chemistry as defined by JPL 94. There is less ozone in the model than in the data, by about 10-25%, the 25% peak being found around 42-46 km. Their baseline model is not constrained by any measurements, and produces its own temperature field.

The first model modification was to force the temperature field by UKMO analysis, which is cooler than the free-running baseline model by as much as 5 K above 40 km, and cooler below. As a result, the ozone deficit decreases as much as 8-10%. This is due to a great sensitivity of the Chapman destruction reaction $O + O_3 \rightarrow 2\ O_2$. The loss rate decreases by 3% for 1 K reduction in temperature. While constraining further the model by the observed NOx field does not modify the deficit, the situation is quite different with ClO. This is

because ozone loss is dominated by the ClO field (in addition to T and NOx), the deficit is reduced to 10%.

By changing further the reaction rate of $HO_2 + O \rightarrow OH + O_2$ (reduction of 40%), the ozone deficit is further reduced to a few percent above 40 km, within the rms errors of the Haloe measurements, but then the deficit is enhanced below 40 km. It is clear that the higher accuracy of GOMOS O_3 measurements would be helpful to determine if there are still systematic discrepancies that would need further changes to the chemistry.

A similar exercise as done by Khosravi et al. could be done with only a subset of GOMOS data, taken during one month, for instance. We not however that , in some sense, the model of Khosravi et al. is manipulated " by hand ": the variables are changed one by one. There are possible alternate routes. One is sequential assimilation of GOMOS data into a CTM model, as is presently foreseen in the MSDOL project funded by EEC. This would serve to establish a difference between model and measurements, especially at high altitudes where the chemical constant of ozone is short, because it is in photo-chemical equilibium (PE). There, the model would relax toward the PE value before a new measurement is assimilated. At each assimilation of a new profile of ozone taken by GOMOS, a discrepancy model-data would be noted. If it has a systematic sign (positive or negative), then it would be a clear sign that the chemistry included in the model (including the abundance of some other species not constrained by assimilation) has to be modified for improvement. In order to estimate to which extent the assimilated field represents the GOMOS data or is dictated by the model chemistry (as in the regions of fast PE), a new variable should be computed as suggested by Bertaux and Hauchecorne (1999): the assimilation factor, which represents on each grid point the ratio of ozone molecules resulting from the GOMOS measurements to the total ozone concentration, the rest having been " fabricated " by the model.

Still, there would be the problem to determine what has to be changed in the model for a better prediction of ozone.One possibility would be to apply a 4 D Var model to a limited period of data, say 3 days to get a full Earth coverage. This variational assimilation technique (Lary et al., 1996; Fonteyn et al., this colloquium) allows to minimize the Q^2 difference by varying the initial field of any species included in the model but not forced by the data . The derivatives of Q^2 w.r.t. the concentrations at each grid point and at t_0 must be calculated, preferably with the technique of the adjoint model (Talagrand and Courtier , 1987) .

In fact, it could also be possible to take the reaction rates as variables that can be optimized, in view of the uncertainties of some reaction rate coefficients. We would also even suggest here that new reaction schemes could be added to the chemistry : besides the 145 reactions between the 46 species typically included in a model, all combinations between two species a and b (or with a third M species) could be included, with a reaction rate K_{ab} set to zero in the nominal model if the reaction is unknown to exist. Then, the optimization process would search for optimization and may point to new reaction schemes by setting some K_{ab} to values different from 0. Of course a critical review with a good knowledge of chemistry would be required to check that the proposed value of K_{ab} would not violate the laws of physics. However, we see here the possibility to perform a new type of exercise with " automatic " chemistry in the stratosphere.

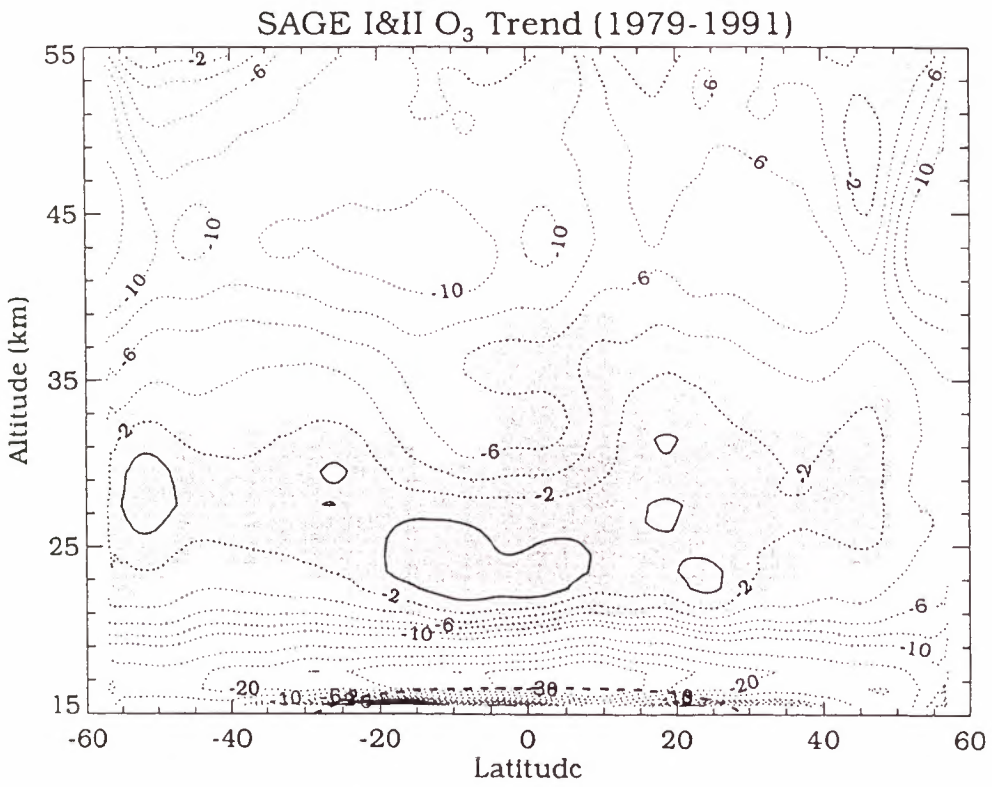

Figure 9. Trends calculated for SAGE I and II for 1979-1991. Hatched areas indicate trends not significant at 2 sigma. Gomos will improve on this situation.

7. Study of ozone trends with GOMOS

While the polar ozone depletion is now well documented and the underlying mechanisms identified (implying heterogenous chemistry on PSC particles), the situation for the other latitudes is less clear. At tropical latitudes, there is no evidence for a total ozone a decrease (from TOMS measurements). At mid-latitudes, a decrease of 2 to 6% per decade seems established. At least three types of explanations have been proposed to explain such a decrease:

- dilution by air migrating from polar regions to mid-latitudes (e.g., Knudsen et al., 1998)
- heterogenous chemistry on aerosol particles, in particular of volcanic origin (sulfate aerosols).
- modulation of ozone transport by upwelling planetary wave activity (e.g., Fusco and Salby, 1998).

In order to discriminate between these mechanims, or to find still another one, it is essential to establish with GOMOS the vertical distribution of the ozone trend. Figure 9 indicates the altitude-latitude variation of ozone as determined between 1979 and 1991 by SAGE I and II (solar occultation). On the whole grey area, the trend found is not statistically significant, and GOMOS, with its high accuracy and daily latitude coverage, would give significant results in this region. Figure 10 indicates the ozone trend as a function of altitude averaged over mid-latitudes, compared with some data and one model prediction. Below 20 km, the observations are somewhat controversial. Sage I and II data might have been hampered by the presence of aerosols, which spectral signature might have been difficult to disentangle from ozone absorption, in view of the small number of spectral channels of SAGE. GOMOS, with its complete wavelength coverage from 250 to 675 nm (and the two IR bands at 760 and 936 nm), should be able to make this discrimination much more easily.

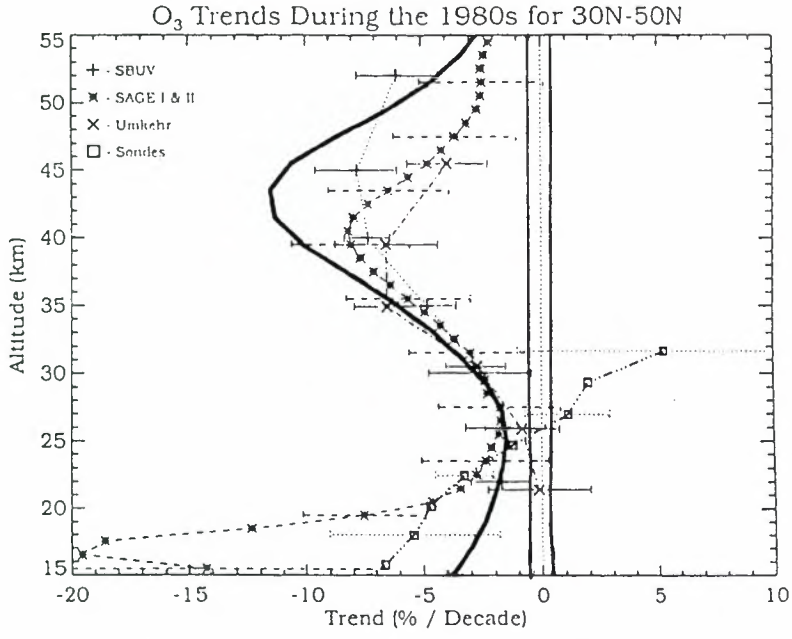

Figure 10. Zonally averaged derived ozone trends for the 80s in the latitude band 30-50° N from SBUV (+), SAGE I and II (*), Umkher (X), sondes (squares) (from WMO, 1995). The solid line is the GSCF-2 model (Jackman et al., 1996).The vertical lines bracketting zero are indicating the GOMOS trend retrieval accuracy.

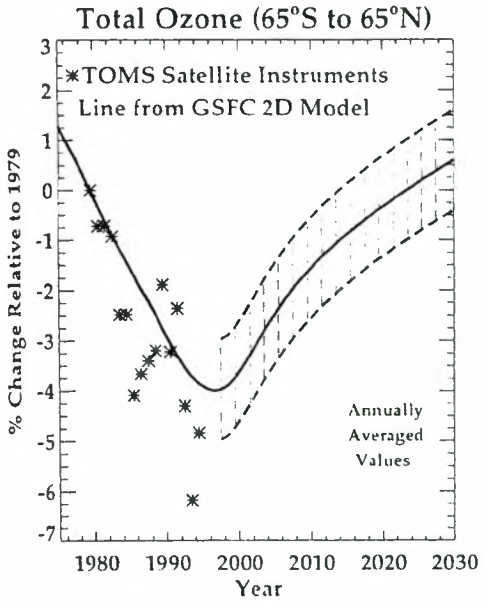

Figure 11. Stars are representing the percentage total ozone changes in the 65° S to 65° N latitude range for TOMS relative to TOMS 1979 values. The solid line is the GSFC-2 model simulation, and its projection into the futur. At the time of ENVISAT, there should be a fast recovery, according to this model.

It is interesting to note that the decrease predicted by the 2D model in the range 35-50 km is larger than the observations. Clearly, it indicates that the model, taken from Jackman et al. (1996), is not perfect. Still, we do need to establish solidly such trend models, since we want to be able to predict the future evolution of ozone and make appropriate political decisions (possibly amendments to Montreal protocol). As an illustration, figure 11 (from Jackman et al., 1996) indicates the past evolution of ozone in the data and in the model, and the model prediction for the future. The model reproduces reasonnably the data, thanks to the inclusion of halogen variations, solar UV variations, and the stratospheric sulphate aerosols linked to volcanic eruptions. Still, there is not a full consensus of the future evolution of ozone : Dameris et al. (1998) argue that the increase of greenhouse gases would modify the temperature and therefore would slow down the ozone recovery especially in the polar regions.
In this respect , it will be essential to correlate the measured ozone GOMOS trends with trends observed on other parameters, in particular the temperature vertical profile and H_2O. Needless to say that both MIPAS and SCIAMACHY on board ENVISAT could contribute for this correlation, in their respective field excellence.

9.Conclusion

GOMOS will provide a large number of ozone profiles, with an unprecedented accuracy, thanks to the self - calibrated method of stellar occultation. Even if no linear trend is obvious over 4 years of ENVISAT lifetime, it will provide a solid ozone reference data base on which later

measurements will be compared to, in particular those obtained with the same methodology, for long term monitoring.

10. Acknowledgements

I wish to acknowledge many useful discussions with GOMOS SAG members, in particular Alain Hauchecorne, Francis Dalaudier, Errki Kyrölä, Gil Leppelmeier, Howard Roscoe and D. Chipperfield on stratospheric studies, Didier Fussen for aerosols. In addition, many other colleagues at Service d'Aéronomie deeply involved in stratospheric research made me quite sensitive to the ozone depletion problem since a long time, in paricular Jean-Pierre Pommereau and Gérard Mégie. Many thanks also to Chris Readings and Joerg Langen for animating the SAG meetings.

REFERENCES

Bertaux, J.L., R. Pellinen, P. Simon, E. Chassefière, F. Dalaudier, S. Godin, F. Goutail, A. Hauchecorne, H. Le Texier, G. Mégie, J.P. Pommereau, G. Brasseur, E. Kyrola, T. Tuomi, S. Korpela, G. Leppelmeier, G. Visconti, P. Fabian, S.A. Isaksen, S.H. Larsen, F. Stordahl, D. Cariolle, J. Lenoble, J.P. Naudet, N. Scott, GOMOS, proposal in response to ESA EPOP-1, A.O.1, January 1988.

Bertaux, J.L., Megie, G., Widemann, T., Chassefiere, E., Pellinen, R., Kyrola, E., Korpela, E., Simon, P.C., Monitoring of ozone trend by stellar occultations : the Gomos instrument, Adv. Space Res., 11(3), 237-242, (1991)

Bertaux J.L., A. Hauchecorne : Un nouveau concept dans les modèles CTM: le facteur d'assimilation, Journées de l'Assimilation, Actes du colloque organisé par le CNFGG, 28 Janv.99

Brasseur, G., and Solomon, S., Aeronomy of the middle atmosphere, D Reidel Publishing Company (1984)

Dameris M., V. Grewe, R. Hein and C. Schnadt, C. Brühl and B. Steil, Assessment of the future devlopment of the ozone layer, Geophys. Res. Lett., 25, pp 3579-3582, 1998

Fonteyn, D., Errera, Q., De Maziere, M.M.H.J., Franssens, G., Fussen, D.,Four -Dimensional Variational Data Assimilation of Chemical Species, this symposium ESAMS (1999)

Frederick, J.E., Measurement Requirements for the detection of ozone trends, ozone Correlative Measurements Workshop, NASA Conference publication 2362, Appendix 3 (1984).

Fusco, A.C., and Salby, M.L., Interannual Variations of Total Ozone and their relationship to variations of planetary wave activity, manuscript (1998)

Gretchko G.M., Gurvich, A.S., Kan V., Pakhomov, A.I., Podviaznyi, Ya.P., Savchenko S.A., Observations of atmospheric turbulence at altitudes of 20-70 km, Trans. Russ. Acad. Sci., Earth Sci. Sect., 357A n°9, 1382-1385 (1997)

Jackman C. H., E.L. Fleming, S. Chandra, D.B. Considine and J. E. Rosenfield, Past present and future modeled trends with comparisons to observed trends, Geophys. Res. Lett., 101, pp. 28,753-28,767, 1996

Khosravi, R., G.P. Brasseur, A.K. Smith, D. W. Rusch, J.W. Waters and J.M. Russell III, Significant reduction in the stratospheric ozone deficit using a three-dimensional model constrained with UARS data, J.Geophys. Res., 103, pp. 16,203-16,219, 1998.

Knudsen B.M., W. A. Lahoz and A. O'Neill, J.J. Morcrette, Evidence for a substantial role for dilution in Northen mid-latitude ozone depletion, Geophys. Res. Lett. 25, pp. 4501-4504, 1998.

Korpela, S., A study of the operational prindiples of the GOMOS instrument, Ph.D.Thesis, FMI, Helsinki, 1991.

Lary D.J., S. Hall, M. Fischer, An overview of atmospheric chemical data assimilation

Popescu A., GOMOS instrument concept and performance, this symposium ESAMS (1999)

Talagrand, O., and Courtier, P.,Variational assimilation of meteorological observations with the adjoint vorticity equation. I. Theory, Q.J.R. Meteorol. Soc. 113, pp.1311-1328, (1987)

Theodore, B., Thesis, (1998)

Thomas, G.E., Mesospheric Clouds and the Physics of the Mesopause Region, Reviews of Geophysics, 29, pp. 553-575, (1991)

The Global Ozone Monitoring by Occultation of Stars (GOMOS) Instrument on ENVISAT: Requirements, Design and Development Status

Alexandru F. Popescu and Torgeir Paulsen
European Space Agency ESA/ESTEC – The Netherlands

ABSTRACT

GOMOS is a medium resolution spectrometer designed to measure the concentrations of, and monitor the trends in, stratospheric ozone with very high accuracy and to observe other atmospheric trace gases. Using the star occultation technique, GOMOS combines the features of self-calibration, high vertical resolution and good global coverage. Due to its high sensitivity down to 250 nm, which is one of its main design drivers, GOMOS can measure ozone profiles from 15 km to 90 km. Accessible altitude ranges, accuracies and global coverage are optimum on the night side. In addition, it can measure high accuracy temperature profiles, which are of interest for understanding the vertical exchange of energy in the Earth's atmosphere. The main mission, instrument and the equipment requirements and performances are presented. The GOMOS instrument development has been completed and the flight model delivered and integrated on the ENVISAT spacecraft.

1. INTRODUCTION

The atmosphere, the land and the sea form a complex interlinked system, whose equilibrium state is essential for life on earth. Herein the atmosphere plays an "interfacing" role with respect to energy and mass transport between the land, the sea and outer space. During the last decades it has become increasingly apparent that the chemical composition of the atmosphere is changing on a global scale and that human activity is partly responsible for this change. ozone plays a central role in the atmospheric chemistry. It is largely responsible for stratospheric heating through absorption of harmful UV radiation, it determines to a large extent the oxidative capacity of the troposphere and is an important "greenhouse" gas. The discovery of the "ozone hole" over the Antarctic has also drawn attention to the global ozone budget.

In order to understand the processes which determine the physical and the photochemical behavior of the atmosphere, detailed global measurements of the amount and of the horizontal and vertical distribution of ozone and of the other gases is necessary. Using measurements from ground-based and satellite-based instruments, ozone trends have been analyzed from 1964 to the present. These measurements agree within their range of errors of several percent but leave a large band of uncertainty (ozone depletion rates have been on the order of fractions of a percent per year, which is much below the measurement accuracy of most of the existing space borne instruments). A comparison of ozone trend measurements with simulation models still shows large discrepancies. Consequently, there is a clear need to increase our understanding of the central processes involved in atmospheric chemistry, and it is vitally important to monitor and investigate global budgets of ozone and other chemically important gases. In order to fulfill this need, accurate altitude-resolved data are necessary.

Starting with its ERS-1 satellite, the European Space Agency (ESA) has initiated a wide earth remote-sensing satellite program. GOME (Global Ozone Measurement Experiment), the first European ozone monitoring instrument, was launched onboard the ERS-2 satellite in 1995. The primary measurement objective of GOME is the measurement of total column amounts and profiles of ozone and of other gases involved in ozone photo chemistry..

The ENVISAT-1 satellite, presently under development and scheduled for launch in 2000 is after ERS-1 and ERS-2 the next milestone of the European "Strategy for Earth Observation" established in 1988. The payload of ENVISAT-1 consists of six ESA Developed Instruments (EDI's) funded under the ENVISAT-1 Program and of three Anouncement of Opportunity (AO's) instruments, funded nationally by the participating states.
The Global Ozone Monitoring by Occultation of Stars (GOMOS) Instrument onboard ENVISAT-1 was proposed in 1989 as a tool to provide altitude resolved global ozone mapping and trend monitoring with very high accuracy as needed for the understanding of ozone chemistry and for model validation.

2. THE GOMOS MEASUREMENT PRINCIPLE

The measurement principle of the GOMOS instrument is shown in Figure 1. It shows schematically the instrument and its accommodation on board the spacecraft. The instrument line of sight can be successively oriented towards preselected

stars and maintained whilst the star is setting behind the Earth's atmosphere observed on the horizon. During the star occultation, the ultraviolet, visible and near-infrared spectra of the star are continuously recorded.

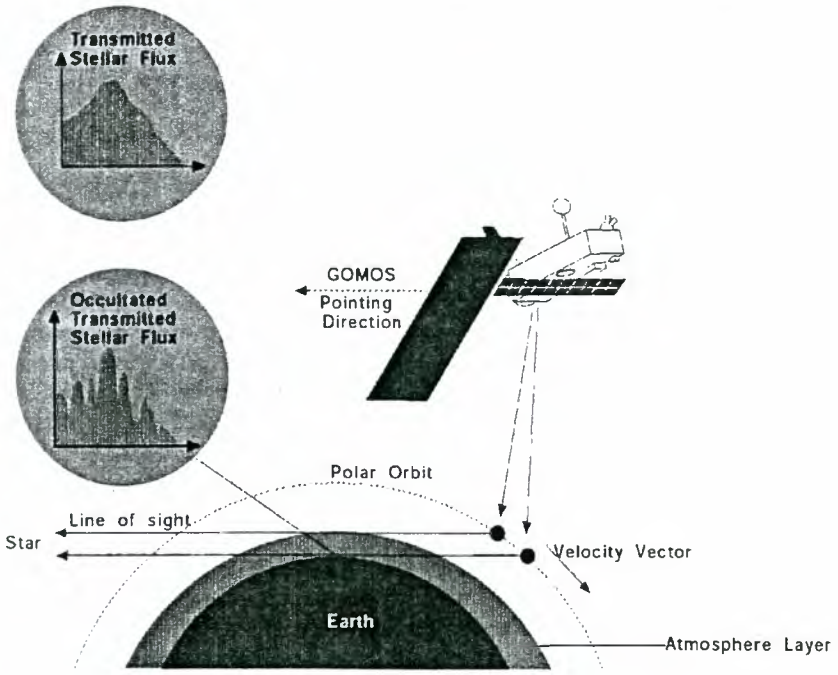

Figure 1 GOMOS Measurement Principle

As the star sets through the atmosphere, its spectrum becomes more and more attenuated by the absorption of the various gases in the atmosphere, each of which is characterized by a known, well-defined spectral signature. Back on the ground, these attenuated spectra recorded by GOMOS will be compared with the unattenuated stellar spectrum measured a few tens of seconds earlier, outside the atmosphere, so allowing the absorption spectra to be derived very accurately. This radiometrically self-calibrating method is protected from sensitivity drifts and is thus capable of fulfilling the challenging requirement of reliably detecting very small trends in ozone (and other gas) profiles.

During day-side observations, the solar radiation scattered by the atmosphere is superimposed to the star signal as the line of sight starts crossing the atmosphere. In order to be able to retrieve the star signal transmitted through the atmosphere without the background component, the (vertically imaging) spectrometers are recording the background spectrum just above and below the star too. These spectra are then used on ground for background removal.

GOMOS uses, as SAGE, the occultation measurement method, which compared to other methods offers the advantage of high measurement accuracy and of very good altitude profiling. However, instead of using the sun as occulting source, GOMOS uses stars for performing the occultation measurements. There are more than 300 stars which are bright enough for GOMOS to observe them as they are setting through the atmosphere Figure 2 shows a typical example of the northern hemisphere coverage of the star occultations available over one day. Over one day/one month there are typically 1600/48000 occultations to be chosen from. Selection criteria like coverage of specific latitudes/longitudes, altitude ranges, etc. can be applied, while still maintaining a good global coverage.

Figure 2: Typical one day coverage over the Northern Hemisphere (21 March)

3. THE GOMOS MISSION OBJECTIVES

The mission objective of GOMOS is to measure vertical profiles of, and monitor the long-term trends in, ozone and other atmospheric trace gases with very high accuracy. The instrument will operate on both the night and the day side of the orbit, thus being able to monitor diurnal variations, and will offer global coverage. GOMOS will perform measurements in the altitude range of 15 km to 90 km. Its altitude sampling interval will be smaller than 1.7 km. GOMOS will perform on the average more than 600 measurements per day over its 4-year lifetime. Figures 3 show the gases which will be measured by GOMOS versus the altitude.

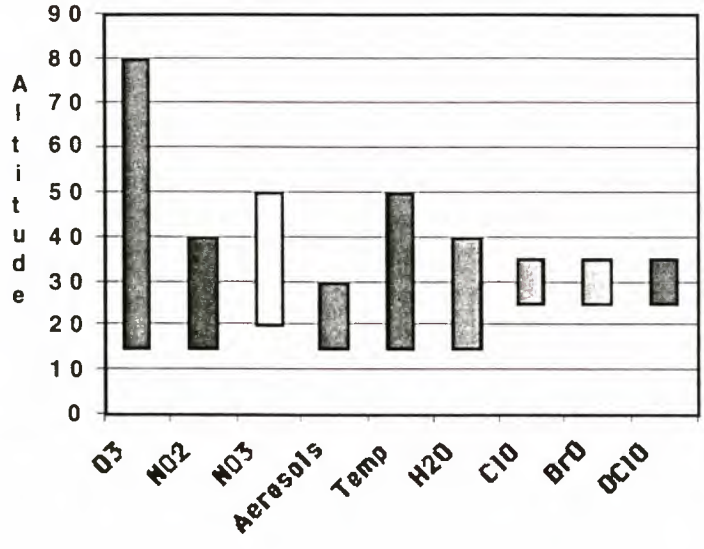

Figure 3 GOMOS Products versus altitude.

4. INSTRUMENT REQUIREMENTS AND DESIGN

4.1 The GOMOS instrument requirements and design drivers

GOMOS is a medium resolution spectrometer covering the wavelength range from 250 nm to 950 nm. The high sensitivity requirement down to 250 nm has been a significant design driver leading to an all reflective optical system design for the UVVIS part of the spectrum and to functional pupil separation between the UVVIS and the NIR spectral regions (thus no dichroic separation of UV). Due to the requirement of operating on very faint stars (down to magnitude 4 to 5) the sensitivity requirement to the instrument is very high. Consequently, a large telescope (30 cm x 20 cm aperture) had to be used to collect sufficient signal, and detectors with high quantum efficiency and very low noise had to be developed to achieve the required signal to noise ratios.

In addition, in order to use the entire star signal, a slitless spectrometer design had to be chosen. The price which had to be paid for this "light efficient" design is that a highly performant pointing system had to be used to keep the star image fixed at the input of the spectrometers in order not to degrade the spectral resolution and the spectral stability.

To achieve a high signal-to-noise ratio when observing the very weak star signal embedded in strong surrounding atmospheric background and stabilizing the star image in spite of the satellite disturbances are major engineering challenges for the GOMOS design.

The main instrument requirements and the resulting design drivers are summarized in Table 1.

Requirement description	Requirement
Spectrometers	
Occulting stars characteristics	Visual magnitude range: max. -1.6 to min. 2.4 to 4 for stars with 30000K and 3000K temperature respectively
Spectral range of the spectrometer:	UV: 250 - 375 nm VIS: 405 - 675 nm IR1: 756 - 773 nm IR2: 926 - 952 nm
Spectrometer spectral resolution	1.2 nm in UVVIS 0.2 nm in NIR
Spectrometer spectral sampling	0.3 nm in UVVIS 0.05 nm in NIR
Spectrometer spectral rejection	UVIS: 85% in 4 samples monochromatic NIR: 85% in 4.5 samples monochromatic
Spectrometer spectral stability knowledge in dark limb	0.07 nm in UVVIS 0.015 nm in IR1 0.018 nm in IR2
Spectrometer spectral stability knowledge in bright limb	0.22 nm in UVVIS 0.025 nm in IR1 0.030 nm in IR2
Relative spectral accuracy	1.5 nm in UVVIS 0.3 nm in IR1 0.3 nm in IR2
Direction of spectral dispersion	Tangential to earth limb within 2 degrees
Dispersion stability	0.12 nm in UVVIS 0.02 nm in IR1 0.02 nm in IR2
Relative dispersion accuracy	1.5 nm in UVVIS 0.3 nm in IR1 0.3 nm in IR2
Spatial extent of spectra UVIS NIR	Target (star) Background Separation 18-70 arcsec 24-96 arcsec 8-20 arcsec 13-52 arcsec 18-70 arcsec 8-20 arcsec
Polarisation sensitivity	< 1 % (Goal)
Integration time Dead time Start time of record precision Photometer/Spectrometer synchronisation	0.5 sec ± 0.5 msec < 10 msec < 5 msec < 100 μsec
Photometers	
Photometer spectral windows and sampling rate	470-520 nm and 650-700 nm 1 kHz sampling rate
Photometer instantanous FOV	> 60 arcsec vertically > 10 arcsec horisontally
Photometer Spatial rejection	> 95% of spatial LSF within 26 arcsec
Short term radiometric stability (over 150 s)	1 %
Sampling frequency Dead time Start time of record precision	1 kHz < 0.1 msec < 5 msec
Linearity	1%
Pointing Requirements	
Pointing stability	Better than 40 microradians peak-peak
Number of occultations per orbit	45 on average, i.e. approximately 920000 occultations during the 4-year mission
Loss of tracking probability	< 10% in dark limb, < 20 in bright limb
Angular coverage	-10 deg. to +90 deg. with respect to the flight direction. Thus, large instrument angular range observability

Table 1 : Instrument requirement summary

4.2 The overall instrument design

The block diagram of the GOMOS instrument is shown in Figure 4. It is based on a 30 cm x 20 cm telescope, whose pupil is shared by the UVVIS and NIR spectrometers and by two redundant star trackers. This function is fulfilled by the optical beam dispatcher. The signal collected by the NIR subpupil is subsequently dichroically splitted between the NIR spectrometer and two photometers (1 and 2). A two-stage steering front mechanism (SFM) moving a 30 cm x 40 cm flat mirror is used to point the line of sight towards the selected star and to track it with very high accuracy as it sets through the atmosphere. The telescope, the optics, all sensors and their associated front-end electronics are mounted on a thermally controlled optical bench. This telescope and optical bench assembly (TOBA) and the SFM are mounted via a GOMOS interface structure (GIFS) to the spacecraft. The entire spacecraft-external GOMOS instrumentation (opto-mechanical assembly: OMA) is covered by an opto-mechanical cover responsible for protecting the instrument from light coming from a different direction than the defined angular range and for ensuring a stable, defined thermal environment. The OMA is connected to the instrument electronics consisting of the sensor detection electronics, the redundant instrument control unit and the redundant mechanism drive electronics in the payload equipment bay of the satellite via a dedicated harness.

The main spacecraft resource requirements of the GOMOS instrument are:

- Instrument mass: 175 kg.
- Instrument power consumption: 200 W.
- Data rate to satellite: 226 kbit/s.

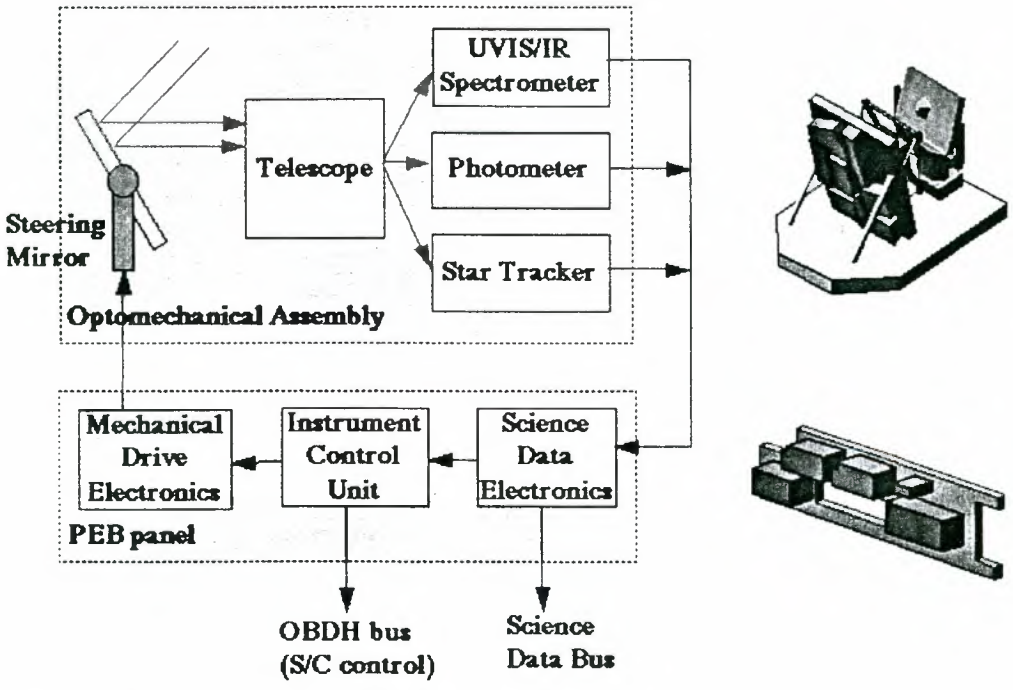

Figure 4 : GOMOS instrument block diagram

4.3 The equipment design and performances

The spectrometer CCD

A special frame transfer CCD has been developed to meet the needs of the GOMOS mission. This is a frame-transfer, thinned, back-side illuminated, radiation-hardened CCD. The main characteristics and performances of the flight models are presented below.

- CCD linearity : < 0.6 %
- pixels : 20 µm x 27 µm
- image zone : 143 x 1353 pixels
- memory zone : 142 x 1353 pixels
- dark signal : < 25 pA/cm^2 at BOL @ 20°C.
- Image zone charge capacity : 5.9×10^5 e$^-$
- Register zone charge capacity : 1.2×10^6 e$^-$

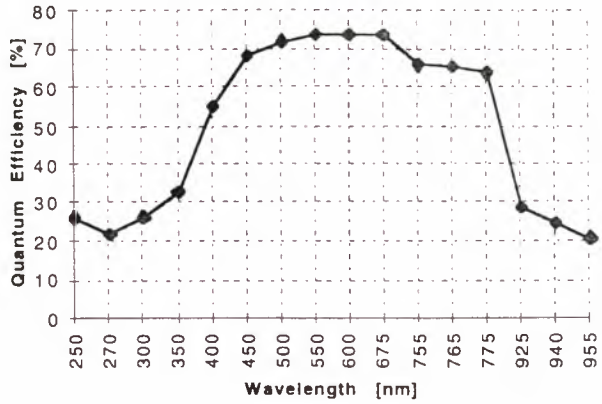

Figure 6 : Flight model quantum efficiency performance

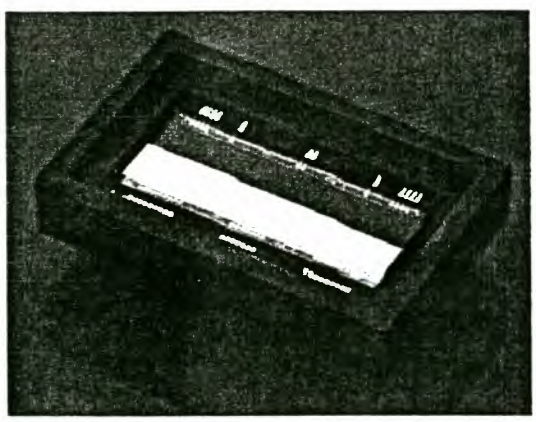

Figure 5 : Flight model spectrometer CCD.

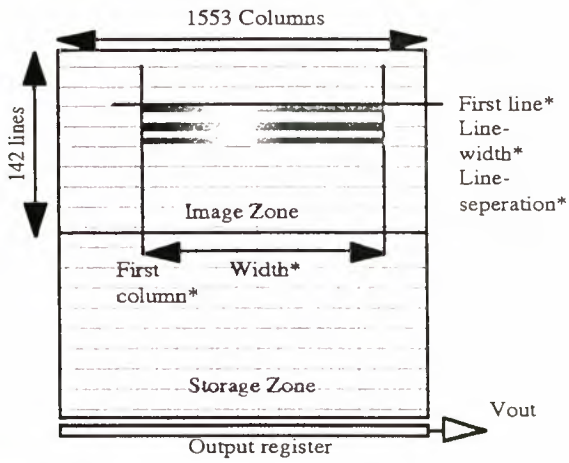

Figure 7 : Spectrometer CCD read-out structure

The steering front mechanism

The steering front mechanism (SFM) consists of a flat mirror of some 40 x 30 cm mounted on a two stage steering mechanism. A coarse steering mechanism, in azimuth only, steers the mirror coarsely towards the occulting stars within a 100-degree angular range, while an azimuth and elevation fine steering mechanism with a range of approximately +/- 4 degrees is performing the acquisition, centering and tracking of the star as it sets through the atmosphere.

The azimuth coarse pointing mechanism is using a ball screw drive, while the fine steering stages are using voice coil actuators. The fine steering stages together with the mirror are inertially mounted so that spacecraft microvibrations are not transmitted to the line of sight. Additionally, electrodynamical dampers are used for microvibration damping. The control bandwidth of the mirror is approximately 5 Hz.

The main requirements together with the resulting technological and design choices are summarized in the table below. Figure 8 shows the steering front mechanism flight model.

Parameter	Requirement	Selected technology / design
Angular range (optical)	100 degrees	Two stage (coarse + fine) design
Open loop pointing accuracy	better than +/- 0.02 degrees bias and +/-0.01 degrees dynamics	High resolution inductosyn angular sensors (1 LSB = 0.0009 degrees)
Torque (acceleration) resolution	5 micro Nm	Voice-coil actuators together with high linearity electronics
Microvibration rejection	3 microradians residual above 10 Hz	Three axis, frictionless mirror mounting
Number of angular travel cycles	> 1.5 million of 70 degrees average	

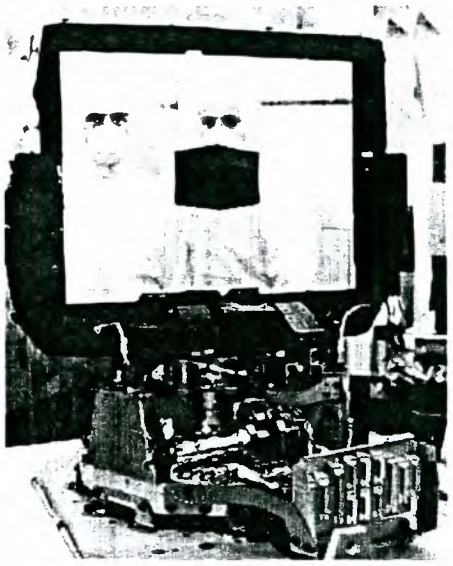

Figure 8 : GOMOS steering front mechanism (flight mode)

The Science Data Electronics (SDE)

The Science Data Electronics (SDE) is the CCD sensor control and signal conditioning unit. It controls a total of 8 CCD's (two for the UVVIS spectrometer, two for the NIR spectrometer, two for the fast photometers and two for the nominal and for the redundant star tracker). This unit has a high degree of programmability.

During the star occultation measurement, three bands of the spectrometer CCD's are read out. They contain the star, the upper and the lower background spectrum. The typically 7 lines of these bands are binned out in the output register of the CCD before reading. The position, the width and the separation of these bands are all programmable. This gives a high degree of flexibility in optimizing the detection performance to specific observation objectives. During specific monitoring modes, the CCD's are read-out in unbinned mode and the integration times are programmable between 0.25 s and 10 s.
The sequencing of the star tracker CCD is adapted dynamically to the different phases of star detection centering and tracking as follows. In the initial phase of star detection the SDE detects the coordinates of the most illuminated pixel of the CCD using a programable integration between 5 ms and 50 ms depending on the star

magnitude. As soon as the star has been detected, a 10x10 pixel window centered around the star is read-out with programmable integration times between 5 ms and 10 ms. This window follows the star as the tracking system centers the star in the field of view. As soon as the star is centered, the read-out window "collapses" to 8x8 pixels and the read-out frequency is set to 100 Hz with 5 ms or 10 ms integration times.
The analog signal conditioning consists of low noise, programmable gain channels. The analog to digital conversion is done with 12 bit ADC's.

The telescope

The GOMOS telescope has a rectangular aperture of 30 cm x 20 cm. It has to operate in a 0.6-degree field of view and has to have very good transmission in the 250nm to 950 nm range. The small allowable volume (intermirror distance < 250 mm) coupled with the high quality imaging and stability requirement and coupled with the high stiffness requirement (first eigenmode above 180 Hz) were very challenging. A Cassagrain design based on aspheric primary and secondary mirrors and based on a CFRP structure has been chosen. Figure 9 shows the layout of the telescope. The main telescope performances together with the resulting technological and design choices are summarized in the table below. Figure 9 shows the telescope flight model.

Parameter	Requirement	Selected technology / design
Field of view	0.6 degrees	Cassagrain design
Optical transmission	> 82 % between 250 nm and 500 nm > 92 % between 500 nm and 952 nm	Al coated UVVIS subpupil and AG coated NIR subpupil
Intermirror distance stability	better than 10 micrometers	coefficient of thermal expansion and coefficient of moisture expansion compensated CFRP structure
Imaging quality	UVVIS: 25 µm @ 85 % encircled energy NIR: 30 µm @ 85 % encircled energy	Cassagrain design with aspheric primary and secondary mirrors

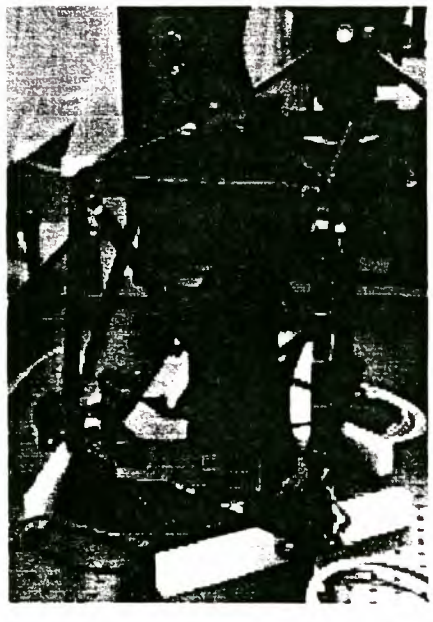

Figure 9 : Telescope flight model

4.4 The instrument operational modes

The main mode of operation of GOMOS is the occultation mode. During this mode the instrument is, as a result of a macrocommand, autonomously acquiring and tracking stars as they set through the atmosphere. The sensors

are operated in binning mode for the star band and for the upper and lower background bands. Both the width and the separation and position of these bands can be programmed. In this way optimum alignment can be ensured over the instrument lifetime and the signal-to-noise ratio can be optimized.

The occultation mode has a specific submode called "fictive star" submode. In this submode the instrument is scanning the limb along a programmable trajectory as if a star were present. This submode can be used for limb sounding under bright limb conditions.

In addition to the occultation mode the GOMOS design supports also three other modes, called monitoring modes, which enable in orbit monitoring and recalibration of important instrument performance parameters used in the ground processing. These monitoring modes are:

The uniformity mode: In this mode the CCD sensors are read out in a non-binned, i.e. pixel by pixel, mode. Depending on weather, the instrument is pointed towards "dark space" or towards uniform limb, the dark current or the photoresponse uniformity of the CCD sensors will be characterized. In this mode the tracking function is disabled. The spectrometer integration time is programmable in the range of 0.25 s to 10 s.

The spatial spread mode: In this mode the instrument operates as in uniformity mode but with the tracking function active. Thus, the optical transfer function of the instrument can be monitored in this mode by observing a star outside the atmosphere.

The linearity mode: In this mode the sensors are operated in binned mode as in occultation mode but with variable integration times (in the range 0.25 s to 10 s). This mode will be used to monitor the linearity of the detection chains during the instrument lifetime by observing stars outside the atmosphere with variable integration times.

5. GOMOS MISSION PLANNING

GOMOS mission planning has been optimised to maximise the scientific return from GOMOS. mission objectives can be grouped under two general headings :

- Long Term Objectives, which are specific to the atmospheric chemistry objectives of GOMOS.
- Campaign Objectives which are needed to validate GOMOS products and to compare them with the other two chemistry instruments on ENVISAT.

Depending on the specific mission objectives, with attached priority factors, the stars to be observed are selected from the star catalogue. The sequencing of observations are done according to the instrument's time line capabilities. The observing schedule will be encoded as a macro-command for uploading to the satellite.

Various simulations have been performed to determine the merit functions of the different observing strategies. Figure 2 gives an example of a set of stars selected to observe stratospheric ozone over a period of one days near the spring equinox ([1]).

The mission planning software is designed to include observation scenarios for long term observations (over days or weeks) as well as for "targeted" short duration observation such as those related to a volcanic eruption.

6. GOMOS PAYLOAD DATA SEGMENT:

All data received on ground are systematically processed and the following products are routinely generated within the ESA Payload Data Segment (PDS): Level 0, Level 1b (transmittance), and Level 2 (profiles of ozone and other species). These products are generated in near real time (i.e. within three hours from sensing) and then regenerated off-line using updated auxiliary data (precise orbits instead of predicted orbits, meteorological analysis fields instead of meteorological predictions, etc...).

[1] Since the rotation of the ENVISAT orbit plane in the inertial reference frame is of the order of 1° per day, there is very little change in the star observing sequence over 3 days; this explains the distribution of the observation and the annular shape of the observation pattern.

With the exception of the quality of the auxiliary data, the algorithms used in "near real time" and "off-line" processing are identical. All ESA processing centres (the Kiruna and ESRIN stations) for the "near real time" products and the German processing and archiving centre (supported by the Finish Meteorological Institute) for the "off-line" products, use the same processing algorithm, so the user will get consistent products irrespective of the processing centre.

The ESA Level 1b and Level 2 algorithms have been defined following the ENVISAT expert support laboratory (ESL) approach where a scientific team gives support to an industrial contractor (ACRI, Sophia Antipolis, F). This scientific team includes members of the Service d'Aéronomie (Paris, F), the Finnish Meteorological Institute (Helsinki, SF) and the Institut d'Aéronomie Spatiale (Bruxelles, Belgium). These algorithms have been prototyped by the ESL and then implemented, within the Payload Data Segment consortium led by ALCATEL Space, by SSF Finland.

Consistency checks in the algorithms and precision estimates of data products have been performed using the simulation tools mentioned above. During ENVISAT commissioning phase, a geophysical validation campaign will be carried out. This will put the Level 2 data of GOMOS and its companion instruments MIPAS and SCIAMACHY in correlation to a large manifold of independent observations by remote sensing and in situ experiments operating on other satellites, aircraft, balloon gondolas and on the ground. The air volumes and observation times of these validation instruments are unlikely to coincide precisely with those of the ENVISAT instruments; atmospheric models will be used to bridge the gap between the different measurements.

7. CONCLUSION

The GOMOS instrument to be carried by ENVISAT-1 has been delivered and integrated on the spacecraft. The instrument performance indicate a performance level compliant with the requirements. GOMOS will exploit for the first time the very accurate star-occultation measuring principle for monitoring the earth atmosphere. It will deliver very accurate ozone profiles and trend measurements. In synergy with the other ENVISAT-1 instruments, GOMOS promises to contribute significantly to environmental monitoring and to our understanding of the mechanisms governing atmospheric chemistry.

8. ACKNOWLEDGMENT

We would like to use this opportunity to express our thanks and recognition to the following people and groups who have so far contributed significantly to the development of the GOMOS instrument:

To the GOMOS Science Advisory Group and in particular to J.L. Bertaux from Service d'Aeronomie France, G. Leppelmeier from the Finnish Meteorological Institute and to C. Readings from ESA, all of whom initiated, promoted and supported very actively the GOMOS mission since its very beginning.

To Gilbert Uguen, Jean Dauphin and Pierre Merat from Matra Marconi Space France, who have led the industrial development consortium during the definition and the design consolidation phases.

To the GOMOS teams of Matra Marconi Space France and to those of the companies of the industrial consortium.

To Odile Fanton d'Andon and Gilbert Barrot of ACRI France, who have developed the GOMOS end-to-end mission performance simulator.

GOMOS mission planning

E. Kyrölä and J. Tamminen

Finnish Meteorological Institute, Geophysical Research Division, P.O. Box 503, FIN-00101 Helsinki, Finland
e-mail: erkki.kyrola@fmi.fi, johanna.tamminen@fmi.fi

ABSTRACT

During each orbit of the ENVISAT-1 satellite there are 150–300 stars that are located suitably and bright enough to be used as the measurement targets for the GOMOS instrument. Since the occultation times overlap each other we have to select between different occultations in order to create an optimum sequence of occultations. In this paper we give an introduction to the scientific mission planning of the GOMOS instrument.

1 INTRODUCTION

Every satellite instrument requires some kind of mission planning. This is because there is usually a division between calibration type of measurements and scientific measurements. In this work we concentrate, however, on the mission planning where we aim to optimize the fulfillment of the scientific objectives of an instrument–in our case GOMOS. The possibility for the scientific GOMOS mission planning arises because at a given time several possible star targets are available (see Figs. 1-3).

Depending on the time of year, there will be 150 to 300 stars that are bright enough for GOMOS to track and that are in its field of view at specific times during an orbit. Since the actual occultation times often overlap each other, they can not all be observed (see Fig. 3). Therefore, a number of alternative occultation sequences can be generated. Each sequence has different characteristics, for example, with respect to the ozone retrieval. This creates an opportunity to find an optimal sequence for a specific mission objective.

The most important properties are the shape of the stellar spectrum and the brightness of the star. Hot stars emit plenty of UV-radiation which penetrates Earth's atmosphere in horizontal direction only at high tangent altitudes. Cold stars, on the contrary, emit a lot of visible and infrared radiation and the atmosphere is fairly transparent down to low tangent altitudes. Different star temperatures mean, therefore, that stars are probing different atmospheric regions. This leads to different retrieval accuracies at different altitudes as exemplified in the Figs. 4 and 5. The brightness of the star is directly likked to the signal to noise ratio (see Refs. 1,2) .

The selection of a certain star to be measured by GOMOS leads first to the determination of the geographical area that the measurement concerns. This is dictated by the spacecraft position and the star direction. The local coverage can be characterized by the movement of the tangent point during the occultation. The individual location of the occultation may be an important property in the selection of stars if we wish to make simultaneous measurements, for example, with ground based instruments.

Because stars are also picked out off the orbital plane the selection of a star may also lead to the specification of the overall altitude coverage of the measurement. Some stars never set seen from the ENVISAT-1 orbit.

The location of the occultation is also attached to time. We can in some cases favor measurements with different diurnal coverage. Different occultations may differ, in addition to the star involved, also by the duration of the occultation and the brightness of the background atmosphere.

In the GOMOS mission planning we are not only targeting to individual stars but we are building sequences of stars to be measured. Different sequences lead to different global coverage of measurements.

In this paper we introduce the main elements of the scientific GOMOS mission planning. The results have been obtained by using the LIMBO-simulator (see Ref. 3). For more information on GOMOS mission planning see Refs. 4–8.

2 GOMOS MISSION PLANNING

In order to accomplish the optimization we need to specify the GOMOS mission objectives and to define criteria for comparing occultations and occultation sequences with one another.

The set of possible stars changes continuously and therefore the optimization of the selected sequence has to be performed repeatedly during the lifetime

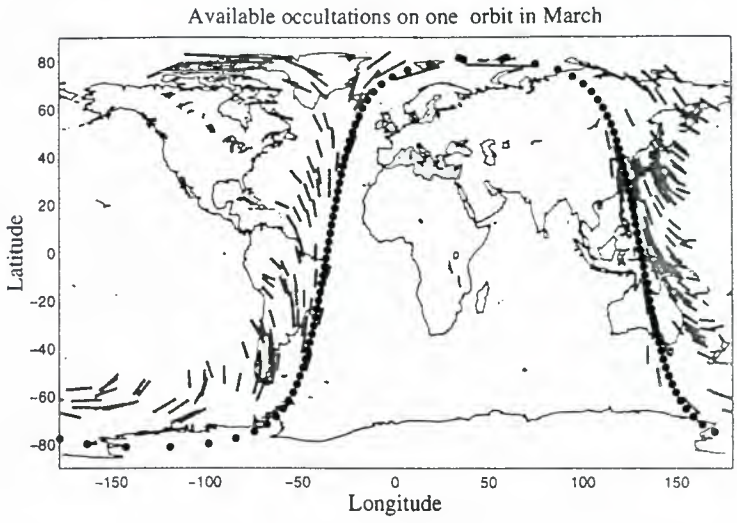

FIGURE 1. An example of the available occultations on one orbit. Each red line corresponds to one occultation. The satellite orbit is denoted with dots.(The figure was created with the LIMBO simulator).

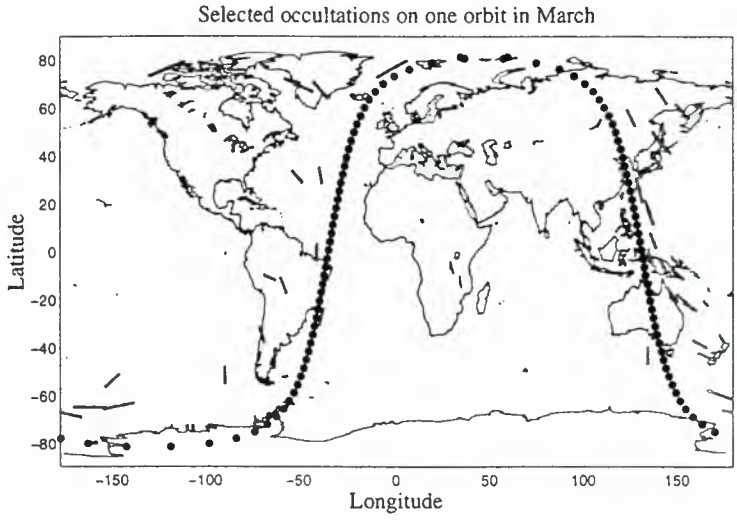

FIGURE 2. An example of the selected occultations on one orbit.

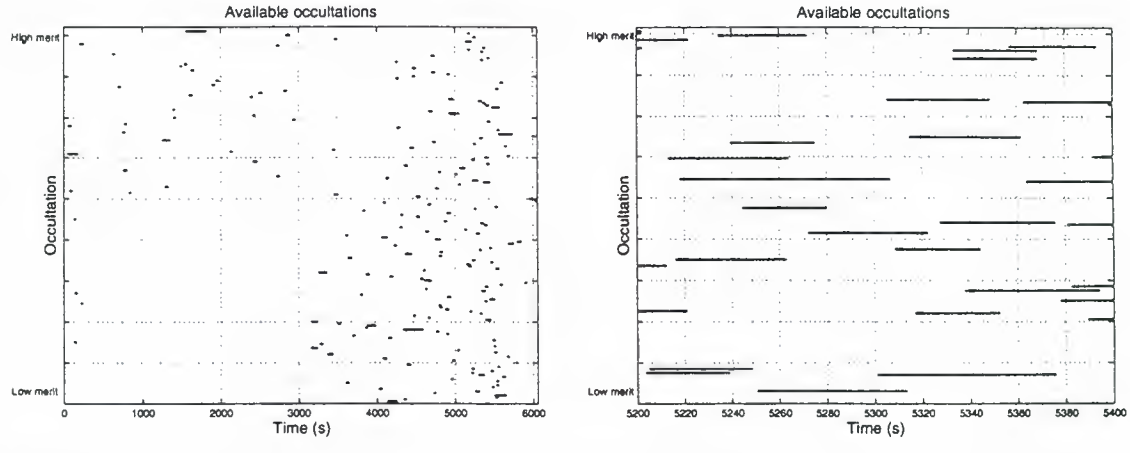

FIGURE 3. On left hand side available occultations during one orbit. On right had side a three minute period of the orbit. Complete occultations are indicated by bars. The vertical axis is proportional to the merit values of the occultations.

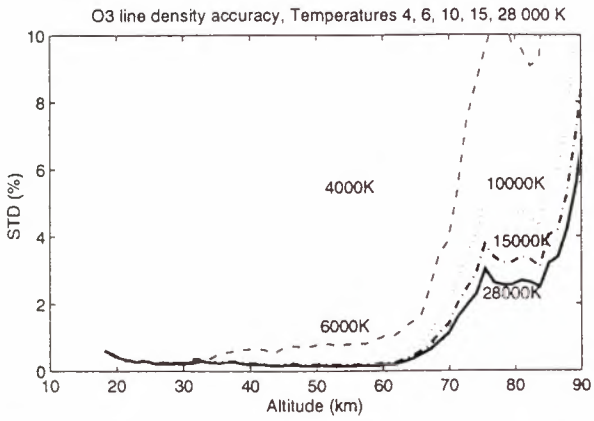

FIGURE 4. Ozone column accuracy vs. tangent height and temperature. (The figure was created with the LIMBO simulator)

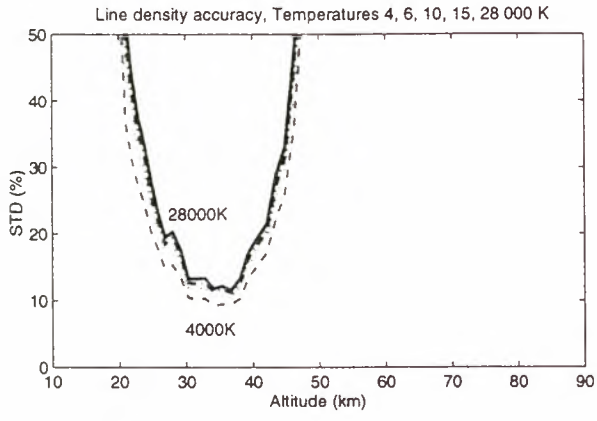

FIGURE 5. NO_3 column accuracy vs. tangent height and temperature.

of the GOMOS instrument. Therefore, an automatic mission planning tool has to be developed to select the optimum sequence with respect to the mission objectives.

GOMOS mission planning includes the steps shown in Fig. 6. Any scientific objective is characterized by a set of criteria. Each mission planning criterion is activated by introducing the data requirements of the criterion. Each data requirement is transformed to a mathematical merit function. From the set of possible occultations and the corresponding mission planning database the mission planning optimization algorithm selects the sequence of occultations which fulfills the requirements in a best possible way.

The GOMOS mission planning inside the occultation mode does not only contain the mission planning tool. An essential element in the mission planning is the selection and updating of the mission objectives and planning how often any single objective is enacted. This will take place in the GOMOS Science

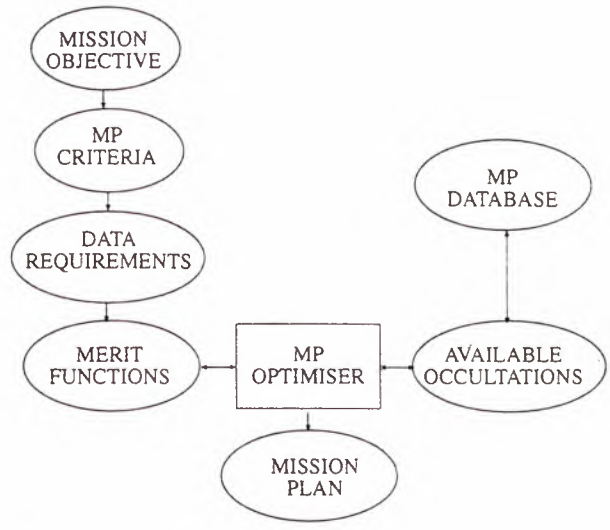

FIGURE 6. Main elements of the GOMOS mission planning.

Advisory Group (SAG).

It is clear that the GOMOS mission planning cannot be operated in isolation. It needs interfaces to the ENVISAT-1 ground segment. Executed mission plans will provide important information about the performance of the GOMOS instrument but also about the already executed mission plans. This experience is fed back to the mission planning operations.

3 GOMOS MISSION OBJECTIVES

The scientific objectives of GOMOS can be divided into three groups. The first group consists of long-term objectives. These objectives are enacted according to the overall GOMOS mission plan during the whole mission lifetime in more or less regular manner. The most important of these objectives is the stratospheric ozone monitoring. The second group consists of campaign type objectives. These have more limited scope than those of the long-term objectives. The activation of a campaign objective is based on an agreement among the partners of the GOMOS mission planning participants. The third group consists of a few permanent objectives that must be considered always when a new mission plan is being prepared. For example, we may be interested in setting some basic standard occultations that either use a set of predefined stars (for example, a few brightest stars) or predefined occultation locations. Once any of these is available in the current mission scenario, it must be selected. Therefore we can also call these overrule objectives. In the following the three groups are listed:

1. Long-term objectives
   - stratospheric ozone monitoring,

- stratospheric chemistry,
- mesospheric ozone monitoring,
- mesospheric noctilucent clouds variation,
- stratospheric dynamics: polar vortex, planetary waves, small scale processes, small scale processes in polar vortex.

2. Campaign type objectives
   - validation of GOMOS products,
   - MIPAS and SCIAMACHY validation,
   - validation and calibration of ground based sensors,
   - campaigns,
   - special events,
   - stellar spectra.
3. Permanent objectives
   - fixed region measurements,
   - fixed stars measurements.

4 CRITERIA CHARACTERISING MISSION OBJECTIVES

The scientific mission objectives of GOMOS listed above are described in details as a set of different criteria. The scientific criteria are divided into three groups in order to clarify their scope. In the first group the characteristics are defined for each star separately. In the second group the characteristics are defined for each occultation separately. In the third group a sequence of occultations is characterised.

1. Star specified criteria
   - For each constituent:
     - For each altitude range:
       - Accuracy type
2. Occultation specified criteria
   - Occultation condition (dark limb, bright limb, terminator).
   - Obliqueness (duration) of occultation with respect to the location.
   - Local coverage.
3. Set of occultation specified criteria
   - Global overage.

Each scientific mission objective is characterised by introducing the *data requirements* linked to these criteria. We include as an example Table 1, which shows how the most important mission objective, the stratospheric ozone monitoring, is characterised.

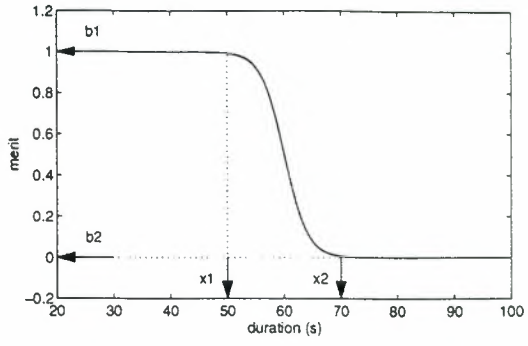

FIGURE 7. Example of merit function for the occultation duration criterion. This merit function favours short occultations.

The importance of each constituent is defined with a priority value. The altitude region and the accuracy type are defined separately for each constituent. The accuracy criterion is specified by two values. They define for each gas separately the accuracy limits where the first one gives the upper limit for accuracies considered still good and the second the lower limit where accuracies are still useful. The favouring of the long lasting occultations at high latitudes is specified as being those occultations whose latitude is more than 70 degrees and which last more than 50 seconds. Occultations which last more than 100 seconds are considered to comply perfectly with the long occultation label. A requirement is made for a good global coverage.

5 MERIT FUNCTIONS

In order to automatically perform the optimisation of the occultation sequence each data requirement has to be defined precisely. In the GOMOS mission planning this has been done by introducing *merit functions* that are used to quantify criteria. The purpose of merit functions is to describe in mathematical form the mission planning criteria. Each criterion, except the global coverage, is characterised by a merit function.

For simplicity we have decided to characterise each criterion with a generic merit function with 4 free parameters. The mathematical formulation of the criteria requires that each of them can be defined by a parameter x which can have real. We define here a merit function which can be used in GOMOS mission planning algorithm:

$$f(x) = b_1 + \frac{b_2 - b_1}{1 + e^{-\gamma(x - \frac{x_1 + x_2}{2})}} \qquad (1)$$

Table 1. Preliminary data requirements on stratospheric ozone monitoring.

Priority	1	2	3	3
Constituent	O_3	aerosol	air	O_2
Altitude region	15-50 km	15 - 50 km	15-50 km	15-50 km
Accuracy type	column	column	profile	profile
Accuracy	2/5 %	10/20 %	2/4 %	2/4 %
Coverage	global	global	global	global
Diurnal condition	not active			
Occultation durat.	long in polar $\lvert\theta\rvert > 70°$ (0.1,50 s;1,100s)			

where parameters b_1, b_2, x_1 and x_2 describe the shape of the function:

b_1 = merit function value at low values of criterion x
b_2 = merit function value at high values of criterion x
x_1 = the last value of the objective x which still approximately gets the merit function value $f(x_1) \approx b_1$
x_2 = the first value of the criterion x which gets the merit function value $f(x_2) \approx b_2$
γ = scaling factor which depends on $|x_2 - x_1|$

The shape of the function is monotonic (see Fig. 7) with maximum equal to one i.e., we put say, $b_1 = 1$. The parameter b_2 defines then the lowest merit attached to the criterion which the merit function quantifies. For crucial criteria (for example, ozone accuracy in the ozone layer) the lowest value is zero whereas for low priority ctiteria it can be any value between zero and one. The parameters x_1 and x_2 give the transition region width.

In Table 2 we present the parameter values which describe the merit functions for the most important mission objective, the stratospheric ozone monitoring.

6 OCCULTATION MERITS

Assuming then that we have identified which occultations are available at one specific time and that we have defined the merit functions which describe our requirements for the occultations. The next step in the mission planning is to compute the merit values related to each occultations. This is done simply by evaluating the function (1) for each requirement separately. This gives us for each occultation a set of merit values which describe the usefulness of the occultation.

In the mission planning algorithm the occultations have to be ranked. We have to decide whether one occultation is better than another one. In order to do this we need to combine the occultation related merit values describing different criteria and interpret them as one *combined merit value*. This combined merit value describes the usefulness of the occultation with respect to all the criteria and by comparing different combined merit values of different occultations we can optimize the occultation scenario.

We have decided to combine the merit values in a following way. Let $m_1, \ldots, m_n$ be different merit values related to one occultation. The combinend merit value M of occultation is defined as the nth root of the multiplication

$$M_i = \sqrt[n]{m_1 m_2 \cdots m_n}.$$

Note, that since the combined merit value is computed by multiplication it gives very strong weight to zero. If one merit value is zero, then the combined merit value of the whole occultation is zero. Therefore, one should be careful about setting the minimum value of merit functions.

7 SELECTING THE OPTIMAL SEQUENCE OF OCCULTATIONS

An algorithm must be developed that finds the sequence of occultations that comes closest to fulfilling the objectives, i.e. has the highest total merit. Since every occultation has a combined merit value (M_i, where i refers to the occultation) corresponding to a particular mission objective, the merit for a sequence of occultations can be obtained simply by adding all the merits of the occultations in the sequence by creating the *merit sum*:

$$B = \sum_{i=1}^{n} M_i.$$

However, since the global coverage criterion can not be taken into account with merit functions, the optimization of B only will not lead to the optimum sequence. In the global coverage criterion he merit is

Table 2. Merit functions for mission objective: Stratospheric ozone monitoring

Criterion	x-variable	b_1	b_2	x_1	x_2
O_3 Column accuracy Priority 1 Alt. range 15 - 50 km	relative accuracy	1	0	2 %	5 %
Aerosol Column accuracy Priority 2 Alt. range 15 - 50 km	relative accuracy	1	0.3	10 %	20 %
Air (T) Profile accuracy priority 3 alt. range 15 - 50 km	relative accuracy	1	0.5	2 %	4 %
O_2 (T) Profile accuracy Priority 3 Alt. range 15 - 50 km	relative accuracy	1	0.5	2 %	4 %
Occultation duration long in polar $\|\theta\| \geq 70°$ (60°)	duration	0	1	50 s	100 s
Diurnal condition	c	not active			

not intrinsic to the parameters of the occultation but rather depends on the distribution of tangent point locations. The goal–all other things being equal–is to seek uniform distribution of occultations over the globe. By the nature of polar orbits, an occultation can be repeated once each orbit at the same latitude, thus achieving uniform coverage longitudinally. So the question of global coverage reduces to seeking a uniform distribution in latitude. There are several possibilities to measure the uniformity of the latitudinal distribution of occultations. For example, we have used the concept of entropy (see Ref. 7) to characterize global coverage.

Regardless of how we characterize the global coverage the *total merit*, for every possible sequence can be calculated by combining the sum of occultation merits B and the global coverage S. This can be done, for example, by defining the total merit P as

$$P = (1 - a)B + aS.$$

Here a is a user-defined trade-off parameter that tells how important are occultation merits compared to the global coverage.

We now can calculate a total merit for every possible sequence. Note that the process presented here, while nominally aimed at one orbit, is equally applicable to more orbits. A sequence could consist of, say, two or three consecutive orbits, not necessarily repeating the same occultations on each orbit, but the sequence would be repeated after two (or three) orbits.

An example how the use of an optimising algorithm may lead to a more efficient measurement program is demonstrated by the Figs. 8–12. In this example the mission objective is the stratospheric ozone monitoring (with some exeptions, namely, the O_2 data requirement has not been implemented and the air data requirement was modified by defining $x_1 = 5\%$ and $x_2 = 20\%$, see Ref. 8). In Fig. 8 we present the latitudinal and merit value distribution of all the 182 available occultations during one orbit in March and in Figs. 9–12 we show the corresponding distribution of the selected occultations, based on different methods. We have also indicated in the figures the total number of occultations selected and the merit sum, which describes the goodness of the occultations with respect to the stratospheric ozone monitoring.

In Fig. 9 the occultations were selected in time order, i.e. the stars are selected according to their entrance into instruments field of view as the satellites progresses along the orbit. In Fig. 10 only the merit sum was optimized whereas in Fig. 11 only the global coverage was optimized. 12 the selection was based on using the mission planning algorithm and optimizing both the global coverage and the merit sum. We can see that by using the algorithm we get the optimal selection of stars. The global coverage is

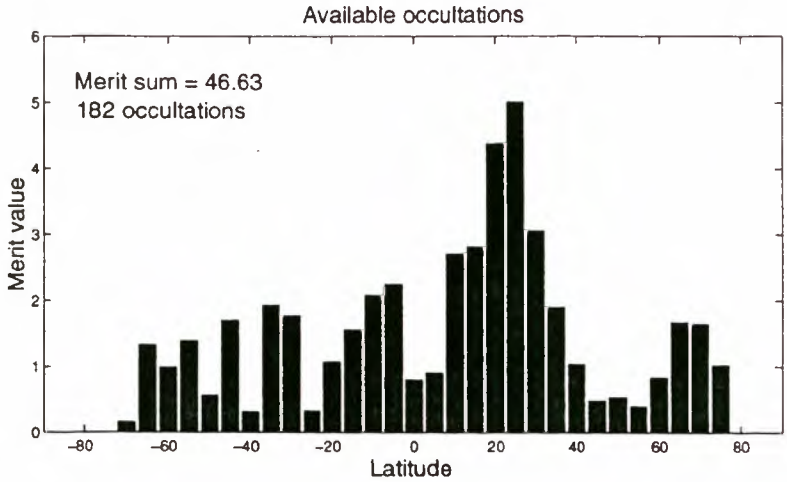

FIGURE 8. An example of the latitudinal coverage and merit values of the available occultations on one orbit in March.(The figure was created with the LIMBO simulator).

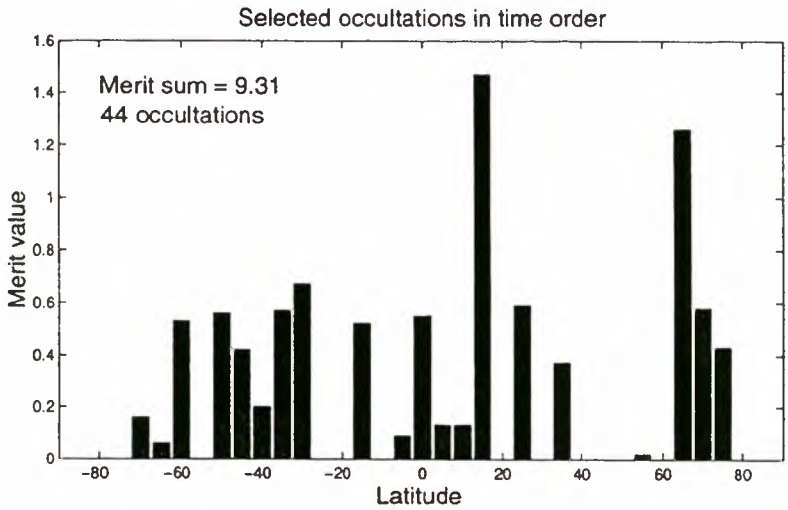

FIGURE 9. An example of the latitudinal coverage and merit values of the selected occultations on one orbit in March. The sequence was created by selecting the occultations in time order.

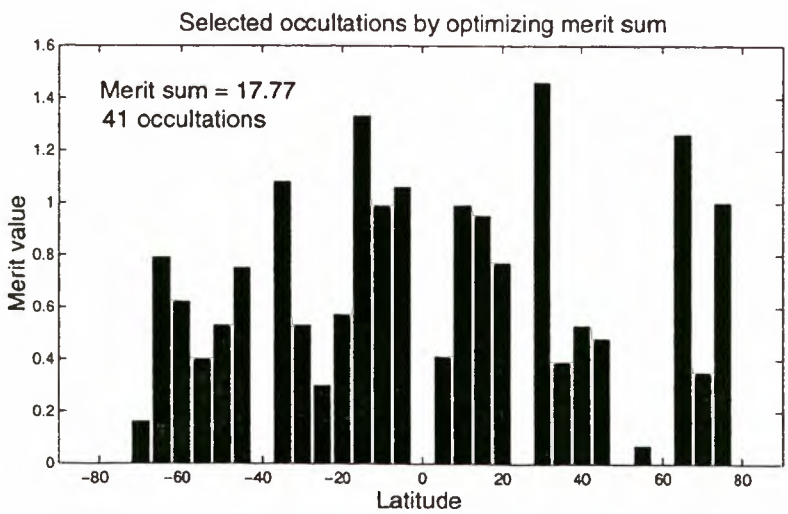

FIGURE 10. An example of the latitudinal coverage and merit values of the selected occultations on one orbit in March. The selection was based on optimizing the total merit sum.

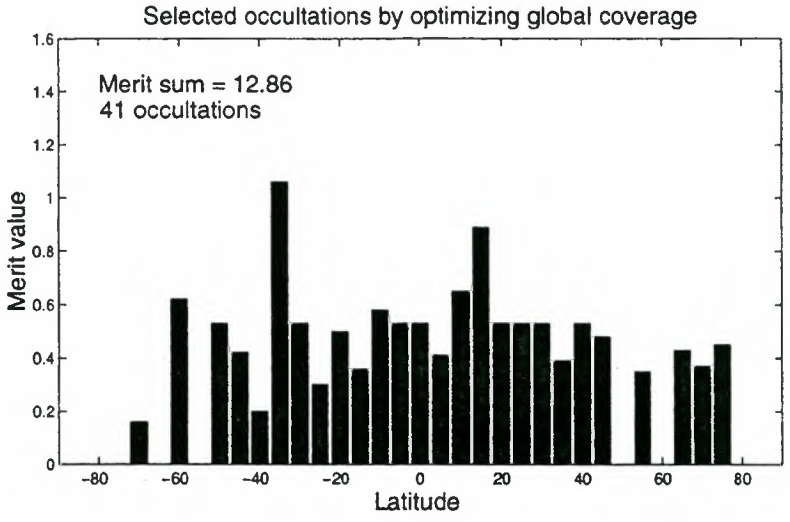

FIGURE 11. An example of the latitudinal coverage and merit values of the selected occultations on one orbit in March. The selection was based on optimizing the global coverage.

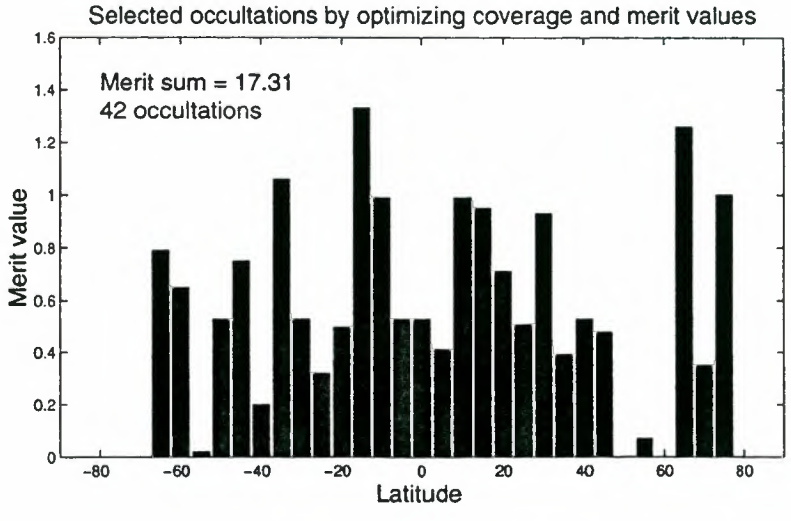

FIGURE 12. An example of the latitudinal coverage and merit values of the selected occultations on one orbit in March. The selection was based on using the mission plannig algorithm and optimizing both the global coverage and the merit values.

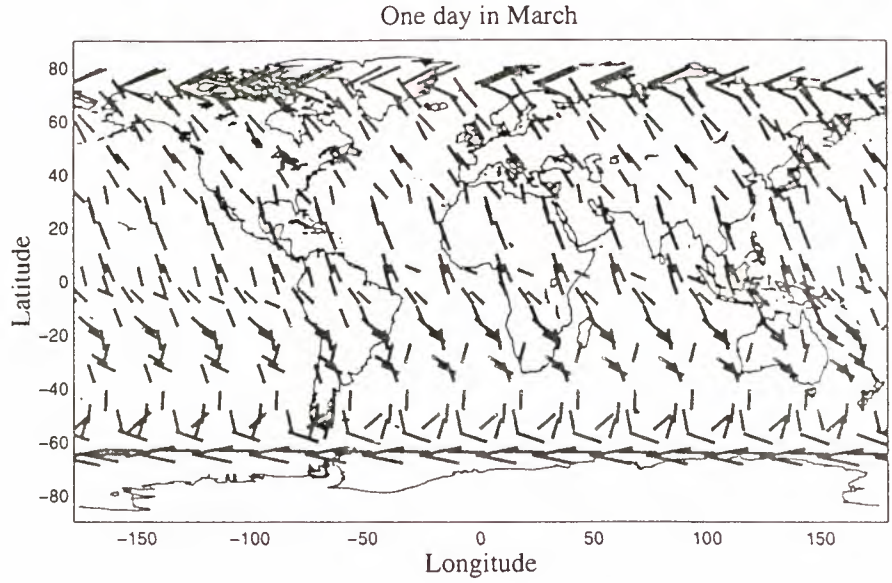

FIGURE 13. Global coverage of the occultations on one day in March. The selection was based on using the missio planning algorithm and optimising both the coverage and the merit sum.(The figure was created with the LIMBO simulator).

very good and the merit sum is almost as good as in the case where we optimized only the merit sum.

During one day the satellite orbits the Earth about 15 times. By repeating the same occultation sequence 15 times we can study the global coverage of GOMOS measurements during one day. This is demonstrated in Fig. 13 where we show the global coverage of the selected occultations in one day. The selection was based on using the mission planning algorithm and optimizing both the global coverage and the merit sum.

8 DISCUSSION

The procedure being developed for the GOMOS mission planning combines a set of merit functions for each occultation with a mechanism for evaluating an overall merit function for any particular combination of occultations, or sequence. The main points of the process are:

1. Set the objectives of the particular mission, either a campaign or a general observation period
2. Identify the relative importance to that mission of the different criteria,
3. Determine the relative merit of each occultation
4. Pick the combination of occultations that has the highest total merit, i.e. best meets the requirements of the particular mission.

We have shown that this process leads to a more effective use of the GOMOS instrument and a better a chievement of the GOMOS mission objectives.

ACKNOWLEDGEMENTS

The main part of the scientific GOMOS mission planning work took place at FMI in spring 1997 within the Mistral project. At FMI the following people have participated in the work: E. Kyrölä, G. W. Leppelmeier, E. Sihvola (now at the University of Helsinki), J. Tamminen; and at ESA: P. Deghaye, J. Langen, A. Popescu.

REFERENCES

1. E. Kyrölä. GOMOS ATBD - Level 2. In this volume, 1999.
2. J. Tamminen, E. Kyrölä, and H. Auvinen. MCMC algorithms for inverse problems in remote sensing. In this volume, 1999.
3. E. Kyrölä and J. Tamminen and L. Oikarinen and E. Sihvola and P. Verronen and G. W. Leppelmeier. LIMBO Limb and occultation measurement simulator. In this volume, 1999.
4. E. Kyrölä. Definition of data requirements and identification of constraints. GOMOS Mission planning and Algorithm Aspects-project, EN-TN-FMI-GM-001, FMI, 1997.
5. E. Kyrölä. Evaluation, optimisation, and consolidation. GOMOS Mission planning and Algorithm Aspects-project, EN-TN-FMI-GM-004, FMI, 1997.

6. GOMOS SAG. GOMOS Science Advisory Group notes. ESA, 1998.

7. E. Sihvola. Mission planning algorithm. GOMOS Mission planning and Algorithm Aspects-project, EN-TN-FMI-GM-003, FMI, 1997.

8. J. Tamminen. Construction of merit functions. GOMOS Mission planning and Algorithm Aspects-project, EN-TN-FMI-GM-002, FMI, 1997.

The GOMOS Data Products

Alexandru F. Popescu and Torgeir Paulsen
European Space Agency ESA/ESTEC – The Netherlands

1. Overall product structure

The GOMOS instrument has two modes of operation; the occultation mode and the monitoring modes. In the occultation mode the scientific relevant products are generated, while the monitoring modes products are used for the monitoring of the instrument engineering performances and for the update of the calibration database.

The GOMOS products are organised on an occultation by occultation basis. The products are grouped in four levels, namely:

- Level 0
- Level 1B
- Level 2
- Auxiliary

All the products have the same format as presented below:

MPH Identification of product and of its main characteristics. Fixed format and length for all ENVISAT products.

SPH General information w.r.t. an occultation, identification of auxiliary data used during processing. Fixed format and size for a product. e.g. occulation start/stop time, latitude/longitude, star, duration.

DSD Indicates the location of the data set in the product: 280 bytes

GADS Contains auxiliary data applicable to the whole product. e.g. wavelength assignment, star spectrum.

ADS Auxiliary data applicable to one measurement only.

MDS Contain the measurements (length is a function of occultation duration.

Acronyms:
MPH: Main Product Header SPH: Specific Product Header
DSD: Data Set Descriptor GADS: Global Annotation Data Set
ADS: Annotation Data Set MDS: Measurement Data Set

2. Level 0 product

The Level 0 product consists of the direct GOMOS spectral measurements geolocated and time tagged using satellite data. These annotations allow for a precise determination of the atmosphere region where the observation is performed and for the precise determination of the observation time.

Level 0 products are going to be produced for the two operation modes of the GOMOS instrument namely for the occultation mode as well as for the calibration operational mode serving the monitoring of the instrument performance and for the in-flight update of the instrument parameters required for the instrument data correction.

3. Level 1b product

The objective of the Level 1B processing is to estimate the set of horizontal transmissions using the spectra measured by the instrument during the occultation. This so-called full transmission functions serve as input data for the Level 2 processing where the atmospheric constituents are being derived.

Although the GOMOS measurement principle is radiometrically self-calibrating, several data corrections are undertaken to ensure maximum data accuracy. The main corrections concern:

- The wavelength assignment. Due to long-term optomechanical drifts of the equipment and due to the pointing evolution shifts of the spectra on the detectors may occur. If not corrected for, these shifts will degrade the correlation of the measured transmission with the known absorption crossection of the atmospheric constituents. In order to minimise this effect the spectral assignment of the detector pixel to wavelength is will be monitored at regular intervals. These monitored shifts together with the monitoring of the instrument pointing performance will be used for reassigning the measured spectra to absolute wavelength.

- Dark charge correction. In addition to the star signal generated photoelectrons, the detector will add dark charge to the measurements. This dark charge is going to be measured using measurements outside of the atmosphere and using the detector temperature information available for subtracting this parasitic signal.

- Background estimation and correction. When the instrument is operating in bright limb condition, i.e. the dayside of the orbit, the limb will also generate photoelectrons which will be added to the star spectrum. This limb spectrum is measured in parallel to the star spectrum and a background estimation and correction is carried out within the Level 1 B processing.

- Flat-filed correction. This corrects for slight variations of the sensitivity of the different pixels of the CCD's, which if uncorrected would degrade the background correction performance of the star spectrum.

In order to arrive at the Level 1B products the following auxiliary products are being used:

- The Instrument physical characteristics database.
- The instrument calibration database.
- The reference atmospheric density profile (from ECMWF), used for geolocation.

At the end of the Level 1B processing the following time-tagged and geolocated products will be available:

- The full transmission spectra and associated error estimation(at 2 Hz).
- The background, i.e. the limb spectra and associated error estimation (at 2 Hz).
- The reference star spectra outside of the atmosphere and associated error estimation (once per occultation).
- The photometer data and associated error estimation (at 1000 Hz).
- The pointing data and associated error estimation (at 100 Hz).
- The geolocation and associated error estimation (at 4 Hz).
- The reference atmospheric profile (at 2 Hz).
- The line of sight direction (at 5 Hz).
- The wavelength assignment and error (at 2 Hz).

4. Level 2 product

In the Level 2 processing the data products which have a direct applicability for atmospheric analysis are generated. The most important are the vertical profiles of the various constituents like Ozone, NO2, NO3, OClo, H20 and aerosols. Intermediate, but not less valuable products are the horizontal column densities of the same constituents. The analysis of the photometer data will produce a high resolution profile for the temperature filed.

The main Level 2 processing steps involve:

- The dilution and chromatic refraction correction. On its path through the atmosphere, the light rays are refracted, wavelength dependent, and "fanned out", which will produce a dilution of the signal. This processing step estimates and corrects for this effect.
- The spectral inversion. This step deals with the determination of the quantity of the atmospheric constituents starting from the atmospheric model and using the crossection database of the different gases. At the output of this step the line densities of the different gases will be available.
- The vertical inversion. This last processing step deals with the derivation of the vertical profiles starting from the horizontal line densities.
- High resolution temperature profiles. The photometer data is the relevant data for the determination of the temperature profiles. The computation of the time delay between the signal seen by the "red" photometer and by the "blue" photometer is used for the determination of the "bending" of the rays induced by temperature related fluctuations of the refractive index of the atmosphere. Starting from this time delay and using the Abel integral the high resolution temperature profiles in the atmosphere can be computed.

At the end of the Level 2 processing the following time-tagged and geolocated products will be available:

- The line density profiles. These are the integrated line densities of Ozone, NO2, NO3, O2, H20 and air.
- The local density profiles (see above). These are the results of the vertical inversion.
- The aerosol product i.e. extinction coefficient and spectral parameters of the extinction coefficient.
- The turbulence product. The tangent altitude of the line of sight, the temperature and the density vertical profiles are retrieved at high resolution.
- The geolocation product. The geolocation data is the same as for Level 1B.
- The accuracy product. This consists of the 12x12 covariance matrix corresponding to 6 gas species, 5 aerosol parameters and one spare.
- The residual extinction product. It was felt necessary to produce the spectral transmission corrected for scintillation and dilution effects, together with the result of the forward model of the transmission with the best-fit values of the parameters.

5. Product size

The product size depends on the occultation duration. The majority (more than 90 %) of the occultations will last less than 75 s. The graph below shows the Level 0, Level 1b and Level 2 products size as a function of the occultation duration

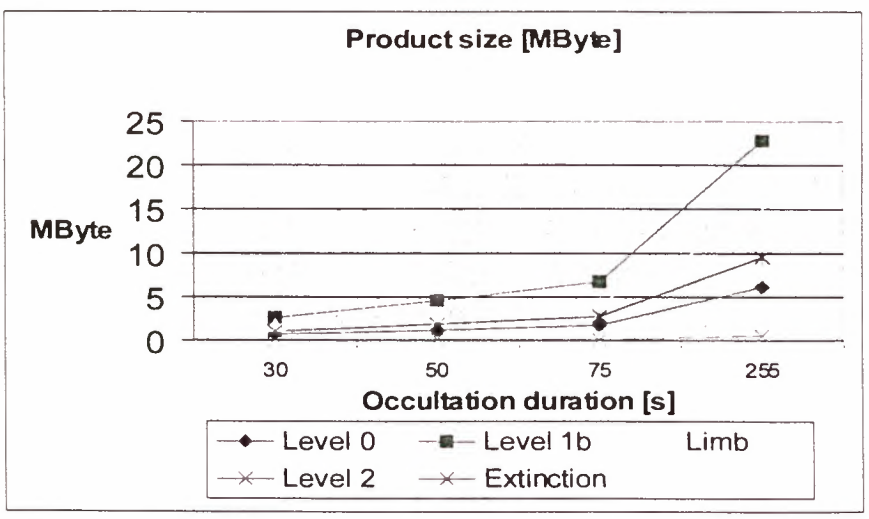

Product size @ 75s occultation duration					
	Level 0:	1.8 Mbyte	Level 1b:	6.7 Mbyte
	Limb:	4.3 Mbyte	Level 2:	0.2 MByte
	Extinct:	9.6 MByte		

6. Auxiliary products

The auxiliary products and their size are summarized below

Instrument physical characteristics	10 kByte
Calibration database	7237 kByte
Level 1b processing configuration	2 kByte
Star catalogue	212 kByte
Stellar spectra database	6268 kByte
Level 2 processing configuration	23 kByte
Cross-section database	11626 kByte

GOMOS ATBD-LEVEL 1b

Jean-Loup Bertaux
Service d'Aéronomie du CNRS, BP.3, 91371 Verrières-le-Buisson, France
e-mail: bertaux@acrov.jussieu.fr

ABSTRACT

The GOMOS instrument, placed on board ENVISAT, is probing the atmosphere by the technique of stellar occultation, in order to map the vertical distribution of ozone and other constituents (NO_2, H_2O, NO_3, T, aerosols...), and to determine accurately their trend over a period of 5 years or longer, when compared to past or future measurements. GOMOS is measuring the atmospheric transmission in the UV-visible-near IR between 250 and 956 nm, and this is the basic product of Level 1b processing. This processing includes the correction of instrumental effects (CCD Dark Charge, cosmic rays, non-linearity, stray-light), the separation of stellar light from the limb light, and a precise geolocation of the line-of-sight with a ray-tracing calculation of the refraction. The limb emission spectrum is also produced as a Limb product, which would allow to compare two different methods of ozone retrieval: direct absorption and more complex solar light scattering by aerosols and Rayleigh diffusion.

1. INTRODUCTION

The principle of stellar occultation is quite simple and straightforward. The spectrum of one star $I_0(\lambda)$ is measured when the line of sight star to spacecraft is well above the atmosphere absorption. Due to the orbiting motion of the spacecraft, the line of sight will go deeper and deeper in the atmosphere (during a star set), and the atmospheric absorption will modify the spectrum of the star as observed from the spacecraft according to the composition of the atmosphere along the line of sight :

$$I(\lambda,p) = I_0(\lambda) \exp(-\Sigma_i \sigma_i(\lambda) N_i(p)) \qquad (1)$$

where p is the impact parameter of the line of sight (the distance to Earth's center of the nearest point to the surface of the Earth along the line of sight), $\sigma_i(\lambda)$ is the wavelength dependence of the absorption cross-section gaseous species i and $N_i(p)$ is the integrated line density of this gaseous species i along the line of sight. The product $\sigma N = \tau$ is the optical thickness, a dimensionless number depending on wavelength.

GOMOS is therefore an instrument which measures the transparency of the atmosphere as a function of wavelength λ, defined by the atmospheric transmission $T(\lambda,p)$:

$$T(\lambda,p) = I(\lambda,p) / I_0(\lambda) \qquad (2)$$

related to the integrated line densities:

$$-\log T(\lambda, p) = \Sigma_i \sigma_i (\lambda) N_i(p) \qquad (3)$$

The great advantage of such a method is that an *absolute* quantity $N_i(p)$ is derived from a *relative* measurement, the comparison of measurements made with the same instrument at a very small interval of time (a few tens of seconds at most). This self calibrated method is therefore protected from instrumental aging and long term drifts, ideally suited when one wants to study variations of the atmospheric compositions (trends) over several years.
The Level 2 contains :

- first, along each line of sight the quantities $N_i(p_j)$ are derived from the measured spectral transmission $T_m(\lambda,p_j)$ (so-called *spectral inversion*).
- second, independently for each species i, all quantities $N_i(p_j)$ are directly inverted to yield the vertical profile of local densities $n_i(z_j)$ (so-called *vertical inversion*).

Kyrölä (Ref.1) is describing in more details the various steps of Level 2 processing, complicated by scintillations, refraction dilution, chromatic effects of refraction and other complications.
In a very natural way, the data processing of GOMOS includes the extraction of the atmospheric transmission as the intermediate product, defining the output of the process which conducts from raw measurements (Level 0) to Level 1b (transmission). Quite obviously also, the data flow of GOMOS is divided into individual occultations, since each of them can be analyzed indepentently of the others.
The estimate of the GOMOS measured transmission from the recorded signal must take into account several instrumental effects (described in Section 5 with more details) and some atmospheric effects : the most important being the subtraction of the limb emission (referred also as "background") from the total signal star + limb, particularly during bright limb daylight conditions.
Another effect is atmospheric refraction, which bends the light path through the atmosphere. Therefore, the exact geolocation of the measurements requires the calculation of the bent ray path (ray tracing), also a major feature of Level 1b. Refraction manifests itself also by dilution and scintillations. The actually measured transmission $T_m(\lambda,z)$ contains therefore the average dilution, the scintillations, and the absorption $T_a(\lambda,z)$ described by eq.(2):

$$T_m(\lambda,z) = T_S(\lambda,z)\, T_d(\lambda,z)\, T_a(\lambda,z) \qquad (4)$$

in which : $T_S(\lambda,z)$ is the scintillation part
$T_d(\lambda,z)$ is the dilution part
$T_a(\lambda,z)$ is the absorption part.

The dilution part $T_d(\lambda,z)$ is due to refraction from the smooth atmospheric profile , while the scintillation part $T_S(\lambda,z)$ results from the fine structure in the temperature profile. At the end of Level 1b, no distinction is made between the three factors: only the product of the factors (actual transmission measurement) is given.

2. INSTRUMENT CHARACTERISTICS

GOMOS is an imaging spectrograph, which records the light from a star in occultation by the Earth (see Popescu, Ref.2, for a more detailed description). As the star sets, GOMOS records successive spectra of the star's light

that has gone through the atmosphere, thus acquiring a set of spectra containing features reflecting the absorption by various molecules at successively lower trajectories through the atmosphere. The spectrometer grating is oriented so that the spectral dispersion is horizontal, yielding a spectrum on the CCD detectors in the horizontal direction, and imaging in the vertical direction. The image of the star is kept inside the slit (10 pixels wide) thanks to a plane mirror in front of the telescope, actively controlled by a Star Acquisition and Tracking Unit (SATU). Residual motions of the star image inside the slit result in displacements of the stellar spectrum on the CCDs both in the spectral (horizontal) direction, and in the vertical direction. The stellar spectrum is distributed over a small number of lines. A larger number of lines (nominally 5 lines, adjustable) , defining the stellar band, are binned together to get the stellar spectrum(SB).

In addition to the star light, there is a contribution from other sources of light, the most intense being the limb brightness on the day side bright limb, integrated on the FOV defined horizontally by the spectrometer slit width, and vertically by the number of lines in the band.

In order to disentangle the stellar light from the sky background, two other blocks of lines (nominally 7 lines, also adjustable) for each CCD are respectively devoted to the limb background above the star (at a higher altitude than the star ray path), and the limb background below the star.

The three bands of CCD lines are producing three spectra, in each spectrometer CCD, which are measured simultaneously and designated in the following by :

- background above the star	BA
- star spectrum + background	SB
- background below the star	BB

While the wavelength assignment of the stellar spectrum on the pixels depends of the pointing and particular position of the star within the slit, for the bakground it does not. Also, the spectral resolution of the Background is degraded, by the 10 pixels wide entrance slit.

The GOMOS instrument consists of four parts:

- a UV-visible spectrograph (250-675 nm),
- an IR spectrograph with two channels (756-773 and 926-952 nm),
- a fast photometer with two channels (470-520 and 650-700 nm),
- a Star Acquisition and Tracking Unit (SATU), controlling a plane mirror to acquire and track the star to keep it in the FOV slit.

The primary function of the two spectrographs is to record spectra which contain absorption features of ozone, NO_2, NO_3, O_2, H_2O, and aerosols.

The history of the SATU during each exposure is used to calculate the mean offset (leading to a wavelength correction) and the distribution of the pointing in time (leading to a correction to the point spread function, PSF).

In addition to the spectrometers, GOMOS is equipped with two fast photometers sampling the stellar signal at 1 kHz in two bandwidths, one in the blue, and one in the red. These data are used to correct for effects of scintillation/refraction in the retrieval processing (Level 2), as well as for studies of atmospheric turbulence. Indeed, because the temperature profile of the atmosphere is not a perfectly smooth function of altitude, the air refractivity experiences small scale fluctuations, and the bending of light rays is not a smooth function of altitude. As a result, the light coming to GOMOS present a series of defocusing and focusing, which are the scintillations. In addition, since the index of refraction is varying with wavelength, the focusing-defocusing pattern is wavelength dependant at GOMOS. The " blue " pattern of scintillations is similar to the " red " pattern, but displaced in altitude (and time) in a deterministic manner.

3. FROM LEVEL 0 TO LEVEL 1b FOR SPECTROMETERS

The data processing to reach Level 1b spectrometers products consists basically of :

- correction of instrumental effects
- separation of stellar light from limb background light and calculation of total transmission
- geolocation of each measurement

The data processing requires a good orbit knowledge, and a good knowledge of instrument characteristics (dark charge, wavelength calibration, wavelength resolution,...), based on ground calibration and in-flight additional measurements (with special monitoring modes of GOMOS). In addition is needed an atmospheric vertical profile, in order to account for atmospheric refraction of the ray path for a more precise geolocation of the transmission measurement.

Level 1b Data Products

The Level 1b data products are listed in Table 1, with their sampling rate. They are grouped occultation by occultation (30 to 50 per orbit). Some comments on these data products are listed below, while details on the data processing are given later.

Reference star spectrum : It is obtained by averaging the 5 first spectra obtained during the occultation ; the averaging is done to minimize the noise.

Reference atmospheric profile : This profile is extracted from a meteorological field analysis (ECMWF) combined with a climatological model (MSIS 90). It is used to compute during Level 1b the refraction of the LOS, by full ray-tracing computation.

Full transmission spectra and covariance : This spectrum is obtained by dividing each spectrum by the reference star spectrum. It is said " full " because it is the actually measured transmission, not corrected from refraction effects (dilution, scintillation, chromatic refraction) nor from variable PSF. The covariance (here, in fact, the variance of each pixel signal) is computed from analysis of S/N ratio.

Central Background estimate: This is the estimated background contribution to the total signal in the central band, which is subtracted to yield the pure stellar signal.

Photometers data : Correction to raw data includes the subtraction of background in the bandwidth of the photometers.

SATU data : This is the position of the centroïd of star image in the SATU CCD (Stellar Tracking Unit), which allows to know where to find each wavelength in the series of pixel.

Wavelength assignment : This is the wavelength of the center of each pixel, for the given measurement of transmission (it may change during one occultation owing to unperfect tracking).

Geolocation : This includes both the position of ENVISAT spacecraft and the position of the tangent point of LOS.

Limb products : This product includes the background actually measured with the two external bands of CCD spectrometers, uncorrected and corrected from straylight and other factors.

TABLE 1. : LEVEL 1b DATA PRODUCTS
(For each single occultation)

Reference star spectrum	**once per occultation**
Reference atmospheric profile	**100 sample per occultation**
Full transmission spectra and covariance	**2 Hz**
Central Background estimate and error	**2 Hz**
Photometers data and error	**1 kHz**
SATU data	**100 Hz**
SFA angle measurements	**5 Hz**
Wavelength assignment of the spectra	**2 Hz**
Geolocation and error	**2 Hz**
Limb products	
Upper and Lower Background Spectra and error	**2 Hz**

4. GEOLOCATION AND ATMOSPHERIC MODEL

In the absence of refraction, the GOMOS line-of-sight (LOS) is defined by the direction of the star and the location of ENVISAT. From the altitude of 850 km , the L.O.S. is ≡ 28° below the horizontal. As a result , a positionning error ΔL "along track" (along the ENVISAT orbit) will reflect immediately in an error Δz for the altitude of the LOS tangent height :

$$\Delta z = \Delta L \cos 28° \equiv 0.5\ \Delta L$$

Therefore GOMOS retrieval accuracy calls for a good accuracy of the orbit knowledge (≡ 50 m), absolute timing of measurements and direction to the star, which must take into account the star proper motion, parallax effect (small), and the aberration of light, which depends on the time of the year, because of the orbital velocity of the Earth along its orbit : 30 km/s, giving a maximum aberration angle of 10^{-4} radian, which projected on the limb, would yield an error altitude of ≡ 300 m if not accounted for.

Because of atmospheric refraction, the LOS is not a straight line, and the exact path must be computed, in particular to geolocate precisely the point along the LOS in altitude, latitude and longitude. The refraction computation (ray tracing) is an important part of Level 1b; it must take into account the Earth's oblateness, characterized by the reference ellipsoïd (fig.1). Then, the atmospheric profile at the time and place of the measurement must be defined. Data processing algorithms of GOMOS are very sensitive to the vertical profile of density and temperature. The ray path from the occulted star to the instrument is very sensitive to the vertical gradient of the index of refraction of air and several phenomena of importance for GOMOS data processing are strongly dependent on the atmospheric profile:

- Rayleigh absorption,
- dilution and scintillations,
- chromatic effects,
- true tangent latitude.

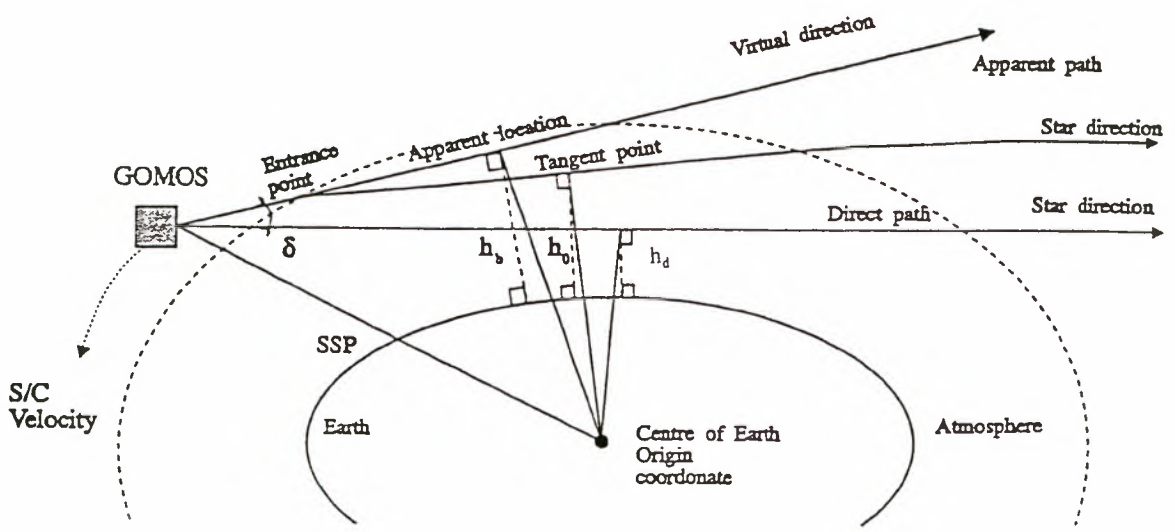

Figure 1. Geometry of the line-of-sight with refraction (from DPM, Ref. 3).

It is then of prime importance to use in the inversion algorithms an atmospheric model of pressure , density and temperature as close as possible to the true state of the atmosphere at the time of the measurement.

For the near real time processing , done within 3 hours after the measurements (for the production of Fast Delivery Products), the atmospheric profile will be computed from the ECMWF 24 hours forecast made the day before for levels up to 10 hPa (or up to 1 hPa if ECMWF is extended) and MSIS90 model above (a climatological model).
The final processing will use ECMWF analysis up to 10 hPa or 1 hPa if extended, and MSIS 90 above. In both cases, a continuous density profile is constructed, verifying the hydrostatic law. Also, the geopotential height (the reference for models) is converted into a geometric altitude, necessary for GOMOS geolocation. The altitude difference between 2 consecutive measurements is 1.7 km at most.

5. FROM RAW DATA (LEVEL 0) TO TRANSMISSION SPECTRA (LEVEL 1b): CORRECTION OF INSTRUMENTAL EFFECTS

Cosmic Rays/Spurious points

It is assumed that Level 0 data contains no TM errors. Saturated samples (ADU=4095) are flagged. Also, permanently "bad pixels" (known from the calibration Data Base) have been eliminated or flagged as such. Still, the CCD detectors are sensitive to high energy particles, which may come from the Earth's radiation belts, the interplanetary/interstellar medium, or even may be generated by radioactive decay of impurities in the spacecraft and GOMOS materials. It will produce an additional charge in one single pixel, or several pixels, when the angle of incidence with respect to the face of the CCD is small. This phenomena is seen in all space flying CCDs. Best proxys to the GOMOS/ENVISAT situation are:

1) the canadian-french instrument WINDII on board UARS.
2) The WFPC/2 instrument on board HST (though the orbit is 500 km, lower than ENVISAT, and therefore encountering less cosmic hits).
3) the LASCO instrument on board SOHO (less relevant, since it is out of the magnetosphere).
The easiest way to identify a cosmic hit on a CCD is to take two images of the same scenery at a short time interval, and to compare them (by subtraction). A hit will appear , above the noise level, either in positive or negative, if it belonged to the first or the second image (cosmic hits are always positive, producing more electrons in one or several contiguous pixels). When only one single image is acquired (full 2D CCD image), the standard way to identify automatically the cosmic hits is to pass a median filter (i.e., 3X3 pixels) on the image and to compare the content of each pixel to the median value of the window centered on this pixel.
For GOMOS, it should be recognized that we do not get a 2D CCD image ; rather, we have several blocks of lines electronically binned together (three per CCD), at each exposure of 0.5 s. Therefore, a pseudo-image is reconstituted for each measuring band of CCDs : the top line of the image being the first measurement in the band, the second line being the second measurement, and so one for a whole occultation. This is because if there is a cosmic hit during one exposure affecting one or several contiguous pixels the same pixels have a large probability not to have been affected by another hit during the preceding and the following exposure, making it easier to recognize its presence than if all exposures were treated independently.
In a sense, we are using both standard methods at the same time (comparison of two nearby exposures, reduced here to a single line per CCD band). Of course, one cosmic hit cannot be distinguihed from noise if it is smaller than k=1 to 5 times the noise level.
Implementation: k and the size of the median window (both vertical/spatial and spectral/horizontal) are read from the Level 1b processing configuration. A theoretical noise level Thr is computed from the known read-out noise and from the shot noise associated with the value of the median on the window. A cosmic ray is detected when the difference between one sample and the median value exceeds k xThr. Caution should be taken with regions of strong gradients in the pseudo-image (both in spectral and vertical/spatial direction). The outlier pixel is flagged.

Instrumental units : ADU versus electrons/pixel

All calculations on the GOMOS data may be made either in ADU (which is actually what comes out of the TM channel) or in electrons per pixel per read-out. This alternative has been extensively debated during DPAD meetings. The use of electrons implies that one knows the conversion factor : number of electrons per ADU (which is the so-called *gain* of the CCD chain). However, if ADU are used instead, the computation of shot-noise errors will require such a knowledge also ; or if a curve S/N = f(ADU) is used, then an analysis of the curve will also give a value of the gain. Also, accurate computations will call for decimal numbers of ADU while the primary output are integer numbers. After long discussions and hot debates it was decided to use electrons rather than ADU. It should also be recognized that, since GOMOS can be operated with at least two different CCD gains, the comparison of signals taken with different gains can be made only when the ADU outputs are converted into electrons with the proper gains.

Electronic Offset or bias

In order to ensure that the output of each pixel readout be included in the range of the Analog to Digital converter, an electronic bias is included, which appears as a minimum digital level. This offset (often called also bias) is subtracted from all measurements. The bias will be different for each CCD chain and will be stored in the Calbration Data Base. It should not be confused with the Dark Current, which is highly temperature dependent and has a variance associated with it, while the offset has none.

Dark Charge correction

In order to simplify the thermal design of GOMOS, the CCDs are not cooled ; rather, they are used in the MPP mode, which reduces very much the build up of Dark Charge (DC), except during the read-out while the content of the pixels are clocked to the CCD output. Therefore the DC is not vanishingly small and should be subtracted from each measurement. Therefore, it must be estimated very accurately. Apparently this problem was very important in the UARS/WINDII data analysis (Ref.4). The estimate of the DC (which will be different for each pixel, in particular because the clocking-time to the output is different for each of them) may be done from several sources of information :

- from other pixels which do not receive light (beware of straylight, though, which should not be

confused with DC) during the same exposure (i.e., in the UV for red stars).

- from other pixels which do not receive light later during the occultation.
- from a temperature measurement of the CCD and the Calibration Data Base.

Actually, three options are implemented in the Level 1b processing:

Option 1: the dark charge correction is not activated.

Option 2: the dark charge is estimated from a calibration dark charge map, provided (in electrons) for each pixel in the Calibration Data Base for a reference thermistor temperture and for an integration of 0.5 s. The temperature dependence of the dark charge is taken into account by a modification of the nominal dark charge map before correction from a parameter giving the temperature variation which doubles the dark charge.

Option 3: the dark charge is estimated from the samples of the background bands of the first frames of an occultation (assumed to be outside the atmosphere). The dark charge of the central band is estimated by scaling the pattern of the dark charge map stored in the calibration auxiliary product, assumed to be independent of the temperature. The scaling factor is obtained by averaging the upper and the lower observed scaling factors.

Stray light (external, internal)

Modules for the correction of both external and internal stray light are implemented in the Level 1b processing chain. However, the level of such a correction is unknown, and the exact way to correct for it will certainly be clarified in flight , during the commissioning phase. External stray light will depend drastically on the solar zenith angle and possibly front mirror angle, while internal stray light, generated inside the spectrometers, will depend on the light entering in the spectrometer (both from the star and from the limb).

Flat Fielding (PRNU)

The specification for GOMOS CCDs is that their response should not vary by more than 5% (pixel-to-pixel, Pixel Response Non Uniformity, PRNU). Actually, flight model CCDs have PRNU of the order of 1.5% or better. Still, a correction for such inhomogeneous response should be taken into account. The difficulty comes from the fact that the various lines inside a band are not uniformly illuminated (particularly the stellar signal which should cover 2 to 3 lines out of 5), and that the GOMOS data output is only a sum of all the lines within a band. In order to make a sensible Flat Field correction, one should use the Star Tracker data (SATU), which tells how was distributed the stellar light among the various lines of the band during one single 0.5 s exposure, and also the Fast Photometer data which tells what was the intensity of the star during each slice of time corresponding to one SATU sample .

Star signal computation

This is done in two steps:
Step 1: Subtraction of the background from central band to get the stellar signal
Step 2: Flat-field correction (PRNU) of the star spectra.

The first step is particularly critical on the bright limb (including dawn/dusk conditions). While the central band of each CCD contains the star spectrum + the limb spectrum, the upper and lower Background (BKG) bands contain only the limb spectrum, but at different altitudes (± 765 m from centre of central background band). Three options are implemented:
Option 1 : no correction (might be valid during the deep night)
Option 2: a linear interpolation in apparent altitude at the limb (or angle) is performed between the two upper and lower background bands BA and BB bands to get an estimate of the background contained in the central band and to subtract it from the total signal of the central band SB to get the star spectrum alone.
Option 3: an exponential interpolation is performed.
Another option was considered , but not implemented yet. The reason to consider it was that when the limb intensity varies rapidly with projected altitude at the limb, all the three bands are containing quite different levels of limb radiance contribution. This more sophisticated variant can be described as follows :

- first, establish an estimate of the altitude variation of the limb emission from the measurements of the backgrounds (a curve of light). It should be recognized that the determination of the altitude of the FOV of background bands can only be made with the help of the knowledge of the star position in the GOMOS FOV from SATU data, because it is the only absolute angular reference to GOMOS . However, when refraction becomes non-negligible, the star is seen deviated from its absolute direction. One must know this deviation angle accurately, and this is only possible through a refraction calculation through the actual atmosphere at the limb. This computation, as well as the exact geolocation , necessitates as input the ECMWF model (prediction for Fast Delivery, analysis for final 1b processing), during the Level 1b processing.

- then, for each measurement, find the altitude of the central band and the corresponding limb radiance for subtraction.The finite FOV and integration time must be taken into account in this exercise. Also, this should be done for groups of pixels, to improve the signal to noise ratio. Testing this variant will be done preferably with real data, during commissioning.

It should be noted that the spectral limb radiance obtained from upper and lower bands, once documented with the altitude, can be analyzed in terms of ozone distribution (and other constituents) since this scattered solar light bears the imprint of gaseous absorption, and aerosols characteristics. Therefore, the limb radiance is a part of the Level 1b data products.

Step 2: Flat-field correction of the star spectra.

There are two options:
Option 1: no correction is performed
Option 2: the correction is performed, taking into account the actual PSF (Point Spread Function) which dynamic part can be retrieved from the SATU data. There are two sub-options, one which considers the time variation (due to scintillations) of the light during the 0.5 s exposure, thanks to FP data, and one which ignores it.

Calculation of transmission $T_m = S_m/S_o$

As an output of level 1b, the atmospheric transmission T_m is the one actually measured by GOMOS: the ratio of the

stellar spectrum S_m measured at each altitude to the spectrum measured outside the atmosphere, the so-called "reference spectrum" S_o, without any correction for scintillations and dilution.

The building of a reference spectrum S_o for each occultation is done by considering the first n spectra (nominal n=5); then to resample them on the common nominal wavelength grid, to compensate for pointing variations which displace the spectrum on the pixels, and average them together.

S_m is computed by resampling all spectra of the occultation (after the first n) on the same nominal wavelength grid, and the transmission is obtained by ratioing $T_m = S_m/S_o$.

One instrumental effect is ignored: the dynamic spectral PSF may have changed from S_o to S_m, because of star pointing variations. Flight data will tell if this effect is important or not. The variance of T_m is computed from the variances of S_m and S_o for each nominal pixel grid, and included in the Level 1b. It takes into account all errors associated to the measurements and their corrections.

Limits on T_m: In principle the atmospheric transmission is a number between 0 and 1. However, owing to scintillations, the measured transmission T_m might be $T_m>1$ occasionally, and still being perfectly correct. Since it was decided that T_m would not be corrected from dilution/scintillation at Level 1b , and rather be the actually measured transmissions, then all values above 1 should be kept. For negative values, a large discussion within DPAD was open to decide what to do with them. Inasmuch as they lie within ± a few σ of 0, (σ being the associated error), they represent "good" values. If they are significantly below zero, it means that perhaps the Background subtraction was in error. One possible solution is to keep these values in the Level 1b product, and to treat them appropriately in the level 2 processing. Also, negative values might be produced at several points in Level 2 processing : transmission, tangential column densities N_i, densities n_i. If considered individually, one negative value has no physical meaning. On the contrary on a statistical point of view, it is quite meaningful. About 65% of negative values should have their 1σ error bar which includes zero ; otherwise, there is a clear shortcoming revealed in the inversion process. In addition, when cumulating a large number of measurements, for which the 1σ error bar includes zero, one will be able to derive a non-zero average, with the error bar shrinked by a factor $1/\sqrt{nb}$ (nb number of measurements). Obviously, if one has discarded all negative values before averaging, then the resulting average will be totally biased, and this is not acceptable, particularly for trend analysis.

6. BACKGROUND SERIES AND LIMB PRODUCT

On the night side, there may be several sources of light superimposed on the light of the star :

- Celestial sources
  - zodiacal light
  - diffuse galactic light
  - extra galactic light
  - minor stars falling in the FOV of the slit
  - planets

These sources have a fixed distribution with respect to the star (neglecting spatial differential refraction).

- Terrestrial sources :
  - Rayleigh scattering + Mie scattering of moonlight
  - aeronomical emissions
  - noctilucent clouds (near the terminator)
  - aurorae (can be considered as sporadic aeronomical emissions at high latitude, linked to solar activity)
  - the recently discovered "sprites", designating intense flashes of light extending from the top of anvil clouds where storms are present up to the ionosphere).

All these terrestrial emissions are altitude-dependent ; some are distributed in such a way that they may actually decrease in intensity during the occultation.

On the day side, all these emissions still exist, but they are dominated (below about 35 km) by solar light scattered either by molecules (Rayleigh scattering) or by aerosols (Mie scattering). Actually, below 20 km the limb is fully bright, and stellar measurements are no longer possible on the dayside below a limiting altitude which depends on the star brightness, somewhere between 20 and 30 km.

In addition, there is some stray-light. One component is the internal straylight generated inside the spectrometer (and should have a weak spectral signature), the other is the external stray light (for instance, bright limb light scattered by the flat entrance mirror). This last component may be derived from measurements in the background bands at high altitude on the day side, for instance.

The processing of the background has several purposes:

- to estimate the contribution of the non-star signal to the total signal recorded in the central band (noted also SB), and to subtract it in order to access the "pure" stellar spectrum.
- to estimate, and to correct for, the contribution of the background to the signal of the fast photometers.
- to establish a distribution of the background emission as a function of altitude.
- to correct for stray-light.
- to disentangle geophysical contribution from possible celestial contribution in the background.
- to extract from the geophysical contribution the solar light scattered by air and aerosols, the limb brightness. From the vertical distribution of this limb brightness it is possible to derive also an ozone vertical profile which absorption is imprinted on the scattered solar light. Because of the complicated geometry and associated radiative transfer, algorithms are more complicated than for the retrieval by occultation. However, they will be developed for SCIAMACHY and OSIRIS/ODIN instruments and could also be applied to GOMOS data, with some modifications. Therefore these background measurements could help to validate the standard retrieval schemes of GOMOS. They are particularly valid in this respect, since the measurements are taken simultaneously in absorption and emission. It can be noted that it requires an absolute calibration of GOMOS, and that it can give also independent estimates of both Rayleigh and aerosols scatterings. With a radiance calibration curve accessed from the Calibration Data Base (established from ground measurements and stellar observations), the background measurements in engineering units can be converted in radiance units (watt/m^2 sr nm) as a function of wavelength.

There are two series of measurements from one single occultation (background bands BA and BB), which are kept, after correction of stray-light, as a Level 1b product, grouped under the name Limb product. It should be noted however that disentangling geophysical from celestial emission, and discriminating aerosol/rayleigh from other sources (like aurorae) are not performed during Level 1b processing, and would necessitate a dedicated variant of Level 2 which is not yet implemented. But all relevant informations are included in Level 1b product (including Limb product).

7. FROM LEVEL 0 TO LEVEL 1b FOR FAST PHOTOMETERS

Each 1 kHz intensity measurement is corrected from Dark Charge contribution and from background contribution estimated from the bands of the spectrometers convoluted by the finite bandwidth of the fast photometers. At Level 1b the sampling is still 1 kHz for these corrected measurements. During Level 2 processing, besides the manipulation of Fast Photometers data made to correct the stellar spectra, these FP data are also used to derive a high-resolution temperature product, from the time delay between the red and the blue photometer. Other than that, the FP data are not kept at the end of Level 2 and one has to rely on Level 1b to make higher level treatments of Fast Photometers. Higher level of data analysis will be used in order to extract turbulence information form these FP data. Also, at high altitude the signal might be occulted by Mesospheric Clouds . A signal drop should be clearly seen, correlated on both photometers. In addition, at lower altitude Polar Stratospheric Clouds (PSC) should also signal themselves by a strong attenuation of the signal.

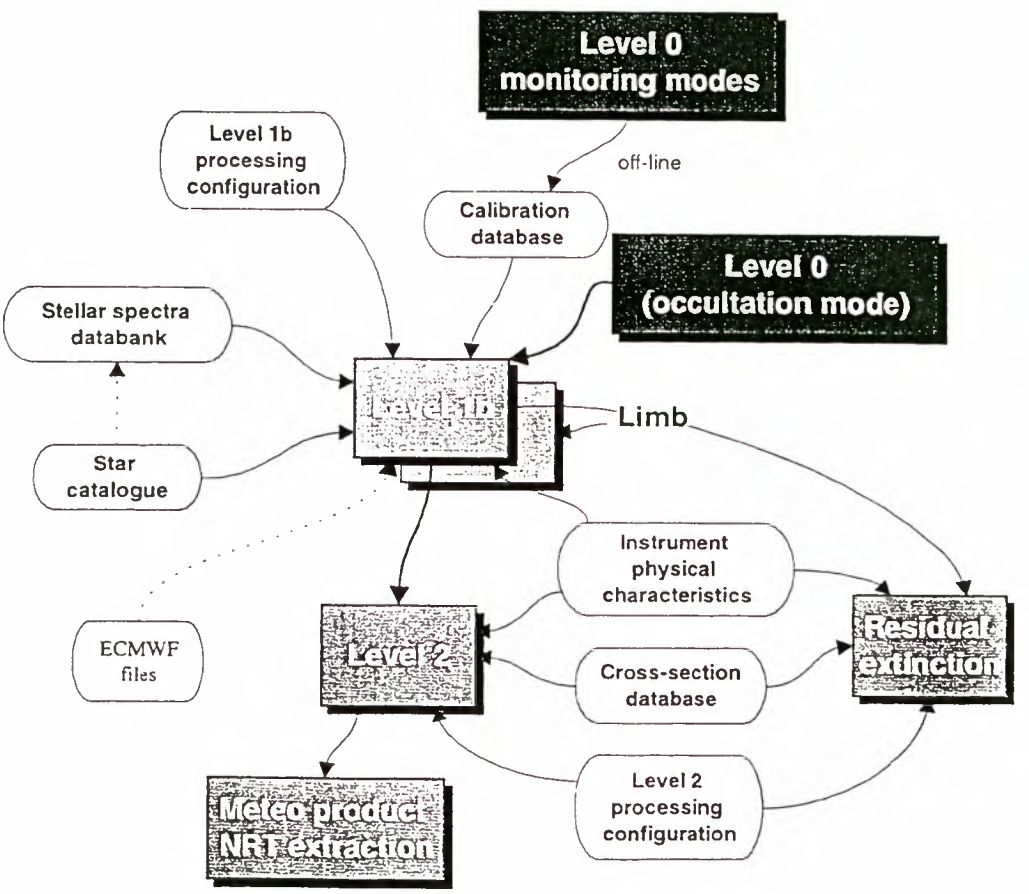

Figure 2. Links between GOMOS products and associated data bases (from DPM, Ref.3).

8. DATA BASES ASSOCIATED TO LEVEL 1b PROCESSING

There are several data bases associated to the Level 1b processing (figure 2).

The **Level 1b processing configuration data base** contains all the configuration parameters and the thresholds used by the different algorithms of Level 1b processing chain as well as the parameters needed in the atmosphere model.

The **Instrument physical characteristics data base** contains the characteristics of the instrument which should

not vary during its lifetime: CCD size, static spatial and spectral PSF, and other parameters.
The **Star catalogue** contains for each of the 960 stars which could be occulted by GOMOS a number of informations: name, identification number in various catalogues, visual magnitude, position, parallax, proper motion (from Hipparcos catalogue), radial velocity, rotational velocity (which determines the Fraunhofer linewidths), spectral type, effective temperature, multiplicity , index describing the proximity of other nearby bright stars and other parameters.
The **Stellar Data Base** contains, for each star of the star catalogue , the spectrum of the star, in absolute units, and in electrons in CCD detectors. It should be used as a back-up of the reference spectrum computed outside of the atmosphere, if for any reason it is not possible to get it for one particular occultation. Remember that a star occulted at one orbit might be occultable for several weeks in a row. Before launch, the stellar spectra has been produced from existing data (IUE data for the UV, Gunn-Stryker Catalog otherwise), either for the star itself, or for a good proxy (a star with the same spectral type, scaled according to the visual magnitude of the GOMOS star). During the flight, each measured reference spectrum will be compared to the spectrum of the star from the Stellar data base to insure proper identification.
The **Calibration Data Base** must contain (non-exhaustive list):
- the absolute sensitivity of spectrometers and photometers chains, both for a point source and an extended source, as a function of λ.
- their detailed spectral bandwidths.
- the gain factors of the CCD chains (number of electrons per ADU) and the read-out noise.
- Flat Fields of CCDs
- linearity curves of CDDs chains and bias levels
- Matrices representing the DC for each pixel, as a function of temperature.
- Calibration factors to allow SATU data interpretation`
- housekeeping engineering calibration curves (i.e., for mirror angles).

All these data may be extracted from the Characterization measurements (on the ground) and from in-flight data, perfomed either with the standard mode of GOMOS operation (occultation) or with the dedicated **Monitoring modes**. Some of the standard occultations may be analyzed for monitoring the instrument (for instance, the sensitivity may be monitored with the signal delivered by stable stars).

In addition to the standard occultation mode, GOMOS may be activated in one of several observation modes (Monitoring modes) dedicated to the monitoring of the instrument. There is the possibility to follow a fictitious star , and a data format identical to the standard mode. In another mode, 33 lines of the CCD are transmitted each 6 sec., allowing to check the response of all individual pixels (which otherwise are merged together to form one spectrum). These Monitoring modes are activated on request for checking the instrument quality and refresh the Calibration data base, on a regular basis. These modes need a special data processing which will be performed off-line.

9. OVERVIEW OF THE GOMOS GROUND SEGMENT

GOMOS Data processing (up to Level 2) is done twice : the first time, in near real time (NRT) with the objective of delivering the data products within 3 hours after reception at the ground (fast delivery products). This processing will be performed at LRAC , in ENVISAT TM reception center (Kiruna). The second processing, for delivery of products within 2 weeks, is performed at several places : Level 1b " final " at LRAC, and Level 2 in the GOMOS PAC (Processing and Archiving Center) located in Finland. The GOMOS data products are then channeled to a " Chemistry " PAC located in Germany, where the data of the 3 chemistry instruments (GOMOS, MIPAS, and SCIAMACHY) are regrouped and made available to the user's community.

The main differences between the two types of processing (3 hours and 2 weeks) are :

- orbit and attitude of ENVISAT are " predicted " during the first processing, while the second processing is made with " definitive " orbit and attitude.

- the description of the atmosphere and related ray-tracing of line-of-sight is based on meteorological predictions of ECMWF during the first processing, while the " final " processing is made with an " actual " description of the state of the atmosphere (also from ECMWF data).
An industrial consortium lead by Thomson was selected by ESA to implement both hardware and software of ENVISAT ground segment. In the case of GOMOS, the operational software is developed by Space System Finland (a member of the Thomson consortium). This development is based on a software prototype, GOPR, which was developed by ACRI (Sofia-Antipolis, France) together with the appropriate documentation and description (Detailed Processing Model, DPM).

As for the other ESA funded Instruments of ENVISAT, the development of GOMOS algorithms was conducted under the responsability of ESA with the Expert Support Laboratory concept. For GOMOS, the ESL selected by ESA includes :

- one industrial company specialised in software development (ACRI, Sofia-Antipolis).

- three laboratories deeply involved in GOMOS Science :
- Service d'Aéronomie du CNRS (Paris area)
- Finnish Meteorological Institute (Helsinki)
- Belgian Institute for Space Aeronomie (Bruxelles).

The algorithm development was done in the following way. The various options were discussed within the Data Processing and Algorithm Development (DPAD, Ref.5), a subgroup of GOMOS SAG (Scientific Advisory Group). The general architecture was first defined, and " sofware boxes " identified and discussed with ACRI . Then algorithms were developed and tested at the three scientific laboratories ; most of time, the algorithm was coded there (under the form of bread board). ACRI had the task to re-code under a unified protocol, link together the various boxes, run the whole code, and write the necessary documentation (Detailed Processing Model, Ref.3).
Finally, the software was validated with the support of ESL involved scientists.

10. ACKNOWLEDGEMENTS

As chairman of DPAD, I wish to thank all my colleagues for the discussions which lead to the definition of Level 1b processing; in particular, Gil Leppelmeier and Erkki

Kyrölä at FMI, Francis Dalaudier and Alain Hauchecorne at Service d'Aéronomie, Howard Roscoe at BAC . Also , I wish to acknowledge the work of Jean-Claude Lebrun , Milena Martic and Bertrand Théodore at Service d'Aéronomie. It was a pleasure to work with Odile Hembise, Gilbert Barrot and Antoine Mangin at ACRI, under the (sometimes demanding) control of ESA staff and with their help , Jacques Louet, Guido Levrini, Alex Popescu, Thorgei Paulsen and François Spiero,. I wish to thank this ESA staff for their continuous support on this project, as well as Nicole Papineau at CNES, which contributed significantly to the support of these software developments.

References

1. E.Kyrölä, GOMOS ATBD-Level 2, ESAMS symposium, January 1999

2. A. Popescu , GOMOS instrument concept and performance, this symposium ESAMS (1999)

3. G. Barrot and O. d'Andon, GOMOS Envisat-1 Ground Segment, Level 1b Detailed Processing Model, ACRI/ESL, Issue 5, September 30, 1998

4. M. Hersé, private communication, 1997

5. J.L. Bertaux, E. Chassefière, F. Dalaudier, A.Hauchecorne, G. Leppelmeier, Erkki Kyrölä, and Paul C. Simon, Data Processing and Algorithm Development (DPAD) Report, 1999

GOMOS ATBD-LEVEL 2

E. Kyrölä

Finnish Meteorological Institute
Geophysical Research Division
P.O. Box 503, FIN-00101 Helsinki, Finland
e-mail: erkki.kyrola@fmi.fi

ABSTRACT

GOMOS is an ozone monitoring instrument onboard ENVISAT-1. GOMOS uses stellar occultations to measure O_3, NO_2, NO_3, O_2, H_2O, aerosol extinction, neutral density, and temperature in the stratosphere on a global scale. In this paper a review of the GOMOS Level 2 retrieval algorithms will be presented. We will show the physical principles behind the retrieval and explain the main algorithms developed.

1 INTRODUCTION

GOMOS will use the occultation measurement principle in monitoring of ozone and other trace gases in the stratosphere (for references and reviews, see Refs. 1–5). It will use specifically stars as source of light. The benefit of the occultation principle is that it is a self-calibrating measurement concept. The reference stellar spectrum is first measured when the star can be seen above the atmosphere. During the occultation measurements through the atmosphere provide spectra with absorption features from the passage through the atmosphere. When these occulted spectra are divided by the reference spectrum, nearly calibration-free horizontal transmission spectra are obtained. These transmissions provide the basis for retrieval of atmospheric constituent densities.

The other advantages of the stellar occultation method are the good global coverage provided by the multitude of stars and the good vertical resolution provided by the point source character of stars. On the other hand, stars are weak sources of light and this makes the retrieval effort a challenging task.

GOMOS is an ESA developed instrument which means that ESA has not only developed the instrument but it has also developed the ground segment scheme. The ground processing is divided to the near-real time processing and the off-line processing and the processing levels are 1b and 2. For GOMOS the division between the Level 1b and the Level 2 is the transmission function.

ESA will take charge the near-real time processing of Levels 1b and 2 and the off-line processing of Level 1b. The off-line processing centre for Level 2 will be located at Finnish Meteorological Institute's Sodankylä observatory (the FIN-CoPAC facility). The dissemination of off-line data will be through DLR's D-PAC in Oberpfaffenhofen. The overall ground processing scheme for ENVISAT-1 is presented in Ref. 6.

The GOMOS data processing algorithms have been developed in the contract between ESA and the ACRI company in Sophia Antipolis France. The scientific institutes, Finnish Meteorological Institute, Service d'Aeronomie and Institut d'Spatiale de Belgique, form the GOMOS Expert Support Laboratory which has supported the algorithm development. The algorithms will be transformed to the processing software by Space Systems Finland-company.

The GOMOS level 1b and Level 2 algorithms have been written down in great detail in the Detailed Processing Model-document (Ref. 7). The theoretical justifications and the higher level presentation of the algorithms is presented in the Algorithms Theoretical Basis Document (Ref. 8). In this paper we present highlights from the GOMOS ATBD concerning the Level 2 processing. The Level 1b ATBD is presented in Ref. 9. The GOMOS mission objectives are presented in Ref 10, the GOMOS mission planning in Ref. 11, the GOMOS instrument in Refs. 12,13, and the GOMOS data products in Ref. 14.

The paper is structured as follows. In section 2 we present the basic measurement physics and emphasize the features which are specific to the GOMOS measurements. In section 3 we outline the inversion strategy. According to this strategy we will first eliminate the modifications from refractive effects on transmissions in section 4. Sections 5-7 explain our data retrieval strategy and explain the transmission model developments. Sections 8-12 detail the spectral and vertical inversion approaches. Finally in Sec.13 we present how fast photometer data can be converted to a high resolution temperature profiles.

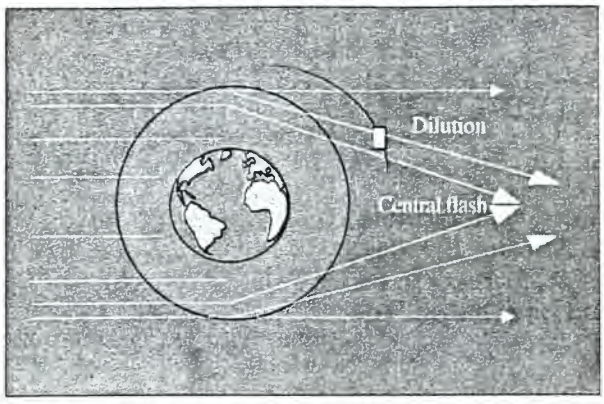

FIGURE 1. Refractive dilution and the central flash.

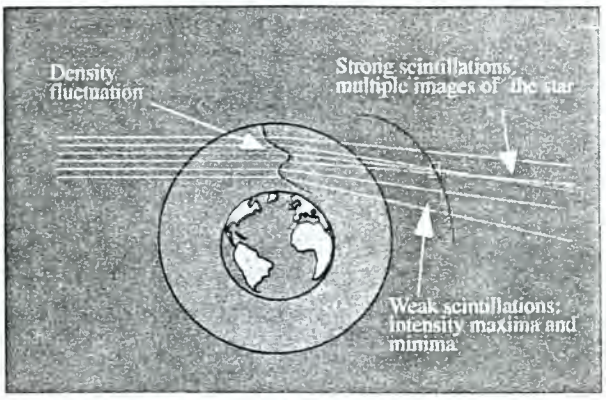

FIGURE 2. Strong and weak scintillations.

2 MEASUREMENT PHYSICS

An occultation measurement can be thought to be a measurement of the atmospheric transmission between the source and the instrument. The transmission cannot be directly observed but it can be calculated by using the measurements through and above the atmosphere.

The transmission can be modelled by using Beer's law

$$T_{ext} = e^{-\tau} \tag{1}$$

where the optical depth is given by

$$\tau(\lambda) = \sum_j \sigma_j(\lambda) \int \rho_j(\bar{r}(s))ds \tag{2}$$

Here ρ_j are the constituent densities depending on the position $\bar{r}$ and σ_j are the absorption or scattering cross sections. The integration is along the line of sight joining the instrument and the source. The modelled transmission gives the desired coupling between measurements and the geophysically interesting constituent profiles.

In the case where the source is point-like, the straightforward connection of Eqs. (1)-(2) fails. The parallel ray bundle from the star will be strongly disturbed by the refractive effects of the Earth's atmosphere.

The first effect is related to the density gradient in the atmosphere. The density gradient will cause a larger deflection to the grazing rays compared to the rays with larger impact parameters. This is shown schematically in Fig. 1. The change of the propagation direction in the atmosphere will result to dilution of the related intensity. We call this attenuation as the refractive dilution. Notice that the rays from different sides of the Earth limb will eventually converge and cause a so-called central flash at large distances from the Earth.

A closely related effect is the scintillation effect. In explaining the dilution we assumed that the atmospheric density decreases monotonically from the ground upwards. If there are fluctuations added to this decrease the ray deviations will also show inhomogeneity. A spacecraft crossing this inhomogeneous light field will record a fluctuating intensity. This is shown schematically in Fig. 2.

The last effect caused by refraction is the chromatic refraction which leads to the spatial separation of different colors. A multi-wavelength measurement of a stellar spectrum through the atmosphere cannot therefore be attached with an unique ray which connects the satellite and the star. If we describe rays by their tangent heights, we see that at a given time the measurement will be characterized by a range of tangent heights. If we want to attach one tangent height we have to combine data from measurements at different tangent heights. This is shown in Fig. 3.

The refractive effects discussed above are not restricted to the stellar occultations in the Earth's atmosphere. In fact they all have been detected and exploited in the data retrieval in stellar occultations of planetary atmospheres (see Refs. 1,5).

In addition to the refractive effects there are two additional measurement features which must be taken into account in the data retrieval. The first one is the finite measurement time (0.5 seconds) of GOMOS. During this time the tangent point altitude can change 1.7 km. This amount is true for occultations in the orbital plane. For off-plane occultations this movement is smaller leading to a better vertical resolution. The movement of the tangent height can, anyhow, be large enough that it must be considered in the inversion. The second item is the finite spectral resolution of the instrument. This means that we cannot simply use the cross sections as such in the inversion but we must take the instrumental resolution into account.

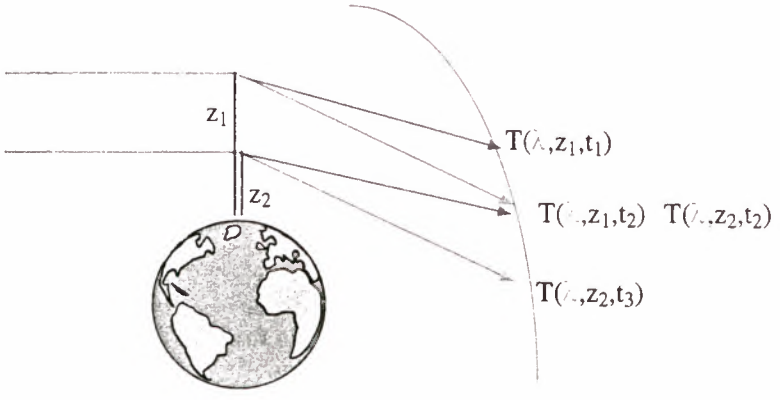

FIGURE 3. Chromatic refraction

3 DATA AND RETRIEVAL STRATEGY

The different GOMOS Level 1 products that are used in GOMOS Level 2 are

- Transmission data (T^{obs})
- Photometer data (I^{obs}_{pho})
- Geolocational data ($\ell(\lambda, t)$)
- A priori atmospheric data ($\rho_{air}(\bar{r}), \mathrm{T}(\bar{r})$)

The main data are the transmission spectra at different tangent heights. Photometric data from the two fast photometers are used to correct the transmissions from the scintillation effects. But photometric data are also used to retrieve a high resolution temperature profile of the atmosphere. The geolocational and the a priori atmospheric data are necessary information in dealing with the refractive effects and in initializing the inversion. These data will be partly replaced by new data from GOMOS Level 2 processing.

In the present GOMOS ground processing we will not use limb spectra from Level 1b. There is some hope that also these spectra could be used for retrieval (see Ref. 15).

The geophysical retrieval strategy in the GOMOS Level data processing assumes that the measured transmission (produced by the GOMOS Level 1b) can be taken as the product of two transmissions:

$$T^{obs} = T_{ref} T_{ext} \tag{3}$$

The transmission T_{ref} is due to refractive effects and the transmission T_{ext} is due to absorption and scattering processes in the atmosphere. The Level 2 processing aims first to estimate the refractive part using the fast photometer data and the geolocational data and then remove it from the measured transmission. The remaining transmission could then be connected to the atmospheric constituent densities, the retrieval of which is the main mission objective of the GOMOS instrument.

In the GOMOS Level 2 processing the data set processed at a time are the measurements from one star occultation. Even if some occultations would probe the same atmospheric region at successive orbits these occultations are treated separately. Therefore, the possibility to carry out some kind of atmospheric tomography by GOMOS will not be considered in the Level 2 processing.

4 REFRACTION CORRECTIONS

As already explained refraction affects GOMOS measurements in various ways. The most obvious is the change in the geolocation of the light path connecting the satellite and a star. This can be taken into account by performing ray tracing calculations but it is further complicated by the chromaticity of the refraction. The ray tracing will need some atmospheric data that will be eventually also generated by GOMOS itself. The other effects are generated by the variation of the air temperature and therefore also the index of refraction in the spatial domain. This causes differential bending of the light rays in the atmosphere which will result in modulation of the intensity detected by GOMOS. In the GOMOS level 2 data processing a distinction is made between the

smooth and the fast variations of the index of refraction. The smooth variation can be calculated analytically whereas the fast variation is best described using GOMOS fast photometer data.

The objective of the refraction corrections is to provide a simple scheme which can be used to estimate the part connected to scintillations and dilution effects.

4.1 Dilution and scintillations

The scintillation and dilution correction process is based on the assumption that the modulation due to dilution and scintillation may be split in two independent terms

$$T_{ref}(t) = T_{dil}(t)T_{sci}(t) \tag{4}$$

where T_{dil} represents the dilution component and T_{sci} represents the effect of scintillation, assumed to be free of direct chromatic effect.

The following approach is assumed: T_{sci} will be estimated using the signal (provided in the level 1b product) of the fast photometer which has the highest signal to noise ratio. The principle is to minimize extinction effects in the photometer bands (the less extinct one is generally the red photometer). The estimation of this term is made with the assumption that all high frequency fluctuations in the photometer signal (if we except noise fluctuations) are due to scintillations and that fluctuations due to structures in vertical profiles of absorbing constituents affect only the low frequency part of the signal. This assumption is justified by the fact that the absorption depends on the integrated density along the line of sight, while the dilution is sensitive to the vertical second derivative of the integrated density. As a matter of fact high frequencies are enhanced by the derivation. T_{dil} is computed using a vertical profile of atmospheric density coming from an external atmospheric model.

The mean dilution is approximated by using the so-called phase screen approximation. Instead of a 3D -atmosphere we assume that it can be replaced by a screen located at the tangent point. The refractive bending takes place at the screen. With this approximation the mean dilution can be written simply as

$$T_{dil}(z,\lambda) = \frac{1}{1 + L\dfrac{d\delta(z,\lambda)}{dz}} \tag{5}$$

where L is the distance from the tangent point (screen) to the satellite and δ is the deviation angle of the ray. In the GOMOS level 2 processing the deviation angle is taken from the ray tracing calculation. If the mean deviation is computed for the first time, the ray tracing calculation is the one performed in Level 1b. For subsequent calls (see Level 2 loops) the ray tracing may be performed again using the GOMOS generated atmosphere.

The scintillation transmission is calculated by

$$T_{sci}(t) = \frac{I_{ph}(t)}{\overline{I}_{ph}(t)} \tag{6}$$

where the numerator is the photometer signal and the denominator is the smoothed photometer signal. The smoothing is performed by the Hanning filter (see Ref. 16) over an adjustable time interval (in vertical distance the default value is about 3 km). The combined effect due to dilution and scintillations during one integration time of the spectrum is now given by

$$\overline{T}_{ref} = \frac{1}{\Delta t}\int T_{ref}(t)\,dt = \frac{1}{\Delta t}\int_{\Delta t} T_{dil}(t)T_{sci}(t)\,dt \tag{7}$$

The transmission due to absorption and scattering can now be calculated dividing the observed transmission by the estimated refractive part:

$$T_{ext}^{obs} = \frac{T^{obs}}{\overline{T}_{ref}} \tag{8}$$

It is important to note that, at this stage, we have transmission corresponding to tangent altitudes depending on wavelength. The chromatic effect is taken into account in the mean dilution term. The chromatic effect which is neglected in scintillation correction is the intensity normalization resulting from difference in "duration" of the same structure when viewed at different wavelengths. In other words, the integration time in Eq. (7) is also wavelength dependent.

Notice also that this algorithm assumes that the absorption does not contain high frequency components. This algorithm does not check either the consistency between the atmospheric model (dilution) and the Rayleigh attenuation.

4.2 Chromatic refraction correction

During its path through the atmosphere, a light ray is refracted by the gradient of the index of refraction. This bending is dependent on wavelength. The smaller the wavelength, the greater the bending. It means that there is no single path through the atmosphere that could be attached to a light field detected at any given time by GOMOS.

The goal of this algorithm is to correct the atmospheric transmission for the chromatic refraction. We calculate the tangent points corresponding to

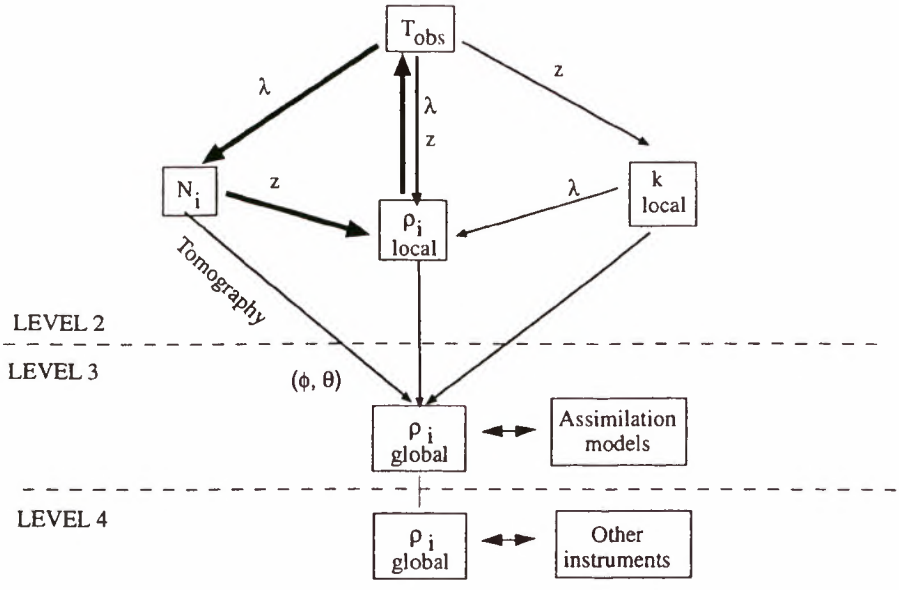

FIGURE 4. Strategy for the spectral and vertical inversion. See text for explanations.

each pixel of each spectrum and then calculate transmission for given tangent altitudes by doing linear interpolations between two acquisitions.

$$\widetilde{T}^{obs}_{ext}(z_j,\lambda) = rT^{obs}_{ext}(z_j,\lambda)+(1-r)T^{obs}_{ext}(z_{j+1},\lambda) \quad (9)$$

$$\widetilde{T}^{obs}_{ext}(z_j,\lambda) = (1-r)T^{obs}_{ext}(z_j,\lambda)+rT^{obs}_{ext}(z_{j-1},\lambda) \quad (10)$$

The first alternative is applied for wavelengths λ smaller or equal to the fixed reference wavelength and the second alternative to the rest. The coefficient r is the interpolation coefficient:

$$r = \pm\frac{z_j(\lambda_{ref}) - z_{j\pm1}(\lambda)}{z_j(\lambda) - z_{j\pm1}(\lambda)} \quad (11)$$

This module represents the first alternative method to correct the chromatic refraction effects. The second alternative is presented in connection to the transmission modelling.

5 ATMOSPHERIC TRANSMISSION

In the previous section we derived from Level 1b transmission reduced transmissions Eq. (8) or Eqs. (9)-10) which should now be connected to the constituent densities of the atmosphere. Notice that the transmission is measured in the horizontal direction and it bears no simple relationship to the vertical transmission which is the relevant quantity in discussions of UV-radiation threats. However, these horizontal transmissions constitute an invaluable data set for the monitoring of the state of the stratosphere.

Unfortunately there are still effects which make necessary some analysis before the connection between transmissions and the profiles can be worked on. These effects are related to the finite integration time of the instrument and to the finite spectral resolution of the imaging system and the combined effect of effects from these two.

For a point source and with nearly ideal imaging we can write the model transmission as the following two-dimensional integral:

$$\bar{T}(\lambda,t) = \frac{1}{\Delta t}\int\int T_{ext}(\lambda',\ell(t,\lambda'))W(\lambda,\lambda',t)\,dtd\lambda' \quad (12)$$

Here W is the instrument point spread function. It is time dependent because pointing movements during the integration time stellar image in the slit plane wanders and its image on the CCD plane does the same. This will cause some spectral smearing. The extinction transmission can be written as

$$T_{ext}(\lambda,\ell(t,\lambda)) = e^{-\tau(\lambda,\ell)} \quad (13)$$

where the optical depth is given by

$$\tau(\lambda,\ell) = \sum_j \int_\ell \rho_j(s)\sigma_j(\lambda,\mathrm{T}(s))ds \quad (14)$$

Equation (12) will be the starting point in the Level 2 inversion. From these formulas we can see that the there is still not a very simple connection between the measured transmissions and the constituent profiles in the atmosphere. First, the spectral and temporal integration cause some averaging in the corresponding directions. Second, all the temperature dependent cross sections cause coupling of the spectral and vertical direction in the problem. Both these problems should be considered.

6 INVERSION STRATEGY

There is no obstacle to an inversion strategy where we use Eqs. (12), (13), and (14) to retrieve the constituent profiles. This approach can be called one-step inversion. In the case of GOMOS it leads to a quite large and heavy inversion problem because every model calculation involve three integrals (over time and wavelength, and along the line of sight) and the size of the input data is about 3000 spectral points (2 spectrometers) at about 50 altitudes. In the GOMOS Level 2 data processing strategy three essential simplifications have been adopted in order to bring the inversion problem into a more manageable form (see Ref. 17). They are

1. Separate UVIS and IR spectrometer data analysis
2. Modify the model function Eq. (12) in order to eliminate the need for repetitive spectral and temporal integrations
3. Decouple spectral and vertical problems so far as possible

The simplifications allow us to perform the inversion in a sequential way. We have still to decide if we carry out the spectral or vertical inversion first. In the first alternative the spectral inversion is performed first and as an intermediate result we produce horizontal column densities of different constituents $N_j(z)$. In the second alternative the vertical inversion is performed first and as intermediate products we produce profiles of the absorption coefficients $k(\lambda, z)$. In the GOMOS ground segment the first alternative is chosen because it leads to a rapid compression in the data volumes processed. The simplifications discussed above lead to some inaccuracies in the modelling but they will be counteracted by performing iteration loops. After performing spectral and vertical inversion we perform the sequence again and so on. The different possibilities are shown in Fig. 4 (see also Ref. 4). We have also shown some further possibilities in the GOMOS data processing.

7 MODEL DEVELOPMENTS

In this section we show how the model transmission is developed so that it can be used effectively in the data inversion (see Ref. 17).

7.1 Effective cross section method

The temperature dependent cross sections cause coupling between the spectral and spatial dimension in the problem. According to our strategy we aim to factorize the problem into spectral and vertical problems as far as possible. This can be achieved by using the effective cross section method. We write

$$\tau(\lambda, \ell) = \sum_j \int \rho_j(s)\sigma_j(\lambda, \mathrm{T}(s))ds$$
$$= \sum_j \sigma_j^{eff}(\lambda, \ell)N_j \qquad (15)$$

where N_j is the line density of the species j

$$N_j = \int_\ell \rho_j(z(s))\, ds \qquad (16)$$

and

$$\sigma_j^{\mathrm{eff}}(\lambda, \ell) = \frac{\int_\ell \sigma_j(\lambda, \mathrm{T}(s))\rho_j(s)\, ds}{N_j} \qquad (17)$$

is the effective cross-section of species j. The use of the effective cross-section has formally separated the inversion problem into two parts. The spectral inversion part is given by Eq. (16) with the line densities N_j as unknowns. The vertical inversion part is given by Eq. (17) with $\rho_j(z)$ as the unknowns. The two parts are, however, coupled together by the unknown effective cross sections. An iterative loop over spectral and vertical inversion is needed to take this into account. Initially we can use the tangent point temperature in Eq. (17).

7.2 Spectral and temporal integration

The other model simplification aims to eliminate the need for the spectral and temporal integrations in the model function Eq. (12). With the perturbation technique we are able to recover the exponential form of the model transmission. The detailed calculations are not shown here (see Refs. 7,17) but the final result is

$$\bar{T}(\lambda, t) = e^{-\hat{\tau}} \qquad (18)$$

where the modified optical extinction is (h's are the tangent heights)

$$\hat{\tau}(\lambda) = -\sum_j \tilde{\sigma}_j(\lambda)\bar{N}_j - \frac{1}{2}\sum_{ij} B_{ij}(\lambda)\bar{N}_i\bar{N}_j$$
$$+(h(\lambda) - h(\lambda_{ref}))\sum_j \tilde{\sigma}_j(\lambda)\frac{d\bar{N}_j}{dh}$$
$$-\frac{(\Delta h)^2}{24}(\sum_j \tilde{\sigma}_j(\lambda)\frac{d\bar{N}_j}{dh})^2 \qquad (19)$$

Here Δh is the vertical coverage of the measurement at the tangent point. The convoluted cross sections are defined by

$$\tilde{\sigma}_j(\lambda) = \int W(\lambda' - \lambda)\sigma_j(\lambda')d\lambda' \qquad (20)$$

Table 1. Different spectral inversion approaches with some advantages and drawbacks.

Method	Advantages	Drawbacks
Spectrally global	All data	Interfering species
Spectral windows	Avoids species interferences	Reduced data, no clean windows
Absolute cross sections	Also air and aerosols retrieved	Aerosol uncertainties may harm other retrievals
Differential cross sections	Aerosols uncertainties not important	No air and aerosols
Linearize problem	Easy linear inverse	Noise deformation, data must be filtered
Non-linear problem	Original noise	Nonlinear inversion
A priori information	More stability	Need to control a priori contamination
No a priori information	No contamination from a priori	Very noisy cases difficult to handle

and the coefficients B_{ij} are coming from the convolution of cross-section correlations:

$$B_{ij}(\lambda) = \int W(\lambda' - \lambda)\sigma_i(\lambda')\sigma_j(\lambda')d\lambda' - \sigma_i(\lambda)\sigma_j(\lambda) \tag{21}$$

Notice that the cross sections here are effective cross sections.

The unknown instantaneous line densities are now replaced by the averaged line densities

$$\bar{N}_j = \frac{1}{\Delta t}\int N_j(t)dt \tag{22}$$

The derivates of the line densities are calculated during the iteration loop only.

The transmission model (18)-(19) includes the chromatic refraction effect, the spectral convolution by the instrument and the time integration effect. Obviously all effects are taken into account in an approximate way only.

7.3 Cross sections

The final ingredient in the model calculation are the cross sections. The cross-sections are taken from the GOMOS cross-section database where they are ordered through species, temperature, and wavelength. The cross sections are obtained from laboratory measurements. There are no cross sections measured by the GOMOS instrument.

The scattering cross-sections can also be approached analytically (for absorbing species the cross-sections are too complex to be derived from first principles). The Rayleigh cross-section needed for scattering by air has the following form:

$$\sigma_R(\lambda) = 1.06\frac{32\pi^3}{3}\frac{(n(\lambda)-1)^2}{\lambda^4 N_{stp}^2} \tag{23}$$

The factor 1.06 is the depolarization factor for air. The index of refraction $n(\lambda)$ follows the Edlen's law. N_{stp} is the air number density at sea level.

The specification of the aerosol scattering cross section is in principle almost impossible. The aerosol content varies all the time in the atmosphere and so varies the effective aerosol cross section. In the retrieval we can either fix a certain best guess cross section or we can try to define a flexible aerosol cross section (actually aerosol extinction) with unknown model parameters. In the latter case the retrieval will hopefully fix the unknown parameters. Both these approaches are possible in the GOMOS Level 2.

Instead of guessing the best cross section we have used in the development a simple Ångström's formula

$$\sigma_a(\lambda) = \frac{\sigma_0}{\lambda^b} \tag{24}$$

A more realistic description of the aerosol extinction will include a more elaborate wavelength dependence. A simple polynomial expression will be used and for the horizontally integrated extinction profile one gets

$$\tau(\lambda) = \int_{LOS}\beta(z(s)),\lambda)ds = c_0 + c_1\Delta\lambda + ... \tag{25}$$

where the coefficients c_i are unknowns to be determined and $\Delta\lambda = \lambda - \lambda_{ref}$.

8 SPECTRAL INVERSION

We are now prepared to start the spectral inversion. We have the experimental transmission function and we have the corresponding model transmission Eq. (19) where the line densities are the unknowns. There are still alternatives how the column

densities are inverted from this comparison. They are listed in Table 1.

In the following we concentrate on the method which is spectrally global, uses absolute cross sections, takes a non-linear approach and assumes no a priori information (see.Refs. 4,17). The other cases will also be available in the GOMOS Level 2 and the best approach will be decided during the actual operation of GOMOS.

The estimations of column densities is based on the standard likelihood method (for a more complete but also computationally more expensive method, see Ref. 18). We aim to minimize of the so-called objective function between the data and the model. We assume that the noise in data is nearly Gaussian (see Ref. 4) and therefore the suitable objective function is the quadratic form

$$S(N) = (T_{ext}(N) - T_{ext}^{obs})^T C^{-1} (T_{ext}(N) - T_{ext}^{obs}) \quad (26)$$

The matrix (in spectral direction) notation is implied. The observed transmission is given by Eq. (8) or by Eqs. (9)-(10). The matrix C is the covariance matrix of the transmission data.

The minimization is done by using the. Levenberg-Marquardt algorithm (see Ref. 16). This algorithm tries to find a minimum starting from a pre-set values. The algorithm also produces an estimate for the covariance matrix. The input covariance for the spectral inversion comes from two sources. The first, the most important one, is the data covariance. If there has been no data operations destroying stochastic independence of data, this covariance is diagonal i.e., it is the variance vector of the data. The second source is the modelling errors. If the data statistics and the model error are Gaussian we can simply add these two error sources

$$C = C_{obs} + C_{mod} \quad (27)$$

The specification of all the modelling errors in still an ongoing activity in the GOMOS project.

9 IR SPECTROMETER SPECTRAL INVERSION

The IR spectrometer will measure the densities of two different constituents O_2 and H_2O in two bands: 756-773 nm and 926-952 nm respectively. Due to the physics of the problem, the individual lines are very thin and saturated, the apparent cross sections change with the integrated densities, and they can no longer be considered as only wavelength dependent. The calculation of the transmission function is computationally very demanding. Therefore, it is difficult to use the same direct inversion method as for the UVIS spectrometer data.

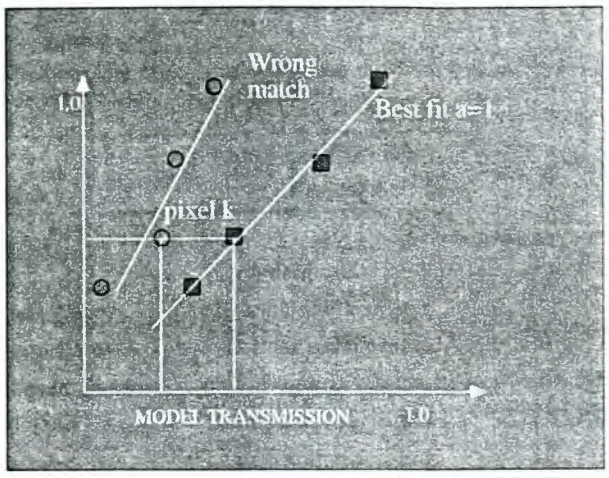

FIGURE 5. IR fitting.

A new algorithm has been developed. The method uses reference transmission spectra ($T_{mod}(\lambda, N)$) which are calculated for different integrated densities of O_2 or H_2O. These reference transmissions depend slightly on pressure. To take into account this dependency, calculations of transmission are performed using a direct model with a standard atmospheric profile. Several such calculations are done for different atmospheric models in order to have the response for different conditions such as tropical, mid-latitude and subarctic profiles. The method fits a function

$$y = a \log(T_{mod}(\lambda, N)) + \frac{b}{\lambda} + c \quad (28)$$

to the data set formed by the observed transmission. The last two terms in Eq. (29) are for the fitting of the background. Varying the model function or varying the altitude where the model function is calculated we aim to minimize the difference $a - 1$. Due to its nature, this method has been called "comparative method ". An illustrative example is shown in Fig. 6.

10 SMOOTHING

A line density retrieved by the spectral inversion is a statistical quantity. If the spectral inversion is attempted for a constituent which is unretrievable the result cannot be relied on. This happens, for example, at very high altitudes where densities decrease rapidly. It may also be the case when data is corrupted (with respect to retrieval). Due to the measurement technique and geometry the measured line densities are integrated along horizontal paths and averaged over 0.5 seconds. Therefore, they should originally be quite smooth quantities. By exploiting this property we can smooth the line densities in the vertical direction. The routine used is CUBGCV

from Ref. 19. The smoothing is an optional step in the GOMOS processing.

11 VERTICAL INVERSION

The vertical inversion problem is to find the vertical profile $\rho(z)$ that fulfills:

$$N(z_t) = \int \rho(z(s))ds \tag{29}$$

where N is any of the line densities inverted in the spectral inversion.

The normal approach to the under-determined inversion problem (29) is to make it even-determined by discretizing the atmosphere into layers. The resulting problem is a readily solvable linear inversion problem. By the triangular nature of the kernel matrix the inversion can be simply done using the so-called onion peeling method.

The vertical inversion method used in the GOMOS data processing makes an attempt to create continuous profiles instead of the layer structure of the onion peel technique. We approximate the local densities to be linear as a function of altitude between two successive GOMOS measurements:

$$\rho(z) = \frac{(z_{j-1} - z)\rho(z_j) + (z - z_j)\rho_{j-1}}{z_{j-1} - z_j} \tag{30}$$

Other approaches have been discussed in Ref. 17 and 20. After a tedious algebra the problem (29) is transformed to a matrix equation

$$A\rho = N \tag{31}$$

where A is a relatively complicated kernel matrix.

As already mentioned the line density we are using as inputs are the result of an integration in time and then should be adapted to the "instantaneous" expression that has been derived (i.e. the linear system is only valid for instantaneous line densities). To pass from integrated to instantaneous data we use an expression derived from Taylor expansion:

$$\bar{N}_j = N_j + \frac{(\Delta t)^2}{24}\frac{\partial^2 N_j}{\partial t^2} \tag{32}$$

Then if we summarize these contributions into a matrix form, the vertical inversion consists of solving the following linear system:

$$\bar{N} = K\rho \tag{33}$$

This matrix equation is solved by standard methods. The covariance matrix will also be produced.

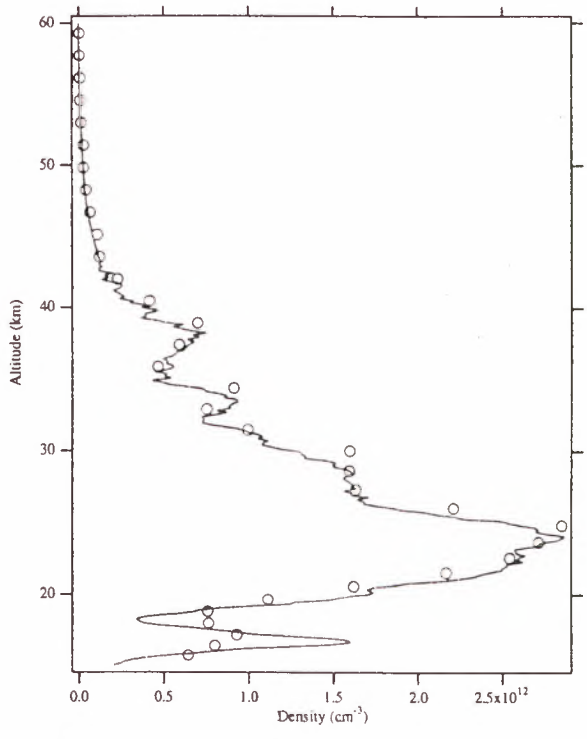

FIGURE 6. An example of the retrieved ozone profile (circles). The original profile is given by the red, continuous curve. The target star visual magnitude is $m_v = 1$ and temperature is T = 6400 K

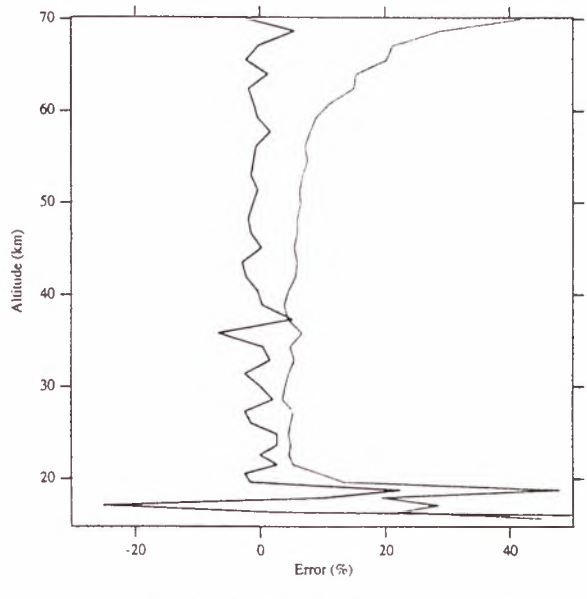

FIGURE 7. Standard deviation from the true value (red curve) and the bias (blue curve) for the ozone retrieval case of Fig.7. Statistics is based on 100 simulations.

12 LEVEL 2 LOOPS

After the vertical inversion we have produced density profiles and a new temperature profile Initially temperature profile is given by the MSIS90 model and ECMWF data. There are several possible sources for the new temperature profile but the most obvious ones are the Rayleigh scattering from the UVIS-spectrometer and the O_2 data from IR-spectrometer. From Rayleigh scattering we can derive neutral density and by using the ideal gas law and by assuming the hydrostatic equilibrium the temperature. From O_2 we can similarly derive neutral density assuming a constant mixing ratio and again temperature from ideal gas law. These two estimates must be assimilated together with weights according to their reliabilities (covariances). If the variance of the new temperature field is smaller than the one attached to the initial a priori temperature field, a new GOMOS atmosphere can be accepted.

These new data are injected to the calculation of the effective cross-sections and the spectral and vertical inversion are carried out again. It has been shown that this iterative process over spectral and vertical inversions significantly improves the final results. Therefore it is routinely applied (at least once and twice most) to reach best results.

Another first estimate has been done to derive the ray geometry. This geometry is computed during the level 1b processing by using a priori information (atmosphere density and temperature profiles) based on the best available information (ECMWF forecast or analysis and MSIS90). As already mentioned a new GOMOS produced temperature profile will emerge after the first vertical inversion. Therefore, a second ray path computation may be activated and the overall loop is launched once again. This requires a combination of the GOMOS retrieved air density with a priori information used from the atmospheric model.

Sample results from the simulation of the GOMOS ground processing is shown in Figs. 6-7. They have been produced by the GOSS- and GOPR-simulators developed by ACRI. The overall Level 2 architecture is shown in Fig. 8.

13 PHOTOMETER DATA ANALYSIS

Besides the manipulation of fast photometer data made to correct the stellar spectra, the photometers signals can be used to detect small structures in the atmosphere. Specifically we can derive high resolution temperature profiles.

The algorithm to derive the high resolution temperature profile is based on the computation of the time delay between the signal of the two photometers. Due to the variation of the index of refraction of air with wavelength, the light beam of an occulted star is more bent in the blue part of the spectrum than in the red part. For a given tangent altitude, the red beam will reach GOMOS before the blue beam. The computation of the time delay gives information on the bending angle which is related to the density and temperature profile in the atmosphere. This method allows us to derive an high resolution temperature profile with a vertical resolution of 100-200 meters.

The algorithm is divided in three main parts:

1. Computation of the chromatic time delay between two photometers
2. Determination of the deviation angle
3. Determination of the atmospheric profile.

The time delay is computed at 40 Hz, corresponding to a vertical sampling of 85 m at the most. This means that 20 time delay values are computed during each 0.5 sec spectrometer measurement. Taking into account the 1000Hz acquisition rate of the photometers, the time delay is computed at intervals of 25 photometer measurements.

The time delay is computed by searching the time shift between the blue and the red signal which gives the largest correlation coefficient between the two signals taken in a time window corresponding to a vertical change of the tangent altitude of 250 m.

The difference of deviation angle between the central wavelengths of the blue and the red photometers is obtained from the time delay Δt (not to be confused with the integration time 0.5 sec):

$$\delta_{blue} - \delta_{red} = \frac{v_z \Delta t}{L} \tag{34}$$

where L is the distance from GOMOS to the limb and v_z the projection of the satellite velocity on the vertical axis at tangent point.

The total deviation is directly proportional to the index of refraction n and is obtained with a linear extrapolation:

$$\delta_{blue} = \frac{(\delta_{blue} - \delta_{red}) n_{blue}}{(n_{blue} - n_{red})} = \frac{\delta_{blue} - \delta_{red}}{(\frac{\Delta n}{n})} \tag{35}$$

The coefficient $\Delta n/n$=0.011 depends on the exact band pass of the photometers.

Once the deviation angle as a function of the impact parameter is obtained (at 40 Hz) , the profile of index of refraction, directly proportional to the atmospheric density, is obtained by inverting an Abel integral

$$n(h_{blue}) = \frac{1}{\pi} \int_{h_{blue}}^{\infty} \frac{\delta_{blue}(h)}{\sqrt{(R+h)^2 - (R+h_{blue})^2}} dh \tag{36}$$

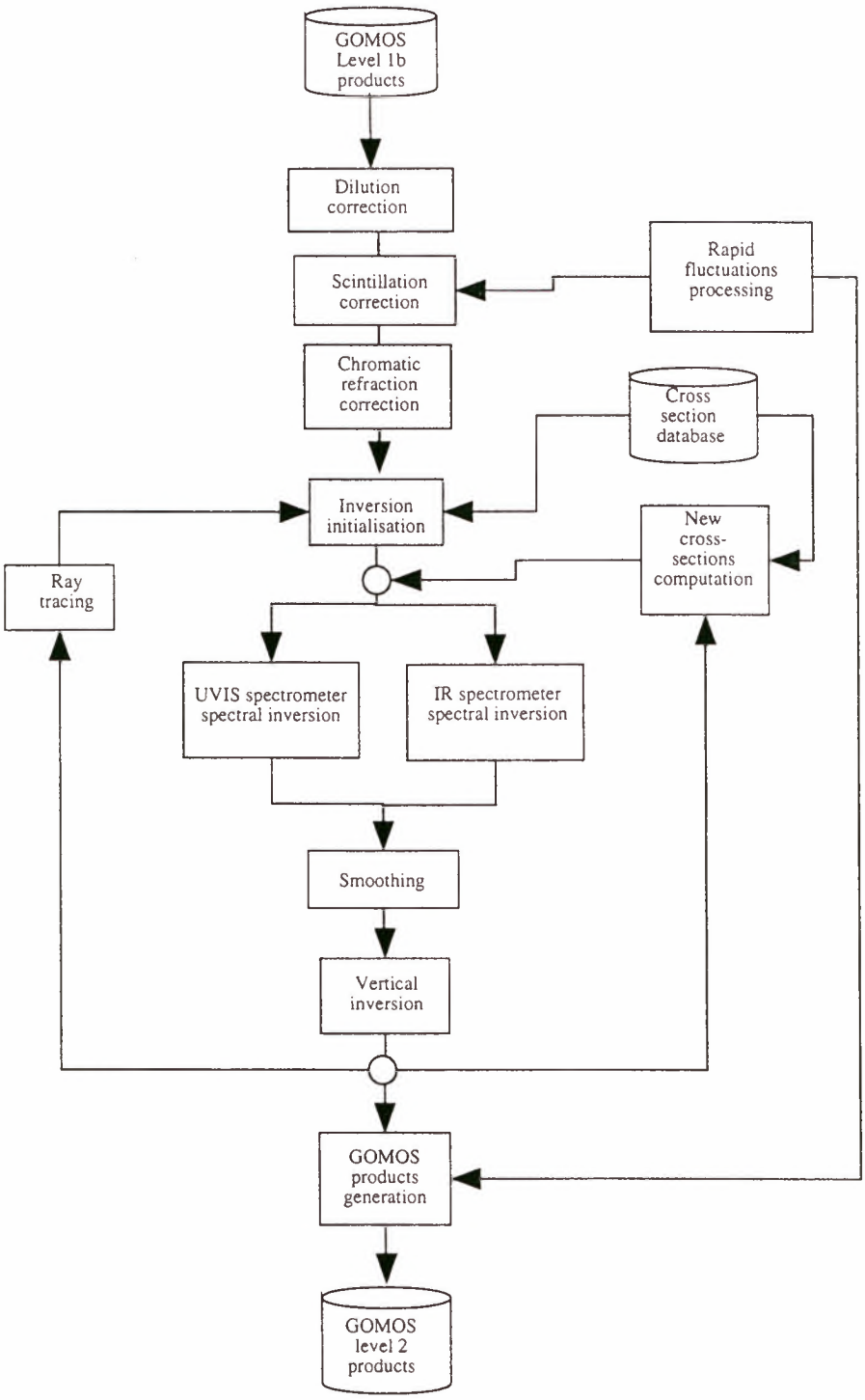

FIGURE 8. GOMOS Level 2 processing architecture.

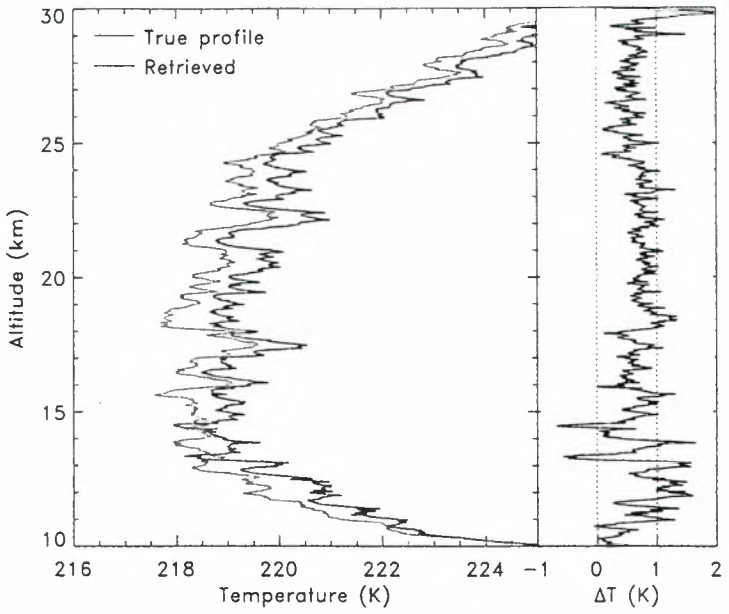

FIGURE 9. High resolution temperature profile and the error (from Ref. 21).

where h_{blue} is the impact parameter and R the Earth radius.

The inversion is done downwards, starting at the top of the high resolution profile (around 35-40 km) and using the model atmospheric profile at the tangent point above this altitude. Once the density profile is obtained, the temperature profile is computed using the hydrostatic equation. An example of the retrieved temperature profile is provided in Fig. 9.

14 DISCUSSION

In this paper we have discussed the ESA GOMOS Level 2 processing main features. The details of Level 1b and 2 algorithms occupy 500 documentation pages and it is quite impossible to go through all this information in this kind of short report. There are still ongoing development work on the following topics:

- Enhanced aerosol modelling
- Inclusion of a priori data
- Error analysis

The GOMOS measurement and the related data retrieval problems looked quite straightforward at the time GOMOS was proposed (1988) but they have turned out to involve quite complicated questions. It is, therefore, perhaps understandable that some theoretical modelling developments and their counterparts in the data processing are not yet at the final mature level where they could be for some more standard instrument. The situation will certainly improve quickly when real data will start to flow from GOMOS.

15 ACKNOWLEDGEMENTS

The author wants to thank J. Tamminen (FMI), L. Oikarinen (FMI), and F. Dalaudier (Sd'A) for useful comments. The result figures in Sec. 12, which certainly present the latest possible outcomes from the GOMOS ground segment, were produced by P. Dorgueil and O. d'Andon at ACRI.

The GOMOS Level 2 processing scheme is a product of many years and many people. At FMI the following people has participated in the development: E. Kyrölä, G. W. Leppelmeier, L. Oikarinen, E. Sihvola (now at the University of Helsinki), J. Tamminen; At Service d'Aeronomie du CNRS: P.Benet, J. L. Bertaux, E. Chassefiere, F. Dalaudier, A. Hauchecorne, J-C. Lebrun,M. Martic, B. Theodore and ; at IASB: D. Fussen, P. Simon. M. Van Roozendael; at ACRI: A. Mangin, O. d'Andon; at ESA: J. Langen, G. Levrini, A. Popescu, F. Spiero. In particular, the team wishes to thank Odile d'Andon for her enthusiasm, encouragement, and leadership, all of which were essential to obtaining a coherent result from such a diverse group.

REFERENCES

1. J. L. Elliot. Stellar occultation studies of the solar system. *Ann. Rev. Astron. Astrophys..*, 17:445–475, 1979.

2. R.G. Hays and P. B. Roble. Stellar spectra and atmospheric composition. *J. Atmos. Sci..*, 25:1141–1153, 1968.

3. S. Korpela. *A study of the operational principles of the GOMOS instrument for global ozone monitoring by the occultation of stars.* Geophysical publications, no. 22. Finnish Meteorological Institute, Helsinki, 1991. Ph.D thesis at the Helsinki University of Technology.

4. E. Kyrölä, E. Sihvola, Y. Kotivuori, M. Tikka, T. Tuomi, and H. Haario. Inverse Theory for Occultation Measurements, 1. Spectral Inversion. *J. Geophys. Res.*, 98:7367–7381, 1993.

5. G. E. Smith and D. M. Hunten. Study of planetary atmospheres by absorptive occultations. *Reviews of geophysics*, 28:117–143, 1990.

6. J. Louet. Envisat ground segment structure. In this volume, 1999.

7. GOMOS ESL. *GOMOS Detailed Processing Model.* ESA, 1998.

8. GOMOS ESL. *GOMOS Algorithm Theoretical Basis Document.* ESA, 1.0 edition, 1998.

9. J.-L. Bertaux. GOMOS ATBD -Level 1b. In this volume, 1999.

10. J.-L. Bertaux. GOMOS Mission objectives. In this volume, 1999.

11. E. Kyrölä and J. Tamminen. Gomos mission planning. In this volume, 1999.

12. J.-L. Bertaux, G. Megie, T. Widemann, E. Chassefiere, R. Pellinen, E. Kyrölä, S. Korpela, and P. Simon. Monitoring of Ozone Trend by Stellar Occultations: The GOMOS Instrument. *Adv. Space Res.*, 11(3):237–242, 1991.

13. A. Popescu. Gomos instrument concept and performance. In this volume, 1999.

14. A. Popescu. Gomos data products. In this volume, 1999.

15. H. Auvinen, L. Oikarinen, E. Kyrölä, J. Tamminen, and G. W. Leppelmeier. Inversion algorithms for OSIRIS and GOMOS bright-limb background term. In this volume, 1999.

16. W. H. Press, S. A. Teukolsky, W. T. Vetterling, and B. P. Flannery. *Numerical Recipes in FORTRAN, The art of scientific computing.* Clasendon Press, Oxford, 1992.

17. E. Sihvola. *Coupling of spectral and vertical inversion in the analysis of stellar occultation data.* Geophysical publications, no. 38. Finnish Meteorological Institute, Helsinki, 1994. Licentiate thesis at the University of Helsinki, Department of Theoretical Physics.

18. J. Tamminen, E. Kyrölä, and H. Auvinen. MCMC algorithms for inverse problems in remote sensing. In this volume, 1999.

19. M. F. Hutchinson. A fast procedure for calculating minimum cross-validation cubic smoothing splines. 12:150–153, 1986.

20. J. Tammienen, E. Kyrölä, E. Sihvola, and L. Oikarinen. Inverse Theory for Occultation Measurements, 2. Vertical Inversion. in preparation, 1999.

21. B. Theodore. *Simulation de la scintillation lors d'occultations d'etoiles par l'atmosphere terrestre; application a la restitution du profil de temperature.* 1998. Ph.D thesis at l'Universite Paris 7.

Algorithm Review
SCIAMACHY

SCIAMACHY: The Mission Objectives

J. P. Burrows, H. Bovensmann, M. Buchwitz, S. Noël
Institute of Environmental Physics and Remote Sensing,
University of Bremen, FB 1, D-28334 Bremen, Germany;
A. P. H. Goede, SRON, Utrecht, The Netherlands;
C. L. C. Muller, BIRA/IASB, Brussel, Belgium

ABSTRACT

SCIAMACHY (SCanning Imaging Absorption spectroMeter for Atmospheric CHartographY) is a spectrometer designed to measure sunlight transmitted, reflected and scattered by the Earth's atmosphere or surface in the ultraviolet, visible and near infrared wavelength region (240 nm - 2380 nm) at moderate spectral resolution (0.2 nm - 1.5 nm). Atmospheric measurements will be performed in nadir, limb, and solar/lunar occultation mode. In addition the extra-terrestrial solar irradiance and lunar radiance will be determined from observations of the sun and the moon above the atmosphere. Inversion of the ratio of earthshine radiance and solar irradiance yields information about the amounts and distribution of important atmospheric constituents and the spectral reflectance (or albedo) of the Earth's surface.

SCIAMACHY was conceived to improve our knowledge and understanding of a variety of issues of importance for the chemistry and physics of the Earth's atmosphere (troposphere, stratosphere and mesosphere) and potential changes resulting from either increasing anthropogenic activity or the variability of natural phenomena.

Inversion of the SCIAMACHY data will provide information on the amounts and distribution of the atmospheric constituents O_3, O_2, $O_2(^1\Delta)$, O_4, BrO, OClO, (ClO), SO_2, H_2CO, NO, NO_2, NO_3, CO, CO_2, CH_4, H_2O, N_2O, and aerosol, as well as the parameters pressure p, temperature T, radiation field, cloud cover, cloud top height and surface spectral reflectance. One unique feature of SCIAMACHY will be the detection of tropospheric column amounts of O_3, NO_2, BrO, CO, CH_4, H_2O, N_2O, SO_2 and H_2CO by the combination of near simultaneous limb and nadir observations.

1. Introduction

The Earth and its atmosphere combine to form a complex biogeochemical system. Within this system conditions, which are essential for life on earth "as we know it", have been maintained for approximately 400 Million years. Recently the growth in the population and its standard of living have resulted in changes in atmospheric composition. It is therefore essential to assess accurately the significance and environmental impact of man's activity.

The potential importance of pollution for global atmospheric change has been recognised in the last 30 years. This has been in large part a result of the knowledge gained from atmospheric measurements. The techniques developed in the post war period have enabled atmospheric parameters, (e.g. temperature, pressure, density, wind speed and direction etc.) and constituents (gases, aerosols and clouds) to be accurately measured for the first time. Passive remote sensing of the atmosphere from orbiting satellites has been and is going to be increasingly exploited in this context.

The changing nature of the atmosphere on a global scale has become a matter of public concern and much scientific debate. Many environmental issues which have been recognised to be of regional and global importance and are and will be the motivation for much scientific research e.g.:

i) Global Warming

Although discussed over 100 years ago, global warming resulting from anthropogenic activity remains a matter of great significance. This is because of the increasing tropospheric abundances of the so-called greenhouse gases and constituents (e.g. CO_2, CH_4, N_2O, Chlorofluorcarbon compounds, CFCs and their substitutes HCFCs, aerosols etc.) and their influence on atmospheric radiative balance ([1] and references therein). The recent Kyoto and Buenos Aires Environmental Summits have developed plans to limit the emission of greenhouse gases

ii) Stratospheric Ozone Depletion

Large depletions of ozone, O_3, have been observed above the poles in spring (better known „ozone holes"). Significant depletions have also been observed at mid-latitudes. These depletions are now known to result from the tropospheric release of long lived halocarbon compounds (CFCs, halons, methyl bromide, CH_3Br) which enter the stratosphere and release species which catalytically remove O_3 [2]. The Montreal Protocol and its amendments are having success in limiting the release of CFCs but the medium term consequences for the atmosphere remains uncertain.

iii) The Coupling of Global Warming and Stratospheric Ozone Depletion

Recently it has been recognised that the coupling of global warming and the mechanism by which stratospheric O_3 is catalytically depleted is poorly understood but of global significance [3, 4].

iv) Industrial Pollution, Oxidising Capacity of the Troposphere and Air Quality

Two types of smog have been identified in the early post war period: in London and Los Angeles. The former is a reducing smog, characterised by high acidity, which results from the reduction sulphur dioxide, SO_2 to sulphuric acid, H_2SO_4 and oxides of nitrogen (NO and NO_2) to nitric acid HNO_3. The latter is a photochemically accelerated oxidation of trace gases, which results in the production of copious amounts of O_3. The background level of tropospheric O_3 is believed to have increased by about a factor of two in the last century. The increasing industrial activity, relying on energy production from fossil fuel combustion and the changing pattern of land usage have increased the anthropogenic emissions to the atmosphere which is expected to have a variety of consequences

v) Increasing of Acid Deposition

The combustion of fossil fuels results in the release of large amounts of nitrogen oxide, NO, and nitrogen dioxide, NO_2, (together denoted as NO_x) and sulphur dioxide, SO_2, into the planetary boundary layer and the free troposphere. With reliance on fossil fuels as an the dominating energy source since the birth of the industrial revolution there has been a corresponding increase of the amount of acid deposition. Acidification was first recognised as an important global ecological issue in the 1970's. Public interest in the consequences of acid deposition peaked in the middle of the 1980's with the concern over forest die-back caused by acidification. This remains an important environmental issue and research area [5].

vi) Biomass Burning

Biomass burning has now been identified as a significant source of many atmospheric trace gases and aerosols [6]. The practice of biomass burning is increasing with growing human population, particularly in the tropics, and it has become a major global environmental issue in its own right [7].

Natural phenomena such as volcanic explosions or the El Nino Southern Oscillation (ENSO) also significantly influence the amounts and distributions of atmospheric constituents. In order to assess accurately the impact of anthropogenic activity on the earth atmosphere biogeochemical system, a detailed knowledge of the physical and chemical processes, which control the atmosphere is required. Knowledge about these processes is obtained from global measurements of the atmospheric constituents. In addition and very importantly such measurements enable the accuracy and predictive power of current models of atmospheric behaviour to be tested.

For long lived atmospheric constituents such as oxygen O_2, carbon dioxide, CO_2, an adequate understanding of their global tropospheric behaviour can be obtained from measurements made at a suitable selected network of ground based stations.

However for shorter lived and highly variable atmospheric species the only feasible approach for obtaining their global distributions is to make regular measurements from space-based platforms. Provided they have sufficient accuracy, global space-based measurements of species with relatively long atmospheric lifetimes can be used to determine source and sink regions and possibly to infer trends.

SCIAMACHY was conceived to improve our knowledge and understanding of a variety of issues of importance for the chemistry and physics of the Earth atmosphere (troposphere, stratosphere and mesosphere) and to investigate potential changes resulting from either anthropogenic behaviour or natural phenomena.

The Scanning Imaging Absorption spectroMeter for Atmospheric ChartographY (SCIAMACHY) was proposed in July 1988 by an international group of scientists in response to the ESA Announcement of Opportunity for the Polar Platform [8]. The latter is now known as ENVISAT and is planned for launch in 2000. SCIAMACHY is intended to exploit the opportunity provided by ENVISAT for atmospheric research and to provide data of significance for scientific and operational users.

2. Measurement Principle

The overall SCIAMACHY mission goal is to be achieved by making passive remotes sounding measurements of the extra terrestrial solar irradiance and the back scattered ultraviolet, visible and infrared radiation.

The heritage of SCIAMACHY [8] lies in both the ground based measurements using Differential Optical Absorption Spectroscopy (DOAS) [9-11] and previous satellite atmospheric remote sensing missions. SCIAMACHY combines and extends the measurement principles and observational modes of the nadir scattered sunlight measuring instruments SBUV and TOMS [12], the solar occultation instrument SAGE [13, 14] and the limb scattered sunlight measuring instrument Solar Mesospheric Explorer SME [15] within one instrument. SCIAMACHY measures in the wavelength range from 240 nm to 2380 nm the following:

- the scattered and reflected spectral radiance in nadir and limb geometry,
- the spectral radiance transmitted through the atmosphere in solar and lunar occultation geometry,
- the extraterrestrial solar irradiance and the lunar radiance.

Figure 1 shows the wavelength range to be observed by SCIAMACHY and the position of spectral windows where atmospheric constituents are to be retrieved.

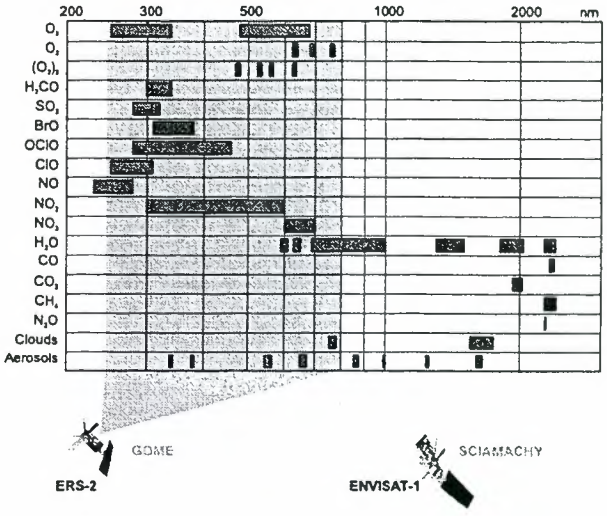

Figure 1: Atmospheric constituents with absorption features in the spectral range covered by GOME and SCIAMACHY.

The SCIAMACHY instrument is a space-based double-spectrometer designed to measure with high sensitivity and accuracy in the ultraviolet, visible and near infrared wavelength region (240 nm - 2380 nm) at moderate spectral resolution (0.2 nm - 1.5 nm). Details about the instrument and the mission are described elsewhere ([16] and references therein). The absorption, reflection and scattering characteristics of the atmosphere are determined by measuring the extraterrestrial solar irradiance and the upwelling radiance observed in nadir, limb, and occultation viewing geometry. During its passage through the earth's atmosphere the electromagnetic radiation emitted by the sun is modified by absorption, scattering and emission processes. SCIAMACHY measures these changes in the different viewing geometries. The ratio of extraterrestrial irradiance and the upwelling radiance will be inverted to provide information about the

amounts and distribution of important atmospheric constituents, which absorb or scatter light, and the spectral reflectance of the Earth's surface. Inversion of the measurements will enable total column amounts and vertical profiles of the targeted atmospheric constituents and parameters to be derived. These retrieved data products are then to be used in combination with simulations of atmospheric behaviour to test our knowledge of atmospheric physics and chemistry. An important focus and unique capability of SCIAMACHY is the retrieval of tropospheric and stratospheric species and parameters.

3. Mission Objectives, Targeted Constituents and Applications

The overall mission objective of SCIAMACHY is to determine globally the amounts and distributions atmospheric constituents and thereby improve our knowledge of the mechanisms, which determine the behaviour of the atmosphere, and the predictive power of our models of the atmosphere. More specifically, SCIAMACHY will be able to detect the atmospheric constituents in the height ranges depicted in figure 2.

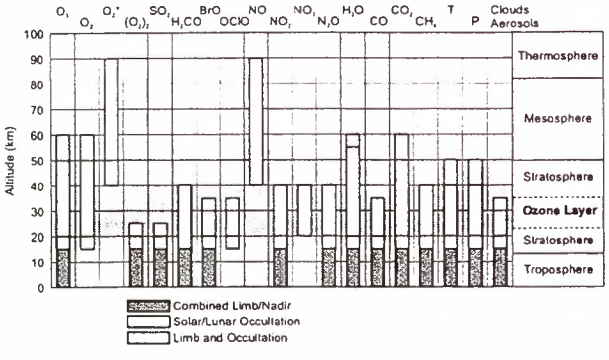

Figure 2: Altitude ranges of atmospheric constituents targeted by SCIAMACHY.

Some of the scientific studies and areas of applications to be pursued using SCIAMACHY data are described below.

i) Tropospheric Chemistry

SCIAMACHY will measure the backscattered sunlight which reaches the Earth surface ($\lambda \geq 280$ nm). The retrieval of tropospheric constituents is influenced and limited by clouds. SCIAMACHY is the only atmospheric chemistry sensor on ENVISAT capable of determining trace gases and aerosol abundances in the lower troposphere including the planetary boundary layer under cloud free conditions. From the SCIAMACHY nadir and limb measurements tropospheric columns of O_3, NO_2, BrO, CO, CH_4, H_2O, N_2O, SO_2 and H_2CO (compare figure 2) will be retrieved. In addition, surface spectral reflectance, aerosol and cloud parameters (cover and cloud top height) and the tropospheric flux from 280 nm to 2380 nm will be retrieved. These data are required for studies of the oxidising capacity of the troposphere, photochemical O_3 production and destruction, and tropospheric pollution (biomass burning, industrial activities, aircraft emissions etc.).

ii) Stratosphere-Troposphere Exchange

For the investigation of stratosphere-troposphere exchange [17] SCIAMACHY measurements of the height resolved profiles of the tracers O_3, H_2O, N_2O, CH_4, and aerosol will be of primary significance. These measurements enable investigations of the downward transport of stratospheric O_3 and upward transport of important species (e.g. aerosol, CH_4, H_2O, and N_2O). The CH_4 and N_2O molecules are emitted into the planetary boundary layer. Their long tropospheric lifetime results in their being transported to the stratosphere, where they are the dominant source of the ozone-destroying HO_x and NO_x radicals. Studies of relatively small scale features such as tropopause folding at mid-latitudes require a high spatial resolution and are unlikely to be unambiguously observed by SCIAMACHY. However larger scale stratosphere-troposphere exchange as envisaged in [17] will be readily observed.

In the neighbourhood of the tropopause the measurement modes of SCIAMACHY will have different vertical and horizontal resolutions. Solar and lunar occultation modes yield measurements with a vertical resolution of 2.5 km and a horizontal resolution of 30 km across track, determined by the solar diameter, and extending roughly 400 km along track. For the limb measurements the geometrical spatial resolution is approximately 3 km vertically and typically 240 km horizontally across track, determined by scan speed and integration time, and extending roughly 400 km along track.

iii) Stratospheric Chemistry and Dynamics

The study of the stratospheric chemistry and dynamics will utilise the simultaneous retrieval of total columns from nadir measurements and vertical stratospheric profiles from limb and occultation measurements of O_3, NO_2, BrO, H_2O, CO, CH_4, N_2O (OClO and possibly ClO under ozone hole conditions), as well as aerosol and stratospheric cloud information. Temperature and pressure profiles can be determined from limb and occultation observations of the well mixed gases CO_2 and O_2 assuming local thermal equilibrium.

SCIAMACHY will be making measurements when halogen loading of the stratosphere maximises around the turn of the century [2]. It has recently been pointed out in [18] that the springtime polar lower stratospheric O_3, specifically the layer from 12 - 20 km, will be the first region to show a response to the international control measures on chlorofluorocarbon compounds (CFCs) defined in the Montreal Protocol 1987 and its Copenhagen and London amendments. SCIAMACHY will enable this preposition to be studied in detail.

In general SCIAMACHY measurements will yield detailed information about the development of stratospheric O_3 above the Arctic and Antarctica, the global stratospheric active halogen species (BrO, (ClO), OClO), and the global O_3 budget as a function of the height in the atmosphere. As SCIAMACHY measures simultaneously the backscattered radiation field and constituent profiles, an important objective is to test the accuracy of current stratospheric photochemical models and their predictive capability.

iv) Mesospheric Chemistry and Dynamics

In the upper stratosphere and lower mesosphere SCIAMACHY measurements yield profiles of O_3, H_2O, N_2O, NO, O_2, and $O_2(^1\Delta)$. These measurements will be used to study the distribution of H_2O and O_3 and their global circulation. There has recently been much discussion of upper stratospheric and mesospheric chemistry in the context of the "ozone deficit problem" [19, 20]. It has also been suggested that monitoring of H_2O in the lower mesosphere may offer an opportunity for the early detection of climate change [21]. The O_3 destruction by mesospheric and upper stratospheric NO will be investigated. Finally the mesospheric source of stratospheric NO_x will be quantified.

v) Climate Research

For use in climate research, SCIAMACHY measurements will provide the distributions of several important "greenhouse" gases (O_3, H_2O, CH_4, N_2O, and CO_2), aerosol and cloud data, surface spectral reflectance (280 nm - 2380 nm), the incoming solar spectral irradiance and the outgoing spectral radiance (240 nm - 2380 nm), and profiles of p and T (via O_2 and CO_2). As it is intended that SCIAMACHY observations are to be made for many years. Together with other relevant data sets, for example from UARS, a longer term data set will provide much unique information useful for the study of the Earth - atmosphere system and variations of the solar output and its impact on climate change.

To provide continuity in the long term record of species such as O_3 determined from measurements by other spectrometers such as SBUV or GOME, it is foreseen to calibrate SCIAMACHY with methods similar to those used for GOME or SBUV calibration [22].

4. SCIAMACHY and GOME

SCIAMACHY and GOME ([23] and references therein), which is a small scale version of SCIAMACHY, represent a new generation of space based remote sounding sensors, which rely on and utilise the simultaneous spectrally resolved measurement of light upwelling from the atmosphere to determine amounts of atmospheric constituents.

Using data from GOME, which was launched on board the European Remote Sensing satellite ERS-2 in April 1995, the feasibility of the instrument and retrieval concepts has been successfully demonstrated for nadir observations. The trace gases O_3, NO_2, BrO, OClO, SO_2 and H_2CO have been observed as predicted (Burrows et al. 1999, and references therein), and studies of NO_3, ClO, NO, and aerosol retrieval are proceeding. The determination of O_3 profile information, including tropospheric O_3, from GOME measurements [23, 24] has a large number of potential applications. In addition the retrieval of tropospheric column information of SO_2, H_2CO, NO_2, and BrO from GOME measurements was demonstrated [23].

There are two main advantages of SCIAMACHY with respect to GOME: its enhanced spectral range and additional atmospheric observation geometries. Whereas GOME concentrates on measurements in the UV and visible wavelength range (240 nm - 785 nm) [23], SCIAMACHY also measures the solar part of the infrared spectral region. SCIAMACHY measures light continuously from 240 nm up to 1750 nm and in two spectral windows in the NIR (1940 nm - 2040 nm and 2265 nm - 2380 nm). This enables SCIAMACHY to detect important atmospheric trace gases with absorption features in the IR, most notably CO, CO_2, CH_4, and N_2O. Pressure, temperature, water vapour and aerosol information can also be obtained from this spectral region.

A second significant advantage of SCIAMACHY is that in addition to the nadir viewing geometry SCIAMACHY will observe the atmosphere in limb and solar and lunar occultation geometry. Limb and occultation measurements will provide height-resolved information about atmospheric constituents on a regular basis. The combination of nadir and limb measurements will be used to derive tropospheric concentrations of several atmospheric trace constituents on a global scale.

5. Viewing Geometries and Typical Orbit

Atmospheric measurements will be performed in nadir, limb and occultation geometry. In nadir mode, the atmospheric volume directly beneath the spacecraft will be observed. Across track scans will be performed covering an area of up to about 480 km left and right of the ground track. In limb mode the instrument observes the edge of the atmosphere. Horizontal scans over a width of approximately 960 km will be performed at tangent altitudes from the ground to about 100 km. In occultation mode the observational geometry is the same as in limb mode, but measurements are performed at times where the sun or the moon are in the instrument's field of view. An alternating limb and nadir measurement sequence will be performed for most time of the sunlit part of the orbit (see figures 3 and 4).

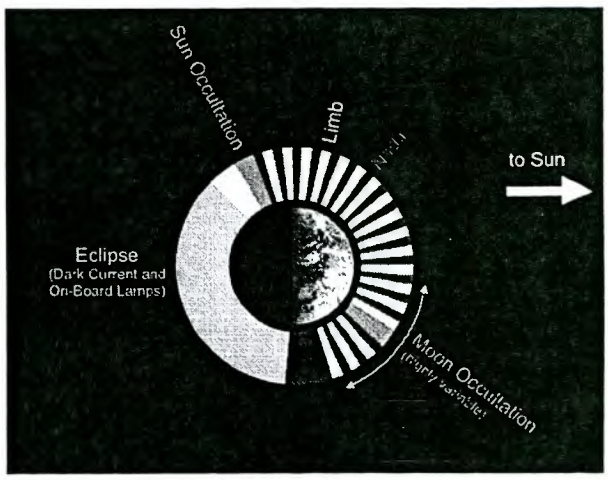

Figure 3: *Typical sequence of scientific measurements during one orbit. The orbit starts with limb measurements prior to sunrise; during sunrise solar occultation measurements are performed. Most of the sunlit part of the orbit consists of alternating limb/nadir measurements. When the moon is visible for SCIAMACHY (which is the case for about one week per month) moon occultation measurements are performed every second orbit on the southern hemisphere; the orbital position of these moon occultation measurements varies strongly over the year. The eclipse phase is dedicated to calibration measurements (mainly dark current measurements and measurements with the internal lamps).*

Similar to ERS-2, ENVISAT-1 will fly in a polar, sun-synchronous orbit with an orbital period of about 100 min. The eclipse part of the orbit is mainly used for calibration measurements, i.e. dark current measurements and measurements using the on-board lamps. During each sunrise solar occultation measurements will be performed over the northern hemisphere. Depending on season, these measurements will cover a latitudinal range at the tangent points from the north pole to 65°N. The moon will be visible for SCIAMACHY for about one week per month over the southern hemisphere. During these times lunar occultation measurements will be performed every second orbit. Lunar occultation measurements provide a challenge for mission planning because the time and place of the visibility of the moon show a large variability over the mission time. Moon

occultation measurements will cover tangent latitudes between 30°S and 90°S over the year.

The spatial resolution of the measurements depends in general on the sensitivity of the instrument to the intensity of the incoming light. Therefore the spatial resolution shows a spectral characteristic. For SCIAMACHY, the available data rate is an important additional factor in this context. Due to the data rate limitations it is necessary to co-add data on board of the spacecraft which essentially reduces the spatial resolution. However, the flexible operational concept of SCIAMACHY enables the definition of special spectral windows with reduced (or even no) co-adding. A typical nadir spatial resolution of about 30 km 60 km (along/across track) will be achieved for all major atmospheric constituents. The vertical resolution for limb and occultation measurements will be about 3 km.

6. Tropospheric Column Information from Combined Limb-Nadir Measurements

A special feature of SCIAMACHY data analysis will be the ability to combine alternating limb and nadir measurements (see figure 4) which enables the tropospheric column amounts of several trace gases to be determined. The approach taken to determine the tropospheric column is to subtract the stratospheric/mesospheric column derived from limb measurements from the total nadir column.

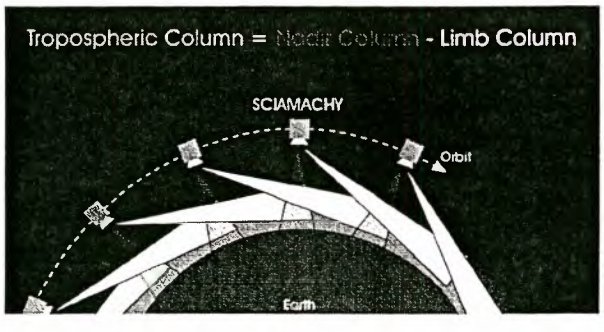

Figure 4: *Tropospheric columns from alternating limb and nadir measurements.*

This residual technique was developed by Fishman et al.[25, 26] who derived tropospheric ozone columns from the combination of TOMS total nadir columns with SAGE II occultation profiles or SBUV nadir profiles. To reduce possible error sources, SCIAMACHY limb and nadir measurements are carefully matched such that effectively the same atmospheric volume will be observed first in limb and then 8 min later in nadir mode. From the combination of the alternating limb and nadir measurements it will be possible to derive tropospheric columns not only for O_3 but also for NO_2, CO, CH_4, H_2O, N_2O, SO_2, H_2CO, and BrO down to the surface or the cloud top. This information will be available on a global scale. At the equator global coverage will be achieved within 6 days.

7. Summary

The study of the mechanisms which control stratospheric ozone, determine the impact of tropospheric pollution arising from industrial activity and biomass burning, enable the troposphere-stratosphere exchange to understood as a global perspective as well as the investigations of special events such as volcanic eruptions, solar proton events, and other related regional and global phenomena are the scientific objectives of the SCIAMACHY mission. SCIAMACHY measurements will yield the amounts and distribution of O_3, O_2, $O_2(^1\Delta)$, O_4, BrO, OClO, (ClO), SO_2, H_2CO, NO, NO_2, NO_3, CO, CO_2, CH_4, H_2O, N_2O, pressure, temperature, aerosol, radiation, cloud cover and cloud top height. A special feature of SCIAMACHY is the combined limb/nadir measurement mode, by which tropospheric information is derived. SCIAMACHY is thereby able to detect tropospheric column amounts of O_3, NO_2, CO, CH_4, H_2O, N_2O, SO_2, H_2CO, and BrO down to the planetary boundary layer under cloud free conditions or to the cloud top. Depending on the type of measurements to be performed during the orbit, global coverage is achieved within 3 or 6 days at the equator.

SCIAMACHY will provide information of unique importance for the environmental issues described above. Provided measurements are made for a sufficient length of time the dataset to be generated by SCIAMACHY will met requirements for assessing the impact of anthropogenic emissions on the atmosphere. Because of its wide range of applications SCIAMACHY is a good candidate instrument for any future global monitoring system. SCIAMACHY must also be recognised as a voyage of scientific discovery. It will survey the atmosphere in a manner previously not possible, thus enabling new effects or atmospheric mechanisms to be discovered.

Acknowledgements

SCIAMACHY is a national contribution to the ENVISAT mission funded by the German Aerospace Centre (DLR) and the Netherlands Agency for Aerospace Programs (NIVR), including a contribution of the Belgian Institute for Space Aeronomy (BIRA-IASB). The SCIAMACHY industrial consortium comprises the prime contractors Dornier Satellite Systems (D) and Fokker Space (NL) and the subcontractors OHB-Systems (D), Jenoptik (D), Space Research Organisation Netherlands SRON (NL), TPD-TNO (NL), OIP (B) and Epitaxx Inc. (USA). The instrument and algorithm development is supported by the activities of the SCIAMACHY Science Advisory Group (SSAG), a team of scientists from various international institutions: University of Bremen (D), SRON (NL), Smithsonian Astrophysical Observatory SAO (USA), BIRA-IASB (B), Max-Planck Institute for Chemistry in Mainz (D), KNMI (NL), University of Heidelberg (D), Institute for the study of Geophysical and Environmental Methodologies IMGA (I), and the Centre National pour la Recherche Scientifique CNRS-LPMA (F). Operational data processing is to be performed by the German Remote Sensing Data Center (DLR-DFD) within the ENVISAT ground segment. The mission operation is supported by the SCIAMACHY Operations Support Team SOST. This work has been funded as part of the SCIAMACHY Scientific Support Study by the German Ministry of Education and Research (BMBF) under grant 50EP9207.

References

1. IPCC (1996) Climate Change 1995: The Science of Climate Change, IPCC, Cambridge University Press, Cambridge
2. WMO (1995) Scientific assessment of ozone depletion. World Meteorological Organisation Global Ozone

Research and Monitoring Project. *Report No. 37*, World Meteorological Organisation, Geneva
3. Shindell, D.T., D. Rind and P. Lonergan (1998) Increased polar stratospheric ozone losses and delayed eventual recovery owing to increasing greenhouse gas concentrations. *Nature* **392**, 589-592
4. Dameris, M., V. Crewe, R. Hein, C. Schnat, C. Brühl and B. Steil (1998) Assessment of the future development of the ozone layer. *Geophysical Research Letters* **25**, 3579-3583
5. Heij, G.J. and J.W. Erisman (1995) (Eds.) *Acid rain research: Do we have enough answers*?. Studies in Environmental Science 64. Elsevier, Amsterdam, 502 pp
6. Watson, C.E., J. Fishman and H.G. Reichle jr. (1990) The significance of biomass burning as a source of carbon monoxide and ozone in the southern hemisphere tropics: a satellite analysis. *Journal of Geophysical Research* **95**, 16443-16450
7. Levine, J. (Editor) (1991) *Global biomass burning: atmospheric, climatic and biospheric implications*. MIT Press, Cambridge, Mass.
8. Burrows J. P., K. V. Chance, P. J. Crutzen, H. van Dop, J. C. Geary, T. J. Johnson, G. W. Harris, I. S. A. Isaksen, G. K. Moortgat, C. Muller, D. Perner, U. Platt, J.-P. Pommereau, H. Rodhe, E. Roeckner, W. Schneider, P. Simon, H. Sundqvist, and J. Vercheval (1988): SCIAMACHY - A European proposal for atmospheric remote sensing from the ESA Polar Platform, published by Max-Planck-Institut für Chemie, 55122 Mainz, Germany
9. Brewer, A. W., C.T. McElroy, J.B. Kerr (1973) Nitrogen dioxide concentrations in the atmosphere, *Nature*, **246**, 129 - 133
10. Platt, U. and D. Perner (1980) Direct measurements of atmospheric HCHO, HONO, O_3, NO_2, and SO_2, by differential optical absorption spectroscopy in the near UV. *Journal of Geophysical Research* **85**, 7453-7465.
11. Solomon, S., A.L. Schmeltenkopf, W.R. Sanders (1987) On the interpretation of zenith sky absorption measurements, *J. Geophys. Res.*, **92**, 8311 - 8319
12. Heath, D.F., A.J. Krueger, H.A. Roeder and B.D. Henderson (1975) The solar backscatter ultraviolet and total ozone mapping spectrometer (SBUV/TOMS) for Nimbus-G. *Optical Engineering* **14**, 323-332
13. McCormick, M.P., P. Hamill, T.J. Pepin, W.P. Chu, T.J. Swissler and L.R. McMaster (1979) Satellite studies of the stratospheric aerosol. *Bulletin of the American Meteorological Society* **60**, 1038-1048
14. Maudlin III, L.E., N.H. Zaun, M.P. McCormick, Jr., J.H. Guy, and W.R. Vaughn (1985) Stratospheric aerosol and gas experiment II instrument: a functional description. *Optical Engineering* **24**, 307-321
15. Barth, C.A., D.W. Rusch, R.J. Thomas, G.H. Mount, G.J. Rottman, G.E. Thomas, R.W. Sanders, and G.M. Lawrence (1983) Solar Mesosphere Explorer: Scientific Objectives and Results, *Geophys. Res. Lett.*, **10**, 237-240
16. Bovensmann, H., J. P. Burrows, M. Buchwitz, J. Frerick, S. Noël, V.V. Rozanov, K.V. Chance, A.P.H. Goede (1999) SCIAMACHY- Mission Objectives and Measurement Modes. *Journal of the Atmospheric Sciences*, **56**, 127 – 150
17. Holton, J.R., P.H. Haynes, M.E. McIntyre, A.R. Douglass, R.B. Hood, L. Pfister (1995) Stratosphere-troposphere exchange, *Rev. Geophys.*, **33**, 403-439
18. Hofmann, D. J. (1996) Recovery of Antarctic ozone hole, *Nature*, **384**, 222
19. Crutzen, P. J., J.-U. Grooß, C. Brühl, R. Müller, J. M. Russel III (1995) A reevaluation of the ozone budget with HALOE UARS data: no evidence for an ozone deficit. *Science*, **268**, 705 - 708
20. Summers, M. E., R. R. Conway, D. E. Siskind, M. H. Stevens, D. Offermann, M. Riese, P. Preusse, D. F. Strobel, J. M. Russel III (1997) Implications of Satellite OH Observations for Middle Atmospheric H_2O and Ozone, *Science*, **277**, 1967 - 1970
21. Chandra, S., C. H. Jackman, E. L. Fleming, J. M. Russel III (1997) The seasonal and long term changes in mesospheric water vapor, *Geophys. Res. Lett.*, **24**, 639 - 642
22. Weber, M., J. P. Burrows, R. P. Cebula (1998) GOME solar UV/VIS irradiance measurements between 1995 and 1997 - First results on proxy solar activity studies, *Solar Physics*, **177**, 63 - 77
23. Burrows, J.P., M. Weber, M. Buchwitz, V. V. Rozanov, A. Ladstätter-Weißenmayer, A. Richter, R. De Beek, R. Hoogen, K. Bramstedt, K.U. Eichmann, M. Eisinger, D. Perner (1999) The Global ozone monitoring experiment (GOME): Mission concept and first scientific results. *J. Atmos. Sci.*, **56**, 151-175
24. Munro, R., R. Siddans, W. J. Reburn, B. J. Kerridge, 1998: Direct measurement of tropospheric ozone distributions from space, *Nature*, **392**, 168-171
25. Fishman, J., C.E. Watson,, J.C. Larsen, J.A. Logan (1990) Distribution of tropospheric ozone determined from satellite data, *J. Geophys. Res.*, **95**, 3599-3617
26. Fishman, J., V.G. Brackett, E.V. Browell, W.B. Grant (1996) Tropospheric ozone derived from TOMS/SBUV measurements during TRACE A, *J. Geophys. Res.*, **101**, 24069-24082

SCIAMACHY INSTRUMENT CONCEPT

A.P.H. Goede
Space Research Organization Netherlands (SRON), Sorbonnelaan 2, 3584 CA Utrecht, the Netherlands
e-mail A.Goede@sron.nl

ABSTRACT

The SCIAMACHY instrument concept is that of a broadband UV-visible-Near Infrared spectrometer at medium spectral resolution designed for atmospheric tracegas studies. This paper focuses on the enhancements of SCIAMACHY in comparison with GOME, presently in operation on the ESA ERS-2 satellite. These enhancements include the limb-viewing mode for atmospheric profile studies and the extension of the spectral range into the near-infrared for greenhouse gas/climate and dynamic transport studies. From an instrument development point of view, the novel near-infrared InGaAs detectors and read-out multiplexers form the most challenging part. Figures are presented on the performance of these detectors and the instrument as a whole.

1. INTRODUCTION

SCIAMACHY (Scanning Imaging Absorption Spectrometer for Atmospheric Cartography) is an advanced UV-vis-NIR spectrometer covering a wide spectral range (240 nm to 2380 nm) at moderate spectral resolution (0.2 to 1.4 nm), which allows for the measurement of a large number of atmospheric tracegases, including those relevant for ozone chemistry and greenhouse radiation studies (Ref.1 and J.P. Burrows, this conference). SCIAMACHY will form part of the atmospheric chemistry instrument complement on the ESA ENVISAT scheduled for launch in the second half of the year 2000. It is an Announcement of Opportunity instrument provided to ESA by the national space agencies DLR (Germany), NIVR (the Netherlands) and BUSOC (Belgium). Delivery is due in April 1999.

SCIAMACHY will observe the Earth atmosphere in alternate (forward) limb and nadir view sampling the same air volume with a spatial resolution of approximately 3 km in the vertical direction and typically 30x60 km^2 to 30x240 km^2 in the horizontal direction. At this spatial resolution the entire globe is mapped in 3 to 6 days periods. In addition to the nadir and limb observation modes the instrument can observe the sun and the moon for occultation and calibration measurements.

The SCIAMACHY instrument system is composed of the following sub-systems:
- the Optical Assembly containing scan mirrors, telescope, spectrometer and detectors, including polarisation detectors
- the Electronic Assembly containing the science data processing unit, the power, mechanism and thermal control unit, and the instrument control unit
- the Thermal Assembly containing the radiant reflector unit connected to the detectors via a (cryo-heatpipe) thermal bus unit, and a flat radiator unit for cooling of the spectrometer. Also decontamination heaters are available.

These sub-systems are mounted on three faces of the ENVISAT satellite, as is shown in Figure 1. The main instrument data are also given in Figure 1 (courtesy DLR, Cologne, 1998, Ref.2).

In this paper I shall concentrate on the Optical Assembly, in particular the enhancements of SCIAMACHY with respect to GOME, presently in operation on the ESA ERS-2 satellite (launched 1995). These enhancements include the limb viewing mode. In combination with the nadir mode this mode enables SCIAMACHY to retrieve global vertical profiles of tracegases and aerosols as well as total column values. GOME has already demonstrated the capability to probe the troposphere. SCIAMACHY will extend this capability by discriminating between lower stratosphere and upper troposphere. Under cloudfree conditions SCIAMACHY will be able to detect tropospheric constituents down to the planetary boundary layer. It will be the only atmospheric chemistry instrument on ENVISAT to do so.

A second enhancement on GOME is the extension of the spectral range into the near infra-red, which contains the spectral signatures of the greenhouse gases CO_2 (CO), N_2O, CH_4 and H_2O. From an instrument development point of view these near infrared (NIR) detectors form the most challenging part of the SCIAMACHY instrument. The detectors are based on novel (extended wavelength) InGaAs technology which in combination with a novel multiplexer read-out system achieves low noise at relatively high operating temperature of 150 K. For the first time InGaAs detector arrays have become space qualified.

2. OPTICAL UNIT

The optical concept is shown in Figure 2. Light from the atmosphere passes the limb and nadir viewing scan mirrors to be collected by an off-axis parabolic telescope and projected into the entrance slit of the spectrometer. This spectrometer is based on predispersion by a prism and subsequent splitting of the lightbeam into 8 spectral channels for final dispersion by individual gratings. This concept allows light dispersion over a wide spectral range with no overlapping orders and with low straylight level, important to cover the large dynamic range of atmospheric light (Ref.3). A compact and modular design was established by stacking the individual channels in two layers with all detectors located at one side of the instrument. The generic design of individual channels consists of optical beam folding and collimation onto a reflecting grating (or echelle for the NIR) and a Petzval type imaging on the detectors. The focal plane in which the detectors are placed is slightly tilted with respect to the optical axis so as to avoid the need for chromatic correction in the imaging objective. Integrated with the housing of the NIR detectors a close coupled cylindrical lens is placed in order to lower the f-number. With the instantaneous field of view (IFOV) and the detector pixel geometry fixed, the optical throughput of the instrument is determined by this f-number. For the UV and visible channels the f# ranges between 2 and 3. For the NIR channels it is nearing 1 in the cross-dispersion direction.

Because light from the atmosphere, in general, is polarised additional information is gained by measuring the polarisation state. This is accomplished by tapping linear p-polarised (parallel

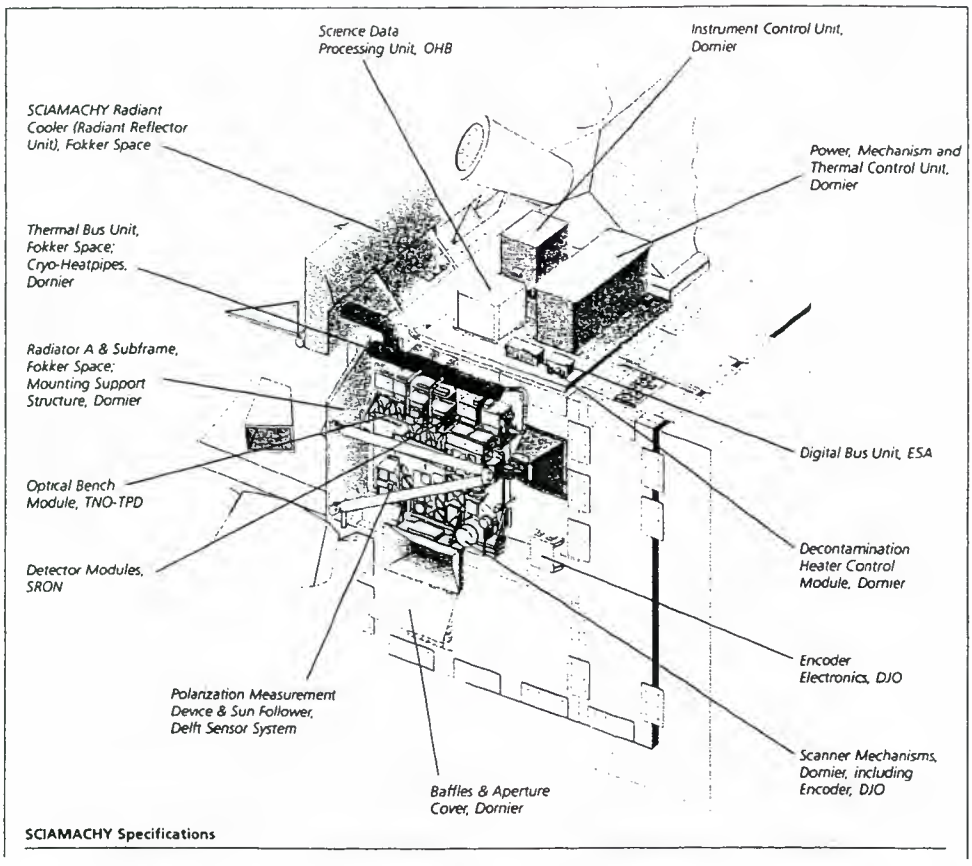

Fig. 1 SCIAMACHY system and main instrument parameters

Instantaneous FOV:	
Nadir measurements	0.045° orthogonal to flight direction 1.8° aligned in flight direction
Limb measurements	0.045° elevation x 1.8° azimuth
Sun measurements	0.045° elevation x 0.72° azimuth
Weight	215 kg
Power consumption	155 W
Data rate	0.4 Mbps Nadir/Limb, 1.9 Mbps Solar Occultation
Mission lifetime	about 5 years

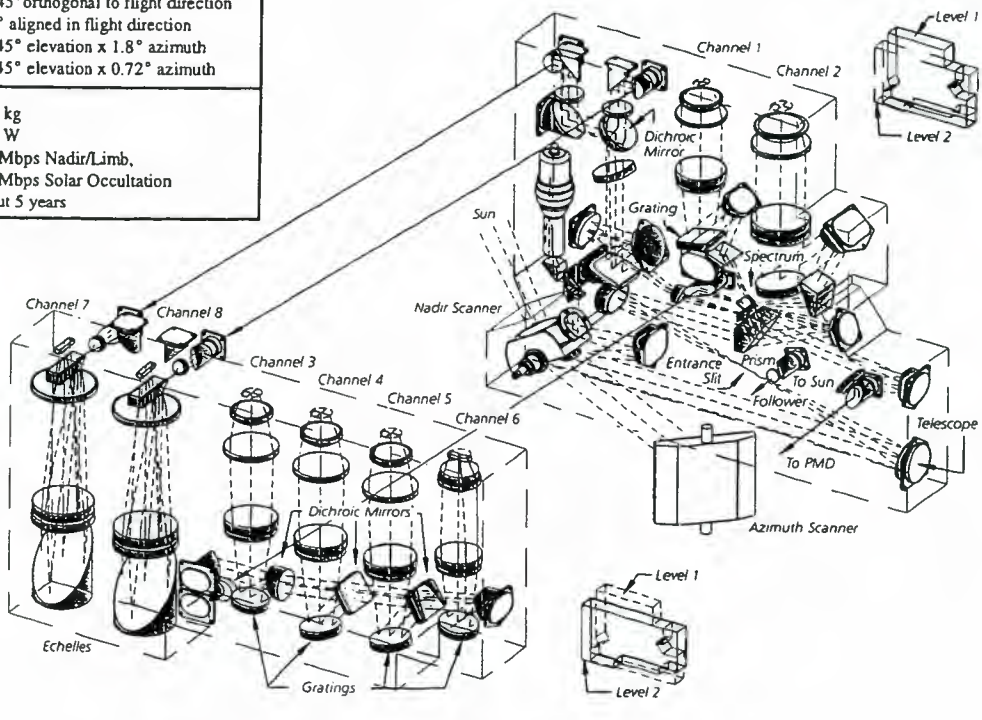

Fig. 2 SCIAMACHY Optical Configuration. Following the light path from the entrance azimuth and nadir scan mirrors, the light is collected by a telescope and projected on the entrance slit of the spectrometer. The light is first dispersed by a prism, after which light is tapped by the PMD and individual channels for final dispersion. At level 1 the individual channel optics of channel 1 and 2 are housed containing grating, imaging optics and detectors. At level 2 the channel optics and detectors of channels 3 to 8 are grouped, optically separated by dichroic mirrors.

to the entrance slit) light from the pre-dispersed prism under the Brewster angle which suppresses the s-polarised light. This p-polarised light is subsequently dispersed into 6 broadband channels corresponding to spectral channels 2 to 8. Thus information on the first two polarisation Stokes parameters can be obtained. The third Stokes parameter is measured by a 45° polarisation detector. This is necessary because of the fact that the limb-scan mirror is out-of-plane with the optical bench which leads to polarisation mixing of incoming polarised light. The fourth circular polarisation Stokes vector is not measured. Atmospheric light is not assumed to be circularly polarised. Additional information on the polarisation state is obtained at the channel overlap regions with different polarisation sensitivity in adjacent channels. Measurements with the GOME breadboard model from the ground have revealed a distinct fine-structure in the polarisation spectrum of the zenith sky light (Ref.4). This fine structure cannot be detected by SCIAMACHY (nor GOME) and has to be corrected for by appropriate modelling. Ongoing research at the Ring effect near the Fraunhofer lines (400 nm) and aerosol scattering near the oxygen band (770 nm) could explain this polarisation structure (see Helderman, this conference).

On-board calibration is established via the nadir scanmirror positioned at the entrance of the instrument, oriented such as to view either the on-board spectral line source (Pt/Cr hollow cathode Ne-discharge), the white light source (UV enhanced quartz tungsten halogen lamp), or the sun via the diffuser plate (Al), fixed at the back of the scanmirror. Further details are given in chapter 4.

In addition to the 8 high-resolution spectral channels, and the 7 broadband polarisation channels, a sun/moon following quadrant Si-detector is mounted next to the spectrometer slit. This detector is used for pointing of the scan mirrors during occultation/calibration measurements. Relevant data on the field of view of the instrument and the spatial resolution for the various observation modes are given in Table 1.

3. DETECTORS

The spectrum produced by the double spectrometer is simultaneously recorded by the 8 detector modules. The channel definition of the detectors is given in Table 2. A detector module consists of a solid-state diode detector array of 1024 pixel elements, a support structure and frontend electronics. The salient part of the detector support structure is a stainless steel labyrinth consisting of three nested concentric cylinders (0.1 mm wall thickness) suspending a cold finger for cooling of the detector. This construction combines good thermal insulation, good mechanical stability and good electro-magnetic shielding. The electronics contain amplification, digitisation and data formatting. It also forms the interface with the Science Data Processing Unit. The type of detector employed is given in Table 2 along with their nominal operating temperatures.

For spectral channels 1 to 5 the space-qualified EG&G Reticon RL 1024 SR detector is employed (Ref.5). This device contains 1024 pixels of dimension 25*2500 μm^2. The light-sensitive material consists of p-type Si with n-type regions defining the pixels. Dark current is low for these devices and is further reduced by lowering the operating temperature to 200 K (Ch 1 and 2) and 235 K (Ch 3 to 5). Quantum efficiencies range from 35% at 240 nm up to 85% at 700 nm, dropping to zero above 1050 nm. The cut-off wavelength shifts to shorter wavelengths upon cooling. The linearity is measured to be in the order of 99.8% or better. The noise in these devices is determined by reset or "kTC" noise. The noise-reduction technique of Correlated Double Sampling (CDS) is employed to eliminate the kTC noise of the video line. The kTC noise of the detector-diode capacitor, however, remains. This CDS feature is not present on GOME.

The individual pixels of the RL 1024 SR can be randomly accessed, making it possible to create "virtual channels", i.e., the possibility to have different integration times for two parts of the array. This feature is employed in channels 1 and 2, where there is a large dynamic range of the atmospheric signal.

A further difference with the Reticon detectors employed for GOME is the faster multiplexer (MUX) read-out time of the detector pixels in 29 msec instead of 97 msec total. This is an improvement which reduces the error introduced by the registration mismatch of different wavelengths observing a different ground pixel during detector read-out while the scan mirror and satellite move to a different position, the so-called spectral aliasing effect.

For channels 6 to 8 the novel InGaAs composite material is used to record the spectrum above 1000 nm where the electronic bandgap of silicon (~1.1 eV) becomes too large to detect the lower energy photons corresponding to 0.5 eV at 2400 nm. The composition of InGaAs can be tuned to match the wavelength response. Detectors using this material have been custom built for SCIAMACHY by Epitaxx Inc., NJ, USA under technical direction of SRON (Ref .5).

The InGaAs material is epitaxially grown on an InP substrate. The main difficulty of $In_xGa_{1-x}As$ lies in the fact that with changing composition for wavelength tuning, also the lattice constant changes which then does not match with the lattice constant of the InP substrate. For channel 6 ($In_{.53}Ga_{.47}As$) a perfect match with the InP substrate exists. It yields the best detector performance in terms of dark current and responsivity. However, at longer wavelength, higher In content is required, which results in lattice mismatch. This causes dislocations which are a source for dark current noise.The practical approach here is to grow the required InGaAs on the InP substrate in such a way that the minimum amount of lattice dislocations are generated. This is achieved by growing intermediate layers of InAsP. This material has a larger bandgap and therefore produces less thermally-activated electron-hole pairs. It has been found experimentally that the best detector performance is obtained if the lattice adjustment by InAsP is performed with discrete stepped layers, with sharp interfaces between the layers. In this case, the lattice dislocations are bent into the plane of growth, rather than extending into the active layer (Refs. 6-8).

On top of the stepped layers the active layer of InGaAs is grown, with the required Indium contents. This is covered by a layer of InAsP equal to the last graded layer for balancing lateral stress. A SiN coating caps the device, which also acts as an anti-reflection coating. Individual pixels are created by Zn diffusion. One detector array consists of 1024 pixels of dimension 500 * 13 μm^2, on a 25 μm grid spacing. The height of the pixels is smaller than that for the Si detectors. A cylindrical lens close-coupled to the detectors compresses the light and adapts for the smaller pixel height. This geometry results in lower dark current at

higher radiance, i.e. better S/N.

The impact of dark current on detector performance is twofold: Firstly, during measurement the full well capacity of the diode is filled with dark signal, reducing the dynamic range. Secondly, dark current increases the noise of the system (shot noise). Both effects can be reduced by reducing detector temperature, bias voltage and integration time.

Operation of the InGaAs detectors at near-zero bias voltage required the development of a custom built charge integrator/multiplexer (MUX) for the SCIAMACHY programme. The features of this MUX are:

- Capacitive Trans Impedance Amplifier (CTIA) for every pixel (2 sets, interleaved at both sides of the array)
- Simultaneous read-out of all pixels (same ground pixel observed at all wavelengths).
- Low noise (Correlated Double Sampling)
- High linearity (≥ 99.9 %)
- Built-in address generators
- Two-directional read-out (count up and count down)
- Integration times from 31.25 ms up to 10 minutes
- Short integration times ($28\mu s < t_{int} < 32$ ms), the so-called hot mode

The detector/multiplexer packaging is shown in Figure 3.

For the most demanding InGaAs detector of channel 8, sensitive to 2400 nm, dark current levels have been achieved as low as 20-100 fA per detector pixel area A of $1.25 \cdot 10^{-4}$ cm^2 (R A=2.5-12.5 MΩ·cm^2) at an operating temperature of 150 K and a bias voltage of 2 mV. Lower temperatures further reduce the dark current, but also decrease the quantum efficiency at long wavelengths, yielding no net gain in performance. Per degree K cooling the cut-off wavelength shifts approx 2 nm to shorter wavelengths. During operation the bias voltage setpoint can be adjusted individually to near-zero values to lower dark current values.

In order to understand and optimise the performance of the InGaAs detectors measurements of dark current and noise have been made as a function of temperature and bias voltage. A theoretical model was developed to explain these measurements (Ref.9). Dark (or leakage) current is the result of thermally generated electron-hole pairs in the solid-state diode in the absence of illumination and is inversely dependent on temperature through the Boltzmann factor exp ($-E_{gap}/2kT$), where E_{gap} is the electronic bandgap energy [eV]. Four components can be identified: interface current, diffusion current, generation-recombination current and tunneling current. From the voltage and temperature dependence these components could be separated out. Results for channel 8 for a typical "good" pixel are shown in Figure 4. It shows that lowering the temperature below 140 K does not further reduce the dark current very much because the tunneling component with weak temperature dependence takes over from the recombination-generation current. The diffusion current component is negligible at these temperatures, whilst the interface current produces a constant offset, independent of bias voltage. Results of a typical "bad" pixel are also shown. The temperature/voltage behaviour suggests tunneling current to be the cause for large dark current. It is proposed that large dislocations in the active layer cause distorted diffusion of p+ doping producing a higher tunneling current. It was concluded (Ref.9) that doping levels should be made high, such as to reduce depletion width (and hence generation/recombination current), but not as high as to cause tunneling to become dominant (at reduced depletion width). The optimum doping concentration was found to be just under 10^{17} cm^{-3}.

Similar to dark current, the Planck black-body radiation of the instrument at room temperature proved to be a significant source of dark signal and noise for channel 8 (Ref.10). The instrument therefore is cooled to approximately -20°C. Small variations in this temperature produce a noise over the integration time, in particular over the sunlit part of the orbit. This is overcome by active thermal control of the optical unit to within 0.25 K. The temperature variation of the NIR detectors themselves is also controlled in order to reduce dark current noise. The thermal stability of the NIR detectors is within a few times 10^{-2} K at 150 K during integration and over an orbit.

The detector noise consists of the following contributions: electronic noise, Johnson noise and shot-noise contributions of the signal, the dark current and the thermal background radiation. Since the detector is operated at a low bias voltage the noise can be described in terms of detector resistance. The noise can be calculated using the expression for the Johnson noise:

$$i_J = \sqrt{(4kTB/R)} \text{ , or } n_J = q^{-1}\sqrt{(2kTt_{int} / R)}$$

where, i_J is the Johnson noise expressed as a noise current, k is Boltzmann's constant, T the detector temperature in Kelvin, B the electrical bandwidth, and R the detector resistance. For charge-integrating read-out electronics, the noise expressed in electrons per read-out becomes $n_J = q^{-1}\sqrt{(2kTt_{int}/R)}$, where t_{int} is the integration time and q the charge of an electron. In addition to Johnson noise the most important electronic noise sources are the preamplifier noise, ADC noise, power-supply noise and the thermal noise of the reset amplifier and the sample circuit. The results of calculations are shown in Table 3a and 3b. These are compared with measured values in Table 4. Improvements are possible on the power supply rejection ratio applying better shielding and filtering. Agreement between theory and measurement is good. Further details can be found in Ref.9.

4. CALIBRATION

Calibration accuracy is at the basis of the quality of the SCIAMACHY data products. This refers not only to photometric and spectral calibration which are both essential for the identification and quantification of the concentration distributions of the target tracegases. It also refers to instrument characteristics such as signal to noise ratio (S/N), instrument line shape (ILS) as well as the field of view (FOV) and the pointing accuracy of the instrument. The SCIAMACHY instrument contains a large number of diffraction gratings, reflecting surfaces and a prism that introduce a polarisation of the incoming light. Since the incoming light is polarised by itself through atmospheric processes, the instrument response not only depends on the magnitude but also on the polarisation state of the signal to be measured. In order to correct for the polarisation sensitivity, SCIAMACHY has been equipped with detectors that can determine the (linear) polarisation state of the light beam entering the instrument.

In order to achieve good calibration accuracy several, partly complementary, calibration modes are available on SCIAMACHY:

Table 1 Spatial resolution and spatial coverage of SCIAMACHY observation modes

		Geometrical FOV	Coverage (scan mirrors)	Typ. spatial resolution
Nadir	along track	25 km	continuous	30 km
	across track	0.6 km	960 km	30 to 240 km
Limb	azimuth	110 km	960 km	240 km
	elevation	2.5 km	0-150 km	3 km vert
Solar Occultation	azimuth	40 km	NA	30 km (tangent point)
	elevation	2.5 km	0-150 km	2.5 km vert

Table 2 SCIAMACHY Channel definition, resolution, light-sensing material and nominal detector temperature

Ch. #	Wavelength [nm]	Resolution [nm]	Light-sensing material	T_{det} [K]
1	240 - 314	0.24	Silicon	200
2	309 - 405	0.26	Silicon	200
3	394 - 620	0.44	Silicon	235
4	604 - 805	0.48	Silicon	235
5	785 - 1050	0.54	Silicon	235
6/6+	1000 - 1750	1.48	$In_{53}Ga_{47}As$+$In_{60}Ga_{40}As$	200
7	1940 - 2040	0.22	$In_{81}Ga_{19}As$	150
8	2265 - 2380	0.26	$In_{83}Ga_{17}As$	150
PMD #	**Spectral range [nm]**	**Resolution [nm]**	**Light-sensing material**	**T_{det} [K]**
1	310-377	broadband	Silicon	253
2	450-525	broadband	Silicon	253
3	617-705	broadband	Silicon	253
4	805-900	broadband	Silicon	253
5	1508-1645	broadband	$In_{53}Ga_{47}As$	253
6	2265-2380	broadband	$In_{83}Ga_{17}As$	253
45 deg	802-905	broadband	Silicon	253

Table 3a Calculated electronic noise (electron rms) at 31.25 ms integration time

	ch 6/6+	ch 7/8
Electronic thermal noise	341	118
Preamplifier noise	79	203
ADC noise	269	90
Power-supply noise	1300	435
Electronic noise	1373	502

Table 3b Diode noise (electron rms) for a reverse bias voltage of 2 mV and an integration time of 31.25 ms. Note the significant contribution of thermal background noise in channel 8

Channel	6 @ 200K	7 @ 150K	8 @ 150K
Johnson diode noise	-	301	355
Thermal back. noise	11	44	198
Dark current noise	1	84	99

Table 4 Total noise (electron rms) of the SCIAMACHY NIR channels (integration time 31.25 ms)

Channel	Modeled value	Measured value
6	1373	1132
6+	1404	1488
7	593	636
8	653	668

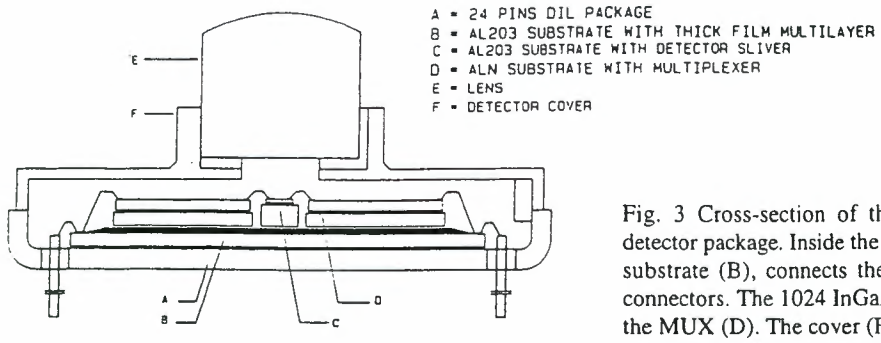

Fig. 3 Cross-section of the SCIAMACHY Channel 6 to 8 detector package. Inside the Invar housing (A) a SiO_2 thick film substrate (B), connects the MUX (D) to the 24-pins outside connectors. The 1024 InGaAs detectors (C) are wire-bonded to the MUX (D). The cover (F) contains a lens (E) for f-matching the detector pixel size.

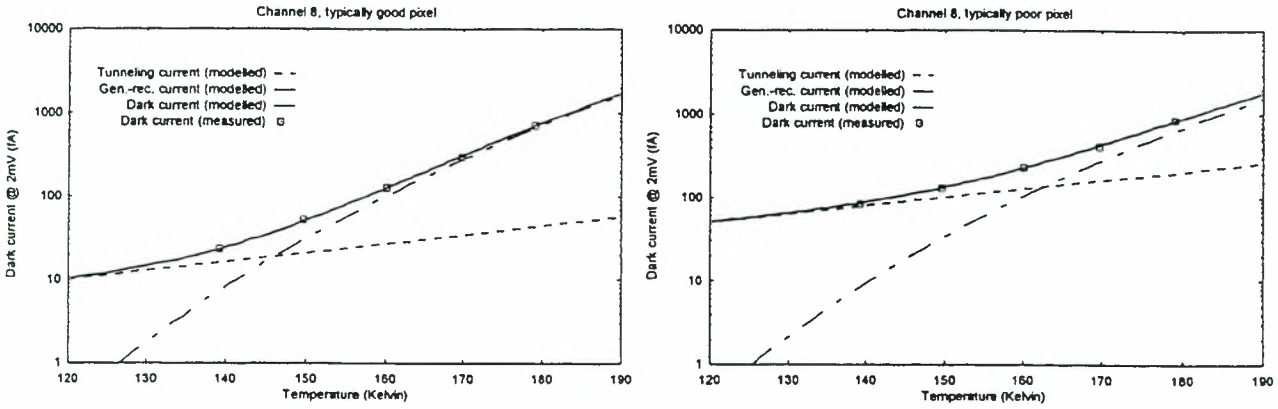

Fig. 4 Modelled and measured dark current components as function of temperature for a typical good pixel of channel 8 (left) and a typical poor pixel (right). Below 140 K the tunneling current takes over, yielding relatively little reduction in dark current by lowering the temperature.

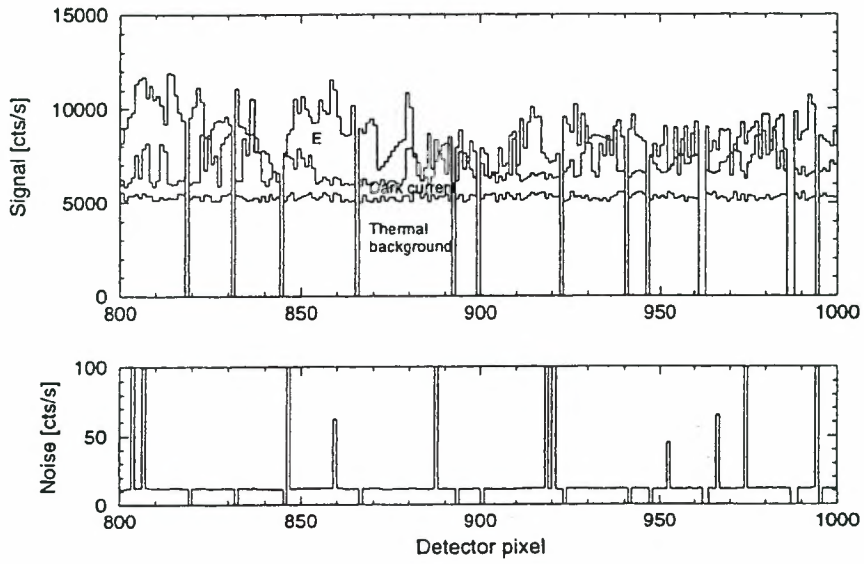

Fig. 5 Simulated detector signal (upper panel) and noise (lower panel) for the nominal instrument in nadir observation for northern hemisphere summer, albedo 30%, solar zenith angle 33°5. In the upper panel the main contributions to the signal (instrumental thermal background, detector dark current, and earthshine spectrum) are indicated separately and in a cumulative fashion. The lower panel shows the noise level and the effects of dead pixels, noisy pixels, and pixel-to-pixel variation of both detector dark current and sensitivity to thermal background. Pixel integration time is 1 sec. For clarity, only a part of the detector (corresponding to 2359-2382 nm) is shown. In this region, absorption lines from CH_4 and CO reside.

- sun via on-board diffuser (for normalisation of earthshine spectra)
- direct sun viewing in different geomeries (for in-flight characterisation and monitoring)
- lunar radiance (for radiance measurements using the same optical path as earthshine)
- white light source (for pixel to pixel gain and etalon correction)
- spectral light source (for spectral calibration)

Spectral calibration can be improved by analysing solar Fraunhofer lines.

The enhancement on GOME calibration is the availability of a white lamp on SCIAMACHY for correction of the etalon effect, i.e. thin interference layers of ice forming on the detector and optical surfaces that are not stable in time. In-flight calibration data combined with on-ground calibration and characterisation data will be used to derive instrument calibration data that will determine data quality. Characterisation data include data such as detector noise, dark current, etalon, polarisation, straylight, vignetting, under-/oversampling, ageing, etc. For more details see Ref. 16. Calibration accuracies achieved are in the order of 3% to 4% (absolute) for photometric calibration and 1/50 of a detector pixel for spectral calibration. Typically two detector pixel elements are used to characterise the spectral line width (resolution) of the instrument (Nyquist criterion).

Unlike GOME on-ground calibration and characterisation of SCIAMACHY has been performed under thermal-vacuum conditions representative for space operation. GOME has displayed various calibration artefacts related to the fact that the on-ground calibration of the instrument was done in air under ambient temperature conditions. In-flight the following air-vacuum effects became apparent:

- outgassing (spectral shift of dichroic mirror, change in polarisation response) and gas desorption from optical surfaces
- ice layer formation on cold detector surface (etalon) from water vapour desorbed from instrument surfaces.

Air-vacuum effects are expected to play a less significant role in SCIAMACHY. At an early date it was recognised that calibration under operational vacuum conditions was mandatory, which has led to the procurement of the OPTEC thermal-vacuum calibration facility. The instrument employs vacuum compatible materials and optical coatings, the construction of the detectors is consistent with operation under vacuum conditions and the instrument is temperature stabilised.

5. PERFORMANCE CALCULATIONS

Signal to noise calculations and sensitivity studies for the detection of tracegases have been carried out using the SRON developed SCIAMACHY Instrument System Simulator SISS (Ref. 11-14). The computation comprises two parts:

- geophysical tracegas target and an atmospheric forward model for the calculation of the input signal to the instrument
- an instrument model (SISS), calculating signal and noise output at the detectors.

Signal to noise values have been calculated for all detector channels, and are generally above 1000. Exceptions are channels 1, 7 and 8. These calculations have been used for instrument design and feedback to instrument development, to optimise the instrument settings and to develop mission scenarios. Recently, the SISS is also employed to test the SCIAMACHY data processing software.

Channel 8 of SCIAMACHY, the most critical channel to develop also contains some of the most interesting science, as it will be measuring global concentration distributions of methane, carbon monoxide, nitrous oxide and water vapour. Results of signal to noise calculations for this channel are shown in Figure 5. For the computations a nominal instrument with a detector dark current level of 30 fA, an instrument thermal background resulting in a detector background signal of 150 fA, and a spectral resolution of 0.24 nm have been assumed. These values correspond to a detector temperature (for infrared channels 7 and 8) of 150 K and a spectrometer optical unit temperature of 253K.

The sensitivity expected for SCIAMACHY nadir observations of CO is in the order of 10%, better in the Northern hemisphere at polluted regions. For CH_4 the sensitivity is better than 1%. N_2O sensitivity is in between. For detailed results of the detection sensitivities of CO, CH_4 and N_2O, see Schrijver (this conference).

6. OBSERVATION MODES AND SPATIAL RESOLUTION

The observation modes of the atmosphere available on SCIAMACHY are: nadir, limb and solar/lunar occultation. Spatial coverage and resolution are given in Table 1. The spatial resolution is determined by S/N values (integration times) and by data rate limitations of ENVISAT. Spectral channel detectors are read out every 31.25 msec (1/32 sec) and this signal is stored in a RAM memory in units of 62.5 msec (1/16 sec). For a nominal measurement integration time of 1 sec, the 16 measurements are co-added on-board before downlinking, resulting in a typical spatial resolution in nadir of 240 km across-track. Better spatial resolution can be obtained by selecting a limited spectral window, so-called clusters, that are read out and processed on-board with less co-adding. In this way 8 cluster readings per second can be downlinked, resulting in a minimum 30 km across-track resolution. This cluster read-out mode is applied for relatively high S/N constituents such as O_3, NO_2, H_2O, aerosol and clouds. Spatial resolution is higher for the PMD detectors because the signal of these detectors is sampled at 40 Hz (25 msec) resulting in 6x30 km ground pixel size resolution. Detector module and PMD signals are not synchronised by a master-clock: Both signals are downlinked, time stamped and co-located by the on-ground dataprocessor with 1 msec relative and 10 msec absolute datation accuracy (for details see Slijkhuis, this conference).

A typical operation sequence of SCIAMACHY, emerging from the eclipse side of the Earth, begins with a limb measurement of the twilight atmosphere, followed by a solar occultation measurement over the North pole and a solar calibration measurement. Solar occultation measurements cover the 65°N to 90°N latitudes. Subsequently, an alternate limb-nadir sequence is started, observing the same air volume first in limb and approx. 7 minutes later in nadir. A detailed mission scenario has been developed (Ref.15) in which integration times and scan mirror movements have been synchronised to achieve an optimum in S/N and spatial resolution/coverage. Global coverage is obtained in 3 to 6 days, depending on latitude and data processing schemes. The observation sequence is supplemented by a moon occultation and calibration measurement. Compared with GOME moon observations are available more frequently, 5 to 8 days per month as compared with a few times a year for GOME. The latitudinal coverage is 30°S to 90°S. The moon calibration mode has proved useful for

GOME. The observation sequence is closed by further limb/nadir measurements. For further details see Ref. 17 and Bovensmann (this conference).

For solar calibration three scan strategies are available: step-wise scanning of the solar disc, co-added several times (similar to SAGE II), stare-mode pointing at one spot of the solar disc (similar to HALOE), and a fast sweep over the solar disc with continuous (125 ms) exposure. Aspects of pointing/ attitude stability of the instrument/platform, the occurrence of sun spots, and solar movement during scan determine the calibration accuracy. The fast sweep mode is the baseline solar calibration mode selected.

All measurements, except lunar observation, are carried out every orbit, i.e. 14 orbits per day. On the eclipse side calibration measurements are performed, including dark current measurements. Spectral lamp and white lamp measurements are performed during eclipse on a weekly to monthly basis. Instrument degradation is monitored both for the spectral channels as well as the polarisation channels, similar to GOME (see Tanzi, this conference).

7. CONCLUSIONS

GOME has demonstrated the capability of acquiring global information on total column amounts of ozone, NO_2, SO_2, BrO, OClO, HCHO, and information on aerosol and clouds. Also, it has proved possible to retrieve height profile information on ozone, BrO and SO_2 to a limited extent. SCIAMACHY will significantly enhance the GOME vertical information through the availability of the limb observation mode. It will extend the range of atmospheric trace constituents with global measurements of CO, CO_2, N_2O, CH_4 and H_2O. This is made possible by the development of InGaAs detectors extending the GOME spectral range to the near infrared.

ACKNOWLEDGEMENTS

SCIAMACHY is a joint national contribution to the ESA ENVISAT mission funded by the German (DLR) and Dutch (NIVR) space agencies, including a Belgian (BUSOC) contribution. The SCIAMACHY industrial consortium comprises the prime contractors Dornier Satellite Systems (D) and Fokker Space (NL), and the subcontractors OHB-Systems (D), Jenoptik (D), SRON (NL), TPD-TNO (NL), OIP (B) and Epitaxx (USA). The instrument and algorithm development is supported by the activities of the SCIAMACHY Science Advisory Group (SSAG), a team of scientists from various international institutions: University of Bremen (D), SRON (NL), SAO (USA), IASB (B), MPI Chemistry Mainz (D), KNMI (NL), University of Heidelberg (D), IMGA (I), CNRS-LPMA (F). Operational data processing will be performed by DLR-DFD within the Envisat ground segment D-PAC. The author would like to thank J.P. Burrows, H. Bovensmann, J. Frerick, I. Aben, R. Hoogeveen, R. van der A, R. Snel and H. Schrijver for providing input to this paper.

REFERENCES

1. J.P. Burrows, K.V. Chance, P.J. Crutzen, H. van Dop, J.C. Geary, T.J. Johnson, G.W. Harris, I.S.A. Isaksen, G.K. Moortgat, C. Muller, D. Perner, U. Platt, J.-P. Pommereau, H. Rodhe, E. Roeckner, W. Schneider, P. Simon, H. Sundqvist and J. Verchéval, "SCIAMACHY - A European proposal for atmospheric remote sensing from the ESA Polar Platform, published by Max-Planck Institut für Chemie, 55122 Mainz, Germany, 1988.

2. J.P. Burrows, E. Hölzle, A.P.H. Goede, H. Visser, W. Fricke, "SCIAMACHY - Scanning Imaging Absorption Spectrometer for Atmospheric Chartography", *Acta Astronautica* 35, pp. 445-451, 1995.

3. C.Smorenburg, H. Visser,"The SCIAMACHY optical system" *Proc. Int. Symp. Optical System Design*, pp. 1780-1851, Berlin, 1992.

4. Aben, I., Helderman, F., Stam, D.M. and Stammes, P., Spectral fine-structure in the polarisation of skylight, Accepted for publication in *Geophysical Research Letters* (1999).

5. R.W.M. Hoogeveen, H. Spruijt, B. Broers, A. Selig, "Near-infrared focal-plane arrays for SCIAMACHY, Advanced and next-generation satellites", Proc. Europto, Ed. H.Fujisada, M.Sweeting, vol.2583, pp 459-470, *SPIE/EOS*, Paris, 1995.

6. K.R. Linga, G.H. Olsen, V.S. Ban, A.M. Joshi, W.F. Kosonocky, "Dark current analysis and characterization of InGaAs/InAsP graded photodiodes with x > 0.53 for response to longer wavelengths (> 1.7 μm)", *J. of Light Wave Techn.* Vol. 10, No 8, Aug. 1992.

7. K.R. Linga, V.S. Ban, A.M. Joshi and S. Mason, "1024 element linear InGaAs/InAsP detector arrays for environmental sensing from 1μm to 2.6μm", *SPIE Proc.*, Vol. 2021, July 1993.

8. K.R. Linga, C.S. Wang, Y. Dzialowsky, M. Louri and S. Mason, "High performance 1024 element InGaAs hybrid focal plane arrays from 1 to 2.6μm", Presented at Opto-94 Conf, Paris April 28, 1994.

9. A, R.J. van der, Hoogeveen, R.W.M., Spruijt, H.J., Goede, A.P.H., Low noise InGaAs infrared (1.0-2.4 um) focal plane arrays for SCIAMACHY, Advanced and Next-Generation Satellites II, H. Fujisada, G. Calamai, M.N. Sweeting, Eds., *Proc. SPIE* 2957, pp. 54-65, 1997.

10. A.P.H. Goede, P. de Groene, R.W.M. Hoogeveen, J. de Vries, R.J. van der A, C.Smorenburg, H.Visser, "SCIAMACHY Instrument Development for POEM-1" (presented at the 29th COSPAR conference, Washington, 1992), *Adv. Space Res.* 14 no.1, pp. 17-20, 1994.

11. A.P.H. Goede, R.W.M. Hoogeveen, S. Slijkhuis, R.J. van der A, and J. de Vries,"SCIAMACHY instrument performance and test" in Atmospheric Radiation, Knut Stamnes, Ed., Proc. *SPIE/EOS* Vol. 2049, pp. 174-182, Tromsö, 1993.

12. R.W.M. Hoogeveen, A.P.H. Goede, S. Slijkhuis, A. Selig, J.P. Burrows, "SCIAMACHY development", *Space Optics* 1994: Earth observation and Astronomy, *Proc. SPIE* 2209, pp. 78-85, 1994.

13. H. Schrijver, S. Slijkhuis, M.G.M. Roemer, and A.P.H. Goede, "Noise related limits on the detectability of concentration variations of CH_4 and CO with SCIAMACHY", in Atmospheric Sensing and Modeling, R.P. Santer, ed., *Proc. SPIE* 2311, pp. 39-46, 1995.

14. S. Slijkhuis, "SCIAMACHY/GOME instrument simulation software, detailed design, issue 2", Tech. Rep. SRON/SCIA/TR 9301, SRON, Utrecht, 1994.

15. SCIAMACHY Operations Concept. I Mission Scenarios - PO-TN-DLRSH-0001/1, issue 2 (May 96).

16. J. Frerick, H. Bovensmann, S. Noël, J.P. Burrows, M. Dobber,"SCIAMACHY on-ground/in-flight calibration, performance verification and monitoring concepts", *Proc. SPIE* 3117, 1997.

17. H. Bovensmann, J.P. Burrows, M. Buchwitz, J. Frerick, S. Noel, V.V. Rozanov, K.V. Chance, and A.P.H.Goede, "SCIAMACHY - Mission Objectives and Measurement Modes, *Journal of Atm. Sciences*, Vol. 56, No. 2, pp. 127-150, 1999.

SCIAMACHY INSTRUMENT CALIBRATION AND PERFORMANCE: FIRST RESULTS

Marcel Dobber, TNO Institute of Applied Physics (TNO-TPD), P.O. Box 155, 2600 AD Delft, The Netherlands. E-mail: dobber@tpd.tno.nl

1. Abstract

This document describes the state of calibration and performance of the SCIAMACHY instrument, to be launched on ENVISAT in 2000, after the main on-ground calibration and performance verification phases. A number of calibration and performance parameters will be discussed and results will be shown. The overall conclusion is that the SCIAMACHY calibration and performance are in very good shape with respect to the instrument requirements.

2. Introduction

The SCIAMACHY instrument, to be launched on ENVISAT in the year 2000, will measure atmospheric gases and aerosols in order to monitor climate processes and climate changes. In order to reach these high-level objectives the instrument has to comply to various calibration and performance requirements. The calibration and performance are the subject of this paper. The instrument bare optical bench is shown in figure 1 and the integrated instrument is shown in figure 2, including the thermal systems for cooling of the detectors (partly) and cooling of the optical bench. Following the light path the instrument consists of an Azimuth Scan Mirror (ASM), an Elevation Scan Mirror (ESM) with an on-board diffuser mounted on the backside, entrance telescope and entrance slit, and a predisperser prism, which performs the first coarse dispersion of the light for the various optical channels. After the predisperser prism the light is separated for the ultraviolet channels 1 and 2, the infrared channels 7 and 8, and the visible-infrared channels 3-6, which proceed to a second level of the optical bench. The visible and infrared channels are separated from each other by means of dichroic mirrors. All channels have dedicated imaging optics, a reflection grating for the final color dispersion and an array detector with 1024 pixels. The detectors for channels 1-5 are Si detectors, whereas the detectors of channels 6-8 are InGaAs detectors. The instrument corrects for the polarisation state of the incident light using a dedicated Polarisation Measurement Device (PMD). The first 6 PMD broadband detectors measure the polarisation component parallel to the entrance slit, while the 7th PMD broadband detector measures the polarisation component with a direction of 45 degrees with respect to the entrance slit. Further important optical components include a Neutral Density Filter (NDF), which can be inserted in channels 3-6 to reduce the light intensity by about a factor of 5, and a small aperture mechanism, which can be inserted for all channels to reduce the light intensity and adapt the instrument Instantaneous Field Of View (IFOV). The small aperture is used for direct sun observations.

The instrument radiometric calibration is based on the Stokes vector and Mueller matrix descriptions of polarised light. In short, a Stokes vector describes polarised light as follows:

$$\begin{pmatrix} I \\ Q \\ U \\ V \end{pmatrix} = \begin{pmatrix} \text{Intensity Unpolarised Light} \\ \text{Intensity } 0^o \text{ - Intensity } 90^o \\ \text{Intensity } +45^o \text{ - Intensity } -45^o \\ \text{Intensity Circular Polarisation} \end{pmatrix} \quad (1)$$

It is well known that the circular polarisation component appearing from atmospheric light can safely be taken as zero. Optical components are described to operate on these Stokes vectors as 4 by 4 Mueller matrices, for example for an aluminium mirror:

$$\begin{pmatrix} I' \\ Q' \\ U' \\ V' \end{pmatrix} = \begin{pmatrix} M_{11} & M_{12} & 0 & 0 \\ M_{12} & M_{11} & 0 & 0 \\ 0 & 0 & M_{33} & M_{34} \\ 0 & 0 & -M_{34} & M_{33} \end{pmatrix} \begin{pmatrix} I \\ Q \\ U \\ V \end{pmatrix} \quad (2)$$

In the SCIAMACHY limb mode the convenient structure of these matrices is broken by the orientation of the ASM with respect to the ESM. In order to describe this in the Mueller matrix formalism a rotation matrix has to be included, resulting in the following result:

$$M_{elevation} \otimes Rotation(\alpha) \otimes M_{azimuth} = \quad (3)$$

$$= \begin{pmatrix} M_{11} & M_{12} & M_{13} & 0 \\ M_{21} & M_{22} & M_{23} & M_{24} \\ M_{31} & M_{32} & M_{33} & M_{34} \\ 0 & M_{42} & M_{43} & M_{44} \end{pmatrix}$$

The light intensity measured by the detectors (array detectors and polarisation detectors) is in principle now described by:

$$I' = M_{11} * I + M_{12} * Q + M_{13} * U \quad (4)$$

depending on I, Q, and U. For the nadir mode it can be shown that only the Stokes parameters I and Q are important to radiometrically calibrate the instrument, when non-depolarising optics are assumed. For these reasons the 7th PMD detector, which measures the U-Stokes-component of the incident light, was introduced into the instrument design for the limb mode. The limb radiometric calibration and the calibration algorithms are much more complicated than for nadir because of this.

The instrument calibration described in short above and the instrument performance must be described and measured accurately in order to fulfil the instrument mission objectives. In this document a number of

calibration and performance parameters are descibed and measurement results are presented.

3. SCIAMACHY Calibration and Performance results

The calibration and performance verification approach of the SCIAMACHY instrument has been such that a number of important calibration and performance parameters, which are anticipated to change from air to vacuum conditions and at different temperature conditions, are measured under thermal-vacuum conditions. The thermal-vacuum measurements have all been performed in the so-called OPTEC thermal-vacuum chamber with accompanying optical stimuli (see figure 3) at Fokker Space in Schiphol-Oost, The Netherlands. In this facility the optical bench can be cooled down to its in-flight temperature of -17.9 degrees Celsius (this is also the temperature of the PMD detectors) and the array detectors can be cooled down to their operational temperatures (channels 7 and 8 are the coldest with temperatures of about 150 K). Since the final in-flight array detector temperatures are not yet known accurately, the relevant calibration parameters were calibrated at 2 detector temperature levels. Figure 4 shows this temperature dependence for the radiometric calibrations. The effect can be as large as 3% per Kelvin. Some calibration and performance parameters are expected to change from air-to-vacuum and at different temperatures as a result of optical component outgassing, prism dispersion changes, and changes in optical characteristics.

3.1 Calibration of scan mirrors and diffuser

The calibration of both scan mirrors, including the on-board diffuser was performed under ambient conditions at the calibration facility at TPD in Delft, The Netherlands, on unit level, i.e. the scan mirror modules were not integrated into the optical bench. This calibration included the polarisation-dependent radiometric calibration and the calibration of the angular dependence of both mirrors. Three operational modes were calibrated:

1) Nadir, only ESM
2) Limb, ASM plus ESM
3) Diffuser, ASM plus on-board diffuser

The diffuser mode is employed in flight to perform sun-over-diffuser measurements. The measurements are performed using either one or two polarisers to present polarised light to the mirrors ot to measure polarised light coming from the mirrors (or both). Five different polarisation directions are necessary to calibrate the instrument: unpolarised (u), s-polarised (s), p-polarised (p), +45-polarised (4), and -45-polarised (m). For example, a measurement with the first polariser in the s-polarised position and the second polariser in the +45-polarised direction is called s4. The required calibration keyparameters are:

nadir us,up,pp,p4
limb us,up,ss,pp,4s,4p,ms,mp,44,s4,p4,sp,ps
diffuser us,up

The geometry of the on-board diffuser is shown in figure 5. Some typical results of the scan mirror calibration are shown in figures 6 (nadir angular dependence as compared to theory [ASAP]), figure 7 (limb reflectance) and figure 8 (diffuser 'reflectance').

3.2 Thermal-vacuum calibration and performance

The absolute radiance calibrations for nadir and limb (figure 9) and the absolute irradiance calibration for the sun-over-diffuser mode (figure 10) were performed under thermal-vacuum conditions. In figure 9 the absolute radiance calibration for the GOME-1 instrument is depicted for comparison. The ND filter transmission characteristics are part of the radiometric calibration keydata. This is shown in figure 11.

The wavelength calibration, instrument slitfunctions, and spectral resolution are derived from measurements with spectral line sources. The instrument has its own internal spectral line source (SLS), the response of which is shown in figure 12. The results are:

Ch.	Spectral resolution (px)	Optimal slitfunction
1	2.0	simple hyperbolic
2	1.9	simple hyperbolic
3	2.0	simple hyperbolic
4	2.0	simple hyperbolic
5	2.0	simple hyperbolic
6	1.8	gaussian
7	4.0 / 2.1*	simple hyperbolic
8	3.5 / 2.1*	compound hyperbolic

Table 1: Spectral resolution and slitfunctions.
** indicates results from after refocussing of channels 7 and 8.*

The infrared channels 7 and 8 were refocussed at some stage to improve the spectral resolution. The simple and compound hyperbolic functions are functions of the type:

$$y = \frac{a^2}{b^2 + (x-c)^2} + \frac{d^2}{b^2 + (x-c)^4} \qquad (5)$$

The internal SLS optical beam is known to be partly blocked by the ESM housing, resulting in slightly narrower and shifted lines with respect to results obtained with external line sources. This effect, which is expected to be stable in flight, has been accurately calibrated and characterised.

The instrument is equipped with an internal Quartz Tungsten Halogen White Light Source (WLS). This lamp emits a spectrally smooth blackbody spectrum with a Planck temperature of about 3050 K. The lamp is used in flight to characterise the radiometric response of the instrument (the WLS has been observed to have a very good radiometric stability on ground), calibrate the pixel-to-pixel gain of the array detectors, which is particularly important for the infrared channels 6-8, and monitor the ND filter transmission characteristics. This is necessary due to the fact that the sun-over-diffuser measurements are performed with the NDF in place in order to avoid saturation in channels 3-5, whereas the nadir and limb measurements are performed without the NDF. For the sun-normalised radiance measurements these nadir and limb measurements are divided by the sun-over-diffuser measurements and therefore the NDF characteristics appear in this ratio. The internal WLS provides a means to monitor this in flight. The regular

WLS measurements are performed with the NDF, also to avoid saturation. However, at a slightly different ESM angle where the WLS measurements do not saturate with and without the NDF, the NDF transmission can be measured. The instrument internal WLS response is shown in figures 13 and 14.

The polarisation calibration consists of a part measured under thermal-vacuum conditions with the scan mirrors in their nominal nadir and limb positions and the ambient scan mirror and diffuser calibration described above. Two polarisation parameters are of direct interest for the calculation of the calibration keyparameters: η and ξ, defined as follows:

$$\eta = \frac{\text{array detector response to s - polarised light}}{\text{array detector response to p - polarised light}} \quad (6)$$

$$\xi = \frac{\text{polarisation detector response to p - pol. light}}{\text{array detector response to p - pol. light}} \quad (7)$$

The η parameter is measured with an external white light source and a Brewster polariser and the ξ parameter with a monochromator and a Brewster polariser, because the PMD detectors are broadband detectors and the ξ parameter needs to be measured at a fine wavelength grid. Both experimental setups are part of the dedicated and fully commissioned optical stimuli setup that pertains to the OPTEC setup. Both η and ξ parameters need to be corrected for setup artefacts. The η and ξ parameters can be combined with the angular-dependent scan mirror and diffuser calibration key parameters to yield a full set of all required calibration keyparameters. The results for the η and ξ calibration parameters are shown in figures 15 and 16, respectively. The spectral sensitivity curves of the polarisation detectors, shown in figures 17 and 18 (uncorrected for monochromator output), can cross over the spectral boundaries of the main optical channels, causing singularities in the ξ parameter. For this reason multiple ξ calibration parameters, made up of combinations with polarisation detector signals with various array detector channels over which the polarisation detector spectral responsivity curve extends, are calculated. The ξ calibration parameters are currently only delivered for the PMD high-gain electrical signals. The dotted line in figure 17 is the PMD #7 curve, which corresponds closely to the PMD #4 curve. The jump at 1650 nm is caused by a grating change of the monochromator.

A number of additional polarisation measurements have been performed during the thermal-vacuum calibration phase. These additional measurements are of interest for a better understanding of the calibration and performance parameters of the instrument, they are not strictly required for the calculation of the calibration keyparameters. Such additional parameters include: ζ in nadir, η and ζ in limb, and η and ζ for the sun-over-diffuser mode, with ζ being defined as:

$$\zeta = \frac{\text{array detector response to } -45\text{ - polarised light}}{\text{array detector response to } +45\text{ - polarised light}} \quad (8)$$

Furthermore, a number of Brewster scans have been performed. In this kind of measurement the polarisation direction is stepped from for example -90 degrees to +180 degrees in steps of 5 degrees and at each step the instrument response is measured. Figure 19 shows an example of such a measurement. In the figure the response of PMD's 6 and 7 are shown. It can be observed that the 6th PMD measures p-polarised light (at about 1.5 radians), whereas the 7th PMD measured +45-polarised light (at about 2.3 radians), in agreement with the instrument design.

Two remarks can be made about the PMD detectors. Firstly, PMD's 1 and 7 are known to measure electrical spikes with an amplitude of about 100-200 above the normal measurement level at a frequency of about once every 10 minutes. The origin of these spikes is currently unknown. In flight, one can look for the existence of such spikes in e.g. the dark signal measurements. Secondly, the PMD detectors suffered from electrical crosstalk in the past. One PMD channel readout could cause a disturbance signal in the next PMD detector of maximally 5-6%. This effect has recently been drastically reduced by a hardware modification, and the effect is now within acceptable limits.

The array detectors can in some cases feature an exhanced noise behaviour. An example of this effect is shown in figure 20. It can be seen that the pixels which are read out later than the pixels at which the strong signal is measured are affected by enhanced noise.

The spectral straylight is also calibrated and characterised under thermal-vacuum conditions. Because the spectral straylight can in principle be polarisation-dependent, measurements were defined with different input polarisations to verify this, but almost no polarisation dependence of the spectral straylight was found. Spectral straylight can be divided into spectral ghost straylight (localised on a few pixels) and uniform straylight (distributed over all pixels in a channel). No spectral ghosts were detected stronger than typically 0.05%. An intrachannel ghost in channel 8 was measured and calibrated when channel 7 is illuminated, its strength being typically 0.1%.

The Instantaneous Field Of View (IFOV) in cross-dispersion direction of all detectors was also measured under thermal-vacuum conditions for the large and the small apertures. The results are shown in figures 21-24. In figures 21 and 23 the measured signals are shown as a function of illumination angle within the IFOV in cross-dispersion direction for a number of pixels in various array detector channels. From such figures the 50% response points can be determined, indicated by the vertical bars in the figures, and the IFOV size and alignment in cross-dispersion direction can be measured for all pixels in the array detectors and for all PMD detectors. The latter results are shown in figures 22 and 24 (neglect the cases in figures 22 and 24 where the results are off-scale in the figures, this is due to measurement artefacts and not a result of instrument performance). The design requirements for the IFOV in cross dispersion direction are 1.80 degrees by 0.045 degrees for the large aperture and 0.72 degrees by 0.045 degrees for the small aperture. It can be seen from figures 22 and 24 that measured results are very close to these design requirements. Furthermore, it can be observed that all detectors are almost perfectly aligned with respect to each other. The results for the small

aperture show a classical diffraction pattern, which changes considerably with wavelength (figure 23). This small aperture is used for solar occultation and calibration measurements over both scan mirrors or over the elevation scan mirror alone (sub-solar mode). If the measurement conditions are always similar, this diffraction pattern causes no additional problems. In any case, the measurement information in order to fully characterise this diffraction pattern is available.
The IFOV in dispersion direction was verified under ambient conditions.
The signal attenuation ratio of the large aperture over the small aperture has been characterised. It is shown in figure 25.

4. Conclusions

A large number of SCIAMACHY instrument calibration and performance verification measurements have been acquired during the on-ground calibration and AIT phases. The first results of these measurements are described in this document and it was shown that for all calibration and performance verification measurements good quality results have been obtained. Furthermore, it was shown that the instrument calibration is in good shape. Further work is required to fit together the calibration keydata and the 0-1 dataprocessing and to test the quality of both in an integrated environment. It was also shown that the instrument performance is very good with respect to the instrument requirements.

6. Acknowledgements

The author wishes to thank for the support of the SCIAMACHY Joint Team (SJT) and of Dornier during the calibration and performance verification phases. In particular, the help of Carina van Eijk, Erik Zoutman, Maurice te Plate (all TNO-TPD), Trevor Watts and Aldert Kamp (both Fokker Space) and Rien van der Linden and Ralph Snel (both SRON) is acknowledged.

7. Figures

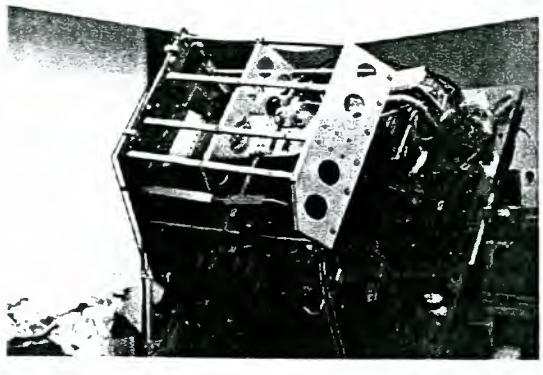

Figure 1: SCIAMACHY optical bench with integrated thermal equipment.

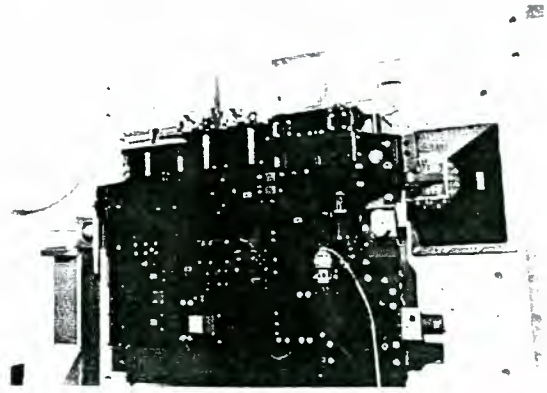

Figure 2: SCIAMACHY bare optical bench.

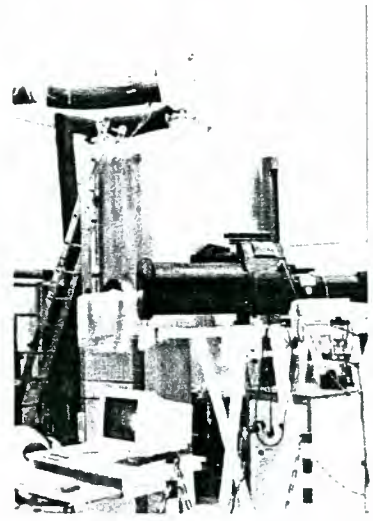

Figure 3: OPTEC thermal-vacuum calibration facility with dedicated optical stimuli.

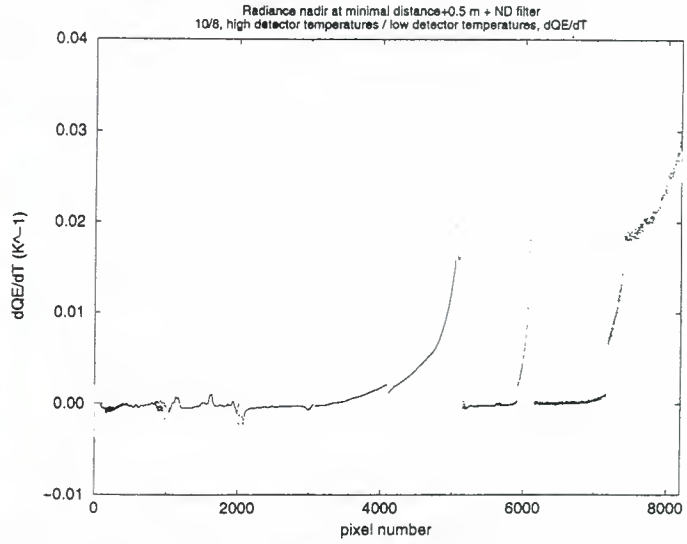

Figure 4: Array detector radiometric sensitivity dependence on detector temperature.

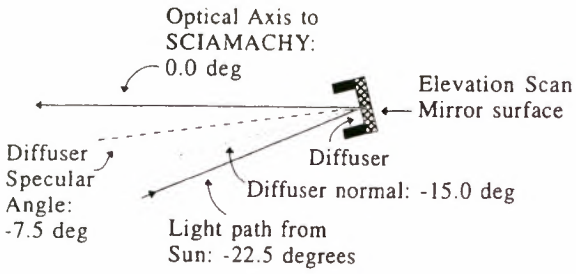

Figure 5: Diffuser geometry for sun-over-diffuser measurements.

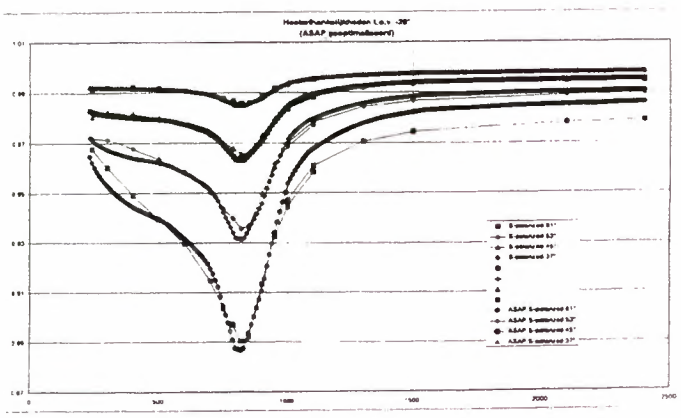

Figure 6: Ambient scan mirror and diffuser calibration: nadir mode scan mirror angle dependence example.

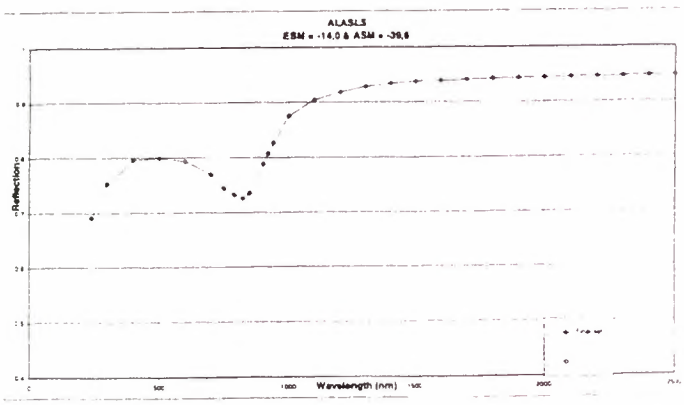

Figure 7: Ambient scan mirror and diffuser calibration: limb mode measurement example.

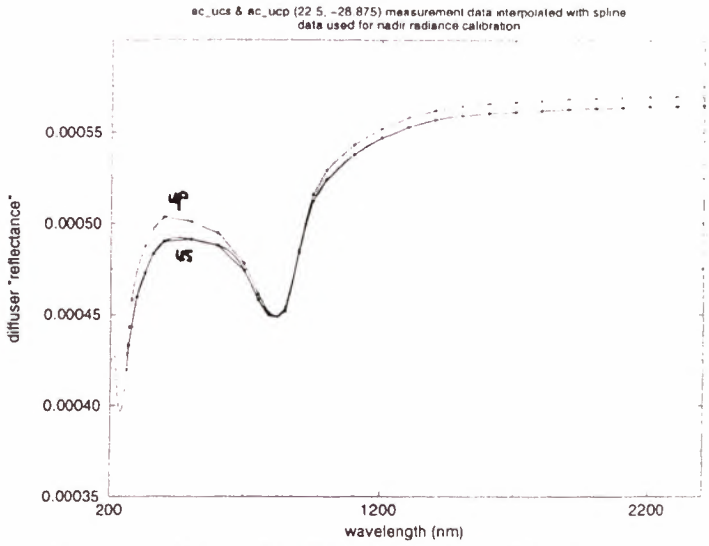

Figure 8: Ambient scan mirror and diffuser calibration: diffuser mode measurement example.

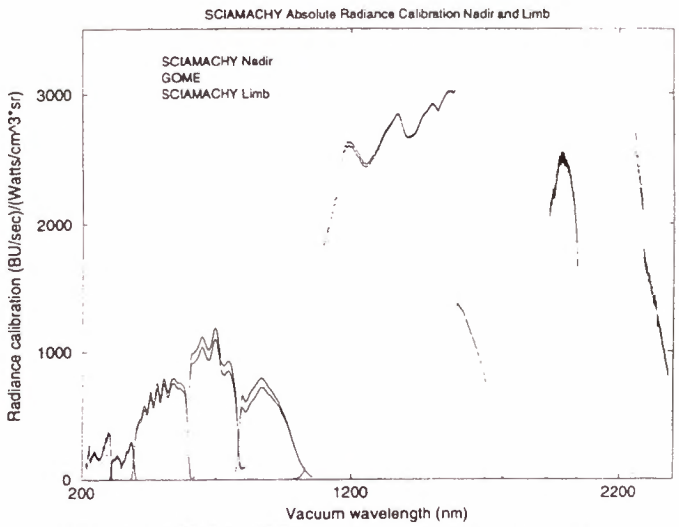

Figure 9: SCIAMACHY nadir and limb absolute radiance calibration. The dotted line is the GOME-1 absolute radiance calibration.

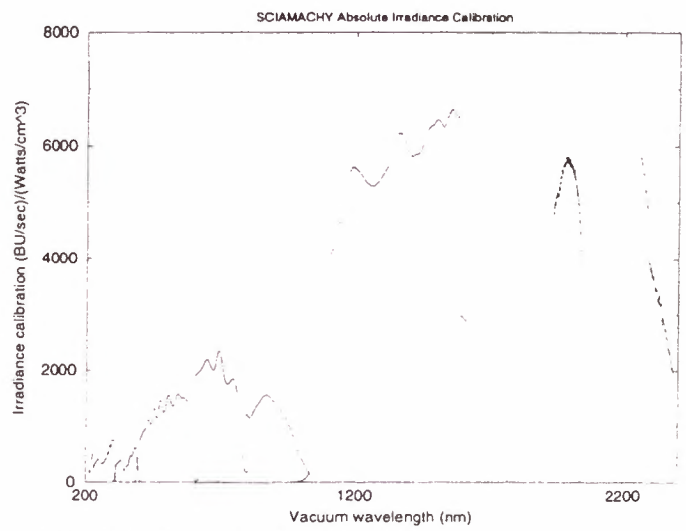

Figure 10: Absolute irradiance calibration results.

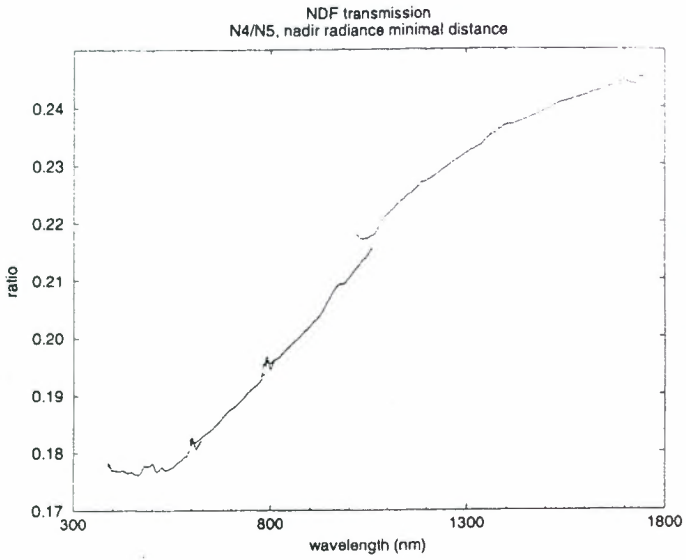

Figure 11: Neutral density filter transmission.

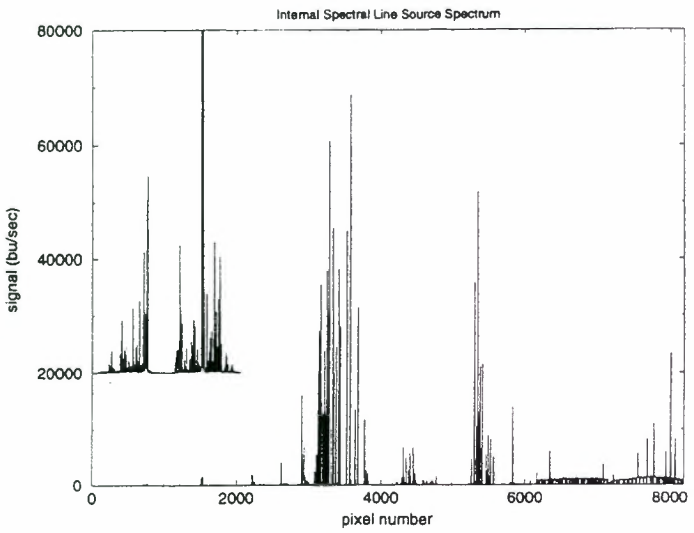

Figure 12: Internal spectral line source measurement.

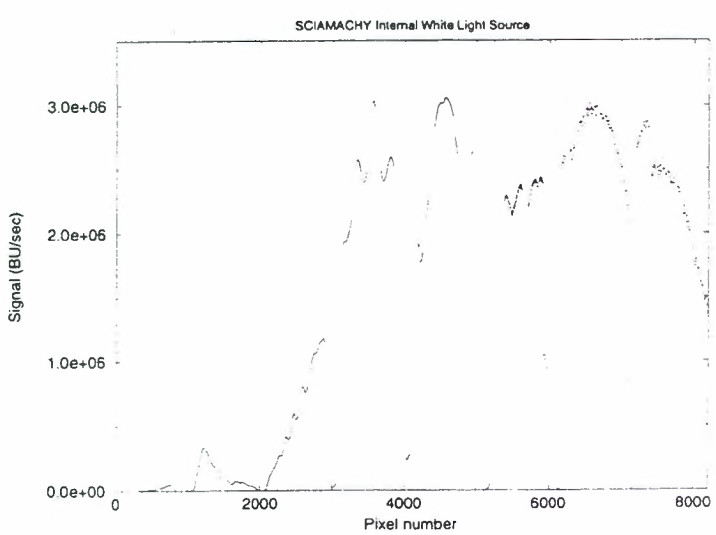

Figure 13: Internal white light source measurement.

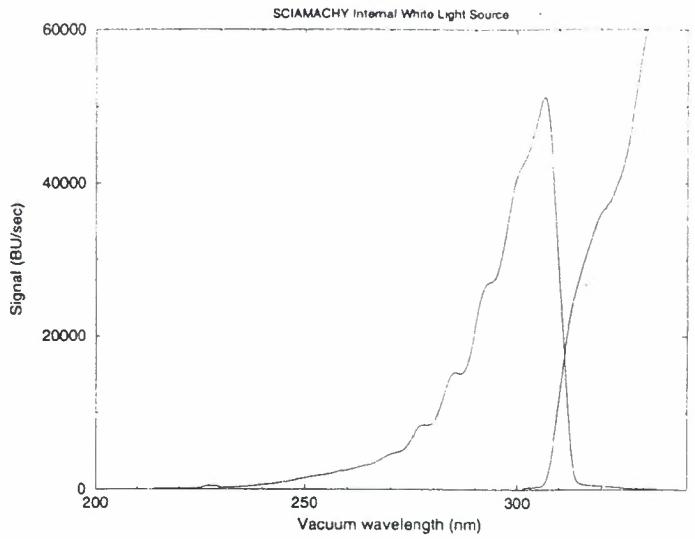

Figure 14: Internal white light source measurement in the ultraviolet.

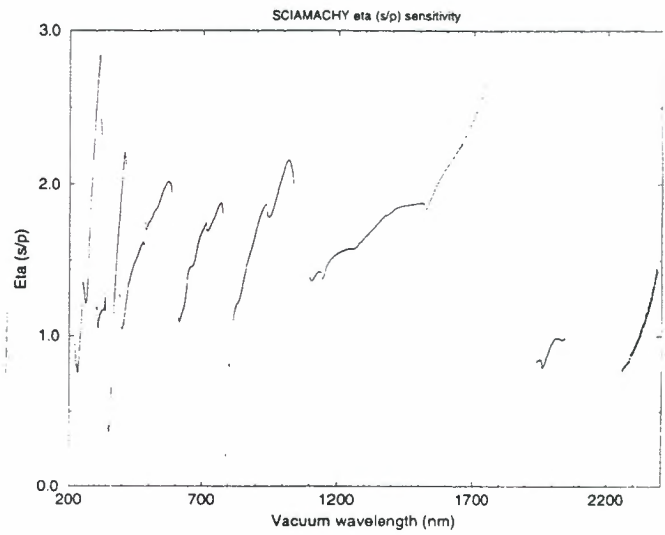

Figure 15: η calibration keyparameter.

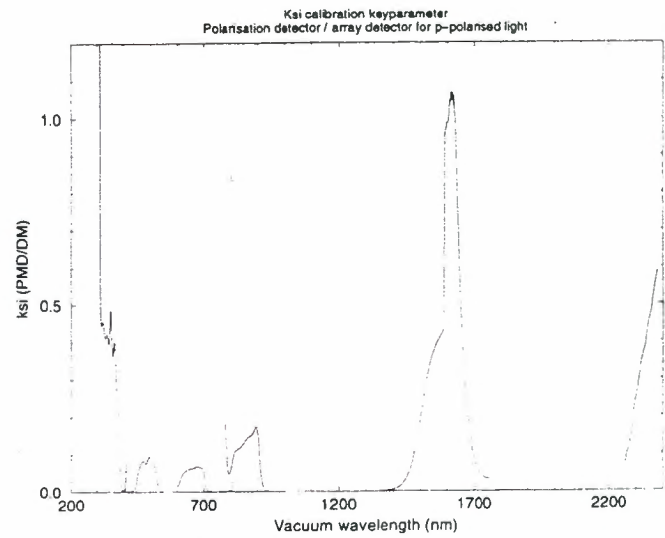

Figure 16: ξ calibration keyparameter.

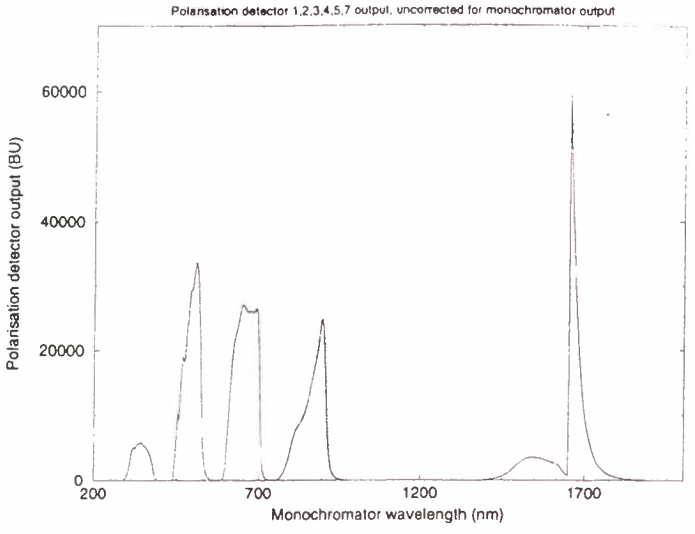

Figure 17: Spectral response of the polarisation detectors 1-5 and 7.

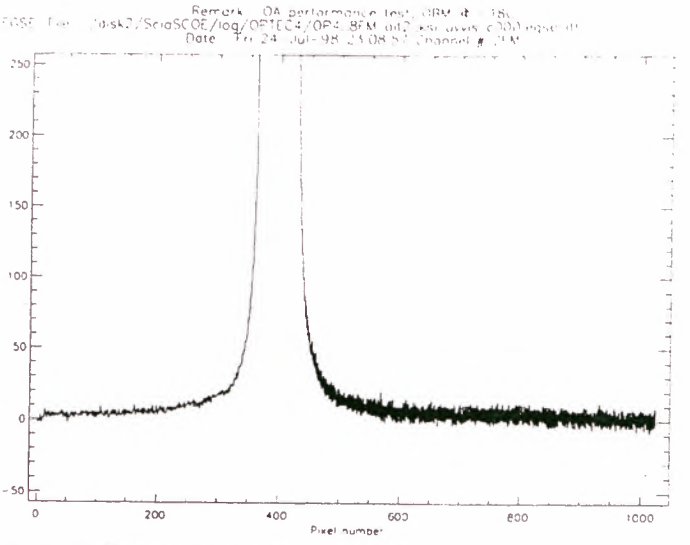

Figure 20: Example of enhanced noise feature.

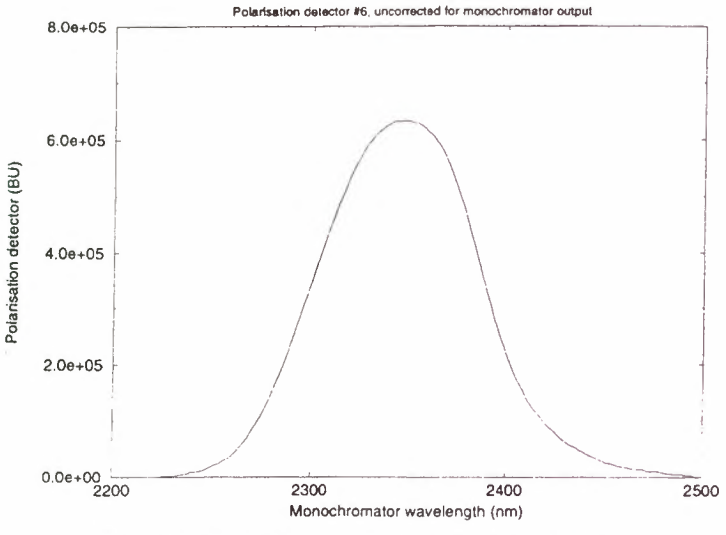

Figure 18: Spectral response of polarisation detector 6.

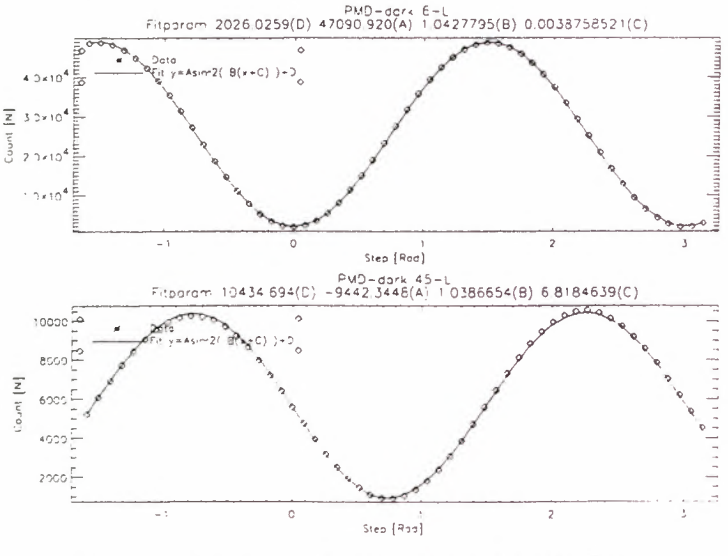

Figure 19: Brewster scan measurement example for polarisation detectors 6 and 7.

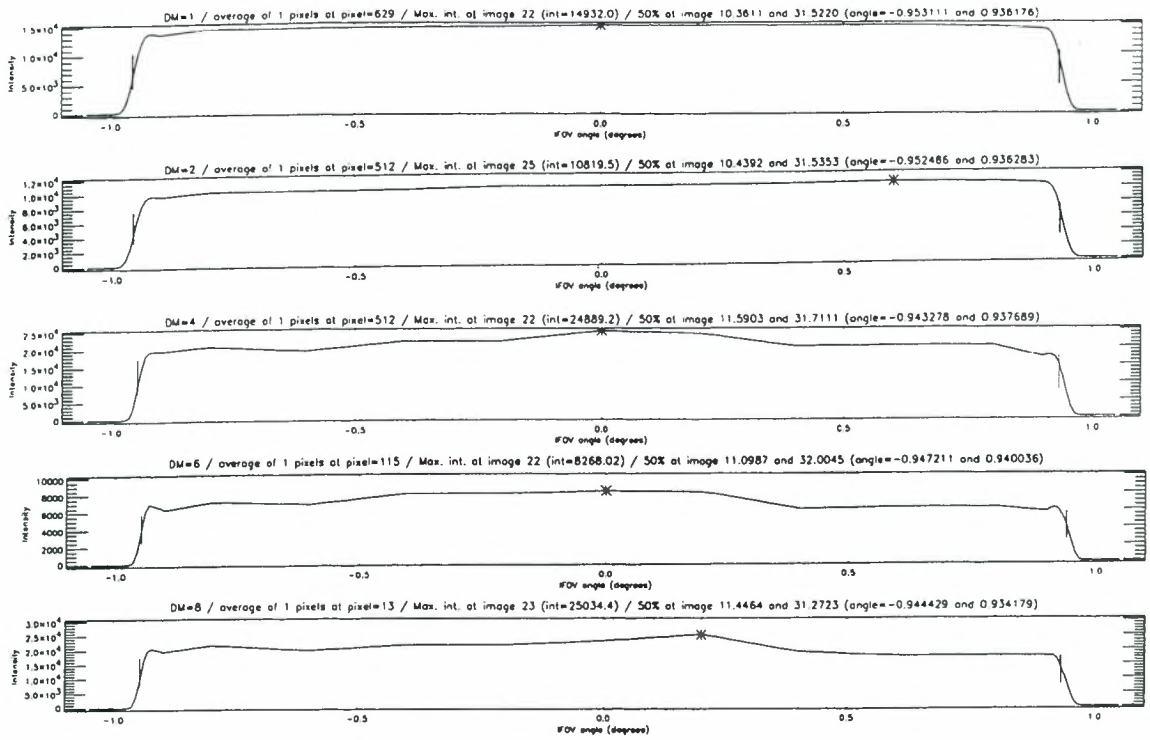

Figure 21: IFOV in cross-dispersion direction for the large aperture for a number of array detector channels.

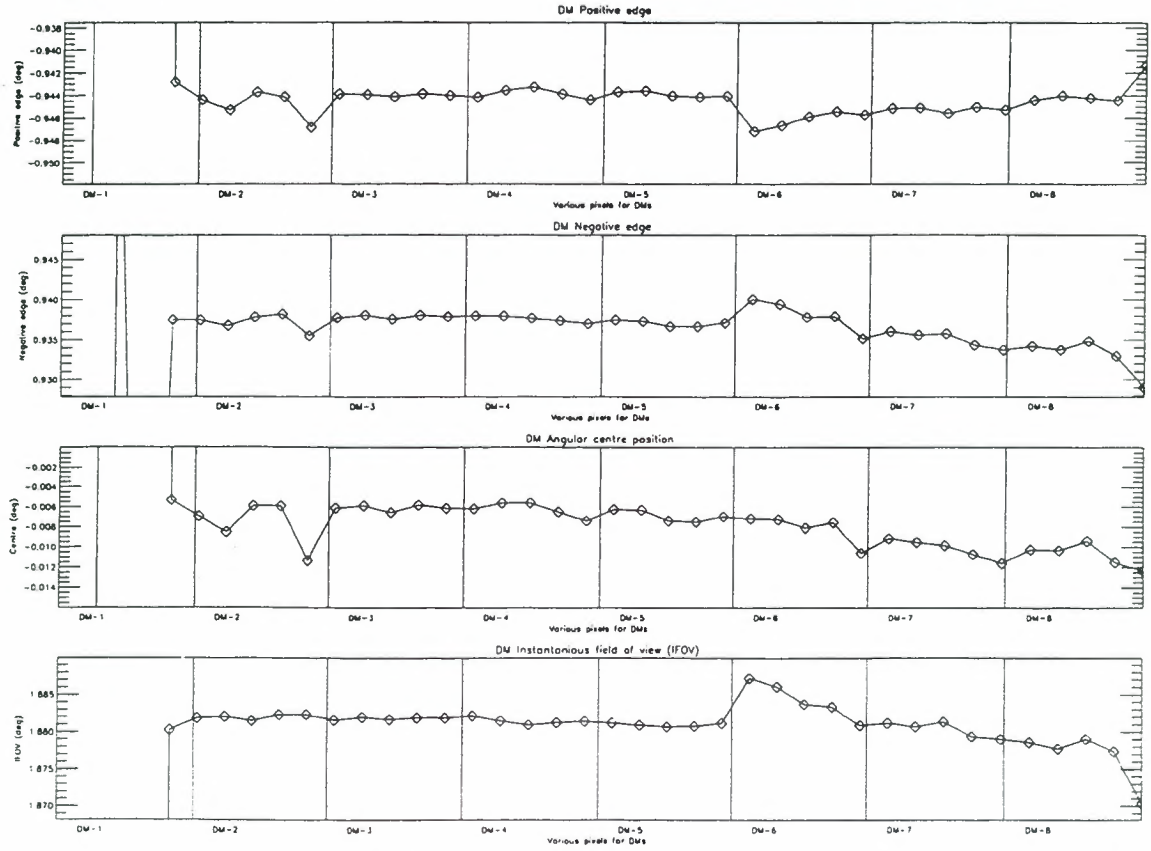

Figure 22: IFOV in cross-dispersion direction for the large aperture for a number of array detector channels: IFOV size and alignment.

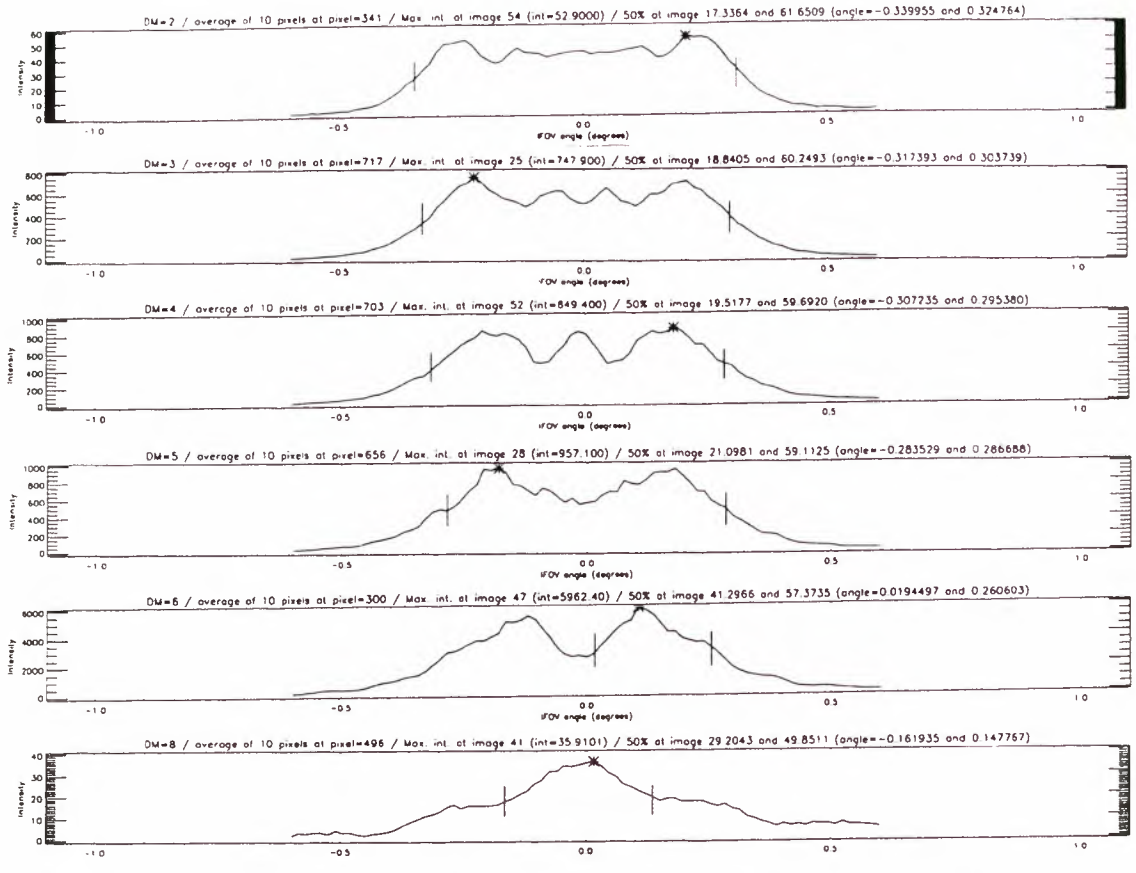

Figure 23: IFOV in cross-dispersion direction for the small aperture for a number of array detector channels.

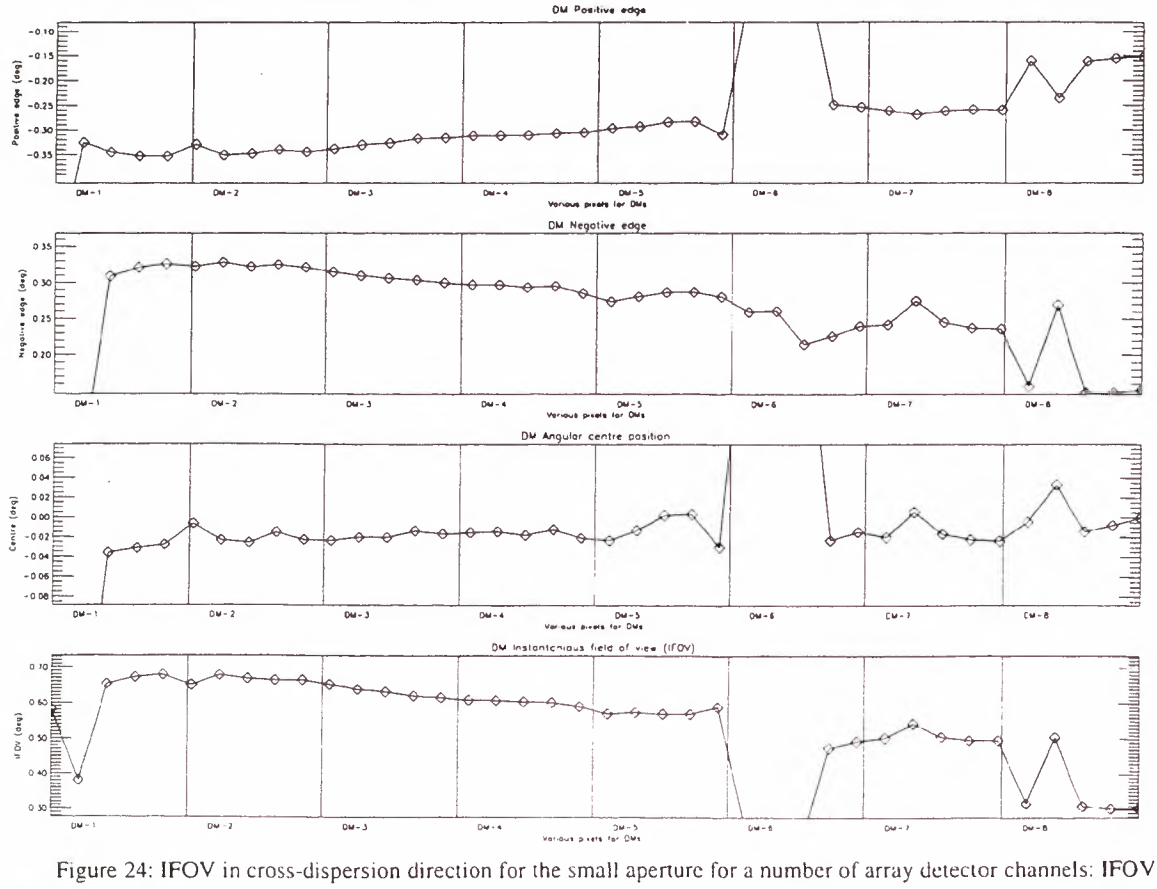

Figure 24: IFOV in cross-dispersion direction for the small aperture for a number of array detector channels: IFOV size and alignment.

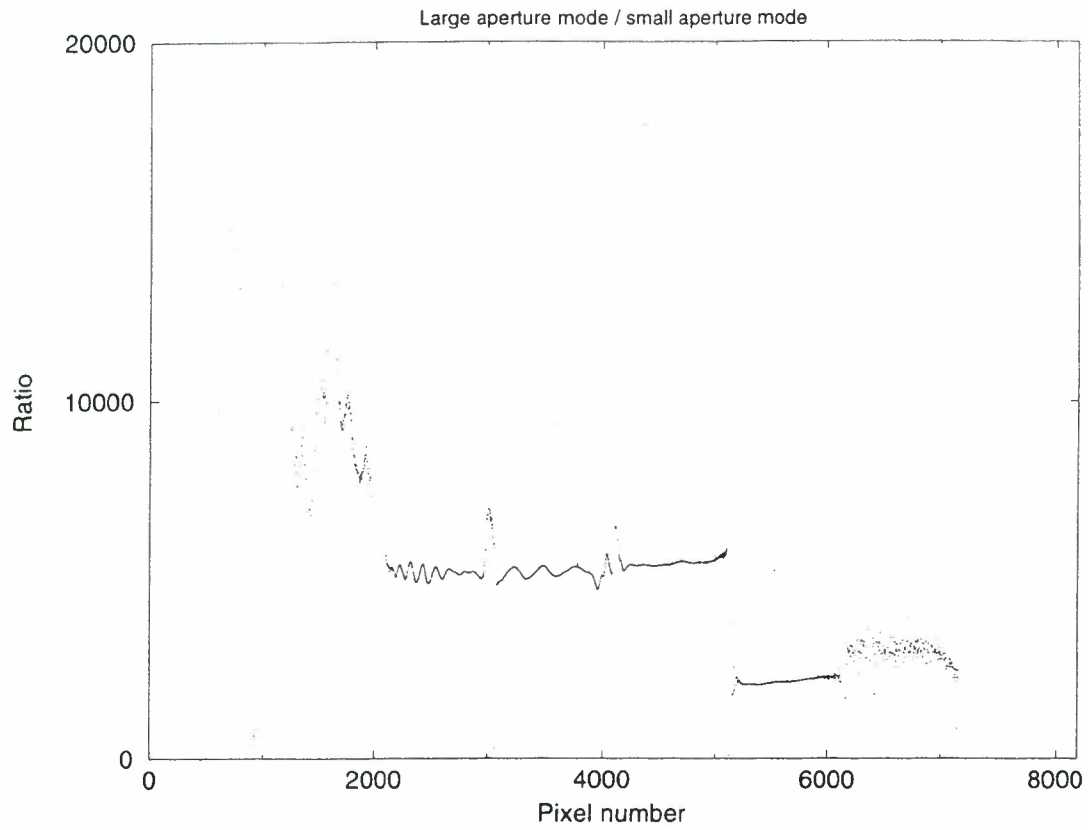

Figure 25: Ratio of large aperture over small aperture showing signal attenuation of the small aperture.

SCIAMACHY NEAR REAL TIME PRODUCTS

European Symposium on Atmospheric Measurements from Space

C. Caspar

Directorate of Observation of the Earth and its Environment
ESTEC, P.O. Box 299, 2200 AG Noordwijk , The Netherlands
Tel +31 71 5655350 , Fax +31 715653191

After introducing formatting rules applicable to all ENVISAT products, this paper describes the Sciamachy Near Real Time products in more details showing how the general guidelines have been applied to this specific instrument.The description begins with an overview of the operation concept introducing the notion of "states" which constitute logical blocks in the measurement sequence and are in this sense driving elements in the design of the products structure. For both level of processing, the discussion continues with a brief description of the content of all products and associated auxiliary information. The format of both level 1b and 2 products is then described down to the record level. Eventually, some Sciamachy specific aspects are developed including for example the use of an "application software".

1. Introduction

In order to offer ENVISAT users a consistent set of products, general format guidelines applicable to all instruments have been defined. As a consequence, all products share a common general structure. A product starts with two ASCII headers: the Main Product Header (MPH) and Secondary Product Header (SPH). Data themselves are organized into several data sets which may be Annotation Data Sets (ADS), Global Annotation Data sets (GADS) or Measurements Data Sets (MDS).This general aspects are further developed in section 2.

Along an orbit, Sciamachy operates under many different modes covering scientific measurements (nadir, limb...) as well as calibration sequences (wavelength calibration...). Each mode requires different instrument settings in order to control various aspects such as the viewing geometry, the duration of the mode or the definition of spectral bands (clusters) together with their associated integration times. Each mode corresponds to one of the 70 possible instrument "states" defined on-board. The variability of source packets content between different states influences the structure of level 1b and 2 products. This aspects are dealt with in section 3.

The discussion is further split into level 1b (section 4) and level 2 (section) specific aspects. For each level of processing, a list of the main and associated auxiliary products together with a brief content description and size consideration is given. The structure of the main product is then described down to the record level. Eventually particular aspects showing in particular the strong GOME heritage are discussed. This include the concept of an application software that will be distributed to users together with the products. It will allow to specify the level of calibration to be applied to the raw measurements increasing the range of potential users of Sciamachy level 1b products.

2. Common ENVISAT products features

All ENVISAT products follow common format guidelines. If this approach simplifies the handling of the numerous products type within the ground segment, it also eases the task of users having to exploit data from several level of products or from several instruments.

Fig.1 depicts the elements common to all products.

They all start with a 1247 bytes long Main Product Header (MPH) which provides general information such as for e.g. start and stop time of processed data, software version, acquisition center or orbital information.

The MPH also contains structure information describing for e.g. the size of the product, or the number of Data Sets.

This first header is followed by a Specific Product Header (SPH) variable for each product type. This header may be empty or provide product wise information such as quality flags. Some specific aspects of the Sciamachy level 2 SPH will be further developed in this paper.

The SPH is followed by several Data Set Descriptors (DSD) i.e. small ASCII records describing a particular data set in the product. They provide information concerning the data set type (GADS, ADS,MDS or reference), the size and the number of records within the data set as well as the byte offset of the data set from the beginning of the product. They therefore constitute con-

venient indexes to access a particular piece of information within a product.

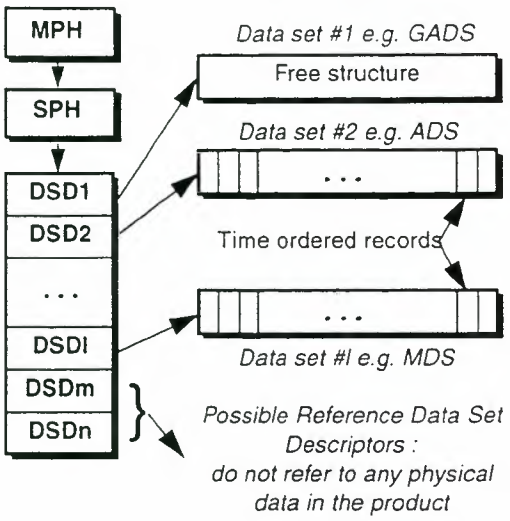

Fig.1: General structure of ENVISAT products

Scientific data are organized into the various data sets of the product. Several type of data sets are defined:

- Measurement Data Sets (MDS)
  In principle these data sets contains the calibrated measurements (level 1b) or geophysical data (level 2) organized into time order records. Each record starts with a time stamp.

- Annotation Data Sets (ADS)
  They include additional time dependent information further describing data in the various MDSs. This could be for example changes in the instrument settings as the satellite moves along the orbit. ADSs are also organized in time ordered records. The time grid is not necessary identical to the one of a given MDS.

- Global Annotation Data Sets (GADS)
  They include additional information necessary to interpret data from the various MDS. The format is free and in general not organized on a time grid. In the case of Sciamachy, this could be for e.g. a solar reference spectrum applicable to the entire product.

More information concerning the general ENVISAT products structure can be found in [R1].

3. Sciamachy operation concept and link to products format.

3.1. Mission planning

Along an orbit, Sciamachy can operate under different modes including scientific measurements: nadir, limb or solar/lunar occultation as well as many calibration modes such as acquisition of a solar reference spectrum or wavelength calibration.

In nominal operation, the instrument executes on the day side alternate limb and nadir measurements so that the same air volume can be seen under the two geometries. When coming out of eclipse, a solar occulation is performed. Whenever possible a lunar occulation is also performed every second orbit in the southern hemisphere (conditions to perform lunar occultations are only verified a few days per month). For most of the eclipse part, Sciamachy performs dark signal measurements as well as nadir measurements using long integration times to study effects such as biomass burning or air glows. Fig.2 illustrates a typical sequence of operations along one orbit.

The routine background operations can be superseded by regular daily, weekly or monthly calibration sequences.

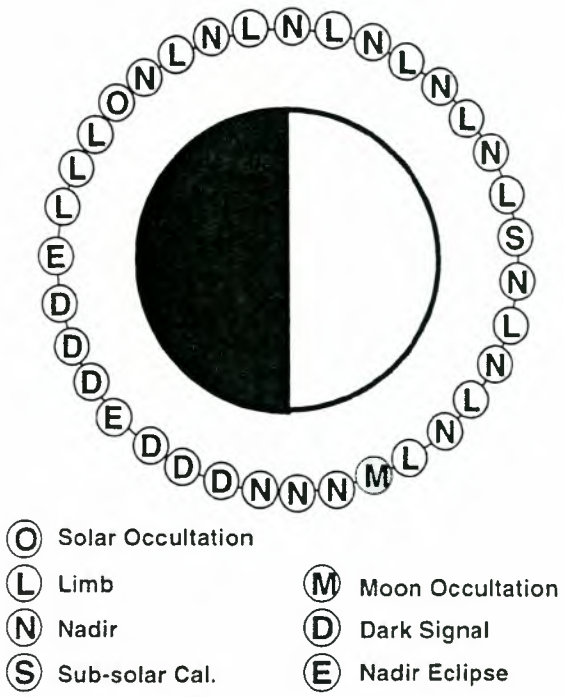

Fig.2: Typical sequence of Sciamachy operations along one orbit

For each measurement mode several parameters needs to be specified including :

- Measurement duration
- Azimuth and elevation scanners motion
- Definition of spectral bands (clusters)
- Exposure time and co-adding factor per spectral band

A given set of parameters defines an instrument state. Up to 70 states can be defined on-board and constitute the basic building blocks for the Sciamachy operations. In terms of products, it is therefore clear that all measurement data corresponding to a given state constitute a logical group or granule.

3.2. States and level 1b products

Level 1b products contains measurement data from all states (scientific measurements and calibration) with the exception of dark signal data as this would considerably increase the products size with little added information.

Because of the many different operation modes, Measurements data are split between four different MDS according to the state they originate from:

- Nadir MDS: contains all nadir measurements data (dayside and eclipse)
- Limb MDS: all limb states
- Occultation MDS: all data from solar and lunar occultations.
- Monitoring MDS: All calibration states (wavelength calibration, sun over diffuser...)

This split between MDSs makes it simple for a particular user to request a child product limited to a particular type of measurements e.g. nadir only.

Within the relevant MDS, all data corresponding to a given state are stored within time ordered records sharing a common structure and with a time span equal to the longer integration time of the state. When changing state, the record structure is modified to take into account changes in cluster definitions and integration times.

3.3. Impact on level 2

Because level 2 NRT products contain only geophysical quantities derived from nadir dayside states, the structure of the product is simpler and more decoupled from the details of the operations.

A separate MDS is dedicated to each retrieved molecule and fitting window. Depending on wavelength, two different algorithms may be used: DOAS for the UV/VIS region and BIAS for the near infrared. All MDSs corresponding to the DOAS algorithm share the same record structure, The same applies to all MDS record relying on BIAS.

3.4. Identification of state boundaries

Because measurement data corresponding to a given state constitute logical blocks of information. It is important to provide simple ways to identify state boundaries in both level 1b and level 2 products.

This task is supported by three ADSs as depicted on fig Fig.3. Each of these three ADS is organized into records containing statewise information. In more details:

- LADS: geolocation of a state (four corner coordinates of ground track or tangent points depending on geometry)
- SQADS: Statewise quality information such as number of missing source packets or sun glint flag.
- State ADS: describes state configuration Start/stop time, measurement category, longest/shortest integration times...

The analysis of this small data sets allow an end user to quickly analyze a product content and access the measurement data of a particular state of interest. (e.g. nadir measurement over a given latitude band).

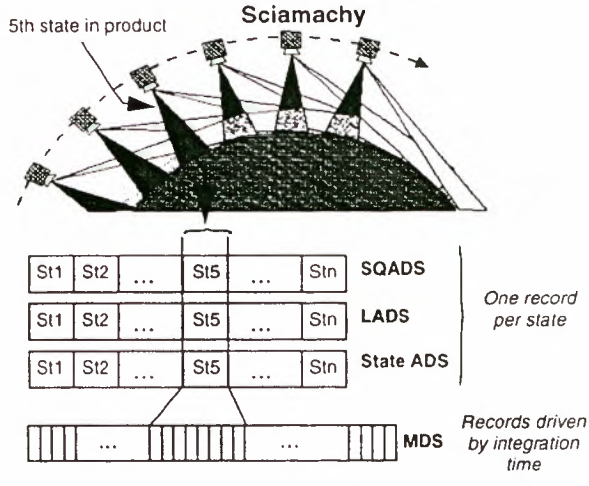

Fig.3: Identification of state boundaries using general ADSs

4. level 0, 1b and associated auxiliary products

4.1. Products list

Table 1 lists all products related to level 1b. For completion, level 0 products have also been inserted into this list.

Product ID	Description	Size
SCI_NL__0P	Raw Sciamachy source packets for all measurement modes, time ordered.	320 Mbytes/orbit
SCI_NL__1P	Geolocated, radiometrically and spectrally calibrated limb and nadir radiance spectra. Spectral coverage: 240 to 1750 nm (channels 1 to 6), 1940 to 2040 nm (ch 7) and 2265 to 2380 nm (CH 8) Resolution: 0.24 to 1.5 nm depending on spectral band. Individual measurements from calibration states	180 Mbytes/orbit
SCI_KD1_AX	On ground calibration parameters (key data) E.g. Polarization sensitivity, absolute radiometric response...	32 Mbytes, exceptional updates only
SCI_MF1_AX	Correction factors for initial calibration parameters.	< 1 Mbyte

Table 1: Level 0, 1b and associated auxiliary products

Product ID	Description	Size
SCI_XX1_1P XX= LK.SP.SU.PE	In flight calibration parameters e.g. spectral calibration curves sun reference spectrum	< 1 Mbyte
SCI_LK1_AX	Processor configuration file e.g. thresholds for identification of bad pixels...	0.1 Mbytes

Table 1: Level 0, 1b and associated auxiliary products

Byte level details of all products can be found in [R2].

4.2. Level 1b products structure

Taking into account the general ENVISAT product guidelines as well as the Sciamachy particular requirements the structure depicted on Fig.4 was derived for Sciamachy level 1b products.

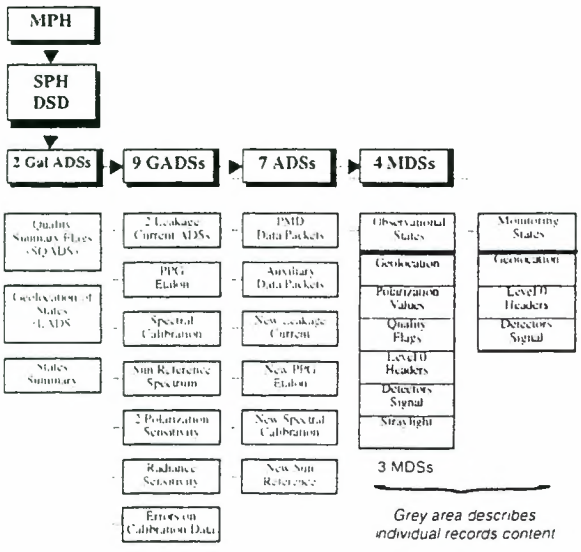

Fig.4 : Level 1b products structure

Besides, various data sets mentioned earlier, one should note the dedicated ADSs (Leakage current... Sun reference) used for the generation of in-flight calibration data by external processing facilities. The Monitoring State MDS will also support calibration activities including the generation of m-factors.

The reason for the different GADSs is explained in the following subsection.

4.3. GOME heritage

Sciamachy has a strong heritage from the GOME project on ERS2. In this sense, it was quite important to ensure some continuity between the products of these two instruments.

In the case of GOME, instead of containing only engineering calibrated (ir)radiances, the level 1b products include the raw measurement data in Binary Units (BU) together with all pre-calculated correction parameters (wavelength, polarization, straylight...) generally stored into dedicated GADSs. The final application of calibration parameters can later be performed in a simple and fast way on the end user platform.

The benefit of this approach is twofold:

- Reduce the size of level 1b products.
- Support a wider community of potential users by allowing precise selection of applied calibration steps.

The same approach is followed for Sciamachy. As a consequence, together with the 1b products, an application software will be delivered to users in order to let them apply a selected set of corrections to earthshine radiances and occulation data.

5. Level 2 and associated auxiliary products

5.1. Products list

Table 2 lists all Sciamachy level 2 related products .

Product ID	Description	Size
SCI_NL__2P	Geolocated vertical and/or slant column amounts of O_3, NO_2, H_2O,N_2O, CO, CH_4,OClO, H_2CO, SO_2 Cloud fractional cover and aerosol absorption indicator.	6 Mbytes/orbit
SCI_RV__2P	Geolocated vertical O_3 column amounts copied from the UV fitting window of SCI_NL__2P for meteo users.	100 Kbytes/orbit
SCI_XX2_AX XX = PR.CL.SF.CS .BL.FM.SL.C C.MF.PF.RC	Climatology Database E.g. Atmospheric profiles, Air Mass Factors LUT, Surface reflectance, cross-sections...	Various sizes Exceptional updates only.
SCI_LI2_AX	Processor configuration file. E.g. definition of wavelength range of the different fitting windows.	10 Kbytes

Table 2 : level 2 and associated auxiliary products

5.2. Level 2 products structure

Fig ?? shows the detailed structure of level 2 products. A separate MDS is used for each retrieved molecule and fitting window. All MDSs based on the DOAS algorithm (UV/Vis) share the same record structure indepent of the originating state. The same applies to all MDSs relying on the BIAS algorithm (near-IR).

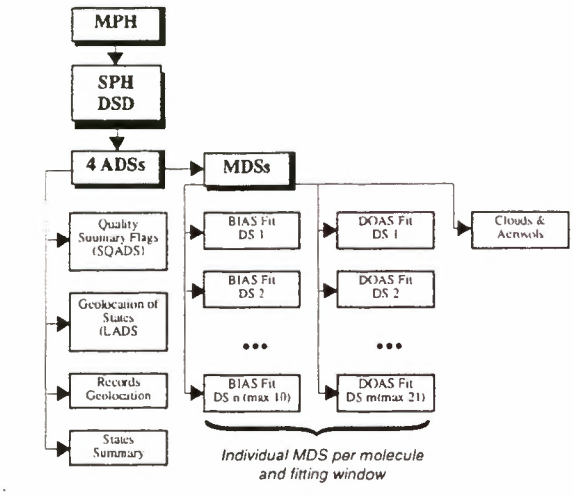

Fig.5 : Level 2 products structure

A last MDS contains information containing cloud cover and aerosol information.

The byte level descrption of the various MDSs can be found in [R2] . A DOAS record for e.g. provides detailed information concerning :

- Time information (measurement start and duration)
- Slant column density and associated error
- Vertical column density and error
- Fitting diagnostic such as number of iterations or χ^2
- Air Mass factors

5.3. Explicit definition of fitting windows

The format of level 2 products is flexible enough to accommodate a variable list of retrieved molecules and fitting windows. The SPH gives an explicit description of the product content as depicted on Fig.6 below.

```
NO_OF_DOAS_FITTING_WINDOWS=+002          } Number and list
DOAS_FITTING_WINDOW_0=" 325-335"         } of DOAS fitting
DOAS_FITTING_WINDOW_1=" 425-450"         } windows
...
NO_OF_BIAS_FITTING_WINDOWS=+003          } Number and list
BIAS_FITTING_WINDOW_0=                   } of BIAS fitting
"2031-2038 2033-2034 2035-2038 "         } windows
BIAS_FITTING_WINDOW_1="2269-2275"
...
DOAS_MOLECULE_00="0_O3    "              } List of fitted
DOAS_MOLECULE_01="1_NO2   "              } species per
DOAS_MOLECULE_02="1_O3    "              } DOAS window
...
NO_OF_BIAS_MOLECULES=+008                } List of fitted
BIAS_MOLECULE_0="0_H2O    "              } species per
BIAS_MOLECULE_1="0_CO2    "              } BIAS window
```

Fig.6: Explicit list of fitting window and molecules within the SPH of level 2 products

6. Conclusion

The detailed format of level 1b , 2 and all associated auxiliary products h as been defined.

This format is expected to be quite stable though outcomes of the instrument on-ground will probably require some changess (mainly for level 1b related files)

On top of the general ENVISAT ground segment facilities which will allow users to extract child product including a selected list of data sets limited to a given time window, Both level 1b and 2 Sciamachy products contain small statewise ADSs supporting user to further perform selection on a finer grid (state level) on his own platform.

Eventually, the use of an application software combined with level 1b products will increase the range of users supporting on top of normal scientific applications more instrument oriented activities such as in-flight calibration or long term monitoring.

7. References

[R1] *ENVISAT Product Specifications*
Volume 5: Product structures
PO-RS-MDA-GS-2009 is. 3 rev. C
October 16, 1997

[R2] *ENVISAT Product Specifications*
Volume 15: Sciamachy Products Specifications
PO-RS-MDA-GS-2009 is. 3 rev. A
July 11, 1998

SCIAMACHY ATBD FOR LEVEL 0 TO 1 PROCESSING

Sander Slijkhuis

Deutsches Zentrum für Luft- und Raumfahrt e.V., Deutsches Fernerkundungsdatenzentrum (DFD),
Oberpfaffenhofen, D-82230 Weßling, Germany
e-mail: Sander.Slijkhuis@dlr.de

ABSTRACT

We present an introduction to the Algorithm Theoretical Basis Document (ATBD) for SCIAMACHY Level 0 to 1 processing. Some aspects of the processing will be addressed more in detail, especially those which differ substantially from the processing for GOME.

This ATBD is publicly available from the DLR-DFD. It can also be found on the ESA www-server.

1. INTRODUCTION

In this Section a short introduction is provided to the SCIAMACHY requirements, to the operational data products, and to the ATBD itself.

Section 2 provides background information on the instrument, on its operation and raw data stream, and on the instrument calibration.

Section 3 gives an overview of the Level 0 to 1 processing algorithms.

Section 4 yields for selected topics a more detailed overview; especially for those algorithms where the processing differs significantly from the GOME processing.

Detailed descriptions of the algorithms are not given in this paper. For these, the ATBD itself is available.

1.1 SCIAMACHY requirements

SCIAMACHY (SCanning Imaging Absorption SpectroMeter for Atmospheric CHartographY) is one of the earth observation research instruments to be included as part of the payload of ESA's ENVISAT platform to be launched in the year 2000. The main scientific objective of SCIAMACHY is to measure distributions of a number of chemically important atmospheric trace species on a global basis. SCIAMACHY has a spectrometer and telescope system designed to observe light transmitted through and reflected and scattered from the earths atmosphere over a spectral range of 240 - 2400 nm. It has an alternate limb and nadir viewing capability, and will be able to perform solar and lunar occultation measurements.

Detailed discussion of scientific objectives for SCIAMACHY may be found in the Phase A Study Report (Ref. 1), and the Scientific Requirements Document (Ref. 3) (currently in draft version). See also the contribution by J.P. Burrows elsewhere in this issue.

Specific scientific requirements on algorithms have been laid down in the Report of the SCIAMACHY Algorithm Development and Data Usage Subcommittee (Ref. 3). Detailed requirements for the level 0 to 1b processing are laid down in the GPPR document (Ref. 2), which amongst others takes account of the SCIAMACHY Calibration Plan (Ref. 7) (based on the instrument design) and of the requirements imposed by the generic environment for all ENVISAT ground processors, by the level 0 data availablility scenarios, and by the data product definition.

1.2 SCIAMACHY Operational Data Products

This section provides a short overview of operational SCIAMACHY Data Products from the ENVISAT ground segment. Data products which may be derived by scientific institutes under their own responsibility are not covered here.

More detailed information on ESA approved products can be found in the review by C. Caspar elsewhere in this issue.

Nadir measurements will provide Top of the Atmosphere (TOA) radiance and reflectance, together with limited polarisation information, in the Level 1c data product; Level 2 processing in the UV/visible part of the spectrum will generate global column distributions of O_3, NO_2 and a number of other trace species (BrO, H_2CO, OClO, SO_2 and possibly ClO), and height-resolved profiles of O_3. Level 2 processing of Nadir infrared measurements will generate column distributions of CO_2, H_2O, CH_4, CO and N_2O.

Limb observations will provide in the Level 1c data product TOA radiance and reflectance and limited polarisation, at ~3 km spacing in tangent height between 0 and 100 km; Level 2 processing will generate vertical profiles of many of aforementioned trace gas species, with particular emphasis on O_3 and NO_2 (from the UV/visible region) and H_2O, CH_4, CO and N_2O (from the infrared). Limb profiles of pressure and temperature will be generated from CO_2

absorption signatures near 2 μm, and possibly from O_2 A band measurements (~760 nm).

Solar occultation measurements will have only crudely calibrated radiance in Level 1c. Operational Level 2 processing to obtain vertical trace gas columns is currently under study.

Aerosol profiles will be available from Level 2 limb (and possibly occultation) retrievals. Cloud parameters and additional aerosol parameters will also be produced from a number of Level 2 pre-processing algorithms.

1.3 ATBD for Level 0 to 1 processing

This Algorithm Theoretical Basis Document (ATBD) describes all algorithms required for the operational processing of SCIAMACHY Level 1b data products, and for the processing from Level 1b to 1c by the end-user. This document also deals with product generation and associated issues appropriate to the implementation of the algorithms in an operational environment, and summarises the necessary input/output requirements for level 0 to 1b data processing.

The Off-line (OL) and Near Real Time (NRT) processing uses the same software elements. Operational level 0 to 1b processing algorithms, and level 1b to 1c algorithms for post-processing by the users, will be implemented by an industrial consortium, with detailed product and algorithm specifications provided by the DLR-DFD (German Remote Sensing Data Centre).

Within the ENVISAT ground segment, the DLR-DFD acts as ESL (Expert Support Laboratory) for ESA.

Inheritance: relation to the GOME Data Processor

The Global Ozone Monitoring Experiment (GOME) was originally conceived as a scaled-down version of SCIAMACHY. It was given fast-track development status by ESA (Ref. 4), and was launched on 21 April 1995 on board the second European Remote Sensing Satellite (ERS-2). It has 4 spectral channels covering the range 240-790 nm, and is a nadir-only instrument. The measurement capability of GOME closely matches the UV/visible nadir capability of SCIAMACHY; the mission objectives are very similar.

The GOME Data Processor (GDP) was developed and implemented at DFD with the help of several scientific institutions (Ref. 5). GDP became operational in July 1996, with calibrated earthshine spectra and retrieved total O_3 columns the main products generated on a routine basis. The experience gained with GOME in the implementation of operational Level 0 to 1 processing has been very valuable. Parts of the current ATBD have their heritance from the descriptions in the GDP Technical Documentation (Ref. 6).

Nevertheless, the enhanced capabilities of SCIAMACHY, the technical differences in optics and electronics, in instrument operation, and last but not least the completely different concept of the ENVISAT ground segment infrastructure, have lead to algorithms which in detail have few things in common with the original GOME algorithms, except for the general scientific background.

ATBD document status

The Draft version of this document was released in December 1998 for the ESAMS conference; the 1st version is from February 1999. Unlike for the other atmospheric instruments on ENVISAT, the official algorithm review did not take place before the ESAMS meeting, but will be held later this year.

The document reflects the status of existing algorithm specifications for the processing software implementation by industry (based on the level 0 to 1b DPM written by S. Slijkhuis and W. Balzer in March 1998).

This first version of the ATBD has been written before detailed results from the on-ground calibration of the SCIAMACHY instrument were available.

Therefore, several algorithms will have to be reviewed when all calibration results are known (especially straylight, etalon properties).

2. BACKGROUND INFORMATION: INSTRUMENT AND CALIBRATION

SCIAMACHY is a medium-resolution UV-VIS-NIR spectrometer, fed by two nearly-orthogonal scan mirrors which enable across-track scanning in Nadir and in Limb, as well as sideways viewing for occultation and calibration measurements of Sun and Moon.

SCIAMACHY contains 8 channels which focus the spectrum on linear detector arrays of 1024 pixels each, and 7 Polarisation Measurements Devices (PMDs) containing photodiodes which measure linearly polarised intensity over a ~50 nm wide spectral band. Six PMDs measure polarisation parallel to the spectrometer slit, and one measures polarisation at a 45° direction.

Channels 1-6 provide continuous spectral coverage of the wavelengths between 240-1750 nm with a resolution between 0.2 nm (at 240 nm) and 1.5 nm (at 1750 nm). Channels 7 and 8 provide 0.2 nm resolution in bands around 2.0 and 2.3 μm. The spectra are formed by reflection gratings. Since the reflecting properties of these gratings are polarisation dependent, the intensity calibration of SCIAMACHY has

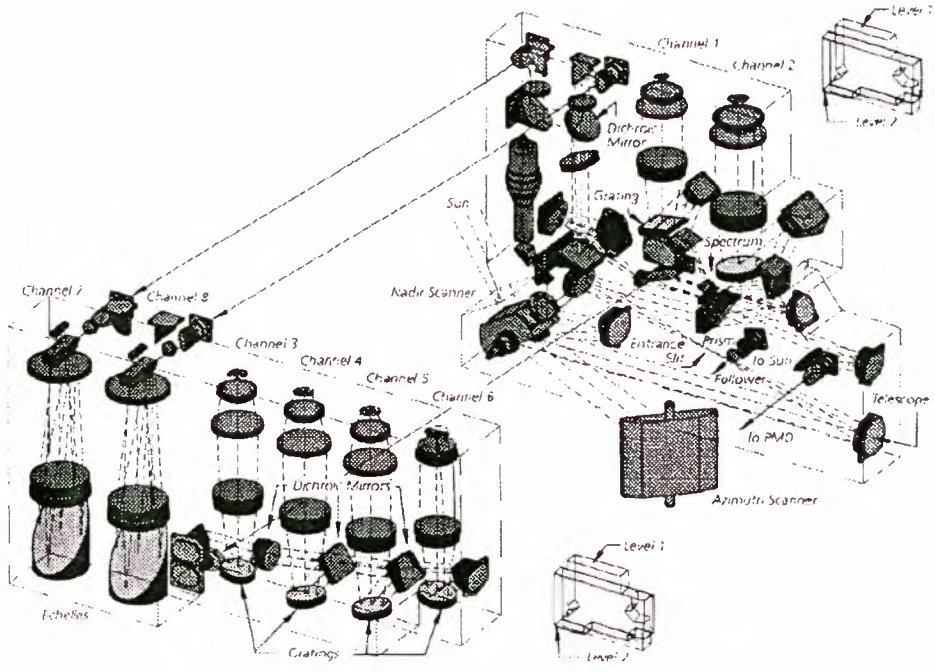

Figure 1: SCIAMACHY optical layout

to take account of the polarisation of the incoming light, using information from the PMDs.

The optical layout of the instrument is schematically shown in Figure 1. Light enters the telescope via two ultra-smooth (reduced straylight) scan mirrors. In Nadir obervation mode only the Nadir scan mirror is used, whereas in Limb and Occultation measuring modes the light is directed to the Nadir Scanner via the Azimuth scanner. In order to monitor a possible degradation of the Azimuth Scanner, which is the optical element most exposed to contaminants and solar UV radiation, a special Sun port is present which enables viewing the Sun over the Nadir Scanner only (if the geometry is favourable). In normal operations, a solar irradiance calibration is performed once a day with the Sun shining over the Azimuth scanner on a diffuser plate which is mounted on the backside of the Nadir scan mirror. Other calibration sources such as the Spectral Light Source (SLS, for wavelength calibration) and the White Light Source (WLS, for pixel-to-pixel gain and etalon correction) are directed to the Nadir scanner using auxiliary optics.

The telescope (3 cm diameter) projects the lightbeam onto the slit which determines the instantaneous field-of-view of 1.8° by 0.045°. For direct Sun viewing, an aperture can be inserted which reduces the amount of light entering the telescope. After the slit, the beam is collimated again and enters a predisperse prism, which has two functions. Brewster reflection at the back of the prism splits off part of one polarisation direction to the PMDs. The prism furthermore forms a low-dispersion spectrum, from which parts are picked-off to separate the light into the channels. Picked off are channel 1, channel 2, channels 3-6, and channel 7+8. In the channel 3-6 lightbeam a 20% Neutral Density filter may be inserted to cut down high light levels. Further channel separation is performed using dichroics. A grating in each channel then further disperses the light which is subsequently focussed onto the detector array.

The detectors are cooled to temperatures between 235 K (UV channels) and 150 K (NIR channels) to reduce dark signal. SCIAMACHY's optical bench is cooled to a stabilised temperature of -18°C to provide a stable, low thermal background for the NIR channels 7 and 8.

2.1 Instrument Operation and Data Packet structure

A basic concept in the operation of the SCIAMACHY instrument, which is also reflected in the structure of the level 0 and level 1 data products, is that of the instrument 'State'. A State is defined by a set of parameters such as scan mirror position, scan swath width, scan rate, detector exposure time, use of sun aperture, ND, or calibration sources. During the orbit the instrument executes a sequence of States, with a typical duration of ~1 minute per State.

There are up to 70 different States possible. The States are subdivided into 19 'Measurement Categories'. The Nadir, Limb and Solar Occultation are

the three measurement categories most relevant to the end-user. Other measurement categories comprise States for calibration and instrument monitoring.

Another important concept for especially the data packet structure is that of the 'cluster'. A cluster is a sub-division of a channel and contains data of a certain wavelength region. The cluster concept was partly driven by the wish to have certain important spectral windows with a higher spatial resolution (i.e. a faster readout during scanning) than would be possible on grounds of data rate limitations.

The consequence is that on the data product not each readout contains the whole spectrum, but that depending on which readout is finished more or less clusters (spectral regions) are present. Several clusters are in fact read out at high rate, but then co-added on-board to reduce the data rate between SCIAMACHY and on-ground receiving stations (in particular, the detector array in each channel can only be read out as a whole, and therefore the cluster with the shortest integration time in the channel determines the detector readout time; clusters which shall have a longer integration time have these short exposures co-added to obtain their nominal integration time).

The readout of the clusters is synchronised via a clock which every 1/16 second sends a BCPS (Broadcast Pulse Signal), hence all detector exposure times are multiples of 1/16 second. The photodiodes of the PMDs are providing a continuous signal which is sampled at 40 Hz through a filter with a time constant of ~20 Hz. Unfortunately, the sampling of the PMDs is in no way synchronised with the BCPS, and one of the tasks of level 0 to 1b processing is to interpolate the PMD signals onto the detector-readout time grid.

For Nadir, the nominal integration time is 1 second, corresponding to a footprint on the ground of 240x25 km. A complete swath of 960 km consist of 4 such integrations, plus one fast reverse scan where the scan mirror returns to the initial position. Channels 2b-6 are read out at a higher rate; the smallest integration time is for the cluster from 425-530 nm (for NO_2, O_3 retrieval) which under sufficiently high light levels attains a minimum footprint of 30x25 km.

For Limb, the nominal integration time is 1.5 second, corresponding to a 'column pixel' of ~960x3 km at the tangent height. The minimum integration time (under sufficiently high light levels) is for channel 3 (400-600 nm) with a column pixel size of ~120x3 km. All clusters in one channel have the same integration time in Limb mode. Limb scanning is performed in 34 steps of 3 km height intervals, starting at approximately 2 km below the horizon up to 100 km. Subesequently a 'dark' exposure is made by looking in dark space at 150 km above the horizon. During the across-track swath of 960 km, the nadir scan mirror follows the Earth's curvature, so that at every point in the swath the field-of-view remains centered on the same tangent height.

In nominal operation, Limb and Nadir viewing is alternated in such a way that a packet of air observed during Limb observation is a few minutes later coverd by the Nadir observation; projected on the Earth surface this leads to footprints where both Limb and Nadir are measured, alternated with footprints where no measurements are available. In order to retain a global latitude coverage, the location of gaps and measurements is alternated every orbit ('chess-board' pattern).

For Sun Occultation measurements, SCIAMACHY is first pointed to the approximate location at which the sun is expected to be situated some 17 km above the horizon (this avoids problems with atmospheric refraction). Because the position of the sun is not known exactly (spacecraft pointing inaccuracies), the elevation mirror scans continuously up and down. When the sun enters the field-of-view, a sun-follower locks the azimuth mirror on the sun, but the elevation mirror continues to scan the slit up and down over the solar image. We thus get a sequence of spectra for which the height in the atmosphere and the position on the solar surface are not accurately known. Since different horizontal slices of the solar image cover different surface areas, there is no accurate radiance calibration of these spectra. In general, platform pointing inaccuracies pose a problem in the determination of tangent height for both Limb and Occultation measurements. Accurate pointing will have to be retrieved during Level 2 processing, e.g. from p,T,z retrieval using the CO_2 lines in SCIAMACHY's channel 7.

2.2 Requirements for Level 0 to 1c processing

There are four basic calibration steps needed to convert the instrument binary data into calibated physical quantities.

1. Signal processing: correction of electronic anomalies (memory effect, cross-talk) and PMD synchronisation; correction for dark signal (including thermal background in channel 7+8), pixel-to-pixel gain, etalonning and straylight
2. Wavelength calibration: assigning to each detector pixel its associated wavelength
3. Radiance calibration: conversion of the corrected detector signals of the earth-shine spectra to radiance units; this includes polarisation correction
4. Irradiance calibration: conversion of the corrected detector signals of the solar spectra to

irradiance units; this includes correction for the BSDF of the diffuser plate.

Furthermore the measurements have to be geolocated, i.e. the geographical position of the footprint on the Earths surface (Nadir) or of the tangent height point (Limb) has to be determined from the instrument's scan mirror angles and from the spacecraft data.

Performing these calibration steps is the task of level 0 to 1c processing. In order to keep the data product as small as possible, the SCIAMCHY processing is done in two steps. All necessary calibration constants are processed from the calibration measurements in the operational processing from level 0 to 1b. The level 1b data product contains the raw detector signals (binary ADC units) of the science measurements plus calibration constants. The enduser has to run an application tool which applies the calibration constants to the data; this inflates the level 1b product to a much larger level 1c product containing fully calibrated data.

An additional advantage of this procedure is that the user can optionally omit certain calibrations to investigate their influence (or perform the calibration himself), and that by optionally filtering out only a subset of the data (i.e. geographical coverage or measurement category) the final level 1c product may be kept as small as possible.

2.3 Calibration Procedures

Calibration of the instrument is performed on 3 different levels:

1. *Onground Calibration*:
determines the instrument response to calibrated radiance and irradiance sources as function of wavelength and scan mirror angles; determines the straylight properties of the instrument; provides preliminary calibration of wavelength and dark signal.

The onground calibration was performed by the SCIAMACHY Joint Team (SJT), a consortium consisting of SRON, TPD/TNO and FSS for the design, building and on-ground calibration of the SCIAMCHY instrument. The output of the on-ground calibration relevant to the operational Level 0 to 1b processing, is a data set containing the so-called 'Calibration Key Data'.

A complication of the onground calibration has been that the instrument had to be calibrated in thermal vacuum, but that the available measurement setup did not allow calibration over the full range of viewing directions. Therefore, the angular dependence of the calibration constants has been derived from measurements on the isolated scanner mechanism alone, but the integration of these angular dependence in the calibration constants leads to a rather complex mathematical description.

In the Level 0 to 1b processing, the evaluation of calibration constants for the exact viewing geometry is performed under the item 'Pre-processing of Mueller Matrix elements.

2. *M-factors*:
uses in-orbit dedicated observing modes ('monitoring States') to obtain the so-called M-factors (monitoring factors) which describe the degradation of the instrument in space.

The degradation of the instrument can be monitored by combining measurements from several instrument States. These States have been designed in such a way that they include or exclude various optical elements, thus enabling to determine the reflectance/transmittance of these elements. End-to-end instrument efficiencies are obtained by using the Sun as a calibration source. This delivers only end-to-end efficiencies for the solar occultation mode, but using information from the single optical components as mentioned above, end-to-end instrument efficiencies can be obtained for nadir, limb and solar diffuser mode as well.

The M-factors are defined as the factors which have to be applied to the measured signals to correct them to begin-of-life levels, such that the onground-calibration data on the (ir)radiance response can be applied. M-factors are to be updated at regular time intervals by the SCIAMACHY Operations Support Team (SOST) consisting of scientists from Univ. Bremen and from DLR-DFD.

In Level 0 to 1c processing, the M-factors are applied to update the radiance- and irradiance response as given by the Calibration Key Data. M-factors are provided externally to the operational processors through the SOST.

3. *Level 0 to 1b Processing of Calibration Constants*:
Calibration constants which can be directly derived from measurements using on-board calbration sources are determined during the operational Level 0 to 1b processing. This comprises dark signal measurements on the night side of each orbit, and at regular intervals (typically once a week) wavelength calibration using the SLS measurements and PPG / Etalon calibration ('flatfielding') using the WLS measurements.

Daily observations of the Sun over a diffuser plate provides a solar reference which is used in the calculation of the reflectivity in Earth-shine spectra. The calibrated solar irradiance spectrum is output as measurement data on the product of the orbit containing the solar measurement; for subsequent orbits it is used as calibration data for reflectivity, until a new Sun is observed. This calibration data is referred

to as the Sun Mean Reference (SMR) spectrum.

3. ALGORITHMS OVERVIEW

In this and the following section, summaries of algorithms are given without references (these will be given in the main text). The summaries given include both the Level 0 to 1b and the Level 1b to 1c algorithms; the latter are often also referred to as 'Applicator' algorithms because they are part of an application tool which has to be run by the end user on the Level 1b data product, in order to generate the level 1c data product.

Noted with underline is if the algorithm belongs to the operational Level 0 to 1b processing (OP) or to the Level 1b to 1c applicator (A).

The sequence below also reflects the sequence of signal processing for the applications.

Pre-processing of Mueller Matrix elements (OP)
These algorithms calculate the Mueller Matrix elements of the instrument from the Calibration Key Data (for an introduction to Mueller Matrix elements see the corresponding algorithm description). These basic calibration data are interpolated to a fine grid of scan angles, and to the wavelength of the SMR spectrum. Those interpolated Mueller Matrix elements which are also needed by the application program are output to the Level 1b product.

Calculate Geolocaltion and synchronise PMDs (OP)
In the geolocation processing, the instrument scan angles and time information is converted to geographical coordinates, and the solar illumination condition is determined. This relies heavily on the use of ESA's ENVISAT Orbit Propagator, whose routines will be referenced but not explained in detail. The stream of PMD signals is synchronised with the BCPS of the channel readout, and the PMD signals are averaged over time chunks of 1/32 second which is an integer fraction of the channel exposure time (2 times the shortest possible readout).

Correct Detector Readout Memory (OP, A)
The magnitude of the memory effect is calculated for channel signals above 10,000 BU using a polynomial function of signal intensity (as described by SJT); in case of co-adding the signals of the individual readouts are estimated by scaling with the PMD signals. The correction is coded as one byte on the Level 1b data product (OP). The memory effect is subtracted from the measurement (OP, A).

Calculate Dark Signal (OP)
The algorithms describe how to use the Dark Measurement States to derive calibration constants for FPN and leakage current (including thermal background). Output to the Level 1b product is a set of calibration constants as function of orbit phase. Similarly, calibration constants for the possible solar straylight from the Azimuth Scanner are derived. The pointing to the dark sky during Limb measurements is not used for dark signal calibration, but a quality flag is set for the limb measurements.

Apply Dark Signal (OP, A)
Applies the calibration constants for Dark Signal to the measurement spectrum and calculates the relevant errors.

Calculate PPG and Etalon Parameters (OP)
Calculates from the WLS calibration data the PPG (detector pixel-to-pixel gain) and the Etalon (interference pattern), using a fourier filtering technique. For the latter a solar spectrum may be used as backup for the WLS.

Apply PPG and Etalon Parameters (OP, A)
Applies the calibration constants for PPG and Etalon to the measurement spectrum and calculates the relevant errors.

Calculate Spectral Calibration Parameters (OP)
All algorithms listed above are applied to detector signals without need of knowledge of the precise wavelength of each pixel. This changes for the algorithms which follow, which need wavelength information in order to use the correct calibration constants. The algorithms described here provide this wavelength calibration, using information from the SLS or from the SMR spectrum.

Apply Spectral Calibration Parameters (OP, A)
Calculates for eacht detector pixel its wavelength [nm] from the spectral calibration parameters.

Determine Spectral Straylight (OP)
Uses pre-flight straylight characteristics and measured polarisation fractions to calculate for each detector pixel the straylight from other wavelengths. The straylight intensity is coded on the level 1b product.

Apply Straylight Correction (OP, A)
Decodes the straylight from the level 1b product (A) and subtracts it from the measurements.

Apply BSDF and calculate SMR (OP, A)
Uses measurements of the Sun over the diffuser to calculate a (daily) Sun Mean Reference spectrum, where the irradiance is calibrated via the BSDF function of the diffuser (OP). The application of BSDF is also performed in the radiometric calibration of science measurements using the Sun (A). The out-of-band signal of the PMDs is calculated (OP).

Apply Radiance Response (A)
Perform the absolute radiometric calibration of the detector signals, including polarisation correction using the wavelength-interpolated Fractional Polarisation Values. Optionally a Sun-normalised spectrum (the reflectivity) is calculated.

Determine Fractional Polarisation Values (OP)
Calculates the Fractional Polarisation Values at 12 wavelengths over the SCIAMACHY range from the

ratio of PMD to channel signals, from the ratio of 2 overlapping channel signals, or from single-scatter theory (at 300 nm). This is not only done for all readouts with the points then available, but also for averaged readouts to cover all possible ground pixel sizes in a State.

Interpolate Fractional Polarisation Values and Apply Polarisation Correction (OP, A)
The Fractional Polarisation Values are interpolated to wavelength (OP, A). This is partly done using modified spline interpolation (Akima), partly using a parameterisation of the polarisation curve in the UV. The interpolated polarisation values are either used in the calculation of the spectral straylight (OP) or in the calculation of the polarisation correction of Earth-shine measurements (A).

Quality Flagging (OP)
Several data quality flags are written to the Level 1b product. These may apply to the whole orbit, or only to a State, or only to a (cluster) readout in a State.

4. SELECTED TOPICS

In this Section we discuss some selected topics more in detailed. Especially those algorithms are covered where the processing differs significantly from the GOME processing.

4.1 Synchronisation of PMDs

The polarisation correction algorithm needs the ratio of channel detector array signal to a PMD signal which is integrated over the same detector exposure time. However, in the raw data there is no synchronisation between PMD signals and detector array readout.

The situation is as follows. The channel detector arrays are integrated with an integration time (IT) which is a multiple of 1/16 sec (62.5 ms); the IT may vary between 1/16 and 10 seconds. The signals of the 7 PMDs are sampled at 40 Hz (25 ms) but not synchronised with the channel readouts. In order to achieve a kind of averaging over the sampling time, the PMDs are filtered before readout with a 3rd order Butterworth filter with a timeconstant of ~50 ms; this filtering induces an apparent signal delay of ca. 16 ms. For each PMD two read-out values (value A and B) are given for one measurement. Value A is the output of the first amplifier stage (low gain), value B the output of the second amplifier stage (high gain) in the PMD electronics. The sampling of the PMDs is sequential in order 1A, 1B, 2A, 2B, ..., 7B with a small timelag (0.5 ms) between each readout.

In the Level 0 to 1b processor we perform the synchronisation and integration of PMD signals over the array detector IT in two steps. First the PMD values are integrated over time intervals of 1/32 second (half the minimum channel integration time) synchronised with the channel detector BCPS. In the second step (in the polarisation correction algorithm) these 'PMD integrals' need only be added to obtain the PMD signal integrated over the actual exposure time of the cluster which is used for the calculation of polarisation parameters. The synchronised PMD integrals are also written to the Level 1b product, where they are useful for e.g. cloud recognition purposes in the Level 1 to 2 processing. Although the PMD integrals probably contain all the information one would usually need, the original PMD data stream is copied to the Level 1b product as well (as annotation data).

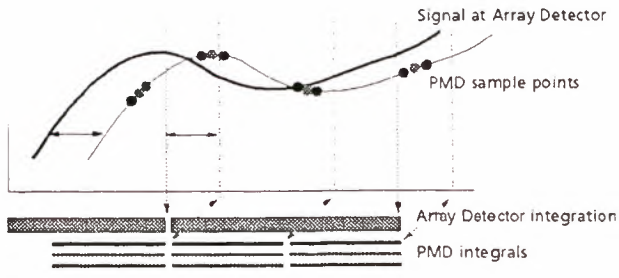

Figure 2: Conversion from sampled PMD points to PMD integrals. The thin line represents the delayed signal after filtering.

The 'PMD integrals' are calculated as:

$$I_{\mathrm{PMD}} = \int_{t\_start}^{t\_end} S_{\mathrm{PMD}}(t_{\mathrm{PMD}} + t\_delay)\ dt$$

where for a channel IT of 1/16 s *t_end* corresponds to the readout time of channel pixel 0 (or 31.25 ms earlier for the 1st integral in the IT), and *t_start* = *t_end* − 31.25 ms; the delay time *t_delay* takes account of the lag of the signal due to filtering.

This integral is numerically calculated using quadratic interpolation and Simpson integration, taking into account the precise time stamps t_{PMD} of the used PMD measurements (e.g. time is different for stage A and stage B of the same PMD).

4.2 Geolocation of measurements

The geolocation information is calculated in granules of the shortest integration time in the present State. Geolocation information for clusters with larger integration times have to be constructed out of the corresponding sets of geolocation information for the shortest integration time.

Geolocation is calculated using ESA's orbit propagator software, which is a requirement from the ENVISAT ground segment applicable to all instruments.

For Nadir, the geolocation parameters are given for the footprint on the ground similar as for GOME, i.e. geographical coordinates (lon,lat) will be given for the 4 corner points and the centre of the footprint. Zenith and azimuth angles are given for the viewing centre for the start, middle and end of the exposure time. For Limb and Occultation measurements, tangent height (geoid) and geographical coordinates, and zenith/azimuth angles of the tangent will be given for the tangent points, for the start, middle and end of the exposure time. For all other measurement modes (calibration and monitoring) only the geographical coordinates for the centre sub-satellite position, and the solar angles for the start, middle and end of the exposure time will be given.

All solar angles are calculated at TOA (prelim. 70 km) for Nadir, Limb, Solar Occultation and at satellite for other observing modes (calibration, monitoring).

All viewing angles are geometrical angles. In Limb/Occulation, this implies that due to atmospheric refraction, 'real' tangent heights have to be calculated using ray-tracing in Level 1 to 2 processing.

4.3 Dark Signal correction

Dark signal from the detectors and PMDs, including the thermal background in the infrared channels, is measured at regular intervals around the orbit by staring at 'Deep Space' (like limb viewing geometry with a tangent height of 150 km). Dark signal has a fixed component, the so-called fixed-pattern noise (FPN), as well as a component due to charge leaking which increases linearly with detector exposure time. The thermal background component also increases linearly with detector exposure time. Therefore, the dark signal can be characterised by 2 calibration constants: the offset (FPN) and the slope of the dark signal versus exposure time. To this end 3 Dark States are implemented, with exposure times of nominal 0.125, 1.5, 40 seconds which are executed after each other, from which the 2 parameters plus error estimate can be derived.

For the NIR channels and PMDs which are affected by thermal background, the dark signal is derived as function of the orbital phase (see below), to allow for thermal gradients over the orbit.

Another background component which increases linearly with exposure time is a possible contamination by solar straylight, which might occur when the Azimuth Scanner is directly illuminated by the Sun for a short period after the instrument emerges from the dark side of the orbit. This component will be modelled as a polynomial function of orbit phase, but only for that part of the orbit where the Azimuth Scanner is directly illuminated. This

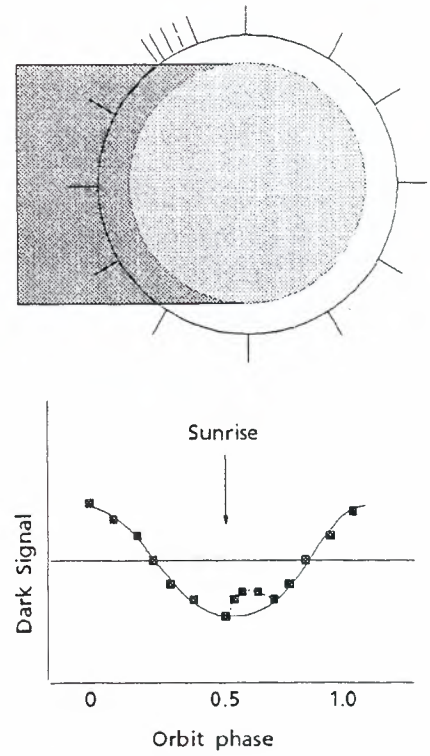

Figure 3: Schematic representation of orbit regions, and of harmonic fit of dark signal over the orbit

component must only be taken into account for Limb/Occultation measurements; in Nadir mode the azimuth mirror may be illuminated but is far outside the field-of-view of the elevation scan mirror and secondary straylight is not expected.

To model the dark signal over the orbit, 'Dark' observations are averaged within a number of predefined regions in the orbit, and offset and slope of the dark signal versus exposure time are determined for each region. Since solar straylight occurs near Sunrise, and thermal background variation is associated with thermal gradients due to heating by the Sun, the regions are defined w.r.t. phase of the orbit after sunrise.

A program external to the level 0 to 1b processor assembles the data from 1 or more orbits and makes a fit of the 'dark signal slope' versus orbit phase. Excluding the region near sunrise (solar straylight) a harmonic fit is made to find the variation of thermal background with orbit phase. After subtraction of this harmonic component, the solar straylight is fitted with a polynomial over the orbit phase for the solar straylight region. Results are output as 1 fitted value of the 'dark signal slope' for the centre of each orbit region, plus the average of FPN over the orbit.

In the application of dark signal correction for the level 1c processing, a 'Dark Spectrum' is calculated for each instrument State, using linear interpolation to calculate for the central time in the State the

'slope' of the Dark Signal from the values given at the centres of the pre-defined orbit regions. Note that a science observation State lasts typically 80 seconds whereas the longest Dark Signal calibration measurement takes 200 seconds. Therefore the approximation of calculating one dark signal for the whole State is justified.

4.4 Spectral calibration

Spectral calibration is performed at regular intervals (typically weekly) using the sharp emission lines of an internal Pt/Cr-Ne hollow cathode lamp (the SLS). The same method of spectral calibration as for GOME is used:

- Line positions are calculated from the centre-of-gravity of the SLS lines (Falk algorithm)
- A correction is made for spectral shifts due to SLS light path blocking; the corrections are to be pre-defined
- For each channel, a 4th order polynomial will be fitted to the spectral line positions to obtain wavelength as a function of pixel number.

For the channels where an insufficient number of lines is available (in the near-infrared), a similar procedure is followed but using the Fraunhofer lines in the Solar Calibration spectrum to derive the line positions. For each channel a fixed window size is taken around selected Fraunhofer lines. A continuum correction is made, where the continuum is calculated from linear interpolation of the intensities at the window edges (edge intensity averaged over 3 pixels). Doppler shifts and a possible wavelength shift of the line due to convolution of the solar spectrum with the SCIA slit function, or due to the continuum subtraction, have to be taken into account; these precalculated shifts are applied like the SLS blocking shifts. This method is fast and delivers stable results; a disadvantage is that the final selection of lines and the calulation of precise wavelength shifts may need results from the commissioning phase.

The wavelength calibration depends on the temperature of the optical bench. Although the instrument is temperature stabilised, thermal gradients may occur as function of orbit phase due to single-sided heating by the Sun. Just as with the Dark Signal, the polynomial coefficients of the wavelength calibration will be modelled by a harmonic (sinusoidal) function, as function of orbit phase. Since within one orbit not all orbit phases may be covered by the measurements, the calculation of the harmonic function is done outside the operational Level 0 to 1b processing chain (in particular, this is a requirement for the NRT processing at the receiving station, which may not have access to orbits received by another station). The result is offered to the processor via an auxiliary input file.

On the Level 1b product the wavelength calibration is given in the instrument rest frame only. Note that the limb spectra and solar spectra will be Doppler shifted due to the motion of the spacecraft in the direction of the light source. These shifts vary from maximally 0.06 detector pixel in channel 1 to maximally 0.6 detector pixel in channel 8. However, this does not in any way influence the wavelength calibration of the instrument as such; the wavelength of each pixel for calibration parameters such as Polarisation Sensitivity or the Radiance Response function is given in the instrument reference frame, not in the moving limb or solar reference frame. Thus for level 0 to 1b processing the Doppler shift is not relevant. The application of Doppler shift would be performed only in level 1b to 1c processing if the end user wishes so. A correction factor describing the Doppler shift [$V.\cos(\alpha)/c$] would be helpful to the user, but is currently not specified on the Level 1b product.

4.5 Bad pixel mask

The new technology array detectors used in SCIAMACHY's NIR channels are not perfect - a fraction of up to 10% of all pixels may be effectively unuseable because they are either dead or have a very high dark current or high readout noise. See also the paper by A.P.H. Goede elsewhere in this issue.

A 'bad pixel mask' will be derived on the basis of unusually low/high pixel-to-pixel gain using the observations of the on-board white light source (WLS). This mask is calculated in the same algorithm where pixel-to-pixel gain (PPG) and Etalon is calculated from WLS data. Unlike the PPG and Etalon, the input bad pixel mask is not automatically updated by the processor; this needs a human intervention. However, bad pixels in this 'diagnostics mask' will not have their calibrated PPG updated.

The reason to omit automatic updating of the mask is twofold. First we wish to avoid spurious 'bad pixels' due to hits of the detector by cosmic particles. Furthermore the original mask supplied by SJT contains several degrees of 'badness' ; e.g. pixels may be designated as 'bad' based on high readout noise values. These subtilities can only be derived from examination of large data sets and not in an operational processing algorithm based on the analysis of one WLS spectrum. Open questions are still where to lie the boundary between 'bad' and 'good', and whether the Level 2 processing shall use the same mask as Level 1 or would we e.g. also allow pixels with higher noise values (at critical locations) in Level 2 processing.

4.6 Polarisation Correction

The sensitivity of the instrument depends on the polarisation of the incoming light. The calculation of this polarisation takes a significant part of the total Level 0 to 1 processing time.

In SCIAMACHY, there are 11 wavelength regions which are covered by at least two detectors having different polarisation sensitivities - thereby allowing for a determination of the input polarisation. These are (a) the six general Polarisation Measurement Devices (PMDs) which cover part of the wavelength ranges of channels 2 (PMD-A), 3 (PMD-B), 4 (PMD-C), 5 (PMD-D), 6 (PMD-E) and 8 (PMD-F), and (b) the five overlapping regions of the six continuous channels 1-6. These PMDs measure the Q component of the Stokes vector. There is also an additional 45° PMD sensor which overlaps PMD-D. This special PMD is required to determine the Stokes U. For channel 7, interpolation between channel 6 and channel 8 has to be used. For channel 1, a theoretical model calculation is used for the wavelength range below 300 nm.

Since we measure the polarisation only at a limited number of wavelengths, interpolating the polarisation parameters to all the wavelengths measured is a significant part of the algorithm. Interpolation is not only necessary for wavelength but also for time, because of the clustered readout not all polarisation points are available at all times. Thus the algorithm requires that the atmospheric polarisation behaves as a smooth function both of wavelength and of time (or equivalently: ground scene). This requirement is not always met, especially at those locations in the orbit where the instrument scans through the rainbow, where polarisation changes rapidly with wavelength during the scanning. For this reason, observing geometries where a rainbow may occur are flagged.

The polarisation correction algorithm is basically the same as in GOME, with the following differences:
- For UV theoretical point solar angles are taken at TOA (70 km) instead of at h=30 km
- The connection of the UV parametrisation ("GDF") to points in the visible is slightly different
- Information from the 45° PMD is used to estimate the full Stokes vector

The latter is especially important for Limb geometry, but may also improve the polarisation correction for Nadir observations.

Since we measure Stokes U only for PMD 45° near 850 nm, interpolation is needed to derive it for the other wavelengths. The assumption is made that polarisation angle is given by a theoretical calculation of the Rayleigh scattering below a wavelength λ_{Ray} and by the 850 nm value above a wavelength λ_{Aer}. In-between a linear interpolation in polarisation angle is used. A practical problem with this interpolation is that the interpolated Stokes U may run into a singularity due to measurement errors when the polarisation angle approaches 45°. Presently this is simply solved by setting a limit on U when this threatens to happen. Whereby it should be noted that the instrument efficiency is only weakly dependent on U, so that even large errors in U may result in small errors on the calibrated radiance.

Unlike geolocation, which is only calculated in units of the smallest ground pixel, polarisation is calculated for all available ground pixels sizes contained in the size of the largest ground pixel. This is done because faster readouts for selected clusters may lead to incomplete knowledge of polarisation vs. wavelength; when polarisation is simply averaged to get the values for 'large pixels' we do not use all available information.

ACKNOWLEDGEMENTS

The author wishes to thank W. Balzer, B. Aberle, T. Wieland, and U. Böttger at DLR, and C. Caspar at ESTEC, for valuable feedback.

REFERENCES

1. Burrows, J. P., K. Chance, P. Crutzen, J. Fishman, J. Fredericks, J. Geary, T. Johnson, G. Harris, I. Isaksen, H. Kelder, G. Moortgat, C. Muller, D. Perner, U. Platt, J. -P. Pommereau, H. Rodhe, E. Roeckner, W. Schneider, P. Simon, H. Sundquist, and J. Vercheval, SCIAMACHY Phase A Study Scientific Requirements Specification, 1991
2. SCIAMACHY Level 0 to 1b Processing, Ground Processing Performance Requirements,ENV-TN-DLR-SCIA-0004, Draft, August 1996
3. Scientific Requirements Document for Data and Algorithm Development, SCIAMACHY Algorithm Development and Data Usage Subgroup, Issue 2A, January 1998
4. GOME Interim Science Report, edited by T. D. Guyenne and C. J. Readings, SP-1151, ESA publications Division, ESTEC, Noordwijk, The Netherlands, ISBN 92-9092-041-6, 1993
5. GOME Users Manual, ESA SP-1182, ESA/ESTEC, Noordwijk, The Netherlands (1996)
6. GOME Level 0 to 1b Algorithm Description, ER-TN-DLR-GO-0022, Issue 4/A, August 1996
7. SCIAMACHY Calibration Plan, PL-SCIA-1000TP/022, Issue 2, 22.1.96
8. SCIAMACHY Level 0 to 1b Processing, Detailed Processing Modules / Parameter Data List, ENV-TN-DLR-SCIA-0006, Issue 1, March 1998
9. SCIAMACHY Level 0 to 1b Processing, Input/Output Data Definition, ENV-TN- DLR-SCIA-0005, Issue 4/C, August 1998

SCIAMACHY LEVEL 1b to 2

ALGORITHM THEORETICAL BASELINE DOCUMENT

Review Presentation

Robert J. D. Spurr

Harvard Smithsonian Center for Astrophysics
60 Garden Street, Cambridge, MA 02138, USA
phone +1 617 496 7819, fax +1 617 495 7389
email rspurr@cfa.harvard.edu

Abstract

This paper is an up-to-date summary of the algorithms under development for the SCIAMACHY Ground Processor (SGP) for level 1b to 2 data processing, as described in the latest version of the Algorithm Theoretical Baseline Document (ATBD) for SCIAMACHY level 1b to 2. Full details may be found in the ATBD itself. Both the Off-line (OL) and Near Real Time (NRT) processing elements are covered.

The two main sections are essentially the same as the first two chapters of the ATBD itself. The first section outlines the document scope, current status, the level 2 product summary and the relation to GOME data processing. The second part of the paper contains algorithm summaries. This includes not only those algorithms now under development and reviewed at ESAMS, but also algorithms to be developed and described in the ATBD for launch and beyond.

1. Introduction to the ATBD

1.1 Document Scope

SCIAMACHY (SCanning Imaging Absorption SpectroMeter for Atmospheric CHartographY) will be included as part of the payload of the ESA (European Space Agency) ENVISAT-1 platform to be launched in the year 2000. The main scientific objective of SCIAMACHY is to measure distributions of a number of chemically important atmospheric trace species on a global basis. SCIAMACHY has a spectrometer and telescope system designed to observe light transmitted through and reflected and scattered from the earth's atmosphere over a spectral range of 240-2400 nm. It has an alternate limb and nadir viewing capability, and will be able to perform solar and lunar occultation measurements (Refs. 1, 2).

Nadir UV/visible measurements will provide global column distributions of O_3, NO_2 and a number of other trace species (BrO, H_2CO, OClO, SO_2 and possibly ClO), and height-resolved profiles of O_3. Nadir infrared measurements will generate column distributions of CO_2, H_2O, CH_4, CO and N_2O. Limb observations will provide vertical profiles of many of these species, with particular emphasis on O_3 and NO_2 (UV/visible) and H_2O, CH_4, CO and N_2O (infrared). Limb profiles of pressure and temperature will be generated from CO_2 absorption signatures near 2000 nm, and possibly from O_2 *A* band measurements (~760 nm). Vertical profiles will also be obtained from solar occultation measurements. Aerosol profiles will be available from limb/occultation retrievals. Cloud parameters and additional aerosol parameters will also be produced from a number of pre-processing algorithms.

Specific scientific requirements on algorithms to retrieve trace gas constituents and other geophysical parameters have been laid down in the Report of the SCIAMACHY Algorithm Development and Data Usage (SADDU) subcommittee (Ref. 3). The design, implementation and maintenance of the SCIAMACHY Off-line Level 1b to 2 processor are the responsibility of the DLR (German Remote Sensing Data Centre). Operational level 1b to 2 Near Real Time algorithms for SCIAMACHY will be implemented by an industrial consortium, on the basis of a sets of detailed product and algorithm specifications provided by DLR (Refs. 4, 5).

Issues of this ATBD from the present to the time of launch will be restricted to algorithms implemented for the retrieval of an established list of level 2 products to be generated on a routine basis at the time of launch. In the interim, it is expected that ongoing scientific investigations will result in changes to some of the algorithms; the development of algorithm prototypes will also generate modifications. This is particularly true for the OL algorithms; there is less flexibility with the NRT processor.

Post-launch updates of this ATBD will reflect experience gained from operational processing during and after the commissioning phase. The algorithms will be fine-tuned in response to results and feedback from verification and validation programmes, and further improved on the basis of relevant scientific research. Once the basic algorithms described in the pre-launch issues of the ATBD are functioning, post-launch updates will probably contain descriptions of

synergies between nadir and limb SCIAMACHY products.

1.2 Document History, Current Status

The original draft of the ATBD was prepared by R. Spurr (Harvard-Smithsonian Center for Astrophysics) in May 1998. This first draft was written as part of the document package produced for the SCIAMACHY Data Processing ADC Review Meeting (June 15, 1998). A number of comments received after this meeting were incorporated in the first issue (July 1998). The first issue was confined to off-line developments.

In September 1998, ESA requested a new ATBD for the level 1b to 2 NRT algorithms. Since the group of NRT algorithms is for the most part a subset of that for the OL, it was agreed that NRT descriptions could be incorporated in the existing document. The second issue was prepared for release in mid-December 1998, in time for the ESAMS conference (18-22 January 1999). In addition to the new material on NRT applications, the section on limb retrieval has been considerably expanded.

In all of the summaries listed in Chapter 2, special considerations for NRT algorithms are noted in italic script. Please note also that the Review Presentation of this ATBD was given by invitation (there was no formal review process at ESAMS for SCIAMACHY ATBDs).

1.3 Level 2 Product Summary

In the AO proposal (Ref. 6), the following gases were targeted for measurement: O_2, O_3, O_4, NO, NO_2, NO_3, CO, CO_2, H_2CO, CH_4, H_2O, SO_2 and possibly ClO and OClO under ozone hole conditions. As a result of the initial sensitivity analysis, N_2O, BrO and O_2 ($^1\Delta_g$) were then included. This list constitutes the set of primary scientific mission objectives. Secondary mission objectives include pressure and temperature profile generation, the determination of selected cloud and aerosol properties, and the derivation of tropospheric distributions from combined limb/nadir results. Detailed discussion of scientific objectives for SCIAMACHY may be found in the Phase A Study Report (Ref. 1), and the Scientific Requirements Document (Ref. 7).

On the basis of the SADDU report on algorithm requirements and as a result of a number of discussions at SCIAMACHY Scientific Advisory Group (SSAG) meetings, a table of SCIAMACHY Data Products was generated by the SSAG; this is given below in Table 1. The basic division here is between nadir-mode total column retrieval products and limb stratospheric profile retrieval products on the one hand, and between off-line (OL) and the fast delivery (NRT) products on the other. Table 1 does not include occultation or nadir profile retrieval products; these have lower priority at present; they include O_3 profiles (nadir) and the set of occultation stratospheric profiles (very similar to the list for limb in Table 1).

	Nadir Total Column Amount			Limb Stratospheric Profiles		
	UV-Vis	*IR*	*UV-IR*	*UV-Vis*	*IR*	*UV-IR*
FD	O_3	H_2O	Clouds			
	NO_2	N_2O	Aerosol			
	BrO	CO				
	SO_2	CH_4				
	OClO					
	H_2CO					
OL	O_3	H_2O	Clouds	O_3	H_2O	Aerosol
	NO_2	N_2O	Aerosol	NO_2	N_2O	
	BrO	CO		BrO	CO	
	SO_2	CO_2			CO_2	
	OClO	CH_4			CH_4	
	H_2CO				P, T	
	UV Index					

Table 1: ***Baseline list of proposed geophysical parameters to be retrieved at the start of operational SCIAMACHY data processing.***

With the exception of the UV Index, the present ATBD will describe all algorithms for off-line and near real time products as listed in the above table. The nadir O_3 profile algorithm will also be described below; even though it does not appear in the above table. The status of this algorithm as far as operational development is concerned is not clear; developments will follow in tandem to those for GOME. Occultation algorithms will be summarised in the ATBD and mentioned briefly in the present paper. Discussion of nadir/limb value-added tropospheric products is beyond the scope of the ATBD.

Since SCIAMACHY channels 1 to 4 are similar in scope to those for GOME, the latter algorithms have been taken over for use in the UV/visible nadir column retrievals for SCIAMACHY (see next section). The first major new development for SCIAMACHY was the specification and generation of an operational prototype algorithm for the NRT processor. This will retrieve total column amounts of trace species (CO, N_2O and CH_4) from channel 7 and 8 nadir measurements.

This algorithm will be taken over for the OL processor, and given greater flexibility and power without the constraint of NRT performance limitations. For the off-line products, limb and occultation retrieval algorithms must be developed from scratch; the first operational prototypes are now under development, and have received their first description in the ATBD.

1.4 Relation to GOME Data Processor

The Global Ozone Monitoring Experiment (GOME) was originally conceived as a scaled-down version of SCIAMACHY. It was given fast-track development status by ESA, and was launched on 21 April 1995 on board the second European Remote Sensing Satellite (ERS-2). It has been in successful operation since launch. It has 4 spectral channels covering the range 240-790 nm, and is a nadir-only instrument. The measurement capability of GOME closely matches the UV/visible nadir capability of SCIAMACHY; the mission objectives are very similar. For details of the instrument, see Ref. 8.

The GOME Data Processor (GDP) was developed and implemented at DLR with the help of several scientific institutions. GDP became operational in July 1996, with earthshine spectra and retrieved total O_3 columns the main products generated on a routine basis (Ref. 9). Total column amounts of NO_2, H_2CO, SO_2, OClO and BrO have been retrieved successfully from GOME back-scatter measurements. The experience gained with GOME in the implementation of operational nadir UV-visible total column retrieval will be invaluable, as there is considerable overlap with SCIAMACHY. Parts of the current ATBD are based on descriptions found in the GDP technical documentation (Ref. 10).

The main algorithm in GDP is the DOAS (Differential Optical Absorption Spectroscopy) fitting for the retrieval of O_3 and NO_2 columns; this can be used directly for SCIAMACHY OL and NRT applications. It is expected that an updated form of the current cloud pre-processing algorithm in GDP will be adapted for SCIAMACHY OL, to include a new PMD cloud-clearing algorithm for cloud fractional cover (the cloud treatment in NRT will be confined to this latter development).

Substantial progress has been made in GOME studies with height-resolved O_3 profile retrieval algorithms, and developments in this field for SCIAMACHY will run in tandem with those for GOME. Study work done for GOME under the aegis of ESA is of relevance to several aspects of SCIAMACHY Data Processing (Cloud and aerosol studies, DOAS retrieval studies, Ring scattering studies). See for example Refs. 11-13.

2. Algorithm Summaries

2.1 Cloud and Aerosol Algorithms

These algorithms will deliver cloud information (fractional cover, cloud optical properties, cloud classification) and initial aerosol information (absorbing index, optical thickness). They are termed 'pre-processing' algorithms; this indicates that they will be the first to be executed in SGP level 1b to 2 processing chain. In particular, the cloud results will be used to correct subsequent UV/visible trace species retrievals for nadir scenes flagged as partially or totally cloudy. There are two main component cloud algorithms; they are listed separately here, but may well be used together in the (off-line) operational processor.

PMD Cloud Coverage Algorithm (PCCA). There are two approaches here, both using sub-pixel PMD (Polarisation Measurement Devices) measurements. One method is based on the use of reflectance and 'colour' thresholds (Ref. 14), the other is based on cloud-free composites (Ref. 15). Both approaches require the dynamic updating of global sets of thresholds or composites. The prototypes recently developed for GOME use 3 PMDs covering channels 2, 3 and 4 of GOME (the 'blue' 'green' and 'red' PMD ranges). The current baseline for SGP will be to use the equivalent 3 PMDs for SCIAMACHY, though it may be possible to use more of the SCIAMACHY PMDs in the infrared (7 PMDs in total).

At present an older version of PCCA is specified for the NRT, but it is expected that the upgrade planned for OL will also be taken on for the NRT.

Revised Cloud Fitting Algorithm (RCFA). An algorithm for the retrieval of cloud optical parameters based on least squares fitting of measured nadir back-scatter intensities with their simulated equivalents in and around the O_2 and O_4 absorption bands in the visible/near-infrared. Main retrieval products will be cloud-top pressure and optical depth; combined with the cloud-cover algorithm, a determination of cloud type will be possible. This is an extension of the original ICFA (Initial Cloud Fitting Algorithm) as developed for GDP. Development of RCFA will again follow that for GOME (Ref. 16). *Not part of the NRT processor.*

Aerosol Absorbing Index Algorithm (AAIA). This index is based on the evaluation of a spectral residue at 340 nm, using an equivalent Lambertian albedo determined from the measured 380 nm back-scatter intensity. The AAI is a measure of presence of soot and dust aerosols that typically show strong UV absorption. The algorithm is stand-alone, and closely follows the original NASA specification (Ref. 17). *Both NRT and OL.*

Aerosol Optical Thickness Algorithm (AOTA). Also intended to be stand-alone, this is a straightforward non-linear least-squares fitting algorithm for the AOT. It uses measurements where trace gas absorption is negligibly small. Developed for operational use in GOME by the Italian Processing and Archiving Facility (see Ref. 18 for details). (Aerosol profiles retrieved from limb and occultation measurements are treated separately). *OL only, not part of the NRT processor.*

2.2 UV/visible Trace Gas Column Retrieval

Applies to NRT and OL.

This algorithm is the one that most closely matches the corresponding DOAS algorithm in GDP. It is based on the least squares fitting of effective slant

column amounts of certain trace species in the UV and visible parts of the spectrum (see Ref. 19 for a review). The DOAS method will be one of the major options: here, optical densities are fitted linearly for trace gas column amounts, and a low-order polynomial in wavelength approximates broad-scale spectral features due to Rayleigh and aerosol scattering, aerosol extinction and surface reflectance.

In DOAS, the multilinear regression is embedded within a non-linear fit for the 'shift and squeeze' parameters to be applied to the reference spectra (due to wavelength calibration uncertainties). One option for trace gas reference cross-sections is to use values derived from pre-flight calibration measurements (O_3 and NO_2 in particular), otherwise cross-sections are taken from literature. Care must be taken with the temperature dependence (O_3 has the well-known quadratic parameterisation for temperature dependence of the Huggins band cross sections). In addition to the trace gas signatures, it is necessary to fit for a differential signature due to inelastic molecular scattering (the Ring spectrum) (Ref. 20).

The baseline will be two windows optimised for O_3 and NO_2 retrieval. Another option to be considered will be the direct non-linear least squares fitting of radiance to determine slant columns. Recent developments with GOME have demonstrated its ability to measure BrO, H_2CO, OClO and SO_2 (Refs. 21-23). Both the SCIAMACHY OL and NRT algorithms will include fitting windows for these species. Columns of O_3, NO_2, BrO, SO_2 and H_2CO will be retrieved on a global basis, while OClO will be retrieved in special cases only (ozone hole scenarios).

The second half of this algorithm is a simulation of the Air Mass Factor (AMF), by which the slant column is divided to get a geometry-independent vertical column result. The AMF represents the enhancement of absorption due to slant path passages through the atmosphere. Experience with GOME has shown that it is preferable to use look-up tables of AMFs in an operational data processing environment, rather than calculate them from scratch using radiative transfer code. Multiple scattering must be accounted for in the simulation of back-scattered intensities.

In the NRT specifications, the conversion to vertical column amounts will be done using a single Air Mass Factor for each trace species and fitting window (this is the classical DOAS approach). So far, AMF look-up tables have been generated only for O_3 (at 325 nm) and NO_2 (at 437.5 nm); results for other trace species will remain as slant columns.

The development for GOME of improved O_3 and NO_2 profile climatology (see for example Ref. 24 for O_3) for the generation of new AMF look-up tables for these species will be incorporated as part of the SCIAMACHY OL algorithms (NRT specifications were frozen before these developments started). The use of profiles classified by column amount in these climatologies allows for the iteration of AMFs and retrieved vertical column amounts. This acts as a kind of quality control on the AMF part of the retrieval (Ref. 25), and is especially relevant in scenarios such as the ozone hole where the AMF depends strongly on the profile shape and total column content.

2.3 Infrared Trace Gas Column Retrieval

Applies to NRT and OL.

This algorithm is based on the direct (non-linear) least-squares fitting of nadir back-scatter spectra measured by SCIAMACHY's infrared channels (channel 7, 1940-2040 nm, channel 8 2265-2380 nm). Vertical column amounts are fitted directly; there is no Air Mass Factor conversion. The algorithm assumes that the back-scatter intensity can be approximated by the solar path transmittance term multiplied by a closure term (low order polynomial in wavelength). Scattering contributions are thus proportional (up to closure) to the transmittance term – an approximation that is valid provided the absorption optical depths are small.

The calculation of the solar path transmittance term is reasonably exact. Line-by-line calculations are carried out at each layer of the reference atmosphere to obtain high-resolution cross-sections. These are combined with ray-traced slant path geometrical factors and volume mixing ratios to obtain cumulative atmospheric transmittance values. The latter are then convoluted with the instrument response function to the wavelength grid of the measurements.

In channel 8, a small selection of micro-windows will highlight retrieval of the relevant species. Only a few absorption lines of CO and N_2O will generate detectable signatures in the SCIAMACHY back-scatter spectrum, and these two gases are the drivers. CH_4 and H_2O are easy to detect in this channel, but they must be included as interfering species in the key CO and N_2O retrievals. The low optical depth requirement of the transmittance-closure approximation is another restraint on window determination (avoid deep CH_4 and H_2O lines).

CO_2 columns can be retrieved from measurements at the upper end of channel 7 (2030-2040 nm). CO_2 absorption is relatively weak here, and it is then possible to use the transmittance/closure approximation. There are only a few interfering H_2O lines in this region.

Studies have shown that this kind of retrieval for CO and N_2O is sensitive to the instrument response width as required by the convolution of high resolution transmittance values (Ref. 26). Until recently, there has been serious concern that the instrument resolution in channel 8 has not been good enough for meaningful CO and N_2O retrieval. It was reported at the ESAMS meeting that this detector focussing problem for channels 7 and 8 has now been solved in a timely manner for SCIAMACHY (FWHM now ~2.1 pixels).

This algorithm can be adapted with only a few modifications for the derivation of the pressure height of an equivalent Lambertian reflecting surface at the lower boundary of the atmosphere. This assumes that the CO_2 content is known, and it uses a window near 2030 nm in channel 7 (relatively low optical depth).

It is more consistent to execute this CO_2 height fit first before attempting the CO and N_2O trace gas retrievals; the height result is used as the lower boundary in the subsequent retrieval of these trace species from Channel 8 infrared measurements. This option has been integrated into the operational NRT and OL algorithms. Apart from this, it is anticipated that all results from the infrared absorption spectroscopy algorithm will be stand-alone (no synergy with UV/visible results or with output from the cloud pre-processing algorithms).

The OL version of this algorithm will include a full line-by-line capability for cross section evaluation for a wide range of temperature and pressure conditions; the use of sets of correlated-k coefficients for these cross-sections is also under investigation (Ref. 27). The OL algorithm will also have a ray-tracing formalism in a curved refracting atmosphere.

The NRT algorithm will use look-up tables of pre-computed trace gas cross-section templates at a high resolution, and an additional table of ray-traced slant path factors. In the specification documents for NRT, the algorithm is named BIAS (Basic Infrared Absorption Spectroscopy).

2.4 UV/visible Limb Profile Retrieval

Off-line only.

At the time of writing, there are still unresolved questions about the overall retrieval strategy for limb profiles. In order to keep options open, both onion peeling and global fit methods will be considered (and perhaps an admixture of the two). There is also a distinction between P-T retrieval and trace gas volume mixing ratio (VMR) (or concentration) vertical profiles. In both cases, aerosol scattering profiles will be retrieved simultaneously. The use of optimal estimation or unconstrained non-linear least-squares has also not been decided for the various limb and occultation applications.

Ideally, P-T retrieval should be performed first, to allow the retrieved temperature and/or pressure profiles to be used in subsequent trace species limb retrievals. So far only the VMR limb retrieval in the UV/visible has received some development in the operational context., and the current version of the ATBD contains some description of the ray-tracing forward model.

The *VMR profile limb algorithm* retrieves volume mixing ratios (VMRs) of selected trace species for layers defined by the limb scan sequence (scan elevation steps translate to tangent height separations of ~3.1 km). For SCIAMACHY channels 1 to 4, the main emphasis is on measurements from the UV (O_3) and visible parts of the spectrum (NO_2, O_3). From two or more micro-windows in channel 8, this algorithm can also retrieve VMRs for trace species N_2O, CO and CH_4 (and possibly H_2O); CO_2 limb profiles can be retrieved from channel 7 measurements. In all cases, aerosol scattering and extinction profiles will be retrieved in conjunction with the main output.

The algorithm will retain options on the use of optimal estimation versus non-linear least squares. It is likely that the first version of the prototype will use the global fit technique (Ref. 28), especially for the UV/visible applications. Also it is probable that 'measurements' as defined in this algorithm will actually be ratios of limb scan radiances at two different tangent heights. This is the approach adopted for the SOLSE/LORE instruments (Ref. 29). It has the advantage that to first order, diffuse scatter contributions from lower troposphere 'cancel out' in the ratio of simulated radiances.

Radiative transfer (RT) for limb scatter retrieval is difficult and time-consuming. The baseline approach will be to perform the single scatter simulations from scratch, and to use correction factors for multiple scatter contributions. The correction factors will be generated off-line using a state-of-the-art fully spherical RT code.

Ray tracing code has been written for the single scatter modelling. Single scatter simulations will be quasi-analytic functions of the retrieval parameters, thus allowing for reasonably exact computations of the Jacobean parameter derivatives (weighting functions) required for non-linear iterative fitting. To first order, it is assumed that the multiple scatter correction terms have no retrieval parameter dependence

Retrieval state vectors will include VMR values at each level of the retrieval height grid, and aerosol scattering and extinction coefficients at these levels. Since there are a number of spectra in a limb scan sequence, we also require a Ring scaling parameter to be fitted for each limb spectrum. Since all targeted species' cross-sections are temperature-dependent, it is important to have accurate and representative P-T profiles. Ideally one should use already-retrieved limb P-T results; failing that, the baseline will be the use of assimilated meteorological data (analysis fiesld from ECMWF for example).

New developments on this algorithm will be coming along in 1999, and it is anticipated that the appropriate sections in the ATBD will be expanded considerably later this year.

2.5 Nadir O_3 Profile Retrieval

(Not in the NRT processor).

This is based in part on the BUV technique (Ref. 30), where the wavelength dependence of O_3 scattering heights in the UV below 300 nm is used to infer

stratospheric O_3 profiles. The algorithm also takes advantage of the temperature dependence of the Huggins bands O_3 absorption (300 - 360 nm) to extract height-resolved information in the troposphere (Ref. 31); inclusion of points in the visible (Chappuis) O_3 absorption region may also provide an additional constraint.

The algorithm uses an iterative optimal estimation technique to update the state vector of profile components. Optimal estimation requires the use of *a priori* values to constrain the fitting problem. In the case of O_3, a priori profiles may be taken from the SAGE II climatology.

The forward part of the algorithm requires repeated calculation of intensities and their parameter derivatives (weighting functions). Radiative transfer simulations (Ref. 32) must be performed with full multiple scatter, and this is (at present) prohibitively time-consuming for realistic inclusion in an operational environment.

However, results derived from GOME back-scatter measurements for special scenarios and campaigns have shown clearly the feasibility of this technique (Refs. 33, 34). It is anticipated that an operational algorithm will be implemented for GOME once the performance bottleneck is overcome (perhaps with the help of extensively parameterised look-up tables). This is currently under investigation at a number of institutions. Developments for SCIAMACHY will follow closely those for GOME.

2.6 Other Algorithms

The following algorithms have not yet started their development as part of the operational level 1b to 2 SGP. At present there is no detailed description of them in the ATBD, but they are summarized in the document and also below. They were omitted from the review presentation. They will not be part of the NRT processor.

The P-T profile limb algorithm. This algorithm will use non-linear least squares or optimal estimation fitting to derive profiles of temperature and pressure from limb scatter measurements of CO_2 in channel 7. Fitting windows for each limb scan must be selected to include suitable combinations of pressure and temperature sensitive CO_2 absorption lines. The atmosphere is assumed to be in hydrostatic equilibrium; exact knowledge of the pressure and temperature at one height will enable the tangent heights to be retrieved.

Simulation of limb scatter intensities and associated weighting functions will be carried out quasi-analytically in the single-scatter line-by-line approximation; multiple scattering effects (small in this part of the spectrum) will again be parameterised, probably with the use of look-up tables of correction factors.

Aerosol scattering and extinction profiles will be retrieved in conjunction with the atmospheric variables. CO_2 amounts are assumed known, and should be taken from a suitable data record (Mauna Loa, for example). Pressure and temperature profiles may also be retrieved from O_2 *A* band limb back-scatter measurements around 760 nm, but this is still under investigation. The question of onion peeling versus global fitting has not been resolved yet for this algorithm.

Occultation algorithms. In principle, the list of products defined for the first limb profile retrievals in SGP (see table 1) can also be retrieved for solar occultation measurements. There is scope for only a few occultation products per orbit due to the limited time (~ 60 seconds) spent in this viewing mode. The forward simulation part of the retrieval algorithms is simpler, because it requires only computation of direct-beam transmittances (scattering can be neglected). Though measurement signal-to-noise and corresponding retrieval precision are high, the retrieval may be hampered due to radiance calibration (and possibly also wavelength calibration) problems resulting from the measurement strategy employed by SCIAMACHY.

2.7 Input/Output and Reference Database Overview

The main input to the level 1b to 2 section of the whole SCIAMACHY Data Processor is the level 1b product, comprising measurements for nadir, limb and occultation states, and an extra-terrestrial sun reference spectrum taken by the instrument. Each atmospheric measurement contains a number of observation records (geolocation information and spectra).

Also required as input is a list of parameters controlling the execution of the component algorithms in level 1b to 2 processing; this comprises the 'Initialisation File'. Additional real-time ancillary data may also be required (assimilated meteorological forecast/analysis fields, CO_2 data for example).

Main output will be level 2 products, as specified in Ref. 35 for the Off-line and Ref. 4 for NRT. Each component algorithm will generate its own component output data set, in addition to the housekeeping and geolocation data required for completeness. In addition to retrieved parameter values, solution covariance output from the fitting algorithms will be specified where possible, though no detailed spectral information will be included in the level 2 products. During the testing and commissioning phases, detailed results and scenarios will also be generated as part of the output.

Reference data may be divided into three classes. The first class contains fixed global and climatological data sets (topography, surface properties, atmospheric profiles including *a priori* values) and reference spectra (spectroscopic line parameters, absorption and

Ring effect cross sections, aerosol and cloud optical properties).

The second class comprises fixed pre-calculated look-up tables of radiative transfer simulated data. These include AMFs for the UV/visible column retrievals, correlated-k coefficients and line-by-line cross sections for the infrared retrievals and multiple scatter correction factors for limb retrievals.

The third class contains data sets that are pre-calculated for each orbit. This will include the preparation of instrument response functions required for the convolution of high-resolution templates to instrument wavelength grids, and the generation of any under-sampling reference spectra required for the least squares column and profile fitting.

Also required for the cloud coverage algorithms are threshold or cloud composite data sets, for which a dynamic update procedure needs to be defined.

3. REFERENCES

1. Burrows, J. P., K. Chance, P. Crutzen, H. van Dop, J. Geary, T. Johnson, G. Harris, I Isaksen, G. Moortgat, C. Muller, D. Perner, U. Platt, J. -P. Pommereau, H. Rodhe, E. Roeckner, W. Schneider, P. Simon, H. Sundquist, and J. Vercheval., SCIAMACHY Phase A Study Scientific Requirements Specification, 1991

2. SCIAMACHY Instrument Requirements Document, PO-RS-DAR-EP-0001, Issue 3/1, December 1995

3. Scientific Requirements Document for Data and Algorithm Development, SCIAMACHY Algorithm Development and Data Usage Subgroup, Issue 2A, January 1998

4. SCIAMACHY Level 1b to 2 NRT Processing, Input/Output Data Definition, ENV-TN- DLR-SCIA-0010, Issue 3/A, 16. July 1998

5. SCIAMACHY Level 1b to 2 NRT Processing, Detailed Processing Modules/Parameter Data List, ENV-TN-DLR-SCIA-0011, Issue 2, 7. July 1998

6. Burrows, J. P., K. Chance, P. Crutzen, J. Fishman, J. Fredericks, J. Geary, T. Johnson, G. Harris, I. Isaksen, H. Kelder, G. Moortgat, C. Muller, D. Perner, U. Platt, J. -P. Pommereau, H. Rodhe, E. Roeckner, W. Schneider, P. Simon, H. Sundquist, and J. Vercheval, SCIAMACHY A European proposal for atmospheric remote sensing from the ESA polar platform, Max-Planck Institut fuer Chemie, Mainz, Germany, 1988

7. SCIAMACHY Requirements Document, SCIAMACHY Scientific Advisory Group, Issue 1A, in preparation, May 1998

8. GOME Users Manual, ESA SP-1182, ESA/ESTEC, Noordwijk, The Netherlands (1996)

9. Loyola D., B. Aberle, W. Balzer, K. Kretschel, E. Mikusch, H. Muehle, T. Ruppert, C. Schmid, S. Slijkhuis, R. Spurr, W. Thomas, T. Wieland and M. Woltmueller, Ground Segment for ERS-2 GOME Sensor at the GERMAN D-PAF, Proceedings of the 3rd ERS Symposium Space at the Service of our Environment, SP-414, 591-596, Florence, Italy, March 1997

10. GOME Level 1 to 2 Algorithm Description, ER-TN-DLR-GO-0025, Issue 2, August 1996

11. Detailed Analysis of the Retrieval Algorithms Selected for the Level 1-2 Processing of GOME data, Final Report, ESA/SERCO 10728/94/NL/CN, July 1995

12. A Study on the effects of Scattering on the Monitoring of Atmospheric Constituents, volume 2: Albedo and Cloud Studies, ESA/ESTEC Final Report, 9740/91/NL/BI, 1994.

13. Study of the Ring effect, Final Report, ESA/SERCO 10996/94/NL/CN, 1996

14. GOME Cloud and Aerosol Data Products Algorithms Development (CADAPA) Study, Final Report, 11572/95/NL/CN, February 1998.

15. Loyola, D., A New Cloud Recognition Algorithm for Optical Sensors, Proceedings of the IGARSS Conference, Seattle, USA, July 1998

16. Kurosu, T. P., K. V. Chance and R. J. D. Spurr, CRAG – Cloud Retrieval Algorithm for ESA's Global Ozone Monitoring Experiment, ESAMS conference, ESTEC, Holland (January 99)

17. Hsu N. C., J. R. Herman, P. K. Bhartia, C. J. Seftor, O. Torres, A. M. Thompson, J. F. Gleason, T. F. Eck and B. N. Holben, Detection of biomass burning smoke from TOMS measurements, *Geophys. Res. Lett.*, **23**, 745-748 (1996)

18. Levoni, C., M. Cervino, R. Guzzi and F. Torricella, Atmospheric aerosol optical properties: a database of radiative characteristics for different components and classes, *Applied Optics*, **36**, 8031-8041 (1997)

19. Platt, U., Differential optical absorption spectroscopy (DOAS), in Air Monitoring by Spectroscopic techniques, ed. M. Sigrist, *Chem. Anal. Ser.*, **127**, 27-84 (1994)

20. Chance K., and R. J. D. Spurr, Ring Effect Studies: Rayleigh Scattering, Including Molecular Parameters for Rotational Raman Scattering, and the Fraunhofer Spectrum, *Applied Optics*, **36**, 5224-5230 (1997)

21. Eisinger, M., and J. P. Burrows, Tropospheric Sulfur Dioxide Observed by the ERS-2 GOME Instrument, *Geophys. Res. Lett.*, **25**, 4177 (1998)

22. Chance K., Analysis of BrO Measurements from the Global Ozone Monitoring Experiment, *Geophys. Res. Lett.*, **25**, 3335 (1998)

23. Perner, D., T. Klüpfel, E. Hegels, P. J. Crutzen, and J. P. Burrows, First results on tropospheric observations by GOME, Proceedings of the 3rd ERS Symposium Space at the Service of our Environment, SP-414, 647-652, Florence, Italy, March 1997

24. Wellemayer, C. G., S. L. Taylor, C. J. Seftor, R. D McPeters and P. K. Bhartia, A Correction for TOMS Profile Shape Errors at High Latitude, *J. Geophys. Res.*, **102**, 9029- 9038 (1997)

25. Spurr, R. J. D.,Improved climatologies and new Air Mass Factor look-up tables for O_3 and NO_2 column retrievals from GOME and SCIAMACHY back-scatter measurements, ESAMS conference, ESTEC, Holland (January 99)

26. Spurr, R. J. D., and K. Chance, BIAS: An algorithm for the retrieval of trace gas vertical column amounts from near-infrared earthshine measurements by the SCIAMACHY spectrometer, Proceedings of the IGARSS conference, Seattle, USA, July 1998

27. Buchwitz, M., V. V. Rozanov, and J. P Burrows, A correlated-k distribution scheme for the radiative transfer models GOMETRAN and SCIATRAN, ESAMS conference, ESTEC, Holland (January 99)

28. Carlotti, M., Global-fit approach to the analysis of limb-scanning atmospheric measurements, *Applied Optics*, **27**, 3250-3254 (1988)

29. SOLSE/LORE, Shuttle Ozone limb Sounding Experiment, Limb Ozone Retrieval Experiment, NASA/GSFC, launched November 1997

30. Bhartia, P. K., R. D. McPeters, C. L. Mateer, L. E. Flynn, C. Wellemeyer, Algorithm for the Estimation of Vertical Ozone Profiles from the Backscattered Ultraviolet Technique, *J. Geophys. Res.*, **101**, 18793-18806 (1996)

31. Chance, K., J. P. Burrows, D. Perner, and W. Schneider, Satellite measurements of atmospheric ozone profiles, including tropospheric ozone, from UV/visible measurements in the nadir geometry: a potential method to retrieve tropospheric ozone, *J. Quant. Spectrosc. Radiat. Transfer*, **57**, 467-476 (1997)

32. Rozanov, V. V., T. Kurosu and J. P. Burrows, Retrieval of atmospheric constituents in the UV/ visible: A new quasi-analytical approach for the calculation of weighting functions, *J. Quant. Spectrosc. Radiat. Transfer*, **60**, 277 (1998)

33. Munro, R., R. Siddans, W. J. Reburn, and B. J. Kerridge, Direct measurement of tropospheric ozone distributions from space, *Nature*, **392**, 168-171 (1998)

34. deBeek, R., R. Hoogen, V. Rozanov, and J. Burrows., Ozone profile retrieval from GOME satellite data 1. Algorithm Description, Proceedings of the 3rd ERS Symposium Space at the Service of our Environment, SP-414, 749-754, Florence, Italy, March 1997

35. SCIAMACHY Level 1b to 2 Off-line Processing, Product Specification Document, ENV-PS-DLR-SCI-2200-0004, Issue 1/A, June 1998

Acknowledgements

The author would like to thank colleagues K. Chance and T. Kurosu at SAO for numerous discussions during the preparation and updating of the ATBD. Thanks also to colleagues at DLR for valuable feedback and help with the document preparation. Thanks also to scientists at KNMI (Holland), RAL (UK) and IFE Bremen (Germany) for helpful comments prior to the first release.

Scientific Session

Ozone: Measurement, Validation & Results

Chair: J.P. Burrows, *University of Bremen*

NASA's Experience with UV Remote Using SBUV and TOMS Instruments

Pawan K. Bhartia (NASA Goddard Space Flight Center, USA)

This paper will discuss key features of the NASA algorithm that has been used to produce several highly popular geophysical products from the SBUV and TOMS series of instruments. Since these instruments have a limited number of wavelengths, many innovative algorithmic approaches have been developed over the years to derive maximum information from these sensors. We will use GOME data to test the assumptions made in these algorithms and show what additional information is contained in the GOME hyperspectral data. At NASA we are using this information to improve the SBUV and TOMS algorithms, as well as to develop more efficient algorithms to process GOME data.

THE SAGE III INSTRUMENT AND LEVEL-1 DATA CORRECTIONS

R. E. Veiga
Science Applications International Corporation, Hampton, Virginia USA

W. P. Chu
NASA Langley Research Center, Hampton, Virginia USA

A. J. Ray
Ball Aerospace Technologies Corporation, Boulder, Colorado USA

e-mail: r.e.veiga@larc.nasa.gov, w.p.chu@larc.nasa.gov,aray@ball.com

ABSTRACT

The EOS program for long term global change monitoring of certain atmospheric constituents includes three Stratospheric Aerosol and Gas Experiment III (SAGE III) instruments. The first will be launched on a Russian platform in mid-1999. The instrument is a self-calibrating Sun photometer with scanning optics which samples the spectrum in the 280-1030nm wavelength range using a CCD array. The IFOV provides 0.5km vertical resolution at the tangent point. The solar Level-2 species retrieval is driven by the Level-1B atmospheric transmission measurements in 86 wavelength bands. Prior to Level-1B processing the digitized counts must be corrected for instrument effects with a Level-1A algorithm. The discussion herein will focus on instrument characterization data and the correction algorithms necessary for the following effects: spectrometer stray light, CCD substrate scattering into the serial register, dark current, charge transfer efficiency, linearity, wavelength calibration, and etaloning.

1. INTRODUCTION

Over the last two decades a series of successful satellite-borne solar occultation radiometers from the NASA Langley Research Center have provided highly vertically resolved profiles of atmospheric aerosol extinction and gases. SAGE III will continue in this line. The first instrument with be launched in 1999 on a Russian Meteor-3M spacecraft in a polar orbit (Ref.1), and the second on the International Space Station (ISS) in 2002 in an inclined orbit. The third instrument is a Flight of Opportunity (FOO) awaiting mission definition. All three instruments were designed and manufactured by the Ball Aerospace Technologies Corporation. The SAGE III lineage, number of channels, spacecraft, orbital inclination, and years of service are listed in Table 1 below.

Table 1. SAGE III and Heritage Instruments

	ch	spacecraft	orbit	years
SAM	1	Apollo-Soyuz	-	1 day
SAM II	1	NIMBUS 7	98°	16
SAGE I	4	AEM-B	53°	3
SAGE II	7	ERBS	57°	15
SAGE III	12	Meteor	96°	-
SAGE III	12	ISS	51°	-

The Stratospheric Aerosol Measurement (SAM) flew on the Apollo-Soyuz Mission in 1975. It sampled 4 extinction profiles was the 'proof of concept' instrument, and paved the way for the subsequent SAM II, SAGE I, and SAGE II instruments. SAM II (1978-1993) flew in a polar orbit and provided the first long term history of 1μm extinction profiles, a record which has been credited with the discovery of Polar Stratospheric Clouds (Ref. 2). The 18 years of SAGE I (1997-1981), and SAGE II (1984-present) data have provided two major contributions to the atmospheric sciences community. The first, in conjunction with SAM II, is a global picture of atmospheric aerosol loading variation caused by numerous volcanic eruptions (Refs. 3-5). The second is the long term record of the lower tropospheric and stratospheric ozone profiles which have been instrumental in the ozone trend studies since 1988 (Refs. 6-9).

2. SCIENCE OBJECTIVES

The five science objectives of the SAGE III mission are the following (Ref. 10):

1. Retrieve profiles of atmospheric aerosol, O_3, NO_2, H_2O, NO_3, OCLO, and air density.
2. Characterize tropospheric and stratospheric aerosol, cirrus and clouds, and investigate their effects on Earth's environment including radiative, microphysical, and chemical interactions.
3. Relate the variability (spatial/temporal) of the measured species to atmospheric chemistry, climate processes, and biogeochemical cycles.
4. Extend the SAGE I/II self-calibrating solar occultation record with prime focus on uncertainty reduction in the estimation of long-term trends.
5. Provide atmospheric data essential for the calibration and interpretation of other satellite sensors.

3. THE OCCULTATION MEASUREMENT AND SENSOR DESCRIPTION

The fundamental measurement in the occultation technique is the attenuation of radiation by the Earth's atmosphere as rays from the source traverse the slant-path into the instantaneous field-of-view (IFOV) of the instrument. The attenuation is solely due to gas

absorption, and scattering from molecules, aerosols, and clouds. The heritage instruments have used the Sun as the source, while for SAGE III the Moon and Earth's limb are additional sources. At the onset of an event the instrument's azimuth control system rotates the scan head from stow to a computed (onboard ephemeris calculation) position to acquire the target. During this stow-to-target pointing operation the CCD controller is in data acquisition mode as the IFOV scans dark space, and numerous dark current frames become available for the detector background offset correction. As the target appears in the azimuth sensor system's 4° (1.2° x 2.6° for lunar) FOV, the system's bi-cell locks the elevation axis on a line which passes through the target's radiometric center of brightness, and continues to keep locked to within 45 arc seconds throughout the event's duration. At azimuth lock-on, the elevation system begins to sweep the scan mirror across the target at a nominal 15 arc minutes per second. After the IFOV moves off the target's edge the scan direction reverses, and the cycle repeats. Precise relative positioning of the instrument's IFOV on the target's disk is provided by the elevation system to within 30 arc seconds. This control is needed in order to geolocate the IFOV in the atmosphere in conjunction with the spacecraft position and target's ephemeris. The scan mirror is the front end of a f/4 Dall-Kirkham telescope which images the target disk onto its focal plane. The scan direction is parallel to the spacecraft's nadir direction, hence the atmosphere is scanned vertically. The focal plane contains a 30 by 300μm slit whose footprint projected onto the target corresponds to an angular extent of 0.5 by 5 arc minutes, respectively. Similarly the footprint of the slit at the tangent point of a light ray passing through the atmosphere corresponds to an area of the atmosphere 0.5 km vertically by 5 km horizontally. The focal plane slit also serves as a spectrometer entrance slit past which a fold mirror directs light onto a holographically recorded concave grating operating in the first order. The grating was designed to eliminate astigmatism at the two wavelengths of 440nm and 868nm. The photoactive part of the detector consists of an 809 by 11 CCD array with 30μm pixels. The grating images the entrance slit without magnification onto the CCD, and the effective IFOV of the instrument can be controlled by how many of the 11 'parallel' pixels are sampled. The only optics between the grating and CCD are a plano-concave field flattener, a colored glass order-blocking filter set, and an air gap. The CCD is rotated 10° along the dispersion axis to reduce reflection back onto the grating. Wavelength calibration on the Meteor instrument indicates the dispersion range is 275nm at pixel 1 to 1034nm at pixel 809. The CCD material is 16μm thick in a thinned backside illuminated configuration, and is fused to a thick bulk glass substrate. The entire detector assembly is bonded to a thermo electric cooler for temperature regulation. The detector assembly also consists of a separate InGaAs photodiode with an interference filter to sense light at 1540nm. The diode is aligned to the CCD by a beamsplitting cube to ensure the FOV of the 1540 and the CCD pixels are coincident in the atmosphere. The zeroth order from the grating is the source for the 1540 channel. The 1540nm channel data are also used to reverse the scan direction for solar sampling, while lunar scan direction change is done by averaging a pixel group of the CCD.

CCD AND SAMPLING MODES

In order to optimize the signal-to-noise ratio in conjunction with the blackbody-like spectral signature of the target and the intrinsic spectral response of silicon, the 809 x 11 active pixels of the CCD which receive diffracted light from the grating are electrically isolated into seven segments. Each segment's integration time is programmable. During an event as the IFOV is trained at some position on the target, photons are converted to photoelectrons in each of the parallel pixels for a given integration time. The photoelectrons are then shifted into the serial pixels corresponding to each of the parallels. All 809 serial pixels comprise the serial register, and are blocked from direct illumination by a mask. The electrons in the serial register are then shifted sequentially to a readout node where an analog-to-digital count conversion is done (~75 electrons/count). The sampling cycle repeats itself at a rate of 64Hz (255 Hz internally with 4 sample averaging) as the scan mirror continues to sweep across the target for subsequent samples until the event terminates. Event termination occurs when the target signal reaching the instrument is too low (Sun/Moonset), or when the target reaches the 300km tangent point during a Sun/Moonrise.

There are six programmable modes for sampling the CCD. These are solar, lunar, wavelength calibration, mirror calibration, charge transfer efficiency (CTE), and serial calibration. In the solar mode 86 pixel groups corresponding to the science requirements are derived from the CCD sampling. These pixel groups are shown in Table 2.

Table 2. Operational Solar Science Sampling (Meteor)

Channel	Start λ	End λ	Pix/D*	Species
1	288	292	5/1	O_3/β*
2	383	387	5/1	β
3	433	450	19/19	NO_2/β
4	519	523	5/1	β
5	562	623	30/10	O_3
6	675	678	5/1	β
7	754	758	4/1	β
8	759	771	14/14	P/T
9	867	871	5/1	β
10	933	959	30/30	H_2O
11	1018	1022	6/6	β
12	1525	1554	1/1	β

*Pix/D denotes (number of CCD pixels shifted into the serial register) / (number of samples put into the data stream). In most cases pixels are averaged to produce one data item. β denotes aerosol extinction.

For lunar mode the CCD sampling is more contiguous, with 340 pixel groups sampled. The wavelength range for lunar spans the three spectral regions of 360-680nm, 740-780nm, and 920-960nm. The species retrieval in lunar mode are the same gases retrieved in solar mode with the additional nighttime species of NO_3 and OCLO.

Wavelength calibration mode samples all 809 active pixels while the tangent point lies above the atmosphere. During wavelength calibration the target is scanned as all active pixels are readout in order to produce a pixel-to-wavelength map for the entire CCD. The wavelength calibration regresses the sampled CCD data against the solar spectral irradiance data set of Kurucz (Ref. 11).

Mirror calibration mode is essentially identical to solar mode, in that the same pixels on the CCD are sampled using the same CCD algorithm. The difference lies in the tangent altitude at which the sampling is performed, namely between 150 and 300km.

CTE mode points the instrument's scan head away from any radiant source while the CCD array is sampled in the following manner: 100 pixels at the center of the array are allowed to accumulate charge for a fixed integration time. Since the detector is not illuminated only dark current electrons accumulate in the parallels. The 100 pixels are then readout while all the parallel pixels are set to drain, i.e. no charge is allowed to accumulate in the parallels. In the process of shifting the 100 pixels through the serial register there will be some electrons which will remain in the current serial pixel and not be shifted to the next serial pixel. After all 100 central pixels are readout the serial register continues to be readout thereby producing a set of virtual pixels. Each virtual pixel will contain only dark current electrons, and electrons not shifted out from the previous clock cycle (charge transfer inefficiency). An estimate of the CTE is derived from the ratio of the instrument counts corresponding to the first few virtual pixels to the instrument counts corresponding to the 100 central pixels. The CCD manufacturer's estimate of the CTE is 0.999995, and analyses predict a 3-year end-of-mission life value of 0.9997.

Serial mode sampling of the CCD sets all parallel pixels to drain as the target is scanned above the atmosphere. The serial register pixels are read out in the identical process to that used for solar sampling. The purpose of this mode is quantify the signal which leaks into the serial register while the active pixels are illuminated by the target.

In CCD characterization mode the scan mirror is preset to a fixed azimuth and elevation, and stares at the target. The mode samples the spectrum with all 809 active pixels, and will be utilized primarily in searching for absorption features in the atmosphere, and in etalon phase change detection.

RADIOMETRIC ERROR SOURCES

The requirements for the maximum radiometric error when the SAGE III instrument views the Sun above the atmosphere are as follows: (1) random error must be less than 0.05%, (2) systematic bias must be less than 0.1%, and (3) stability must be less than 0.03% of the target signal during an event. The instrument vendor has isolated the components of each of the above error sources as follows:

1. (random) quantizing noise, dark current, readout noise, and processing noise
2. (systematic) linearity, offset bias, stray light, red leakage, CTE calibration, and scan mirror calibration
3. (stability) electronic drift, quantum efficiency stability, temperature stability, etalon effects

Data acquired during instrument testing indicate that the errors from most of the above sources are within specification. Several effects must be managed with algorithms in order to meet specifications, and these will be discussed below.

Mirror Angle. The scan mirror reflectivity depends on view angle and wavelength. Relative reflectance differences of up to 0.6% throughout the range of mirror travel can occur during an event. For the full range of mirror angles experienced in an event, the SAGE III scan mirror reflectance has been shown to be a linear function of view angle. Relative mirror reflectance measurements will be performed on every orbit.

CTE. The radiation environment of the Meteor's 1020km satellite orbit will affect the charge transfer efficiency of the CCD. If no CTE correction is applied, errors exceeding the 0.1% radiometric budget will occur near strong absorption features. The estimation of the CTE is based on either an autoregressive model, or on simple ratios between the 100-pixel plateau and the subsequent virtual pixels (see CTE mode above). CTE is projected to linearly decrease 0.000014 per month. CTE mode will be performed monthly to update its current estimate, and the CTE correction will be applied continuously. The CTE correction algorithm is currently being evaluated.

Linearity. The CTE mode repeatedly run for a sequence of increasing integration times allows the detector linearity to be periodically assessed on-orbit. Test data indicate that the budgeted specification of 0.03% is met by all SAGE III CCDs except for the FOO CCD in the red. Quadratic correction will yield further linearity improvement in the event detector degradation will decrease detector linearity throughout the mission life.

Stray Light. Several sources contribute to unwanted light collected at any given pixel. One source is due to scatter from the CCD substrate as NIR photons are transmitted through the thinned, backside-illuminated CCD, and scatter back into the CCD from the thick glass substrate. The phenomenon is termed 'red leakage', and the primary effect is a broadening of the wings of the detector's spectral response. Second order stray light effects arise from light scattered back to the grating from the detector, and rediffracted onto the detector. The spectral response was characterized for each of the SAGE III instruments by illuminating the spectrometer/telescope with a monochromator at a set of 15 specially selected wavelengths. At each of the

wavelengths all 809 CCD pixels were scanned, and the resulting data were interpolated to arrive at a set of spectral response functions for each pixel of the CCD. Figure 1 shows a sample of the straylight response when the 680nm pixel is illuminated on the Meteor and FOO instruments. Characterization of the spectral response was performed at numerous wavelengths using monochromator, bandpass, as well as numerous discrete line source measurements. The results of fitting gaussian functions to the core of the response measurements are shown in Fig. 2. Note that the two minima in the spectral response measurements closely coincide with the spectrometer's design stigmatic points. A polynomial fit to the measurements shown in Fig.2 allows continuous interpolation to all wavelengths.

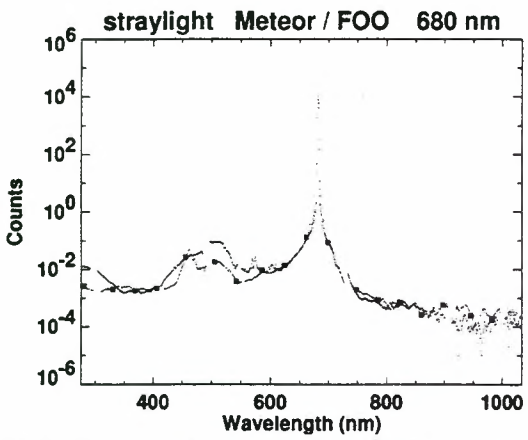

Figure 1. Monochromator-based straylight for Meteor and FOO. FOO marked by black squares.

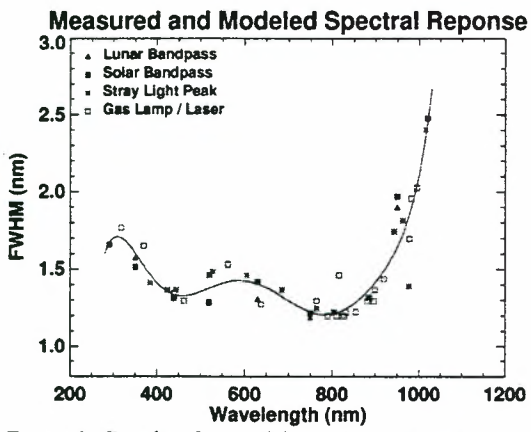

Figure 2. Core bandpass of the Meteor instrument.

The data in Fig. 2 characterize only the core of the spectral response. The wing response is empirically fitted separately from the core response. The combination of both wing and core responses form a basis for the set of point spread functions which are used for algorithm and database development. It is expected that the central core of these measurements adequately characterize the in-band instrument response, and that the out-of-band response, including the parallel red leakage component, are characterized by the wing measurements. Calculations based on the above spectral response measurements convolved with an exoatmospheric solar signal indicate that the greatest out-of-band (OOB) contributions are to the UV and NIR regions of the CCD (mesospheric ozone, O_2-A band, and H_2O). OOB to in-band relative contributions for the above spectral regions range from 0.25-1.0% in the UV, 0.06-0.08% in O_2, to 0.2-0.5% in H_2O.

Serial Leakage. The serial register on the CCD is blocked from receiving direct illumination, however photon scattering from the glass substrate below the CCD, especially in the NIR region, reaches serial pixels. As a consequence a complex sequence of leaked photoelectrons are added to the parallel signal as these parallel pixels are shifted along the serials toward the readout. The fast/slow shifting of the serial during a solar mode readout causes the leakage to be highly dependent on the read process, and on the radiant image on the parallels. All other CCD sampling modes do not use a fast/slow serial shift process, hence serial red leakage does not contribute biases to the parallel signal. The serial mode sampling allows the deterministic evaluation of the serial leakage, however this mode only operates on the solar signal above the atmosphere. An algorithm using an atmospheric model coupled with the instrument signal in the atmosphere would have been needed in order to remove the serial leakage component from the data samples acquired during an event. Work with instrument test data indicated that the success of a serial red leakage algorithm was not good. Thus a renewed effort was made to develop an on-orbit CCD solar sampling algorithm to remove the serial red leakage. After substantial testing an in situ algorithm was developed which utilized one of the 4 over sampling periods that existed in the flight code to sample the serial register pixels while the parallels are set to drain. The other 3 periods shift the parallel image into the serials. The serial signal is automatically subtracted from the parallel signal during solar mode, thus the instrument counts at readout are free from serial leakage and only require a parallel dark current subtraction.

Spectral Calibration. Several exoatmospheric scans of the Sun during wavelength calibration mode will provide the data for a regression function to calculate wavelength as a function of pixel number. The calibration is driven heavily by the solar Fraunhoffer lines.

Etaloning and Spectral Stability. Due to the semi-transparency of the CCD in the NIR, reflections between the nearly parallel back and front surfaces of the 16μm thick CCD causes it to act as an etalon, albeit an imperfect one. Fig. 3 shows this effect in the Meteor test data beginning at 750nm, where the etaloning amplitude is small, and extending to 1030nm where the amplitude is the largest. The phase of the etaloning signal is primarily controlled by the relative orientation between the grating and the detector. This orientation is controlled by temperature-induced

flexure of the spectrometer thermal enclosure. As long as the etalon phase remains constant throughout a nominal 3 minute event duration, the instrument remains radiometrically self-calibrated. Instrument test data were gathered for a temperature controlled thermal vacuum chamber experiment where an approximate 4°C gradient was imposed across the spectrometer enclosure. Analysis of the resulting test shows that the drift in the etaloning phase induced a relative radiometric change less than 0.03%. Although these results are encouraging, meeting the budgeted 0.03% radiometric stability requirement, a series of on-orbit test data will need to be measured in order precisely estimate the magnitude of etalon phase change.

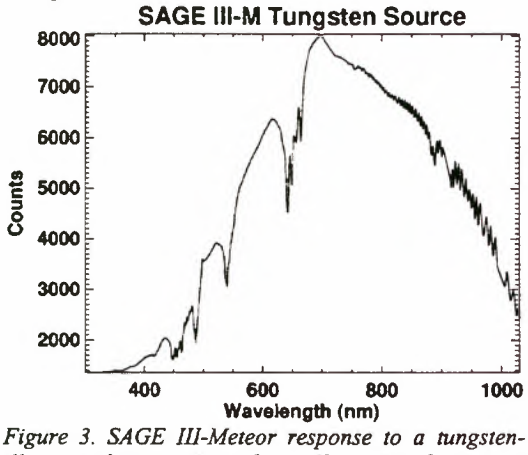

Figure 3. SAGE III-Meteor response to a tungsten-illuminated integrating sphere. Absorption features at 450, 540, and 640nm are due to rare earth elements in the integrating sphere coating.

A variant of wavelength calibration mode can be used to sample the contiguous spectrum throughout an event. A potential etalon detection channel is also available for each event by using the six pixels assigned to solar channel 11. In this channel the etalon amplitude is quite large, and little gaseous absorption exists.

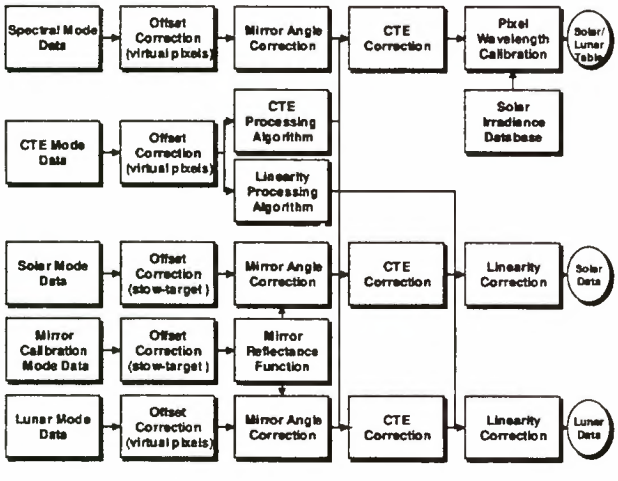

Figure 4. SAGE III flight data processing flow.

FLIGHT DATA CORRECTION PROCESSING

Fig. 4 shows the ground processing needed for correcting the instrument count data prior to injection of the Level-1B transmissions into the species retrieval algorithm. Implementation of all the corrections will yield a data accuracy specification of 0.1%. The background offset and CTE correction are essential components, and CTE processing is likely to be the most processor intensive. Linearity correction is optional, and not required to meet specification. The mirror angle correction will be a simple product based on scan mirror position measurement. The reflectance data suggests that a linear relationship exists between mirror angle and correction.

The point spread function (PSF), as derived from the straylight, bandpass, and spectral test data does not appear in the processing sequence in Fig. 4. However a PSF correction is incorporated into the Level-2 processing.

REFERENCES

1. Mauldin, L.E. et al., Meteor-3M(1)/Stratospheric Aerosol and Gas Experiment III (SAGE III) jointly sponsored by the National Aeronautics and Space Agency and the Russian Space Agency, *SPIE, 3501,*355, 1998.
2. McCormick, M.P. , et al., Polar stratospheric cloud sightings by SAM II, *J. Atmos. Sci., 39,*1387, 1982.
3. McCormick, M. .P., Stratospheric aerosols, in Atlas of Satellite Observations Related to Global Change, edited by R. J. Gurney, et al., Cambridge University Press, 1993.
4. Veiga, R. E., and M. P. McCormick, SAGE II measurements of early Pinatubo aerosols, *Geophys. Res. Lett., 19,* 155, 1992.
5. Trepte, C. R., R. E. Veiga, and M. P. McCormick, The poleward dispersal of Mt. Pinatubo volcanic aerosol, *J. Geophys. Res, 98,*563, 1993.
6. Report of the International Ozone Trends Panel – 1988, R. D. Watson, Chair, World Meteorological Organization (WMO), Global Ozone Research and Monitoring Project-Report No. 18, 1988.
7. Scientific Assessment of Stratospheric Ozone: 1989, D. L. Albritton and R. D. Watson, Co-Chairs, WMO, Global Ozone Research and Monitoring Project-Report No. 20, 1989.
8. Scientific Assessment of Ozone Depletion: 1991, D. L. Albritton and R. D. Watson, Co-Chairs, WMO, Global Ozone Research and Monitoring Project-Report No. 25, 1991.
9. Scientific Assessment of Ozone Depletion: 1994, D. L. Albritton, R. D. Watson, and Piet J. Aucamp, Co-Chairs, WMO, Global Ozone Research and Monitoring Project-Report No. 37, 1994.
10. Chu. W. P. and R. E. Veiga, SAGE III / EOS, *SPIE, 3501,*52, 1998.
11. Kurucz, R. L. The solar irradiance by computation, in *Proeedings of the 17th Annual Conference on Atmospheric Transmission Models,*PL-TR-95-2060, G. P. Anderson et al., eds., (Phillips Laboratory, Hanscom Air Force Base, Mass., 1995) pp 333-334.

Total Ozone Comparisons using EP-TOMS and GOME

James Gleason
NASA/Goddard Space Flight Center, USA

Total ozone from two operational satellite total ozone data sets, NASA's Earth Probe TOMS and ESA's GOME instrument will be compared. Differences as a function of time and latitude will be presented. Algorithmic differences will be explored by using a specially created GOMETOMS data set. This data set was created by using the GOME radiances in the TOMS total ozone algorithm. Comparisons of the operational total total ozone data with this data set will illustrate the algorithmic assumptions of both retrieval methods.

ERROR ANALYSIS OF THE GOME OZONE COLUMN RETRIEVAL METHOD

P. Stammes and R.B.A. Koelemeijer

Royal Netherlands Meteorological Institute (KNMI), P.O. Box 201, 3730 AE De Bilt, The Netherlands
phone: +31 30 2206459, fax: +31 30 2210407, email: stammes@knmi.nl

ABSTRACT

Differential absorption spectroscopy is the method used for ozone retrieval from GOME measurements of the Earth's ultraviolet (UV) spectrum. The two main elements of this retrieval method are: (i) the slant column determination, using spectral fitting to an ozone reference spectrum, and (ii) the air mass factor calculation, to convert the slant ozone column into the vertical ozone column. Both elements are discussed here. Firstly, we propose to use an effective ozone cross-section spectrum, which is integrated over the entire atmosphere. Secondly, we propose a new formula to calculate the air mass factor with a radiative transfer model. It appears that the traditional formula is an approximation for small optical thickness, which is not valid for ozone in the UV fitting window of 325–335 nm. The old air mass factor formula leads to an overestimation of the air mass factor, and thus an underestimation of the ozone column. We finally conclude that the wavelength at which the air mass factor is calculated should be representative for the ozone absorption optical thickness in the ozone fitting window.

1. INTRODUCTION

The Global Ozone Monitoring Experiment (GOME) on board the ERS-2 satellite has been designed to measure ozone and other trace gases by means of the differential absorption spectroscopy method [Ref. 1]. This method has been developed for ground-based observations of trace gases in the troposphere and the stratosphere, i.e. for transmitted sunlight, and has become well-known under the name DOAS [Ref. 2 and references therein]. GOME is the first satellite instrument for which the differential absorption spectroscopy method is applied in order to retrieve trace gas column densities from measurements of reflected sunlight. From extensive intercomparisons of GOME ozone data with ground-based measurements, it has been shown that systematic errors exist for the GOME ozone column [Ref. 3]. In order to understand these errors – at least in part – we here analyze the main aspects of the GOME ozone retrieval method and its assumptions. A full discussion of the new air mass factor formula is given in [Ref. 4].

2. PRINCIPLE OF DIFFERENTIAL ABSORPTION SPECTROSCOPY OF SCATTERED SUNLIGHT

2.1 Overview

In the differential absorption spectroscopy method, the depth of atmospheric absorption features is compared to the depth of features in (laboratory) absorption spectra of trace gases. From the fit of a (laboratory) reference spectrum to an atmospheric spectrum, the slant column density of an absorber is found, denoted by N^s (in molecules/cm^2). The depth of an atmospheric absorption line depends on the average photon path in the atmosphere, which is determined by scattering and absorption processes. The average path of sunlight scattered in the atmosphere and detected by the observer, relative to the vertical path, is described by the air mass factor, denoted by $\mathcal{A}$. Assuming that the effective cross-section of ozone along a slant atmospheric path is the same as along the vertical atmospheric path, the vertical column density, N (in molecules/cm^2), is given by:

$$N = \frac{N^s}{\mathcal{A}}. \qquad (1)$$

This equation shows that the retrieval of N has two main elements: (i) determination of

the slant column, N^s; (ii) calculation of the air mass factor, $\mathcal{A}$. Both elements will be discussed in this paper. Another element of the GOME ozone retrieval algorithm is the effect of clouds on the air mass factor. This topic is discussed in [Ref. 5; this issue].

2.2 Principle

The principle of differential absorption spectroscopy is based on separation of absorption features, which have a high-frequency structure, and scattering features, which have a low-frequency structure in their wavelength dependence. We first define the reflectivity at top-of-atmosphere, $R(\lambda)$:

$$R(\lambda) = \frac{I(\lambda)}{\mu_0 F(\lambda)}, \qquad (2)$$

where $I(\lambda)$ is the Earth's radiance, $\pi F(\lambda)$ is the solar irradiance perpendicular to the beam, and μ_0 is the cosine of the solar zenith angle, which is denoted by θ_0. Let us now assume that the atmospheric path of the radiation at λ_1 is the same as the atmospheric path of the radiation at λ_2, which is chosen close to λ_1, but only with a *slightly* different amount of absorption along the way, due to spectral structure of the absorption cross-section (of, e.g., ozone) . Then the atmospheric reflectivities $R(\lambda_1)$ and $R(\lambda_2)$ are related according to:

$$\frac{R(\lambda_1)}{R(\lambda_2)} = \exp[-(b^s(\lambda_1) - b^s(\lambda_2))], \qquad (3)$$

where $b^s(\lambda)$ is the slant absorption optical thickness of the absorber, in the present case ozone. Equation (3) is the basic formula of differential absorption spectroscopy of scattered sunlight.

3. OZONE SLANT COLUMN DETERMINATION

3.1 Spectral fitting

We assume that the slant column density is proportional to the slant optical thickness, so that Eq. (3) can be written as:

$$\ln R(\lambda_1) - \ln R(\lambda_2) = -N^s[\overline{\sigma}(\lambda_1) - \overline{\sigma}(\lambda_2)], \quad (4)$$

where $\overline{\sigma}(\lambda)$ is the effective absorption cross-section of ozone, which we define as:

$$\overline{\sigma}(\lambda) = \frac{1}{N}\int_0^\infty \sigma(\lambda, T(z))\ \rho(z)dz, \qquad (5)$$

where $\sigma(\lambda, T(z))$ is the temperature (T) dependent ozone absorption cross-section, $\rho(z)$ is the ozone concentration (in molecules/cm^3) at altitude z (in cm), and N is the vertical column density of ozone (in molecules/cm^2), given by $N = \int_0^\infty \rho(z)dz$. In Eqs. (4–5) we have approximated the effective cross-section of a slant path by the effective cross-section of the vertical path. We note that by employing the concept of effective cross-section, the vertical optical thickness exactly obeys:

$$b(\lambda) = N\ \overline{\sigma}(\lambda). \qquad (6)$$

The slant column density, N^s, is now found by applying Eq. (4) to many wavelengths belonging to a "fitting window". We thus obtain:

$$N^s = \frac{-\Delta \ln R(\lambda)}{\Delta \overline{\sigma}(\lambda)}. \qquad (7)$$

Here $\Delta f(\lambda)$ denotes the differential of the function $f(\lambda)$, in which a smooth spectral function is subtracted, leaving only the differential spectral structure of $f(\lambda)$ in the chosen fitting window. In the case of the operational GOME ozone retrieval from UV spectra, the spectral fitting window 325–335 nm has been chosen, and a second-order polynomial is assumed for the smooth function which is subtracted [Refs. 6–7].

3.2 Ozone reference spectra

As an example, we discuss here the ozone reference spectrum for one atmospheric model, namely the midlatitude summer (MLS) atmosphere [Ref. 8]. In Fig. 1 the vertical profile of the ozone volume mixing ratio and of the ozone concentration belonging to this atmosphere are shown. Apparently, the maximum in the ozone concentration lies at a much lower altitude (at about 25 km) than the maximum of the ozone mixing ratio (at about 35 km). The effective ozone cross-section for the MLS atmosphere, calculated by Eq. (5), is shown in Fig. 2. Here

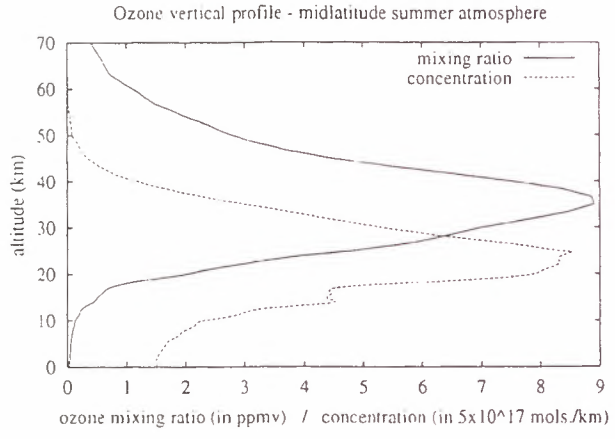

Figure 1: Vertical profiles of ozone volume mixing ratio (in ppmv) and ozone concentration (in 5×10^{-17} molecules/cm^2) for the midlatitude summer atmosphere [Ref. 8].

we used the temperature-dependent ozone cross-section data of [Ref. 9]. For comparison, the ozone cross-section spectra at the temperatures of the maximum mixing ratio ($T = -28°$C at 35 km) and the maximum concentration ($T = -48°$C at 25 km) are also shown.

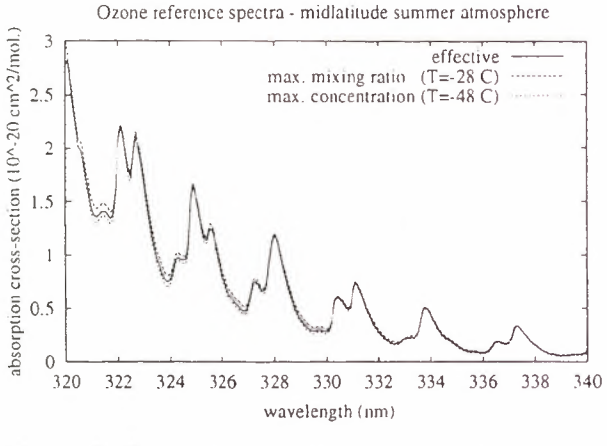

Figure 2: Three ozone cross-section spectra between 320 and 340 nm relevant to the MLS atmosphere: the effective cross-section (solid line), the cross-section at the temperature of the maximum mixing ratio (upper dashed line), and the cross-section at the temperature of the maximum concentration (lower dashed line).

This choice is made, because in the early version of the operational GOME ozone column algorithm, the cross-section at the maximum mixing ratio was chosen as reference spectrum. Presently, the cross-section at the maximum concentration is chosen as reference spectrum. However, neither agrees with the effective cross-section – in fact, the effective cross-section just lies between the cross-sections for $T = -28°$C (maximum mixing ratio) and $T = -48°$C (maximum concentration). This becomes more clear in Fig. 3, where the relative difference between the effective cross-section and the cross-section at $-28°$C and $-48°$C is shown. Clearly, the ozone cross-section at one temperature cannot represent the ozone cross-sections through the entire atmosphere.

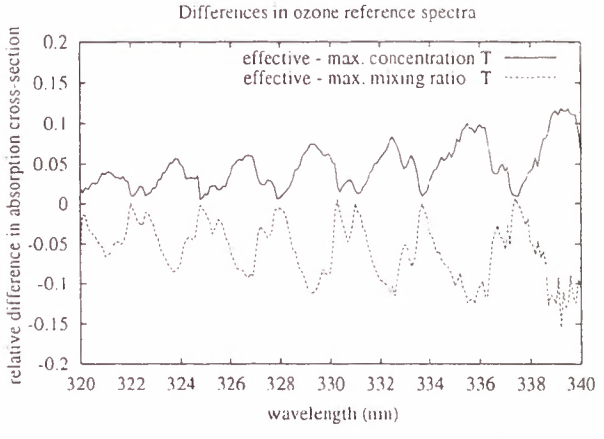

Figure 3: Relative difference, defined as $(\overline{\sigma} - \sigma_T)/\overline{\sigma}$, between the effective ozone cross-section $\overline{\sigma}$ and the ozone cross-section σ_T at the specific temperatures of Fig. 2.

The relative difference in cross-section has a smooth bias of a few % *and* a differential structure of up to 10 % peak-peak. The former is subtracted in the spectral fitting but the latter is not, and will affect the ozone slant column determination. From Fig. 3 we see that, around 330 nm, the ozone cross-section at the temperature of maximum concentration is about 6 % (peak-peak) smaller than the effective cross-section. This means that the ozone slant column using the cross-section at this temperature is a few % larger than using the effective cross-section (Eq. 7). In contrast, the ozone cross-section at the temperature of maximum mixing ratio is about 10 % (peak-peak) larger than the effective cross-section. This leads to a slant column which is several % smaller than when using effective cross-section. We observed the same tendency for two other atmospheric cases, namely the subarctic winter and the tropical atmospheres [Ref. 8]. We therefore conclude that

using the ozone cross-section spectrum at the temperature of maximum ozone concentration as the reference spectrum, instead of the effective cross-section spectrum, leads to a systematic overestimation of the ozone slant column in the GOME data processor.

4. AIRMASS FACTOR

4.1 Airmass factor formula

We define the air mass factor $\mathcal{A}$ as the ratio of the slant optical thickness of ozone to its vertical optical thickness:

$$\mathcal{A} \equiv b^s/b. \tag{8}$$

Starting with the differential principle, Eq. (3), and employing the air mass factor definition Eq. (8), the *new air mass factor formula* for differential absorption spectroscopy of scattered sunlight reads [cf. Ref. 4]:

$$\mathcal{A} = \frac{-d \ln R(\lambda, b(\lambda))}{d\, b(\lambda)}, \tag{9}$$

which may also be written in terms of the vertical ozone column density N:

$$\mathcal{A} = \frac{1}{\overline{\sigma}(\lambda)} \frac{-d \ln R(\lambda, N)}{d\, N}. \tag{10}$$

The derivative in Eq. (9) is evaluated at the actual ozone absorption optical thickness, b. This formula is used to calculate the air mass factor for a given atmospheric case, using a radiative transfer model.

The old air mass factor formula, which is mostly used for interpreting differential absorption spectroscopy measurements of scattered sunlight, reads [e.g. Refs. 10, 7]:

$$\mathcal{A} = \frac{\ln R_0 - \ln R}{b}, \tag{11}$$

where R_0 is the atmospheric reflectivity calculated for an atmosphere without ozone. This formula is an approximation of Eq. (9) for small absorption optical thickness, which is, however, not correct for ozone in the UV.

In Fig. 4, the general behaviour of $\ln R$ versus b for scattered light is sketched. This shows

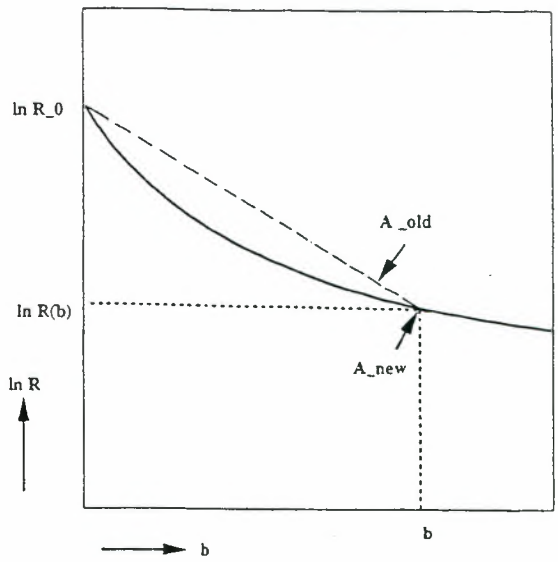

Figure 4: Behaviour of $\ln R$ versus ozone absorption optical thickness b, sketched by the curve. The new air mass factor is the absolute value of the slope of the curve at b, whereas the old air mass factor is the absolute value of the slope of the long-dashed line through $(0, \ln R_0)$ and $(b, \ln R(b))$ (cf. Eq. (11).

that the hollow curvature of $\ln R(b)$ leads to an overestimation of the air mass factor if the old formula is used.

4.2 Airmass factor results

As an example, we here compare the old and new ozone air mass factors for the case of reflected light in nadir. The wavelength chosen is 325 nm, as it is in the GOME data processor. The new air mass factor is calculated using Eq. (10), whereas the old air mass factor is calculated using Eq. (11). The reflectivities occuring in these equations are calculated using the Doubling-Adding KNMI radiative transfer model including polarization [Refs. 11–12].

In Fig. 5 the new and old air mass factors are shown as a function of ozone column for the mid-latitude summer atmosphere [Ref. 8], for nadir view and $\theta_0 = 75^\circ$. The MLS ozone profile has been scaled to the ozone column (in Dobson Units) given on the x-axis. Here only Rayleigh scattering and ozone absorption are taken into account. The surface albedo is 0.05. The difference between the old and new air mass factors

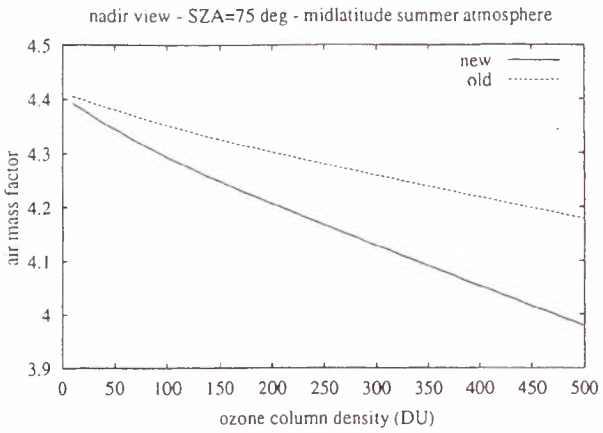

Figure 5: New and old air mass factors as a function of the ozone column, for nadir view and $\theta_0 = 75°$. Atmospheric model: midlatitude summer, no aerosols and clouds, surface albedo 0.05.

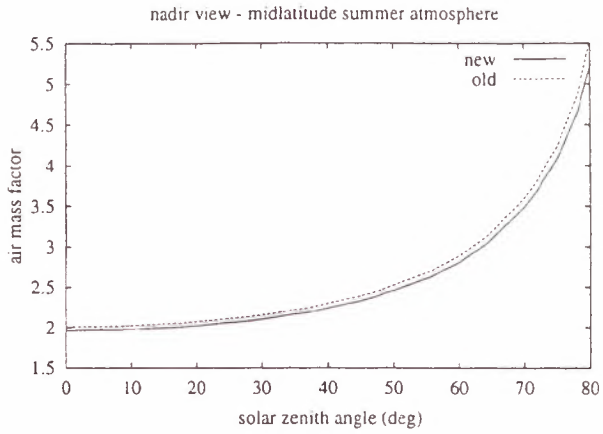

Figure 6: New and old air mass factor as a function of solar zenith angle, for nadir view and the standard ozone column (335 DU). Other parameters are the same as in Fig. 5.

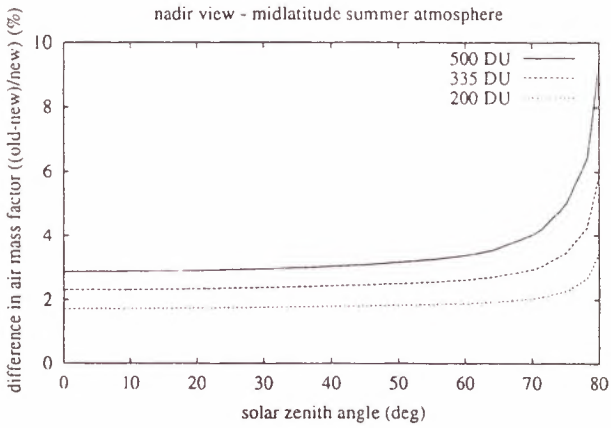

Figure 7: Relative difference (in %) between the old and new air mass factors as a function of solar zenith angle, for nadir view and three values of the ozone column: 500, 335, and 200 DU, using the (scaled) MLS ozone profile. Other parameters are the same as in Fig. 5.

increases with ozone column and amounts in this case to 5 % at $N = 500$ DU.

In Fig. 6 the new and old air mass factors are shown as a function of solar zenith angle for the standard ozone column (335 DU) of the midlatitude summer atmosphere. Both the old and new air mass factor increase with θ_0; the rate of increase is different, as is more clearly shown in Fig. 7. Here the difference between the old and new air mass factors is shown as a function of θ_0 for three values of the ozone column, using the scaled MLS ozone profile. Clearly, the difference between the old and new air mass factor increases with increasing θ_0, but especially rapidly for $\theta_0 > 60°$. Thus, using the old air mass factor the ozone column is underestimated, especially for large solar zenith angles.

5. CONCLUSIONS

GOME is an experiment in applying the method of differential absorption spectroscopy to measurements from space. By this method, GOME has obtained exciting results about the chemical composition of the atmosphere [for a recent overview, see Ref. 13]. In the past years, a lot of effort has been devoted to validation of especially the GOME ozone column derived from UV spectra. This validation has revealed considerable systematic deviations between GOME and ground-based ozone values as a function of solar zenith angle and season [see e.g. Ref. 3]. Therefore, it is important to understand the basis of the differential absorption retrieval method and its assumptions.

In this study and in [Ref. 4] we have found that the two main elements of the GOME ozone retrieval method, namely the ozone slant column determination and the air mass factor calculation, can be improved considerably. Our recommendations for improvement of the GDP can be summarized as follows:

1. In the slant column determination, the *effective* ozone absorption cross-section spectrum (Eq. 5) should be used as the reference

spectrum, in stead of the absorption spectrum of ozone at a specific temperature as is presently done.

2. The new air mass factor formula given by Eq. (10) should be used for ozone retrieval from the fitting window 325–335 nm, in stead of the old formula Eq. (11) which is presently used.

3. The wavelength for which the air mass factor is calculated should be representative for the optical properties of the entire fitting window, in stead of taking the wavelength at the extreme end of the window (325 nm) as is presently done [Ref. 4]. For example, for the MLS atmosphere the window-average ozone optical thickness is 0.04934, whereas the ozone optical thickness at 325 nm is as large as 0.14142.

4. Polarisation should be included for accurate radiance calculations in the UV. Neglecting polarisation in the air mass factor calculations around 330 nm has an effect of at most about 1.5 %.

5. Because the air mass factor depends on the ozone column (cf. Fig. 5), an iterative scheme is needed in the GOME ozone column retrieval method. The first-guess air mass factor could be calculated using a climatological value of the ozone column.

It appears that in the GDP a fortuitous cancellation of errors occurs for certain atmospheric profiles and geometries [Ref. 4]. The error due to the incorrect air mass factor formula is largely compensated by taking the wavelength of 325 nm for the evaluation of the air mass factor. Neglecting polarisation adds to the error balance. However, the GOME ozone column retrieval method should be based on solid grounds, in order to fully exploit the strength of the spectral coverage and resolution of GOME, and at the same time using the efficiency of the differential absorption spectroscopy method.

The above suggested improvements for GOME are also important for developing the ozone column retrieval algorithm for future satellite instruments which will employ differential absorption spectroscopy, such as SCIAMACHY on Envisat, GOME-2 on Metop-1, and the Ozone Monitoring Instrument on EOS-CHEM.

ACKNOWLEDGEMENTS

Discussions on differential absorption spectroscopy in the GOME science team, especially with Prof. U. Platt, Dr. A. Richter, and Dr. A. Piters, are gratefully acknowledged.

The Space Research Organisation of the Netherlands (SRON) and the Netherlands Agency for Aerospace Programmes (NIVR) are acknowledged for the financial support of part of this work.

REFERENCES

[1] ESA, 1993, *GOME Interim Science Report*, ESA SP-1151, ESA/ESTEC, Noordwijk

[2] Platt, U., Differential Optical Absorption Spectroscopy (DOAS), in *Air Monitoring by Spectroscopic Techniques*, edited by M. W. Sigrist, pp. 27-84, John Wiley & Sons, New York, 1994.

[3] Lambert, J.-C., et al., Combined characterisation of GOME and TOMS total ozone using ground-based observations from the NDSC, submitted to: *Advances in Space Research, Proc. of the 32nd COSPAR assembly, Nagoya, Japan, 12-19 July 1998*, Nagoya, 1998

[4] Stammes, P., and R. B. A. Koelemeijer, A new air mass factor formula for the interpretation of differential absorption spectroscopy measurements of scattered sunlight, submitted to *J. Geophys. Res.*, 1999

[5] Koelemeijer, R. B. A., and P. Stammes, Influence of clouds on GOME ozone retrieval, *Proc. of ESAMS '99* (this issue), ESA, Noordwijk, 1999

[6] DLR, GOME level 1 to 2 algorithms description, *Tech. Rep. ER-TN-DLR-GO-0025*, 32 pp., DLR, Oberpfaffenhofen, 1994

[7] Diebel, D., J. P. Burrows, R. de Beek, B. Kerridge, L. Marquard, K. Muirhead, R. Munro, and U. Platt, Detailed Analysis of the Retrieval Algorithms Selected for the Level 1-2 Processing of GOME Data, *Final Report ESA Contract 10728/94/NL/CN*, ESA/ESTEC, Noordwijk, 1995

[8] Anderson, G. P., S. A. Clough, F. X. Kneizys, J. H. Chetwynd, and E. P. Shettle, AFGL Atmospheric Constituent Profiles, *Tech. Rep. AFGL-TR-86-0110,* Air Force Geophysics Laboratory, Hanscom AFB, MA, 1986

[9] Bass, A. M., and R. J. Paur, The ultraviolet cross-sections of ozone, I. Measurements, *Proc. of the Quadrennial Ozone Symposium, Halkidiki, Greece,* edited by C. Zerefos and A. Ghazi, 606–610, D. Reidel, Dordrecht, 1984

[10] Perliski, L. M. and S. Solomon, On the Evaluation of Airmass Factors for Atmospheric Near-Ultraviolet and Visible Absorption Spectroscopy, J. Geophys. Res. *98,* 10363–10374, 1993

[11] De Haan, J. F., P. B. Bosma, and J. W. Hovenier, The adding method for multiple scattering calculations of polarized light, *Astron. Astrophys.* **183**, 371–391, 1987

[12] Stammes, P., Errors in UV reflectivity and albedo calculations due to neglecting polarisation, *Proc. of SPIE, Atmospheric Sensing and Modeling,* Vol. 2311, 227–235, 1994

[13] Burrows, J. P., et al., The Global Ozone Monitoring Experiment (GOME): Mission Concept and First Scientific Results, *J. Atm. Sci.*, in press, 1999

Intercomparison of GOME with Balloon and Groundbased Observations

D. Perner, H. Harder, and T. Klüpfel (Max-Planck-Institut für Chemie, Germany)
E. Hegels (Deutsches Zentrum für Luft- und Raumfahrt, Germany)
K. Pfeilsticker, U. Platt (IUP, Univ. Heidelberg, Germay)

Groundbased DOAS and balloon-borne DOAS experiments were carried out and the results are compared to GOME. The ground DOAS measured vertical columns of bromine monoxide, BrO, ozone, O3,and nitrogendioxide, NO2,in zenith scattered sunlight at Leon, Spain, in spring and at Söndre Strömfjord, Greenland, in spring and summer.

In addition reliable height distributions of those compounds in the stratosphere are obtained in balloon experiments when the sun is followed during ascend and during occultation.

At this time the vertical columns of those species in the stratosphere measured by balloon seem to deviate from the coresponding columns observed by GOME.

COMPARISON OF THE GOME NO2 TOTAL CONTENT DATA WITH THE RUSSIAN GROUND-BASED MEASUREMENTS

Yuriy M. Timofeyev, Dmitriy V. Ionov, Alexandr V. Polyakov

St. Petersburg State University, Russia
e-mail: tim@troll.phys.spbu.ru

Nikolay F. Elansky, Alexandr.S. Elokhov, Alexandr M. Gruzdev, Oleg V. Postylyakov
Institute of Atmospheric Physics RAN, Moscow, Russia
e-mail: Nikolai@selansky.home.bio.msu.ru

Eugene V. Rozanov, Michael E. Schlesinger
University of Illinois at Urbana-Champaign, USA
e-mail: rozanov@atmos.uiuc.edu

Igor L. Karol, Vladimir A. Zubov,
A.I.Voeikov Main Geophysical Observatory, St.Petersburg, Russia
e-mail: karol@main.mgo.rssi.ru

ABSTRACT

Information on a method, measurement instrumentation, interpretation algorithms used by the Institute of Atmospheric Physics RAS (Zvenigorod Scientific Station) for deriving the column abundance and vertical distribution of NO_2 from the measurements of diffused solar zenith radiation during morning and evening twilight is given. Comparison of the NO_2 ground-based and GOME measurements revealed the large deviations between the satellite and ground-based data. Possible causes of these mismatches (NO_2 daily run, town influence, etc.) are analyzed.

Three-dimensional Atmospheric Chemical Transport Model (ACTM) of the atmosphere has been used for computing the NO_2 column abundance fields. Some examples of comparing the GOME measurements with the model prediction are given.

1. INTRODUCTION

Understanding of NO_2 and NOx global distribution is very important due to well known very active participation of these radicals in sources and sinks of the ozone and other climatically active photochemical gases. In particular the information on NO_2 content and horizontal distribution in a layer involving the tropopause is crucial for estimation of NOx emissions from the current fast growing world fleet of subsonic air transport aircrafts. These emissions affect the ozone content in the above layer, which produces the maximal greenhouse effect. NOx emissions in the stratosphere by future supersonic massive transports have also to be monitored.

For the most part the NO_2 content measurements from satellites use the slant path geometry. The SAGE-2 and POEM-2 instruments have measured the NO_2 atmospheric profiles by the solar radiation absorption in visible spectral range at sunrise and sunset [Refs. 1, 2]. Similar measurements in IR spectral range were carried out in a number of satellite experiments with the Spacelab grill spectrometer [Ref. 3] and the ATMOS interferometer [Refs. 4, 5]. Studies of spatial - temporal variations of the NO_2 vertical structure were also conducted by measurements of thermal radiation of the Earth horizon [Ref. 6, 7]. Beginning in 1995, nadir measurements of the NO_2 total content have been carried out by the GOME spectrometer (ERS-2 satellite) through interpreting the scattered and reflected solar radiation in visible spectral range [Ref. 8].

Ground-based, aircraft and balloon measurements collocated in time and space with the satellite ones are of great importance in estimating the real accuracy of satellite data (e.g. [Ref. 9]). In this study, the results of comparing the GOME data on NO_2 total content with ground-based measurements at Zvenigorod Scientific Station (1996, 1998) and with the prediction of three-dimensional ACTM are given.

2. GROUND-BASED THE NO_2 MEASUREMENTS

Zvenigorod Scientific Station (ZSS) of the Oboukhov Institute of Atmospheric Physics (56°N, 38°E,) is located at a distance of 50 km to the west from Moscow. However, because of the westerly winds prevail in this region through out the year the influence of the polluted air from Moscow on the observations is not too important. In the region of station there are no sources of pollution of the environment. The highways and main roads are far from the station.

The regular measurements of column abundances and vertical profiles of NO_2 at ZSS have been performed since March 1990. The station is a member of the International Network for Detection of Stratospheric Change (NDSC) as a station for complimentary measurements of column NO_2. Vertical NO_2 profiles are retrieved out of the framework of the NDSC activity. First retrievals of NO_2 vertical distributions from ground-based measurements were undertaken by McKenzie

et al. [Ref. 10]. In the papers [Ref. 11,12], the NO_2 total content measurements at ZSS were analyzed.

Column amount NO_2 contents are obtained from zenith-scattered solar radiation measured by the grating spectrometer MDR-23 operating in the 435-450 nm wavelength range with spectral resolution 0.7 nm and time of scanning 40 s. A photomultiplier optimized in the visual wavelength range is used as a detector. The measurements are taken at twilight in mornings and evenings at solar zenith angles 84°-96°, and during daytime , if necessary, to control NO_x pollution of the boundary layer. Detected spectrum is proposed to be the sum of the solar spectrum exponentially attenuated by NO_2 and O_3 absorption and by Rayleigh and aerosol scattering, and a constant. The constant is believed to include effects of detector dark current, spectrometer stray light leakage, and the Ring effect. The slant NO_2 contents are derived from the observed spectra with the use of differential NO_2 absorption.

To retrieve columnar NO_2 contents and NO_2 vertical distributions from the slant NO_2 contents, air mass factors for NO_2 are needed. They are computed using a spherical scattering model for solar radiation and a non-stationary one-dimensional photochemical model including the O_x and NO_x photochemistry. The spherical scattering model takes into account ozone and NO_2 absorption, single molecular and aerosol scattering, refraction and refraction divergence. Parameters of the models: ozone, temperature and air density vertical distributions are seasonally dependent and taken from simultaneous measurements, if available, or from empirical models [Refs. 13-15] specified for the latitude of observations.

The photochemical model provides the altitude-dependent diurnal variation of NO_2, which is the input parameter in the scattering model. Taking into account photochemical processes is very important as NO and NO_2 undergo rapid changes at sunrise and sunset.

Given calculated air mass factors for NO_2, the NO_2 contents in 5-km thick layers and in the thin near-surface layer are then obtained as a solution of the inverse mathematical problem, with the use of modified method similar to that used by McKenzie et al. [Ref. 10] (Chahine method). The modification is concerned with introducing into consideration the thin near-surface layer where NO_2 concentration can be large during pollution episodes. The NO_2 content in the 0-5 km layer does not include NO_2 in the near-surface layer. Derived quantities are (1) NO_2 contents within 5 km thick layers in the stratosphere and the troposphere (0-50 km), (2) NO_2 content in the thin atmospheric surface layer, and (3) columnar NO_2 contents in the troposphere (0-10 km) and the stratosphere (10-50 km) as integrals over appropriate layers. Comparison of the NO_2 profiles retrieved from ground-based and SAGE-2 measurements demonstrated a good agreement of the data.

The precision of determination of NO_2 slant abundances using the only spectrum is about 3 % at the solar zenith angle 90°, the precision of determination of NO_2 slant abundances with a step 0.5° is better than 1 %.

3. COMPARISON OF THE GOME AND GROUND-BASED NO_2 MEASUREMENTS

The results of comparing all the ground-based (GS) and satellite (GOME) total NO_2 measurements in pairs are given in Fig. 1. The sets of compared data consisted from 331 GOME measurements with 280 sunrise and 286 sunset ground-based observations for 1996. The simplest approximation was used to consider the diurnal variation of total NO_2 - the GOME measurements were compared with a half-sum of corresponding sunrise and sunset ground-based observations. The reason for such approach is that the GOME measurements occur near the local noon time, as the ERS-2 satellite has a so-called sun-synchronized orbit.

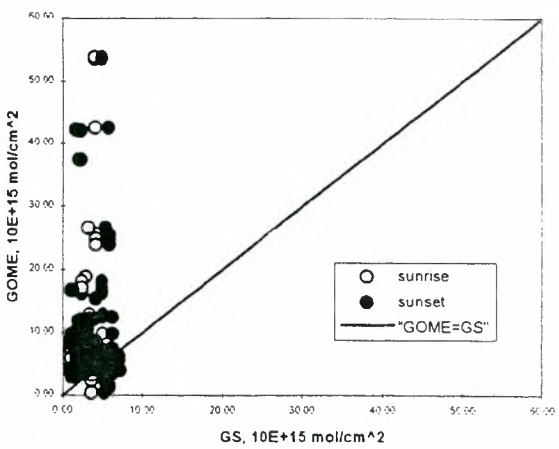

Figure 1. Comparison of satellite (GOME) and ground-based (GS) total NO_2 measurements over ZSS in 1996 (Solid line - the equality "GOME = GS")

Results of comparison demonstrate a very poor agreement between satellite and ground-based measurement systems (it should be taken into account that even negative values were found in the satellite data set, and those were excluded from the comparison). Statistical characteristics of observed discrepancies between GOME (s) and ground-based (g) total NO_2 measurements also prove that conclusion. The mean deviation Δ_{s-g} between the GOME measurements and a half-sum of ground-based observations is 176 % ("sunrise" and "sunset" observations separately deviate from satellite ones by 260 % and 114 %, respectively); standard deviation σ_{s-g} is 549 % (727 % and 394 % for comparison of GOME with "sunrise" and "sunset" observations, respectively); the coefficient of correlation R is - 0.04±0.05 (when comparing GOME measurements with "sunrise" and "sunset" observations those are + 0.01±0.06 and - 0.05±0.06, respectively). It is clear that the GOME significantly (several times!) overestimates the value of total NO_2 in comparison with ground-based observations.

Fig. 2 presents the similar comparison for the limited data set of satellite and ground-based observations - only relatively accurate the GOME measurements (error < 25 %) at the high sun (sun zenith angle SZA < 55°) were included. Results of that comparison demonstrate much better agreement between satellite and ground-based data. The mean deviation Δ_{s-g} for the comparison of GOME measurements with a half-sum of

ground-based observations is - 0.1 %, with standard deviation σ_{s-g} = 23.7 %. Although the absolute values of satellite and ground-based measurements agree rather well, correlation of these data sets is still very poor - $R = 0.13 \pm 0.14$. 49 satellite measurements were compared with 39 "sunrise" and 43 "sunset" observations, covering time period from 26 of March to the 5 of September 1996. The corresponding temporal variation of the GOME NO_2 total content data together with a half-sum of "sunrise" and "sunset" observations is presented in Fig. 3. It is clearly seen, that GOME measurements hardly reproduce variation of daily total NO_2 over the time, if compared with ground-based observations.

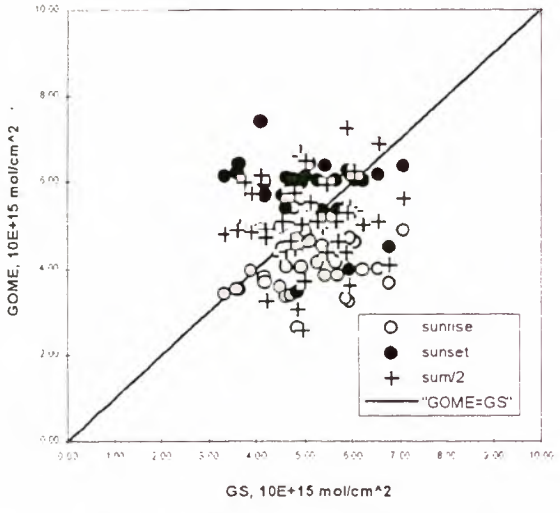

Figure 2. Comparison of satellite (GOME) and ground-based (GS) total NO_2 measurements over ZSS in 1996 (limited dataset).

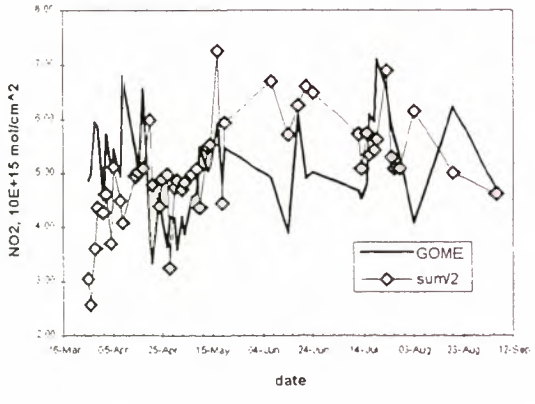

Figure 3. Temporal variation of NO_2 total content from satellite (GOME) and ground-based measurements over Zvenigorod (limited dataset)

Additional comparison was performed for the GOME NO_2 total content data (s) with ground-based observations (g) over Zvenigorod station in March 1998 ("sunset" measurements only). The temporal variations of total NO_2 satellite and ground-based observations are presented in Fig. 4. Satellite measurements give the total NO_2 values exceeding, on the average, by 30.5 % the ground-based ones, with corresponding standard deviation σ_{s-g} = 60.0 %. The number of measurements in the comparison (only 10 pairs were available) is insufficient to make any strong conclusion, but it is possible to note that the agreement between two data sets is much better than it was in 1996 (the average discrepancies were Δ_{s-g} = 114 %, σ_{s-g} = 394 %). GOME measurements performed on March 26 and 29 are nearly 2 times higher the ground-based ones; an elimination of these data from the comparison reduces the average discrepancy between satellite and ground-based systems to 8.9 %, with corresponding standard deviation σ_{s-g} = 20.2 % relative to 30.1 % in 1996. So, there is some reason to conclude that the GOME data processed by new improved code are better agree with ground-based measurements.

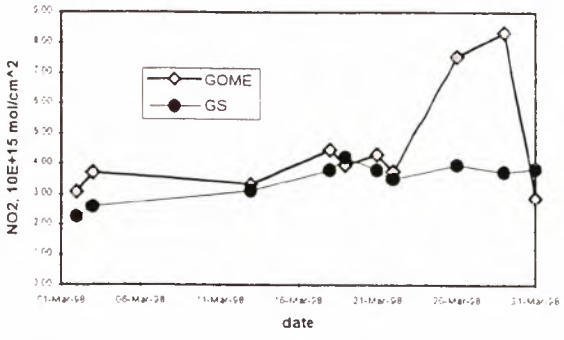

Figure 4. Comparison of satellite (GOME) and ground-based "sunset" (GS) total NO_2 measurements over ZSS in March 1998

Diurnal cycle of total NO_2 is well expressed. Total NO_2 value changes several times, with a rapid decrease at sunrise, growing slowly during daylight until sunset, when it quickly reaches the maximum and starts to reduce gradually until the next dawn. An example of one-day total NO_2 variation, calculated with a use of special photochemical routine of the UIUC 3-D ACTM (see sec. 4) is presented in Fig. 5. Simulation was performed for the first day of each month, giving diurnal cycle of total NO_2 over location of Zvenigorod station. It is clearly seen from this Figure, that the "noon" value is found between "sunrise" and "sunset" values. According to ACTM simulations, the relative variation of total NO_2 over Zvenigorod during the daylight is minimal in May - less than 7 %, and maximal in August - up to 15 %.

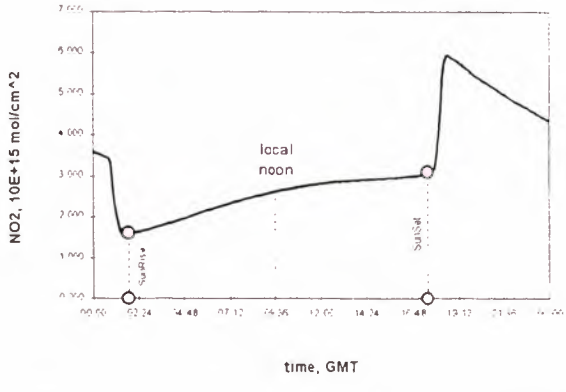

Figure 5. Diurnal cycle of total NO_2 over Zvenigorod (August 1998) (dashed lines indicate the time of sunrise, sunset and local noon)

4. NUMERICAL SIMULATION OF NO_2 GLOBAL FIELDS

In modeling, the 24-layer 3-Dimensional Atmospheric Chemical Transport Model, developed at University of Illinois at Urbana-Champaign, USA (UIUC 3-D ACTM) [Ref 16] have been used. It consists of 3 main modules: (1) a Hybrid advective transport routine, which includes Prather scheme for vertical transport and Semi-Lagrangian scheme for horizontal transport, (2) a photochemical routine that includes the principal gas-phase and heterogeneous reactions and uses a pure implicit iterative Newton-Raphson routine for solving the set of continuity equation for gas species, (3) a module with prescribed temperature, tropospheric humidity and circulation fields. The developed ACTM is global with a horizontal resolution of 4^0 latitude and 5^0 longitude. In the vertical direction the model extends from the earth's surface to 1 hPa. The sources of NO_X and CO as well as near surface mixing ratio of other source gases (CFC's, CH_4 and N_2O) are prescribed for 1995 conditions. The circulation and temperature fields are acquired from 24-L UIUC AGCM as well as from assimilated UKMO (U. K. Meteorological Office) dataset.

Evaluations of 3-D ACTMs have been performed using observed climatological data or observed species distributions for particular locations or time periods. These comparisons showed that 3-D models can reproduce many features of the observed species distributions. However, substantial disagreements between model-simulated and observed data have also been reported in these studies. On the other hand, an extensive validation of the model results (that reflect the current level of theoretical knowledge) with observation data and especially the evaluation of any kind of substantial disagreement between measured and simulated trace gas distributions can be very useful for further progress of the science and may also help to improve the quality and accuracy of the measurements.

4.1. Comparison of the GOME total NO_2 global distribution with model prediction

Comparing the GOME total NO_2 global measurements with simulated spatial distributions may help to understand the reasons of the observed discrepancies between satellite and ground-based systems.

As an example, 3-days averaged total NO_2 GOME data (25-27 July 1996) was compared with corresponding local noon ACTM simulation. Satellite measurements were averaged and interpolated onto the ACTM spatial grid. Fig. 6 presents a map of relative difference of the observed total NO_2 from simulated values, in %. The GOME NO_2 total content data significantly deviate from the simulation - up to 130%. The best agreement between modeled and GOME data is found in the low latitudes of northern hemisphere, and in some parts of southern hemisphere - the relative discrepancy is less then $\pm$ 30 %. In most part of northern hemisphere the GOME total NO_2 data exceed the simulated ones- discrepancy is more than 30 %. On the south, results are opposite - the GOME total NO_2 values are less the simulation by 30-90 %. It is necessary to note, that both data sets (satellite and modeled) produce similar zone distribution of total NO_2 over the globe - it is maximal in the high northern latitudes and decrease to the south. So, it is possible to conclude, that GOME overestimate (in comparison with ACTM) the high NO_2 total contents and underestimate the low ones. Of course, these results are just preliminary; such investigations are at the initial stage and will be continued.

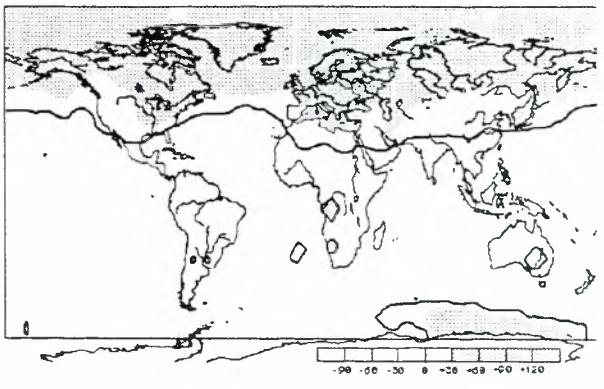

Figure 6. Relative difference of the GOME total NO_2 from simulated (ACTM) values, in % (25-27 July 1996).

4.2. Comparison of the ground-based total NO_2 measurements with model prediction

The results of an 8-year steady-state model run have been reprocessed and the total vertical NO_2 column compared with the data collected at Zvenigorod in 1996 an 1997 years. In this case the model NO_2 values were sampled every 6 minutes for the first day of every month to describe better the diurnal NO_2 variations. Results of comparison for sunrise conditions show that the model mimics rather good the observed seasonal cycle which is characterized by the maximum of vertical column NO_2 in June and minimum vertical column NO_2 during the winter season. However, the difference between simulated and observed data could be rather substantial. The model underestimates vertical column NO_2 from April to August up to 20-40 %. During January and February simulated vertical column NO_2 exceeds measured values by almost 100%. More or less reasonable agreement (within uncertainty of the measurements) occurs in March and from August to November. The causes of such disagreements can be connected with not accurate time coincidence of the measured and simulated data. The other possible sources of the disagreement are rather rough horizontal resolution of the model and the using of GCM generated wind fields to drive ACTM.

It is evident that the agreement between NO_2 ground-based and simulated data is much better then that between the GOME and modeled values.

5. SUMMARY

1. Results of comparison between GOME and ground based NO_2 column amount measurements in 1996 (ZSS, Russia: 56°N, 38°E) (331 GOME measurements, 280 sunrise and 286 sunset ground-based observations) demonstrate a very poor agreement between satellite and ground-based

measurement systems. The mean deviation Δ_{S-g} between the GOME measurements and a half-sum of ground-based observations is 176 %, standard deviation σ_{S-g} is 549 %, the coefficient of correlation R is - 0.04±0.05. It is clear that GOME significantly overestimates the value of total NO_2 in comparison with ground-based observations.

2. The similar comparison for the limited data set of satellite and ground-based observations in 1996 - only relatively accurate the GOME measurements (error < 25 %) - demonstrates much better agreement between satellite and ground-based data. The mean deviation Δ_{S-g} for the comparison of GOME measurements with a half-sum of ground-based observations is - 0.1 %, with standard deviation σ_{S-g} = 23.7 %. Although the absolute values of satellite and ground-based measurements agree rather well, correlation of these data sets is still very poor - $R = 0.13 \pm 0.14$.
3. Comparison of the GOME NO_2 total content data and ground-based observations over Zvenigorod station in March 1998 shows that satellite measurements give, on the average, 30.5 % higher the total NO_2 values than ground-based system, with corresponding standard deviation σ_{S-g} = 60.0 %. GOME measurements performed on March 26 and 29 are nearly 2 times higher than the ground-based ones. Elimination of these data from comparison reduces the average discrepancy between satellite and ground-based systems to 8.9 %, with corresponding standard deviation σ_{S-g} = 20.2 %. Our preliminary conclusion is that the GOME data of March 1998 has the better quality than data of 1996.
4. Comparative analysis of total NO_2 measured by GOME and modeled by three-dimensional Atmospheric Chemical Transport Model for 25 - 27.07.96 shows some differences both in tropical and in polar zones. Model overestimates the total NO_2 in polar regions and underestimates it in tropics relative to GOME results, but their globally averaged values are close to each other. The more smoothed latitudinal distribution of the modeled total NO_2 relative to GOME data is partly due to using the climatic July wind field in calculations having no actual wind field data for the considered period.

6. REFERENCES

1. Chu, W & McCormic M P 1996, SAGE observations of stratospheric nitrogen dioxide, *J. Geophys. Res.*, 91, 5465-5476.
2. Bevilacqua, R M 1997, Introduction to special section: Polar Ozone and Aerosol Measurement (POAM II), *J. Geophys. Res.*, 102, D19, 23591-23592.
3. Laurent, J & al 1985, Middle atmospheric NO and NO_2 observed by the Spacelab grill spectrometer, *Nature*, 315, 126-127.
4. Allen, M & Delitsky 1990, Stratospheric NO, NO_2, and N_2O_5: A comparison of model results with Spacelab 3 Atmospheric Trace Molecular Spectroscopy (ATMOS) measurements, *J. Geophys. Res.*, 95, D10, 14077-14082.
5. Newchurch, M J & al 1996, Stratospheric NO and NO2 abundunces from ATMOS solar-occultation measurements, *J. Geophys. Res. Let.*, 23, 17, 2373-2376.
6. Russel, J M & al 1984, Validation of nitrogen dioxide results measured by the Limb Infrared Monitor of the Stratosphere (LIMS) experiment on Nimbus 7, *J. Geophys. Res.*,89, D4, 5099-5118.
7. Reburn, W J & al 1996, Validation of nitrogen dioxide measurements from the Improved Stratospheric and Mesospheric Sounder, *J. Geophys. Res.*, 101, D6, 9873-9895.
8. Burrows, J P & Chance K V 1992, SCIAMACHY and GOME: the scientific objectives, *Proc. of SPIE*, 1715, 502-512.
9. GOME Geophysical Validation Campaign, Final results Workshop Proceedings, 24-26.1.96 (ESA-WPP 108, 1996)
10. McKenzie, R L & al 1991, Altitude distributions of stratospheric constituents from ground-based measurements at twilight, *J. Geophys. Res.*, 96, 15499-15511.
11. Elokhov, A S & Gruzdev A N 1993, Spectrometric measurements of total NO_2 in different regions of the globe, *Proc SPIE*, 2107, 111-121.
12. Elokhov, A S & Gruzdev A N 1995, Estimation of tropospheric and stratospheric NO_2 from spectrometric measurements of column NO_2 abundances, *Proc SPIE*, 2506, 444-454.
13. Barnett, J J & Corney M 1985, Middle atmosphere model derived from satellite data, *Handbook for MAP*, 16, 47-85.
14. Keating, G M & Pitts M C 1987, Proposed reference models for ozone, *Adv. Space Res.*, **7**, (9)37-(9)47.
15. Gruzdev A N & Sitnov S A 1994, Analysis of the annual variation of tropospheric and stratospheric ozone derived from ozonesonde data, *Izvestiya, Atmos. Oceanic Phys.*, 30, 491-500.
16. Rozanov, E V & al 1998, The UIUC 3-D Atmospheric Chemical Transport Model: Description and evaluation of the simulated source gases and ozone, *J. Geophys. Res* (submitted).

A PSEUDO-GLOBAL CORRELATIVE STUDY OF ERS-2 GOME NO_2 DATA WITH GROUND-, BALLOON-, AND SPACE-BASED OBSERVATIONS

J.-C. Lambert, J. Granville, M. Van Roozendael, and J.-F. Müller

Belgian Institute for Space Aeronomy (IASB-BIRA), Avenue Circulaire 3, B-1180 Brussels, Belgium
phone: +32-2-373 04 68; fax: +32-2-374 84 23; lambert@bira-iasb.oma.be

J.-P. Pommereau, F. Goutail, and A. Sarkissian

Service d'Aéronomie du CNRS (CNRS/SA), BP3, F-91371 Verrières-le-Buisson Cedex, France
phone: +33-1-64 47 42 88; fax: +33-1-69 20 29 99; pommereau@aerov.jussieu.fr

ABSTRACT

After nearly four years of successful operation aboard ERS-2, the current total NO_2 data record inferred routinely from GOME measurements allows a year-round evaluation of both versions 2.0 and 2.3 of the operational GOME Data Processor (GDP). Their respective performance is investigated by means of high-quality correlative observations performed by a pseudo-global ground-based network of UV-visible spectrometers, under a variety of relevant geophysical conditions. The study concludes that the total NO_2 data product derived with GDP 2.0 is unreliable, mainly due to the use of a partially inadequate NO_2 database in the evaluation of optical enhancement factors. Improved with a more acceptable database, GDP 2.3 provides a more consistent data product. However, latitudinal and seasonal changes in stratospheric NO_2 as well as tropospheric emissions of NO_x distort the shape of the actual NO_2 vertical distribution and hence affect the optical enhancement factor. To assess the resulting impact on the retrieved vertical column amount, a suitable NO_2 reference atmosphere is built up, combining long-term space-, balloon-, and ground-based measurements and modelling results. The investigation highlights the need to improve the GDP with a NO_2 database including relevant stratospheric features and a consistent three-dimensional tropospheric background.

1. INTRODUCTION

Operating since July 1995 aboard the ESA's Earth observation heliosynchronous polar satellite ERS-2, the Global Ozone Monitoring Experiment (GOME, ESA 1995) observes at nadir, between 240 nm and 790 nm, with a resolution of 0.2 to 0.4 nm, the solar radiation backscattered by the atmosphere. The atmospheric abundance of several trace species, including nitrogen dioxide (NO_2), is derived from GOME spectra using the Differential Optical Absorption Spectroscopy (DOAS). Line-of-sight column amounts, or apparent slant columns, are retrieved with an iterative least-squares procedure, fitting the observed differential optical thickness with differential absorption cross-sections derived from laboratory measurements. Slant columns are converted into vertical columns using an optical enhancement factor, or air mass factor (AMF). The AMF is evaluated with a radiative transfer model assuming vertical distributions of the target absorber and of the atmospheric constituents controlling the path of the solar radiation through the atmosphere. For several decades, the DOAS has also been widely used for the interpretation of ground-based observations of the UV-visible sunlight scattered at zenith by the atmosphere. Deployed from the Arctic to the Antarctic within the framework of the Network for the Detection of Stratospheric Change (NDSC), about 30 zenith-sky UV-visible spectrometers monitor total NO_2 twice daily at twilight (Lambert *et al.*, 1999, and references therein).

The performance of the GOME total NO_2 data product has been investigated at every step of its maturation by means of ground-based observations associated with the NDSC. After evaluation of the successive developmental versions 1.x of the GOME Data Processor (GDP), a preliminary ground-based analysis of the first operational version GDP 2.0 was carried out with a limited set of GOME data from July through November 1996 (Lambert *et al.*, 1997). The study highlighted the high sensitivity of nadir-viewing AMFs to the shape of the NO_2 vertical distribution. The NO_2 profile database used in GDP 2.0 was also shown to be partially inadequate for the evaluation of GOME AMFs. According to recommendations drawn from this preliminary study, a more acceptable NO_2 database was implemented in GDP 2.3, operational since January 1998. A first verification exercise concluded to the better general consistency of GDP 2.3 total NO_2 data (Lambert and Simon, 1998). However, it also stressed the need to investigate the impact of seasonal and latitudinal changes in stratospheric NO_2 and of tropospheric emissions of NO_x, on the GOME AMF due to alteration of the NO_2 profile shape.

Described in section 2, the data record available at the time of the present study allows the pseudo-global, year-round evaluation of both versions 2.0 and 2.3 of the GOME total NO_2 product reported in section 3. Seasonal and latitudinal biases of stratospheric origin in both the GDP 2.3 and ground-based vertical columns are estimated in section 5 by means of a composite climatology built up from ground-, balloon-, and space-based observations and modelling results, described in section 4. The impact of tropospheric NO_x emissions on the GOME AMFs is assessed in section 6. The paper concludes with recommendations to improve the quantitative derivation of the NO_2 vertical column amount from GOME data.

2. DATA SETS

2.1 GOME level-2 data record

The GOME total NO_2 data record available at the time of the present study was obtained with two versions of the operational level-1b-to-2 retrieval algorithm: GDP 2.0 for 1996-1997, and GDP 2.3 since January 1998 and also for 1995.

Between the two versions, most relevant improvements to total NO_2 processing are connected with the evaluation of AMFs: (a) substitution of the NO_2 profile database; (b) use of multiple scattering look-up table of AMFs computed with an upgraded radiative transfer model; (c) new weighting and time/latitude interpolation schemes; and (d) correction of a known error in the detection of clouds. Two time periods identified by dashed boxes in the time-series of Figures 1 and 2 are affected by irrelevant retrieval due to wavelength registration problems in the spectral channel 3 of the instrument. The atmospheric profile database used in GDP 2.0 is based on results of a two-dimensional chemical transport model of the atmosphere developed at the Max Planck Institute (hereafter MPI-2D, Crutzen and Gidel, 1983). MPI-2D profiles represent seasonal mean estimates in 10° latitude belts. GDP 2.3 AMFs are based on the daytime estimate for United States (US Standard) included in the AFGL Reference Atmosphere (Anderson *et al.*, 1986).

2.2 Ground-based vertical column amounts

Measurements of the NO_2 vertical column amount at twilight have been collected from 24 zenith-sky UV-visible DOAS spectrometers operating at the stations listed in Table 1: (a) 5 instruments developed by NIWA since the late 1970s (McKenzie and Johnston, 1982); (b) 15 SAOZ instruments (Système d'Analyse par Observation Zénithale) developed by CNRS and performing automated network operation since the late 1980s (Pommereau and Goutail, 1988); and 4 spectrometers of a similar design developed at (c) IASB (Van Roozendael *et al.*, 1995), (d) IFE (Richter *et al.*, 1998), and (e) NILU (Arlander *et al.*, 1998), respectively. Using high-resolution Fourier transform infrared (FTIR) solar spectrometry, the NO_2 column amount throughout the day has also been measured at the Jungfraujoch station by the University of Liège, as part of its monitoring activities initiated in the 1950s (Delbouille and Roland, 1995). Most of the contributing UV-visible sensors have been certified for the NDSC after fruitful participation to major intercomparison campaigns organised through the NDSC or the EC Environment Programme. During such campaigns, the agreement between the various instruments generally falls within 5-10% (e.g., Vaughan *et al.*, 1997; Roscoe *et al.*, 1999). The figure is consistent with an estimated 5-10% accuracy of the retrieved slant column amount taking into account the 5% uncertainty of the NO_2 absorption cross-sections (Merienne *et al.*, 1995), their temperature dependence (Harwood and Jones, 1994; Coquart *et al.*, 1995), and the average 1.5% one sigma confidence level of the least-squares spectral fit. The largest uncertainty in the vertical column remains the AMF, which varies by large factors with the time of the day, the latitude and the season, and has been difficult to characterise until recently due to the near absence of profile measurements. Most of the contributing total NO_2 data records are based on single profiles measured in 1983 during the MAP/GLOBUS balloon campaign (Pommereau *et al.*, 1987), or on the AFGL Reference Atmosphere. Usually, ground-based data are obtained with two different levels of data processing: (i) a version 0 (NIWA) or real-time (SAOZ) spectral analysis, generally performed at the station and transmitted via the ARGOS satellite collection system or the Internet, aiming at a quick evaluation and dissemination of preliminary data; and (ii) a state-of-the-art analysis providing high accuracy data. A characteristic of real-time data consists of their retrieval with absorption cross-sections at room temperature. Consequently, slant columns must be reduced by about 15% due to the large temperature dependence of the NO_2 cross-sections. Data acquired with instruments equipped with uncooled detectors and operating in a severely changing environment must also be corrected for the temporal variation of the instrument slit function arising from instrument temperature changes. State-of-the-art data are all retrieved with low temperature cross-sections and, when relevant, with a dynamic slit function. They have been used here for quantitative investigation of the GOME NO_2 data product, while real-time data have provided valuable support for the pseudo-global extension of the investigation and for the regular monitoring of the GOME performance since the beginning of its operation in July 1995.

Table 1. Contributing ground-based stations

Location	Lat.	Long.	Institute
Ny-Ålesund	79°N	12°E	NILU, IFE
Longyearbyen	78°N	16°E	NILU
Thulé	77°N	69°W	DMI
Scoresbysund	70°N	22°W	CNRS/DMI
Sodankylä	67°N	27°E	CNRS/FMI
Salekhard	67°N	67°E	CNRS/CAO
Zhigansk	67°N	123°E	CNRS/CAO
Harestua	60°N	10°E	IASB
Bremen	53°N	9°E	IFE
Aberystwyth	52°N	4°W	U. Wales
Jungfraujoch	47°N	8°E	IASB, U. Liège
Haute Provence	44°N	6°E	CNRS
Mauna Loa	20°N	156°W	NIWA
Tarawa	1°N	172°E	CNRS, NIWA
Saint Denis	21°S	55°E	U. Réunion
Bauru	22°S	48°W	CNRS/UNESP
Lauder	45°S	170°E	NIWA
Kerguelen	49°S	70°E	CNRS
Macquarie	55°S	159°E	NIWA
Faraday	65°S	64°W	BAS
Dumont d'Urville	67°S	140°E	CNRS
Rothera	68°S	68°W	BAS
Arrival Heights	78°S	167°E	NIWA

3. PSEUDO-GLOBAL GROUND-BASED COMPARISONS

3.1 GOME Data Processor version 2.0

Comparisons of the GOME and ground-based total NO_2 are illustrated in Figure 1 at six typical stations from north to south. Except at Kerguelen, ground-based data displayed in the figure are all retrieved with state-of-the-art algorithms, including NO_2 absorption cross-sections at stratospheric temperatures and dynamic instrument slit function. Conclusions drawn from the first pole-to-pole study (Lambert *et al.*, 1997) remain valid throughout the time period of operational processing with GDP 2.0. The agreement is found to vary significantly with the season and the latitude. A striking feature is the difference between latitudes below 30°N and beyond. Although GOME reports lower values than the ground-based instruments, the general agreement can be considered as reasonable at southern latitudes and up to 30°N, that is, within 5% to 20%. On the opposite, the agreement at higher northern latitudes is mediocre and its quantification often is irrelevant. GOME total NO_2 data beyond 30°N are affected by 3-months shifts of significant amplitude, leading to

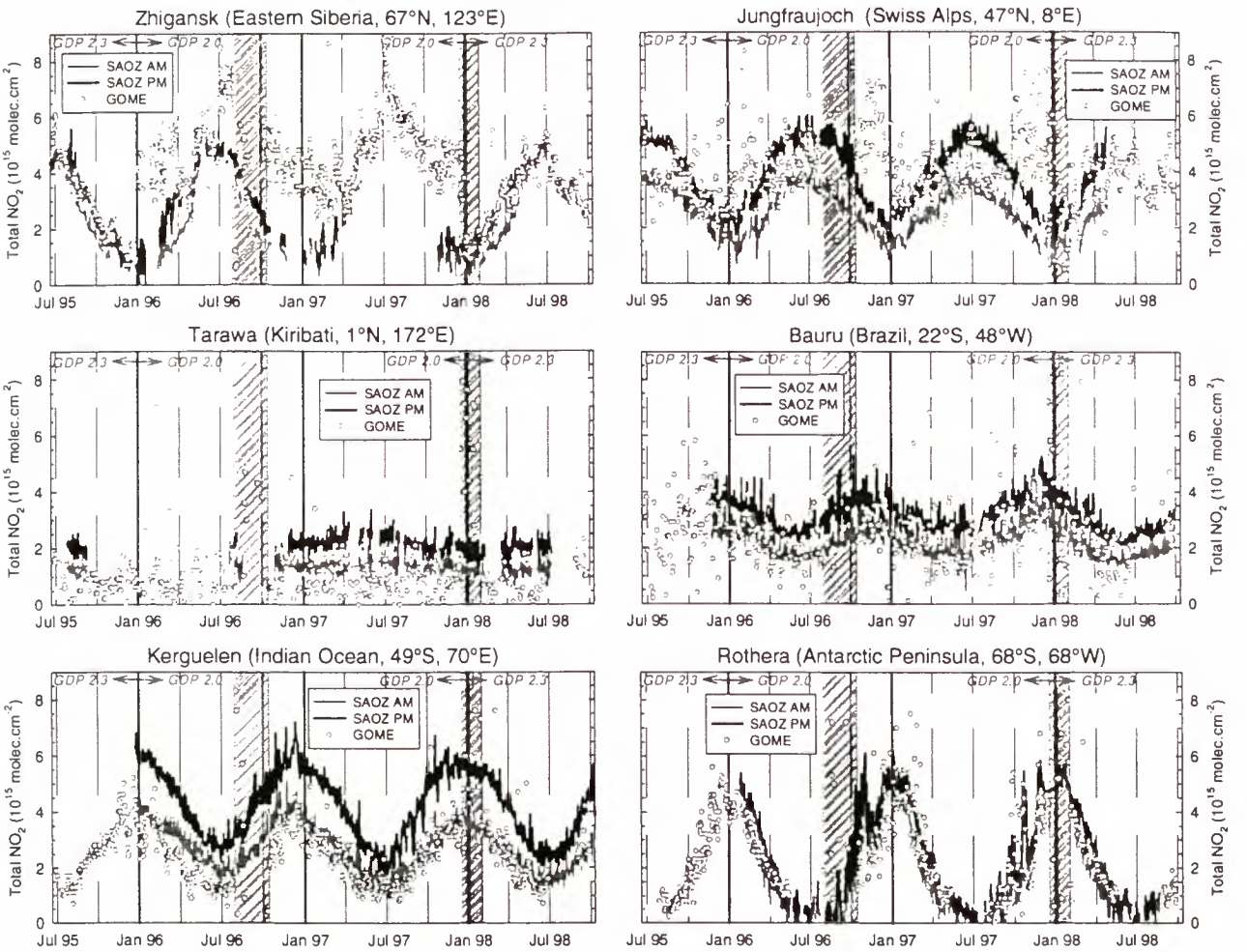

Figure 1. Time-series of the NO_2 vertical column amount derived from ERS-2 GOME and from ground-based observations at six typical stations from north to south. Dashed areas indicate time periods when NO_2 retrieval is dramatically affected by known problems in the spectral channel 3 of the GOME instrument.

a seasonal variation inconsistent with ground-based observations. Enhanced in most of the cases, the day-to-day variability of GOME data is also found to vary with the season and the latitude. The lowest dispersion is observed at middle and high southern latitudes, except during overpass of the station by the border of the polar vortex. It is already larger in the subtropics, where the measured differential optical depth and the signal-to-noise ratio are weaker. Finally, the day-to-day dispersion increases to unrealistic values at northern latitudes, especially in fall and winter, exceeding by far both the day-to-day and dusk-to-dawn differences observed from the ground. The qualitative analysis of global NO_2 maps inferred from GOME level-2 data highlights aberrant spatial structures in the Northern Hemisphere. Anomalies are also detected along orbits, such as the high dispersion of total NO_2 values from pixel to pixel along track, or an unphysical increase of the NO_2 column over summer polar regions in midnight sun conditions. The study also confirms the frequent occurrence of aberrant individual values in the vertical column amounts: negative, or too high by one and sometimes two orders of magnitude, associated with unacceptable error values on the DOAS fitting. There is also a major concern as to the reliability of GDP 2.0 slant column amounts from July 1996 through June 1997: from north to south, they are found to be systematically quantified, as illustrated in Figure 2 over the Alpine region. The apparent dispersion of total column values during this period arises from the division of the slant columns by an AMF influenced by pseudo-random parameters, such as the cloud cover in the line-of-sight, the surface albedo, or the effective line-of-sight angles.

Except aforementioned problems specific to the retrieved slant column amounts which suggest possible problems in the spectral fitting segment of the processing chain, major geophysical inconsistencies of the GDP 2.0 vertical column amount can be explained partly by looking at the corresponding AMF time-series. The three-month shifts observed in Figure 1 in the agreement with ground-based observations at the Jungfraujoch correlate with three-month shifts in the GDP AMF appearing in Figure 2. The principal cause of the problem at latitudes higher than 30°N has already been pointed out in the study reported by Lambert *et al.* (1997). It originates from the use of partially inadequate NO_2 vertical distributions in the calculation of the GOME AMF combined with the enhanced sensitivity of this latter to the actual atmospheric profile shape. The weak consistency of the GDP 2.0 total NO_2 product arises from unreasonable tropospheric burden and shape of the MPI-2D profiles at those latitudes, which decrease drastically the AMF and in addition increase the sensitivity of the AMF to the troposphere. Regions with a relatively clean troposphere – e.g.,

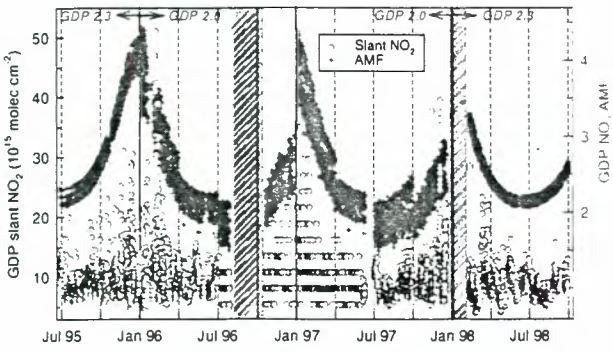

Figure 2. ERS-2 GOME NO_2 slant column amount and down-to-ground AMF over the Alpine region, extracted from level-2 data files generated with GDP 2.0 and 2.3.

the Eastern Siberian station of Zhigansk in Figure 1 - are particularly affected since AMFs are calculated with zonal mean profiles, strongly biased towards the extreme values characteristic of heavily polluted regions. Three-month shifts originate in the strong seasonal difference of the tropospheric burden of the MPI-2D profiles. The effect vanishes towards south where tropospheric amounts become insignificant.

3.2 GOME Data Processor version 2.3

Typical comparisons illustrated in Figure 1 show that the geophysical consistency of the GOME total NO_2 data at northern latitudes has improved significantly with GDP 2.3, especially in fall and winter. The implementation of the US Standard profile in the AMF calculation has produced the expected effect. Three-month shifts seem to have disappeared in both the vertical columns (e.g., Figure 1) and the AMFs (e.g., Figure 2). The seasonal variation of the vertical column is in better agreement with that observed from the ground. From the northern Tropic through the Southern Hemisphere where MPI-2D tropospheric burdens were already more realistic than beyond 30°N, the mean agreement remains reasonable but GOME persists in reporting generally lower values than the ground-based instruments. As demonstrated in section 5, both GOME and NDSC time-series are affected by cyclic biases due to changes in stratospheric NO_2. However, after taking those cyclic biases into account, differences persist, or even increase by a few percent. E.g., GOME total NO_2 at the Equator remains lower than ground-based data by a factor of two. At all latitudes, the quantitative comparison of GDP 2.3 data acquired in 1995 and 1998 does not reveal any significant long-term drift. The occurrence of aberrant individual values of the vertical column amount is less frequent, however, negative or highly scattered values are detected in both the slant and vertical columns and error values on the DOAS fitting remain high, suggesting that the spectral analysis in GDP still needs to be refined.

4. COMPOSITE NO_2 REFERENCE ATMOSPHERE

The evaluation of the optical enhancement of scattered light requires an accurate knowledge of the atmospheric parameters affecting the radiative transfer. An improved database of NO_2 atmospheric profiles has been built up, combining long-term observations from ground-, balloon- and space-based sensors, and modelling results. The concept is illustrated in Figure 3

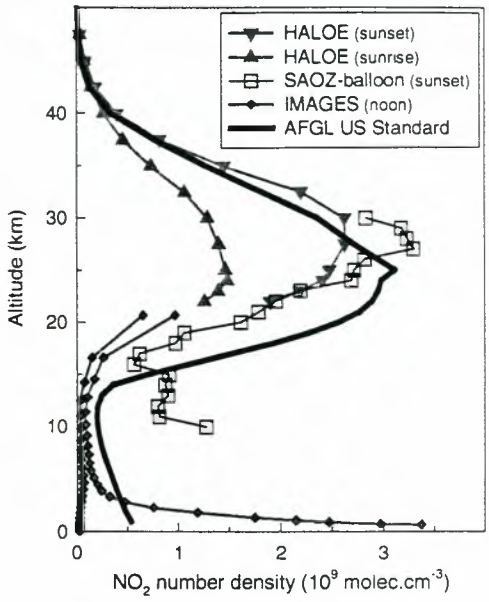

Figure 3. Vertical distribution of NO_2 over Bauru (Brazil) at the end of November, derived from: (a) climatological study of HALOE sunrise and sunset zonal means; (b) SAOZ-balloon measurement at Bauru on 29 November 1996; (c) IMAGES modelling results typical of a clean (Pacific ocean) and polluted (Brazil) troposphere; and (d) AFGL US Standard.

where the different sources for a Brazilian station are compared to the US Standard profile. The information in the middle and upper stratosphere relies on twilight profiles measured for more than 7 years by the Halogen Occultation Experiment (HALOE, Russell *et al.*, 1993) aboard the US UARS platform. HALOE NO_2 data cover altitudes spanning from above the stratopause down to 20 km, however, the accuracy of version 18 used here degrades at altitudes below 25 km, mainly because of Mie scattering by stratospheric aerosols. A three-dimensional chemical transport model of the global troposphere, named Intermediate Model of Global Evolution of Species (IMAGES, Müller and Brasseur, 1995), has been developed jointly at IASB-BIRA and at the National Center for Atmospheric Research (NCAR) to study the global distributions, budgets and trends of 41 chemical compounds, including nitrogen oxides. Modelling results are found to be generally in good agreement with correlative airborne *in situ* measurements. IMAGES has been run to provide monthly means of the vertical distribution of tropospheric NO_2 at local noon, onto a 5° x 5° grid. A database of NO_2 profiles measured during more than 80 flights of the SAOZ-balloon experiment (Pommereau and Piquard, 1994) at middle and high northern latitudes in various seasons and in Brazil, fill in the altitude gap between the HALOE and IMAGES data sets. Covering altitudes from 8 km up to 30 km, the long-term SAOZ-balloon data record gives also a unique opportunity to evaluate the quality of the HALOE and IMAGES information at altitudes where their accuracy might degrade. Climatological information on temperature, pressure and geopotential height has been derived from statistical analyses of European Centre for Medium Range Weather Forecasts data (Trenberth, 1992) and from the COSPAR International Reference Atmosphere (Fleming *et al.*, 1990). Taking into account the high sensitivity of the AMF to the profile shape of the NO_2 vertical distribution, a special care has been given to each step of the

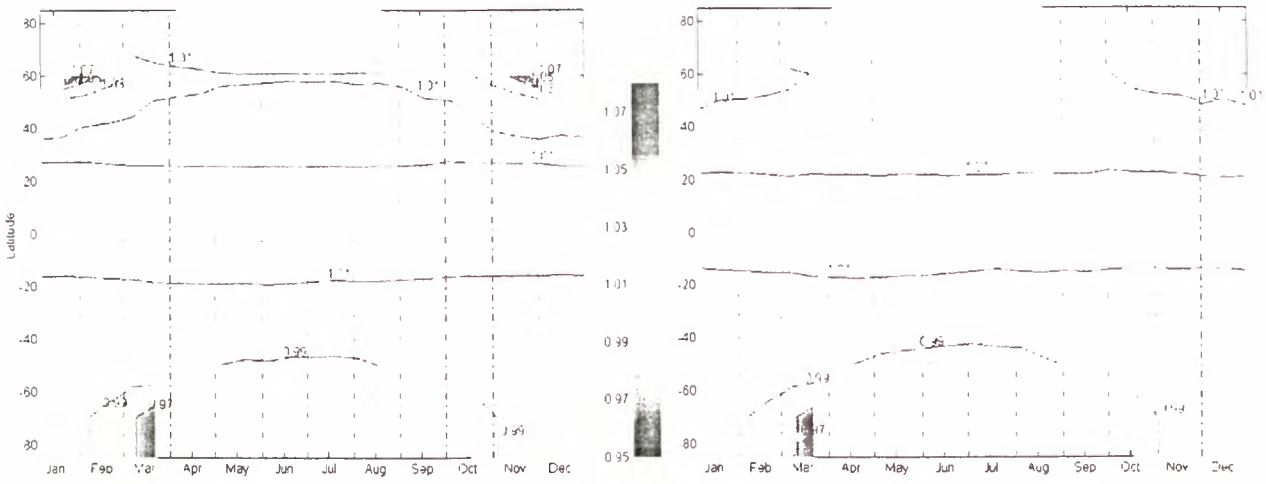

Figure 4. Ratio of nadir-viewing optical enhancement factors for NO_2 calculated with the US Standard and climatological NO_2 atmospheric profiles, as a function of latitude and time, for a sunrise (left panel) and sunset (right panel) stratosphere.

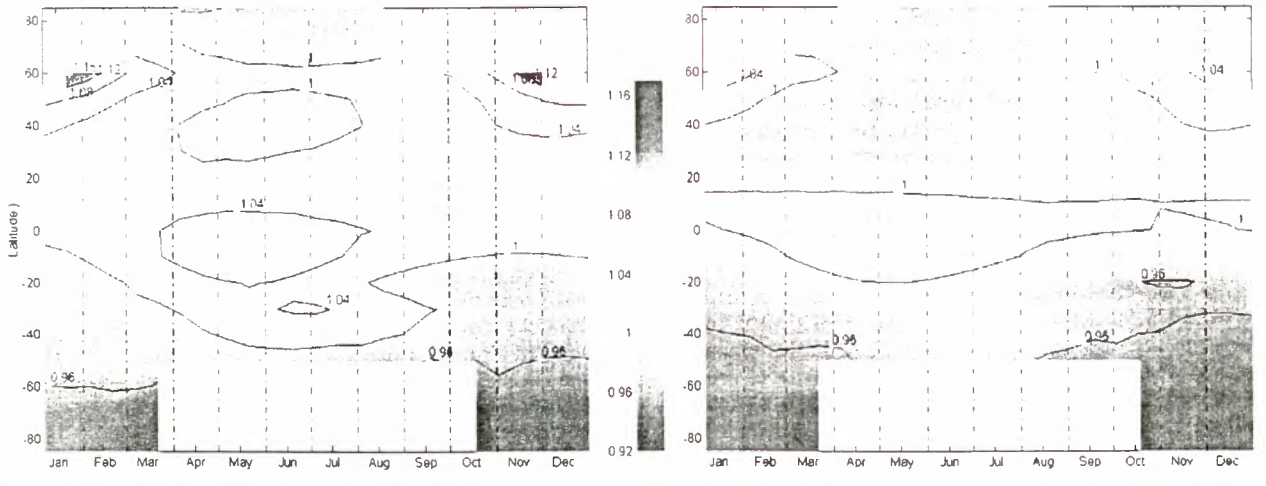

Figure 5. Same as Figure 4, but at 90° SZA in the zenith-sky observation geometry, at sunrise (left panel) and sunset (right panel).

database compilation. The geophysical consistency and the accuracy of the final composite database have been verified from pole to pole, among others by comparison with long-term ground-based observations of stratospheric NO_2. Finally, the database has been implemented in an AMF processor based on both an in-house single scattering radiative transfer model (Sarkissian *et al.*, 1995) and the UVSPEC package (Kylling, 1995) using a pseudo-spherical adaptation of the multiple scattering Discrete Ordinate Radiative Transfer model (DISORT, Dahlback and Stamnes, 1991).

5. CYCLIC SIGNATURES OF STRATOSPHERIC ORIGIN

Seasonal and latitudinal changes in solar illumination, temperature, and distribution of N_2O, the main stratospheric source of NO_2, cause the NO_2 stratospheric profile shape to vary significantly, resulting in a seasonal and latitudinal variation of the AMF. The single profile used by GDP 2.3 or by the ground-based retrieval algorithms cannot take the effect into account, and its use generates in the resulting total columns, fictitious cyclic signatures superimposed on the real total NO_2 variations observed by the instrument. To assess the NO_2 stratospheric profile shape effect and the resulting bias in both the GDP 2.3 and NDSC NO_2 vertical columns, US Standard AMFs have been compared with climatological AMFs. Seasonal and latitudinal components of stratospheric origin have been estimated from the climatological study of the aforementioned HALOE and SAOZ-balloon empirical database. Stratospheric profiles have been completed with IMAGES tropospheric profiles representative of regions free from surface emissions for each latitude belt. From pole to pole, the geophysical consistency of the resulting semi-empirical model has been verified in the long term by comparison with ground-based observations of stratospheric NO_2. Nadir-viewing AMFs have been estimated at the actual mid-morning GOME SZA. Other relevant parameters are: surface albedo of 5%; aerosols: background; line of sight: 0°; wavelength: 437 nm.

5.1 ERS-2 GOME

Figure 4 depicts seasonal and latitudinal variations of the ratio between AMFs calculated in the nadir viewing geometry with the US Standard profile and the stratospheric climatology. The

AMF ratio is a first approximation of the factor by which GDP vertical column amounts should be multiplied to take into account the seasonal/latitudinal bias of the US Standard AMF. The ratio can show more pronounced amplitude with a sunrise stratosphere. This is likely due to the reduced amount of stratospheric NO_2 before the daytime photolysis of its nighttime reservoir N_2O_5, combined to other effects affecting the profile shape, such as the possible relative importance of the tropospheric NO_2 burden and, in winter, the higher sensitivity of the AMF at large SZA to stratospheric variations. During midnight sun and polar night when the diurnal variation of NO_2 is significantly attenuated, and in regions with negligible tropospheric background, the AMF ratio exhibits no clear sunrise/sunset difference. Although sometimes different in amplitude, results with a sunrise and sunset stratosphere are qualitatively consistent, and the ratio at mid-morning should fall between sunrise and sunset values. In the subtropics, the US Standard AMF would yield underestimated vertical column amounts by 1% to 3%. At middle and high latitudes, a clear seasonal variation appears. In summertime, the overall agreement generally falls within 1%. At polar latitudes in fall and spring, the drastic reduction of stratospheric NO_2 distorts the profile shape in such a way that the US Standard AMF would lead to vertical columns too high by 2% in the Arctic to 5% in Antarctica. Denoxification inside the polar vortex would increase the effect. At northern middle latitudes, GDP vertical columns in fall and winter would be underestimated by 1% to 8%. The obvious difference between southern and northern middle latitudes might reflect the difference in the contribution of the troposphere to the net profile shape effect.

5.2 NDSC/UV-visible spectrometers

Figure 5 depicts seasonal and latitudinal variations of the ratio between US Standard and climatological AMFs calculated in the zenith-sky viewing geometry at 90° SZA. Similar results are reached when the US Standard is replaced with other profiles of the AFGL Reference Atmosphere or from the MAP/Globus balloon campaign. Qualitatively, the seasonal and latitudinal variations of the AMF ratio in the zenith-sky geometry display similar patterns compared to those of the AMF ratio at nadir. Quantitatively, variations of the zenith-sky ratio are more pronounced especially at 60°N when they would reach at sunrise a maximum of 15% between summer and winter, against 8% at nadir. Another illustration is the increase of the sunrise underestimation in May at the southern subtropics, from 3% at nadir up to 6% at zenith. Again, the amplitude of the AMF ratio and of its variations at sunrise exceeds sunset values.

6. IMPACT OF TROPOSPHERIC NO_2

Due to its viewing geometry at nadir, GOME is particularly well suited to detect absorbers located in the troposphere. On global maps of NO_2 derived from GOME observations (not shown here), massive emissions of NO_x associated with biomass burning or urban pollution are clearly identifiable by the striking enhancement of the NO_2 slant column amount. As shown in Figure 3, tropospheric emissions bend spectacularly the NO_2 profile shape in the first five kilometres. Consequently, they are expected to modify dramatically the optical enhancement factor. Moreover, it is pointed out in the previous section that the tropospheric background, although moderate, can affect AMF variations of stratospheric origin at northern latitudes. To assess the impact of the tropospheric NO_2 field on the global scale, nadir-viewing AMFs have been evaluated at the actual mid-morning GOME SZA for a variety of representative geographical distributions of tropospheric emissions. The clean zonal tropospheric background used in section 5 has been replaced by three-dimensional IMAGES modelling results, completed by associated climatological stratospheric profiles.

The ratio of AMFs calculated with a clean and a loaded troposphere in March and July is displayed in Figures 6 and 7 with two different colour scales. The dilated colour scale of Figure 6 shows the striking decrease of the AMF in the vicinity of massive NO_x emissions. Tropical biomass burning is associated with an AMF reduction reaching 5% to 20%, while urban and industrial pollution over extended areas can cause the AMF to decrease by 30% in extreme cases. In this exercise, the surface albedo has been fixed to a value of 5%, representative of oceanic conditions. At higher albedo, the reduction of the AMF is less pronounced, and this latter effect is more significant for a loaded than for a clean troposphere. Consequently, the estimated ratio clean/loaded AMF would be reduced over vegetation and ice. The impact of tropospheric emissions depends not only on their strength but also on their relative importance compared to the stratospheric column. Figure 6 shows the significant reduction of the AMF ratio over Europe between March and July, that is, for two very different stratospheric profiles. This latter finding demonstrates the importance of a reliable stratospheric climatology. The reduced colour scale of Figure 7 highlights the influence of the long-range transport of species. AMFs decrease systematically by several percent over the continents, except in a few desert regions. Changes in the AMF ratio over the oceans clearly correlate with changes in the global atmospheric circulation depicted in Figure 8. In particular, the decrease of the loaded AMF over the northern Pacific and Atlantic in March arises from the contamination of the tropospheric background by polluted air masses transported from Asia through the Pacific and from northern America through the Atlantic, respectively.

7. CONCLUSIONS AND RECOMMENDATIONS

The geophysical consistency of the GOME NO_2 data record available at present time has been investigated from pole to pole by means of high-quality ground-based observations associated with the NDSC. The reliability of the data record processed with the version 2.0 of the GDP - operational in 1996 and 1997 - is questionable due to serious problems in both the retrieved slant column amounts and the AMFs. Problems in GDP 2.0 AMFs arise clearly from the use of a partially inadequate NO_2 atmospheric profile database in the AMF evaluation, and the implementation in GDP 2.3 of the AFGL/US Standard NO_2 profile constitutes a first step towards a geophysically consistent total NO_2 product from GOME. However, due to significant variations of the actual profile shape in both the stratosphere and the troposphere, the use of the single US Standard profile generates in the retrieved vertical columns fictitious signatures superimposed on the real total NO_2 variations observed by GOME. Those signatures have been assessed by means of a composite, semi-empirical NO_2 reference atmosphere combining space-, balloon- and ground-based observations and modelling results. Seasonal and latitudinal changes in the stratospheric profile shape result in relative cyclic biases of a few percent, however, the net effect on the AMF is controlled by the tropospheric profile shape. Tropospheric NO_2 reduces the AMF considerably in the vicinity of tropospheric NO_x emissions. Although to a less

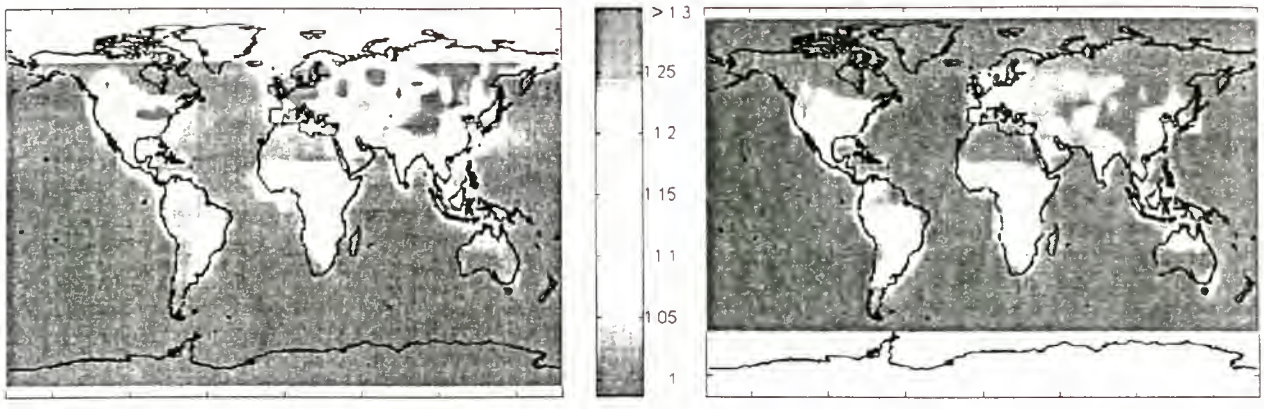

Figure 6. Ratio of nadir-viewing optical enhancement factors for NO_2 calculated with a clean and a loaded noon troposphere. Left panel: March; right panel: July.

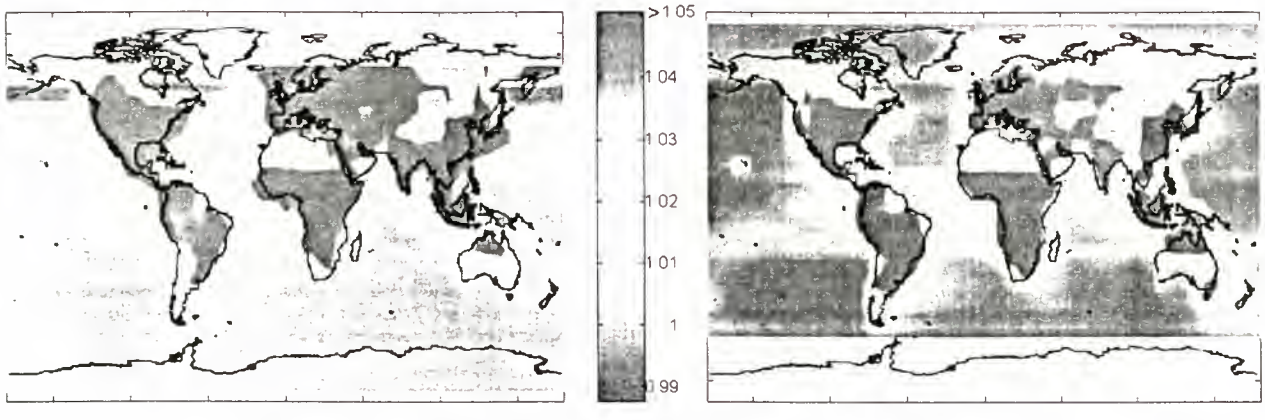

Figure 7. Same as Figure 6, but with colour scale saturated at 1.05

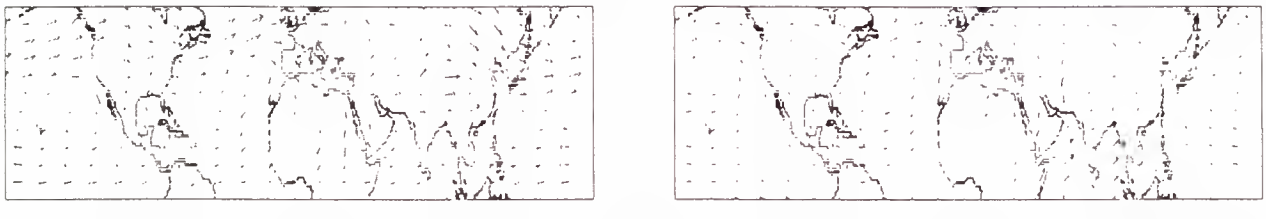

Figure 8. March (left panel) and July (right panel) monthly means of the atmospheric circulation (direction and relative intensity) over the northern Pacific and Atlantic oceans at altitudes between 500 and 850 hPa (derived from Trenberth *et al.*, 1992).

extent, the effect is also observed in remote geographical areas free of tropospheric emission sources, due to the long-range transport of polluted air masses. It is timely to emphasise that the coupled stratospheric and tropospheric profile shape effects will affect the scientific exploitation of nadir total NO_2 data from the progammed GOME series as well as tropospheric information derived from the interleaved limb/nadir mode of the SCIAMACHY to be flown aboard ENVISAT-1.

According to the conclusions drawn from the present study, it is vigorously recommended to improve the operational GDP with an adequate NO_2 reference atmosphere inspired from that developed here, including relevant stratospheric features as well as a consistent 3-dimensional tropospheric background. Over regions affected by intense NO_x emissions, the extreme spatial and temporal variability of the NO_2 field makes the use of a fixed tropospheric database hazardous. Moreover, the enhanced sensitivity of the retrieved vertical column amount to the profile shape is inherent to the static retrieval approach adopted up to now in GDP. Therefore, it might be preferred to adopt for polluted conditions an iterative approach, e.g., consisting of the selection of an adequate reference troposphere after first retrieval of information on the tropospheric burden from GOME data themselves. Finally, the observed bias between the GOME and ground-based total NO_2 time-series persists or increases after deduction of the stratospheric profile shape effect on both the GOME and ground-based data records. This latter finding suggests that other issues related to the retrieval of the slant column amount remain to be addressed, among others, the quality of the DOAS fitting procedure, or the impact of the temperature dependence of the NO_2 absorption cross-sections.

8. ACKNOWLEDGEMENTS

The authors address all their acknowledgements to the contributing instrument PIs and operators for providing high quality data and for fruitful discussions. They would like to thank especially: S.B. Andersen and P. Eriksen (DMI), D.W. Arlander, K. Karlsen Tørnkvist, and B.A. Kåstad Høiskar (NILU), N.A. Bui Van (UNESP), P. Demoulin and R. Zander (U. Liège), V. Dorokhov (CAO), A.C. Green and G. Vaughan (U. Wales), J. Hill and H.K. Roscoe (BAS), P.V. Johnston and K. Kreher (NIWA), E. Kyrö (FMI), J. Leveau (U. Réunion), K. Munderloh, A. Richter, and F. Wittrock (IFE/IUP), and W. Thomas (DFD/DLR). The logistic support provided by P. Gerard (IASB-BIRA) and J. Hottier (CNRS/SA) is greatly appreciated. GOME level-2 products were processed at DFD/DLR on behalf of ESA. The HALOE operation and science teams are acknowledged for supplying data via the NASA/GSFC DAAC. The reported work has been supported by the PRODEX ERS-2 project and by the Belgian Science Policy Office (OSTC) in Belgium, by the Programme de Chimie de l'Atmosphère in France, by the EC within the framework of the SCUVS, ESMOS and COSE projects, and by an INTAS/CNES grant.

9. REFERENCES

Anderson, G.P., S.A. Clough, F.X. Kneizys, J.H. Chetwynd, and E.P. Shettle, 1986: AFGL Atmospheric Constituents Profiles (0-120 km), AFGL-TR-86-0110, Env. Res. Papers, No. 954 (43 pp.), AFGL (OPD), Hanscom AFB, MA 01736.

Arlander, D.W., K.K. Tørnkvist, and G.O. Braathen, 1998: Ground-based UV-Vis Validation Measurements of Stratospheric Molecules above Spitsbergen, in *Proc. 24th Annual European Meeting on Atmospheric Studies by Optical Methods, Andenes 1997*, ISBN 82-994583-0-7, pp. 185-188.

Coquart, B., A. Jenouvrier, and M.-F. Merienne, 1995: The NO_2 Absorption Spectrum II. Absorption Cross Sections at Low Temperature in the 400-500 nm Region, *J. Atm. Chem.*, 21, pp. 251-261.

Crutzen, P.J., and L.T. Gidel, 1983: A two-dimensional model of the atmosphere, 2: The tropospheric budgets of the anthropogenic chlorocarbons CO, CH4, CH3Cl, and the effects of various NOx sources on tropospheric ozone, *J. Geophys. Res.*, 88, pp. 6641-6661.

Dahlback, A., and K. Stamnes, 1991: A new spherical model for computing the radiation field available for photolysis and heating at twilight, *Planet. Space Sci.*, 39, pp. 671-683.

Delbouille, L., and G. Roland, 1995: High resolution solar and atmospheric spectroscopy from the Jungfraujoch high-altitude station, *Optical Eng.*, 34, pp. 2736-2739.

ESA, 1995: Global Ozone Monitoring Experiment (GOME) Users Manual (191 pp.), ESA SP-1182.

Fleming, E.L., S. Chandra, J.J. Barnett, and M. Corney, 1990: COSPAR International Reference Atmosphere, Chapter 2: Zonal mean temperature, pressure, zonal wind and geopotential height as functions of latitude, *Adv. Space Res.*, 10(12), pp. 11-59.

Harwood, M. H., and R. L. Jones, 1994: Temperature Dependent Ultraviolet Cross-sections of NO_2 and N_2O_4: Low Temperature Measurements of the Equilibrium Constant $2NO_2$ <--> N_2O_4, *J. Geophys. Res.*, 99, pp. 22 955-22 964.

Kylling, A., 1995: UVspec, a program package for calculation of diffuse and direct UV and visible intensities and fluxes.

Lambert, J.-C., M. Van Roozendael, J.-F. Müller, P.C. Simon, M. De Mazière, *et al.*, 1997: Pole-to-pole validation of the ERS-2 GOME level-2 products with the SAOZ ground-based network, *Proc. 3rd ERS Scientfic Symp., Florence 1997* (3 Vol.), ESA SP-414, Vol. II, pp. 629-636.

Lambert, J.-C., and P.C. Simon, 1998: Geophysical Comparison of the GOME Data Processors GDP 2.0 and 2.3 by Means of Ground-based Networks, in GOME Data Improvement Validation Report (58 pp.), B. Greco (Ed.) - ESA/ESRIN APP/AEF/17/GB, pp. 34-42.

Lambert, J.-C., M. Van Roozendael, M. De Mazière, P.C. Simon, J.-P. Pommereau, *et al.*, 1999: Investigation of pole-to-pole performances of spaceborne atmospheric chemistry sensors with the NDSC, *J. Atmos. Sci.*, 56, pp. 176-193.

McKenzie, R.L., and P.V. Johnston, 1982: Seasonal variations in stratospheric NO_2 at 45°S, *Geophys. Res. Lett.*, 9, pp. 1255-1258.

Müller, J.-F., and G.P. Brasseur, 1995: IMAGES: A three-dimensional chemical transport model of the global troposphere, *J. Geophys. Res.*, 100, pp. 16 445-16 490.

Pommereau, J.-P., P. Fabian, G. Flentje, M. Helten, H.W. Patz, *et al.*, 1987: Intercomparison of stratospheric NO_2 and NO_3 measurements during MAP/GLOBUS 1983, *Planet. Space Sci.*, 35, pp. 615-629.

Pommereau, J.-P., and F. Goutail, 1988: Ground-based Measurements by Visible Spectrometry during Arctic Winter and Spring 1988, *Geophys. Res. Lett.*, 15, pp. 891-894.

Pommereau, J.-P., and J. Piquard, 1994: Ozone and nitrogen dioxide vertical distributions by UV-visible solar occultation from balloons, *Geophys. Res. Lett.*, 21, pp. 1227-1230.

Richter, A., M. Eisinger, F. Wittrock, S. Schlieter, A. Ladstätter-Weißenmayer, and J. P. Burrows, 1998: Zenith sky and GOME DOAS measurements of atmospheric trace gases above Bremen, 53°N: 1994 - 1997, in *Polar Stratospheric Ozone - Proc. 4th European Workshop, Schliersee 1997*, N.R.P. Harris, I. Kilbane-Dawe, and G.T. Amanatidis (Eds.), Air Pollution Research Report 66 (CEC DG XII), pp. 482- 485.

Roscoe, H.K., P.V. Johnston, M. Van Roozendael, A. Richter, J. Roscoe, *et al.*, 1999: Slant column measurements of O_3 and NO_2 during the NDSC intercomparison of zenith-sky UV-visible spectrometers in June 1996, *J. Atmos. Chem.* (in press).

Russell, J.M. III, L.L. Gordley, J.H. Park, S.R. Drayson, W.D. Hesketh, *et al.*, 1993: The Halogen Occultation Experiment, *J. Geophys. Res.*, 98, pp. 10 777-10 797.

Sarkissian, A., H.K. Roscoe, D.J. Fish, M. Van Roozendael, M. Gil, *et al.*, 1995: Ozone and NO_2 air-mass factors for zenith-sky spectrometers: Intercomparison of calculations with different radiative transfer models, *Geophys. Res. Lett.*, 22, pp. 1113-1116.

Trenberth, K. E., 1992: Global Analyses from ECMWF and Atlas of 1000 to 10 mb Circulation Statistics, NCAR Technical Note NCAR/TN 373+STR (191 pp. + 24 fiche), NCAR, Boulder, CO.

Van Roozendael, M., C. Hermans, Y. Kabbadj, J.-C. Lambert, A.-C. Vandaele, *et al.*, 1995: Ground-Based Measurements of Stratospheric OClO, NO_2 and O_3 at Harestua, Norway (60°N, 10°E) during SESAME, in *Proc. 12th ESA Symp. on European Rocket and Balloon Programmes & Related Research, Lillehamer 1995*, ESA SP-370, pp. 305-310.

Vaughan, G., H.K. Roscoe, L.M. Bartlett, F. O'Connor, A. Sarkissian, *et al.*, 1997 : An intercomparison of ground-based UV-Visible sensors of ozone and NO_2, *J. Geophys. Res.*, 102, pp. 1411-1422.

OZONE DEPLETION IN THE ARCTIC SPRING, CALCULATED FROM GOME-OZONE PROFILES

K. Bramstedt, K.-U. Eichmann, M. Weber, R. Hoogen, V. Rozanov, and J.P. Burrows

Institute of Remote Sensing and Environmental Physics, University of Bremen, Bremen, Germany
klaus.bramstedt@iup.physik.uni-bremen.de

ABSTRACT

The Global Ozone Monitoring Experiment (GOME) aboard ERS-2 measures the reflected and backscattered UV/visible radiation from the Earth in nadir geometry. The FUll Retrieval Method (FURM), an advanced Optimal Estimation inversion scheme using the radiative transfer code GOMETRAN as forward model derives ozone profiles frome the UV spectra. FURM was used to retrieve ozone profile distributions in the Arctic region at selected days during the Arctic springs 1997 and 1998.

In 1997 the polar vortex formed late in winter and record low temperatures were reached in late March. In the lower stratosphere depleted levels of ozone were observed by GOME. In spring 1998 the lower stratospheric temperatures were comparable to the longterm mean and the polar vortex was relatively weak. Under these different meteorological conditions the ozone profile distributions retrieved by FURM were used to estimate a lower limit of chemical ozone loss rates on selected isentropic levels inside the polar vortex.

1. INTRODUCTION

Since the end of the seventies, a dramatic decline in total ozone over Antarctica has been observed in late winter and spring. Heterogenous chemical reactions occurring on polar stratospheric clouds (PSC) lead to chlorine-catalyzed ozone destruction. Above the Arctic stratospheric temperatures are higher and stratospheric dynamics are larger, which are the reason for less ozone depletion. Since the beginning of the nineties, however, chemical ozone depletion has also been identified during the Arctic winter and spring (1, 2).

The GOME spectrometer is capable to measure total columns of ozone and other trace gases (3). The UV/visible spectral range of the instrument also contains information about the vertical distribution of ozone in the Hartley–Huggins band. The retrieval algorithm FURM (FUll Retrieval Method), an advanced optimal estimation scheme, utilizes this information to retrieve ozone profiles by an iterative inversion scheme . A detailed description can be found in Ref. (4)

The aim of this paper is to present first results of using FURM observations to calculate ozone depletion in the Arctic winters 96/97 and 97/98 (Section 4). Section 2 gives an overview on the meteorological situation in both seasons.

2. THE ARCTIC WINTER/SPRING 96/97 AND 97/98

The meteorology of the Arctic winter and spring shows much more variations from year to year than the Antarctica ones. Dynamical processes can cause strong ozone variations in the Arctic atmosphere, which makes it difficult to quantify chemical ozone loss due to heterogenous reactions on PSC surfaces (1).

Temperatures are tightly coupled to ozone in the Arctic lower stratosphere through dynamics and photochemistry. Low temperatures (below 195 K or -78° C) are necessary for the development of Type I PSCs. Heterogeneous chemical reactions on PSCs enhance the production of reactive chlorine compounds, namely ClO, leading to ozone depletion in the presence of sunlight.

The 1996-1997 northern hemisphere spring polar vortex was very strong, stable, and cold. It did not form until late in December and was very symmetric and close to the pole from February into late April. It was the latest in formation and dissipation in the last 18 years using the National Centers for Environmental Prediction (NCEP) dataset (5). The core region of the vortex was very isolated from outside mixing. The temperatures decreased markedly and were low enough to form PSCs from the middle of January to the end of March. Record low temperatures were found inside the vortex at the isentropic height of 475 K at the end of March and early April. No substantial stratospheric warming occurred in the lower and middle stratosphere (5).

The 1997-1998 Arctic winter/spring period differs from the previous three winters, as it was comparingly warm and no record low temperatures were observed. The polar vortex formed at the end of November at higher altitudes and dissipated by the end of March. The coldest temperatures were reached in December over Scandinavia, low enough to form type I PSCs at isentropic heights of 550 K. Due to warming events the vortex was displaced from the polar regions towards Scandinavia and Russia and the shape of the vortex was constantly distorted in January and February.

Fig. 1 shows the effect of the different meteorologies to the total ozone column as measured by GOME. In 1997 (Fig. 1a), the stable and cold vortex leads to ozone values about 125 DU less than the monthly mean from 1979 to 1993 using the Nimbus-7 TOMS Version 7 dataset (6) (Fig. 1c). The polar region shows a characteristic ozone hole structure. In 1998 (Fig. 1b), the ozone pattern is very similar to the TOMS longterm mean, only a small reduction over the Barents Sea and North Atlantic could be observed.

Figure 1: *Gridded and smoothed contour maps of northern hemispheric monthly mean total ozone from a) March 1997 (top) and b) March 1998 (middle) as measured by GOME and c) a climatology as measured by Nimbus-7 TOMS averaged over the years 1979-1993 (bottom). The GOME means were calculated using the GDP Level 2 Version 2.4 dataset. The projection is stereographic with 0° at the bottom and extends from 30° N to the North pole. The contour interval is 25 DU.*

Figure 2: *Gridded and smoothed FURM ozone for the layer of 15 km to 23 km on 1 April 1997, during the largest extension of polar vortex. The projection is stereographic with 0° at the bottom and extends from the North pole to 40° N. The contour interval is 20 DU. Superimposed in grey is the PV isoline of 38 PVU showing the vortex boundary region. The PV data is taken from the European Centre for Medium-Range Weather Forecasts (ECMWF).*

3. THE FURM DATASET

The short-wave region of GOME covers the Hartley-Huggins ozone bands and therefore contains information about the vertical ozone distribution. The retrieval algorithm FURM (FUll Retrieval Method) has been developed to derive ozone profiles from the UV/visible spectral range.

FURM consists of two major parts: first, a forward model, the pseudo-spherical multiple scattering radiative transfer model GOMETRAN (7), calculating the top of atmosphere (TOA) radiance for a given state of the atmosphere, second, an iterative inversion scheme, that adjusts this state to match the calculated with the measured TOA radiance, utilizing the so-called weighting functions also provided by GOMETRAN (8). Because this inversion problem is under-constrained, an optimal estimation (9) approach was chosen, which combines the information from the measurement with statistical a-priori information from a climatology. A detailed description and first validation with ground-based and satellite measurements of FURM can be found in Refs. (4) and (10).

In this work, the spectral range from 290 nm to 355 nm of the GOME spectra is used for the retrieval. The a-priori ozone distribution is taken from an ozone climatology derived from combined ozone sonde and satellite measurements during 1980-1991 (11). Temperature and pressure profiles is taken from the United Kingdom Meteorological Office (UKMO) assimilated dataset (12). Information about the surface height and albedo are taken from a database (13). The cloud cover is calculated from the measurements of the broadband Polarisation Measurement Devices (PMD) of GOME. From the fractional cloud cover an effective cloud albedo is determined.

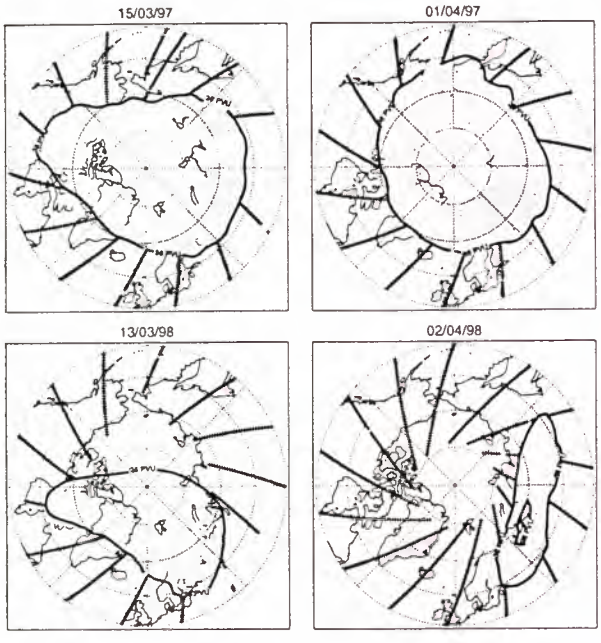

Figure 3: *Coverage of the polar vortex by GOME ground pixels used for FURM profile retrieval. From top left to bottom right: a) 15 March 1997, b) 1 April 1997, c) 13 March 1998, and d) 2 April 1998.*
The grey shaded area indicates the covered area, the crosses marked the centre of the footprint of profiles not used in the depletion calculations. The thick line marks the vortex boundary, defined as the potential vorticity isoline at 38 PVU on 475 K. The PV data is taken from the European Centre for Medium-Range Weather Forecasts (ECMWF).

FURM profiles were retrieved for selected days in spring 1997 and 1998 in the northern hemisphere, starting at 40° N. In 1997, the days are 10, 15, 20, 25 March, 1, 5, 11, 16, 21 and 26 April. In 1998 the days 21 February, 3, 8, 11, 12, 13, 18, 23, 28 March and 2 April are used. In Fig. 2 the results of FURM for 1 April 97 at the layer 15 km to 23 km, containing the ozone maximum at about 20 km, is plotted. Low ozone of 120 DU and less are found inside the polar vortex, indicated by the 38 PVU isoline, whereas values of about 160 DU are observed outside the vortex.

Fig. 3 shows for two days each year the coverage of the polar vortex by GOME ground pixel used for profile retrieval. The potential vorticity (PV) data are taken from the European Centre for Medium-Range Weather Forecasts (ECMWF). All ground pixels with centre coordinates within the vortex area are used for further analysis. Because the ground pixel area (100 km x 960 km) is mostly orientated parallel to the isoline, only small fraction of GOME ground pixel crosses the vortex boundary.

The currently used setup of FURM limits the usable GOME spectra to a solar zenith angle (SZA) of 76°. At larger SZA the GOME instrument switches to a scan mode with longer integration times. At the middle of March, this limits the retrieval to the area south of 75°N.

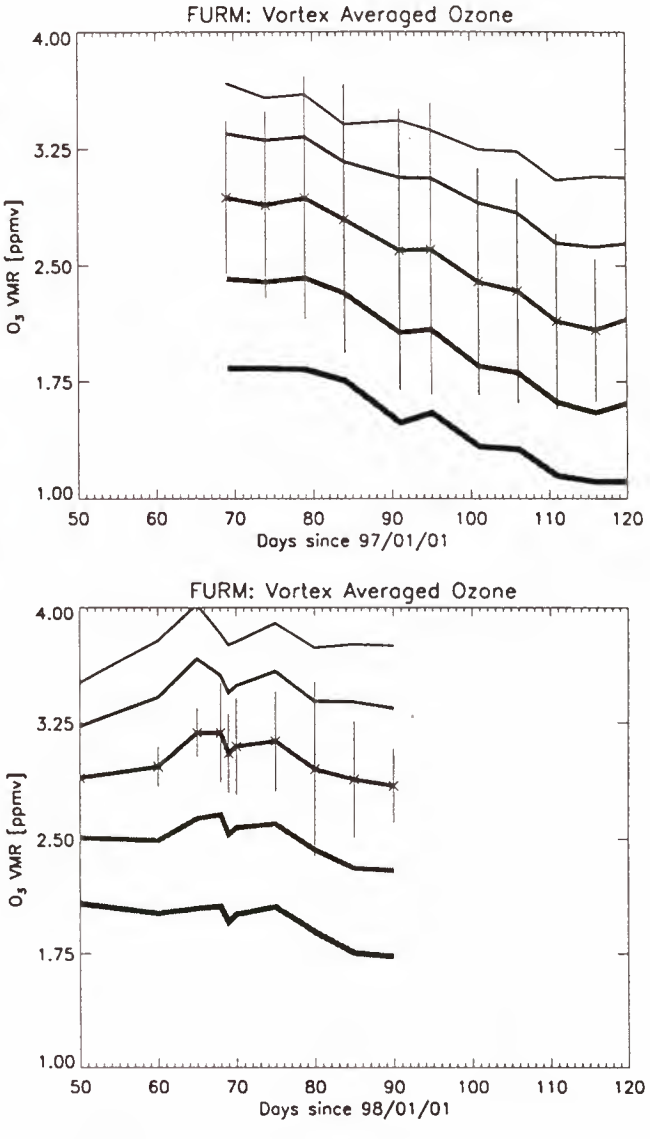

Figure 4: *Ozone decline inside the polar vortex for the layer of 425 K to 525 K as calculated with FURM: a) During the Arctic Spring 1997 from 10 March to 26 April (top). b) During the Arctic Spring 1998 from 21 February to 2 April (bottom).*
The lines represent the ozone as volume mixing ratio (VMR) in ppmv for the isentropics of potential temperatures of 425, 450, 475, 500, and 525 K (from thick to thin and from light grey to black, respectively), corresponding to 16-21 km altitudes. Vertical bars denote the 1σ errors for the vortex average at 475 K.

The north pole is reached by FURM on about 10 April.

In 1997 coverage of about half the vortex area is achieved in the middle of March. Because the vortex is centred over the pole, no vortex profiles could be retrieved before 10 March. The vortex remained stable until the end of April (see Sec. 2) in 1997, therefore the last inspected day was 26 April.

In 1998, the dynamical situation was much different,

the vortex was weak and displaced from the pole. On 21 February 98, the vortex has moved towards Russia. Therefore, the first vortex profiles could be retrieved over Siberia earlier than the year before. In Fig. 3c, the GOME coverage on 13 March is displayed. The vortex reached from the Hudson Bay to Western Russia with a centre over Spitsbergen. Profiles could be retrieved over the Hudson Bay, Scandinavia and West Siberia, whereas in 1997 profiles all around the much larger vortex could be seen. In the beginning of April, the polar vortex break up. Only a small area remained over Siberia at 2 April (3d), the last day for our analysis.

4. OZONE DEPLETION

Strong stratospheric ozone depletion in the springtime Arctic was not observed for a long time, but the winter/spring periods in 1996 and 1997 showed extremely low ozone inside the polar vortex (1, 14, 15, 16, 17). The stratosphere were particularly cold in Spring 1997 for the fifth time in a row (18) and stratospheric temperatures cold enough to form PSCs were observed late in the season when the sunlight has already returned to higher northern latitudes. Chemical ozone reductions in the lower stratosphere of about 80 DU has been estimated by the end of March (15). In contrast, the winter/spring period 1998 show ozone distributions comparable to the longterm mean, see Section 2 and Fig. 1.

The FURM data are used to calculate vortex-averaged and area-weighted ozone concentrations as a function of time at certain isentropics (425–525 K, every 25 K) in the lower stratosphere.

The results are presented in Fig. 4. During the observed time period from 10 March to 26 April 1997 the ozone concentration is reduced about 0.75 ppmv at all isentropic levels, which is a reduction from 40 % at 425 K to 20 % at 525 K. The meteorological conditions (low temperatures and a stable vortex, see section 2) lead to the ozone depletion in the 1997 polar vortex.

Knudsen et al. (17) derived a chemical loss rate of 46 and 43 percent, respectively, during a 3 month period (January - March 1997). Our rates are limited to the period March-April and are difficult to compare. The GOME results are also obtained at less vertical resolution than the sonde measurements and, therefore, less depletion is expected from our calculations, if the loss is confined to rather thin layers. We have not yet included ozone increases due to diabatic descent inside the vortex, which shall be accounted for in future studies. Therefore, the rates given here present lower limits of the expected chemical loss.

Fig. 4b, the ozone concentration in the time period from 21 February to 2 April 1998 is shown. Up to middle of March, no significant ozone depletion can be observed. In the higher levels, the ozone concentration even increases. From 18 March to 2 April, the ozone is reduced by about 30 ppmv at 425 K decreasing to 20 ppmv at 525 K. Because the polar vortex break up after 2 April, no further ozone depletion is expected.

During the time period covered by our analysis in both seasons, the ozone concentrations at all levels are higher in 98, starting with about 15 ppmv at 10 March to 25 ppmv to 2 April. This agrees with the mean total ozone columns, as displayed in fig. 1. The observed ozone loss in 1997 was much higher than in 1998, as expected from the different meteorological situations, e.g. the much longer stable period of the polar vortex and the lower temperatures, falling below the critical temperature for the formation possible PSC formation.

5. CONCLUSION AND OUTLOOK

FURM has been successfully used to derive lower limits of mean ozone depletion rates for the polar vortex. Because of the geographical limits of the usable GOME data, the calculations usually cannot be started in the first half of March, depending on size and location of the polar vortex. Since June 1998, the operating mode of GOME has been changed, so that the complete spectral range used by FURM is integrated at the nominal integration time of the visible channels. This gives the possibility to use smaller ground pixel sizes for all profiles, and a raise in the limit for the solar zenith angle is expected.

We are currently attempting to determine diabatic descent inside the vortex in order to separate dynamical ozone changes from chemical loss. Work on this point is in progress. Furthermore, the FURM algorithm needs a clear speedup to extend the calculations on every day in the Arctic spring.

ACKNOWLEDGEMENTS

We express our thanks to DLR-DFD for producing the operational GOME level-1 and level-2 data, the ECMWF for providing the potential vorticity data, and UKMO for providing pressure and temperature profiles. This work has been funded by the national Ozone Research Program (OFP), the BMBF (German Ministry of Research) within the national Ozone Research Program (OFP, grant 01L09607), the European Space Agency (ESA), the State of Bremen, and the University of Bremen.

REFERENCES

1. Müller R & al 1997, HALOE observations of the vertical structure of chemical ozone depletion in the Arctic vortex during winter and early spring 1996-1997, *Geophysical Research Letters*, 24, 22, 2717–2720.

2. Rex M & al 1998, In situ measurements of stratospheric ozone depletion rates in the Arctic winter 1991/1992: A Lagrangian approach, *Journal of Geophysical Research*, 103, D5, 5843–5853.

3. Burrows J & al 1999, The Global Ozone Monitoring Experiment (GOME): Mission concept and first scientific results, *Journal of the Atmospheric Sciences*, 56, 151–175.

4. Hoogen R & al 1998, Ozone profiles from GOME satellite data: Algorithm description and first validation, submitted to JGR.

5. Coy L & al 1997, Meteorology of the polar vortex: Spring 1997, *Geophysical Research Letters*, 24, 22, 2693–2696.

6. McPeters R & Labow G Dec 1996, An assessment of the accuracy of 14.5 years of nimbus 7 TOMS version 7 ozone data by comparison with the Dobson network, *Geophysical Research Letters*, 23, 25, 3695–3698.

7. Rozanov V & al 1997, GOMETRAN: A radiative transfer model for the satellite project GOME, the plane-parallel version, *Journal of Geophysical Research*, 102, D14, 16683–16695.

8. Rozanov V & al 1998, Retrieval of atmospheric constituents in the uv-visible: A new quasi-analytical approach for the calculation of weighting functions, *Journal of Quantitative Spectroscopy and Radiative Transfer*, 60, 277–299.

9. Rodgers C 1976, Retrieval of atmospheric temperature and composition from remote measurements of thermal radiation, *Reviews of Geophysics and Space Physics*, 14, 4, 609–624.

10. Hoogen R & al 1998, Ozone profiles from GOME satellite data - i: Comparison with ozonesonde measurements, *Physics and Chemistry of the Earth*, this issue.

11. Fortuin P & Kelder H 1997, An ozone climatology based on ozonesonde and satellite measurements, *Journal of Geophysical Research*, submitted.

12. Swinbank R & O'Neill A 1994, A stratosphere-troposphere data assimilation system, *Monthly Weather Review*, 122, 686–702.

13. Guzzi R 1993, Surface type and height database, private communication.

14. Rex M & al 1997, Prolonged stratospheric ozone loss in the 1995/96 Arctic winter, *Nature*, 389, 835–838.

15. Müller R & al 1997, Severe chemical ozone loss in the Arctic during the winter of 1995–1996, *Nature*, 389, 709–712.

16. Newman P & al 1997, Anomalously low ozone over the Arctic, *Geophysical Research Letters*, 24, 22, 2689–2692.

17. Knudsen B & al 1998, Ozone depletion in and below the Arctic vortex for 1997, *Geophysical Research Letters*, 25, 5, 627–630.

18. Collins G Jan 1998, Springtime Arctic ozone levels fall further in 1997, *Physics Today*, 18–19.

STRUCTURE OF OZONE MINI-HOLES FROM GOME OBSERVATIONS

K.-U. Eichmann, K. Bramstedt, M. Weber, R. Hoogen, V.V. Rozanov, and J.P. Burrows

Institute of Environmental Physics, University of Bremen, FB 1,
P.O. Box 330440, D-28334 Bremen, Germany
phone: +49 421 218 2362, fax: +49 421 218 4555
email: eichmann@iup.physik.uni-bremen.de

ABSTRACT

Ozone mini-holes frequently form in mid-latitude regions during hemispheric spring. A mini-hole is an area of strongly reduced total ozone, which lasts only a few days. It is related to upper tropospheric circulations. Intrusion of ozone poor subtropical air into higher latitudes raises the tropopause causing a horizontal divergent transport of ozone in the above lying lowermost stratosphere. In the northern hemisphere mini-holes are mostly observed in the regions over the North Atlantic and Europe. Northeastward tropospheric air flow occur just east of the North Atlantic storm track.

In both arctic spring seasons 1997 and 1998 ozone mini-hole events were observed by GOME, where the total ozone amount inside the hole decreases by more than 70 DU. Vertical ozone profile distributions derived from observations by the Global Ozone Monitoring Experiment (GOME) aboard ESA's ERS-2 satellite have been used to investigate the two dimensional structure of these mini-hole events.

1. INTRODUCTION

Since the discovery of the Antarctic ozone hole in 1985 (1) a lot of scientific studies and public debate about the ozone layer was initiated. There are several mechanisms that are responsible for the thickness of the ozone layer. The need to distinguish between reversible, dynamically induced and irreversible, chemically induced ozone losses became important.

One example of transient depressions of total ozone are known as mini-holes (2, 3, 4). During such events exchange of air masses from the sub-tropics with low total ozone towards the polar vortex occur, which leads to a high tropopause at higher latitudes. These tropospheric ridges cause adiabatic cooling at the vortex edge and can possibly lead to the formation of polar stratospheric clouds (5). As an example GOME ozone profiles inside an ozone mini-hole have been observed in March 1998.

In Fig. 1 an example of the ozone mini-hole, discussed in this paper, over the North Atlantic sector on 11 March 1998 is shown. Lowest total ozone of below 250 DU can be found at the southern tip of Greenland near Cape Farewell. The area of low ozone extends from the east coast of North America to the British isles. The polar vortex edge is depicted by the white 38 PVU line at the isentrope of 475 K (about 20 km). 1 PVU is 1 x $10^{-6} Km^2/(kgs)$. The tropospheric ridge (see Section 3) as the reason for the ozone mini-hole is touching the polar vortex edge.

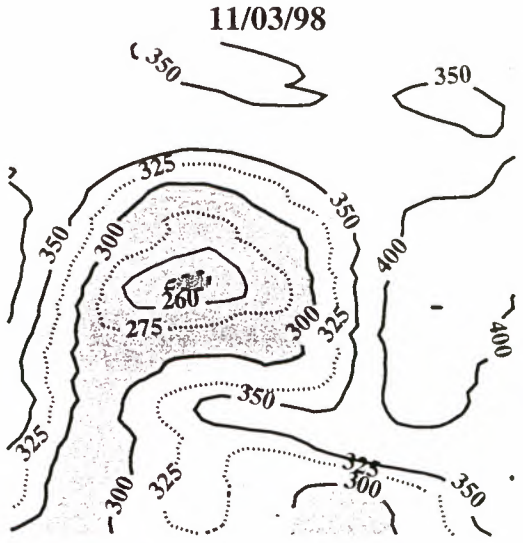

Figure 1. GOME Level 2 Version 2.4 total ozone above the North Atlantic sector on 11 March 1998. The map reaches from 30° N to 80° N and from 80° W to 20° E. The overplotted white PV isoline of 38 PVU depicts the vortex boundary region in the lower stratosphere and is just north of the mini-hole. The PV data is taken from the European Centre for Medium-Range Weather Forecasts (ECMWF).

The inversion algorithm FURM (Full Retrieval Method) calculates ozone profiles from GOME satellite data have been applied to derive northern hemisphere (NH) vertical ozone distributions for ozone mini-hole conditions. Results for selected days during the Arctic spring season 1998 are presented and discussed. The inversion scheme to derive ozone profiles from GOME data is presented in Section 2. The characteristics of ozone mini-holes are described in Section 3. Results from GOME ozone data analysis and ECMWF meteorological datasets are discussed in Section 4.

2. GOME OZONE PROFILE RETRIEVAL

The Global Ozone Monitoring Experiment GOME measures the backscattered and reflected solar radiation from the atmosphere and the surface of the Earth. The primary objective of the GOME mission is the determination of global distributions of total ozone and NO_2. Furthermore, total column amounts of other relevant atmospheric trace constituents, for instance, O_3, BrO, OClO, HCHO, and SO_2, can be determined (6). Column amounts are retrieved using the differential optical ab-

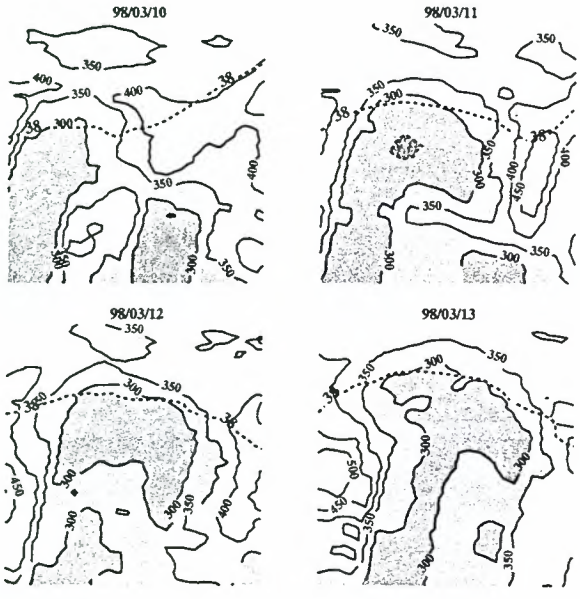

Figure 2. Gridded and smoothed GOME total ozone for the North Atlantic region for a four day period from 10 to 13 March 1998. The maps reach from 30° N to 82° N and from 70° W to 20° E. The superimposed, black and white PV isoline of 38 PVU, taken from ECMWF data, depicts the vortex boundary region in the lower stratosphere.

sorption spectroscopy method DOAS (7). However, total O_3 and NO_2 columns are currently the only trace gases publically available as GOME level-2 data products (8).

Using the broad spectral range (240–790 nm) of GOME with its moderate spectral resolution (0.2–0.4 nm), height-resolved ozone information can be derived from the short-wave Hartley-Huggins ozone bands. The FUll Retrieval Method FURM derives ozone profiles from GOME sun normalized spectra using an iterative optimal estimation scheme (9). It consists of two parts: (i) the pseudo-spherical, multiple scattering, radiative transfer model (RTM) GOMETRAN (10), calculating the top of atmosphere (TOA) radiance for a given atmospheric state, defined by the vertical distribution of ozone and other trace gases, the surface albedo, and the aerosol scenario among others, and (ii) the advanced optimal estimation scheme, matching the calculated TOA radiance to the measured GOME radiance iteratively by adjusting the atmospheric model parameters, like the vertical ozone distribution. The inversion scheme utilizes appropriate weighting functions provided by GOMETRAN (11). A detailed account on the retrieval methodology applied to GOME is given by Hoogen et al. (9, 12).

For this work, the spectral range from 290 nm to 355 nm of the GOME spectra is used for the retrieval. The a-priori ozone distribution is taken from an ozone climatology derived from combined ozone sonde and satellite measurements during 1980-1991 (13). Temperature and pressure profiles is taken from the United Kingdom Meteorological Office (UKMO) assimilated dataset (14). Information about the surface height and albedo are taken from a database (15). The cloud cover is calculated from the measurements of the broadband Polarization Measurement Devices (PMD) by GOME (16). From the fractional cloud cover an effective cloud albedo is determined.

The ozone number density is retrieved in 81 equidistant altitude levels from 0 to 81 km. Additional scalar fit parameters are the surface albedo, aerosol extinction, a scaling factor for the pressure profile, the Ring amplitude, and an offset for the temperature profile. This version also contains corrections to the instrument calibration (9). Although the ozone number density is calculated on 81 levels, the vertical resolution is limited to 6–8 km between 20 km and 35 km and about 10 km below and above (12). The root mean square error for FURM profiles in northern mid-latitudes from the upper troposphere above 10 km into the middle stratosphere is below 10%.

3. DYNAMICS OF OZONE MINI-HOLES

Correlations between total ozone and synoptic meteorological situations have been known since the dawn of atmospheric spectrometry (17, 18). Ozone mini-holes are synoptic-scale regions (10^6 km^2) of low total ozone (compared to the surrounding areas). They are persistent for several days over extra-tropical latitudes most dominantly in winter/spring and generally move northeastward. These transient disturbances of several tens of DU's (Dobson units = 2.67 x 10^{16} molecules cm^{-2}) are associated with anticyclones (high-pressure systems), primarily of upper-tropospheric origin. The northward transport of subtropic and tropospheric airmasses along an extended anticylonic ridge lifts the tropopause in higher latitudes. There will be both horizontal and vertical movement of air and ozone during the passage of an anticyclone. The intrusion of low-ozone tropospheric air in a column leads to lifting and divergence of ozone-rich stratospheric air out of the column by mass continuity, as the volume mixing ratios of ozone are invariant to adiabatic processes. The net effect is a reduction of total ozone in the column. Extremely low total ozone can be observed at the edge of the polar vortex, when the vortex air is lifted and thus adiabatically cooled due to the blocking upper-tropospheric anticyclone. This vertical motion both lowers the temperature and the total ozone content in the lower stratosphere (19, 4, 20).

Ozone mini-holes are in two ways important for the polar ozone study. (i) They contribute to the meridional transport in the lower stratosphere. Ozone mini-hole can induce strong irreversible deformation of the circumpolar circulation. (ii) They have an important role for the chemical balance of the ozone layer. The strong adiabatic cooling due to the lifting of airmasses can induce formation of polar stratospheric clouds (PSCs). Heterogeneous processes which leads to ozone depletion can occur on the surfaces of PSCs (5).

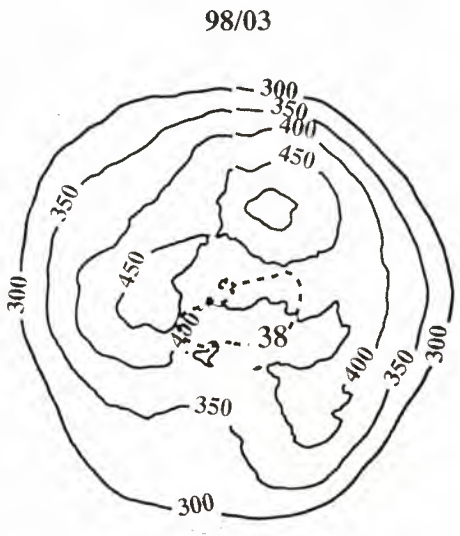

Figure 3. Gridded GOME Level 2 Version 2.4 monthly mean total ozone in March 1998. The projection is stereographic with 0° at the bottom and extends from 20° N to the North pole. The contour interval is 50 DU. A monthly mean of the polar vortex as shown by the dashed 38 PVU line has been overplotted.

4. RESULTS AND DISCUSSION

4.1. 11 March 1998 Ozone Mini-Hole

The ozone mini-hole event can both be seen in total ozone maps and in meteorological datasets like temperature, geopotential height and potential vorticity distributions. As an example of the evolution of an ozone mini-hole, a sequence of four days from 10 to 13 March 1998 is shown in Fig. 2. Subtropical tropospheric air is streaming along the east coast of the United States and Canada, on 10 March the airmass has reached south of Greenland and the edge of the vortex. In the lower stratosphere at 475 K the air is streaming along the vortex boundary above Greenland. On 11 March the subtropical air turns slightly eastward and then south again on 12 March. Very low ozone of less than 250 DU was observed on 11 March. A reduction of more than 100 DU is found, when compared to the total ozone monthly mean as shown in Fig. 3.

On 12 March an isolated area with low ozone below 300 DU just south of Iceland can be seen. The mini-hole moves northeastwards on 13 March and vanishes the following days. In the course of the mini-hole event the polar vortex, as indicated by the 38 PVU contour line at 475 K on the maps, becomes distorted and pushed north by the mini-hole.

4.2. Meteorological Conditions

Various ECMWF meteorological parameters for the mini-hole event on 11 March 1998 are displayed in Fig. 4 showing the upper-tropospheric situation. The geopotential height [Dm] at 300 hPa (about 9 km) is depicted in the

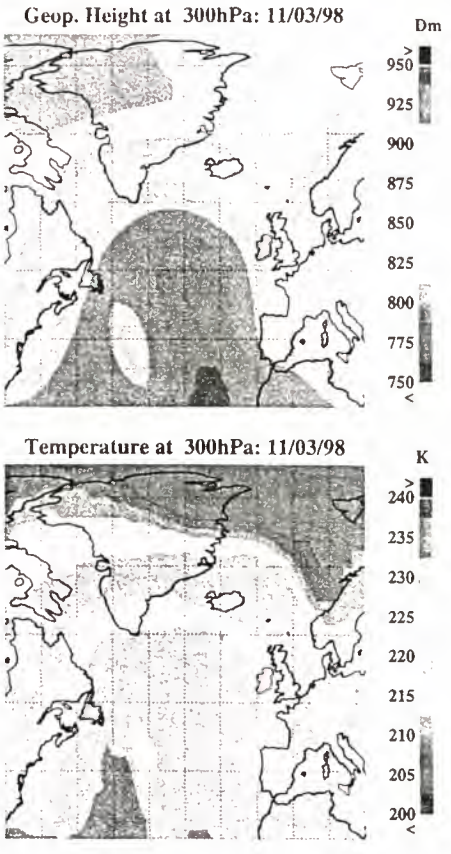

Figure 4. ECMWF geopotential height (top) in Dm and temperature (bottom) in K for the upper troposphere at 300 hPa (below 10 km) for the 11 March 1998 mini-hole event. The maps reach from 30° N to 80° N and from 80° W to 20° E.

top panel. High values are generally found in the extratropics, which are associated with high pressure areas. Low values are more typical for higher latitudes. The poleward extension of the ridge is associated with strong intrusion of subtropical air over the North Atlantic. The warm, subtropical air moving to higher latitudes can also be seen in the temperature map at 300 hPa (bottom panel). Note that at 200 hPa (about 12 km, not shown here) near the tropopause the temperature were significantly lower by more than 20 K. Thus we find a cold high tropopause inside the mini-hole. The wave-breaking behavior can be seen by the coincident tongue of low potential vorticity [PVU] at the 350 K isentrope (about 12 km, Fig. 5). Areas of low PV depict subtropical, tropospheric air with a higher tropopause, whereas stratospheric air is associated with high PV units. Two high pressure systems were merged near the European continent as seen in the geopotential height.

All maps show the wave-breaking of airmasses in the vicinity of the tropopause. This event also has an impact on the lower stratosphere, which can be seen in Fig. 6. At 50 hPa (about 20 km) the geopotential height tends to be more zonally averaged, but the wave of high values coming from the subtropics can also be found at this height.

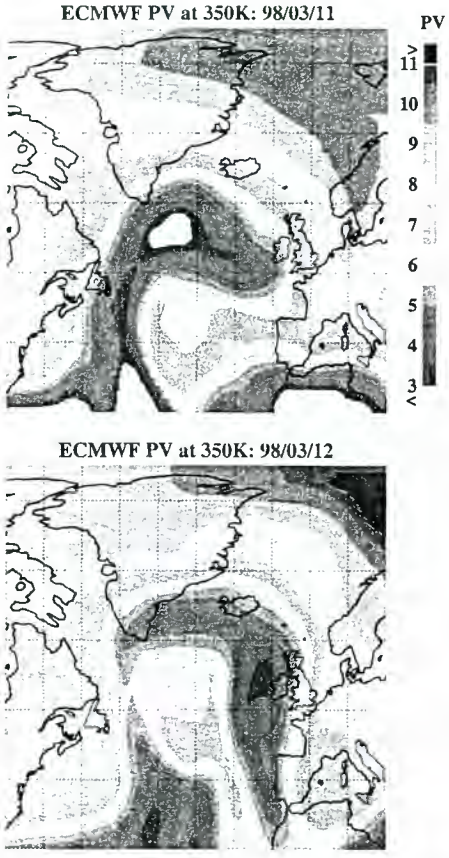

Figure 5. ECMWF Potential vorticity in PVU for the upper troposphere at 350 K (about 12 km) for the 11 (top) and 12 March 1998 (bottom). The maps reach from 30° N to 80° N and from 80° W to 20° E.

The distortion of the vortex by the mini-hole event at the southern tip of Greenland can be detected in the potential vorticity map at 475 K (about 20 km) depicting the polar vortex (more than 38 PVU) and its surf zone. Temperatures below 195 K are found at the vortex surf zone over southern Greenland and near Iceland. This is due to adiabatic cooling of the uprising polar wind jet streaming along the polar vortex edge, where the windspeed is largest.

4.3. Vertical structure of the mini-hole

The vertical structure of the ozone mini-hole is shown in Fig. 7. The top panel displays the GOME level 2 total ozone [DU] taken from our webpage 'www.iup.physik.uni-bremen.de/ifepage/gomenrt.html' for each ground pixel for 11 March 1998. The orbit over Europe from Scandinavia to Spain is shown in the middle panel and over Greenland to the east coast of North America in the lower panel as latitude-altitude charts of ozone number density [$10^{18}m^{-3}$]. The middle figure depicts normal March conditions. High values of ozone (>6x$10^{18}m^{-3}$) can be found in the ozone belt in the lower stratosphere around 475 K for latitudes above 40° N. The tropopause can be defined as the region of strong gradients in ozone number density around 350 K,

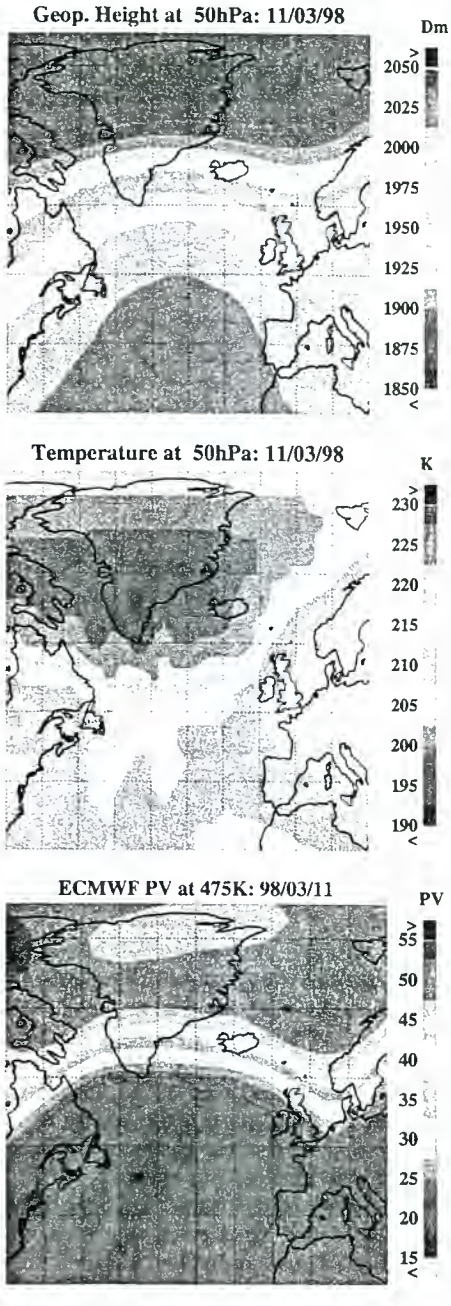

Figure 6. ECMWF meteorological datasets for the lower stratosphere at about 20 km for the 11 March 1998 mini-hole event. The maps reach from 30° N to 80° N and from 80° W to 20° E.

the ozone content of tropospheric air is low. A slight decrease in tropopause height is seen towards higher latitudes. The ozone mini-hole can clearly be detected in the lower figure reaching from 40° N to 65° N. This can be confirmed by the total ozone maps in Fig. 7(top panel) and Fig. 1. Ozone poor air is streaming along the bottom of the the tropopause, lifting it from normal heights of roughly 10 km to tropical 16 km. The thinning of the stratospheric ozone belt can also be seen, highest values at 475 K are below 5x$10^{18}m^{-3}$. An interesting feature seen in the data is the intrusion of subtropical

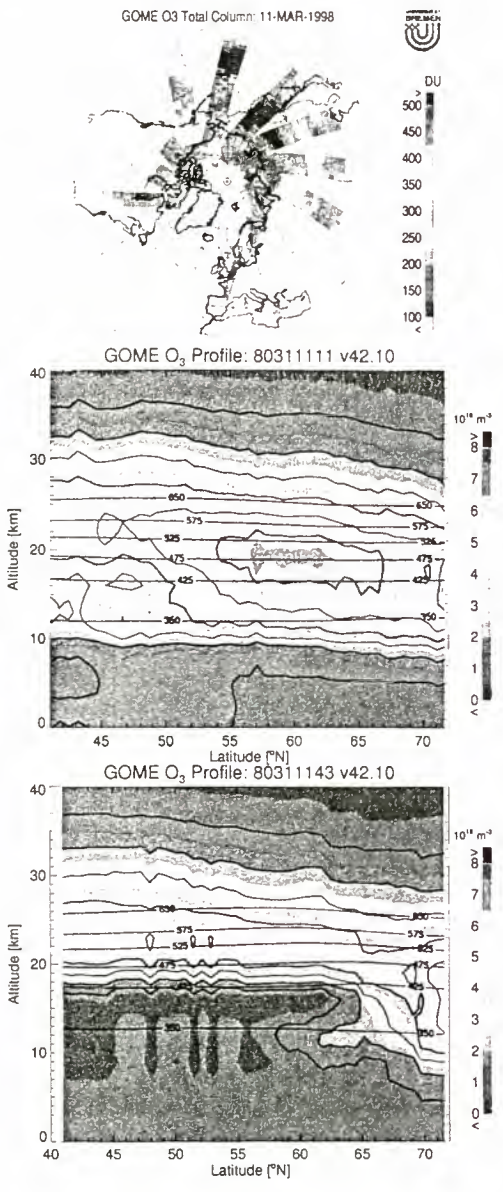

Figure 7. Total ozone [DU] for each ground pixel of GOME measurements for 11 March (top panel). The projection is stereographic with 0° W at the bottom and extends from 30° N to the North pole. Latitude-altitude charts of ozone in number density from 40° N to 72° N and from 0 km to 40 km height for the GOME orbit over Europe (middle panel) and for the orbit over Greenland (bottom panel).

air into the vortex edge region near 63° N. This could be the reason for the deformation of the vortex, where the wind pattern changes in this region and adiabatic cooling occurs due to uplifting of air. The tongue of relatively high ozone contents below 350 K is the area where strong irreversible stripping of stratospheric airmasses out of the vortex can be seen.

5. SUMMARY

This paper investigates the dynamics and structure of a typical northern hemisphere ozone mini-hole event occurring at the edge of the polar vortex around 11 March 1998. This was done by using meteorological data from ECMWF, GOME level 2 total ozone and the FURM algorithm to derive ozone profiles from GOME data. The results are in good agreement with literature (21, 22). Very low ozone columns with high temperatures in the troposphere and low temperatures in the stratosphere were seen at the edge of the polar vortex on 11 March 1998. Vertical motions changes both stratospheric ozone and adiabatically lower the temperature with less than 195 K. This could lead to formation of PSCs, activation of chlorine and, consequently to depletion of ozone downstream (5).

A comparison of FURM latitude-altitude charts under normal and mini-hole conditions shows an elevated tropopause up to 16 km, low ozone number densities in the lower stratosphere, and low ozone just below the tropopause. The vortex was disturbed by the upper tropospheric anticylonic ridge. Transport of vortex air out of the vortex into the upper troposphere below 400 K were found.

ACKNOWLEDGMENTS

We express our special thanks to DLR-DFD and ESA for producing the operational GOME level-1 and level-2 data, the ECMWF for providing the meteorological data, and UKMO for providing pressure and temperature profiles. This work has been funded by the BMBF (German Ministry of Research) within the OFP program NO. 01L9607/1O, the State of Bremen, and the University of Bremen.

REFERENCES

1. Farman J & al 1985, Large losses of total ozone in Antarctica reveal seasonal ClO_X / NO interaction, *Nature*, 315, 207–210.

2. Newman P & al 1988, The morphology and meteorology of southern hemisphere Spring total ozone miniholes, *Geophysical Research Letters*, 15, 923–926.

3. McKenna D & al 1989, Diagnostic studies of the Antarctic vortex during the 1987 Airborne Antarctic Ozone Experiment: Ozone miniholes, *Journal of Geophysical Research*, 94, D9, 11641–11668.

4. Hood L & McCormack J 1997, An investigation of dynamical contributions to midlatitude ozone trends in winter, *Journal of Geophysical Research*, 102, D11, 13079–13093.

5. Grewe V & Dameris M 1997, Heterogeneous psc ozone loss during an ozone mini-hole, *Geophysical Research Letters*, 24, 20, 2503–2506.

6. Burrows J & al 1999, The Global Ozone Monitoring Experiment (GOME): Mission concept and first scientific results, *Journal of the Atmospheric Sciences*, 56, 151–175.

7. Burrows J & al 1993, Global Ozone Monitoring Experiment: Interim science report, Tech. Rep. SP–1151, ESA, ESTEC, Publication Divisions, Noordwijk, The Netherlands.

8. 1995, GOME Users Manual, ESA SP–1182, European Space Agency/ESTEC, Nordwijk.

9. Hoogen R & al 1998, Ozone profiles from GOME satellite data: Algorithm description and first validation, JGR, accepted.

10. Rozanov V & al 1997, GOMETRAN: A radiative transfer model for the satellite project GOME, the plane-parallel version, *Journal of Geophysical Research*, 102, D14, 16683–16695.

11. Rozanov V & al 1998, Retrieval of atmospheric constituents in the uv-visible: A new quasi-analytical approach for the calculation of weighting functions, *Journal of Quantitative Spectroscopy and Radiative Transfer*, 60, 277–299.

12. Hoogen R 1998, Inversion globaler Ozonvertikalverteilungen aus Messungen des Satelliteninstruments GOME, Ph.D. thesis, Universität Bremen.

13. Fortuin P & Kelder H 1998, An ozone climatology based on ozonesonde and satellite measurements, *Journal of Geophysical Research*, 103, D24, 31709–31719.

14. Swinbank R & O'Neill A 1994, A stratosphere-troposphere data assimilation system, *Monthly Weather Review*, 122, 686–702.

15. Guzzi R 1993, Surface type and height database, private communication.

16. Guzzi R & al 1998, Gome cloud and aerosol data products algorithms development, Tech. Rep. ESA Contract 11572/95/NL/CN, European Space Agency, ESA/ESTEC, PO Box 299, 2200 AG Noordwijk, The Netherlands.

17. Dobson G & al 1929, Measurements of the amount of ozone in the earth's atmosphere and its relation to other geophysical conditions, *Proc. R. Soc. London, Ser. A*, 122, 456–486.

18. Reed R 1950, The role of vertical motions in ozone-weather relationships, *Journal of Meteorology*, 7, 263–267.

19. Rood R & al 1992, Episodic total ozone minima and associated effects on heterogeneous chemistry and lower stratospheric transport, *Journal of Geophysical Research*, 97, D8, 7979–7996.

20. McCormack J & Hood L 1997, The frequency and size of ozone mini-hole events at northern midlatitudes in february, *Geophysical Research Letters*, 24, 21, 2647–2650.

21. Petzold K & al 1994, Correlation between stratospheric temperature, total ozone, and tropospheric weather systems, *Geophysical Research Letters*, 21, 13, 1203–1206.

22. Orsolini Y & al 1995, Ridge formation in the lower stratosphere and its influence on ozone transport: A general circulation model study during late january 1992, *Journal of Geophysical Research*, 100, D6, 11113–11135.

DESCENT FROM STRATOSPHERE TO TROPOSPHERE IN THE ANTARCTIC WINTER: DOES IT EXIST, WHY IS IT IMPORTANT, AND CAN IT BE MEASURED BY GOMOS?

Howard K Roscoe

British Antarctic Survey (BAS)
Cambridge UK
email h.rosocoe@bas.ac.uk

ABSTRACT

Descent within the winter stratosphere over Antarctica is well established, but significant descent to the troposphere is challenged, despite there being no well-defined tropopause. Such descent implies a different isotope fractionation of H2O in ice-cores, and so an altered calibration of temperature from ice-cores in palaeoclimates; a dry upper troposphere, and so a reduced possibility of increased precipitation in global warming; and a larger supply of ozone, and so a modified budget of ozone in the unpolluted troposphere. Measurements of H2O in the upper troposphere would identify such descent; measurements of lack of cloud and of O3 might help confirm it. GOMOS has a unique capability for upper-tropospheric measurements in the Antarctic winter, but new operational rules might be necessary. A new observation mode of extended sources might also be necessary. Such a mode might also observe cloud to the high-altitude Antarctic surface, and so identify if precipitation formed in the boundary layer and falling from a clear sky is ubiquitous.

1. DESCENT IN THE STRATOSPHERE AND TROPOSPHERE IN WINTER

Absorption of sunlight by O3, which creates the warm stratosphere, ceases in winter in Antarctica as the sun sets. This causes the stratosphere to cool by radiation, and the denser air descends. This well-known descent is observed in profiles of N2O [1] and other gases, and its accompanying convergence causes the stratospheric vortex because the Coriolis force turns the Southerly air flow to the East.

In the troposphere in winter, radiative cooling of the surface to space causes nearby air to cool. Cooling of nearby air occurs more readily than in winter at mid-latitudes because of the longer night. Where there is a sloping surface this cooler and denser air flows downhill (katabatic flow - see Figure 1). Much of Antarctica is in the form of a dome so that the flow is everywhere outward, and the resupply of air must occur by descent at least at the central flat part of the Antarctic Plateau, if not more generally during the inward flow.

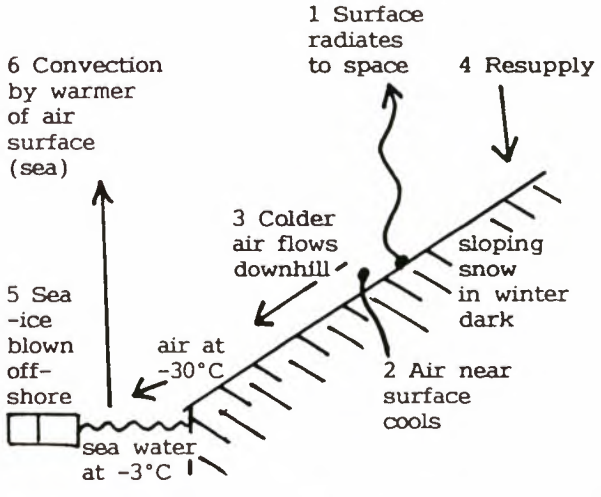

Figure 1. Sketch showing the sequence of events which create katabatic flow in winter in Antarctica, thereby causing descent in the troposphere over the Plateau. Events 5 and 6 are not universal, but increase the forcing of katabatic flow when they occur.

2. DESCENT FROM STRATOSPHERE TO TROPOSPHERE IN WINTER

A well-defined minimum in temperature creates a tropopause which acts as a barrier to rapid transport upwards or downwards. However, in winter in Antarctica there is no well-defined minimum (Figure 2), again because of the lack of absorption of sunlight by ozone. Hence there is no theoretical obstacle to descent through the tropopause.

Few model studies have considered such descent in isolation from general Southern Hemisphere stratospheric-tropospheric exchange, much of which occurs via tropopause folds at mid-latitudes, or in isolation from outward flow from the stratospheric vortex in the lowermost stratosphere. One of the few studies [2] estimates over 60% of the mass flow out of the stratospheric vortex to be to the tropopause; however, the study was heavily criticised for the lack of accuracy of the meteorological analyses upon which it relied [3] in this data-poor area.

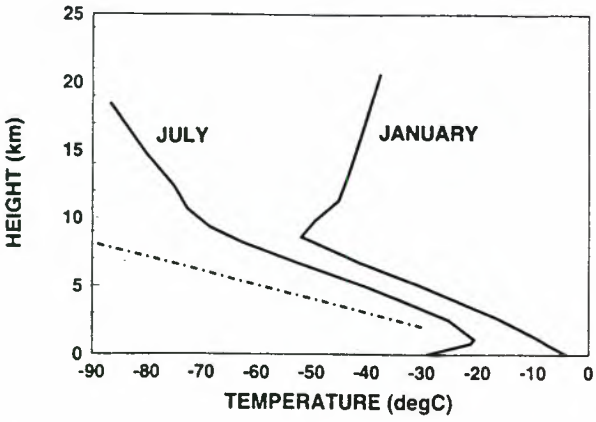

Figure 2. Mean temperature profiles at Halley (75°S) in summer (January) and winter (July), from 1957 to 1993 (taken from Turner & King [4]). Note the lack of a tropopause in winter - the temperature profile is closer to that of radiative equilibrium, such as that seen on Mars [5]. The dashed line illustrates the dry adiabatic lapse rate.

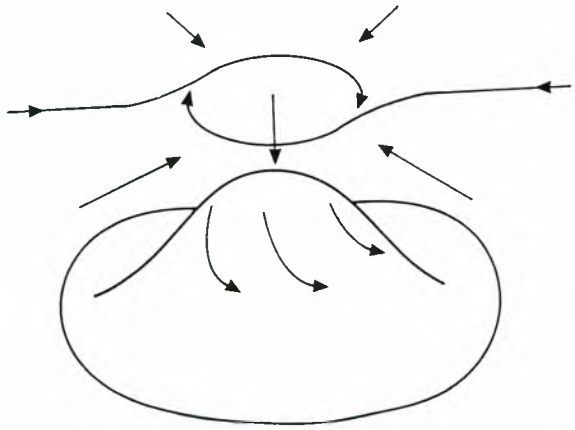

Figure 3. Cartoon of the flow induced over the Antarctic Plateau by katabatic forcing, taken from Turner & King [4]. The inward flow in the troposphere is diverted to form a vortex by the Coriolis force, as in the stratosphere.

In the troposphere, temperatures over the pole are colder than at lower latitudes at the same height, so if the inward spiralling flow (Figure 3) of moist air from further North were horizontal until reaching the centre, then clouds should result. Clouds would probably reduce the radiative cooling of the surface and should switch off the katabatics. But measurements of katabatic winds at 81°S show steady winds throughout winter [6] except for some dips probably attributable to storms. Hence it is probable that the spiralling flow descends as it goes inwards, leaving a cone of air that must surely have come from the stratosphere. If so, it will be dry and cloud-free.

3. THE IMPORTANCE OF POSSIBLE DESCENT FROM STRATOSPHERE TO TROPOSPHERE IN ANTARCTICA

(a) Oxygen Isotope Ratios in Ice Cores

Temperature in ice cores is routinely deduced from the ratio of H2O18 to H2O16 in the ice [7]. In fact, this ratio is only a proxy for temperature, being a measure of the degree of fractionation that has occured from sub-tropics to pole (Figure 4), i.e. of the number of condensation events on the way to the pole. This approximates to the temperature difference between tropics and pole, but the empirical calibration which must be used will vary with the nature of the poleward flow. Hence for accurate use in earlier glacial periods, the calibration must be corrected with a palaeoclimate model.

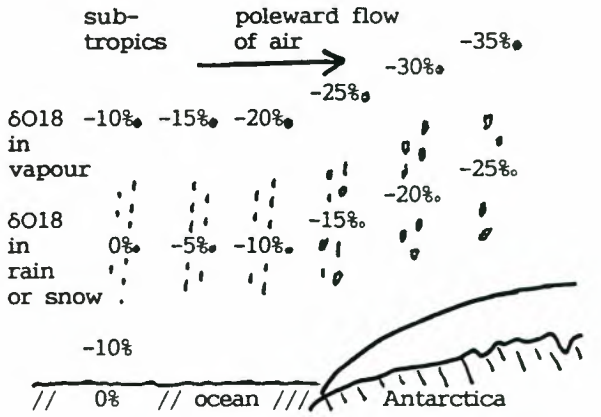

Figure 4. Sketch showing the fractionation of the heavier isotope H2O18 in water vapour as it is transported to the pole. H2O18 has a lower boiling point and so lower vapour pressure; recondensation fractionates the vapour left behind, which becomes an ever lighter fraction.

However, if descent occurs from the stratosphere, it will bring down water vapour which arises in a very different way (Figure 5). Because the O2 which reacts with CH4 has a similar isotopic composition to sea water, the stratospheric water vapour will have a δ018 of -4‰, compared to that of the tropospheric H2O with -35‰. In earlier climates, the proportion with -4‰ is invariant, but the tropospheric value would differ, so that calculations of the difference would be wrong unless they included descent from the troposphere.

(b) The possible increase in precipitation accompanying global warming.

Many climate models predict that there will be a global increase in precipitation if global warming occurs, due to the extra water vapour evaporating from a warmer ocean. The Poles are no exception, and it is probable that there would be more ice rather than less in Antarctica and Greenland [8].

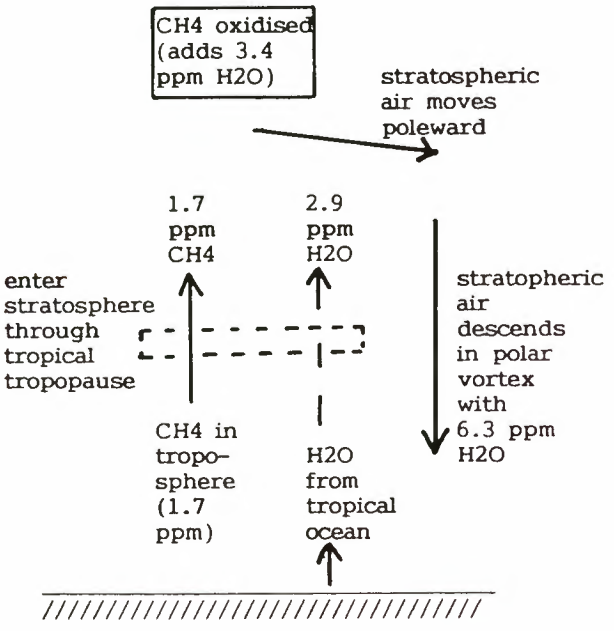

Figure 5. Sketch showing the cycle of stratospheric water vapour. Much of the return path from the stratosphere to the troposphere occurs via tropopause folds at mid-latitudes, but any descent at the Pole would also supply dry air to the upper troposphere. Note that no fractionation of H2O occurs in this cycle, unlike that of tropospheric H2O transported to the Pole.

However, the core of dry air in upper troposphere that would exist if air descended from the stratosphere would be present irrespective of water vapour amounts in the rets of the troposphere. Henec descent must reduce the propensity for increased precipitation over the Antarctic Plateau during global warming

(c) Tropospheric ozone budget

Ny descent from the stratopshere must bring ozone-rich air into the troposphere, and so alter our perception of the tropospherеic ozone budget. A recent model of tropspheric chemistry reproduced measured ozone amounts very accurately at all locations except South Pole [9]. There, the model underestimated the observed ozone in the lower and middle troposphere, suggesting that descent does indeed take place but is not represented in the model.

4. POSSIBLE MEASUREMENTS OF DESCENT

If descent is occuring, there will be a pool of dry air in the upper troposphere except during the few storms which penetrate the Antarctic interior, so frequent observation of cloud would say descent is not occuring.

The international cloud study ISCCP concluded that mean cloudiness was frequently 40% in winter over the Plateau [4], but this is deduced from satellite images which are difficult to interpret given similar reflectivity, emissivity and temperature of cloud and surface.

By contrast, at S Pole which is near the edge of the Plateau during the 3 winter months in the 1990s, 57% of the days (nights) were observed to be zero octas cloud cover, with a mean of 23% cloud cover [10]. However, such observations are rendered very difficult by the frequent presence of aurora, and so cannot be considered definitive.

One can appeal to the constancy and strength of the katabatic winds as a diagnostic that thick cloud is infrequent, as otherwise the reduction in radiative cooling of the surface would cause a reduction and variability in the winds. Dudenay et al [6]found winds between 12 and 18 ms^{-1} throughout winter at their automated observatory on the Plateau slope at 81°S.

Hence there is considerable but inconclusive evidence that cloud amounts over the Plateau in winter are small. However, this is not a sufficient condition for descent, as cloud could be limited by the supply of ice nuclei (IN) rather than by water vapour amount.

At mid-latitudes in the upper troposphere, IN are mostly carbonaceous material, i.e. soot [11], unlike other condensation nuclei which are mostly sulphate. It is possible that the very fine IN remain suspended during poleward transport, but soot in aerosol at the surface at S Pole in winter is less than 0.2 ng m^{-3}.

Hence it is possible that ice nuclei are limiting. This is certainly borne out by the frequent observation of clear-sky precipitation [12]. This requires major supersaturation, which gives rise to very rapid growth of ice-crystals on the few IN present, thereby creating large enough crystals that they fall from the sky (so-called diamond dust). This arises in the boundary layer because of descent through the extreme inversion, which often exceeds 30°C at Vostok in the centre of the Plateau in winter [13], but the same arguments apply in the boundary layer and the upper troposphere.

If measurements of cloudiness are not sufficient to identify decsent from the stratosphere, we must measure the water vapour in the upper troposphere.

5. POSSIBLE GOMOS MEASUREMENTS

The instrument Global Ozone Monitoring by Occultation of Stars (GOMOS), to be launched on ESA's Envisat, can measure in winter over the Pole. It measures H2O at its strong absorption band near 720 nm, and so would seem ideal for measurement of descent from the stratosphere.

However, there is a difficulty with GOMOS measurements in the troposphere. Refractive dilution (Figure 6) increases at lower altitude, giving rise to a weaker image of the star; and turbulent layers in the troposphere cause varying refraction and so scintillation. Either phenomenon might prevent the GOMOS active tracker from following a setting star in the troposphere, even in the very clean and probably cloud-free Antarctic. Even to test the mode woulod require a revision of GOMOS operational rules, whereby tracking is ceased at the tropopause.

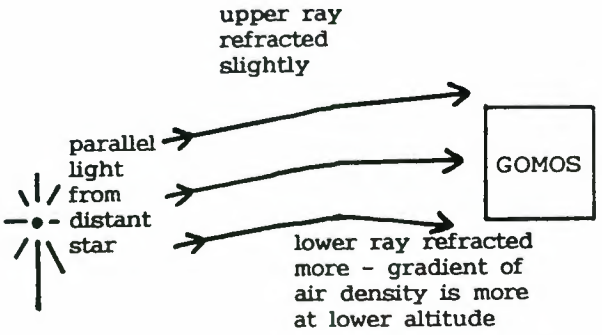

Figure 6. Refractive dilution of input signal from a star, at lower altitudes in the atmosphere.

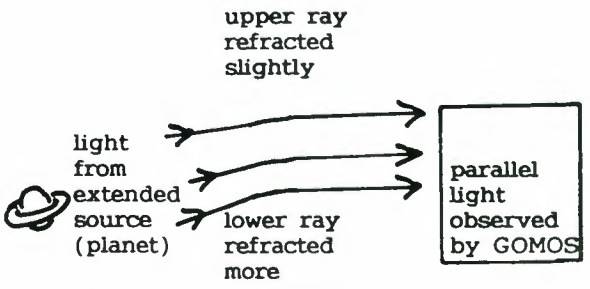

Figure 7. GOMOS' viewing of an extended source. The lack of refractive dilution and scintillation occurs because non-parallel light can arrive from an extended source such as a planet or the moon. The increase in the range of tangent heights is not significant.

However, refractive dilution and scintillation would be absent if GOMOS viewed a planet or the moon (Figure 7). In this configuration GOMOS would be unable to track as the source would be too large, but could instead passively point to follow the predicted course of the planet (so-called fictitious-star mode of GOMOS operation). This would require a new operational mode to be adopted for GOMOS.

Because of the large size of the planets, in this mode the location of the tangent point is less certain - when tracking a star it is defined by the accurately-known direction of the star. However, extinction at the surface would define a fixed point of reference which would enable the immediately preceding tangent points to be defined during the setting of the planet. The probability of GOMOS' being able to observe to the surface of the Antarctic Plateau in winter is increased by the extreme cleanliness of its atmosphere, the probable lack of clouds, and the low pressure at the high-altitude surface (< 700 mbar).

This extinction would be far from complete because the surface is highly-reflective snow and ice, viewed at grazing incidence. Fortunately the surface of Antarctic snow is highly corrugated by wind action, with small peaks over 100 mm high at about twice the separation of their height. The shadows they create will cause a massive loss of albedo at grazing incidence.

The probability of GOMOS' viewing the surface suggests the exciting possibility of detecting the clear-sky precipitation in the boundary layer. Such precipitation has an optical depth of less than 0.05 in the vertical, but could well be 0.1 or 0.2 when viewed tangentially. If would probable not be observed by the spectrometers because their 0.5 s integration is usually too long to distinguish the boundary layer, often less than 600 m in thickness, from the surface. But it might indeed be observed by the fast photometers on GOMOS. If so, GOMOS might help identify if precipitation from a clear sky is ubiquitous over much of the Plateau in winter, as believed by some workers.

References

1. Cheng D et al 1997, Millimeter wave spectrospcopic measurements over the South Pole 4 O3 and N2O during 1995 and their correlations for two quasi-annual cycles, J. Geophys. Res. 102, 6109-6116.
2. Wauben W M F et al 1997, Reply, J. Geophys. Res. 102, 28,219-28,221.
3. Tuck A F & Proffitt M H 1997, Comment on "On the magnitude of transport out of the Antarctic polar vortex" by Wiel M.F.Wauben et al, J. Geophys. Res. 102, 28,215-28,218.
4. King J C & Turner J 1997, Antarctic meteorology and climate, CUP, London, ISBN 0-521-56560-5.
5. Wayne R P 1985, Chemistry of atmospheres, OUP, ISBN 0-19-855176-2.
6. Dudenay J R, Kressman R I, Rodger A S 1998, Automated observatories for geospace research in polar regions, Antarctic Science 10, 192-203.
7. IPCC Woking Group 1 1990, Scientific assessment of climate change, Policymakers' summary, WMO/UNEP.
8. Hulme M, Osborn T J, Johns T C 1998, Precipitation sensitivity to global warming: comparison of observations with HadCM2 simulations, Geophys. Res. Lett. 25, 3379-3382.
9. Wang Y, Logan J A, Jacob D J 1998, Global simulation of tropospheric O3-NOx-hydrocarbon chemistry 2. Model evaluation and global ozone budget, J. Geophys. Res. 103, 10,727-10,755.
10. King J C 1999, private communication.
11. Chen Y et al 1998, Single particle analysis of ice nucleating aerosols in the upper troposphere and lower stratosphere, Geophys. Res. Lett. 25, 1391-1394.
12. Tape W 1994, Atmospheric Halos, Antarctic Research Series 64, AGU, Washington DC, ISBN 0-87590-834-9.
13. Connolley W M 1996, The Antarctic temperature inversion, Int. J. Climatology 16, 1333-1342.

Scientific Session

Retrieval & Radiative Transfer

Chair: B. Carli, *Universitá degli Studi di Firenze*

MONTE CARLO SIMULATIONS OF RADIATIVE TRANSFER FOR LIMB SCAN MEASUREMENTS

Liisa Oikarinen

Finnish Meteorological Institute,
Geophysical Research Division, Helsinki, Finland
e-mail: liisa.oikarinen@fmi.fi

ABSTRACT

Limb scanning from a satellite is a new geometry for radiance measurements in the near-UV, visible and near-IR wavelength range. It is used by two instruments on ENVISAT-1, SCIAMACHY (Scanning Imaging Absorption Spectrometer for Atmospheric Cartography), and by GOMOS (Global Ozone Monitoring by Occultation of Stars), which will measure the backscattered solar radiance as a background term of bright limb stellar occultation. Retrieval of geophysical parameters from the measured spectra requires accurate radiative transfer modeling in the atmosphere. In this wavelength range the backscattered radiance forms in a complex way through multiple scattering of light in the atmosphere. Most multiple scattering algorithms assume approximations (e.g. plane-parallel geometry) which are not valid in limb-viewing geometry. We have developed a backward Monte Carlo algorithm "Siro" especially for realistic and accurate radiative transfer modeling of limb measurements. The model is fully three-dimensional, i.e. it does not require spherical symmetry of constituent density profiles or boundary conditions. Siro is a tool for the development of constituent retrieval algorithms, but it requires too much computer time to be used in an iterative inversion algorithm. Siro can be used as a reference against which to validate faster but more approximate models.

1. INTRODUCTION

Two UV, visible and near-IR instruments on ENVISAT-1 have been designed to be able to measure atmospheric radiance spectra in limb-viewing geometry. These instruments are SCIAMACHY (Scanning Imaging Absorption Spectrometer for Atmospheric Cartography) and GOMOS (Global Ozone Monitoring by Occultation of Stars), which will measure the solar radiance spectrum as a background term of bright limb stellar occultation. Also the OSIRIS instrument on the Swedish Odin satellite (launch scheduled for Sept. 1999) will have a limb-viewing UV-visible spectrometer. The instruments scan the limb vertically and record spectra at different tangent altitudes from about 10 to 100 km (Figure 1). The density profiles of several atmospheric constituents (e.g. O_3, NO_2, BrO, OClO, neutral density and aerosols) are retrieved from one vertical scan.

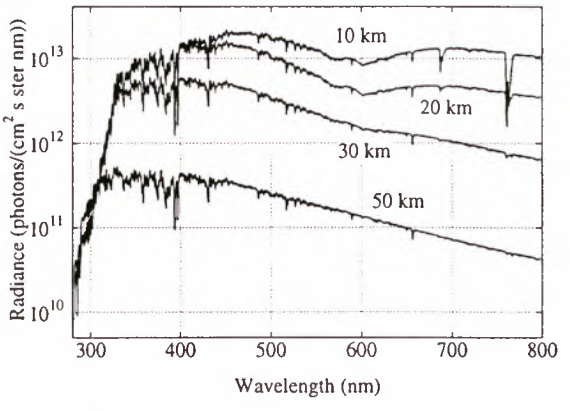

Figure 1. Single scattering radiance simulated by the MODTRAN 3.5 model using U.S. Standard atmospheric model and Background Stratospheric aerosol model. Tangent altitude of detector's line-of-sight is 10, 20, 30 and 50 km, zenith angle of Sun θ_T=80° and azimuth φ_T=90°. Spectra have been smoothed to 1 nm spectral resolution.

Before, UV-visible measurements of backscattered radiance have been conducted in nadir-viewing geometry (e.g. by the GOME instrument). Limb-viewing measurements are expected to yield constituent profiles at a better altitude resolution (1 - 3 km) than measurements in nadir-viewing geometry (vertical resolution about 5 km). For example, studies of stratospheric chemistry and dynamics would benefit from the improved vertical resolution. In limb-viewing the stratospheric optical depth of the line-of-sight is longer than in nadir-viewing, so a better sensitivity to small amounts of stratospheric absorbers is to be expected.

Retrieval of geophysical parameters is based on fitting a modeled spectrum to the measured spectrum of scattered solar light. Therefore, accurate radiative transfer (RT) modeling is necessary for the development of retrieval algorithms for the measurements. Due to the essentially different geometry RT models used with ground-based measurements or nadir-viewing instruments (Ref. 1) can not directly be applied to the limb-viewing case. A RT model for simulating limb-viewing measurements must be able to model:

- a spherical atmosphere,
- multiple scattering and
- refractive bending of light.

Monte Carlo RT models working in limb-viewing geometry have been published (Refs. 2-4) as well as a model which uses Gauss-Seidel iteration (Ref. 5). However, no accurate and validated RT model for this geometry has been made publicly available.

In Monte Carlo simulation of radiative transfer the radiance is determined statistically by following a large number of individual photon trajectories through the atmosphere. A minimal amount of geometrical approximation is required, so limb-viewing geometry can be modeled accurately. The conceptual simplicity of this method also allows one to introduce easily new physical processes to the simulation.

An effective Monte Carlo approach in limb-viewing geometry is the backward (or adjoint) Monte Carlo method. The word "backward" refers to time reversal: the photons are started from the detector and their path is followed backwards from the detector to the point where they leave the atmosphere towards the source, the Sun. The backward Monte Carlo method was introduced to atmospheric optics in the 70's (Refs. 2-4, 6). More recently, it has been used for computing air mass factors for ground-based zenith sky measurements, where during twilight conditions the sphericality of the atmosphere becomes important (Refs. 7-8).

In this paper we describe a Monte Carlo algorithm "Siro" ("sirota" is the Finnish word for "to scatter") which is similar to the backward Monte Carlo methods presented by the authors above, but Siro is especially tailored for simulations in limb geometry with a realistic model atmosphere. While previous algorithms used a spherical-shell model atmosphere, the implementation of Siro is fully three-dimensional. The model does not require spherical symmetry of the atmosphere or boundary conditions.

Two examples of simulations by Siro are presented in the end of this paper. The first example shows how the backscattered radiance and the proportion of multiple scattered light to total radiance depend on the relative orientation of the tangential line-of-sight and the Sun. In the second example mean photon path lengths at different altitude layers are calculated, which illustrates the coupling of the vertical and spectral dimensions of the retrieval problem (coupling of vertical and spectral inversion).

2. RADIATIVE TRANSFER EQUATION

The radiance spectrum $I_\lambda(\vec{r}_{det},\Omega_{det})$ detected by an instrument at location $\vec{r}_{det}$ from direction Ω_{det} is modeled by solving the radiative transfer equation in a model atmosphere

$$\vec{\Omega}\cdot\vec{\nabla}I_\lambda^{SS+MS}(\vec{r},\vec{\Omega}) = -k_\lambda^{ext}(\vec{r})I_\lambda^{SS+MS}(\vec{r},\vec{\Omega}) + J_\lambda(\vec{r},\vec{\Omega}). \qquad (1)$$

The incoming solar beam at the top of the atmosphere sets an upper boundary condition and a lower boundary condition is set by the reflective properties of the ground or a cloud top surface. In (1) $I_\lambda^{SS+MS}(\vec{r},\Omega)$ is the radiance (single and multiple scattering) at point $\vec{r}$ in the atmosphere propagating to direction $\vec{\Omega}$. The first term in the right hand side of (1) presents loss of radiation. Total volume extinction coefficient $k_\lambda^{ext}(\vec{r})$ includes absorption and scattering by molecules and particles. The source function $J_\lambda(\vec{r},\vec{\Omega})$ gives the gain of radiation.

At the wavelengths and atmospheric region studied in this work the source function is only due to elastic scattering by molecules and particles

$$J_\lambda(\vec{r},\vec{\Omega}) = \int_{4\pi} P_\lambda(\vec{\Omega},\vec{\Omega}',\vec{r})\, k_\lambda^{scatt}(\vec{r})\, I_\lambda^{SS+MS}(\vec{r},\vec{\Omega}')\, d\Omega'.$$

Scattering phase function $P_\lambda(\Omega,\Omega',\vec{r})$ is a weighted sum of phase functions for molecular and particle scattering

$$P_\lambda(\vec{\Omega},\vec{\Omega}',\vec{r}) = P_\lambda^m(\vec{\Omega},\vec{\Omega}',\vec{r})\frac{k_\lambda^{m\,scatt}(\vec{r})}{k_\lambda^{scatt}(\vec{r})} + P_\lambda^a(\vec{\Omega},\vec{\Omega}',\vec{r})\frac{k_\lambda^{a\,scatt}(\vec{r})}{k_\lambda^{scatt}(\vec{r})}.$$

Function $k_\lambda^{m\,scatt}(\vec{r})$ is the coefficient for scattering from molecules (equal to the product of the spectral scattering cross section and the local density) and $k_\lambda^{a\,scatt}(\vec{r})$ is the coefficient for scattering from aerosols. Total scattering coefficient $k_\lambda^{scatt}(\vec{r})$ at wavelength λ and point $\vec{r}$ is

$$k_\lambda^{scatt}(\vec{r}) = k_\lambda^{m\,scatt}(\vec{r}) + k_\lambda^{a\,scatt}(\vec{r}).$$

We call single scattering (SS) that part of radiation where a photon reaching the detector has undergone only one scattering event on its way through the atmosphere. All other photons belong to the multiple scattering term (MS). We consider also those photons, which have been scattered only once by an atmospheric molecule or particle, but have also been reflected by the ground to belong to the multiple scattering. The SS component I_λ^{ss} can be expressed as an integral over the line-of-sight (LOS) of light scattering towards the detector

$$I_\lambda^{ss}(\vec{r}_{det},\vec{\Omega}_{det}) = I_\lambda^{Sun}\int_{LOS} T_\lambda^{ps}(s)\, T_\lambda^{op}(s)\, P_\lambda(\vec{\Omega}_{det}(s),\vec{\Omega}_0(s))\, k_\lambda^{scatt}(s)\, ds. \qquad (2)$$

Here $T_\lambda^{ps}(s)$ is the transmittance of the path from Sun to the scattering point s on detector LOS and $T_\lambda^{op}(s)$ is the transmittance of the path from the scattering point to the detector. The solar irradiance incident on the atmosphere is denoted by I_λ^{Sun}. It arrives to the LOS with direction $\Omega_0(s)$. The single scattering term can easily be solved by numerical integration of (2) and is therefore a commonly used approximation for the scattered radiance.

3. BACKWARD MONTE CARLO ALGORITHM SIRO

In a Monte Carlo computation one photon at a time is followed along its three-dimensional path through the atmosphere. The photon's probability to be absorbed or scattered at a given point in the atmosphere is calculated and random numbers are used to select the results of collisions. Because the propagation of light is reversible

the probability of a photon going through the atmosphere along a particular path is independent of the direction in which we follow the path. The backward Monte Carlo method uses this idea (Ref. 2). We shoot photons from the detector and trace their paths backwards. This increases the speed of the simulation, because those photons, which in the forward method escape from the atmosphere outside the field-of-view of the detector, will now not be simulated at all. An other advantage over a forward method is a simpler description of the photon source, which is now the detector instead of the solar beam illuminating the whole day side of the atmosphere (Ref. 2). In a typical limb case the backward method selects the first scattering event most likely near the tangent point of the LOS, which is exactly the area where largest contribution to the scattered radiance can be expected to originate.

The basic formulation of Siro is similar to the method presented in Ref. 2. Siro starts with a computation of the line-of-sight of the instrument. The LOS is traced with short steps of length Δs and the optical depth τ_i to each point i of the LOS is calculated. The first (or last if counting in the forward direction) scattering cell is determined by finding the largest τ_i which satisfies

$$\tau_i \leq -\ln\left[1 - RN \cdot (1 - T^{LOS})\right],$$

where RN is a uniformly distributed random number between 0 and 1. Transmittance to the last point of the LOS is denoted by T^{LOS}. Scaling factor $1 - T^{LOS}$ forces a scattering to occur at some point of the LOS. The photon weight, initially equal to 1.0, is multiplied by the single scattering albedo $k_\lambda^{scat}(\vec{r}_1)/k_\lambda^{ext}(\vec{r}_1)$ at the selected first scattering point $\vec{r}_1$ to remove the bias from requiring the interaction to be a scattering event and by $1 - T^{LOS}$ to remove bias from forcing a scattering to occur along the LOS.

The SS contribution from this photon is then calculated by multiplying the photon weight by the probability that the photon would have come directly from Sun to point $\vec{r}_1$. This probability is the product of the transmittance of path $\vec{r}_1$-Sun multiplied by the scattering probability to the direction of Sun. The resulting SS photon weight is added to the cumulative SS weight. Several different solar positions can be simulated together, in which case the transmittance of $\vec{r}_1$-Sun and the scattering probability are calculated separately for each solar position.

We then continue tracing the photon path from $\vec{r}_1$ to simulate higher scattering orders. A random number is used to decide whether the first scattering occurs from a molecule or an aerosol particle. The probabilities are scaled according to the ratio of the corresponding scattering coefficients $k_\lambda^{m\,scat}(\vec{r}_1)$ and $k_\lambda^{a\,scat}(\vec{r}_1)$. A new propagation direction for the photon is obtained by sampling the cosine of the scattering angle $\cos(\Omega,\Omega')$ from the phase function and determining scattering plane δ by $\delta = 2\pi \cdot RN$.

Next a new path through the atmosphere is calculated starting from $\vec{r}_1$ to the new direction. We proceed to draw a scattering point $\vec{r}_2$, update photon weight and calculate second order scattering contributions as in the case of the LOS and SS component. If the photon hits the ground a Lambertian reflection is modeled and photon weight multiplied by the surface albedo. The photon's history is followed until its weight becomes smaller than a given minimum value. After the simulation of a sufficiently large set of photons the cumulative weight of each solar position and scattering order is divided by the total number of photons shot from the detector, which gives the ratio of the detected radiance to incident solar irradiance.

Atmospheric density profiles enter the simulation in the form of stepwise analytical functions of altitude, latitude and longitude. No shell structure is introduced to the model to allow full three-dimensionality. Also surface albedo and scattering phase functions could be allowed to vary as a function of geographical location. Refractive bending of the photon trajectory is taken into account by bending the ray path at the middle point of each short step Δs. Bending angle for a step is calculated by Snell's law from the values of refractive index at the end points of the step. For the scattering point - Sun paths refractive bending is solved by iteration.

The statistical error in the retrieved radiance is estimated by dividing the simulation to ten independent subsets (for example, 10 000 photons are simulated in sequences of 1000 photons). The standard deviation of statistical error in the full simulation is estimated from the standard deviation of the results from the ten subsets. Some thousands of photons (depending on model details, wavelength, geometry etc.) usually have to be simulated for a statistical accuracy better than 1 %. When photons are followed to minimum weight 10^{-6} with a step of 1 km this takes from a minute to more than an hour in a Silicon Graphics Origin 200 computer (simulation of radiance at one wavelength).

4. MODELLING RESULTS

In a fixed static spherically symmetric atmosphere the scattered solar radiance is only a function of wavelength, tangent altitude of the line-of-sight and the relative direction of the Sun. The radiance spectrum (Figure 1) reflects the wavelength dependence of molecular and aerosol scattering and absorption. Limb radiance is largest at visible or long UV wavelengths. It decreases fast towards shorter UV because of increasing absorption by ozone. Radiance decreases slowly towards IR because the molecular and aerosol scattering coefficients decrease. In the optically thin limit the radiance measured along a fully illuminated LOS increases about exponentially as the tangent altitude decreases.

4.1 Model atmosphere

The model atmosphere of the Monte Carlo simulations below includes scattering by molecules and aerosols and absorption by ozone. The vertical distribution of absorption and scattering coefficients $k_\lambda^{abs}(z)$ and

$k_\lambda^{m(a)scatt}(z)$ is shown in Figure 2 for 250 nm, where O_3 absorption is the dominating process, and 500 nm, where absorption coefficient of O_3 is of the same order of magnitude or smaller than the scattering coefficients. The profiles present the U.S. Standard Atmosphere, rural boundary layer aerosols with surface visibility 23 km, summer tropospheric aerosols and background stratospheric aerosol conditions.

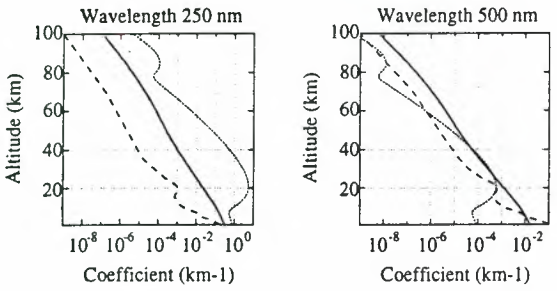

Figure 2. Absorption and scattering coefficients used in the simulations at 250 and 500 nm. Rayleigh scattering coefficient is drawn by a solid, aerosol scattering by a dashed and ozone absorption by a dotted line.

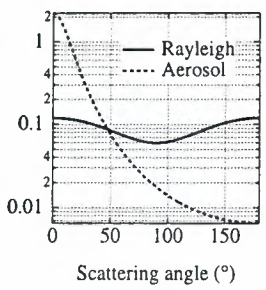

Figure 3. Phase functions used in the simulations for Rayleigh scattering and aerosol scattering (Henyey-Greenstein with asymmetry factor g=0.75).

We model the Rayleigh scattering phase function by

$$P^m(\gamma) = \frac{3}{16\pi}(1+\cos^2(\gamma))$$

where γ is the scattering angle. Aerosol scattering phase function for all wavelengths is modelled by the Henyey-Greenstein phase function with asymmetry factor $g = 0.75$ (presents background stratospheric aerosols)

$$P^a(\gamma) = \frac{1}{4\pi}\frac{1-g^2}{\left[1+g^2-2g\cos(\gamma)\right]^{3/2}}.$$

The phase functions have been plotted on Figure 3. Reflection from the ground is assumed to be Lambertian, with surface albedo 0.3.

4.2 Variation of radiance with the relative position of Sun

Figure 4 explains the co-ordinates that are used in this work to specify the direction of Sun: zenith θ_T and azimuth φ_T relative to tangent point of LOS. Figure 5, which has been produced by a simplified orbit propagator, gives an idea of the range of solar co-ordinates (θ_T, φ_T) occurring in the measurements by SCIAMACHY, GOMOS and OSIRIS. Figure 5 assumes that the LOS of SCIAMACHY and OSIRIS lies in the orbit plane. For SCIAMACHY and OSIRIS the possible directions of Sun (θ_T, φ_T) form approximately a circle, the radius of which depends on the orbit (descending node of Envisat is 10 a.m., Odin's 6 a.m.) and the month of the year. The maximum radius occurs at summer solstice, the minimum in February. GOMOS is pointed at stars of varying azimuths relative to the orbit plane and the relative direction of Sun is more scattered.

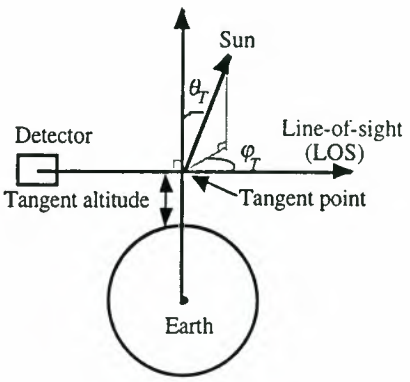

Figure 4. Co-ordinates for characterizing the geometry of a limb measurement. The direction of Sun relative to detector LOS is defined by the zenith angle θ_T and azimuth angle φ_T at the LOS tangent point. The zenith angle is defined as the angle between the z-axis and the direction of the Sun. The azimuth is the angle between the LOS and the projection of Sun's direction on the plane perpendicular to the z-axis.

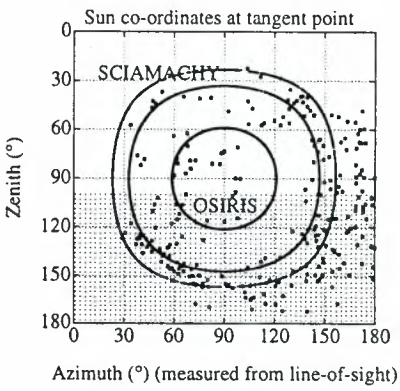

Figure 5. The direction (θ_T, φ_T) of the incident solar beam relative to the LOS of SCIAMACHY, OSIRIS and GOMOS. For OSIRIS the possible directions are inside the innermost circle, for SCIAMACHY within the two outermost circles. The dots present the direction of Sun for GOMOS (all possible occultations with stars brighter than magnitude two, one orbit/month). For GOMOS azimuths $180° < \varphi_T < 360°$ have been mapped to the mirror image in $0° < \varphi_T < 180°$. The shaded area gives approximately the dark limb where no scattered solar light is measured.

We study how limb radiance depends on the direction of the Sun (θ_T, φ_T) in an average case: tangent altitude of line-of-sight 20 km, wavelength 500 nm. In this case most of the radiation originates near the tangent point of the LOS (except for cases where θ_T = 100°) and the absorption and scattering coefficients are of the same magnitude (Figure 2).

The Rayleigh scattering phase function peaks for forward and backward scattering, and the aerosol phase function has a strong forward maximum (Figure 3). The observed radiance as a function of the relative direction of Sun reflects this angular dependency clearly (Figure 6). Even photons that have undergone two or three collisions (second and third order scattering) show small maxima for forward and backward Sun. The radiance decreases rapidly as the Sun get's colser to the horizon (large θ_T).

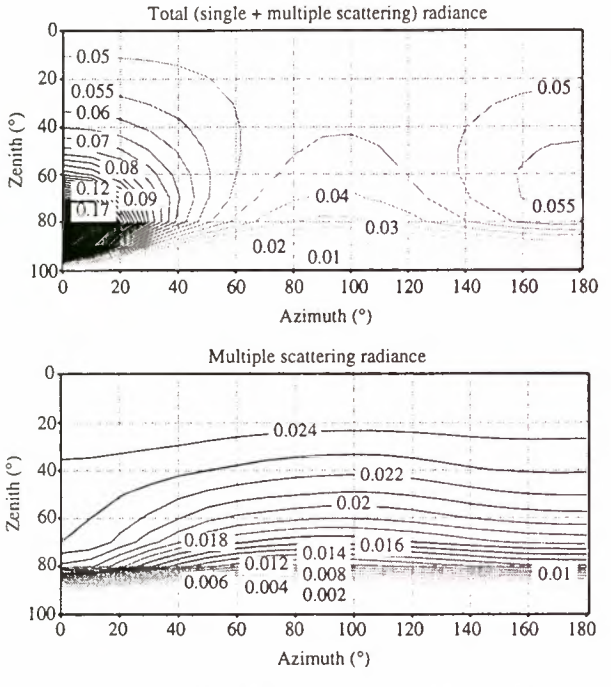

Figure 6. Upper plot: the ratio of total limb radiance to incident solar irradiance at 500 nm as a function of Sun's direction (θ_T, φ_T) simulated by Siro. Tangent altitude of line-of-sight is 20 km. Lower plot: multiple scattering term alone (second order and higher orders of scattering). The statistical accuracy of the simulation is better than 1 % for $\theta_T \leq 90°$, and better than 10 % for $\theta_T = 100°$.

The proportion of multiple scattering to total radiance as a function of solar position is shown in Figure 7, upper plot. Multiple scattering is most important, constitutes about half of the total radiance, when the solar zenith angle θ_T is small. In the region of strongest total radiance (detector looking almost directly to Sun), and also for near-horizon sun, the relative contribution of multiple scattering is at smallest.

The effect of surface albedo on the measured radiance can be seen from the proportion of photons whose trajectory includes a reflection from ground (Figure 7, lower plot). The effect of surface albedo is largest for high solar elevation angles and smaller for geometries where Sun is close to the horizon. When the surface albedo is 0.3 light reflected from the ground constitutes about half of the multiple scattering term when θ_T is small. Extreme albedos of 0.0 and 1.0 would give correspondingly 30% and 70 % multiple to total scattering ratios at high solar elevation angles.

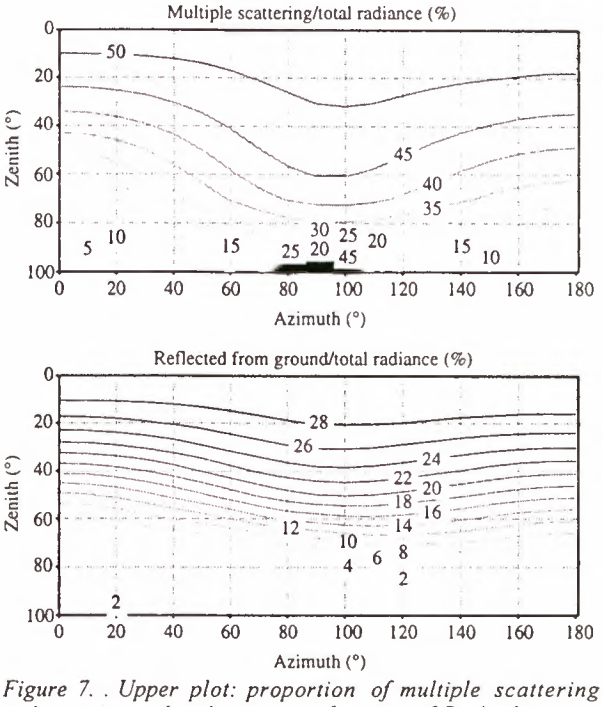

Figure 7. . Upper plot: proportion of multiple scattering radiance to total radiance as a function of Sun's direction (θ_T, φ_T) at 500 nm and tangent altitude 20 km simulated by Siro. Lower plot: proportion of light that has undergone at least one reflection from ground. Statistical error of the simulation is better than 3% for $\theta_T \leq 90°$, better than 30% for $\theta_T = 100°$..

4.3. Mean photon path lengths at different altitude layers of the atmosphere

When the transmittance to the tangent point of the LOS is above about 0.1 (for example visible and near-IR wavelengths and tangent altitude ≥ 15 km), most of the radiation observed by a limb-viewing instrument originates near the tangent point of the LOS. To study more closely the altitude region relevant for the radiance measurement we calculate mean photon path lengths Δs_i (photon path lengths weighted by the weights of individual photons) at different 1 km thick altitude layers i in the atmosphere. The path length Δs_i can be interpreted as the derivative of the radiance with respect to the absorption coefficient (e.g. of ozone) at altitude z_i relative to total intensity I_λ^{SS+MS}

$$\Delta s_i = \frac{dI_\lambda^{SS+MS}}{dk_\lambda^{abs}(z_i)} \cdot \frac{1}{I_\lambda^{SS+MS}}. \qquad (3)$$

Figure 8 shows examples of mean path lengths for wavelength 500 nm and different tangent altitudes.

Because of strong absorption by ozone in the UV (Figure 2) photons at wavelength 300 nm or below reaching the detector have only visited upper parts of the stratosphere. This is illustrated by Figure 9, where mean photon path lengths for a measurement at tangent altitude 10 km have been plotted for different wavelengths.

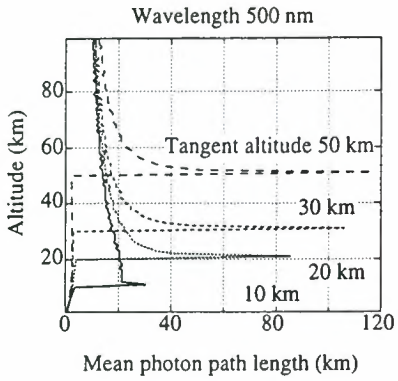

Figure 8. Mean photon path lengths (3) for wavelength 500 nm and different tangent altitudes of LOS simulated by Siro (θ_T=80°, φ_T=90°).

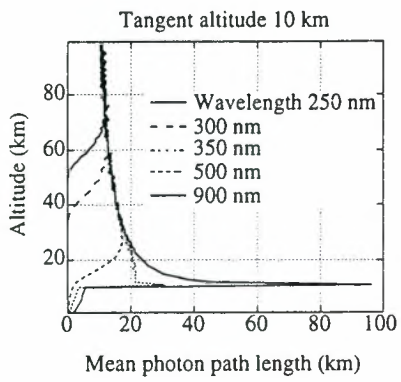

Figure 9. Mean photon path lengths (3) for different wavelengths simulated by Siro (tangent altitude 10 km, θ_T=80°, φ_T=90°).

5. CONCLUSIONS

We have presented a backward Monte Carlo algorithm Siro which has proven to be a versatile tool for studying the limb-viewing measurement technique. Siro is a good tool for validating approximations adopted by other faster methods, but it is too slow to be used as part of an iterative retrieval algorithm. Comparisons between Siro and some other models are going on.

In limb-viewing geometry multiple scattering constitutes 10 - 50 % of the total radiance at visible wavelengths (background stratospheric aerosols and albedo 0.3), depending on the solar position relative to the detector LOS. Volcanic aerosol conditions or a surface albedo close to 1.0 (snow or cloud cover) can increase the proportion of multiple scattering well over 50 % at visible wavelengths. A single scattering model would be a poor approximation of limb radiance in this wavelength range.

The mean photon path lengths at different altitude layers (altitude weighting functions) depend strongly on wavelength, especially at near-UV wavelengths (Figure 9). A common retrieval approach in occultation measurements separates the inversion to two parts: a spectral inversion and a vertical inversion (e.g. onion peeling). For limb radiance measurements this approach must be used with caution: the wavelength dependence of weighting functions shows that spectral and geometrical effects are not decoupled. Measurements in the UV can only give information of the abundances of atmospheric constituents in the upper stratosphere (Figure 9). For good profile retrieval down to 10 – 20 km measurements at visible and near – IR wavelengths are also needed.

A future version of Siro will perform the radiative transfer calculation separately for different polarisation directions of light. Neglecting the vector nature of light may cause an error of a few per cent to the scalar intensity (Ref 9). A very realistic simulation would also take into account the Ring effect, i.e. the filling of solar Fraunhofer lines by inelastic scattering processes in the (Ref. 10).

REFERENCES

1. Rozanov, V.V., D. Diebel, R.J. Spurr, and J. P. Burrows, GOMETRAN: A radiative transfer model for the satellite project GOME, the plane parallel version, *J. Geophys. Res., 102,* 16683-16695, 1997.

2. Collins, D.G., W. G. Blättner, M.B. Wells, and H. G. Horak, Backward Monte Carlo calculations of the polarization characteristics of the radiation emerging from spherical-shell atmospheres, *Appl. Opt. 11,* 2684-2696, 1972.

3. Adams, C.N., and G.W.Kattawar, Radiative transfer in spherical shell atmospheres, I., Rayleigh scattering, *Icarus, 35,* 139-151, 1978.

4. Kattawar, G.W., and C. N. Adams, Radiative transfer in spherical shell atmospheres, II., asymmetric phase functions, *Icarus, 35,* 436-449, 1978.

5. Herman, M.B., A. Ben-David, and K. J. Thome, 'Numerical technique for solving the radiative transfer equation for a spherical shell atmosphere, *Appl. Opt. 33,* 1760-1770, 1994.

6. Marchuk, G.I., G.A. Mikhailov, M.A. Nazaraliev, R.A. Darbinjan, B.A. Kargin, B.S. Elepov, *The MonteCarlo Methods in Atmospheric Optics,* 208 pp., Springer, Berlin Heidelberg, 1980.

7. Lenoble, J., and H.B. Chen, Monte Carlo study of the effects of stratospheric aerosols and clouds on zenith sky absorption measurements, Paper presented at the International Radiation Symposium, IAMAP, Tallin, Estonia, Aug. 1992.

8. Perliski L. M. and S. Solomon, On the evaluation of air mass factors for atmospheric near-ultraviolet and visible absorption spectroscopy, *J. Geophys. Res., 98,* 10363-10374, 1993.

9. Lacis, A.A., J. Chowdhary, M.I. Mishchenko, and B. Cairns, Modelling errors in diffuse sky radiation: Vector vs. scalar treatment, *Geophys. Res. Lett., 25*, 135-138, 1998.

10. Graigner, J., and J. Ring, Anomalous Fraunhofer line profiles, *Nature, 193*, 762, 1962

INTERPRETATION OF THE LIMB RADIANCE MEASUREMENTS ACCOUNTING FOR THE NON-LTE CONDITIONS

Kostsov V.S. (1), Timofeyev Yu.M. (1), Grossmann K. (2), Vollmann K. (2), Fischer H. (3)

1) St.Petersburg State University, Ulyanovskaya 1, St.Petersburg-Petrodvorets, 198904 Russia
Email: vlad@troll.phys.spbu.ru
2) Wuppertal University, Gauss-str. 20, 42097 Wuppertal, Germany
3) Institut für Meteorologie und Klimaforschung, Forschungszentrum Karlsruhe, 76021 Karlsruhe, Germany

ABSTRACT

The multiparameter inverse problem relevant to the interpretation of the limb radiance measurements with account for the non-LTE conditions in the atmosphere is considered. The method of joint retrieval of the kinetic temperature, gas concentrations and vibrational temperatures which characterize the nonequilibrium populations of the vibrational states of molecules is described. The method is based on the optimal estimation algorithm and does not require preliminary modeling of the processes driving non-LTE. The applicability of the method to the processing of the limb infrared radiance spectra measured from satellites is demonstrated on the basis of the 15μm data obtained by the CRISTA instrument during 1994 mission. The applicability of the method to the processing of the MIPAS data is discussed.

1. INTRODUCTION

The development of the high accuracy and medium/high spectral resolution satellite instruments, e.g. CRISTA, MIPAS (Refs. 1, 8) measuring the infrared spectra made it possible to register weak limb emissions of the middle and upper atmosphere and investigate the non-LTE effect which is most pronounced in the upper atmospheric layers.

There are different approaches to the interpretation of the limb radiance spectra measurements influenced by the non-LTE effect:

a) Microwindow selection aimed to avoid spectral regions with considerable non-LTE effect and performed on the basis of theoretical modeling of the non-LTE populations of molecular states and estimations of the magnitude of the non-LTE effect (Ref. 6). This approach is the most applicable in the case when the primary goal of the remote sensing experiment is the determination of the parameters which are not relevant to non-LTE.
b) Approximate accounting for the non-LTE effect on the basis of pre-calculations of the non-LTE populations of molecular states using available models of the non-LTE processes and utilization of these data in the inversion procedure (the process can be iterative). This approach is also the most applicable in the case when the primary goal is the determination of the parameters which are not relevant to non-LTE.
c) Derivation of the parameters which characterize the non-LTE conditions together with other atmospheric parameters (kinetic temperature, gaseous content, etc.) directly from spectra without preliminary modeling of the processes driving non-LTE. Such approach is applicable in general case and gives the opportunity to investigate the non-LTE atmospheric conditions, but the inverse problem becomes more complicated and the requirements to the measurement data quantity and quality increase.

The latter approach is used in the present study for the problem of the multiparameter sounding of the non-LTE atmosphere in the 15 μm CO_2 band using spectra measured by the CRISTA and MIPAS instruments. General consideration of the problem was done in a number of papers (Refs. 2,3). The detailed description of the simultaneous retrieval approach to the remote sensing problems of the non-LTE atmosphere can be found in several studies (Refs. 4, 5, 10).

In the present study only the "vibrational non-LTE" is considered, though in general the population of the rotational molecular states may be influenced by non-LTE too. The non-LTE populations of molecular vibrational states are described by so-called vibrational temperatures (which is rather common approach).

In the subsequent sections the description of the method and the formulation of the specific inverse problem are given. The results of the derivation of the kinetic temperature and the CO_2 vibrational temperatures from the CRISTA data are presented. The problem of sounding the non-LTE atmosphere by the MIPAS instrument is discussed.

2. RETRIEVAL METHOD

2.1 Formalism

Radiative transfer equation for limb radiance I at wavenumber ν and tangent altitude z_t can be expressed as a complex functional depending on a number of parameters including the vibrational temperature profiles:

$$I(\nu,z_t) = F\,[\,T_k(z),\, p(z),\, n_g(z),\, T_v^{gs}(z)\,]\,, \qquad (1)$$

where z is the altitude coordinate, T_k is kinetic temperature, p is pressure, n_g is the concentration of atmospheric gas of the number g and T_v^{gs} is the vibrational temperature of the vibrational state s of the gas "g". After linearization Eq. 1 may be written in a vector-matrix form:

$$\delta\mathbf{y} = I_{measured}(\nu, z_t) - I_{mean}(\nu, z_t) = \mathbf{A}\delta\mathbf{x}\,, \qquad (2)$$

where $\delta\mathbf{y}$ is a vector composed of the variations of limb radiance at wavenumber gridpoints for different tangent

altitudes, **A** is forward operator, and $\delta\mathbf{x}$ is a vector of unknowns:

$$\delta\mathbf{x}^{+} = (\delta T_k(z_1), \delta T_k(z_2), \ldots, \delta T_k(z_N), \delta p(z_1), \delta p(z_2), \ldots, \delta p(z_N), \delta n_g(z_1), \delta n_g(z_2), \ldots, \delta n_g(z_N), \delta T_v^{gs}(z_1), \delta T_v^{gs}(z_2), \ldots, \delta T_v^{gs}(z_N)),$$

where δ denotes variations from mean values, N is a total number of altitude levels, here and below "+" denotes transposition. The problem of the inversion of Eq. 2 is a well-known ill-posed one. The solution of such problem can be obtained on the basis of the regularization algorithm in the iterative process:

$$\mathbf{x}_{k+1} = \mathbf{x}_{mean} + \delta\mathbf{x}_{k+1} = \mathbf{x}_{mean} + (\mathbf{A}_k^{+}\Sigma^{-1}\mathbf{A}_k + \mathbf{R})^{-1}\mathbf{A}_k^{+}\Sigma^{-1}(\delta\mathbf{y}_k + \mathbf{A}_k\delta\mathbf{x}_k), \quad k = 0, 1, \ldots, \qquad (3)$$

where Σ is the matrix describing measurement random errors, **R** is the regularization operator, $\delta\mathbf{y}_k$ denotes the discrepancy between measured spectra and spectra calculated on the basis of the set of profiles obtained at the *k*th iteration (not in linear approximation). If **R** is assigned to the inverted covariance matrix of unknown parameters, we obtain the so-called "optimal estimation" algorithm. The diagonal elements of the error matrix:

$$\mathbf{E} = (\mathbf{A}^{+}\Sigma^{-1}\mathbf{A} + \mathbf{R})^{-1}, \qquad (4)$$

are the estimates of the retrieval errors at different altitudes for different parameters.

2.2 Physical background

Physical background for the joint retrieval of atmospheric parameters including the vibrational temperatures for different molecular vibrational states comprises several aspects:

a) The main principle is the utilization of measurements in spectral regions corresponding to different vibrational bands in order to achieve separation of the variables.
b) True or model covariance matrices can be used in order to incorporate a priori information into the retrieval procedure for obtaining unique solution.
c) Different physical constraints may be applied to the inversion process which diminish the number of unknowns, for example: hydrostatic equation with reasonable accuracy, vibrational temperature coupling for closely located (by energy) vibrational states (so-called "internal LTE"), identification of layers where non-LTE is not expected (on the basis of model predictions, if any), non-variable volume mixing ratio for certain gases.
d) Different approximations may be applied, e.g. the equivalence of certain vibrational temperatures with reasonable accuracy (on the basis of model predictions, if any).

Combination of spectral separation of the variables with minimum a priori information (e.g. on expected mean values and variability of parameters) eliminates the necessity for rigorous preliminary modeling of the processes driving non-LTE. It should be mentioned that the requirements to the accuracy of mean values of the vibrational temperatures (used also as initial guess) are not strong and the estimation of these values can be done on the basis of general considerations.

3. INTERPRETATION OF THE CRISTA DATA

3.1 Formulation of the problem and error analysis

The limb radiance spectra from 645 cm^{-1} to 675 cm^{-1} (the 15 μm region) measured by the CRISTA instrument during 1994 campaign were taken for the interpretation. Fig. 1 shows sample spectrum and indicates the location of the most intensive Q-branches of vibrational bands for four CO_2 isotopes, thus demonstrating spectral separation of the variables. The resolving power of the instrument was estimated as 520. Tangent altitude range of measurements was from 40 km up to 150 km. The random noise was estimated to be about 0.005 mW/(m^2 sr cm^{-1}).

The vibrational states of the CO_2 molecule for which the non-LTE effect was taken into account are shown in Fig.2. For other states the approximation of the validity of LTE was used.

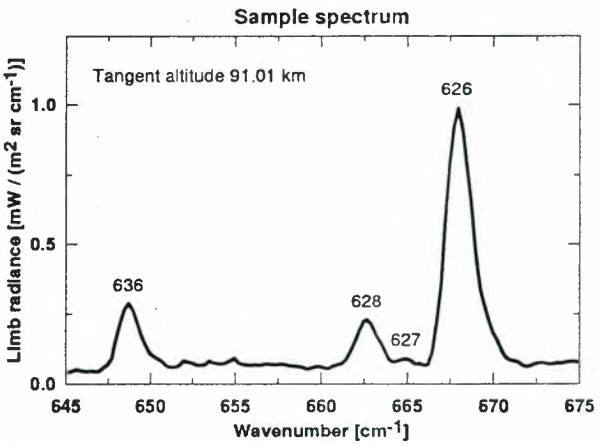

Figure 1. Sample spectrum. Demonstration of the spectral separation of the variables (see text).

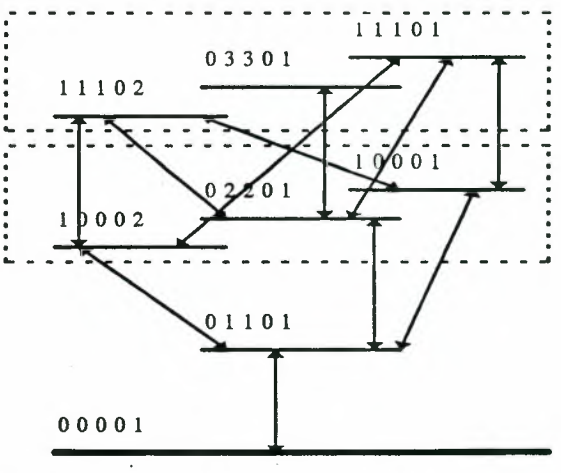

Figure 2. The vibrational states of the CO_2 molecule for which the non-LTE effect was considered. Boxes show the "internal LTE" groups of states.

The following details of the formulation of the inverse problem and the retrieval process should be mentioned:

a) A priori information
Mean profiles: T_k - MSIS90, gases -AFGL86, all T_v=T_k up to 110 km, T_v=260 K above 110 km.

b) Covariance
Matrix of the model type with exponential dependence of covariances was used. A priori uncertainty for T_k and all T_v was constant and equal to 50 K, correlation radius was set to the value of 7 km.

c) Constraints
LTE conditions for all levels up to 60 km were assumed. Internal LTE for the groups of levels: (10001, 02201, 10002), (11101, 03301, 11102) was assumed. Volume mixing ratio profiles for all gases were taken equal to correspondent mean profiles. Hydrostatic constraint with 15% accuracy was applied.

d) Approximations
The vibrational temperatures of the levels 01101, 02201, and 03301 for each isotope were set equal since the spectral resolution was insufficient for the separation of correspondent variables.

The following error sources were taken into account: random noise, tangent altitude pointing errors, wavenumber calibration errors, offset calibration errors.

As a result, the inverse problems was formulated with respect to 5 unknowns: (1) - kinetic temperature T_k, (2-5) - vibrational temperatures T_v of the 01101 level of the CO_2 isotopes 626, 636, 628, 627. The retrieval errors for these parameters estimated on the basis of the error matrix are shown in Fig. 3. For the sake of convenience it is useful to set the criterion identifying the upper boundary up to which the parameters could be retrieved with reasonable accuracy. We selected the criterion of 50% decrease of a priori uncertainty which resulted in the error value of 25 K for all temperatures. One can see from Fig.3 that the altitude levels of the 50% decrease of a priori uncertainty for T_k and Tv are the following: T_k-130 km, T_v(626)-higher than 130 km, T_v(636)-120 km, T_v(628)-115 km, T_v(627)-105 km. It should be mentioned that the numerical experiments confirmed the error estimations based on the error matrix calculations.

3.2 Retrieval results

We present the results of the interpretation of several limb scans obtained at different geographic locations (scan numbering is valid only for the present study). The plots show the retrieved kinetic temperature and the vibrational temperatures of the state 01101 for the 626, 636, 628, and 627 isotopes in the altitude range 40-130 km. The "upper limit" identification marks designate the altitude levels of 50% decrease of a priori uncertainty (25 K error) for T_v(01101) of the 636, 628, and 627 isotopes. There are no marks for other parameters since corresponding levels are 130 km and higher. It should be stressed that the retrieval results for the atmospheric layers higher than the upper limit are not suitable for analysis due to large errors, however they are plotted for the sake of consistency. The error bars correspond to the error estimations made on the basis of the error matrix calculations.

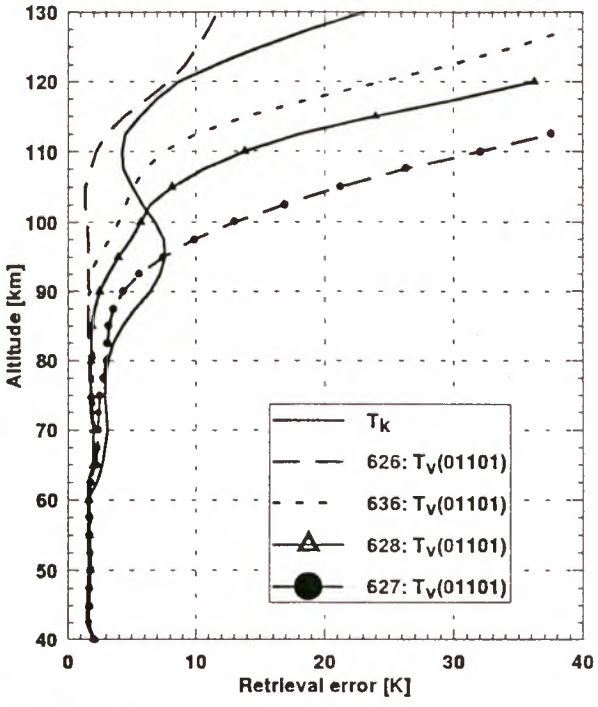

Figure 3. Retrieval errors of the kinetic temperature T_k and vibrational temperatures T_v of the 01101 state (for different CO_2 isotopes) estimated on the basis of error matrix calculations (the CRISTA 15 μm measurements)

Together with the results of joint kinetic-vibrational temperature retrieval, we plotted the results of the independent retrieval of kinetic temperature by the Wuppertal University scientific team (referred below as WU) under the assumption of LTE.

The retrieval results obtained for scan S09 are presented in Fig 4. All vibrational temperatures are very close to the kinetic temperature up to the altitude of 75 km indicating the validity of the LTE conditions. In the upper layers vibrational temperatures start to deviate from the kinetic temperature and the deviations in the vicinity of the mesopause are larger for T_v of minor isotopes. The considerable deviations of the vibrational temperatures from the kinetic temperature start at about 107 km where the vibrational temperature profiles become relatively constant if compared to the kinetic temperature profiles. The results of the kinetic temperature profile retrieval are very close to independent retrieval by the Wuppertal University group up to 80 km, except the 50-60 km region where the independent retrieval profile is slightly oscillating. In the 80-90 km range the WU results are larger and closer to the vibrational temperature of the 01101 state of the major isotope.

The retrieval results for scan S11 are presented in Fig. 5. The non-LTE effect in this case starts at about 73 km, however there are small deviations of vibrational temperatures from the kinetic temperature in the vicinity of 67 km altitude. There is a strong temperature inversion at 90 km altitude. Above this temperature inversion the vibrational temperatures are close to the kinetic temperature. As it was for the S09 scan, the most pronounced non-LTE effect starts at about 107 km altitude. We stress that large retrieval errors

for the vibrational temperatures of minor isotopes make the comparative analysis of different vibrational temperatures problematic. The independent kinetic temperature retrieval results are in very good agreement with the results obtained by the joint retrieval method up to 72 km altitude. Above this altitude, they coincide with the $T_v(01101)$ of the 626 isotope.

The results for scan S13 are interesting since the kinetic temperature profile in this case is characterized by two very strong inversions, see Fig. 6. One can see that the non-LTE effect is considerable in the inversion area and in the vicinity of mesopause (the temperature minimum at 95 km can be attributed to the mesopause).

Let us consider one more example of the retrieval - scan S15, which is characterized by a very high mesopause at 105 km and two temperature inversions at 88 km and 98 km. The results are shown in Fig. 7. One can see that the non-LTE effect starts at about 80 km altitude, however the deviations of the vibrational temperatures from the kinetic temperature are not large up to 100 km altitude. In the vicinity of mesopause, the deviations increase, and the magnitude of deviations is larger for minor isotopes. Starting from 112 km the vibrational temperature $T_v(01101)$ of the 626 isotope is practically constant. As far as the comparison with the kinetic temperature independent retrieval is concerned, we stress that the situation is similar to other scans: in the LTE layers there is a very good agreement, but in the non-LTE areas the independent results are more close to the vibrational temperature $T_v(01101)$ of the 626 isotope.

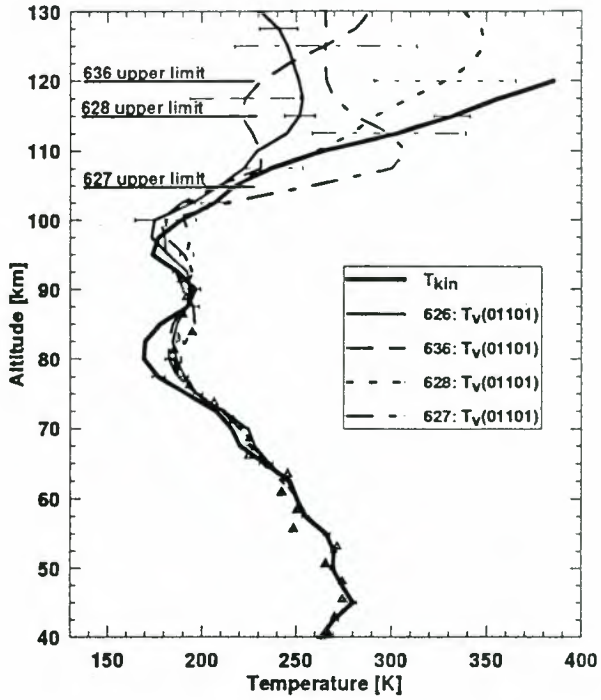

Figure 5. Same as Fig. 4 but for scan S11, -42.4LAT, -112.9LONG, 14:01GMT, 05.11.1994.

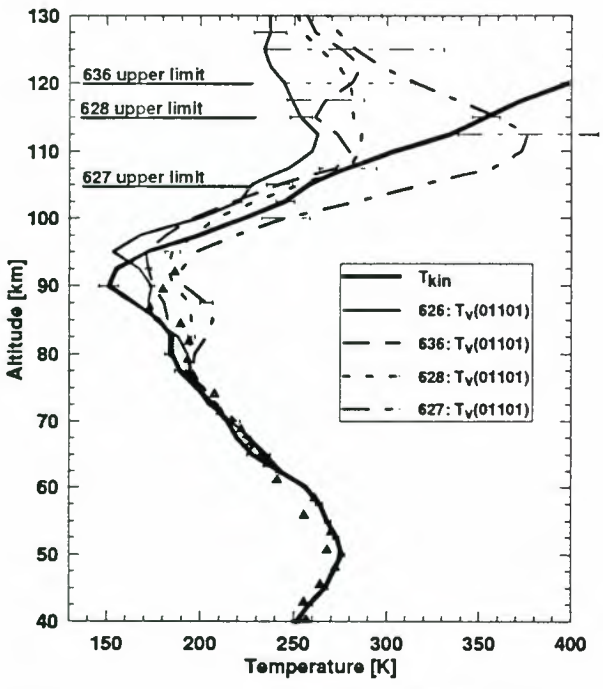

Figure 4. The CRISTA retrieval, scan S09, -51.9LAT, -150.7LONG, 13:54GMT, 05.11.1994. Triangles show the independent retrieval of kinetic temperature by the Wuppertal group without accounting for non-LTE.

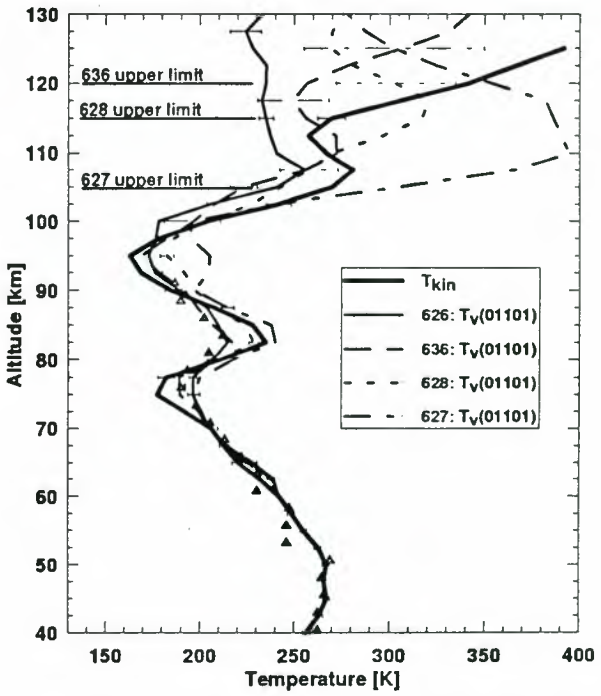

Figure 6. Same as Fig. 4 but for scan S13, -22.9LAT, -90.2LONG, 14:08GMT, 05.11.1994.

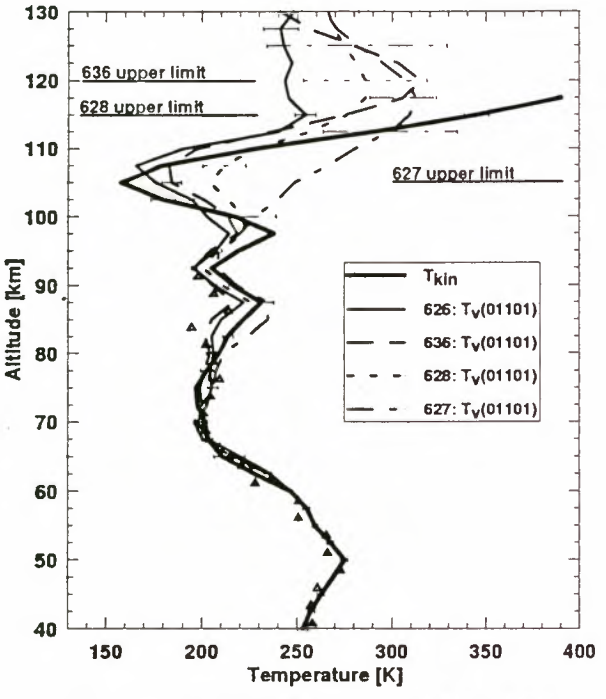

Figure 7. Same as Fig. 4 but for scan S15, -0.09LAT, -75.2LONG, 14:15GMT, 05.11.1994.

4. APPLICABILITY OF THE METHOD TO THE PROCESSING OF THE MIPAS DATA

The Michelson Interferometer for Passive Atmospheric Sounding (MIPAS) will operate on board ENVISAT-1 polar platform (Ref.1). The operational scenario of measurements will cover tangent altitudes in the range of 8-70 km, however besides the operational scenario, special observations will be performed up to the tangent altitude of 150 km which will be of particular interest with respect to the investigation of non-LTE effects.

In order to estimate the potential possibilities of the applying the developed approach to the interpretation of the MIPAS measurements, we simulated the 15 μm limb radiance measurements using the performance characteristics of the MIPAS instrument, and made calculations of the error matrix. The spectral resolution of measurements was taken equal to 0.055 cm^{-1} and the noise equivalent spectral radiance was set equal to 0.32 $mW/(m^2\ sr\ cm^{-1})$. It should be stressed that we did not take into account the error sources other than random noise. We performed the numerical experiment on the joint retrieval of atmospheric parameters using the same wavenumber interval as in the case of processing the CRISTA data. The non-LTE atmospheric model for the numerical experiment was provided at our disposal by Dr. V.P.Ogibalov (Refs. 7, 9).

The results of the error matrix calculations are shown in Fig 8. One can see that the limb radiance measurements by the instrument of the MIPAS type can provide the information on the vibrational temperature of the 01101 state of the major CO_2 isotope with reasonable accuracy up to 130 km altitude. For the vibrational temperatures of other isotopes the retrieval errors are considerably larger. If the criterion of 50% decrease of a priori uncertainty is assumed, then the upper altitude limits for the retrievals will be: T_k - 117 km, $T_v(626)$ - higher than 130 km, $T_v(636)$ - 108 km, $T_v(628)$ - 103 km, $T_v(627)$ - 94 km. Taking into account the fact that the non-LTE effect for the considered CO_2 vibrational states can start from about 70 km altitude, there is the opportunity to derive new information on the non-LTE conditions from the MIPAS measurements even for minor isotopes.

In Fig. 9 we present the results of the retrieval of the kinetic temperature and the vibrational temperature of the state 01101 of the major CO_2 isotope in the numerical experiment simulating limb measurements by the MIPAS-type instrument and in Fig. 10 - the results if averaged over 10 samples. The error bars correspond to the error estimations made on the basis of the error matrix calculations. As one can see, the retrieval of the $T_v(01101)$ of the 626 isotope is very good in the whole altitude range. The kinetic temperature profile retrieval is very good up to 110 km altitude if averaging is applied. In the whole altitude range the retrieved and true profiles coincide within the limits of error matrix estimations.

5. CONCLUSIONS

The interpretation of the CRISTA measurements in the 15 μm spectral region provided the information on the vertical profiles of the kinetic and vibrational temperatures of the 01101 state of the CO_2 626, 636, 628, and 627 isotopes up to the altitude of 105-130 km for different geographic locations.

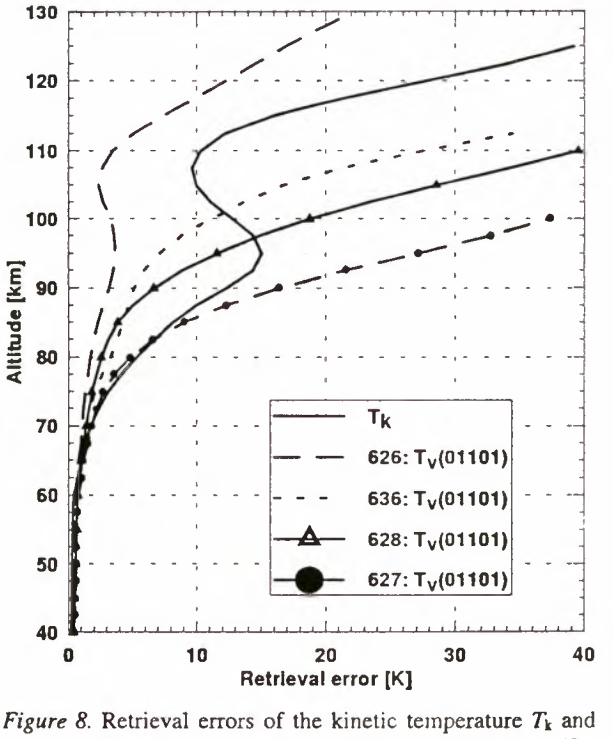

Figure 8. Retrieval errors of the kinetic temperature T_k and vibrational temperatures T_v of the 01101 state (for different CO_2 isotopes) estimated on the basis of error matrix calculations (15 μm measurements simulated for the instrument of the MIPAS type).

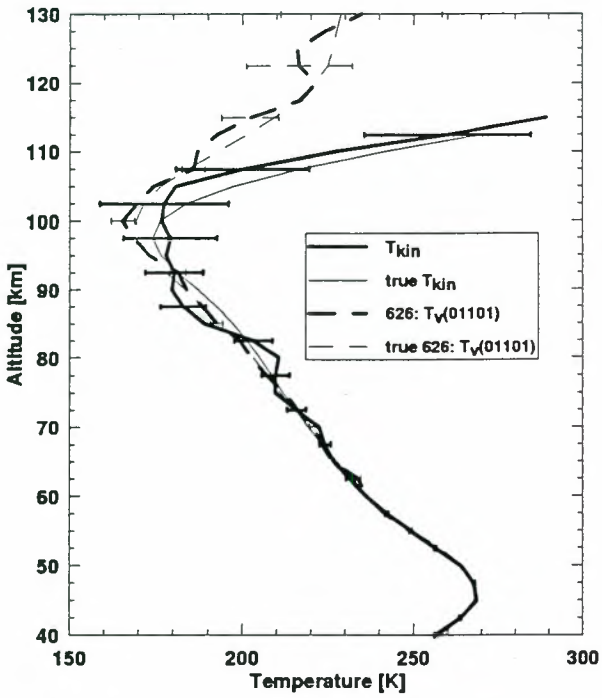

Figure 9. Retrieval in the MIPAS numerical experiment. The non-LTE model (true profiles) has been provided by Dr. V.P.Ogibalov. Only the random noise error source has been taken into account. Bold lines show the retrieved profiles, thin lines show true profiles. Random noise 0.32 mW/(m^2 sr cm^{-1}).

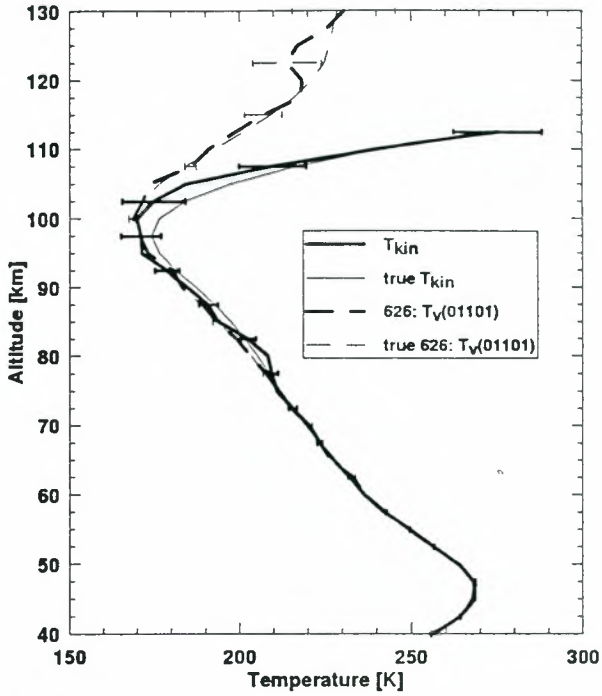

Figure 10. Same as Fig. 9 but with averaging over 10 samples.

Numerical experiments and error matrix calculations have shown that the most accurate are the retrievals of the kinetic temperature T_k and the vibrational temperature $T_v(01101)$ of the 626 isotope.

Processing of the CRISTA measurements in the 15 μm domain has shown that the non-LTE effect for CO_2 starts at about 80 km if the T_k profile is smooth but can start lower in case of kinetic temperature inversions.

The vertical behavior of the kinetic and vibrational temperatures is highly variable for different geographic locations and can be rather complicated (characterized by multiple inversions).

Comparison of the kinetic temperature retrievals with independent retrievals of T_k performed by the Wuppertal University scientific group without accounting for non-LTE has shown, first, very good agreement in the LTE layers, and second, considerable discrepancies in the regions with noticeable non-LTE effect.

Numerical experiments and error matrix calculations have shown the possibility to sound the non-LTE atmosphere in the 15 μm region by the MIPAS-type instruments. For such instruments the highest retrieval accuracy is expected for the vibrational temperature of the 01101 state of the major CO_2 isotope and for the kinetic temperature. The vibrational temperatures $T_v(01101)$ for minor isotopes can be derived with reasonable accuracy up to the altitude of 90-100 km.

6. REFERENCES

1. Fischer, H., and H. Oelhaf 1996, Remote sensing of vertical profiles of atmospheric trace constituents with MIPAS limb-emission spectrometers, *Appl. Opt.*, 35, 16, 2787-2796.
2. Kostsov, V.S., Yu.M.Timofeyev, and H.Grassl 1992, *Atmos. Ocean. Phys.*, 28, 6, 457-465.
3. Kostsov, V.S., Yu.M.Timofeyev, H.Grassl, and H.-D.Hollweg 1993, Possibilities of thermal sounding of the atmosphere under non-LTE conditions, in Optical Methods in Atmospheric Chemistry, Harold I.Schiff, Ulrich Platt, Editors, Proc. SPIE 1715, 550-561.
4. Kostsov, V.S., H.Fischer, Yu.M.Timofeyev, and G.Stiller 1997, *Journal of Geophysical Research*, 102, D25, 30,003-30,015.
5. Kostsov, V.S. 1998, *Advances in Space Research*, 21, 3, 405-408.
6. Lopez-Puertas, M., et al. 1996, Evaluation of non-LTE effects in MIPAS pressure, temperature and volume mixing ratio retrievals (Non-LTE study), ESTEC Purchase Order 151625/1995, Final Report.
7. Ogibalov, V.P., A.A.Kutepov, and G.M.Shved 1998, *Journal of* Atmospheric *and Solar-Terrestrial Physics*, 60, 3, 315-329.
8. Riese M. et al. 1997, Measurements of trace gases by the Cryogenic Infrared Spectrometers and Telescopes for the Atmosphere (CRISTA) experiment, *Adv. Space Res.*, 19, 563-566.
9. Shved, G.M., A.A.Kutepov, and V.P.Ogibalov 1998, *Journal of Atmospheric and Solar-Terrestrial Physics*, 60, 3, 289-314.
10. Timofeyev, Yu.M., V.S.Kostsov, and H.Grassl 1995, *J.Quant. Spectrosc. Radiat. Transfer*, 53, 6, 613-632.

NON-LTE STUDIES FOR THE MIPAS INSTRUMENT

M. López-Puertas[1], M.Á. López-Valverde[1], F.J. Martín-Torres[1], G. Zaragoza[1], A. Dudhia[2], T.v. Clarmann[3], B.J. Kerridge[4], K. Koutoulaki[4], and J.-M. Flaud[5]

[1]Instituto de Astrofísica de Andalucía (CSIC), Granada, Spain
[2]Atmospheric, Oceanic and Planetary Physics, Oxford University, UK
[3]Institut für Meteorologie und Klimaforschung, Forschungszentrum Karlsruhe, Germany
[4]Rutherford Appleton Laboratory, UK
[5]Laboratoire de Photophysique Moleculaire, CNRS, Univ. Paris-Sud, France
e-mail: puertas@iaa.es

ABSTRACT

A summary of the non-local thermodynamic equilibrium (non-LTE) studies carried out for assessing the non-LTE effects in the MIPAS spectra is presented. For that purpose, LTE and non-LTE limb radiance spectra have been computed in the 685-2410 cm^{-1} range with a spectral grid of 0.025 cm^{-1} at tangent heights from 8 to 83 km. These calculations include non-LTE populations of a large number of vibrational levels of the CO_2, CO, O_3, H_2O, CH_4, NO, N_2O, NO_2 and HNO_3 molecules which originate the most prominent atmospheric infrared emissions. The impacts of these effects on the retrieval of pressure, temperature and species abundances from MIPAS spectra are presented. In addition, a number of non-LTE issues that could be addressed with MIPAS data are discussed.

1. INTRODUCTION

MIPAS (Michelson Interferometer for Passive Atmospheric Sounding) is one of the ESA-developed instruments to be launched on board the ENVISAT-1 polar platform. This instrument will measure atmospheric limb emission spectra in the infrared (4.15–14.6 μm) in the 8–150 km altitude range with a spectral resolution of 0.05 cm^{-1} and a sensitivity which varies from 50 $nW/(cm^2\ sr\ cm^{-1})$ at 14 μm to 4.2 $nW/(cm^2\ sr\ cm^{-1})$ at 4 μm. The main objective of MIPAS is to derive the pressure-temperature distribution and the abundances of the minor atmospheric constituents O_3, H_2O, CH_4, N_2O, and HNO_3 (Ref. 1). Global measurements of these parameters will be provided by operating the instrument from space in the emission mode.

The principle of atmospheric sounding by measuring infrared emissions to derive geophysical parameters such as temperature, pressure, and trace species abundances is based on the assumption that the atmospheric compounds emit according to the Planck function at the local kinetic temperature. It is known, however, that many of the vibrational levels of atmospheric constituents responsible for infrared emissions have excitation temperatures which differ from the local kinetic temperature in the stratosphere and mesosphere and hence can affect the limb radiances at those tangent heights and below (Refs. 2–9).

In this paper we briefly describe the work performed to evaluate the potential effects of non-local thermodynamic equilibrium (non-LTE) on the retrievals of pressure, temperature, and of O_3, H_2O, CH_4, N_2O, HNO_3, CO, NO, NO_2, N_2O_5 and $ClONO_2$ abundances in the 10–60 km altitude interval.

Further to the main objective of MIPAS of studying the stratospheric chemistry, the instrument offers an unprecedented opportunity to study the upper atmospheric regions (mesosphere and lower thermosphere). At those altitudes, non-LTE processes are most important and are essential for deriving the energy balance (eg, CO_2, O_3 and NO) and for determining the concentration of tracers such as H_2O, CH_4, and CO. Its high spectral resolution, wide spectral coverage, and high sensitivity makes this instrument ideal for pursuing those studies. Thus, in this paper we also describe the non-LTE aspects of the upper atmosphere that could be tackled with MIPAS measurements.

2. NON-LTE EFFECTS IN OPERATIONAL RETRIEVALS

The goal of these studies was to evaluate the effects of the breakdown of local thermodynamic equilibrium (LTE) in the atmosphere with respect to the retrieval of pressure, temperature, and the volume mixing ratios (VMR's) of O_3, H_2O, CH_4, N_2O, HNO_3, CO, NO, NO_2, N_2O_5 and $ClONO_2$ in the 10–60 km altitude interval (the operational altitude range). Once evaluated, it was also aimed at finding the best way of treating non-LTE in the operational retrieval scheme. From this point of view, the following schemes were considered:

a) To avoid non-LTE by a proper selection of small spectral regions (microwindows, see Ref. 11). Given that the handling of non-LTE would severely increase the retrieval computer time, this option was the most desirable. The high spectral resolution (allowing for selecting individual rotation-vibration lines) and the wide spectral coverage of MIPAS (covering various vibrational bands of the species at work) make this selection plausible.

b) To evaluate the non-LTE effects if they are significant (either very large or small but need to be corrected for). Two ways were considered: 1) to use pre-calculated non-LTE populations (eg, vibrational temperatures) and 2) to use a direct computation of the vibrational temperatures

in the retrieval scheme in conjunction with the forward radiance model. The latter option is more adequate if the non-LTE model is not very time consuming (eg, the cases when radiative transfer is not important).

c) Finally, we evaluate if, simultaneously with the VMR of the species at work, information on the non-LTE population of the emitting states was retrievable, eg, retrievals of vibrational temperatures. Examples of these are the works presented in Refs. 12 and 13.

To evaluate the non-LTE effects we selected a set of reference atmospheres for temperature, species abundances, solar illumination and tropospheric conditions that covers both, typical and extreme atmospheric conditions for which the potential non-LTE effects vary from weakest to moderate to strongest. A set of four reference atmospheres was established corresponding to mid-latitude day- and night-time conditions, and typical polar winter and polar summer cases (see Ref. 14).

The method followed to evaluate the non-LTE effects consists of the following steps. First, LTE and non-LTE MIPAS synthetic spectra were generated. The computation of the non-LTE ones requires, in turn, the calculation of new spectroscopic data (mostly of hot bands originating in high energetic levels), and the non-LTE populations of all the emitting levels of all molecules known to be (or likely to be) in non-LTE in such conditions. From those spectra retrievals were performed including all known sources of errors. For those retrievals, Jacobians from the calculated synthetic spectra were precomputed. The differences between the quantities retrieved from the non-LTE and from the LTE spectra were assumed as the errors of non-LTE, ie, the errors we would commit if non-LTE were neglected.

2.1 Spectroscopic Data

In the analysis of atmospheric spectra and the retrieval of atmospheric parameters such as concentration profiles, the spectroscopic line parameters are usually taken from atmospheric spectral databases such as HITRAN (eg, Ref. 16). However, the spectroscopic data in these databases are given with an intensity cut-off (different for each molecule) corresponding to a 'minimum' absorption observable through a 'maximum' path length in an atmosphere under LTE conditions. Thus, hot bands involving highly excited vibrational states are not available. These weak isotopic and hot bands, which do not emit a significant radiance in the atmosphere under LTE conditions, might contribute with radiances similar to those from fundamental bands when the high energetic upper levels of these transitions are highly populated under non-LTE conditions. Therefore, line parameters for many of these hot bands were needed for computing the non-LTE spectra. The spectroscopic linelist used in these non-LTE studies was extended from HITRAN 96 with 199 bands of the ozone molecule involved in 17 polyads, and with 30 bands involved in 7 polyads of NO_2. These calculations represent a large increase in the number of spectral lines since the final dataset was approximately twice as large as the original HITRAN 96 data.

2.2 Non-LTE Vibrational Populations

Already existing non-LTE models for some species and other recently developed, eg, for N_2O, CH_4, NO_2, and HNO_3, have been used to obtain the non-LTE populations of the vibrational levels originating the most important atmospheric infrared emissions. We briefly list below the species and levels included. A detailed description of the non-LTE models used to calculate them can be found in Ref. 14.

For CO_2 we have included 47 vibrational levels, including those emitting the strongest emissions at 15, 10, and 4.3 μm. For CO only the major CO(1-0) band near 4.6 μm was included. For O_3, up to 245 levels were introduced, including those emitting at 14.6 μm, many hot bands near 10 μm, and the combination bands around 4.8 μm. For H_2O, 7 vibrational levels emitting at 6.3 and 4.7 μm were introduced. The levels emitting the ν_2 and ν_4 fundamental bands at 7.6 and 6.5 μm of the two major CH_4 isotopes were incorporated. For HNO_3, 8 'equivalent' states, which originate the 5.9, 7.5, 11, and 22 μm bands were also introduced. For the NO_2 molecule, the highest 7 ($00\nu_3$) levels, originating the ν_3 fundamental and 6 hot bands emitting in the 6.2–7.0 μm interval, were included. For the N_2O molecule, 16 vibrational levels originating the 8.6, 7.8, 4.5, 4.0, 3.6, and 3.0 μm bands were incorporated. Finally, the NO(1-0) transitions near 5.3 μm were also introduced.

The non-LTE populations of these levels were calculated for the four reference atmospheres mentioned above, including day- and night-time mid-latitude conditions and polar winter and summer conditions. Those are the situations for which we expect non-LTE populations to be fro the smallest, to moderate and to the largest, In addition, we also included maximum and minimum non-LTE populations based on the uncertainties in the model's input parameters. A detailed description of the models and the results obtained can be found in Ref. 14.

2.3 LTE and Non-LTE Spectra

In order to evaluate the non-LTE effects on the retrievals of the atmospheric parameters, LTE and non-LTE limb radiance spectra as measured by MIPAS were computed by using the Reference Forward Model (RFM) radiative line-by-line code (Ref. 17). Spectra were generated at a spectral resolution of 0.025 cm^{-1} (internal resolution of $5\times10^{-4}cm^{-1}$) for the 5 MIPAS filters: A (685-970), AB (1020-1170), B (1215-1500), C (1570-1750), and D (1820-2410) cm^{-1}. They were computed for each of the 4 reference atmospheres (mid-latitude day and nighttime, polar winter, and polar summer). Tangent heights from 8 km up to 83 at 3 km steps were covered, except for the NO(1-0) bands for which they were extended up to 200 km. The spectra were calculated for LTE as well as for non-LTE conditions, covering the nominal and extreme (maximum and minimum) non-LTE conditions with the corresponding vibrational temperatures described in the previous section.

The target species (eg, those which are intended to be retrieved) were the following 11 gases: CO_2, O_3, H_2O, CH_4, N_2O, HNO_3, NO_2, CO, NO, N_2O_5, and $ClONO_2$. Apart from those, other 21 gases were also incorporated

in the limb radiance calculations as contaminants: SO_2, NH_3, HNO_4, ClO, HOCl, HCN, H_2O_2, C_2H_2, C_2H_6, OCS, CF_4, CCl_4, COF_2, SF_6, CCl_3F, CFC-11, CFC-12, CFC-14, CFC-22, CCl_2F_2, CHF_2Cl.

The spectroscopic data included are the HITRAN 96 linelist (Ref. 16), in addition to the many hot bands of O_3, and NO_2 described in Section 2.1. Molecular cross-section data (as opposite to line data) were used for the following species: CCl_4, $ClONO_2$, CFC-11, CFC-12, CFC-14, CFC-22, HNO_4, and N_2O_5.

To simulate the instrument line response and apodization, the high-resolution spectra calculated at 5×10^{-4} cm^{-1} were convolved with a function representing the Norton-Beer 'strong' apodization.

Three different field-of-view convolutions were used to approximate the nominal MIPAS field-of-view response function (a trapezium of 4 km base and 2.8 km altitude) for all spectral and altitude regions. In order of decreasing accuracy these convolutions correspond to 12-, 5-, and 3-points sampling of the trapezium.

The spectra were computed treating all lines with a Voigt line shape except for the CO_2 ones in filter A (685-970 cm^{-1}) for which a sub-Lorentzian behaviour in the line wings was assumed by including a suggested χ-factor (see Ref. 14).

The vibrational temperatures for all the species and levels mentioned in the previous section were introduced in the calculation.

In addition to the spectra, the Jacobians, J_{ij}, defined as $\partial R_i/\partial x_j$ where R_i is the radiance at some spectral grid-point/tangent, and x_j is a parameter which represents a retrieved quantity, were calculated. Jacobians were calculated for all gases abundances considered, temperature, continuum and spectroscopic uncertainties. They were used to map the resulting error in radiance to the corresponding error in the retrieved parameters. Details on the calculations of the Jacobians can be found in Ref. 14.

2.4 Error Analysis

These simulated LTE and non-LTE spectra, together with their corresponding Jacobians, were used to select narrow spectral regions (microwindows) for retrieving the pressure-temperature and VMR's. The selection was performed in such a way that the total error budget induced by the different sources, including the non-LTE errors, was minimized. The sources of error included are: measurement noise, gain calibration error, pointing uncertainties, uncertain abundances of interfering species, spectroscopic data uncertainties, variability of isotopic fractioning of species, temperature uncertainty (for the retrieval of the VMR's), and errors induced by non-LTE effects. The latter were evaluated from the difference of retrieving the p-T and VMR's from the LTE spectra and from the non-LTE ones.

The inclusion of non-LTE modelling into the operational retrieval scheme would be very time consuming. So the major idea was to find out microwindows for the retrieval of p-T and VMR's in which the non-LTE effects are negligible in comparison with the other sources of errors. So, a procedure was followed to explore among all possible microwindows until we found those which minimized the

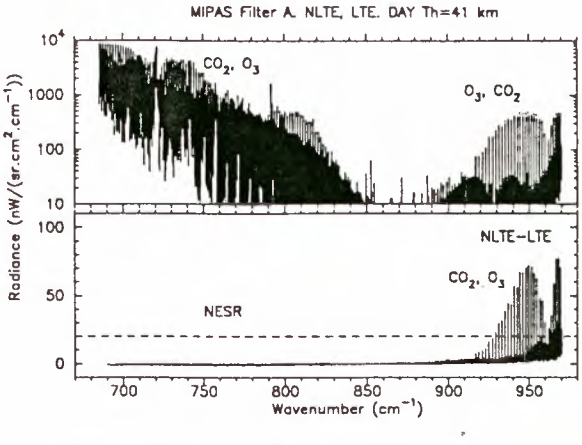

Figure 1: MIPAS synthetic limb radiances for filter A at a tangent height of 41 km for the daytime mid-latitude atmosphere. Top panel: Non-LTE (dotted) and LTE (solid) radiances. Lower panel: Non-LTE–LTE radiance difference; the noise equivalent spectra radiance (NESR) of MIPAS is also plotted for comparison.

total error. The calculation of the total error, including the combination of random and systematic errors, is described in detail in Ref. 14.

The selection of the microwindows was done on the basis that a 'Global Fit' (Ref. 15) operational retrieval scheme will be used and that, for tangent altitudes below 30 km, the continuum will be jointly retrieved with pressure, temperature or the VMR of the species at work.

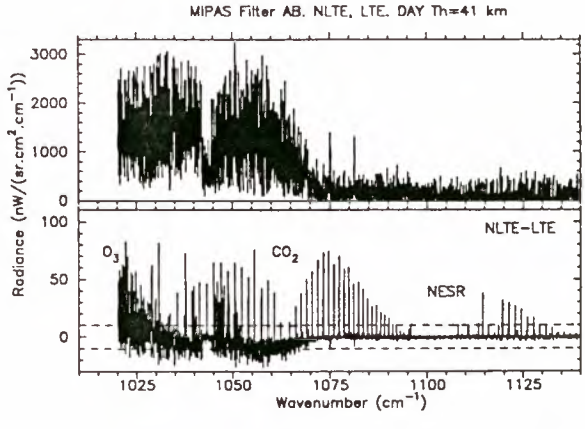

Figure 2: As Fig. 1 but for filter AB at a tangent height of 41 km.

2.5 Results

Our calculations showed that the high spectral resolution and wide spectral coverage of MIPAS allows one to select a set of microwindows free from non-LTE effects for the most important gases (p-T, O_3, H_2O, CH_4, N_2O, HNO_3, and NO_2) in the altitude range of the operational retrieval (10–60 km). As an example, Fig. 1 (lower panel) shows that the effects of non-LTE are negligible in the

15 μm region (around 700 cm^{-1}) where strong bands of CO_2 and O_3 are located and where most microwindows for the retrieval of temperature and O_3 VMR have been selected. In contrast, the CO_2 and O_3 bands near 10 μm (see the shorter wavelength part of Fig. 1, and Fig. 2) clearly show very large non-LTE effects, and hence were avoided for operational retrievals.

For the CO and NO molecules, however, which have only one strong vibrational transition in the mid-infrared, non-LTE effects are important in the whole operational altitude range, and hence, require the inclusion of non-LTE modelling into the retrieval scheme. Direct calculation of their non-LTE populations is the most accurate approach, although in the case of CO this might be difficult due to the dependence of the CO(1) excitation temperature on the CO VMR itself (Ref. 18).

For the remaining 'target' gases expected to be retrieved from MIPAS spectra, N_2O_5 and $ClONO_2$, non-LTE populations were not included. These are not expected to be important in the stratosphere. We considered, however, the non-LTE effects due to possible contamination from non-LTE emissions of the 9 species described in Section 2.2, and found that a sufficiently large number of microwindows 'free' from non-LTE can be selected for their retrieval.

3. FUTURE NON-LTE STUDIES

The MIPAS instrument will expectedly offer highly resolved limb emission spectra with a full coverage of the mid-IR, high sensitivity and a full global and seasonal coverage. These characteristics make it a very useful instrument to study the non-LTE processes taking place in the atmosphere. On one hand, its high spectral resolution will allow us to distinguish between the contributions of different bands, both from different molecules and also between the fundamental, isotopic and hot bands of some molecules, shuch as CO_2. The fact that MIPAS covers a wide spectral range in the infrared is also very useful since it allows to retrieve the kinetic temperature and, in some cases (eg, CO_2 and O_3), the abundance of the species at work, from one part of the spectrum (usually at longer wavelengths, where non-LTE effects are smaller) and to analyse the non-LTE emissions from the other (shorter-wavelengths) part.

In addition, the possibility of taking near-collocated (both in space and time) measurements with 'Non-LTE–free' instruments (like GOMOS and SCIAMACHY both in the ENVISAT platform) are very useful for studying non-LTE since they will provide independent measurements of the VMR's of the species at work, which will be crucial to discriminate between the species abundances and the excitation temperatures of the emitting states. We discuss in the next paragraphs some potential non-LTE studies that could be carried out with MIPAS data.

The kinetic temperature, T_k, is usually retrieved from the CO_2 15 μm spectral region. Fig. 3 shows a good signal-to-noise ratio (S/N) in MIPAS filter A up to 83 km. Hence it would be possible to retrieve T_k from his filter up to around the mesopause (90 km). The CO_2 VMR starts being not well mixed above about 80 km. It is expected, however, that it can be retrieved from filter D spectra (see below).

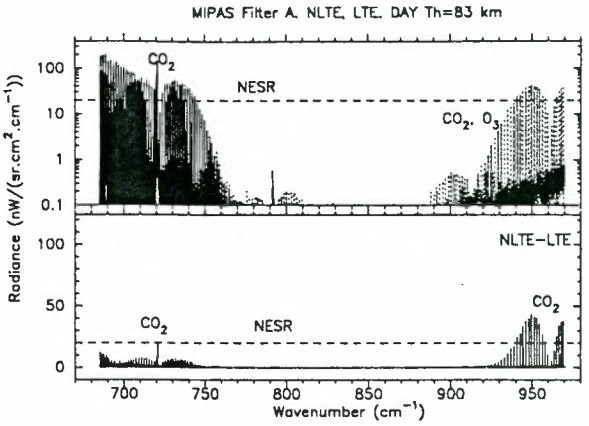

Figure 3: As Fig. 1 but for a tangent height of 83 km.

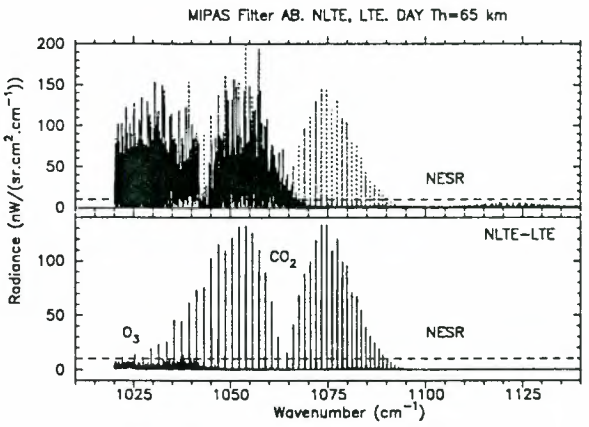

Figure 4: As Fig. 1 but for filter AB at a tangent height of 65 km.

It is also interesting to note that the CO_2 10 μm laser bands in filters A and AB (Figs. 3 and 5) have a high S/N up to and above 83 km. These bands are both originated by the $CO_2(001)$ level which also originates the 4.3 μm fundamental band. These emissions can be used to study the excitation of $CO_2(001)$ from $O(^1D)$ through $N_2(1)$ in the stratosphere and mesosphere (see, eg, Ref. 8). $O(^1D)$ abundances can be estimated by using chemical transport models and the O_3 abundances measured by MIPAS. In addition, these emissions, which are rather optically thin in the stratosphere and mesosphere, can be used in conjunction with the CO_2 emissions in filter D (Fig. 12) (many of them rather optically thick) to derive the CO_2 VMR and to understand the vibrational-vibrational exchange of ν_3 quanta between the $CO_2(\nu_1,\nu_2,\nu_3)$ states and $N_2(1)$.

The O_3 non-LTE emissions around 10 μm are expected to be greatly improved with the analysis of MIPAS spectra, particularly in filters A and AB. A large fraction of the fundamental and hot bands could be resolved by MIPAS. As shown in Figs. 4 and 5, the non-LTE effects could be

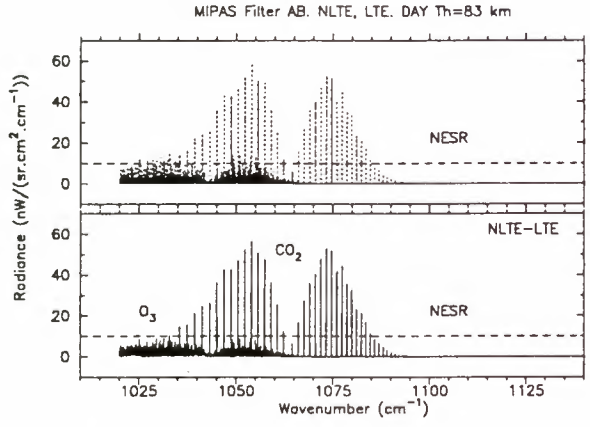

Figure 5: As Fig. 1 but for filter AB at a tangent height of 83 km.

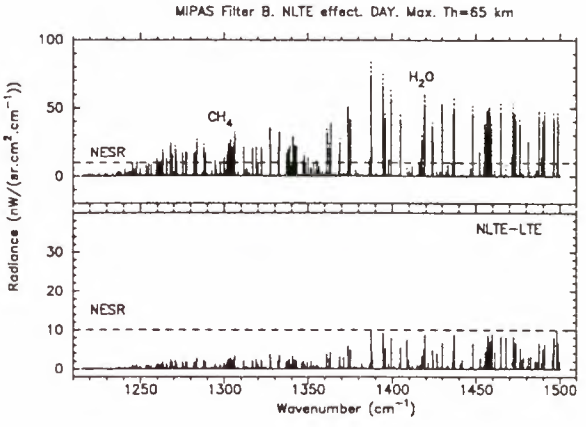

Figure 7: As Fig. 1 but for filter B at a tangent height of 65 km.

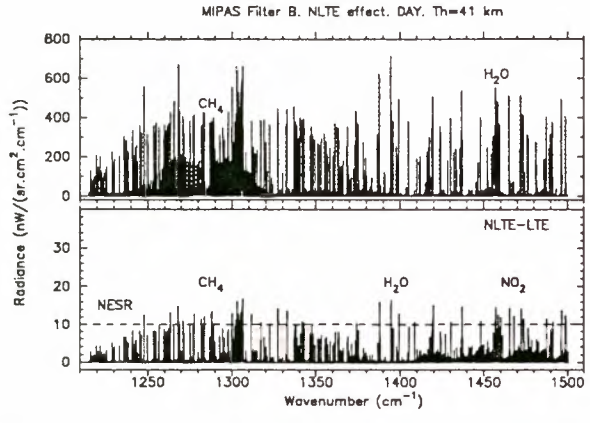

Figure 6: As Fig. 1 but for filter B at a tangent height of 41 km.

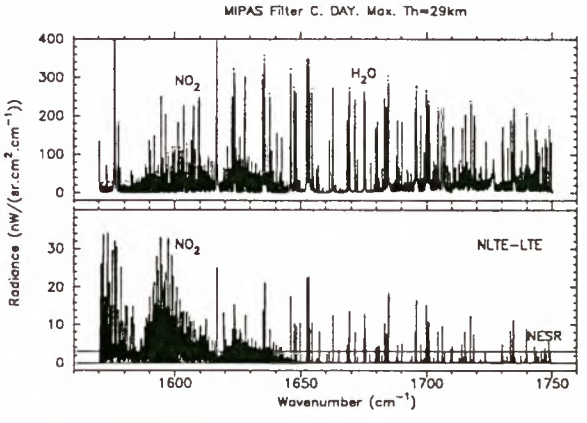

Figure 8: As Fig. 1 but for filter C at a tangent height of 29 km. Note than maximum expected non-LTE T_v's were included.

detected up to the mesopause by integrating over the band's interval. In addition, T_k and O_3 VMR (the latter at least up to 60 km) could also be retrieved from the spectra in filter A. The collisional relaxation as well as the nascent distribution of the O_3 vibrational states are expected to be improved from MIPAS data (Ref. 13 discusses these possibilities in detail).

Filter B is mostly dominated by CH_4 and H_2O bands, as well as by some possible contribution of NO_2 ν_3 hot bands in the shorter-wavelength region of this filter. Figs. 6 and 7 show synthetic spectra in this filter for stratospheric and mesospheric tangent heights, respectively. In the stratosphere, the CH_4 and H_2O non-LTE effects are very small. In the shorter-wavelength a significant non-LTE contribution is appreciated due to NO_2 ν_3 hot bands. These predicted non-LTE enhancements might be measured by MIPAS. In the mesosphere, the non-LTE effects of CH_4 are predicted to be small. So far no experimental evidence of non-LTE in the CH_4 bands has been reported. MIPAS could confirm these predictions. On the other hand, the non-LTE contribution in the water vapour lines are at the noise limit. However, both the CH_4 and H_2O signals are well above the noise up to 65 km. Hence, CH_4 and H_2O VMR's are likely to be measured in the mesosphere by MIPAS and hence allow to study the mesospheric chemistry and dynamics.

Filter C is dominated by NO_2 ν_3 bands in the lower atmosphere (longer-wavelength part) and by H_2O lines. Fig. 8 shows spectra and the non-LTE contribution for a lower-stratospheric tangent height in which the maximum expected non-LTE populations of the $NO_2(\nu_3)$ levels were included. MIPAS will clearly be able to detect such large non-LTE contribution in the fundamental and first hot bands of $NO_2(\nu_3)$. In the mesosphere, the H_2O lines have a good S/N up to 74 km (see Fig. 9) and non-LTE can be well measured in both the fundamental and first hot bands of $H_2O(\nu_2)$.

Filter D, in the shorter-wavelength region, is the richer part of the MIPAS spectra in non-LTE effects. Figs. 10 and 11 show synthetic spectra for stratospheric and upper mesospheric tangent heights for mid-latitudes conditions

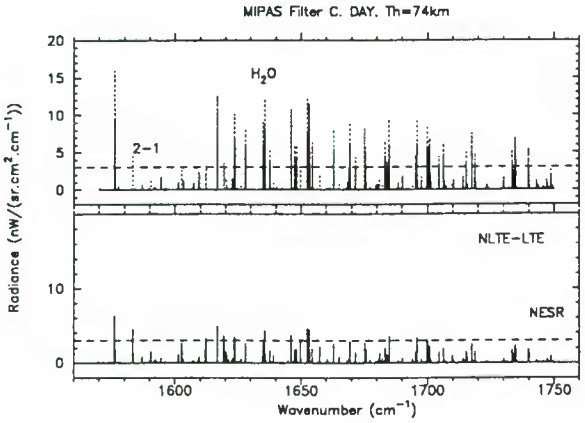

Figure 9: As Fig. 1 but for filter C at a tangent height of 74 km.

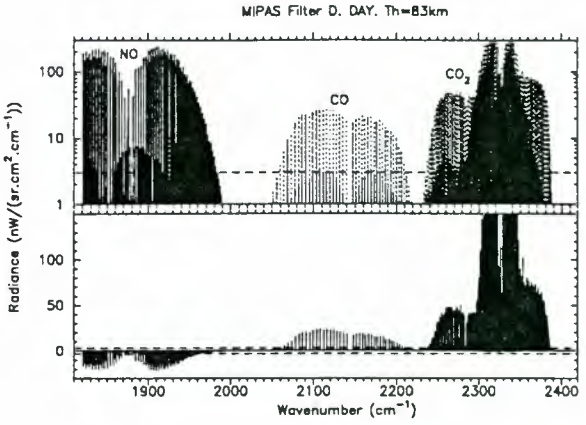

Figure 11: As Fig. 1 but for filter D at a tangent height of 83 km.

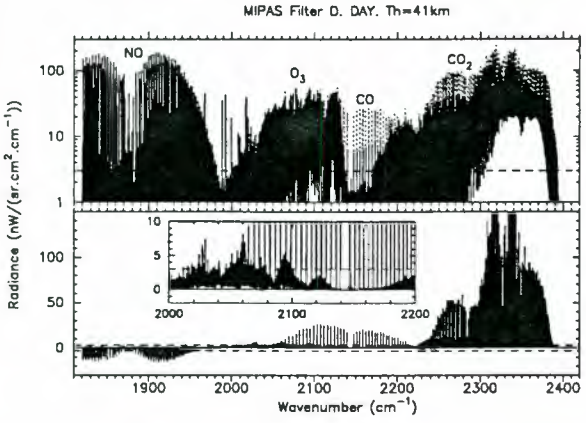

Figure 10: As Fig. 1 but for filter D at a tangent height of 41 km. The inset in the lower panel shows an extended region of the non-LTE–LTE radiance differences.

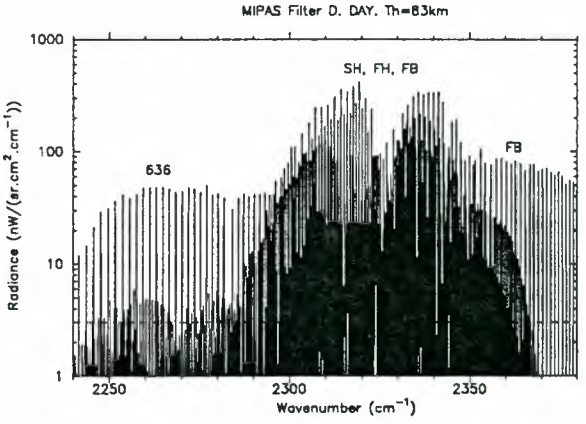

Figure 12: Non-LTE radiances for filter D at daytime conditions and a tangent height of 83 km in the CO_2 spectral region. Note that most of the lines are spectrally resolved. The symbols 636, FB, FH and SH denotes the CO_2 4.3 μm 636 isotopic, fundamental, first hot, and second hot bands, respectively.

at daytime. Focussing in the stratosphere, we see first the prominent bands of NO(1-0). Non-LTE effects in these bands are negative for retrievals of NO VMR because most of the radiation seen even at stratospheric tangent heights comes from the upper thermosphere (above 120 km), where the vibrational excitation of NO(1) is much smaller than the very high thermospheric temperature. A detailed study of the possibilities of retrieving NO VMR and non-LTE parameters related to the NO(1) levels is presented in a companion paper (Ref. 12).

We also observe the large contribution of the O_3 combinational bands near 4.8 μm. Their non-LTE contributions is predicted to be well above the noise of the instrument (see inset in lower panel of Fig. 10). This additional piece of information, in addition to the measurements in the 10 μm region, would help in understanding the non-LTE populations of the $O_3(\nu_1,\nu_2,\nu_3)$ levels. The contribution of carbon monoxide is also seen very clearly, being most of it in non-LTE because CO(1) is in non-LTE in the mesosphere and the large mesospheric gradient of CO VMR makes the mesospheric contribution very important at stratospheric tangent heights. Also is clearly seen the large contributions of the fundamental, isotopic, and hot bands of CO_2, with the large non-LTE contributions even at stratospheric tangent altitudes. A simulation for a 29-km tangent height shows that all these non-LTE contributions are very similar, hence being important in nearly the whole altitude coverage in this filter.

Fig. 11 shows a spectrum at 83 km. At this altitude, the signal from NO, CO and CO_2 bands is well above the noise of the instrument. Particularly important is the CO contribution for which it is expected to be retrieved up to the lower thermosphere, and hence contribute to the understanding of the mesospheric dynamics, eg, the meridional circulation and the mesosphere-stratosphere exchange particularly at the polar winter. CO_2 contributions are very strong, too. The high spectral resolution

of MIPAS will allow us to distinguish between the contributions of the different CO_2 bands near 4.3 μm, eg, the fundamental, isotopic, and first hot bands (see Fig. 12). This will allow us to understand better the ν_3 vibrational exchange between the upper states of these bands and, in consequence, be able to retrieve the CO_2 VMR with a high accuracy. Simulations for high altitudes with the CO_2 VMR retrieved from ISAMS measurements (Ref. 10) show that MIPAS spectra are expected to have a good S/N in the CO_2 4.3 μm bands up to 120–130 km. From these high-altitude spectrally resolved bands, the kinetic temperature can also be retrieved. Hence, together with the retrieved CO_2 VMR and a CO_2 15 μm non-LTE model, it will be possible to derive the radiative cooling of the upper mesosphere.

Although not included in these simulations, MIPAS filter D is also sensitive to the emission from OH(v) vibrationally excited in the 4.2-4.5 μm interval at nighttime. MIPAS has a sensitivity similar to the ISAMS instrument on UARS, which has been able to detect such emissions (Ref. 19). Finally, also MIPAS might be able to measure the NO^+ emission around 4.3 μm which seems to have been detected by ISAMS (Ref. 10).

4. CONCLUSIONS

Non-LTE studies have been carried out to evaluate the potential impacts of our current knowledge of non-LTE atmospheric emissions in the operational retrievals of pressure, temperature, and VMR's of O_3, H_2O, CH_4, N_2O, HNO_3, and NO_2 from ENVISAT/MIPAS spectra. Our results show that the high spectral resolution and wide spectral coverage of MIPAS allows us to select microwindows (narrow spectral regions) 'free' from non-LTE effects for the most important gases (CO_2 (p-T,) O_3, H_2O, CH_4, N_2O, HNO_3, and NO_2) in the altitude range of the operational retrieval (10–60 km). The simulations carried out for the CO and NO infrared emissions show that non-LTE effects are important in the whole altitude of the operational retrieval and their retrievals require the inclusion of non-LTE modelling into the retrieval scheme.

For the N_2O_5 and $ClNO_2$ gases, non-LTE populations were not included. These are not expected to be important in the stratosphere. The non-LTE effects due to possible contamination from non-LTE emissions of the most abundant atmospheric species were found to be negligible.

The high spectral resolution, wide spectral coverage, high sensitivity and full global and seasonal coverages makes MIPAS an ideal instrument for studying non-LTE processes in the atmosphere. We have performed simulations for all the MIPAS filters and shown the large potential of this instrument to study non-LTE atmospheric emissions. Most of the non-LTE atmospheric emissions will be measured by MIPAS with a high spectral resolution, and a large step forward in understanding these processes is expected to be achieved from MIPAS measurements. In addition, the understanding of these processes will allow MIPAS to measure the most important constituents of the upper atmosphere, eg. CO_2, O_3, H_2O, CH_4, and NO, and hence to contribute to the understanding of the energy balance, dynamics, and chemistry of the upper atmosphere.

5. ACKNOWLEDGEMENTS

Main parts of this work have been performed under ESA contracts No. P.O. 151625/1995 and 12054/96/NL/CN. The IAA team was also supported by Spanish CICYT under contracts ESP96-0623 and ESP97-1798.

REFERENCES

1. Endemann, M. & H. Fischer 1993, Envisat's high-resolution limb sounder: MIPAS. *ESA bulletin*, 76, 47-52.

2. Kerridge, B. J. & E. E. Remsberg 1989, Evidence from the limb infrared Monitor of the Stratosphere for non-local thermodynamics equilibrium in the ν_2 mode of mesospheric water vapour and the ν_3 mode of stratospheric nitrogen dioxide, *J. Geophys. Res.*, 94, 16323-16342.

3. López-Puertas, M. & F.W. Taylor 1989, Carbon dioxide 4.3 μm emission in the earth's atmosphere: A comparison between Nimbus 7 SAMS measurements and non-LTE radiative transfer calculations, *J. Geophys. Res.*, 94, 13045-13068.

4. Solomon, S. & al. 1986, Evidence for nonlocal thermodynamic equilibrium in the ν_3 mode of mesospheric ozone. *J. Geophys. Res.*, 91, 9865-9876.

5. López-Puertas, M. & al. 1992, Analysis of the upper atmosphere $CO_2(\nu_2)$ vibrational temperatures retrieved from ATMOS/Spacelab 3 observations, *J. Geophys. Res.*, 97, 20469-20478.

6. López-Puertas, M. & al. 1998, Non local thermodynamic equilibrium (LTE) atmospheric limb emission at 4.6 μm 1. An update of the CO_2 non-LTE radiative transfer model, *J. Geophys. Res.*,103, 8499-8513.

7. López-Valverde, M. A. & al. 1996, Validation of measurements of carbon monoxide from the improved stratospheric and mesospheric sounder, *J. Geophys. Res.*, 101, 9929-9955.

8. Edwards, D. P. & al. 1996, Non-local thermodynamic equilibrium limb radiance near 10 μm as measured by CLAES, *J. Geophys. Res*, 101, 26577-26588.

9. Nebel, H. & al. 1994, CO_2 non-local thermodynamic equilibrium radiative excitation and infrared dayglow at 4.3 μm: Application to spectral infrared rocket experiment data, *J. Geophys. Res.*, 99, 10409-10419.

10. López-Puertas, M. & al. 1998, Non local thermodynamic equilibrium (LTE) atmospheric limb emission at 4.6 μm 2. An analysis of the daytime wide-band radiances as measured by UARS improved stratospheric and mesospheric sounder, *J. Geophys. Res.*,103, 8515-8530.

11. Echle, G. & al. 1999, Spectral microwindows for MIPAS-ENVISAT data analysis. In *Proc. European Symposium on Atmospheric Measurements from*

Space, ESAMS'99, 18-22 Jan 1999, Noordwijk. European Space Agency, ESTEC, Noordwijk, The Netherlands.

12. Funke, B. & al. 1999, Retrievability of NO volume mixing ratio and non-LTE parameter from stratospheric midlatitude daytime MIPAS-ENVISAT limb spectra at 5.3 μm.In *Proc. European Symposium on Atmospheric Measurements from Space, ESAMS'99, 18-22 Jan 1999, Noordwijk*. European Space Agency, ESTEC, Noordwijk, The Netherlands.
13. Martín-Torres, F.J. & al. 1999, Retrievability of O_3 concentration profiles and critical parameters in non-LTE models from MIPAS/ENVISAT limb spectra. In *Proc. European Symposium on Atmospheric Measurements from Space, ESAMS'99, 18-22 Jan 1999, Noordwijk*. European Space Agency, ESTEC, Noordwijk, The Netherlands.
14. Clarmann, T. v. & al. 1998, Study on the simulation of atmospheric infrared spectra. Technical report, European Space Agency. Final Report of ESA Contract 12054/96/NL/CN.
15. Carlotti, M. 1988, Global Fit approach to the analysis of limb-scanning atmospheric measurements. *Appl. Opt.*, 27, 3250-3254.
16. Rothman, L.S. & al. 1998, The HITRAN molecular spectroscopic database and HAWKS (HITRAN Atmospheric Workstation) 1996 Edition, *J. Quant. Spectrosc. Radiat. Transfer*, 60, 665-710.
17. ESTEC, 1997, Reference Forward Model-Software User's Manual (SUM), *PO-MA-OXF-GS-0003*, ESTEC, Noordwijk, The Netherlands.
18. López-Puertas, M. & al. 1993, Non-local-thermodynamic-equilibrium populations of the first vibrational excited state of CO in the middle atmosphere, *J. Geophys. Res.*, 98, 8933-8947.
19. Zaragoza, G. & al. 1998, The Detection of the Hydroxyl Airglow Layer in the Mesosphere by ISAMS/UARS, *Geophys. Res. Lett.*, 25, 2417-2420.

MICROWINDOW SELECTION FOR MIPAS USING INFORMATION CONTENT

Victoria L. Bennett, Anu Dudhia, Clive D. Rodgers

Atmospheric, Oceanic and Planetary Physics,
University of Oxford, UK
e-mail: vbennett@atm.ox.ac.uk, dudhia@atm.ox.ac.uk, rodgers@atm.ox.ac.uk

ABSTRACT

Measurements from MIPAS (Michelson Interferometer for Passive Atmospheric Sounding) contain a large amount of information - up to 10^6 spectral points are obtained from each limb scan. To use these data efficiently we need to select a subset of the measurements which are most useful in the retrieval of atmospheric profiles. The use of 'microwindows', sections of spectrum containing a number of adjacent points, increases the efficiency of forward model calculations. An objective scheme was developed to select microwindows using the Shannon information content as a figure of merit. The Shannon information content represents the reduction in retrieval error due to the inclusion of a measurement, using the full error covariance of the retrieval. The use of the full covariance matrix allows selection of microwindows which are optimal both in spectral and in altitude range, and takes correlations between levels into account. Sources of retrieval error (random and systematic, e.g. forward model errors) were considered and measurements were selected sequentially to build up an optimal list of microwindows. Initial results compare favourably with current MIPAS microwindow sets. Analysis of information content can also be used to select a subset of microwindows in an optimal sequence from an existing microwindow list.

1. INTRODUCTION

High-resolution Fourier Transform Spectrometers such as MIPAS, the Michelson Interferometer for Passive Atmospheric Sounding, use a huge number of channels and obtain many atmospheric spectra: a typical limb scan measures 16 spectra in 75 seconds, each containing 60,000 spectral points. The spectra cover the mid-infrared region (685-2410 cm^{-1}) with $\sim$0.035 cm^{-1} resolution (unapodised) at 0.025 cm^{-1} spacing (Ref. 4). In order to use these data efficiently it is usual to select sections of spectrum, 'microwindows', containing a limited number of spectral points, where each microwindow targets an atmospheric parameter to be retrieved. The width of a microwindow is usually limited by the presence of spectral lines of contaminants or regions contributing no significant information to the retrieval. The use of microwindows in retrievals has a number of advantages over the use of isolated spectral points, including more efficient forward model calculations and continuum and offset fitting.

Traditionally, microwindows have been selected on an *ad hoc* basis but work has been done to select microwindows in more objective and reproducible manners (e.g. Refs. 2, 7). Rodgers, 1996 [7] uses information content to optimise the selection of channels for retrieval, but only accounts for random errors. The approach described by von Clarmann and Echle [2] constructs microwindows by minimising the retrieval error, taking systematic errors into account, but assuming a single-layer retrieval. In this paper, a method is described which uses a multi-layer approach to microwindow selection. A multi-layer method allows microwindows to be defined which are optimal both in frequency and in altitude range, and allows for inter-level correlations to be included in the analysis. Full covariance matrices are intercompared to fully represent the multi-layer retrieval, and the Shannon information content is used as a figure of merit to perform the selection. Using this method microwindows can be generated by analysing and evaluating the information content of individual spectral points and combining useful points optimally.

In addition, it is possible to select microwindows from an existing list in the most useful order: the order which improves the information content, or reduces the total retrieval error most efficiently. This has a potential advantage in operational systems where the microwindow list can be arbitrarily truncated or extended according to available processing time.

Some theory of the retrieval problem and information content as a selection criterion will be presented, followed by a test case where microwindows are generated for a MIPAS O_3 retrieval. The results are compared to some existing MIPAS microwindow lists.

2. THEORY

2.1 DEFINITIONS

The retrieval aims to obtain a profile $\hat{\mathbf{x}}$ with n elements from a set of measurements $\mathbf{y}$, where the state and measurements are related by the weighting function matrix $\mathbf{K}$ as $\mathbf{y} = \mathbf{K}\mathbf{x}$. As individual measurements y are included in a retrieval at stage i, the estimate of the retrieved parameter and the retrieval covariance are sequentially updated from their previous values at stage $i-1$ as follows. Using the contribution function $\mathbf{d}$:

$$\mathbf{d}_i = \hat{\mathbf{S}}_{i-1}\mathbf{k}_i^T(\sigma^2 + \mathbf{k}_i\hat{\mathbf{S}}_{i-1}\mathbf{k}_i^T)^{-1} \quad (1)$$

where $\mathbf{k}$ is the weighting function, $\hat{\mathbf{S}}$ the (random) error covariance, and σ^2 the measurement error. It can be shown (Ref. 6) that

$$\hat{\mathbf{x}}_i = \mathbf{d}_i y_i + (\mathbf{I}_n - \mathbf{d}_i\mathbf{k}_i)\hat{\mathbf{x}}_{i-1} \quad (2)$$

i.e. the retrieval combines the measurement and the state at the prior stage $i-1$ weighted by the measurement noise and the (random) error covariance $\hat{\mathbf{S}}_{i-1}$. The covariance matrix is then updated as:

$$\hat{\mathbf{S}}_i = (\mathbf{I}_n - \mathbf{d}_i\mathbf{k}_i)\hat{\mathbf{S}}_{i-1} \quad (3)$$

In optimal estimation (Ref. 6) a measurement vector $\mathbf{y}$ is combined with an *a priori* state vector $\mathbf{x}_a$ and *a priori* error covariance $\mathbf{S}_a$ to provide a new estimate of the state $\hat{\mathbf{x}}$. The 'sequential update' contribution function given here is equivalent to that used in optimal estimation. However, the retrieval by sequential update is optimal only if errors are uncorrelated between channels.

2.2 INFORMATION CONTENT

The information gained by including a measurement can be expressed by its 'information content'. The information content expresses the improvement in knowledge, or the reduction in uncertainty. Shannon, 1949 (Ref. 8) uses the logarithm to the base two of the ratio of the prior and posterior uncertainties. It can be shown that:

$$I = \frac{1}{2}\log_2|\hat{\mathbf{S}}_{i-1}| - \frac{1}{2}\log_2|\hat{\mathbf{S}}_i| \quad (4)$$

where I is the information content expressed in bits (Refs. 7,8). The use of the full covariance matrix in this way allows off-diagonal elements in the covariance matrices to be considered. Using equation 3 the covariance and hence the information content can be updated sequentially, as points are added to the microwindows for use in the retrieval. If there are no correlations between measurement errors, the information content can be computed efficiently as in Ref. 7.

2.3 SYSTEMATIC ERRORS

An optimal retrieval should account fully for both uncorrelated and correlated errors. The latter will include systematic forward model errors, such as contributions from absorbers that are not retrieved, spectroscopic errors, etc. However for efficiency the MIPAS retrieval considers only errors which are uncorrelated between measurements, and is therefore not optimal. The sequential update approach described above is also efficient only for uncorrelated errors for the same reason. In selecting microwindows the effect of ignoring correlated errors on the information content must therefore be considered, so that the process can avoid using measurements which are degraded by systematic errors. On evaluating the change in information content due to a non-optimal update, we find that it may be positive or negative. A negative change clearly indicates a channel that should not be used in the retrieval, and so is likely to determine the boundary of a microwindow.

The effect of systematic errors in the sequential update can be tracked as follows. Systematic errors in the forward model act as errors in radiance but are also carried through as errors in the prior state. An example: if water vapour is unknown in an ozone retrieval at stage i, there is a contribution δy_i due to unknown water vapour radiance but also a contribution $\delta\mathbf{x}_{i-1}^{H_2O}$ which is the error in the retrieval so far due to the unknown water vapour. The corresponding retrieval error due to the water vapour uncertainty is given by:

$$\hat{\mathbf{S}}_i^{H_2O} = \mathcal{E}\langle(\delta\mathbf{x}_i^{H_2O})(\delta\mathbf{x}_i^{H_2O})^T\rangle \quad (5)$$

where

$$\delta\mathbf{x}_i^{H_2O} = \mathbf{d}_i\delta y_i^{H_2O} + (\mathbf{I}_n - \mathbf{d}_i\mathbf{k}_i)\delta\mathbf{x}_{(i-1)}^{H_2O} \quad (6)$$

and $\mathcal{E}$ indicates the expected value of the expression in brackets. The total error covariance of the retrieval is the sum of the random and systematic error covariances:

$$\hat{\mathbf{S}}_i^{\text{total}} = \hat{\mathbf{S}}_i + \Sigma_j\mathbf{S}_{ji}^s \quad (7)$$

where superscript s denotes systematic error contribution. The last term is the sum over j error sources each contributing an error $\mathbf{S}_{ij}^s$ at stage i, as in equations 5 and 6:

$$\mathbf{S}_{ij}^s = \mathcal{E}\langle(\delta\mathbf{x}_{ij}^s)(\delta\mathbf{x}_{ij}^s)^T\rangle \quad (8)$$

and

$$\delta\mathbf{x}_{ij}^s = \mathbf{d}_i\delta y_{ij} + (\mathbf{I}_n - \mathbf{d}_i\mathbf{k}_i)\delta\mathbf{x}_{j(i-1)}^s \quad (9)$$

The total error covariance should be used to obtain the true information content of a measurement. The random error component will always be reduced by the use of a measurement: $I > 0$, but the systematic error component can lead to negative information.

3. MICROWINDOW SELECTION

3.1 GENERAL APPROACH

Starting with a suitably chosen *a priori* covariance, the information content of every spectral point at each altitude can be computed as outlined above. Using the point with the highest information contribution as a starting point it is then possible to add adjacent points to form a microwindow. The adjacent point or group of points with the highest information content is added at each stage. When the microwindow has reached a predetermined maximum size, or if the addition of adjacent points no longer adds information, the microwindow is complete and a new starting point is selected from the remaining points in the spectrum. The next microwindow always starts from the prior state assuming all previous microwindows have already been used in the retrieval.

The selection of individual channels (not microwindows) as in Ref. 7 leads to a more rapid increase in information content with number of points used, but microwindows have many advantages both in the retrieval (more efficient forward model calculations) and in the channel selection procedure. It is much faster to grow microwindows as the search through the spectra is only performed once per microwindow and not for each individual channel.

3.2 STARTING POINT SELECTION

The single point with maximum information content is not necessarily the best place to start growing a microwindow: it is possible that the single point is surrounded by low information points. It is more useful to start growing microwindows in an 'information-dense' area, where area is given by a spectral and altitude range. There are many possible approaches to select such an area from the spectra but in this case the following was used: the spectrum was surveyed in blocks of 4 spectral points by 4 tangent altitude points. The microwindow growing procedure was started in the block of points with maximum information content. This approach avoided the generation of many very small microwindows as obtained by the single point search.

3.3 MICROWINDOW GENERATION

The microwindows were grown from the single point with the most information in the high-information block, by increasing the size in spectral or altitude directions, retaining a rectangular shape at all times. The constraint of rectangular microwindows makes the definition of the completed microwindows very simple: each microwindow can be defined just by tangent height and spectral boundaries. The procedure itself however could generate any shape microwindows if required.

3.4 MICROWINDOW ORDERING

A microwindow list generated in this way or from another source can also be re-ordered according to information content. In this case the information content of each complete microwindow is computed, the microwindow with the highest information content selected and all the covariances updated. The best microwindow can then be selected from the remaining list and so on. The resulting list contains the most useful microwindows in the most efficient order.

4. A TEST CASE

4.1 DESCRIPTION OF TEST CASE AND INPUT DATA

Microwindows were computed for O_3 using the method described above.

The state vector was constructed with 25 elements: O_3 volume mixing ratio at 16 tangent heights (8-53 km in 3 km steps), continuum at 8 tangent heights (8-29 km) and radiometric offset. The information content was optimised for O_3 only, using the first 16×16 elements of the covariance matrix only to compute I (equation 4).

An *a priori* covariance was chosen to be diagonal (100% O_3 uncertainty, 10% continuum absorption and 50 $nW/(cm^2\ sr\ cm^{-1})$ offset).

All spectral calculations for weighting functions and systematic error terms were performed using the Reference Forward Model (Ref. 5) with 0.025 cm^{-1} spacing. Systematic error terms were included for temperature uncertainty at each altitude (3K), LOS uncertainty at each altitude (150m), 22 different contaminant species with realistic uncertainties (Ref. 3), non-LTE, spectroscopic errors and gain. Each of these terms was generated by differencing spectra generated with unperturbed input parameters to the forward model and spectra generated with input parameters perturbed by the appropriate uncertainty. The difference spectra were then handled as in equation 9. Spectroscopic and gain errors were treated as microwindow-specific errors which are correlated between points in the same microwindow, but uncorrelated between microwindows.

The instrument noise was taken as a diagonal matrix with values of σ from MIPAS specifications. The off-diagonal elements of measurement noise introduced by convolution with the apodised instrument lineshape have not been considered.

4.2 RESULTS

The first ten microwindows are listed in table 1 with the incremental information content in bits in the right hand column. It can be seen that the first microwindow contributes a large amount of information and that subsequent microwindows contribute less. Figure 1 shows how the information content increases with the number of spectral points used (logarithmic scale).

mw	spec. range [cm^{-1}]	alt. range [km]	info. [bits]
1	723.600 - 723.875	14 - 53	25.80
2	760.800 - 761.175	8 - 26	35.61
3	1044.575 - 1044.875	29 - 53	38.34
4	779.500 - 779.650	8 - 29	39.46
5	748.175 - 748.300	20 - 32	40.12
6	753.075 - 753.250	17 - 32	40.69
7	717.000 - 717.100	35 - 53	41.03
8	760.450 - 760.600	14 - 53	41.92
9	761.750 - 762.000	14 - 32	42.61
10	766.825 - 767.175	8 - 17	43.19

Table 1: First ten O_3 microwindows in order of selection

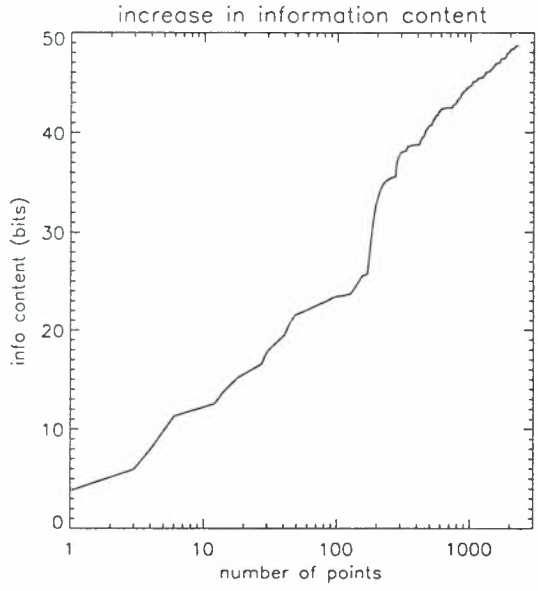

Figure 1: Information content vs number of points

The first 40 microwindows were taken and re-ordered according to microwindow information content. The first ten from the resulting list are shown in table 2. The first three microwindows appear as in the original list, followed by microwindows from further down the original list. The re-ordered list achieves a higher information content for fewer microwindows, but larger microwindows tend to be selected earlier as their information contribution is relatively high. The first 10 microwindows in the re-ordered list contain 946 points, before re-ordering the first 10 microwindows contained 801 points. Larger microwindows imply larger computing costs, so there is scope for a selection method where computing costs are taken into account and a measure of e.g. information content per unit cpu time used.

mw	spec. range [cm^{-1}]	alt. range [km]	info. [bits]
1	723.600 - 723.875	14 - 53	25.80
2	760.800 - 761.175	8 - 26	35.61
3	1044.575 - 1044.875	29 - 53	38.34
24	759.275 - 759.650	8 - 17	39.92
21	781.875 - 782.100	14 - 53	40.94
9	761.750 - 762.000	14 - 32	41.80
13	765.250 - 765.525	8 - 20	42.48
8	760.450 - 760.600	14 - 53	43.13
5	748.175 - 748.300	20 - 32	43.65
16	1074.875 - 1075.100	32 - 53	44.12

Table 2: Top ten O_3 microwindows after re-ordering

4.3 MICROWINDOW COMPARISONS

Full retrieval error simulations were made to compare these and existing MIPAS microwindow lists based on the MIPAS Global Fit approach (Ref. 1). Random and systematic errors were computed using the same error contributions and weighting functions for all microwindow sets. The weighting functions and systematic error contributions were calculated by a method independent from that used in the microwindow selection procedure. Results are plotted in figure 2.

The 'Old' microwindow set is one obtained by visual inspection of spectra (Ref. 3) and subsequently reduced by a selection algorithm to a subset based on MIPAS retrieval runtime and error requirements. The selection algorithm uses a single-layer retrieval analysis. The 'H3' microwindow set is one generated by von Clarmann *et al.* (Ref. 3), where each microwindow is allowed up to 3 different 'masks' blanking out spectral points over an altitude range. The use of masks allows for further optimisation of microwindows as sections contributing large unknown errors can be left out.

MW10, MW20, MW30, MW40 are the top 10, 20, 30 and 40 microwindows generated and re-ordered according to information content as described above. The number of spectral points in these microwindows is 946, 1549, 1999, 2241 respectively. The 'Old' microwindow set contains 15 microwindows and 2268 spectral points, the 'H3' set contains 25 microwindows and 4158 spectral points, including the 'masked' points. As expected the random error decreases as the number of spectral points is increased (MW10, 20, 30, 40). However, for a similar number of

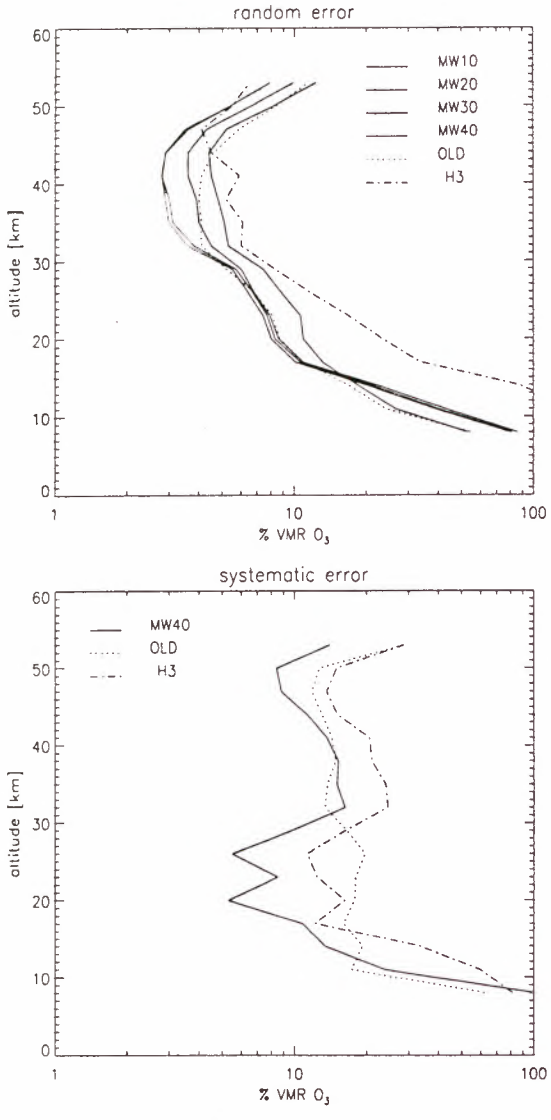

Figure 2: Comparison between microwindow sets. **top:** *random error covariance (diagonal elements),* **bottom:** *total systematic error covariance (diagonal elements)*

spectral points, the 'Old' microwindow set has higher random errors than MW40 at most altitudes. The 'H3' microwindow set has higher random errors at all but the highest tangent altitude. It is important to note though that the 'H3' microwindow subset has been obtained in an *ad hoc* manner from the full 'H3' database. A more rigorous selection method would probably improve these results.

The systematic error plot shows that our microwindow list performs better than the other lists at most altitudes. The 'H3' has higher systematic errors at all but the lowest altitude and the 'Old' list has slightly lower errors at 32-35 km and at 8 km.

Overall, it seems that the performance in terms of retrieval error of the microwindows generated in this test case is better than both the 'Old' and 'H3' lists. The use of masks in our microwindow list should further decrease the systematic error and increasing the number of microwindows and thus spectral points used should decrease the random error further. The effect of using a non-diagonal measurement covariance matrix should also be investigated.

A further important consideration is the computational cost of a retrieval. The inclusion of some 'cpu cost function' for each spectral point would allow information content to be optimised for minimum cpu time.

5. CONCLUSIONS

It has been shown that information content can be used to select channels and to grow microwindows for use in retrievals. Information content may also be used to put an existing microwindow list into the most useful sequence. Initial results indicate that O_3 microwindows generated in this way compare well with existing MIPAS microwindow lists. The method is objective, reproducible and simple to adapt to generate lists for other gases. Further work will allow microwindow lists to be generated for all target species and temperature and pressure retrievals. If required the constraint of rectangular microwindows can be dropped or additional features could be added.

REFERENCES

1. Carlotti M & al 1997, High level algorithm definition and physical and mathematical optimisations, Tech. Note TN-IROE-RSA9601, Issue 2, IROE-CNR, Firenze, Italy

2. Clarmann T von & Echle G 1998, Selection of optimized microwindows for atmospheric spectroscopy, *Applied Optics*, 37, 7661-7669

3. Clarmann T von & al 1998, Study on the simulation of atmospheric infrared spectra, Final Report, ESA Contract No. 12054/96/NL/CN

4. Dudhia A 1996, RFM Software User's Manual, ESA Document PO-MA-OXF-GS-0003, ESTEC, Noordwijk, Netherlands

5. Endemann M & al 1997, MIPAS: Design overview and current development status, in *Optics in Atmospheric Propagation, Adaptive Systems, and Lidar Techniques for Remote Sensing*, Devir A & Kohnle A & Werner C, eds., Proc. SPIE, 2956, 124-135

6. Rodgers C D 1976, Retrieval of atmospheric temperature and composition from remote measurements of thermal radiation, *Review of Geophysics and Space Physics*, 14, 4, 609-624

7. Rodgers C D 1996, Information content and optimisation of high spectral resolution remote measurements, in *Optical and Spectroscopic Techniques and Instrumentation for Atmospheric and Space Research II*, Hays P B & Wang J, eds., Proc. SPIE, 2830, 136-147

8. Shannon C E & Weaver W 1949, *The Mathematical Theory of Communication*, University of Illinois Press, eighth edition

INVERSION ALGORITHMS FOR OSIRIS AND GOMOS BRIGHT-LIMB BACKGROUND TERM

Harri Auvinen, Liisa Oikarinen, Erkki Kyrölä, Johanna Tamminen and Gilbert W. Leppelmeier

Finnish Meteorological Institute,
Geophysical Research Division,
Helsinki, Finland
e-mail: harri.auvinen@fmi.fi, liisa.oikarinen@fmi.fi, erkki.kyrola@fmi.fi, johanna.tamminen@fmi.fi and gilbert.leppelmeier@fmi.fi

ABSTRACT

OSIRIS is a UV-visible near-IR instrument on the Swedish satellite Odin (launch in autumn 1999). It measures atmospheric radiance spectra in limb viewing geometry at different tangent altitudes. Finnish Meteorological Institute is developing level 2 algorithms and the processing chain for the UV-visible spectrometer of OSIRIS. GOMOS bright-limb background term and the OSIRIS measurements are essentially similar, except for the worse spectral resolution of the GOMOS background term.

Different inversion methods proposed for OSIRIS include onion peeling, DOAS and optimal estimation. The subject of this paper is the onion peeling method in OSIRIS level 2 data processing. Constituent retrieval error of OSIRIS is estimated by using simulated measurements. To analyze the onion peeling method we determine marginal posteriori distributions. Marginal posteriori distributions illustrate how noise level of the measurement and choice of wavelength points will affect the confidence of the result. Posteriori distributions are calculated by the Markov chain Monte Carlo (MCMC) method. The results are also applicable for the GOMOS bright-limb background term.

1 INTRODUCTION

The OSIRIS instrument is a part of the Swedish Space Corporation's (SSC) Odin satellite, which will be launched in autumn 1999 (Ref. 1). The UV-visible spectrometer of OSIRIS measures atmospheric radiance spectra in limb-viewing geometry at different tangent altitudes. GOMOS bright-limb background term and the OSIRIS measurement are essentially similar, except for the worse spectral resolution of the GOMOS background term. Table 1 compares some characteristics of OSIRIS and GOMOS. Figure 1 illustrates the measurement geometry of OSIRIS and GOMOS.

Finnish Meteorological Institute (FMI) is developing level 2 algorithms and the processing chain for OSIRIS. Different inversion methods proposed for

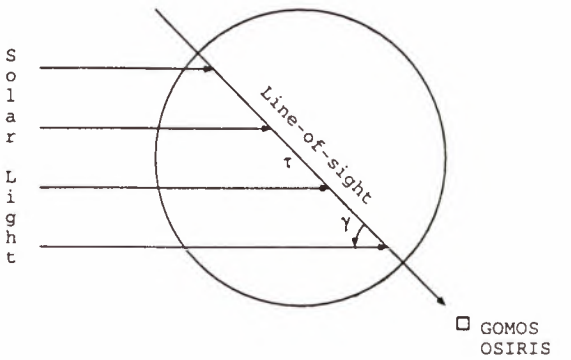

Figure 1: *Measurement geometry of OSIRIS and GOMOS bright-limb background term from above the atmosphere. Tangent point of the line-of-sight is marked with τ and γ is the azimuth angle. The circle illustrates the atmosphere.*

OSIRIS include onion peeling, DOAS and optimal estimation. In this paper we concentrate in the onion peeling method applied to OSIRIS inversion problem and the reliability of this method. Constituent retrieval error of OSIRIS is estimated by using simulated measurements. The advantage of using simulated data is that we can directly validate the results. The results are also applicable for the GOMOS bright-limb background term. To analyze the onion peeling method we determine marginal posteriori distributions. Marginal posteriori distributions illustrate how variance and choice of wavelength points will affect the confidence of the result. Posteriori distributions are calculated by the Markov chain Monte Carlo (MCMC) method.

This paper is organized in the following way. In Section 2 we explain the measurement principle of the OSIRIS instrument. The inversion problems of OSIRIS data processing are introduced in Section 3. In Section 4 we discuss the Markov chain Monte Carlo (MCMC) method which we have applied to the data processing of the OSIRIS instrument. In Section 5 we will show retrieval results and some examples of the posteriori distributions computed with the MCMC methods to analyze the onion peeling method.

Table 1: Some characteristics of the UV, visible, and near-IR spectrometers of GOMOS and OSIRIS compared with the GOMOS background term. OSIRIS parameters are from technical reports of the Odin group.

	GOMOS background term	OSIRIS
Spectral range	250-375 nm UVIS1 405-675 nm UVIS2 756-773 nm NIR1 926-952 nm NIR2	280-800 nm
Spectral resolution	$\geq$ 5.0 nm (vis) $\geq$ 0.7 nm (IR)	1 nm (UV) 2 nm (vis)
Sampling ratio	16 (vis) 11-14 (IR)	2.5 (UV) 5 (vis)
Field-of-view	min. vert. 0.015° min. horiz. 0.013° $\approx$ 1 km * 1 km	vert. 0.02° horiz. 0.8°
Integration time	0.5 s	0.1-10 s
Noise level (% of signal)	0.05 - 2.0	$\approx$ 0.1 - 2.0

2 OSIRIS MEASUREMENT PRINCIPLE

We introduce here shortly the measurement principle of the OSIRIS instrument. The OSIRIS instrument contains one UV-visible spectrometer at (280-800 nm) it measures ozone,NO_2, OClO, BrO, aerosols and neutral density.

Nominally OSIRIS looks only at the limb in the orbit plane of the satellite, but it can also be directed $\pm 32°$ out of plane. In nominal measurement geometry the solar zenith and azimuth angle are between 58.7° and 121.3° measured at the tangent point of the line-of-sight.

The instrument will measure scattered light at limb. The measured radiance spectra include spectral information of scattering and absorption processes. The radiance spectrum is measured repeatedly at different tangential altitudes (100–15 km) as the satellite moves. During each vertical scan spectra are measured at about 30-60 different line-of-sights with tangential altitudes between 15 and 100 km. During one day the satellite takes about 15 rounds around the earth. One round includes about 60 scans, which gives a good global coverage in a day.

We will use a pure solar spectrum as a reference spectrum. Note that the measured signal is corrected for instrument response at Level 1 data processing. By dividing the radiance spectrum measured at tangent altitude j by the reference spectrum we obtain the transfer spectrum:

$$F(\lambda, j) = \frac{I(\lambda, j)}{I^{ref}(\lambda)}, \qquad (1)$$

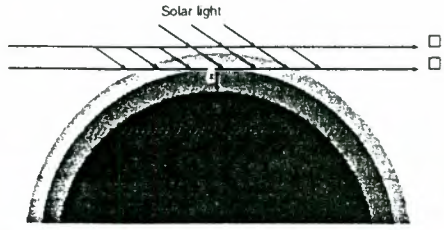

Figure 2: *The principle of a radiance spectra measurement at tangent altitude z.*

where $I(\lambda, j)$ is the radiance spectrum at wavelength λ measured along ray path j and $I^{ref}(\lambda)$ is the reference spectrum. The transfer spectrum includes information of how much stellar light was absorbed and scattered in the atmosphere. It is proportional to the amount of absorbing or scattering gases in the atmosphere. In Figure 3 we present simulated transfer spectra at different altitudes.

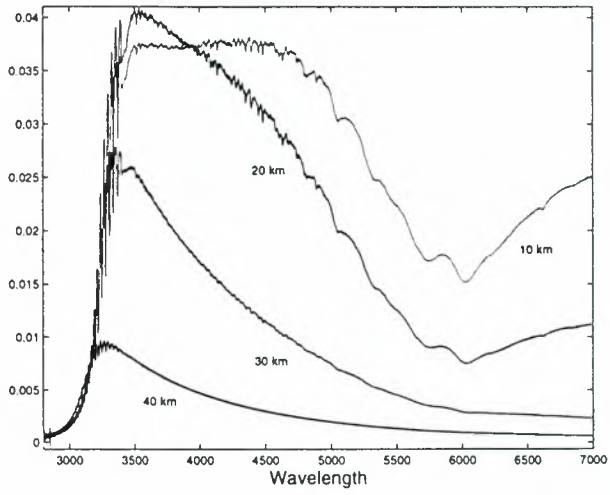

Figure 3: *Simulated transfer spectra at tangent altitudes 10, 20, 30 and 40 km. The spectra have been simulated by a single scattering model.*

3 OSIRIS INVERSION PROBLEM

By using the onion peeling method we can retrieve the vertical profile of each gas. Hence, the unknown quantities are the different gas densities in layers ($j = 1 \ldots n$). To formulate the inversion problem we have to determine the forward model. Let us have a closer look for the term $I(\lambda)$. Actually $I(\lambda)$ forms in a complex way. It includes single and multiple scattering effects. In this paper we will use a forward model which includes only the single scattering effect. Multiple scattering effect will be included later and a similar approach can be used.

Let $I(\lambda)$ be the radiance spectrum measured at a given tangent altitude. When we are using only the

single scattering model, radiance $I(\lambda)$ can be written

$$I(\lambda) = I^{sun} \int_{LOS} T_1(\lambda, s) S(\lambda, \gamma, s) T_2(\lambda, s) ds, \quad (2)$$

where $S(\lambda, \gamma, s)$ is the scattering term, $T_1(\lambda, s)$ is the transmittance of the paths from the Sun to the scattering point s on the line-of-sight and $T_2(\lambda, s)$ term is the transmittance from the scattering point to the detector.

The scattering term $S(\lambda, \gamma, s)$ can be written

$$S(\lambda, \gamma, s) = P_m(\lambda, \gamma)\rho_m(s)\sigma_m(\lambda, s) + P_a(\lambda, \gamma)\rho_a(s)\sigma_a(\lambda, s), \quad (3)$$

where P_a is the phase function of scattering from aerosols and similarly P_m is the phase function of Rayleigh scattering.

By Beer's law transmittance functions $T_1(\lambda, s)$ and $T_2(\lambda, s)$ are:

$$T_1(\lambda, s) = exp(-\int_{Sun}^{s} \sum_{i=1}^{k} \rho_i(u)\sigma_i(\lambda, u)du), \quad (4)$$

$$T_2(\lambda, s) = exp(-\int_{s}^{detec.} \sum_{i=1}^{k} \rho_i(u)\sigma_i(\lambda, u)du), \quad (5)$$

where ρ_i is the density of gas i and σ_i is the cross section, which is known and typical for each gas.

In practice we have to discretize the forward model for layer structure. In the discretized model we have replaced integrals with sums. In OSIRIS level 2 data processing the number of unknown quantities per layer is 4-6.

The detector measures actually photons (i.e.discrete counts) and hence the measurement error is Poisson distributed with variance proportional to the amount of signal measured. Due to the great amount of detected photons the noise due to photon counting statistics can be assumed to be normally distributed with variance proportional to the amount of photons.

In this work we further assume that there is no correlation in the noise between detector pixels.

3.1 Onion peeling method

In a standard onion peeling method we assume that the atmosphere consists of layers. Within each layer the densities of the different gases are constant. Figure 4 illustrates the layer construction for one specific measurement. In this approach we use measurements in the following way. Let us have measurements $1 \ldots n$ from up to down. We construct the layer structure so that there is exactly one tangent point of a measurement in each layer. Hence the number of layers is the same as the number of measurements.

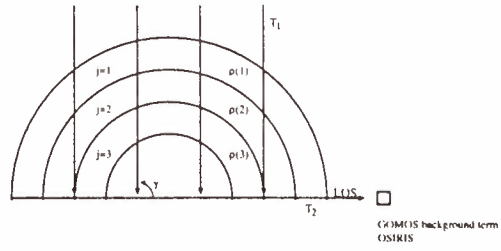

Figure 4: *Layer structure of the atmosphere.*

Like we can see in Figure 2, the line-of-sight of the first measurement is going through only the uppermost layer. When the zenith angle is ≤ 90 the measurement is independent of the gas densities $\rho_i(k)$, where $k \geq 2$.The main aim in onion peeling method is to find gas densities for each layer one by one by using measurements from up to down. The first step in our case is to find gas densities for the uppermost layer using a non-linear least-squares fitting method. Then next step is to find gas densities for the next layer by using the already known densities in upper atmosphere. When we continue like described above we will get the vertical profile for each gas.

3.2 Minimising the sum of squared residuals

Let us next derive an expression of the sum of squared residuals. Let $\rho_i(j)$ be the density of gas i in layer j and $F(\lambda, j)$ be the observed transfer spectrum, which now includes also noise. Note, that transfer spectrum $F(\lambda, j)$ is independent of gas densities $\rho_i(k)$, where $k > j$ in case where zenith angle is ≤ 90.

The traditional approach to inverse problems is to seek for the solution which minimises the sum of squared residuals (SSR) term also known as the least squares solution (see for example Ref. 2). Using matrix notation this term in OSIRIS inversion is following:

$$\mathrm{SSR_j} = (M(\rho) - F(j))^{\mathrm{T}}\, \mathbf{C}^{-1}\, (M(\rho) - F(j)), \quad (6)$$

where M is the response of the forward model at different wavelengths and given gas densities $\rho = \rho_i(1 \ldots k)$. In the OSIRIS case the covariance matrix of the measurement error $\mathbf{C}$ is a diagonal matrix and $\mathbf{C}^{-1}$ denotes the inverse of it.

The non-linear least-squares solution can be found by using an iterative routine. We have applied the Levenberg–Marquardt routine (Ref. 3) to OSIRIS inversion problem. The method is based on combining the steepest descent and the inverse Hessian methods and the error estimates are computed by assuming that the SSR term can be linearised around the minimum value.

3.3 Statistical solution for inverse problems

In statistical inversion theory both the measurements and the unknown quantities are treated as random variables and they are characterized with probability distributions. Hence the solution is not only a point equipped with an error bar, but instead, it is a whole distribution of probable solutions. The Bayesian approach expresses the inverse problem as a conditional posteriori probability distribution of the unknown parameters with the condition that the measurement $F(\lambda)$ has been made. Applied to OSIRIS inversion the posteriori distribution reads

$$P(\rho \mid F) = \frac{P(F \mid \rho) P(\rho)}{P(F)}, \tag{7}$$

where $P(\rho)$ is the *a priori* knowledge of the gas densities, $P(F)$ is a scaling factor (and can be ignored hereafter). The *likelihood function* $P(F \mid \rho)$ is the probability density of the transfer data with the condition that the estimated parameters are ρ. Since the noise in the OSIRIS data is normally distributed the likelihood function is

$$P(F \mid \rho) = \frac{1}{(2\pi)^{d/2}\sqrt{|\mathbf{C}|}} \times$$
$$\exp[-\frac{1}{2}(M(\rho) - F)^{\mathrm{T}}\, \mathbf{C}^{-1}\, (M(\rho) - F)], \tag{8}$$

where d is the number of unknown parameters (dimension of the parameter space) and $|\mathbf{C}|$ is the determinant of the covariance matrix. We see that in the case of normally distributed noise the estimate of ρ which maximises the posteriori probability density function equals with the one that minimises the SSR term if we ignore the a priori knowledge of ρ.

4 Markov chain Monte Carlo (MCMC) methods

In this section we discuss how the posteriori density can be computed in practice. We shortly introduce the Markov chain Monte Carlo (MCMC) method by which posteriori distributions can be determined numerically (see for example Ref. 4). The basic idea of MCMC methods is to generate a Markov chain of random samples from the posteriori distribution so that the set of sampled points converges towards the unknown posteriori distribution.

By analysing the generated chain we can approximate, for example, the expectation value and the covariance matrix with sample averages in a following way. Let us assume that we have sampled d-dimensional states $\mathbf{X}_1, \ldots, \mathbf{X}_n$ from the posteriori distribution (7). The expectation values of the unknown gas densities are now computed simply by approximating

$$\mathrm{E}[\rho] \approx \frac{1}{n} \sum_{i=1}^{n} \mathbf{X}_i. \tag{9}$$

Similarly the covariance matrix is approximated with

$$\mathrm{E}\left[(\rho - \mathrm{E}[\rho])\,(\rho - \mathrm{E}[\rho])^{\mathrm{T}}\right] \approx$$
$$\frac{1}{n-1} \sum_{i=1}^{n} (\mathbf{X}_i - \mathrm{E}[\rho])\,(\mathbf{X}_i - \mathrm{E}[\rho])^{\mathrm{T}}. \tag{10}$$

4.1 Random walk Metropolis-Hastings algorithm

There are many variations of the MCMC methods depending on how the Markov chains are created see for example Adaptive Proposal (AP) method, introduced in (Ref. 5 and Ref. 6) for the GOMOS spectral inversion. In this paper we use only the standard random walk Metropolis algorithm (Ref. 7). Our intention is to draw samples $\mathbf{X}_1, \ldots, \mathbf{X}_n$ from the posteriori distribution (7). Let $\mathbf{X}_t$, (t=1) be our starting point. Now each state $t > 1$ in the chain is sampled in two steps:

1. Sample a candidate point $\mathbf{Y}$ from a fixed symmetric proposal distribution $Q(\cdot)$ (e.g. Gaussian centered at the current point)

2. Accept the candidate point with the probability

$$\alpha(\mathbf{Y}, \mathbf{X}_t) = \min\left\{1, \frac{P(\mathbf{F} \mid \mathbf{Y}) P(\mathbf{Y})}{P(\mathbf{F} \mid \mathbf{X}_t) P(\mathbf{X}_t)}\right\}. \tag{11}$$

   If $\mathbf{Y}$ is accepted put $\mathbf{X}_{t+1} = \mathbf{Y}$ else $\mathbf{X}_{t+1} = \mathbf{X}_t$.

These steps are repeated until $t = t_{mar}$. The required length t_{mar} of the chain has to be carefully studied (see for example Ref. 8). After making sure, that the Markov chain has converged, we can use the chain to approximate the posteriori distribution and we may compute the expectation values and the covariance matrix defined above. It is advisable to leave out the early part of the chain (called the burn in period) so that the starting point does not affect the solution.

5 RESULTS

In this section we present some retrieval results of OSIRIS level 2 data processing by using the onion peeling method. We also take a closer look on the inversion problem at one specific zenith and azimuth angle and altitude. In this study we use the MCMC method described above.

To study how the onion peeling method works in the OSIRIS case we have performed the inversion at 48 altitudes between 10 and 80 km. In this case we set the zenith angle to 80° and the azimuth angle to 90°. A set of simulated spectra was produsedused using the profiles of Figure 5.

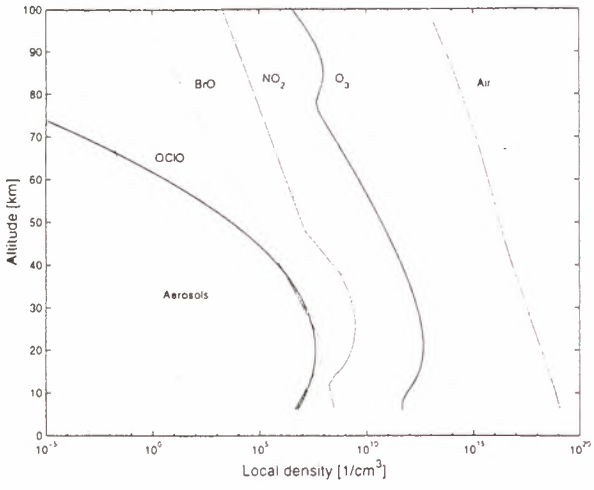

Figure 5: *Gas and aerosols density profiles (U.S. Standard air and O_3) as a function of altitude (y-axis). Note that the x-axis is logarithmic.*

The Levenberg–Marquardt method was run twice to optimize the starting points. The results are presented in table 2, where we have relative error of different gases. The relative error corresponding to each layer j, $(j = 1, \ldots, n)$ is calculated in a following way:

$$\mathrm{err}(j_i) = \left(\frac{\rho_i^{est}(j) - \rho_i^{true}}{\rho_i^{true}(j)} \right) \times 100\%, \qquad (12)$$

where $\rho_i^{est}(j)$ is the estimate of gas density i in layer j and similarly ρ^{true} is the true value of the simulations.

Next we study how the choice of wavelength points will affect the size and the shape of the posteriori distribution. The posteriori distribution varies a lot depending on the altitude and on the signal to noise level. As the a priori information of the gas densities we have used non-informative density.

We have run exactly the same case by using onion peeling method with the Levenberg-Marquardt and with the MCMC method. In order to get a starting point for the MCMC method we run the Levenberg-Marquardt method first. The MCMC chain length was 17000 and we discarded the 2000 first states. In Figure 6 we present two sets of two-dimensional marginal posteriori distributions of the retrieved gas densities at 30 km altitude. The upper row corresponds to a case where we have data point at every 3 nm and the lower row corresponds to a case where we have a data point at every 1 nm. It is clear from the figure that when we use less spectral data points the posteriori distributions are flatter and the confidence limits are wider. We see that ozone, NO_2 and aerosol densities can be identified quite well in both cases. However, estimates are more accurate when we have a data point at every 1 nm.

From the two-dimensional marginal distributions it is easy to observe possible correlations between gases. The Figure shows that there exists a positive correlation between ozone and NO_2 at 30 km.

Table 2: Relative error of different gases when zenith angle is 80° and azimuth angle is 90°. Simulated measurements are made at tangent altitudes 10-80 km.

alt	O_3	NO_2	Air	Aer	BrO	OClO
80	259.8	–	71.2	107.6	–	–
78	339.9	–	21.7	38.4	–	–
76	309.1	–	9.26	18.6	–	–
74	39.1	–	4.32	11.4	–	–
72	-31.1	–	2.57	6.38	–	–
70	-24.0	–	1.47	4.23	–	–
68	-4.57	–	0.81	3.16	–	–
66	2.08	–	0.50	2.49	–	–
64	6.70	–	0.43	-0.03	–	–
62	-6.00	–	-0.05	2.72	–	–
60	0.56	–	0.24	0.75	–	–
58	-0.37	–	0.21	0.07	–	–
56	0.23	–	-0.12	0.51	–	–
54	-0.10	–	0.02	0.19	–	–
52	-0.13	–	-0.13	1.71	–	–
50	-0.54	–	0.11	-1.06	–	–
48	-0.05	–	0.07	-0.85	–	–
46	-0.67	–	-0.07	-0.62	–	–
44	0.84	–	-0.04	0.38	–	–
42	0.43	102.3	0.18	0.56	–	–
40	-0.73	-12.1	-0.06	0.19	–	–
38	-0.97	-27.0	-0.44	1.96	–	–
36	0.48	1.84	-0.12	2.61	–	–
34	-0.16	16.0	0.56	-4.86	–	213.4
32	1.12	-1.19	-0.04	1.04	117.0	-59.27
30	-0.84	-3.91	-0.18	0.17	83.95	-41.22
28	0.53	5.63	0.29	-0.96	-44.15	13.04
26	0.38	4.40	0.32	-1.07	29.05	-0.72
24	0.15	-0.42	0.03	-0.04	-2.28	-6.92
22	-0.04	-1.60	-0.05	0.46	9.45	2.36
20	0.04	0.83	0.14	0.18	-9.59	-35.48
18	0.27	10.3	0.25	-0.90	6.65	14.82
16	-0.68	-21.5	-0.16	0.29	43.11	21.86
14	-0.35	-33.4	-0.07	0.82	–	–
12	0.89	–	0.19	1.32	–	–
10	0.81	–	0.07	-0.32	–	–

6 CONCLUSIONS

The onion peeling method with Levenberg-Marquardt has turned out to be a useful approach in OSIRIS data inversion. The method is fast and it gives quite accurate results when the signal to noise ratio is fairly good. The method gives us the possibility to use spectral data efficiently. Hence, we can use more

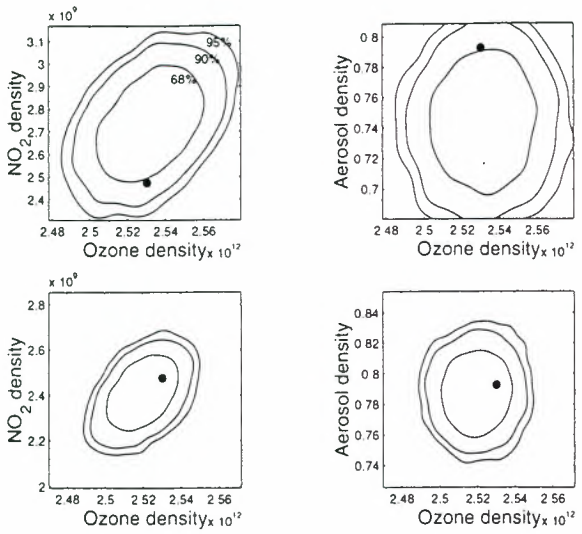

Figure 6: *Two dimensional kernel estimates of the marginal posteriori distributions of the gas densities at 30 km. The contours refer to 68, 90, and 95% confidence regions. On the left ozone and NO_2. On the right ozone and aerosols. Upper plots corresponds to a case where we have data point at every 3 nm and lower plots corresponds to a case where we have a data point at every 1 nm. The true value is denoted by a dot.*

than 400 different wavelength points simultaneously. The analysis of posteriori distributions in Section 5 shows the advantage of using as many data points as possible.

In this work a single scattering radiative transfer model was used. A more realistic forward model would include multiple scattering effects. With multiple scattering we can't, in principle, use the onion peeling method. In Figure 7 we compare Monte Carlo simulations (Ref. 9) of single and multiple scattering effects at tangent altitude 10 km. We see that the optical depth of ozone at different altitude layers is quite similar in both models. Therefore, with suitable use of a priori information, it seems to be possible to use the onion peeling method also with multiple scattering effect.

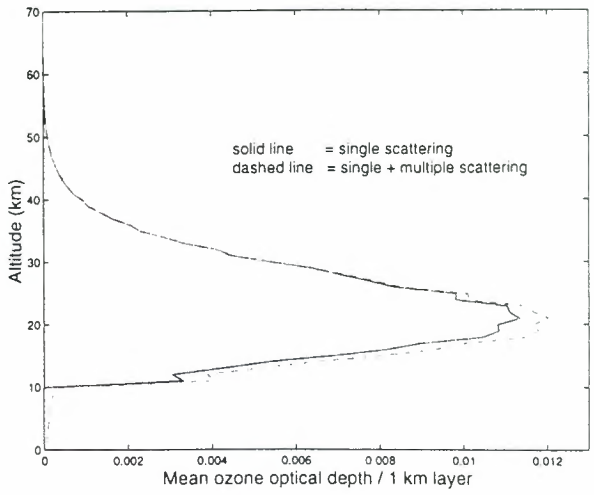

Figure 7: *Comparison of single and multiple scattering effects by Monte Carlo simulation of a measurement at tangent altitude 10 km and wavelength 500 nm.*

References

[1] Odin home page at. `http://irg.usask.ca/`.

[2] W. Menke. *Geophysical Data Analysis: Discrete Inverse Theory.* Academic press, inc., San Diego, California, 1989.

[3] W. H. Press, S. A. Teukolsky, W. T. Vetterling, and B. P. Flannery. *Numerical Recipes in FORTRAN, The art of scientific computing.* Clasendon Press, Oxford, 1992.

[4] W. R. Gilks, S. Richardson, and D. J. Spiegelhalter. Introducing Markov chain Monte Carlo. In W. R. Gilks, S. Richardson, and D. J. Spiegelhalter, editors, *Markov Chain Monte Carlo in Practice*, pages 1–19. Chapman & Hall, 1995.

[5] H. Haario, E. Saksman, and J. Tamminen. Adaptive proposal distribution for random walk metropolis algorithm. Reports of the Department of Mathematics, University of Helsinki, Preprint 176, 1998.

[6] J. Tamminen, E. Kyrölä, and H. Auvinen. MCMC algorithms for inverse problems in remote sensing. *Proceedings of European Symposium on Atmospheric Measurements From Space, 18-22 Jan 1999, The Netherlands.*

[7] N. Metropolis, A. W. Rosenbluth, M. N. Rosenbluth, A. H. Teller, and E. Teller. Equations of state calculations by fast computing machine. *J. Chem. Phys.*, 21:1087–1091, 1953.

[8] S. P. Brooks. Markov Chain Monte Carlo Method and its Application. *The Statistician*, 47:69–100, 1998.

[9] L. Oikarinen. Monte Carlo Simulations of Radiative Transfer for Limb Scan Measurements. *Proceedings of European Symposium on Atmospheric Measurements From Space, 18-22 Jan 1999, The Netherlands.*

IMPROVED CLIMATOLOGIES AND NEW AIR MASS FACTOR LOOK-UP TABLES FOR O_3 AND NO_2 COLUMN RETRIEVALS FROM GOME AND SCIAMACHY BACKSCATTER MEASUREMENTS

Robert J. D. Spurr

Harvard Smithsonian Center for Astrophysics
60 Garden Street, Cambridge, MA 02138, USA
phone +1 617 496 7819, fax +1 617 495 7389
email rspurr@cfa.harvard.edu

ABSTRACT

A column-classified climatology of O_3 profiles is used to generate a global look-up table of Air Mass Factors (AMFs) for the conversion of fitted ozone slant columns to vertical columns, in the GOME and SCIAMACHY level 1-2 operational processing algorithms. The column classification may be used to optimize the choice of AMF and vertical column. The O_3 AMF dependence on surface albedo is also examined. More representative AMFs can be found by computing area-weighted average albedos for the nadir footprints.

A suggested climatology for NO_2 profiles is derived from HALOE stratospheric NO_2 measurements, while the tropospheric burden is approximated by a set of analytic curves based on the ground concentration as a free parameter. A look-up table of NO_2 AMFs is constructed on this basis. The climatology facilitates the selection of an AMF (and hence vertical column) which reflects the tropospheric burden of NO_2 implicit in the slant column result.

1. INTRODUCTION

GOME was launched on board ERS-2 in April 1995. Operational ozone total column products have been available from July 1996 to the present. The level 1 to 2 GOME Data Processor (GDP) has used the DOAS (Differential Optical Absorption Spectroscopy) spectral fitting method for the retrieval of O_3 and NO_2 columns. DOAS comprises a least-squares fit of the measured optical density spectrum to retrieve slant column amounts, followed by an Air Mass Factor (AMF) division to achieve the (geometry-independent) vertical column result. A first-order correction is made to the vertical column result to allow for partial or total cloud cover in the footprint. See [1] and [2] for details on the instrument and data processing algorithms.

In addition to O_3 and NO_2, spectral fitting of slant column amounts from GOME backscatter measurements has now been demonstrated for a number of minor but chemically important trace species. These include BrO and SO_2, which have been retrieved on a global basis, and OClO and HCHO, retrieved in special scenarios. Some of this work is summarized in [3] and references therein. While there has been considerable research into improving spectral fitting and deriving new or improved reference spectra, less attention has been paid to the AMF issue.

AMFs are simulated quantities calculated using radiative transfer (RT) models. For determination on a global basis, suitable trace gas profile climatology is required. In the first versions of GDP level 1-2 processing, AMFs for O_3 and NO_2 are computed using a quasi-exact single scatter radiative transfer model, and a look-up table of multiple scatter correction factors generated off-line with another RT model. Profiles used in these simulations are taken from model output (no climatology. The need for improved AMFs has been recognized as an essential ingredient in level 2 data product upgrades for GOME. The motivation for the present work is to create a consistent set of look-up tables of AMFs for O_3 and NO_2 for use on a global basis in the operational environment of the GDP and (in the near future) the SCIAMACHY Data Processor.

In section 2, we consider the AMF situation for O_3. A suitable column-classified climatology for this trace species is now available from SAGE II and balloon results [4]. Based on this climatology, a look-up table of AMFs for use in the operational framework has been generated using the GOMETRAN radiative transfer model [5] (sections 2.1 and 2.2). The O_3 column classification in the table may be used to return an AMF that corresponds more closely to the real atmospheric burden; this is especially true for O_3 hole scenarios where the depleted profile shape has a significant effect on the AMF value. In addition, it is shown how error covariance values in the profile climatology translate into AMF errors that contribute to the overall Level 2 O_3 product error (section 2.3).

A wrong choice of surface albedo from climatology data can produce a significantly incorrect AMF. By using an area-weighted coverage algorithm, a "footprint-representative albedo" can be derived from the surface database to ensure that the correct AMF is returned from the look-up table (section 2.4).

The situation for global NO_2 AMF values is less clear (sections 3.1 to 3.3). The GDP default uses just one model output profile for every AMF simulation: there is no climatology. We show how a set of analytic NO_2 profiles may be generated from HALOE NO_2 occultation profile retrievals [6] in the stratosphere, together with an assumed tropospheric shape that has the ground concentration as the single free parameter. We examine the corresponding look-up table of NO_2 AMFs constructed using GOMETRAN. We show how it may be used to improve the vertical column estimation, and to derive a tropospheric ground-level concentration as a by-product of the AMF correction.

2. O_3 Air Mass Factors

2.1 Column-classified climatology

We use the column-classified climatology developed by NASA for use in the TOMS retrieval (algorithm version V7) [4]. The data has been compiled from an analysis of several years of SAGE II data, together with a large number of balloon sonde profiles for tropospheric coverage. The data is divided into 3 broad latitude zones. There are 6 low latitude profiles with total columns from 275 to 475 Dobson Units [DU], at intervals of 50 DU. There are 10 mid-latitude profiles and 10 high latitude profiles, both sets ranging from 125 to 575 DU at intervals of 50 DU. O_3 profiles are expressed in Umkehr columns (in DU),. Umkehr layer boundaries are specified as pressure levels decreasing in exponential half steps (scale height ~5 km in lower atmosphere). The top Umkehr layer extends to the top of the atmosphere; there are 11 Umkehr layers in all. Temperatures in [K] are given for each Umkehr layer, and for all 26 profiles. There is also a single symmetric 11x11 matrix of error covariances in $[DU]^2$, valid for all profiles. (The data set also includes principal components from an eigenvector analysis, but these ae not used in the AMF derivation). Figure 1 illustrates the Umkehr data for 10 mid-latitude profiles.

The creation of O_3 profiles expressed as number concentrations $[mol.cm^{-3}]$ on a user-defined height grid is done by first computing the *cumulative* Umkehr column amounts, then taking the derivative to get number concentration values. A 4-point Lagrangian interpolation scheme is suitable for the cumulative column interpolation to user-defined height levels, and some small modifications were made to ensure continuity of the profile.

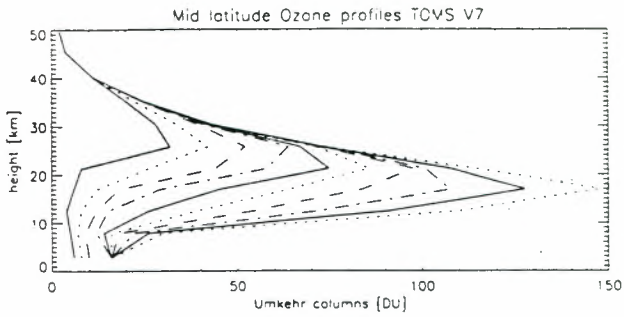

Figure 1. NASA-TOMS O_3 Umkehr column mid-latitude profiles.

Profile error covariance matrices may be derived from the database Umkehr covariance matrix using the Jacobean of transformation between the Umkehr column profile in the original data set and the profile number concentrations. For each profile we require also a set of tropospheric columns up to a set of pre-specified heights (up to 10 km, resolution 1 km is sufficient). This adjunct set of columns is required for the "ghost column" evaluation in the vertical column cloud correction (section 2.3). We may also define an error covariance for this set. Mathematical details of all these derivations are not given here, but can be obtained from the author.

2.2 Derivation of an O_3 AMF Look-up table

Let q_i be the O_3 concentration profile defined on a user defined height grid z_i, and S_{ij} is the corresponding covariance matrix. The standard AMF definition is:

$$AMF_{O3} = \frac{Ln(I_{NoO3} / I_{total})}{\tau_{O3}} \qquad (1)$$

Here I_{total} is the simulated backscatter intensity with all absorbers present, and I_{noO3} is the intensity simulated without O_3 absorption; τ_{O3} is the vertical depth given in terms of the concentrations q_i and cross sections σ_i as:

$$\tau_{O3} = \sum_{i=1}^{N-1} 0.5(q_i\sigma_i + q_{i+1}\sigma_{i+1})(z_i - z_{i-1}) \qquad (2)$$

The AMF variance is computed from S_{ij} as follows:

$$\mathrm{var}(AMF_{O3}) = \frac{\partial A}{\partial q_j} S_{ij} \frac{\partial A}{\partial q_i} \qquad (3)$$

$$\frac{\partial A}{\partial q_j} = \frac{1}{\tau}\left[- A\frac{\partial \tau}{\partial q_j} - \frac{1}{I_0}\frac{\partial I_0}{\partial q_j} \right] \qquad (4)$$

Note that I_{noO_3} has (by definition) no dependence on q_i (the subscript O_3 has been dropped in the last two equations). The derivative of optical depth may be calculated directly from equation (2).

The forward model GOMETRAN [5] (Version 2.1) was used to carry out the intensity calculations. Note that the derivative of I_{total} in equation (4) is related directly to the weighting function output from this model. A 37-level atmosphere was used both for the profile derivations from database, and for the subsequent RT simulations. Wavelength dependence of the AMF across the DOAS fitting window range (325-335 nm) has not been used in GDP to date. It has been demonstrated that the value at 325 nm is the most representative single AMF to use for this window and this is the default in the present work.

For each of the 26 NASA-TOMS Umkehr profiles, we calculate AMFs for 6 albedo values (assumed Lambertian, from 2% to 90%), for 6 lower boundary heights from 0 to 10 km at 2 km resolution, and for a set of viewing geometries. This latter includes 16 solar zenith angles from 16° to 91.5°, 8 line-of-sight zenith angles from 0° to 35°, and 6 azimuth angles from 0° to 180°. Figure 2 gives an example of the dependence on the column amount for the 10 mid-latitude Umkehr profiles of Figure 1.

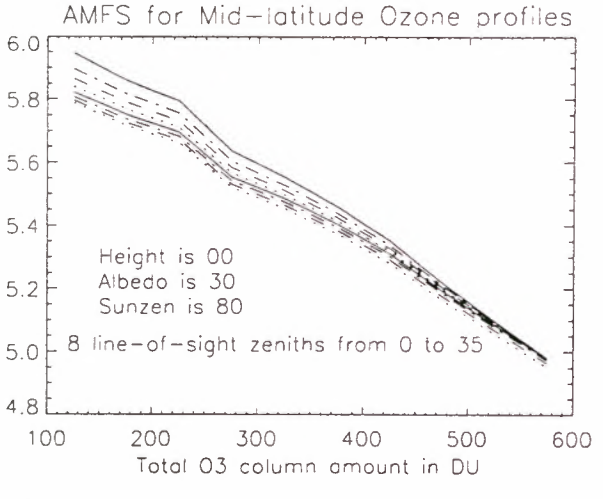

Figure 2. AMF variation with mid-latitude O_3 profiles for albedo 30%, solar zenith 80°, azimuth 0° and 8 line-of-sight zenith angles.

For a given geophysical scenario, the extraction of a correct AMF from this table needs to be fast and accurate. For the viewing geometry, 4-point Lagrangian or Akima polynomial interpolation is performed over the 3 sets of reference angles (should interpolate using cosines). Linear interpolation is sufficient for the albedo and height dependence (see Figure 4 below for example). An alternative for the viewing geometry extraction is to use a double parameterization scheme for the zenith angle dependencies (this assumes that AMFs can be linearly regressed to polynomials in zenith angle cosines). Such a parameterization scheme is used in GDP for the extraction of multiple scatter correction factors, and for all scenarios encountered by GOME, the accuracy is better than 1.5%.

The azimuth angle interpolation may be avoided. Since the GOMETRAN RT model output is expressed in terms of a Fourier cosine series in azimuth, one can store Fourier *components* of the backscatter intensities instead of the actual AMF values. The number of Fourier terms determines the accuracy of the azimuth expansion. Another approach using neural networks has been proposed recently [7]: once the network is trained the extraction is very rapid.

Further work on the look-up tables is needed to establish the dependence of the O3 AMF at 325 nm on aerosol burden. All calculations presented here were done with a single aerosol class ("maritime" boundary layer, background stratospheric loading). However, a land/sea distinction in the aerosol boundary layer is allowed for in the GDP operational algorithm. The look-up table makes no distinction between cloud-top and ground reflectance – both are assumed Lambertian. A version of GOMETRAN with the treatment of clouds as bi-directional reflecting surfaces has recently been released, and this will be used in future to deal more accurately with AMFs for O_3 absorption in an atmosphere with a reflecting cloud layer as the lower boundary.

2.3 Vertical column computation and error

The following equation is used in GDP to make the first-order correction for cloud contamination in the vertical column (VC) evaluation:

$$V = \frac{S + F \cdot G \cdot A_2}{F \cdot A_2 + (1 - F) \cdot A_1} \qquad (5)$$

G is the tropospheric "ghost" column below cloud-top, F is the cloud fraction (a result from the operational cloud coverage algorithm) and S is the slant column value (from spectral fitting). A_1 and A_2 are the AMFs to ground level and cloud-top level respectively. Equation (5) reduces to the clear sky result $V=S/A_1$ when $F=0$. G may be found readily by integrating part of the appropriate climatology profile from ground level to cloud-top. Error bars on G, A_1 and A_2 may be

expressed in terms of the climatology profile covariance, with the help of equations (3) and (4) and suitable Jacobeans of transformation.

In the classical DOAS approach, AMFs and the VC are calculated using a single O_3 profile chosen as most representative for the geophysical scenario. The wrong choice of profile may result in significant errors in the AMF values and hence the level 2 total column product. At low latitudes, the AMF values are in general only weakly dependent on the total column content and the usual approach is sufficiently accurate.

However, using AMFs from a high latitude profile with (say) 400 DU column content in an O_3 hole scenario will lead to a significant error (8-10% from Figure 2). We may use equation (5) to adjust the AMF values to reflect the actual content of atmospheric O_3 implicit in the slant column result. The first guess V_0 for the vertical column may be taken for example from the TOMS zonal mean total ozone climatology. (An alternative for the operational environment is to take a nearest neighbor previously retrieved O_3 total column). From the look-up table of AMFs, we compute A_1 and A_2 using the built-in column classification to interpolate to V_0. The ghost column G is also evaluated for a profile with total column V_0. Equation (5) is then used to update the vertical column to a new value V_1. The process is iterated until the difference between successive vertical column estimates is less than some pre-set convergence criterion ε:

$$\left| 1 - \frac{V_{n+1}}{V_n} \right| < \varepsilon \qquad (6)$$

Setting $\varepsilon=10^{-3}$ ensures convergence after 3-5 iterations. Clearly this iteration is a form of quality control on the AMF computation, and it provides an answer to the classic dilemma inherent in the DOAS approach. (How can you retrieve vertical column amount when you need to know the profile accurately in advance for the AMF evaluation?). From equation (5) and the Gaussian error propagation law, we may compute the total error on V from knowledge of errors on the fitted quantities (S and F), and uncertainties on G, A_1 and A_2 due to O_3 profile climatology covariance errors. The latter errors are assumed independent of the spectral fitting errors. (So far in GDP, only errors on S and F have been considered).

The look-up table and vertical column quality control iteration have been used to re-process whole orbits of GOME level 2 O_3 total column data. The slant column and cloud fraction results are taken as read from the intermediate records in the level 2 product. Climatological and reference databases are used as they appear in GDP (with the exception of O_3 profiles). Instead of computing the AMFs using the GDP scheme, we get them straight from the look-up table described here, and then apply the vertical column calculation as outlined above.

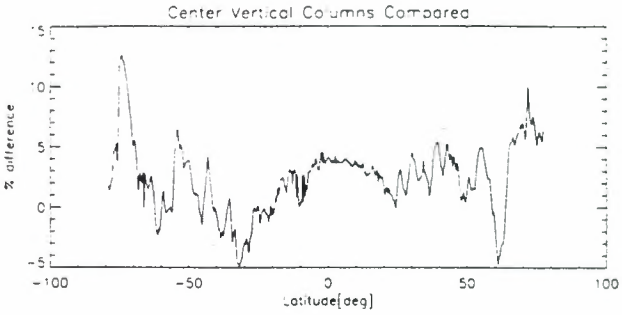

Figure 3. Comparison between re-processed and GDP original O_3 total column amounts.

Figure 3 illustrates the comparison between original GDP total ozone level 2 data and the re-processed values using the AMF look-up table and quality control iteration (center pixels, part of ERS-2 orbit 70930005). The comparison reveals some of the faults noticed in the original data; the "west pixel bias" is clearly seen in the third panel (absent in the re-processed results). Some of the differences (particularly at high latitudes) can be attributed to the mixing of two RT model results in the original GDP AMF algorithm.

The re-processing is a fast and effective tool for investigating and improving the AMF formalism in the global operational environment. The use of a look-up table for O_3 AMFs has already been implemented for GOME, and this will be done also for SICAMACHY, at least in the Near Real Time application. The work can be taken further by looking at a number of validation orbits in order to assess the impact of the look-up table AMF extraction in operational processing for total column retrieval of ozone. This work has already started at DLR, and validation studies will begin in Spring 1999.

2.4 Albedo dependence and footprint averages

In GDP the surface albedo selected for AMF determination is taken from a climatological database of Lambertian albedos and associated vegetation types (land surface indices). The database resolution is 1°x1° (latitude and longitude). The requisite albedo is selected by examination of the surface coordinates of the footprint center. If the center lies over a dark ocean (albedo 2-5%) surrounded by an ice shelf (albedo 75-

90%), the low albedo is not representative of the level of reflected light from the whole footprint. This can lead to large errors in the resulting AMF values. This is evident in the example shown in Figure 4, where the ice/ocean albedo variation mentioned above would generate a 10-12% change in AMF.

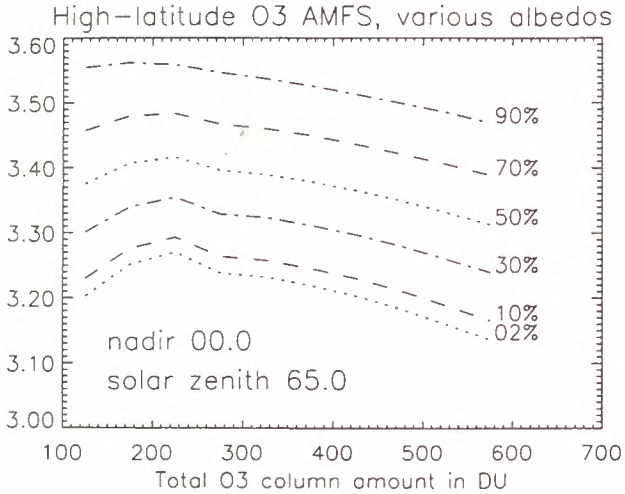

Figure 4. AMF dependence on albedo for high latitude O_3 profiles. Direct nadir, sun zenith 65°.

This effect was noticed round the arctic ice shelf in a comparison between GDP O_3 total columns and those derived from coincident profile measurements from Ny-Ålesund (Spitzbergen). GDP results were too high due to underestimated AMFs brought about in large part by just the sort of incorrect albedo assignment mentioned above. To remedy this fault, it is necessary to ensure that a representative albedo is chosen.

The obvious answer is to assign an area-weighted albedo. A footprint will be covered by several 1°x1° latitude/longitude bins, each with a different albedo value. Some bins will lie entirely inside the footprint, others will be split in various ways by the 4 sides and corners of the footprint. If each tessellating bin has an albedo A_j and area (total or partial) S_j, then the average albedo is

$$\hat{A} = \sum_j A_j S_j \Big/ \sum_j S_j \qquad (7)$$

This value should be used in the AMF selection. The computation of areas is straightforward, but care has to be taken with the partial areas included by footprint sides and corners. A rectilinear approximation to the grid area computations only really works near the equator. Elsewhere one should use spherical geometry. To a very good approximation the footprint sides can be treated as great circle sections, and this allows for a straightforward analytic solution to the curvilinear area determination. In Figure 5 we given an example of the area tessellation algorithm applied to a section of an orbit from 10/10/96 over Antarctica. There are just two values in the database (one for ocean, the other for ice). The variety of area-weighted albedos near the ice shelf boundary ensures that representative AMFs are returned for these footprints.

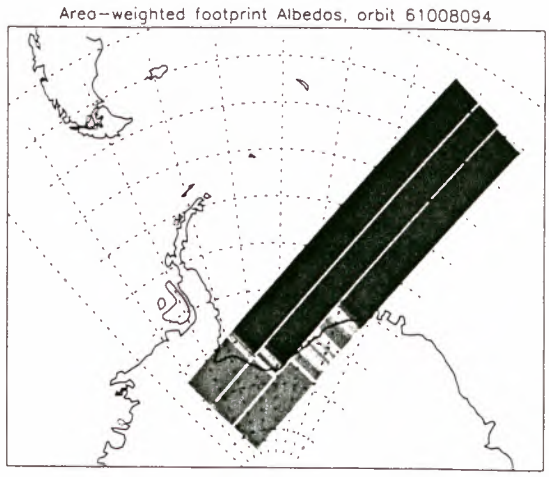

Figure 5. Footprint average albedos near Antarctic ice shelf, 10/10/96. Red 75%, black 5%.

3. NO_2 Air Mass Factors

3.1 Introductory Remarks

For an NO_2 DOAS retrieval from measurements in the visible part of the spectrum (425-450 nm), it is sufficient to compute the AMF at a single wavelength (437.5 nm). Ideally for GOME, we require a global climatology of NO_2 profiles as an auxiliary database. GDP currently uses the single USA-standard atmosphere NO_2 profile that may be completely unrepresentative of the actual NO_2 burden. NO_2 profiles have been measured in the stratosphere by a number of limb and occultation instruments but there is no global climatology. The nearest equivalent is the database of NO_2 profiles derived from occultation measurements by the UARS HALOE instrument [6].

Tropospheric NO_2 is variable; boundary layer amounts are especially dependent on local sources of combustion (industrial, automotive, biomass burning, etc.). To date, it has proved impossible to generate any sort of tropospheric climatology based on sets of ground-based measurements. Unfortunately the AMF for NO_2 is sensitive to the tropospheric burden. This source of uncertainty, in addition to the slant column error from the spectral fitting, may be enough to seriously compromise the accuracy of the desired

vertical column result. Here we indicate a solution to this problem for a global remote sensing application.

First we attempt to create a convenient and simple 'analytic' NO_2 profile climatology (section 3.2). A profile is constructed by piecing together sections of analytic curves; parameters for stratospheric curves may be inferred from HALOE data. Next (section 3.3) we describe a look-up table of NO_2 AMFs based on this climatology, and examine the dependence on ground-level concentration (a free parameter in the climatology choice). Finally in section 3.4, by allowing this parameter to vary, we find an iterative solution for the AMF (and hence the vertical column result) which matches the NO_2 burden implicit in the slant column value. This process also provides an estimate of the ground level concentration.

3.2 Towards an NO_2 climatology

We examine a set of stratospheric NO_2 profiles from a year's worth of HALOE sunrise and sunset occultation events. Retrieved profiles of pressure, temperature and NO_2 volume mixing ratios are given at a resolution of ~0.3 km, from a top height of about 54 km down to the upper troposphere (~9 km). Profile retrieval errors below the tropopause are too great for the results to be reliable. Number density profiles and total column amounts (plus error estimates for both) may be derived easily from the retrieval data. Concentration profiles show a characteristic maximum (25-33 km, depends on latitude) and fall off to a minimum around the tropopause. There is little longitudinal variation, and large-scale zonal variations are relatively smooth. Figure 6 shows concentration extreme values for NO_2 profiles retrieved for a number of events in early 1997.

In constructing an analytic climatology for stratospheric NO_2 based on this data, we make some simplifying assumptions. First, profiles from the top of the atmosphere down to the tropopause are approximated by two curves $P_I(z)$ and $P_{II}(z)$, with profile and gradient continuity at the transition height $z=z_2$. The second assumption is that the profile can be accurately reproduced (at least from the viewpoint of AMF computation) determined by a small set of parameters taken from an examination of the HALOE profiles. This parameter set comprises the profile maximum concentration C_0 at height z_0, the tropopause minimum concentration C_1 at height z_1, and the total column content U (down to height z_1). Errors $E(C_0)$, $E(C_1)$ and E(U) can be determined readily from the HALOE standard deviation data. We assume that the curves P(z) have the generalized distribution function (GDF) shape, expressed by

$$P(z) = P_0 + \frac{\omega \exp[-\beta(z - z_0)]}{(1 + \exp[-\beta(z - z_0)])^2} \qquad (8)$$

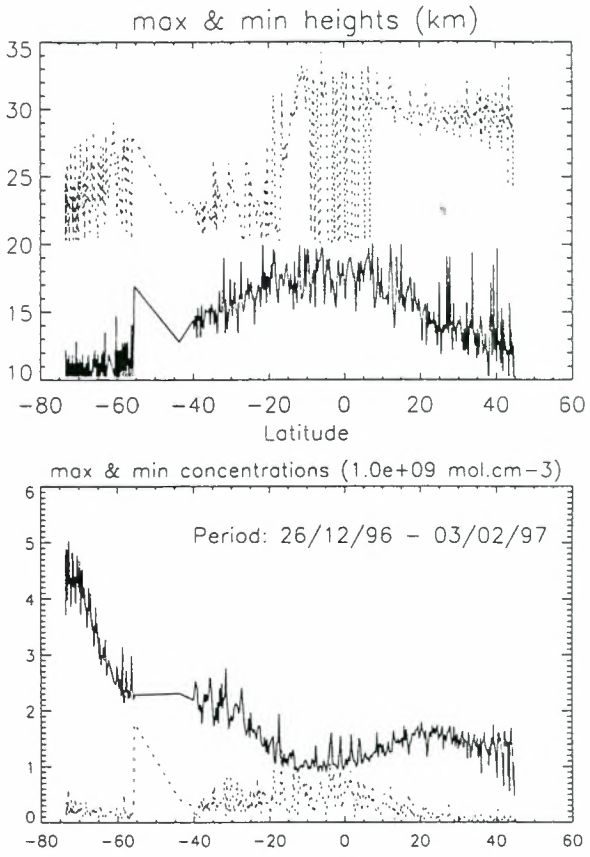

Figure 6. Maximum and minimum concentrations of NO_2 for HALOE occultation events from 26/12/96 to 03/02/97. Also shown are the heights of occurrence.

The GDF function is characterized by the 3 parameters $\{P_0,\omega,\gamma\}$ and an abscissa z^* at which the function reaches an extreme. We take the upper curve $P_I(z)$ with its maximum value C_0 at $z=z_0$; also, $P_I(z)$ vanishes as z goes to space. $P_{II}(z)$ has the minimum value C_1 at height $z=z_1$. Function and gradient continuity at $z=z_2$ provide two equations for parameter determination. A third is provided by the column constraint (U is the integral of P(z) from space to the tropopause height z_1). The value of z_2 may be set by imposing a shape constraint (curves should look same at the changeover). The derivation of z_2 and parameters that characterize $P_I(z)$ and $P_{II}(z)$ is straightforward. In determining error bars for these profiles, we assume that z_2 is fixed and that uncertainties depend only on errors $E(C_0)$, $E(C_1)$ and E(U) through the Gaussian error propagation law. A profile error covariance matrix can be constructed

from these errors and from suitable Jacobeans of transformation.

For the tropospheric part, we assume the concentration C_g at ground level $z=z_g$ is the only free parameter determining the distribution. We use again two GDF curves $P_{III}(z)$ and $P_{IV}(z)$, with function and gradient continuity at a second changeover height $z=z_3$ in the troposphere. We assume the concentration reaches its maximum value at ground level, and we require continuity with the stratospheric curve $P_{II}(z)$ at the tropopause minimum height $z=z_1$. To determine z_3 and the appropriate GDF parameters, we again impose continuity and shape conditions; and the solution is similar to that derived for the first curves. (Tropospheric profiles are dependent on the choice of HALOE-derived parameters). Figure 7 shows analytic profiles for a single HALOE parameter set, and for 5 values of ground concentration.

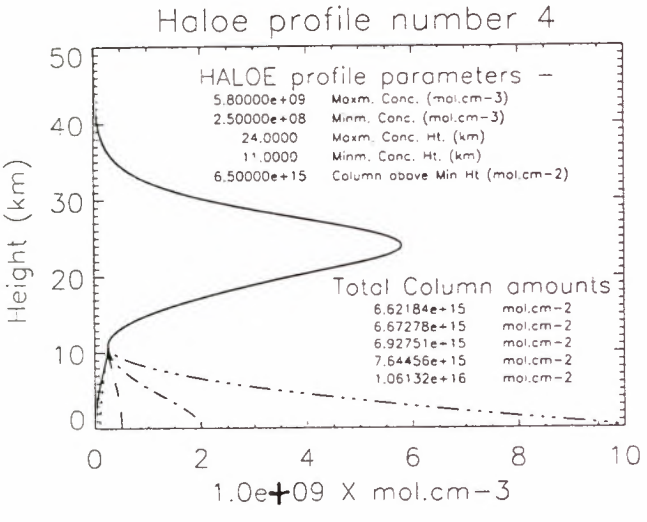

Figure 7. Analytic profiles for a single set of HALOE-derived stratospheric parameters, and for 5 tropospheric ground level concentrations.

The assumptions above for the tropospheric profile represent just one possibility. A number of other profile shapes should be considered, as it turns out that the AMF is sensitive to profile shape and loading in the troposphere (J.C. Lambert, private communication).

3.3 Look-up tables and tropospheric dependence

AMFs for NO_2 are calculated in a similar manner to those for O_3. The definitions in section 2.2 are relevant, and the classification system is similar. We use 16 solar zenith angles from 16° to 92°, 8 line of sight zenith angles, and 6 albedos and lower boundary heights as before. Again we can compute AMFs directly or store the Fourier cosine harmonic components of intensity to deal with azimuth angle dependence. We compute AMFs for 5 profiles parameterized in Table 1, and for 5 different values of tropospheric ground level concentration (total 25 profiles in complete data set).

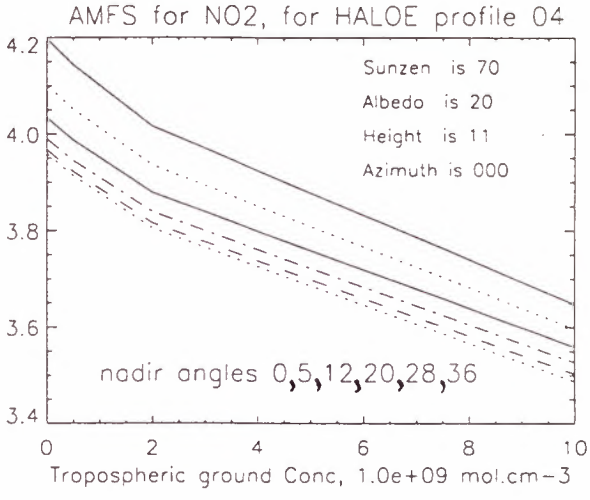

Figure 8. AMF dependence on NO_2 column content for 5 tropospheric burdens. Sun zenith 70°, 6 nadir zeniths, albedo 0.2, azimuth 0°.

Extraction of AMFs from the look-up table proceeds as before. 4-point Lagrangian interpolation is performed for the determination at intermediate solar and line-of-sight zenith angles, while linear interpolation is again sufficient for height and albedo values. The recovery of AMF parameter derivatives follows in the same way (derivatives of the optical depths are also stored in an auxiliary data set).

Figure 8 shows the dependence of the AMF on profile column amount for one choice of HALOE stratospheric profile, and for the choice of geometry and height/albedo indicated. It is clear that AMFs are strongly dependent on ground-level concentration (and thus on total column amount). Similar values for other profiles indicate that the AMFs are only weakly dependent on the stratospheric HALOE-based parameterization.

3.4 Vertical column computation

The calculation here is preliminary. One may use the vertical column formulation to iterate on the AMF in the manner suggested earlier for O_3. So far this works well for cloud-free cases, but problems have been encountered with the first-order cloud correction formula as used for the O_3 tropospheric correction

(equation (5)).

An alternative is to use an equivalent Lambertian approach, which has been used in a number of TOMS applications (see [8] and references therein). An effective Lambertian albedo for the footprint as that value of the surface albedo that generates a simulated intensity at 380 nm equal to the measured intensity at this wavelength. The simulations are done in an atmosphere with trace absorption and molecular scatter (look-up tables are suitable for the albedo determination). This equivalent albedo is then used as the baseline in the AMF extraction.

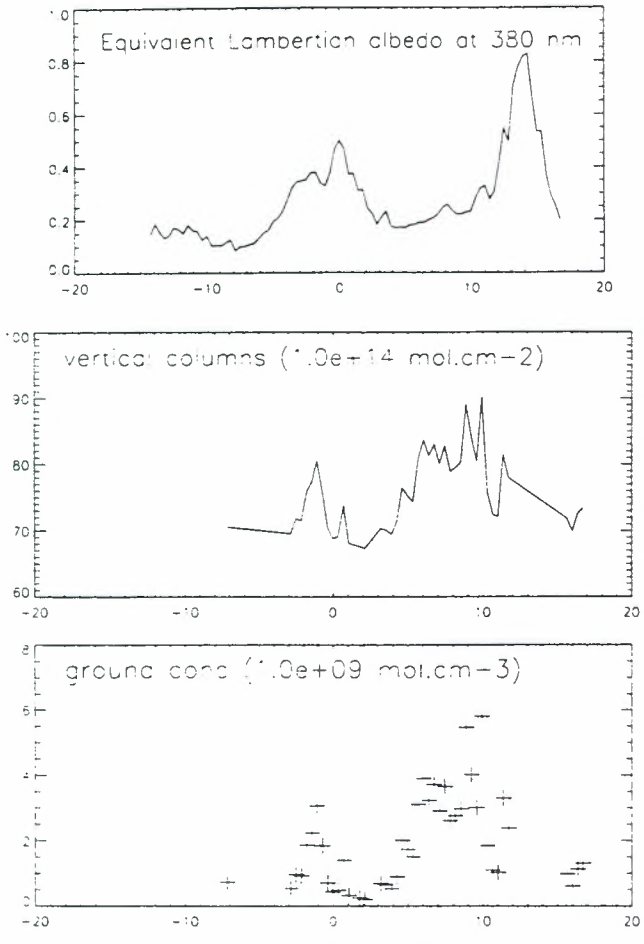

Figure 9. NO_2 columns and ground concentrations for part of orbit 70927024 over S. E. Asia. Note also the equivalent Lambertian albedos

If the stratospheric part of the profile is assumed known, then the variation of AMF with the free ground level concentration parameter may be used to iterate the vertical column. The use of an analytic form for the profile shape provides a simple relationship between the ground level concentration and the vertical column. Thus the tropospheric ground level concentration emerges as an adjunct to the vertical column retrieval. Figure 9 illustrates these computations for part of an orbit over tropical SE Asia, at a time of biomass burning (27 September 1997, center pixels over Borneo near the equator). The general level of NO_2 is high. Note the large dip in slant column values for pixels with total or near total cloudiness – in these cases GOME misses the NO_2 boundary layer amount below the cloud layer.

The initial examination of HALOE data presented here will be extended to cover all the data, and an examination of tropospheric profile shapes and AMF dependence is required. An extensive table of AMFs will be created so that the vertical column estimation (and ground level concentration) can be made effective on a global basis. This work will be done in conjunction with improvements in the fitting for NO_2 slant columns. It should then be possible to validate re-processed NO_2 results and upgrade the level 2 product.

4. REFERENCES

[1] GOME User's Manual, European Space Agency, SP-1182 (1995)

[2] GOME Level 1 to 2 Algorithm Description, ER-TN-DLR-GO-0025, Issue 2, (August 1996)

[3] K. Chance, R. Spurr and T. Kurosu, Atmospheric Trace Gas Measurements from GOME and SCIAMACHY, this conference

[4] C. G. Wellemayer, S. L. Taylor, C. J. Seftor, R. D McPeters and P. K. Bhartia, A Correction for TOMS Profile Shape Errors at High Latitude, J. Geophys. Res. 102, 9029 (1997)

[5] V. Rozanov, D. Diebel, R. Spurr and J. Burrows, GOMETRAN: A Radiative Transfer Model for the Satellite Project GOME - the Plane Parallel Version, J. Geophys. Res., 102, 16683 (1997)

[6] L. Gordley et. al., Validation of Nitric Oxide and Nitrogen Dioxide Measurements Made by HALOE for the UARS Platform, J. Geophys. Res., 101, 10241 (1996)

[7] D. Loyola, Using Artificial Neural Networks for the Calculation of Air Mass Factors, this conference

[8] O. Torres, P. K. Bhartia, J. R. Herman, Z. Ahmad, and J. Gleason, Derivation of Aerosol Properties from Satellite Measurements of Backscattered Ultraviolet Radiation: Theoretical Basis, J. Geophys. Res., 103, 17099 (1998)

Acknowledgements. The author would like to thank Albrecht von Bargen and Werner Thomas of DLR for helpful discussion on O_3 AMFS, and Ken Jucks at SAO for stimulating feedback on the NO_2 climatology.

Retrieval of carbon monoxide, methane and nitrous oxide from SCIAMACHY measurements

Hans Schrijver

SRON, Sorbonnelaan 2, 3584 CA Utrecht, The Netherlands

ABSTRACT

SCIAMACHY's channel 8 covers the wavelength range 2265–2380 nm (with resolution 0.27 nm) and will allow the global determination of concentrations of methane, carbon monoxide and nitrous oxide. Sensitivity studies using the most recent values for the instrument parameters have shown that the minimum values for the accuracies for total vertical columns (as determined by the noise) are of order 5 Dobson units (DU) for carbon monoxide, 3 DU for methane, and 6 DU for nitrous oxide, for a 1 s SCIAMACHY nadir observation and ground albedo 0.3. Using data from small spectral windows only increases these values by a factor of 4–5.

The detection of the infrared spectra features novel InGaAs detectors, specially developed for the SCIAMACHY project. While providing the required sensitivity in this wavelength domain, these detectors are limited by noise levels (mainly due to dark current and thermal background) that vary strongly from pixel to pixel. This poses special challenges to the retrieval of molecule concentrations from the measured detector signals.

The retrieval process is hampered by a lack of knowledge on the spectroscopic parameters. This situation is expected to improve in the near future.

1. INTRODUCTION

SCIAMACHY will be able to measure atmospheric spectra in nadir, limb, and (solar and lunar) occultation in 8 channels (each comprising 1024 detector diodes) covering the spectral ranges 240–1750 nm (channels 1–6), 1940–2040 nm (channel 7), and 2265–2380 nm (channel 8), with resolutions down to 0.22 nm (FWHM).[1-9]

In this paper, the focus is on channel 8, measuring with a resolution of about 0.27 nm (FWHM) in a wavelength region where the absorption spectrum is almost entirely determined by the molecules H_2O, CH_4, CO, and N_2O. The vertical trace gas column retrieval precision is dependent on many factors. In practice, however, it will be dominated by the noise generated by the dark current of the detector and the instrumental thermal background. In a realistic retrieval, the eventual accuracy may also be determined by factors external to the instrument: knowledge of a priori physical quantities, clouds, variations over the scene. In other words, the retrieval precision will be dependent on the extent that these effects can be accurately modelled in the forward model.

In the first part of this paper, an answer is sought to the question: what is the contribution of the instrument to this accuracy, in other words: what are the limits to the sensitivity of SCIAMACHY channel 8 brought about by the detector noise, even with the best retrieval methods?

In order to answer this question model spectra for a number of scenarios have been computed, involving various model components for gas distribution, radiative transfer, and the instrument. A convenient method to relate the expected instrument noise values to limits in sensitivity is to compute Cramér-Rao limits by inverting the Fisher matrix.[11] Besides giving an estimate of the minimum retrieval precision, the non-diagonal elements give an indication of the expected correlations.

An early assessment by Mewe[12] of the measurement sensitivity of SCIAMACHY for these species resulted in values of 0.5% for CH_4 and 2.6% for CO. Other results, obtained using preliminary values for the instrument parameters have been reported by Chance et al.,[13] Schrijver et al.,[14] Roemer et al.,[15] and Schrijver et al..[16] The results presented here use definitive values for the instrument parameters as far as available, and differ from those previously reported mainly because of a larger entrance slit width, improved noise characteristics of the detector, a lower quantum efficiency for the longest wavelengths, a corrected spectral resolution, and the inclusion of the effects of the so-called dead and bad pixels.

In the second part of the paper, some of the problems to be addressed in the development of the forward model are dealt with. The detection of the infrared spectra in SCIAMACHY is done using a novel InGaAs detector system built and characterised at SRON. It has been shown to provide the desired sensitivity in the relevant wavelength domain. The sensitivity is limited by a noise level caused by instrumental thermal background and dark current. Moreover the noise level related to dark current varies considerably from (detector) pixel to pixel. In addition a small number of pixels appear to be non-respondent ('dead'). This poses special requirements to the retrieval process. Details are given in section 3.2.

Spectroscopic knowledge in the relevant wavelength region, such as line strengths, temperature and pressure dependency is far from complete, as was already noticed in the SCIAMACHY Scientific Requirements Document. This problem is discussed in section 3.3

2. SENSITIVITY OF THE NOMINAL INSTRUMENT

2.1. Method

The measured spectrum is read out in 1024 detector pixels. The signal eventually measured in these pixels is a complicated function of all physical and instrumental parameters contributing to the measured result: extraterrestrial solar irradiance, atmospheric properties, earth surface albedo, observation geometry, optical and electronical properties of the instrument. In this paper, for a selected choice of most of these parameters, the effects of variations in the concentrations of the four gases that contribute to SCIAMACHY channel 8 will be investigated. More precisely, while keeping the relative distribution over the column fixed, the effect of changes in the total column amount will be studied.

Thus the expected contents of pixel k can be written as a function of the four total column amounts:

$$I_k = f(n_{H_2O}, n_{CH_4}, n_{CO}, n_{N_2O}, \alpha) \tag{1}$$

where the n's are the total column amounts of the various gases, and α stands for all other parameters, kept fixed in this analysis.

The computed noises ϵ_k in the pixels can be translated back to a variation in the n's by computing the Fisher (or information) matrix **F**, the elements of which can be shown (for Poisson noise) to be:

$$F_{ij} = \sum_k \frac{\partial I_k}{\partial n_i} \frac{\partial I_k}{\partial n_j} \epsilon_k^{-2} \tag{2}$$

where the sum can be over all or over a subset of the pixels. The inverse of this (4 × 4) matrix is the Cramér-Rao matrix; its diagonal values give the Cramér-Rao limits for the estimation of the values of n from observations I_k with noise ϵ_k. The non-diagonal elements are estimates of the covariances, and hence of the correlations between the n's. For probability distributions such as the Poisson distribution, it can be shown that the Cramér-Rao limit is a good estimate for the real (co-)variances following from the statistics of the noise. But it presents a lower limit in the sense that systematic effects introduced by modelling errors are not taken into account, so the final accuracy of the results, in general, will be worse. In the context of this paper a change of three times the Cramér-Rao limit (3σ) is considered to be the minimally detectable change in the concentration.

The computation of the expected SCIAMACHY detector signal involves three main steps. First, one needs a model of the distribution of the relevant molecules in the atmosphere. Then, the problem of radiative transfer from the original extraterrestrial solar spectrum through the atmosphere (downwards and upwards, including the scattering) must be solved. Finally, the radiance arriving at the entrance of the instrument must be translated into detector pixel counts.

The vertical distribution of the various species in the atmosphere is taken from results from the two-dimensional model of TNO.[17,14,15] The results have a north-south resolution of 10 degrees and a vertical resolution of 1 km, and they are available for all months of the year.

For observations in nadir mode, the geometry of the problem follows from the date of observation and the geographical latitude (as related to the distribution model). The orbit and attitude rules of Envisat fix the local mean solar time of the nadir point for a given latitude. This allows to compute the solar zenith angle for the observation, taking into account the equation of time. The date also fixes the sun distance, and hence the absolute value of the extraterrestrial solar irradiance.

As discussed in Refs. 14,15, the radiative transfer can be computed by running the line-by-line program FASCODE[18] twice, the first time to compute the transmission $T_s(\lambda)$ along the path from the sun to the earth surface, and a second time for the transmission $T_n(\lambda)$ along the path from the surface to the satellite. The line list fed to FASCODE is provided by the HITRAN 1996 database.[19] The spectral radiance at the top of atmosphere I_λ may be calculated as:

$$I(\lambda) = S(\lambda) R_\odot^{-2} T_s(\lambda) \cos(\theta) A \pi^{-1} T_n(\lambda), \tag{3}$$

where $S(\lambda)$ is the solar irradiance for a sun distance of 1 astronomical unit (as provided by the MODTRAN program[20]), $R_\odot$ is the distance of the sun in astronomical units, θ the solar zenith angle, and A the albedo of the earth surface. This procedure has been validated using results from MODTRAN. Although this procedure neglects scattering, extensive comparison with MODTRAN results has shown that reliable results can be obtained using an 'effective' albedo,[15] that corrects for the effects of scattering. Typical values for such an effective albedo are in the range 1.1–1.3 times the ground albedo.

The GOME/SCIAMACHY instrument software simulator (ISS) developed by SRON[21] has been used for the computation of detector pixel contents and signal-to-noise ratios from the computed radiances. The ISS simulates all optical and electronical components of the SCIAMACHY instrument; a so-called travelling spectrum is passed through consecutive modules representing the components. The physical parameters of each component are continuously updated as new calibration and characterisation results become available. The output of the version of the program used in this investigation consists of the computed detector spectrum and its associated noise level. For the computations a detector dark current level of 30 fA, and an instrument thermal background resulting in a detector background signal of 150 fA have been assumed. These values correspond to a detector

temperature (for infrared channels 7 and 8) of 150 K and a spectrometer optical unit temperature of 253 K. The dark signal values are slightly overestimated, but on the other hand, the real dark current is variable from (detector) pixel to pixel (see section 3.2). Higher values of the noise lead to larger statistical errors (higher values of the sensitivities), so that the values of the latter will be on the safe side. A spectral resolution of 0.27 nm FWHM has been assumed; this corresponds to the value of 2.1 detector pixels currently applicable (after the refocusing activities aimed at improvement of the degraded spectral resolution that became evident in the calibration period).

In order to produce the present results, the so-called dead and bad pixels (cf. section 3.2) have been excluded from the computations.

In Table 1 the sensitivities (expressed in Dobson units) for a 1 s SCIAMACHY observation in nadir mode for various geographic latitudes and times of the year are presented, assuming a ground albedo of 0.3, and assuming that all detector pixels are contributing to the sensitivity (i.e., the sum in Eq. 2 is from 1 to 1024). These values can be compared with typical values of the total vertical column of 1300 DU for CH_4, 250 DU for N_2O and varying from 20 DU in southern summer to 120 DU in northern winter for CO.

It appears that sensitivities do not strongly depend on latitude or time of year; differences are mainly related to differences in solar zenith angle.

Except for very high values of the earth albedo, detector noise is dominated by instrument noise (and not by earthshine photon shot noise, cf. Figure 2). As a consequence, the sensitivities are approximately inversely proportional to the earth albedo, as is illustrated in Table 2 for one of the cases of Table 1.

In this spectral region, low albedos are expected over water and snow, whereas the albedo will be 0.3–0.4 over soil and vegetation. Higher albedos can be expected for clouds, but in this case only part of the atmosphere is sounded, either the upper atmosphere in the case of continuous thick cloud cover, or a fraction (variable with height) of the full vertical column in the case of partial cloud cover, or semi-transparent clouds like cirrus. A good estimate of the air mass contributing to the absorption might be obtained by estimating the absorption by CO_2 from SCIAMACHY channel 7 (1940–2040 nm). Additional

Table 1. 3-σ sensitivities for SCIAMACHY nadir observations of 1 s exposure time for different geographic latitudes, times of year, and a ground albedo of 0.3, expressed in Dobson units. The corresponding solar zenith angles (SZA) are included.

Month	Latitude	SZA	CO [DU]	CH_4 [DU]	N_2O [DU]
Jan	50° N	73°5	7.5	4.7	5.6
	0°	38°0	5.9	2.6	4.6
	40° S	38°8	5.4	2.3	4.4
Apr	50° N	42°3	5.3	2.4	4.3
	0°	31°6	5.8	2.5	4.6
	40° S	61°4	6.1	3.1	5.0
Jul	50° N	33°5	5.6	2.5	4.5
	0°	37°3	6.2	2.7	4.9
	40° S	70°9	6.7	4.1	5.5
Oct	50° N	61°1	6.5	3.3	5.1
	0°	27°9	5.6	2.4	4.5
	40° S	42°6	5.0	2.2	4.2

Table 2. 3-σ sensitivities for a 1 s SCIAMACHY nadir observation at 50° north in July for different values of the ground albedo, expressed in Dobson units.

Albedo	CO [DU]	CH_4 [DU]	N_2O [DU]
0.01	152	64	110
0.03	51	22	37
0.1	16	6.8	12
0.3	5.6	2.5	4.5
1	2.0	0.9	2.1

information on cloudiness may be gained from SCIAMACHY's polarisation measurement devices which sample the ground pixels with a higher spatial resolution.

Retrieval using all detector pixels assumes that spectroscopic line parameters (wavelengths, line strengths, broadening parameters) are available with good precision for all lines in the relevant spectral range. Imperfect knowledge of these parameters obviously introduces additional errors, because of under/overestimation of the total absorption, and by correlation effects between the different molecules. Unfortunately, for the wavelength region considered, knowledge of the spectroscopic data is inadequate. Details can be found in section 3.3.

A way to overcome this problem is to select small windows where (almost) isolated and well known lines are available. The disadvantage of such an approach is clearly less sensitivity, since only a part of the statistical information is used. Also, there is a more critical dependence on the good functioning of the relevant detector pixels (cf. section 3.2). In Table 3 minimum sensitivities are reported that may be expected for the spectral windows now selected for the standard near-real time retrieval of CO, CH_4, and N_2O from SCIAMACHY data in the operational processing employed for the Envisat data product (R. Spurr, private communication).

Sensitivities are reduced considerably when using the spectral windows, with values higher by factors 4 to 20. It should also be noted that the correlation between N_2O and H_2O becomes rather strong (about -0.8) compared to -0.25 in the full detector case; in the latter case the strongest correlation is between CH_4 and H_2O (about -0.6). The determination of the N_2O vertical column may therefore become sensitive to the precision of the result for H_2O.

It is instructive to examine the matrix $K_{ki} = \partial I_k / \partial n_i$, i.e., the sensitivity of the detector pixels (labeled k) for changes in the column amounts of the four species (labeled i); see also Eq. 2. An example is shown in Figure 1. This matrix makes clear which pixels contain information on a species, and what fraction of sensitive pixels fall within the small spectral windows.

The conclusion is that restricting the retrieval to small spectral windows will considerably reduce the accuracy of the results. It seems necessary to find an optimal retrieval strategy between the two above extremes of using either the entire detector pixel array for retrieval, or only a small fraction. By applying a sophisticated pixel-to-pixel weighting scheme which takes into account the level of accuracy of the spectroscopic data such an optimum might be found.

3. FORWARD MODEL

3.1. Instrumental effects

All the above results have been derived for a nominal instrument. This represents the instrument as built knowing the calibration and characterisation results up to this moment in time, with one exception: the detailed noise characteristics of the detector have been represented by average values (as quoted in section 2.1).

As an example, Figure 2 shows a simulated detector spectrum , together with the computed noise level, for the above nominal detector. The main contributing terms to the total signal (instrument thermal background, detector dark current, and earthshine spectrum) are displayed in a cumulative fashion. The good signal-to-noise ratio is apparent.

Table 3. 3-σ sensitivities for SCIAMACHY nadir observations of 1 s exposure time for different geographic latitudes, times of year, and a ground albedo of 0.3, expressed in Dobson units, for a partial spectral window (2269.0–2275.3 nm for N_2O, and 2359.5–2366.0 nm for CO and CH_4) as selected for producing the operational Envisat data product. Results should be compared with those in Table 1.

Month	Latitude	SZA	CO [DU]	CH_4 [DU]	N_2O [DU]
Jan	50° N	73°.5	24	80	26
	0°	38°.0	23	44	21
	40° S	38°.8	20	37	22
Apr	50° N	42°.3	19	37	22
	0°	31°.6	22	43	21
	40° S	61°.4	21	52	25
Jul	50° N	33°.5	21	40	21
	0°	37°.3	24	47	22
	40° S	70°.9	22	70	27
Oct	50° N	61°.1	23	56	25
	0°	27°.9	21	40	20
	40° S	42°.6	17	34	21

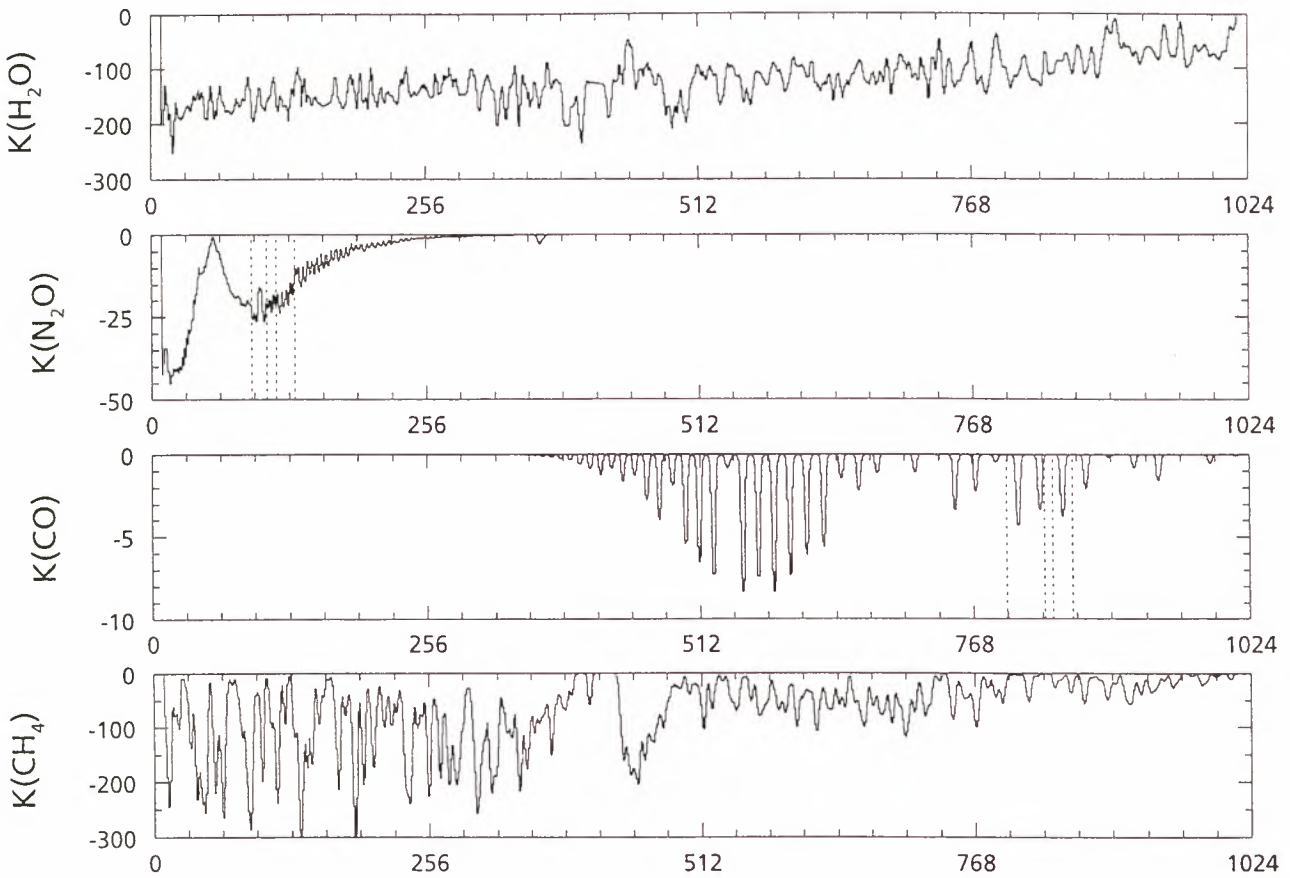

Figure 1. Sensitivity of detector signal to variations in column amount of the various species ($K = \partial I_k / \partial n_i$, arbitrary units), not modelling dead and bad pixels. The dashed lines indicate the windows selected for the retrieval of the operational (near real-time) CO and N_2O products.

3.2. Noise characteristics

The SCIAMACHY detector units built and characterised at SRON feature novel InGaAs diode arrays for the infrared channels. These arrays have rather complex noise properties. First, the detector dark current (with an overall level which depends on the voltage bias applied, and which is close to the value assumed in the computations presented in the previous sections) varies considerably from pixel to pixel, and so does the associated shot noise. About 80 ('dead') pixels out of 1024 do not or hardly respond to photons. Furthermore, about 80 ('bad') pixels have a much higher noise level or another quantum efficiency than specified, and must be considered unsuitable for scientific return.

Figure 3 reproduces Figure 2, but now taking into account these effects. All three identified effects are clearly visible.

The following conditions have to be fulfilled for a reliable retrieval given the detector characteristics: 1) the dark current must be sufficiently stable, and well calibrated as a function of detector temperature. A realistic estimate of variations must be introduced as a noise term in the retrieval process. Note that, in general, much time is available at the night side of the earth to perform dark measurements. Note also that the instrument thermal background may vary with instrument temperature, but its variable part may be accounted for by fitting a low-order polynomial over the detector. 2) Dead and bad pixels must be excluded from the retrieval procedure, although it might be possible to include some of the bad pixels at a lower weight.

Now that the precise wavelength registration of the detector has been measured, it has become possible to estimate the sensitivities including the effects of dead and bad pixels. As was expected, the results for the case where the entire detector is taken into account is only marginally influenced (a few percent).The results for spectral windows do not change too strongly (in the unfavourable sense) by coincidence of dead or bad pixels with crucial spectral lines.

3.3. Spectroscopic data

It has been known since the early phases of the SCIAMACHY project that the current level of knowledge on spectrocsopic data such as line identification, line strength, influence of temperature and pressure is well below what would be desirable for an

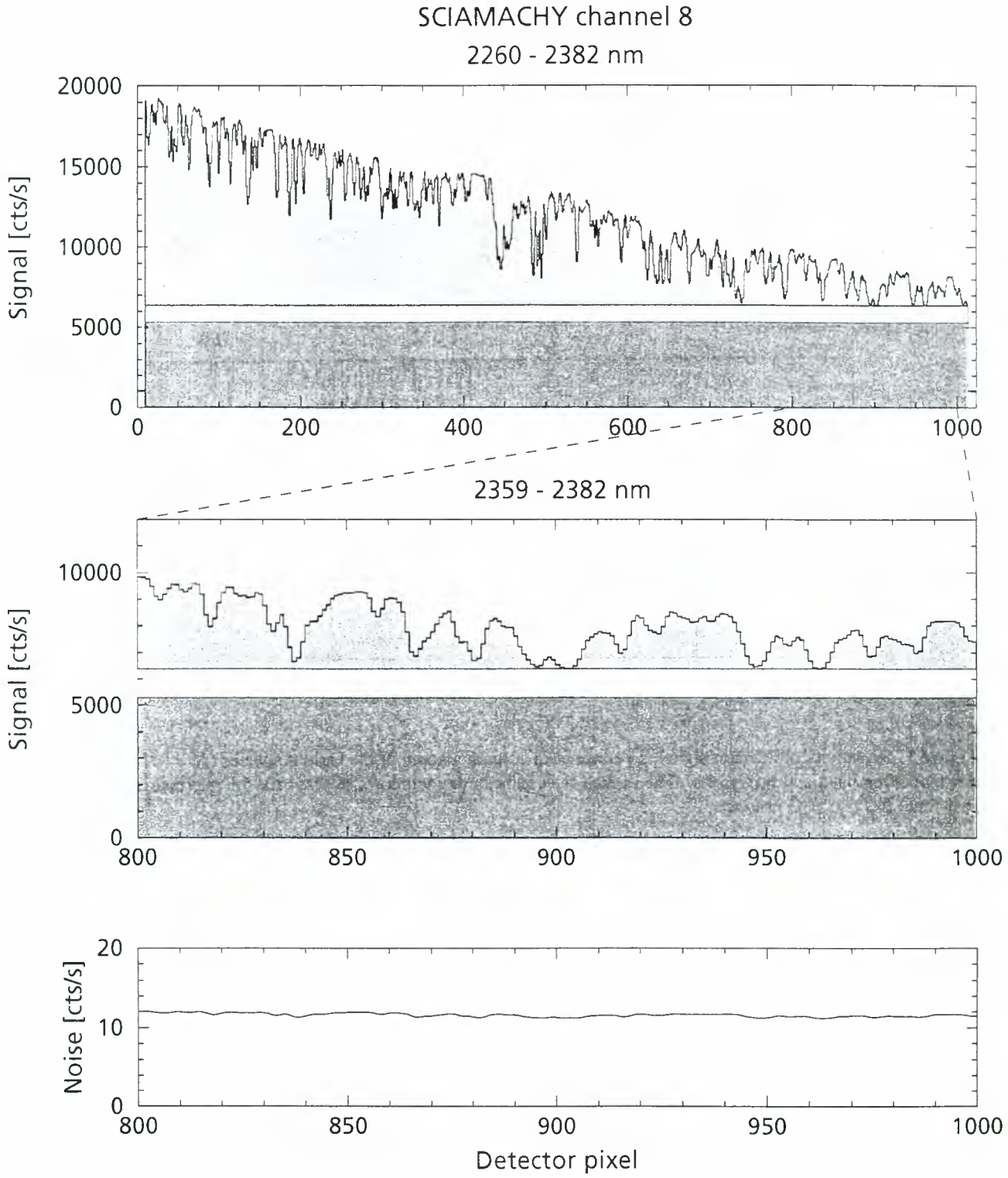

Figure 2. Simulated detector signal (upper two panels) and noise level (lower panel) for the instrument with nominal detectors for northern hemisphere summer and albedo 30%, solar zenith angle 33°.5. The total expected detector signal is represented by the upper curve (in the upper two panels). The main contributions to this signal (instrumental thermal background , detector dark current , and earthshine spectrum) are indicated separately, in a cumulative fashion. For clarity, the middle panel shows a zoom into a part of the detector (corresponding to 2359–2382 nm). The lower panel refers to the same range. In this region, absorption lines from CH_4 and CO reside.

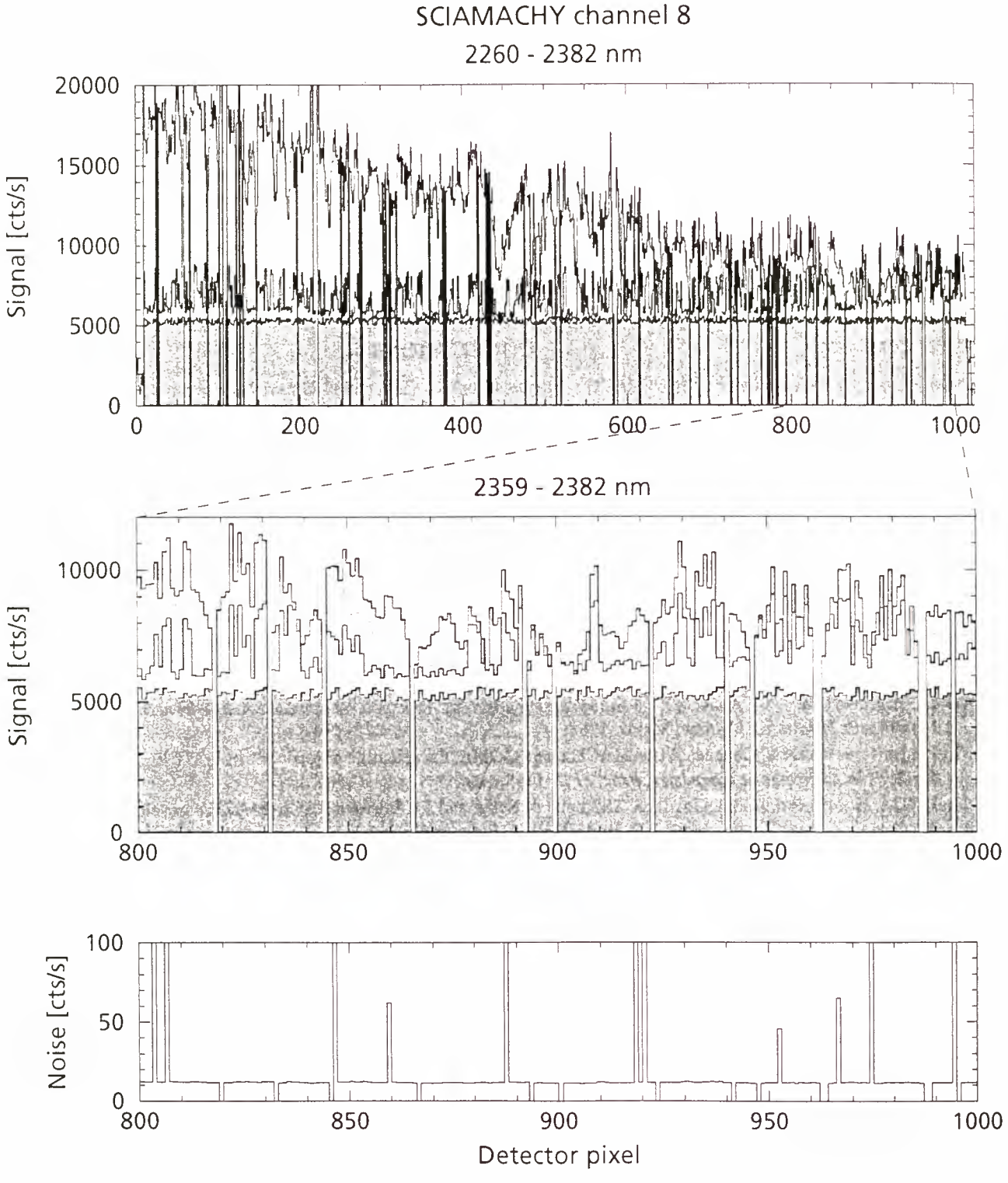

Figure 3. As Figure 2 but for a simulation with the real detector, showing the effects of dead pixels, noisy pixels, and the pixel-to-pixel variation of both detector dark current and sensitivity to thermal background.

accurate retrieval. The information has been collected in the SCIAMACHY Scientific Requirements Document and is copied in Table 4. The approximate numbers of known lines represent all lines in this wavenumber domain irrespective of their line strength; as a consequence the number of lines relevant for the retrieval may be lower.

The importance of an accurate knowledge of line data can be recognised from Figure 4. It is apparent that the atmospheric spectra in the studied wavelength region are dominated by water and methane. Relatively small errors in the modelling of lines of the latter species may influence considerably the interpretation of the faint lines of carbon monoxide and nitrous oxide.

Fortunately, there is some improvement to be expected. First, after the on-ground calibration period, the SCIAMACHY flight model has been used to measure gas cell spectra of the various species, together with atmospheric measurements. These measurements have the advantage of being taken with the instrument itself; but they give no insight in the underlying spectral structure. Second, the University of Bremen plans to perform comprehensive high-resolution spectroscopy in this wavelength region. Third, the Free University of Amsterdam (W. Ubachs) is planning to extend their 'cavity ring down' experiment, which has successfully obtained high-resolution water spectra in the visual range, towards the wavelength region of interest here, and measure spectra of the various species in windows to be selected in consultation with the retrieval algorithm development.

4. CONCLUSIONS

Lower bounds for the sensitivity of SCIAMACHY channel 8 for CO, CH_4, and N_2O have been computed using the most recent values of the instrument parameters. For a 1 s nadir observation, sensitivity values of order 5 Dobson units (DU) for carbon monoxide, 3 DU for methane, and 6 DU for nitrous oxide were derived. Due to uncertainties in the spectroscopic data, only part of the detector data can be used, resulting in less favourable values; an example for a particular choice of spectral windows shows a degradation of a factor of 4 for CO, about 20 for CH_4, and 1.5 for N_2O. This means that efforts should be devoted to include as much spectral information as is available from the detector. This may be achieved by i) improving the spectral line data base, and ii) careful selection and weighting of spectral windows during retrieval.

The impact of the specific noise and background characteristics of the InGaAs infrared detectors should be minimised by i) careful and systematic on-board calibration of the dark signal, and ii) 'switching off' or downweighting suspect pixels in the retrieval (for which ongoing on-board calibration is also a requirement).

REFERENCES

1. J.P. Burrows *et al.*, *'SCIAMACHY', A European Proposal for Atmospheric Remote Sensing from the ESA Polar Platform*, Max Planck Institut für Chemie, Mainz, 1988.
2. J.P. Burrows and K.V. Chance, "SCIAMACHY and GOME: the scientific objectives," in *EOS/SPIE, Int. Symp. on Optical Methods in Atmospheric Chemistry, Proc. SPIE* **1715**, 1992.
3. R.W.M. Hoogeveen, A.P.H. Goede, S. Slijkhuis, A. Selig, and J.P. Burrows, "SCIAMACHY development," in *EOS/SPIE, Int. Symp. on Space Optics, Garmisch-Partenkirchen, Proc. SPIE* , 1994.
4. J. Frerick, H. Bovensmann, S. Noël, J.P. Burrows, and M. Dobber, "SCIAMACHY on-ground/in-flight calibration, performance verification and monitoring concepts," in *Earth Observing Systems II, SanDiego, California, 28–29 July 1997, Proc. SPIE* **3117**, pp. 176–187, 1997.
5. H. Bovensmann, J.P. Burrows, M. Buchwitz, J. Frerick, S. Noël, and V.V. Rozanov, "The SCIAMACHY mission," in *Proceedings of the 4th European Symposium on Polar Stratospheric Ozone, Schliersee, Germany, 22–26 Sept 1997*, pp. 633–636, European Commission, DG XII, EUR 18032, 1997.

Table 4. Spectroscopic data knowledge in the 4130–4450 cm^{-1} wavenumber region (from the SCIAMACHY Scientific Requirements Document)

Molecule	Known lines	Remarks
H_2O	1100	accuracy 5–60%
CH_4	2000	accuracy 5–40%; no systematic spectroscopy; weak lines missing; many lines not identified
CO	500	accuracy 10%
N_2O	400	accuracy 5–40%; data obtained by a mixture of observations and (non-systematic) calculations

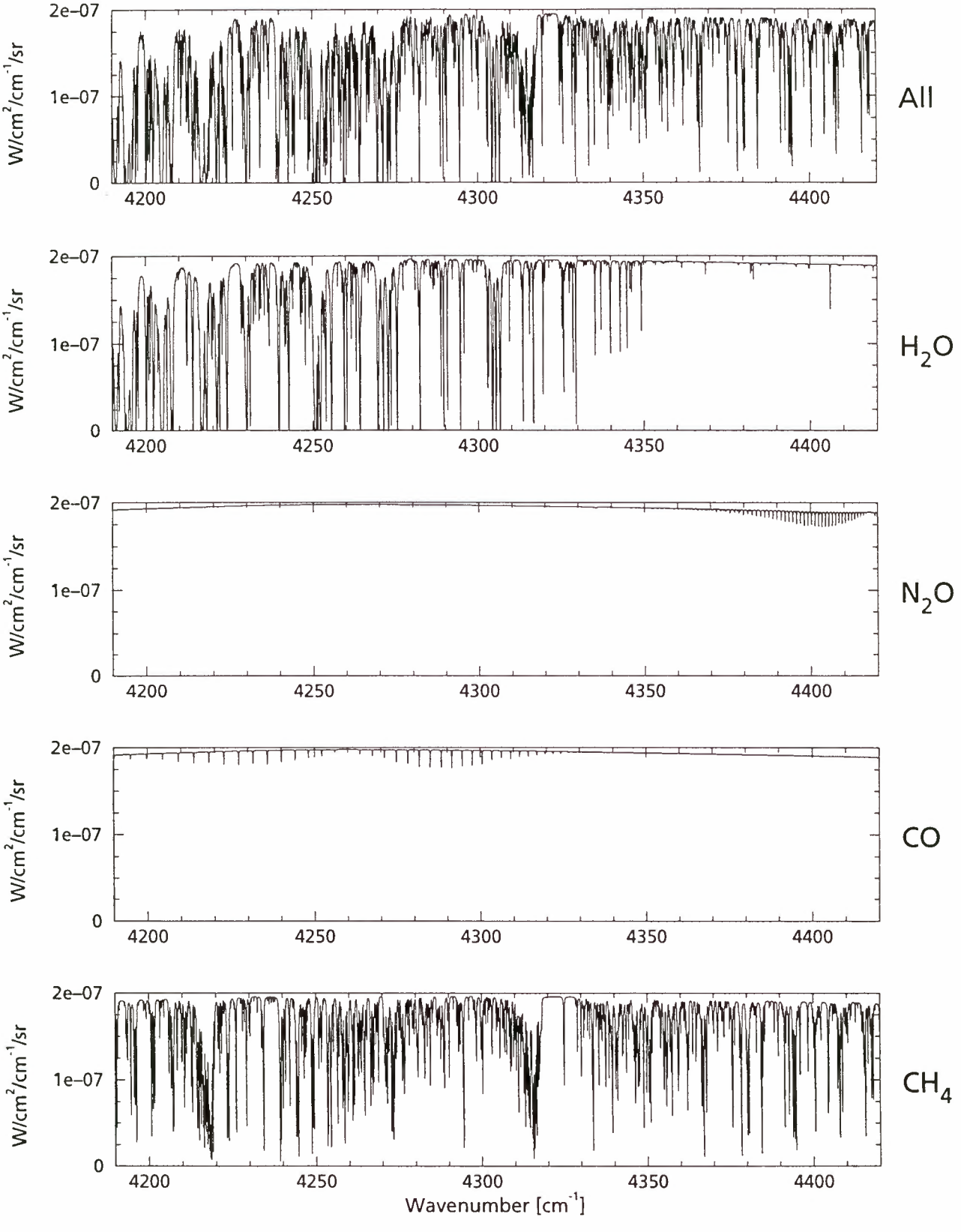

Figure 4. Top panel: typical atmospheric backscatter spectrum. Lower four panels: the same assuming that only one of the contributing species is present in the amount used for the computation of the spectrum in the top panel.

6. S. Noël, H. Bovensmann, J.P. Burrows, J. Frerick, K.V. Chance, and A.P.H. Goede, "Global atmospheric monitoring with SCIAMACHY." Presented at the symposium of the European Geophysical Society, Nice, 1998, submitted to Physics and Chemistry of the Earth.
7. H. Bovensmann, J.P. Burrows, M. Buchwitz, J. Frerick, S. Noël, V.V. Rozanov, K.V. Chance, and A. Goede, "SCIAMACHY - mission objectives and measurement modes." Submitted to Journal of the Atmospheric Sciences, GOMAC Conference special issue, 1998.
8. J.P. Burrows, "Sciamachy mission concept." This symposium, 1999
9. A.P.H. Goede, "Sciamachy instrument concept." This symposium, 1999
10. J.P. Burrows, "Sciamachy instrument performance." This symposium, 1999
11. M. Kendall and A. Stuart, *The Advanced Theory of Statistics, Vol. 2*, Griffin, London, 1979.
12. R. Mewe, in A.P.H. Goede *et al.*, *Voorstudie atmosferisch ruimteonderzoek*, BCRS 90-02, Delft, 1990.
13. K.V. Chance, J.P. Burrows, and W. Schneider, "Retrieval and molecule sensitivity studies for the Global Ozone Monitoring Experiment and the SCanning Imaging Absorption spectroMeter for Atmospheric CHartographY," in *Remote Sensing of Atmospheric Chemistry*, *Proc. SPIE* **1491**, pp. 151–165, 1991.
14. H. Schrijver, S. Slijkhuis, M.G.M. Roemer, and A.P.H. Goede, "Noise related limits on the detectability of concentration variations of CH_4 and CO with SCIAMACHY," in *Atmospheric Sensing and Modeling*, R. P. Santer, ed., *Proc. SPIE* **2311**, pp. 39–46, 1995.
15. M.G.M. Roemer, H. Schrijver, I. Aben, S. Slijkhuis, and A.P.H. Goede, *Analysis of the potential of CO and CH_4 measurements by SCIAMACHY for the validation of tropospheric models*, BCRS NRSP-2 96-36, Delft, 1998.
16. H. Schrijver, A.P.H. Goede, M.R. Dobber, and M. Buchwitz, "Retrieval of carbon monoxide, methane, and nitrous oxide from SCIAMACHY measurements," in *Optical Remote Sensing of the Atmosphere and Clouds*, J. Wang *et al.*, ed., *Proc. SPIE* **3501**, pp. 215–224, 1999.
17. M.G.M. Roemer and K.D. van den Hout, "Emissions of NMHCs and NO_x and global ozone production," in *Proc. 19th NATO/CCMS Int. Techn. Meeting on Air Pollution Modeling and its Applications, 29 Sept.–4 Oct. 1991, Crete, Greece*, van Dop and Kallos, eds., Plenum Press, New York, 1992.
18. H.J.P. Smith, D.J. Dube, M.E. Gardner, S.A. Clough, F.X. Kneizys, and L.S. Rothman, *FASCODE — Fast Atmospheric Signature Code (Spectral Transmittance and Radiance)*, AFGL-TR-78-0081, Air Force Geophysics Laboratory, Hanscom, Mass., 1978.
19. L.S. Rothman *et al.*, "The HITRAN molecular database editions of 1991 and 1992," *J. Quant. Spectr. Rad. Transfer* **48**, pp. 469–507, 1992.
20. A. Berk, L.S. Bernstein, and D.C. Robertson, *MODTRAN: A Moderate Resolution Model for LOWTRAN-7*, GL-TR-89-0122, Geophysics Laboratory, Hanscom AFB, MA 01732, 1989.
21. S. Slijkhuis, "SCIAMACHY/GOME instrument simulation software, detailed design, issue 2," Tech. Rep. SRON/SCIA/TR9301, SRON, Utrecht, 1994.

OZONE PROFILE RETRIEVAL AND ITS APPLICATION TO THE POLAR VIEW MODE OF GOME

Ronald J. van der A

Royal Netherlands Meteorological Institute,
P.O.box 201, 3730 AE De Bilt, The Netherlands
e-mail: avander@knmi.nl

ABSTRACT

GOME is a high resolution spectrometer, which observes the backscattered atmospheric radiation in nadir direction. From July 1995 till June 1997 the GOME instrument has made additional observations in polar view mode above the Arctic and Antarctic region. The polar view mode means that GOME is observing with a zenith angle of about 135 degrees in the azimuth direction of the Poles. Results are shown for height-resolved ozone densities in both troposphere and stratosphere. Special attention is paid to the polar view GOME observations of 1996 at the Antarctic region.

1. INTRODUCTION

Since the late seventies satellites routinely monitor the global ozone distribution. The early TOMS/SBUV instruments measured the backscattered radiation for several frequencies, resulting in an accurate estimate of the total column densities of ozone. Apart from this limited information is obtained about the vertical ozone distribution in the stratosphere. However, a growing need evolved for more accurate profile measurements in stratosphere and in troposphere. Knowledge on tropospheric ozone is important for different reasons. First, because ozone belongs to the greenhouse gases and because of the toxic nature of ozone for humans and vegetation. In addition, the ozone concentrations in the troposphere are a measure for the oxidising capacity of the atmosphere and therefore important for understanding the chemical processes in the troposphere. Chemical modelling will benefit from global measurements of tropospheric ozone. In 1995 GOME (Global Ozone Monitoring Experiment [*Burrows et al.*, 1997]) has been launched to measure in nadir direction the backscattered sunlight from the atmosphere in the range from 240-790 nm. The GOME spectrometer is a unique instrument to retrieve height-resolved ozone densities in the stratosphere as well as in the troposphere [*Munro et al.*, 1998]. The improvement in comparison to former satellite instruments is the high spectral resolution of the observations in the ozone absorption bands (the Huggins, Hartley and Chappuis bands). The steep rise of ozone absorption from 350 to 270 nm offers the possibility to infer height-resolved information on the ozone concentration from backscattered sunlight. The reason for this is that highly absorbed photons at the short- wavelength side penetrate the atmosphere only shallowly, whilst weakly absorbed photons on the long-wavelength side travel through the full height of the atmosphere. Therefore, backscattered short-wave photons carry only information on the upper layers of the atmosphere and photons with increasing wavelength reveal information on lower layers. Combining the measured reflectances in this wavelength range then gives the desired height-resolved atmospheric properties. The full spectrum between 270 and 350 nm can be used to infer the ozone height profile in a global fit (or retrieval) using the ozone concentrations at a number of specific heights as unknowns and the measured reflectances as known parameters. The retrieval necessitates a radiative transfer calculation to obtain reflectances given the ozone profile and other atmospheric properties. Below the details of the retrieval method are outlined. Ozone profile retrievals are done from GOME observations in Polar View Mode of the Antarctic region during the polar spring of 1996. The possibilities and some results of these retrievals will be discussed.

2. RETRIEVAL APPROACH

For the retrieval at KNMI [*van der A et al.*, 1998] the optimal estimation method [*Rodgers*, 1990] is used on a linearisation of the forward model utilising an iterative process to account for the non-linearity. With this algorithm it is possible to retrieve height-resolved ozone densities in both stratosphere as troposphere. In addition aerosol, albedo, NO_2 and cloud information can be obtained from the GOME observations. To perform the retrieval of some of these parameters in parallel improves the accuracy of the retrieved ozone profile. A vital component of the retrieval algorithm is the radiative transfer model. In our retrieval algorithm we use MODTRAN 3.7 [*Berk et al.*, 1989]. MODTRAN is a semi-spherical radiative transfer model which uses a frequency step size of 5 reciprocal cm. The multiple scattering calculation within MODTRAN is based on the discrete ordinates radiative transfer (DISORT) algorithm. For fast multiple scattering calculations a two-stream approximation is available, which give good results for radiances with wavelengths below 300 nm. This approximation

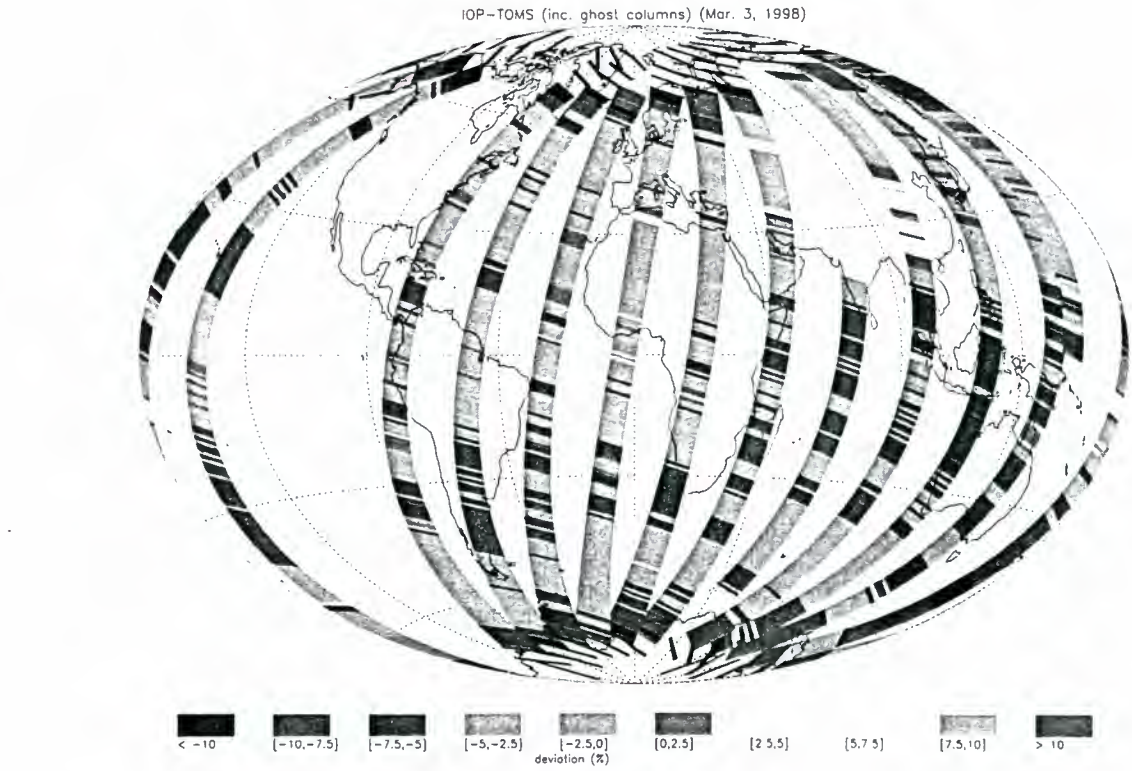

Figure 1. Relative differences between the integrated ozone profiles from GOME and the total ozone observations of TOMS. May 5, 1998.

is used for most calculations and results in less accurate values for the troposphere. Because of the high resolution of the GOME spectrometer, the Ring effect, which is not included in MODTRAN, can not be neglected in the radiative transfer modelling. The Ring effect shows up in the spectrum of the backscattered sunlight as a filling-in of solar absorption lines and is caused by inelastic (Raman) molecular scattering. To account for the Ring effect the magnitude and a wavelength shift of a theoretic Ring spectrum is fitted in parallel to the retrieval of ozone. The optimal estimation method requires a-priori information when available. A-priori profiles are taken from a US standard atmosphere and an ozone climatology of Fortuin [*Fortuin and Kelder,*1998]. This is a zonal mean ozone climatology based on a 12 year observation period of ozone sonde stations and satellites. The temperature profiles are also based on climatological data. The a-priori albedo is calculated from the GOME measurement at 400 nm where the absorption of ozone can be neglected. A mask is used to reject parts of the spectrum that show NO-γ emission lines, because these features are not included in the forward model.

The presented results are for retrieval of the ozone profile (parallel to the fit of the albedo and the Ring parameters) from the spectral interval of 260 to 340 nm. The ozone profile is given at 4 km steps at the altitude range from 12 to 48 km and an additional value at 6 km. Clouds are not directly modelled in this study, but are represented by a high albedo value. For validating the resulting profiles we have applied three methods. Firstly, a selected number of ozone profiles are compared to co-temporal and co-spatial ozone sonde measurements. Secondly, the resulting retrieval errors are compared to the a-priori errors on the ozone values in order to check the quality of the retrieval on every altitude. Finally, the retrieved profiles are integrated to yield ozone columns which are compared to the ozone columns as calculated by the GOME Data Processor from the GOME observations and as calculated by NASA from the TOMS observations. These ozone column densities from GOME and TOMS are thoroughly validated. Figure 1 shows the differences between the integrated ozone profiles and the TOMS total column densities. On average the integrated profiles have 3 to 5 % lower values than the TOMS total ozone columns. Both total columns are corrected for the ozone column below the cloud surface. In general, the retrieved profiles compare good to sonde measurements in stratosphere, while there is lesser agreement in troposphere.

3. THE POLAR VIEW MODE

From the launch in 1995 of GOME till July 1997 the GOME instrument has observed the polar regions in a special mode: the polar view mode. When switching to polar view mode the viewing angle changes from 180 degree (nadir) to 135 degree in the azimuth direction of the pole. The advantage of this mode at the Antarctic region is that GOME is viewing further into the day-side of Earth, with the consequence

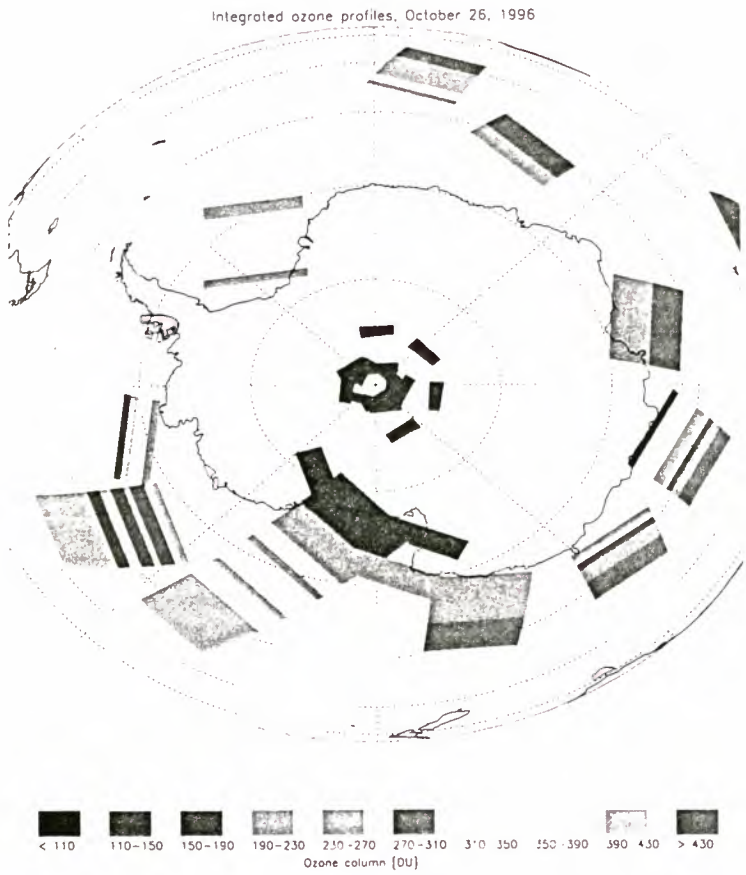

Figure 2. Integrated ozone profiles from GOME Polar View Mode observations on Oct. 26, 1996.

that the signal, and thus signal-to-noise ratio, of the measurements increases. In addition, the polar view mode allows observations at latitudes as low as -89 degrees instead of the minimum latitude of -81 degrees for nadir observations. This means that during polar spring from the end of September ozone profiles could be retrieved in the complete Antarctic region.

A series of ozone profile are retrieved from polar view mode observations in the Antarctic region during polar spring in 1996. In Figure 2 an example is given of the integrated retrieved profiles of GOME observations in the Antarctic region on October 26, 1996. The normal observations can be identified by their broad swath width. From the Figure it can be seen that observations in normal mode does not produce profiles on lower latitudes than -75 degree, while the observations in polar view mode (smaller swath width) still result in ozone profiles at about -89 degree.

Figure 3 shows a retrieved profile from an observation in polar view mode at September 27, 1996 (latitude= - 89.1°, longitude= 321.2°). Clearly visible are the low ozone concentrations at every altitude, especially at 16 km. The strong difference between a-priori profile and retrieved profile indicates that the observation contains enough information for the retrieval over the whole altitude range. On the other hand, it shows that the climatology, which is mainly based on measurements in the eighties, is not suitable for the situation with strong ozone depletion in 1996. The climatology, however, has recently been extended with a series of sonde observations from the ozone hole in recent years to cover also these cases (Fortuin, private communication).

4. CONCLUSIONS

The spectrum of backscattered solar radiation measured by GOME is used to gain information on the distribution of ozone over altitude. Due to its high spectral resolution and accuracy the GOME spectrometer can be used to obtain ozone profiles in stratosphere and in troposphere. A state-of-the-art atmospheric radiation transport model is used as a forward model in the retrieval code. With this retrieval method, it is feasible to retrieve ozone values at a step size of 4 km in stratosphere and one or two values in the troposphere. Validation shows that the retrieved ozone profiles closely match sonde data in stratosphere and the tropopause. The retrieval of the ozone profile in the troposphere produces a poorer resolution, but improves on climatological data. The resulting retrieval errors and the comparison of the integrated profiles with total column values gives us confidence in the retrieval algo-

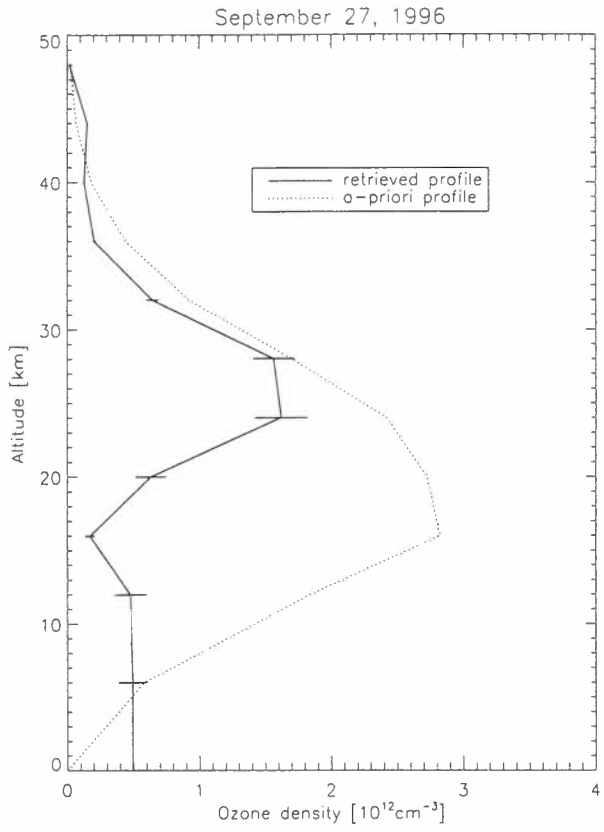

Figure 3. Ozone profile at -89 degrees latitude on Sept. 27, 1996 from a GOME observation in Polar View Mode

rithm. However, during polar spring, it is difficult to retrieve ozone profiles from normal observations in nadir mode due to the high solar zenith angle. Though, due to the switched viewing direction the polar view mode provides us a tool to research the height-resolved ozone distribution within the polar vortex during polar spring. A series of ozone profiles are retrieved for the polar spring of 1996 in the Antarctic region. For the first time ozone profiles in both stratosphere and troposphere are retrieved from satellite measurements at latitudes less than -85 degree. The retrievals showed that ozone profiles could be retrieved from the end of September at latitudes close to the absolute South Pole.

REFERENCES

van der A, R. J., and H. M. Kelder, Ozone profile retrieval with GOME, *Earth Observational Quaterly* no.58, March, 1998.

van der A, R. J., R. F. van Oss, H. M. Kelder, Ozone profile retrieval from GOME data, *Satellite Remote Sensing of Clouds and the Atmosphere III*, J.E. Russell, Editor, Proceedings of SPIE Vol. 3495, pp. 221-229, 1998.

Berk, M. A., L. S. Bernstein, D. C. Robertson, MODTRAN: A moderate resolution model for LOWTRAN7, *Tech. Rep. GL-TR-89-0122*, Geophysics Laboratory, Hanscom AFB, Mass., 1989.

Burrows, J.P., M. Buchwitz, V. Rozanov, M. Weber, A. Richter, A. Ladstätter-Weißenmayer, M. Eisinger, The global ozone monitoring instrument (GOME): mission, instrument concept, and first scientific results. Proc. 3rd ERS Symp. on Space at the service of our Environment, ESA SP-414, 3 Vols., pg 585, 1997.

Fortuin, J.P.F. and H.M. Kelder, An ozone climatology based on ozonesonde and satellite measurements, *J. Geophys. Res. 103,* no.D24, December, 1998.

Munro, R., R. Siddans, W. J. Reburn, B. J. Kerridge, Direct measurement of tropospheric ozone distributions from space, *Nature*, Vol.392, March, 1998.

Rodgers, C. D., Characterization and error analysis of profiles retrieved from remote sounding measurements, *J. Geophys. Res. 95*, no.D5, April, 1990.

HEIGHT-RESOLVED OZONE RETRIEVALS SPANNING THE TROPOSPHERE AND STRATOSPHERE FROM GOME

R. Siddans[1], B.J. Kerridge[1], W.J. Reburn[1], A. Stevens[1], R. Munro[2]
[1]Rutherford Appleton Laboratory Chilton, Didcot, Oxon OX11 0QX, U.K.
[2]European Centre for Medium Range Weather Forecasting, Reading RG2 9AX, U.K.

ABSTRACT

A retrieval scheme has been developed at the Rutherford Appleton Laboratory to obtain height-resolved ozone profiles spanning the troposphere and stratosphere from GOME data, thereby providing the first direct measurement of tropospheric ozone from a single satellite instrument and offering greatly increased horizontal and temporal coverage of the lower stratosphere than previous satellite instruments. The generation of a global dataset (sampling 1 day in 10 for 12 months), for release via the British Atmospheric Data Centre, is currently underway. Synergistic use of ATSR-2 data for cloud information and critical elements of a fast retrieval scheme to allow more comprehensive processing of GOME data is discussed. Some early results are presented showing, (i) *in situ* production of tropospheric ozone as a result of biomass burning and (ii) transport of sub-tropical tropospheric air into the mid-latitude lower stratosphere.

Key words: GOME; ozone; inversion algorithm.

1. INTRODUCTION

The Global Ozone Monitoring Experiment (GOME) was launched on ESA's ERS-2 satellite in April 1995. GOME is a downward viewing spectrometer which measures back-scattered solar radiation from 237-790nm at moderate spectral resolution (0.2 - 0.4nm). Due to contiguous spectral coverage and higher spectral resolution, GOME provides height-resolved ozone data of higher quality than previous UV back-scatter instruments. In particular ozone information extends down into the lower stratosphere and troposphere, a region not measured extensively by previous satellite sensors.

A retrieval scheme capable of generating ozone profiles on a global basis from GOME measurements has been developed and optimised at the Rutherford Appleton Laboratory (RAL), thereby providing the first direct measurements of tropospheric ozone distributions from space (Munro 1998). (The tropospheric ozone column had previously been inferred indirectly from TOMS and SAGE observations (Fishman 1990) and from TOMS observations at different locations Jiang 1996.)

Section 2. contains a basic description of the prototype retrieval scheme, developed to demonstrate the potential of the GOME dataset for this application. Validation of this scheme is then described in section 3. and some preliminary results are presented in section 4.. Optimisation of the scheme to allow large scale processing of a sub-set of the GOME data is described in section 5., followed by an outline of developments to provide auxiliary information on cloud from ATSR-2 in section 6.. Finally, the status of current data processing is detailed in section 7.

2. OVERVIEW OF THE RETRIEVAL SCHEME

Profile retrieval is carried out using Optimal Estimation (OE) (Rodgers 1990), which solves an otherwise under-constrained problem by combining information from measured spectra with that from *a priori* profiles. The primary input required is the GOME Level 1 Product, comprising measured backscattered spectra, and measurements of direct-sun spectra acquired in-flight via a diffuser. The wavelength calibration of the GOME spectra is refined by fitting to a high resolution solar reference spectrum (Chance 1996). *A priori* ozone profiles and uncertainties were taken from a monthly zonal mean climatology constructed from SAGE II data (McCormick 1989).

The GOMETRAN radiative transfer model (Rozanov 1997), developed by the University of Bremen, is interfaced to the retrieval scheme to synthetic reflectance spectra. It incorporates gaseous absorption, surface reflection and multiple scattering by air molecules, aerosol and clouds. In this study, a fixed single profile was adopted for aerosol scattering and cloud was not included in the radiative transfer.

Due to differences in viewing geometry and ozone absorption properties, a two-step approach is adopted, in which an ozone profile is first retrieved from the 237-307nm region (known as GOME Band 1A), which primarily contributes information on ozone down to, or just below, the stratospheric concentration peak. This profile is then used as *a priori* in a retrieval from 312-405nm (Band 2B). In addition to the ozone profile it is necessary to retrieve: (i) a scaling

factor for filling in of Fraunhofer lines by the Ring effect; (ii) wavelength shifts of the back-scattered spectrum with respect to the reference ozone absorption cross-section and the direct-sun spectrum and (iii) total column amounts of BrO and NO_2. As a precursor, an effective surface reflectance is retrieved from measurements near 340nm, where absorption by ozone and other gases is relatively small.

The current scheme retrieves the ozone mixing ratio on a fixed altitude grid: 0, 6, 12km, then 4km intervals up to 80km. These levels have been chosen to slightly oversample the intrinsic resolution of the GOME measurements, while maintaining retrieval stability.

3. VALIDATION

GOME retrievals using the prototype scheme have been compared to 34 co-located ozone sonde measurements made over Europe (including Northern Scandinavia) between July 1995 and February 1997. Means and standard deviations in the fractional differences in integrated sub-columns between the retrieval levels are shown in figure 1 for: (i) *a priori* profiles (SAGE II climatology); (ii) Band 1A (step 1) retrieved profiles and (iii) Band 2B (step 2) retrieved profiles. The Band 1A retrievals generally have much smaller biases and standard deviations than the *a priori* profiles, and Band 2B results provide very valuable extra information in the lower stratosphere and troposphere. The standard deviation in fractional difference between the final (Band 2B) retrievals and the ozone-sonde measurements is seen to be <10% in the stratosphere and <40% in the troposphere, with biases <5% above 6km and -30% below that altitude, where a negative bias is expected as GOME cannot detect ozone below optically thick cloud and no screening was performed for this inter-comparison.

The stratospheric profiles have also been validated by comparison to other satellite sensors (Stoffelen 1998). The zonal mean ozone field constructed from nine orbits processed on 11 January 1996 were compared with with those obtained from SSBUV and MLS. Agreement is generally within 10% between 1 and 40 hPa, the common altitude range within which the three sensors provide information.

4. RESULTS

4.1. Observations of *in situ* production of tropospheric ozone as a result of biomass burning

Figure 2 shows retrieved distributions of surface ozone (representative of a lower tropospheric column) from 9 orbits processed on the 11th January 1996 and 14 orbits on the 4th July of the same year. Measurements obscured by cloud have been omitted and only a limited number of retrievals are successful in the Brazil / South Atlantic region as a consequence of GOME Band 1A data corruption by the South Atlantic anomaly (SAA). Care must be exercised in interpreting the gridded fields, as large data gaps exist in some locations, particularly the SAA region. A limited comparison with fields from a 3-D UKMO chemistry-transport model (Collins 1997) has been performed and the following features are worthy of note:

- On the 11 January elevated ozone values are observed over Central America and Central Africa, whereas in July, highest concentrations are found further South. This picture is qualitatively consistent with the predictions of the model and is a consequence of the seasonal variation of biomass burning.
- The lowest ozone values are found in remote, low latitude maritime locations, again consistent with the model.
- Higher mixing ratios are observed over Northern mid-latitudes in summer than in winter (due to enhanced photochemical production of ozone arising from pollution in industrial regions), although the model predicts a larger enhancement than observed.

Further comparisons with model tropospheric ozone distributions, more rigorously taking into account possible cloud contamination in the GOME data, are planned for the future.

4.2. Transport of sub-tropical tropospheric air into the mid-latitude lower stratosphere in March '97.

At the suggestion of workers at the University of Aberystwyth, retrievals were carried out to determine the ozone distribution over the E. USA / N. Altantic / W.Europe region (from 20°N to 70°N and 80°W to 50°E), on several days in March 1997. During this period, air of sub-tropical origin had been observed in the mid-latitude lower stratosphere by a number of ozone-sondes (O'Connor 1998), resulting in a characteristic minimum in the ozone concentration profile at approximately 15km.

The potential for GOME to detect such structure in the lower stratosphere was clearly demonstrated by results from the period. Figure 3 shows a comparison between GOME and co-located ozone-sonde. The relatively coarse vertical resolution of the GOME retrieval is apparent, but the ozone minimum at 15km is detected in the Band 2B retrieval. In this case, the contribution of the Band 2B measurements to the retrieval in the lower atmosphere is clearly evident - the step 1 retrieval, which makes use of measurements in Band 1A only, produces a reasonable profile down to 20km but fails to capture the structure below.

A height / latitude (Band 2B) cross section of the orbit containing this profile is provided in figure 4(a). The figure also shows (b) the corresponding equivalent latitude [1] derived from the UKMO

[1] Equivalent latitude at a given point on a potential temperature surface is defined as the latitude circle which encloses the same area as the potential vorticity contour passing through the point. In adiabatic, frictionless motion, potential vorticity and hence equivalent latitude are conserved.

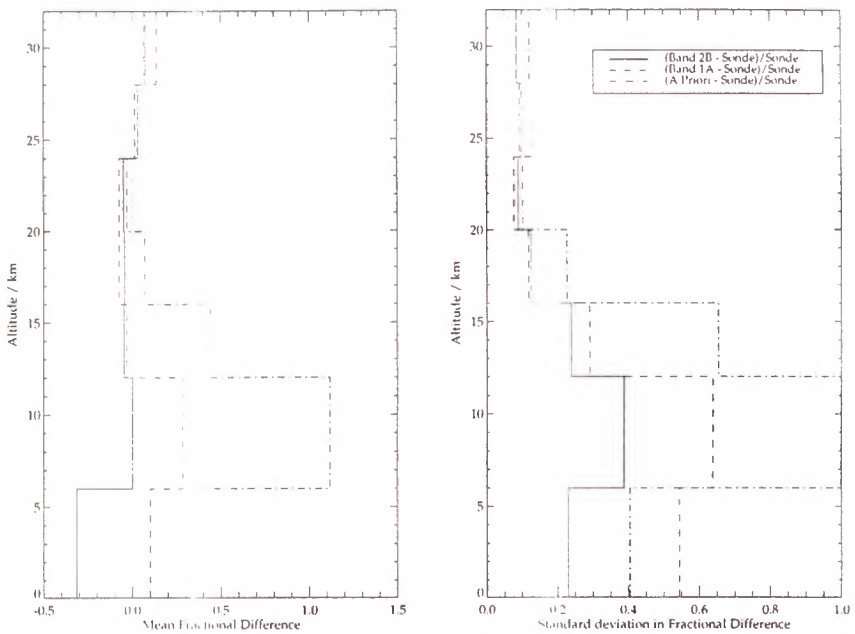

Figure 1. Inter-comparison of retrieved, a priori and sonde integrated sub-columns.

UARS-assimilation analysis for 12UT . In addition, an "equivalent ozone" field is also shown (c), constructed by sampling the Fortuin 1994 monthly zonal ozone climatology in equivalent latitude / potential temperature space (treating ozone as a passive tracer). Despite the limitations of this technique, there is a certain correspondence in structure near the tropopause with the retrieved distribution, e.g. the behaviour of the 2×10^{12} molecules/cm^3 contour which, proceeding northwards, descends near 30°N, then rises near 30°N, before descending again near 47°N. The 15km ozone minimum near 50°N is identified as arising from air originating at 35°N overlying air from 60°N.

5. OPTIMISATION OF RETRIEVAL SCHEME EFFICIENCY

In order that large scale processing of GOME data be feasible the prototype scheme (operating at 1 profile per hour c.f. measurement time of 1.5 seconds) required optimisation. Processing speed is limited by multiple-scattering, high-resolution. radiative transfer (or *forward*) calculations required to synthesise GOME spectra during the retrieval process. Approximations to these radiative transfer calculations were considered:

Band 1A obtains information, down to just below the stratospheric ozone peak, from the steep wavelength dependence of ozone optical depth in the Hartley band. In this region, information of adequate quality can be obtained by matching measured spectra at the 1% level (in reflectance, defined as the ratio of back-scattered radiance to direct solar irradiance). In order that profile information be extended down into the lower stratosphere and troposphere by the Band 2B retrieval , however, measurements in the Huggins bands must be matched to at least 0.1% (ESA 1991) to exploit the temperature-dependent structure of the band. Forward model accuracy must therefore be significantly better than 1% and 0.1%, respectively, for retrievals from Bands 1A and 2B to be of similar quality to those of the prototype algorithm.

A scheme has been developed which meets the Band 1A accuracy requirement by making use of exact, GOMETRAN calculations at 24 wavelengths. These are interpolated in absorption and scattering optical depth space to obtain spectra at the required resolution, by making use of the analytic weighting functions provided by GOMETRAN. The scheme relies upon the temperature dependence of the band being relatively weak, as a consequence of which the relationship between total optical depth and reflectance is only a weak function of wavelength. The scheme is accurate at the 0.2% level and rapid enough to allow real-time processing of the Band 1A data within the available computational resource (5 Dec Alpha 433au machines).

The temperature dependence in the Huggins bands, coupled with the more stringent accuracy requirement, precludes the use of a similar scheme for the Band 2B retrieval. Instead, work is proceeding on a look-up table approach to parametrise the effects of multiple scattering in the band. The accuracy achieved so far (0.2%) is not adequate for this band. (Retrieved ozone from this approximate scheme deviated by up to 100% in the lower stratosphere from reference calculations performed by the prototype scheme).

Large scale processing is currently under way using the Band 1A optimised scheme but retains the accurate, prototype Band 2B scheme. Single profile processing time is now 10 minutes on a single machine.

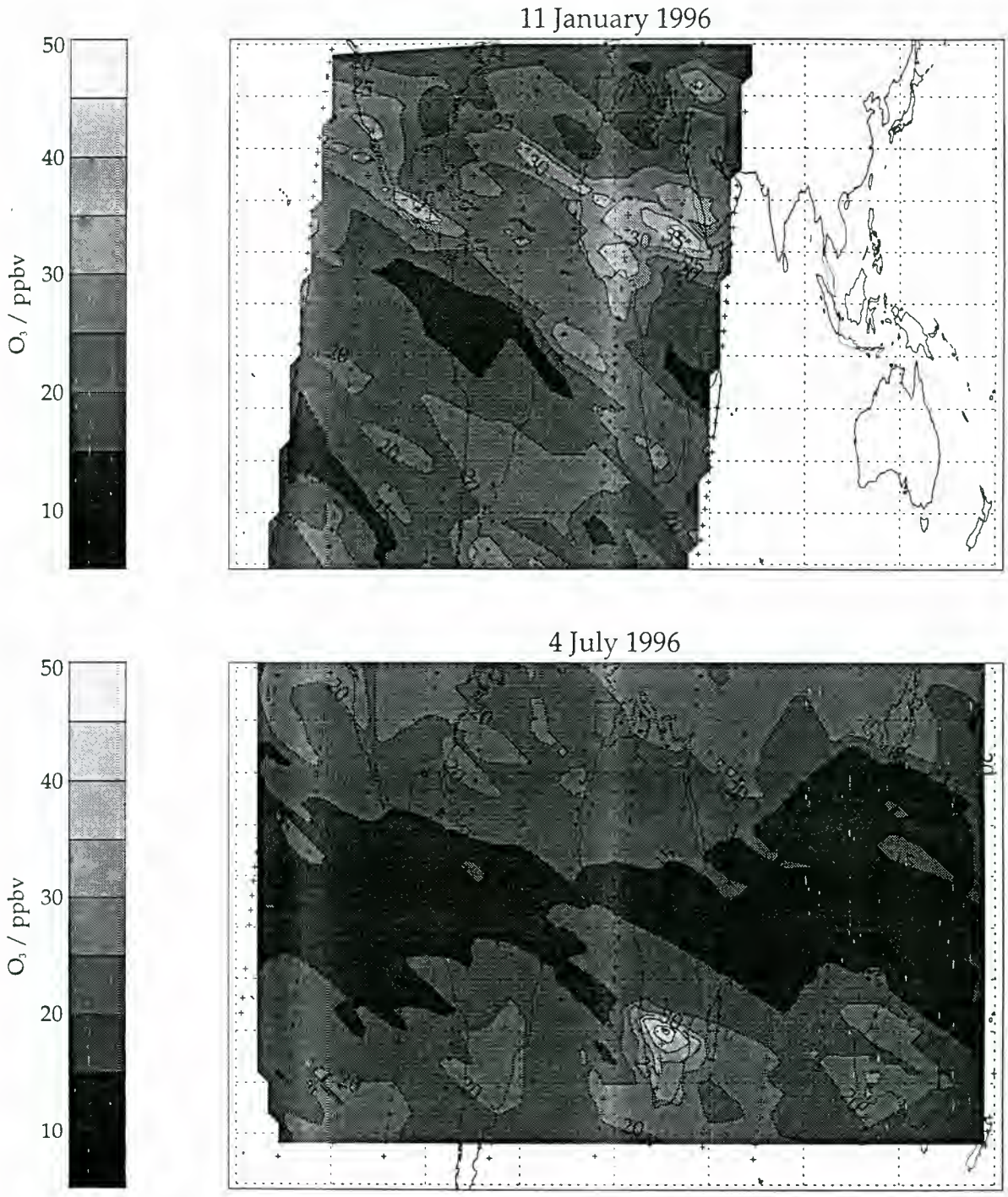

Figure 2. Retrieved ozone mixing ratios at the surface on 11th January and 4th July 1996. "+" symbols indicate the centre of each GOME observation used to construct the map (values between which are obtained by linear interpolation of the triangulated dataset).

The look-up table approach is being refined in parallel so as to allow accurate retrieval from Band 2B at a rate approaching real time in future processing.

6. SYNERGISTIC USE OF ATSR-2 DATA TO DERIVE CLOUD INFORMATION

In the presence of optically thick cloud, GOME cannot see ozone at lower altitudes, and the retrieval

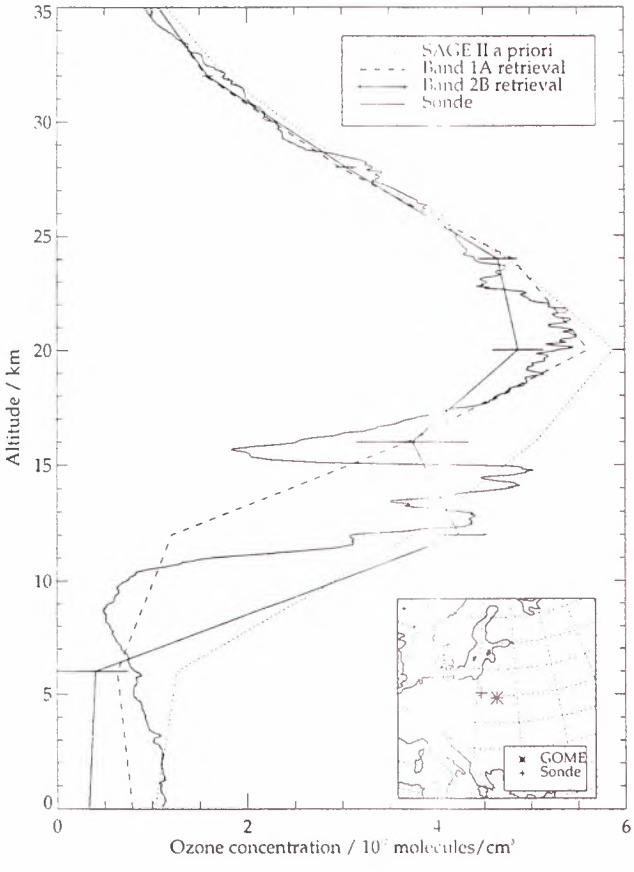

Figure 3. Comparison of GOME ozone retrieval with an ozone-sonde measurement from Legionowo (52.4°N,21.0°E) at 11:30 on 7 March 1997. The solid line with error-bars is the final (Band 2B) GOME retrieval. The dotted line shows the a priori profile used and the dashed line shows the output of the first retrieval step (using Band 1A measurements only).

scheme therefore returns values which are erroneously low. To properly interpret the retrieved tropospheric distribution therefore requires accurate knowledge of cloud fraction and altitude within the GOME field of view (FOV). A scheme is currently being developed to derive such information using data from the ATSR-2 instrument (also on board ERS-2).

ATSR-2 provides visible and infra-red measurements in 7 channels (0.56, 0.66, 0.87, 1.6, 3.7, 11 and 12μm) at a spatial resolution of 1km × 1km. For the purposes of characterising each GOME scene the more readily available "GBROWSE" product, sampled every 4km along and across track was found to be sufficient. ATSR-2 / GOME co-location as been verified using spatially (ATRS-2) and spectrally (GOME) averaged measurements made by both instruments at 0.55 μm. For each GOME FOV:

1. Each ATSR-2 sub-pixel within the GOME FOV is classified from visible channel ratios. Scene type is identified as thick cloud, cloud-free land, cloud-free sea, thin/partial cloud etc.
2. A histogram of occurrence of each scene type vrs. infra-red brightness temperature within the GOME FOV is constructed.
3. Height is inferred from infra-red brightness temperature using the appropriate temperature profile from the UKMO analysis.
4. ATSR-2 views the same scene twice by scanning in the forward and nadir directions. From the two views, cloud height is also inferred by a parallax technique. This approach provides information on high-altitude optically thin clouds which can otherwise be incorrectly assigned to lower altitudes by the infra-red brightness temperature technique.
5. Parameters representative of the GOME FOV are derived from the histograms: e.g. total cloud fraction, mean and standard deviation cloud reflectance, mean and standard deviation cloud height etc.

7. CONCLUSIONS AND FURTHER WORK

A *prototype* processing scheme has been developed at RAL which retrieves height-resolved ozone profiles spanning the troposphere and stratosphere, providing the first direct measurement of tropospheric ozone from space and representing a significant advance (in terms of temporal / spatial coverage) over previous measurements in the lower stratosphere by occultation techniques. The potential of GOME to obtain tropospheric ozone distributions consistent with a 3-D CTM and to resolve ozone structure associated with upper troposphere/ lower stratosphere dynamics has been demonstrated.

A more efficient scheme allows large-scale processing of GOME data at a rate of approximately 10 minutes per profile per CPU, including processing of Band 1A data at a real-time rate to provide information down to just below the stratospheric ozone concentration peak. Work is continuing on development of a fast forward model from Band 2B with the aim of accurate retrievals at a real-time rate for this band.

. The scheme is capable of real time processing of Band 1A data to provide information down to just below the stratospheric concentration peak, however the recovery of information at lower altitudes requires Band 2B measurements to be fitted to a level of accuracy not yet achieved with the approximate radiative transfer model developed thus far. Work is continuing on this model with the aim of enabling full retrievals at a real-time data rate.

The scheme, as it stands, is currently being used to process 1 day in 10 of the GOME data globally for one year starting on 24th March 1998. Sampling was selected to make use of the narrow-swath mode GOME data and the commencement of a special view mode of the ATRS-2 instrument (also on board ERS-2), designed to ensure full coverage of the GOME FOV. A scheme to make use of this ATSR-2 data to obtain accurate cloud coverage and altitude information for interpretation of the GOME retrievals is currently under development at RAL.

It is intended that the profile data, together with ATRS-2 derived cloud information will be made

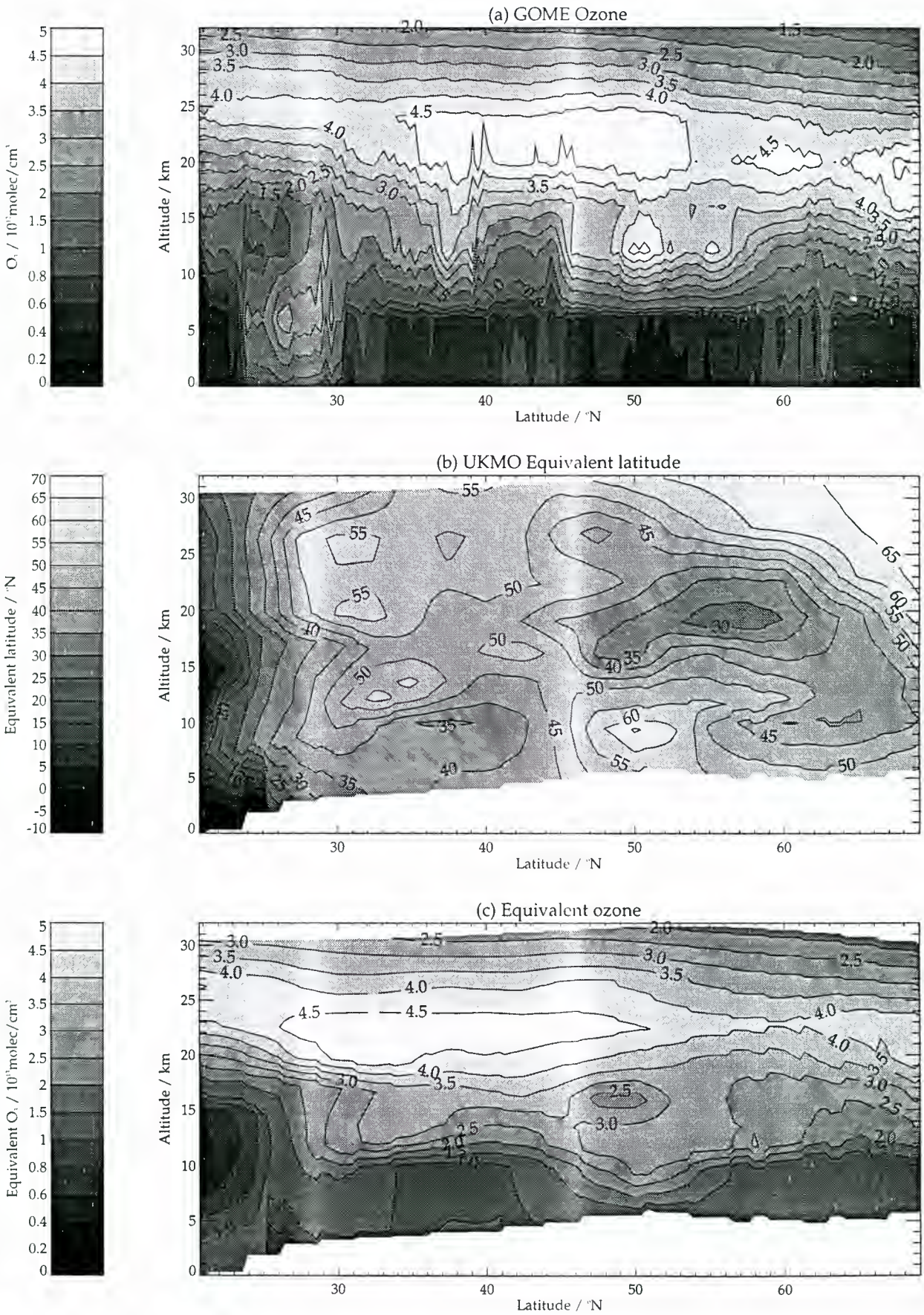

Figure 4. (a) Height vrs. latitude distribution retrieved from GOME orbit commencing 09:20 on 7 March 1997. (b) Corresponding equivalent latitude distribution derived from the UKMO analysis and (c) "equivalent ozone" derived by interpolating the Fortuin climatological distribution in equivalent latitude / potential temperature space.

available via the British Atmospheric Data Centre (http://www.badc.rl.ac.uk/).

ACKNOWLEDGEMENTS

We would like to acknowledge the UK Natural Environment Research Council and the EC (via the SODA project) for providing the funding to process and validate the GOME data. Permission to use GOME data prior to its public release was granted by ESA and GOME Data Products were provided by DLR. The GOMETRAN radiative transfer model and the high resolution solar reference spectrum used in this study were supplied by Prof. J.Burrows (University of Bremen) and Dr. K.Chance (Harvard-Smithsonian Astrophysical Observatory), respectively. UK Met.Office temperature was acquired through the BADC at RAL and ozone-sonde data was obtained from NILU. The "Fortuin" climatology was made available by its author. We would also like to acknowledge NERC, ESA and the RAL project team for the use of ATSR-2 data.

REFERENCES

Chance, K., and R. Spurr, "Ring effect studies, GOME Geophysical Validation Campaign". Workshop Proceedings., ESA WPP-108, pp.69-74, 1996.

Collins, W.J., D.S. Stevenson.C.E. Johnson, R.G. Derwent, Tropospheric Ozone in a Global-Scale Three Dimensional Lagrangian Model and Its Response to NOx emission Controls. Journal of Atmospheric Chemistry, v26, pp223-274, 1997.

ESA, "A study of advanced techniques for monitoring atmospheric trace gases". ESA Contract 8915/90/NL/BI, Final Report (1991).

Fishman, J., Watson, C.E., Larsen, J.C. and Logan, J.A., "Distribution of tropospheric ozone determined from satellite data", Journal of Geophysical Research, D95(4), pp.3599-3617. 1990.

Fortuin, J. P. F., and U. Langematz, "An Update on the Global Ozone Climatology and on Concurrent Ozone and Temperature Trends", Atmospheric Sensing and modelling, R. P. Santer (Ed.) pp. 207-216, Proc. SPIE 2311 Washington, DC., 1994.

Jiang, Y.B. and Yung, Y.L., "Concentration of tropospheric ozone from 1979 to 1992 over tropical pacific South-America from TOMS data", Science, v272(5262), pp.714-716, 1996.

McCormick, M.P., J.M. Zawodny, R.E. Veiga, J.C. Larsen, and P.H. Wang, "An Overview Of SAGE I And II Ozone Measurements" Planet. Space Sci., 37, 12, 1567-1586; 1989.

Munro, R., R. Siddans, W.J.Reburn and B.J.Kerridge, "Direct Measurement of Tropospheric Ozone from Space" Nature, v392(6672), pp.168-171, 1998.

O'Connor, F.M. and G. Vaughan, "Observations of sub-tropical air in the European midlatitude lower stratosphere", Q.J.R.Meteorol.Soc., in press, 1998.

Rodgers, C. D., "Characterisation and error analysis of profiles retrieved from remote sounding measurements", Journal of Geophysical Research, 95(D5), pp.5587-5595, 1990.

Rozanov, V., D. Diebel, R. Spurr, and J. Burrows. Gometran: A radiative transfer model for the satellite project gome, J. Geophys. Res., v102(D18), pp. 21809-21823, 1997.

R.Siddans, B.J.Kerridge, W.J.Reburn and R. Munro, "Height-resolved ozone retrievals in the troposphere and lower stratosphere from GOME", Earth Observation Quarterly, v58, pp.11-13, 1998.

Stoffelen, A. (ed.) "Satellite Ozone Data Assimilation". 1st Annual European Union project report, 1998.

Four-Dimensional Variational Data Assimilation of Chemical Species

Dominique Fonteyn, Quentin Errera, Martine De Maziere, Ghislain Franssens and Didier Fussen
BIRA-IASB, Belgium

Advances in chemical modelling, assimilation techniques and computing power, allowed the use of chemical models for the assimilation of chemical species. At BIRA-IASB a 4D-VAR model for the assimilation of stratospheric chemical species is developed. It is based on the 3-D chemical transport model with detailed chemistry and uses ECMWF's analysed dynamical fields.

Results will be presented using a sample of a passed spaceborne mission. The topics addressed in this presentation will be:

- description of 4D-VAR assimilation system,
- issues about observations of chemical species with respect to the assimilation,
- technical implementation,
- results on chemical composition and evolution, and,
- possibilties for the ENVISAT 'chemistry' instruments and measurements.

ASSIMILATION OF SIMULATED GOMOS DATA OF VERTICAL OZONE PROFILES IN A 3-D CHEMISTRY-DYNAMICS-TRANSPORT MODEL IN THE FRAME OF MSDOL PROJECT

A. Hauchecorne, B. Théodore, J.L. Bertaux, C. Cot, C. Deniel
Service d'Aéronomie du CNRS, BP 3, 91371 Verrières-le-Buisson Cedex, France, hauchecorne@aerov.jussieu.fr

A. Mangin, G. Bérenger, O. Hembise
ACRI, 260, Route du Pin Montard, 06904 Biot,

O. Talagrand, LMD, ENS, 24 Rue Lhomond, 75231 Paris Cedex 05

D. Fussen, IASB, 3 Avenue Circulaire, 1180, Bruxelles, Belgium

E. Kyrölä, S. Hassinen, J. Damski, FMI, Vuorikatu 24, P.O. Box 503, SF 00101, Helsinki, Finland

H. Roscoe, BAS, Madingley Road, Cambridge, United Kingdom

and G.P. Brasseur, NCAR, P.O. Box 3000, Boulder, Colorado 80307-3000, USA

ABSTRACT

Here, we show assimilation results from GOMOS simulated ozone data. The model is derived from the stratospheric 3-D chemistry-dynamic model ROSE developed at NCAR, and is forced by ECMWF winds below 30 hPa and internally computed above this level. An Eulerian advection scheme has been adapted in ROSE in order to have a better mass conservation. The model is first used to create a set of simulated observations randomly noised. These observations are then assimilated in a second version of the model with an initial field which may differ from the first version. The ability of the model to converge toward the true 3-D ozone field when observations are assimilated is assessed. Results are discussed in terms of the time constant of the ozone photochemistry and the assimilation process. This allow us to define a new concept, the assimilation factor.
These results form part of an EC-funded project Monitoring of Stratospheric Depletion of Ozone Layer (MSDOL), which is preparing for data from the European Space Agency's ENVISAT, due to be launched in 2000.

1. INTRODUCTION

ENVISAT polar platform, to be launched by the European Space Agency in 2000, will carry 3 instruments for the study of the chemistry of the atmosphere and particularly the stratosphere, GOMOS, MIPAS and SCIAMACHY. These 3 instruments will provide a large quantity of measurements of chemical constituents for the study of the ozone layer and its possible depletion. In the present paper, we concentrate on GOMOS experiment. A detailed description of the experiment is given in (Ref. 2). GOMOS is a stellar occultation experiment. It will measure UV-visible spectra of stars occulted by the atmosphere, giving access to about 400 vertical profiles per day of ozone and other constituents. However, the accuracy of each individual profile will be very dependent upon several parameters as the star magnitude and temperature and the local time of the occultation (day/night). Furthermore, the geographical location of the profiles will not be uniformly distributed over the globe. It is therefore not so easy to obtain, using a simple interpolation scheme, global 3-D fields of ozone needed for modelling and climatology studies.

2. OPTIMAL INTERPOLATION

The goal of the data assimilation is to make the optimal use of observations in order to improve model data. In the sequential assimilation technique used in the present study, an observation is assimilated at the nearest time step from the measurement time. If one wants to make this assimilation optimal in a statistical sense, one has to modified the model field in the direction of the measurement in order to minimise the model error. This minimisation should be obtained in the full area where the model field is correlated with the model value at the location of the observation. This method, called optimal or statistical interpolation, has been described in details in (Ref. 9) and a more recent update is given in (Ref. 1). Here we just want to recall the basic principle of the method.
When an observation of the variable g is available at a grid point (i,j), the best estimate of g at a grid point (i',j') is given by :

$$g^{a}_{i',j'} = g^{b}_{i',j'} + G(g_{obs} - g^{b}_{i,j})$$

where G is referred as the Kalman gain and a and b refer to the analysed and background values of g. The minimisation of the analysed model error leads to the expression of G :

$$G = \frac{\sigma_{i,j}\sigma_{i',j'}r_{(i,j),(i',j')}}{\sigma^{2}_{i,j} + \sigma^{2}_{obs}}$$

where $\sigma_{i,j}$ and σ_{obs} are the model and observation errors.

In the present study, the correlation function r, also called neighbouring function, is assumed to have a Gaussian shape in the zonal and meridional direction and can be expressed as :

$$r_{(i,j),(i',j')} = \exp\left(-\frac{(x_{i'} - x_i)}{2L_x^2} - \frac{(y_{j'} - y_j)}{2L_y^2}\right)$$

where (x_i, y_j) and $(x_{i'}, y_{j'})$ are the co-ordinates of points (i,j) and (i',j') and L_x and L_y are the zonal and meridional correlation lengths of the error of model ozone field. In the present study, they are fixed to L_x = 1000 km and L_y = 500 km.
The analysed model error is computed taking into account the weight given to the observation in the analysed model value. In absence of observation, the model error is assumed to tend exponentially toward an asymptotic value of 25% of the model value with a 3 days time constant.

3. DESCRIPTION OF THE MODEL

The ROSE model was developed at Free University Berlin for the dynamics (Ref. 7) and at NCAR for the chemistry (Ref. 8). Published descriptions of former versions of the model can also be found in (Refs. 3, 5, 10). A version of ROSE driven by daily UKMO analyses have been used to assimilate MLS data (Ref. 6).
ROSE is a grid point model extending from the upper troposphere to the mesopause with an adjustable resolution fixed for the present study to:
32 grid points in longitude, resolution 11.25° ;
36 grid points in latitude, resolution 5° ;
24 pressure levels from 10 to 80 km, resolution about 3 km.

3.1 Chemistry

The model includes 45 chemical species or families, among them 30 long-lived species or families are explicitly transported and 15 short-lived species are assumed to be in photochemical equilibrium in their family. The photodissociation rates are calculated taking into account the diurnal variation. In ROSE chemistry, ozone belongs to the odd oxygen family O_x which is the sum of O_3 + O. The variable to be assimilated is then O_x but in the stratosphere O_3 represents more than 99% of O_x. By convenience of language, we refer to ozone instead of odd oxygen in the continuation of the paper.

3.2 Dynamics

In this version of ROSE, wind and temperature fields below 30 hPa are nudged to ECMWF fields taken every 6 hours and averaged at the ROSE resolution. In order to avoid unrealistic gravity waves in the model, the nudging is introduced smoothly during the 15 days initialisation period. Above 30 hPa the dynamics is computed internally using primitive equations of the motion.

3.3 Transport

The advection scheme originally implemented in ROSE was a semi-Lagrangian scheme described (Ref. 11). It has the advantage to have a relatively low numerical diffusion but at the cost of unrealistic negative mixing ratios or non-conservation of the mass. Following the recommendation of (Ref. 4), the initial scheme has been replaced by an Eulerian scheme referred as VanLeer I (Ref. 12) in which the mixing ratio is assumed to vary linearly within each elementary cell of the model with a condition on the slope to insure monotonicity. It has the advantage to conserve perfectly the mass and present an acceptable numerical diffusion.

4. STRATEGY OF USE OF THE MODEL

In the final stage MSDOL, a set of randomly noised simulated ozone profiles will be generated taking into account the mission planning of GOMOS and the estimation of ozone error bars as a function of altitude and magnitude and temperature of the occulted star. In order to better understand the efficiency of the assimilation scheme, a more simple experiment is made in the present study. We consider that we have each day one occultation at each second grid point in latitude and longitude, all occurring at OO UT. This corresponds to 288 occulations per day. The random error bar is assumed to be constant and equal to 5% at all altitudes. We define 4 runs of the model.
Run 1 : ROSE run freely and the output is considered as the "true" atmosphere. Randomly noised ozone profiles are extracted from the output of Run 1.
Run 2 : ROSE starts from the same ozone field than Run 1 and profiles created using Run 1 are assimilated.
Run 3 : ROSE starts with an ozone field increased by 50% everywhere and runs freely.
Run 4 : ROSE starts with an ozone field increased by 50% everywhere and profiles created using Run 1 are assimilated.

The 4 runs start on 22 January 12 UT and end 6 days later. Root mean square (hereafter RMS) differences Run 2 - Run 1, Run 3 - Run 1 and Run 4 - Run 1 are represented respectively on Figures 1, 2 and 3 as a function of time (every 6 hours) and for several altitudes in the stratosphere. All observations are assimilated just after hours 00, 24, 48, 72, 96 and 120. It means that for instance the point at 48 hours is obtained 24 hours after the previous time of assimilation when the point at 54 hours is only 6 hours after.

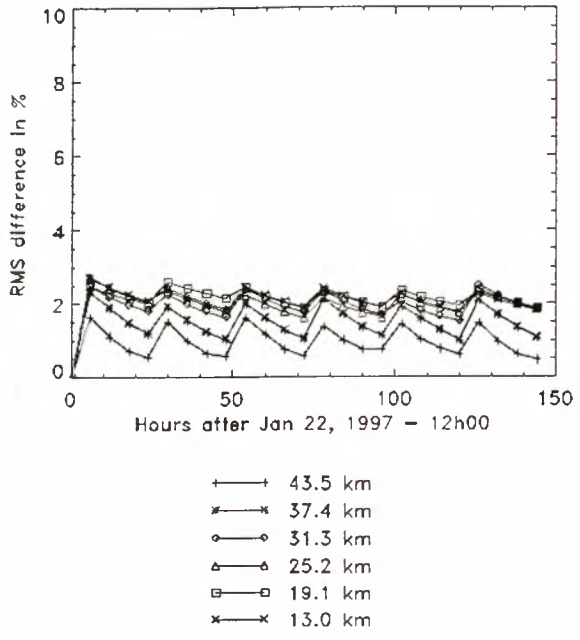

Figure 1 : Time evolution of the rms difference between Run 1 and Run 2 at several altitudes in the stratosphere. Highest curves correspond to lowest altitudes.

The difference Run 2 – Run 1 is representative of the noise in the model due to the noise in the observations. In this case the RMS difference increases just after the assimilation. The RMS difference never reaches 5% but has a maximum of the order of 2.5 %. This is due to the fact that each grid point is influenced by several observations made during the previous days, what tends to average statistical fluctuations of the noise. At higher altitudes the RMS difference tends to be smaller than in the lower stratosphere. This is related to the faster photochemistry of ozone in the upper stratosphere where the model tends to converge rapidly toward its photochemical equilibrium in absence of measurement.

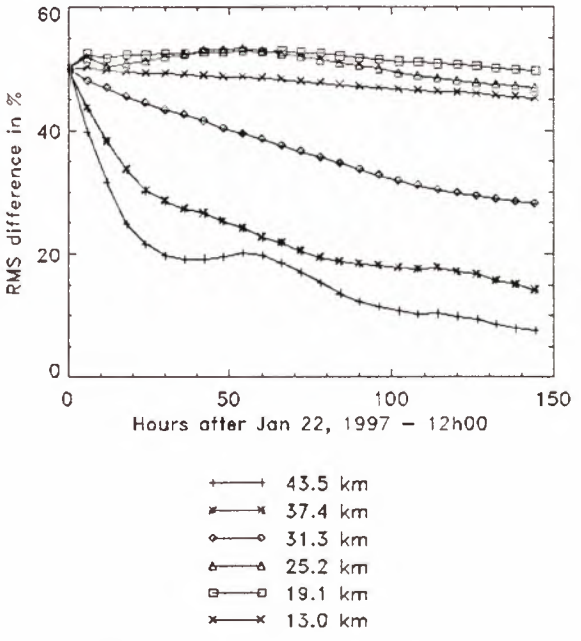

Figure 2 : Time evolution of the rms difference between Run 3 and Run 1 at several altitudes in the stratosphere. Highest curves correspond to lowest altitudes.

The difference Run 3 – Run 1 is representative of the tendency of the model to converge toward its photochemical equilibrium when it has been displaced. As expected, in the lower stratosphere (13.0 to 25.2 km), the RMS difference decreases very slowly with time due to the very low photochemistry in this region. On the contrary, on the upper stratosphere (43.5 km) the ozone concentration tends to converge toward its photochemical equilibrium and after 6 days the ozone field is only weakly dependent on its initial state. However the convergence is not totally reached. It is very fast during the first 24 hours but much slower after that. This may be due to the fact that some other constituents have been modified by the 50% increase of ozone and take some time to return to their equilibrium.

The difference Run 4 – Run 1 is representative of the efficiency of the assimilation scheme to force the model field to converge toward the "true" field. The convergence is faster at high levels but after 5-6 days it is reached at all altitudes and the RMS difference is about the same than in the case of Run 2 – Run 1. This means that the memory of the initial state of the model is lost and the ozone field in the model is totally driven by the assimilation of observations made during the 5-6 days period. This proves the efficiency of the assimilation process.

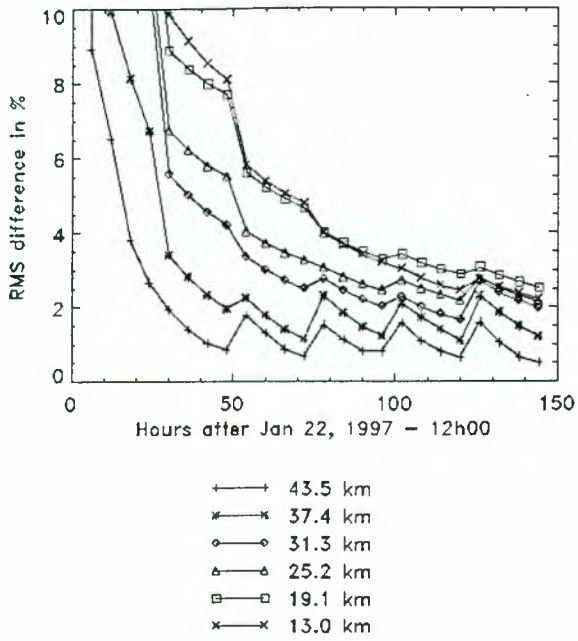

Figure 3 : Time evolution of the rms difference between Run 4 and Run 1 at several altitudes in the stratosphere. Highest curves correspond to lowest altitudes.

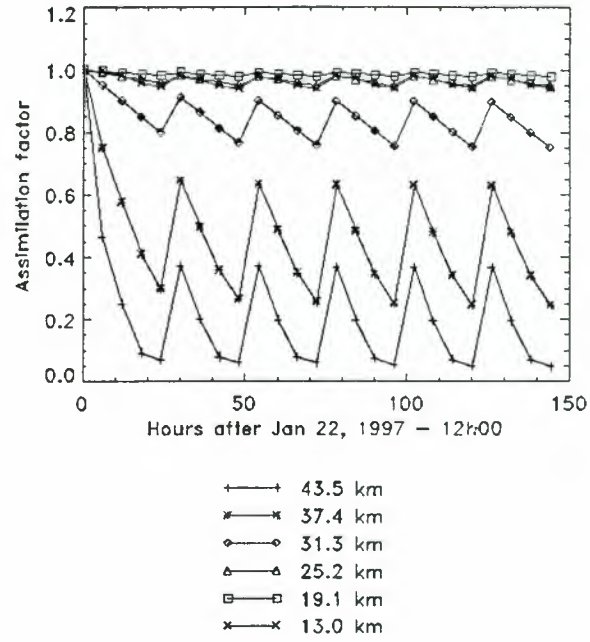

Figure 4 : Time evolution of the mean value of the factor of assimilation in Run 2 at several altitudes in the stratosphere. Highest curves correspond to lowest altitudes.

5. ASSIMILATION FACTOR

The results presented above indicate the difference of behaviour of the model when observations are assimilated in the lower stratosphere where the photochemistry is slow and in the upper stratosphere where it is very fast. In order to better visualise the effect of the assimilation process in the model output, we defined a new concept, the assimilation factor. It corresponds to the proportion of ozone molecules assimilated at the time of one of the previous observations and never destroyed after to the total number of molecules.

During the assimilation process, the assimilation factor α is increased according to the Kalman gain :

$$\alpha_a = \alpha_b(1 - G) + G$$

In the chemical module the assimilation factor α is decreased as a function of the chemical evolution of ozone concentration N(t):

$$\alpha(t + \Delta t) = \alpha(t) + \frac{N(t) - L\Delta t}{N(t) + (P - L)\Delta t}$$

where Δt is the chemical time step (7.5 min in our case) and P and L are the production and loss rates of ozone.

The assimilation factor is transported as long-lived species.

Figure 4 represents the evolution with time of the factor of assimilation in the case of Run 2. The difference of behaviour as a function of altitude is very clear. In the lower stratosphere up to 25.2 km (and to a less extent at 31.3 km), α is always above 90%, indicating that the time constant of ozone photochemistry is much larger than the assimilation time constant (mean time between the assimilation of 2 observations for a given grid point) and ozone can be considered as a quasi-passive tracer. Therefore, the ozone field in the model is dominated by the assimilation of observations. In the upper stratosphere (43.5 km), α is much lower, which indicates that the photochemistry time constant is smaller than the assimilation time constant. In this case, the ozone field in the model is more driven by the photochemistry of the model than by the assimilation of observations and by the transport. The middle stratosphere (37.4 km) is a region of transition where both the assimilation of observations and the photochemistry of the model have a significant contribution to the ozone model field.

Contrary to the 4D-Var assimilation where it is possible to constraint species which are not measured, in the optimal interpolation technique presented here, we modify only the measured species. Differences between model and observations may be due to differences in unmeasured species or inaccuracies in the model photochemistry and transport. In order to assess the quality of the assimilated ozone field even in the case where the model is wrong, we assume an intrinsic error E_m for the ozone field in the freely running model and a contribution of this error to the total error in the assimilated ozone field proportional to $1-\alpha$. This gives for the error E_a of the assimilated ozone field:

$$E_a^2 = (RMS)^2 + (1-\alpha)^2 E_m^2$$

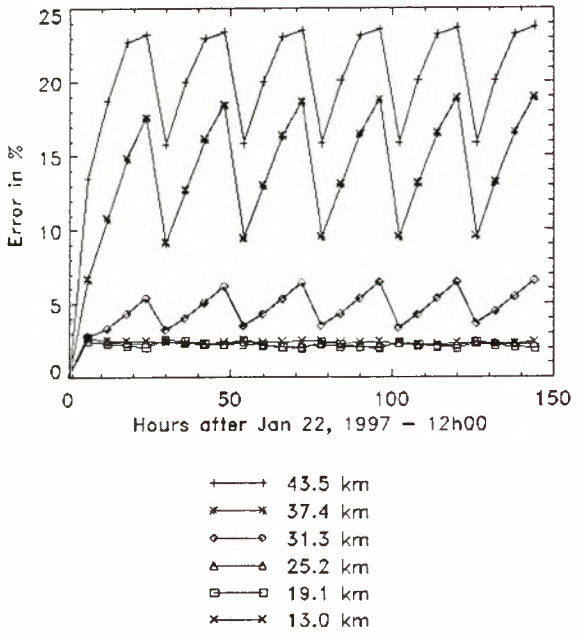

Figure 5 : Time evolution of the mean value of the error on the assimilated ozone field in Run 2 at several altitudes in the stratosphere assuming a 25% error on the ozone field of the free running model. Lowest curves correspond to lowest altitudes.

Figure 5 presents the evolution of the error in the assimilated ozone assuming a model error of 25%. This value is perhaps pessimistic but is chosen high in order to show that it is possible to assimilate observations in the lower stratosphere even if they are high uncertainties in the photochemistry of the model. Below 25.2 km, the error remains below 3%. In the upper stratosphere (43.5 km) where the assimilated ozone field is mainly imposed by the photochemistry of the model, the error is of course near the 25% value of the model error.

6. DISCUSSION

The goal of this preliminary study within the European MSDOL project was to assess the potential of optimal interpolation technique to assimilate ozone profiles in a 3-D chemistry-dynamics-transport model. The simplified exercise presented here allows us to conclude that the technique is working very well in the lower/middle stratosphere up to 30/35 km where the time constant of photochemistry is longer than the time constant of assimilation. In this altitude range the accuracy obtained in the assimilated ozone field is smaller than the accuracy of a single ozone profiles due to the fact that the value at a given time and a given grid point can be influenced by several observations during the previous days. This result is in agreement with (Ref. 6) who have shown that the assimilation of UARS- MLS observations in a version of ROSE resulted in improved global 3-D distributions of ozone. In the upper stratosphere, the time constant of the photochemistry is shorter than the time constant of assimilation and the assimilated field reflects the photochemical equilibrium in the model. However, this does not mean that the model will be useless in this altitude range. If we observe a systematic difference between the model and the observations, it will mean that there is some discrepancy in the model (concentration of other constituents or/and rate of photochemical reactions). Some modification of the model photochemistry could be done off-line in order to improve the agreement.

The next step within MSDOL will be to generate realistic GOMOS profiles taking into account the mission planning and the estimation of errors on ozone profiles as a function of star magnitude and temperature. This will help us to estimate what will be the final accuracy of the 3-D assimilated ozone field.

7. ACKNOWLEDGMENTS

The MSDOL project is supported by the European Commission's RTD programme on Environment and Climate (contract N° ENV4-CT97-0386) in the theme "Space techniques for environmental monitoring and research".

8. REFERENCES

1. Banfield, D., A.P. Ingersoll & C.L. Keppenne 1995, A steady-state Kalman filter for assimilating data from a single polar orbiting satellite, *J. Atmos. Sci.*, **52**, 737-753.

2. Bertaux, J.L., G. Mégie, T. Widemann, E. Chassefière, R. Pellinen, E. Kyrölä, S. Korpela & P. Simon 1991, Moitoring of ozone trend by stellar occultations : the GOMOS instrument, *Adv. Space Res.*, **11 (3)**, 237-242.

3. Granier, C. & G.P. Brasseur 1991, Ozone and other trace gases in the Arctic lower stratosphere during winter 1989-1990, *J. Geophys. Res.*, **96**, 2995-3011.

4. Hourdin, F. & AA. Armengaud 1999, On the use of finite volume methods for atmospheric advection of trace species : I. Test of various formulations in a general circulation model, *Mon. Weath. Rev.*, in press.

5. Lefèvre, F., G.P. Brasseur, I. Folkins, A.K. Smith & P. Simon 1994, Chemistry of the 1991-1992 stratospheric winter : three-dimensional model simulations, *J. Geophys. Res.*, **99**, 8183-8195.

6. Levelt, P.F., B.V. Khattatov, J.C. Gille, G.P. Brasseur, X.X. Tie & J.W. Waters 1998, Assimilation of MLS ozone measurements in the global three-dimensional chemistry transport model ROSE, *Geophys. Res. Lett.*, **25**, 4493-4496.

7. Rose, K. 1983, On the influence of nonlinear wave-wave interaction in a 3-D primitive equation model for sudden stratospheric warmings, *Beitr. Phys. Atmosph.*, **56**, 14-41.

8. Rose, K. & G.P. Brasseur 1989, A three-dimensional model of chemically active trace species in the middle atmosphere during disturbed winter conditions, *J. Geophys. Res.*, **94**, 16387-16403.

9. Rutherford, I.D. 1972, Data assimilation by statistical interpolation of forecast error fields, *J. Atmos. Sci.*, **29**, 737-753.

10. Smith, A.K. 1995, Numerical simulation of global variations of temperature, ozone and trace species in the stratosphere, *J. Geophys. Res.*, **100**, 1253-1269.

11. Smolarkiewicz, P.K. & P.J. Rasch 1991, Monotone advection on the sphere : an Eulerian versus semi-Lagrangian approach, *J. Atmos. Sci.*, **48**, 793-810.

12. VanLeer, B. 1977, Towards the ultimate conservative difference scheme : IV. A new approach to numerical convection, *J. Computational Phys.*, **23**, 276-299.

Scientific Session

Ultraviolet Radiation, Clouds & Aerosols

Chair: P. Simon, *Telecom PTT*

MAPPING SURFACE UV RADIATTION OVER EUROPE, USING GOME AND METEOSAT DATA

Jean Verdebout

Space Applications Institute
Joint Research Centre of the European Commission
21020 Ispra (VA), Italy
e-mail: jean.verdebout@jrc.it

ABSTRACT

This paper presents a methodology for mapping the ultraviolet radiation (UV) with a spatial resolution of approximately 5 km and potentially on a half hourly basis. It consists in using a standard radiative transfer code (UVspec) and in exploiting various sources of information to assign values to the influencing parameters. GOME total column ozone data (or TOMS for pre GOME years) are used for the total column ozone. The attenuation of radiation by clouds is estimated using the MVIRI/METEOSAT visible channel data. In practice, for each METEOSAT pixel, a cloud liquid water path is derived from the enhancement of the signal with respect to the cloudless situation. Other influencing factors taken into account include the tropospheric aerosols (using the observations by the ground meteorological stations), the surface elevation and the enhancement of the UV surface albedo in presence of snow. First results on maps at the European scale are presented. A preliminary comparison of the satellite derived surface UV irradiance with the measurements performed at the Environment Institute in Ispra is also discussed.

1. INTRODUCTION

The increase in the intensity of the UV radiation reaching the ground is one of the most important direct consequences of ozone depletion. As exposure to higher levels of UV radiation is potentially harmful to human health (skin cancer, cataract, immunosuppression), and could induce modifications in natural systems, it is obviously important to monitor the changes that occur in this environmental parameter. Not directly linked with ozone depletion there is anyway an increasing awareness that exposure to solar radiation plays a role in the risk of contracting some diseases or simply on skin aging. Be it for impact studies on the environment or epidemiological studies, it would therefore be very desirable to obtain geographically and temporally extended information on the surface UV radiation. The work reported here is a contribution to generating this information.

We have adopted an incremental approach and the method presented here should be considered as a first version that can certainly be improved following an assessment of the results accuracy and as new sources of information on the influencing factors become available. In this respect, the processing scheme is not fundamentally bound to any particular sensor or data set as the UV maps are ultimately obtained by interpolation in look up table, the entries of which are physical parameters. In this version, these are solar zenith angle, total column ozone amount, cloud liquid water path, near surface horizontal visibility and surface elevation and albedo. Most of the processing actually consists in estimating the values of these parameters in each pixel of the desired UV map. In this work, we have focused on Western Europe and have generated maps on an area extending from 34 to 74 deg. North and from 12 deg. West to 32 deg. East. A regular grid in latitude and longitude with a 0.05 deg. resolution was chosen. It roughly corresponds to the typical resolution of the METEOSAT images over Europe.

2. METHODOLOGY

We have used without any modification, the 1.51 version of the UVspec package [Refs 1, 2]. This radiative transfer code offers several options for solving the radiative transfer equation; we have systematically used the well known DISORT routine [Ref 3], in its classical plane parallel version and with six streams. We used UVspec to generate two Look Up Tables (LUT), one giving ultraviolet dose rates at the surface and the other simulating the radiance at the input of the MVIRI sensor on board the METEOSAT satellites. The entries of these tables are a selection of the UVspec parameters describing the radiative characteristics of the atmosphere and the Earth surface.

2.1 The UV Look Up Table

The retained entries for the ultraviolet LUT are solar zenith angle, total column ozone amount, cloud liquid water path (CLWP), horizontal visibility at the surface, Lambertian equivalent UV surface albedo and surface elevation. We chose these parameters on the basis of their significant influence on the surface UV radiation intensity and/or because of the possibility of assigning them geographically and/or temporally resolved values. Figure 1 shows the overall scheme for producing UV maps using this LUT.

Solar zenith angle, horizontal visibility and surface albedo are explicit input parameters of the radiative transfer code. The visibility parameter modulates the tropospheric aerosol optical thickness (the code equates the extinction coefficient at 550 nm to ~3 times the inverse of the visibility expressed in km). A background standard aerosol model was used [Ref 4], the method is therefore unable to take into account the variability in the spectral radiative properties of different aerosol species or in vertical aerosol profiles. Changing the total column ozone amount and/or surface elevation requires modifying the atmospheric profiles. For the result presented here, a standard mid-latitude summer atmosphere was used as the basis [Ref 5]. To take into account the surface elevation, the profiles are truncated in their lower part, up to the surface altitude. The resulting total column ozone amount is then computed and set to the desired value by multiplying the ozone concentration by the adequate scaling factor. This procedure obviously neglects the variability in the ozone profile shape. UVspec uses four parameters to describe the low clouds: thickness, altitude, effective water droplet radius and density. As the cloud information is later derived using only the visible band image of the MVIRI sensor, we needed to reduce the cloud

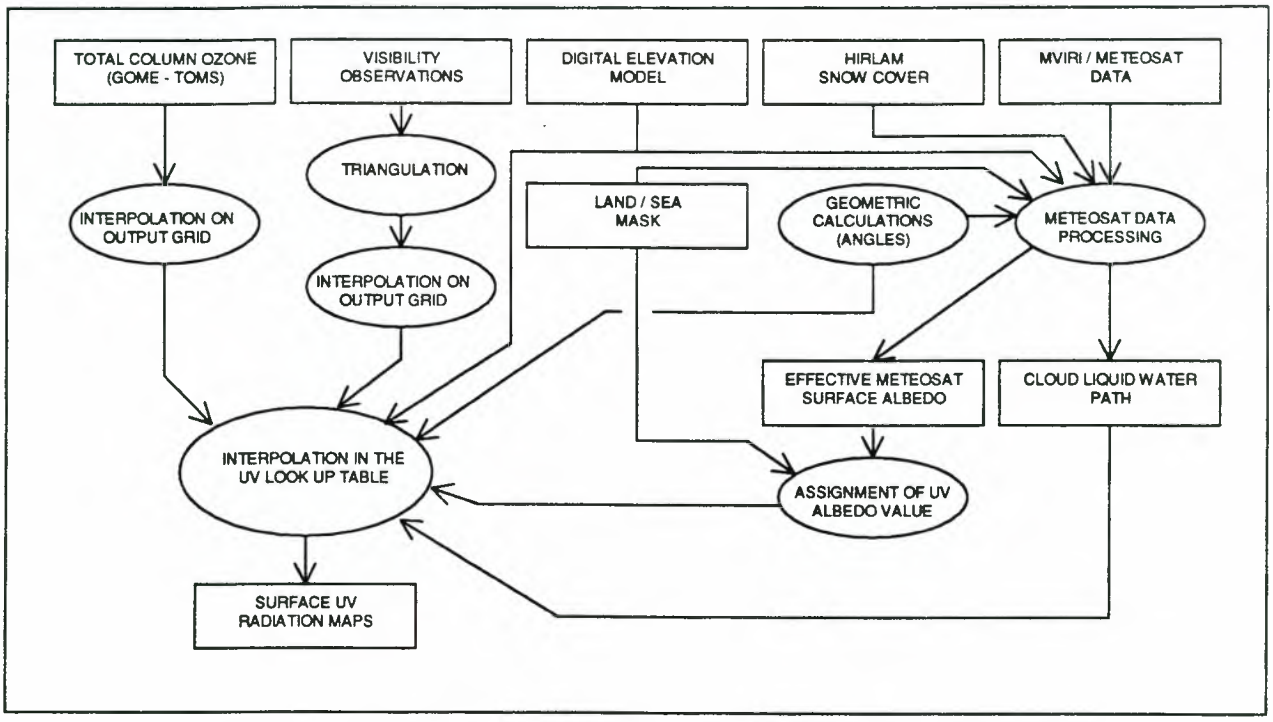

Figure 1. Overall structure of the algorithm to produce surface UV radiation maps.

description to a single parameter, equivalent to the cloud optical thickness. We chose fixed values for the altitude, thickness and droplet radius (respectively 1 km, 1 km and 7μm) and left the density variable, which then determines the liquid water path. The value for the effective drop radius is a climatological value adapted to clouds over land [Ref 6].

2.2 The METEOSAT Look Up Table

This second LUT is used to retrieve a liquid water path from the MVIRI/METEOSAT images. This time, the top of atmosphere radiance is computed as a function of solar zenith angle, viewing zenith angle, difference between the illumination and viewing azimuth angles, cloud liquid water path (CLWP), the effective surface albedo in the MVIRI visible band and the surface elevation. The three angles are explicit input parameters of UVspec and the other parameters are treated in the same way as for the UV LUT. The MVIRI visible channel has a broad spectral band extending from 500 to 900 nm and it takes quite a large CPU time to perform the calculations over the entire band. To keep the computing time reasonable, a narrower band centered on the maximal spectral sensitivity was used. Furthermore, the METEOSAT LUT does not include the variability due to water vapour and ozone amount. These are admittedly drastic simplifications. However, we use the LUT only to compare the cloudy and non cloudy signal. The absolute values are only of a second order importance and this should reduce the impact of the approximations on the results.

2.3 Retrieval of values for the cloud liquid water path

The overall scheme for processing the METEOSAT data is illustrated in Figure 2. Given the date and time slot, for which the UV maps have to be produced, the first step is to reconstruct a map of effective surface albedo. For this purpose, we use a series of images acquired during ten days centered on the considered date and for the same time slot, in order to find a cloudless situation. For each pixel, the various illumination and observation angles are computed. Using also the elevation data, the METEOSAT LUT is reduced to two entries: effective surface albedo and cloud liquid water path. For low values of the surface albedo (large majority of cases) the signal increases with cloud thickness. A first guess is therefore to assign the lowest observed signal to the cloudless situation and to compute the corresponding surface albedo. The METEOSAT signal dependence on CLWP is then estimated from the LUT, for the retrieved effective albedo. If the signal is indeed found to increase with CLWP, the effective albedo value is accepted. In the opposite case (i.e. the signal decreases with increasing CLWP), the logic is reversed and the surface signal is associated with the maximal signal observed during the ten days. In practice the latter case only occurs over snow covered areas. This procedure assumes that the surface reflectivity is stable during the ten day period. It should be stressed that the effective albedo obtained in this way does not pretend in any way to represent the real surface albedo. It is only the value of the albedo parameter, in the modelling scheme described above, that reproduces the signal intensity for the given date and time slot.

Although most of the clouds are eliminated, a substantial fraction remains, especially in the Arctic. The effective albedo map is further processed to eliminate part of the remaining cloudy pixels, on the basis of separate histograms of effective albedo over land and seas/ocean. These histograms show an asymmetrical peak with a trailing edge on the high value side. The albedo values above a certain threshold are rejected and substituted by value on neighboring pixels. The high albedo values are however kept where the pixel may be snow covered. These are identified using the HIRLAM data, giving the snow cover over Europe on the basis of synoptic observations and modelling.

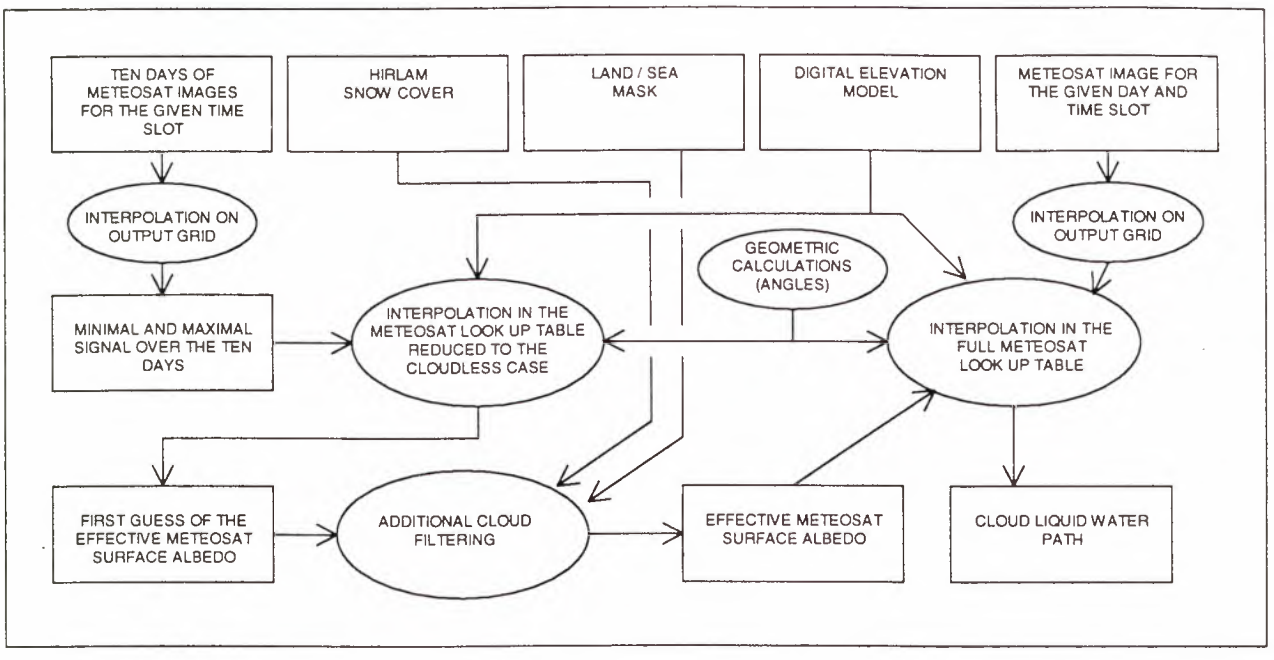

Figure 2. Overall scheme for estimating the cloud liquid water path from MVIRI/METEOSAT data.

Finally, the cloud liquid water path for the selected day and slot is retrieved from the corresponding original METEOSAT image and effective albedo map. For each pixel, we determine the value of CLWP that reproduces the METEOSAT signal, using the full METEOSAT LUT.

2.4 Assignment of values to the other influencing parameters

For surfaces not covered by ice or snow, the UV Lambertian equivalent reflectivity typically varies between 0.01-0.04 (land) and 0.05-0.1 (water). These ranges of value are supported both by ground or airborne measurements [Ref 7] and estimation from satellite observations [Ref 8]. Several sensitivity studies have shown that for these low values of surface reflectivity, the influence on the surface downwelling UV intensity is very limited [Refs 7, 9]. The bright surfaces that make the exception are sand deserts and, more important for Europe, snow covered areas. The UV effective reflectivity of a snow covered surface depends on a number of factors such as grain size, purity, illumination angle, layer thickness. A range of values from 0.6 to close to 1 are reported in the literature [Refs 10, 11]. Furthermore, for mapping the UV radiation, we are interested in the effective reflectivity of an area corresponding to a map pixel. While the reflectivity of pure clean snow may approach 1, partial snow cover, the presence of trees and other similar factors will very often significantly reduce the effective pixel reflectivity. The detailed information that would be necessary to correctly assign the value to the UV albedo is clearly not available at the chosen spatial resolution and scale. For generating the maps, we have thus assigned values of 0.06 to sea/ocean pixels and 0.03 to non snowy land pixels. We assigned a value equal to 70% of the effective visible albedo to the pixels identified as snowy from the METEOSAT data processing. The rationale for proportionality between the albedo in the two spectral ranges is that partial snow cover should affect them in a similar way. The value of 70% was chosen to set the values of the UV albedo in the reported experimental range.

Tropospheric aerosols are an important factor in determining the intensity of the surface UV radiation. They backscatter and absorb the radiation, leading to a diminution of the surface radiation. Different types of aerosols vary considerably in their UV single scattering albedo: between 0.9 and 1 for maritime aerosols and antropogenic sulfate, down to 0.6 for urban aerosols and smoke [Ref 9]. Their efficiency in reducing the surface radiation vary accordingly. In any case, the aerosols should be taken into account for mapping UV radiation, in particular if the results are intended to be exploited for change studies. An increase in the aerosol load could indeed reduce the upward trend due to stratospheric ozone depletion [Ref 12]. However, historical and geographically resolved maps of aerosol load and optical thickness are not readily available. In most UV mapping processors, this constrains to assume a constant background aerosol characterisation. One exception is the use of the TOMS UV aerosol index [Ref 13]. This data set is definitely pertinent for global studies but is not ideally adapted for high spatial resolution maps. While the new satellite ocean colour sensors (OCTS, SEAWIFS) provide aerosol optical thickness over seas and oceans with 1 km resolution, there aren't yet similar products over land. In the present version of the processor, we make an attempt to use the observations of horizontal visibility reported by the ground meteorological stations. More precisely, we exploit a database of meteorological observations compiled by the MARS (Monitoring Agriculture with Remote Sensing) project at the JRC. This data set is made of information obtained from national meteorological services, either directly or via the Global Telecommunication System. The data are preprocessed to convert them in a standard format. The database spans a period from 1974 to present. We use the mean daytime visibility, expressed in kilometers. Over the area covered by the UV maps, approximately one thousand stations report this daily value. The meteorological observations are interpolated on the UV map grid. This is

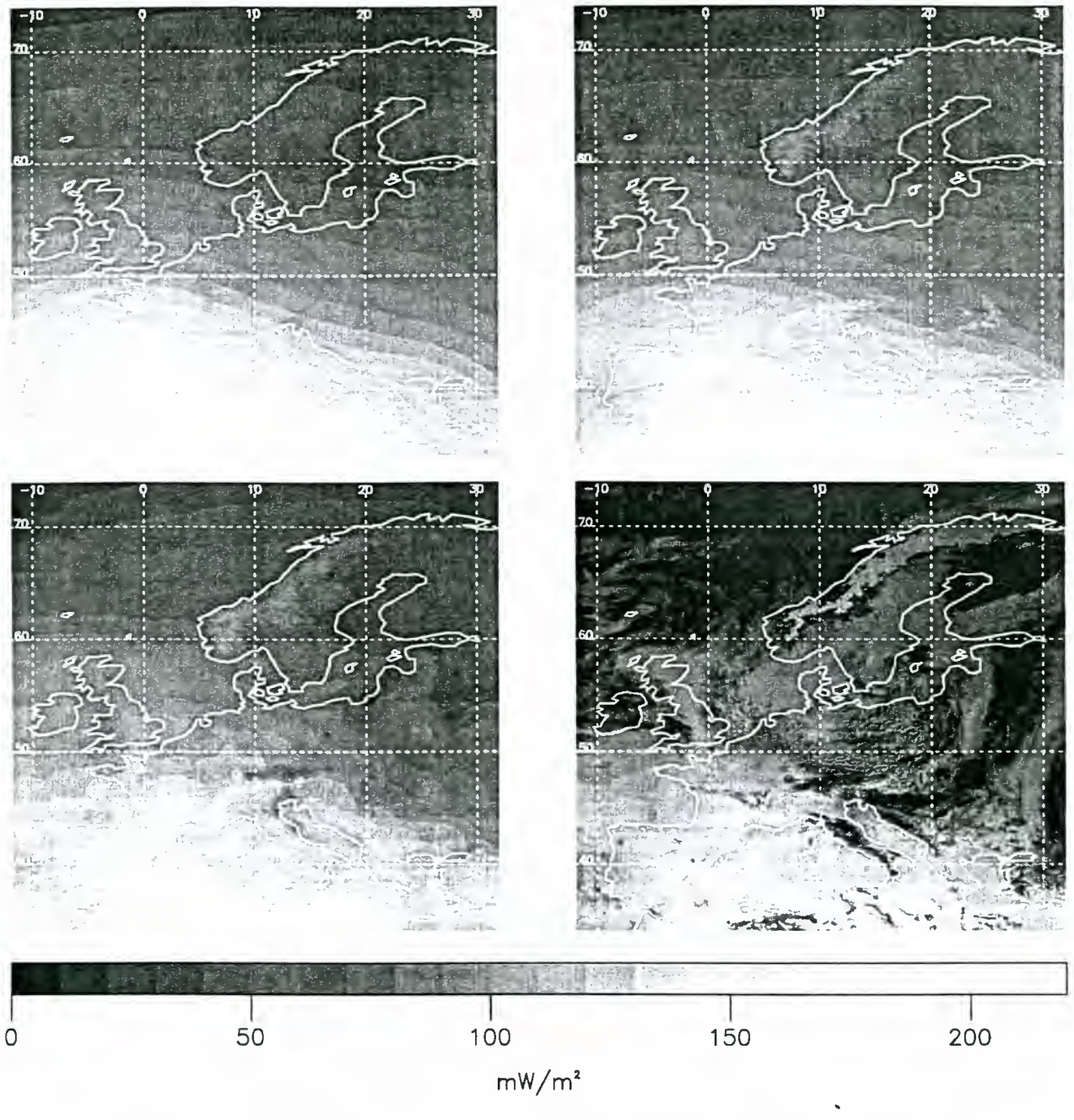

Figure 3. A series of UV maps showing the influence of various factors. All maps represent erythemally weighted UV dose rate, on April 15th 1997 at 11:22 UTC. Top left: only solar zenith angle and total column ozone are taken into account (surface elevation = 0, Lambertian equivalent UV surface albedo = 0.03, visibility = 20 km). Top right: after inclusion of surface elevation and albedo. Bottom left: after inclusion of surface visibility. Bottom right: after inclusion of attenuation by clouds.

performed in a simple way by finding the Voronoi polygon of stations associated to each node of a 0.5 degree grid in latitude and longitude, following a spherical Delaunay triangulation. The visibility value at each node is then computed by weighting the contributing stations values in inverse proportion to their distance to the considered grid node. Finally, the values on the finer UV map grid are interpolated on the 0.05 deg. grid with a bi-linear algorithm.

The method described here only needs the total column ozone amount, which can be obtained from various sources. For the recent years (after July 95), we use the level 3 GOME data available from the ATMOS User Center at DLR (http://auc.dfd.dlr.de/GOME/index.html). These daily maps are obtained by interpolating the level 2 data on the basis of an atmospheric planetary wave model (the level 2 data provide global coverage in three days). For earlier years, we use the TOMS version 7 level 3 gridded data (1 degree latitude x 1.25 degree longitude). In both cases, the ozone data are interpolated on the UV map grid with a simple bi-linear algorithm.

The information on surface elevation comes from the GTOPO30 world digital elevation model (DEM) elaborated by and available from the U.S. Geological Survey's EROS data center (http://edcwww.cr.usgs.gov/eros-home.html). This truly global data set contains the elevation for land surfaces, on a regular grid in latitude and longitude, with a spatial resolution of 30 arc seconds. For the purpose of this work, the DEM was resampled both on the METEOSAT grid and the grid chosen for the UV maps. In both cases, the resampled DEMs contain the mean elevation inside the pixel. We also generated masks of land and sea/ocean used in the processing scheme.

3. EXAMPLE OF RESULTS AND PRELIMINARY COMPARISON WITH GROUND MEASUREMENTS

Although the processor also generates other dose rates, we systematically present here maps of the erythemally weighted UV radiation (CIE87); in order to make the comparison easier. Figure 3 shows the results obtained when the influencing factors are taken into account step by step. In the first image (top left), only the solar zenith angle and total column ozone are included, the other parameters are given uniform values (0.03 Lambertian equivalent UV albedo, 20 km visibility, 0 m elevation). The image corresponds to 11:22 UTC when the solar zenith angle is minimal at approximately 9.5 deg. of longitude East. In the image however, the maximal surface UV radiation is shifted to the west because of lower values of the total ozone column, which on this day typically varied from 300 to 350 DU over the Iberian peninsula, France and the British Isles and between 370 and 400 DU over the rest of Europe. In the next image (top right) we have introduced the elevation and the surface Lambertian equivalent UV albedo. The increase in surface UV radiation is due to both elevation and snow cover in Scandinavia and over the Alps, while the effect in Spain and Northern Africa for instance is solely due to the altitude. The procedure assigned typical values between 0.5 and 0.7 to snowy pixels in Norway and between 0.3 and 0.6 in the Alps. The typical increase in surface erythemal dose rate is from 55 to 70 mW/m^2 and from 150 to up to 200 mW/m^2 respectively. If we take the example of the highest pixel in the Sierra Nevada (37.6 deg. N- 4.25 deg. W, snow free), for which the mean altitude given by the resampled DEM is 1420 m, the erythemal dose rate increases to 190 mW/m^2 from 177 mW/m^2 when calculated as if at the sea level. In the following image (bottom left), we have used the horizontal visibility interpolated from ground observations instead of the relatively high uniform value of 20 km. Areas most affected are Southern Germany and Wales but, as these are also heavily covered by clouds, the low visibility value could result from rain. A decrease is also visible for instance in Catalonia, where a cloud free condition prevails. If we choose the pixel containing Barcelona (41.37 deg. N - 2.12 deg. E), the visibility is found to be 13.8 km and the erythemal dose rate is reduced from 179 mW/m^2 to 166 mW/m^2. Finally, the attenuation by clouds is introduced (bottom right) and it is of course the major factor determining the instantaneous surface dose rate.

With the exception of HIRLAM snow cover, all the input data are available back to the early eighties. The possibility of consistently generating information on the past situation at a decadal scale has been tested by producing maps for the year 1984. In this case, the total column ozone data are from TOMS.

Figure 4 shows a map of the erythemal daily dose on April 15th 1997. We have sampled the dose rate at half-hourly intervals from 4:52 to 17:52 UTC, using 27 METEOSAT images and integrated over this time range to obtain the dose. A correction factor was applied to take into account the fact that the fraction of the full daily cycle covered by the 27 time slots varies according to the geographical position. It should be remembered that only the attenuation by clouds is actually temporally sampled in this way, as we only have a daily average for the other influencing factors. The attenuation by clouds is however the most dynamic influencing factor. As expected, the cloud features are smoother than in the dose rate map of Figure 3. It should also be noticed that the patterns over Spain are significantly different. This is due to rapidly evolving meteorological conditions over this area, with clouds forming in the afternoon. This illustrate the interest of using the half hourly sampling rate of METEOSAT to better estimate the daily dose in such conditions.

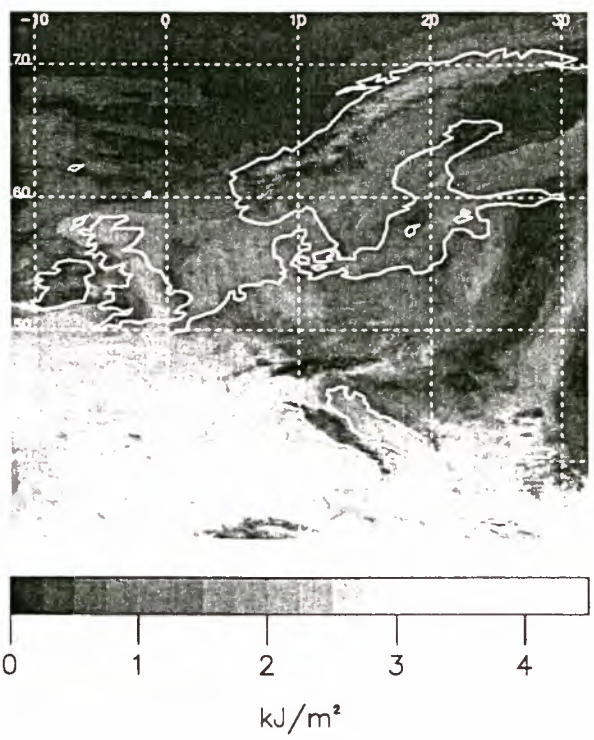

Figure 4. A map showing the erythemally weighted day dose on April 15th, 1997. This map was obtained by integration on time of dose rate estimated every half hour from 4:52 to 17:52 UTC.

In this paper we present a very preliminary comparison between the results obtained with the mapping methodology and ground measurements performed at the Environment institute of the JRC, in Ispra. The spectral measurements were performed with a Brewer instrument and extend from 290 to 325 nm. As longer wavelengths still significantly contribute to the erythemally weighted dose, we have chosen to compare the unweighted UV-B (280 to 315 nm). When comparing the instantaneous dose rate, the agreement can be quite good on cloudless days. In the presence of a broken field on the contrary, the model does not reproduce the high dynamic of the measurement. This is expected as the satellite derived dose averages over an area of about 25 km^2 while the ground instrument reacts to the passing of a single cloud. The broken

cloud field is also a case where plane parallel modelling, which considers a horizontally homogeneous atmosphere, is in principle not valid. The same is true in general wherever a strong horizontal gradient in any of the influencing factors is present. Another example is the fact that high albedo surfaces (snow covered) increase the surface radiance in snow free adjacent areas [Ref 14]. These "3D" effects are significant for high spatial resolution UV maps such as those presented here. On the other hand, the implied CPU time still makes three-dimensional modelling impracticable for generating maps.

However, in the case of a broken cloud field, and because of ergodicity, we can expect that the errors will partly average out when performing the integration to obtain the daily dose. This is what suggests Figure 5, which shows quite encouraging agreement when we compare the results for the daily dose of ten days in July 1996. In this figure and to illustrate the relative importance of the influencing factors, we have also plotted the doses obtained for absolutely clear sky and constant ozone amount and when introducing step by step the observed ozone amount and estimated visibility. Over these tens days, total column ozone varied between 303 and 323 DU and visibility between 9.7 and 19.5 km.

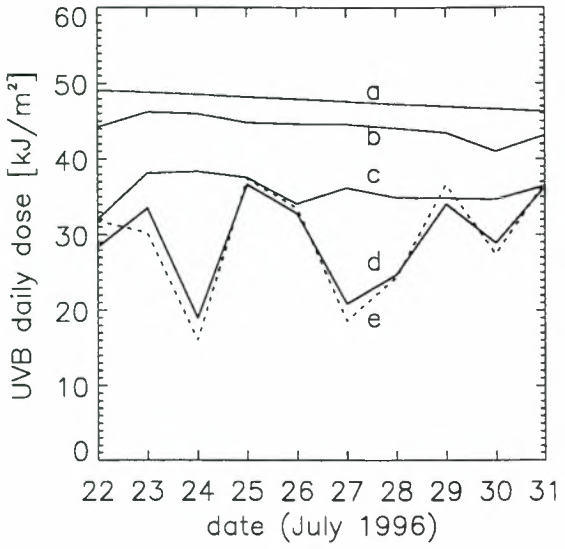

Figure 5. Comparison between modelled and measured UV-B (280-315 m) daily dose at Ispra (45.8 deg. N – 8.63 deg. E – 220 m altitude) during a ten-day period from July 22nd to July 31st, 1996. The dotted line (e) represents the measurement. The solid lines represent the modelled values, a: only the solar zenith angle is variable (total column ozone= 290 DU, no aerosols and no clouds), b: the actual total column ozone is additionally taken into account, c: the visibility observations are used to modulate the attenuation by aerosols, d: after inclusion of cloud attenuation.

This single comparison is certainly not sufficient to draw a conclusion on the quality of the UV maps. We have plans to systematically assess the maps' accuracy by comparing the results with a comprehensive set of ground measurements. These will be chosen to be representative of the variability in influencing factors encountered in Europe during a full year (geographical, meteorological and environmental). We see this exercise as a vital step to determine the usefulness of satellite derived maps with regard to various potential applications.

4. CONCLUSION

The technical capability of generating surface UV irradiance maps over Europe that take into account the geographical variability of solar zenith angle, total column ozone, attenuation by clouds and tropospheric aerosols, surface elevation and albedo with a spatial resolution of 0.05 deg. has been demonstrated. These maps could be produced on a half-hourly basis and used to compute the UV dose integrated on a day. The same information could also be consistently generated with 1984 data. This suggests that the methodology is adapted to enable change studies. All included influencing factors have been found to significantly affect the surface UV irradiance in the context of the geographical and temporal variability encountered in Europe. The accuracy of the produced information has not yet been systematically assessed but a preliminary comparison with a single set of ground measurements in Ispra is encouraging for the quality of the daily dose estimation.

5. ACKNOWLEDGMENTS

The author thanks F. Cappellani and C. Koechler of the Environment Institute of the JRC for providing the ground measurements of UV-B. He also thanks M. Amsellem and C. Attardo of the MARS project for the meteorological synoptic data. The HIRLAM snow cover data were kindly provided by P. Taalas and S. Kalliskota of the Finnish Meteorological Institute. This work was supported under contract No ENV4-CT97-0401 of the Environment and Climate RTD Programme of the European Commission.

6. REFERENCES

1. Kylling, A., UVspec, A program package for calculations of diffuse and direct uv and visible intensities and fluxes, available by anonymous ftp to kaga.gi.alaska.edu, cd pub/arve, 1995.

2. Mayer B., Seckmeyer G. and Kylling A., Systematic long-term comparison of spectral UV measurements and UVSPEC modelling results, J. Geophys. Res., 102, 8,755-8,767, 1997.

3. Stamnes, K., S.-C. Tsay, W. Wiscombe and K. Jayaweera, Numerically stable algorithm for discrete-ordinate-method radiative transfer in multiple scattering and emitting layered media, Appl. Opt., 27, 2502-2509, 1988.

4. Shettle, E.P., Models of aerosols, clouds and precipitation for atmospheric propagation studies, in AGARD Conference Proceedings No. 454, Atmospheric propagation in the uv, visible, ir and mm region and related system aspects.

5. Anderson, G.P., S.A. Clough, F.X. Kneizys, J.H. Chetwynd and E.P. Shettle, AFGL Atmospheric constituents Profiles (0-120 km), AFGL-TR-86-0110, AFGL (OPI), Hanscom AFB, MA 01736, 1986.

6. Rogers, R.R. and M.K. Yau, A short course in cloud physics, Pergamon Press, Oxford, pp 293, 1989.
7. Madronich, S., UV Radiation in the Natural and perturbed Atmosphere, in UV-B Radiation and Ozone Depletion – Effects on Humans, Animals, Plants, Microorganisms, and Materials, edited by M. Tevini, pp 17-68, Lewis Publishers, 1993.

8. Herman, J.R., and E.A. Celarier, Earth surface reflectivity climatology at 340-380 nm from TOMS data, J. Geophys. Res., 102, 28003-28012, 1997.

9. Krotkov, N.A., P.K. Barthia, J.R. Herman, V. Fioletov and J. Kerr, Satellite estimation of spectral surface UV irradiance in the presence of tropospheric aerosols- 1. Cloud-free case, J. Geophys. Res., 103, 8779-8793, 1998.

10. Warren, S. G., Optical properties of snow, Rev. Geophys. Space Phys., 20,67-89, 1982.

11. Feister, U. and R. Grewe, Spectral albedo measurements in the UV and visible region over different types of surfaces, Photochem. Photobiol., 62, 736-744, 1995.

12. WMO, Scientific Assessment of Ozone depletion: 1994, Global Ozone Research and Monitoring project, WMO Rep. No 37, Geneva, 1995.

13. Herman, J. R., P.K. Barthia, O. Torres, C. Hsu, C. Seftor and E. Celarier, global distribution of UV-absorbing aerosols from Nimbus 7/TOMS data, J. Geophys. Res., 102, 16,911-16,922, 1997.

14. Degünther, M., R. Meerkötter, A. Albold and G. Seckmeyer, Case study on the influence of inhomogeneous surface albedo on UV irradiance, Geophys. Res. Lett., 25(19), 3587-3590, 1998.

SURFACE UV MODELLING AND VALIDATION USING GOME DATA

A. Menkhaus, M. Weber, C. Haite, J. P. Burrows

Institute of Environmental Physics,
University of Bremen FB1,
P.O. Box 330 440,
28334 Bremen, Germany.
(e-mail: anja.menkhaus@iup.physik.uni-bremen.de; mark.weber@iup.physik.uni-bremen.de;
christine.haite@iup.physik.uni-bremen.de; john.burrows@iup.physik.uni-bremen.de)
Uwe Feister
Deutscher Wetterdienst,
P. O. Box 60 05 52,
14405 Potsdam, Germany.
(e-mail: ufeister@dwd.d400.de)

ABSTRACT

Three different satellite based methods for the calculation of the UV radiation from GOME spectral data at the earth surface are presented. The main difference between the three methods is the way cloud information is derived from GOME data and how it is implemented in the algorithms. The first idea in how to handle the clouds is based on an empirical cloud correction factor which is derived from reflectivity measurements at 380nm. The second method calculates the UV surface spectra by taking a weighted sum of clear sky and overcast spectrum where the weight f is the partial cloudiness in percent, computed from the GOME data in two alternative ways. All radiative transfer calculations are done by a multiple scattering pseudospherical radiative transfer model (RTM) including aerosols and clouds as layers.

For the validation of the three models data from ground based Brewer spectroradiometers operated by the German Weather Service (DWD) are used. The spatial and temporal coincidence between the satellite overpass and the ground based measurement deeply affects the quality of the UV field estimation. The presence of broken clouds and the short time scale cloud variability within the field of view of the satellite are the major factors giving rise to significant discrepancies. Provided that the atmospheric conditions are mostly unperturbed, the overall agreement is good. A higher resolution cloud detection algorithm is a very promising tool to deal with more disturbed situations.

1. INTRODUCTION

Due to the depletion of stratospheric ozone an enhancement of the biologically harmful UVB radiation reaching the earth surface is expected (Ref. 21). Other effects such as possible increases in aerosol loading and variations in the cloud coverage have also to be taken into account to study longterm trends in UV surface radiation. One disadvantage of ground based UV measurements is that they mainly look at local effects. A satellite based method in deriving UVB radiation, however, is able to produce global maps of UV fluxes and analyse global UV trends with respect to cloud, aerosol and ozone variability.

The first approach to derive UV radiances from satellite measurements was based on data from the NIMBUS 7 solar backscattered ultraviolet (SBUV) instrument (Ref. 8). It uses atmospheric radiation budgets and the law of energy conservation to compute the biologically active UV radiation. A second method calculates the surface UV radiation over Antartica with the help of NOAA/AVHRR cloud information and NIMBUS 7/TOMS total ozone data (Ref. 17, 16). Another algorithm was developed by NASA/GSFC to determine UVB fluxes from the NIMBUS 7/TOMS instrument using total ozone and reflectivity measurements for cloud correction (Ref. 3, 12, 13). In this paper GOME data are used to derive surface UVB radiation. GOME provides in addition to total ozone auxiliary information about the atmosphere, for example fractional cloud cover and UV/VIS reflectivity. It is, therefore, possible to derive the UV index from a single satellite instrument.

2. GOME INSTRUMENT

The Global Ozone Monitoring Experiment (GOME) is a new passive remote sensing instrument launched by ESA aboard the second European Research satellite (ERS-2) in late April 1995 (Ref. 5, 1, and references therein).

The primary objective of GOME is the derivation of vertical columns of relevant atmospheric trace gases, such as O_3, NO_2, BrO, OClO, SO_2, H_2CO, from the backscattered radiance and direct solar irradiance measurements (Ref. 1, 18, 10, 22, 4). GOME comprises entrance optics, a spectrometer, as well as electronic and thermal subsystems. The spectrometer is basically a double monochromator, where the light is separated into four spectral channels. Each of the latter contains a holographic grating and a Reticon Si diode array detector with 1024 pixels. In this manner the entire spectrum from 240 to 790 nm is observed simultaneously and the spectral resolution varies between 0.2 and 0.4 nm depending on the spectral channels (Ref. 1). Part of the light which reaches the predisperser prism is branched out and recorded with three broadband polarization monitoring devices (PMD), which approximately cover the spectral range of the GOME spectral channels 2 (300-400nm), 3 (400-600nm), and 4 (600-800nm), respectively. The PMDs measure the amount of light at an instrument defined polarization angle. GOME is a nadir viewing instrument and the measurement sequence consists of

three across-track scans lasting 1.5 sec each. Each forward scan covers a surface area of 40 km along-track × 320 km across-track. The readout time of the PMDs is 93.75 msec, such that each spectral scan of 1.5 sec includes 16 PMD measurements. Besides measuring the fractional polarisation of the backsattered radiances, the PMD measurements can be used to obtain additional information on cloud distribution and surface reflectivity variation at a higher spatial resolution (40×20 km^2) than is possible from the spectral channels alone.

3. GOME UV MODELS

One of the most important and challenging needs in computing the UV radiation reaching the ground from satellite data is the knowledge of the atmosphere's composition. The actual and local amount of the main absorbers in the UV region like oxygen and ozone is measured by the GOME instrument. However, the correlation between stratospheric ozone depletion and an enhancement of ultraviolet radiation reaching the earth's surface can be only studied if other impacts to the incoming solar light are considered. Particularly clouds have a dramatic screening effect on the UV flux. The probability that a GOME pixel (40 x 320 km^2) is contaminated with clouds is estimated to be more than 99.8% (Ref. 2). Thus, the necessity of correcting UV calculations for clouds is obvious and one main aspect in this work. In Figure 1 the two extreme cases of clear and complete overcast sky and its impact on the UV index are shown in the time series of GOME derived UV indices in Bremen (53°N, 9°E). Under partial cloud cover the derived UV index lies between the two extreme values shown in the bottom of Figure 1, if the fractional cloud cover information from GOME is used (see section 3.2). In early March an ozone mini-hole with total ozone as low as 210 DU passed through Bremen causing an increase of UV exposure by a factor of almost two, which is, however, still less than half of that reached in the summer.

3.1. Reflectivity Models

The following method was first applied for TOMS satellite data (Ref. 3). An empirical correction factor determined from the top of atmosphere reflectivity at 380 nm is used:

$$F = F_{clr}[1 - (R - 0.05)/0.90]\,, \qquad (1)$$

with F being the actual surface flux and F_{clr} the clear sky surface flux. The reflectivity R is obtained by averaging the GOME sunnormalised radiances from 380 to 381 nm. F_{clr} is calculated with a radiative transfer model GOMETRAN (Ref. 19), which includes the total ozone column information obtained from GOME. The RTM calculation includes full multiple scattering, pseudospherical geometry, and an aerosol parametrization scheme. The aerosol optical thickness is taken from the global aerosol data set (Ref. 11). For reflectivities $R > 0.5$ the ground albedo, described by the off-set 0.05 in the above formula, can be neglected and the surface flux can be expressed as follows:

$$F = F_{clr}(1 - R) \qquad (2)$$

(Ref. 3).

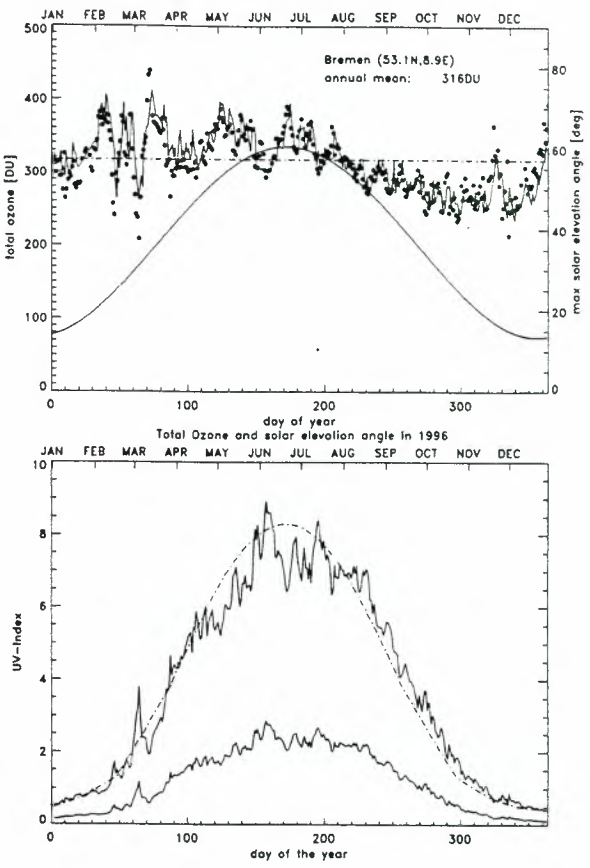

Figure 1: 1996 time series of daily total ozone measured by GOME (solid line) and ground based ozone data from an UV zenith sky spectrometer in Bremen, Germany (53°N, 9°E, solid points). All GOME data recorded within a distance of 500km from Bremen were averaged. The horizontal line corresponds to the GOME annual mean of 316DU. Also shown are the annual variation of the maximum solar elevation angle above horizon each day. Bottom: Using the daily GOME total ozone and the daily maximum solar zenith angle a time series of the UV index under clear-sky condition (top curve) and overcast condition (bottom curve) are shown in the bottom. A reference UV index time series calculated from the annual total ozone mean is shown as a smooth line. An uniform altostratus cloud with vertical extent from 1.5 to 2 km and optical depth of 20 has been assumed, which reduces the UV index by a factor of about 3.2 from that under clear sky condition.

3.2. Cloud Cover Models

The second and third model use the GOME observation of fractional cloud cover which is derived in two different ways. In the radiative transfer model GOMETRAN clouds can be parametrized in two ways: as a bidirectional reflecting surface or as a scattering layer with radiation penetrating the clouds. In both methods the cloud is assumed to be extended homogeneously over the entire GOME ground pixel. Since the most common scenario is

a sky with partial cloud cover, the radiative transfer calculation ist done twice, once for clear sky situation (F_{clr}) and then for a completely overcast scene (F_{cloud}). These two results are combined to a weighted average, where the weight is determined by the fractional cover f:

$$F = (1 - f) * F_{clr} + f * F_{cloud}. \quad (3)$$

There are two independent methods to derive the cloud fraction f from GOME: the ICFA (Initial Cloud Fitting Algorithm) method and the PMD (Polarization Measurement Device) algorithm.

3.2.1. The Initial Cloud Fitting Algorithm (ICFA)

The Initial Cloud Fitting Algorithm (ICFA) was first proposed by Kuze and Chance in 1994 and has been extended to be part of the operational GOME level 1 to level 2 processing (Ref. 20). The major aim of ICFA is to obtain a cloud correction to the retrieved trace gas columns (Ref. 1).
The algorithm is based on the following idea: The missing O_2 absorption below the cloud top measured in the oxygen A band at 760 nm gives an estimate of the fractional cloud cover. By least squares fitting, the cloud fraction is searched which minimizes the difference between measured and precomputed transmittances, exploiting the moderately high spectral resolution of GOME (Ref. 1).
The calculated UV spectra are finally multiplied with the CIE function resulting in the erythemally weighted spectrum. Integration over the UV wavelength region and multiplying by 40 leads to an UV index between 0 and 16.

3.2.2. The PMD algorithm

An alternative way to obtain a more accurate and detailed measure of the cloudiness is to enhance the spatial resolution. The three broadband Polarization Measurement Devices (PMDs) of the GOME instrument, which are used to determine the polarization state of the incoming radiances, are read out 16 times faster than the diode arrays, yielding an improved spatial resolution of 40 x 20 km^2.
The three reflectivity signals from the PMDs, approximately covering the red, green and blue part of the visible GOME spectrum, are tested against user-defined thresholds (Ref. 14). Pixels showing a reflectivity lower than a predefined minimum are identified as cloud free and pixels, whose PMD signals exceed a certain maximum threshold are declared complete overcast. For partially cloudy scenes, i.e. the signal P lies between P_{min} and P_{max}, the fractional coverage f is computed as follows:

$$f = \frac{|P_i - P_{i,min}|}{P_{i,max} - P_{i,min}}, \quad (4)$$

where the index i denotes the number of the device (i=1,2,3).
Due to the different spectral reflection properties of different earth surface types the actual test varies with the surface type detected. The surface dependence of the *ratios* of certain pairs of the signals is also exploited. Furthermore a permanent update of the thresholds is performed, thus providing an optimum basis for cloud classification, derived directly from the instrument's signal.

4. VALIDATION OF THE UV MODELS

For the validation of the UVB models ground based measurements by Brewer spectroradiometers operated by the German Weather Service (DWD) in Potsdam, Hohenpeissenberg and Lindenberg were collected. The Brewer instruments in Lindenberg and Hohenpeissenberg are single monochromators while in Potsdam measurements are made with a single and, in addition, with a double monochromator. Spectra from Hohenpeissenberg and Potsdam are corrected for the cosine error (Ref. 7) while the correction is not applied to measurements from Lindenberg leading to an error of up to a maximum of 10% to 15%. At days with partial cloudiness it is difficult to compare model values with measurements since clouds have a large effect on the UV spectra. Even short time differences between the GOME overpass and the ground based measurement can lead to large deviations in the UV index because the satellite and the ground measurement might see different sky conditions. One ground based spectral measurement takes about eight minutes and quick cloud passages can lead to inconsistent surface measurements. It should be mentioned that GOME cloud detection with PMDs has a maximum spatial resolution of 40 x 20 km^2 and GOME sees therefore spatially averaged cloudiness, whereas only *local* cloud information is important for the ground based measurements.

Figure 2 shows the UV indices for all coincidences between GOME overpasses and DWD measurements in the months April to September in 1996 and 1997. Spatial coincidence was fulfilled if the PMD subpixel (40 x 20 km^2) contained the DWD station. The time differences between the two measurements had to be less than 30 minutes. The best correlation between the GOME and the DWD UV index is found with the PMD model. Both the ICFA and the Reflectivity Model tend to underestimate the UV index. The ICFA cloud fraction calculated with the GOME Data Processor (GDP) Version 2.0 (1996-1997) is known to be overestimated (see Figure 3) which may explain the underestimation of the UV index by the Bremen ICFA model. Better agreement shall be obtained for the new version 2.3 (1998-present).

The Hohenpeissenberg measurement station lies at a sea level of 970m. Our assumption for the aerosol optical thickness of 0.2 may be too high leading to GOME UV indices too small for this station. The scattering of the points in Figure 2 can be mainly explained by the influence of broken clouds.

In Figure 4 only those points where the averaged cloud fraction over the 16 PMD-subpixels (16 sequential PMD measurements occur during one high spectral resolution scan) is lower than 10% are plotted and the time gap between the measurements is smaller than 5 minutes. Under such restricted circumstances there is an excellent correlation between our model and the DWD data. In the bottom of Figure 4 we can see that the best correlation is found for the data from Potsdam. For Lindenberg

the deviations seem to be larger because the spectra are not corrected for the cosine error. The GOME UV indices for Hohenpeissenberg seem to be a bit too low perhaps due to a too heavy aerosol loading assumed as mentioned already above.

The difficulties in modelling the UV index under broken cloud condition are shown in Figure 5. Greatest deviations should occur in the region where the averaged cloud fraction lies between 0.3 to 0.7 which can be seen in the upper plot of the picture. As the cloud fraction approaches 1 one would expect small deviations between model and measurement as for clear-sky conditions. This is not the case in general because of unknown parameters for the complete description of the clouds (cloud optical thickness, cloud type and height), which have to be estimated.

In the bottom of Figure 5 we can see that with increasing variability of the cloud fraction from PMD pixel to PMD pixel within the agreement between model and measurement becomes worse because of the fluctuating cloud conditions.

5. CONCLUSIONS

We have shown that GOME specific products can be used efficiently for the estimation of global surface UV irradiance. However the most problematic issue is the time lag between satellite observation and ground measurement. If broken clouds are shielding the field of view at the time of overpass, accurate UV index is difficult to estimate. To solve this problem, the use of higher resolution PMD measurements seems to be the most promising methodology for detecting and taking this situation into account. This validation is limited both in time and space. Together with improvements in the models, a more comprehensive intercomparison is needed that would include the effects of ground albedo and aerosol attenuation.

One great advantage of GOME is that the satellite actually measures backscattered UVB radiation. Because GOME measures a broad spectral range (240nm - 790nm) it is possible to perform direct aerosol retrieval (Ref. *Guzzi et al.* 1998) using the decreasing behaviour of the part of the spectrum, where trace gas absorption does not play such a important role. Furthermore, we plan to implement a cloud retrieval code which consists of a combination of the absorption of the O_2 A band and the PMD algorithm to simultaneously derive the cloud fraction, cloud top height and perhaps cloud type (Ref. 9). Further improvements are expected from the use of O_3 profiles retrieved from GOME (Ref. 1) in place of the total column. In the model calculations we currently use the 1D radiative transfer code GOMETRAN++ (Ref. 15, 19). The next step beyond is to test our computations with a 3D radiative transfer model in order to improve the GOME UV index under inhomogenous cloud condition (Ref. 6). The combination of UV surface flux, cloud and possibly aerosol properties may provide important contribution to the further understanding of longterm trends of surface UV in conjunction with stratospheric ozone depletion and variability in meteorological conditions.

ACKNOWLEDGEMENTS

This work was funded in part by BMBF project 01 LU 9704/2, the state of Bremen, and the University of Bremen.

REFERENCES

1. Burrows, J.P. , M. Weber, M. Buchwitz, V. Rozanov, A. Ladstaetter-Weissenmeyer, A. Richter, R. De Beek, R. Hoogen, K. Bramstedt, K.-U. Eichmann and M. Eisinger, The Global Ozone Monitoring Experiment (GOME): Mission concept and first scientific results, *J. Atmosph. Sciences*, in press, 1998.

2. Derrien, M., Influence of the size of field of view on the contamination by clouds, Technical report, Meteo-France, 1992.

3. Eck, T., P. Barthia and J. Kerr, Satellite Estimation of Spectral UVB Irradiance Using TOMS Derived Total Ozone and UV Reflectivity, *Geophys. Res. Lett.*, *22*, 611-614, 1995.

4. Eisinger, M., and J. P. Burrows, Tropospheric Sulfur Dioxide observed by the ERS-2 GOME instrument, *Geophys. Res. Lett.*, 25, 4177–4180, 1998.

5. ESA, GOME Science Interim Report, eds. T.D. Guyenne and C. Readings, ESA SP-1151, European Space Agency Publication Division, Nordwijk, Netherlands, 1993.

6. Evans, K. F., The Spherical Harmonic Discrete Ordinate Method: Application to 3D Radiative Transfer in Boundary Layer Clouds, *J. Atmos. Sci.*, *55*, 429-446, 1998.

7. Feister, U., R. Grewe and K. Gericke, A Method for Correction of Cosine Errors in Measurement of spectral UV Irradiance, *Solar Energy*, 60, 6, 313-332, 1997.

8. Frederick, J. E., D. Lubin, The Budget of Biologically Active Ultraviolet Radiation in the Earth-Atmosphere System, *J. Geophys. Res.*, 93, D4, 3825-3832, 1988.

9. Guzzi, R., J. Burrows, V.V. Rozanov, K. Chance, M. Cervino, T. Kurosu, P. Watts, F. Torricella and K. Muirhead A Study of Cloud Detection, ESA, Final Report, ESA Contract 10997/94/NL/CN, (1996).

Guzzi et al. 1998. Guzzi, R., J. Burrows, M. Cervino, and T. Kurosu, GOME Cloud and Aerosol Data Products Algorithms Development (CADAPA). Tech. Rep. 11572/95/NL/CN, European Space Agengy, ESA/ESTEC, Noordwijk, The Netherlends (1998).

10. Hegels, E., P.J. Crutzen, T. Klüpfel, D. Perner, and J.P. Burrows, Global distribution of atmospheric bromine monoxide from GOME on Earth-observing satellite ERS-2, *Geophys. Res. Lett.*, 25, 3127–3130, 1998.

11. Köpke, P., M. Hess, I. Schult, and E. P. Shettle, Global Aerosol Data Set, *Theoretical and Applied Climate*, submitted, 1997.

12. Krotkov, N.A., P.K. Barthia, J. Herman, V. Fioletov and J. Kerr, Satellite estimation of spectral surface UV irradiance in the presence of tropospheric aerosols. 1. Cloud-free case, *J. Geophys. Res.*, 103, D8, 8779–8793, 1998

13. Krotkov, N. A., J.R. Herman, P.K. Bhartia, Z. Ahmad, and V.Fioletov Satellite estimation of spectral surface UV irradiance 2: Effect of horizontally homogeneous clouds, *J. Geophys. Res.*, this issue

14. Kurosu, T., PMD Cloud Detection Algorithm for the GOME Instrument; Algorithm Description and User's Manual, European Space Agency, Draft Final Report, ESA Contract 11572/95/NL/CN (1997).

15. Kurosu, T., V. Rozanov, and J. Burrows, Parametrization schemes for terrestrial water clouds in the radiative transfer model GOMETRAN. *J. Geophys. Res.*, *102*, 21,809-21,823 (1998).

16. Lubin, D., and E. Jensen, Effects of clouds and stratospheric ozone depletion on ultraviolet radiation trends, *Nature*, 377, 710-713, 1995.

17. Lubin, D., P. Ricchiazzi, C. Gautier, and R. Whritner, A Method for Mapping Antarctic Surface Ultraviolet Radiation Using Multispectral Satellite Imagery, Ultraviolet Radiation in Antartica: Measurements and Biological Effects, Antartic Research Series, Volume 62, 53-81, 1994.

18. Richter, A., F. Wittrock, M. Eisinger, and J.P. Burrows, GOME observations of tropospheric BrO in Northern hemispheric spring, *Geophys. Res. Lett.*, 25, 2683–2686, 1998.

19. Rozanov, V., D. Diebel, R. Spurr and J. Burrows, GOMETRAN: A Radiative Transfer Model for the Satellite Project GOME, the Plane-parallel Version, *Journal of Geophysical Research*, 102, No. D14, 16683-16695 (1997).

20. Spurr, R., GOME level 1 and 2 algorithms description, Technical Note ER-TN-DLR-GO-0025, Iss./Rev. 1/A, DLR, Oberpfaffenhofen, Germany.

21. Teveni, M. (eds.), UVB radiation and ozone depletion : effects on human, animals, plants, microorganisms, and materials, Lewis Publishers, 1993.

22. Thomas, W., E. Hegels, S. Slijkhuis, R. Spurr, and K. Chance, Detection of biomass burning combustion prodcuts in Southeast Asia from backscatter data taken by the GOME spectrometer, *Geophys. Res. Lett.*, 25, 1317–1320, 1998.

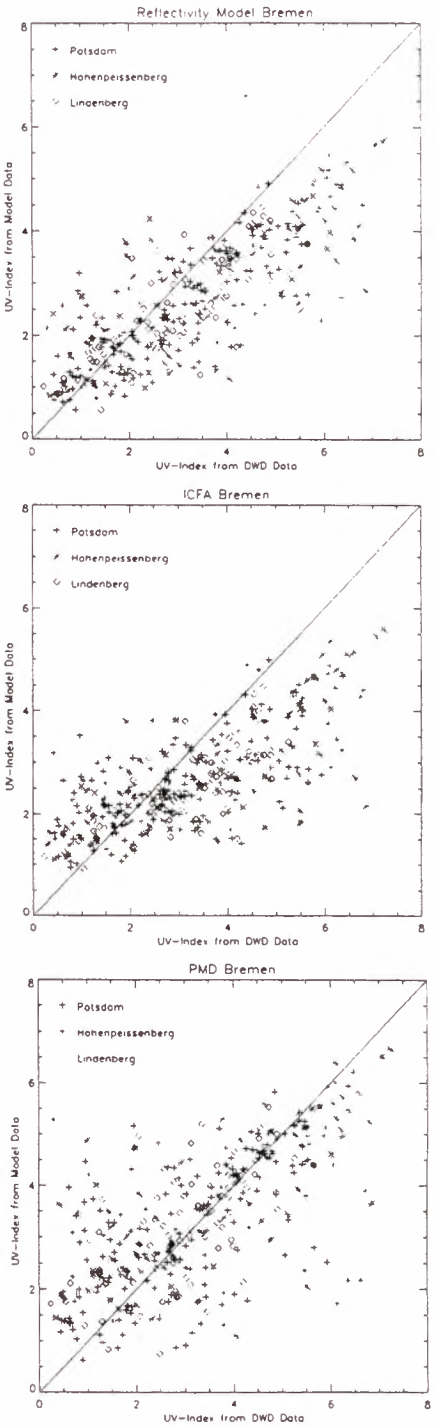

Figure 2: Scatter plot for the GOME UV index from the three models versus ground based DWD data (April to September 1996 and 1997). Top: Reflectivity model, ICFA model (middle); bottom: PMD model.

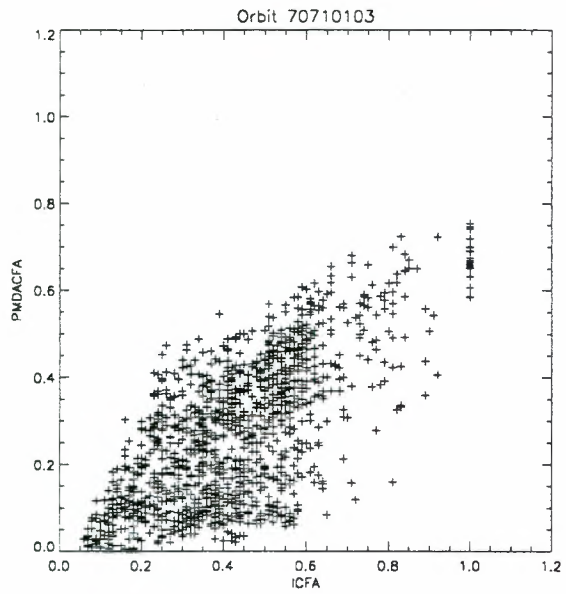

Figure 3: Operational ICFA product versus a cloud fraction derived from averaging over the 16 PMD cloud fractions. ICFA overestimates the fractional cloud cover with respect to the PMD algorithm.

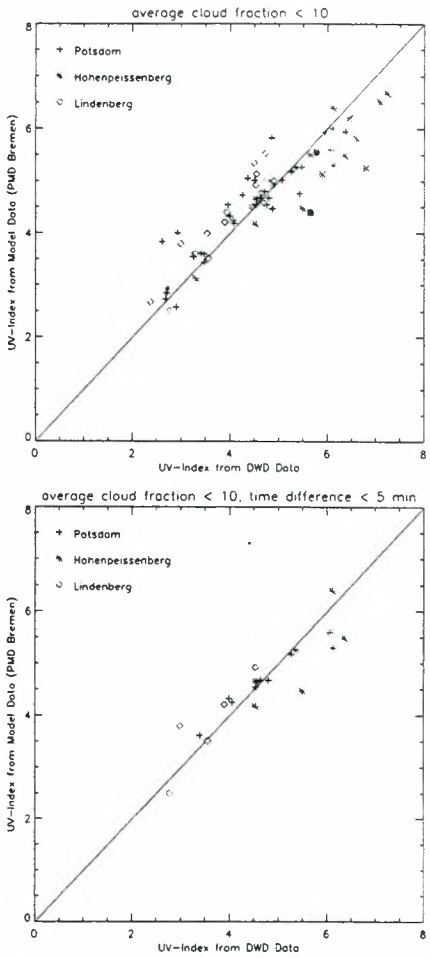

Figure 4: These plots demonstrate the difficulties to calculate the UV Index in the presence of clouds. Top: Scatter plot using GOME UV index under nearly clear-sky conditions (fractional cloud cover less than 0.1). Bottom: in addition time gap between GOME overpass and ground based measurement is limited to 5 minutes. By restricting the time gap and limiting the maximum averaged cloud fraction, the agreement is much better (bottom).

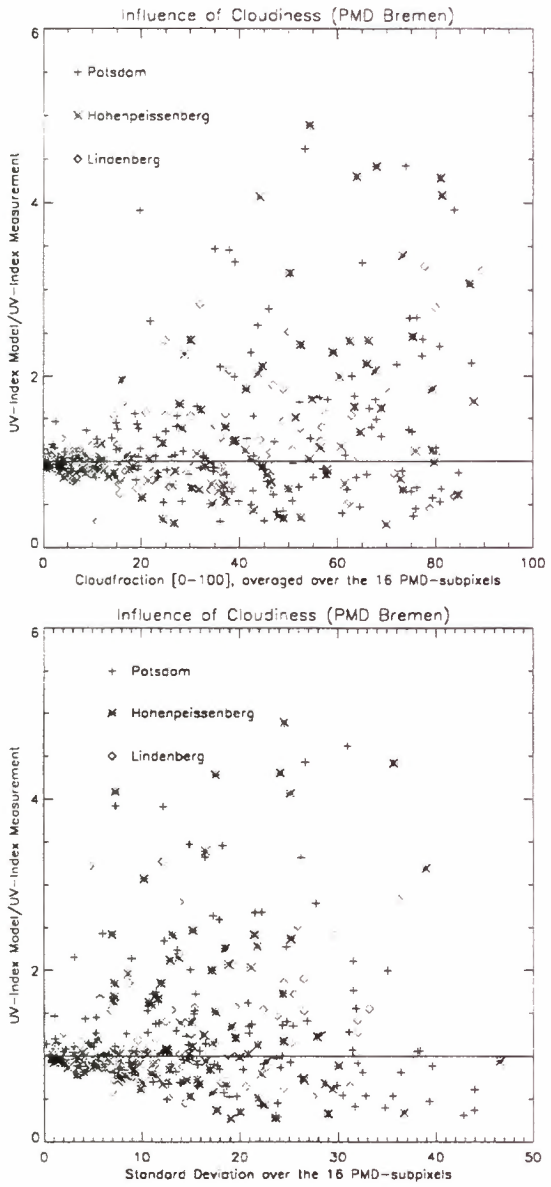

Figure 5: The influence of the cloudiness on the difference between GOME derived and ground based data: The standard deviaton of the 16 PMD cloud fractions is a measure of the broken clouds.

SATELLITE REMOTE SENSING OF TROPOSPHERIC AEROSOLS OVER LAND FROM ATSR-2 AND GOME

J.P. Veefkind and G. de Leeuw

TNO Physics and Electronics Laboratory, The Hague, The Netherlands
email: veefkind@fel.tno.nl, deleeuw@fel.tno.nl

ABSTRACT

Two aerosol retrieval algorithms are compared for a case study over northwestern Europe for 25 July 1995. The first method uses data from the Along Track Scanning Radiometer (ATSR-2) to compute the aerosol optical depth in the visible and near infrared. The second algorithm uses data from the Global Ozone Monitoring Experiment (GOME) in the wavelength range between 0.340 and 0.400 μm. ATSR-2 and GOME are both on board the ERS-2 satellite. Results from the two algorithms agree within 0.1 optical depth. Also good agreement is observed with ground-based aerosol measurements.

1. INTRODUCTION

Aerosol effect on the global radiation balance are a leading uncertainty in predicting climate change. To a large extent, these uncertainties are caused by a lack of aerosol data on a global scale. Due to the short lifetimes of aerosols in the lower troposphere (days to a week), and the large number of different aerosol sources with different spatial extents and source strengths, the aerosol is highly variable in both and space time and time. Only the use of satellites can give the spatial resolution combined with regional and global coverage required by climate models (Ref. 1).

Until recently it was thought that aerosol satellite retrieval was only possible over dark surfaces, such as large water bodies. New sensors, with improved calibration and more spectral information make it possible to retrieve aerosol properties over land as well (Ref. 2). The key problem in aerosol retrieval over land is to distinguish between atmospheric and surface reflection contributions to the top of the atmosphere radiance. Several methods are proposed to perform this difficult task (Ref. 2).

At TNO Physics and Electronics Laboratory retrieval algorithms are developed for the retrieval of aerosol properties over land and water, see Table 1. In this paper, two aerosol retrieval algorithms, using different instruments and different methods are compared. The first method is the dual-view algorithm (Ref. 3), which uses both the spectral and directional information of the Along Track Scanning Radiometer 2 (ATSR-2). The second algorithm uses data from the Global Ozone Monitoring Experiment (GOME) in the 0.340 to 0.400 μm wavelength range. Results from both methods are compared to ground-based measurements. Synergistic use of both algorithms is discussed.

	Ocean	Dual-View	GOME UV
Wavelength	VIS/NIR	VIS/NIR	340-400 nm
Surface	Sea	Land/Sea	Land/Sea
Sensors	Various	ATSR-2 (AATSR)	GOME (Sciamachy)
Refs.	4	3,5	5

Table 1. Characteristics of the aerosol retrieval algorithms developed at TNO Physics and Electronics Laboratory. Future missions are in brackets.

2. ALGORITHM DESCRIPTION

2.1 The dual-view algorithm

The ATSR-2 is a dual-view imaging spectrometer on board the ERS-2 satellite with four wavelength bands in the visible and near infrared (0.555, 0.659, 0.865, and 1.6 μm). The conical scanning mechanism produces two views of each region, first a forward view and two about minutes later a nadir view. The dual-view algorithm uses both the spectral and directional information in the ATSR-2 data to distinguish between atmospheric scattering and surface reflection contributions to the satellite measured radiance (Ref. 3). Once the atmospheric contribution is determined, the aerosol optical depth (AOD) is computed using a two-mode aerosol size distribution. The ratio between these modes is derived from the spectral behavior of the atmospheric radiance contribution. The dual-view algorithm was first validated during the TARFOX experiment, which was conducted at the USA east coast in July 1996. Comparisons with ground-based sunphotometers showed that the AOD and its spectral behavior can be retrieved accurately.

2.2 GOME UV method

Aerosol retrieval is best possible over surfaces with a low and preferably constant albedo. Herman et al. (Ref. 6) showed that between 0.340 and 0.380 μm the albedo of most land surfaces is between 0.02 and 0.04, and nearly independent of the wavelength. GOME is a four channel grating spectrometer with a spectral range between 0.240 and 0.790 μm. Five spectral bands (0.342, 0.355, 0.368 and 0.400 μm) with widths of 1 nm were selected from the GOME spectra. The atmospheric and surface reflection contributions are separated using a prescribed value for the surface albedo. The AOD is computed by fitting a two-mode aerosol model through the spectral data. Since this method is based on aerosol scattering, it differs from the UV aerosol index (Ref 7) which detects mainly absorbing aerosols.

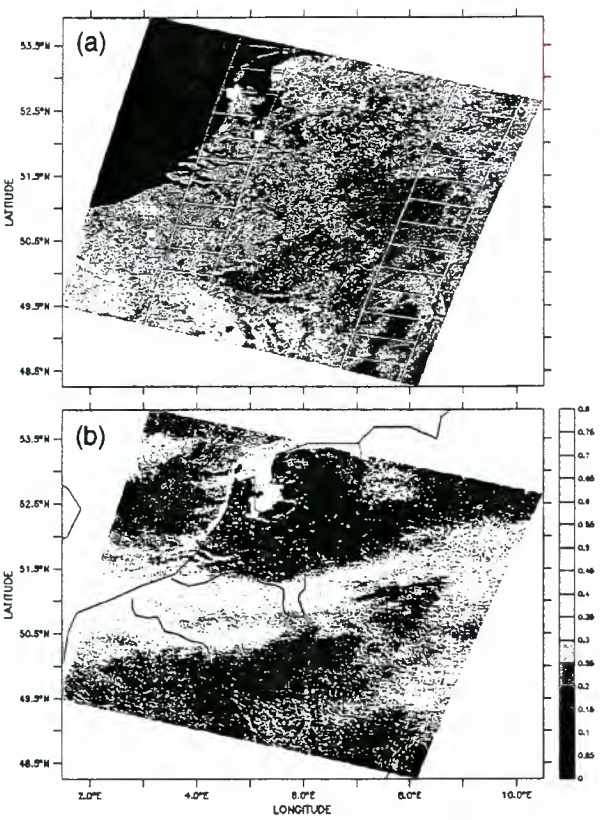

Figure 1. (a) Near-infrared (1.6 μm) ATSR-2 image over northwestern Europe, for 25 July 1995, 1050 UTC. Squares indicate location of ground stations. Lines indicate ground track of GOME nadir and east pixels. (b) Aerosol optical depth at 0.555 μm for the scene shown in Fig. 1a, as retrieved with the dual-view algorithm.

3. CASE STUDY

On 25 July 1995 the ERS-2 satellite passed over northwestern Europe at 1050 UTC. As can be seen in Figure 1a, the area over the Netherlands, Belgium and northern France was cloud-free. AVHRR images for this day showed that the cloud-free area extended further south covering most of France. Since aerosol retrieval is impossible when a pixel is cloud contaminated, this is an exceptionally good case for comparing retrieval algorithms.

3.1 ATSR-2 retrieval

The AOD retrieved for the ATSR-2 image, using the dual-view algorithm, is shown in Figure 1b. This image shows a large aerosol plume, extending over Germany, Belgium and northern France. In the plume, AOD values as high as 0.5 are reached, whereas north and south of the plume the AOD is less than 0.15. The large gradients in Figure 1b, with variations in AOD of more than a factor of three over less than 100 km, clearly demonstrates the large variability of the aerosol. Figure 1b also shows some artifacts of the retrieval algorithm. Especially over shallow water bodies the dual-view algorithm frequently shows very high values. Apparently the assumptions used to separate the atmospheric and surface reflection contributions, that were developed for use over land, do not hold over these shallow waters.

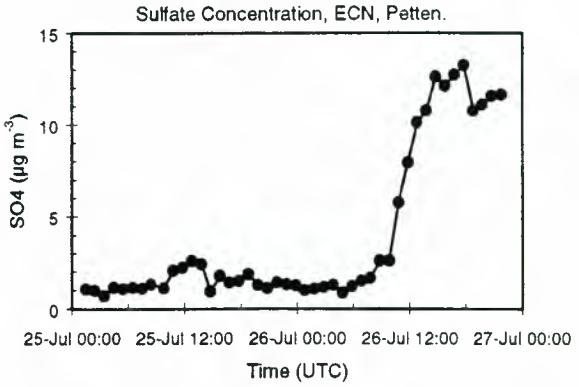

Figure 2. Sulfate aerosol concentration as measured in Petten, the Netherlands (52.75°N, 4.65°E) for 25 and 26 July 1995. Preliminary results.

In Figure 2, hourly values of the sulfate aerosol concentration are shown for Petten, the Netherlands, for 25 and 26 July 1996. Sulfate aerosol accounts for approximately 40% of the aerosol scattering in The Netherlands (Ref. 8). Trajectory analysis indicates that for this site the air mass on 25 July was coming from the North Sea, whereas on 26 July the air mass first passed over Germany. The high pressure area, which was located over the North sea on the 25th moved to southern Scandinavia on the 26th. The strong increase in sulfate concentration on 26 July at noon (Fig. 2) reflects this change in air mass. The data presented here indicate that the aerosol plume located over Belgium on 25 July moved north under the influence of the pressure gradients. Thus the strong spatial gradient on the 25th (Fig. 1b) manifested as a strong temporal change the day after, at a location some 150-200 km further north.

Aerosol satellite retrieval algorithms can be applied for monitoring purposes only when they are validated with ground-based measurements. Such comparison permits the assessment of measurement uncertainties, and can establish credibility for the retrieval method. Aerosol satellite retrieval is best validated when compared with sunphotometers, since both methods derive the (spectral) AOD. In Lille, France (50.60°, 3.15°) a sunphotometer of the AERONET network (Ref. 9) is stationed. One of the main objectives of the AERONET network is validation of satellite measurements. In Figure 3, the AOD from the sunphotometer at Lille and simultaneous ATSR-2 dual view algorithm values for the same area are plotted as a function of the wavelength. Unfortunately, the instruments have their spectral bands at different wavelengths. However, aerosol optical properties are smooth functions of the wavelength, and thus the data points can be interpolated. The results show that the ATSR-2 and sunphotometer agree within 0.05.

The spectral behavior of the AOD is determined by the size of the aerosol particles that dominate aerosol scattering. When the AOD decreases strongly with the wavelength, the particle scattering is dominated by small particles. When large particles dominate the scattering, no decrease, or even an increase, of the AOD with the wavelength is expected. Figure 3 shows that the slope of the ATSR-2 retrieved AOD is in good agreement with that of the sunphotometer. This is a very important observation, since it indicates that also information on the aerosol size distribution can be retrieved from satellite observations.

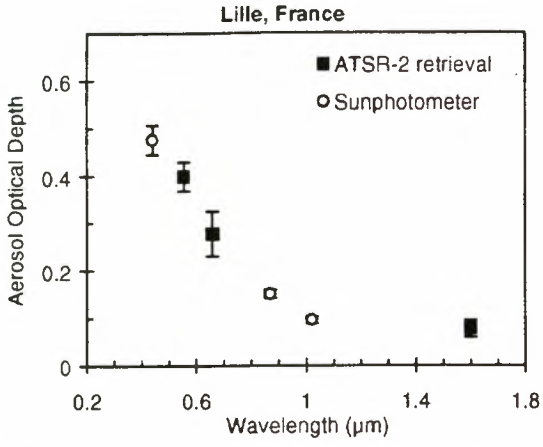

Figure 3. Aerosol optical depth as a function of the wavelength for Lille (50.60°N, 3.15°E), for 25 July 1995 1050 UTC. Squares are for the ATSR-2 dual view retrieval and circles are for the AERONET sunphotometer. Error bars indicate spatial standard deviation for ATSR-2 retrieval, and temporal standard deviation for the sunphotometer.

3.2 GOME retrieval

The ground tracks of the GOME nadir and east pixels are shown in Figure 1a. July 1995 was in the commissioning and validation phase of GOME, during which the pixel size was 80x40 km^2. Because most of the ground data was closest to the GOME nadir track and some pixel clouds were detected in the east track, we focused on the nadir track. As described above, the GOME UV retrieval method uses prescribed values for the surface reflection. For this area values of 0.01 to 0.02 were derived for the surface albedo (Ref. 5). In Figure 4, the GOME retrieved AOD at 0.400 μm is plotted as a function of the latitude, for the nadir track. The aerosol plume is also clearly apparent in the GOME AOD. Given the large pixel of GOME, it is difficult to compare GOME data with ground based observations. Therefore, an inter-comparison between GOME and ATSR-2 retrievals was made. For the nadir GOME track the ATSR-2 retrieved AOD was averaged over the GOME pixels. A power law fit was used to convert the ATSR-2 AOD to 0.400 μm. As can be seen in Figure 4, for latitudes between 49.5 and 53.5°N the agreement between the GOME and ATSR-2 retrieval is within 0.1 AOD. At higher latitudes the ATSR-2 is higher. However, these higher values are an artifact caused by the shallow water in this area.

3.3 Combining ATSR-2 and GOME data

Combining the retrieval results from the two algorithms yields information on the AOD from the UV to the near-infrared. Figure 5a shows the AOD over this wavelength range for the GOME pixel covering De Bilt, The Netherlands (51.1°N,5.18°E). Figure 5b is similar to 5a, but for the GOME pixel closest to Lille. Also shown in Figure 5a and 5b are power law fits trough the combined GOME and ATSR-2 data. For The Ångström wavelength exponent, determined from these power law fits, is 0.7±0.1 for De Bilt. For the pixel near Lille a value of 1.6±0.1 is found. The latter is in good agreement with the Ångström exponent of 1.8±0.2 derived from the Lille sunphotometer data. It is noted that this is a comparison between a point measurement to a GOME pixel of 80x40 km^2. Not only the spatial average in the GOME pixel may yield a higher value for the Ångström exponent in Lille, also the GOME pixel was some distance east of Lille.

The difference in Ångström exponent between Lille and De Bilt (Fig. 5), indicates that in the aerosol plume relatively more smaller particles were present than in the relatively clean air north of the plume. This is a further indication of the previously noted similarity between the transport of the plume and the increase of the sulfate concentration on the 26th in Petten.

Combining the retrieval algorithms can be done at different moments during the retrieval process. In Figure 5 the algorithms were combined at the end of the process, i.e. when both algorithms separately finished their retrieval. Interaction between the retrieval algorithms can also be performed during an earlier stage. This concept is especially attractive for satellite sensors with a very wide wavelength range, such as SCIAMACHY.

4. CONCLUSIONS

Aerosol optical depth retrieved over land from GOME and ATSR-2 are compared for a case study over northwestern Europe for 25 July 1995. The retrieval algorithms that are used for these two sensors apply to different wavelength ranges, and differ in viewing directions, and in the assumptions that are used for the surface reflection. The ATSR-2 shows very large variations in the spatial aerosol distribution for this day. Over less than 100 km the aerosol optical depth varies by more than

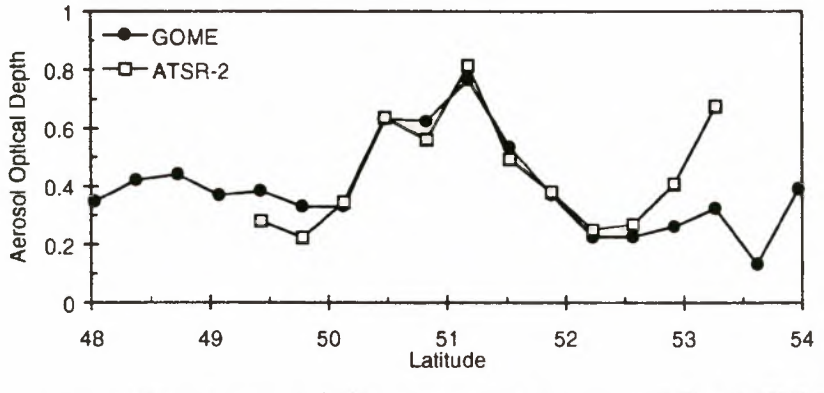

Figure 4. Aerosol optical depth at 0.400 μm as retrieved from the GOME and ATSR-2 data, plotted as function of the latitude, for 25 July 1995 1050 UTC.

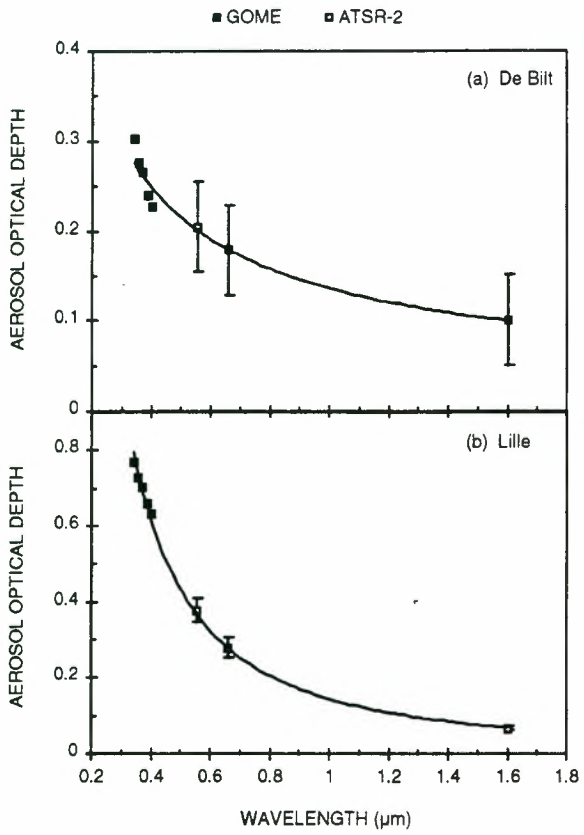

Figure 5. Aerosol optical depth versus wavelength as retrieved from ATSR-2 and GOME data, for the GOME pixel covering De Bilt (Fig. 5a) and the GOME pixel nearest to Lille (Fig. 5b). Lines are power law fits through the combine GOME and ATSR-2 data points.

a factor of three, clearly demonstrating the variability of the aerosol field expected form the short lifetimes of aerosols in the lower troposphere. The ATSR-2 retrieval agrees within 0.05 optical depth with sunphotometer data. The results indicate that the retrieval data can be used to assess the aerosol size distribution. To inter-compare the two retrieval algorithms, the ATSR-2 data was averaged over the GOME pixels. The inter-comparison showed agreement within 0.1 optical depth for most of the pixels. By combining the two methods, aerosol optical depths from the UV to the near-infrared can be retrieved from the same platform.

5. ACKNOWLEDGMENTS

This work is supported by the Netherlands Space Research Foundation (SRON), contract EO-008. The ATSR-2 and GOME data were kindly provided by the European Space Agency (ESA) through DLR and ESRIN. The authors would like to thank Piet Stammes and Robert Koelemeijer of the Royal Netherlands Meteorological Institute (KNMI) for the cloud screening product, and Harry ten Brink and Arjan Hensen of the Netherlands Energy Research Foundation (ECN) for the sulfate concentration data. The ECN contribution is supported by the National Research Programme on Global Air Pollution and Climate Change (NRP), contract number 951205. The AERONET data were provided by Dr. D. Tanré from the Laboratoire d'Optique Atmospherique (LOA), Université de Lille.

6. REFERENCES

1. IPCC1995, Aerosols, In Climate Change 1994, Eds. Anderson & co-authors, pp 127-157.
2. Kaufman, YJ & Tanré D & Nakajima T & Lenoble J & Frouin R & Grassl H & Herman B & King MD & Teillet PM 1997, Passive remote sensing of tropospheric aerosol and atmospheric correction for the aerosol effect, *J. Geophys. Res.*,102, 16,815-16,8130.
3. Veefkind JP & De Leeuw G 1998, A new algorithm to determine the spectral aerosol optical depth from satellite radiometer measuremets, *J. Aerosol Sci.*, 29, 1237-1248.
4. Veefkind JP & De Leeuw G & Durkee PA, 1998, Retrieval of aerosol optical depth over land using two-angle view satellite radiometry during TARFOX, *Geophys. Res. Letters*, 25, 3135-3138.
5. Veefkind JP & De Leeuw G & Stammes P & Koelemeijer RBA, 1999, Regional distribution of aerosol over land derived from ATSR-2 and GOME, *manuscript in preparation.*
6. Herman JR & Celarier EA, 1997, Earth surface reflectivity climatology at 340-380 nm from TOMS data, *J. Geophys. Res.* 102, 28,003-28,011.
7. Herman JR & Barthia PK & Torres O & Hsu C & Seftor C and Celarier E, 1997, Global distributions of uv-absorbing aerosols from nimbus 7/toms data, *J. Geophys. Res.*, 102, 16,911-16,922.
8. Ten Brink HM & Veefkind JP & Waaijers-Ijpelaan A & Van der Hage JCH, 1996, Aerosol light scattering in the Netherlands, *Atmos. Environ.*, 30, 4251-4261.
9. Holben B & co-authors, 1998, AERONET- a federated instrument network and data archive for aerosol characterization. *Rem. Sens. Environ.*, 66, 1-16.

RETRIEVING AEROSOL PROPERTIES OVER LAND AND OCEAN FROM GOME AND ATSR–2 DATA

Thomas Holzer–Popp and Marion Schroedter

Deutsches Zentrum für Luft– und Raumfahrt e.V. (DLR)
Deutsches Fernerkundungsdatenzentrum (DFD)
Oberpfaffenhofen, D–82234 Weßling, Germany
phone: ++49–8153–28–1382, fax ++49–8153–28–1445
e–mail: Thomas.Holzer–Popp@dlr.de, Marion.Schroedter@dlr.de
www: http://www.dfd.dlr.de

ABSTRACT

Currently satellite observation of aerosols is limited to the oceans (NOAA–AOT product) or a selected class of aerosols (TOMS algorithm). To overcome these restrictions the new aerosol retrieval method SYNAER (SYNergetic AErosol Retrieval) was developed within the ESA–AO2 project PAGODA (Project for ATSR and GOME Data Application). SYNAER delivers boundary layer aerosol optical thickness (BLAOT) and type over both land and ocean, the latter as BLAOT percentage contribution of 10 representative components from the OPAC (Optical Parameters of Aerosols and Clouds) dataset. The high spatial resolution of ATSR–2 permits cloud detection, BLAOT calculation over automatically selected dark pixels and surface albedo correction for a set of different boundary layer aerosol mixtures. After spatial integration to GOME pixels these parameters are used to simulate GOME spectra for the same set of different aerosol mixtures. A least square fit of these spectra to the measured spectrum delivers the BLAOT value and – if a uniqueness test is passed – the aerosol mixture. Within the ESA–AO3 project PAGODA–2 (Extending the Applicability of New Methods from PAGODA) SYNAER will be validated. First case studies using ground based sun–photometer measurements of the spectral aerosol optical thickness from NASA's Aerosol Robotic Network (AERONET) show a good agreement.

1. INTRODUCTION

Aerosol particles affect climate directly by interacting with solar and terrestrial radiation and indirectly by their effect on cloud microphysics (aerosols act as cloud condensation nuclei), albedo and precipitation [Refs. 9, 10]. Tropospheric aerosol forcing is comparable to global net cloud forcing of approximately –1 Wm^{-2} [Ref. 1]. However, on regional scale the mean direct radiative forcing by aerosols can be as large as –10 Wm^{-2} (mineral dust over ocean [Ref. 24]). Anthropogenic changes of the global aerosol distribution may delay or temporarily mask greenhouse warming. Our understanding of aerosol impact is extending beyond the sulfate aerosol which has been used as sole aerosol component in climate models upto now: It is recognized that smoke aerosol and mineral dust are equally important and may regionally enhance greenhouse warming. For a review of aerosol impact on climate see Charlson and Heintzenberg [Ref. 1].

In order to assess the impact of aerosols on climate there is thus a growing need for more detailed information on the aerosol spatial distribution and variation together with its composition. More specifically, we need to know aerosol optical thickness (AOT), its absorption, scattering properties, vertical profiles, size distributions and chemical composition. Currently there is only limited capability for aerosol monitoring. Available products are restricted to the oceans (NOAA [Refs. 8, 22]; planned: GOME/SCIAMACHY [Ref. 3]), UV absorbing aerosols (TOMS [Ref. 4]) or the stratosphere (SAGE). With the exception of singular case studies only values of the aerosol optical thickness can be derived so far.

Within the next few years a number of new spaceborne instruments promise a large step forward in the aerosol monitoring capabilities. Among these are SCIAMACHY and AATSR onboard ENVISAT (with their predecessors GOME and ATSR–2 onboard ERS–2), POLDER, TOMS and OCTS onboard ADEOS–2 (ADEOS–1 was active for 8 months in 1996/97) and MISR and MODIS onboard the EOS–AM–1. In principle aerosol retrieval can be exhibited by inversion from data of several groups of sensors: (1) Multispectral near nadir viewing (MODIS [Ref. 23]; SCIAMACHY), (2) multiangle, multispectral viewing (MISR [Ref. 11]; AATSR), (3) multiangle, multispectral viewing with polarization (POLDER [Ref. 16]), (4) limb viewing (SCIAMACHY, SAGE). A detailed summary of the current status and plans on aerosol retrieval can be found in Kaufman et al. [Ref. 12].

In order to overcome restrictions due to current monosensoral methods a new synergetic aerosol retrieval method was developed at the German Remote Sensing Data Center (DFD) of the German Aerospace Center (DLR).

2. THE NEW METHOD

ATSR–2 measures radiances in 7 spectral bands centered at 550 nm, 670 nm, 870 nm, 1.6 µm, 3.7 µm, 11 µm and 12 µm under two viewing angles (nadir, forward around 52°) with a ground resolution of approximatelly 1.1 km. GOME observes near–nadir reflection in the range from 240 nm to 790 nm with a spectral resolution of 0.2 nm to 0.4 nm and a pixel size of 320 x 40 km^2 or 80 x 40 km^2. Both instruments measure the solar illumination regularly and are thus self–calibrating. The use of reflectance values obtained from onboard solar irradiance measurements for both instruments reduces calibration errors significantly as compared to the use of calibrated radiances.

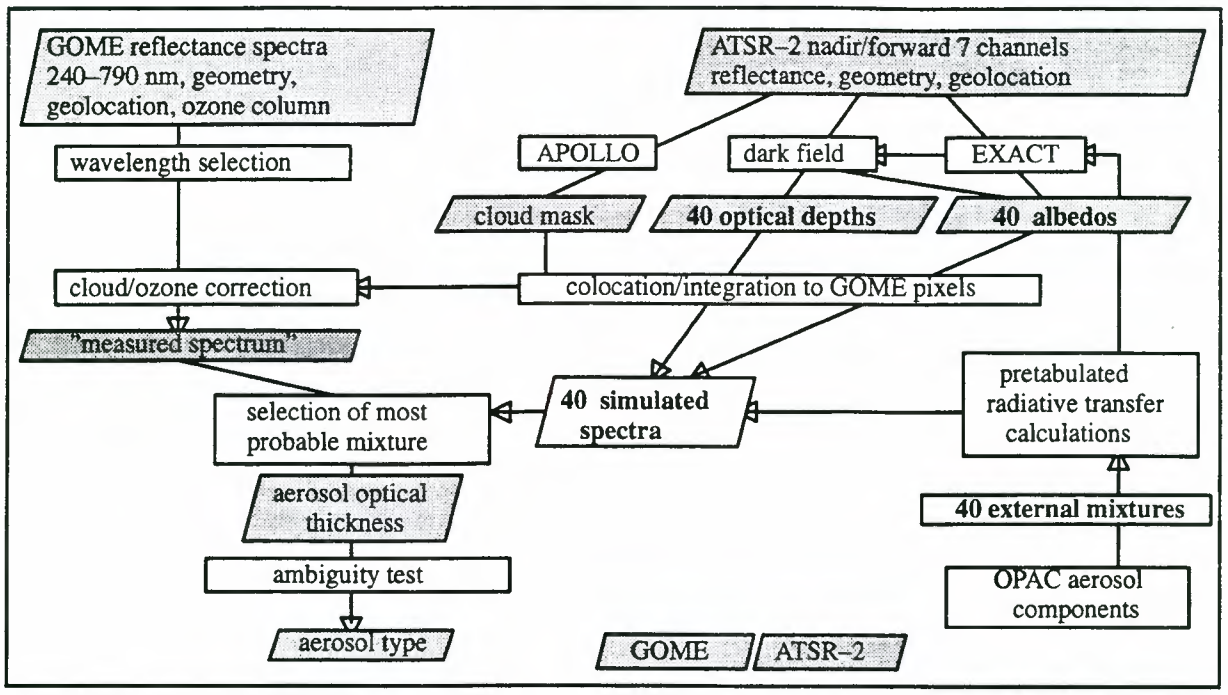

Figure 1: Flow chart of the aerosol retrieval major steps

Aerosol parameters are retrieved from a combination of simultaneous ATSR–2 and GOME data with the software SYNAER (SYNergetic AErosol Retrieval [Refs. 19,7]): Boundary layer aerosol optical thickness (BLAOT) values are derived from automatically selected dark ATSR–2 pixels (dark forest, water bodies) for which the surface albedo can be estimated with good accuracy. Using the atmospheric correction scheme EXACT [Ref. 18] which has been validated with Landsat–TM and NOAA–AVHRR data, BLAOT can be estimated for the dark fields and interpolated to all cloudfree ATSR–2 pixels. Then the surface albedo values for the 3 wavelengths 560 nm, 670 nm and 870 nm are obtained for all pixels. The ATSR–2 derived data are then colocated to GOME pixels and interpolated spectrally. Using the ATSR–2 calculated values of optical thickness and surface albedo, GOME spectra for different mixtures are simulated. A least square fit of the simulations to the measured GOME spectrum results in the selection of the most plausible type of aerosol and its corresponding BLAOT value in a GOME pixel. Finally, an ambiguity test is applied. Figure 1 gives an overview of processing steps in SYNAER.

Dark land pixels are selected on the basis of the 1.6 μm channel. As the aerosol effect at this wavelength can be neglected for most aerosol types, all cloud/snowfree pixels with a 1.6 μm reflectance below a given threshold are selected. To reject wet bare soil pixels which are also dark in the 1.6 μm channel but brighter in the visible the normalized differential vegetation index (NDVI) must be larger than a preset minimum value. For the pixels selected through this scheme the dark field albedo values at 560 nm and 670 nm can then be estimated from the 1.6 μm reflectance by application of a conversion factor. Kaufman et al. [Ref. 13] suggest a similiar selection scheme based on the 2.1 μm and 3.8 μm channels of the MODIS sensor onboard the EOS–A platform. Water pixels are exploited over deep ocean with a fixed albedo.

The accuracy of the retrieved spectral optical thickness values depends highly on the exact knowledge of the surface albedo of the dark fields and decreases with increasing surface albedo. The BLAOT retrieval based on dark field selection and estimation of their surface albedo values from the 1.6 μm channel shows a significant scatter in the retrieved values of neighbouring pixels. Therefore, a minimum number of adjacent pixels must be exploited to allow for an appropriate averaging. In areas with sparse dark fields singularities must be rejected. To overcome these difficulties dark fields are grouped into 4 different classes with increasing surface albedo, i. e. decreasing retrieval accuracy. For boxes of 25x25 ATSR–2 pixels only dark pixels of the lowest available, i. e. most accurate category are exploited. Furthermore, pixels are rejected if their retrieved values differ by more than the local variance from the average of their neighbourhood. The range for this variance test is increased stepwise until a minimum pixel number guarantees statistical significance.

Aerosol optical thickness and surface albedo values are derived for 40 different boundary layer aerosol mixtures because the retrieved values depend strongly on the type of aerosol. For the modelling of aerosols the external mixing approach [Ref. 25] based on 10 components from the OPAC database (Optical properties of aerosols and clouds [Ref. 5]) is used in the boundary layer. The same set of 40 mixtures is used in the ATSR–2 BLAOT and albedo retrieval and the GOME simulations. For humidity dependent components two models with 50% and 95%

relative humidity have been included. The free tropospheric and the stratospheric aerosol are fixed based on World Climate Program [Ref. 25].

In the current version GOME spectra are calculated at 10 wavelengths which are free of severe instrument errors (e.g. noise in band overlap regions) and gas absorption lines. The broad ozone absorption in the Chappuis band is corrected utilizing GOME retrieved ozone columns. The ambiguity test checks if the GOME fit error value of the best and second best mixtures differ at least by a noise induced error value. This test refuses pixels with large cloud fraction, radiometric differences or bright surface because their aerosol sensitivity is low. A before–hand refusal is impossible because of the complex geometry– dependent influence of the interaction between atmosphere and surface on the radiance field.

All radiative transfer calculations are conducted with an iterative code (successive orders of scattering, SOS; [Ref. 17]) which includes full multiple scattering. They assume the surface at sea level. For a fast application the actual radiative transfer calculations in EXACT and SOS are replaced by interpolations using precalculated tables.

Clouds are detected by the well established APOLLO (AVHRR Processing Scheme Over CLoud Land and Ocean [Refs. 21, 2, 15]) software extended to ATSR–2 data. APOLLO/ATSR–2 [Ref. 7] exploits reflectances and temperatures in the solar and terrestric spectral range. Five ATSR–2 channels which are equivalent to the AVHHR spectral bands are used for cloud detection; the additional 1.6 μm channel is used to separate clouds from snow and ice. A number of threshold tests is applied to differentiate types of clouds. APOLLO yields cloud fraction, 4 cloud layers and cloud optical parameters.

Within the project PAGODA–2 (Extending the Applicability of New Methods from the Project for ATSR and GOME Data Application) accepted in the 3. ERS AO we will further improve and validate the aerosol retrieval method. A scheme for retrieving three vertical layers of the aerosol optical thickness will be tested. Furthermore, we will investigate the possibilities for aerosol retrieval from partly cloudy GOME pixels in order to assess the interaction between clouds and aerosols directly. We will also revise the set of predefined aerosol mixtures.

The method will be adapted to similiar sensors AATSR and SCIAMACHY onboard ENVISAT–1 (launch planned May 2000) and applied within the accepted ENVISAT–AO proposal SENECA (Synergetic ENVISAT Data Exploitation for Cloud, Aerosol and Ozone Retrieval). SCIAMACHY and AATSR provide some valuable additional features for global aerosol monitoring in comparison to GOME and ATSR–2: As far as SCIAMACHY is concerned, there is the wider spectral range (upto 2400 nm, GOME upto 790 nm) which enables a better investigation of the type of aerosol especially for large particles and the additional limb viewing geometry for stratospheric aerosol retrieval. Both AATSR and SCIAMACHY offer an improved data transmission rate with small SCIMACHY pixels throughout the entire mission and orbitwise AATSR products (ATSR–2: framewise products). Furthermore, other ENVISAT instruments (MERIS, MIPAS) also measure parts of the global aerosol distribution and may be used for comparisons.

3. FIRST VALDIATION RESULTS

The validation of SYNAER results has been started. For the first case studies ground based measurements taken by the AERONET (AErosol RObotic NETwork) stations were used. The objective of AERONET [Ref. 6] is to monitor aerosols by ground based spectral radiometers. It was especially designed for the validation needed for all upcoming satellites like ENVISAT, EOS–AM 1 and ADEOS–2 that will be capable of retrieving aerosol information. The measurements are processed in near real–time, archived and made available to the public by NASA's Goddard Space Flight Center through their www pages (http://aeronet.gsfc.nasa.gov:8080). AERONET provides spectral aerosol optical thickness (AOT) values and aerosol size distributions taken by automatic sun–sky scanning spectral radiometers since 1993 at approximately 50 ground stations worldwide.

pixel	*1*	*2*	*3*	*4*
date	*15/8/97*	*5/10/97*	*15/11/97*	*14/7/98*
UTC	*9:39*	*9:36*	*10:24*	*14:28*
latitude	*45:18N*	*45:18N*	*45:48N*	*16:00S*
longitude	*12:30E*	*12:30E*	*8:37E*	*62:01W*
altitude	*10m*	*10m*	*235m*	*500m*
orbit number	*12129*	*12859*	*13446*	*16898*
	818	*589*	*419*	*1596*
location	*Venice*	*Venice*	*Ispra*	*Concepcion*
country	*Italy*	*Italy*	*Italy*	*Bolivia*
clouds	*5.4%*	*11.4%*	*6.1%*	*0.0%*
author	*GZ*	*GZ*	*GZ*	*BH*
type	*nadir*	*nadir*	*west*	*nadir*

Table 1: Specifications of validation pixels (authors: GZ=Giuseppe Zibordi/JRC, BH=Brent Holben/NASA–GSFC)

So far, about 2500 GOME pixels were analysed, but only 66 pixels include ground stations inside the pixel boundaries. Additional criteria for validation pixels (cloudfree ground based measurements, less than 15% cloud coverage inside the GOME pixel, a maximum of 15 minutes difference between ground measurement and satellite overpass) left four pixels with corresponding ground measurements of spectral aerosol optical thickness val-

ues. For these pixels ground measurements of size distributions are not available.

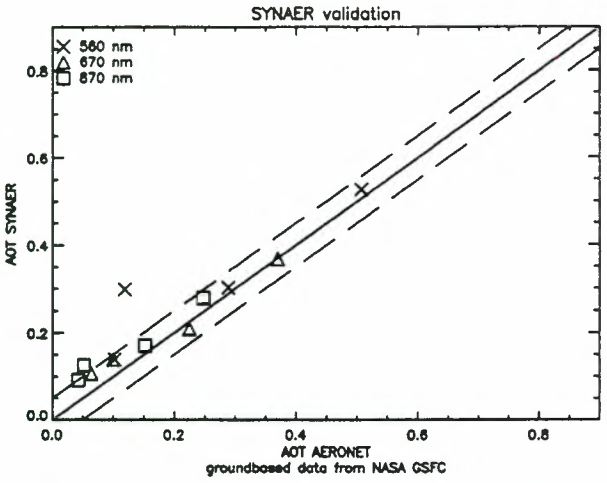

Figure 2: First validation results: Comparison of spectral AOT values measured by the groundbased AERONET stations at Ispra, Venice and Concepcion to AOT values retrieved by SYNAER. AERONET data were acquired through the AERONET website of NASA–GSFC (http://aeronet.gsfc.nasa.gov:8080).

In all four cases the SYNAER retrieval was driven by land dark fields. The specifications of the four test cases are given in table 1. All GOME pixels have a size of 80x40 km^2. Figure 2 shows the retrieved AOT values at 3 wavelengths against the groundbased sun–photometer measurements from the AERONET database. A good agreement with errors less than 0.05 for the AOT values can be seen. However, for one case the 500 and 870 nm values show a significant deviation indicating the detection of a wrong aerosol mixture. Direct validation of the retrieved mixing contributions of the basic aerosol components is planned through the exploitation of airborne measurements acquired in August 1998.

4. CONCLUSIONS

A new unsupervised retrieval method for aerosol optical thickness and type in the boundary layer over cloudfree land and ocean from GOME and ATSR–2 data was delevoped and applied. A first case study validation showed good agreement of retrieved spectral aerosol optical thickness values to ground based sun photometer measurements (error below 0.05 at 560, 670 and 870 nm). Difficulties in the selection of the right aerosol mixture, i. e. the correct spectral dependence of AOT values occur which have to be addressed in the future. Due to a very small number of exploitable ground measurements only four case studies could be performed so far. We plan a more detailed validation of this approach with airborne measurements that were conducted in August 1998. Additionally the AERONET data base was completed remarkably and therefore, the availability of ground measurements has been improved much.

Within the setup of a processor for atmospheric value added products DFD will operationalize the SYNAER method. Our final aim is to contribute a satellite based climatology of tropospheric aerosols from 10 years of ERS–2 and ENVISAT data (7/1995 to 6/2005) to improve the understanding of the global temporal–spatial distribution of aerosol loading and its major components. The direct implementation of the SYNAER resulting climatology dataset in the global circulation model ECHAM [Ref. 20] is prepared as our dataset follows the characteristics of the groundbased dataset GADS (Global Aerosol Data Set [Ref. 14]) which is currently under implementation in ECHAM. Thus this dataset may easily enable a more detailed treatment of aerosols in climate models. Furthermore, a direct comparison of the groundbased GADS and the satellite derived SYNAER climatologies is possible since both datasets rely on the same set of representative aerosol components from the OPAC database.

5. ACKNOWLEDGEMENTS

The results presented in this paper were achieved within the ESA–AO projects PAGODA (AO2.D107–1) and PAGODA–2 (AO3.218) through which the input data (GOME and ATSR–2) were acquired. Our thanks go to G. Zibordi/JRC and Brent Holben/NASA–GSFC for the provision of AERONET validation data from the Venice, Ispra and Concepcion stations.

6. REFERENCES

1. Charlson, R. J., Heintzenberg, J. (Eds.), Dahlem Workshop Report on Aerosol Forcing of Climate, 416 pp., John Wiley, New York, 1995

2. Gesell, G., An Algorithm for Snow and Ice Detection using AVHRR data: An Extension to the APOLLO Software Package, *Int. J. Rem. Sens.*, 10, 897–905, 1989

3. Guzzi, R., Burrows, J., Cattani, E., Kurosu, T., Cervino, M., Levoni, C., Torricella, F., GOME Cloud and Aerosol Data Products Algorithm Development – Final Report, ESA Contract 11572/95/NL/CN, 1998

4. Herman, J. R., Bhartia, P. K., Torres, O., Hsu, C., Seftor, C., Celarier, E., Global distributions of UV–absorbing aerosols from NIMBUS 7 TOMS data, *J. Geophys. Res.*, 102, 16911–16922, 1997

5. Hess, M., Köpke, P., Schult, I., Optical Properties of Aerosols and Clouds: The Software package OPAC, *Bull. Am. Met. Soc.*, 79, 831–844, 1998

6. Holben, B. N., Eck, T. F., Slutsker, I., Tanre, D., Buis, J. P., Setzer, A., Vermote, E., Reagan, J. A., Kaufman, Y. J., Nakajima, T., Lavenu, F., Iankowiak, I., Smirnov, A.,

AERONET – A Federated Instrument Network and Data Archive for Aerosol Characterization, *Rem. Sens. Environ.*, 66, 1–16, 1998

7. Holzer–Popp, Th., Kriebel, Th., Böttger, U., Dameris, M., Gesell, G., König, Th., Meerkötter, R., Rother, T., Schroedter, M., PAGODA final report, Schriften des Deutschen Fernerkundungsdatenzentrums Nr.1, DLR, Oberpfaffenhofen, 1998

8. Husar, R. B., Prospero, J. M., Stowe, L. L., Characterization of tropospheric aerosols over the oceans with the NOAA advanced very high resolution radiometer optical thickness operational product, *J. Geophys. Res.*, 102, 16889–16909, 1997

9. IPCC (Intergovermental Panel on Climate Change), Climate Change: the 1990 and 1992 IPCC assessments, WMO/UNEP, June, 1992

10. IPCC (Intergovermental Panel on Climate Change), Climate Change 1994, Cambridge Univ. Press, 1995

11. Kahn, R., West, R., McDonald, D., Rheingans, B., Mishchenko, M. I., Sensitivity of multiangle remote sensing observations to aerosol sphericity, *J. Geophys. Res.*, 102, 16861–16870, 1997

12. Kaufman, Y. J., Tanre, D., Gordon, H. R., Nakajima, T., Lenoble, J., Frouin, R., Grassl, H., Herman, B. M., King, M. D., Teillet, P. M., Passive remote sensing of tropospheric aerosol and atmospheric correction for the aerosol effect, *J. Geophys. Res.*, 102, 16815–16830, 1997

13. Kaufman, Y. J., Tanre, D., Remer, L. A., Vermote, E. F., Chu, A., Holben, B. N., Operational remote sensing of tropospheric aerosol over land from EOS moderate resolution imaging spectrometer, *J. Geophys. Res.*, 102, 17051–17067, 1997

14. Köpke P., Hess, M., Schult, I., Shettle, E. P., Global Aerosol Data Set, Max–Planck–Institut für Meteorologie, Report No. 243, 1997

15. Kriebel, K. T., Saunders, R. W., Gesell, G., Optical Properties of Clouds Derived from Fully Cloudy AVHRR pixels, *Beitr. Phys. Atmos.*, 62, 165–171, 1989

16. Leroy, M., Deuze, J. L., Breon, F. M., Hautecoeur, O., Herman, M., Buriez, J. C., Tanre, D., Bouffies, S., Chazette, P., Roujean, J. L., Retrieval of atmospheric properties and surface bidirectional reflectances over land from POLDER/ADEOS, *J. Geophys. Res.*, 102, 17023–17038, 1997

17. Nagel, M. R., Quenzel, H., Kweta, W., Wendling, P., Daylight Illumination–Color–Contrast–Tables, New York, Academic Press, 1978

18. Popp, Th., Correcting atmospheric masking to retrieve the spectral albedo of land surfaces from satellite, *Int. J. Rem Sens.*, 16, 3483–3508, 1995

19. Popp, Th., Gesell, G., König, Th., Kriebel, Th., Meerkötter, R., Mannstein, H., Exploiting GOME and ATSR–2 data: First results of the PAGODA project, in: *Proc. 3rd ERS Symp. on Space at the service of our Environment*, Florence, Italy, 17–21 March 1997, ESA SP–414, Vol II, 761–766, 1997

20. Röckner, E., Arpe K., Bengtsson, L., Brinkop, S., Dümenil, L., Esch, M., Kirk, E., Lunkeit, F., Ponater, M., Rockel, B., Sausen, R., Schlese, U., Schubert, S., and Windelband, M., Simulation of the present–day climate with the ECHAM model: Impact of model physics and resolution. Max–Planck–Institut für Meteorologie, *Report No.* 93, 171pp, 1992

21. Saunders, R. W., Kriebel, K. T., An Improved Method for Detecting Clear–Sky and Cloudy Radiances from AVHRR–data, *Int. J. Rem. Sens.*, 9, 123–150, 1988

22. Stowe, L. L., Ignatov, A. M., Singh, R. R., Development, validation, and potential enhancements to the second–generation operational aerosol product at the National Environmental Satellite, Data, and Information Service of the National Oceanic and Atmospheric Administration, *J. Geophys. Res.*, 102, 16923–16934, 1997

23. Tanre, D., Kaufman, Y. J., Herman, M., Mattoo, S., Remote Sensing of aerosol properties over oceans using the MODIS/EOS spectral radiances, *J. Geophys. Res.*, 102, 16971–16988, 1997

24. Tegen I., Lacis A.A., Fung I., The influence on climate forcing of mineral aerosols from disturbed soils, *Nature*, 380, 419–422, 1996

25. World Climate Program (WCP), A Preliminary Cloudless Standard Atmosphere for Radiation Computation, WCP–112, *WMO/TD* No. 24, Boulder, 1986

A STUDY OF PSC ACTIVATION OF CHLORINE DURING THE AUSTRAL WINTER 1997

L.Hild, A. Richter, F. Wittrock, M. Weber, A. Ladstätter-Weißenmayer, R. Spang*, K. U. Grossmann*, J. P. Burrows

Institute of Environmental Physics (IUP), University of Bremen, Germany
*Department of Physics, University of Wuppertal, Germany

e-mail: hild@iup.physik.uni-bremen.de

ABSTRACT

During the second flight of the CRyogenic Infrared Spectrometers and Telescopes for the Atmosphere (CRISTA) Polar Stratospheric Clouds (PSC) were detected between 70°S and 55°S on the 9th to 11th of August 1997 under sunlit conditions. Simultaneous measurements by the Global Ozone Monitoring Experiment (GOME) enables synoptic studies of the PSC using both datatsets to be undertaken.
The PSC processing of reservoir gases has been investigated by using measurements of chlorine nitrate ($ClONO_2$) and nitric acid (HNO_3) from CRISTA2 and ozone (O_3), nitrogen dioxide (NO_2), bromine oxide (BrO) and chlorine dioxide (OClO) from GOME, and meteorological parameters from the UKMO analysis.
A low pressure anti cyclone in the troposphere appears to induce an O_3 minihole. The NO_2 values are also low in the region of the O_3 minihole as is expected in the cold vortex. OClO is observed in large amounts inside the vortex downwind from the PSC. The total columns of BrO appear to increase due to tropospheric activation of bromine, but no large stratospheric increase of BrO was identified within the vortex. $ClONO_2$ and HNO_3 are depleted in the vortex but maximum values are observed at the edge of the vortex.

1. INTRODUCTION

During the polar winter and spring, the stratosphere above Antarctica regularly cools to temperatures, which are sufficiently cold for the formation of PSC. These particles, which are mixtures of solids and liquids containing HNO_3, H_2SO_4 and H_2O, provide a surface which is suitable for the processing of photostabile species such as the chlorine and bromine reservoirs HCl, $ClONO_2$, HOCl, HBr, $BrONO_2$, and HOBr to photolabile species such as Cl_2, ClONO, BrCl, and Br_2. (Ref. 9)

(1) $ClONO_2\ (g) + HCl\ (g) \rightarrow Cl_2\ (g) + HNO_3\ (s)$
(2) $HCl\ (g) + HOCl\ (g) \rightarrow Cl_2\ (g) + H_2O\ (s)$
(3) $HCl\ (g) + N_2O_5\ (g) \rightarrow ClONO\ (g) + HNO_3\ (s)$
(4) $HCl\ (g) + BrONO_2\ (g) \rightarrow BrCl\ (g) + HNO_3\ (s)$

During polar spring Cl_2 and BrCl are readily photolysed and the resultant Cl and Br radicals react with O_3 to form ClO and BrO.

(5) $Cl_2 + h\nu \rightarrow Cl + Cl$
(6) $Cl + O_3 \rightarrow ClO + O_2$

(7) $BrCl + h\nu \rightarrow Br + Cl$
(8) $Br + O_3 \rightarrow BrO + O_2$

In the lower stratosphere, the effective denitrification resulting from production of the PSC and the elevated production of ClO yields two important catalytic removal processes for O_3.

(9) $ClO + ClO + M \rightarrow Cl_2O_2 + M$
(10) $Cl_2O_2 + h\nu \rightarrow Cl + ClOO$
(11) $ClOO + M \rightarrow Cl + O_2 + M$
(12) $2\ (Cl + O_3 \rightarrow ClO + O_2)$
(13) $2\ O_3 \rightarrow 3\ O_2$

(14) $BrO + ClO \rightarrow \alpha\ (Br + OClO)$
(15) $\rightarrow \beta\ (Br + Cl + O_2)$
(16) $\beta\ (Cl + O_3 \rightarrow ClO + O_2)$
(17) $Br + O_3 \rightarrow BrO + O_2$
(18) $(1+\beta)\ O_3 + \alpha\ ClO \rightarrow (1+2\beta)\ O_2 + \alpha\ OClO$

During sunlight OClO is rapidly photolysed:

(19) $OClO + h\nu \rightarrow ClO + O$
(20) $\rightarrow Cl + O_2$

The OClO amount is therefore strongly dependent on solar zenith angle (SZA). In the Antarctic spring the heterogeneous processing reduces the O_3 in the lower stratosphere to very low values within the vortex. Stratospheric models predict qualitatively the behaviour but not quantitatively.
In this study, measurements by the CRISTA2 and GOME instruments are used to study a PSC episode above Antarctica: the objective being to identify processing both inside and outside of the vortex.

2. CRISTA

On its second flight the CRISTA instrument observed the atmosphere for the period from the 8th to 16th of August 1997. The platform ASTRO-SPAS containing CRISTA was launched and recaptured by STS-85 Space Shuttle Discovery at an altitude of 300 km. The latitude range for the measurements was between 74°N and 74°S.
CRISTA measured the thermal emissions of 18 trace gases (e.g. O_3, NO_2, CO_2, HNO_3, $ClONO_2$, CFC-11, CH_4, N_2O, H_2O) in the spectral range of 4 - 71 µm. CRISTA scans the atmosphere in the limb viewing mode. To reduce the thermal noise levels for the high vertical resolution (2 -3 km) the optical equipment was cooled with liqiud helium. More details about CRISTA are provided by Ref. 5.
For the retrieval of HNO_3 and $ClONO_2$ the characteristic peaks at λ_{HNO3} = 11.3 µm and λ_{ClONO2} = 12.8 µm were used. The results for this reservoir gases are preliminary. The background radiance at 12,1 µm was used for the PSC detection.

3. GOME

In April 1995 the GOME nadir spectrometer mounted on the ERS-2 satellite was launched in a polar, sun-synchrononous orbit at an altitude of 795 km. GOME scans solar back scatter spectra between 240 and 790 nm with a spectral resolution of 0.2 - 0.4 nm. More details about GOME are provided by Ref. 1.

The retrieval of slant column densities (SCD) from GOME measurements is based on the Differential Optical Absorption Spectroscopy (DOAS) method. For the spectral fitting a wavelength window of 365 – 390 nm was selected for OClO, 425 – 450 nm for NO_2, 344.7 - 359 nm for BrO and 325.5 - 334.5 nm for O_3.

Air Mass Factors (AMF), which are used to convert SCD to vertical column densities (VCD), have been calculated using the radiative transport model GOMETRAN++ developed at the IUP Bremen and the MPI trace gas climatology (Ref. 7).

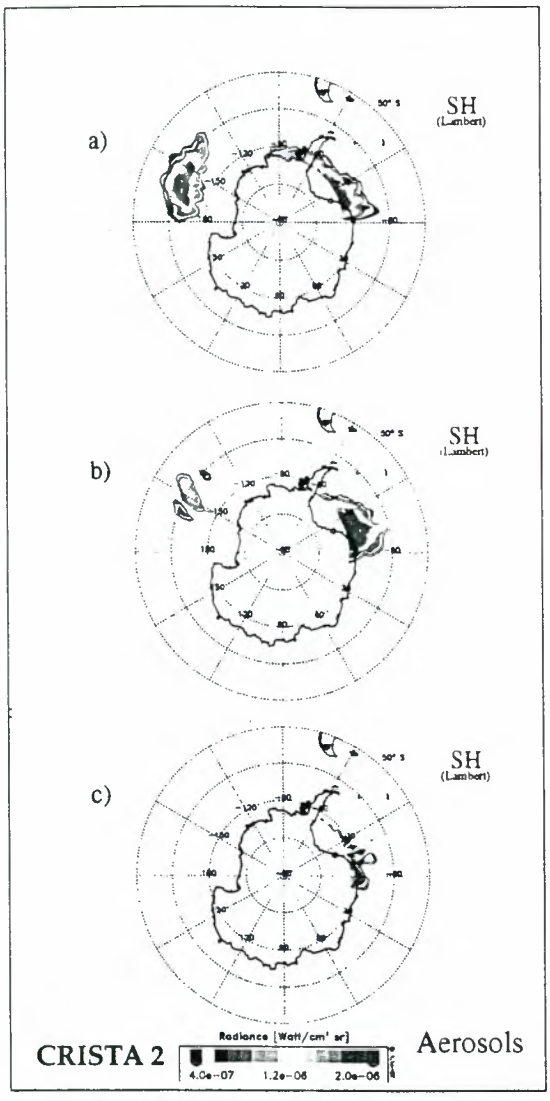

Figure 1. The CRISTA2 radiances of aerosols at an altitude of 20 km and the wavelength of 12.1 µm. The daily picture shows the measurement between 12 pm UTC and 12 pm UTC of the next day

a) 09 August 1997
b) 10 August 1997
c) 11 August 1997

4. DETECTION OF PSC

On August the 9th 1997 CRISTA observed two aerosol clouds near Antarctica. The first cloud was situated between 70°S and 55°S at the edge of the polar vortex, above the Pacific Ocean: the second being south of 65°S and clearly inside the vortex above sea ice. The tops of both clouds were detected at a height of 24 – 25 km.

In Figure 1 the temporal development of both PSCs is shown. It seems that the PSC disappear rather than move with the vortex. After three days the PSC have almost vanished completely.

A necessary condition for the formation of PSCs is a sufficiently low temperature inside the clouds. For the isolated PSC the UKMO temperature is below 188 K, cold enough for ice formation. The temperature may be even colder, according to priminilary CRISTA2 retrieval.

Analysis of the -3.5 PVU isoline, which can be regarded as an estimate of the dynamical tropopause (Ref. 4), shows that the tropopause in the PSC region is elevated (see Figure 2). It therefore appears that lifting of the tropopause induced by the tropospheric low pressure region in turn induces an adiabatic cooling in the lower stratosphere and resultant growth of PSC.

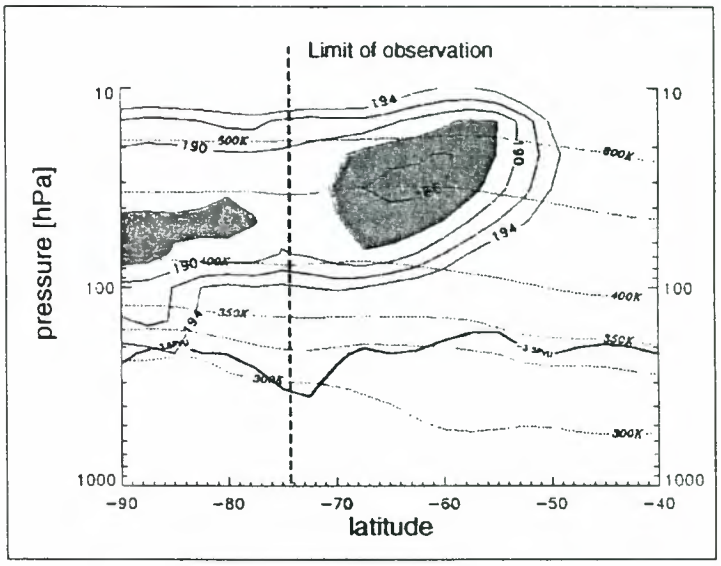

Figure 2. UKMO meterological data for the longitude 172.5° W crossing through the isolated PSC on the 9th of August 1997. The –3.5 PVU isoline shows the lifting of the tropopause in the PSC region and the temperature isolines at 188 K which coincide with the observed PSC.

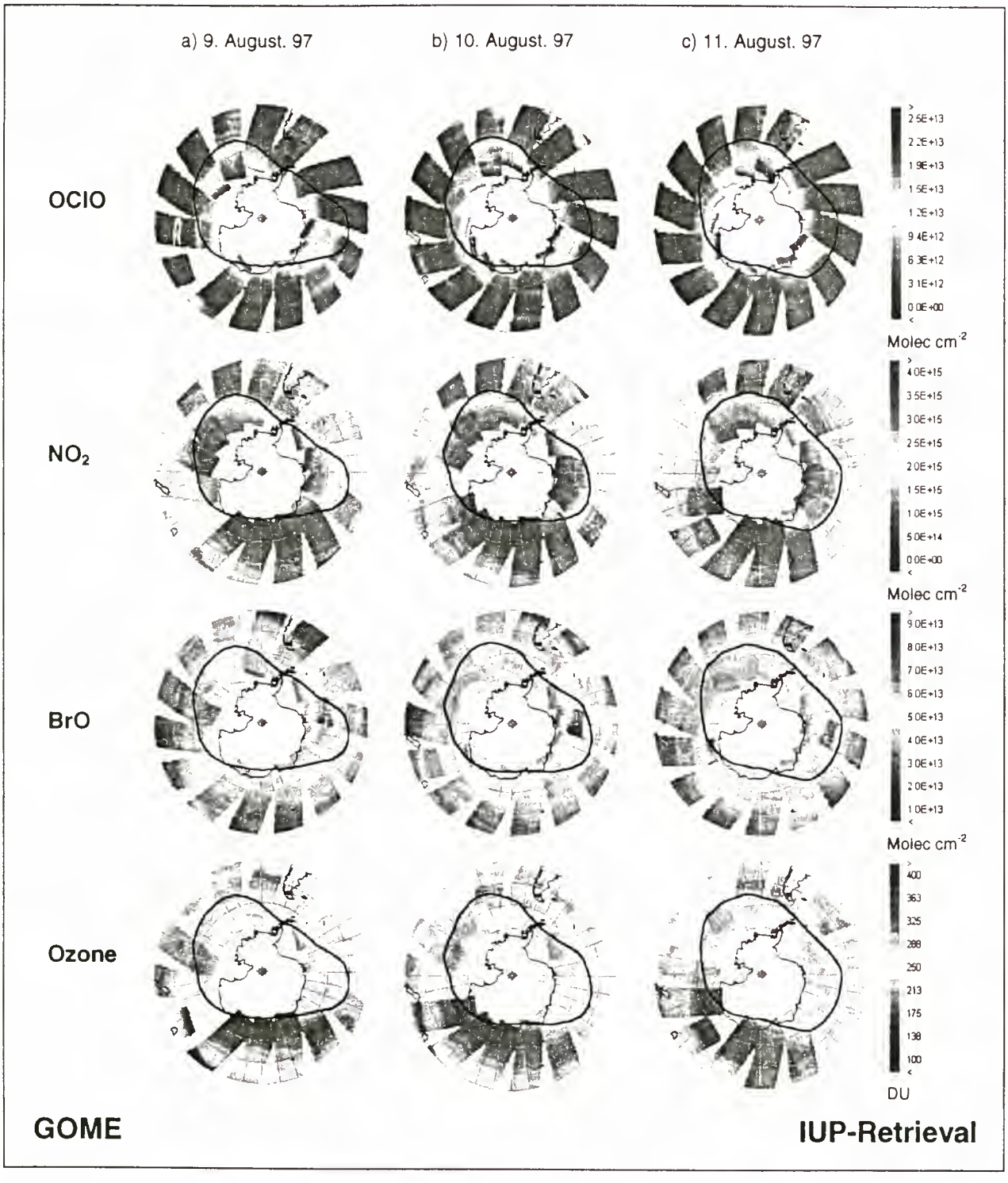

Figure 3. GOME retrieval of OClO, NO_2, BrO, and O_3. The picture shows the daily vertical column densities (12 pm UTC to 12 pm UTC). The black line represents the isoline of 42 PVU (Potential Verticity Units) which is a rough estimate of the vortex edge.

5. THE TRACE GASES

The vertical column densities of OClO, NO_2, BrO and O_3 are shown for the 9th to 11th of August 1997 in Figure 3. OClO appears to be present in copious amounts downwind from the PSC. This indicates processing of Cl-reservoirs and the production of OClO by the mechanism described above.

O_3 is not significantly chemical depleted in early August. The PSC is optically thin in GOME nadir viewing geometry and does not introduce significant error in the retrieved total O_3 amount. The lower O_3 in the region of

the PSC is rather a dynamic effect, resulting from the higher tropopause.
No large increase of BrO is observed downwind from the PSC feature. Rather evidence for tropospheric BrO is found, similar to that observed previously by in the southern hemisphere (Ref. 8) and in the northern hemisphere (Ref. 6).
The preliminary CRISTA retrieval of $ClONO_2$ and HNO_3 shows high values along the edge of the vortex. The low values of these reservoir gases correlate with the low column densities of NO_2 inside the vortex. Outside the vortex, the concentrations of $ClONO_2$ and HNO_3 decrease towards the equator, as expected (Ref. 9).
The minimum of O_3 at the edge of the vortex close to and in the PSC region is typical for a so-called O_3 mini-hole events (Ref. 2), created by the lifting of the tropopause. The resultant adiabatic cooling of the lower stratosphere reduces locally the temperature of the region inside of the polar vortex, which is colder than the surrounding air.
Inside of the vortex NO_2 is expected to be depleted by the formation of N_2O_5 which reacts on the ice to form HNO_3. However NO_2 is also low in the region of the elevated tropopause outside of the vortex. This may due to loss of N_2O_5 on liquid aerosols outside of the vortex as a result of tropopause lifting combined with possible mixing of vortex air with non vortex air.

6. CONCLUSIONS AND OUTLOOK

On the 9^{th} to 11^{th} of August 1997 CRISTA observed PSC in the southern hemisphere. This event remained stationary with time and did not move with the polar vortex. After three days the clouds vanished. The formation seems to be caused by adiabatic cooling as a result of a dynamic lifting of the air caused by the pushing of a low pressure system in the troposphere.
Downwind of the PSC large OClO column densities were observed inside the displaced vortex. This indicates chlorine activation in the air processed by the PSC. Within the vortex the region of high OClO and low NO_2 column densities rotated with the vortex. Elevated BrO regions however did not. They are attributed to tropospheric activation in or on sea ice.
The chlorine activation and the low column densities of NO_2 are in agreement with our current qualitative understanding of vortex chemistry and heterogeneous activation of chlorine reservoirs on PSC. The preliminary retrievals of the reservoir gases HNO_3 and $ClONO_2$ indicate that within the vortex, as excepted, these gases have very low amounts. At the edge of the vortex high values are observed which decrerase towards mid-latitudes.
The column densities of O_3 are low in the PSC region, mainly as a result of the lifting of the tropopause and the horizontal advection of lower stratospheric O_3 away from the tropospheric ridge. Any chemical O_3 destruction over three days of PSC existence is much smaller than the observed dynamical changes.
This study will be continued by comparing the observed PSC events with simulations using the BRemen Atmospheric PHOtochemical model (BRAPHO). This will provide a more detailed test of our knowlegde of polar chemistry and dynamics in the lower stratosphere.

7. ACKNOWLEDGMENTS

H. Kromminga and K. U. Eichmann are gratefully acknowledged for valuable discussions. Cooperation with the CRISTA team from the University of Wuppertal has been essential to this work. Parts of this work have been funded by the BMBF project 01LO9607/1 and by the University of Bremen. We thank UKMO for providing the meteorological datatset.

8. REFERENCES

1. Burrows, J.P. at al, The Global Ozone Monitoring Experiment (GOME): Mission Concept and First Scientific Results, J. Atmos. Sci., 56, 151-175, 1999.
2. Eichmann, K. U. at al, Ozone profile distributions in the Arctic from GOME satellite observations during spring 1997 and 1998, Satellite Remote Sensing of Clouds and the Atmosphere III, Proc. Of SPIE, Vol. 3495, 357-366, 1998.
3. Eisinger, M. at al. Studies on the precision of GOME irradiance and radiance products and GOME measurements of OClO and BrO over Antarctica. GOME Geophysical Validation Campaign. Final results workshop proccedings, ESA-WPP 108, 93-105, 1997.
4. Hoerling, M. P. at al, Global Objective Tropopause Analysis, Monthly Weather Review, 119, 1816-1831, 1991.
5. Offermann, D at al, Cryogenic Infrared Spectrometers and Telescopes for the Atmosphere (CRISTA) and Middle Atmosphere Variability, J. Geophys. Res., in print, 1999.
6. Richter, A. at al, GOME observations of tropospheric BrO in Northern Hemisphere spring and summer 1997, Geophys. Res. Lett., 25, 2683-2686, 1998.
7. Rozanov, V at al, GOMETRAN: A radiative transfer model for the satellite project GOME - the plane parallel version, J. Geophys. Res., 102, 16683, 1997.
8. Wagner, T. at al, Satellite mapping of enhanced BrO concentrations in the troposphere. Nature, 395, 486-490, 1998.
9. WMO Report, Scientific Assessment of Ozone Depletion, 1994.

SPECTRAL INTERPOLATION OF AEROSOL EXTINCTION COEFFICIENTS

Ghislain Franssens, Didier Fussen, Martine De Mazière, Dominique Fonteyn, and Quentin Errera

Belgian Institute for Space Aeronomy
Ringlaan 3, B-1180 Brussels, BELGIUM
E-mail: ghislain.franssens@oma.be

ABSTRACT

A new approach to the problem of spectral interpolation of aerosol extinction coefficients is presented. The proposed algorithm is applicable to non-absorbing, spherical particles and is based on the Anomalous Diffraction Approximation (ADA). The interpolant consists of a linear combination of carefully designed basis functions, each possessing the correct spectral behaviour of an extinction function. The expansion coefficients are obtained by minimising a fitting cost function, using a Generalized Reduced Gradient Method (GRGM), with constraints.
The performance of the algorithm has been examined when applied to sparse data, corrupted by errors. The usefulness of the algorithm in solving the spectral inverse problem, i.e. in deriving the aerosol size distribution from the extinction coefficient, is discussed. A number of numerical test examples are shown.

1. INTRODUCTION

Measurements of the optical extinction coefficient β [1/m] are typically performed at a limited number of discrete wavelengths or in limited, densely sampled bands.
For certain applications, one needs to know β also at wavelengths where no measurements were made. An example is the retrieval of the concentration of an atmospheric trace constituent from total optical extinction, measured at a particular wavelength. To find the contribution from the constituent alone, one must subtract the aerosol component at that wavelength (e.g. O_3 at 0.6 μm).
Another application is the retrieval of derived aerosol parameters, which requires the knowledge of $\beta(\lambda)$ over a broad range (UV to the far IR) [Refs. 1-2]. An example is the aerosol number density distribution $N(r)$ [1/m^4], obtained from the spectral inversion of the extinction coefficient.
Spectral interpolation and this spectral inversion are closely related. On one hand, experimental data requires interpolation or fitting before spectral inversion can be carried out. On the other hand, the spectral interpolation problem becomes trivial, once the underlying aerosol number density is known. In the approach presented here, we consider the problems of interpolation and inversion together.
General light scattering and absorption is described by Mie theory and is mathematically complex [Ref. 9]. A convenient approximation to Mie scattering theory is the Anomalous Diffraction Approximation (ADA). It is valid for spherical particles, with radius r and (complex) refractive index $m = n - in'$, when $|n-1| << 1 << kr$, $k = 2\pi/\lambda$. The ADA is sufficiently accurate for most practical purposes and is mathematically more tractable. It incorporates both the Rayleigh limit for small r (extinction efficiency tends to zero) and the geometrical-optics limit for large r (extinction efficiency tends to 2), and therefore possesses the major features of light scattering by spherical particles larger than the wavelength.

A number of interpolation and inversion methods have been presented in the literature before [Refs. 3-8]. In this paper we present some first results obtained by a new algorithm for spectral interpolation. As a by-product, we also get an approximation for the underlying aerosol number density distribution. We focus attention on the practical case where $\beta(\lambda)$ is measured at only a limited number of wavelengths and the data is corrupted by experimental and/or processing errors [Ref. 8].
We begin with a brief summary of spectral inversion theory and present an explicit analytical inversion formula. Based on this formula, we propose a discrete set of basis functions, and represent the spectral interpolation function as a linear combination of these basis functions. The interpolation function is then fitted to the given data, by minimising a cost function, using a Generalized Reduced Gradient Method (GRGM), with constraints [Refs. 11-12]. Finally, expressions are given to compute the aerosol total number density, total surface density and total volume density, (assuming spherical particles).
Our method was tested on simulated data for single and bimodal distributions, using ADA as forward model, and for non-absorbing, non-dispersive particles (i.e. having a real and constant refractive index). The noise tolerance of the algorithm and the accuracy of the interpolation were examined, and this is illustrated by a number of examples.
This work is still in progress and efforts are underway to also incorporate absorption and dispersion effects in the algorithm.

2. THEORY

For our theoretical framework we use the ADA, applied to non-absorbing, non-dispersive, spherical aerosol particles. That is, the refractive index n of the particles is assumed to be real and independent of the wavelength. The extinction efficiency $Q_{eff}(2\kappa r)$, where $\kappa = (n-1)k$ is the effective wavenumber, is given by [Ref. 9]

$$Q_{eff}(2\kappa r) = 2 - 4\frac{\sin(2\kappa r)}{2\kappa r} + 4\frac{1-\cos(2\kappa r)}{(2\kappa r)^2} \qquad (1)$$

valid when $\kappa r >> |n-1|$.
The relation between the aerosol extinction function $\beta(\kappa)$ and the aerosol number density distribution $N(r)$ is

$$\beta(\kappa) = \int_0^{+\infty} \pi r^2 Q_{eff}(2\kappa r) N(r) dr \qquad (2)$$

It is mathematically more convenient to use the effective wavenumber κ instead of the wavelength as independent variable and to work with a modified extinction function $B(\kappa)$, instead of the function $\beta(\kappa)$. Eq. (2) is rewritten as

$$B(\kappa) = \int_0^{+\infty} K(\kappa, r) S(r) dr \tag{3}$$

with

$$B(\kappa) \stackrel{\Delta}{=} b_\infty - b(\kappa),\ b(\kappa) \stackrel{\Delta}{=} 2\beta(\kappa) \tag{4a}$$

$$b_\infty \stackrel{\Delta}{=} \lim_{\kappa \to +\infty} b(\kappa) = \int_0^{+\infty} S(r) dr \stackrel{\Delta}{=} S_{tot} \tag{4b}$$

$$\begin{aligned} K(\kappa, r) &\stackrel{\Delta}{=} \frac{1}{2}\left(2 - Q_{eff}(2\kappa r)\right) \\ &= 2\left(\frac{\sin(2\kappa r)}{2\kappa r} - \frac{1-\cos(2\kappa r)}{(2\kappa r)^2}\right) \end{aligned} \tag{4c}$$

$$S(r) \stackrel{\Delta}{=} 4\pi r^2 N(r) \tag{4d}$$

The quantity (4d) is the aerosol surface density distribution, in [1/m^2]. Eq. (3) is a Fredholm integral equation of the first kind, with symmetric kernel $K(\kappa, r)$, over the domain $R^+ \times R^+$. In [Ref. 10] it is proved that (3) has the explicit inverse

$$S(r) = \frac{4}{\pi} \int_0^{+\infty} (\kappa r)^2 K(\kappa, r) B(\kappa) d\kappa \tag{5}$$

and that this inverse is unique.

The inversion formula is mainly of theoretical importance and served as a basis for the construction of a more practical algorithm. Due to the oscillatory behaviour of the inverse kernel, this formula will be of little use, when only a few spectral measurements are available. For these more difficult cases we now introduce a more practical algorithm.

Consider an ordered sampling of the r-axis, $\{r_n,\ n = 0, N\}$ and define a set of discrete basis functions $\{B_n(\kappa),\ n = 1, N\}$, by

$$\begin{aligned} B_n(\kappa) &= \frac{2}{\sqrt{\pi}} \frac{r_n^c}{h_n} \kappa \int_{r_{n-1}}^{r_n} K(\kappa, r') dr' \\ &= \frac{2}{\sqrt{\pi}} \frac{r_n^c}{h_n} \left(\frac{1-\cos(2\kappa r_n)}{2\kappa r_n} - \frac{1-\cos(2\kappa r_{n-1})}{2\kappa r_{n-1}} \right) \end{aligned} \tag{6}$$

where

$$\begin{aligned} h_n &= r_n - r_{n-1} \\ r_n^c &= (r_n + r_{n-1})/2 \end{aligned} \tag{7}$$

The discrete basis functions are such that $\frac{B_n(\kappa)}{\kappa}$ is the extinction function of a block-like surface density distribution $S_n(r) = \frac{2}{\sqrt{\pi}} r_n^c \frac{\Pi(r - r_n^c; h_n)}{h_n}$.

The discrete basis functions are orthogonal over the continuous domain [Ref. 10]

$$\int_0^{+\infty} B_n(\kappa) B_m(\kappa) d\kappa = \frac{1}{h_n} \frac{(r_n^c)^2}{r_{n-1} r_n} \delta_{nm} \tag{8}$$

but not over the discrete domain. In the limit when all h_n tend to zero, they satisfy

$$\lim_{\{h_n\} \to 0} \sum_{n=1}^{+\infty} B_n(\kappa) B_n(\kappa') h_n = \delta(\kappa - \kappa') \tag{9}$$

We can therefore call the discrete basis functions 'pseudo-orthonormal' over the discrete domain, in the sense that, in the limit for ever smaller discretisations, they become truly orthogonal.

We use as discrete representation for the modified spectral extinction function

$$B(\kappa) = \frac{\sqrt{\pi}}{2} \frac{1}{\kappa} \sum_{n=1}^{N} c_n B_n(\kappa) \tag{10}$$

It can be shown that, if we take

$$c_n = \frac{h_n}{r_n^c} S(r_n^c) \tag{11}$$

the representation (10) converges to the correct continuous limit (i.e. the integral (3)) when the $\{h_n\}$ tend to zero [Ref. 10]. From (11) it is obvious that our interpolation method also solves the inversion problem. The coefficients $\{c_n\}$ are, up to a factor fixed by the r-axis sampling, values of the underlying surface density distribution.

By substituting the discrete representation (10) in the inversion formula (5), and by integrating over r, we can compute expressions for some integrated distribution quantities (i.e. density quantities), in terms of the coefficients $\{c_n\}$.

For the aerosol total number density we find [Ref. 10]

$$N_{tot} \stackrel{\Delta}{=} \frac{1}{4\pi} \int_0^{+\infty} \frac{S(r)}{r^2} dr = \frac{1}{4\pi} \sum_{n=1}^{N} c_n \frac{(r_n^c)^2}{r_{n-1} r_n} \tag{12}$$

For the total surface density we get

$$S_{tot} \stackrel{\Delta}{=} \int_0^{+\infty} S(r) dr = \sum_{n=1}^{N} c_n r_n^c \tag{13}$$

and for the total volume density

$$V_{tot} \stackrel{\Delta}{=} \frac{1}{3} \int_0^{+\infty} r S(r) dr = \frac{1}{3} \sum_{n=1}^{N} c_n (r_n^c)^2 \tag{14}$$

Up to now, we worked with the modified extinction function $B(\kappa)$, which contains the usually unknown constant $b_\infty = S_{tot}$. From the definition (4a) and by using (10) and (13) we can now write down the discrete representation for the true extinction function $\beta(\kappa)$, as follows

$$\beta(\kappa) = \frac{1}{2} \sum_{n=1}^{N} c_n \left(r_n^c - \frac{\sqrt{\pi}}{2} \frac{1}{\kappa} B_n(\kappa) \right) \tag{15}$$

Expression (15) is the spectral interpolation function used in the numerical implementation.

Finally, we need to determine the coefficients $\{c_n\}$.

Consider given extinction measurements $\{\beta_m,\ 1 \le m \le M\}$ with absolute errors $\{\varepsilon_m,\ 1 \le m \le M\}$ at wavelengths $\{\lambda_m,\ 1 \le m \le M\}$, or equivalently at effective wavenumbers $\{\kappa_m = (n-1)2\pi/\lambda_m,\ 1 \le m \le M\}$. The aim is to determine the coefficients such that the extinction function $\beta(\kappa)$, given by (15), closely passes through the measured data. The most straightorward solution is a least square fit with cost function

$$J_1(\{c_n\}) \stackrel{\Delta}{=} \frac{\sum_{m=1}^{M} w_m(\beta_m - \beta(\kappa_m))^2}{\sum_{m=1}^{M} w_m(\beta_m)^2} \qquad (16)$$

and positive weights $\{w_m,\ 1 \le m \le M\}$, which typically depend on the errors. When this was applied to data with a high degree of uncertainty, it was found necessary to introduce a regularisation of the minimisation problem. This was done by introducing a second cost term, of the form

$$J_2(\{c_n\}) \stackrel{\Delta}{=} \rho^2 \frac{\int_0^{+\infty} \frac{1}{S(r)}\left(\frac{dS(r)}{dr}\right)^2 \frac{dr}{r}}{\int_0^{+\infty} S(r)\frac{dr}{r}} \qquad (17)$$

where ρ is an empirical constant of dimension [μm] and of the order of 0.1. The effect of this term is to reduce the oscillatory behaviour of the coefficients and hence of the resulting surface density distribution. Functional (17) is implemented by discretising the integrals and by relating the discrete values $S(r_n^c)$ to the unknown coefficients, using (11).

The coefficients are then obtained by minimising the total cost function

$$J(\{c_n\}) = aJ_1(\{c_n\}) + bJ_2(\{c_n\}) \qquad (18)$$

with constants a and b, subject to the constraints

$$\beta_m - \varepsilon_m \le \beta(\kappa_m) \le \beta_m + \varepsilon_m,\quad m = 1,\ldots M \qquad (19)$$

and

$$\begin{aligned} &0 \le c_1 < 10^{-6} \\ &0 \le c_n < +\infty,\quad n = 2,\ldots N-1 \\ &0 \le c_N < 10^{-6} \end{aligned} \qquad (20)$$

Constraints (19) assure that the interpolant passes through the error bars of the extinction measurements, while conditions (20) result in a surface density distribution that is positive and zero at the edges of the r-axis discretisation region. The constants a and b are to be fixed by numerical experimenting.

We solved the problem (18)-(20) with a Generalized Reduced Gradient Method [Refs. 11-12].

3. NUMERICAL RESULTS

To examine the applicability of the inversion formula (5) and of the interpolation algorithm, numerical tests were done with computer simulated extinction data, using ADA as forward model. In all subsequent examples, aerosol size is measured in μm and densities (concentrations) are expressed per m^3. Test number density distributions were taken to be log-normal

$$N(r) = N_{tot}\frac{1}{\sqrt{4\pi}}\frac{1}{\ln\sigma}\frac{1}{r}e^{-\frac{\ln^2\frac{r}{r_m}}{2\ln^2\sigma}},\quad \int_0^{+\infty} N(r)dr = N_{tot} \qquad (21)$$

A) Inversion by the continuous formula (5).

Consider a bimodal number density, consisting of the sum of two log-normal distributions with parameters r_m=0.7, σ=1.4, amplitude A=0.9 and r_m=3.0, σ=1.3, amplitude A=0.09. We computed the modified extinction function $B(\kappa)$ and then applied the inversion formula (5) to reconstruct the surface density distribution. The integrals were numerically calculated with the trapezium rule. A low pass filter in wavenumber space was used to limit the infinite integration range. This truncation is the main cause of error. Increasing the range of integration and the density of the discretisation of the integrands both reduce the errors, in the forward and inverse calculation. For 10000 wavelength points and 2000 radius points, we get a root mean square (rms) error between the original and reconstructed surface density distributions of 0.9% over a 0.1 – 10.0 μm range. Fig. 1 shows the computed extinction function associated with the bimodal distribution plotted in Fig. 2. This example shows that a straightforward discretisation of the inversion formula can give very good results, provided the extinction function is very densily sampled and the data is exact.

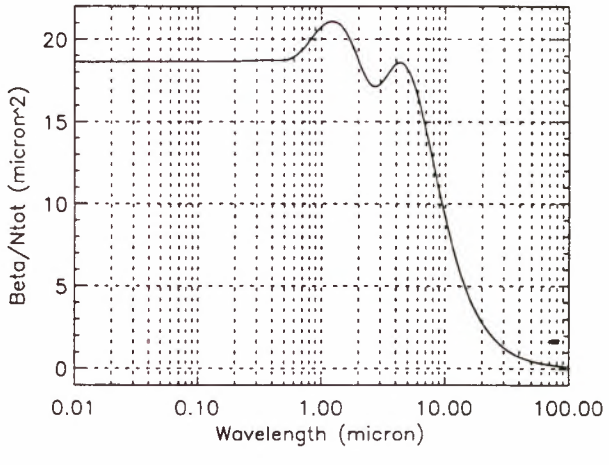

Fig. 1 : Normalized extinction coefficient as function of wavelength, obtained by the ADA for the $S(r)$ in Fig. 2.

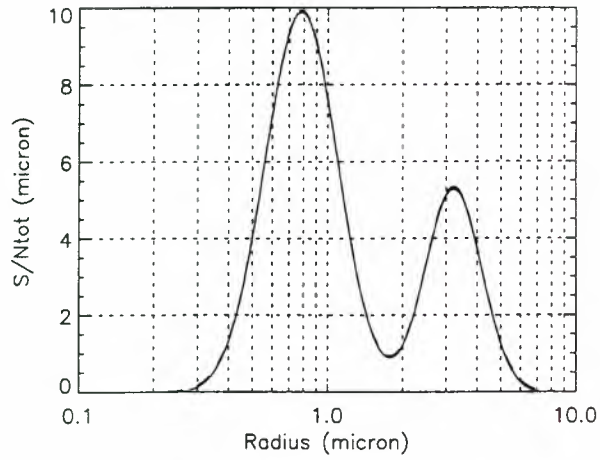

Fig. 2 : Normalized surface density distribution as function of radius. The (invisible) dashed line is the initial distribution, the solid line the reconstruction obtained by (5).

The reason for the necessity of the high number of sample points is the fast oscillatory behaviour of the inverse integrand, when reconstructing the larger radius part of the surface density distribution. Real atmospheric data are not sufficiently densily measured, do not cover a sufficiently large wavelength range and have error bars. For these reasons, a straightforward application of the inversion formula cannnot be used.

B) Results obtained with the discrete algorithm.

The following examples show the behaviour of the algorithm for varying number of measurement points and error bars.

Consider again the bimodal from A. We computed the extinction function $\beta(\kappa)$, sampled it in M=51 points, and reconstructed the original distribution with N=15 basis functions. Reconstructed surface density distributions were interpolated by cubic splines from the N discrete values. Uniformly distributed random noise was added to the extinction samples, giving error bars of a) 3% and b) 10%.

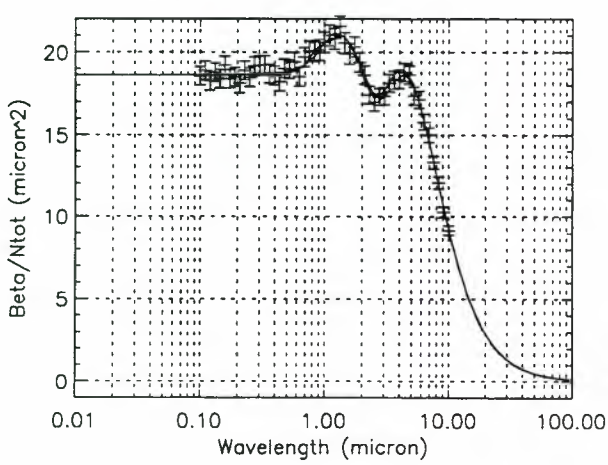

Fig. 3. Initial (dashed) and interpolated (solid) normalized extinction from 51 samples with 3% error.

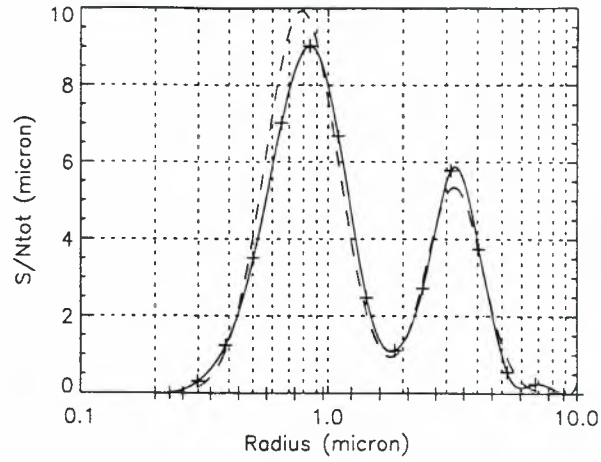

Fig. 4. Initial (dashed) and reconstructed (solid) normalized surface density distribution from 51 samples with 3% error.

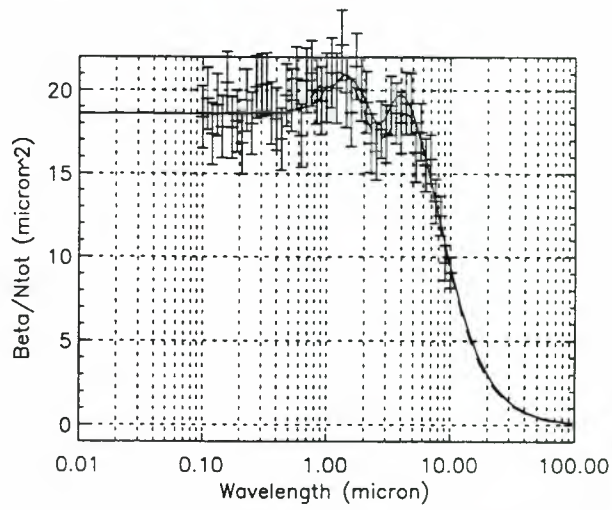

Fig. 5. Initial (dashed) and interpolated (solid) normalized extinction from 51 samples with 10% error.

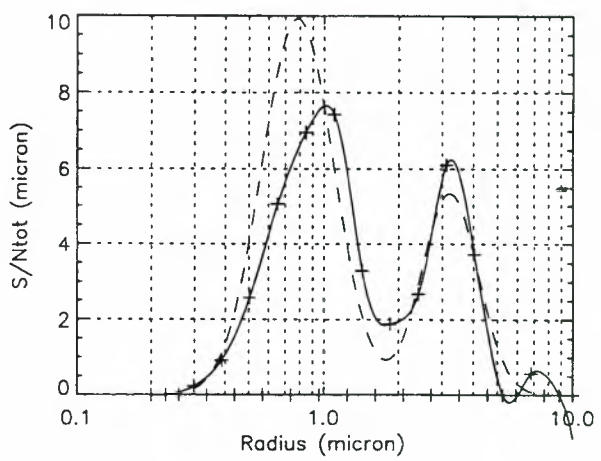

Fig. 6. Initial (dashed) and reconstructed (solid) normalized surface density distribution from 51 samples with 10% error.

Figs. 3 and 5 show the interpolation of the extinction function and Figs. 4 and 6 the surface density distributions. The rms errors are : on the extinction function 0.8% and 2.4% and on the surface density distribution 12.4% and 31.8%, for cases a and b, repectively. The relative errors on the total surface density S_{tot} and total volume density V_{tot} are respectively 0.05% and 1.3% for a and 0.2% and 3.9% for b. This shows that, although the shape of the reconstructed surface density distribution is in error, the integrated quantities are obtained with a smaller error than the error on the original extinction samples. The reason for these good results is that the interpolation algorithm predicts with good accuracy the low wavelength limit of the extinction function, and $S_{tot} = 2 \lim_{\kappa \to +\infty} \beta(\kappa)$.

Fig. 7 shows the interpolation of $\beta(\kappa)$ when $b = 0$ in (18), for error case a. Fig. 8 shows the resulting surface density distribution. It is clear, by comparing Figs. 3, 4 with 7, 8, that the presence of J_2 is necessary to stabilize the inversion. However, J_2 has little effect on the quality of the interpolation (rms error 0.5%). So this means that the surface density distributions of Figs. 4 and 8, although largely different, produce almost the same extinction interpolation curve. This example shows that the inversion problem is much more sensitive to measurement errors than the interpolation problem and one can still have a good interpolation with a bad surface density distribution.

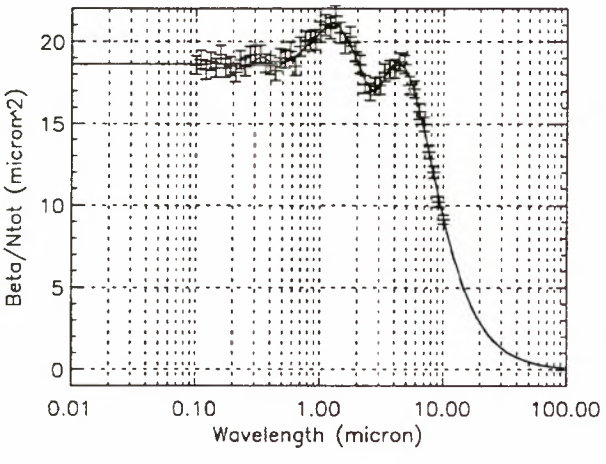

Fig. 7. Initial (dashed) and interpolated (solid) normalized extinction from 51 samples with 3% error, without using the second term in the total cost function (18).

We now consider a single log-normal number density distribution with parameters r_m=1.0, σ=1.35, A=1.0. We use only M=5 extinction samples and again N=15 basis functions, and consider the same relative error bars of a) 3% and b) 10%. Figs. 9 and 11 show the interpolation of the extinction function, while in Figs. 10 and 12 the respective surface density distributions are plotted. The rms errors are : on the extinction function 2.8% and 8.2% and on the surface density distribution 15.0% and 27.5%, for cases a and b repectively. The relative errors on the total surface density S_{tot} and total volume density V_{tot} are respectively 0.6% and 1.6% for a and 2.6% and 8.0% for b.

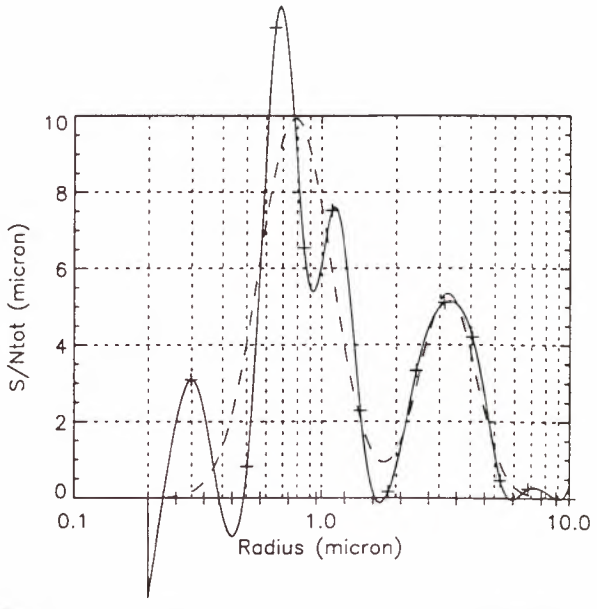

Fig. 8. Initial (dashed) and reconstructed (solid) normalized surface density distribution associated with Fig. 7.

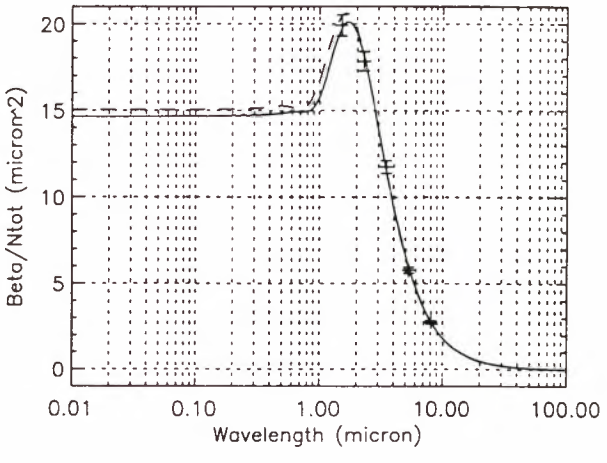

Fig. 9. Initial (dashed) and interpolated (solid) normalized extinction from 5 samples with 3% error.

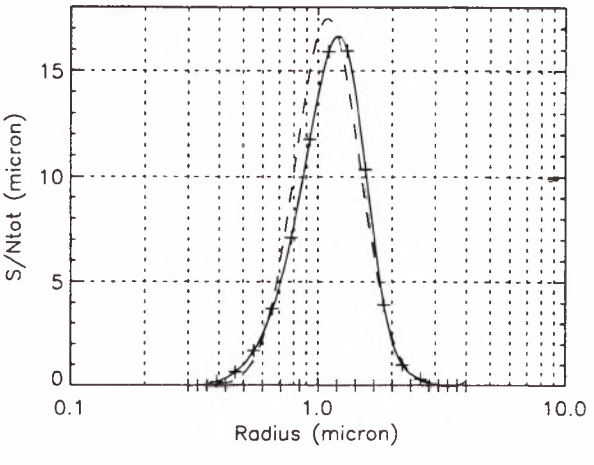

Fig. 10. Initial (dashed) and reconstructed (solid) normalized surface density distribution from 5 samples with 3% error.

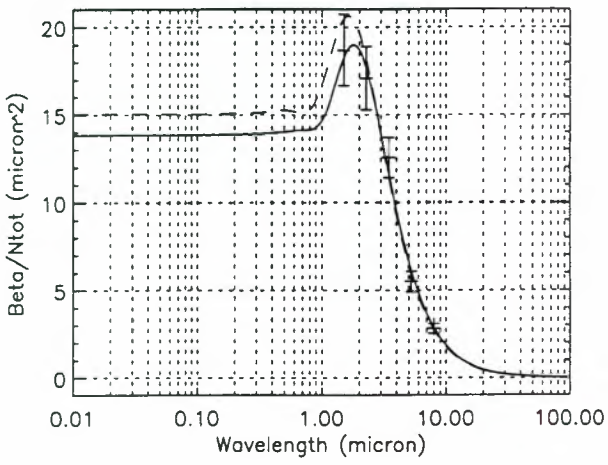

Fig. 11. Initial (dashed) and interpolated (solid) normalized extinction from 5 samples with 10% error.

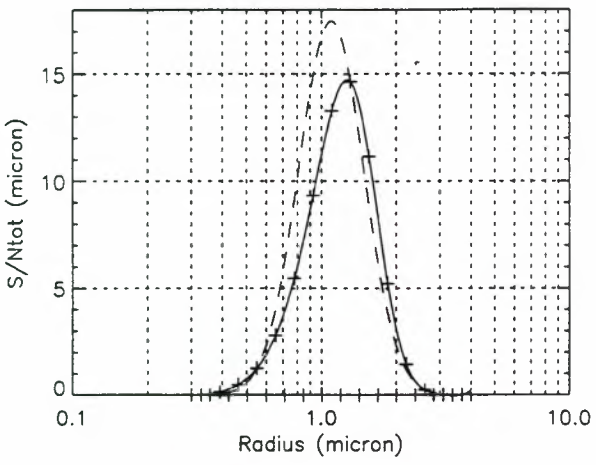

Fig. 12. Initial (dashed) and reconstructed (solid) normalized surface density distribution from 5 samples with 10% error.

Figs. 9-12 are to be compared with Figs. 13 and 14, which show the interpolation and inversion for the same case, but now with exact samples. This shows that the algorithm is very powerful in reconstructing the extinction and surface density distribution from very few points, provided the data is accurate, at least for single mode log-normal distributions. We now obtain a rms error on the extinction function of 0.5% and 7.2% on the distribution. The relative error on the total surface density is 0.06% and on the total volume density 0.4%. In this example, the algorithm extrapolates the extinction into the UV region very well, from data that was only available in the IR region.

4. CONCLUSIONS

Numerical tests demonstrated the usefulness of the proposed algorithm for spectral extinction interpolation. Examples for a single and bimodal distribution show that our method is stable when applied to noise-corrupted data. It is capable of reconstructing $\beta(\kappa)$ with a relative rms error that is smaller than the relative error on the initial extinction samples, even when only very few data points are available. For example, interpolating from 5 samples, having a 10 % relative error, in the case of a single log-normal number density distribution, results in an interpolation error of about 8% rms over the whole spectrum. The method produces, as by-product, the underlying size distribution (number, surface and volume density distributions), to a reasonable degree of accuracy. The relative error on the inversion is about 3 to 4 times higher than that on the samples, for single and bimodal log-normal number density distributions. But integrated quantities, such as total surface and volume densities, are retrieved to a much higher accuracy. For the case already mentioned above, total surface and volume density were retrieved to within 0.6% and 1.6%, repectively. In general, it was found that the inverse problem was much more sensitive to noise, than the interpolation problem.

More work is planned to further improve the algorithm. In particular, the choice of the functional (17) needs to be examined in more detail.

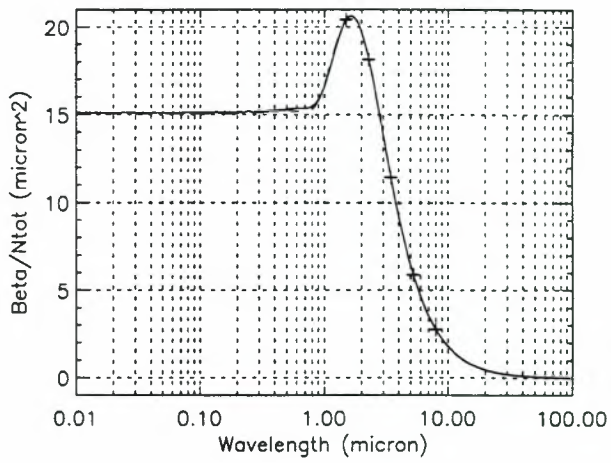

Fig. 13. Initial (dashed) and interpolated (solid) normalized extinction from 5 exact samples.

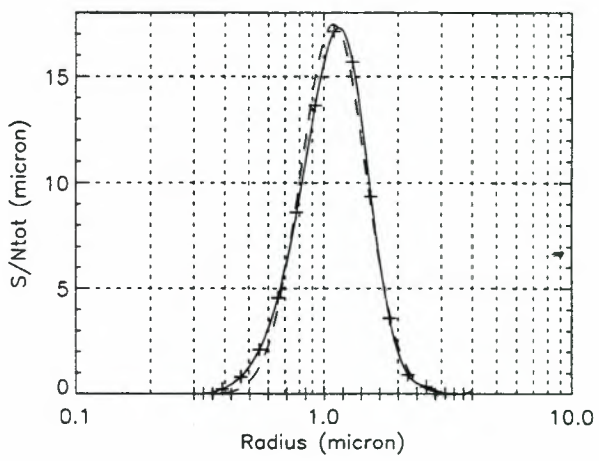

Fig. 14. Initial (dashed) and reconstructed (solid) normalized surface density distribution from 5 exact samples.

5. ACKNOWLEDGEMENT

This research was funded by the European Space Agency in the framework of the Data User Programme (http://styx.esrin.esa.it:8099/), contract AMASDU (Aerosol Mapping Algorithms for Satellite Data Users, contract no. 12526/97/I-HE).

6. REFERENCES

1. Box G. P., Box M. A. and Krücker J., 1996, Information content and wavelength selection for multispectral radiometers, *J. Geophys. Res.*, 101, 19211-19214.

2. Lambert, A., Grainger R. G., Rogers H. L., Norton W. A., Rodgers C. D. and Taylor F. W., 1996, The H_2SO_4 Component of stratospheric aerosols derived from satellite infrared extinction measurements: Application to stratospheric transport studies, *Geophys. Res. Lett.*, 23, 2219-2222.

3. Twomey S., 1975, Comparison of constrained linear inversion and an iterative non-linear algorithm applied to the indirect estimation of particle size distributions, *J. Comput. Phys.*, 18, 188-200.

4. Smith C. B., 1982, Inversion of the anomalous diffraction approximation for variable complex index of refraction near unity, *Applied Optics*, 21, 3363-3366.

5. Klett J. D., 1984, Anomalous diffraction model for inversion of multispectral extinction data including absorption effects, *Applied Optics*, 23, 4499-4508.

6. Wang J. and Hallett, F. R., 1996, Spherical particle size determination by analytical inversion of the UV-visible-NIR extinction spectrum, *Applied Optics*, 35, 193-197.

7. Amato U., Di Bello D., Esposito F., Serio C., Pavese G. and Romano F., 1996, Intercomparing the Twomey method with a multimodal lognormal approach to retrieve the aerosol size distribution, *J. Geophys. Res.*, 101, 19267-19275.

8. Thomason L. W., Poole L. R. and Deshler T., 1997, A global climatology of stratospheric aerosol surface area density deduced from SAGE II measurements: 1984-1994, *J. Geophys. Res.*, 102, 8967-8976.

9. van de Hulst H. C., 1981, Light scattering by small particles, *Dover Publications Inc.*, New York.

10. Franssens G., 1999, Determination of particle size distributions from extinction data based on the anomalous diffraction approximation, pre-print.

11. Lasdon L. S., Waren A. D., Jain A. and Ratner M., 1978, Design and Testing of a Generalized Reduced Gradient Code for Nonlinear Programming, *ACM Trans. on Math. Software*, 4, 1, 34-50.

12. Lasdon L. S. and Waren A. D., 1979, Generalized Reduced Gradient Software for Linearly and Nonlinearly Constrained Problems, in *"Design and Implementation of Optimization Software"*, Greenberg H., ed., Sijthoff and Noordhoff, pubs.

CLOUD CLASSIFICATION USING IMAGE SEQUENCES OF GOME DATA

Mark Wenig[1,2], Carsten Leue[1,2], Bernd Jähne[1,2] and Ulrich Platt[1]

[1]Institute for Environmental Physics
[2]Interdisciplinary Center for Scientific Computing
Heidelberg University, Germany
e-mail: mark.wenig@iwr.uni-heidelberg.de

Abstract

An algorithm is presented which calculates the degree of cloud cover by means of image sequence and color space (HSV) analysis of GOME PMD-data (Polarization Monitoring Device). The developed algorithm uses two characteristic properties of clouds, being white and varying with time. The PMD-data can be interpreted as RGB images and hence a color space analysis can be used for the classification of clouds. Following that first classification, an iterative fix point method is applied to the PMD image sequences to create clear sky and maximum cloud cover images of the entire globe. From comparison of the PMD images to that reference data, the fractions of the amount of light reflected at the earth's surface and by clouds can be calculated which indicates the fractional cloud cover. The results of the method are compared to the cloud detecting algorithm ICFA and are validated using other satellite images. It is also shown that the method improves the interpretation of the DOAS (differential optical absorption spectroscopy [6]) results by providing more information on the cloud cover which is necessary for accurately calculating the Air Mass Factors (AMFs).

1 Introduction

For trace gas retrieval with the DOAS technique it is necessary to consider the Air Mass Factor to receive a representation of the vertical column densities which is independent from the geometry of the lightpaths. One of the most important parameters for the calculation of the AMF is also the cloud cover at the measurement pixel. The pathlength of the light in clear and cloudy skies differ in a wide range. In order to calculate the pathlength it is necessary to consider whether the light beam is reflected at the earth's surface or a cloudy layer. Therefore a cloud detecting algorithm is needed. Possible influences of clouds on the lightpath are shown in figure 1.

The cloud detection algorithm presented here relies on information from the spatially high resolved PMD data. The data yields an integral of the light intensity over the three wavelength intervals as shown in table 1 and will thus be regarded as proxies for RGB intensities used for further image processing. The cloud detecting algorithm

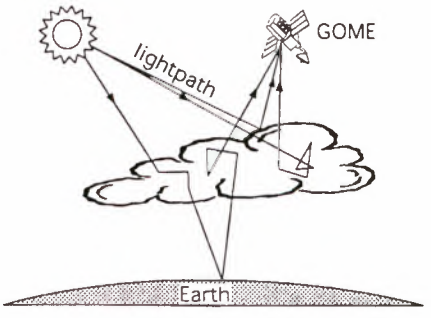

Figure 1: Possible Influences of clouds on the lightpath.

focuses on two characteristics of clouds, their degree of whiteness and that clouds form a moving layer in front of a static background. A visualization of PMD values from June 29 1997 can be seen in figure 2.

PMD chanel	wavelength [nm]
1. (UV)	295-397
2. (blue)	397-580
3. (red)	580-745

Table 1: Wavelength bands of the three PMD channels (see [1])

2 Color Space Analysis

One of the clouds' characteristic is their degree of whiteness compared to the background pixels. The most evident approach uses the three PMD channels themselves as the feature space to analyze the cloudy and clear-sky scenes in the RGB color space. This distribution of corresponding features gives a first hint to the quality of the chosen color space. A histogram plot of the distribution of channel 2 (blue) and channel 3 (red) over the global data from an image sequence of one month can be seen in figure 3. In figure 3a all scenes cluster into a single area with a single maximum, so the two object classes *clouds* and *background* are not well separated. The contribution of cloudy scenes to this distribution is shown in figure 3b

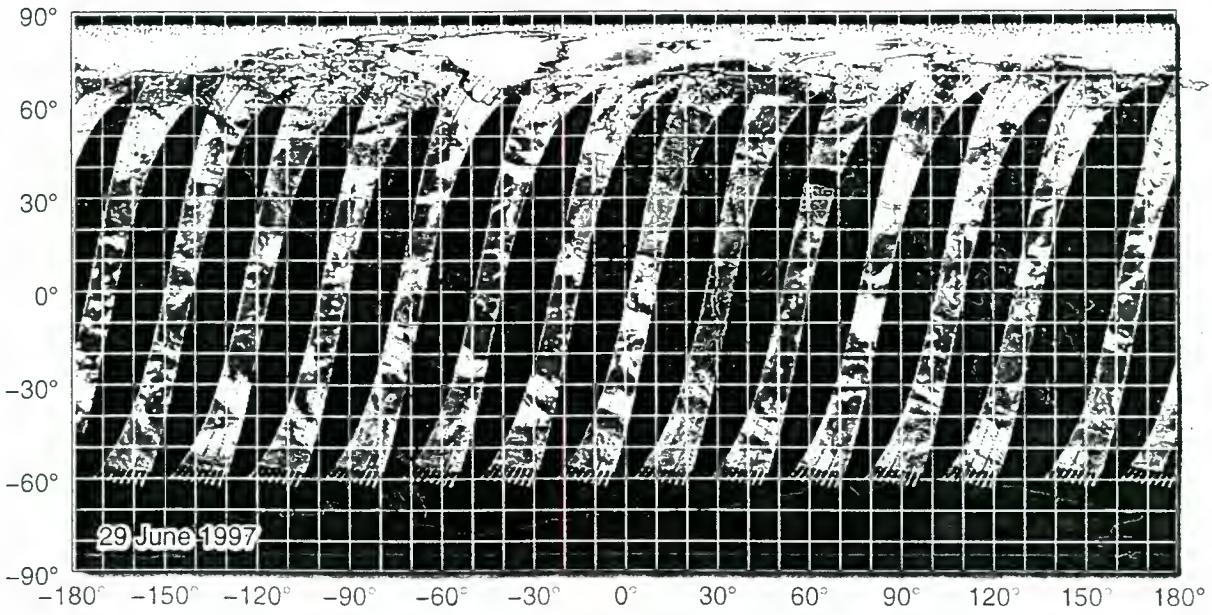

Figure 2: A visualization of PMD values. The values are taken from June 29 1997.

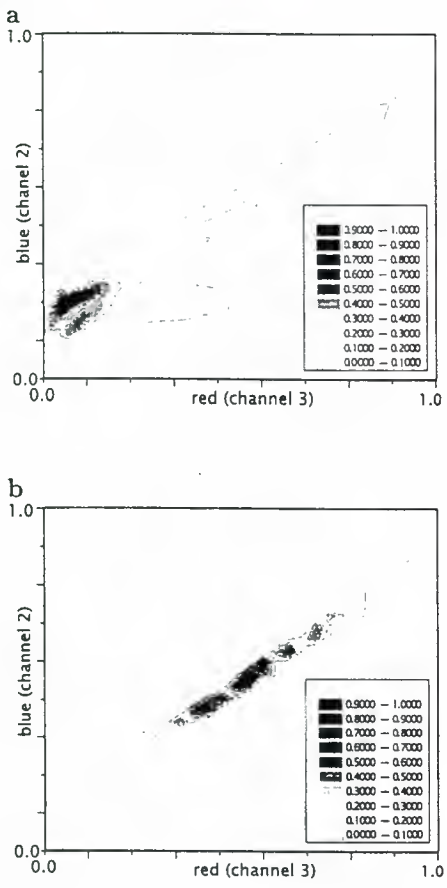

Figure 3: Histogram plot of the distribution of channel 2 (blue) / channel 3 (red) over the global data from one month. **a** Whole image sequence **b** Visually classified clouds

with cloudy pixels sorted out visually. Another finding is that the two PMD channels are strongly correlated, expressed by the concentration along the diagonal. The histograms referring to the other possible pairs of channels produce similar results. Other linear or nonlinear combinations of the PMD values might be better.

In fact the *whiteness* of the clouds seems to provide a better classification feature. This leads to a color model in which the color white plays a decisive part. An appropriate color model to measure whiteness is the HSV color model [2]. In this model, the RGB color space is transformed to a cylindrical coordinate system in which H is the hue and is measured by the angle around the vertical axis, S is the saturation of the color relative to the color gamut and V specifies the brightness value.

Again we take a look at the histogram plot with the new parameters, saturation and brightness value (figure 4). In this parameter space clear and cloudy pixels spread more widely, showing two maximums, one in the cluster of clouds and one in the cluster of the background.

Another quality control of the classification features is the *covariance matrix* (see [4]):

$$C_{pq} = \langle (m_p - \langle m_p \rangle)\,(m_q - \langle m_q \rangle) \rangle$$

For the RGB color space this results in:

$$\mathbf{C}_{RGB} = \begin{pmatrix} 2.283 & 2.227 & 1.698 \\ 2.227 & 2.229 & 1.707 \\ 1.698 & 1.707 & 1.324 \end{pmatrix} 10^{-2},$$

and for the HSV color space:

$$\mathbf{C}_{HSV} = \begin{pmatrix} 2.999 & 0.125 & -1.504 \\ 0.125 & 0.393 & -0.023 \\ -1.504 & -0.023 & 2.103 \end{pmatrix} 10^{-2}$$

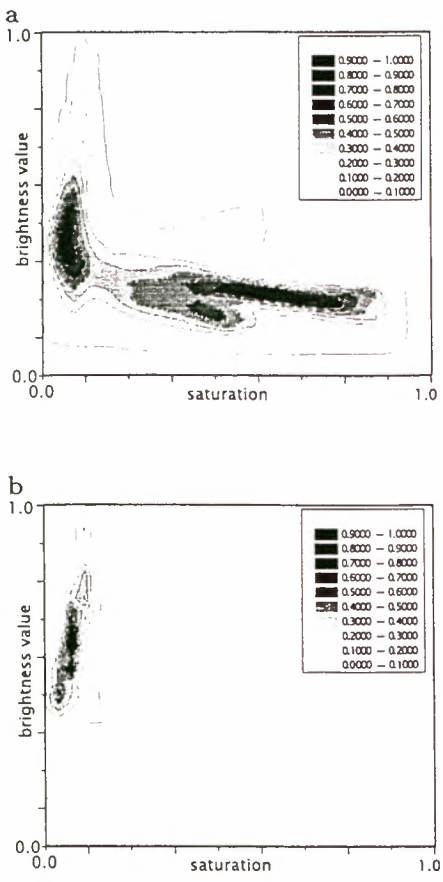

Figure 4: Histogram plot of the distribution of the brightness value and the saturation over the global data from one month. **a** Whole image sequence **b** Manually classified clouds

Although a direct comparison of this two matrices is not possible, the variances of the RGB values are in the same order of magnitude as the cross covariance. In contrast the values differ for the elements saturation and brightness value in the HSV matrix. Therefore these two parameters are taken for further analysis.

We can now define a subset of the HSV space which characterizes the clouds. Since there is only a small overlap between the region classifying the background and the region of clouds, an efficient separation can be achieved by applying a threshold in the S-V space.

Although the results are very promising, the method only allows us to determine whether or not a cloud is detected but it does not allow us to infer the degree of cloud cover. Moreover, the limiting values for the cloud subspace are to a certain degree arbitrary and disregard local conditions like the ground albedo. Our method can serve as a pre-classification for the second, iterative cloud detection method hereinafter described.

3 Iterative Fix Point Method

The results of the HSV method can be improved by considering that clouds are moving, forming and dissolving. Therefore those SV values nearly constant with time are likely to belong to the background whereas those which change should belong to cloudy pixels. That approach is successful, if the majority of days are cloud-free. Apparently, that condition is fulfilled through the HSV-pre-classification. The implementation of this idea is realized in the employed iterative algorithm.

- First we use the HSV-pre-classification to generate a PMD image sequence with less cloud cover.
- Then we calculate the mean RGB values over this series of pictures. This average picture serves as a first estimate for the background picture $\mathbf{B}^0$.
- In the third step the background image $\mathbf{B}^n$ allows us to measure the deviation of each pixel from the PMD images $\mathbf{A}_k$. For this purpose a weighting function $W(||\mathbf{A}_k(\mathbf{x}) - \mathbf{B}^n(\mathbf{x})||) \in [0,1]$ is required, which is set to 0 if the actual pixel $\mathbf{A}(\mathbf{x})$ has nearly the same SV values as the one from the background image $\mathbf{B}(\mathbf{x})$, and is set to 1 otherwise.
- The calculated weighted mean over the picture series (using the weighting function W) allows us to reiterate $\mathbf{B}^n$. By yielding a better estimate for the background picture, we go back to the third step.
- The algorithm terminates when the background image converges.

If $\mathbf{B}^n(\mathbf{x})$ is the background picture of the n^{th} iteration and $\mathbf{A}_k$ the k^{th} picture of the time series, the cloud free background image is given by the fix-point of the following function:

$$\begin{aligned} f(\mathbf{B}^n(\mathbf{x})) &= \mathbf{B}^{n+1}(\mathbf{x}) \\ &= \frac{\sum_k^K \mathbf{A}_k(\mathbf{x}) W(||\mathbf{A}_k(\mathbf{x}) - \mathbf{B}^n(\mathbf{x})||)}{\sum_k^K W(||\mathbf{A}_k(\mathbf{x}) - \mathbf{B}^n(\mathbf{x})||)} \end{aligned}$$

Finally the background image $\mathbf{B}^\infty(\mathbf{x})$ can be used to calculate a degree of cloud cover.
In sensitivity tests using different weighting functions W the fastest convergence is found for the step function Θ of the Euclidean distance in the S-V color space, where the threshold is set to the average distance between clouds and background seen in figure 4 (≈ 0.3). Actually, that function requires the least iterations and the results of cloud detection are acceptable. A flow chart of the described algorithm is shown in figure 5.

The described method allows us to get full information about the ground albedo and the local measuring conditions (e.g. solar zenith angles etc.). It is not necessary

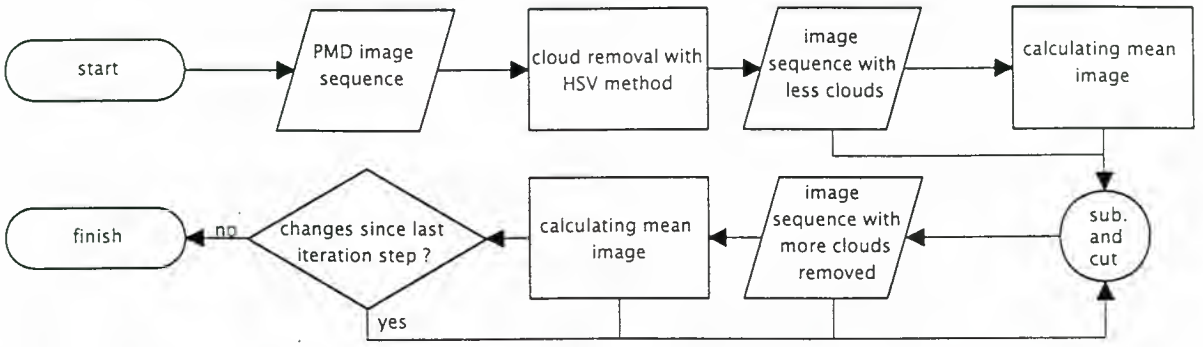

Figure 5: A flow chart of the described method to determin a PMD background image.

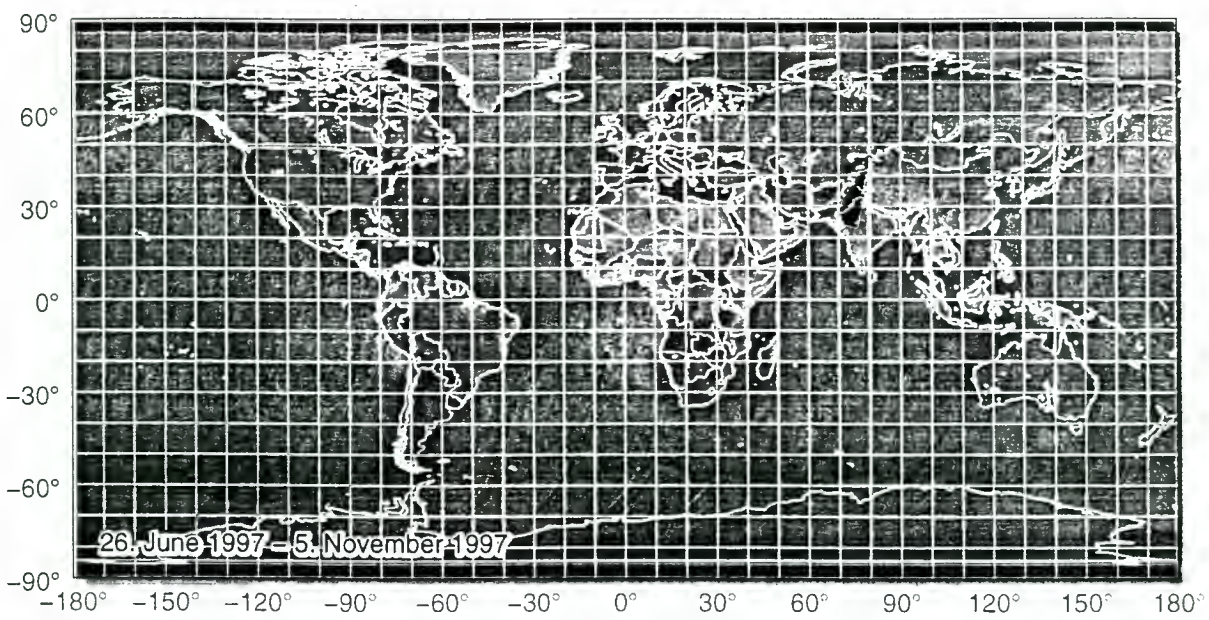

Figure 6: The result of the iterative background image processing.

to correct the PMD values with AMFs because the algorithm corrects for it automatically. With a similar algorithm, it is possible to determine a reference image of overcast cloud cover. The pre-classification has to be reversed and after applying the iterative algorithm, a maximum filter with respect to whiteness is applied to the image.

However, some parameters which are included in the background image can vary on a long time scale, e.g. the vegetation cycle. To consider these effects, it is possible to generate several images for different seasons.

4 Calculation of the HSV-Cloud Cover

After the data is processed according to the technique described above, a tool is built to calculate the cloud cover. Since that parameter not only includes the fraction of cloud covered space of one GOME-pixel but also regards the transparence of a cloud, we call this parameter *HSV-Cloud Cover* (HSV-CC).

The PMD values of the actual pixel are likely to be linear combinations of the values from the two reference images. As far as the two parameters, saturation and brightness value, are concerned the parameters of the actual pixel are not constrained to the connecting line of the reference values. Therefore the least square solution is taken for further processing. The notations for the different images are as follows:

$\mathbf{a}(\mathbf{x})$: current image
$\mathbf{b}(\mathbf{x})$: background image
$\mathbf{c}(\mathbf{x})$: maximum cloud image

Thus the definition of the HSV-CC is:

$$f = \frac{(\mathbf{a}-\mathbf{b})(\mathbf{c}-\mathbf{b})^{\mathrm{T}}}{||\mathbf{c}-\mathbf{b}||}$$

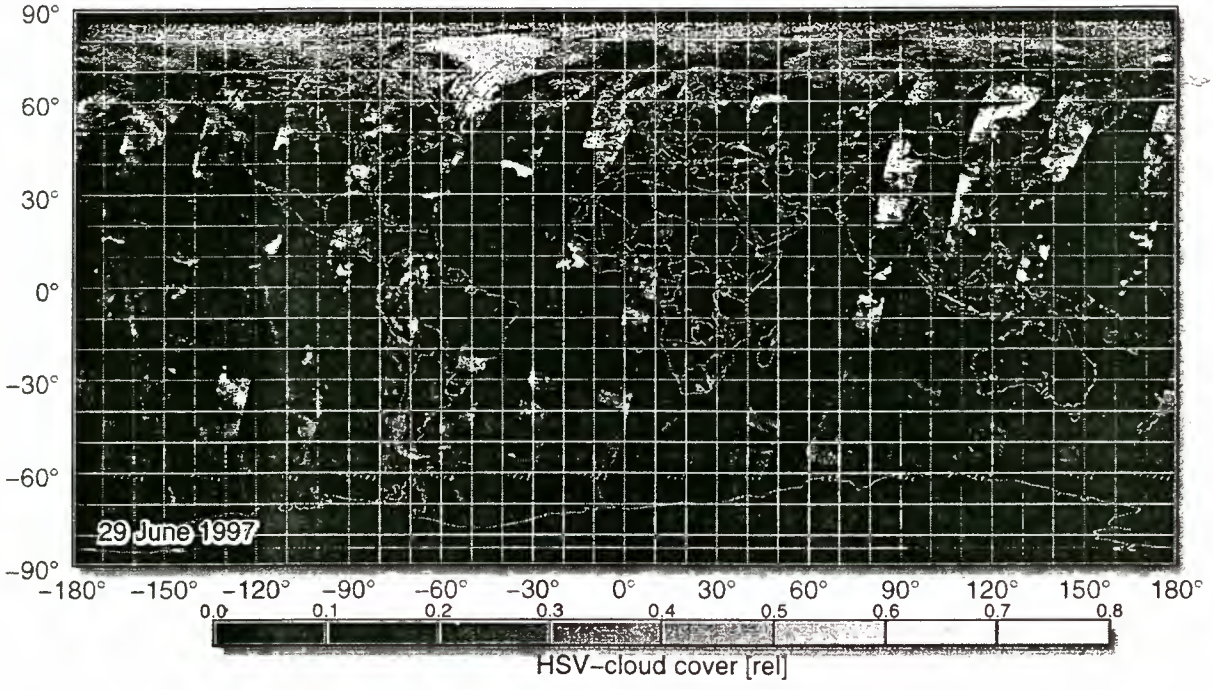

Figure 7: A visualization of global HSV-Cloud Cover. These parameters are calculated on the PMD values shown in figure 2.

5 Results

The results of our algorithm are global images of the HSV-CC (figure 7). With figure 2 in mind, the results are promising. The results were compared to another cloud detecting algorithm, the *Initial Cloud Fitting Algorithm* (ICFA V2.0, see [3]). This comparison is visualized in figure 8, where the relative frequency of corresponding cloud parameters, the ICFA fractional cloud cover and the HSV-CC, is shown. It is striking that on the right side of the diagonal there are few data. Therefore the HSV-CC is generally smaller than ICFA. This effect can be explained by the fact that ICFA regards the changing ground albedo differently. The ground albedo in ICFA is a fitting parameter whereas the HSV-CC algorithm uses pre-calculated ground albedos. These differences are predominantly over bright areas, e.g. North Africa. An other explanation is the different dependence of this two parameters on the cloud optical thickness. The HSV-CC is measured relative to maximum clouds, concerning cloud cover and cloud optical thickness whereas in ICFA a priori-chosen cloud optical thicknesses are used. Therefore the HSV algorithm yields smaller cloud covers than ICFA, in particular for optically thin clouds.

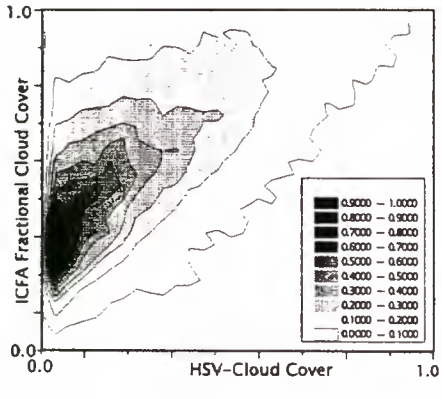

Figure 8: Histogram plot of the ICFA fractional cloud cover in dependence on the HSV-Cloud Cover.

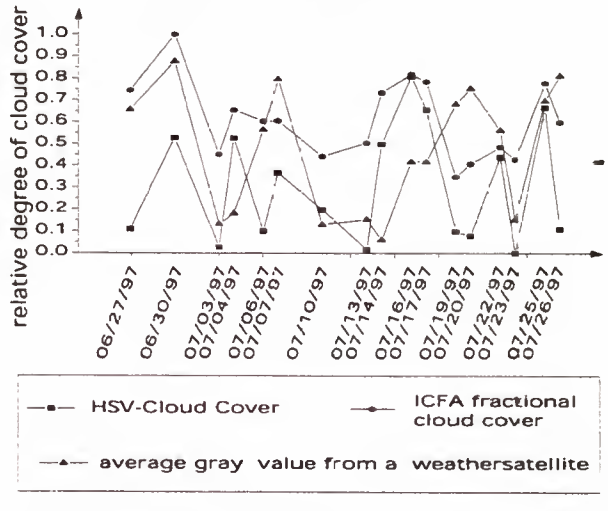

Figure 9: Comparison of the HSV-Cloud Cover with ICFA and a mean gray value from a weather satellite [5].

This effect is displayed in figure 9, where time series of several cloud parameters are compared, i.e. the HSV-CC with ICFA cloud cover and a mean gray value inferred from an image which is operated by the AVHRR (Advanced Very High Resolution Radiometer) aboard the weather satellite NOAA 14 (National Oceanic and Atmospheric Administration) [5]. Although the three values differ they correlate somehow. Again the discrepancy can be explained by the different adaptation of the ground albedo and the different influence of the clouds' optical thickness.

6 Influence of Clouds on the Trace Gas Retrieval

In order to analyze the influence of clouds on the trace gas retrieval we generate statistical values of vertical column densities of several trace gases as a function of the HSV-CC. We use the data integrated globally over a long observation period in order not to be sensitive to short time variations and local events. As an example, the average global relative vertical column density of the trace gases O_2, O_4 and NO_2 as a function of the HSV-CC is calculated. That comparison is performed for the whole earth's surface and for an area over the Pacific intended to discard influences like NO_x emitted from biomass burning or industrial areas. For all these values the same AMFs assuming a typical NO_2 distribution were used (fig.figure 10).

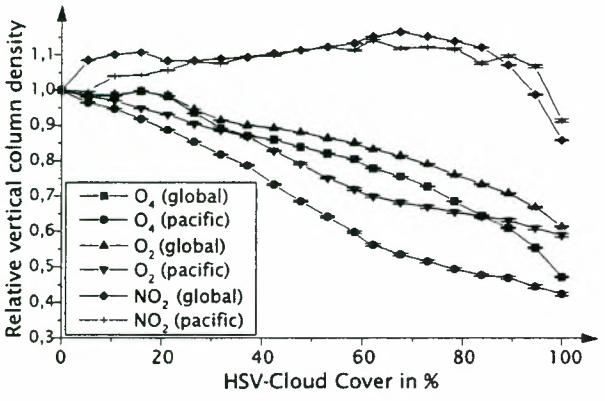

Figure 10: Average global relative vertical column density as a function of the HSV-CC.

There is a noticeable reduction of the vertical column densities for O_2 and O_4 due to clouds with a stronger effect for O_4 than for O_2. This is due to the quadratic dependence of O_4 with pressure leading to a corresponding more rapid decrease of O_4 than O_2 with atmospheric height. For NO_2 the effects of clouds are different, mainly because the bulk of atmospheric NO_2 resides in general above the cloud, i.e. in the stratosphere. These statistical curves can be used for doing a simple cloud correction.

7 Conclusion and Outlook

The algorithm makes use of two characteristics of clouds, the color and the temporal variation. The algorithm is based on image sequences so it primarily enables us to calculate the global cloud cover for longer periods. Once the reference images (cloud-free background and maximum cloud) are generated, the cloud cover calculation is very fast (approx. 5 sec./800x400 pixel image on Pentium 166 MHz). The algorithm is very robust because invalid values are easily removed without affecting the reference images and it can simply be extended. Once reference images for different seasons are generated, annual changes, such as variations due to vegetation cycles, are also considered. Finally the results of this algorithm, the HSV-Cloud Cover can serve as an input for other algorithms to calculate other cloud parameters. For a more detailed description see [7].

Acknowledgements

This work is supported by the DFG research unit "Image Sequence Analysis to Investigate Dynamic Processes" (Ja395/6).

References

[1] F. Bednarz. Global ozone monitoring experiment, gome, users manual. Technical report, ESA Publications Division, 1995.

[2] J.D. Foley, A. van Dam, S.K. Feiner, and J.F Hughes. *Computer Graphics: Principles and Practice, Second Edition.* Addison-Wesley Systems Programming Series. Addison-Wesley, 1990.

[3] R. Guzzi, E. Cattani, M. Cervino, C. Leconi, F. Torricella, and T. Kurosu. Gome cloud and aerosol data products algorithms development. *Final Report Draft ESA Constract 11572/95/NL/CN*, 1998.

[4] B Jähne. *Digital Image Processing: Concepts, Algorithms and Scientific Applications.* Springer Verlag, 1991.

[5] (Natural Environment Research Council) NERC. Www-page of the dundee satellite receiving station, dundee university, uk, 1998. http://www.sat.dundee.ac.uk.

[6] U. Platt. Differential optical absorption spectroscopy (doas). In M.W. Sigrist, editor, *Air Monitoring by Spectrometric TechniquesSigrist, M.W.*, volume 127. John Wiley & Sons, Inc., 1994.

[7] M. Wenig. Wolkenklassifizierung mittels bildsequenzanalyse auf gome-satellitendaten. Master's thesis, University of Heidelberg, 1998.

GOME NO2 and ATSR temperature data analysis: a hint to the role of biomass burning in trace gasses concentration variations

S. Casadio[1], C. Zehner[2], P. Colagrande[3] and A. Buongiorno[2]

1) SERCo s.r.l. under contract to ESA/ESRIN, Frascati, Italy
e-mail: scasadio@esrin.esa.it
2) ESA/ESRIN, Directorate of Applications, Remote Sensing Exploitation Dep., Frascati, Italy
e-mail: Claus.Zehner@esrin.esa.it; Alessandra.Buongiorno@esrin.esa.it
3) VITROCISET s.p.a. under contract to ESA/ESRIN, Frascati, Italy
e-mail: paola.colagrande@esrin.esa.it

ABSTRACT

An experimental version of a diagnostic tool for the detection and monitoring of NO_2 sources in the atmosphere has been developed at ESA/ESRIN. Input data are the GOME level 2 vertical columnar concentrations of NO_2 and the ATSR temperature images. A preliminary step consists of the creation of NO_2 "mean" or "climatic" fields using the level 2 products. Statistical analyses of these fields lead to the selection of areas characterized by high variability (both in time and space) of NO_2 concentration; single orbit analyses are then carried out over the area of interest. The ATSR temperature data are used for validation (fires) and detection of smoke plumes eventually present in the scene. A case study is here described in detail.

1.INTRODUCTION

A new and attractive possibility of monitoring the atmosphere is represented by GOME (Global Ozone Monitoring Experiment) launched on ERS-2 in April 95 and functioning continuously since then. The main scientific objective of the GOME mission is to measure the global distribution of ozone and of several trace gasses, namely NO_2, BrO, OClO and SO_2 (Ref. 1). Evidence of NO_2 production due to biomass fires and antropogenic pollution has been reported in the last years; in recent publications (Refs. 2,3) an attempt to evaluate the excess of NO_2 produced by the Borneo fires of 1997 using the GOME data has been described. In our case GOME and Along Track Scanning Radiometer (ATSR) products have been used to investigate the role of biomass burning in the variations of the NO_2 columnar concentration. GOME level 2 products, generated operationally at D-PAF, consist of slant and vertical amount of atmospheric constituents (O_2 and NO_2), and related uncertainties, retrieved from calibrated geolocated radiances; they also include essential information on cloud parameters (Ref. 4). Here we use NO_2 vertical column data; the cloud information is also used to select cloud free scenes imposing a threshold for the cloud fraction of 0.3. ATSR-2 products used for our analyses are the GBT, geolocated gridded calibrated brightness temperature/reflectance products generated with RAL's SADIST-2 ATSR data processing software (Ref. 5). Although the NO_2 GOME product has not been thoroughly validated as the corresponding O_3 measurements and has to be carefully interpreted (Ref. 6), the attempt to retrieve useful information on the processes involved in trace gasses concentration variations appear to be quite successful.

2.METHOD DESCRIPTION

Biomass fires are usually sporadic and highly localized events. This sources of trace gases are therefore short lasting and the resulting excess of tracers can be detected if considered as a deviation from a mean undisturbed field. The most challenging task is the construction of a suitable "mean field". The proposed solution is the creation of an ensemble of gridded mean fields, using the GOME level 2 products: orbits relative to periods of two-three days are selected and grouped; then a regular gridded fields from the instantaneous GOME data is constructed by geometric interpolation; these fields are smoothed to reduce noise and point sources contribution. Each of these gridded fields is assumed to represent the "instantaneous global distribution" of NO_2 for the selected period. Finally, gridded fields are averaged over periods of ten days; the variances are also computed at each grid point. Ten days is here assumed to be the maximum time scale over which seasonal variation of NO_2 concentration can be neglected. This procedure has been applied to the GOME products dated on February-August 1998 producing more than twenty mean and standard deviation fields, which are assumed to represent the "global undisturbed distribution" for the ten day period. The mean fields cannot be considered as NO_2 climatologies since climatic means, by definition, a mean taken over a period of at least 10 years. Moreover, the assumption of mean fields as "undisturbed fields" is incorrect due to the correlation between instantaneous and mean field; this limitation will be taken into account in discussing the results. High values in the standard deviation fields correspond to highly localized sources of NO_2; in most cases these sources are due to antropogenic pollution and can be seen in the same places all the year long. Since the object of this

study are only sporadic events, the antropogenic sources will not be discussed in this paper.

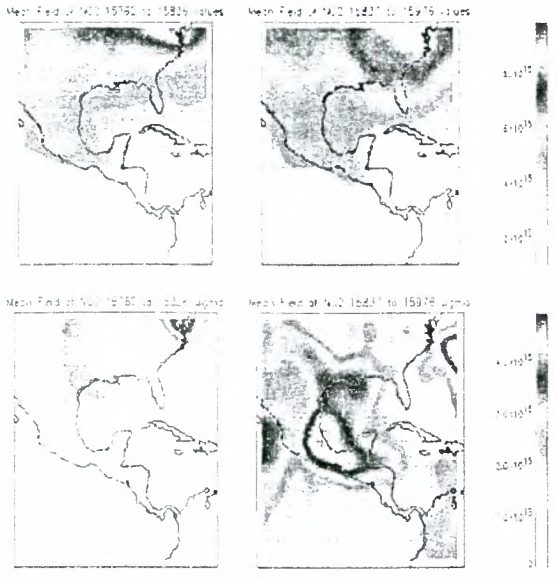

Fig. 1 Mean and standard deviation fields in the Mexico Gulf for two different periods. The upper plots refer to mean field, the lower plots to standard deviation. Large differences in standard deviation reveal the occurrence of a sporadic event over Mexico in the second period.

FIG(1) shows two examples of mean field and standard deviation field over the Mexico Gulf during April and May 1998: the upper plots show mean field values, the lower plots refer to standard deviation fields. The first case (left plots) refers to the period from the 20th to the 30th of April, the second to the period from the 1st to the 10th of May. In the second case, highest values in the SF are present over the Mexico State and the western part of the Mexico Gulf, suggesting the occurrence of events such as long lasting and wide spread biomass fires, which can produce non stationary instantaneous field of NO_2. This type of information can be used to select period and areas of probable interest. The data for those periods are processed by subtracting, for each center pixel location, a single mean field value, computed using bilinear interpolation, to the original NO2 datum. The resulting "deviation from the mean" is plotted vs. latitude together with its uncertainty (UD) estimated from the instantaneous field's uncertainty (UI), and the mean field's standard deviations (SF) as:

$$UD = \sqrt{UI^2 + SF^2}$$

Actually, the UD's definition is valid for uncorrelated variables, which is not the case here; moreover, the standard deviation field values contain the contribution of both instrumental noise and atmospheric phenomena, which result in an overestimate of the "true" deviation's uncertainty. In addition, since the single mean field is computed from the instantaneous fields, which are constructed using the instantaneous data ensemble, the deviation values are an underestimate of the "true" disturbance. An important assumption, to be validated using the ATSR products, is that the deviation values are produced by phenomena taking place in the lower troposphere (fires and industrial pollution).

3.CASE STUDY

During the first half of May 1998 vast forest fires continued to burn in five Mexican states (Oaxaca, Chiapas, Veracruz, Coahuila and Durango) and in the Yucatan peninsula. Smoke from this fires reached the Southwestern United States polluting the air from Florida to California. As shown in FIG(1) high values of standard deviation are reported for the period 1st to 10th of May indicating that GOME has been able to detect the occurrence of a sporadic NO_2 production event. The above described method has been carried out and the results are reported in the following. FIG(2) and FIG(3) show the time evolution of the deviation values for the Mexico Gulf area in the period ranging from May 7 to May 10 for FIG(2) and May 13 to May 19 for FIG(3), and 10m wind field analysis (ECMWF) relative to the closest in time available. For each day three graph are presented reproducing the deviation values at their geographical location (left plot), deviation vs. latitude along with the related uncertainty (center plot) for the left (upper), central (center) and right (lower) GOME pixel, and wind field in which the arrow length is proportional to the wind intensity.

On May 7th small NO_2 plume are detected over the states of Chiapas and of Honduras while the ECMWF wind analysis reveals strong winds blowing in the NW direction over the two states (see FIG(2a)). The situation has developed at the next passage of ERS-2 over the Mexico state during May 9th as shown in FIG(2b). Extremely high values of deviation are found over the states of Oaxaca and Guerrero. The NO_2 plume is generated in the Eastern part of the Sierra Madre del Sur and advected over the Gulf of Mexico, up to the Southern United States, by the strong winds still blowing from the South in that area. The two spikes in the central pixel plot located at 20 and 30 [deg] are due to the contribution from Mexico City and Houston, due to their highly polluted atmosphere; the antropogenic contribution is superimposed to the NO_2 plume generated by the fire. Deviation values are, in this case, as high as 3.5 10^{15} mol/cm^2, with the mean field value of 2.5 10^{15} mol/cm^2. The NO_2 concentrations are more than doubled in that area. FIG(2c) shows the plume still spreading over the Yucatan peninsula, the Oaxaca state and the Gulf of Mexico during May 10th. The fires are still active during the May 13th ERS-2 passage (see FIG(3a)). It can be noted that the high deviation values in the Gulf of Mexico are found in the area of low wind intensity, while in the region interested by the wind jet blowing from the Yucatan Channel to Texas the instantaneous data are close to the mean values. In FIG(3b), relative to the 15th of May, the plume intensity is

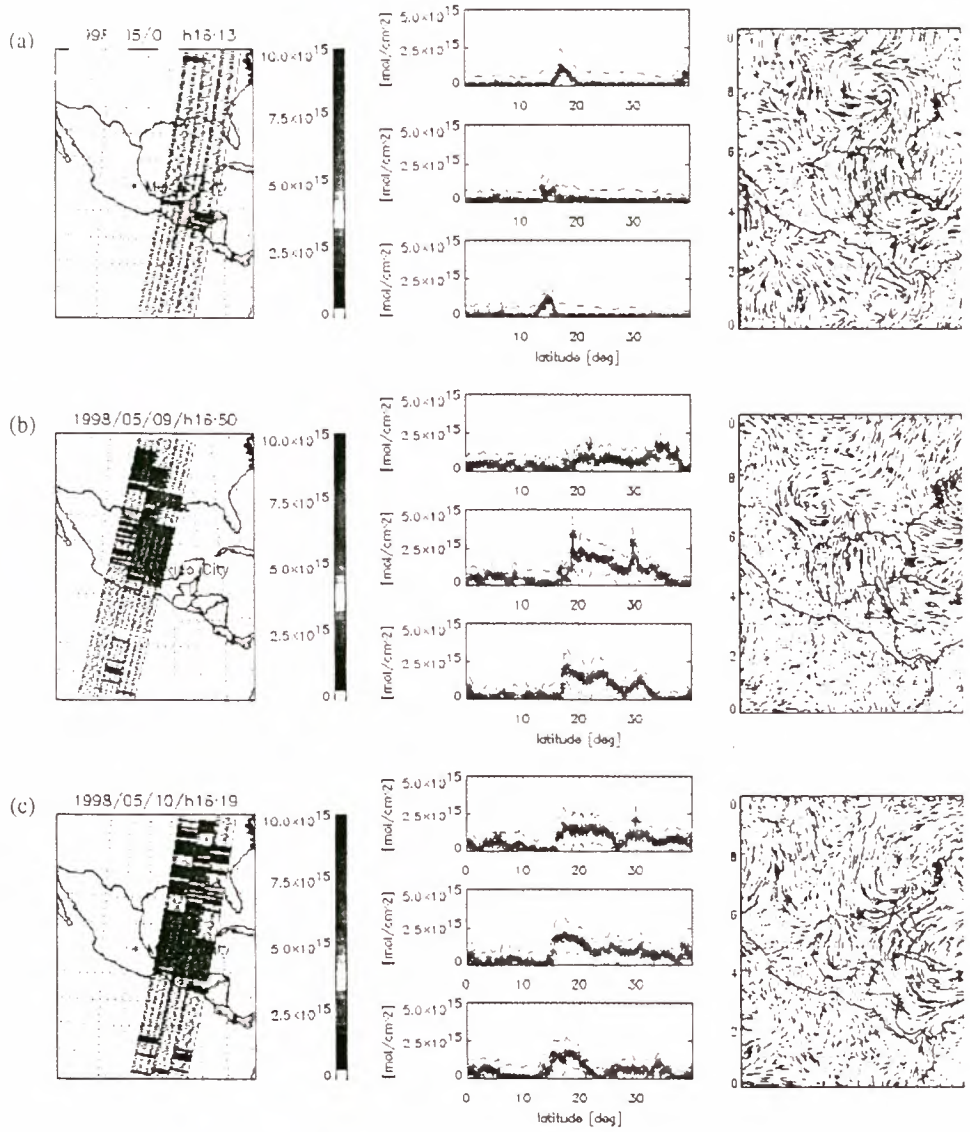

Fig. 2 Time evolution of the deviation from the mean for the period 7-10 of May. Plot (a) refers to May 7th, plot (b) to May 9th, plot (c) to May 10th. The arrow plots show the closest in time wind intensity and direction (ECMWF analysis)

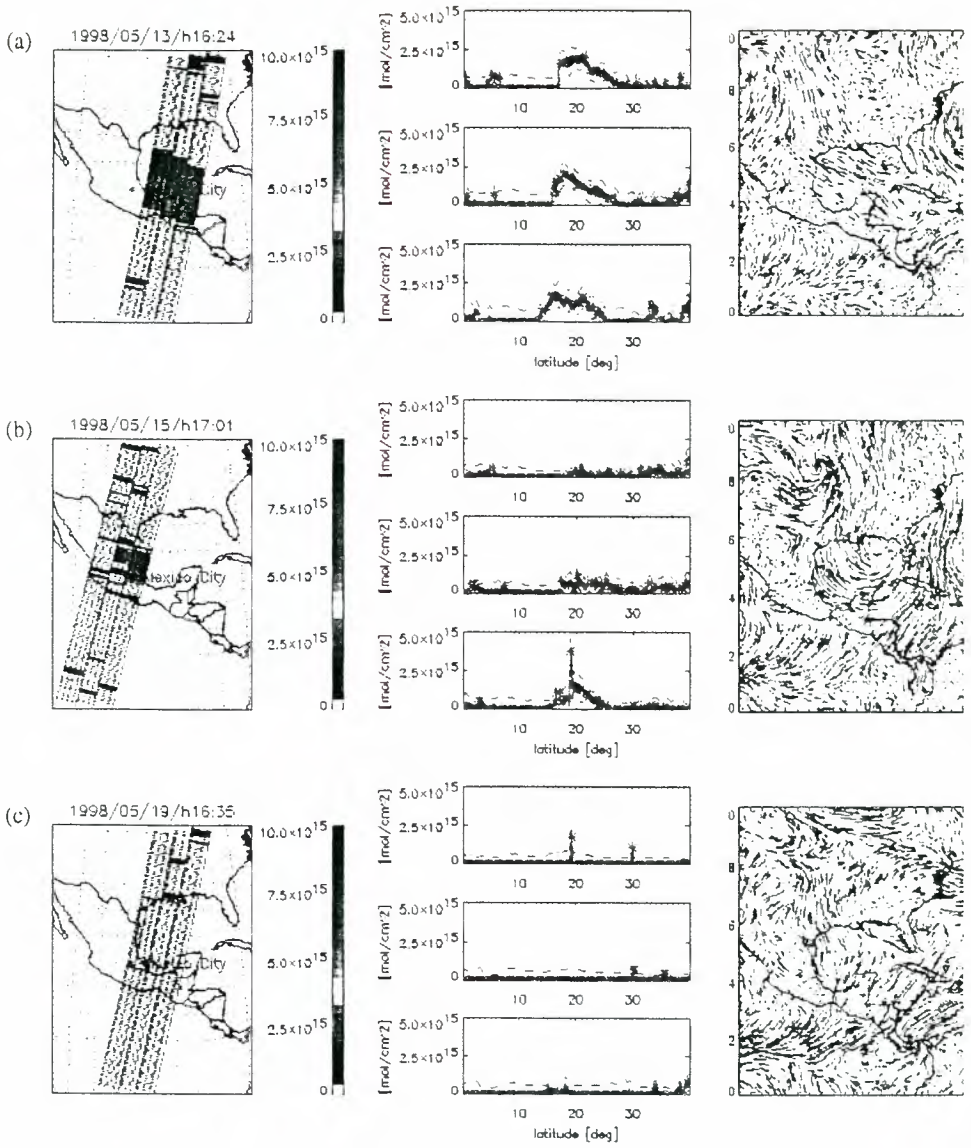

Fig. 3 Time evolution of the deviation from the mean for the period 13-19 of May. Plot (a) refers to May 13th, plot (b) to May 15th, plot (c) to May 19th.The arrow plots show the closest in time wind intensity and direction (ECMWF analysis)

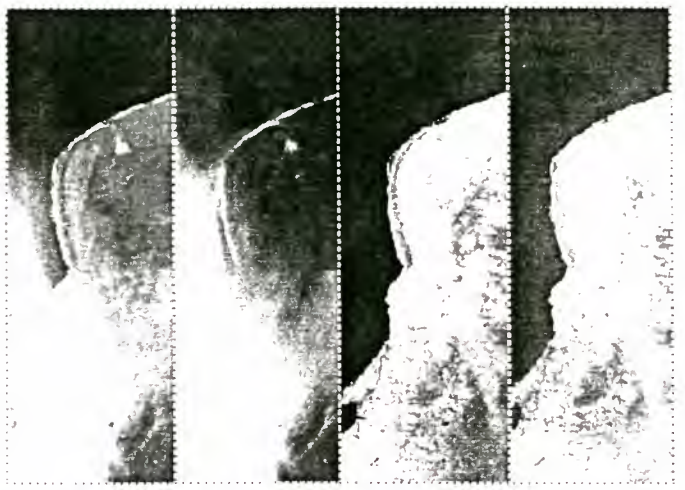

Fig.4 Set of visible, near and thermal infrared channels of ATSR-2 image over Yucatan Peninsula on 10th May 1998. a) False colour combination of VIS and NIR channels (Red: average of 0.87 and 1.6 μm; Green: 0.67 μm; Blue: 0.55 μm; b) 0.55μm channel; c) 1.6 μm channel; d) 11 μm channel.

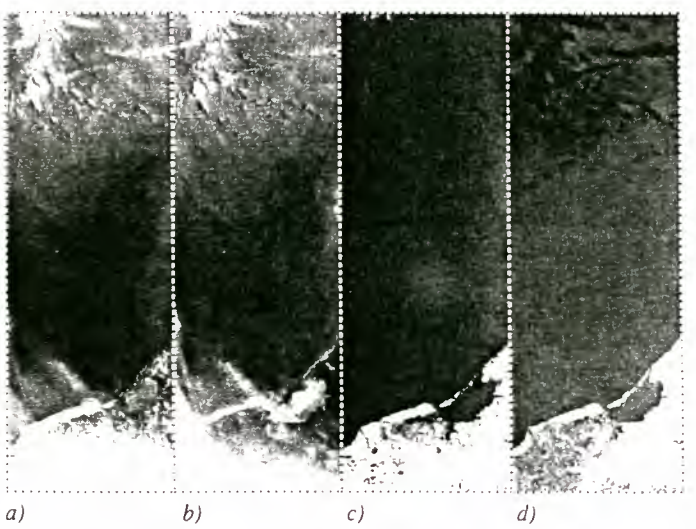

Fig.5 Set of visible, near and thermal infrared channels of ATSR-2 image over Yucatan Peninsula on 13th May 1998. a) False colour combination of VIS and NIR channels (Red: average of 0.87 and 1.6 μm; Green: 0.67 μm; Blue: 0.55 μm; b) 0.55μm channel; c) 1.6 μm channel; d) 11 μm channel.

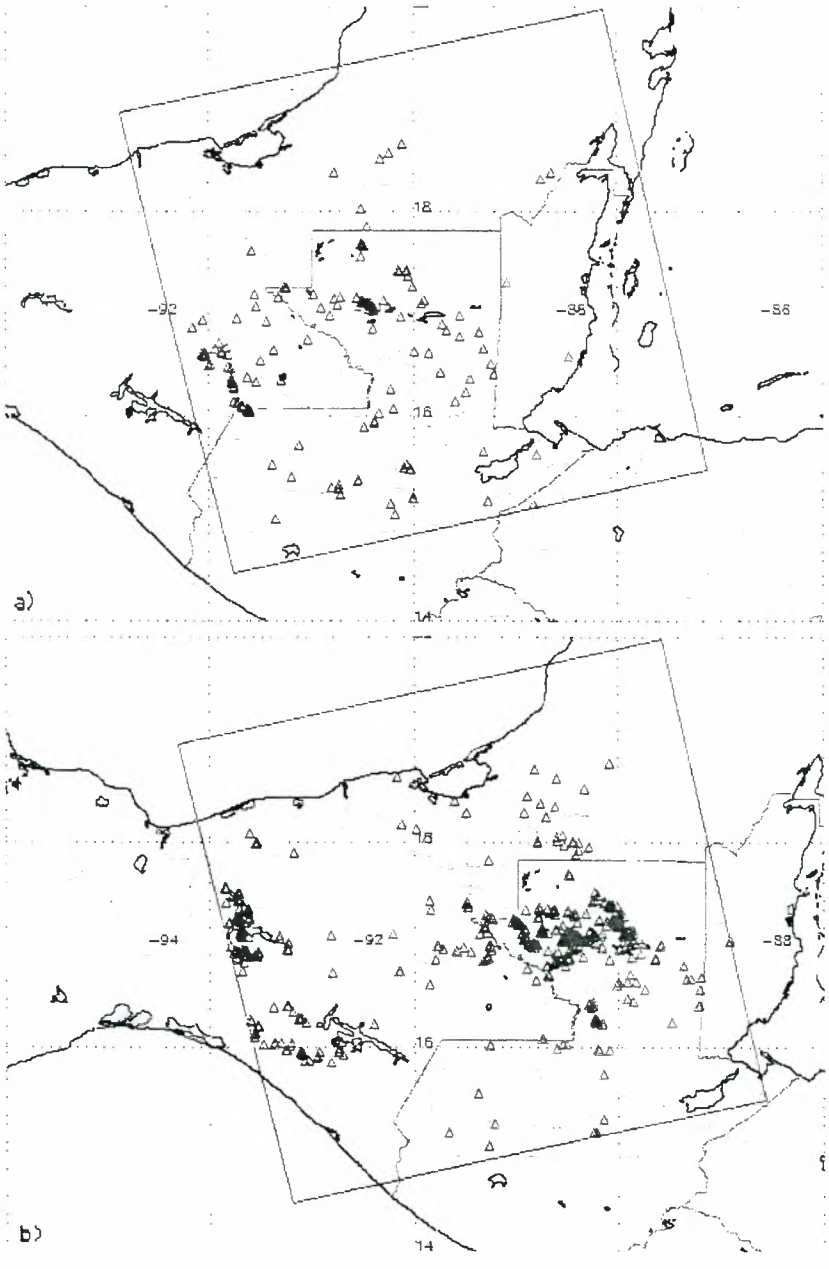

Fig.6 ATSR-2 fire maps in Central America. a) 10th May 1998 and b) 13th May 1998. The first image shows the strong presence of fires on 10th May and the second their dramatic increasing three days later in the same region.

reduced; high deviation values can still be found in correspondence of Mexico City and its surroundings. Over this area the wind is almost absent, while strong wind is blowing in the NW direction over the Gulf of Mexico. FIG(3c), relative to the 19th of May, shows a typical "undisturbed" NO_2 field where the DD values are close to zero, except in the Mexico City, Houston and New Orleans locations, where the deviation is 2 10^{15} mol/cm^2. The adopted method seems to allow the monitoring of point sources of pollution such as urban and industrial sites.

The 1 km resolution ATSR-2 IRR Gridded Brightness Temperature/Reflectance products were used to point out the huge amount of smoke produced by fires occurred during the period of interest in Central America. From the spectral analysis of visible, near-infrared and thermal-infrared channels of ATSR-2, it is possible to see the smoke cover on the Yucatan Peninsula. While the near infrared 1.6 μm channel seems to be poorly sensitive to attenuation by smoke (Ref, 7) (see images in FIGG 4c and 5c, where the reflectance of smoke particles appear very low), the presence of smoke is well detected in visible channel 0.55 μm (see images (b) in FIGG 4 -5, where in the bottom half of images the reflectance is very high). What leeds to exclude the presence of clouds in the region is the high temperature resulting form the analysis of 11 μm thermal channel data. In fact, whilst usually clouds are highly reflecting and have low temperature, as can be seen in the top half of FIGG 5b and 5d, the image sequence shows high temperature and low reflectance in the region covered by the smoke. It is interesting to remark that in parallel, the GOME instrumentation has recorded a massive presence of NO_2 over the same region and in the reference time period. High concentration of fires at the too different ATSR-2 acquisition dates is well demonstrated in the relevant fire distribution maps shown in FIGG 6a and 6b. FIGG 4.a and 5.a show a false color combination of visible and near-infrared reflectance channels, where the presence of smoke particles is well detected over land and sea near the coast.

The above described synergy of GOME and ATSR-2 promises new results on the monitoring of the atmosphere: the optical features of clouds and aerosols are well described by ATSR-2, the chemical components of the atmosphere can be analyzed using information from the GOME spectra. Moreover, the ATSR-2 capability to detect fires can be used to validate the GOME NO_2 products.

Some limitations to the proposed analysis need to be pointed out:

a) due to the low time resolution of the ERS-2 orbit and GOME field-of-view geometry only long lasting fires can be monitored;

b) analysis is performed for cloud free scenes (cloud fraction < 0.3);

c) NO_2 variations are assumed to occur in the troposphere;

d) low signal-to-noise ratios may affect the results in regions between the tropics (30 S to 30 N);

e) the NO_2 mean field is correlated to the instantaneous values and is not representing a climatic field.

From the above listed points it is evident that the results from the proposed analysis need to be carefully interpreted and further investigation will be necessary to define, and eventually remove, the possible sources of error.

4.CONCLUSIONS

In this paper a simple diagnostic tool is presented to monitor biomass burning by using GOME level 2 and ATSR products. The main objectives are the detection of fire location and the tracking of NO_2 plumes produced by wide spread and long lasting fires. GOME gives the possibility to study and prepare applications (e.g. air pollution monitoring) for the atmospheric payload to be flown on the satellite ENVISAT including the instruments GOMOS, MIPAS and SCIAMACHY. Information content of Earth Observation measurements can be enhanced by the synergy of atmospheric and optical measurements as presented here by the instrument GOME and ATSR for air pollution monitoring.

5.REFERENCES

1. Burrows, J.P. et al. 1997, The Global Ozone Monitoring Experiment (GOME): mission, instrument concept, and first scientific results, ESA SP-414, volume II, 585-590

2. Buongiorno, A. et al. 1997, ERS-2 monitors exceptional fire event in South-East Asia, Earth Observation Quarterly, 56-57, 1-5

3. Thomas, W. et al 1998, Detection of biomass burning combustion products in Southeast Asia from backscatter data taken by the GOME spectrometer, Geophys. Res. Letters, 25, 1317-1320

4. Product Specification Document of the GOME Data Processor 1996, ER-PS-DLR-GO-0016. Iss./Rev. 3/A

5. Bailey, P. 1995, SADIST-2 v100 Products, ER-TN-RAL-AT-2164

6. Attema, E. et al. 1996, GOME Geophysical Validation Campaign - Final Results Workshop Proceedings, ESA-WPP-108

7. Eva, H.D. et al. 1998, The advance of burnt areas in Central Africa as detected by ERS-1 ATSR-1, Int. J. Remote Sensing, 19, no. 9, 1635-1637

GOME: BIOMASS BURNING AND ITS INFLUENCE ON THE TROPOSPHERE

A. Ladstätter-Weißenmayer, John P. Burrows, P. Crutzen and A. Richter

Institute of Environmental Physics, University of Bremen, Germany
Max Planck-Institut for Chemistry, Mainz, Germany
e-mail:lad@gome5.physik.uni-bremen.de

ABSTRACT

The Global Ozone Monitoring Experiment (GOME) onboard ESA's 2nd European Remote Sensing Satellite (ERS-2) has been measuring backscattered earth radiances and solar irradiances in the UV/visible wavelength range between 240 and 790 nm since its launch in April 1995. In this study GOME measurements have been inverted to yield column amounts of formaldehyde (HCHO), ozone (O_3), and nitrogen dioxide (NO_2).These trace gases have been derived by applying the method of differential absorption spectroscopy (DOAS). Both total column amounts and the tropospheric excess columns have been derived. The tropical region from 20°N to 20°S between 90°E and 120° E covering Indonesia has been investigated. During the period from summer 1997 to spring 1998 forest fires burned extensively in Indonesia. Analyses have been made for summer and autumn 1995, where no burning occurred and for the period from July 1997 to March 1998. The observation of excess tropospheric HCHO, NO_2 and O_3 show the influence of the biomass burning and air pollution from the cities in this region. The largest HCHO tropospheric excess column densities observed for the GOME pixel (40x320 km^2) were around 2x10^{16} molec/cm^2 above the burning forest. Significant NO_2 was observed above urban areas and biomass burning regions. O_3 plumes were produced downwind from the biomass and urban areas. The results demonstrate that the measurements of GOME are useful for investigation of the impact of biomass burning and urban pollution.

1. INTRODUCTION

Biomass burning comprises both moderately high and low temperature combustion processes. Hydrocarbons, aldehydes, ketones, organic acids, and other oxygenated hydrocarbons are emitted. As is well known tropospheric HCHO is formed during the oxidation of methane (CH_4) and non methane hydrocarbons (NMHC). In unpolluted regions of the tropical troposphere, the dominant source of HCHO is the oxidation of CH_4 and mixing ratios in the boundary layer are typically around 400 pptv. In polluted regions HCHO is produced additionally in significant amounts during the oxidation of hydrocarbons emitted from both anthropogenic and biogenic sources. The HCHO photolysis and its reaction with OH result in the formation of HO_2 radicals.

NO_2 is produced by industrial combustion processes, biomass burning and lightning in the troposphere. Tropospheric O_3 is considered to have two sources: Transport from the stratosphere and chemical production. The latter comprises a catalytic photochemical chain reaction in air masses that have sufficient NO_x ($NO + NO_2$) and volatile organic compounds (VOC) [1],[2].

In the troposphere, the background level of O_3 is considered to be determined by transport from the stratosphere and methane and carbon monoxide (CO) oxidation chemistry. However in the planetary boundary layer the oxidation of NMHC and NO results in effective chain reactions producing copious amounts of O_3 [3]. Such conditions are associated with summer smog episodes [4].

In this study the region around Indonesia has been analysed using GOME measurements. The objective of the study has been to investigate the production of ozone from biomass mass burning and pollution. To achieve this goal, two cases have been studied: a period without biomass burning in 1995 and two periods including biomass burning in 1997/1998. The observations from September 1995 are those from a typical year for the region around Indonesia. No significant El Niño occurred and the monsoon behaved normally. In contrast, the monsoon was significantly disturbed by the large El Niño event 1997/98. This resulted in a long dry period. Unfortunately this appears to have been exploited by locals in their need for arable land. Fires raged in Kalimantan from July to September 1997 with significant burning occurring up to March 1998.

2. THE GOME INSTRUMENT AND MEASUREMENTS ON ERS-2

GOME is a small scale version of the SCIAMACHY (SCanning Imaging Absorption spectroMeter for Atmospheric ChartographY) [5]. The ERS-2, including GOME, was launched in April 1995 into a near-polar sun-synchronous orbit at an altitude of 780 km. The GOME instrument and some results from inversions of GOME data have been described and reviewed elsewhere [6]. Briefly, GOME is a nadir-scanning double monochromator. The spectrometer comprises four spectral channels in GOME each having a grating, transmissive optics and a 1024 element diode array detector. In this manner the spectral region between 240 to 790 nm at a spectral resolution of between 0.2 and 0.4 nm is observed simultaneously. In addition three broad band polarisation monitoring devices (PMDs) observe the same scene as the array detectors. These are used to measure the polarisation of the up-welling radiance, which is required to perform accurate radiometric calibrations and as cloud cover detectors.

A mirror directs the up-welling radiance from the earth and its atmosphere to the GOME spectrometer. Scanning across track enables full coverage at the equator to be obtained within 3 days. The swath width is then 960 km across-track swath and the ground pixel size is 40 x 320 km^2 for the array detectors. The broad band PMD are read out 16 times faster than the array detectors and have ground scenes of approximately 16x20 km^2.

On three days of the month a smaller swath width of 240 km is used. The solar irradiance is measured daily. GOME measurements are available since July 1995.

3. DATA ANALYSIS

For this study GOME radiance and irradiance (level 1 data) from channels 2 and 3 have been analysed using the DOAS technique. Cloud data have been inferred from the Polarisation Monitoring Devices (PMD) observations. GOME observes the total column of O_3 and NO_2 globally [7], [8], [9], [10]. HCHO column densities are derived from the near UV GOME radiance/irradiance measurements.

For the DOAS derivation of slant columns, the fitting-window 338-357 nm was used for the HCHO analysis,325-335 nm for O_3 and 425-450 nm for NO_2. The DOAS routine used is described elsewhere [11].

GOME data were used to identify periods of high NO_2. O_3 and NO_2 total columns were reprocessed using the IUP/IFE DOAS algorithm to determine the slant columns. The total column amount is then derived by combining the slant column and the appropriate AMF, determined using the forward radiation transfer model GOMETRAN [12], [13].

In the tropics, the stratospheric O_3 and NO_2 can be considered to a first approximation to be longitudinally homogeneous. Subtraction of the total column amount for a longitude, associated with an unpolluted region, from that for the same latitude but at a longitude experiencing pollution in the tropics yields therefore an excess tropospheric column. Care must be taken in generating and interpreting these values as changes in the position of the Inter-Tropical Convergence Zone (ITCZ) or wave activity resulting in loss of homogeneity in the stratosphere, could be falsely interpreted. For this study the region above the Pacific at longitudes around 180° is identified as being unpolluted. Data from the UARS (NASA Upper Atmospheric Research Satellite)-HALOE and SAGE-II indicate that the assumption of stratospheric longitudinal homogeneity is reasonable for columns of O_3 and NO_2. The amount of stratospheric HCHO compared to the tropospheric burden is small. Using the above procedure, the tropospheric excess column amounts of HCHO, NO_2 and O_3 have been calculated for the different periods studied.

During the period analysed the prevailing wind direction in the boundary layer above the region selected for analysis is from the east, being roughly parallel to the equator. For the case studies the wind speeds were relatively low (5-7 m s^{-1}).

For this analysis the presence of clouds has been determined using the PMD retrievals. Smoke can clearly be seen above burning regions. An appearent systematic dependence of PMD true colour image on the scan position is observed. This most likely arises from an error in radiometric calibration of the PMDs. The slant column amount retrieved is that above the ground under cloud free conditions. However it is important to point out that for cloudy skies GOME measurements are made effectively to the top of the cloud. For partially cloudy conditions some uncertainties are introduced to the AMF values. These depend on the penetration of radiation in the cloud or smoke region. For the present this will not be further discussed, as studies are being undertaken to quantify better these issues.

Finally another important limitation of GOME measurements is that they are made at the sites under consideration once every three days and at approximately 10.30 a.m. local time. For short lived species such as tropospheric O_3, and NO_2, which exhibit strong diurnal variations, this implies that atmospheric models need to be coupled with such measurements to generate a more complete understanding of the observations. Nevertheless the combined set of retrievals from an instrument such as GOME provide a unique view of the troposphere.

4. RESULTS

The large fires over Kalimantan (0°, 115°E) lasted from July to September 1997, with some minor burnings continuing into the spring of 1998. The monsoon rains normally expected during these months were absent (related to the El Niño weather phenomena) which caused an unusual dry condition in this region. Smog is usually observed only in the metropolitan areas around the cities of Jakarta, Kuala Lumpur, and Singapur. During this biomass burning period clouds of smog could be regulary observed covering a large area.

Data from a period having no biomass burning in September 1995 and the entire period of large biomass burning event in Indonesia from the beginning of June 1997 to the end of March 1998 have been analysed as part of this study. In order to demonstrate the observed behaviour, selected periods have been chosen to illustrate different types of behaviour.

A series of GOME overpasses for the periods 1-12 September 1995, 1-12 September 1997 and 16-28 March 1998 have been analysed for the trace gases NO_2, HCHO and ozone. These are described and discussed below.

Case 1: Indonesia without Biomass Burning – 1st-12th September 1995.

Figure 1 shows composite pictures of the excess NO_2, HCHO and O_3 tropospheric columns and true colour images for the period 01-12.09.1995.

Some small amounts of excess NO_2 are observed above Kalimantan and Thailand. The Kalimantan plume is above a cloud. The Thailand plume above a partically cloudy scene is downwind of the Kuala Lumpur and Singapur regions. The event above Kalimantan may be related to convective clouds. The evidence for significant tropospheric excess columns of HCHO was observed. Some tropospheric excess O_3 is observed downwind from the Bangkok area.

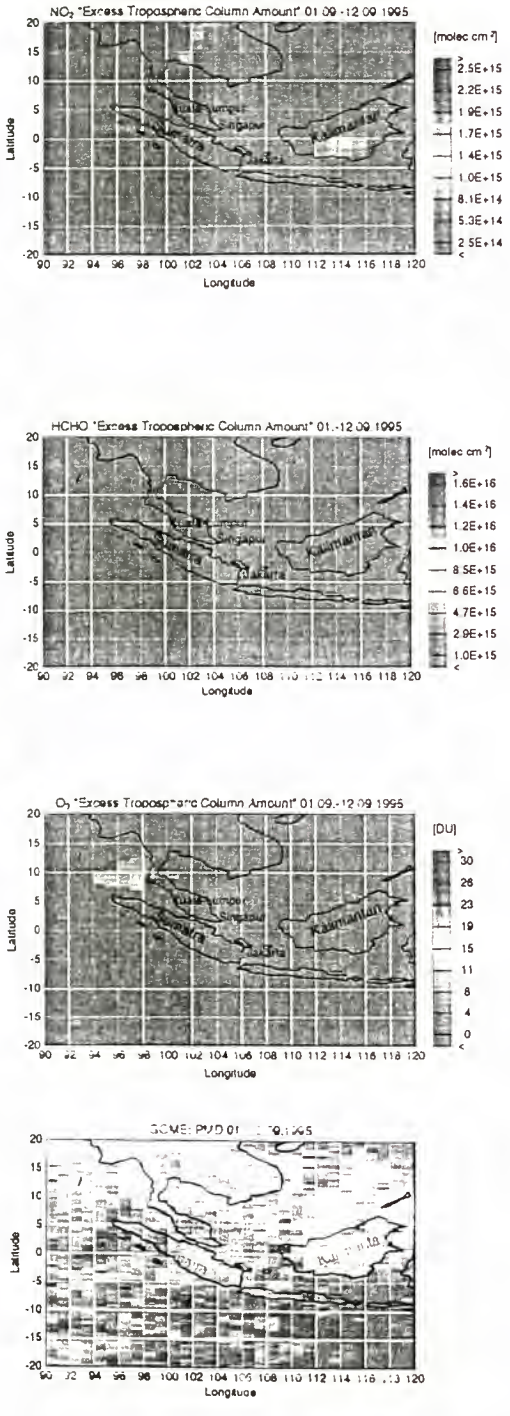

Figure 1. Composite pictures of the excess NO_2, HCHO, O_3 tropospheric columns and true colour image for the period 01-12.09.1995.

Case 2: Biomass Burning – 1st-12th September 1997.

During this period significant biomass burning took place and figure 2 shows a set of composite pictures similar to these of figure 1. Relatively few clouds are present and regions of smoke can be observed over Kalimantan and elsewhere. These are identified by the darker clouds between 5°N 120°E and 3°N 100°E, and above 5°S 120°E between 4°S 100°E. Significant production of NO_2 and HCHO can be readily seen associated with this fire plumes.

The excess column amount of NO_2 increased from being less than $0.8x10^{15}$ in non polluted regions to between 2 and $4x10^{15}$ molec/cm^2 in urban and biomass burning regions of Kalimantan. Some small tropospheric excess NO_2 can be seen below the ITCZ in the southern hemisphere. The origin of these signals may be effectively noise or could perhaps indicate that lightning may have been present. Further work is required to understand this phenomenum.

The tropospheric excess columns of HCHO reached values up to ~$2.6x10^{16}$ molec cm^{-2} (~ 5-10 ppbv for a height of 2 km) over Kalimantan. HCHO is well correlated with the plume from the biomass burning regions over Kalimantan and Sumatra. Some excess HCHO can be also be seen to the south of Kuala Lumpur where smoke clouds are visible. For the Kalimantan fire region the ratio of HCHO/NO_2 excess column amounts is approximately 10. Although it is likely that some of the HCHO is produced by the oxidation of NMHCs and that some of the NO_2 may be lost by reaction with OH to form HNO_3 within the fire plume observed by GOME, this can be assumed to appropiate the ratio HCHO/NO_2 being emitted. Combining this value with the literature estimate of the ratio of NO_2/CO_2 emitted by fires, which has been determined to be around $2x10^{-3}$, [14], [15], [16], [17] yields the ratio of HCHO to CO_2 emitted by the fire to be about 0.02. This represents quite a large emission of HCHO and needs to be confirmed by other independent techniques.

Excess tropospheric O_3 is observed in both hemispheres. Above the ITCZ in northern hemispheric air a plume of O_3 appears to begin over Kalimantan and then increases downwind of Sumatra: the maximum columns being around 25 to 30 DU (~ 125-150 ppbv for a height of 2 km).

In southern hemispheric air significant but lower excess tropospheric O_3 is observed. This may partly result from limitations in the "excess" concept, but at least provisionally is attributed to result in part from the outflow convected to the upper troposphere from African biomass burning emissions.

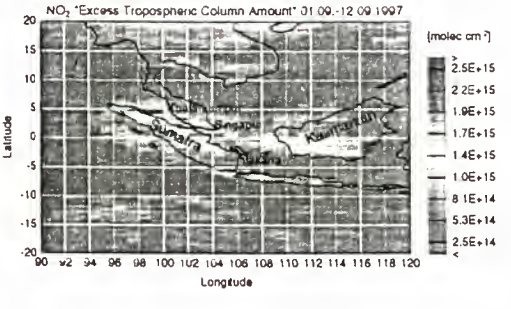

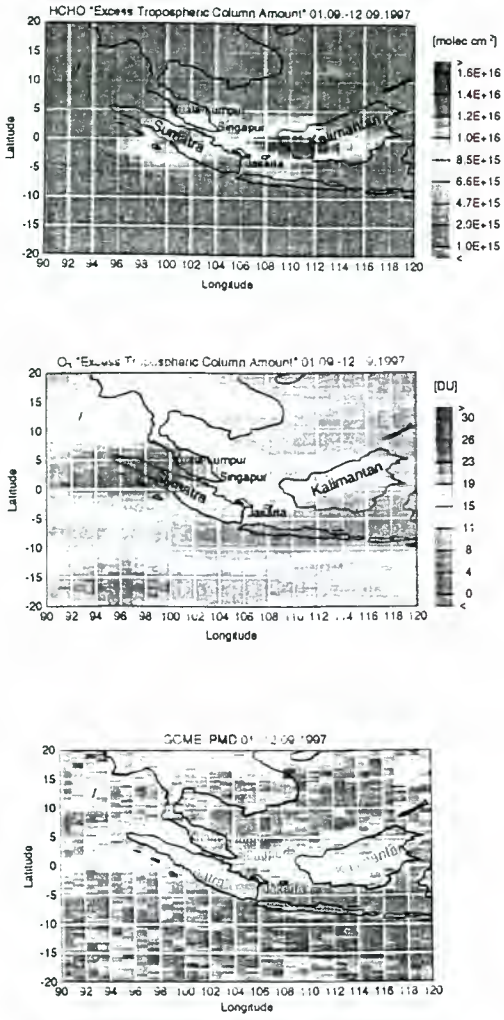

Figure 2. Composite pictures of the excess NO_2, HCHO, O_3 tropospheric columns and true colour image for the period 01.-12.09.1997.

Case 3: Biomass Burning – 16th-28th March 1998.

Another biomass burning event took place in early 1998. Figure 3 shows the excess tropospheric columns of NO_2, HCHO, O_3 and true colour image similar to figures 1 and 2. In this case a significant smoke cloud is observed over Kalimantan. Convective activity appears to be relatively low with scatterd clouds being present.
In addition to the city plumes, a strong excess NO_2 plume above the forest fire is observed. A large feature can be seen for HCHO above Kalimantan. The observed ratio of HCHO to NO_2 is about 8 for this period of fire burning, similar to that observed in September 1997.

As in September 1997 a large plume of excess O_3 is observed in northern hemispheric air. However significant southern hemispheric plume is observed. At this time of year there was no significant biomass burning over Africa in the southern hemisphere.

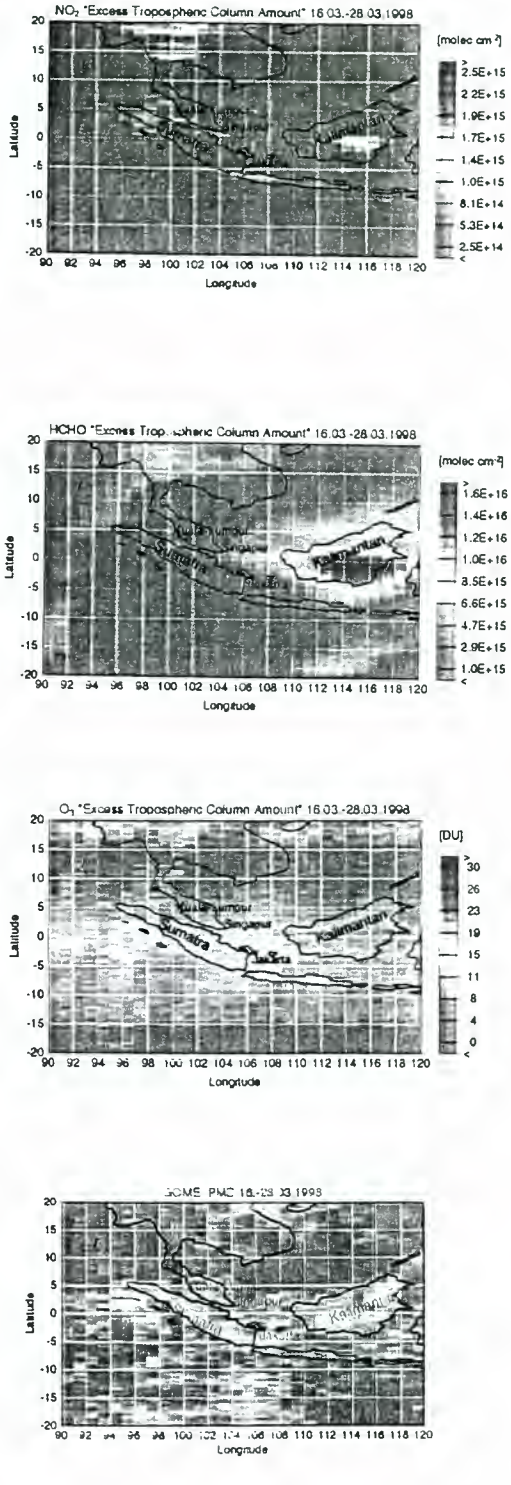

Figure 3. Composite pictures of the excess NO_2, HCHO, O_3 tropospheric columns and true colour image for the period 16.-18.03.1998.

5. CONCLUSIONS

The cases studied and described above demonstrate the importance of air pollution and biomass burning during the large fires which burned in Indonesia between June 1997 and April 1998. Significant emissions of both NO_2 and HCHO are observed from the fires. HCHO may also be generated in the plumes by the oxidation of NMHCs.
A simple analysis indicates that HCHO is about 2% of CO_2 emitted from the fire for both periods of burning reported.

Tropospheric O_3 appears, as is to be expected downwind of biomass burning plume. It appears that the production of O_3 in the plume is NO_x limited, because O_3 increases downwind from the urban areas of Singapur and Kuala Lumpur. Evidence for some tropospheric excess O_3 being produced in the southern hemisphere is also observed. This is attributed tentatively to convection and outflow of emissions from biomass burning in Africa.
This study demonstrates that GOME data will be most useful for observing certain aspects of tropospheric chemistry. However these observations need to be coupled to atmospheric models as they provide information only about one particular time of the day when GOME flies by.

6. ACKNOWLEDGEMENTS

We would like to thank our colleagues at the University of Bremen for useful discussions. ESA provided the CDs of the GOME level 1 data products used in this study and generated by the GDP Version 1.30 at the DLR-DFD.
This study has been funded in part by the ATMOS Project of the German Ministry of Education and Research (BMBF) and the University of Bremen.

7. REFERENCES

[1] Burkert, J., Andrés Hernández, M.D., Schwöppe, D., Stöbener, D., Weißenmayer, M., and J.P. Burrows (1996). "Ozone production calculated by using peroxy radical measurements". *Proceedings of EUROTRAC Symposium 96*, pp 627-631 (1996).

[2] Andrés Hernández, M.D., Burkert, J., Stöbener, D., and J.P. Burrows. "Role of peroxy radicals in tropospheric ozone formation". *Proceedings of the 7th European Symposium on the physicochemical behaviour of atmospheric pollutants*, pp 149-152, Venice (1996).

[3] Crutzen, P. J., and L. T. Gidel, A Two-Dimensional Model of the Atmosphere. 2: The Tropospheric Budget of the Anthropogenic Chlorocarbons, CO, CH4, CH3Cl and the Effect of Various NO_x Sources on Tropospheric Ozone, *J. Geophys. Res.*, 88, 6641-6661, 1983

[4] Altshuller, A. P., "Review: Natural Volatile Organic Substances and Their Effect on Air Quality in the United States, "Atmos. Environ., 17, 2131 (1983); Duce, R. A., V. A. Mohnen, P. R. Zimmermann, D. Grosjean, W. Cautreels, R. Chatfield, R. Jaenicke, J. A. Ogren, E. D. Pellizzari, and G. T. Wallace, "Organic Material in the Global Troposphere, *"Rev. Geophys. Space Phys.*, 21, 921 (1983)

[5] H. Bovesmann, J. P. Burrows, M. Buchwitz, J. Frerick, S. Noël, V. V. Rozanov, K. V. Chance, A. P. H. Goede 1999, "SCIAMACHY- Mission Objectives and Measurement Modes", J. Atmospheric Sciences 56, 126-150.

[6] Burrows J. P., 1999: Current and future passive remote sensing techniques used to determine atmospheric constituents, in scaling of trace gas fluxes between terrestrial and aquatic ecosystems and the atmosphere, *Ed. A. Bouwmann, Elsevier Science B.V.*

[7] J.P. Burrows, M. Weber, M. Buchwitz, V. Rozanov, A. Ladstätter-Weißenmayer, A. Richter, R. DeBeek, R. Hoogen, K. Bramstedt, K.-E. Eichmann, M. Eisinger, and D. Perner, 1999: The Global Ozone Monitoring Experiment (GOME): Mission Concept and First Scientific Results, *J. Atmos. Sci.*, 56, 151-175.

[8] Ladstätter-Weißenmayer, A., J.P. Burrows, A. Richter, F. Wittrock, M. Buchwitz, M. Weber, M. Eisinger, and R. Neuber, 1996: Validation of GOME O_3 and NO_2 Measurements in Bremen, Ny Alesund, and Neumeyer, GOME Geophysical Validation Campaign Proc., Frascati, *ESA-WPP 108*, 153-160.

[9] Perner D., T. Klüpfel, E. Hegels, P.J. Crutzen und J.P. Burrows, First Results on Tropospheric Observations by the Global Ozone Monitoring Experiment, GOME, on ERS 2, *Proceedings to the 3rd ERS-2 Users Conference*, Florence, Italy, Vol II, 647-650 (1997)

[10] Thomas W., E. Hegels and S. Slijkhuis, R. Spurr und C. Chance 1998: Detection of biomass burning combustion products in Southeast Asia from backscattered measurements taken by the GOME spectrometer, *J. Geophys. Res.* 25, 1317-1320 (1998)

[11] Richter A., 1997: Absorptionsspektroskopische Messungen stratosphärischer Spurengase über Bremen, 53°N, PhD thesis, University of Bremen, Germany

[12] Rozanov, V.V., D. Diebel, R.J.D. Spurr, and J.P. Burrows, 1997: GOMETRAN: A Radiative Transfer Model for the Satellite Project GOME, The Plane Parallel Version, *J. Geophys. Res. 102(D14), 16683-16695.*

[13] Rozanov, V., et al., GOMETRAN: A Radiative-Transfer Model for the Satellite Project GOME - The Plane-Parallel Version, submitted to *J. Geophys. Res., 1996*

[14] Andreae, M. O., E. V. Browell, M. Garstang, G. L. Gregory, R. C. Harriss, G. F. Hill, D. J. Jacob, M. C. Pereira, G. W. Sachse, A. W. Setzer, P. L. S. Dias, R. W. Talbot, A. L. Torres, et al., Biomass-burning emissions and associated haze layers over Amazonia. *J. Geophys. Res., 1988. 93: p. 1509-1527*

[15] Evans, L. F. N. K. King, P. R. Pockhaun, and L. T. Stephens. 1974. Ozone Measurements in Smoke from Forest Fires, *Environ. Sci. Technol., 8, 75-79*

[16] Crutzen, P. J. , L. E. Heidt, J. P. Krasnec, W. H. Pollock, and W. Seiler. 1979. Biomass Burning as a Source of Atmospheric Gases CO, H_2, N_2O, NO, CH_3Cl, and COS. *Nature, 282, 253-256*

[17] Crutzen, P. J. , A. C. Delany, J. Greenberg, P. Haagenson, L. E. Heidt, J. P. Krasnec, R. Lueb, W. H. Pollock, and W. Seiler. 1979, A. Wartburg, and P. Zimmerman, Tropospheric chemical composition measurements in Brazil during the dry season, *J. Atmos. Chem., 2, 233-256, 1985.*

WATER VAPOUR RETRIEVAL FROM GOME DATA

S. Noël, M. Buchwitz, H. Bovensmann, R. Hoogen, and J. P. Burrows

Institute of Environmental Physics, University of Bremen,
FB 1, P.O. Box 330440, D-28334 Bremen, Germany
phone: +49 421 218 4081, fax: +49 421 218 4555
email: Stefan.Noel@iup.physik.uni-bremen.de

ABSTRACT

A method to derive the atmospheric vertical column of water vapour from the near-infrared measurements of the Global Ozone Monitoring Experiment (GOME) is presented. These columns are determined by a modified DOAS approach, taking into account effects of strong wavelength dependent absorption. The radiative transfer model MODTRAN is used to calculate appropriate reference spectra for different scenarios, i.e. different solar zenith angles (SZAs) and different model atmospheres. This paper shows the feasibility of this approach and gives first estimates on the retrieval precision and the accuracy of a possible new GOME H_2O data product by comparison with selected radio sonde and SSM/I data.

1. INTRODUCTION

The accurate assessment of the impact of present and future anthropogenic pollution and natural phenomena of the atmosphere and the climate-chemistry coupling requires a detailed global knowledge of the temporal and spatial behaviour of atmospheric trace constituents (gases, aerosols, clouds). Water vapour is one of the most abundant atmospheric gases. More than 99% of water vapour is located in the troposphere where it significantly contributes to atmospheric chemistry and of course weather and climate. For example, H_2O plays a major role in the production of OH, the most important oxidising agent. Water vapour is arguably the most variable greenhouse gas. Variations of water vapour are closely related to atmospheric pressure and temperature; thus water vapour may be considered as a tracer for the spatial and temporal variability of the troposphere and particularly of climatic changes. The amount of water vapour is therefore of great importance for global atmospheric models which aim to predict the future climate.

Currently, global water vapour concentrations are mainly estimated from satellite based measurements in the infrared – e.g. with the TIROS-N Operational Vertical Sounder (TOVS) – and in the microwave spectral region – e.g. with the Special Sensor Microwave Imager (SSM/I) at 22 and 37 GHz – in combination with in-situ radio sonde measurements (see Ref. 1, and references therein).

This paper describes a method to derive water vapour column amounts from measurements of the Global Ozone Monitoring Experiment (GOME) which is operating successfully from the ERS-2 satellite since 1995. The GOME instrument is a grating spectrometer which measures solar irradiance and earthshine radiance from the UV to the visible and near-infrared wavelength region (≈240-800 nm). The inversion of the ratio of measured radiances and irradiances provides information about the amount and distribution of atmospheric constituents. The main task of GOME is the determination of global distributions of O_3 and NO_2, but it has been shown that concentrations of much more atmospheric constituents can be derived as well, e.g. BrO, OClO, SO_2, HCHO (see Ref. 2).

The method described in this paper uses GOME measurements in the near-infrared wavelength region (around 720 nm) to retrieve water vapour total vertical column amounts. In contrast to microwave measurements this approach is not limited to ocean areas. As with IR measurements it is possible to determine H_2O concentrations also over land. However, the determination of total H_2O columns is limited by the comparably low spatial resolution of GOME of about 320×40 km. So far, the retrieval algorithm is applied only to (almost) cloud-free scenarios, but in principle water vapour columns above the cloud top can be derived for cloudy pixels.

H_2O columns from GOME measurements are of special interest for users of the other GOME data products. Moreover, water vapour data from GOME measurements complements well other ERS-2 data products. Combination of GOME water vapour with e.g. cloud detection by ATSR and liquid water content from the Microwave Sounder will increase our knowledge on the global hydrological cycle in addition to demonstrating the pre-operational potential for meteorological applications.

As the retrieval method described here does not explicitly rely on GOME data, it may be applied to data from other similar sensors, such as the Scanning Imaging Absorption Spectrometer for Atmospheric Chartography (SCIAMACHY) (see e.g. Refs. 3, 4). SCIAMACHY is an enhanced version of GOME, which will operate from the ENVISAT-1 platform to be launched in late 2000.

2. RETRIEVAL METHOD

The retrieval of vertical H_2O columns is based on the Differential Optical Absorption Spectroscopy (DOAS) approach which was originally developed for on-ground observations (see e.g. Ref. 5) but has proven to be applicable also for ground-based zenith and space-based nadir measurements (Ref. 6).

2.1. Standard DOAS

DOAS exploits the Beer-Lambert law:

$$I = I_0 \exp(-\tau)$$

where I and I_0 are the measured and the unattenuated intensity, and τ is the optical depth along the light path.

The main idea of DOAS is to separate components which vary slowly with wavelength (resulting from Rayleigh and Mie scattering, surface reflection, and broadband absorption) from differential absorption structures. The broadband spectral features are approximated by a low-order polynomial P, which leads to

$$\ln\left(\frac{I}{I_0}\right) = P - \tau_A \tag{1}$$

where τ_A is the slant optical depth due to differential absorption.

For one absorber in the selected wavelength interval, which is the case for the H_2O band used in this study, the slant optical depth is given by

$$\tau_A = \int_s \sigma_A \, n \, ds \tag{2}$$

where σ_A is the differential absorption cross section and n is the number density of the atmospheric species; the integration is to be performed along the light path s.

If σ_A is independent of atmospheric pressure and temperature, the slant optical depth is proportional to the amount of the absorbing species integrated along the light path:

$$\tau_A = \sigma_A \, C_S \tag{3}$$

where

$$C_S := \int_s n \, ds$$

is the slant column density which is related to the vertical column density C_V by the so-called air mass factor:

$$m := \frac{C_S}{C_V}$$

C_V is defined similar to C_S:

$$C_V := \int_0^{\mathrm{TOA}} n \, dz$$

where n is integrated in the vertical direction, z, from the ground (altitude 0) to the top of the atmosphere (TOA).

Combining the above yields

$$\ln\left(\frac{I}{I_0}\right) = P - \sigma_A \, m \, C_V \tag{4}$$

Using measured values of I and I_0, known absorption cross sections σ, and an air mass factor m (usually derived from radiative transfer calculations), a linear fit provides the polynomial coefficients and the vertical column density C_V.

If the differential absorption cross sections depend on pressure and temperature (which is the case for H_2O), σ_A is not constant, and equation (3) no longer holds. However, it is possible to use a slightly different approach for this case which uses the slant optical depth τ_A instead of the slant column density C_S in the fitting process (see e.g. Ref. 6).

2.2. Modified Approach

The main assumption of "standard" DOAS is that the relative depth of an absorption feature is linearly proportional to the amount of the absorbing species integrated along the light path. This does not hold for molecules like H_2O where differential absorption features strongly depend on wavelength and are not resolved by the measuring instrument. In this case, the Beer-Lambert law is not applicable. The differential absorption depth becomes a nonlinear function of the absorber amount, and equation (4) is no longer valid unless at spectral regions where absorption is low, e.g. at the outer edges of a band structure. Unfortunately, this is also the region where absorption cross sections are typically less accurately known.

To make use of the usually much better signal-to-noise ratio of spectral regions with strong absorption, which may enable us to additionally derive H_2O vertical profile information out of the GOME data, it is necessary to include the saturation effect in the calculations. This is done by analogy to an approach described by Halthore & al. (Ref. 7) who determined water vapour columns from ground-based occultation measurements using sun photometers operating in the 940-nm band. Although the instrumental setup of Halthore & al. differs from the GOME observational geometry, spectral resolution and wavelength range, it will be shown that the general parametrisation of the saturation effect is applicable to GOME data.

Instead of equation (3) the following relationship between the slant optical depth τ_A and the slant column density C_S is assumed:

$$\tau_A = a \, C_S^b \tag{5}$$

The parameters a and b depend on wavelength, observational geometry (mainly solar zenith angle), spectral resolution and atmospheric properties, in particular on the vertical distribution of water vapour, i.e. the shape of the profile. It is a main assumption of the method described here that a and b do not depend on the actual amount of water vapour in the atmosphere, i.e. the total vertical column density. The parameter a contains the differential absorption cross sections (for different temperatures/pressures, averaged along the light path) at instrument resolution, whereas b is directly related to saturation where usually $b \leq 1$. For their broadband photometer measurements Halthore & al. determined single values for a and b which were quite insensitive to atmospheric changes. To use the higher spectral resolution of GOME data a and b are assumed to have a spectral dependence.

If we define

$$c := a \, m^b \tag{6}$$

the slant optical depth may also be written as a function of the vertical column density:

$$\tau_A = c \, C_V^b \tag{7}$$

This leads to the following basic equation which replaces (4):

$$\ln\left(\frac{I}{I_0}\right) = P - c \, C_V^b \tag{8}$$

The parameters b and c are obtained from radiative transfer calculations for different model atmospheres and observational geometries (i.e. solar zenith angles). This is explained below. For given values of b and c, the vertical column amount C_V may then be determined by a non-linear fit similar to the standard DOAS approach.

2.3. Determination of Parameters b and c

The first step in the determination of b and c is the derivation of the slant optical depth. For a given scenario, the slant optical depth is calculated by performing two radiative transfer calculations: one for an atmosphere which contains the relevant absorbing species (in our case water vapour), and one for an atmosphere which does not contain this species, i.e. for a zero column density. Using equation (1) the corresponding simulated intensities (i.e. radiances) I_{with} and I_{without} are:

$$\ln\left(\frac{I_{\text{with}}}{I_0}\right) = P - \tau_A$$

and

$$\ln\left(\frac{I_{\text{without}}}{I_0}\right) = P$$

which leads to

$$\tau_A = \ln\left(\frac{I_{\text{without}}}{I_{\text{with}}}\right) \tag{9}$$

This implicitly assumes that the polynomial P does not depend on the vertical column amount. This appears to be a good approximation in our case.

Taking the logarithm of equation (7) a linear relation between the logarithms of vertical column density and slant optical depth is obtained:

$$\ln \tau_A = \ln c + b \ln C_V \tag{10}$$

Varying the vertical column density and computing the corresponding slant optical depths yields b and c for each wavelength by a linear fit. To retrieve parameters which are specific for a given model atmosphere, the shape of the water vapour profile is kept constant in this process. This is achieved by scaling the assumed H_2O profile of the model atmosphere by factors from 20% to 100% without changing the other atmospheric parameters. It is not useful to apply scaling factors larger than 1 because this may result in a relative humidity larger than 100% at certain altitudes. On the other hand, taking into account only atmospheric columns which are smaller than the reference column may cause an under-estimation of the retrieved columns. This is (at least partly) compensated by adding more weight to the 100% atmosphere in the fitting process.

In this study, all radiative transfer calculations are performed with MODTRAN 3.7 (Ref. 8) for the wavelength range between 710 and 740 nm where water vapour is the dominant absorber. However, the method has also been successfully applied to other spectral regions where H_2O absorbs. The simulated spectra are computed at the highest spectral resolution of MODTRAN (1 cm^{-1}, equivalent to about 0.05 nm in this wavelength region) and then convoluted to the GOME spectral resolution (about 0.345 nm in this spectral range) before further processing.

Parameter sets of b and c are computed for solar zenith angles between 0° and 80° and each of the six MODTRAN standard atmospheres: tropical (TRO), mid-latitude summer (MLS), mid-latitude winter (MLW), sub-arctic summer (SAS), sub-arctic winter (SAW), and 1976 US Standard (STD) atmosphere. MODTRAN is run in multiple scattering mode in nadir viewing geometry assuming no clouds/precipitation, and tropospheric/background stratospheric aerosols. A surface albedo of 0.05 is assumed for ocean scenarios and 0.3 for land.

As an example, Figure 1 shows the slant optical depths computed with MODTRAN assuming a solar zenith angle of 40°, a surface albedo of 0.05, and a tropical background atmosphere (TRO) with water vapour profiles scaled by the indicated factors. As can be seen from the resulting spectra for b and c which are displayed in Figure 2, values of low c, equivalent to low absorption, correspond to values of b close to 1, equivalent to few saturation. At these regions the current approach is equivalent to standard DOAS. In fact, both methods produce similar results there.

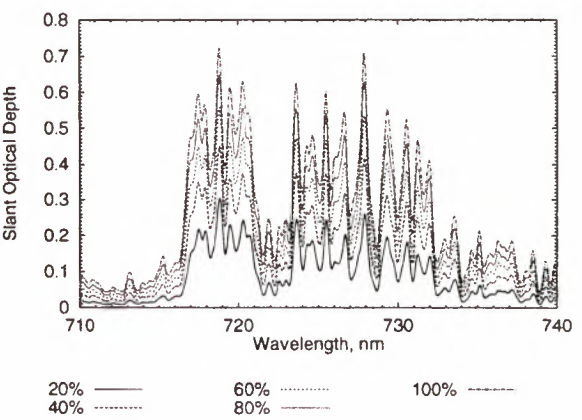

Figure 1. Slant optical depths computed with MODTRAN for a solar zenith angle of 40°, a surface albedo of 0.05 (equivalent to ocean), and a tropical model atmosphere in which the water vapour profile has been scaled by (from bottom to top) 20%, 40%, 60%, 80%, and 100%.

2.4. Selection of Parameter Set

As described above, the parameter sets b and c depend on model atmosphere, solar zenith angle, and surface albedo. Thus for each measured spectrum it has to be determined which parameter set will be used for the retrieval.

The surface albedo is chosen with respect to the geographical location of the measurement. Presently, only two different albedo values are used: 0.05 for ocean scenarios and 0.3 as an average value for measurements above land.

Since the solar zenith angle is known, an appropriate parameter set may be selected in one of the following ways:

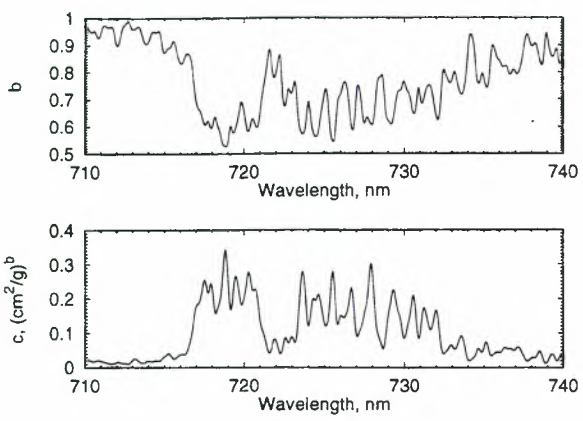

Figure 2. Parameters b (top) and c (bottom) computed with MODTRAN from the optical depths shown in Figure 1.

1. Use the parameter set with the smallest difference between model and measured solar zenith angle.
2. Interpolate the parameter sets for the measured solar zenith angle.
3. Compute the parameters b and c for the measured solar zenith angle.

The third possibility is the most accurate one, but it is very time-consuming because it requires individual radiative transfer calculations for each measured spectrum. The two other possibilities rely on tables of pre-calculated parameter sets and are therefore very useful when applied to a large data set (like the GOME data). Therefore the present study uses method (2). Since the solar zenith angle dependence of b and c has turned out to be rather smooth for SZAs $< 80°$ (higher solar zenith angles are currently not covered) it is sufficient to pre-calculate b and c for the solar zenith angles 0°, 20°, 40°, 50°, 60°, 70°, and 80°. For intermediate SZA values interpolation is performed.

The selection of an appropriate model atmosphere is difficult and requires in general a-priori information, e.g. a climatological data base. In our case, this data base is provided by the six MODTRAN atmospheres. Knowing the time and geolocation of a measurement, a parameter set which has been calculated for a suitable scenario (e.g. use the MLS atmosphere for measurements in mid-latitudes during summer) could be selected. However, this method relies on the quality of the climatological data base. This is why a different approach is used here: Retrievals are performed for each of the six atmospheres and then the result which has the smallest residual, i.e. the one which reproduces the measurements best, and for which the retrieved column does not exceed the column of the reference atmosphere is selected. The second criterium avoids extrapolation of column densities which may produce unphysical results. This approach is less dependent on the choice of the model atmosphere. Obviously, performing the retrieval six times is not the most computationally efficient, but it is sufficient at the present time. Other, more sophisticated algorithms will be subject to future investigations.

3. APPLICATION TO SIMULATED DATA

In a first verification the water vapour retrieval algorithm is applied to spectra computed with MODTRAN for the combination of the six MODTRAN atmospheres with the seven different solar zenith angles (see above) each for a surface albedo of 5% and 30%.

Figure 3 shows a comparison between the retrieved water vapour columns and the reference values corresponding to the atmospheric model used in the simulation. The results are very similar for both albedos.

The relative deviation between the retrieved and the reference column density is always below 0.7% and typically around 0.4% (see Figure 4). The retrieved column amounts are always smaller than the reference columns. As explained above, this is characteristic for the approach used here and due to the fact that in the determination of b and c no atmospheres with columns larger than the MODTRAN reference can be used.

As can be seen from Figure 5, the relative error of the retrieved water vapour column derived from the non-linear fit is generally less then 0.25% which indicates that this error is a good estimate for the retrieval precision.

There is a small dependence on solar zenith angles visible from Figures 5 and 4 as both estimated retrieval error and deviation from reference columns slightly increase with higher SZAs. However, this effect is very small, which indicates that the algorithm is quite insensitive to different viewing geometries.

It may be noted here, that the atmosphere selected by the retrieval is always the one which has been used in the radiative transfer calculations. This does not only show that the "minimum residual" approach works, but also gives confidence that information on the vertical distribution of water vapour can be retrieved from the data. However, the resulting columns are not too sensitive to the reference atmosphere, as long as the retrieved column is similar to or lower than the reference column, which is ensured by the selection process (see above).

4. APPLICATION TO GOME DATA

This section describes some results applying the water vapour total column retrieval algorithm to radiance/irradiance spectra measured by the GOME instrument.

4.1. Comparison with Radio Sonde Data

As sonde data are commonly used for validation purposes, the retrieval algorithm has been applied to a set of GOME measurements which fulfil the following criteria:

- Radio sonde data and GOME data are available for the same day.
- The distance between the centre of a GOME ground pixel and the location of the radio sonde station is

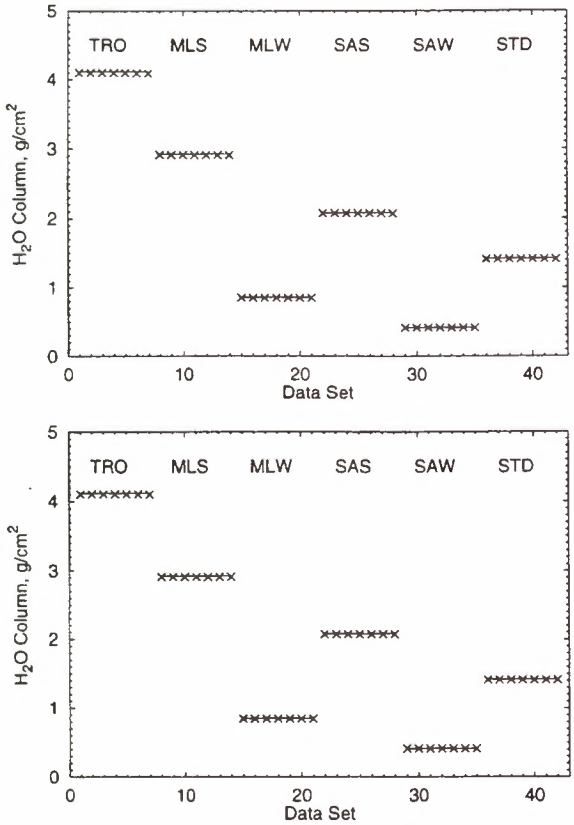

Figure 3. Comparison between retrieved water vapour columns (crosses) and reference values (lines) for simulated data assuming a surface albedo of 5% (top) and 30% (bottom). The reference atmospheres for the different data sets are indicated. Within each block of reference atmospheres solar zenith angles increase from left to right (0°, 20°, 40°, 50°, 60°, 70°, and 80°).

less than 480 km (which is half of the typical GOME swath width).

- GOME pixels have a cloud fraction smaller than 25%.
- Only GOME centre pixels are used.

Sonde data obtained at several stations at middle and higher latitudes on the northern hemisphere have been taken from the NADIR data base of the Norwegian Institute for Air Research (NILU). The above criteria are met by 47 data sets between July 1996 and June 1997 which cover solar zenith angles between 30° and 80°. Because all sonde measurements are performed over land, the 30% albedo parameter set has been used in the retrieval.

The results are shown in Figure 6. A good correlation between both data sets is obtained, but a systematic offset is visible: low sonde columns being under-estimated by the retrieval. This deviation is most likely caused by surface albedos different from (i.e. in the average lower than) the assumed value of 30%. Further studies will have to use an appropriate albedo data base to minimise this effect. Albedo information may also be obtained

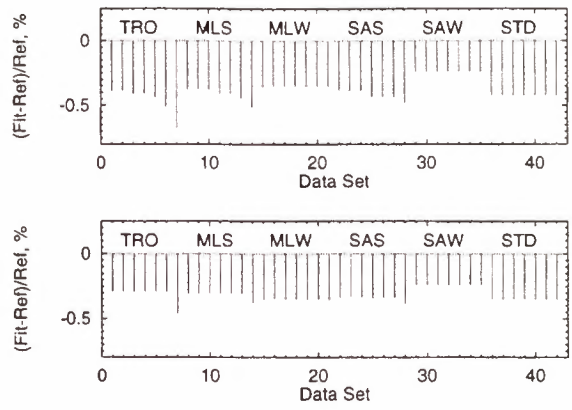

Figure 4. Relative deviation of retrieved water vapour columns from reference values for the simulated data presented in Figure 3. Top: Surface albedo 5%. Bottom: Surface albedo 30%

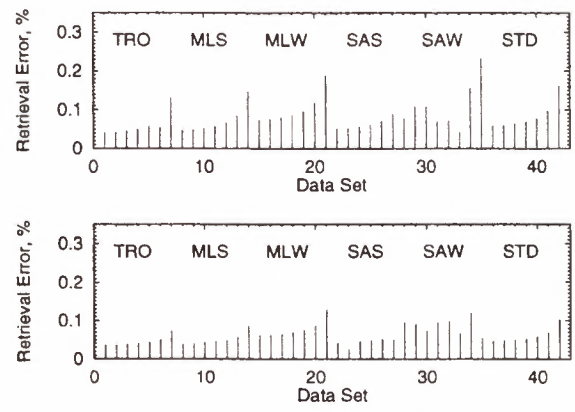

Figure 5. Estimated relative retrieval error for the simulated data presented in Figure 3. Top: Surface albedo 5%. Bottom: Surface albedo 30%

from the measured radiances and irradiances outside the H_2O band, e.g. at around 750 nm.

The average relative deviation between GOME and radio sonde data is approximately 16% with a standard deviation of 28%. Although this is a significant scatter, almost the standard deviations (up to 20%) are observed when comparing radio sonde data with SSM/I or TOVS results (see Ref. 1). As the estimated retrieval error is generally smaller (average value about 1.3%) the observed scatter most likely arises from differences in the sonde effective pixel and the large GOME ground pixels (about 320 km×40 km) coupled with the high spatial and temporal variability of atmospheric water vapour.

The relatively small number of appropriate sonde measurements does not allow a more detailed analysis of the relation between radio sonde and GOME water vapour columns. This will be subject to further investigations.

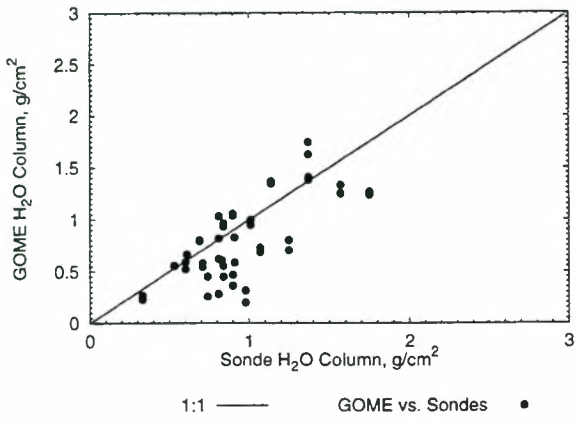

Figure 6. Correlation of GOME and radio sonde total water vapour columns assuming a surface albedo of 30%.

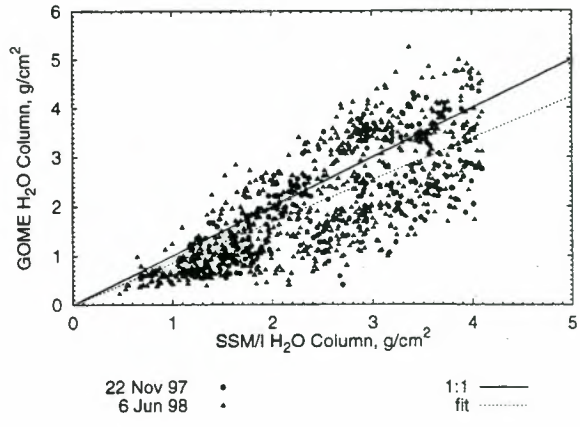

Figure 7. Correlation of GOME and SSM/I total water vapour columns assuming a surface albedo of 5%. The dotted curve shows the result of fitting a straight line with zero bias to the data.

4.2. Comparison with SSM/I Data

Because of the limited availability of appropriate ground based in-situ measurements, satellite remote sensing results are better suited to assess the quality of the GOME water vapour retrieval algorithm as their spatial and temporal coverage is generally larger.

Therefore, GOME total water vapour columns are compared with daily gridded Integrated Water Vapor (IWV) data produced by the Global Hydrology Resource Center (GHRC). These IWV data are based on measurements of the Special Sensor Microwave Imager (SSM/I) from the Defense Meteorological Satellite Program (DMSP) F-14 satellite. Data are available on a global scale but – due to limitations of the microwave sensing retrieval method – only above ocean. Further information may be found at the GHRC web site (http://ghrc.msfc.nasa.gov).

For the comparison we arbitrarily select two SSM/I water vapour data sets obtained during the descending orbits on two days roughly half a year apart (22 November 1997 and 14 June 1998). For each GOME ground pixel the average of all SSM/I data which cover the same area is computed. To simplify the boundary conditions the data set is further reduced by only taking into account cloud-free GOME pixels (i.e. cloud fraction < 0.1). Furthermore no data sets with an SSM/I column larger than 4.1 g/cm^2 are taken into account which is the largest water vapour column of the MODTRAN reference atmospheres. All higher columns are currently not covered by an appropriate model atmosphere. This leaves a number of 1030 GOME measurements for which the total water vapour column is retrieved and compared with the corresponding SSM/I data. Since all reference data are valid for ocean areas, computations are performed with the 5% albedo parameter set.

As can be seen from Figure 7, similar results are obtained for both days. Despite the significant scatter a clear correlation between the GOME and SSM/I data sets is visible, but there seems to be a systematic offset as the mean GOME water vapour columns tend to be about 10–20% smaller than the corresponding SSM/I columns. This is indicated by the dotted curve in Figure 7 which shows the result of fitting a straight line with zero bias to the data.

The average deviation between both data sets is about 18% with a standard deviation of 29%. This is the same magnitude as it turned out in the comparison between GOME and radio sonde columns. The scatter is significantly larger than the average retrieval error of 1.6%. Therefore, the variability of atmospheric conditions is considered to be a major source of deviations. This is supported by the statistical error of approximately 14% arising from averaging several SSM/I measurements over one GOME ground pixel. Taking into account that SSM/I measurements show a scatter of up to 20% when compared with radio sonde data (Ref. 1) the SSM/I and GOME results agree considerably well. The retrieval error may be reduced by using more sophisticated retrieval methods which e.g. correct for spectral shifts and use a larger atmospheric data base covering in particular also the higher columns.

In agreement with the results of the comparison between GOME and radio sonde data, the systematic offset is especially visible for small columns. The reason for this discrepancy between SSM/I and GOME is still unclear. In contrast to the radio sonde measurements, it is unlikely that this discrepancy between SSM/I and GOME data may be attributed to an inaccurate albedo value in the determination of b and c. Since the observed deviation is higher than expected from the results for simulated spectra, it is most likely not a problem inherent to method. At the moment, the following are considered as potential sources of error in the GOME H_2O retrieval:

1. Influence of partially cloudy ground pixels.
2. Incorrect air mass factors resulting from conditions which differ from the modelled ones (e.g. aerosols, clouds, albedo).
3. Errors in the absorption cross sections for water vapour.
4. Approximations in the calibration of GOME, espe-

cially w.r.t. polarisation.

5. Water vapour line filling due to Ring effect.

As deviations of the same order of magnitude have been found in comparisons between TOVS and SSM/I water vapour columns at higher latitudes (Ref. 1), potential error sources in the SSM/I will also be investigated.

5. SUMMARY AND CONCLUSIONS

A method to derive total water vapour column densities from GOME data has been presented. This method is based on a modified DOAS approach which considers saturation effects. By application on simulated data self-consistency of the method has been shown, and the retrieval precision has been estimated to be better than 1%.

Comparison of total water vapour columns derived from GOME data with radio sonde measurements and SSM/I Integrated Water Vapor results show a significant scatter in the order of 25–30%. This is slightly larger than typical deviations between SSM/I or TOVS and radio sonde data which may be attributed to the larger GOME ground pixel size in combination with the spatial and temporal atmospheric variability. Between SSM/I and GOME water vapour columns a systematic offset of about 18% is found. It will be a task of further studies to investigate reasons for this offset. Nevertheless, it has been shown that water vapour columns may derived from GOME measurements and that the results are in general agreement with other data sources.

Currently, several improvements of the retrieval algorithm are under development. This includes using the radiative transfer model GOMETRAN (Ref. 9) instead of MODTRAN. GOMETRAN has been specifically developed for use with GOME-like instruments. Recently, GOMETRAN has been extended and accurately simulates H_2O and O_2 absorptions (Ref. 10). The introduction of an air mass correction factor derived from measured O_2 absorption features will also improve the method such that the resulting water vapour columns will be less influenced by the particular atmospheric conditions. This will also be the first step in the development of a retrieval algorithm which can handle cloudy scenes.

ACKNOWLEDGEMENTS

GOME data are provided by ESA. Radio sonde data are taken from the NILU NADIR data base. SSM/I data have been obtained from the Global Hydrology Resource Center (GHRC). Part of this work was funded by the BMBF under grant 07 UFE 12/8 and the University of Bremen.

REFERENCES

1. Chaboureau J P & al 1998, Remote sensing of the vertical distribution of atmospheric water vapor from the TOVS observations. Method and validation, *J. Geophys. Res.*, 103, 8743–8752.

2. Burrows J P & al 1997, The Global Ozone Monitoring Experiment (GOME): Mission, instrument concept, and first scientific results, *Proc. 3rd ERS Symposium, 17-21 March 1997*, Florence, 585–590.

3. Noël S & al 1998, The SCIAMACHY instrument on ENVISAT-1, *Sensors, Systems, and Next-Generation Satellites II* (H Fujisada, ed.), vol. 3498 of *Proc. of SPIE*, 94–104.

4. Bovensmann H & al 1999, SCIAMACHY — Mission objectives and measurement modes, *J. Atmos. Sci.*, 56, 2, 127–150.

5. Perner D & Platt U 1979, Detection of nitrous acid in the atmosphere by differential optical absorption, *Geophys. Res. Lett.*, 6, 917–920.

6. Burrows J P & al 1999, The Global Ozone Monitoring Experiment (GOME): Mission concept and first scientific results, *J. Atmos. Sci.*, 56, 2, 151–175.

7. Halthore R N & al 1998, Sun photometric measurements of atmopheric water vapor column abundance in the 940-nm band, *J. Geophys. Res.*, 102, D4, 4343–4352.

8. Anderson G P & al 1995, FASCODE / MODTRAN / LOWTRAN: Past / present / future, *18th annual review conference on atmospheric transmission models, 6–8 June 1995.*

9. Rozanov V V & al 1997, GOMETRAN: A radiative transfer model for the satellite project GOME – The plane parallel version, *J. Geophys. Res.*, 102, D14, 16683–16695.

10. Buchwitz M & al 1998, Development of a correlated-k distribution band model scheme for the radiative transfer program GOMETRAN / SCIATRAN for retrieval of atmospheric constituents from SCIAMACHY/ENVISAT-1 data, *Satellite Remote Sensing of Clouds and The Atmosphere III*, vol. 3495 of *Proc. of SPIE*, 171–186.

Scientific Session

Trace Gases
– Retrievals & Geophysical Results –

Chair: K. Chance

Harvard Smithsonian Center for Astrophysics, USA

Determination of the Tropospheric NO_X Source Strength from GOME Data

C. Leue[1,2], T. Wagner[1], M. Wenig[1,2], U. Platt[1] and B. Jähne[1,2]
[1]Heidelberg University, Institute of Environmental Physics
[2]Heidelberg University, Interdisciplinary Center for Scientific Computing
carsten.leue@iwr.uni-heidelberg.de

Abstract

This contribution presents an algorithm to estimate the NO_X source strength of ground sources from GOME data. For the calculation of the source strength the separation of the tropospheric and stratospheric proportions of the retrieved vertical column density is necessary. The stratospheric background is estimated by calculating regional mean latitudinal slices of global NO_2 maps over regions unaffected by tropospheric emissions. The stratosphere can then be interpolated from those slices. Afterwards an annual mean image of the tropospheric NO_2 vertical column density in conjunction with the mean wind vector field is used to estimate the mean NO_2 life time. With this information rough estimates of the global NO_X budget can be given.

1 Introduction

Nitrogen oxides NO_X (NO and NO_2) play an important role in the atmospheric chemistry, moreover their concentrations have increased due to human activities in the past.
Biomass burning (forest fires, bush fires, etc.), especially in the tropics, have been identified as a major source of nitrogen oxides. However the global amount emitted by biomass burning is very difficult to quantify, as observations are extremely sparse, especially in the tropics. In addition there is a surprising uncertainty in the estimation of the amount of NO_X emitted by the burning of fossil fuel.
In this contribution we will show that in principle it is possible to derive information on the global tropospheric NO_X budget, in particular the geographical distribution of sources, from GOME satellite data.

1.1 Analysis procedure

Starting point for the NO_2 analysis is the GOME level1 data [1] i.e. earthshine spectra (see Figure 1). In order to retrieve slant column densities from the spectral information we apply a fast DOAS algorithm[1] [4], [6], [9] in the wavelength window between 425 nm and 450 nm. For the conversion from slant to vertical columns air mass factors for a *stratospheric* trace gas profile are calculated with the program AMFTran [5]. The stratospheric profile is important because the next step in the analysis is the estimation of the stratospheric background. For quantitative column densities for tropospheric columns these values have to be corrected with the corresponding tropospheric air mass factors (see Section 4).
Parallel to the trace gas retrieval cloud cover information is calculated from the PMD data of the GOME level1 product. Cloud information is important for the estimation of quantitative NO_X burdens, since clouds hide part of the NO_2 column visible for GOME.
For further analysis it is now important to exploit neighborhood information of local NO_2 concentrations.

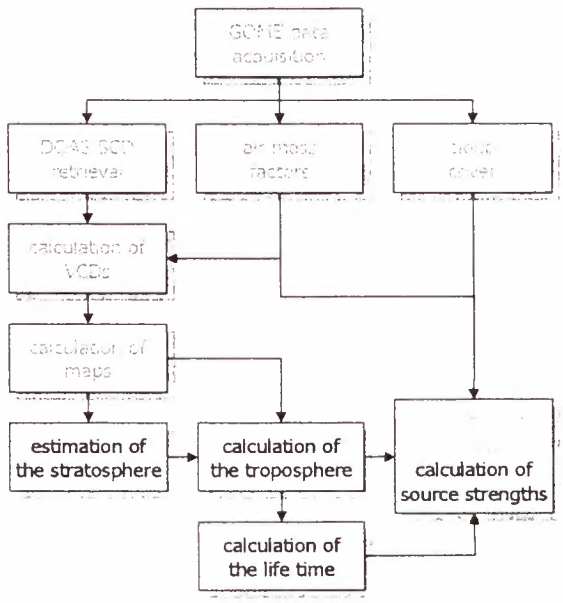

Figure 1: Flowchart of the analysis procedure: GOME level1 data is analyzed with a standard DOAS procedure to calculate NO_2 slant column densities. After the separation of stratosphere and troposphere (see Section 2) NO_X the source strength can be estimated (see Section 4) globally.

Therefore the sequential data of one orbit is assembled into bitmaps of global NO_2 concentrations. Such maps are formed as three day composite images with a dimension of 800 × 400 pixels which corresponds approximately to the spatial resolution of the GOME instrument. Missing pixels in the image are interpolated with normalized convolution [4]. For image processing we use the platform independent commercial software package *heurisko* [2].

[1] 60 ms per spectrum on a Pentium Pro 200MMX

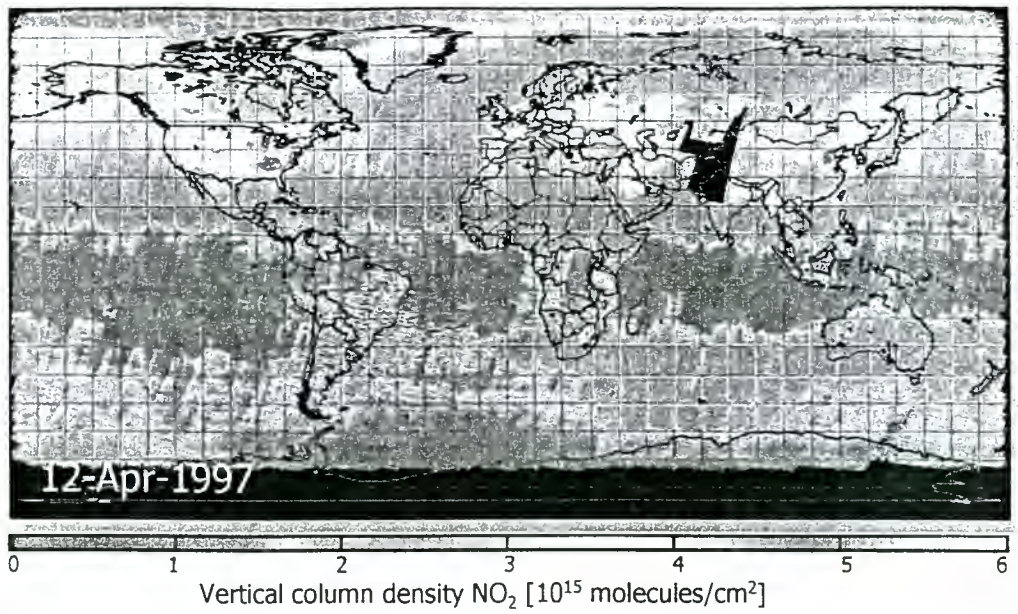

Figure 4: Typical global NO_2 distribution for a three day composite image derived from GOME for April 12 1997. Tropospheric and stratospheric contributions to the total column can be distinguished by their different spatial scale.

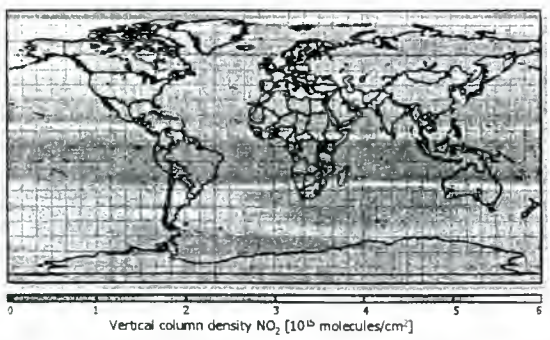

Figure 2: Estimated stratospheric background for the scenario of Figure 4.

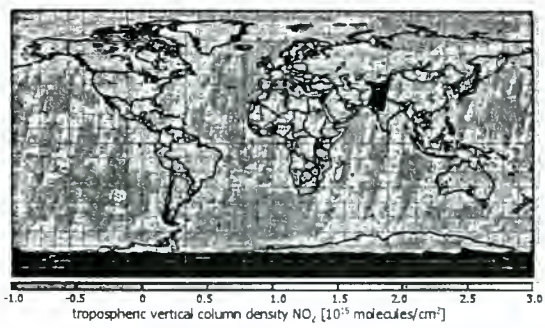

Figure 3: Tropospheric residual derived from the difference between the original NO_2 vertical column density in Figure 4 and the estimated stratosphere in Figure 3.

2 Separation of Stratospheric from Tropospheric NO_2 Columns

The stratosphere contains a considerable amount of NO_2 (typical stratospheric column densities are 1-5 10^{15} cm^{-2}) from the total observed column.
First step in the subsequent analysis is therefore the separation of the stratospheric and the tropospheric contribution to the total NO_2 column as we are only interested in the tropospheric NO_2 emissions. This step will be executed with an image processing approach on three day composite NO_2 vertical column density images considering the following assumptions of the spatial distribution of stratospheric NO_2.

2.1 Assumptions

Figure 4 shows the typical distribution of the vertical column density of NO_2 for April 12 1997. On this map the basic assumptions to discriminate troposphere and stratosphere can be observed:

- The stratospheric NO_2 column varies on a much larger scale than the tropospheric contributions. The tropospheric emissions usually take place on a scale of only several hundreds of kilometers as they are mainly caused by punctual emissions of industrial sources or biomass burning events. This can be observed very well over European and North American regions in Figure 3, as well as in South Africa near Johannesburg.
- In particular the stratospheric distribution is less variable in longitudinal direction than in latitudinal direction where apparently a typical profile is established.
- As most of the tropospheric NO_2 is emitted by burning events or by emissions from soil observed columns over the ocean are most likely due to stratospheric NO_2 contributions.

2.2 Algorithm

Based on the observation from Section 2.1 we developed an image processing approach to estimate the stratospheric background: First land regions are masked out to avoid errors in the stratospheric signal due to tropospheric contributions. The resulting image

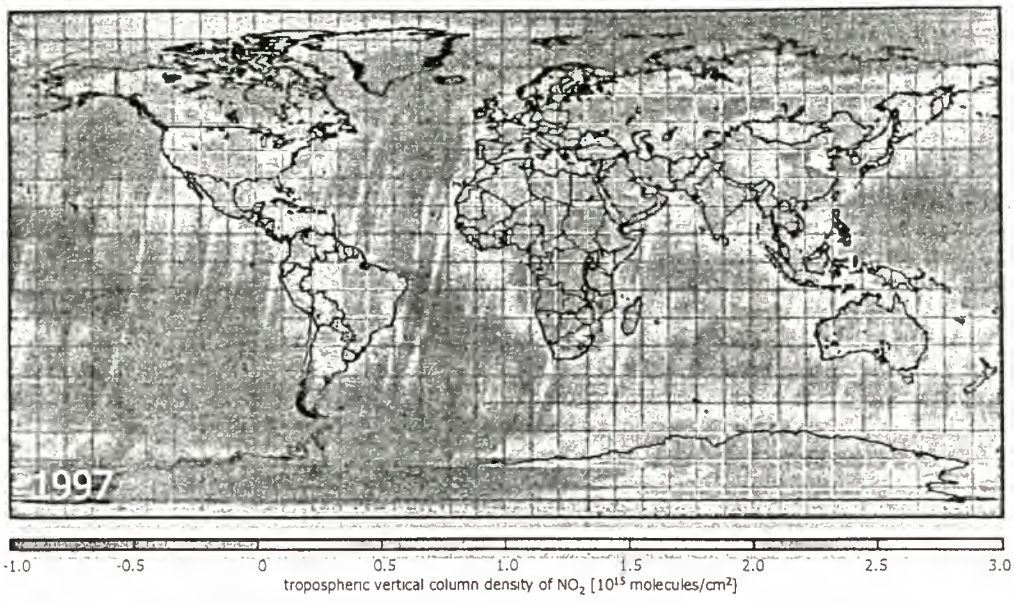

Figure 5: Global mean image of the tropospheric NO_2 residual for the year 1997. The image shows a strong correlation between the land masses and an elevated column density. Furthermore it can be seen that on the lee side of the coastlines there are increased NO_2 concentrations over the ocean as well.

is low-pass filtered with a B_5 filter[2] to suppress single emission peaks that cannot belong to the stratosphere. The resulting signal is then interpolated to give an estimate for the masked land regions. For this purpose the image is split into several longitudinal regions calculating the mean longitudinal distribution over each such region. The regions are selected such that at any latitude at least one pixel information is present resulting in mean latitudinal sections without gaps representing the typical NO_2 distribution in latitudinal direction for each region. This step considers the different variability of the NO_2 distribution in longitudinal and latitudinal direction.

The interpolation step is done by a cyclic spline interpolation between the sections for each latitude. For simplicity we chose Catmul-Rom splines [8] because they can be implemented efficiently and do not tend to create wiggles at their nodes which would result in an over or underestimation of the stratosphere. The result of the spline interpolation is then assumed to represent the stratospheric background of the total NO_2 column.

2.3 Results

An example can be seen in Figure 2 which corresponds to the original NO_2 map in Figure 4. The image shows that the background could be estimated very well and is smoothly interpolated over the land regions which had been masked out for the calculation of the latitudinal sections.

The tropospheric contribution can now be estimated by calculating the difference between the original image and the estimated stratosphere. In the resulting image Figure 2 we see that localized emission sources appear pronounced whereas the global stratospheric trend could be suppressed nearly completely. Moreover it emerges that the NO_2 column over land is systematically higher than that over the oceans which confirms our assumptions. This feature is even more pronounced in the annual mean image (see Figure 5) of the tropospheric residual of 1997. It shows out that in regions with strong industrial emissions tropospheric NO_2 columns of up to $3\ 10^{15}$ molecules/cm^2 can be found. Localized emission sources appear pronounced whereas the global trend over the image could be suppressed.

3 Estimation of the Mean NO_2 Life Time

For the determination of the mean NO_2 source strength from the measured NO_2 burden the knowledge of its atmospheric life time is necessary. This quantity can now be estimated from the decay behavior of NO_2 on the lee side of coastlines with strong tropospheric emissions.

The annual mean image (see Figure 5) of the tropospheric NO_2 residual shows increases NO_2 columns over the ocean near coasts in wind direction whereas in the opposite direction no such feature can be found. This behavior is due to the chemical decay of NO_2 over the ocean where there is no net production but only chemical decay (see Figure 6). From this decay curve we estimate the mean NO_2 life time from a case study in North America.

The basic assumption for the method is that in the annual mean the wind speed u and the life time τ can be substituted by their mean values and that the chemical decay can be described by a linear model. In the approach the plume dispersion does not have to be taken into account because in the vertical case it is invisible to GOME, which measures the integrated concentrations (vertical columns). Also lateral diffusion does not play a role if we can assume a similar NO_2 distribution in the neighborhood of the measured case because of the conservation of mass.

The decay curve c(x) of NO_2 then shows a static behavior and can be expressed by the following equation (in x-direction) with the NO_2 concentration c and the mean wind speed in x-direction u_x:

[2] The B_n filter describes a binomial filter with a mask size of n.

$$c(x) = c_0 \exp(-\frac{x}{\bar{u}_x \tau})$$

The mean NO_2 life time τ over one year can thus be calculated by the determination of the 1/e width of the decay curve, which is found to be $x_e \approx 491$ km. Information on the wind vector field can be found at NILU's database[3] with a temporal resolution of six hours. The annual mean wind speed in x-direction for 1997 was found by calculating the average over this data to be $u_x \approx 6.7$ m/s for the lower troposphere.
From this information we derive an average life time of $\tau \approx 73300$ s ≈ 20.5 h which corresponds well to values found in literature of approximately one day.

4 Estimation of the Mean NO_X Budget

From our annual mean images of tropospheric NO_2 vertical column density and an estimate of the mean NO_2 life time we can try to estimate the global NO_X budget. This time of course we rely on quantitative values for the tropospheric vertical column densities whereas in the previous sections only relative columns respectively their relative distribution were of importance.

For a quantitative estimate of the vertical column densities of NO_2 we have to be aware of the following facts:

- It is important to note that NO_2 which can be observed by GOME is in an equilibrium with NO. Both species are distributed approximately in equal proportions. To estimate the contents of nitrogen we have therefore to increase the observed concentrations by a factor of the order of 2.
- Pixels observed by GOME are never cloud free but they are (at least partially) covered with clouds with an probability of above 99.8 % [3] which shield the observed NO_2 column. We estimate that GOME underestimates the NO_2 column due to clouds by approximately 50 % in the annual mean. This means that we have to correct the measured values by another factor of the order of 2.
- GOME can only measure slant column densities. The conversion to vertical columns is done by the division by the air mass factor which itself strongly depends on the trace gas profile in the atmosphere. In particular the tropospheric air mass factor is smaller than the air mass factor calculated with the assumption that all NO_2 resides in the stratosphere. To be able to discriminate troposphere and stratosphere we applied air mass factors for a stratospheric NO_2 profile. Evidently this underestimates the column for the tropospheric residual. Hence we have to correct the tropospheric residual with the correct tropospheric air mass factor:

$$VCD_{trop} = VCD_{residual} \frac{AMF_{strat}}{AMF_{trop}}$$

Model calculation show that the correction factor lays between 2 and 3 for mid latitudes.

[3] ftp://zardoz.nilu.no

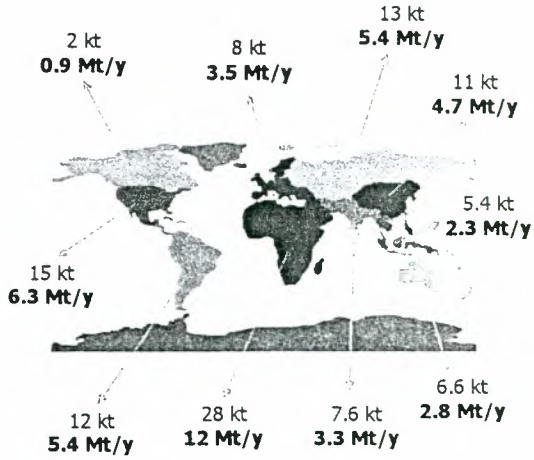

Figure 6: Estimate of the annual tropospheric NO_X emissions by region (in units of nitrogen) in 1997. The first number denotes the total contents of nitrogen in the atmosphere over the specified region (in the annual mean), the second number gives the mean sources strength. For details of the calculation procedure see Section 4.

As a summary we conclude that the observed NO_2 vertical column densities have to be increased by a factor of 10 to correctly estimate the global contents of nitrogen in the atmosphere.

The estimation of the NO_2 source strength (production rate) λ can now be done from the data of the annual mean image of the tropospheric NO_2 residual considering the correction factor from Section 4.1. Assuming that the production rate is constant over the year as well as the life time τ. The temporal development of the NO_2 concentration is then described by

$$\frac{dc}{dt} = \lambda - \frac{1}{\tau} c$$

To derive the mean production rate over a time period T we integrate over c(t) over this period. For long integration times T>>t the steady state solution for this problem is

$$\lambda = \frac{c_T}{\tau T}$$

By comparison with the measured columns c_T (see Figure 5) and the life time τ from Section 3 we can now estimate the global nitrogen budget and the mean production rate λ over one year.

Results of the determination of the global source strength and nitrogen budget are presented in Figure 7. Whereas the absolute values contain still uncertainties of approximately a factor of 2 at least their relations show the relative source strengths of the regions. It shows out that Africa emits most nitrogen though it is only a poorly industrialized region. This is most likely due to biomass burning.

5 Summary and Outlook

In this article we presented a method to discriminate the tropospheric and stratospheric NO_2 contribution to the vertical NO_2 column from GOME satellite data. The method only uses intrinsic image information and can thus be applied self consistently to each global NO_2 map of an image sequence (see Section 2). From the tropospheric data information about the mean NO_2 life time can be obtained by analyzing its decay behavior in coastal regions (see Section 3). The estimated life time of 20.5 h corresponds very well to values found in literature of about one day.
The determination of the global NO_X budget is more difficult because of large uncertainties in the knowledge of the 'right' air mass factors and the mean cloud coverage. Nevertheless first estimates of the mean NO_X budget for the year 1997 could be presented for several world regions assuming a-priory values for the uncertainties mentioned before.
We are - of course - aware of the fact that the NO_2 source strength data presented here are very rough estimates. However considerably better estimates can be made by several improvements that will be implemented in the near future:

- First more appropriate NO_2/NO_X ratios can be calculated by taking the latitudinal dependence of the sun zenith angle into account.
- Furthermore we will improve the air mass factor subject by the application of AMF lookup tables for tropospheric air mass factors which take into account seasonal changes in the ground albedo.
- Time resolved cloud information is now available from the HSV cloud cover algorithm [7] and will help to calculate the cloud cover more accurately.

With these improvements it will also be possible to study the seasonal variation of the NO_2 source strength and to resolve the relative emission rates more accurately.

Acknowledgements

This work was supported by *DFG research unit "Image Sequence Analysis to Investigate Dynamic Processes" (Ja395/6)*. C. Leue is supported by a grant by the *Studienstiftung des Deutschen Volkes*.

References

[1] W. Balzer and D. Loyola. *Product specification of the GOME data processor.* Technical Report, Deutsche Forschungsanstalt für Luft- und Raumfahrt, Deutsches Fernerkundungszentrum, 1996. ER-PS-DLR-GO-0016

[2] Walter H. Dorn. *Heurisko Benutzerhandbuch, Version 2.3* Aeon Verlag & Studio, 12 1995

[3] L. Kurosu. *Die Modellierung des Strahlungstransports in Wolken für atmosphärische Fernerkundung im ultravioletten und sichtbaren Bereich.* PhD thesis, University of Bremen, 1997

[4] C. Leue, M. Wenig and U. Platt. *Handbook of Computer Vision and Applications*, volume 3. Academic Press, 1998

[5] L. Marquardt. *Modellierung des Strahlungstransports in der Erdatmosphäre für absorptionsspektroskopische Messungen im ultravioletten und sichtbaren Spektralbereich.* PhD thesis, University of Heidelberg, February 1998

[6] J. Stutz and U. Platt, *Numerical analysis and error estimation of Differential Optical Absorption Spectroscopy Measurements with Least-Squares Methods.* Applied Optics, 35:6041-6053, 1996

[7] M. Wenig, *Wolkenklassifizierung mittels Bildsequenzanalyse auf GOME Satellitendaten.* Master's thesis, University of Heidelberg, 1998

[8] Foley, J.D. and van Dam, A. and Feiner, S.K. and Hughes, J.F, *Computer Graphics: Principles and Practice, Second Edition* Addison-Wesley, 1990

[9] Ottoy, J.P. and Vansteenkiste, G.C. *A computer algorithm for non-linear curve fitting.* Advances in Engineering Software, vol. 3, pp55-61, 1981

DOAS-OCM retrieval of water vapor from GOME and new CRD spectroscopy.

R. Lang[1,2,3], A.N. Maurellis[1], W.J. van der Zande[1], I. Aben[2], P. Levelt[4], H. Naus[3], W. Ubachs[3]
[1]FOM-Institute AMOLF. Amsterdam. [2]SRON. Utrecht. [3]VU. Amsterdam. [4]KNMI. De Bilt.

Abstract

We report on the application of a single reference spectrum standard DOAS technique as well as a new, multiple-spectrum, modified DOAS technique to the retrieval of absolute H_2O vertical column densities from GOME data. The modified technique implements a new kind of radiative treatment to correctly sample the net contribution to the total absorption of altitude-dependent (ie. temperature- and pressure-dependent) cross-sections for each detector pixel. The standard DOAS technique yields estimates of total water column which correlate remarkably well against ECMWF estimates. Our techniques were also applied to a single radiosonde KNMI measurement for cloud coverage smaller than 20%. Unfortunately, absolute values produced by standard DOAS are too low. The modified DOAS algorithm reveals better absolute agreement with the data and lends itself easily to level-2 product generation of H_2O columns without requiring an independent calculation of airmass factors.

We also report on the new measurements of H_2O absorption bands between 580 and 605 nm using Cavity Ring Down Spectroscopy (CRDS). These measurements reveal good agreement with existing lines in the HITRAN96 database and add some 800 additional lines.

1. Introduction

The GOME experiment on the ERS-2 satellite continues to provide powerful opportunities for mapping the distributions of many trace gases and aerosols. Many species have absorption features in a number of spectral regions covered by GOME, and many trace gas density retrieval algorithms, among them the DOAS (Differential Optical Absorption Spectroscopy) technique, have been developed and successfully implemented in the past. In this work, we focus on a weak water vapor absorption band in the visible spectrum which appears to be optically thin to absorption from all species other than water. In section 2 we show that standard DOAS provides results that correlate very well with ECMWF (European Centre for Medium-Range Weather Forecasting) and KNMI (Royal Dutch Meteorological Institute) radiosonde data although DOAS underestimates absolute H_2O. DOAS also underestimates total precipitable water vapor (PWV) columns for pixels with fractional cloud cover above 20%. In section 3 we outline a new algorithm, which we dub DOAS-OCM (OCM stands for Optical Density Coefficient Method). This algorithm correctly samples altitude-dependent absorption cross-sections and mixing ratios and behaves more robustly in the presence of clouds. Furthermore, both DOAS techniques require accurate reference spectra, as a function of temperature and pressure. This requirement has prompted new laboratory measurements (discussed in section 4) of the above-mentioned water band using the novel CRDS technique which displays a number of advantages over traditional spectroscopy.

2. Initial tests with standard DOAS and validation data sets

Figure 1 shows the spectral region (586nm - 597nm) to which we applied our fitting techniques. This region contains a weak absorption band of water just between two

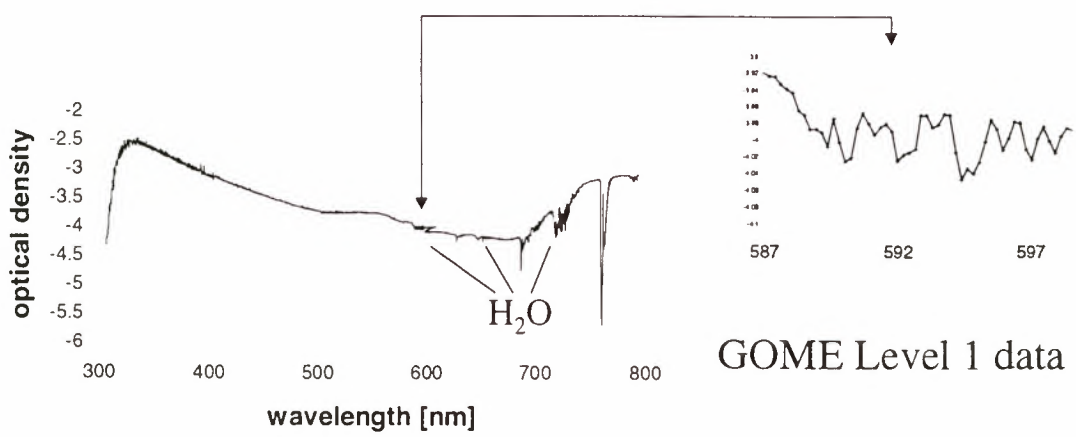

Fig 1. *Sample wavelength band from GOME level 1 data used in H_2O vapor retrieval with explosion of specific region of interest: a weak water band in the visible.*

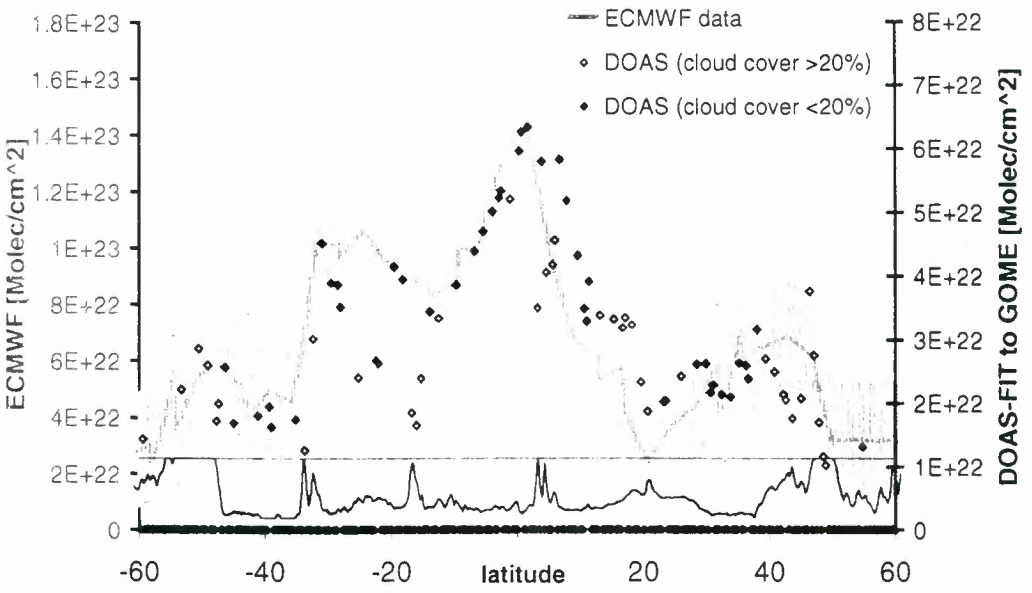

Fig 2. *Comparison of standard DOAS technique with ECMWF data. ECMWF data (red line) are interpolated. A nominal error bar (shaded gray region) of 0.6 mm PWV surrounds each ECMWF point. The lowest curve gives an indication of cloud cover (taken from GDP level 2). DOAS vertical column density fit results for low cloud cover (filled points) correlate better with ECMWF data than DOAS results for high cloud cover (unfilled points).*

$(O_2)_2$ collisional bands (at 577.2 nm and 630.0 nm) and the $O_2(\gamma)$ band (at 628.8 nm) (Ref. 1). Apart from the possibility of sodium line absorption at 588.99 nm and 589.59 nm, this band appears to be uncontaminated by other molecular absorptions. Initially, we used an implementation of DOAS developed at SRON (Ref. 2). This procedure requires the input of a single reference absorption cross-section spectrum. We computed such a spectrum using lines from the HITRAN96 database, for a temperature and pressure corresponding to the ground level of each GOME pixel. Temperature and pressure profiles were taken from the MSIS-E model (Ref. 3). The output, an estimate of vertical column density, is shown in figure 2 along with a longitudal slice through assimilated ECMWF data (http://www.ecmwf.int/), correlated in epoch and geolocation to GOME pixel data. (Note that ECMWF pixels are approximately 4-5 times larger than GOME pixels and thus reflect a smoothed average of a few GOME pixels). As a first approximation airmass factors (AMFs) were estimated geometrically. Although the derived columns correlate rather well with the expected data, this method is clearly not able to generate absolute columns.

3. New results from DOAS-OCM

Water vapor may well exist at a number of different altitude levels rather than being concentrated over a single, fairly narrow range of altitudes as, for example, is the case with ozone. Thus a single reference absorption spectrum at one particular temperature and pressure might fail to adequately represent the variation in the spectrum that might be expected for the combined effect of both stratospheric and tropospheric water. The DOAS-OCM technique (Ref. 4), allows for a wide variation in absorption characteristics as a function of altitude (and hence temperature and pressure). The OCM technique correctly samples the absorption strength as a function of optical depth for a set of absorption cross-section profiles. This profiles are calculated at altitude levels which adequately represent the neutral temperature dependence on altitude. Rather than simply averaging absorption strengths and then applying Beer's law, the OCM technique wavelength-averages the transmittance after Beer's law has been differentially applied to absorption cross-section structure, for each detector pixel. This has the advantage that the altitude dependence of the optical density (α_i) is separated from the cross-section dependence (ξ_i) in the expression for net transmittance per detector pixel (see equation) which facilitates easy altitude interpolation and the construction of look-up tables.

$$\frac{I_{out}}{I_{in}} = \int_{\lambda_1}^{\lambda_2} \exp\left(- \int \sigma(\lambda, s) n(s) ds \right) d\lambda$$

$$\approx \sum_{i \in \Re} \left(\frac{\int_{z_1}^{z_2} \alpha_i(s) n(s) ds}{\int_{z_1}^{z_2} n(s) ds} \right) \exp\left[-\xi_i \int_{z_1}^{z_2} n(s) ds \right] \Delta\lambda$$

Here λ_1, λ_2 refer to the wavelength bin limits of a detector pixel, z_1, z_2 refer to the altitude bounds of a layer of atmospheric water vapor and *n(s)* refers to the altitude profile of the water vapor number density. Since such a profile is, of course, not known *a priori*, we assume that the water vapor distribution follows the background neutral density scale heights but with unknown mixing ratios as a function of altitude. The mixing ratios are then fitted as free parameters to the GOME data. In particular, we assume a simple 3-layer radiative transfer model with ground and cloud reflectivity and then obtain a fit for three mixing ratios between altitude levels chosen to match cloud-top height (taken from climatology GDP level 2) and neutral background temperatures in excess of freezing. DOAS-OCM appears to yield good estimates of PWV (see figure 3) notwithstanding a small amount of scatter induced by a lack of spatial averaging of GOME ground pixels over the large ECMWF pixel. The KNMI measurement is also reproduced. Cloud cover does not appear to significantly reduce the accuracy of the method. Note that AMFs are not required to calculate column densities in DOAS-OCM since the method yields vertical mixing ratios directly, although the method does generate AMFs as a by-product.

4. CRDS

Cavity Ring Down Spectroscopy is a relatively new technique in which pulsed laser radiation is transmitted through a high-finesse stable optical cavity, built from two mirrors with extremely high reflectivities of 99.99% or better. In transmission an exponentially decaying light flux can be measured outside the cavity. The time constant represents the photon round trip time in the cavity and is a function of mirror reflectivity. If the cavity contains species that lead to loss of light out of the cavity due to absorption or scattering then the observed decay rate for light leaking out of the cavity increases. In fact, the absorption coefficient can be deduced from the decay rates only, since the incident light intensity and hence fluctuations in this intensity do not affect the determination of decay rates. Thus CRDS has two major advantages: the outcome is not a function of the laser intensity or its temporal stability, as in conventional absorption spectroscopy, and the sensitivity is greatly enhanced because the high reflectivity of the mirrors results in an absorption path length of more than 100 kilometers. Ideally, the spectral width of the light source should be smaller than the width of individual absorption lines in order to ensure well-behaved single exponential decay. In the present experiment this is not realized, as the laser line-width (0.05 cm^{-1}) nearly equals the Doppler width. As a result the absolute absorption cross sections for the lines are not extractable in a simple manner and will be the subject of future work.

In figure 4 the CRDS spectrum has been transformed into integrated band intensities. These intensities were used to build up a spectrum with the same line-shape parameters as the corresponding HITRAN96 spectrum. Note the excellent agreement of line positions although the strongest lines appear to be somewhat underestimated by CRDS. Furthermore, although not obvious from the figure, the laboratory spectrum contains some 800 weak lines (with peak cross-sections less than 10^{-24} cm^2) that do not appear in the HITRAN96 database.

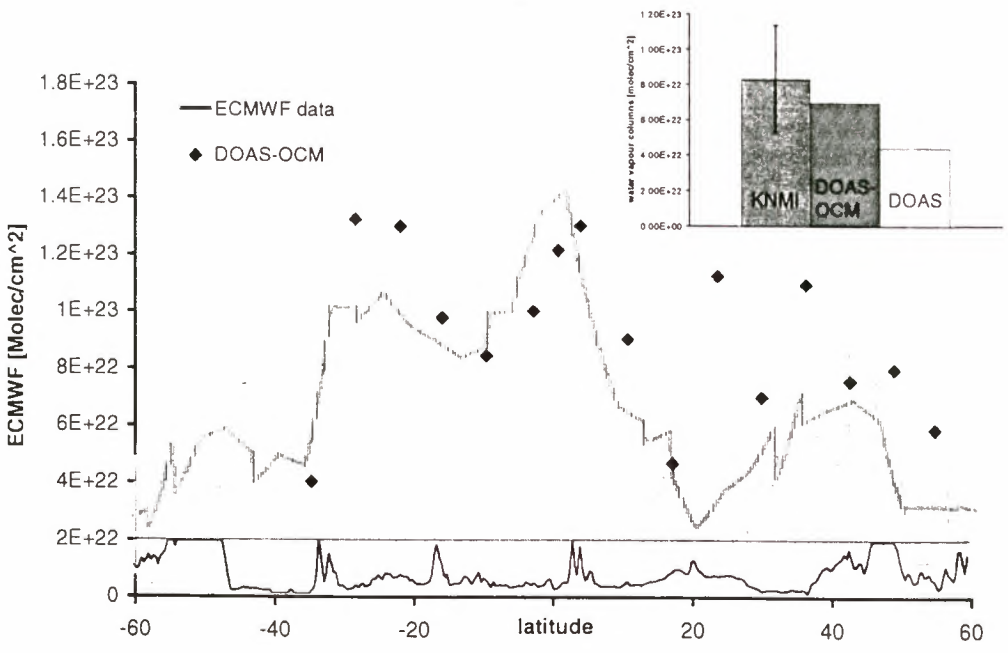

Fig 3. *Comparison of DOAS-OCM technique with ECMWF data. ECMWF data (red line) and fixed error bar (shaded gray region) as in figure 2. The method appears to reproduce the ECMWF and KNMI data more reliably.*

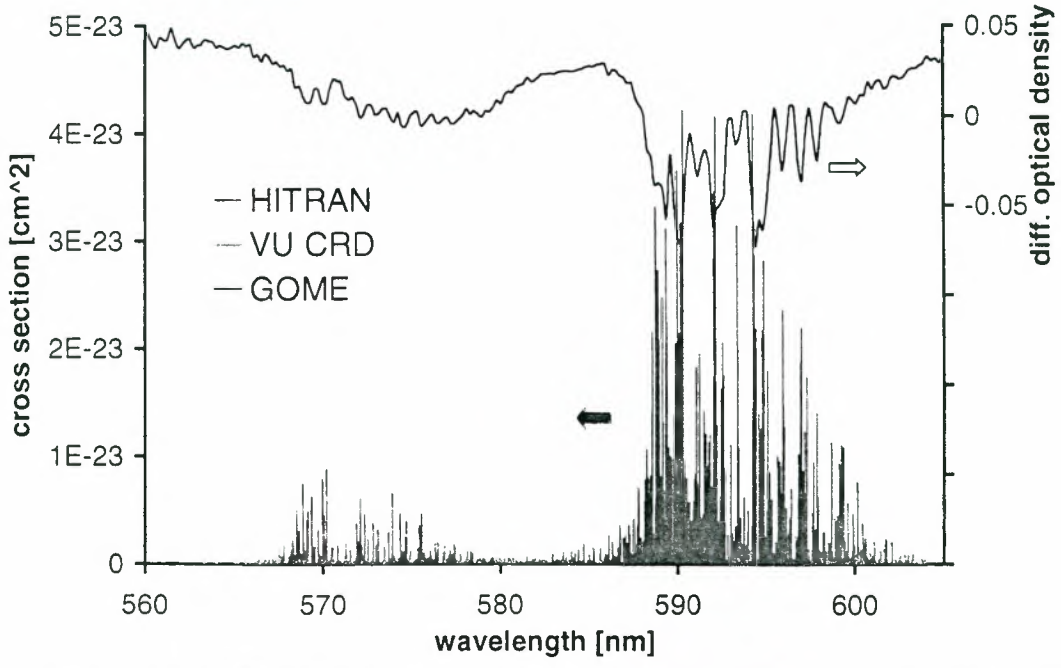

Fig 4. Comparison of HITRAN96 realization of water vapor absorption with CRDS data taken at the Vrije Universiteit. A sample GOME spectrum is overlaid in order to highlight the area of interest to this work, viz. the right-hand absorption band.

5. Summary and Conclusions

We have described a progress report of the use of GOME data for routine precipitable water vapor column retrievals as well as some new laboratory spectra for H_2O absorption.

We used HITRAN96 spectra in a standard implementation of single reference spectrum DOAS as well as in a new multiple reference spectrum (DOAS-OCM) implementation. For validation purposes we compared our results to assimilated data from ECMWF and a single radiosonde measurement above KNMI. Any algorithm for trace gas retrieval must ultimately reproduce currently available PWV measurements, and the use of these and other data validation sources still needs to be investigated further.

The DOAS-OCM algorithm operates under a simple radiative transfer model that is computationally well suited to near-real-time retrieval of trace gas columns for any unsaturated absorption band. Apart from reproducing the columns, the method also provides some altitude resolution, determines airmass factors and takes into account cloud reflectivity. Because we compare GOME ground pixels with lower resolution ECMWF pixels there appears to be some scatter in the comparison. Thus further development, in the form of reliable error estimates, more testing of robustness of column retrieval under different conditions, and spatial averaging for proper comparison with validation data, is needed. The use of a variety of absorption windows might also strengthen the technique considerably.

A preliminary comparison of the new CRDS spectrum with the HITRAN96 database reveals reasonable quantitative agreement with the approximately 1000 lines found in HITRAN96 and adds 800 more. Thus CRDS appears to support our use of the HITRAN96 database in the application of DOAS-OCM in this work, but further calibration is required before the CRDS line profiles can be used in on-line water vapor retrieval.

Acknowledgements

We thank ESA for making available the GOME data. The authors acknowledge support from SRON through project grants E0-023 and E0-0123 respectively. ANM is supported by Marie Curie Environment & Climate grant ERB4001GT980174.

References

1. Newnham, D. A. & J. Ballard 1998, Visible Absorption Cross Sections and Integrated Absorption Intensities of Molecular Oxygen (O_2 and O_4), *J. Geophys. Res.*, **103**, 28,801-28,816.
2. Pasterkamp, R. 1998, Differential Optical Absorption Spectroscopy, Research Document, Space Research Organisation of the Netherlands.
3. Hedin, A. E. 1991, Extension of the MSIS Thermosphere Model into the Middle and Lower Atmosphere, *J. Geophys. Res.*, **96**, 1,159-1,172.
4. Maurellis, A. N. 1998, A New Basis Set for Weighting Functions in Atmospheric Transmittance Determination, in preparation.

MEASUREMENT OF WATER VAPOUR IN THE UPPER TROPOSPHERE AND LOWER STRATOSPHERE with MIPAS/ENVISAT

M. Milz, T.v. Clarmann, G.P. Stiller, H. Fischer

Institut für Meteorologie und Klimaforschung, Forschungszentrum Karlsruhe, Germany
e-mail: mathias.milz@imk.fzk.de

ABSTRACT

Measurements of water vapour in the upper troposphere and lower stratosphere (UT/LS) with good vertical and horizontal resolution are required to assess its influence on the radiation budget of the earth and for its use as a suitable tracer for the study of troposphere-stratosphere exchange processes (STE). Compared to the vertical structures of the real water vapour distribution (e.g. hygropause), the field of view of MIPAS is rather wide. Our aim is to derive UT/LS water vapour profiles from MIPAS/ENVISAT data with optimized spatial resolution and accuracy requirements. Microwindows were selected for a standard retrieval scenario (retrieval of H_2O level values on tangent heights) and a tropical reference atmosphere in the range 5 - 25 km. The related retrieval errors were assessed. Improvements by joint retrieval of the temperature were investigated, in particular for saturated H_2O signatures originating from the troposphere.

1. INTRODUCTION

The knowledge of the composition of the earth's atmosphere and the distributions of single components is necessary to assess the radiation budget of the atmosphere and thus to understand the natural and antropogenic greenhouse effect. Some of the constituents, e.g. water vapour, are much more relevant to the earth's radiation budget than others. Especially water vapour is the most effective and most variable greenhouse gas in the earth's atmosphere. In order to assess its influence on the radiative transfer, good knowledge of its vertical and horizontal distribution is essential. Satellite-borne instruments like MIPAS/ENVISAT provide global coverage with vertically and horizontally resolved measurements. Water vapour distributions are highly variable in the temporal and spatial domain which complicates the assessment of its radiative influence. Especially for climatological analysis satellite borne instruments like MIPAS provide useful results.

On the other hand water vapour is a suitable tracer for the study of exchange processes between the upper troposphere and the lower stratosphere (STE). These processes are described by different models e.g. the tropical pipe model (Ref. 1), where upward transport of tropospheric air into the stratosphere occurs in the inner-tropical convergence zone (ITCZ) and downward transport is supposed to appear in middle and high latitudes. In these altitudes water is chemically inert and thus an indicator on the source of observed air masses. Comparatively dry air parcels in the tropical lower stratosphere are likely to have tropospheric origin and relative dry air-masses in the midlatitude upper troposphere may originate from the stratosphere.

With this background our aim is to derive well resolved water vapour profiles for the UT/LS-region. With its global coverage MIPAS/ENVISAT is a suitable tool to map water vapour distributions and use these results to investigate STE and radiative budget.

2. MICROWINDOW SELECTION

Successful retrieval depends on the appropriate selection of microwindows. In order to obtain good results it is necessary to use spectral intervals containing maximum information on the target quantities while they are affected by a minimum of random and systematic error sources. To achieve this goal we follow the approach by (Ref. 2), which provides sets of optimized microwindows for user defined measurement scenarios.

For the selection of microwindows the following assumptions have been made: The chosen observation scenario is the MIPAS standard scenario with limb scanning altitude steps of 3 km in a range from 5 to 23 km. For the retrieval we assumed that it will be performed on these tangent altitudes within a global fit approach. As a reference atmosphere, tropical conditions have been used. In this case the tropopause occurs at about 17 km and the hygropause at about 20 km height.

Two different cases have been considered for the retrieval scenario: In the first case water vapour was assumed to be the only retrieval parameter. In the second case temperature (T) and H_2O were assumed to be jointly fitted. Proper microwindows show minimized retrieval error Δx_i of the target parameter i. In our first case the water vapour profile is the target parameter vector X with the dedicated error vector ΔX.

The retrieval error Δx_i for each target quantity i can be expressed by the equation

$$\Delta x_i = \sqrt{\sigma_i^2 + \sum_{j=1}^{j_{max}} (\Delta x_{i,j})^2} \qquad (1)$$

σ_i^2 is the ith diagonal element of the retrieval covariance matrix S_x. Without application of of any regularisation, S_x is given by

$$S_x = (K^T K)^{-1} K^T S_y K (K^T K)^{-1}, \qquad (2)$$

Table 1: Assumed systematic uncertainties for the microwindow selection and the retrieval error assessment

Source of error	Troposphere	Lower Stratosphere
H_2O	200%	40%
CO_2	0.5%	0.5%
O_3	200%	150 %
N_2O	3%	50%
CH_4	3%	15%
HNO_3	150%	150%
NO_2	1000%	1000%
N_2O_5	1000%	150%
$ClONO_2$	250%	60%
NH_3	1000%	1000%
HNO_4	1000%	150%
ClO	300%	1000%
OCS	10%	50%
HOCl	1000%	200%
HCN	10%	50%
C_2H_2	50%	150%
C_2H_6	40%	150%
CCl_4	10%	70%
COF_2	500%	200%
SF_6	10%	30%
CFC-11	10%	70%
CFC-12	10%	70%
HCFC-22	10%	70%
SO_2	1000%	1000%
H_2O_2	1000%	1000%
CF_4	5%	5%
CO	70%	40%
NO	300%	300%
Offset	200 $\frac{nW}{cm^2\ sr\ cm^{-1}}$	200 $\frac{nW}{cm^2\ sr\ cm^{-1}}$
Frequency shift	$1.0 \cdot 10^{-03}$ cm^{-1}	$1.0 \cdot 10^{-03}$ cm^{-1}
Line of sight	0.2 km	0.2 km
Scale	$2.0 \cdot 10^{-03}$	$2.0 \cdot 10^{-03}$
Temperature	3 K	3 K

and $\Delta x_{i,j}$ is the i^{th} component of the error vector ΔX_j due to the error source j:

$$\Delta X_j = (K^T S_y^{-1} K)^{-1} K^T S_y^{-1} (y_{err,j} - y_{ref}) \qquad (3)$$

where K is the Jacobian matrix, S_y the measurement covariance matrix, and j_{max} is the number of *a priori* errors.

Error sources under consideration are volume mixing ratios (vmr) of interfering species, line of sight, frequency shift, and radiometric calibration in terms of offset and scale factor. In the case of water vapour-only retrieval temperature uncertainty is handeled as error source, too. The assumed errors for the individual sources are listed in Tab. 1.

Combination of several microwindows was done in order to minimize the resulting retrieval error for each tangent height.

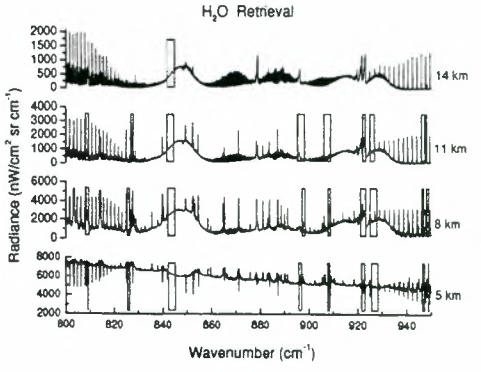

Figure 1: Selected microwindows in MIPAS channel A for H_2O-only retrieval

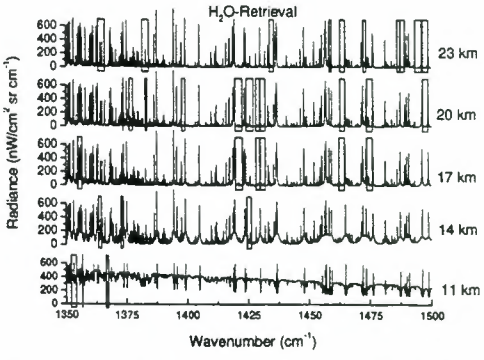

Figure 2: Selected microwindows in MIPAS channel B for H_2O-only retrieval

Selected optimized microwindows differ partly between altitudes. A selection of microwindows for the H_2O-only retrieval case are shown in Figs. 1 and 2. In the UT/LS region a high number of interfering signals contribute to the signals of the target parameter. Saturated lines and increasing optical density of the atmosphere give reasons to examine joint retrieval scenarios.

Joint retrieval with strong interfering species were performed and microwindows were selected accordingly. Simultaneous retrieval of H_2O together with N_2O or CH_4 did not improve the retrieval in terms of total retrieval error.

As saturated lines and radiation continuum show high temperature dependence, microwindows were selected for the case of joint retrieval of water vapour and temperature. The selected microwindows are shown in Figs. 3 and 4 for the same spectral ranges as for Figs. 1 and 2 . Under consideration of temperature as additional retrieval parameter different microwindows than in the case of H_2O-only retrieval were found. While optimized microwindows for the H_2O-only and the H_2O-T joint fit case have a lot of transitions in common, the joint fit microwindows are typically wider; spectral regions where the atmosphere is quite opaque, typically at the line centers or in the vicinity of strong lines, can better be utilized.

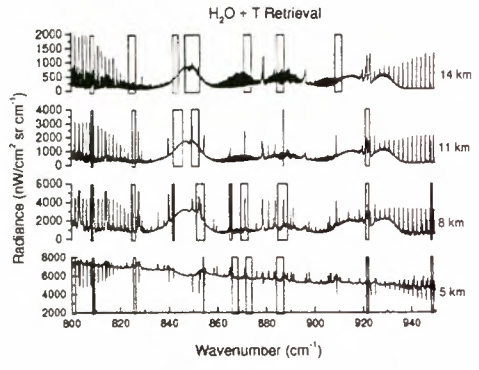

Figure 3: Microwindows in MIPAS channel A for H_2O and temperature joint fit

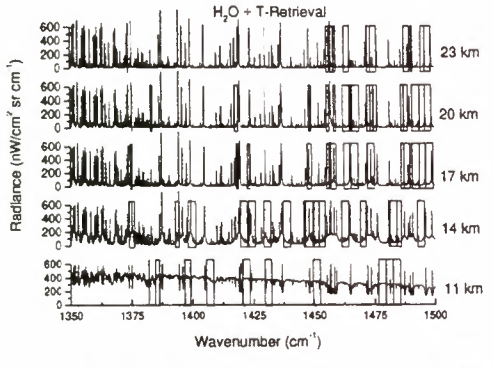

Figure 4: Microwindows in MIPAS channel B for H_2O and temperature joint fit

3. ESTIMATED RETRIEVAL ERRORS

The possibility to distinguish different air masses and interesting areas in the UT/LS is the driving force in posing requirements to measurement accuracy. Tropopause temperatures in the tropics show values below 200 K. Thus air parcels on their way from the troposphere into the stratosphere are freeze dried. According to this effect, tropical air in the lower stratosphere is dry compared to subtropical stratospheric air. Inside of the "tropical pipe" (Ref. 1) volume mixing ratio values of below 3.7 ppmv can be found. Outside of this "pipe" vmrs increase up to 4.5 ppmv (Ref. 3). To resolve horizontal gradients and to distinguish tropical and extra-tropical air errors smaller than 10% in the water vapour retrieval would be appropriate. With this accuracy the hygropause could be resolved and quantified.

The estimated retrieval errors vary for the individual tangent altitudes. In Fig. 5 the resulting retrieval errors for each height are shown. Obviously the joint-retrieval of water vapour and temperature provides significantly better results. In the following, these results are discussed.

The retrieval in the tropopause and hygropause region is not very accurate (20% (H_2O + T joint fit) to 30% (H_2O-only retrieval)). This is due to very low temperatures below 200 K and resulting low radiances in the tropopause region. The very small vmr values in the hygropause with increasing values above this minimum in 20 km complicate the water vapour retrieval since the sensitivity of the signal to the target quantity is small. These errors do not satisfy the desirable accuracy of 10%.

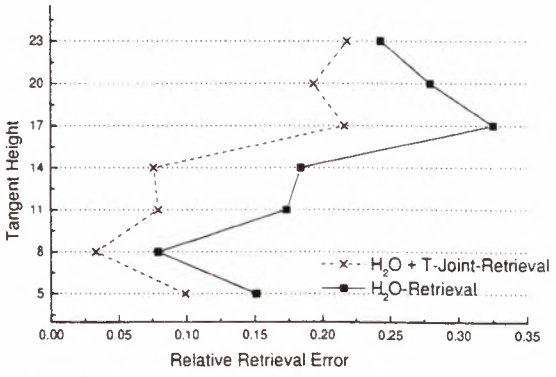

Figure 5: Errors at different tangent levels for the H_2O only and the H_2O + T joint fit case.

As temperature and concentrations increase with decreasing tangent heights the resulting radiances become stronger. This results in a significantly better retrieval accuracy of about 7% (H_2O + T) and 17% (H_2O-only) at 14 and 11 km tangent height, respectively. For the joint fit case the desired accuracy can be achieved.

At tangent altitude 8 km the retrieved results are very good. The estimated error is below 10% (3% (H_2O + T joint fit)/7%(H_2O-only retrieval)).

At 5 km tangent height the results become worse again due to the dominance of the continuum radiation in the spectra. Saturation effects reduce the spectral sensitivity. The sensitivity of the spectrum to changes at levels above the tangent height is significantly higher than the one related to changes at the tangent level.

As can be seen in Fig. 5, the joint retrieval of water vapour and temperature leads to a better retrieval accuracy at all retrieval levels. The reason is that especially at their centers, saturated lines are highly temperature dependent. The measured intensity is primarily determined by the atmospheric temperature distribution. Variations of vmr only influence the line-wings. Retrieval of H_2O only avoids this source of error by restriction of the microwindows to the line wings. On the contrary, optimum microwindows for the joint-fit case containing strong lines are wider and include the line center which makes the retrieval more robust.

The temperature retrieval performed simultaneously with the vmr retrieval provides the radiance temperature for the individual line which does not necessarily coincide with the expected value which would be the mass-weighted (Curtis-Godson) temperature in case of optically thin lines. Especially in layers with high vertical temperature gradient or saturated spectra the observed H_2O radiance temperature may differ from the Curtis-Godson mean and vary from line to line. Moreover, the temperatures retrieved in a prior step of processing are of limited accuracy for several reasons and these errors directly map onto the water vapour retrieval, in particular in the case of saturated H_2O lines.

By joint fit of H_2O and T these uncertainties are avoided. The accuracy of the simultaneously retrieved temperature is below 2 K and thus significantly below the assumed uncertainty of 3 K used in the H_2O-only retrieval. Above the hygropause level the difference between the joint-retrieval and vmr-only retrieval becomes smaller. As the number of saturated lines decreases, the influence of temperature on the results is smaller.

4. VERTICAL RESOLUTION

Water vapour structures occuring in the UT/LS-region show comparatively small horizontal and vertical extention. Some of these small scale features are important for STE processes. Observation of these structures provides information on magnitude and intensitiy of exchange processes. For example, in regions characterized by tropopause foldings or cut-off lows the small scale downward transport of dry stratospheric air might be observed in the comparatively moist tropospheric air. Thus assessment of the vertical and horizontal resolution of MIPAS/ENVISAT is required. Along the satellite's flight path the horizontal resolution of MIPAS is limited by the line of sight on its way through the tangent layer, by the satellite's speed and the time passing between two successive limb scans. Furthermore horizontal resolution is limited by the flight path with successive orbits separated by 2000 to 3000 km.

Vertical resolution is dominated by the vertical field of view (FOV), the tangent altitude spacing and possible regularization in the retrieval process. The MIPAS instrument FOV is a trapezoid with sidelengths of 4 km and 3 km. The distance of successive limb steps determines the vertical resolution. The use of smaller altitude steps increases the vertical resolution. At altitude steps smaller than the vertical field of view, uncertainties at one tangent layer affect the neighbouring layers. Thus, an increase in vertical resolution is accompanied by a decrease of accuracy.

The selection of a suitable retrieval base also determines the resolution. As shown by (Ref. 5) the used retrieval base influences the results noticeably. Different combinations of retrieval bases and tangent altitude steps lead to different results according to accuracy and resolution.

One way to assess vertical resolution is the usage of so called averaging kernel matrices described by (Ref 4). The averaging kernel matrix is given by:

$$A = (K^T S_y^{-1} K + \lambda L^T L)^{-1} K^T S_y^{-1} K = K^{@} K \qquad (4)$$

Here $K^{@}$ is the generalized inverse of the matrix K. L is a regularisation operator and λ is a Lagrangian multiplicator. This averaging kernel matrix represents the smoothing effect of applied regularization on the achievable resolution. In our scenario the global-fit retrieval method is chosen; thus, no regularization is applied, but the solution is kept stable by the choice of a coarse retrieval grid, which usually is identical to the measurement grid. The observation assumed was a MIPAS-standard mode with 3 km altitude steps and retrieval performed on these tangent heights. Using this retrieval base the inverse problem is quite good determined. Then A is by definition unity according to Eq. 4.

Thus, another way to calculate the averaging-kernel-matrix is needed which reflects smoothing through the use of the coarse grid. We chose a methodology similar to that described in (Ref. 5). The reference profile of the target parameter is given on a grid finer than the retrieval grid. On a grid-point l of this highly resolved profile a disturbance is applied. The related spectra for this disturbed profile are calculated on all tangent levels i. For these disturbed spectra the correction vector ΔX_l related to a disturbance in level l compared to the reference profile X_{ref} is calculated by:

$$\begin{aligned} \Delta X_l &= (X_l - X_{ref}) \\ &= (K^T S_y^{-1} K)^{-1} K^T S_y^{-1} (Y_l - Y_{ref}) \end{aligned} \qquad (5)$$

ΔX_l is the response of the retrieval on the coarse grid to a disturbance in altitude l in the reference profile. Y_l represents the spectra of all tangent heights related to the perturbation in level l. The vectors ΔX_l are calculated for each level l in the reference profile i. They are normalized and used as column-vectors of a matrix A which is a kind of averaging-kernel-matrix of dimension $l_{max} \times i_{max}$, where i_{max} is the number of retrieval grid levels and l_{max} the number of fine-grid-levels, where $l_{max} > i_{max}$. The row i of this matrix give an assessment how much the value in the fine-grid-point l contributes to the retrieval result on a retrieval level i. This means consideration of the influence of a coarse retrieval grid on the resolution.

These rows show a broadend peak. The width of this peak can be used to determine the vertical resolution. The definition of the resolution is not unique (Ref. 5). Here the so-called modulation transfer functions (MTF) are applied to the rows of the averaging-kernel-matrix. This is the Fourier transform of the rows of the averaging-kernel-matrix. The resolution is defined as the reciprocal of twice the frequency at which the value of the MTF drops on 50% of the starting value.

First calculations have been applied to simplified scenarios. Studies to more realistic cases are ongoing. These averaging kernels shall be used to do a trade-off between vertical resolution and resulting retrieval error. This trade-off will be done for different retrieval scenarios with retrieval levels offset against the measurement grid, retrieval levels more dense and more coarse compared to the measured tangent levels then requiring regularization. Also different measurement scenarios with fine and coarse grids, with high and low spectral resolution shall be assessed. Trade-off for different combinations of retrieval bases and measurement scenarios are to be made. In these cases we will investigate the impact of regularization.

REFERENCES

1. Plumb RA 1996, A "tropical pipe" model of stratospheric transport. *J. Geophys. Res.*, 101, D2, 3957–3972.

2. von Clarmann T & Echle G 1998, Selection of optimized microwindows for atmospheric spectroscopy. *Appl. Opt.*, 37, 33, 7661–7669.

3. Chiou EW & al. 1993, Intercomarison of stratospheric water vapor observed by satellite experiments: Stratospheric aerosol and gas experiment II versus limb infrared monitor of the stratosphere and atmospheric trace molecule spectroscopy. *J. Geophys. Res.*, 98, D3, 4875–4887.

4. Rodgers CD 1976, Retrieval of atmospheric temperature and composition from remote measurements of thermal radiation. *Rev. Geophys. Space Phys.*, 14, 4, 609–624.

5. Carli B & al. 1998, Study of the retrieval of atmospheric trace gas profiles from infrared spectra. Technical report, European Space Agency. Final Report of ESA Contract 12055/96/NL/CN.

Evidence of Troposheric BrO from Stratospheric BrO Profile Measurements and Total BrO Measured from Ground or Satellite (GOME)

Pfeilsticker, Klaus et al.
IUP, University of Heidelberg, Germany

Stratospheric BrO profiles were measured at different latitudes and in different seasons in 1996/97 during three flights of the LPMA/DOAS balloon gondola (LPMA\-/Laboratoire Physique Mol\'{e}culaire et Application and DOAS/Differential Optical Absorption Spectrometry).

Overall the measured BrO profiles are found to agree well with those formerly measured using the resonance flourescence in-situ technique, and with predictions based on photochemical model calculations. Conversely collocated ground-based and satellite total atmospheric BrO measurements, however, show significantly more total atmospheric BrO (50 - 100$\%$) than the integrated stratospheric BrO balloon profiles can account for. This indicates a global tropospheric BrO background, estimated at 1~-~2~ppt.

ATMOSPHERIC TRACE GAS MEASUREMENTS FROM GOME AND SCIAMACHY

K. Chance, R.J.D. Spurr, and T.P. Kurosu

Harvard-Smithsonian Center for Astrophysics
Atomic and Molecular Physics Division
60 Garden Street, Cambridge, Massachusetts, USA
e-mail: kchance@cfa.harvard.edu

ABSTRACT

We review Smithsonian Astrophysical Observatory (SAO) developments for GOME and SCIAMACHY data analysis and algorithm development and update recent progress on a selection of particular problems currently being addressed. Developments in data analysis and algorithm development include: The initial UV/Vis/IR measurement sensitivity analyses for GOME and SCIAMACHY; discovery of the now-standard method for ozone profile determination from GOME nadir measurements; development of the full molecular physics of the Ring effect, along with re-parameterization of the wavelength-dependent index of refraction and Rayleigh scattering coefficients, and re-analysis of ground-based solar FTS measurements to produce a high-resolution Fraunhofer reference spectrum (contributions to the ESA Study of the Ring Effect); intrinsic wavelength calibration studies; and discovery of the correction for undersampling of the GOME instrument. Current GOME-related science studies at the SAO include: Development of operational-speed ozone profile determinations; improvements in trace gas fitting techniques; and climatology and pollution studies on O_3, NO_2, BrO, OClO, H_2CO, SO_2, and aerosols.

1. INTRODUCTION

The SAO has been involved on first SCIAMACHY, and then GOME, since their inceptions. This conference presentation is intended to summarize and provide appropriate references for some of our past developments and contributions, as well our current research and future directions. Additional information on our research presented at this conference includes cloud parameterization (Ref. 1), improved climatologies and air mass factors for O_3 and NO_2 (Ref. 2), and participation in the overall development of the SCIAMACHY Level 1-2 operational processor development (Ref. 3). More extensive information (as well as figures!) can be found in these and our other references.

In the beginning of SCIAMACHY, and for the first several years, the program was largely carried on by J. Burrows and W. Schneider of the Max Planck Institute for Chemistry in Mainz, Germany (MPI) and K. Chance of the SAO, with support from D. Perner, P. Crutzen, C. Brühl, U. Platt, and several others. Early support on aerosols, for example, came from C. Muller of the IASB.

SAO calculated the sensitivities for measurements of molecules and aerosols, with extensive input from the other investigators. J. Geary of the SAO provided estimates of the realistic capability for measurements using (then) modern array detectors based upon experience in the design and operation of astronomical instruments. Sensitivities were calculated by forward spectroscopic modeling and retrieval calculations using these estimates, an initial instrument model developed by the investigators, and abundances calculated with an MPI atmospheric model, provided by C. Brühl.

2. SENSITIVITY STUDIES

The results from the initial sensitivity studies are tabulated in the initial SCIAMACHY proposal (Ref. 4). For those species measured by GOME, the early predictions have been remarkably good. We expect that the same will be true for additional measurements to be made by SCIAMACHY.

BrO One very nice surprise of these initial sensitivity studies was being able to show that BrO globally can be measured globally by SCIAMACHY (and also, of course, by GOME). This has turned out to be the case. Several groups, including our own, are now able to do this routinely. Of course, we did not predict the blooming events in polar springtime BrO that several groups (Heidelberg, Bremen, and SAO, at least) have now seen with GOME data (Refs. 5-8). BrO is now also being studied as a potential operational product (Ref. 9).

SO_2 has turning out to be somewhat better for measurement than initially predicted, although it possesses some particular challenges. Several groups, including the SAO, are readily able to measure SO_2 output from volcanos in GOME data. Our current status is that we have a measurement sensitivity for the total slant column of about 2 Dobson Units (DU; 1 DU = 2.6868×10^{16}), with near-term prospects for a factor of three improvement. SO_2 retrieval is complicated by the fact that the fitting window is located near to the beginning of GOME channel 2, where the instrument transfer function width varies considerably (Ref. 10 and C. Caspar, private communication, 1997).

OClO was difficult to predict because we did not know the photolysis behavior in twilight well enough, but it is seen robustly in GOME through a range of polar springtime conditions and beyond by several of the research groups in GOME (Ref. 11).

ClO is very difficult to measure, although we have seen it (just barely) in ozone hole conditions.

NO_2 is measured operationally. There have been some algorithm difficulties, but these have recently been solved by DLR, with input from SAO and other investigators from the GOME Scientific Advisory Group; remaining difficulties with the climatology, needed to obtain vertical columns from slant columns, have been addressed earlier in this conference (Ref. 2).

H_2CO has been measured by several groups, including the SAO (Ref. 12). It has turned out to be somewhat better than the initial predictions, permitting measurement of background concentrations. SAO currently working on determining a global climatology of formaldehyde as part of the NASA Atmospheric Chemistry Modeling and Analysis Program (ACMAP), in collaboration with the tropospheric modeling group from Harvard University, and NASA/GSFC. The fitting is not yet optimized, so no results are presented here.

O_3 The most exciting discovery from the initial SAO sensitivity studies was that we could measure ozone profiles, including the tropospheric component of the ozone, from nadir measurements - as well as how to do it. This came about from the difficulty in quantifying the sensitivity for measuring ozone in the UV Huggins bands, because of their strong temperature dependence (this is due to the onset of vibrational hot band absorption in these only partly predissociated bands at increasing temperatures). It was then realized that the problem could be turned around: if the temperature structure of the atmosphere is known well enough (3-5 K turns out to be sufficient) information is gained on the distribution of the ozone, particularly below the (usual) 22-23 km maximum and down into the troposphere. Adding this to the height information from penetration depth (the BUV information, Refs. 13,14) now gives complete ozone profiles. Fitting of the full spectrum (or carefully selected portions) with proper modeling and retrieval thus produces the entire ozone profiles, at about atmospheric scale-height resolution, down to the ground or cloud-top. Once the cross sections and the instrument calibration are fully justified across the wavelength range, measurements in the visible Chappuis bands will help to improve the accuracy further at the lower altitudes because the full penetration at these wavelengths provides a better lock on the total ozone column.

These studies went into the SCIAMACHY proposal, and later into other documents, including the GOME Interim Science Report (Refs. 4,15,16). We later did a complete least-squares retrieval study on synthetic data, at the beginning of the 1990's (although it has only recently been published, Ref. 17) showing the capability in detail. The Rutherford Appleton Laboratory took up the development after the initiation of the GOME program, applying the full optimal estimation machinery to the retrieval (Refs. 18,19) and have produced very impressive results (Ref. 20). More recently, other groups have have implemented the method, with results that are also very gratifying (Refs. 21-23). SAO has provided an operational prototype of the method (Ref. 24) and is currently developing improvements to speed it up to operational levels. We hope within the year to have an improved implementation, based on some further ideas now under development, that runs at a speed comparable to the trace gas fitting methods we have developed.

3. ISSUES IN DATA ANALYSIS AND ALGORITHM DEVELOPMENT

3.1. The Ring Effect

The Ring effect is very important for the fitting of UV atmospheric spectra; it can easily be an order of magnitude larger in GOME spectra, for example, than the absorptions of trace gases being fitted. SAO participated in the ESA-sponsored Ring effect study (Ref. 25), developing the complete molecular physics for the rotational Raman scattering that is the inelastic component of Rayleigh scattering and the major part of the Ring effect. The cross sections for individual transitions in N_2 and O_2 are derived statistically and quantum mechanically (including the triplet structure of the O_2 lines). The wavelength-dependent index of refraction, the Rayleigh scattering cross sections and phase functions, and the polarizability anisotropies were updated using the best currently available measurements and calculations (Ref. 26). This was all developed for the first time into a comprehensive database which can be used at any wavelength and scattering angle. It is combined with a high resolution solar Fraunhofer spectrum (Ref. 27) so that Ring effect cross sections can be directly calculated (using the computer program supplied) for use in fitting of atmospheric spectra. All of the relevant equations describing the detailed Ring effect properties, including their wavelength and polarization dependences, were also assembled in this work for convenient reference. The comprehensive results have since been published independently (Ref. 28).

3.2. Wavelength Calibration

In the fitting of trace gases, SAO has re-examined the underlying details of the physics as well as the basic principles of the retrieval. For example, we proposed that ways be found to avoid shifting and squeezing of reference spectra (a common practice in DOAS fitting) in GOME data processing. In order to help accomplish this, SAO developed methods for the independent absolute

vacuum wavelength calibration of GOME irradiance and radiance spectra (in collaboration with C. Caspar of ESTEC, Ref. 10) that are good to several times 10^{-4} nm (better than 1/100 of a GOME detector array pixel) in parts of the GOME wavelength range - for example, where BrO and H_2CO are fitted. This also permits accurate re-determination of the GOME slit (ITF) function, usually to better than 1%. The methods use the Fraunhofer reference spectrum of Ref. 27, and either directly fit or cross-correlate to obtain wavelength calibration. Coupled with better determinations of the wavelength calibration of reference spectra (in the example of BrO, by colleagues at Harvard University), we are now able to fit spectra without shifting and squeezing.

3.3. Correction for Spectral Undersampling by GOME

SAO has had many years of experience in fitting atmospheric spectra, sometimes for very small spectroscopic features. This is usually accomplished by directly calculating spectra and iterating to match the measurements to within preset convergence criteria. It was decided to try this approach before adopting the spectral filtering used in DOAS, and found that it works very well. Like our colleagues who employ the DOAS fitting method, we found that that there are substantial systematic features remaining in the fitting residuals. We have been able to demonstrate that most of these systematic residuals are due to undersampling of the spectrum by GOME and that they can be reduced (by more than 90% in favorable cases, such as the region used for fitting BrO) by the use of undersampling corrections calculated entirely using an oversampled Fraunhofer reference spectrum (Ref. 27) and properly re-sampling - that is, without the use of GOME data, except for the use of the GOME slit function width determined during wavelength calibration (see above). This was first presented at the GOME/SCIAMACHY data and algorithm working session in April 1998 and is illustrated in Ref. 7. It is also the subject of a poster at this meeting (Ref. 29). This correction improves the fitting of GOME data for trace gases, including the fitting statistics and uncertainties, by a full order of magnitude. It has has allowed us to make very precise quantitative measurements of trace gases from GOME and to provide the full fitting statistics and uncertainties from the fitting (Ref. 7). This undersampling correction is now also being taken up by other groups fitting GOME data, including its application to DOAS fitting, with similar improvements, now permitting them to make quantitative trace gas measurements from GOME as well, and to do so without smoothing the spectra before fitting (A. Richter and J.P. Burrows, *private communication*, 1998).

4. CONCLUSIONS

Work currently in progress at the SAO includes:

- Determination of global climatology for BrO.
  - Tropospheric BrO is being investigated from correlation with clouds and the use of orographic techniques. The best current estimate gives $\leq$0.5 pptv BrO below cloud top level.
- Optimizing of H_2CO fitting, and global climatology and pollution studies.
  - An ACMAP project, in collaboration with Harvard University and NASA/GSFC.
- Optimizing of SO_2 fitting and volcano and pollution studies.
  - Positive correlation with O_3 being investigated.
  - Background SO_2 and industrial pollution should be measurable.
  - Additional algorithmic difficulties must be resolved.
- Enhancement of the ozone profiling capability of GOME.
  - Operational speed should be obtained within a year, using a new approach being developed at the SAO.
  - Open to active collaboration with GOME investigators.
- Development of the Cloud Retrieval Algorithm for GOME (CRAG).
  - Subject of a presentation at this conference (Ref. 1).

ACKNOWLEDGEMENTS

We gratefully acknowledge the cooperation and support of the European Space Agency and the German Remote Sensing Data Center; particular thanks are due to A. Hahne, C.J. Readings, and W. Balzer. Research at the Smithsonian Astrophysical Observatory (Harvard-Smithsonian Center for Astrophysics) was supported largely by NASA, through Grants NAGW-2541 and NAG5-3461.

REFERENCES

1. Kurosu, T & al, 1999, CRAG - Cloud Retrieval Algorithm for ESA's Global Ozone Monitoring Experiment, this conference.

2. Spurr, R, 1999, Improved climatologies and new air mass factor look-up tables for O_3 and NO_2 column

retrievals from GOME and SCIAMACHY backscatter measurements, this conference.
3. Spurr, R, 1999, SCIAMACHY ATBD - Level 2, this conference.
4. Burrows, J P & al 1988, SCIAMACHY - A European proposal for atmospheric remote sensing from the ESA polar platform, Max Planck Institute for Chemistry, 55122 Mainz, Germany.
5. Hegels, E & al, 1996, Satellite measurements of halogen oxides by the Global Ozone Monitoring Experiment, GOME, on ERS2: Distribution of BrO and comparison with groundbased observations, *Proc. XVIII Quadrennial Ozone Symposium.*
6. Richter, A & al, 1998, GOME observations of tropospheric BrO in northern hemisphere spring and summer 1997, *Geophys. Res. Lett. 25* 2683-2686.
7. Chance, K, 1998, Analysis of BrO measurements from the Global Ozone Monitoring Experiment, *Geophys. Res. Lett. 25*, 3335-3338.
8. Hegels, E & al, 1998, Global distribution of atmospheric bromine-monoxide from GOME on earth observing satellite ERS-2, *Geophys. Res. Lett. 25*, 3127-3130.
9. Van Roozendael M & al, 1999, Development of a bromine oxide product from GOME, this conference.
10. Caspar, C & Chance, K, 1997, GOME wavelength calibration using solar and atmospheric spectra, *Proc. 3rd ERS Symp. on* Space at the Service of our Environment, Ed. T.-D. Guyenne and D. Danesy, European Space Agency publication SP-414, ISBN 92-9092-656-2, 600-614.
11. Wagner, T & al, 1999, Measurement of atmospheric BrO and OClO from GOME, this conference.
12. Thomas, W & al, 1998, Detection of biomass burning combustion products in Southeast Asia from backscatter data taken by the GOME spectrometer, *Geophys. Res. Lett. 25*, 1317-1320.
13. Singer, S F & Wentworth, R C, 1957, A method for the determination of the vertical ozone distribution from a satellite, *J. Geophys. Res. 62*, 299-308.
14. Heath, D F & al, 1975, The solar backscatter ultraviolet and total ozone mapping spectrometer (SBUV/TOMS) for Nimbus G, *Opt. Eng. 14*, 323-331.
15. Chance, K V & al, 1991, Retrieval and molecule sensitivity studies for the Global Ozone Monitoring Experiment and the SCanning Imaging Absorption spectroMeter for Atmospheric CHartographY, *Proc. S.P.I.E., Remote Sensing of Atmospheric Chemistry, 1491,* 151-165.
16. Burrows, J P & al, 1993, *Global Ozone Monitoring Experiment Interim Science Report*, ed. T. D. Guyenne and C. Readings, Report ESA SP-1151, ESA Publications Division, ESTEC, Noordwijk, The Netherlands, ISBN 92-9092-041-6.
17. Chance, K V & al, 1997, Satellite measurements of atmospheric ozone profiles, including tropospheric ozone, from UV/visible measurements in the nadir geometry: A potential method to retrieve tropospheric ozone, *J. Quant. Spectrosc. Radiat. Transfer 57*, 467-476.
18. Munro, R & al, 1992, Ozone profile retrievals from the ESA GOME instrument, *Proc. XVII Quadrennial Ozone Symposium.*
19. Rodgers, C, Retrieval of atmospheric temperature and composition from remote measurements of thermal radiation, *Rev. Geophys. Space Phys. 14*, 609-624, 1976.
20. Munro, R & al 1998, Direct measurement of tropospheric ozone distributions from space, *Nature 392*, 168-171.
21. Eichmann, K-U & al, 1998, Ozone profile distributions in the Arctic from GOME satellite observations during spring 1997 and 1998, *Proc. S.P.I.E., Satellite Remote Sensing of Clouds and the Atmosphere III, 3595*, 357-366.
22. Hoogen, R & al, 1998, Validation of ozone profiles from GOME satellite data, *Proc. S.P.I.E., Satellite Remote Sensing of Clouds and the Atmosphere III, 3595*, 367-378.
23. van der A, R J & al, 1998, Ozone profile retrieval from GOME data, *Proc. S.P.I.E., Satellite Remote Sensing of Clouds and the Atmosphere III, 3595*, 221-229.
24. Spurr, R J D, 1997, Development of a prototype algorithm for the operational retrieval of height-resolved products from GOME, *Proc. 3rd ERS Symp. on* Space at the Service of our Environment, Ed. T.-D. Guyenne and D. Danesy, European Space Agency publication SP-414, ISBN 92-9092-656-2, 621-628.
25. Burrows, J P & al, 1996, Study of the Ring Effect, Final Report, ESA Contract 10996/94/NL/CN, European Space Agency.
26. Bates, D R, 1984, Rayleigh scattering by air, *Planet. Space Sci. 32*, 785-790.
27. Kurucz, R L & al, 1984, Solar Flux Atlas from 296 to 1300 nm, National Solar Observatory, Sunspot, New Mexico, 240 pp.
28. Chance, K & Spurr, R J D, 1997, Ring effect studies: Rayleigh scattering, including molecular parameters for rotational Raman scattering, and the Fraunhofer spectrum, *Appl. Opt. 36*, 5224-5230.
29. Slijkhuis, S & al, 1999, Calculation of "undersampling correction spectra" for DOAS spectral fitting, this conference.

GOME OBSERVATIONS OF TROPOSPHERIC BRO

Andreas Richter, Folkard Wittrock, and John P. Burrows

Institute of Environmental Physics, University of Bremen, Germany
e-mail: Andreas.Richter@iup.physik.uni-bremen.de

ABSTRACT

Several years of data from the Global Ozone Monitoring Experiment (GOME) have been analysed for BrO absorptions. In both hemispheres, periods with locally enhanced BrO are observed throughout polar spring and are attributed to tropospheric BrO events. Most of the regions with enhanced BrO are located over sea ice and along the coasts of Antarctica and the Arctic Sea, confirming the model of bromine release from sea salt and activation on sea ice or snow. The seasonal variation and the observed columns are similar in both hemispheres indicating that similar mechanisms are operating in the Arctic and Antarctic. Comparable results have been obtained for 1995, 1996, 1997 and 1998, leading to the conclusion that enhanced tropospheric BrO is a typical feature of the polar troposphere in spring.

1. INTRODUCTION

Long-term observations of tropospheric ozone concentrations in polar regions have repeatedly shown periods of low ozone values in spring (refs 20, 4, 30). These "low ozone events" have been reported for both the Arctic and the Antarctic and are believed to be mostly of natural origin. Measurements of filterable bromine showed enhanced Br levels before and during such events (ref 3). More recently the presence of up to 30 pptv of BrO, an active form of bromine has been shown by long-path Differential Optical Absorption (DOAS) measurements (refs 13, 17). Ground-based zenith sky DOAS experiments have also provided evidence for periods of elevated tropospheric BrO in both Arctic (refs 31, 19) and Antarctic spring (ref 15). It now is widely accepted that catalytic cycles invoking BrO are responsible for the majority of the observed ozone losses, smaller contributions being proposed for cycles involving ClO and IO. Some recent modelling studies conclude that locally the rate of ozone loss is well explained assuming that sufficient halogen is present (ref 24). However, the sources of bromine in polar spring are not well understood. Two different sources have been proposed: organic bromine compounds like $CHBr_3$ (refs 3, 16) and sea salt aerosols ((refs 18, 29) and references therein).

With the Global Ozone Monitoring Experiment (GOME) instrument, BrO, one of the key species in polar spring tropospheric ozone depletion can for the first time be monitored globally. These measurements offer a unique opportunity to study the geographical and temporal evolution of the low ozone events and contribute to the continuing search for the sources and mechanisms of bromine release in the polar troposphere.

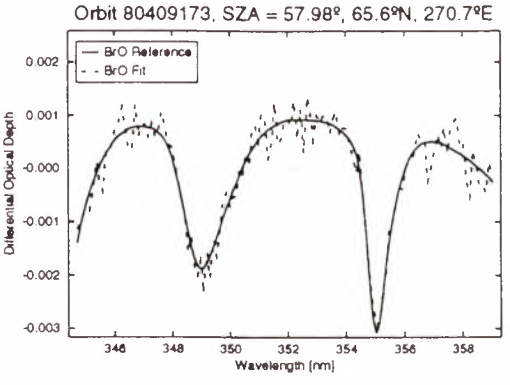

Figure 1. Example of a BrO fit during a tropospheric BrO event. The solid line is the scaled laboratory reference, the dotted line the fit result.

2. DATA ANALYSIS

The GOME is a UV/VIS double monochromator with a spectral range of 240–793 nm and a resolution of 0.2 nm (< 400 nm) and 0.4 nm (> 400 nm). GOME observes the light scattered from the earth's atmosphere and reflected by the ground in near nadir viewing geometry. It operates on board of ERS-2 which is on a sun-synchronous orbit since April 1995. The spatial resolution of GOME is 40×320 km^2 for solar zenith angles (SZA) below 86°. Global coverage is achieved within 3 days at the equator and within 1 day at a latitude of 67°.

The main objective of the GOME instrument is the global measurement of vertical columns of O_3 and NO_2. However, other trace gases including H_2O, SO_2, OClO and HCHO can be retrieved by means of the DOAS technique (ref 7). After the first detection of BrO in GOME measurements (ref 9), several studies of stratospheric and tropospheric BrO from GOME have been performed (refs 14, 27, 22, 8).

In this study, GOME data have been analysed for BrO using the well known DOAS technique developed for ground-based measurements. Calibrated earth shine and solar irradiance spectra were used as provided by ESA through DLR-DFD. In order to get the best spatial resolution, only the three forward scans have been included, limiting the available range of solar zenith angles to values below 86°.

2.1. Spectral fitting

For the BrO retrieval, a spectral fitting window of 344.7 – 359 nm was selected. This spectral range is similar to that used for the ground-based measurements (ref 10) and was chosen to provide large differential BrO signals

and small interference from other absorbers. In the fit, the absorption cross-sections of BrO (ref 28), O_4 (ref 11), NO_2 (ref 5) and O_3 (ref 6) at 221 and 241 K have been used together with a synthetic Ring spectrum (ref 26) compensating the effect of Raman scattering in the atmosphere. The wavelength calibration of BrO has been corrected by +0.17 nm as suggested by (ref 2) and recently confirmed by FTS measurements in Bremen (*O. Fleischmann, private communication*). After cross-calibration with the FTS measurements of (ref 25), both O_3 and NO_2 cross-sections have been shifted by +0.03 nm to correct for an error in wavelength calibration.

The slit function of channel 2 of the GOME instrument is to narrow for sufficient sampling of the spectra with the diode array used as detector. Due to a small doppler shift, GOME earth-shine and direct sun measurements have a systematic difference of approximately 0.008 nm in the wavelength sampling. In addition, small thermal drifts of the instrument calibration have to be corrected in the fit. Therefore, interpolation of the earth-shine spectra is necessary for the analysis, leading to large residuals from undersampling errors. This can be accounted for by either averaging over adjacent spectral points and thereby reducing the undersampling or by fitting a simulated undersampling spectrum as suggested by (ref 8). In this study, an undersampling spectrum and no smoothing were used. One example of a BrO fit result is shown in figure 1. The BrO slant column for this particular pixel is $4.25 \cdot 10^{14}$ molec/cm^2, this large value being attributed to a tropospheric BrO event. For the plot, an averaged residual has been included in the fit to compensate for constant instrument effects. This reduces the residuals but has negligible influence on the retrieved BrO columns. It therefore has not been used in the analysis discussed below.

2.2. Airmass factors

The DOAS fit results are slant columns, i.e., the integral of the absorber concentration along the line of sight. To convert slant into vertical columns, airmass factors (AMFs) have been computed with the radiative transfer model GOMETRAN (ref 23).

2.2.1. Stratospheric airmass factors For solar zenith angles below 70°, the AMF is essentially independent of the assumed vertical profile of the absorber. However, at larger SZA significantly different airmass factors result from different profiles as shown in figure 2. The profiles used for the calculations were taken from two BrO measurements of (ref 12), one at high latitudes in February and one in mid-latitudes in November. Little is known about the latitudinal and seasonal changes of stratospheric BrO profiles. Therefore, the same airmass factor (based on the high latitude profile of (ref 12)) has been used for all latitudes and seasons. Assuming that the two profiles used in figure 2 are extreme cases, the maximum error introduced from the use of a constant airmass factor is of the order of 10% for GOME measurements below 86° SZA.

2.2.2. Tropospheric airmass factors In the wavelength region used for BrO retrieval, a significant part of the

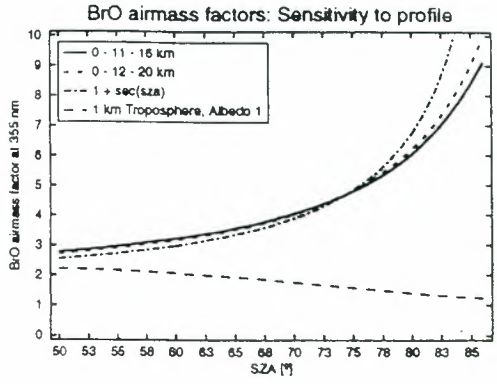

Figure 2. Airmass factors for different vertical BrO profiles. All values are for 355 nm. The two stratospheric profiles have been adapted from (ref 12) and are zero below the tropopause at 11 (12) km, increase linearly to 16 (20) km and are constant above that height.

photons measured by GOME are scattered in the upper troposphere and do not penetrate the atmosphere to the ground. This is particularly true for situations with low albedo, where photons reflected from the ground are only a small contribution to the overall intensity of the earth-shine spectrum. As a result, airmass factors for tropospheric absorbers depend strongly on the albedo as shown in figure 3. For an absorber layer in the lowest 1000 m of the atmosphere, the airmass factor at high sun increases from 0.25 to 2.25 for a change of albedo from 0 to 1. This implies, that GOME measurements in the UV are much more sensitive to tropospheric absorbers above ice than above open water. For solar zenith angles below 50°, the tropospheric and stratospheric airmass factors are of the same magnitude. For lower sun, the sensitivity towards tropospheric absorptions decreases significantly while at the same time the stratospheric airmass factor increases (fig. 2). This implies that tropospheric absorbers are difficult to detect with GOME at low sun (high latitudes in spring, autumn and winter).

2.2.3. Separation of stratosphere and troposphere The BrO slant columns measured with GOME are the sum of both tropospheric and stratospheric columns, weighted with different airmass factors. As BrO is not a strong absorber, the GOME measurements themselves contain not enough information to determine the vertical profile of the molecule.

There are however several arguments which give strong support to the interpretation of the large BrO absorptions as tropospheric events:

- On several occasions, GOME observations of high BrO columns coincide with ground-based measurements of enhanced tropospheric BrO (see *Wittrock et al.* and *Wagner et al.*, this issue for a more detailed validation of GOME BrO measurements).
- The large BrO absorptions coincide with low cloud cover fraction
- Many of the observed BrO events are strongly localised and not associated to the movements of the

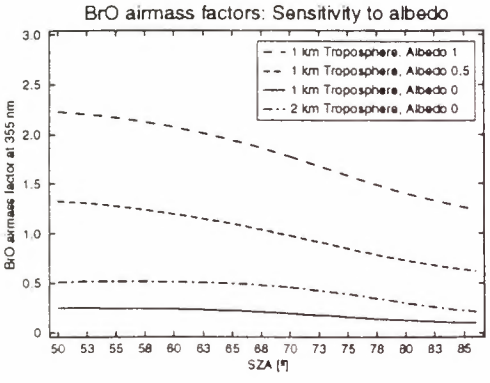

Figure 3. Sensitivity of tropospheric airmass factors to changes in albedo and profile height. All airmass factors are at 355 nm, nadir viewing geometry and include multiple scattering.

polar vortex.

- Assuming a stratospheric origin of the observed BrO peaks would imply stratospheric mixing ratios of more than 30 ppt in some cases, inconsistent with previous measurements and model predictions.

In order to determine the tropospheric BrO column, the stratospheric column has to be estimated and subtracted from the measured signal. Estimates of the stratospheric column can be based on other GOME measurements assuming temporal and/or spatial homogeneity of the stratospheric BrO (ref 22) or from model predictions. Clearly, both approaches can lead to large errors in the derived tropospheric values. In this study, no attempt was made to separate tropospheric and stratospheric columns. Tropospheric BrO events are identified by the magnitude of the total column and stratospheric airmass factors used. Therefore, all plots should be interpreted in a qualitative way only.

2.3. Error discussion

Several error sources have to be considered for the accuracy of the GOME BrO columns: instrumental errors, systematic analysis errors and errors in the airmass factors. Two methods have been used to estimate the random error in the BrO slant columns: the statistical error as determined from the fit and the difference between the three forward scans and the following back scan that covers approximately the same area. Both approaches result in similar values of an absolute error in the BrO slant column of less than $3 \cdot 10^{13}$ molec/cm^2 for an individual pixel.

The main systematic error source in the DOAS fit is the uncertainty in the BrO cross section, which is in the order of 20%. In addition, there are other, smaller error sources like stratospheric temperature changes, the I_0-effect or errors in the wavelength calibration that are discussed in detail in (ref 1). As discussed above, both stratospheric and tropospheric airmass factors for BrO depend on the assumed scenario. In addition, the weighting between tropospheric and stratospheric airmass factor depends on the cloud fraction. Without accurate values for albedo, aerosol loading, cloud fraction and vertical profile of the absorber, uncertainties in airmass factors can exceed 50% and will dominate the total error of the tropospheric BrO columns.

Additional errors arise in the determination of the tropospheric BrO column. As the stratospheric contribution has to be subtracted from the total columns, any error in the estimation of the stratospheric BrO results in an error in the tropospheric column. Local changes in the stratospheric column (resulting for example from changes in tropopause height) can potentially be misinterpreted as tropospheric BrO enhancements.

3. RESULTS AND DISCUSSION

In this study, several years of GOME BrO data have been analysed in the regions poleward of 40° in both hemispheres. To facilitate the discussion of the temporal and spatial behaviour of the tropospheric BrO, monthly averages of vertical BrO columns have been derived. For the conversion from slant to vertical columns, airmass factors based on the high latitude profile described in section 2.2.1 have been used independent of season and latitude. As discussed above, the resulting error is in the order of 10% for stratospheric BrO, but much larger for the tropospheric columns.

3.1. Northern hemisphere

In figure 4, BrO vertical columns in the northern hemisphere are shown for February to July 1998. On average, GOME measures a vertical column of about $6 \cdot 10^{13}$ molec/cm^2 in February and $4 \cdot 10^{13}$ molec/cm^2 in July. This is in good agreement with values from zenith-sky measurements (ref 21), but clearly in excess of model estimates for the stratosphere and the integrated columns from balloon borne measurements. This discrepancy between total and stratospheric columns has prompted the hypothesis of a significant BrO background concentration in the upper troposphere (see *Pfeilsticker et al.*, this issue). However, up to now no direct evidence was found for such a tropospheric BrO layer.

3.1.1. Seasonal variation Starting in late February, localised regions with enhanced BrO columns appear in the GOME data. Most of these measurements are in the Hudson Bay area and along the coastlines of the Arctic Ocean, but in April and May high values are also detected over the arctic ice. The last such events are observed in early June and do not reappear for the rest of the year.

Individual BrO events usually extend over several hundred kilometres and disappear after a few days. This is in agreement with ground-based measurements in Ny-Ålesund showing episodes of high BrO in connection with rapid boundary layer ozone destruction and very low O_3 values for periods of hours to days. However, GOME data show that in some areas the frequency of BrO events is much higher than in Ny-Ålesund or Greenland. In fact, as shown in figure 4, BrO columns along the cost of the Arctic Sea are enhanced by a factor of 1.5 in the monthly

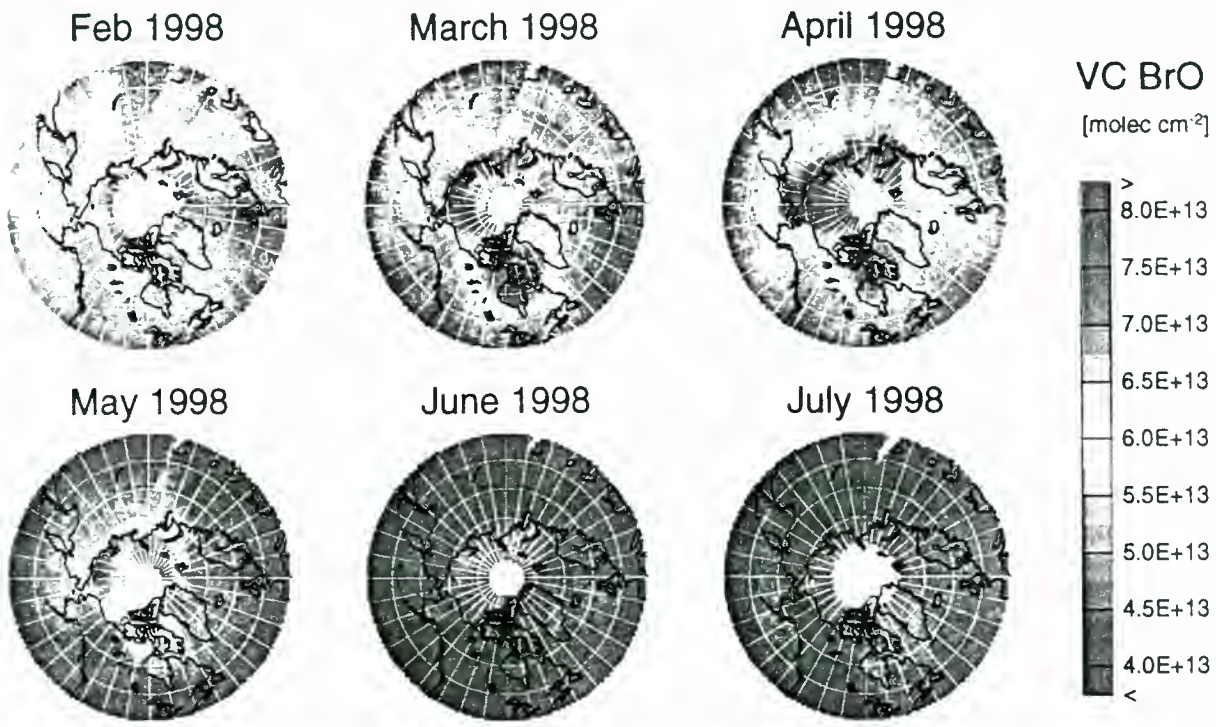

Figure 4. Monthly averages of GOME BrO in the northern hemisphere. Vertical columns have been derived using an airmass factor appropriate for stratospheric BrO. Therefore, tropospheric BrO columns are underestimated at high latitudes.

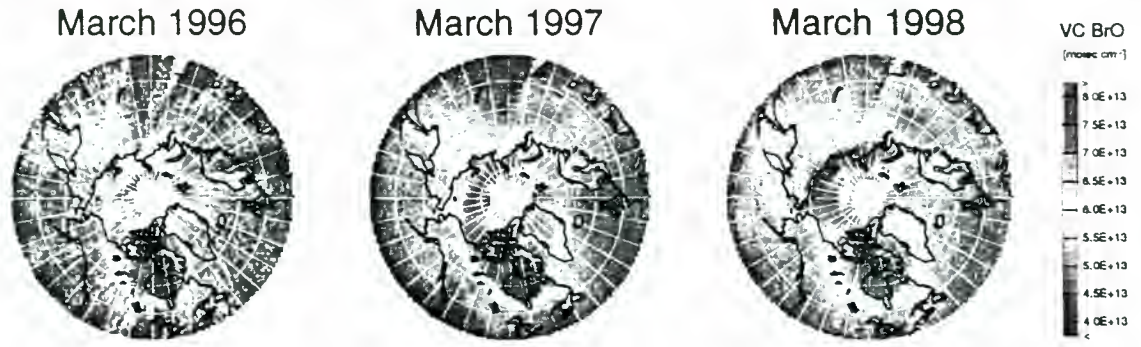

Figure 5: Monthly averages of GOME BrO in the northern hemisphere.

average, indicating the large impact of the BrO events on boundary layer chemistry in the Arctic spring.

Most of the observed BrO events are located near the coast or over the ice cap. This supports the assumption, that bromine is released from sea-salt and that sea-ice (or the snow covering the ice) is involved in bromine activation. Tropospheric BrO events observed by GOME seem to move northwards from February to May, in agreement with the assumption that ice with some cracks is necessary to release bromine. However, as the solar zenith angle increases with season, GOME sensitivity towards tropospheric BrO increases and this could explain part of the observed trend.

3.1.2. Year to year variation In fig. 5, BrO vertical columns are shown for March 1996, 1997 and 1998. As can be seen from the plot, the general pattern and absolute values of the BrO events is comparable from year to year. There are however differences in the number and distribution of the events, which for example were much less frequent along the Russian coast in March 1996 than in 1998. Possible reasons for the differences from year to year are changes in temperature and sea ice cover, but cloudiness is also a factor for measurements from space.

3.2. Southern hemisphere

In figure 6, monthly averages of GOME BrO columns are shown for the southern hemisphere from August 1997 to January 1998. From August to November, BrO events occur frequently in a ring around the Antarctic continent. In late November and December, some periods of enhanced BrO columns are also observed over the Antarctic continent near parts of the coast where the ice breaks up

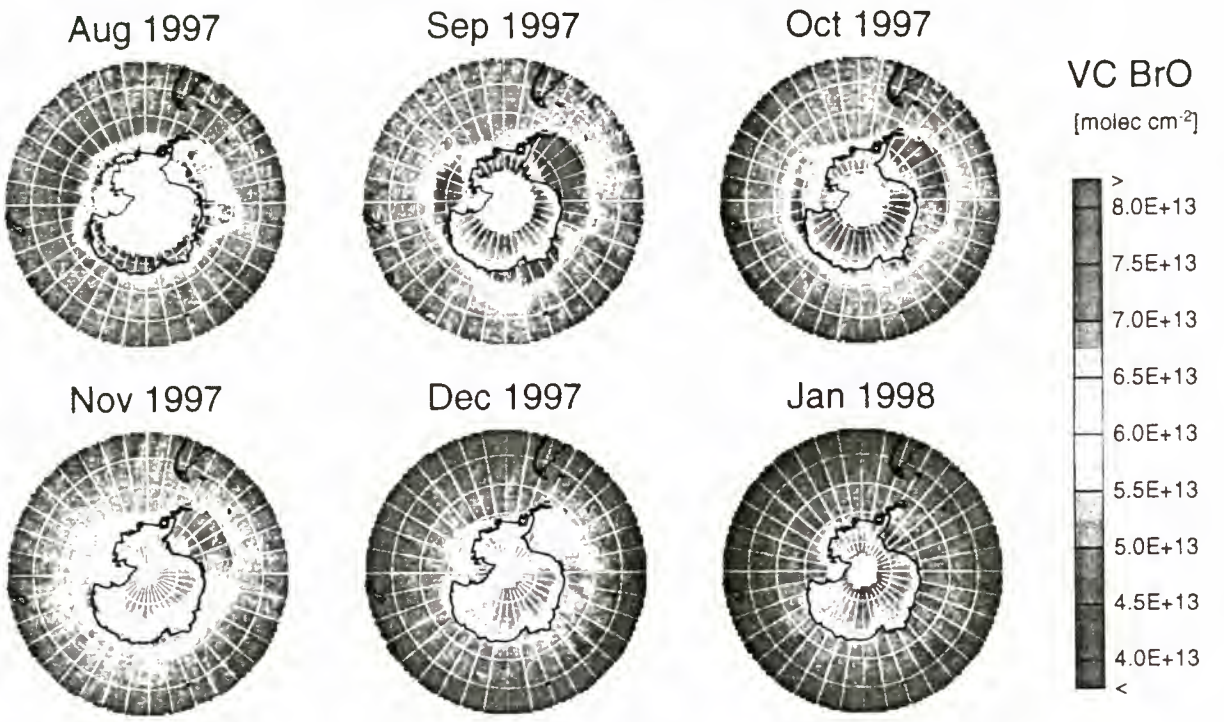

Figure 6. Monthly averages of GOME BrO in the southern hemisphere. Vertical columns have been derived using an airmass factor appropriate for stratospheric BrO. Therefore, tropospheric BrO columns are underestimated at high latitudes.

early. The ring structure of the enhanced BrO explains the small number of tropospheric BrO events observed from ground-based measurements on Antarctica - obviously most of these events are located over the ice. The strong correlation between sea-ice coverage and BrO enhancements is shown in figure 7, where BrO and reflected intensity in the southern hemisphere are compared for September 1995, 1996 and 1997. The intensity of the GOME earth-shine spectra has been averaged over the wavelength interval used for the BrO fit and corrected for the cosine response. In a monthly average, cloud influences are smoothed out and reflectivity gives a good idea of ice coverage. A striking correlation exists between intensity and BrO columns, indicating that BrO enhancements are constrained to the ice covered region. This is similar to the observations in the northern hemisphere and again confirms the model of bromine release over sea ice. However, the pronounced sensitivity of tropospheric airmass factors to changes in albedo can clearly influence this result. If present, BrO events over water would lead to much smaller BrO slant columns than comparable events over ice.

3.3. Comparison of the hemispheres

Both the seasonal variation and the column amounts of the tropospheric BrO in the two hemispheres are comparable. The differences in sea-land distribution are reflected in the spatial pattern of the BrO events and with the exception of the Hudson Bay area, the bulk of the BrO in the northern hemisphere is closer to the pole than in the southern hemisphere. Most of the BrO is observed over sea ice and along the coasts of the continents. The similarity of the BrO distribution in the two hemispheres is an indication that similar chemical and physical processes are involved in the bromine activation in arctic and antarctic spring.

4. SUMMARY AND CONCLUSIONS

Several years of data from the GOME satellite instrument have been analysed for BrO absorptions. Stratospheric BrO columns show a small seasonal variation with a maximum of $6 \cdot 10^{13}$ molec/cm^2 during winter at high latitudes and about $4 \cdot 10^{13}$ molec/cm^2 in summer. Superimposed on the stratospheric columns are events of large BrO enhancements attributed to tropospheric BrO. These events start in early spring and continue for 4 months, both in the southern and in the northern hemisphere. Most BrO enhancements are observed over sea ice and along the coasts of Antarctica and the Arctic Sea. The general pattern is similar in 1995, 1996, 1997 and 1998, but differences in the frequency and the spatial distribution of the events exist, probably because of differences in temperature, sea-ice and cloud coverage.

The presented GOME observations agree well with ground-based observations of sporadic BrO events at coastal stations and continuous O_3 depletion over the arctic ice. The distribution of the BrO enhancements supports the model of bromine release from sea salt and a role of sea-ice in the activation of the bromine. The similarities between the two hemispheres indicate that the same mechanisms could be responsible for the bromine release in the Arctic and Antarctic. From the GOME

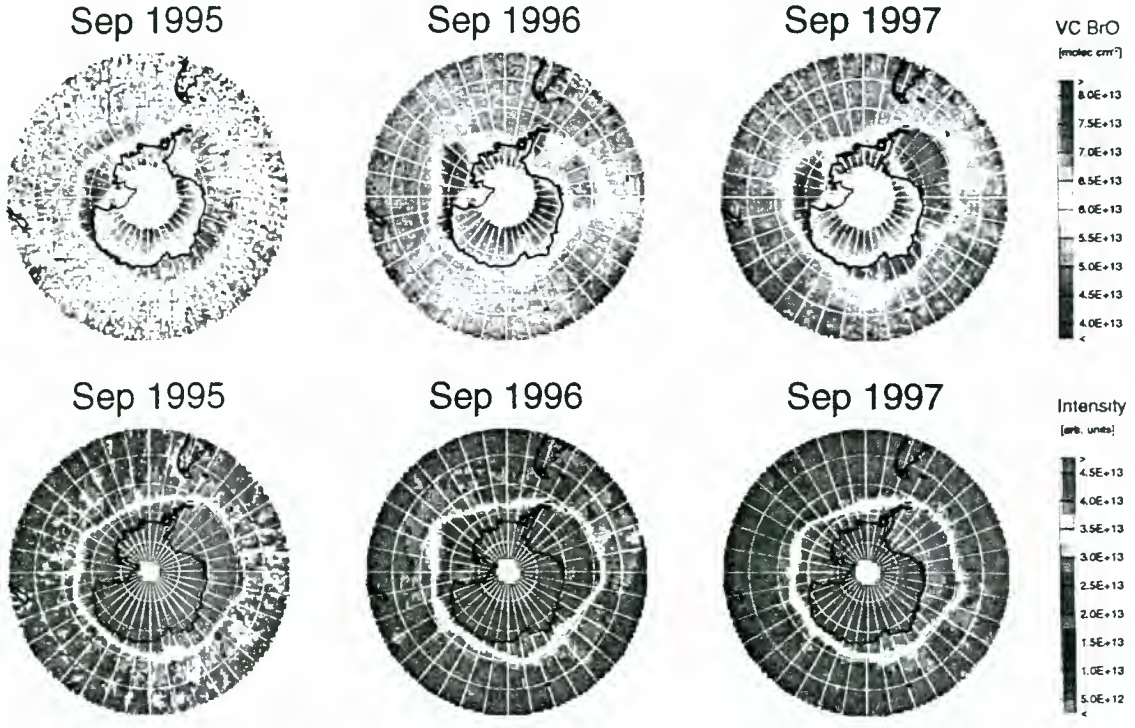

Figure 7. Monthly averages of GOME BrO and Reflectivity in the southern hemisphere. Averaged reflectivity can be used as a proxy for sea-ice coverage. Measurements in 1995 were subject to instrumental problems and noisier than in the following years.

data it appears, that enhanced BrO concentrations are not sporadic events in the polar boundary layer, but rather a frequent and common feature of polar spring. The presence of these large halogen amounts in the lower atmosphere at high latitudes should have a strong impact on tropospheric chemistry in the polar regions and could possibly also be important for mid-latitudes.

ACKNOWLEDGMENTS

The authors would like to thank M. Vountas for the preparation of the synthetic Ring spectrum. Helpful discussions with T. Wagner, H. Harder and M. Eisinger are gratefully acknowledged. GOME data have been supplied by the German Aerospace Centre / DLR. Parts of this work have been funded by the University of Bremen, the European Union and the German Space Agency (DARA).

REFERENCES

1. S. R. Aliwell, P. V. Johnston, A. Richter, M. Van-Roozendael, T. Wagner, D. W. Arlander, J. P. Burrows, D. J. Fish, R. L. Jones, K. Karlsen-Tornkvist, J. C. Lambert, K. Pfeilsticker, and I. Pundt. Analysis for BrO in zenith-sky spectra - an intercomparison exercise for analysis improvement. *to be submitted to J. Geophys. Res.*, 1999.

2. S. R. Aliwell, R. L. Jones, and D. J. Fish. Mid-latitude observations of the seasonal variation of BrO. 1. Zenith-sky measurements. *Geophys. Res. Lett.*, 24:1195–1198, 1997.

3. L. A. Barrie, J. W. Bottelsheim, R. C. Schnell, P. J. Crutzen, and R. A. Rasmussen. Ozone destruction and photochemical reactions at polar sunrise in the lower Arctic atmosphere. *Nature*, 334:138–141, 1988.

4. J. W. Bottenheim, A. G. Gallant, and K. A. Brice. Measurements of NO_y species and O_3 at 82°N latitude. *Geophys. Res. Lett.*, 22:599–602, 1986.

5. J. P. Burrows, A. Dehn, B. Deters, S. Himmelmann, A. Richter, S. Voigt, and J. Orphal. Atmospheric remote-sensing reference data from GOME: Part 1. Temperature-dependent absorption cross-sections of NO_2 in the 231–794 nm range,. *J. Quant. Spectrosc. Rad. Transfer*, 60:1025–1031, 1998.

6. J. P. Burrows, A. Richter, A. Dehn, B. Deters, S. Himmelmann, S. Voigt, and J. Orphal. Atmospheric remote-sensing reference data from GOME: Part 2. Temperature-dependent absorption cross-sections of O_3 in the 231–794 nm range,. *J. Quant. Spectrosc. Rad. Transfer*, 61:509–517, 1999.

7. J. P. Burrows, M. Weber, M. Buchwitz, V. Rozanov, A. Ladstätter-Weißenmayer, A. Richter, R. DeBeek, R. Hoogen, K. Bramstedt, K. U. Eichmann, M. Eisinger, and D. Perner. The Global Ozone Monitoring Experiment (GOME): Mission Concept and First Scientific Results. *J. Atmos. Sci.*, 56:151–175, 1999.

8. K. Chance. Analysis of BrO measurements from the Global Ozone Monitoring Experiment. *Geophys. Res. Lett.*, 25:3335–3338, 1998.

9. M. Eisinger, J. P. Burrows, and A. Richter. Studies on the precision of GOME irradiance and radiance products and GOME measurements of OClO and BrO over Antarctica. *GOME Geophysical Validation Campaign. Final results workshop proceedings*, 1996.

10. M. Eisinger, A Richter, Burrows Ladstätter-Weißenmayer, and J. P. DOAS zenith sky observations: 1. BrO measurements over Bremen (53°N) 1993-1994. *J. Atm. Chem.*, 25:93–108, 1997.

11. G. D. Greenblatt, J. J. Orlando, J. B. Burkholder, and A. R. Ravishankara. Absorption measurements of oxygen between 330 and 1140 nm. *J. Geophys. Res.*, 95:18577–18582, 1990.

12. H. Harder, C. Camy-Peyret, F. Ferlemann, R. Fitzenberger, T. Hawat, and H. Osterkamp. Stratospheric BrO Profiles Measured at Different Latitudes and Seasons: Atmospheric Observations. *Geophys. Res. Lett.*, 25:3843–3846, 1998.

13. M. Hausmann and U. Platt. Spectroscopic measurement of bromine oxide and ozone in the high Arctic during Polar Sunrise Experiment 1992. *J. Geophys. Res.*, 99:25399–25413, 1994.

14. E. Hegels, P. J. Crutzen, T. Klüpfel, D. Perner, and J. P. Burrows. Global distribution of atmospheric bromine oxide from GOME on the earth observing satellite ERS-2. *Geophys. Res. Lett.*, 25:3127–3130, 1998.

15. K. Kreher, P. V. Johnston, S. W. Wood, B. Nardi, and U Platt. Ground-based measurements of tropospheric and stratospheric BrO at Arrival Heights, Antarctica. *Geophys. Res. Lett.*, 24:3201–3024, 1997.

16. G. LeBras and U. Platt. A possible mechanism for combined chlorine and bromine catalyzed destruction of tropospheric ozone in the arctic. *Geophys. Res. Lett.*, 22:599–602, 1995.

17. M. Martinez-Walter, T. Arnold, D. Perner, R: Seuwen, and F: Stordal. The role of halogen oxides and peroxy radicals in the boundary layer during arctic ozone depletion 1995/1996. *Proceedings of XVIII Ozone Symposium in L'Aquila*, 1996.

18. J. C. McConnell, G. S. Henderson, L. Barrie, J. Bottenheim, H. Niki, C. H. Langford, and E. M. J. Templeton. Photochemical bromine production implicated in Arctic boundary-layer ozone depletion. *Nature*, 355:150–152, 1992.

19. H. L. Miller, A. Weaver, R. W. Sanders, K. Arpag, and S. Solomon. Measurements of Artic sunrise surface ozone depletion events at Kangerlussuaq, Greenland (67°N, 51°W). *Tellus*, 49, 1997.

20. S. J. Oltmans and W. D. Komhyr. Surface ozone distributions and variations from 1973-1984 Measurements at the NOAA Geophysical Monitoring for Climatic Change Baseline Observatories. *J. Geophys. Res.*, 91:5229–5236, 1986.

21. A. Richter, M Eisinger, Burrows Ladstätter-Weißenmayer, and J. P. DOAS zenith sky observations. 2. Seasonal variation of BrO over Bremen (53°N) 1994-1995,. 1998. J. Atm. Chem., in press.

22. A. Richter, F. Wittrock, M. Eisinger, and J. P. Burrows. GOME observations of tropospheric BrO in Northern Hemispheric spring and summer 1997. *Geophys. Res. Lett.*, 25:2683–2686, 1998.

23. V. Rozanov, D. Diebel, R. J. D. Spurr, and J. P. Burrows. GOMETRAN: A radiative transfer model for the satellite project GOME - the plane parallel version. *J. Geophys. Res.*, 102:16683, 1997.

24. R. Sander, R. Vogt, G. W. Harris, and P. J. Crutzen. Modeling the chemistry of ozone, haolgen compounds, and hydrocarbons in the arctic troposphere during spring. *Tellus*, 49:523–532, 1997.

25. S. Voigt. Hochauflösende Fourier-Transform-Spektroskopie atmosphärischer Spurengase im ultravioletten, sichtbaren und nahinfraroten Spektralbereich: CO, NO_2 und O_3. *PhD thesis, University of Bremen*, 1998.

26. M. Vountas, V. V. Rozanov, and J. P. Burrows. Ring effect: Impact of rotational Raman scattering on radiative transfer in earth's atmosphere. *J. Quant. Spectrosc. Radiat. Transfer*, 60:943–961, 1998.

27. T. Wagner and U. Platt. Satellite mapping of enhanced BrO concentrations in the troposphere. *Nature*, 395:486–490, 1998.

28. A. Wahner, A. R. Ravishankara, S. P. Sander, and R. R. Friedl. Absorption cross section of BrO between 312 and 385 nm at 298 K and 223 K. *Chemical Physics Letters*, 152:507–512, 1988.

29. S. Wessel. Tropospheric ozone variations in polar regions. *Berichte zur Polarforschung*, 1997.

30. P. Winkler, S. Brylka, and D. Wagenbach. Regular fluctuations of surface ozone at Georg-von-Neumayer-Station, Antarctica. *Tellus*, 44:33–40, 1992.

31. F. Wittrock, M. Eisinger, A. Ladstätter-Weißenmayer, A. Richter, and J. P. Burrows. Ground-based UV/vis measurements of O_3, NO_2, BrO and OClO over Ny-Ålesund, 78°N. *Proceedings of XVIII Ozone Symposium in L'Aquila*, 1996.

MEASUREMENT OF ATMOSPHERIC BRO AND OCLO BY GOME

Thomas Wagner, Klaus Pfeilsticker, Carsten Leue, Ulrich Platt

Institut für Umweltphysik, University of Heidelberg, Germany
e-mail: wat@uphys1.uphys.uni-heidelberg.de

ABSTRACT

In April 1995 the GOME (Global Ozone Monitoring Experiment) instrument was launched aboard the European research satellite ERS-2. It allows to detect the absorptions of several atmospheric trace gases like O_3, NO_2, BrO, SO_2 and OClO on a global scale. Compared to measurements from the ground or from aircraft and balloon platforms it thus offers the unique opportunity to detect both the temporal and spatial evolution of atmospheric species. Here we present GOME measurements of atmospheric BrO and OClO. Both species are involved in catalytic ozone depletion. We show BrO results for the stratosphere and the boundary layer. In addition we present strong indications for a 'tropospheric background concentration' of BrO of about 1 ppt. OClO is formed by the reaction of BrO and ClO and its detection can be used as an indicator for the halogen activation of the stratosphere during the polar night. We present OClO measurements during polar winter/spring for both hemispheres.

1. INTRODUCTION

The GOME instrument (Ref. 1) consists of a set of four spectrometers measuring sunlight reflected from the earth in the wavelength range between 240 and 790 nm with moderate spectral resolution (0.2 nm/0.4 nm) and therefore allows to detect the absorptions of different atmospheric trace gases (Refs. 2-8). The satellite operates in a nearly polar, sun-synchronous orbit at an altitude of 780 km with a local equator crossing time of ≈10:30. While the satellite flies in an almost north-south direction the GOME instrument scans in east west direction. During each scan three individual measurements are performed, the corresponding 'ground pixels' (west-, centre- and east-pixel) each cover an area of 320 km (east-west) by 40 km (north-south). At the equator the earth's surface is covered during three days, polewards from ≈70° it is covered daily.

In recent years many spectroscopic observations of BrO and OClO were made from the ground (Refs. 9-15), from balloon platforms (Ref. 16) as well as from aircrafts (Ref. 17). From these measurements it became clear that halogen oxides play an important role in the chemistry of the troposphere and the stratosphere. Satellite measurements, however, offer now the unique possibility to observe the atmospheric content of BrO and OClO on a global scale. Thus it is now possible to a) quantify the areas where BrO and OClO show enhanced absorptions (e.g. the ozone hole), b) to separate the spatial and temporal evolution of the atmospheric BrO and OClO content, c) to directly compare the halogen activation in both hemispheres and d) to determine maximum values within specific areas (e.g. the entire polar vortex).

2. DATA PROCESSING

OClO and BrO show characteristic absorption features in the UV spectral range which can be clearly detected in the atmospheric spectra measured by GOME. From the measured raw spectra of the GOME instrument slant column densities (SCD, i.e. the integrated concentration along the light path) are calculated applying **D**ifferential **O**ptical **A**bsorption **S**pectroscopy (DOAS, Ref. 18). In brief the measured spectra are modelled using suitably weighted trace gas- and sunlight reference spectra. From the model parameters and the trace gas absorption cross sections (for OClO and BrO the data from Wahner et al. (Refs. 19,20) were used) the desired trace gas SCDs are calculated. In Fig. 1 the results of the spectral retrieval for the BrO- and OClO absorption detected in a GOME spectrum is shown.

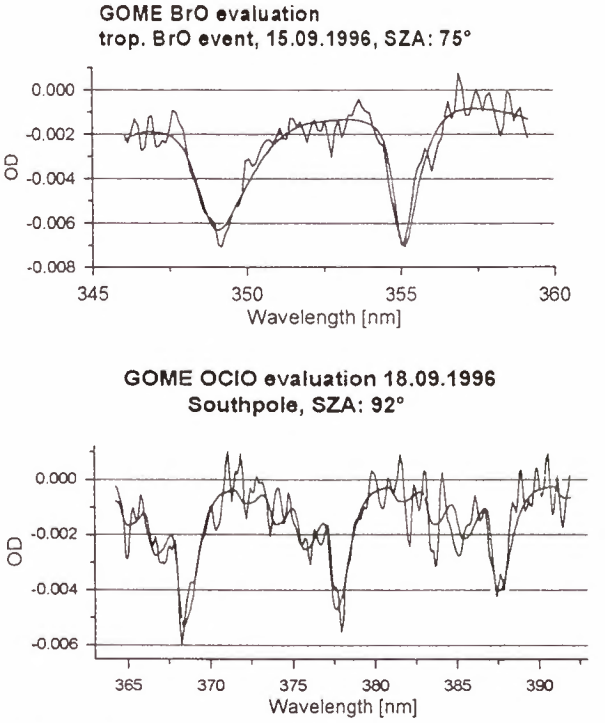

Figure 1. Results of the spectral evaluation for BrO (top) and OClO (bottom). The thick lines show the trace gas absorption spectrum scaled to the respective absorptions detected in the measured spectrum (thin lines).

The light, which reaches the instrument is either reflected from the earth's surface or scattered back from the atmosphere. Therefore the determination of the vertical column density (VCD, the vertically integrated trace gas concentration) from the measured SCD requires radiative transport modelling, e.g. to derive air mass factors (AMF), where AMF = SCD / VCD. We calculated AMFs using a Monte Carlo radiative transport

model including spherical geometry and multiple scattering (Ref. 21).

3. RESULTS

In this section we present GOME observations of stratospheric OClO as well as of BrO located in the boundary layer or in the free troposphere.

3.1 STRATOSPHERIC OCLO

All OClO data presented here are expressed as slant column densities (SCD), the integrated OClO concentration along the light path through the atmosphere. Thus one has to keep in mind that the SCD is strongly dependent on the solar zenith angle (SZA) and that different OClO SCDs at different latitudes (and different SZA) do not necessarily represent different degrees of the atmospheric halogen activation. In addition, due to photo-dissociation the atmospheric OClO concentration depends strongly on the SZA. In Figure 2 the OClO SCD measured on January 19, 1997 is shown. Enhanced values of OClO indicating a chlorine activated stratosphere are found within the complete polar vortex, even at relatively low SZA below 80°. Since areas of temperatures deep enough for the formation of PSCs often exist only on distinct locations inside the polar vortex, this can is a strong indication for very effective transport mechanisms inside the polar vortex. For SZA above 90° the SCD OClO further increases due to slow photolysis of the OClO molecule. On January 19, 1997 when GOME observes high SCD OClO above Scandinavia enhanced values were also measured from ground based observations (Ref. 22).

In Fig. 3 the maximum OClO SCDs around SZA=90° are presented for polar winter/spring in both hemispheres. Satellite measurements allow to compare the OClO absorptions from both hemispheres with one instrument under constant calibration conditions which can be used for a direct comparison. It can be seen that the period of enhanced stratospheric OClO concentrations is much longer and the magnitude of the OClO absorption is stronger in the Antarctic than in the Arctic. This can be expected as a result of the deeper temperatures and the more stable polar vortex. However, although there is a large variability of the measured OClO abundance in the northern hemisphere there also exist periods during which the OClO concentration continuously stays enhanced. In particular the beginning and the ending of the chlorine activation can be nearly as soon or late as in the southern hemisphere. This is of great importance since the total degree of ozone depletion depends critically on the duration of chlorine activation.

3.2 ENHANCED BRO CONCENTRATIONS IN THE BOUNDARY LAYER

It was expected that the GOME instrument would be in particular sensitive to stratospheric BrO. However, besides these stratospheric measurements (Refs. 6, 23) it turned out that GOME was also well suited to measure BrO concentrations in the troposphere. In particular it was possible to determine the temporal and spatial evolution of events of enhanced BrO concentrations during polar spring (Ref. 8).

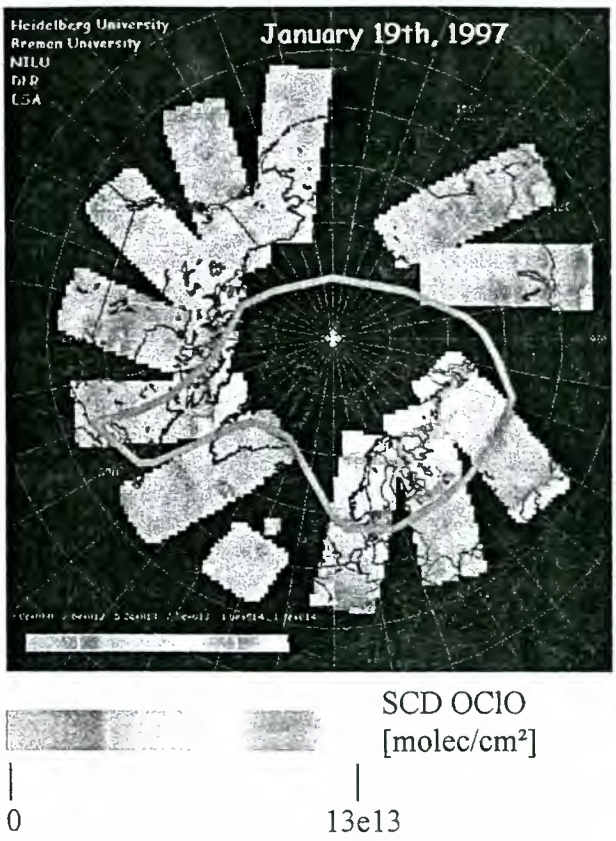

Figure 2. OClO SCD observed by GOME on January 19, 1997. High OClO SCDs are seen in the entire polar vortex which is indicated by the thick line (35 PV units at 475K lvel, ECMWF data) .

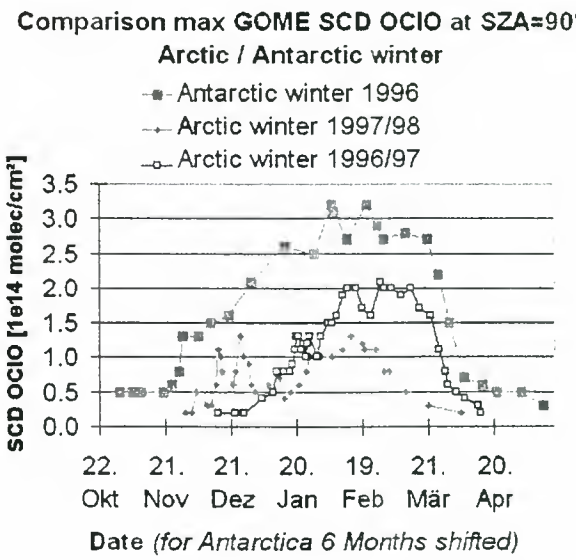

Figure 3. Evolution of the maximum SCD (for a SZA of 90°) found during polar winter in both hemispheres.

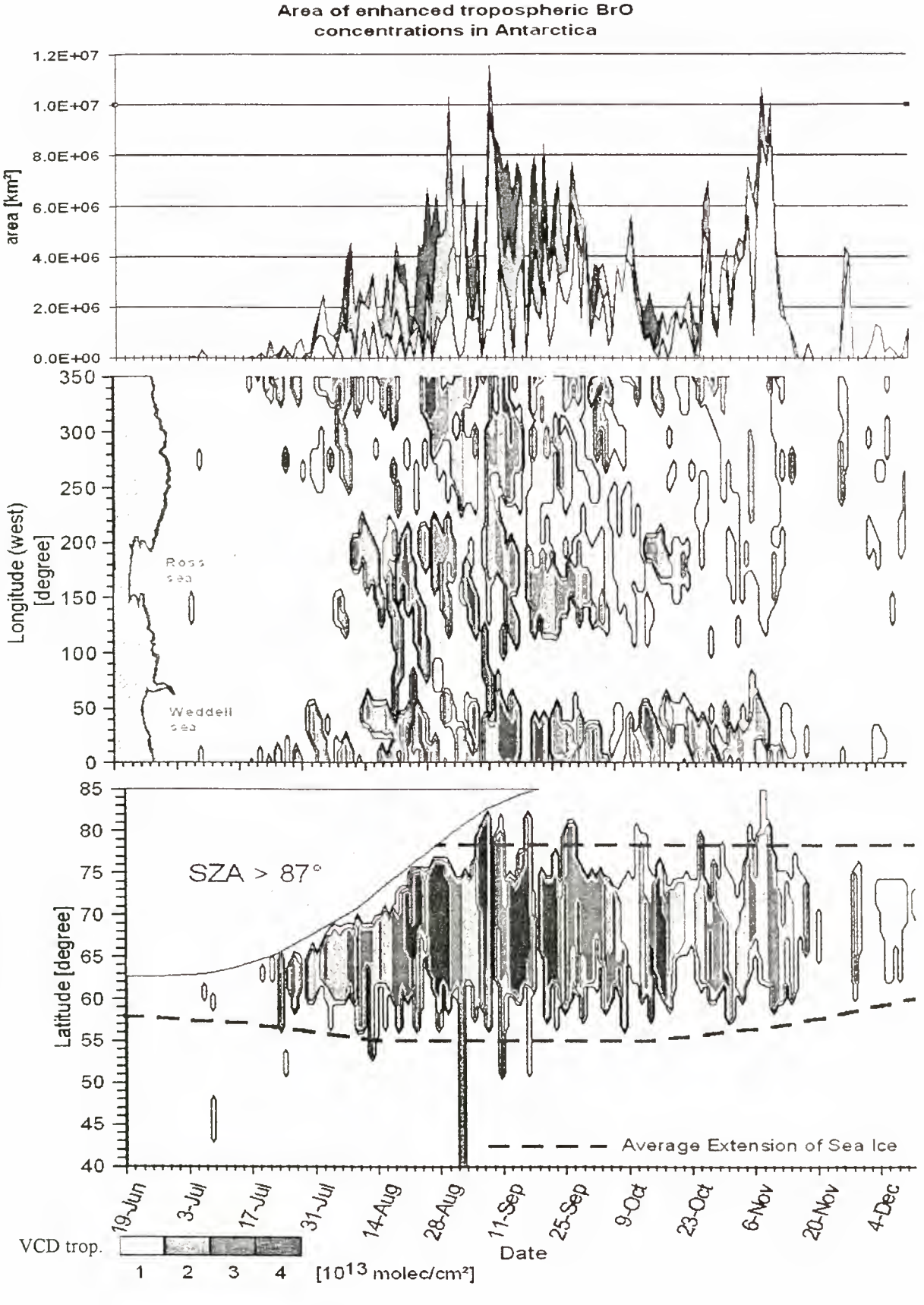

Figure 4. Events of enhanced BrO concentrations in the boundary layer during Antarctic winter/spring 1997. In the upper panel the total area of such events around Antarctica is shown. The middle panel displays the longitudinal and the lower panel the latitudinal distribution of these BrO events (displayed are the maximum values appearing in the respective latitude or longitude interval).

In Fig. 4 time series of such events during Antarctic spring are presented. They appear first in July and last until December. The maximum total extension is about more than 10^7 km², about the area of Antarctica. The events appear at the sea ice border around Antarctic, in particular at the Weddell- and Ross-sea where the ice reaches a rather large extension. Only very few events occurred above the ocean or above the Antarctic continent, maybe caused by transport from the sea ice. Two maxima of the total area of enhanced BrO concentrations were found, one in August/September and one in November. During August/September the observed BrO concentrations were about 2 to 4 times higher than in November.

3.3 BRO CONCENTRATIONS IN THE FREE TROPOSPHERE?

Recently it was speculated that there might exist a BrO 'background' concentration of about 1 to 2 ppt in the free troposphere. This was in particular concluded from the comparison of balloon borne measurements with ground based and satellite measurements (Refs. 6, 24, 25) as well as from the comparison of ground based with modelled BrO data (Ref. 26). Here we present a new method to estimate the magnitude of the BrO concentration in the troposphere. Assuming a considerable part of the total atmospheric VCD BrO was located in the troposphere. Then satellite measurements of BrO should be largely affected by the appearance of clouds (Refs. 5, 8). In particular there should be a correlation between the absorptions of BrO and those of the oxygen dimer O_4 which is mainly located in the troposphere. To investigate this assumption we chose ground GOME pixels in the tropics, subtropics and at mid latitudes (SZA<55°) for which the AMF is relative constant (about 2.2 for SZA=20° to 2.9 for SZA=55°) and clouds frequently reach into the upper troposphere (see Figure 5). It can be seen that for several latitudes where largely decreased O_4 absorptions indicate the appearance of clouds also the SCD BrO is decreased. A reduction of about 50% for the O_4 absorption corresponds with a decrease of about 30% for the BrO SCD.

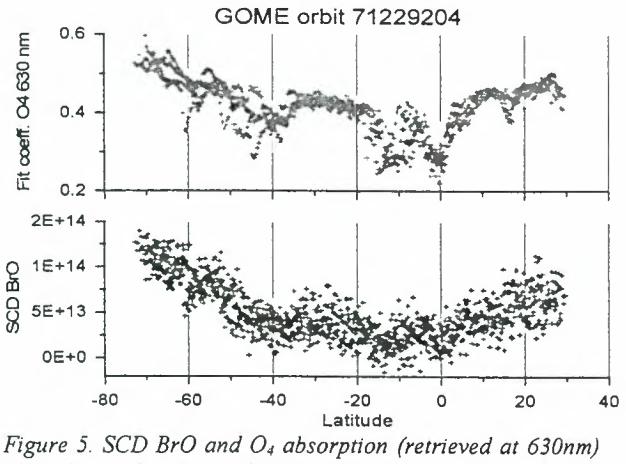

Figure 5. SCD BrO and O_4 absorption (retrieved at 630nm) plotted as function of the latitude (measurements for SZA<55° were chosen). When decreased O_4 absorptions indicate the appearance of clouds also the SCD BrO is decreased.

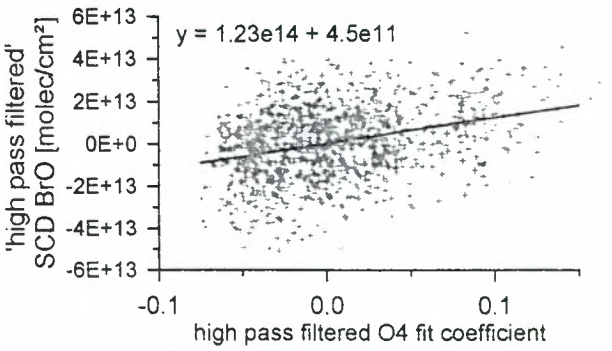

Figure 6. The High pass filtered' SCD BrO is plotted as a function of the O_4 absorption (to minimise the SZA dependence of the BrO and O_4 measurements both data sets were high pass filtered by the subtraction of a polynomial of degree 2 as a function of the latitude).

This dependence is also confirmed by Fig. 6 where the SCD BrO is plotted as a function of the O_4 absorption (to minimise the SZA dependence of the BrO and O_4 measurements both data sets were high pass filtered by the subtraction of a polynomial of degree 2 as a function of the latitude).

A reduction of the O_4 absorption of about 50% can be caused by a) a total cloud layer at a height of about 3 km or b) a high cloud (a cloud at about 12km hides about 97% of the total O_4 column) which covers about a half of a ground pixel (These are the easy cases. Typically GOME ground pixels are partly covered by clouds at different heights). For case a) from a reduction of the total BrO VCD of about 30% it can be concluded that 30% of the total BrO VCD is located ithin the lowest 3 km of the atmosphere. For case b) it can be concluded that 60% of the total BrO VCD is located below 12 km. Both conclusions are in agreement with the assumption of a tropospheric BrO background concentration of about 1 ppt (for a total BrO VCD of about $3*10^{13}$ molec/cm² as typically found in the tropics).

4. CONCLUSIONS

We presented GOME observations of OClO and BrO in the stratosphere and the troposphere. From our observations we can draw the following conclusions:

a) In the Antarctic winter the chlorine activation stays enhanced for a period of about 4 months (November until March).

b) In the Arctic winter the periods of continuously enhanced OClO absorptions are typically by about one month shorter than in Antarctica. Nevertheless, in different years the beginning or the ending of the chlorine activation can be nearly as early or as late as in Antarctica.

c) The maximum OClO SCD (at SZA = 90°) found during the Arctic winter are by about 30% lower than the maxima in Antarctica.

d) We searched for events of enhanced BrO concentrations in the boundary layer around Antarctica from June to December 1997. From mid of July until mid of November such events occurred continuously around the continent. Most of the individual events stayed for about 1 to 3 days. However, some events continued for up to 10 days.

e) The maximum extension of the total area of the 'BrO events' is about more than 10^7 km² (this is approximately the area of Antarctica). Such large total extensions appear in August/September and November.
f) The events appear at the sea ice border around Antarctica, in particular at the Weddell- and Ross-sea where the ice reaches a rather large extension. Only very few events occurred above the ocean or above the Antarctic continent, probably caused by transport from the sea ice.
g) The observed BrO concentrations in the boundary layer decrease from August to December. During August/September the observed BrO VCD in the boundary layer is about 2 to 4 times higher than in November.
h) From the simultaneous measurement of BrO and O_4 we estimated the magnitude of an assumed tropospheric background BrO concentration of about 1 ppt.

5. ACKNOWLEDGEMENTS.

The financial support of the Deutsche Agentur für Raumfahrtangelegenheiten (DARA) and the data supply from the ESA operation centre in Frascati (Italy) and the DLR, in Wessling (Germany) is highly acknowledged. Fruitful discussions with I. Pundt (CNRS), A. Richter, F. Wittrock (IUP Bremen) M. Van Roozendael (IASB) and H. Harder (MPI Mainz) are highly appreciated.

6. REFERENCES

1. ESA Publication Division, GOME, Global Ozone Monitoring Experiment, Users manual. European Space Research and Technology Centre (ESTEC) 1995, edited by Floyed Bednarz.
2. Burrows, JP & al 1998, Global ozone monitoring experiment (GOME): Comparison of back scattered measurements and O_3 DOAS/BUV retrievals, *Proceedings of the XVIII Quadrenial ozone symposium, L'Aquila, 12-21 September, Italy, edited by R. Bojkov and G. Visconti, Internal ozone commission*, 657-660.
3. Eisinger, M & Burrows, JP 1998, Tropospheric sulfur dioxide observed by the ERS-2 GOME instrument, *Geophys. Res. Lett., 25, in press.*
4. Wagner, T & al 1998, Cloud properties deduced from GOME observations of O_2 and O_4 absorptions, *Air pollution report 66, Polar stratospheric ozone 1997, proceedings of the fourth European symposium, 22 to 26 Sepetember, Schliersee, Germany, European communities*, p514-517.
5. Wagner, T & al 1998, GOME global BrO observations, Validation with ground based and balloon measurements, *Air pollution report 66, Polar stratospheric ozone 1997, proceedings of the fourth European symposium, 22 to 26 Sepetember, Schliersee, Germany, European communities*, p397-400.
6. Richter, A & al 1998, GOME observations of tropospheric BrO in northern hemispheric spring and summer 1997, *Geophys. Res. Let.*, 25, 2683-2686.
7. Wagner, T & Platt, U 1998, Satellite mapping of enhanced BrO concentrations in the troposphere, Nature, 395, 486-490.
8. Hausmann M & Platt, U 1994, Spectroscopic measurement of bromine oxide and ozone in the high Arctic during Polar Sunrise Experiment 1992, J. Geophys. Res. 99, 25,399-25,414.
9. Eisinger M & al 1997, DOAS Zenith sky observations: 1. BrO measurements over Bremen (53°N) 1993-1994, *J. Atmos. Chem.*, 26, 93-108.
10. Otten, C & al 1998, Groundbased DOAS UV/visible measurements at Kiruna (Sweden) during the SESAME winters 1993/94 and 1994/95, *J. Atmos. Chem.*, 30, 141-162.
11. Solomon, S & al 1987, Visible Spectrospcopy at McMurdo Station, Antarctica 2. Observations of OClO, *J. Geophys. Res*, 92, 8329-8338.
12. Fiedler, M & al 1993, Groundbased spectroscopic measurements of stratospheric NO_2 and OClO in Arctic winter 1989/90, *Geophys. Res. Let.*, 21, 963-966.
13. Kreher, K & al 1996, Ground based measurements of OClO and Hcl in austral spring 1993 at Arrival Heights, Antarctica, Geophys. Res. Let., 23, 1545-1548.
14. Gil., M & al 1996, OClO, NO_2 and O_3 total column obsrvations over Iceland during the winter 1993/94, Geophys. Res. Let., 23, 3337-3340.
15. Pommereau, JP & Piquard, J 1994, Observations of the vertical distribution of stratosperic OClO, Geophys. Res. Let., 21, 1231-1234.
16. Erle, F & al 1998, Transall DOAS measurements of nighttime column abundances of stratospheric O_3, NO_2, OClO and NO_3, Air pollution report 66, Polar stratospheric ozone 1997, proceedings of the fourth European symposium, 22 to 26 Sepetember, Schliersee, Germany, European communities, 435-438
17. Platt U 1994, Differential optical absorption spectroscopy (DOAS), In: Air Monitoring by Spectroscopic Techniques, M.W. Sigrist, Ed., Chemical Analysis Series, Vol 127, John Wiley & Sons, Inc.
18. Wahner A & al 1988, Absorption cross section of BrO between 312 and 385 nm at 298 and 223 K, Chem. Phys. Lett. 152, 507-512.
19. Wahner A & al 1987, Absorption cross sections for OClO as a function of temperature in the wavelength range from 240-490 nm, J. Phys. Chem., 91, 2735-2738.
20. Marquard, LC & Platt, U 1997, AMFTRAN: A new Monte Carlo radiative transfer model for the calculation of air mass factors, Proceedings of the NATO ARW, Athens, Nov. 1995, Springer Heidelberg, London, New York.
21. Enell, C-F & al 1998, UV/visible O_3, NO_2, OClO, and BrO startospheric column amount measurements at Kiruna/Sweden in the Arctic winter 1996/97, Air pollution report 66, Polar stratospheric ozone 1997, proceedings of the fourth European symposium, 22 to 26 Sepetember, Schliersee, Germany, European communities, p431-434.
22. Hegels, E & al 1998, Global distribution of atmospheric bromine monoxide from GOME on earth observing satellite ERS-2, Geophys. Res. Lett., submitted.
23. Pundt, I 1997, Distribution verticale de la concentration de IO et de BrO dans la basse stratosphère : Mesure et interprétation, PhD thesis, University of Paris 6.
24. Van Roozendael, M & al 1999, Developement of a Bromine oxide product from GOME, this issue.
25. Friess, U & al 1999, Intercomparison of measured and modelled BrO slant column amounts for the Arctic winter 1994/95, submitted to Geophys. Res. Lett, 1998.

GOME OBSERVATIONS OF TROPOSPHERIC SULFUR DIOXIDE

Michael Eisinger[1,2,*] and John P. Burrows[2]

[1] Alfred Wegener Institute for Polar and Marine Research, Potsdam, Germany
[2] Institute of Environmental Physics, University of Bremen, Germany
e-mail: meisinge@estec.esa.nl, John.Burrows@iup.physik.uni-bremen.de

ABSTRACT

Column densities of tropospheric sulfur dioxide have been derived from UV radiance measurements of the Global Ozone Monitoring Experiment (GOME) on board ESA's Second European Remote Sensing Satellite (ERS-2). GOME combines the advantages of contiguous ground coverage and contiguous spectral sampling, the latter enabling highly sensitive and specific SO_2 measurements. The detection limit for SO_2 is currently estimated to be 0.4 DU in the vertical column. This enables both volcanic and anthropogenic SO_2 to be detectable by GOME.
After a brief summary of GOME observations of volcanic SO_2, examples of SO_2 "hot spots" as detected by GOME between 1996 and 1998 over Europe and East Asia are presented. They are ascribed to combustion of sulfur-rich lignite and brown coal in power plants.

1. INTRODUCTION

SO_2 enters the atmosphere as a result of anthropogenic activity and natural phenomena, the most important sources being combustion of fossil fuels – mainly lignite, coal, and oil –, oxidation of dimethyl sulfide (DMS) over oceans, and emissions from volcanoes. The anthropogenic contribution is estimated to account for about 85 % of the total SO_2 emissions.
SO_2 is very reactive and has a lifetime of a few days in the troposphere where it is removed by H_2O_2 and O_3 oxidation in the aqueous phase, OH oxidation in the gas phase, and dry and wet deposition. This implies that the tropospheric amount of SO_2 is very variable and the background concentration is very small. Clean continental air contains less than 1 ppb SO_2. In contrast, SO_2 concentrations may exceed 40 ppb (the WHO guideline 4-hour average value) in heavily polluted areas and reach tens of ppm in volcanic or power plant plumes [*Berresheim et al.*, 1995].

2. DATA ANALYSIS

The strong absorber ozone is the primary target species of GOME. However, the column amounts of a number of important atmospheric trace gases which have comparably weak atmospheric absorptions can also be retrieved, among them SO_2.
Earth radiances and solar irradiances are taken from the operational GOME Data Processor (GDP) level 1 products. Slant column densities of SO_2 are derived from the UV radiances by the standard differential optical absorption spectroscopy technique in a 315.5–327 nm wavelength window. After the absorption signature of the ozone Huggins bands, which is more than one order of magnitude larger than the SO_2 absorption, and the contribution of NO_2 absorption and the Ring effect have been removed from the measured optical density, a clear SO_2 signal is obtained in regions of elevated SO_2. Slant column densities are then converted to vertical column densities by means of a simple geometric air mass factor, applicable for small solar zenith angles where the geometric light-path is an adequate approximation. SO_2 vertical column densities are traditionally given in equivalent Dobson Units (1 DU = 300 t SO_2 per 40x320 km^2 GOME groundpixel).

*Now at ESA-ESTEC, Noordwijk, The Netherlands.

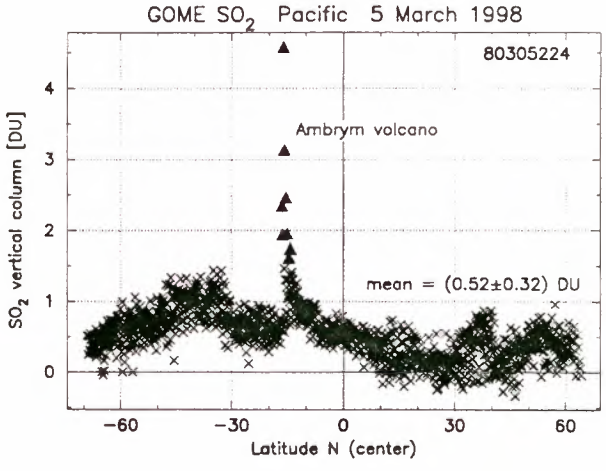

Figure 1: GOME SO_2 observations over the Pacific on 5 March 1998. The mean value and standard deviation given in the figure has been calculated for the background values (crosses).

3. VOLCANIC SO_2

Nyamuragira, Zaire, and Popocatépetl, Mexico, were the first volcanoes where SO_2 has been identified from GOME measurements. Maximum SO_2 column densities of 33 DU for Nyamuragira and 6 DU for Popocatépetl have been reported [*Eisinger and Burrows*, 1998]. This section presents examples of volcanic events where even lower SO_2 column densities arising from intermittently emitting volcanoes have been observed.
Figure 1 shows an orbit passing over the Pacific Ocean

on 5 March 1998. SO_2 columns are generally found to be low, with the exception of a few values which can be attributed to the effusive activity of Ambrym volcano (16.25°S, 168.12°E, summit elevation 1334 m), Vanuatu. In March 1998, enhanced SO_2 is frequently observed close to this volcano.

At Mt Etna (37.73°N, 15.00°E, 3315 m), Sicily, localised SO_2 maxima up to 2 DU could be observed on several days between August and October 1997 (Fig. 2). This corresponds to the vigorous activity of the Bocca Nuova and Southeast Crater reported for that period [*Bull. Global Volcanism Network*, 1997]. SO_2 from Mt Etna is frequently transported towards the East, which is consistent with the prevailing winds.

4. ANTHROPOGENIC SO_2

Figure 3 displays observations of enhanced SO_2 over southeastern Europe for selected days in winter 1998. The meteorological situation on 8 February 1998 is typical for these examples [*Berliner Wetterkarte*, 1998]. On this day a high pressure region was centred near Sofia leading to favourable observing conditions. From the GOME broadband spectral measurements, the scene is classified as cloud-free, which is in agreement with the station reports from Belgrade and Bucharest. Accumulation of pollutants was favoured by the meteorological situation. Upward dispersal of pollutants was prevented by a stable temperature inversion, and SO_2 removal by wet deposition was effectively suppressed. Horizontal wind speeds were below 2.5 m/s, making other than local SO_2 sources improbable.

We conclude that the enhanced SO_2 observed by GOME is mainly emitted by large thermal power plants indicated in Figure 3. This is consistent with the fact that public power generation is considered to contribute the major fraction to the SO_2 emissions in Bulgaria and Romania.

Averaged GOME SO_2 measurements over Europe during the second half of February 1996 (Fig. 4) show that regions of enhanced SO_2 in eastern and southeastern Europe. Highest SO_2 values are to be found over Romania and Hungary, followed by Ukraine, Moldova, and Bulgaria. Enhanced SO_2 is also observed over Poland and the "Black Triangle" at the borders of Poland, the Czech Republic, and Germany.

In all of these countries locally produced sulfur-rich lignite provides a significant fraction of the energy supply. It is used mainly in power plants, but also for household heating. With surface air temperatures in February 1996 being significantly below the long-term average [*Berliner Wetterkarte*, 1996], lignite consumption and SO_2 emissions probably have been above the average. Furthermore, frequent temperature inversions favoured accumulation of pollutants.

Finally, Figure 5 shows monthly mean SO_2 column densities measured in February 1998 over East Asia. Sulfur-rich coal provides a major fraction to the energy supply of China. Enhanced SO_2 values are observed over the Red Basin. Pollutants can easily accumulate in this highly industrialised area which is nearly completely surrounded by mountain ranges.

5. DISCUSSION

The detection limit for SO_2 retrievals from GOME measurements depends on both the observing conditions and the retrieval algorithm. For cloud-free scenes at low solar zenith angles, a reasonable estimate is 0.4 DU in the vertical column, corresponding to 150 t of SO_2 in a 40 × 320 km^2 GOME groundpixel. This comparably high sensitivity arises from the multi-wavelength advantage of GOME. Furthermore, interferences from varying ground albedo, aerosol and ozone content can be cleanly separated from the SO_2 signal, leading to highly specific measurements.

Sensitivity to tropospheric SO_2 is expected to be lower at high latitudes where less UV radiation penetrates to the surface. Similarly, larger effective absorptions of ozone are likely to result in a somewhat poorer detection limit. However, it has been demonstrated above that heavy and sustained anthropogenic SO_2 pollution events may be observed using GOME data. Further work is required to establish the detection limit at higher latitudes.

No attempt has been made in this work to account for clouds. SO_2 below clouds is "hidden" for GOME; therefore cloud masks will have to be applied for a proper interpretation of the observed SO_2 columns. Furthermore, the influence of the ground albedo on the air mass factors has to be considered. Otherwise SO_2 vertical columns tend to be overestimated for high ground albedos. Finally, as SO_2 and aerosols are in most cases emitted together, the GOME SO_2 product should be combined with aerosol products from GOME and ATSR-2.

REFERENCES

Berliner Wetterkarte (1996–1998).

Bull. Global Volcanism Network (1997), online edition: http://www.nmnh.si.edu/gvp/gvn.

Berresheim, H., Wine, P. H., and Davis, D. D. (1995), Sulfur in the atmosphere, in: *Composition, chemistry, and climate of the atmosphere*, ed. by Hanwant B. Singh, New York: Van Nostrand Reinhold, 251–307.

Burrows, J. P., *et al.* (1998), The Global Ozone Monitoring Experiment (GOME): Mission concept and first scientific results, *J. Atmos. Sci.*, in press.

Eisinger, M., and J. P. Burrows (1998), Tropospheric sulfur dioxide observed by the ERS-2 GOME instrument, *Geophys. Res. Lett.*, 25, 4177–4180.

ACKNOWLEDGEMENTS

We thank our colleagues Andreas Richter and Marco Vountas at iup/ife Bremen for valuable contributions. GOME level 1 products have been provided by the German Aerospace Centre (DLR-DFD) on behalf of ESA. This contribution has partly been funded by ESA-ESRIN.

Paper presented on European Symposium on Atmospheric Measurements from Space, ESTEC, Noordwijk, The Netherlands, 18-22 Jan 1999.

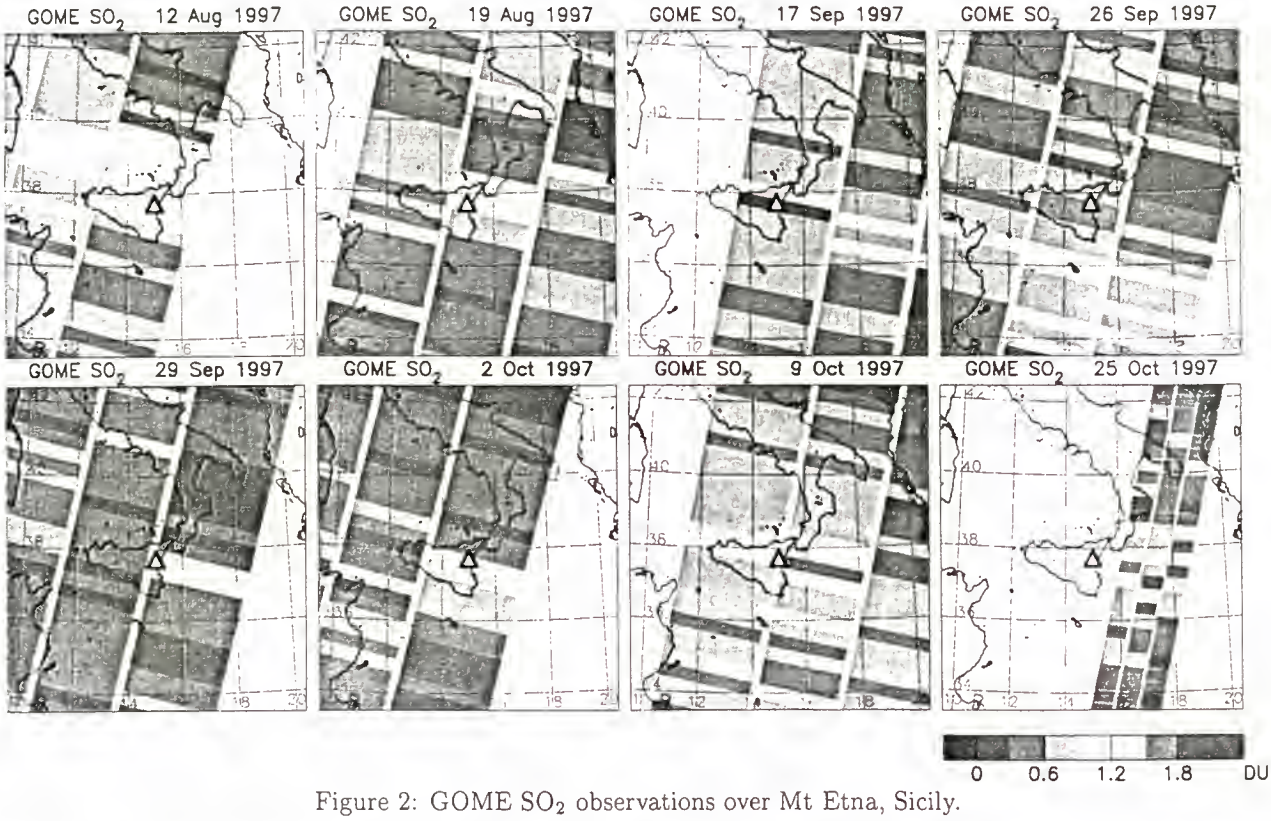

Figure 2: GOME SO_2 observations over Mt Etna, Sicily.

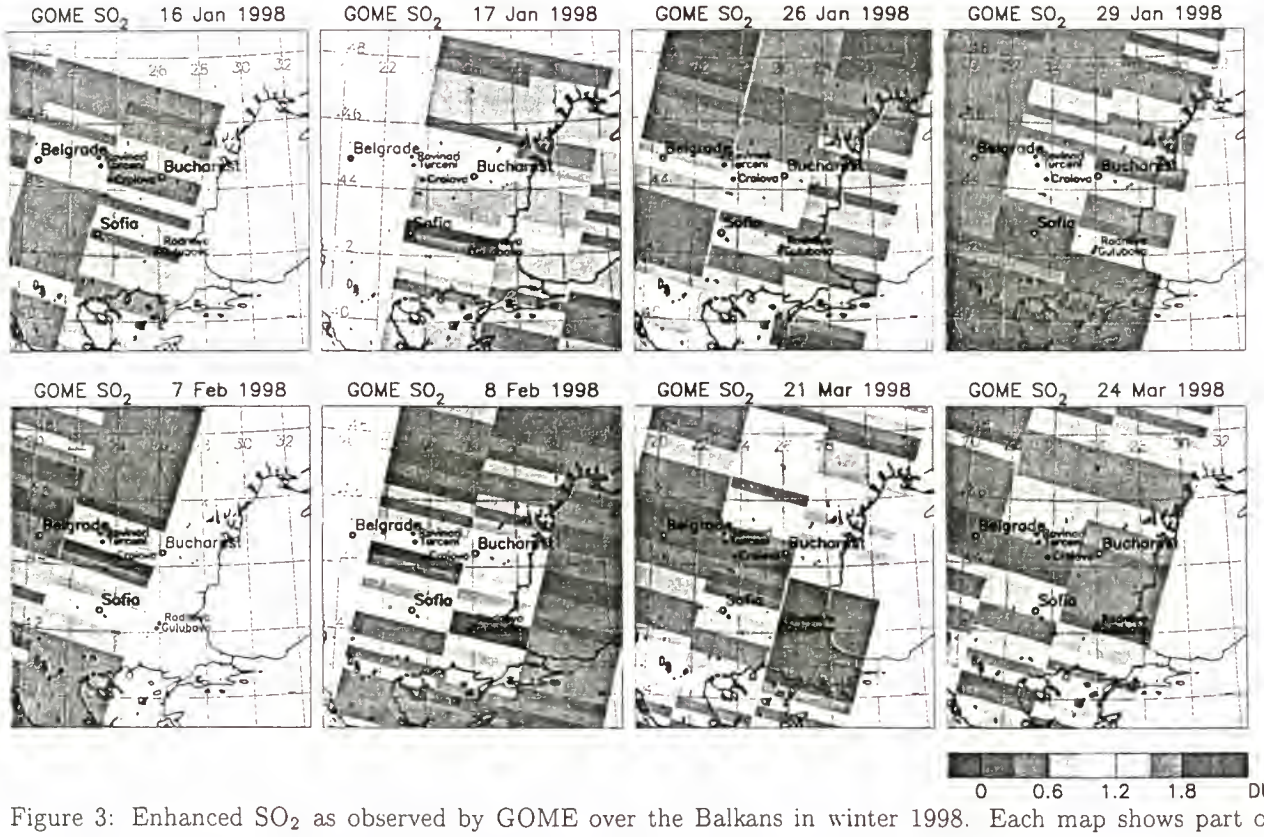

Figure 3: Enhanced SO_2 as observed by GOME over the Balkans in winter 1998. Each map shows part of a single orbit (forward scan only). The small dots indicate the locations of the largest thermal power plants burning lignite in Romania (Turceni, Rovinari, and Craiova, total 5065 MWe) and Bulgaria (Gulubovo and Radnevo, forming the Maritsa-Iztok complex, total 3485 MWe). Together, these plants represent 27 % of the electric power capacity installed in the two countries.

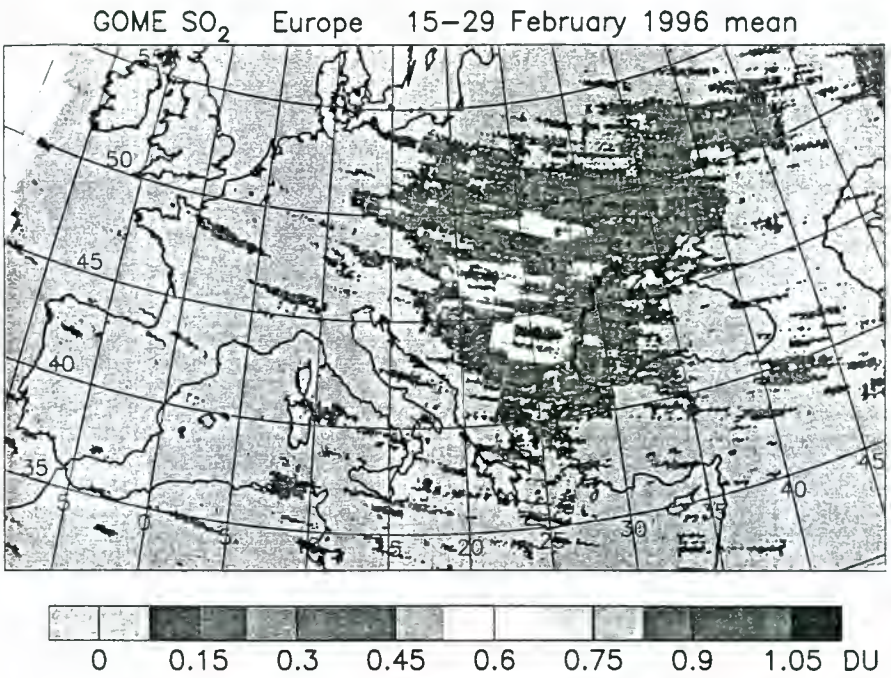

Figure 4: GOME SO_2 measurements over Europe averaged over the last two weeks of February 1996. Note that no cloud correction has been applied, i.e., some additional SO_2 may be hidden below clouds.

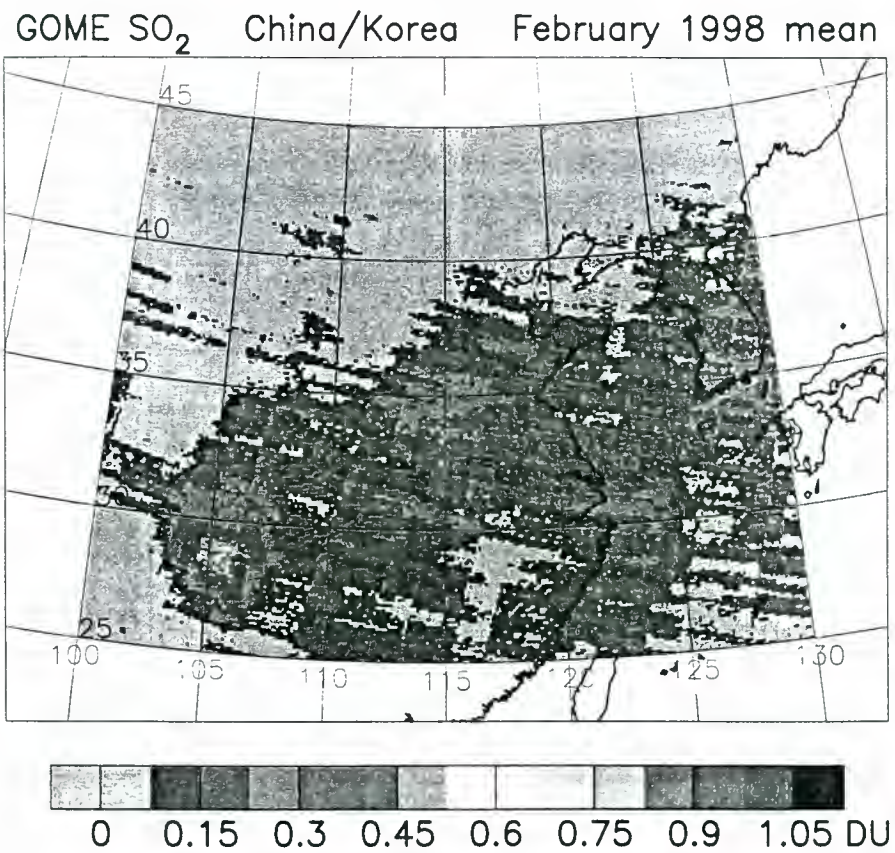

Figure 5: GOME SO_2 measurements over East asia, February 1998 monthly mean.

RETRIEVABILITY OF NO VOLUME MIXING RATIO AND NON-LTE PARAMETER FROM STRATOSPHERIC MIDLATITUDE DAYTIME MIPAS-ENVISAT LIMB SPECTRA AT 5.3 μm

B. Funke, M. Lopéz-Puertas[a], G.P. Stiller, T.v. Clarmann, and M. Höpfner

Institut für Meteorologie und Klimaforschung, Forschungszentrum Karlsruhe,
Postfach 3640, D-76021 Karlsruhe, Germany
[a]Instituto de Astrofísica de Andalucía (CSIC), p.o.b. 3004, Granada, Spain
e-mail: bernd.funke@imk.fzk.de

ABSTRACT

The Michelson Interferometer for Passive Atmospheric Sounding (MIPAS) on the ENVISAT polar platform will continuously record limb radiance from which, among other species, NO abundances are planned to be retrieved. Stratospheric NO will be retrieved from the NO(ν = 1) emission at 5.3 μm which is strongly affected by non-LTE in a wide altitude range. Moreover, due to the large NO(ν = 1) concentration in the thermosphere, radiances from altitudes above 100 km contribute considerably to spectra related to stratospheric tangent heights. These thermospheric radiance contributions are disturbed by the breakdown of rotational and spin LTE above approx. 110 km. This paper presents a new retrieval approach for the NO volume mixing ratio vertical profile which accounts for the non-LTE situation. This approach additionally enables the simultaneous determination of the nascent vibrational distribution of the NO_2 photolysis which is an important non-LTE parameter. Vibrational, rotational and spin non-LTE is included with a model specifically developed and optimized for this application. Retrieval errors due to instrumental noise and systematic error sources have been assessed. The tangent altitude range of the limb sequence used in the retrieval was found to show a strong impact on the accuracy of the retrieved stratospheric NO profile. A limb scanning range up to at least 70 km is necessary to keep systematic errors due to uncertainties in the *a priori* information on the NO vertical distribution above the upper scanning limit reasonable small.

1. INTRODUCTION

Nitric oxide is an important trace constituent throughout the lower atmosphere. The distribution of stratospheric NO is very important for understanding the odd nitrogen chemistry, especially the cyclic short time conversions between NO and NO_2 (Ref. 1). In the near future, the Michelson Interferometer for passive Atmospheric Sounding (MIPAS) (Ref. 2) on board of the European polar platform ENVISAT will record highly resolved limb emission spectra enabling the inversion of numerous atmospheric trace gases including nitric oxide.

It is well known that NO($\nu \geq 1$) populations depart from local thermodynamic equilibrium (LTE) in the terrestrial atmosphere down to stratospheric altitudes. Kaye and Kumer (Ref. 3) have demonstrated that NO($\nu > 1$) vibrational populations are significantly larger than those for LTE at daytime in the stratosphere mainly due to the photochemical production of NO from NO_2. This effect is strongly correlated with the cyclic short time (day/night) variations of NO and NO_2 abundances. The analysis of CIRRIS-1A data has shown that the rotational and spin degrees of freedom of thermospheric NO($\nu > 1$) are highly non-equilibrated (Ref. 4–7). The ratio of the spin orbit populations $N(S = 3/2)/N(S = 1/2)$ was found to be much lower than its LTE value at thermospheric altitudes. The rotational distribution was found to consist of a subthermal part, equivalent to a Maxwell-Boltzmann distribution with a rotational temperature of approximately 100 K below the kinetic temperature, and a superthermal part with rotational temperatures of 3000 - 5000 K. Several theoretical studies have shown that the origin of the 'hot' NO($\nu > 1$) population is related to the nascent rotational distribution of NO produced by chemical recombination of atomic nitrogen with molecular oxygen (Ref. 8–10), while the subthermal part arises from collisions of NO with atomic oxygen (Ref. 7).

As a consequence of all these evidences, it is clear that the retrieval of NO volume mixing ratio (vmr) profiles from space- or airborne limb radiance measurements at 5.3 μm requires the consideration of non-LTE populations in the retrieval scheme. Limb radiance spectra at

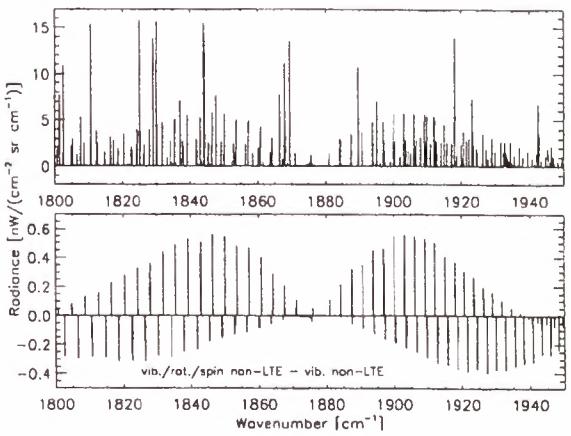

Figure 1: Calculated limb radiances with and without consideration of rotational/spin non-LTE for 60 km tangent height.

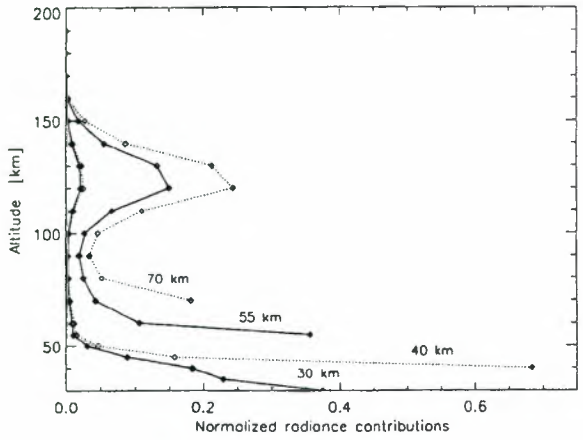

Figure 2: Normalized contribution function at the R(J=6.5, S=1/2) line center of the fundamental band at 1900.05 cm^{-1} for 30, 40, 55, and 70 km tangent height.

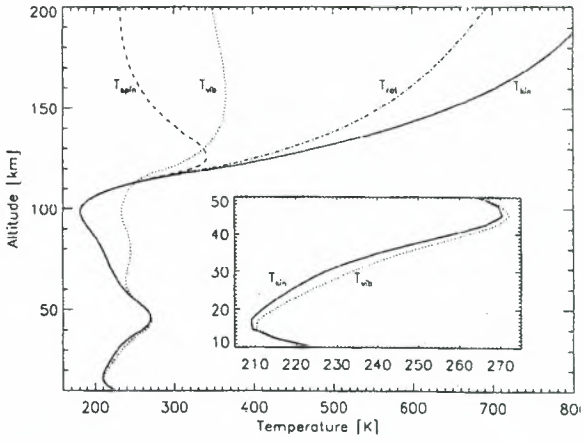

Figure 3: Vibrational, rotational and spin temperatures for the NO($\nu = 1$) state at midlatitude daytime conditions.

5.3 μm essentially contain information on the NO($\nu = 1$) population. However, spectral information on NO($\nu = 0$) and NO($\nu > 1$) populations is poor. Thus, the NO vmr, which in first order is essentially proportional to the NO($\nu = 0$) abundance, can only be derived if the non-LTE state distribution is known. Furthermore, thermospheric NO($\nu = 1$) emission, affected also by rotational and spin non-LTE, contributes significantly to measured stratospheric and mesospheric limb spectra due to the high thermospheric NO densities (see Figures 1 and 2). These non-LTE emission contributions, which show a high local variability, have to be correctly modeled within the retrieval procedure in order to avoid systematic errors in the retrieved NO vmr's.

The aim of this paper is to describe a retrieval approach for the stratospheric NO volume mixing ratio (vmr) profile, which accounts for the non-LTE situation including the breakdown of rotational and spin non-LTE in the thermosphere.

2. NON-LTE STATE DISTRIBUTION OF NO

The non-LTE vibrational, rotational and spin state distribution of NO($\nu = 1, J, S$) is calculated with a recently developed model (Ref. 11) covering the atmospheric altitude range up to 200 km. The model includes all important non-LTE driving processes, which are absorption of solar and tropospheric radiation, spontaneous and induced emission, collisional processes of NO with molecular and atomic oxygen, chemical production of NO by photolysis of NO_2 and by NO_2+O→NO+O_2 in the stratosphere, and the chemical recombination N+O_2 in the thermosphere.

The population of the vibrational NO($\nu = 1$) state is described, as commonly defined, by the vibrational temperature, T_{vib}. The NO rotational non-LTE state distribution above approximately 110 km can be described by a sum of two Boltzmann distributions (Ref. 11) which correspond to a sub-thermal part arising from the inter-vibrational NO+O relaxation and a super-thermal part produced by the N+O_2 reaction. For NO($\nu = 1$) the sub-thermal part characterized by the rotational temperature T_{rot} dominates the state distribution. Since both spin-orbit states ($S = 1/2$ and $S = 3/2$) show the same rotational distribution, the ratio of the two spin-orbit states can be expressed by a spin temperature, T_{spin}, given by

$$T_{spin} = -E_{spin} \left[k \ln(n_{1,J,3/2}/n_{1,J,1/2}) \right]^{-1} , \qquad (1)$$

where E_{spin} is the energy difference between the two spin-orbit states.

Figure 3 shows the calculated profiles of T_{vib}, T_{rot}, and T_{spin} for midlatitude daytime conditions. Vibrational temperatures are about 3 - 7 K above the kinetic temperature in the whole stratosphere (15 - 50 km), equivalent to a 30% enhancement due to non-LTE of the NO($\nu = 1$) population. This non-LTE effect is mainly produced by the chemical production of NO($\nu = 1$) by the NO_2 photolysis. The impact of the NO_2 photolysis on the NO($\nu = 1$) population depends on the NO/NO_2 abundance ratio, i.e. vibrational daytime temperatures increase with decreasing NO abundance and increasing NO_2 abundance. Due to the diurnal NO↔NO_2 conversion maximum values of T_{vib} at sunrise are about 15 - 20 K above T_{kin}.

Mesospheric (60 - 90 km) NO($\nu = 1$) populations are mainly affected by radiative processes (absorption of solar and tropospheric radiation) and hence very much controlled by the tropospheric conditions (T_{kin} profile, cloud coverage, humidity). Vibrational temperatures are higher than T_{kin} and take values of about 240 K.

Thermospheric vibrational temperatures are generally lower than T_{kin} since radiative losses dominate over the collisional excitation (NO+O). Maximum values of T_{vib} are about 360 K.

Above 110 km NO($\nu = 1, J, S$) rotational and spin distributions start to depart from LTE caused by collisional relaxation time being longer than radiative lifetime. The deviations of T_{rot} and T_{spin} from the kinetic temperature are increasing with altitude. At 200 km T_{rot} and T_{spin} are very close to the effective rotational

and spin temperatures of the nascent distribution produced by NO+O collisions as found by Sharma and Duff (Ref. 12) to be $T_{rot}^{NO+O}(z) = 0.74\ T_{kin}(z) + 24$ K and $T_{spin}^{NO+O}(z) = 200$ K, respectively.

The non-LTE state distribution of NO thus mainly depends on a) atmospheric profiles of pressure, kinetic temperature, and the vmr's of O, NO_2, and NO itself, b) kinetic temperature, water vapour, and cloud coverage in the troposphere, c) the nascent vibrational state distribution of the stratospheric NO_2 photolysis, and d) the rate constant and nascent vibrational, rotational and spin distribution of the thermospheric NO+O collisional relaxation.

3. A NEW NON-LTE RETRIEVAL APPROACH

The retrieval of stratospheric NO abundances from limb radiance spectra requires the simultaneous determination of the non-LTE state distribution since this distribution is not given by the Boltzmann law. A simultaneous retrieval of vmr and T_{vib} profiles has already been proposed for trace gases affected by non-LTE (Ref. 13). However, in the case of NO this approach is not practicable for two reasons. First, NO non-LTE limb radiances show at maximum a signal-to-noise ratio of 10 which leads to small sensitivities with respect to NO profile parameters (vmr and T_{vib}). Second, the poor degree of saturation of stratospheric NO lines reduces the content of spectral information on the ground state density which results in a high correlation between the profile parameters vmr and T_{vib}. Also, the *a priori* calculation of the NO state distribution is not suitable, since the vibrational NO state distribution depends on the unknown NO abundance itself, if there is a significant chemical production of excited NO($\nu > 0$). This occurs in the stratosphere due to the NO_2 photolysis and, to a lesser extent, in the thermosphere due to the $N+O_2$ reaction.

In order to account for this dependence in the NO-vmr retrieval, our retrieval approach incorporates a non-LTE model into the retrieval process, i.e., the NO state distribution is recalculated in each iteration of the retrieval process to update the NO vmr profile.

Also, in order to achieve convergence in the retrieval, the calculation of the Jacobian matrix elements, i.e the spectral derivatives with respect to NO vmr, needs to include the dependence of the vibrational NO state distribution on the NO vmr. For this purpose the non-LTE model additionally provides analytical derivatives of the NO state distribution with respect to NO vmr.

The inversion approach consists of the non-LTE model described in Section 2, which provides the NO state distribution and their derivatives with respect to the retrieval parameter, and the radiative transfer code KOPRA which allows for vibrational, rotational and spin non-LTE populations (Ref. 14–16) (see Figure 4). The presented retrieval approach additionally enables the the simultaneous determination of non-LTE model parameter, if spectral information on the relevant vibrational, rotational or spin states is available. In the NO case, spectral information on NO($\nu = 0$) in the lower stratosphere due to saturation effects allows for the simultaneous determination of the nascent vibrational distribution ϵ of

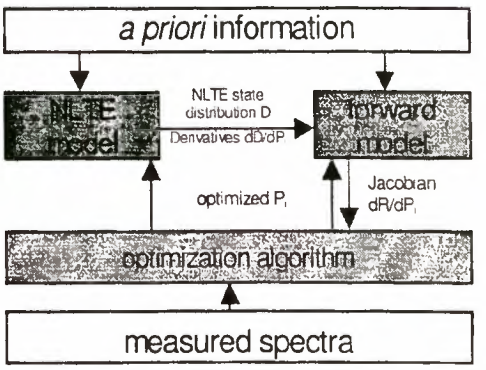

Figure 4: The non-LTE retrieval scheme. P_i are the retrieval vector elements and R is the modeled limb radiance.

the NO_2 photolysis, and thus enables the determination of the stratospheric vibrational state distribution. The advantages of this approach compared to the simultaneous T_{vib}/NO vmr retrieval are evident: The reduction of retrieval parameters due to the scalar nature of ϵ in contrast to the vector nature of T_{vib} improves the spectral sensitivity with respect to the vibrational state distribution significantly. Furthermore, the constraint on the altitude dependence of the state distribution by the model leads to smaller correlation between the parameters NO vmr and ϵ than in the case of a T_{vib}/vmr retrieval.

4. RETRIEVAL SCENARIOS AND ERROR ASSESSMENT

The retrieval scenarios were chosen according to the expected MIPAS-ENVISAT observational altitude range. The calculation of limb radiance spectra and the spectral derivatives with respect to the target parameter were performed with the KOPRA algorithm assuming scanning geometries from 10 to 70 km tangent height and an observer altitude of 800 km (see Fig. 1). The vertical spacing of the limb sequence was set to 5 km below 60 km and to 10 km above. Radiances have been calculated for midlatitude daytime conditions. Kinetic temperature, pressure, and NO profiles were taken from Ref. 11. The interfering species H_2O, CO_2, O_3, and N_2O have been considered with profiles taken from the US76 Standard Atmosphere (Ref. 17). An aerosol continuum has been considered below 30 km according to Ref. 18. The spectra have been apodized to a final spectral resolution of 0.05 cm^{-1}.

An altitude-dependent microwindow approach was chosen in order to reduce the number of spectral gridpoints needed, and the errors produced by interfering gases and other systematic error sources. In a first step, microwindows including NO lines were determined by minimizing the expected retrieval error with a method proposed by Ref. 19. In a second step the 'best' microwindows were combined, again by minimizing the expected retrieval error. The resulting microwindow selection is shown in Fig. 5.

Three different retrieval scenarios have been chosen in

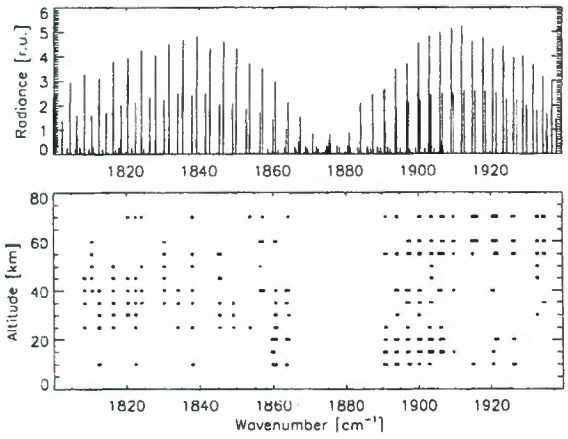

Figure 5: The altitude dependent microwindow selection used in the retrieval error assessment. For comparison, a limb radiance spectrum of the NO fundamental band at 150 km tangent altitude is shown in the upper panel. r.u. is defined as nW/(cm^2 sr cm^{-1}).

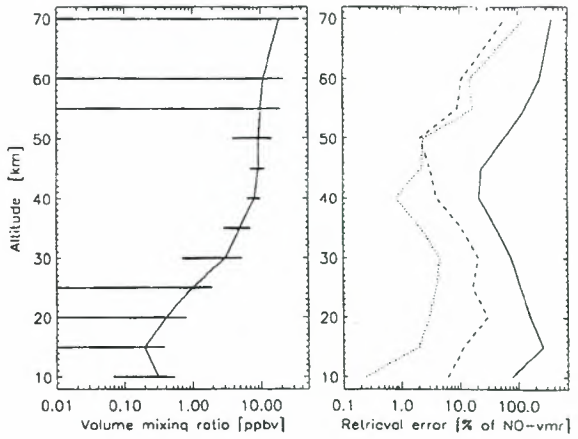

Figure 6: Absolute noise-induced NO retrieval errors (left) and relative errors (right) due to noise (solid), uncertainties of interfering gas profiles (dashed), and uncertainties of the non-LTE model parameter (dotted), all for case B.

order to investigate the feasibility of a simultaneous retrieval of NO vmr and non-LTE parameter, and to assess the optimal upper scanning limit:

- CASE A: The measurement vector was built up from the simulated radiance spectra from 10 to 70 km with a resulting dimension of 2734 gridpoints. The retrieval parameter vector consists on the NO vmr sampled according to the tangent altitudes up to 70 km, and a scalar scaling factor α for the **a priori** NO vmr profile from 70 - 200 km.
- CASE B: This case is equivalent to case A but the nascent vibrational distribution $\epsilon(\nu = 1)$ is added to the retrieval parameter vector.
- CASE C: The measurement vector was built up from the simulated radiance spectra from 10 to 55 km with a resulting dimension of 2089 gridpoints. The retrieval parameter vector consists on the NO vmr sampled according to the tangent altitudes up to 55 km, a scalar scaling factor α for the *a priori* NO vmr profile from 55 - 200 km, and the nascent vibrational distribution $\epsilon(\nu = 1)$.

In all cases a scalar instrumental offset parameter and a profile of aerosol optical depth sampled according to the tangent altitude grid up to 30 km was added to the retrieval parameter vector. The expected retrieval error for NO vmr and ϵ were assessed using the method proposed by Ref. 19. Covariances of spectral gridpoints were considered. Random retrieval errors due to instrumental noise were assessed by assuming an instrument noise level (NESR) of 3 nW/(cm^2 sr cm^{-1}) according to the MIPAS-ENVISAT instrument specifications (Ref. 20). Systematic error sources investigated in this study are:

- uncertainties of interfering gas profiles (all cases),
- uncertainties of non-LTE model parameter (case B),
- neglection of vibrational non-LTE in the stratosphere due to the NO_2 photolysis (case A),
- neglection of thermospheric rotational/spin non-LTE (case B),
- uncertainties in the thermospheric kinetic temperature profile (case B), and
- uncertainties in the vertical distribution of NO above 55 km (case B and C).

The expected noise-induced retrieval error for the NO vmr profile was estimated at 0.5 - 20 ppbv, increasing with altitude. Thus, relative noise-induced errors below 100% of the NO vmr are only reached between 25 - 50 km altitude. The highest accuracy of the retrieved NO vmr is achieved at 40 km. Systematic errors due to uncertainties of interfering gas profiles are about one order of magnitude smaller than the noise-induced errors (see Figure 6). Uncertainties in the non-LTE parameters (excluding the nascent vibrational distribution of the NO_2 photolysis) result in relative NO retrieval errors up to 4% below 50 km and 10 - 100% above. The resulting total retrieval error of the nascent vibrational distribution $\epsilon(\nu = 1)$ in case B was estimated at 136%. The accuracy of this parameter is mainly restricted by instrumental noise, while systematic error sources are much smaller (see Table 1).

The neglection of NO($\nu = 1$) production by NO_2 photolysis in case A leads to systematic errors about 1.5 times higher than the noise-induced error. This corresponds to an overestimation of stratospheric NO up to 40% (see Figure 7). The neglection of thermospheric rotational/spin non-LTE in case B maps into oscillating systematic errors of the retrieved NO vmr with magnitudes of 10 - 150% of the noise-induced error, increasing with altitude. These errors result from the spectral sensitivity to the spin state distribution describing the intensity ratio of neighboring spin-orbit line pair, rather than

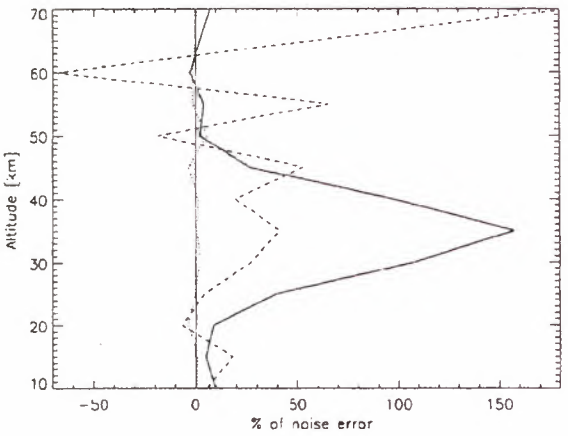

Figure 7: Systematic NO retrieval errors relative to the noise-induced retrieval errors. Solid: Error due to neglection of the NO_2 photolysis in case A. Dashed: Error due to neglection of rotational/spin non-LTE in case B. Dotted: Error due to 50 K increased thermospheric temperature in case B.

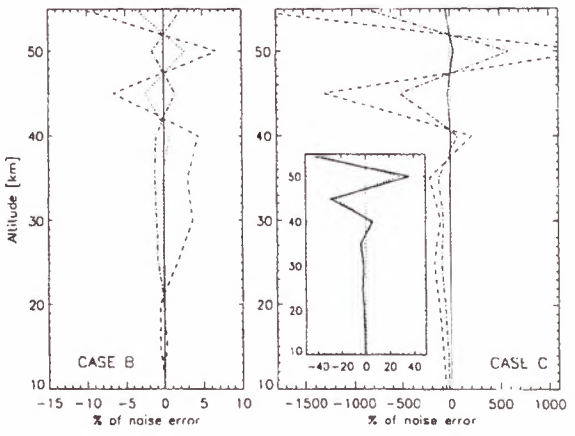

Figure 8: Systematic NO retrieval errors relative to the noise-induced retrieval error due to 100% increase of NO vmr at 70 (solid), 90 (dotted), 120 (dashed), and 150 km (dashed-dotted) for case B (left) and case C (right). The inset in the right panel zooms the errors due to an NO increase at 70 km and 90 km for case C.

to the rotational state distribution describing the rotational envelope of the band. Since the spin temperature T_{spin} is nearly independent of the kinetic temperature above 140 km, systematic errors in the retrieved stratospheric NO vmr due to uncertainties in the thermospheric kinetic temperature are very low. A 50-% increase of the kinetic temperature above 100 km leads only to errors below 10% of the noise-induced retrieval error (see Figure 7).

The retrieval error due to the uncertainty of the vertical distribution of NO above the upper scanning limit has been assessed by calculating the systematic error induced by an 100-% increase of the NO vmr at given altitudes (which is in the frame of climatological variability). For case B, 100-% variations in the NO vmr at all altitudes above 70 km produce retrieval errors below 15 % of the noise-induced retrieval error (see Figure 8). For case C 100-% NO-vmr variations between 70 and 100 km produce retrieval errors below 50 % of the noise-induced retrieval error. However, due to the high thermospheric NO abundance the impact of thermospheric 100-% NO-vmr variations is much higher, mapping into retrieval errors of over 1000% of the noise-induced retrieval error (see Figure 8). The reduced upper scanning limit of 55 km in case C does not allow for a proper separation of thermospheric radiance contributions. Radiance spectra at 55 km tangent height contain information on both, thermospheric and stratospheric NO (see Figure 2), and thus, no independent information on the vertical distribution of NO. If spectra of higher tangent altitudes are added to the measurement vector (case B), the necessary information on the vertical distribution of NO can be provided.

Table 1: Relative retrieval errors of the NO_2 photolysis nascent vibrational distribution $\epsilon(\nu = 1)$ and the scaling factor α of the thermospheric NO profile for case B.

Parameter	noise	interfering species	non-LTE model parameter
$\epsilon(\nu = 1)$	136%	38%	34%
α	19%	12%	14%

5. CONCLUSIONS

The presented inversion approach enables the accurate retrieval of stratospheric NO by taking into account the strong vibrational, rotational and spin non-LTE effects all over the atmospheric range. The dependence of the NO non-LTE state distribution on the target parameter NO vmr itself due to chemical production of $NO(\nu > 1)$ by NO_2 photolysis in the stratosphere and the reaction $N(^4S)+O_2$ in the thermosphere is taken into account by inclusion of the non-LTE model into the retrieval procedure. This treatment allows for simultaneous inversion of particular non-LTE parameter, if there is any spectral information on the non-LTE state distribution in the altitude range of interest. Thus, the nascent vibrational distribution of the stratospheric NO_2 photolysis can be determined simultaneously with the NO vmr from limb emission spectra of the NO fundamental band.

Due to the weak intensity of the NO fundamental band the accuracy of the NO vmr retrieval is restricted mainly by noise-induced retrieval errors with values below 100% of the NO vmr only between 25 - 50 km, while uncertainties in the interfering gas profiles and in the non-LTE model parameter are minor error sources. Thus, the resulting retrieval error can be reduced by a statistical evaluation of many NO vmr parameter sets derived from single measurements of comparable atmospheric conditions (i.e. same latitude). The accuracy for the nascent vibrational distribution of the stratospheric NO_2 photolysis

was estimated at 136%. However, due to the independence of this parameter on atmospheric conditions, the accuracy can be improved significantly by averaging retrieved results of several limb scans.
Systematic errors in the retrieved NO vmrs higher than the noise-induced retrieval error caused by neglection of particular non-LTE effects, such as the NO_2 photolysis in the stratosphere or the rotational/spin non-LTE in the thermosphere, indicate that non-LTE has to be considered in order to accurately retrieve NO abundances.
Strong thermospheric non-LTE radiance contributions in spectra related to stratospheric tangent heights give rise for additional systematic errors due to the high variability of the NO profile and uncertainties in the thermospheric kinetic temperature. The impact of the thermospheric NO variability on the accuracy of the stratospheric NO retrieval can be significantly reduced by expanding the MIPAS scanning range up to at least 70 km. Uncertainties in the thermospheric kinetic temperatures affect the accuracy of the NO-vmr retrieval less than expected under assumption of LTE due to the weak temperature dependence of the thermospheric non-LTE spin distribution.
The inversion approach presented is not restricted to the retrieval of NO abundances, but can be generally applied to the inversion of non-LTE affected trace gases with a limited amount of spectral information on the non-LTE state distribution. As an example, the retrievability of O_3-vmr and rate constants of several V-V and V-T processes affecting the O_3 vibrational state distribution by means of the presented approach is currently investigated by Martín-Torres et al. (Ref. 21).

REFERENCES

1. Newchurch M & al. 1996, Stratospheric NO and NO_2 abundances from ATMOS solar-occultation measurements. *Geophys. Res. Lett.*, 23, 2373–2376.

2. Endemann M & Fischer H 1993, Envisat's high–resolution limb sounder: MIPAS. *ESA bulletin*, 76, 47–52.

3. Kaye J & Kumer J 1987, Nonlocal thermodynamic equilibrium effects in stratospheric NO and implications for infrared remote sensing. *Appl. Opt.*, 26, 22, 4747–4754.

4. Armstrong P & al. 1994, Highly rotationally excited NO(ν, J) in the thermosphere from CIRRIS 1A limb radiance measurements. *Geophys. Res. Lett.*, 21, 2425–2428.

5. Lipson S & al. 1994, Subthermal nitric oxide spin-orbit distributions in the thermosphere. *Geophys. Res. Lett.*, 21, 2421–2424.

6. Sharma R & al. 1996, On the rotational distribution of the 5.3 μm 'thermal' emission from nitric oxide in the nighttime terrestrial atmosphere. *J. Geophys. Res.*, 101, 17,129–17,135.

7. Sharma R & al. 1996, Production of vibrationally and rotationally excited NO in the nighttime terrestrial atmosphere. *J. Geophys. Res.*, 101, 19,707–19,713.

8. Solomon S 1983, The possible effects of translationally excited nitrogen atoms on lower thermospheric odd nitrogen. *Planet. Space Sci.*, 31, 135–139.

9. Gérard JC & al. 1991, Non thermal nitrogen atoms in the earth's thermosphere 2. a source of nitric oxide. *Geophys. Res. Lett.*, 18, 1695–1698.

10. Duff J & Sharma R 1997, Quasiclassical trajectory study of NO vibrational relaxation by collisions with atomic oxygen. *J. Chem. Soc. Faraday Trans.*, 93, 2645–2649.

11. Funke B & López-Puertas M 1998, Non–LTE vibrational, rotational and spin state distribution for the NO(ν= 0,1,2) states. Unpublished.

12. Sharma R & Duff J 1997, Determination of translational temperature of the high altitude terrestrial thermosphere from the rotational distribution of the 5.3 μm emission from NO(ν = 1). *Geophys. Res. Lett.*, 24, 2407–2410.

13. Timofeyev Y & al. 1995, Numerical investigations of the accuracy of the remote sensing of non-LTE atmosphere by space-borne spectral measurements of limb IR radiation: 15 μm CO_2 bands, 9.6 μm O_3 bands, and 10 μm CO_2 laser bands. *J. Quant. Spectros. Radiat. Transfer*, 53, 613–632.

14. Stiller GP & al. 1998, The Karlsruhe optimized and precise radiative transfer algorithm. Part I: Requirements, justification, and model error estimation. In J Wang, B Wu, T Ogawa & Z Guan, editors, *Optical Remote Sensing of the Atmosphere and Clouds, Beijing, China, 15 17 September 1998*, Volume 3501, 257–268.

15. Höpfner M & al. 1998, The Karlsruhe optimized and precise radiative transfer algorithm. Part II: Interface to retrieval applications. In J Wang, B Wu, T Ogawa & Z Guan, editors, *Optical Remote Sensing of the Atmosphere and Clouds, Beijing, China, 15–17 September 1998*, Volume 3501, 186–195.

16. Kuntz M & al. 1998, The Karlsruhe optimized and precise radiative transfer algorithm. Part III: ADDLIN and TRANSF algorithms for modeling spectral transmittance and radiance. In J Wang, B Wu, T Ogawa & Z Guan, editors, *Optical Remote Sensing of the Atmosphere and Clouds, Beijing, China, 15–17 September 1998*, Volume 3501, 247–256.

17. *U.S. Standard Atmosphere* 1976, NOAA–S/T 76–1562,10.

18. Carli B & al. 1998, Study of the retrieval of atmospheric trace gas profiles from infrared spectra. Technical report, European Space Agency. Final Report of ESA Contract 12055/96/NL/CN.

19. von Clarmann T & Echle G 1998, Selection of optimized microwindows for atmospheric spectroscopy. *Appl. Opt.*, 37, 33, 7661–7669.

20. v. Clarmann T & al. 1998, Study on the simulation of atmospheric infrared spectra. Technical report, European Space Agency. Final Report of ESA Contract 12054/96/NL/CN.

21. Martín-Torres F & al. 1999, Retrievability of O_3 concentration profiles and critical parameters in non-LTE models from MIPAS/ENVISAT limb spectra. In *Proc. European Symposium on Atmospheric Measurements from Space, ESAMS'99, 18-22 Jan 1999, Noordwijk*. European Space Agency, ESTEC, Noordwijk, The Netherlands.

Retrieval of Stratospheric NO Distributions from MIPAS on Envisat

B.J. Kerridge, R.Siddans, W.J. Reburn, K. Koutoulaki
Rutherford and Appleton Laboratory, United Kingdom

Nitric oxide (NO) is the predominant form of active nitrogen (NOy) in the upper stratosphere. It is intimately involved in stratospheric ozone chemistry and provides one of the possible links between stratospheric composition, the upper atmosphere and solar activity. High-quality, global, height-resolved observations of stratospheric NO would therefore be useful for a number of research studies. Limb-viewing emission spectra measured by MIPAS in the NO fundamental band (5.3micron) will contain information on stratospheric NO, although this will be difficult to interpret due to intense, ``non-thermal" emission from NO in the overlying thermosphere. The initial (PAC) MIPAS data processing scheme will therefore not generate NO products.

As part of a recent study for ESA on non-thermal emission effects on MIPAS data, preliminary NO retrieval simulations have been performed. The results, to be presented here, demonstrate that the spectral coverage and resolution of MIPAS will, in due course, offer significantly improved capabilities over previous satellite IR emission sensors for discriminating stratospheric NO and determining its global distribution.